Report No. CCEER-06-02

LARGE-SCALE EXPERIMENTAL AND ANALYTICAL SEISMIC STUDIES OF A TWO-SPAN REINFORCED CONCRETE BRIDGE SYSTEM

Nathan S. Johnson
M. "Saiid" Saiidi
David H. Sanders

Center for Civil Engineering Earthquake Research
Department of Civil and Environmental Engineering/258
University of Nevada
Reno, Nevada 89557

March 2006

Abstract

A quarter-scale, 67 ft (20.5 m) long asymmetric reinforced concrete bridge model with two-spans supported on three, two-column piers was tested using the shake table system at the University of Nevada Reno. In addition, extensive analytical studies were conducted. The shake table testing was part of a multi-university research project utilizing the Network for Earthquake Engineering Simulation (NEES) to investigate the effects of soil foundation structure interaction. The shake table testing objective was to study the response of a reinforced concrete bridge model subjected to mostly transverse earthquake excitations. This included the effects of in-plane rotation irregularities on distribution of forces among different piers and the interaction of different components of the bridge.

Upon completion of testing, in depth analytical modeling was conducted to evaluate the accuracy of conventional methods in reproducing the bridge model response and to develop a model for further study. Three aspects of bridge system response were studied utilizing the analytical model. 1) Performance of the bridge compared to the design performance objectives. 2) The effect of differences between the target and achieved shake table motions on the progression of damage in the bridge. 3) Investigation of the system effect, comparing the system and response of individual bents as well as the response of several other bridge models.

Contemporary analytical methods were accurate in determining the response of the flexurally dominated system up to bent failure. The NCHRP 12-49 design methodology was shown to satisfy earthquake performance requirements. Incoherency of achieved table motions did not affect failure progression of the bridge; however, it was affected by acceleration inconsistencies.

The introduction of higher modes and interaction among the bents (system effect) changed the amount of damage the bents underwent compared to the damage they would have experienced had they been individually tested. A simple irregularity index was found to be a good indicator to identify whether the system will have an effect on the bents. The failure progression of the bridge model and the analytical comparisons suggested that the reserve capacity from varied column heights could provide a beneficial substructure redundancy.

Acknowledgements

The research presented in this report was sponsored by the National Science Foundation through Pre-NEES award number CMS-0324326. The NSF program directors were Steven McCabe and Joy Pauschke. The study was a part of multi-institution project under the overall direction of Sharon Wood of the University of Texas, Austin. Research collaborators Richard Ranf and Mark Eberhard at the University of Washington are thanked for their involvement with the shake table testing.

The authors are indebted to Patrick Laplace and Paul Lucas of the UNR structures lab for their dedicated support throughout the project. Kevin Nieznanski and others at Granite Construction are thanked for their interaction and care during the construction of the bridge. Thanks are due to UNR students Melissa O'Brien, Hoon Choi, Jessica Doyle and Robert Nelson who helped during instrumentation and testing.

This report is based on a PhD dissertation by the first author supervised by the other authors.

Table of Contents

List of Tables

Chapter 6

Chapter 7

Chapter 10

List of Figures

Chapter 3

Chapter 4

Chapter 6

Chapter 7

Chapter 8

Chapter 9

Chapter 10

Chapter 1: Introduction

1.1 Background

Catastrophic earthquakes over the past two decades which have caused immeasurable devastation, including extensive economic impacts and loss of lives, have directed considerable effort toward improving the seismic performance of the world's infrastructure. Notable recent events in developed nations are the 1994 M6.7 Northridge, California earthquake, which caused 60 deaths and $20 billion in direct damage; and the 1995 M6.9 Kobe, Japan earthquake, which caused 5500 deaths and $147 billion in direct damage (Working Group, 2003). Because of these catastrophes, a performance based philosophy of design for highway bridges has evolved. Currently, rather than attempting to resist seismic excitation with a system that remains elastic, typical bridges are designed to undergo a substantial amount of ductile inelastic deformation without collapse. This philosophy saves lives but permits localized structural damage, which can alleviate the need for structure replacement. In order for the design to be effective, structural performance during inelastic response from earthquake excitation must be well understood and engineers should be able to calculate the performance using reliable, and readily available analytical tools.

A vast amount of experimental research has been concentrated on broadening technology to calculate the nonlinear response and understanding performance of highway bridges under earthquake loads. Past experiments have primarily focused on components of bridge systems to improve and validate modeling techniques, to test performance of new designs, or to evaluate old designs and to develop retrofit measures to improve response of existing structures that have insufficient details to adequately resist earthquake forces. However, due to limitations of earthquake testing facilities, and because system testing of bridges requires a large scale specimen, system tests have generally not been conducted.

In the United States, the National Earthquake Hazards Reduction Program (NEHRP) was created in 1977 to reduce the risks to life and property in the United States resulting from Earthquakes. Under NEHRP, through the National Science Foundation (NSF), the George E. Brown Network for Earthquake Engineering Simulation (NEES) was created so that collaborative research integrated through information technology (IT) could be conducted throughout the United States to advance means for earthquake loss reduction. As stated by Dr. Eugene Wong, the Assistant Director for Engineering at the National Science Foundation, the NSF believes that the partnership of earthquake engineering and advanced IT of NEES will enable the earthquake engineering research field to move from a reliance on physical testing to model based simulation (Wong 1999). Fifteen experimental research facilities are a part of NEES, including the multiple shake table facility at the University of Nevada, Reno, which plays a significant role in the research that is discussed subsequently.

The research that is presented in this document is part of a collaborative Pre-NEES study to investigate soil-foundation-structure-interaction (SFSI) of bridge systems. Data from this test is to be used by research collaborators to integrate the bridge structural response into computer models to study SFSI. The design of the prototype

bridge for the global project is discussed. The major focus in this research was on the multiple shake table testing of a reinforced concrete bridge system including the analytical modeling of bridges and investigation of bridge system response.

1.2 Previous Work

The main aspects of this study were experimental testing of bridge systems, response and interaction of bridge sub-structural components, and the computer modeling of nonlinear bridge response. This section presents relevant past research. An extensive amount of experimental research has been conducted on the seismic response and performance of bridges. However due to limitations of testing facilities and the large specimen scale required to model bridges, past research has primarily focused only on component testing much of which has not included dynamic effects. No available literature discusses system testing of a complete large scale reinforced concrete bridge frame on multiple shake tables.

1.2.1 Component Testing

Component tests of typical reinforced concrete bridges have mostly been on bridge substructures, which, due to strong and stiff superstructures, is where the primary nonlinearity during earthquakes occurs. Substructure testing includes single and multiple column bents that are modeled as being tributary to a portion of a complete. The interaction with the rest of the bridge system is generally excluded. Past tests have included quasi-static cyclic testing, pseudo-dynamic testing, and shake table testing. The shake table testing is the most realistic of the test methods because it includes the most dynamic effects. Cyclic load testing is the most common technique but potentially important dynamic effects such as the influence of strain rate is excluded in these tests. Hybrid test methods have only recently been developed. Hybrid methods use the aforementioned methods to test large scale models of components, but also include active control of boundary conditions to simulate adjacent structural response. A major difficulty in hybrid testing is that it requires an accurate integrated computer model of structural system response to command additional excitation to the specimen based on achieved specimen response.

In a collaborative effort between the Public Works Research Institute of Japan and the Federal Highway Administration of the United States guidelines focusing on quasi-static testing were developed for the testing of seismic performance of bridge columns (Hoshikuma and Unkoh, 2002). Preliminary proposed generic methods for quasi-static cyclic loading tests of ductile reinforced concrete columns were presented including measurement of column curvature and standard cyclic loading displacement histories.

Past research that was conducted at the University of Nevada, Reno compared the response of quasi-static loading with dynamic loading on large scale flared bridge columns (French and Saiidi, 2000). The column that was subjected to quasi-static loading failed due to low-cycle fatigue of the longitudinal reinforcement. The column that was tested dynamically failed due to rupture of the lateral tie reinforcement. It was concluded that shake table testing of structural elements could lead to results that are different than those obtained from commonly applied slow cyclic loading due to effect of high strain rate combined with variations in loading history.

Unidirectional shake table research of three 0.3 scale two-column bents having aspect ratios ranging from 2.5 to 6.64 was also conducted at the University of Nevada, Reno (Moustafa et al. 2004). The columns were hinged at the base and were designed according to contemporary California Department of Transportation (Caltrans) earthquake design requirements. Testing consisted of increased amplitude shake table excitation in the in-plane direction of the bent using the Sylmar record from the 1994 Northridge earthquake. Analytical models of the bents using Drain-3DX (Prakash and Campbell 1994) lumped plasticity Takeda elements in the columns led to good correlation with measured dynamic response for the bents dominated by flexure. For the columns with the lowest aspect ratio (2.5) where shear was significant, the calculated response deviated slightly from the measured response. The Caltrans (Caltrans 2004) shear design equation was determined to be conservative for all of the columns tested in the study, and was recommended for design.

Biaxial shake table tests in Japan (Nishida and Unjoh, 2004) were conducted at approximately quarter-scale on three types of flexurally dominated single column bents (square, circular, and rectangular) having longitudinal steel ratios of approximately 1 percent. The square column had a width of 23.6 in (600 mm) and clear height of 78.7 in (2000 mm). The circular column had a diameter of 23.6 in (600 mm) and height of 84.3 in (2140 mm). The rectangular column had a cross section of 31.5 x 17.7 in (800 x 450 mm) and a clear height of 78.7 in (2000 mm). The columns were all tested with two sets of biaxial motion. The first was approximately up to the yield level of the longitudinal reinforcement. The second was to induce bar buckling and crushing of confined concrete. It was concluded that a different failure for bilateral excitation occurred because of buckling on all four sides instead of just two. Inelastic time history analyses were conducted using fiber elements and it was concluded that the fiber model simulated the dynamic biaxial response well before deterioration of strength due to bar buckling.

1.2.2 Bridge System Shake Table Tests

Reported past bridge system testing on shake tables is extremely limited. No previous work as been conducted on testing a complete large scale reinforced concrete bridge frame to failure.

Williams and Godden (1975) tested a 1/30 scale model of a curved bridge on a single shake table at the University of California, Berkeley. The model included abutments and end expansion joints and focused on their interaction. The columns were made of micro-concrete and four #2 bars. The model included two weak columns with a rectangular section of 2.5 x 1.5 in and two strong columns with a rectangular section of 2.25 x 4 in. Stiffness properties were measured for the components of the experimental model and were integrated into an analytical model. It was concluded that the linear computer models were accurate for reproducing low amplitude vibration response as long as values of damping and low frequency characteristics were specified to match the specimen. Linear methods were inaccurate to predict the response when collisions took place even if damping and low frequency characteristics were adjusted. The nonlinear response of the model was duplicated well using nonlinear analytical models.

Tests of a steel plate girder bridge superstructure on multiple shake tables (Carden et al. 2004) were conducted at the University of Nevada, Reno. The model was

supported on a base isolation system which was rigidly attached to the shake tables. The specimen was subjected to seismic excitation to determine the performance of superstructure end cross frames. This test model did not include columns and hence the substructure response was not studied.

1.3 Objectives and Scope

The primary objective of the study presented in this document was to determine the seismic response of a two-span reinforced concrete bridge system under different levels of excitations through an experimental study of large-scale bridge model and analytical studies. This project was a component of a larger multi-university study. The following sections provide details about the object and scope of the overall project and the study presented in this document.

1.3.1 Overall Project

This research is a part of a larger project that has two goals: (a) to try and demonstrate the Network for Earthquake Engineering Simulation (NEES) system for studying soil-foundation-structure-interaction (SFSI) (Wood et al. 2004), (b) conduct a comprehensive study of SFSI effect by integrating analytical and experimental tools at multiple universities. Experimental studies were conducted at four sites across the United States (Fig. 1-1): (1) Centrifuge tests at the University of California, Davis, to determine the effects of foundation behavior on 1/48th scale models of single piles, two-column bents, and a two-span bridge, (2) Field tests at the University of Texas, Austin, using the mobile shaker to dynamically excite the soil near a series of quarter-scale single extended piles and two-column bents on extended piles, (3) Shake table tests of a quarter scale model of a two-span bridge at the University of Nevada, Reno (UNR), to provide direct measurements of bridge response to coherent motions under small- and large-amplitude simulated ground motions, and (4) Quasi-static structural component testing of quarter-scale and half-scale single column and two-column pier models at Purdue University to determine the effect of reinforcement detailing on the cyclic response. The shake table tests were a joint effort between UNR and the University of Washington.

The prototype for the experimental studies (Fig. 1-2) is a two-span frame of a cast-in-place post-tensioned reinforced concrete box girder bridge. The span lengths are 120ft (37m), and the substructure is composed of 1.2 m (4 ft) diameter 2-column piers on extended pile foundations. Columns have a 1.56 percent longitudinal steel ratio and a spiral reinforcement ratio of 0.9 percent. The lateral reinforcement is designed to satisfy the current Caltrans (Caltrans 2004), and NCHRP 12-49 (ATC/ MCEER 2001) criteria.

Multiple experiments were conducted for the SFSI study because it is currently impractical to test a complete large scale model including the effects of both the pile foundations and the bridge system. Results from the UNR bridge test will be compared and combined with the experimental tests that were conducted at the other three sites. This will provide integrated computer models that will allow for further investigation to understand the effects of SFSI.

1.3.2 Study of Two-Span Bridge Model

This document focuses on the shake table testing and analytical studies of a quarter-scale two-span reinforced concrete bridge specimen that was part of the SFSI project. The scope includes the design of the prototype structure for the global project, development and implementation of an effective technique for experimentally testing bridges on multiple shake tables, analytical modeling of bridge model, and parametric studies of system effects. The analytical model that was developed and experimentally validated was used in conjunction with the measured data from testing to conduct further study on bridge system response and shake table testing of bridges.

Seismic detailing of the prototype was based on the Caltrans SDC (Caltrans 2003) and NCHRP 12-49 *Recommended LRFD Guidelines for the Seismic Design of Highway Bridges* (ATC/MCEER 2001). General design of the prototype was based on the American Association of State Highway and Transportation Officials AASHTO bridge specifications (AASHTO 2002). The bridge specimen, which was composed of 11 major components, was designed to model the system interaction between three two-column bridge bents of varying heights. It was created at quarter scale to maximize the size of the specimen while remaining below the capacity of the shake tables. The 11 components were such that the specimen could be assembled on the shake tables, easily disassembled, and, except for the three bents, be reusable. The total height of the specimen to the top of the superstructure was 10.75 ft (3.28 m); the total length was 67.3 ft (20.5 m). Span lengths were 30 ft (9.14 m) and the columns of the three bents had clear heights of 6 ft, 8 ft, and 5 ft (1.83, 2.44, and 1.52 m) with the tallest bent in the middle. The superstructure was composed of a solid slab that was post-tensioned in both the longitudinal and transverse direction of the bridge. It was designed to maintain generally un-cracked stiffness properties throughout the tests and its stiffness matched the stiffness of the prototype about both bending axes.

Both low and high amplitude testing was conducted on the bridge model. Earthquake motions that were used were calculated based on the measured records at the Century City Country Club from the 1994 Northridge, California earthquake. The low amplitude tests included transverse coherent and incoherent, and biaxial coherent target motions. Low amplitude motions were such that the longitudinal reinforcement in the columns did not yield. High amplitude tests were a transverse coherent motion that was applied in increments from a pre-yield demand (0.075g PGA) until bent failure (1.66g PGA) when the shortest of the bents failed in flexure from crushing of confined concrete and buckling of longitudinal reinforcement.

Two computer models were used in attempt to reproduce the response of the bridge specimen. Standard methods using nonlinear fiber elements were employed to define column nonlinearity using the measured material properties of the bridge. Because of the achieved motion incoherency, the measured accelerations from the shake tables were filtered and double integrated for input to the computer models. Both SAP2000 version9 (CSI 2005) and Drain-3DX (Prakash and Campbell 1994) were used in the analytical modeling. It was concluded that the Drain-3DX results provided the best match to the measured structural response of the model due to a more refined distributed plasticity fiber element and an element that explicitly modeled reinforcement bond-slip. Because of the good correlation with the measured results and more efficient computation

of the Drain-3DX model, it was used to conduct parametric studies of the bridge response.

Beyond the valuable information that was learned directly from the measured and observed results of the shake table tests and from the computer modeling, three aspects of bridge system response were studied. The first was the performance level of the bridge model compared to the design performance objectives using the measured and calculated bridge response. The second was the effect of the deviations between the target and achieved table motions on the damage progression of the bridge. The third was differences in the amount of damage between the system and individual response of the bents for both the shake table model and for other models with different column heights.

Chapter 2: Prototype Properties and Specimen Design

2.1 Introduction

The prototype bridge is a continuous post-tensioned reinforced concrete box girder structure. For the shake table model, it was decided to create a reduced scaled bridge having two spans that are representative of one frame of the prototype bridge. The two spans are supported on three piers. The columns of the bridge are in the form of two-column bents having varying heights among the piers, thus making the model asymmetric with respect to the transverse axis passing through the center. The lack of symmetry leads to in-plane rotation of the model, an effect studied in this project. Based on span length between the bents, the general dimensions of the prototype superstructure were determined. The National Cooperative Highway Research Program (NCHRP) 12-49 *Recommended LRFD Guidelines for the Seismic Design of Highway Bridges* (ATC/MCEER 2001) was utilized for design of the columns and the joints. The prototype was scaled into an equivalent quarter scale model that was designed so that it could be tested on the shake tables and would structurally match the prototype. Components of the specimen were designed utilizing current design codes. This chapter discusses in detail the design process of the specimen from the span length selection in the prototype, to the complete plans of the test model. The plans for the model bridge are shown in Figs. 2-1 through 2-24. Renderings are shown in Figs. 2-25 through 2-27.

2.2 Prototype Dimensions

A span length of 120 ft (36.6 m) governs the geometry of the prototype bridge. This span length was chosen because it is within the range of a typical span for a post-tensioned box girder bridge, which can extend from 100 ft (30.5 m) to 250 ft (76.2 m) (Caltrans 2001). Section width of the prototype, and transverse column spacing were determined from average section properties for typical highway bridges built in California (Pulido et al. 2002). The width of the prototype superstructure section is 41.5 ft (12.6 m); this allows for two 12 ft (3.7 m) wide lanes and wide shoulders. The space between columns is 25 ft (7.6 m) with 6.25 ft (1.91 m) overhangs. The depth of the superstructure was calculated using Equation 2-1 from the AASHTO Standard Specifications (AASHTO 2002) for the minimum depth of continuous post-tensioned box girder bridges.

$$\textit{Superstructure Depth} = 0.04 * \textit{Span Length} \tag{2-1}$$

The resulting depth of the superstructure was 5 ft (1.52 m), rounded up from the calculated depth of 4.8 ft (1.46 m). The girder spacing, web thickness, deck thickness, and soffit thickness were estimated using typical geometry provided by AASHTO Standard Specifications. A prototype bent cap width of 5 ft (1.52 m) was determined by adding 1 ft (305 mm) to the preliminary column diameter of 4 ft (1220 mm). The idealized section of the prototype bridge superstructure is shown in Fig. 2-28.

Considering the geometry of the prototype including barrier rails, the estimated dead load of the bridge per bent is approximately 1490 kips (6628 kN). A prototype

column diameter of 4 ft (1.22 m) was chosen because the axial load index for the columns from the tributary dead load resulted in 0.082, a representative index for typical columns. Axial load index is defined as the axial load divided by the product of column area and the specified concrete compressive strength. Design of the columns is discussed later in this chapter.

Since most bridges do not have bents of all the same height, column heights were varied along the length of the prototype bridge in an asymmetric pattern. This is important because the primary direction of the shake table testing was to be in the transverse direction of the bridge model. Variation of column heights led to in-plane rotation and provided a slight coupling of the longitudinal and transverse bridge response. The substructure was assumed to be cast-in-place drilled pile shafts extended as columns. The column heights from the superstructure to the point of base fixity of the piles were assumed to be 20 ft (6.1 m), 32 ft (9.8 m), and 24 ft (7.3 m), for the three piers supporting the two-span bridge frame.

Because of soil flexibility, the point of fixity for drilled shafts is located below the ground level. Figure 2-29-a shows an idealization of soil pressure, and Fig. 2-29-b presents the resulting moment in a drilled shaft. The columns are considered to be fixed at the pile point of maximum curvature. A linear variation in soil pressure causes a square function of moment variation. Because of the square function, the shaft is subjected to a moment approaching the ultimate value at a depth of approximately one half of the depth to the point of fixity. This half depth can be approximated with a linear function. The effective column height, "Hcol", is from the bottom of the superstructure soffit to the half depth point. The location of maximum moment was estimated to be a distance of 2 times the column diameter, which for the prototype is 6 ft (1.83 m).

2.3 Model Scaling Factor

The geometric scale used to create the shake table model of the prototype was 0.25. The model for shake table testing needed to be as large as possible and at the same time be able to reach failure without exceeding the capacity of the University of Nevada, Reno shake tables. Using realistic materials in the model would provide a better match to the actual prototype response. Quarter scale allowed the column longitudinal steel to be composed of conventional reinforcing bars with the correct configuration, and was sufficiently large to accommodate regular concrete instead of micro-concrete.

Specifications of the shake tables are listed in Table 2-1. To ensure that the tables could fail the bridge model, the demands were compared to capacities of the shake table. Shake table torsion about the vertical axis of the table was a concern. Maximum table torsion due to a two-column bent was calculated based on column plastic shear demand creating a force couple across the distance between the columns. Figure 2-30 shows the maximum torsion that 1 ft (0.305 m) diameter columns could impose on the shake table. Considering a column spacing of 75 in (1.91 m), and 5 ft (1.52 m) high columns subjected to double curvature, the maximum torsion demand of the two column bent on the table is 134 kip-ft (182 kN-m). This moment is approximately one-third of the yaw capacity of the table (Table 2-1). This is the safety factor for the shortest and the most critical of the bents in a quarter scale model of the prototype frame.

A similar but more complete analysis was conducted upon completion of the specimen design and the selection of shake table input motions. This analysis is discussed in Section 4.6.

2.4 Column Design

Columns for the bridge were designed using the NCHRP Recommended LRFD Guidelines for the Seismic Design of Highway Bridges (ATC/MCEER 2001). The NCHRP guidelines are based on Load Resistance Factor Design (LRFD) and were developed for possible incorporation in the American Association of State Highway and Transportation Officials (AASHTO) Specifications. The NCHRP guidelines were to replace the seismic design provisions of the AASHTO Specifications. The seismic design section of the AASHTO code is over 20 years old. Although this version of NCHRP recommendations was not yet adopted into AASHTO at the design time, the recommendations were used in this project in anticipation that the NCHRP provisions for column design would be eventually adopted in a form close to that proposed. The Caltrans SDC and the existing AASHTO code were used to provide comparison with the design results from NCHRP. The resulting NCHRP 12-49 design for the columns of the shake table model is shown in Fig. 2-3.

2.4.1 Column Design Moment

The longitudinal steel of the bridge specimen columns was assumed to be 16-#3 bars. This provides a longitudinal steel ratio of 1.56 percent, which is considered a representative steel ratio for typical bridge columns. To determine if this amount of longitudinal steel was sufficient, the column design moment for a corresponding prototype was calculated using the NCHRP code. The demand in the NCHRP design code is site specific. To determine a location requiring a longitudinal steel ratio of approximately 1.56 percent, the design was iterated using the USGS design maps. Using USGS map data (Frankel et al. 1996) based on latitude and longitude, earthquake probabilities for both the expected and rare earthquakes were determined. The 0.2 second and 1.0 second period spectral accelerations were calculated and used to construct the design spectrum. Moment demands were calculated for both the longitudinal and transverse directions of the bridge. The design moment was calculated by using the 100% - 40% combination of the longitudinal and transverse design directions, respectively.

The Los Angeles area was chosen for the general location of the bridge because it represents a region of the country that is well known for its seismic activity and has a substantial range of seismic demand. A site at least 10 km from active faults was chosen to avoid the inclusion of near-fault ground motion effects, as they were not within the scope of this study. A location determined to have a demand approximately equivalent to the capacity of the prototype bridge having a longitudinal steel ratio of 1.56 percent is located at 33.60 degrees latitude, -117.45 degrees longitude (Fig. 2-31). Earthquake hazard curves for the 0.2-second and 1.0-second period spectral accelerations associated with soil type C are shown in Figs. 2-32 and 2-33, respectively (Frankel et al. 1996). Values from the hazard curves for both the rare (3% probability of exceedance, PE, in 75 years), and the expected (50% PE in 75 years) events were used and combined with the

soil type modification to construct both the rare and expected design spectra. Using the Southern California Earthquake Center (SCEC) shear wave velocity calculator (SCEC 2000), which calculates shear wave velocity in the Los Angeles area based on latitude and longitude, soil at this location was type B. The soil map associated with the velocity calculator is shown in Fig. 2-34. Design spectra for the rare and expected earthquakes for soil type B are shown in Figs. 2-35 and 2-36, respectively.

The seismic hazard level for the location was determined to be level IV, the highest of NCHRP seismic hazard levels. Seismic Design and Analysis Procedure (SDAP) E, an elastic response spectrum analysis procedure that considers cracked section properties was used to calculate design moments. SDAP E is similar to SDAP D except SDAP E requires displacement capacity verification (pushover analysis) to take advantage of higher response modification factors, which lead to reduced design forces. The Life Safety performance objective was employed and resulted in R-factors of 6.0 for the rare earthquake and 1.30 for the expected earthquake for both the longitudinal and transverse directions of the bridge. An elastic SAP2000 (Computers and Structures 2002) model and the uniform load method were used to determine the fundamental periods, which for the prototype were 0.758 seconds in the transverse and 0.748 seconds in the longitudinal direction. Column slenderness effects were considered for the tallest of the columns, which had an aspect ratio slightly larger than the threshold to include slenderness.

The expected earthquake was the controlling factor for the design. For the transverse and longitudinal directions of the bridge, the design accelerations were 0.175 g and 0.177 g, respectively. The prototype moment demand resulting from the 100% - 40% combination was 37600 kip-in (4248 kN-m). This is equivalent to 587 kip-in (66.3 kN-m) for the specimen. The calculated nominal plastic moment for the quarter scale column was 605 kip-in (68.4 kN-m). The longitudinal steel ratio of 1.56 percent was representative of a location of low to moderate seismic demand for the Los Angeles region. Had a location such as San Diego, CA or Portland, OR been chosen, the column design would represent what is required for a moderate to high regional demand for those locations.

To allow for the higher R-factors associated with SDAP E, displacement capacity verification was conducted for each of the bents. Moment curvature analysis was performed using the program RCMC2.0 (Wehbe et al. 2003). Nominal material properties and the change of axial load due to overturning were included. RAM Perform (RAM Int. 2003), a structural analysis program was used to model the bent systems. Elasto-plastic idealizations of the moment-curvature relationships from RCMC were used as input to the RAM Perform model, which utilized moment-rotation hinges at the ends of the columns. The displacement capacity was calculated to meet the higher R-factor code requirement, which was the elastic deflection from the seismic demand multiplied by a factor of 1.5.

2.4.2 Lateral Reinforcement Design

Lateral reinforcement of the columns was designed for the quarter scale model. This was because the model was to be built in quarter scale and scaling down from a prototype design was unnecessary. The design (Fig. 2-3) was conducted for each of the

scaled prototype column heights, which were 5 ft (1.52 m), 6 ft (1.83 m), and 8 ft (2.44 m). The columns were designed for double curvature and a dead-load axial load index of 0.082, which is equivalent to 46.5 kip (206.8 kN) per column. To match the test specimens used in experimental tests at other universities participating in the larger pre-NEES project a concrete cover of 0.75 in (19 mm) was used. The lateral reinforcement consisted of spiral steel that was continuous throughout the height of the columns. For comparison, the lateral steel was designed using four bridge design codes: NCHRP 12-49, Caltrans SDC (Caltrans 2003), AASHTO Standard Specifications, and AASHTO LRFD (AASHTO 1998). All of the design codes contain two basic design requirements, confinement reinforcement to increase plastic hinge rotation capacity, and shear reinforcement to prevent shear failure. The spiral reinforcement was first designed based on confinement requirements and then was checked to ensure sufficient shear capacity. Comparisons of lateral reinforcement ratio requirements for each of the four design codes are made in Table 2-2. Table 2-3 is a comparison of the shear factors of safety that resulted from each design, which are presented as the ratio of shear capacity and plastic shear demand for each column. The design that was implemented in the shake table model was that resulting from NCHRP 12-49. The NCHRP 12-49 design is discussed below.

2.4.2.1 NCHRP 12-49 Design

NCHRP 12-49 considers both confinement and longitudinal bar restraint for the required lateral steel in plastic hinge zones. The minimum confinement steel volumetric steel ratio is obtained from the following equation:

$$\rho_s = 0.008 \frac{f'_c}{U_{sf}} \left[12 \left(\frac{P_e}{f'_c A_g} + \rho_l \frac{f_y}{f'_c} \right)^2 \left(\frac{A_g}{A_{cc}} \right)^2 - 1 \right] \qquad (2\text{-}2)$$

where

ρ_s = *volumetric spiral steel ratio,* $\rho_s = \dfrac{4A_{bh}}{sD''}$

A_{bh} = *bar area of transverse hoops*
s = *vertical spacing of hoops*
D'' = *center to center diameter of perimeter hoop or spiral*
f'_c = *unconfined concrete strength*
U_{sf} = *strain energy capacity*
P_e = *factored axial load including seismic effects*
A_g = *gross area of column*
ρ_l = *longitudinal reinforcement ratio*
f_y = *yield strength of reinforcing bars*
A_{cc} = *area of column core concrete*

Equation 2-2 was developed by Dutta and Mander (1998). The commentary of NCHRP 12-49 states that for typical columns with low levels of axial load, this equation rarely

governs. This was the case for the columns in the model bridge, which had a relatively low axial load index of 0.082.

As shown in Table 2-2, the lateral steel for all the three column heights designed using NCHRP 12-49 was controlled by longitudinal bar restraint. The NCHRP 12-49 equation for longitudinal bar restraint is the following:

$$\rho_s = 0.016\left(\frac{D}{s}\right)\left(\frac{s}{d_b}\right)\rho_l \frac{f_y}{f_{yh}} \tag{2-3}$$

where

D = diameter of circular column
d_b = diameter of longitudinal reinforcing bar
f_{yh} = transverse reinforcing bar yield stress

Local buckling between spirals is prevented by the code spacing requirements. Equation 2-3 is intended to prevent global buckling of the longitudinal steel that extends over several spirals. Although the global buckling equation is located in the commentary of NCHRP 12-49 and not in the specification section, the commentary specifies that designers should not ignore the possibility global buckling. Prevention of global buckling to ensure the yield capacity of longitudinal reinforcement is maintained is a life-safety requirement. The commentary states that the equation has not been fully studied to determine its validity.

Lateral reinforcement for shear is specified in NCHRP by both an implicit and an explicit design method. Either method may be used for SDAP E, the elastic response spectrum method with displacement capacity verification, which was used for the bridge model design. However, the explicit method must be always checked.

The equation for the implicit shear design method is as follows:

$$\rho_s = 2K_{shape}\Lambda\frac{\rho_l}{\phi}\frac{f_{su}}{f_{yh}}\frac{A_g}{A_{cc}}\tan\alpha\tan\theta \tag{2-4}$$

where

K_{shape} = 0.32 (circular)
Λ = 2 (fixed-fixed)
f_{su} = ultimate tensile stress of longitudinal reinforcement (1.5fy)
f_{yh} = transverse reinforcement yield stress
α = geometric aspect ratio
$\tan\alpha = \frac{D'}{L}$
D' = center-to-center diameter of longitudinal reinforcement
L = column length
θ = angle of principle crack plane

$$\tan\theta = \left(\frac{1.6}{\Lambda} \frac{\rho_v}{\rho_t} \frac{A_v}{A_g} \right)^{0.25}$$

A_v = *shear area of concrete = 0.8A_g*
ρ_t = *volumetric ratio of longitudinal reinforcement*
ρ_v = *volumetric ratio of shear reinforcement*

The implicit method assumes that the contribution of shear carried by concrete is zero. The required lateral reinforcement, which is based on the plastic overstrength demand carried by concrete arch action and steel truss action, is directly proportional to the amount of longitudinal reinforcement in the column. The shear crack angle was calculated to be 33.3 degrees for all three of the column heights (Table 2-2).

Shear design by the explicit method considers concrete arch action, steel truss action, as well as shear carried by the concrete tensile section. The design shear capacity, Vu is determined using the following equation:

$$V_u = \phi(V_p + V_c + V_s) \tag{2-5}$$

where

V_p = *contribution due to arch action*
V_c = *contribution of the tensile concrete*
V_s = *contribution of the transverse reinforcement*
ϕ = *0.85*

$$V_p = \frac{\Lambda}{2} P_e \tan\alpha \tag{2-6}$$

where

P_e = *compressive axial force including seismic effects*

$$V_c = 0.05\sqrt{f'_c}\,A_v \quad (f'c = MPa)$$

$$V_c = 0.6\sqrt{f'_c}\,A_v \quad (f'c = psi) \tag{2-7}$$

$$V_s = \frac{\pi}{2} \frac{A_{bh}}{s} f_{yh} D'' \cot\theta \tag{2-8}$$

Program RCMC2.0 (Webhe et al. 2003) was used to conduct moment-curvature analysis on the sections for each column to determine shear demand. Factors of 1.7 and 1.3 were used to calculate over strength for the concrete and steel, respectively. The controlling amount of lateral reinforcement in the plastic hinge zone, which was provided for longitudinal bar restraint, was used to calculate the confining pressure. Confinement properties were calculated using the Mander model for confined sections (Mander et al. 1988). Table 2-2 lists the shear design values for each of the three column heights. Contribution carried by concrete tensile action is constant as shown by Equation 2-7 and accounts for approximately ten percent of the total shear strength for all of the columns. Contribution of shear resistance carried by the arch action, presented in Equation 2-6, accounts for six to ten percent of the total shear strength. Arch action participation is

relatively low because it is directly proportional to the axial load, which due to overturning during seismic excitation only provides an axial load index of about 4.7 percent. Lateral reinforcement provides between 81 to 84 percent of the shear strength for the 5 ft (1.52 m) to 8 ft (2.44 m) columns, respectively. The reinforcement contribution is relatively high because the equation for shear crack angle, shown in Equation 2-4, resulted in an angle of 33.3 degrees for all columns.

2.4.2.2 Design Comparisons

Comparisons of the design requirements for the lateral column reinforcement of the bridge model are discussed in the following sections. The comparisons are grouped into two categories: shear and confinement. The Caltrans provision used in this comparison was the displacement based design. A target displacement ductility of 5 was used because this is the minimum global displacement ductility specified in the code for a 2 column bent. Table 2-2 lists the reinforcement ratio requirements, as well as the controlling factor for each of the twelve combinations of the four design codes and the three column heights. Reinforcement to prevent longitudinal buckling, which could be considered as a type of confinement, controlled the design of all three columns for NCHRP 12-49. Requirements for confinement controlled all three of the columns considering both of the AASHTO codes, and controlled the tallest column considering the Caltrans SDC. For the short and medium height columns, Caltrans lateral reinforcement requirements were controlled by shear.

2.4.2.3 Confinement Requirement Comparisons

Confinement requirements for both Caltrans and AASHTO were compared to the NCHRP 12-49 design as shown in Table 2-2. The table shows the required lateral reinforcement ratio of each code for the three column heights. The amount of reinforcement that was included as spirals in all three sets of the columns for the shake table model provided a lateral reinforcement ratio of 0.009.

NCHRP 12-49 required a lateral reinforcement ratio of 0.0028 for lateral confinement and 0.0079 for prevention of longitudinal reinforcement buckling. These values were the same for all three column heights. Both Caltrans and AASHTO had requirements for confinement but did not explicitly specify a requirement for prevention of longitudinal bar buckling. The Caltrans method for confinement requirements is such that enough confinement is provided so that the column can achieve the design ductility without crushing the confined concrete. This amount varied from a ratio of 0.0037 to 0.0079 for the 5 ft (1.52 m), and 8ft (2.44 m) tall columns, respectively. Confinement requirements of both the AASHTO Standard Specifications and AASHTO LRFD Specifications were both specified by the same equations, which are dependant on the steel and concrete strengths, and the column longitudinal reinforcement ratio. The AASHTO requirements for all three column heights were the same value of 0.0115.

The amount of lateral reinforcement that was provided in the columns satisfied both the Caltrans and NCHRP 12-49 requirements. However, the amount of lateral steel that would be required by both of the AASHTO codes was deficient in the bridge model columns by approximately twenty percent.

2.4.2.4 Shear Requirement Comparisons

The required lateral reinforcement ratios to satisfy shear capacity for the three column heights and the four design codes are listed in Table 2-2. Table 2-3 lists the resulting shear strengths and the ratio of the shear capacity over demand for each design case. Shear requirements of all three column heights are satisfied for both Caltrans and NCHRP with the 0.009 lateral reinforcement ratio that was provided in the bridge model. For both AASHTO codes, the 0.009 ratio satisfies requirements for the medium and tall columns, but is not sufficient for the 5 ft (1.52 m) column. The AASHTO LRFD code requires the most lateral shear reinforcement for all three of the columns compared to the other three design codes. The column with the smallest aspect ratio, which is the 5 ft (1.52 m) tall column, has factors of safety for shear reinforcement ratio of 1.28, 1.05, 0.82, and 0.80 for the NCHRP, Caltrans, AASHTO, and AASHTO LRFD codes, respectively. The 6 ft (1.83 m) column has factors of safety of 1.58, 1.21, 1.03, and 1.00 for the NCHRP, Caltrans, AASHTO, and AASHTO LRFD codes, respectively. The 8 ft (2.44 m) column has factors of safety of 2.24, 1.49. 1.52, and 1.45 for the NCHRP, Caltrans, AASHTO, and AASHTO LRFD codes, respectively.

2.5 Specimen Design

Column properties and general dimensions of the shake table model are directly correlated to the prototype bridge. However, components of the model such as the cap beams, beam-column joints, superstructure, and footings, required a hybrid design that would satisfy the following three conditions: provide a realistic representation of the prototype response, be relatively easily constructed and assembled/disassembled, and be able to be attached to and safely tested on the shake tables. This section discusses the component designs and their implications on the shake table tests. Material properties that were used in the design were grade 60 reinforcement steel and 5000 psi (35 MPa) concrete.

2.5.1 Bent Cap Design

This section describes the design of the cap beams for the bridge model. The dimensions, design loadings, and reinforcement detailing are discussed. Other parts of the cap beam that are not discussed in this section, but are in the following sections are the beam-column joint design (Sec. 2.5.2), the lift points (Sec. 2.5.3.3), the cantilevers on bents 1 and 3 (Sec. 2.5.5), and the ledges that supported the superstructure beams (Sec. 2.5.6). The cap beams were designed as standalone members. However because the cap beams were post-tensioned to the superstructure, which was a solid section, and because the cap beams had additional components such as cantilevers and ledges, the cap beams had both additional strength and stiffness beyond what they would have in the prototype. This was not considered to be an issue for modeling since the prototype was representative of contemporary design, in which case, the cap beams are designed to remain elastic. The primary goal of the shake table model was to capture the nonlinear bridge response that occurs in the columns. In continuous reinforced concrete bridges nonlinearity occurs essentially in the substructure and the superstructure remains elastic.

2.5.1.1 Dimensions

The dimensions for the cap beams were influenced by both the prototype dimensions and the dimensions of the bridge model superstructure. The model dimensions are shown in Fig. 2.2. The depth of the cap beams was 15 in (0.38 m), which is the same depth of the scaled down prototype cap beam. The total length of the cap beams (perpendicular to the longitudinal axis of the bridge) was 98 in (2.49 m), which is approximately 21 percent less than that of the scaled prototype. There are two reasons that the length of the cap beams is less than the prototype equivalent. The first is because the calculated equivalent solid superstructure width (discussed in 2.5.3) is 90 in (2.28 m), which is also less than the quarter scale prototype. To transfer the transverse superstructure bending loads, it was not necessary for the cap beams to be longer than the width of the superstructure. The second reason is because the length of 98 in (2.49 m) was sufficient to include the two columns in the bent, and to provide sufficient cantilever length for the joints to transfer moments from the columns to the beam.

The widths of the beams (in the longitudinal direction of the bridge) were 15 in (0.38 m), which is the same as that of the scaled prototype. However, all three of the cap beams contained additional components to allow for assembly and for modeling of the prototype masses. As seen in Fig. 2-2, the middle bent (bent 2) contained beam ledges on both sides, which were to support the superstructure beams. Bents 1 and 3 contained a beam ledge on one side to support the superstructure beams, and a cantilever to support additional masses on the other to balance the column moment due to frame action in the longitudinal direction of the bridge. The beam ledges, masses, and cantilevers are discussed later in this chapter.

2.5.1.2 Design Loads

The cap beams were designed for two loading types. The first was for the scaled version of the prototype loads and the second was for the specimen under the shake table test loads. The model was designed according to the first case, and was checked for the second case. In addition to the capacity of the beams resulting from this design, the beams contained supplementary capacity from the beam ledges and cantilevers, as well as the confinement from the longitudinal post tensioning of the superstructure.

In the first design the specimen was designed using the AASHTO bridge design provisions for vertical loading. Moments and shears were calculated for the prototype and scaled down for design of the model. This included the combined dead loads, live lane loads, and earthquake loads on the prototype bridge. The combinations that were considered were Strength I with one lane loaded, Strength II with two lanes loaded, Dead loads only, and Extreme Event I. The demands from load cases were calculated at each tenth of the span length along the cap beam span between the columns, and at 1/5 increments of overhang length along the cap beam overhangs. To scale the prototype moment demands and shear demands into model form for design, scale factors of 1/64 and 1/16 were used, respectively.

For the second design case, the beams needed to resist the distributed dead load on the shake table model, and the plastic moments of the columns during a lateral pushover. The second case is the case that the bridge model would actually experience on the shake tables. A safety factor of 1.5 was used in the second case design.

2.5.1.3 Reinforcement

Once the design loads were calculated as discussed in the previous section, the longitudinal and shear reinforcement of the beams was designed and detailed. Bent cap reinforcement was designed to satisfy both the AASHTO standard specifications as well as the requirements of Caltrans BDS (Caltrans 2000). As if the beams were designed in a typical bridge, consideration was given for crack control, reinforcement due to the effective slab width, and the side face reinforcement that is required by Caltrans BDS. Reinforcement that was provided to satisfy design loads was the same along the length of the beams. This was because it would have been impractical to terminate the reinforcement along such a short distance, and the reinforcement variation would not affect the results of the shake table modeling, which was intended to keep the superstructure elastic.

The amount of shear reinforcement that was required in the beams to resist shear from loading discussed above was controlled by the forces at the face of the columns (Caltrans BDP). The required shear reinforcement in the model was 0.4 in^2 (258 mm^2) at a spacing of 3.3 in (84 mm). As shown in Fig. 2-8, the actual reinforcement was greater. This is because additional reinforcement was required due to the ledges, which are discussed in Sec. 2.5.6, as well as to satisfy the joint force transfer discussed in Sec. 2.5.2.

Flexural reinforcement was provided in both the negative and positive moment regions. As shown in Fig. 2-8, the required flexural reinforcement was four #6 bars in the positive moment regions and six #6 bars for negative moment. In addition to the top and bottom flexural reinforcement, additional reinforcement was provided on the faces of the beams. This reinforcement was calculated according to Caltrans BDS requirements for cap side face (also known as skin) reinforcement, and was three #3 bars equally spaced across each face.

2.5.2 Beam-Column Joint Design

Although beam-column joints were not modeled as an exact representation of the prototype because the bridge model superstructure provided additional strength and stiffness, the joints were designed to satisfy both the Caltrans SDC and NCHRP 12-49 requirements. Both requirements are very similar having the same design method with only slight variations in the quantity of reinforcement. It was critical for this test that the joints would not be damaged, and that the column bars were fully anchored into the beam. Joint details of the model are shown in Figs. 2-5 and 2-8.

The joints were first checked to make sure that they were correctly proportioned according to principal stresses. Following this check, the reinforcement in the joint region was designed to satisfy requirements for joint shear, as well as joint force transfer. Reinforcement for joint shear was satisfied by the column lateral reinforcement spirals that extended into the joint.

Joint force transfer reinforcement was required in the joints because the principal tensile stress in the joint region exceeded the maximum concrete tensile strength. The transfer reinforcement was provided in the form of vertical reinforcement, clamping reinforcement, and horizontal reinforcement. The vertical reinforcement was provided in the form of stirrups, which included the shear stirrups from the cap beam design.

Vertical reinforcement was provided to satisfy the requirements in the four zones adjacent to the four faces of the column as required by both design codes.

Clamping reinforcement is not required by Caltrans, but is a requirement of NCHRP 12-49, and therefore was provided in the bridge model. The clamping reinforcement hooks on to the flexural reinforcement in the top of the cap beams directly above the columns, and extends vertically into the joint above the columns. The purpose of the clamping reinforcement is to aid in the transfer of moment from the columns to the flexural reinforcement of the beam. The requirement of clamping steel was 0.16 in^2 (103 mm^2). The minimum clamping reinforcement length was two-thirds of the depth of the beam. For ease of construction, four #3 bars were provided with a cross sectional area of 0.44 in^2 (284 mm^2). The clamping reinforcement is shown in Figs. 2-5 and 2-8 and is labeled as "C-4".

The requirement for horizontal reinforcement for joint force transfer is additional cap beam flexural reinforcement in the region of the joint. This reinforcement is in addition to what is already required for cap beam flexure. This requirement was already satisfied by the amount of flexural reinforcement that was provided when rounding the flexural reinforcement up to the nearest bar size during the cap beam design.

2.5.2.1 Anchorage of Column Bars

The column longitudinal reinforcement for the specimen extended into the joint region a distance of 13.5 in (0.343 m), which was the available development length after subtracting the cover concrete and the beam reinforcement. This length is approximately 106 percent of the ACI 318 (ACI 2002) requirement for straight #3 bars using a yield stress of 60 ksi (414 GPa). Because the development length in the specimen for straight bars was at such a close margin and because it was desired for this test that the columns fail at the column ends rather than the column reinforcement slipping out of the beams, the column reinforcement into the beams needed to have an additional measure for development. There were two options that were considered to increase the development length: (1) providing a hook, and (2) providing a mechanical anchorage at the end of the longitudinal column reinforcement in the cap beams.

A standard hook at the top of the column reinforcement would have provided a significant safety margin against column reinforcement bond failure in the cap beam. However, the hooks could not be used because if the hooks faced away from the center of the columns, they would not allow for the cardboard formwork to be slipped onto the column cages after pouring the footing concrete during construction. If the hooks faced toward the center of the column, the placement of the column concrete would have been difficult.

It was decided to provide the additional anchorage of the column reinforcement into the beams by attaching mechanical anchorage to the ends of the column bars after the columns were cast, but before the beams were cast. Since headed bars are not avaliable for small bar sizes, the mechanical anchorage was made by welding cross pieces at the top of the bars as shown in Fig. 2-4 and designated as bar type "C-25". The weld was designed according to ACI 318 code to be able to fully develop the # 3 bars.

2.5.3 General Superstructure Design

The superstructure was designed to match the scaled prototype response in bending, as well as to be easily assembled on the shake tables. This section describes the derivation of the superstructure dimensions, the design of the general reinforcement, and the design and placement of lifting hooks so that the beams could be transported from their off-site construction location. Upon completion of the general design of the superstructure, the mass configuration, superstructure end cantilevers, beam ends, and post-tensioning systems were designed. These designs are discussed in Sections 2.5.4-2.5.7.

2.5.3.1 Dimensions

Because of the high relative strength and stiffness of the prototype superstructure compared to the substructure, the superstructure remains essentially elastic when the bridge is subjected to seismic excitation. Also, because the bridge is post-tensioned, the superstructure remains generally un-cracked. For these reasons, it was not necessary to model the superstructure in detail, which would have been very difficult considering transportation after construction, and constructability of cells having scaled web widths of only 3 in (76 mm). Instead, the model superstructure was a solid rectangular section with bending properties equivalent to those of the prototype.

The quarter-scale moment of inertias for bending about both orthogonal axes of the superstructure were calculated to match the prototype section (Fig. 2-28) by multiplying the prototype moments of inertias by 1/256, which is the fraction of the length scale to the fourth power. The resulting section for the two spans, essentially a slab, was a rectangular section having a width of 90 in (2.29 m), a depth of 14 in (0.36 m) and a length of 324 in (8.23 m). So that the two spans could be easily transported, stored, and assembled on the shake tables, it was decided to construct each span with three beams that each had a cross section of 30 in (0.76 m). The resulting dimensions are shown in Fig. 2-1.

2.5.3.2 General Reinforcement

The six beams were designed to sustain their own weight as well as superimposed weight (discussed in Sec. 2.5.4) without the use of the longitudinal post-tensioning system. The longitudinal post-tensioning, discussed in Section 2.5.7, was applied after assembly of the beams and before addition of the masses. Because the superimposed weights were added to the bridge model after the post-tensioning, the general flexural reinforcement should not have been required to resist moments due to superimposed weights. However, because the bridge was to be tested to failure, which subjected the superstructure to large forces, and because there was a chance that during testing the post-tensioning strands could suffer an extreme loss of tension, the beams were designed to be able to support all the dead loads including both the beam self weight, and the superimposed weights.

Design forces of the superstructure beams for both shear and moment design were derived from the maximum of three different load cases. The first was self weight of the beam when lifted by the lifting hooks, which is discussed in the following section. The second and third cases were for the beams subjected to self weight and superimposed

loads while supported at the ends for a fixed case and for a pinned case. Although the fixed case was not realistic since the beams would be simply supported without the longitudinal post-tensioning, it was still analyzed because the end conditions could a have partial fixity.

The superimposed load on each beam was a moving distributed load that was equivalent to 1/3 the distributed load of the 20 kip (89 kN) reaction blocks that are used in the University of Nevada, Reno laboratory. The reaction blocks are 4 x 4 x 8 ft (1.2 x. 1.2 x 2.4 m), and the 8 ft (2.4 m) sides were oriented perpendicular to the axis of the beams. The load was divided by three because there were three beams side by side. The distributed load, which traveled from end to end, varied from a length of zero to the entire length of the beam. When the load was equal to the beam length, it was equivalent to reaction blocks covering the entire length of the beams. An example of the loading for the pinned end case is shown in Fig 2-37. This load case is greater than what was to be expected in the bridge model loading. However, in case the beams were to be used in the future for additional bridge models with different loadings, this extreme case was considered. The moment and shear demands were calculated at tenth points along the span of the beams for each of the three cases and were then used for design.

Flexural reinforcement for the superstructure beams was designed according to ACI 318 using an over design factor of 1.5. The resulting design is shown in Fig. 2-14. Figures 2-38 and 2-39 show the reinforcement demand and the amount of flexural reinforcement that was provided in the beams for the positive and negative moments, respectively. For the positive moment reinforcement, fifteen #6 bars were placed toward the center of the beams where the maximum moment occurred. The positive moment reinforcement was reduced down to nine #6 bars toward the ends of the beams. The negative moment reinforcement for the beams was five #6 bars throughout the length of the beams. Although the calculated negative moment demand at the beam ends required a greater amount of reinforcement, this was not provided because the negative moment at the beam ends would only develop when the post-tension cables were in place. Any negative moment demand would be resisted by the cables.

Shear reinforcement of the beams was also designed according to ACI 318, but with an over design factor of 2. Had the post-tension force been included in the shear design, the over design factor would have been larger because of a decrease in crack angle due to the sectional compression. A larger safety factor was considered for shear than for moment because the longitudinal post tensioning that would be included in the beams would make a greater contribution to the moment capacity than the shear capacity. The shear reinforcement is shown in Fig. 2-15. A constant spacing of 5 in (127 mm) was used throughout the span to space the #3 stirrups. The design was controlled by the shear at the beam ends.

2.5.3.3 Lift Points

As shown in Figs. 2-7, 2-12, and 2-13, lifting anchors were included in the end bents (bents 1 and 3), the footing spacer blocks (discussed in Sec. 2.5.9), and the superstructure beams. The hooks, shown in Fig. 2-12, were 8-ton (71 kN) Swift-Lift anchors that are specifically designed for lifting reinforced concrete. This type of anchor was used because it is set into the concrete and has no protrusions, which would make it

possible to stack the beams and footing blocks for storage upon completion of the shake table testing, as well as to place the masses on top of the superstructure after the beams were assembled on the shake tables.

Four anchors were used in each beam, and were placed in pairs at approximately 4 ft (1.22 m) from the beam ends. The weight of each beam is approximately 11.8 kips (52.5 kN), which for the 4 anchors there is a safety factor of 5.42 beyond the specified strength of the anchors. In case one of the anchors was not attached properly, or they were not loaded evenly, the safety factor with two anchors (one at each end), is 2.71. The lifting hooks in the two spacer blocks had a safety factor of 2.5 beyond the specified anchor strength.

Lifting hooks were provided in the end bents so that they could be lifted on to the shake tables. The hooks were placed in the cantilever cap beams (Fig. 2-7) so that the center of the hooks was in the same location of the center of mass of the bents. The safety factor of the anchors for the bents was 3.2. Although this was a very conservative design, four anchors were used so that the irregularly shaped bents would be stable during lifting.

An important part of the lifting hook design for the bents was to make sure that when the bents were lifted at the top of the cap beams, the columns would not crack under the gravity load of the footing. The gravity load was checked for the most extreme case, which was for bent 3. The tension at the top of the columns due to the footing and column was compared to the tensile strength of the concrete. The safety factor against concrete cracking based on the modulus of rupture using the specified concrete compressive strength of 5000 psi (34.5 GPa) was 10.6. Although this is a very conservative check, the footing would likely be subjected to lateral rocking during lifting of the cap beam, which would place additional demand on the columns.

2.5.4. Superstructure Masses

Column axial load level was designated by the axial load index, which is defined as the ratio of the axial load and the product of the gross section and the specified concrete compressive strength. The target axial load index for the bridge model was 8.2 percent, which represents a typical bridge column axial load level. An axial load index of 8.2 percent in the model is equivalent to a column axial load of 46.5 kips (206.8 kN). Due to the scaling effect, masses of the quarter scale model provide a smaller axial stress than in the prototype scale. Some of the required axial load was provided by the self weight of the bridge model. The rest was provided by superimposed dead load that was attached to the top of the superstructure.

2.5.4.1 Additional Masses

The mass that was already available for use in the University of Nevada laboratory that could be placed on the top of the bridge was six, 8 kip (35.6 kN) lead pallets, four, 2.55 kip (11.3 kN) lead buckets, and twenty-four, 20 kip (89kN) concrete blocks that are 4 x 4 x 8 ft (1.2 x. 1.2 x 2.4 m). To determine the configuration of masses that was required to produce the target axial load in each of the columns, an elastic model was developed and different trials of locations of masses were checked. It was determined that in order to produce the target axial load index in bents 1 and 2 without

stacking concrete blocks, superstructure cantilevers extending past the ends of the model were required in the bridge model. The cantilevers were also required so that there was not a significant out-of-plane bending moment due to the dead load on the columns of the two end bents. The dead load moments including effects of the post-tensioning are further discussed in Section 2.5.7.2.

To achieve a dead load and tributary mass corresponding to an 8.2 percent axial load index, the length of required cantilevers beyond the column centerlines of the two ends of the bridge model was 43.5 in (1.1 m). This was determined by placing the densest mass that was available, which was three of the 8 kip (35.6 kN) lead pallets stacked together, at the extreme ends of the model. In the computer analysis, the cantilevers were extended until a reasonable match of the axial load index was achieved. The cantilevers are shown in Fig. 2-1. Cantilever design is discussed in Section 2.5.5. The superimposed load that satisfied the axial load index requirements consisted of 120kip (534kN) of concrete blocks and 58kip (258kN) of lead pallets as shown in Fig. 2-40 and the renderings of Figs. 2-25 through 2-27.

2.5.5 Cantilever Design

The cantilevers that were attached to bents 1 and 3 were required to support a portion of the superimposed weights on the superstructure. General dimensions are shown in Fig. 2-2. The plans resulting from the cantilever design are shown in Fig. 2-7. The loading that was considered for the cantilever design was the self weight of the concrete added to the distributed load from the three lead pallets that were on top of the superstructure (Fig. 2-40). The cantilevers were designed according to ACI 318 for moment and shear at the face of the columns using an over design factor of 2. Similar to the design of the superstructure beams, the additional strength that was provided from the longitudinal post tensioning was ignored in the cantilever design.

2.5.6 Design of Beam Ends and Cap Beam Ledges

To allow for the pieces of the bridge model to be assembled on the shake table, ledges were designed for the ends of the longitudinal superstructure beams and the portions of the cap beams that the superstructure beams rested on. The system was designed so that the six superstructure beams, discussed in 2.5.3, could be placed on the three bents after the bents were attached to the shake tables. Similar to the design of the superstructure beams, the ledges were designed to support the weight of the beams, as well as the superimposed weights that were later attached to the beams. To be conservative, the additional strength of post tensioning was not considered in the design. The general locations of the ledges for the three bents are shown in Fig. 2-3. The detail of the ledge designs are shown in Fig. 2-6 and 2-9 for end bents and the middle bents, respectively. The general location and the detail of the design for the ledges of the superstructure beams are shown in Figs. 2-13 and 2-15.

Bearing pads for the ledges were designed according to the strut-and-tie model guidelines in ACI 318, as well as AASHTO standard specifications. The AASHTO design was used to determine the optimal spacing and size of the bearing pads, as well as to determine the initial dimensions of the ledges. The design for the bearing plates was for both punching shear and bearing, and was controlled by punching shear capacity.

Bearing pads were 0.75 in (19 mm) thick, 6 in (152 mm) x 3 in (76 mm) steel plates and each had a tributary ledge width of 15 in (381 mm).

The ledges were designed using the strut-and-tie method according to ACI 318. The calculated dead loads discussed above were multiplied by a factor of two prior to the design. As shown in Figs. 2-6 and 2-9, each ledge for the bents had six bearing pads. Each of the three beams had two bearing points that rested on the pads. The design was conducted for the ledge area tributary to one bearing pad for each of the ledge types. Because the bearing pads were at equal spacing, only one design was necessary for each ledge type. The bridge model had two ledge types. The first type was a typical beam ledge, and was used in bents 1 and 3, as well as in the beam ends. The second type, for bent 2, was a T-beam type ledge.

The strut-and-tie configuration that was used for the typical beam ledge design, which was for the 12 superstructure beam ends and the ledges of bents 1 and 3, is shown in Fig. 41. A tributary ledge width of 15 in (381 mm) was used to determine the design loads. The primary tension reinforcement in the ledges tributary to two bearing plates, which has a ledge width of 30 in, was provided by five #6 headed bars that were anchored with straight bars into the primary section. The headed bars for the cantilevers and beams are designated "C-14" in Fig. 2-6, and "B-7" in Fig. 2-15, respectively. The shear from the ledges was transferred into the flexural reinforcement of the main section using #4 stirrups. The stirrups for the cantilevers and beams are designated "C-26" in Fig. 2-7, and "B-6" in Fig. 2-15, respectively.

The strut-and-tie configuration that was used for the T-beam ledge design, which was for the two cap beam ledges of bent 2, is shown in Fig. 2-42. Similarly to the typical beam ledge design discussed above, a tributary ledge width of 15 in (381 mm) for each bearing pad was used to determine the design loads. The primary tension reinforcement for the ledge, designated as "C-8" in Fig. 2-9, was provided with five #6 bars that were headed at each end of the ledges. The headed end of the bars provided development at the extreme edge of the ledges. The anchorage length for each headed bar was taken from the face of the cap beam at the ledge connection to the head at the other end of the bar. The shear transfer from the ledge into the primary member, which was the cap beam, was provided by increasing the shear reinforcement in the cap beam. The increased reinforcement, which provided resistance for ledge shear transfer, joint shear near the columns, and for transfer of ledge shear, is designated as "C-1 and C-5" in Fig. 2-8.

2.5.7 Post Tensioning Design

The superstructure components of the bridge model were post-tensioned in both the longitudinal and transverse directions creating a solid post-tensioned slab. As discussed in section 2.5.3, the superstructure slab was designed so that the bending moments of inertia matched the scaled inertias of the prototype. The prototype bridge is a post-tensioned box girder bridge that due to post-tensioning generally exhibits un-cracked behavior. This section describes the purpose as well as the design of the post-tensioning in the model.

2.5.7.1 Transverse Post-Tensioning

Transverse post tensioning, which was perpendicular to the longitudinal axis of the bridge, was required so that the two sets of three beams that spanned the bents across the shake tables acted integrally. This was necessary because the spans were each constructed as three beams (Fig. 2-1) to facilitate transportation and assemblage of the model. The design for the transverse post-tension force was such that the transverse tension rods created compression perpendicular to the beam interfaces. This compression led to a friction force between the beams greater than the interfacial shear that was caused by superstructure bending in the transverse direction.

The design bending moment was determined as the largest lateral bending moment on the superstructure from the following three cases: (1) elastic pushover analysis until the first bent reached its calculated lateral load capacity, (2) inelastic analysis under the Sylmar record from the 1994 Northridge, California earthquake (0.6g PGA), and (3) inelastic analysis under the Sylmar record from the 1994 Northridge, California earthquake scaled to a 1.0 g peak acceleration. The computer analyses were conducted using RAM Perform, which is a general purpose nonlinear structure analysis program (RAM International 2003). The elastic model was composed of linear beam column elements with cracked concrete properties for the columns and un-cracked properties for the remainder of the bridge. The nonlinear model was the same as the linear model, except for the plastic hinge zones at the top and bottom of each column modeled by a nonlinear element. The nonlinear element was a lumped rotational spring that included axial load interaction, and a surface function to account for biaxial bending. It provided a simple bilinear hysteresis load-deflection relationship, which had the same unloading and loading stiffness and no degradation. This model was sufficient to capture the approximate moments that would be caused in the superstructure.

The maximum moment from the three cases discussed above was located at the center bent. This is because the middle bent (bent 2), which is the tallest of the three bents, is very flexible in comparison to the end bents. The transverse response is essentially that of a simply supported beam. The maximum moment, which was 4343 kip-in (491 kN-m), was controlled by the elastic pushover analysis. An over strength factor of 1.2 was applied to this value for the design.

The transverse post tensioning was provided by 1.25 in (32 mm) diameter Dywidag post-tension rods that went through the mid-depth of the beams. The total transverse post-tensioning force of all of the rods was 1000 kip (4450 kN). The layout resulting from the design of the transverse post-tension system is shown in Fig. 2-16. The spacing of the ducts along the length of the superstructure was determined assuming that the force spread from the bearing plates into the beams at 45 degree angles as shown in the plan view of Fig. 2-43. The 45 degree spreading combined with a 5 in (0.13 m) bearing plate provided a 65 in (1.65 m) tributary width for each rod. Figure 2-44 shows a plan and section view of the force propagation for one of the rods. The required clamping force was calculated assuming a friction coefficient of 0.6 between the two beams, which is typical for smooth concrete on concrete. However, the design was conservative because during construction it was determined that it was necessary to pour hydrostone, a grout like material, between the beams to fill excess voids. Because of the hydrostone, the friction coefficient between the beams was actually greater than 1. Ducts

for the 1.25 in (32 mm) rods were provided in the beams as shown in Fig. 2-44 using 2 in (51 mm) PVC pipes at the mid-height of the beams. No extra reinforcement were used in the anchorage zone of the transverse post-tensioning bars because special plates were provided at the ends of the bars to transfer compression to the concrete. Also, the concrete in the beams was well confined and the force in each bar was relatively low.

2.5.7.2 Longitudinal Post Tensioning

Longitudinal post tensioning of the model served two purposes. This first was to keep the superstructure under axial compression so that it did not experience cracking throughout testing. The second was to form a continuous superstructure across all three bents. This section describes the post tension design, the moments and axial loads in the columns that resulted from the combination of dead loads and post-tensioning, as well as the design of the anchorage zones in the cantilevers of bents 1 and 3.

Plans resulting from the post-tension design are shown in Figs. 2-16 and 2-17. The system was designed so that when the bridge was subjected to its self weight and the superimposed weights, the tension in the concrete remained below one-half of the concrete modulus of rupture, and the concrete compression remained below 0.45 multiplied by the concrete compressive strength. Upon completion of the design for concrete stresses, the second purpose of the post-tensioning, which was to prevent separation of the superstructure beams and cap beams was checked. The design check for beam separation utilized the same superstructure design moments as those determined in the transverse post-tension design discussed in the previous section. The difference in this design was that instead of compressing the beams transversely, the beam-slabs were compressed onto the bents in the longitudinal direction to overcome the transverse bending stresses. The longitudinal post tensioning from the concrete stress design, which is discussed in the next paragraph, provided a calculated safety factor of 2.8 against separation of the superstructure beams from the bents.

An elastic model using beam-column elements in SAP 2000 was used to determine the required path and tension of the longitudinal system. A computer model was needed because the system is indeterminate and iterations needed to be performed to determine the optimal path. The system was composed of three ducts, one in each beam, with 0.5 in (13 mm) diameter 270 ksi (1860 GPa) low relaxation strands. The sequence of loading was an important factor in this design. For the self-weight of the model, which included the bent caps, and the superstructure beams, the seat joints at the end of the beams were considered to be zero-moment (pinned) connections. For the superimposed loads, which were placed after the post-tensioning, the joints were considered to be moment connections. This is because the rotations of the joints that occurred from the self weight of the beams would remain after the beams were placed. The construction sequence was then to grout the joints, post-tension the bridge, and to place the lead and concrete blocks. Due to the post-tensioning and the grout, the joints had moment resistance to resist the moments from the superimposed loads.

It was attempted to design the cable paths to have a constant eccentricity. However, because of the highly varied moments throughout the superstructure, the eccentricity of the tendons had to be varied from 3 in (76 mm) below the centroid at the cantilevers to 4 in (102 mm) above the centroid at the middle bent. Part of the challenge

in designing the path for the tendons was avoiding the transverse post tension ducts which ran transversely through the mid-depth of the superstructure at 65 in (1650 mm) intervals (Fig. 2-16). This did not allow for the most efficient path. The other obstacle was that near the outer bents of the bridge in the superstructure spans (bents 1 and 3); there were highly concentrated masses which caused large positive moments. The large positive moments were very close to the cap beams and cantilevers, where the superstructure was subjected to large negative moments. For this reason, it can be seen in the plans in Fig. 2-16 that the cable path has a negative eccentricity over bent 2 and a positive eccentricity over bent 3. The final design consisted of nine 0.5 in diameter 270 ksi tendons for each of the three ducts having an effective post tensioning force of 230 kip per duct after all losses.

Losses that were considered were elastic shortening, steel relaxation, creep, anchorage set, and friction. Time dependant losses were assumed to occur over a period of 35 days. This was the estimated amount of time that it would take to assemble the model on the shake tables. Approximately 70 percent of the losses were due to friction and anchorage set. The jacking force that was required was calculated to be 258 kip (1148 kN) per tendon.

2.5.7.2.1 Column Axial Loads and Bending Moments

As discussed in Section 2.5.4.1, the target axial load index for the columns was 8.2 percent which translates to an axial load of 46.5 kips (207 kN) per column. The distribution of axial loads to the columns was affected by two factors. One was the tributary dead loading of the model self weight and the superimposed loads, and the other was column axial loads due to secondary effects from the post-tensioning. The elastic SAP 2000 model that was used in the design of the post-tensioning strands path was also used to determine the axial loads resulting from post-tensioning. Similar to the calculation of moments for post tensioning, two bridge systems were required to determine the axial loads. The first system, which was used to determine the axial loads due to self-weight of the model, had pinned connections at the four ledges that supported the superstructure beams. The second system, which was used to determine the axial loads due to the secondary effects from post-tensioning and the superimposed weights, had full fixity at the ledge joints.

The axial load distribution from the model was such that the columns in the short (bent 3) and medium (bent 1) bents had an axial dead load of 47.1 kips (210 kN). The columns of the middle bent (bent 2) had an axial dead load of 41.0 kips (182 kN). These loads translate to axial load indices of 7.3 and 8.3 percent in the middle and end bents, respectively. Because the end bents would experience the most damage during testing, it was more important that they had an index close to the target of 8.2 percent. The slight deviation of axial load in the center bent was not important for three reasons. The first was that the center bent is very flexible and would not control the response of the model. The second is that slight differences in the axial load generally do not have significant effect on the response of reinforced concrete columns. The third is that the computer modeling of the bridge after completion of the testing would include the actual axial loads provided in the model and not the target loading.

The distribution of masses combined with the secondary effects of the post tensioning caused slight moment demands on the columns in the longitudinal direction of the bridge model. The same computer model that was utilized in the post-tension design was used to determine these moments. The maximum longitudinal moment on the center bent was 7 kip-in (0.8 kN-m) per column. The maximum longitudinal moments on the end bents were 85 and 92 kip-in (9.6 and 10.4 kN-m) for bents 1 and 3, respectively. Moments in the end bents were greater than the middle bent because the secondary moments due to post-tensioning combined with the moment from the cantilevers, did not completely counteract the moment from the bridge spans that was caused by the concrete blocks. The unbalanced moments were relatively small compared to the calculated effective yield moment of the columns, which was approximately 700 kip-in (79 kN-m). Also, the model was to be tested primarily in the transverse direction which made the longitudinal moments less significant. However, the moments were taken into consideration in the extensive computer modeling that was conducted upon completion of the shake table tests.

2.5.7.2.2 Anchorage Zones

Proper detailing of anchorage zones in the cantilevers was required to accommodate the large post-tensioning forces from the three longitudinal ducts. The general anchorage zone reinforcement, described in this subsection, was designed according to AASHTO standard specifications. The spiral reinforcement for the local zone was provided by the vendor of the post-tensioning system. The reinforcement for the general anchorage zones in the cantilevers is shown in Fig. 2-45. This part of the plans is separate from the plans in Figs. 2-1 through 2-24 because the anchorage zones were designed after the contractor selected the system.

Each cantilever was divided into three general anchorage zones for the design. Each zone had a width of 30 in (0.76 m), which was tributary to each of the three ducts. The design for the general zone consisted of bursting reinforcement for the lateral and vertical directions, and spalling reinforcement directly under the bearing plates. As shown in Fig. 2-45, the bursting reinforcement was provided by two #4 hoops (designated as “A-1”) in each zone. The spalling reinforcement was provided by two #4 bars across the three anchorage zones at the end of each cantilever (designated as “A-2”).

2.5.8 Spacer Block Design

As shown in both Fig. 2-1 and the renderings of Figs. 2-26 and 2-27, the footings of bents 1 and 3 were attached to the shake table through spacer blocks. The spacer blocks, were required so that the top of the bents, which all had different column heights would all be at the same level for connection to the superstructure. The plans for the two blocks are shown in Fig. 2-12. The design of the blocks was based on the moment and shear demands due to self weight during transportation. However, the ACI 318 requirements for minimum reinforcement controlled the design. PVC ducts with a 3 in (76 mm) diameter were placed in the blocks so that anchor rods could pass through the blocks to attach the footings to the shake tables.

2.5.9 Footing Design and Anchorage to the Shake Tables

The general locations of the footings for the shake table model are shown in Fig. 2-1. The footings in the model were designed to be strong and stiff to avoid any footing damage. The footings needed to resist the moments and shears of the columns, as well as the clamping forces between the footings and the shake tables. Plans for the footings are shown in Fig. 2-10 for bents 1 and 2, and Fig. 2-11 for bent 3. The footings for bents 1 and 2 are identical because the 2 ft (610 mm) spacer blocks provide bent 1 with the additional height needed to match the height of bent 2, which had columns that were 2 ft (610 mm) taller. The footing for bent 3, the shortest of the three bents, was approximately 1 ft (305 mm) taller than the other footings. This is because bent 3 was 1 ft (305 mm) shorter than bent 1.

Design of the footings consisted of the following six components: punching shear, overturning, grout compression, sliding, one-way shear, and moment. The components that directly affected the capacity design of the footings were punching shear, one-way shear, and the moment. The design for these components was according to ACI 318. The components that affected the footing size and the required clamping force were overturning, grout compression, and sliding. These components were designed at all of the column bases and at the bases of the spacer blocks.

An example of the loading condition for the design of bent 1 is shown in Fig. 2-46. A linear distribution of loading was assumed to occur at the base of both the footing and the spacer blocks. A spreadsheet was developed for the design of the footing to calculate the safety factor for all six components, as well as the minimum overturning stresses. The overturning and one-way shear were the most critical parameters of the designs. The lowest safety factor of the three footings for one-way shear was 1.9 for bent 2. The required clamping force on the footings to prevent overturning was controlled by the base of the footing of bent 3. A clamping force of 300 kips (1330 kN) was provided by ten 1-in (25.4-mm) diameter threaded rods through each footing. The rods were tensioned to 30 kips (133 kN) each at the top of the footings. The other end of each rod was threaded into the shake tables beneath the footings. PVC ducts that were 3in (75 mm) in diameter were placed in the footings to allow the threaded rods to pass through.

2.5.10 Anchorage of Masses

The superimposed weights that were placed on top of the bridge model (discussed in section 2.5.4) were tensioned on to the superstructure so that they did not move during testing. Two types of mass were attached to the model, concrete blocks and lead buckets/pallets.

The concrete blocks were attached to the superstructure beams using 1.25 in (32 mm) diameter post-tensioned Dywidag rods. The post tensioning force that was required was achieved by using two rods for each of the six 20-kip (89 kN) concrete blocks. A lateral acceleration of 2.0 g and friction coefficient of 0.6 for concrete on concrete was assumed. The 2.0 g lateral acceleration was conservative by a factor of approximately 2. The friction resistance was calculated accounting for both the self weight of the blocks and the clamping force of the rods. PVC ducts having a diameter of 2 in (51 mm), as shown in Fig. 2-16 were cast in the beams to allow for the Dywidag rods to pass through.

The lead pallets and buckets were attached to the top of the superstructure using 0.5 in (13 mm) diameter A325 bolts. The plans for the anchors in the beams that supported the lead buckets, and the cantilevers that supported the lead pallets are shown in Fig. 2-18. The same lateral design acceleration as for the concrete blocks, which was 2.0 g was used in this design. The anchored bolts were designed according to ACI 318 Appendix D. The bolts were designed to provide sufficient vertical tension to increase the friction between the containers of lead and the concrete beyond the lateral design acceleration. The anchors were designed for tension, and checked for shear. The shear design was checked to determine if it was necessary for the bolts to be fully tensioned. The tension design included concrete breakout strength, tensile strength of the anchors, pull-out strength of the anchors, and concrete side-face blowout strength of the headed anchor. The shear capacity included steel strength in shear, concrete breakout strength in shear, and concrete pry-out strength in shear.

The bolt tension design for the 24 kips (107 kN) of lead pallets that were on the cantilevers, was controlled by the concrete breakout strength in tension. It was conservatively determined that the shear capacity of the bolts provided approximately the 2g resistance as was provided from the tension design. As shown in Fig. 2-19, the bolts at the end of the cantilever had additional reinforcement in the form of u-shaped bars. This reinforcement was provided because the bolts were close to the edge of the concrete.

The bolt design for the 2.55 kip (11.3 kN) lead buckets that were attached to the beam was very conservative. This was because bolts were attached at each of the four corners of the buckets, and for consistency of design, the same 0.5 in (13 mm) diameter bolts were used as for the pallets. The safety factor for the buckets in tension was 4.2 for the design acceleration of 2.0g. The shear capacity of the bolts was sufficient for a lateral acceleration of approximately 14g.

Chapter 3: Specimen Instrumentation and Safety System

3.1 Instrumentation

The shake table model was instrumented with 298 working channels of displacement transducers, accelerometers, and strain gauges. The data were recorded at a rate of 100 Hz using both National Instruments and Pacific Instruments data acquisition systems. Instrumentation plans are shown in Figs. 3-1 through 3-8. Geodetic orientation, which is shown in the figures, is such that the longitudinal axis of the bridge is in the north-south direction. The longitudinal axes of the bents are in the east-west directions. Bent 1 is located at the north end of the model. Table 3-1 lists the number of instruments for each transducer type.

Twelve instruments, internal to the shake tables, were used to measure the achieved response of the tables. Each of the three shake tables had two accelerometers and two displacement transducers to directly measure acceleration and displacement in the north-south and east-west directions. The polarity of the shake table measurements is such that positive measurements are to the east and south directions.

Each type of instrument is discussed in the following sections. All instrumentation except for the internal shake table measurements are included in the instrumentation plans.

3.1.1 Curvature Transducers

Plans for column curvature measurements are shown in Fig. 3-1. Column curvature was measured using TR50 and TR75 Novotechnik displacement transducers having strokes of 2 in (51 mm) and 3 in (76 mm), respectively. The polarity of the transducers was such that extension of the transducers was positive. The transducers were attached to 5/16 in (8 mm) diameter rods embedded into the concrete. The rods were located in pairs on opposing faces of the columns. As shown in the figure, the notation of the curvature instruments is five characters per instrument. The characters are in the following order: bent number, East or West column, Top or Bottom of column, type of measurement (Rotation), and instrument number.

Curvature was measured at both the top and bottom of both columns in each of the three bents in both the transverse and longitudinal directions of the bridge. The curvature transducers were concentrated in the plastic hinge zones over a length equal to the diameter of the columns. The plastic hinge zones were at both the top and bottom of each column because the columns were deformed in double curvature when subjected to lateral deformations. A photograph of a typical column end curvature measurement is shown in Fig. 3-9

Since the primary direction of excitation for the model was in the transverse direction of the bridge, the curvature measurement was more concentrated to capture in-plane bending of the bents. For in-plane bending curvature measurements, the twelve plastic hinge zones had curvature rods located in pairs at two levels, 5 in (127 mm) from the ends, and then 7 in (178 mm) following.

In the longitudinal direction of the bridge, which is the out-of-plane direction of the bents, the curvature was only measured with one pair of rods at 5 in (127 mm) from

each column end. On bent 2, curvature in the out-of-plane curvature was only measured on the east column since bent 2 would be the most unlikely bent to fail during the shake table tests.

The same instruments used to measure curvature were also used to measure uplift of the footings (Fig. 3-1). The uplift was measured for bent 3, the shortest of the bents because the shortest bent would be subjected to the greatest shear. Measurement was taken at the footing-spacer block interface, and at the spacer block-shake table interface. This measurement was important during testing because if the footings were not attached securely to the shake tables, the test results would be altered.

3.1.2 Strain Gauges

The primary purpose of strain gauges was to measure damage progression, and most importantly, to identify when reinforcement in the columns yielded. Reinforcement strains for the columns in the bridge model were measured using 160 YFLA-2-5L strain gauges manufactured by Tokyo Sokki Kenkyujo Co., Ltd. of Japan. The YFLA type of strain gauge is designed for post-yield strain measurement of steel and is accurate for strains of up to 20 percent. Plans for the strain gauge locations are shown in Figs. 3-2 through 3-6. Strains were measured on two types of reinforcement, the #3 longitudinal column bars, and the W2.9 lateral column spiral reinforcement. The strain gauge polarity was such that extension strain was recorded as positive. To avoid damage during construction, all strain gauge wires were covered with plastic tubing and strain gauges were wrapped in vinyl tape (Fig. 3-10).

Notation for the strain gauges (Fig. 3-2) was similar to that for the curvature measurements. Each gauge was identified using six characters, which are in the following order: bent number, East or West column, Top or Bottom of column, Strain measurement, Longitudinal or Transverse reinforcement, and gauge number.

Strain gauges for the longitudinal reinforcement are shown in Figs. 3-2 through 3-4. One-hundred and four working longitudinal gauges were placed at the critical flexural sections of the columns, which were located at the extreme column ends. At each end of the columns, strain was measured at the following three levels: the critical section (column-footing or column-cap beam interface), and at 6 in (152 mm) above and below the critical section. As shown in the figures, the strain gauges for longitudinal reinforcement were more concentrated on the east and west sides of the column sections. This is because the primary direction of shake table excitation was to be in the transverse direction of the bridge. Large amounts of flexural damage were expected in the transverse direction, and longitudinal reinforcement resisting east-west excitation would be subjected to high strains.

Plans for the transverse strain gauges are shown in Figs. 3-5 and 3-6. The purpose of the 56 transverse strain gauges was to measure strain on the lateral reinforcement due to column shear and confinement stresses. Concentration of the gauges was greatest in bent 3, the shortest of the bents, which was subjected to the highest amount of shear. The transverse strain gauges were located at both ends of each column at two 4 in (102 mm) intervals from the column ends. The concentration was near the column ends because the ends of the columns had the greatest confinement

stresses due to bending, and because wide flexural cracks could extend into shear cracks placing relatively high demands on the spirals.

3.1.3 Shear Transducers

Displacement transducers to measure shear deformation were attached to the west column of bent 3 (Fig. 3-6). The transducers were the same NovoTechnik type as those discussed in Section 3.1.1. The transducers were arranged in four 15 x 12 in (381 x 305 mm) panels oriented in the east-west direction (Fig. 3-11) so that column shear deformations could be differentiated from column flexural deformations. The panels were attached to bent-3 because this was the shortest of the three bents and therefore experienced the largest amount of shear deformations.

3.1.4 Superstructure Accelerometers and Displacement Transducers

The superstructure of the bridge model was instrumented with 14 accelerometers and 25 displacement transducers (Figs. 3-7 and 3-8). The accelerometers were Crossbow high sensitivity LF series with a measurement range of plus or minus 2g. The displacement transducers were UniMeasure PA series displacement transducers with a stroke of 40 in (1.02 m). The acceleration and displacement measurements were identified using the following three character notion: Displacement or Acceleration, Transverse, Longitudinal, or Vertical, and instrument number.

Displacements of the superstructure (Fig. 3-7) were measured in the transverse (east-west) and vertical directions at the top of each bent and at each superstructure mid-span. Longitudinal (north-south) superstructure displacements were measured at the four corners at the extreme ends of the superstructure. Vertical bent displacements were also measured at each of the three bents in the form of four transducers on each cap beam measuring from the cap beam to the top of the footing.

Superstructure accelerations (Fig. 3-8) were measured at the top of each of the three bents in both the longitudinal (north-south) and lateral (east-west) directions of the superstructure. At both mid-spans of the superstructure, accelerations were measured in all three orthogonal directions. Vertical acceleration was measured at the end of the superstructure cantilevers in case the cantilevers, which had a large amount of mass, were excited by higher modes in the vertical direction during testing.

While testing was in progress, an additional accelerometer was added to one of the safety frames. The safety frames are discussed in the next section. The accelerometer was used to measure frame vibrations on the center shake table, to see if it had an impact on the table response.

3.2 Safety System

As shown in the renderings of Figs. 2-25 and 2-27, a steel frame safety system was attached to the shake tables beneath the superstructure of the bridge model. The safety system included four steel frames located between the bents within the two main bridge spans. Two frames, identified in this document as type 1 and shown as brown in the renderings, were located next to bents 1 and 3. Two other frames, identified as type 2 in this document, and shown as grey in the renderings, were located next to and on

opposite sides of bent 2, the center bent. This section discusses the design loads and design method for the safety frames.

3.2.1 Design Loads

The purpose of the safety frames was to provide restraint in the transverse (east-west) direction to "catch" the leaning superstructure if and when it collapsed. Because the columns of the bents were designed to fail in flexure, it was highly unlikely that the columns would completely lose vertical load carrying capacity. However the full vertical dead load of the bridge model was included in the design. The lateral design force for the safety frames was based on 1.0 g peak acceleration for the superstructure. This was a conservative estimate of the lateral loading because the preliminary analysis suggested the model would fail under a superstructure lateral acceleration of approximately 0.6 g. The design load for the frames was the combination of a 1.0 g lateral acceleration in either horizontal direction multiplied by the mass of the superstructure, and the superstructure vertical dead load of the bridge model.

The two type 1 frames next to bents 1 and 3 at the ends of the model were each designed considering the dead load tributary to one bent. The smaller type 2 frames that were next to bent 2 were each designed considering half of the dead load tributary to bent 2.

3.2.2 Design of Safety Frames

Safety frames were designed using SAP2000 and the loading discussed in the previous subsection. The frames were constructed utilizing existing frames that were available in the laboratory from past experiments. SAP2000 section designer was used to check the frames considering AISC LRFD specifications (AISC 1993). The automated design checking process included beam, tension, and compression member design. The type 1 frame had sufficient capacity to satisfy the design loads. However, it was determined that the existing type 2 frames for bent 2 had insufficient lateral load carrying capacity. Back to back double angle cross frames were welded to each of the type 2 frames in order to increase lateral load capacity to satisfy the design. As shown in the renderings, braces were also attached to the top of the type 2 frames to tie them together so that they were more stable in the longitudinal direction of the bridge model.

Timber that was slightly longer than the width of the superstructure was attached to the top of each safety frame using silicone glue (Fig. 3-12). The purpose of the timber, which was between 6 and 8 in (152 and 203 mm) thick was to bring the frames close to the bottom of the superstructure. A gap of 3 in (76 mm) was left between the top of the timber beams and the bottom of the superstructure. With this configuration, the superstructure would come in contact with, and rest on the frames if its vertical downward displacement exceeded 3 in (76 mm).

Chapter 4: Selection of Shake Table Motions and Preliminary Analyses

4.1 Introduction

This chapter discusses selection of input motions for the shake table tests and the preliminary analyses of the bridge model. Preliminary analyses were conducted to determine the optimal motions to excite the model as well as to make sure that the parameters of the shake table motion required to fail the model did not exceed the capacity of the shake tables.

Earthquake records used in the experiment were all the modified versions of the motions obtained from the measured Century City station records of the 1994 Northridge, California earthquake. As discussed later in this chapter, the derivations of the motions were conducted as a joint effort between researchers at the University of California, Davis and the University of Washington, who were involved with the SFSI project.

The bridge was subjected to two sets of excitation, low amplitude and high amplitude. The low-amplitude testing consisted of transverse coherent, transverse incoherent, and biaxial shake table motions. Low amplitude tests were conducted prior to high amplitude tests and their peak amplitude was controlled such that the longitudinal reinforcement of the columns did not yield. High amplitude testing was based on a single transverse coherent input motion with amplitudes increasing in subsequent runs from a pre-yield motion until the failure of the first bridge bent. All of the low and high amplitude excitations, except for one low amplitude biaxial test, were in the transverse direction of the bridge frame. This was because the end conditions of the bridge model were not accurately modeled for the longitudinal interaction with the rest of the structure. The main purpose of the shake table experiments was to evaluate bridge frame response in the transverse direction.

Material testing is discussed at the end of this chapter. The material tests were important for two reasons. The first was to make sure that the material properties were in an acceptable range. The second was to determine the constitutive relationships so that the post-test computer modeling would be more accurate.

4.2 Preliminary Analysis Models

Preliminary analyses of the specimen were conducted using SAP2000 (Computers and Structures 2002) and RAM-Perform (RAM International 2003). The SAP2000 model was used for low amplitude analysis where the system could be linear. The RAM-perform model was used for the high amplitude analysis where there was a coherent motion, but the system was highly nonlinear. RAM-Perform was not used for the low amplitude motions because it does not allow for input of different support excitations. The results from the two models were compared using low amplitude coherent motions to make sure that they were consistent and did not contain any apparent errors.

Analysis of the specimen prior to testing was conducted for two reasons. The first was to choose which amplitudes to use as input for the shake tables. The second was to ensure that the shake tables were capable of producing the amplitudes of the motions, and

that the demand would not exceed the capacity of the tables. The capacity of the tables was only an issue for the high amplitude testing.

4.2.1 SAP2000 v8

The SAP2000 model (CSI 2002) that was used for the pre-test analysis of low amplitude testing was the same as the computer model that was discussed in Sec. 2.5.7 for post-tension design. The reason that SAP2000 was used instead of RAM-Perform for the low amplitude analysis was because the low amplitude tests included incoherent multiple support excitation. At the time of this study, SAP2000 was capable of this type of analysis, whereas RAM-Perform was not.

The model was defined using linear beam column elements. Gross section properties were used for all of the elements except for the columns. The column elements were assumed to be cracked. The cracked moment of inertia for the columns was calculated using the slope of the elasto-plastic idealized moment-curvature relationship obtained from program RCMC analysis (Wehbe and Saiidi 2003). The calculated moment-curvature relationship and idealization are shown in Fig. 4-1. The resulting cracked moment of inertia was 33% of the gross moment of inertia.

SAP2000 was not used for the nonlinear pre-test analysis because the nonlinear biaxial moment-rotation hinge element in RAM-Perform was better suited to model reinforced concrete. For nonlinear models of reinforced concrete, accurately modeling the hysteretic relationship is important because when the system is highly nonlinear most of the damping is hysteretic. Unlike the RAM-Perform biaxial hinge element, the SAP2000 biaxial hinge element does not include a parameter to describe the unloading stiffness. In SAP2000, the unloading stiffness is assumed to be the same as the loading stiffness. The use of fiber elements to model plastic hinges would have alleviated this problem since a "correct" unloading stiffness is implicitly included in a fiber model. However, fiber models for the column nonlinearity were not used for this model because the version of SAP2000 that has the capability of fiber section modeling (version 9 and later) was not yet released. Nonlinear analysis using SAP2000 version 9 with fiber models is discussed in Chapter 7. Analytical results from the SAP2000 analyses for low amplitude testing are discussed in Section 4.4.

4.2.2 RAM-Perform

The nonlinear RAM-Perform model used for pre-test analysis of the high amplitude motions was generally the same as the nonlinear RAM-Perform model used for the post-tension design that was discussed in Sec. 2.5.7. The major difference between the two models was a modification to the hysteretic relationship for the nonlinear elasto-plastic column hinges, which is discussed subsequently.

In addition to the beam elements that were discussed for the linear SAP2000 model in the previous section, the RAM-Perform model included nonlinear plastic hinge elements at the column ends. The nonlinear hinge elements utilized the same moment-curvature analysis that was discussed in Section 4.2.1 for the cracked beams of the SAP2000 model, except axial load interaction was included. Therefore a complete set of moment-curvature relationships was required. Biaxial interaction was also defined so that the element considered the interactions of axial load and bending about both axes of

the column sections. This is known as a P-M-M hinge. Plastic hinge rotations were obtained using the calculated curvatures and the plastic hinge length equation by Paulay and Priestley (1996), which defines an empirical plastic hinge length as a function of column height and diameter of longitudinal bars.

4.2.2.1 Hysteretic Relationship for M-θ Hinges

The RAM-Perform nonlinear column hinge model that was used to determine forces for the superstructure design, discussed in Sec. 2.5.7, did not include any stiffness degradation for the unloading slope. Instead, the unloading slope matched the loading slope, which created a hysteretic relationship in the shape of a parallelogram. An example of this is shown in Fig. 4-2 labeled "elasto-plastic". In order for the pre-test analysis model to be more accurate, the unloading slope of the hinge was modified to create a more realistic amount of hysteretic energy dissipation.

In RAM-Perform, the method to specify hysteretic energy dissipation for the P-M-M hinge, including effects of unloading stiffness degradation, is to directly specify an area modification to the hysteresis loop. The program implements the modification through a reduction in the unloading stiffness. The hysteresis area modification is specified by a degradation coefficient, which is equal to the modified area divided by the original area of the loop. The degradation coefficient becomes effective after a specified rotation of the element is reached. Multiple coefficient-rotation pairs can be specified so that as the amount of damage increases, the degree of degradation increases.

The degradation coefficients in the analysis model were specified to match the hysteretic energy within a loop of the Q-hyst model (Saiidi 1982). The Q-hyst model is a realistic reinforced concrete hysteresis model that takes stiffness degradation effects into account. Degradation coefficients were calculated for each of the three two column bents by calculating the area inside of the Q-hyst loop and dividing it by that of an elasto-plastic loop without stiffness degradation. An example of this comparison is shown in Fig. 4-2. The hinge rotation and corresponding coefficient were calculated and were input to the RAM-Perform model at four different ductility values for each bent, 1.5, 2, 4, and 10. The degradation coefficients were approximately 0.89, 0.65, 0.5, and 0.47, at the four ductility values, respectively.

4.2.3 Modal Shapes of Superstructure

In order to have a better understanding of how the bridge specimen would respond to shake table motions, the elastic modal shapes and periods were calculated. This allowed for the comparison of response spectra to easily determine the effect of different motions on the bridge. Because the primary excitation of the bridge was to be in the transverse direction, and in the transverse direction the bridge was unsymmetrical, the transverse modes were viewed as the most important modes. Modal properties were calculated using both the RAM-Perform and the SAP2000 models using cracked column properties and including column reinforcement bond slip. The results were consistent between the two computer models.

The calculated superstructure modal shapes in the transverse direction of the bridge are shown in Fig. 4-3. Modal mass participation factors for the mass in each direction and periods for the first 6 modes are listed in Table 4-1. Mass participation can

be used to determine the contribution of each mode to the response. Only the first six modes are listed because as shown in the table, six modes are sufficient to define 99.9 percent of both the longitudinal and transverse modal response.

As shown in Fig. 4-3, the transverse elastic response of the superstructure is composed of 3 mode shapes, modes 2, 3, and 6. Mode 2, at the top of the figure shows the primary transverse mode, which has a period of 0.40 seconds and mass participation factor of 0.819. This mode is primarily superstructure translation with slight in plane rotation and a peak amplitude at bent 1, which is the medium height bent. Mode 3, the mode shape in the center of the figure, is the second transverse mode, which has a period of 0.30 seconds and a participation factor of 0.180. This mode is primarily in-plane rotation of the superstructure with slight translation and a peak amplitude at bent 3, the shortest of the bents. The third transverse mode, shown in the bottom plot of the figure, has a period of 0.08 seconds and a mass participation factor of 0.001. This mode is superstructure bending in the transverse direction. The third transverse mode is included in the figure for completeness. Because the superstructure is very stiff in comparison to the substructure, the third transverse mode plays very little role in the transverse displacement response of the bridge model.

The longitudinal elastic response of the bridge is dominated by the first mode, which has a period of 0.41 seconds and mass participation of 0.819. This mode is from the combined lateral stiffness of the columns in the longitudinal direction of the bridge.

4.2.4 Pushover Analyses

Pushover analysis was required to help estimate how much excitation the shake tables would need to provide to fail the bridge bents. The predicted load-deflection relationships for the three two-column bents are shown in Fig. 4-4. Table 4-2 lists a summary of the results that are shown in the figure.

The analyses were conducted using the same SAP2000 and RAM-Perform models that were discussed in Sec. 4.2.1 and 4.2.2. Lateral deflections of the columns included flexure, reinforcement bond slip, and shear (Wehbe et. al. 1997). The columns were assumed to be cracked in both flexure and in shear. The post-yield deflection was calculated considering rigid body rotation at the column ends. The rotation was calculated according to the Priestley plastic hinge length (Priestley 1997), and the Mander model for confined concrete in compression (Mander 1988).

Typically, failure is assumed to occur when the confined concrete at the extreme compression fiber of the core concrete reaches the ultimate concrete compressive strain. To be conservative and to ensure that the displacement capacity of the columns would not be greater than expected, the rotation at the point where the concrete failed in compression was multiplied by a factor of 2. It was important not to underestimate the failure deformation of the columns because a major portion of pre-test analysis was to make sure that the columns could be excited to failure.

4.3 Input Motions

The motions that were used for the shake table tests were calculated based on the 1994 Northridge earthquake as recorded from the ground station at the Century City Country Club North. The Century City station is owned by the California Strong Motion

Instrumentation Program, and is located at 34.063 Latitude, -118.418 Longitude. Both the 90 degree and 360 degree lateral components were used. Throughout this paper, the two components are referenced as motion 1 and motion 2, respectively. The calculation of the motions was a joint effort between researchers from the University of California at Davis and the University of Washington (Shin et. al 2006) as part of the collaborative SFSI project (Wood et. al. 2006). The main purpose of the calculated motions was to provide excitation that would be consistent for both the shake table tests at the University of Nevada, Reno, and the centrifuge tests that were conducted at UC Davis. The general method is discussed below.

The calculation was a two step process that was conducted in prototype scale. The initial motion recorded at location (1) in Fig. 4-5, was the original Century City recorded acceleration history. Program ProShake (EduPro 1999) was used to transfer the original motions from the top of the soil down to an assumed bedrock location at a depth of 91.2 ft (27.8 m) of soil. The soil type was a medium-dense Nevada sand. The bedrock acceleration history of motion 1 and motion 2 were used as the starting point for the calculation of all of the motions that were used in the shake table tests. Program OpenSees (Opensees 2002), an open source finite element program, was then used to propagate the calculated bedrock motion up to the level of the point of fixity in the piles (taken the same as the base of the columns in the shake table specimen). The motion was propagated through the same soil type that was used to calculate the bedrock motion. As discussed in Section 2.2, the length of the pile from the top of the soil down to the point of fixity in the pile was assumed to be 2 times the diameter of the columns. The location of the final motion at the pile point of fixity is shown as (4) in the figure. Because of soil structure interaction, the motion of the pile at this location was slightly different than the motion of the adjacent soil. However, as discussed in Section 4.3.1, this difference was negligible. Therefore, it was the soil motions that were used in the shake table tests (and other studies of the SFSI project).

Two parameters were varied for the OpenSees calculation of the motions, the peak ground acceleration of the bedrock excitation, and the depth of soil from bedrock to the point of column fixity. The depth of the soil was denoted in terms of the constant "d", which was 87.2 ft (26.6 m) (the total soil depth, less two times the pile diameter). The parameters were both fixed values for the high amplitude tests. For the low amplitude tests, the bedrock peak ground acceleration was scaled to a constant value and the depth to bedrock was varied. Details of the depth and bedrock acceleration amplitude parameters for the low and high amplitude tests are discussed in sections 4.4 and 4.5, respectively.

4.3.1 In-Situ vs. Free field response

The calculated pile level motions were determined for both the in-situ response and the free field response (Shin et. al. 2006). Soil in the OpenSees model was nonlinear but the piles were assumed to remain elastic. The motion at the pile included the interaction of the pile and soil. The free-field response (the motion at the adjacent soil) did not include the effect of the pile, and the interaction between pile and soil was ignored. A comparison of the motions showed that for the pile and soil configuration considered, there was not a significant difference between the pile and the free-field

motions. Therefore the free-field motions were used in both the high and low amplitude shake table tests.

4.4 Low Amplitude Tests

The low amplitude tests were a series of tests that included transverse coherent, transverse incoherent, and biaxial shake table motions. In addition, the achieved centrifuge motions from the UC Davis tests (Shin et. al. 2006) were applied so that the centrifuge and shake table tests could be better correlated. Motions were applied to the bridge so that the calculated maximum moment in each of the columns remained below seventy-five percent of the moment from moment-curvature analysis where extreme longitudinal column reinforcement yielding was initiated. This moment was equal to approximately half of the effective column yield moment from the moment curvature analysis that was discussed in Chapter 2. Adjustment of the amplitude of the calculated earthquake motions so that their demand would remain below the allowable moment in the columns was made by changing the amplitude of the excitation motion at bedrock. The reason that care was taken to make sure that the longitudinal reinforcement of the columns did not yield was because for the high amplitude tests, it was desired to have a system with essentially no damage so that the complete system response up to failure could be captured.

Table 4-3 lists the shake table input motions for each of the low-amplitude tests. Bedrock excitation for all of the motions that were applied to the transverse direction of the bridge model was from the calculated bedrock excitation of motion 1, which was discussed in the beginning of this section. Motion 1 was used in the transverse direction to be consistent with the high amplitude tests that are discussed in section 4.5.

The analyses to determine the amplitude of bedrock excitation were conducted using the elastic SAP2000 model that was discussed in 4.2.1. To keep the estimated column moments below seventy-five percent of the first yield moment, the peak acceleration of the bedrock excitation was limited to 0.06 g for all of the low-amplitude motions. The three types of low amplitude tests, transverse coherent, transverse incoherent, and biaxial, are discussed in the following subsections. Section 4.4.4 presents the target response spectra and histories for the motions. More details about the test schedule are discussed at the end of the next chapter.

4.4.1 Transverse Coherent and Incoherent motions

A significant portion of the low amplitude testing on the shake tables was devoted to subjecting the model to differential excitation beneath the three bents. Differential motions at bridge foundations are known to be caused by three different phenomena (Yang et. al 2002): the incoherency of the earthquake waves, the wave passage, and the local site conditions. For the prototype bridge in this study, the distance from one end of the bridge frame to the other was not significant enough to consider the wave passage effect. The incoherency of the earthquake waves was also ignored. The only source of incoherency used in the analysis was hence the site characteristics beneath each bent. For consistency with the high amplitude tests and other experimental studies that were part of the SFSI project, the soil type was assumed to be the same beneath all foundations.

However, the depth of soil from the point of column fixity to the bedrock was varied in each run to achieve incoherent motions.

The variation of bedrock depths needed to consider a wide variability of configurations, and at the same time, the number of test runs needed to be relatively small to avoid accumulation of damage in the bridge model during low-amplitude runs. Two different methodologies were considered for the variability of soil depth to bedrock beneath each bent. In the following paragraphs, both methodologies are described. However, the second methodology was chosen for the shake table tests because it contained a consistent variable of average bedrock depth beneath the column fixity.

The first methodology consisted of two different sets (Fig. 4-6). In each set, one of the bents at the end of the bridge was directly connected to the bedrock and soil depth beneath the foundation point of fixity increased linearly toward the other two bents. Essentially, one of the end bents was fixed to bedrock and the slope of the soil depth beneath the other bents was pivoted about that bent. The multiple cases in the figure, numbered 1 through 14 were at an increasing depth which ranged from all of the bents on bedrock, to one bent on bedrock and the end bent having a large depth of soil beneath it. Although it is not realistic for a pile foundation to be directly on bedrock at its point of fixity, this was included so that the extreme case of a zero soil depth to bedrock could be represented. In order to keep the amount of experimental runs to a minimum, select cases from each of the two sets would have been chosen.

The second methodology of bedrock depth variation, which was chosen for the low amplitude shake table tests, is shown in Fig. 4-7 and listed in Table 4-3. For this pattern, the average soil depth beneath each bent from the pile point of fixity to the bedrock was held constant. The constant depth was chosen to be "d/3", which is based on the variable d, discussed in section 4.3. Six different combinations of depths beneath the bents were included. The first was a depth of d/3 beneath each of the three columns. This was a benchmark configuration and was considered to have zero incoherency. Cases 2 and 3 in the figure are similar to the first methodology. Each of the end bents for cases 2 and 3 was directly on bedrock (outcrop motion), with the middle bent and bent at the opposite end of the frame having soil depths of d/3 and 2d/3, respectively. For cases 4, 5, and 6, two of the bents had soil depths of d/2 and the other bent was directly on bedrock. The bent on bedrock was bent 1, bent 2, and bent 3, for cases 4, 5, and 6, respectively. So that the motions resulting from the bedrock depth configurations and motion 1 excitation at the bedrock did not overstress the columns, the bedrock record resulting from motion 1 was scaled to a PGA of 0.06g before the propagated motions were calculated.

4.4.2 Biaxial Coherent Motions

One set of low amplitude biaxial motions was applied to the bridge model (Table 4-3). To be consistent with the transverse incoherent motions, the depth to bedrock was set to be d/3. Because the target biaxial excitation was coherent, this value was constant beneath all of the bents. Also for consistency, a bedrock excitation from motion 1 was applied in the transverse direction, and excitation from motion 2 was applied in the longitudinal direction. Motions 1 and 2 were used for biaxial excitation because these motions were actually recorded as biaxial motions. Similarly to the incoherent motions

discussed in the previous subsection, to make sure that the columns were not overstressed, the bedrock excitation was scaled to 0.06g.

4.4.3 Centrifuge motions

Centrifuge tests that were conducted at UC Davis (Shin et. al. 2006) were based on the same prototype as that of the shake table tests. The centrifuge model was 1/52 scale and included both the piles beneath the bents, and the surrounding soil. The columns and piles were composed of aluminum tubing that matched the scaled moments of inertia and moment capacity of the prototype. The soil was medium-dense Nevada sand, which was the same type of soil that was used to calculate the propagated motions for the shake table tests. In order for researchers UC Davis to have better correlation between the shake table tests and the centrifuge tests, the achieved centrifuge motions were included as two runs in the low amplitude shake table testing. The centrifuge test was for a motion 1 with the target peak amplitude scaled to 0.1 g applied uniformly to the centrifuge bridge model in the transverse direction. The achieved motions from each of the three bents in the centrifuge model were input to the corresponding bent on the shake table. Two sets of motions were considered, the motions that were measured at the pile points of fixity, and the motions that were measured in the soil free field adjacent to the point of pile fixity. In order for the column moments to remain below that of the first yield, the achieved centrifuge motions were multiplied by a factor of one-half before being applied to the model.

4.4.4 Input Acceleration Histories and Response Spectra

Acceleration response spectra and acceleration and displacement histories of the shake table target motions were calculated and plotted for each low amplitude test. The time axis of the prototype motions were compressed by a factor of 2 for the bridge specimen to account for the quarter scale of the bridge specimen. After the time compression, each record was 20 seconds long. The response spectra were calculated for 5 percent damping. The spectra used along with the elastic transverse modes of the bridge were utilized both to evaluate the motions before testing, as well as to understand the excitation as the testing progressed. The displacement and acceleration histories were used as input to the computer models to calculate the bridge response, and to evaluate the incoherency among the motions. This section presents the spectra and histories of the motions for the transverse coherent and incoherent, biaxial, and centrifuge low amplitude tests that are listed in Table 4-3.

The spectra for the four different target motions of the incoherent tests 1 through 8 in Table 4-3 are shown in Fig. 4-8 Superimposed on the spectra are the three calculated vibration periods that contribute to the transverse response. The spectrum labeled “outcrop motion” is for the 0.06g bedrock excitation. It is shown that the 0.33d motion has the greatest spectral acceleration response. As the soil depth increases to 0.5d and 0.66d, the peak spectral acceleration is reduced and shifted toward longer period response. The acceleration and displacement histories for the four target motions of the incoherent tests are shown in Figs. 4-9 through 4-12, and 4-13, respectively. The displacements of the four motions are very similar in both amplitude and in frequency. However, the acceleration records and the response spectra show that the accelerations of

the four motions are very different. Because the displacements are similar and the accelerations are different, most of the incoherent response for multiple support excitations would come from the dynamic acceleration response and not the pseudo-static response from differential displacements.

The target response spectra for the two motions of the biaxial tests are shown in Figure 4-14. Motion 1 and motion 2 were propagated through a 0.33d depth of soil starting with a bedrock PGA of 0.06g. Motion 1 was applied in the transverse direction of the bridge and motion 2 was applied in the longitudinal direction. The acceleration history of the 0.33d motion 1 record was already discussed for the incoherent motions, and is shown in Fig. 4-10. The acceleration history for the 0.33d motion 2 record is shown in Fig. 4-15. The displacement histories of both records are superimposed in Fig. 4-16. It can be seen that the motions are very similar and have comparable frequency content. However, the 0.33d motion 1 record, which was applied in the transverse direction of the bridge, had a slightly greater amplitude.

Centrifuge motions that were applied to the bridge were from two sets of measured centrifuge motions: the measured centrifuge soil motions and the measured pile motions. Figures 4-17 and 4-18 show the response spectra for each of these two sets of motions with the transverse modes of the bridge superimposed. The time axis of the achieved centrifuge motions was amplified to account for the scale effect. Figures 4-19 through 4-21 and 4-22 through 4-24 show the acceleration histories of bents 1 through 3 for the soil and pile motions, respectively. The three bent motions within each set of spectra are slightly different from each other. Also, each set of motions while having similar amplitudes and frequencies are slightly different. The entire test apparatus from the centrifuge tests was excited with the same motion. However, there are differences in the motions at and near each bent as well as from bent to bent because within the centrifuge soil box that contained the bridge model and soil, the soil deformed, the model deformed, and there was soil-structure interaction. The displacement histories of the three bents for the soil and pile motions are shown in Figs. 4-25 and 4-26, respectively. Displacement histories of the three bents within each set and between the two sets of motions are comparable throughout, showing that the target motions for the shake tables had relatively small amounts of differential displacement.

4.5 High Amplitude Tests

The high amplitude shake table tests were conducted upon completion of the low amplitude “pre-yield” shake table tests. The purpose of the high amplitude testing was to excite the bridge in the transverse direction until failure. In order to capture the bridge response from initial yielding of reinforcement through column failure, a motion was applied to the bridge at low amplitude and was scaled up for the successive tests until failure. Unidirectional coherent excitation was used because the end conditions of the model were such that longitudinal response would only be accurate up to closure of the scaled prototype hinge gap. Although the transverse response of the bridge was coupled, which created some response in the longitudinal direction of the bridge under transverse excitation, this response was not expected to exceed the gap width of a typical hinge. The hinges and the bridge boundary conditions in the longitudinal direction were not modeled in this study because this test was the first time a concrete bridge of this

magnitude was shaken to failure on shake tables and the model had to be kept reasonably simple.

The schedule of motions that were used for the high amplitude tests is shown in Table 4-4. A complete schedule including all tests is discussed at the end of the next chapter. The motion that was chosen was derived from the motion 1 bedrock excitation scaled to 0.4 g and propagated through a depth of "d" from the bedrock to the pile point of fixity. A bedrock excitation of 0.4g was used because it is representative of the average high amplitude motion that was to be applied to the bridge, and is relatively close to the amplitude of bedrock excitation derived from the measured Century City motion. The motion 1 record was scaled by its peak acceleration and applied in sequential tests of increasing amplitude with PGA from 0.075 g to 1.66 g. The method that was used to choose motion 1 and the scaling of PGA in the sequential tests is described in Section 4.6.

4.5.1 Input Acceleration Histories and Response Spectra

The target motions for each high amplitude test were the same for all three shake tables. For successive tests, the same motion was used, but was scaled by the peak ground acceleration. The 5 percent damping response spectra for the tests ranging from target PGA of 0.075 to 0.50 g are shown in Fig. 4-27. Figure 4-28 shows the response spectra for the tests ranging from PGA of 0.75 to 1.66 g. The three calculated elastic transverse modes of the bridge are superimposed on the spectra. The period for the second transverse mode is approximately the same as the period at the large peak in the spectra. Although the modes would shift as testing progressed and damage increased in the bridge, the high spectral acceleration at this mode lends to the idea that the second mode would have a major contribution, especially within the elastic range of the bridge. It was to be expected that during testing the periods of the first and second transverse modes would lengthen due to damage in the bents. Because the spectral acceleration is reduced at periods exceeding approximately 0.4 seconds, the lengthening of the periods of the bridge would reduce the demand on the bridge model.

The acceleration and displacement histories of the input motions are shown in Fig. 4-29 and 4-30, respectively. The peak accelerations in the eight consecutive motions shown in Fig. 4-29 range from 0.075 to 1.66 g. The target peak acceleration and displacement of the final 1.66 g run are approximately 22 times greater than that of the first high amplitude run with PGA of 0.075 g, and 3.5 times greater than the original calculated motion.

4.6 High Amplitude Motion Demand

For high amplitude tests, the nonlinear RAM-Perform analysis model that was discussed in 4.2.2 served two purposes; the first was to determine the response of the bridge model in order to choose which motion to use during testing. The second was to calculate the demands on the shake table. Both motion 1 and motion 2 having a bedrock PGA of 0.4g and depth equal to "d" were considered for the high amplitude tests. The motion that was chosen for testing was the one that would provide the most demand on the bridge model and remain within the limits of the shake tables. Because selecting the motion depended on the bridge model response and demands on the shake tables and

because the shake table response depended on the motion, many trial runs were attempted while planning the testing program. A spreadsheet was developed to determine the capacity-demand ratios for different shake table parameters and the displacement of the bridge model.

4.6.1 High Amplitude Response

To choose the motion for the high amplitude tests, motion 1 and motion 2 were applied to the computer model. The motions were scaled by PGA as they would be in the tests, and successive motions were analyzed considering the state of the model at the end of the previous motion. Table 4-5 lists the transverse displacement ductility demands for the bents for motion 1 and motion 2. Table 4-6 lists the transverse displacement demand divided by the calculated ultimate displacement capacity.

The yield displacements and ultimate displacement capacities used to calculate the values in the tables were both those from the pushover analyses discussed in section 4.2.4. The ultimate displacement capacity was conservatively high because the plastic rotation capacity was doubled as discussed in 4.3.4. The conservatism was important because it was the goal to be able to make sure that the shake tables would be able to fail the model with the same motion throughout high amplitude testing. If it were discovered during the pre-test analysis phase that the tables could not fail the model with the motion that was being considered, then a more demanding motion would have been selected for all of the high amplitude tests, or the specimen design would have been changed. Changing motions during high amplitude testing would be undesirable because the experiment would not have been consistent.

As shown in the tables, two other motions were used in the analyses as benchmarks, the 90 degree component of the Sylmar Hospital parking lot record from the 1994 Northridge earthquake, and the El-Centro record from the 1940 El Centro earthquake. These motions were included in the analysis as benchmarks because they have been used extensively in structural research as well as on the University of Nevada, Reno shake tables. The 1.5 g analyses for the Sylmar and El-Centro motions are not included in the tables because the computer model became unstable and would not converge during part of the analysis.

It was determined that excitation calculated from motion 1 with a 0.4 g bedrock excitation with PGA of 1.5 g would be able to fail the model. As shown in the tables, for motion 1 scaled to 1.0 g, bent-1 was predicted to reach a displacement ductility of approximately 10, which was 95 percent of the calculated ultimate displacement. Also at the 1 g motion, bents 1 and 3 were predicted to reach 40 and 62 percent of their ultimate displacement capacity, respectively. The bridge model was predicted to fail somewhere between the amplitude of 1.0 g and 1.5 g for motion 1.

Analyses showed that motion 2 and a 0.4 g bedrock excitation would not be able to fail the bridge model even for a scaled PGA of 1.5 g. When subjected to a 1.5g scaled version of the motion, the analysis predicted that the bent closest to failure would be bent-1, which had a displacement demand of 83 percent of the capacity. Analysis also showed that neither the Sylmar nor the El-Centro motion would be able to fail the model with a 1.5 g PGA.

Because motion 1 was the most demanding motion on the bridge model while placing the least demand on the shake tables (discussed in the next section) for the amount of specimen response, it was chosen for the high amplitude testing (Table 4-5). Although the preliminary test schedule reflected the same maximum PGA of 1.5 g as these analyses, the final schedule, which was modified during testing, was updated, replacing the 1.5 g motion with a 1.66 g motion. The amplitude modification was applied to make sure that the model would reach failure. Also, the actual test schedule contained additional motions having amplitudes between the motions in the analysis so that there was a finer gradation of the high amplitude tests. These additional tests were to ensure that the full range of response of the bridge would be captured. A more thorough discussion of the complete test schedule is discussed at the end of the next chapter.

4.6.2 Shake Table Demands

The demands of the bridge specimen on the shake table for given input motions needed to be estimated to ensure that the shake tables could fail the bridge. The demands on the shake tables were calculated with the use of column moments, axial loads, and shear forces obtained from the RAM-Perform model, combined with the known properties of the specimen, motions, and tables. The limits on the parameters of each shake table, which were discussed in Chapter 2, are listed in Table 2-1. The parameters that are included in Table 2-1 are the table displacement, velocity, acceleration, the maximum pitch, yaw, and roll moments, the mass, and the actuator force. Many of these parameters are directly or indirectly related to each other. Therefore, a spreadsheet was required to calculate the demands. The ratio of the capacity and demand was designated as the "safety factor" for each parameter. The safety factors for each of the limits (Tables 4-7 through 4-11) were calculated for the bridge system and for both motion 1 and motion 2 at the same scaled accelerations as the analyses in the previous section.

Table 4-7 shows the specimen weight that was tributary to the shake tables for each of the three bents compared to the payload limit of each table. The specimen weight includes the weight of the superstructure as well as the bents. The weight limits of the shake table are based on shake table actuator force limit and the shake table bearings. However, the shake table bearing limit was satisfied by the combination of checks for pitch and roll moments which were conservative because the limits in Table 2-1 are for maximum pitch and yaw achieved simultaneously. Because the shake table does not see the entire tributary weight of each bent for actuator capacity, only the weight of the footings and blocks combined with whatever shear force is in the column, the safety factor for specimen weight was not included in the summary of Table 4-12.

The safety factors for yaw moment (moment about the vertical axis of the table) are listed in Table 4-8. Yaw moment evaluation was independent of the motion of the shake tables. As discussed in Chapter 2, the yaw moment for each bent was calculated as the maximum torsional moment that could be imposed from the couple created by the plastic shear vectors of the two columns in each bent. The minimum safety factor for yaw moment on the three tables was for the shortest bent (bent 3), and was 3.0.

Table 4-9 lists the pitch moment demand for each table. Pitch moment is bending about the horizontal table axis that is perpendicular to the primary direction of the bridge excitation. Pitch moment at the centerline of the top of each shake table for each run was

calculated by adding the transverse moments at the base of the columns, to the moment from the shear of the columns about the table centerline, to the moment from footing mass acceleration about the table centerline, to the calculated overturning of each bent. The minimum safety factor for the pitch moment using motion 1 was 1.04, which was for the 1.5 g scaled motion. Motion 2 was more demanding for pitch moment having a safety factor of only 0.89 for the 1.5 g motion. The roll moment (moment about the axis of the shake table running parallel to longitudinal axis of the bridge model) was assumed to be negligible because the bridge was not explicitly excited in the longitudinal direction under the high amplitude motions.

Displacement and velocity demands of the two motions compared with the capacities of the tables are listed in Table 4-10. These demands directly depend on the motions and analysis of the specimen was not required. Velocity was the controlling factor for both motion 1 and motion 2. For the 1.5 g scaled motions, the safety factors were 1.2 for motion 1 and 0.96 for motion 2.

The maximum table actuator force demands compared to the capacity are listed in Table 4-11. The calculation of actuator force for each run considered the mass of the shake table and footings multiplied by the table acceleration and added to the shear force of the columns. This calculation was conservative because the acceleration that was used was the maximum acceleration of the motions and the shear was the maximum column shear from the RAM-Perform analyses. These maximums would not necessarily be concurrent. As shown in the table, motion 1 is generally a more demanding motion with respect to the actuator force. The minimum safety factor of actuator force for the 1.5 g motion was 0.86 for bent 3.

Table 4-12 presents a summary of the controlling calculated safety factors of the shake tables for each run as well as the values of calculated displacement ductility for each bent. As shown in the table, the safety factors are slightly lower for motion 1 than for motion 2. However, the ductility demands of motion 1 are substantially greater than those of motion 2. In general, motion 1 provides a greater demand than motion 2 on the bents for the amount of shake table capacity that is required. The minimum safety factor of the shake tables for motion 1 scaled to 1.5 g is 0.86 for bent 3, and is controlled by actuator force. This was not a significant issue for two reasons. The first is that the analysis suggested that the required amplitude of motion 1 to fail bent 3 was between 1.0 and 1.5 g. The second is that the calculated ultimate displacement required to fail the bent was a conservatively high value.

4.7 Material Tests/Properties

Testing of the materials for the bridge served two purposes. The first was to make sure that the concrete and reinforcement had properties that satisfied the design and reflected the properties of the prototype bridge. The second was to be able to use the measured constitutive relationships in the post-test analytical modeling. Testing was conducted for all concrete in the model and for both types of column reinforcement.

4.7.1 Concrete

The concrete had a 3/8 in (9.5 mm) maximum aggregate size and was rated for an unconfined compressive strength of 5000 psi (34.5 MPa). Concrete was ordered with a

specified 28 day compressive strength of 5000 psi (34.5 MPa), expecting a cured strength ranging from 4500 psi (31.0 MPa) to 6000 psi (41.4 MPa) from past experience with the supplier. The small aggregate size was required because of reinforcement congestion and small cover that was a result of scaling. Table 4-13 lists the test data for the concrete from each pour. There were five different pours: footings, columns, superstructure beams, spacer blocks, and cap beams. Standard 6 x 12 in (150 x 300 mm) cylinder compressive strength was measured at 7 days, 28 days, and at the end of the shake table tests. Only one set of cylinders was tested at the time of the shake table experiments because the duration of testing was relatively short compared to the life of the concrete. Strength of the column concrete was most important because of its effect on bridge stiffness and strength. The measured unconfined compressive strength of the concrete used in the columns at the end of shake table testing was 5900 psi (40.7 MPa). The unconfined concrete compressive strength for the cap beams, spacer blocks, beams and footings ranged from 4800 psi (33.1 MPa) for the footings, to 7200 psi (49.6 MPa) for the superstructure beams.

4.7.2 Steel

Tensile testing was conducted for both the lateral W2.9 spiral wire reinforcement and the longitudinal #3 bar reinforcement in the columns. Grade 60 bar was used throughout the bridge model. The W2.9 wire used in the columns was the same batch of Bright Basic wire that was used in both the quarter-scale in-situ two-column bent tests at University of Texas, Austin, and the quarter-scale column component tests at Purdue University.

Figures 4-31 and 4-32 show the measured stress-strain curves for two of the wire tests. Yield stress for all reinforcement tests was determined using the 0.2 percent offset method. The average measured yield stress of the wire was 67 ksi (462 MPa) and the average ultimate stress was 80 ksi (552 MPa). The measured elastic modulus was approximately 27600 ksi (190000 MPa). Prior to the results shown in the figures, another set of wire tests was conducted. It was determined from those tests that accurate strain could not be measured by using the frame displacement of the test machine because of a slight curvature in the wire. For the stress-strain curves shown in the figure, the strain was measured as the average strain of two strain gauges that were placed on opposite sides of the wire. The average of the data from the two opposite gauges excluded bending strains.

Tensile test results for the #3 rebar are shown in Figs. 4-33 through 4-36. Figures 4-33 through 4-35 show the stress-strain curves for three tests that were conducted. Figure 4-36 shows the average of the three measured curves. The average stress-strain curve was calculated by averaging each of the measured stress-strain points along the three measured curves. For the pre-yield portion of the curve, the elastic modulus was assumed to be 29000 ksi (200000 MPa). The average yield and ultimate strength for the #3 bar was 66.5 ksi (459 MPa) and 97 ksi (669 MPa), respectively. It can be seen in the curves that there was not a yield plateau for the column reinforcement.

Chapter 5: Construction of Test Model and Testing Protocol

5.1 Introduction

This chapter describes the construction and assembly of the bridge specimen (Section 5.2) including discussion of issues for each components construction, the schedule of time spent on the shake tables, and details of the assembly stages. Also in this chapter, the final test protocol is discussed (Section 5.3) including changes that were made to the test schedule as the testing progressed.

5.2 Construction and Assembly

This section describes the construction and assembly of the bridge. The schedule of use of the shake tables is presented in Section 5.2.1. Construction is described in Section 5.2.2. The bridge was constructed as 11 structural components, both on and off-site of the laboratory at University of Nevada, Reno. Because of the magnitude of the project, manufacturing of the components was contracted out to a construction company but was guided by UNR staff. Photos in Figs. 5-1 through 5-20 show different stages of construction of the components.

Stability of the bents, which was an important issue during both the construction and the assembly stage, is discussed in Section 5.2.3. Section 5.2.4 discusses assembly of the bridge. All the components were assembled on the shake tables, and the bridge was prepared for testing. Because of the complexity and care that was involved in the assembly of the bridge, complete assembly was carried out by UNR staff. Figures 5-23 through 5-42 show assembly of the bridge on the shake tables.

5.2.1 Schedule

The schedule of events on the shake tables is listed in Table 5-1. The duration of the shake table usage, beginning with table preparation and ending with the completion of disassembling the model and cleaning off the tables, was the 73 days from December 13, 2004 to February 23, 2005. The schedule includes table preparation, assembly of the bridge on the tables, attaching instrumentation, both low and high amplitude testing, disassembly of the bridge, and cleaning the shake tables. Time on the tables is an important aspect of shake table testing, especially when testing on multiple shake tables. This is because there is a high demand for use of the tables both singly and in combination for a multitude of projects, and time is limited. This is the first test of a complete concrete bridge frame on multiple shake tables. This section documents all the necessary steps in constructing a large-scale bridge model. The material in this section could help improve the efficiency of testing and streamlining future projects.

5.2.2 Construction of Components

The bridge model was composed of 11 major structural components: six superstructure beams, three two-column bents, and two footing spacer blocks. Design of the components was discussed in Chapter 2. Because of the size of the project and to insure that the craftsmanship would be of sufficient quality so that the components would fit together correctly, the construction of the complete set of bridge components was

carried out by a local contractor. The contractor was the Sparks, NV branch of Granite Construction, which is headquartered in Watsonville, CA. It was advantageous for construction to be conducted by a construction company with experience in both bridges and post-tensioning because the quality of construction was an important factor. Furthermore the required manpower to build a model was not available at UNR. The beams were constructed off-site at a construction yard belonging to the contractor in Sparks, NV. Level concrete pads, which were dedicated to the construction of the beams, were created prior to construction.

The bents and footing blocks were constructed on concrete pads owned by the university that are dedicated to structural research projects. The pads are located adjacent to the structures laboratory at UNR. It was important that the bents were constructed at the university because extensive instrumentation was embedded into the concrete of the bents, which required substantial interaction between the contractor and UNR during construction. Throughout construction of the off-site beams as well as on-site bents and blocks, consistent instruction and inspection was provided by the designer from UNR.

5.2.2.1 Superstructure Beams

Figure 5-1 shows the formwork for the superstructure beams located at the Granite Construction site. The formwork was constructed so that the beams could be built side by side. Upon completion of the forms, guides were placed inside the forms on the concrete pad for the vertical post-tensioning ducts that were to be used for post-tensioning of the concrete blocks during assembly of the bridge. Also, guides were placed on the inside walls of the forms for placement of the lateral ducts that were to be installed for lateral post-tensioning of the beams. It was advantageous that the beams were cast side-by-side so that the lateral post-tensioning ducts of each beam could be in line during construction so that they would match up well during assembly on the shake tables.

The beam reinforcement cages, which included the general flexural and shear reinforcement, were assembled outside of the forms. Prior to placing the cages into the forms, a test-run of placement of the longitudinal and transverse ducts was conducted (Fig. 5-2). It was important that the longitudinal post tensioning duct could be placed correctly and would easily form to the specified duct path while avoiding the ducts that were placed for lateral post-tensioning. After verification of the longitudinal duct paths, the ducts were taken out and the beams cages were placed into the forms. The lateral and vertical ducts were then installed and the end details of the reinforcement cages, including the beam ledges were completed. Upon completion of the reinforcement cages, the ends of the formwork were finished and the lifting hooks and threaded anchors that were to be on top of the beams were put in place. Figure 5-3 shows the completed beam reinforcement prior to placement of concrete. The beams after the placement of the concrete are shown in Fig. 5-4. Thermal blankets were spread over the top of the beams for protection from the cold during curing. After curing, the beams were transported to the laboratory for assembly of the bridge (Fig. 5-5).

5.2.2.2 Bents

Construction of the bents was conducted according to the following eleven stage process that included three separate concrete pours: construction of footing formwork, assembly of the footing and column cages, instrumentation the column cages, attachment of column cages to footing cages, placing concrete for the footings, construction of platform at the top level of the columns, assemble column formwork, placing concrete for columns, assembly of cap beam cages, assembly of cap beam formwork, and placing concrete for the cap beams. The bents were constructed on site at the university.

Figure 5-6 shows the instrumented column cages prior to attachment of the cages in the footings. Extreme care was required so that the delicate strain gauges were not damaged during transportation of the cages, integration of the cages, or placement of concrete. Assembled footing cages and column cages that were placed after instrumentation of the columns are shown in Fig. 5-7. Special attention was given to the orientation of the columns during placement of the cages because as discussed in Chapter 3, the configuration of column strain gages was complex and varied in different directions. Once the construction was complete, it would be very difficult to verify location of the strain gauges. A photograph of the footing joint region after placement of a column cage and before the concrete was poured is shown in Fig. 5-8. The columns were tied in place with both wire ties and timber struts that extended from the columns to the ground. The ties remained attached to the columns after the footings were cured and until the column formwork was added. Before placement of the footing concrete, vertical PVC ducts were passed through the footing cages and secured with timber cross pieces that spanned across the top of the forms. The vertical ducts allowed for rods to pass through the footing to attach it to the shake tables.

After the concrete in the footings had cured, a single frame was built around all the columns in order to support a construction platform. Figure 5-9 shows placement of supports and timber bracing of the frame. The construction platform served two purposes. The first was to have a platform to work on for placing the concrete in the columns and assembling the cap beams. The second was to provide support for the large concrete cantilevers and the cap beams. The completed support frame is shown in Fig. 5-10. Railings were included around the perimeter of the platform for safety. Figure 5-11 is a photograph of the top of the platform. Circular cutouts were made in the the platform to accommodate the column bars that extended into the joints.

Sono-tubes were used for column forms. The columns were centered using wood wedges that were kept in place until the completion of the placement of column concrete (Fig. 5-11). Prior to placement of the concrete, holes were drilled in the sono-tubes and the rods for the curvature transducers were inserted into the columns (Fig. 5-12). As shown in the figure, wood blocks were glued to the sono-tubes to support the instrument rods until after the concrete was placed. Concrete was brought up to the top of the platform to place the concrete into the sono-tubes using 5 gallon (0.019 m^3) buckets. The buckets were lifted up to the platform using a forklift. Buckets were used for the concrete placement of columns instead of a concrete pump or a boom truck with a large lift bucket because the volume of concrete required for the columns was only 1.1 yd^3 (0.28 m^3).

After the concrete in the columns had cured, the steel cages of the cap beam of bent 2 (Fig. 5-13) and the cantilevers of the end bents (bents 1 and 3) (Fig. 5-14) were assembled on the platforms around the top of the column cages. Upon completion of assembly of the cages, the ducts for the longitudinal post-tensioning were passed through. Figure 5-15 shows the installation of the anchors and anchorage zone spirals for the anchorage zones of the longitudinal post-tensioning strands. The anchorages were slid into the end of the cantilever reinforcement cage and the formwork next the anchors was completed. Six anchors were required, three in each cantilever end for the three ducts that ran the length of the bridge. Following installation of the anchors, the formwork around the completed steel cage of bent 2 was completed (Fig. 5-16).

Prior to placement of the concrete, the threaded anchors and lifting hooks were set in place at the top of the forms. Placement of the concrete is shown in Fig. 5-17. Care was required so that the lifting hooks remained in place during placement of the concrete since the hooks were not rigidly attached to the formwork. The completed bents after curing of the cap beam concrete and removal of the forms are shown in Fig. 5-18. Thermal blankets were used to cover the bents during each concrete pour to protect the concrete from the cold during the curing process. The approximate ambient night time low was 22 deg. F (-5.6 deg. C). Extreme care was required during removal of the formwork so that the curvature rods and strain gauge wires protruding from the concrete were not damaged. As will be discussed in Section 5.2.3, temporary supports were placed under the cantilevers for added stability.

5.2.2.3 Spacer Blocks

The two spacer blocks were the simplest of the eleven structural bridge components to construct. Figure 5-19 shows the reinforcement cages inside the forms. The forms were constructed and the cages were assembled within them. Prior to placement of the concrete, vertical PVC ducts were passed through the cages that would later allow for the blocks to be tensioned onto the shake tables. Also, the lifting hooks were set in place. Timber cross pieces to laterally support the ducts and hold the lifting hooks in place were spanned across the top of the forms as shown in Fig. 5-20.

5.2.3 Bent Stability during Construction

Stability was an important issue for all of the structural components of the bridge model both during storage and during the construction phase. Because the six beams, spacer blocks, and bent 2 were all vertically symmetric about both axes and because they all had a relatively large footprint, stability was not an issue. However, the eccentric mass that was on top of bents 1 and 3 due the cantilevers was a cause for concern because of its lack of symmetry. Stability of the cantilevered bents was checked by two different methods. An example of the stability checks is subsequently provided for bent 1. Bent 1 was the more critical of the two bents since bent 1 had a smaller footing mass to counteract the overturning moment caused by the cantilever and was the taller of the two bents.

The weight of the bent was divided into three components as shown in Fig. 5-21: cantilever, columns, and footing. The two cases that were considered for stability are shown in Fig. 5-22. Case A was a check for uplift of the footing due to overturning

moments. A linear distribution of stress at the bottom of the footing was assumed and a check was made to determine if the stress beneath the footing would be entirely compressive under self weight. Under self weight, the pressure distribution under both bents 1 and 3 was such that there was pure compression. Next, as shown in case B, the amount of lateral force at the top of the bent required to overturn the bent was calculated. It was determined that for bents 1 and 3, a lateral forces of 1.9 and 2.2 kip (8.5 and 9.8 kN) were required to overturn the bents, respectively. Although this is a significant amount of force, it was concluded that for the safety in the vicinity of the bents, and so that if the bents were accidentally "bumped", they did not tip over, supports should remain beneath the cantilevers until construction of the bridge was completed. As shown in Fig. 5-23, the cantilevers were braced with temporary supports for storage. Also, when the cantilevered bents were placed on the shake tables, supports were provided until the bents were secured to the tables.

5.2.4 Assembly

This section describes the assembly process of the bridge model on the shake tables. Extensive planning was required so that the model would be correctly assembled in an efficient manner without damaging any components.

5.2.4.1 Transportation

All of the components were transported from the construction locations to the structures laboratory. Once inside the lab, transportation of components was conducted utilizing two overhead cranes.

Superstructure beams were transported from the construction yard in Sparks, NV using a flat bed semi-truck. The beams were lifted off of the construction pad using a crane and were lowered onto the truck. The beams were transported in two sets of three because of the large mass of each beam, which was approximately 12 kip (53 kN). The truck was driven partially into the structures lab so that the beams could be lifted directly from the truck using the two cranes in the laboratory.

The spacer blocks and three bents were transported from the concrete construction pads into the lab using a forklift. For the cantilever bents, the forks were placed beneath the cantilever for lifting. Forks were inserted on the side opposite from the ledges so that the ledges would not be damaged. Once inside the lab, the four lifting hooks that were embedded on top of each cantilever were used to lift the components with the overhead crane.

To move the center bent (bent 2) from the construction pads, forks of the forklift were inserted into the bar lifting hooks in the footings. Forks were not placed directly beneath the cap beams as for the cantilevered bents because the two beam ledges, were on either side of the bent 2 cap beam and any damage to the ledges was undesirable. Once inside the lab, the crane was attached to the bar lifting hooks in the footing. To avoid damage to the beam ledges, portions of a railroad tie were placed against the cap beams above the ledges so that the cables of the crane would not come in contact with the ledges.

The spacer blocks were lifted inside the laboratory using the forklift attached to the swift-lift anchors that were installed at the top of the blocks. Once inside the laboratory, the blocks were attached directly to the crane using the lifting hooks.

5.2.4.2 Placement of Bents on Shake Table

Figure 5-24 shows the bare shake tables before assembly of the bridge. The shake tables were prepared prior to placement of the spacer blocks and bent-2 by inserting the threaded rods that were to be used to post-tension the footings and safety frames to the tables, and by spraying form release on the footprint where the blocks and footing would be grouted on to the tables. Square 7x7 in (180 x 180 mm) pieces of high density foam with a hole in each center were used to seal the ducts beneath the footings to keep grout out of the ducts and the anchor holes in the shake tables. The foam pieces were 0.5 in (13 mm) thicker than the target thickness of the grout beneath the footings and blocks so that the weight of the footings and blocks would compress the foam and seal the duct region. The 1.5 in (38 mm) spacing beneath the spacer blocks was provided using 6 in (150 mm) long pieces of standard 2 x 4 in (51 x 102 mm) dressed lumber. A 2.5 in (64 mm) gap for the grout was provided beneath the center bent. The extra 1 in (25 mm) of grout was provided for the center bent so that the top of the three bents would be at the same elevation, since an additional 1 in (25 mm) layer of grout was required on the end bents between the spacer blocks and footings.

Once the tables were prepared, the spacer blocks and safety frames were lowered on to the end shake tables (Fig. 5-25). The middle bent, which did not have a spacer block, was placed directly on the middle shake table (Fig. 5-26). Upon centering of the bent and spacer blocks on the shake tables, formwork was constructed so that the footing grout could be poured. After the grout was poured and had cured, the top of the spacer blocks were prepared in a similar manner to the preparation of the surface of the shake tables. The top of the spacer blocks were sprayed with a form release oil, high density foam was placed, and the bents were lowered onto the blocks. Figure 5-27 shows bent 1 attached to the crane in the lab prior to moving the bent to the shake table. Figure 5-28 shows bent 3 after it was placed on the shake table. The distances between the top corners of each of the three bents were measured to make sure that the bents were square and that they had the correct spacing to accommodate the superstructure beams. Bents were moved within ¼ in (6 mm) of their target locations. After the bents were in place, the grout was poured between the bents and spacer blocks. Upon curing of the grout, the three bents were tensioned on to the shake tables.

5.2.4.3 Assembly of Superstructure

The superstructure assembly consisted of the attachment of the six superstructure beams to the three two-column bents. This included attachment of bearing plates, placing of the beams, grouting the joints, and both laterally and longitudinally post tensioning the beams to each other and to the cap beams.

Figure 5-29 shows the installation of the bearing pads on the beam ledges. Each of the four ledges had six steel bearing plates. The bearing plates were made to provide bearing for the beams so that there was a 1 in (25 mm) gap between the bent ledges and the beam ledges. This was accomplished using a 0.25 in (6.4 mm) gap of hydrostone

between the beam ledges and the plates. Hydrostone was required on the top of the beam ledges because the concrete of beam ledges was finished by hand and did not have a perfectly even surface. However, the surfaces of the ledges on the six superstructure beams were placed against the forms and were therefore perfectly flat. Forms for the hydrostone were constructed using strips of 0.5 in (13 mm) thick plywood. The bearing plates were 0.75 in (19 mm) thick. Care was taken to make sure that the plates were level and at the same height so that the top of the superstructure beams would all be at the same elevation.

Superstructure beams were lowered on to the cap beam ledges using the dual overhead cranes in the lab (Figs. 5-30 and 5-31). The beams were placed in an order which put the least amount of moment on the columns of the center bent and created the most even amount of loading distribution possible. The center beams were placed first, followed by the east beam of span 1 and the west beam span 2, followed by the west beam of span 1 and the east beam of span 2. As the beams were placed, they were adjusted to ensure that the longitudinal post-tensioning ducts of the beams matched the longitudinal post-tensioning ducts of the bents and that the transverse joints at the end of the beams were approximately equal.

Grout was placed in the transverse joints of the superstructure where the beams rested on the cap beam ledges. The grout provided continuity between the bents and superstructure beams so that the superstructure could be compressed for post-tensioning. Sealing of the transverse joints prior to pouring the grout is shown in Fig. 5-32. The joints, which ranged from 0.5 to 1.25 in (13 to 32 mm) wide, were filled with cut strips of high density foam. The foam was sealed between the foam and concrete using silicone sealant. As shown in Fig. 5-33, U-shaped inserts of foam were required to prevent grout from entering the longitudinal post-tension ducts. The inserts also allowed for viewing of the post tension strands during installation in case the strands were caught up at one of the joints while being pushed through the ducts during installation.

Initially, it was hoped that the faces on the sides of the superstructure beams would be sufficiently uniform and smooth so that the beams could be set up side-by-side and post-tensioned transversely together without the use of grout. Although the surfaces of the beams were ground for smoothness before installation, the uniformity was not sufficient to allow for full contact between the beams after the transverse post-tensioning was applied without damaging the beams. Because the gap between the beams varied from zero to approximately 1/8 in (3 mm) thick, grout was not an option because it was too viscous. Therefore, it was decided to use hydrostone between the beams. Hydrostone has essentially the same consistency as water, so it can form within a very small gap. Figure 5-34 shows the sealed longitudinal joints beneath the superstructure between the beams prior to the pouring of hydrostone from the top of the deck.

The grout at the end joints between the cap beams and superstructure was poured and cured prior to pouring the hydrostone. Grout was poured directly into the transverse joints, which were approximately 1 in (25 mm) wide. However, because of the small width of the longitudinal joints between the beams and the low viscosity of the hydrostone, funnels were used to pour the hydrostone. The funnels were made of high density foam glued to the top of the beams, are shown in Fig. 5-35. Figure 5-36 shows the top of the superstructure after the hydrostone was poured.

Upon curing of the grout and hydrostone, the lateral post-tensioning was applied to the superstructure. Lateral post tensioning consisted of ten Dywidag rods, five in each span (Fig. 5-37). The rods were post-tensioned in each beam starting with the mid-span and working outward. Lateral post-tensioning was conducted prior to the longitudinal post-tensioning so that during longitudinal post-tensioning, the two sets of beams each behaved as a single slab.

Longitudinal post-tensioning of the superstructure is shown in Fig. 5-38. There were three ducts over the entire length of the bridge. Each duct contained nine 0.5 in (13 mm) strands. The strands were pushed through the ducts by hand, one at a time. Once the strands were in place, collars were placed on each end and the strands were tensioned (Fig. 5-39). The strands were tensioned one at a time using a mono-strand jack. The strands in the middle duct were tensioned first to half of the target jacking stress. Strands on the east and west side followed, which were all tensioned to half stress. The process was repeated again starting with the strands in the middle duct and ending with the strands in the west duct until all the strands were tensioned to full target jacking stress. Because a mono-strand jack was used, which created greater elastic shortening losses than would a multi-strand jack; all strands were re-tensioned in the same sequence a second time to the full jacking stress. The strands were marked at the collar so that if slippage at the collars occurred, it could be measured.

5.2.4.4 Addition of Superimposed Weights

Figure 5-40 is a photograph of the bridge model after post-tensioning was completed, and before the superimposed weight was attached to the superstructure. The sequence of the addition of masses was important so that excessive out-of-plane bending moments would not be imposed on the columns of bents 1 and 3. The superimposed weights were placed symmetrically on the bridge in the following order: 1) the concrete block closest to the center of each span, 2) the center concrete block in each three block set, 3) two of the three lead pallets at the cantilever ends, 4) the remaining concrete block in each three block set, 5) the remaining pallet of lead on each cantilever (Fig. 5-41), 6) the lead buckets at each mid-span. After the weights were added to the bridge, the concrete blocks were post-tensioned on to the superstructure. The lead pallets were bolted to the top of the bridge using the threaded rods that were cast into the top of the beams and cantilevers during construction. A photograph of the complete bridge after the weights were attached is shown in Fig. 5-42.

5.2.4.5 Attachment of Instrumentation

Instrumentation for the bridge was attached in three stages. The first stage was attaching the strain gauges to the column cages during construction. The second stage was attaching the strain gauges to the data acquisition system after the superstructure beams were placed and before the beams were post-tensioned. The final stage was the attachment of all transducers, other than strain gauges, after longitudinal post-tensioning. The last stage was completed two days before start of shake table testing.

Ideally, the strain gauges in the columns would have been monitored throughout the construction process of the model, including transportation of the bents, the placement of superstructure beams, post-tensioning, and addition of masses. However,

the gauges were not attached to the data acquisition until after the superstructure beams were placed. For both the longitudinal post-tensioning, and the addition of masses, the strain gauges were monitored in real time to make sure that the strains in the columns were close to the predicted strains that were discussed in Section 2.5.7.2.1. After the placement of the weights, it was determined that the strains in the bar were consistent with strain that was predicted from analysis. Because the measured strain in the gauges did not include strain from placement of the beams, which heavily counteracted the strains due to longitudinal post-tensioning, and because actual the resultant strain in longitudinal reinforcement of the columns after assembly was close to zero, the strain gauges were restored to zero prior to testing.

5.3 Test Protocol

Table 5-2 lists the complete test schedule for all of the shake table tests. Target table motions and derivation of these motions were discussed in the previous chapter. This section discusses the test schedule, and additions to the schedule that were made during testing.

5.3.1 Low Amplitude Tests

Motions that were applied to the shake table for the low amplitude tests were discussed in Section 4.4. As shown in Table 5-2, low amplitude testing was conducted as two sets of motions that were numbered 1 through 11. The first set of tests on January 27, 2005, included tests 1 through 8, the transverse coherent and incoherent motions. The second set, on February 8, 2005, included tests 9 through 11, the biaxial motion and the centrifuge motions. Test 7, which was scheduled to have the same target motions as test 8, except on a different day, was not conducted and is therefore not included in the table. The second set of tests was conducted at a later date because the centrifuge motions to be used were the achieved motions, and the centrifuge tests had not yet been conducted at the time of the first set of tests. White noise and snap tests were conducted at various stages of low amplitude testing as discussed in Sec. 5.2.3.

As shown in the table, certain tests, denoted with "A" at the end of the test name were half amplitude tests. Half amplitude tests were conducted for the first uniaxial coherent motion, the first two uniaxial incoherent motions, the first white noise test, and the first biaxial motion. The reason that the half amplitude tests were conducted prior to the actual tests at the beginning of testing was because this was the first two-span bridge frame test on the shake tables and there was some uncertainty about the system response and the response of the shake tables. It was also important to make sure that the longitudinal reinforcement strains in the columns would remain below yield for the actual tests.

5.3.2 High Amplitude Tests

Shake table target motions for the high amplitude tests were discussed in Section 4.5. The schedule for high amplitude testing is shown in the lower half of Table 5-2 and includes tests 12 through 22. High amplitude testing was conducted over a span of two days, February 9 and 10, 2005. The purpose of the first day of tests was to excite the bridge model past yielding of the column longitudinal reinforcement in the bents, up to

just before failure of the most critical bent. Testing on the first day was completed at a scaled target motion of 1.33 g. The failure test, test 19, which was conducted on the second day, was the target motion scaled to 1.66 g. Test 19 signified failure of the bridge when the first bent (bent 3) reached failure. The original test schedule for tests 18 and 19 was scaled motions of 1.25 and 1.5 g, respectively. However, during testing it was decided to amplify tests 18 and 19 to 1.33 and 1.66 g, respectively, to increase the size of the steps between motions. After the bridge was subjected to the 1.66g motion (failure run), a 1.0g motion, test 20, was applied to induce additional damage without collapsing the model.

Test 20 signaled the completion of the high-amplitude tests of the bridge in the original configuration. However, bents 1 and 2 had only reached the point of insipient buckling of the longitudinal reinforcement. The weights above bent 3, three 20kip (89.0kN) concrete blocks and 24kip (106.8kN) of lead, were removed and further tests were conducted in an attempt to inflict further damage to bents 1 and 2 while minimizing the demand on bent 3. The bridge model was then subjected to 2 additional high-amplitude motions, tests 21 and 22, which were the same as the target motion of the high amplitude testing scaled to 1.0 and 1.5 g, respectively.

5.3.3 White Noise and Snap Tests

Both white noise and snap tests were included in the test schedule to allow for calculation of the change in low amplitude frequency response of the bridge as a measure of damage progression. As shown in the test schedule, the name for each white noise and square wave test begins with the letters WN, and SQ, respectively. Each test is identified with four digits following the two letter identification. The first two digits are the previous test and the second two digits are the subsequent test. For cases where testing was concluded on one day and began on another, two sets of white noise and square waves were conducted. These tests are identified numerically at the end of the name by the order they were performed.

Each set of white noise testing included excitation in the transverse, followed by the longitudinal direction. White noise tests were low amplitude coherent motions that were not large enough to induce any damage to the bridge. The acceleration history used for the “white noise” was a random motion having a peak acceleration of 0.1 g and a frequency range of 1 – 30 Hz that lasted for approximately 60 seconds. The advantage of the white noise was that it excited all of the modes of the bridge in both the transverse and longitudinal directions. Square wave motions were applied following several of the white noise tests. The square wave motions were applied in the transverse direction only, at amplitude that was comparable to the white noise motions. The purpose of square wave tests was to subject the bridge to free vibration.

Chapter 6: Shake Table Test Results

6.1 Introduction

This chapter discusses the observed behavior and the measured results from the shake table testing of the bridge. Observations and results from this experiment served two purposes. The first was to evaluate the experimental method of testing the bridge on shake tables. The second was to document the behavior of the bridge to improve the understanding of bridge system response. Observations during low amplitude testing were to make sure that the bridge had not sustained significant damage. Observations of the high amplitude tests were primarily to document the failure progression of the bridge.

Experimental results that are based on measurements from the instruments discussed in Chapter 4 are presented in Sections 6.3 through 6.5. Much of the data collected required post processing, which is described as the corresponding data is presented in this chapter. The material in this chapter refers to the instrumentation plans and channel labels that were discussed in Chapter 3.

6.2 Observed Results

Observations that were made during testing are discussed in this section in two groups, low amplitude testing and high amplitude testing. The observations included physical inspection of the state of the bridge between tests that were documented as written events, drawings, and photographs at key locations. During each test, video of the bridge was recorded at four locations. A wide angle camera, which filmed the entire bridge, was placed on the east side of the bridge near the middle. The second camera was placed at the northeast end of the bridge and also filmed the entire bridge. The third and fourth cameras were placed at the north and south ends of the bridge and recorded the motions of bents 1 and 3, respectively.

Data such as strains, displacements, and accelerations were also observed during the tests to track the response and understand the damage state of the bridge. The measured data is discussed later in this chapter in the results section.

6.2.1 Low Amplitude Tests

The bridge was not expected to be, and was not significantly damaged during low amplitude testing. The columns were allowed to exceed their flexural cracking moment, but not the moment that would initiate yielding of the longitudinal reinforcement. Therefore, the purpose of observations that were made during the low amplitude tests was to make sure that the bridge had not sustained any damage other than tensile cracking of the concrete in the columns. The strain history data was reviewed after each test to make sure that the reinforcement in the columns was had not yielded during the test. Special attention was given to the longitudinal reinforcement in the plastic hinge zones of the columns that would yield from transverse excitation.

Cracking of the concrete in the superstructure and substructure of the bridge was monitored, and throughout the low amplitude tests none was observed. It was understood that thin column cracks would be closed by the axial loads and would not be visible after the tests. The superimposed weights attached to the top of the superstructure were

evaluated after alternating tests to check for any slippage. At the same interval, the longitudinal post-tensioning tensioning tendons were inspected to check for any slippage in the collars at each end of the bridge. The slippage was monitored by measuring marks that were made on the tendons extending out of the superstructure (Fig. 5-39) after the tendons were stressed.

6.2.2 High Amplitude Tests

Observations of the high amplitude tests served two purposes. The first was to determine if parts of the bridge model that where expected to be damage free (the superstructure, joints, post-tensioning, and footings) were indeed intact. The second was to document the bridge response including the damage progression of the columns up to failure. Similar to the low amplitude tests, no damage was observed in the superstructure including the concrete in the cap beams and superstructure beams, as well as the longitudinal post-tensioning. Nor there was any visible damage in the footings that were bolted to the shake tables or the weights that were attached to the superstructure.

High amplitude testing included tests 12 through 20 (see Table 5-2). The bridge was considered to have failed during test 19 when the columns of bent 3 failed. After the bent 3 failure, the bridge was subjected to an additional test, test 20, of reduced amplitude to attempt to further damage bents 1 and 2. The purpose was to study the redistribution of loads after the loss of lateral load capacity in bent 3. Two additional tests of the bridge with a different superimposed weight configuration were conducted after test 20. However since the change in the mass altered the dynamic characteristics of the bridge model, observations of these tests are discussed separately in Section 6.2.3.

Tables 6-1 through 6-6 list the observations of the columns in a hierarchal order from bent 1 to 3, east column to west column, east side to west side, and top to bottom. Damage was concentrated on the east and west sides because the bridge was excited in the transverse (east-west) direction. Because of the relatively large aspect ratio of the columns in bents 1 and 2, no shear cracks were observed in these columns. Shear cracking was only observed on the north and south sides of the columns of the shortest bent, bent 3. Shear cracking is not listed in the tables, but was documented with photographs and is discussed in Section 6.2.2.3. Observations that were documented in the tables for each high amplitude test included the maximum crack width (determined by comparing with a crack size chart), spall height and description, number of exposed lateral and longitudinal bars, extent of longitudinal reinforcement buckling, and the number of ruptured longitudinal bars and spirals.

Figures 6-1 through 6-24 are photographs of the damage progression of columns for all high amplitude tests. Each figure shows the damage progression throughout the high amplitude tests in one zone. The zones are in the same hierarchical order as Tables 6-1 through 6-6: bents 1 through 3, followed by east and west column, east and west side, and top and bottom.

No damage was observed in the bridge until after test 13. During test 13, initial hairline flexural cracks developed in bent 1. Flexural cracking began in bent 3 and became significant in the columns of both bents 1 and 3 during test 15. Also during test 15, initial hairline cracks began to develop in bent 2. During test 17, significant concrete spalling exposed the column lateral reinforcement in both bents 1 and 3. Significant

spalling and exposure of lateral column reinforcement in bent 2 became evident during test 18. Also during test 18, the longitudinal reinforcement of bent 3, the shortest of the bents, became exposed and initial buckling was observed on the bottom west side of the west column. Both columns of bent 3 failed in flexure during test 19. The top and bottom of bent 3 columns experienced significant plastic hinging and crushing of the core concrete. Four bent 3 spirals fractured, and 36 longitudinal bars buckled. During test 20, seven longitudinal bars in bent 3 fractured and most of longitudinal reinforcement buckled. The increase of damage in bents 1 and 2 was minor during test 20.

6.2.2.1 Bent 1 Observations

Descriptions of damage progression for bent 1, the medium height column, are listed in Tables 6-1 and 6-2. Photographs of the damage progression are shown in Figs. 6-1 through 6-8. Prior to yielding of bent 3, which occurred during test 14, most of the damage in the bridge was concentrated in bent 1. Initial flexural cracking in the columns began during test 13. During test 15, flexural cracking increased and flaking of concrete in the plastic hinge regions was initiated. Additional concrete flaking and initiation of spalling was observed after test 16. During tests 17 and 18, there were slight increases in flexural cracking and spalling in all of the plastic hinge zones. Also, the spiral reinforcement was exposed on the top and bottom west side of the east column as well as bottom west side of the west column. During test 19, spalling at the top end bottom of the columns increased and the longitudinal reinforcement was exposed on the top west side of the east column. During test 20, only slight increases of spalling and flexural cracking were observed, namely at the top west side of the east column and the bottom west side of the west column.

6.2.2.2 Bent 2 Observations

Descriptions of damage progression for bent 2, with the tallest of the columns, are listed in Tables 6-3 and 6-4. Photographs of the damage progression are shown in Figs. 6-9 through 6-16. No damage in bent 2 was visible until test 15 when thin flexural cracks became apparent in some of the plastic hinge zones. During tests 16 and 17, flexural cracking became apparent at all plastic hinge zones and minor flaking occurred in the concrete. During test 18, spalling initiated in the top west side of the east column and in all but the top west side of the west column. Spalling increased during test 19 and became apparent on the east and west side of the top and bottom of both columns. Slight increases in both flexural cracking and spalling were observed after test 20. However, the column reinforcement was not exposed.

6.2.2.3 Bent 3 Observations

Descriptions of damage progression for bent 3, the shortest of the columns, are listed in Tables 6-5 and 6-6. Photographs of the damage progression are shown in Figs. 6-17 through 6-24. Figure 6-25 shows the progression of shear cracks on the south side of the east column where shear cracks were most prevalent. Other than initiation of shear cracks during tests 15 and 16, no significant shear damage was observed in the columns.

No cracks were observed in the columns of bent 3 until test 15. After test 15, significant flexural cracking was apparent at all 8 faces of the plastic hinge zones. Also

as a result of test 15, flaking of cover concrete was apparent on three of the four faces of the east column and spalling initiated at the top east and bottom west sides of the west column. After test 16, additional flexural cracking was observed at the top and bottom of both columns. Also, flaking occurred at two and spalling occurred at five of the eight faces of the plastic hinge zones. At the bottom west side of the west column, spalling increased to the point where the spirals became exposed. Slight shear cracking could be seen as shown in Figure 6-25. No significant increase in damage occurred during test 17. A slight increase in spalling was observed and lateral reinforcement was exposed at the top west side of the west column.

Significant additional spalling in the plastic hinge zones occurred as a result of test 18. After test 18, spalling was observed at all 8 faces of the hinge zones. Eleven spirals were exposed, including 3 spirals on the top east side of both columns. Six longitudinal bars were exposed, 2 bars at each the top east and bottom west side of the west column and the top west side of the east column. Also during test 18, incipient buckling could be observed in one of the longitudinal bars at the bottom west side of the west bent (Fig. 6-24).

Bent 3 failed during test 19. Spalling increased to the point where three-quarters of the circumference at three of the four column ends spalled off and the average maximum spall height at the faces of the plastic hinge zones was 6.3 in (160 mm). The spalling of bent 3 at plastic hinge zones exposed a total of 31 of the spiral hoops with an average of four spirals at each face. Fifty of the 64 longitudinal column bars at the hinge zones were exposed. Significant crushing of the core concrete occurred and 36 longitudinal column bars buckled. Four of the spirals fractured, 2 at the bottom east side of the east bent (Fig. 6-18) and one at both the bottom west and top east sides of the west column.

Although the columns of bent 3 had failed during test 19, additional damage was imposed during test 20. Spalling increased and 58 of the 64 longitudinal column bars and one additional spiral was exposed. Seven longitudinal bars fractured, four at the top west side of the east column, two bars at the top east and one bar at the bottom west of the west column.

Even though bent 3 failed during test 19 and was further damaged in test 20, the failure was ductile. As a result the bridge did not collapse and the superstructure did not drop on the steel catch frame that had been placed as a part of the safety system.

6.2.3 Post Failure Tests

The purpose of the post failure tests was to further excite the bridge as an attempt to inflict more damage to bents 1 and 2. The superimposed weights above bent 3 were removed and the bridge was subjected to two additional motions. Similar to the observations that were made during high amplitude tests, description of damage progression for the bents during the post failure tests, tests 21 and 22, are listed in Tables 6-1 through 6-6. Photographs of damage progression from the final high amplitude test, test 20, through the final post-test for bents 1 and 2 are shown in Figs. 6-26 through 6-33. Four of the eight sides of the plastic hinge zones are included in the figures. The hierarchal order of the zones in the bents where damage is shown is the same as that for high amplitude tests. Bents 1 and 2 are first, followed by east and west columns, east and

west sides and top and bottom of the columns. Photographs of damage to bent 3 are excluded in these figures because bent 3 had already reached failure and the purpose of tests 21 and 22 was to record damage for the other two bents.

Relatively little increase of damage was observed in bents 1 and 2 as a result of test 21. During test 21 a slight increase on spalling was observed in bent 1. Two longitudinal bars were exposed on the bottom west side of the west column. No notable additional damage was imposed on bent 2 during test 21.

After test 22, three additional longitudinal bars for a total of six longitudinal bars, and one additional spiral, for a total of ten spirals were exposed in bent 1. One longitudinal bar at the bottom west side of the west column of bent 1 showed signs of buckling. In bent 2, spalling increased significantly causing the first of two longitudinal bars and four spirals to be exposed. The most notable damage increase for bent 2 was at the top east side of the west column where 2 longitudinal bars and 2 spirals were exposed (Fig. 6-33). One of the bent 2 longitudinal bars in this zone buckled and was separated approximately 0.25 in (6.3 mm) from the core concrete.

6.3 Measured Results

Results from the instruments that were discussed in Chapter 4 were recorded at a rate of 100Hz and were filtered through a low pass filter to cut out noise above 50 Hz. Much of the data required post processing, which is described as the data is presented in this section.

6.3.1 Transverse Acceleration-Deflection Relationships

Typically when columns are tested in a laboratory, the primary descriptions of global column response to earthquake motions are displacement and force in the direction of testing. The displacement is typically measured using displacement transducers and the force is measured using a load cell. The deflections of the columns for this experiment were measured using the displacement transducers at the top of the columns that were attached to a fixed wall in the laboratory, subtracted from the measured displacement of the shake tables. Since the columns in this test were in a bridge system and there was not a practical way to include a load cell in the columns, there was not a direct measurement of shear force for the columns or the individual bents. Therefore the acceleration at the top of the bents was used as an indicator of the force acting on the bents. Implicit in this approach was the assumption that the inertial forces applied to each bent are proportional to the tributary mass of each bent and the top acceleration.

The bent force obtained using the acceleration and the tributary mass is only an estimate. In a nonlinear multi-degree-of-freedom system such as the bridge tested in this study, tributary masses can be shifted among the bents. For the purpose of determining approximate yield displacements and amount of nonlinearity in each of the bents, accelerations were sufficient. Since exact yield points of the columns could not be calculated accurately using the accelerations, the yield displacements that were used in any evaluation of the bridge in this study are those calculated from the analytical models that are discussed in the next chapter.

As discussed in Section 6.4, the lateral shake table force calculated from the pressure in the hydraulic fluid in the shake table actuators was used to estimate the force

in the columns for select tests. This estimate was compared with the force calculated from assuming a constant tributary mass at each bent utilizing the measured accelerations. In Chapter 7, the lateral forces are further compared with the results from the Drain-3DX model, which is demonstrated in Chapter 7 to accurately duplicate the response of the bridge. The comparisons of the forces provide some insight to the accuracy of both the acceleration estimated and actuator pressure calculated column forces so that their reliability is known for future tests.

6.3.1.1 Filtering of Results

The measured acceleration-deflection relationships of the three bents that were filtered at 50 Hz appeared to be irregular compared to typical data from past experiments on bridge bents. The loops exhibited dual reversals as shown in the upper left plot of Fig. 6-34 as well as the upper left plot of Fig. 6-37. To determine whether the irregular loops were a result of insufficient filtering or were the actual response of the bridge, the frequency content was examined. Figures 6-34 through 6-36 show the cumulative high amplitude lateral acceleration vs. deflection plots for bents 1 through 3, respectively low pass filtered at 50Hz, 20Hz, 15Hz, and 10Hz. Figures 6-37 through 6-39 show the filtered lateral acceleration vs. displacement plots for test 1, a representative low amplitude test.

Between the data that were filtered at 15 Hz and higher, there was no significant difference in the response. It can therefore be seen in comparing the filtered hysteresis curves of both the high and low amplitude tests that the "irregularities" in the acceleration-deflection relationships were caused by response below 15 Hz. Modal shapes of the superstructure were described in the pre-test analysis description in Chapter 4. The measured modal properties of the bridge are discussed later in this chapter. The frequency of the third transverse mode, bending of the superstructure, is approximately 12-13 Hz, which was cut out of the response when a 10Hz filter was applied to the data. The frequency of the second transverse mode, which is superstructure translation and in plane rotation is approximately 4Hz, which was not eliminated with the 10Hz filter. It can be seen in Figs. 6-34 through 6-39 that when the 10Hz filter was applied, much of the irregularity in the hysteresis was removed. As shown in Fig. 6-37 some irregularity remained after the 10 Hz filer was applied. This irregularity is believed to be caused by the second transverse mode combined with the first when the superstructure response was translating and rotating in the lateral plane. Upon reviewing of the measured transverse superstructure displacements that were animated utilizing MathCAD (Mathsoft 2002), it was further confirmed that the reversals that were within the hysteresis loops were caused by the combination of the three modes due to column interaction and superstructure bending. It was therefore determined that the 50 Hz filtered data was appropriate for use and that characteristics of the acceleration-deflection relationship were indeed a part of the actual response of the bridge. Acceleration-deflection relationships that are discussed throughout this document as well as all other recorded data from the bridge were all low pass filtered at 50Hz.

6.3.1.2 Low amplitude tests

Cumulative acceleration vs. deflection plots of tests 1 through 11 for the transverse response of bents 1 through 3 are shown in Figs. 6-40 through 6-42, respectively. The plots are shown on the same scale as high amplitude plots, which are discussed in the following section, to demonstrate the relative magnitude of the response. As shown in the figures, no significant hysteretic energy dissipation resulted from the low amplitude tests which were intended to remain well below the yield point of the columns.

Figures 6-43 through 6-46 show the acceleration vs. deflection relationships for bent 1 for each of the low amplitude tests 1 through 11. The relationships for bents 2 and 3 are plotted in Figs. 6-47 through 6-50 and 6-51 through 6-54, respectively.

6.3.1.3 High Amplitude Tests

Cumulative acceleration-deflection curves from high amplitude tests 12 through 20 for bents 1 through 3 are shown in Figs. 6-55 through 6-57, respectively. It can be seen in the figures that all of the bents underwent large deformations and dissipated considerable amounts of hysteretic energy. It is also shown that bent 3, the shortest bent, underwent the largest deformations.

Figures 6-58 through 6-66 show the acceleration-deflection curves of bent 1 for each test. Some degree of nonlinearity was seen in test 14. The first test to show significant energy dissipation and yielding was test 15 (Fig. 6-61). Amplitudes of accelerations and displacements after test 12 increased for all subsequent runs until test 19 except for test 17. It can clearly be seen that during test 17 either the vibration frequencies of system changed and there was less demand on bent 1, or the demand of the test 17 motion was less than that of test 16. As the hysteresis curves of other bents are discussed in the following paragraphs of this section and from the achieved shake table motions discussed in Sec. 6.3.9 it is shown that the reduction in bent response for test 17 is due to a smaller achieved motion of the shake tables. Test 20 was the motion with a target PGA of 1 g that was applied to the bridge after failure of bent 3 (occurred during test 19 with a target PGA of 1.66 g). The maximum displacement and acceleration of bent 1 were less for this test than those of test 19.

Individual acceleration-deflection curves of bent 2 for all high amplitude tests are plotted in Figs. 6-67 through 6-75. Significant energy dissipation is not evident in the bent 2 curves until test 15 (Fig. 6-70). Although the opening of hysteresis loops during this run suggests that bent 2 is well past its yield displacement, this cannot be verified from acceleration-deflection curves because the general response at bent 2 including acceleration was highly influenced by the much stiffer end bents 1 and 3, which dominated the response. Similar to the progression of the curves for bent 1, a reduction of amplitude is shown for test 17 (Fig. 6-72), with the 1.0 g target PGA, compared to test 16 (Fig. 6-71), with the 0.75 g target PGA.

Bent 3 acceleration-deflection hysteresis curves for tests 12 through 20 are plotted in Figs. 6-76 through 6-84. Test 15 is the first test where significant energy dissipation can be observed (Fig. 6-79). As shown in Fig. 6-81, similarly to the hysteresis of the other bents, the response of test 17 was reduced relative to test 16. The plot for test 18 (Fig. 6-82) reveals large displacements and hysteretic loops for the bent. The plot for test 19, which was the failure test of bent 3 (Fig. 6-83), shows comparable hysteretic energy

dissipation to test 18 except for a large bias of the displacement in the positive direction. A decrease in maximum acceleration that is shown in the largest of the positive displacement hysteretic loops suggests a loss of lateral load capacity for the bent. It is shown in the hysteresis plot for test 20 that the stiffness and maximum accelerations of the bent were greatly reduced after being subjected to test 19.

6.3.1.4 Post-Failure Tests

The purpose of tests 21 and 22 was to further excite the bridge with the intent of inflicting increased damage to bents 1 and 2. Since bent 3 had failed, (the evidence being crushing of confined concrete, rupture of reinforcement, and a significant loss of lateral load capacity), the superimposed weights above bent 3 were removed for these tests. Plots of the combined acceleration-deflection relationships for tests 21 and 22 for bents 1 through 3 are plotted in Figs. 6-85 through 6-87. Each plot is superimposed on the cumulative curves from high amplitude testing.

It is shown in the bent 1 plot that relatively little increase in displacement was achieved for bent 1 during the post-failure tests. A greater increase of displacement was achieved in bent 2 (Fig. 6-86), caused by large displacements of bent 3, which had low stiffness and lateral load resistance after failure during test 19. As shown in Fig. 6-87, the displacements and acceleration of bent 3 during the post-failure tests were significantly greater than for the high amplitude tests. The large amplitude accelerations for bent 3 were not due to high forces in the bent, but were caused by the large reduction of the mass that was tributary to bent 3 during previous tests and the whipping action from the more stiff bents 1 and 2. The maximum lateral displacement of the bent cap in bent 3 reached close to 7 in. (178 mm). Given that the cap beam remained connected to the columns, it is reasonable to assume that the maximum column displacement was close to this value. It is likely that the column displacement was slightly lower than the cap beam displacement due to severe damage at the top of the column that could cause shear deformations at the top plastic hinges.

6.3.1.5 Backbone Curve Idealizations

Since bent lateral forces could not be directly measured, acceleration-deflection response was used to estimate the bent yield displacements. Yield displacements were used to calculate displacement ductility in order to quantify the displacement demands on the bents for each shake table excitation. Acceleration provides a good estimate of the yield displacement; however, the acceleration can be highly influenced by the interaction among different bents in the system. A more exact yield displacement is discussed in Chapter 7 that is based on the calculated load-deflection relationship. Other than within this section, the calculated yield displacements were used throughout this study when defining ductility of the columns.

Backbone curves of the acceleration-deflection hysteresis curves for bents 1 through 3 are plotted in Figs. 6-88 through 6-90. The backbone curves were plotted based on the acceleration-deflection envelopes from tests 12 through 20. Post-failure test data were not included since the bridge system for the post-failure tests was drastically different after the weights were removed. The positive and negative backbone curves for each bent were both plotted in the positive quadrant and each was idealized as elasto-

plastic by setting the initial slope to pass through the first yield point and adjusting the plastic portion so that areas above and below the idealized curves were balanced with the original backbone curves. The failure deflection of bent 3 was defined as the deformation where the acceleration was reduced to 80 percent of the maximum measured acceleration. The backbone curves and idealizations for bents 1 through 3 are plotted in Figs. 6-91 through 6-93, respectively.

Measured maximum lateral deflections of each column for all shake table tests and the displacement ductility calculated using acceleration estimated yield displacements are listed in Table 6-7. The yield displacements used in the ductility calculation were the average of the displacements calculated from the positive and negative backbone curves for each bent. Although a more exact version of this table using the calculated yield displacements is discussed in Chapter 7 the following general observations of the achieved displacements are made. It will be seen in Chapter 7 that the conclusions are similar to those shown in this section.

The maximum displacement ductility that was achieved for the low amplitude tests was 0.32 for bent 3 during test 2. The maximum displacement ductilities achieved for bents 1 and 2 were 0.29 and 0.19 during test 3. The maximum achieved ductilities during the low amplitude tests confirm that the bents remained well below their yield displacements, which was desired for the low amplitude tests.

The first bent to surpass yield displacement was bent 1 during test 14. During test 15, both bents 2 and 3 were subjected to displacements that exceeded yield. The failure ductility of bent 3 was 7.6 during test 19. This ductility is slightly lower than the ductility value of 8.9 discussed in Chapter 7 using the more accurate calculated yield displacement. The maximum ductilities for bents 1 and 2 during high amplitude tests were 5.33 and 5.22, respectively. During the post-failure tests bents 1 and 2 reached displacement ductilities of 4.9 and 6.4, respectively.

6.3.2 Transverse Superstructure Displacement Envelopes

Displacement envelopes for transverse deformation of the superstructure during low and high amplitude tests relative to the shake tables are plotted in Figs. 6-94 through 6-103 and Figs. 6-104 through 6-112, respectively. Envelopes from the post-failure tests are plotted in Figs. 6-113 and 6-114. In each of the figures, there are three graphs, one for each bent. Each graph contains two plots of transverse displacement of the superstructure. One plot is at the instant of maximum displacement and the other at the minimum displacement of the bent.

A general trend of displaced shapes is shown in the low amplitude plots and is more pronounced for the high amplitude plots where the motions had synchronous target motions for tests 12 through 15 (pre-yield runs). The superstructure deformation at the maximum displacement of bent 1 shows a combination of superstructure translation and in plane rotation about bent 3. The superstructure deformation at maximum displacement of bent 3 shows a combination of superstructure translation and a slight in plane rotation about bent 1. Plots of the displaced shape of the superstructure at the maximum deformation of bent 2 appear to be a combination of the deformed shapes at maximum displacements of bents 1 and 3. All plots show a slight contribution of superstructure bending to the total displaced shape.

As shown in comparing the plots of Figs. 6-106 and 6-107, the trend of superstructure displacements at maximum bent deformations after yielding of the bents in test 15 changed slightly so that the maximum superstructure deformations were mostly composed of translation. However, the pivoting of the superstructure about the bent at the other end of the bridge in the plots of bents 1 and 3 remained an underlying characteristic of displacement envelopes through failure of bent 3.

6.3.3 Longitudinal Superstructure Displacements

Except for test 9, the biaxial test, and low amplitude vibration testing to determine the longitudinal modes, all shake table excitation to the bridge was in the transverse direction. Although the primary direction of excitation was in the transverse direction, the superstructure underwent longitudinal displacements that were caused by the unsymmetrical bent stiffness. Longitudinal displacements relative to the laboratory floor were measured at the four corners of the north and south ends of the superstructure. In order to calculate the relative displacements, the shake table displacements for table 1 and table 3 were subtracted from displacements at the north and south ends of the bridge, respectively.

Table 6-8 lists the measured maximum and minimum relative displacements for each test at the four corners of the superstructure. The instrumentation plan is shown in Fig. 3-7. The measurements at the northeast and northwest corners are labeled as DL1 and DL2, respectively. The measurements at the southeast and southwest corners are labeled as DL3 and DL4, respectively. Relative displacement history plots at the four corners of the bridge for the both the half-scale and full-scale low amplitude biaxial tests and tests 12 through 19 of the high amplitude tests are shown in Figs. 6-115 through 6-118.

As shown in Table 6-8, and on the displacement history plots, the maximum longitudinal deflection of the superstructure was 0.5 in (13 mm), which was measured at the southwest corner during test 19. The maximum longitudinal deflection of the superstructure corners during tests 12 through 18 was 0.22 in (5.5 mm). The maximum longitudinal displacement measured during the biaxial tests was 0.12 in (3.0 mm) at both of the north corners of the superstructure. For concrete box girder bridges the gap at superstructure hinges is typically 2 in (51 mm). This translates to a gap of 0.5 in (13 mm) for the quarter-scale of the shake table model. Since the maximum measured longitudinal displacement measured at the corners of the superstructure during the tests was 0.5 in (13 mm), and most of the response was at amplitudes of less than 0.25 in (6.4 mm), the bridge model tested on the shake table would not have any interaction at the ends of the frame with the adjacent spans if they were present because the hinge gaps would not generally close. This validates the lack of modeling the impact of adjacent spans in the shake table test setup.

The north and south longitudinal displacements of the superstructure were calculated by averaging the displacements for each set of corner displacement measurements at the north and south ends. Table 6-9 lists the maximum and minimum values of the north and south displacements. Plots of the histories of north and south end relative displacements for the two low amplitude biaxial tests and for tests 12 through 19 are shown in Figs. 6-119 and 6-120. There are slight differences between the north and

south end displacements. These differences are from two sources, axial deformation of the superstructure, and slight longitudinal displacements in the three shake tables that varied among them.

Longitudinal shake table displacements for the north and south shake tables during biaxial tests and high amplitude tests 12 through 19 are plotted in Figs. 6-121 and 6-122, respectively. Maximum and minimum values of the displacements for all tests are listed in Table 6-9. As shown in the plots, the shake tables underwent slight displacements in the longitudinal direction during the tests due to force feedback from the bridge. The maximum amount of differential longitudinal displacement between adjacent tables before failure of bent 3 was 0.02 in (0.5 mm) during test 19.

6.3.4 Reinforcement Strains

As discussed in Chapter 3, and shown in the instrumentation plan sheets of Figs 3-2 through 3-6, strain of both the lateral and longitudinal reinforcement in the columns was measured during testing. The strain histories for all high amplitude tests and the post-failure tests are shown in Appendix A. The histories were included in the appendix and not in this chapter because the findings from them are similar and can be demonstrated by observing a selected number of the plots. Figures A-1 through A-160 show the strain histories for high amplitude tests. Figures A-161 through A-320 show plots of the histories for low amplitude tests. As shown in the figures, strain gauges can be reliable for strains up to approximately 200000 microstrain (20 percent). The scale of each of the plots is such that it begins focusing on the range close to yield strain and increases as needed for subsequent tests up to 200000 microstrain. Tables 6-10 through 6-29 list the maximum and minimum strains measured in each of the strain gauges for all tests including low amplitude, high amplitude, and post-failure tests. Both the figures in Appendix A and Tables 6-10 through 6-29 present the strain gauge data in the same hierarchal order, which is as follows: longitudinal and horizontal reinforcement, bents 1 through 3, west and east columns, top and bottom of column. The instruments are further labeled at the top and bottom of each column with a number.

One of the main purposes of the strain gauges was to measure if and when yielding took place at various column locations. In the figures of Appendix A, the measured yield strains from tensile tests of longitudinal reinforcement and horizontal spiral reinforcement are marked as dashed lines. In the strain tables, strain values for reinforcement that has exceeded its yield strain are listed in bold. While strain gauges are accurate instruments, cracks and interaction of aggregates and ribs on the bars with the cement paste can cause highly localized strains. Therefore, erratic measurements may be recorded during some tests.

6.3.4.1 Longitudinal Reinforcement

Tables 6-10 through 6-22 list the maximum measured strains for the longitudinal reinforcement. Other than gauge 3ETSL3 (Table 6-21) located in bent 3, none of the longitudinal reinforcement strains exceeded yield during the low amplitude testing. It was determined that the irregular strain measured at this location was due to localized strain effects. Slippage was not an issue for the longitudinal reinforcement because more than adequate anchorage was provided into both the cap beam and the footings.

Longitudinal strain envelopes for bent 1 are listed in Tables 6-10 through 6-14. The first yield of longitudinal reinforcement for bent 1 was measured during test 13. During this test, 22 out of 35 measured bars yielded. Longitudinal strain envelopes for bent 2 are listed in Tables 6-14 through 6-18. The first yielding of the longitudinal reinforcement in bent 2 was during test 15. During test 15, 21 out of 33 of the bars with strain gauges passed yielding. Longitudinal strain envelopes for bent 3 are listed in Tables 6-18 through 6-22. The first yielding of longitudinal reinforcement for bent 3 was measured during test 13. However, only four of 36 bars that were instrumented reached yield strains. During test 14, 23 of the 36 bars reached strains beyond yield.

In comparing the longitudinal strain gauge data of the three bents during yield, it is shown that the first bent to fully yield was bent 1, the medium height bent during test 13. Also during test 13, initial yielding began in bent 3, the shortest of the bents. During test 14, bent 3 became fully yielded. Bent 2, the tallest of the bents yielded during test 15.

6.3.4.2 Lateral Reinforcement

Tables 6-23 through 6-29 list the strain maxima for the strain gauges that were located on the spirals in the columns. The strain in the spirals was due to a combination of confinement stress from the concrete and from column shear. As shown in the tables, none of the spirals reached the yield strain during the low amplitude tests.

Lateral reinforcement strains for bent 1, the medium height bent are listed in Tables 6-23 through 6-25. The maximum measured lateral strains in bent 1 occurred during test 19 and reached approximately one half of the yield strain.

Lateral reinforcement strains for bent 2, the tallest of the bents, are listed in Tables 6-25 through 6-26. One of the 12 bent 2 strain gauges, 2EBSH2, located on the bottom south side of the east bent, measured strains that were greater than yield beginning at test 18. The greatest strain measured with the other 11 gauges on bent 2 was in one gauge that measured approximately 2/3 of the yield strain during tests 17 and 18. The remaining ten lateral strain gauges in the bent did not measure strains above 20 percent of yield for any of the tests. Since bent 2 was the tallest of the bents, shear demand was low.

The maximum strains for the lateral reinforcement of bent 3, the shortest of the bents are listed in Tables 6-26 through 6-29. Bent 3 should have had the largest lateral reinforcement strains of all the bents because bent 3 had the smallest aspect ratio, therefore the largest shear demand, and bent 3 reached a flexural failure, which caused high confinement stresses. Other than two gauges, which were impacted by localized effects, strains in bent 3 generally remained low and well below yield throughout testing up through test 18. During test 19, strains in several of the spirals exceeded yield and in select spirals showed signs that the spiral approached failure. The high strains during test 19 and through the completion of testing were a result of the plastic hinging at the ends of the columns. As discussed in the observed results, after test 19, many of the spirals were exposed and deformed from extensive spalling, buckled longitudinal rebar, and crushing of confined concrete.

6.3.5 Column Curvature Data

Curvature within the plastic hinge zones of the columns was calculated using the measured displacements that were discussed in Chapter 3 and are shown in Fig. 3-1. Curvature was measured in both the transverse and longitudinal directions of the bridge. In the transverse direction, curvature was measured at two intervals from the point of fixity over a distance of 12 in (305 mm) at each end of all of the columns. The first interval was over a distance of 5 in (127 mm) from each point of fixity; the second was over an additional adjacent 7 in (178 mm). In the longitudinal direction of bending, curvature was measured at one 5 in (127 mm) interval from each point of fixity at the top and bottom of the columns. Longitudinal curvature measurement was included on all columns except for the west column of bent 2. Instruments to measure curvature in the longitudinal direction were excluded on this column because the number of the available displacement transducers was limited and since bent 2 was the most flexible of the columns and excitation in the longitudinal direction was minimal, this was seen as the least important curvature measurement.

Curvature was calculated by dividing the rotation at each set of curvature rods by the gauge length. Rotation at each transducer pair was calculated by dividing the combined measured displacements by the horizontal distance between the transducers. Histories for the measured curvatures for the high amplitude tests 12 through 20 are plotted in Figs. 6-123 through 6-156. Histories for the post-failure tests, tests 21 and 22 are shown in Figs. 6-157 through 6-190. Maximum and minimum values of curvature for all runs are listed in Tables 6-30 through 6-38. Curvature measurements are not included for bent 3 during test 22 because the instruments were removed from the bent after test 21 so that they would not be damaged from the large deflections and crushing concrete of the bent 3 columns. The hierarchal order that the curvature data is presented for both the tables and figures is the following: bents 1 through 3, west and east column, top and bottom, transverse and longitudinal bending, and first and second interval from point of fixity (footing surface at the bottom and the bottom of the beam at the column top).

The calculated yield and ultimate curvatures from the elasto-plastic idealization of moment-curvature analysis discussed in Chapter 4 were 0.00046 and 0.00718 rad/in (0.000018 and 0.00028 rad/mm), respectively. A direct comparison between the measured curvatures and calculated curvature cannot be made because the calculated curvature is for a section of the column whereas the measured curvatures represent an average curvature over the gage length. Also, the measured curvatures for the intervals that are adjacent to the point of fixity on the columns include bond slip, which causes a concentrated rotation at the column ends that is not included in the moment-curvature calculations. However, the calculated yield and ultimate curvatures can be compared to the measured values to determine approximately how much the columns have deformed on a relative scale.

The maximum measured curvature in the transverse direction of bent 3 located at 5 in (127 mm) intervals from the column ends during test 18, the test before failure of bent 3, ranged from 0.0066 to 0.0093 rad/in (0.00026 and 0.00037 rad/mm). During the failure run, the maximum measured curvature at these locations ranged from 0.012 to 0.015 rad/in (0.00047 and 0.00059 rad/mm). These maximum measured curvatures of bent 3 exceeded the calculated ultimate curvature from moment-curvature analysis.

However, the measured curvatures included bond-slip, which is not accounted for in the moment-curvature calculation.

The maximum measured transverse curvatures for bent 3 during test 18 for the second intervals from the column ends, which were over a gauge length of 7 in (178 mm), ranged from 0.00093 to 0.0016 rad/in (0.000037 to 0.000063 rad/mm). During test 19, the maximum measured curvatures at these locations ranged from 0.00090 to 0.0021 rad/in (0.000035 to 0.000083 rad/mm).

6.3.6 Cap Beam Bending

Plans for the displacement transducers that were used to measure cap beam bending, discussed in Chapter 3, are shown in Fig. 3-7. Each of the cap beams had four displacement transducers spaced equally across the beam to measure the vertical displacement between the bottom of the cap beam and the top of the footing. The vertical displacements of the cap beam were calculated by subtracting the cosine of the lateral deflections at each bent from the measured displacements of the vertical displacement transducers. Figures 6-191 through 6-199 are plots of the displaced shape of the three cap beams at the instant when each of the cap beam ends is at a maximum positive displacement for tests 12, 15, and 19. The displaced shape at maximum positive end deformation corresponds to the point in time when the forces are greatest in the cap beams. These tests were chosen because they are representative of the bridge before yielding, after yielding, and at failure.

The maximum cap beam bending deformation between the columns for test 12 was 0.010 in (0.25 mm) for bent 3 during positive deformation on the west side of the beam. Maximum cap beam bending deformations for tests 15 and 19 were 0.040 and 0.068 in (1.02 and 1.73 mm) for the bent 3 beam at the instant of maximum deformation at the west and east ends of the beam, respectively. The maximum bending deformations are further discussed in Chapter 7, where they are quantified relative to moment demand in the columns using the computer model that was developed to predict response of the bridge.

6.3.7 Damping

Damping ratio of the bridge response in the transverse direction were calculated using accelerations measured at the top of each bent during the transverse square wave tests. The square wave tests, discussed in Section 5.2.3, were a series of displacement pulses in the transverse direction of the bridge that subjected the bridge to free vibration. Damping was calculated using the log decrement method (Chopra 2001) considering the first five cycles of acceleration for each free vibration. Three damping ratios were calculated for each test and for each bent. Each bent damping ratio was the average of two of the free vibrations from each square wave test.

Table 6-39 lists the values of damping for each bent during each of the square wave tests, which were conducted at various stages of damage progression beginning with test 8 through after test 19. The average amount of damping which was for low amplitude response, remained relatively constant for all tests that were conducted throughout the range of damage states of the bridge. Average damping for bent 1, the medium height bent, was 3.9 percent. This value was slightly less than the average

damping at bent 3, the shortest bent, which was 4.9 percent. The damping measured at bent 2, which was dominated by the response of the stiffer bents 1 and 3, was 4.2 percent. The average damping of the bridge model was 4.3 percent. Damping is further discussed in the next chapter with regards to analytical modeling of the bridge.

6.3.8 Modal frequencies of superstructure

Frequencies of the superstructure modes measured between progressive tests of the bridge were determined from the white noise tests that were discussed in Section 5.2.3. These modes are similar to the calculated elastic modes from preliminary analysis, which considered the bridge in a cracked state prior to yielding and were discussed in Section 4.2.3. The calculated modes from preliminary analysis included three primary modes in the transverse direction. The first was superstructure translation with slight in-plane rotation; the second was superstructure in-plane rotation with slight translation; the third was superstructure bending. The calculated longitudinal modal response was composed of two modes. The first longitudinal mode was translation and dominated the longitudinal response. The second longitudinal mode was bending of the superstructure beams about the transverse axis of the bridge. Modal frequencies that were measured from the tests were comparable to the modes from preliminary analysis. However, the measured modal frequencies as testing progressed, which are discussed in this section, provided information about the frequency shifting of the modes as the bridge was increasingly damaged. After the measured frequencies are discussed, they are compared with the calculated frequencies from preliminary analysis.

Each white noise test consisted of two sets of excitation, transverse, followed by longitudinal. Frequency contents at each bent were calculated utilizing plots of the Fourier Transform from the recorded accelerometer data. The Fourier Transforms (FFT) were calculated using a Hanning window (Ramirez 1985) function and a shifting window that considered 2048 terms of recorded data shifted 20 times. The 20 shifted FFT functions were averaged to create a single more uniform function. The purpose of the Hanning window was to weight the beginning and end of the data to zero with a cosine function to compensate for an inherent error in the FFT algorithm that causes the frequencies to be more spread out than well defined at a concentrated point.

FFT plots for the white noise tests are shown in 6-200 through 6-243. The plots are first displayed for each of the three top of bent accelerometers in the transverse direction followed by a longitudinal superstructure accelerometer, and are in chronological order of the white noise tests. The modal frequencies, which were determined with a 3 point moving average of the FFT functions, are superimposed on the plots. The FFT of the accelerometer data where each mode was most dominant was used to determine the corresponding modal frequency. For example: the first mode in the transverse direction was most dominant in bent 1, and the second mode was more dominant in bent 3. Therefore the accelerometer measuring transverse acceleration of bent 1 was used to calculate the frequency of the first mode in the transverse direction. The accelerometer measuring the transverse acceleration of bent 3 was used to calculate the frequency of the second mode in the transverse direction.

Although the transverse response is mostly governed by the first three transverse modes, the first five modes were determined. In the longitudinal direction there were

only two prevalent modal frequencies; both were determined for each longitudinal test. The five transverse and two longitudinal measured modal frequencies for each test are listed in Table 6-40. Table 6-41 lists the modal periods.

6.3.8.1 Variation of Period with Achieved Ductility

Plots of periods for the first two transverse modes and the third through fifth transverse modes vs. maximum achieved bent 1 displacement ductility are shown in Figs. 6-244 and 6-245, respectively. Figures 6-246 and 6-247 show the results for bent 3. Figures 6-248 and 6-249 are plots of the two longitudinal modal periods vs. maximum achieved ductility for bents 1 and 3, respectively. There is an almost linear relationship between increase of the first two transverse modal periods and the damage progression of bents 1 and 3. A similar relationship is shown for the first longitudinal mode. The relationship of damage increase to lengthening of the periods for the first two transverse modes and primary longitudinal mode is expected because these modes are dominated by response of the columns, which were subjected to increased damage with ductility. The first and second transverse modes are combinations of superstructure translation and rotation that are governed by bents 1 and 3, respectively. The first longitudinal mode is longitudinal deformation governed by the combined stiffness of all columns.

The third transverse and second longitudinal modes do not have significant relationships with the increase of damage in the bents. This is not surprising since these modes are related to superstructure deformations and no significant superstructure damage was observed.

It is apparent in reviewing this data that low amplitude modal frequencies of a bridge could be a valuable tool in assessing and quantifying post earthquake damage assuming that the benchmark frequency for the undamaged structure is available. Significant changes in modal frequencies were measured after achieved column displacement ductilities of approximately 0.5. At ductility values of 2.0 for bents 1 and 3, lengthening of periods for the first two transverse modes ranged from approximately 25 to 50 percent. In a system such as a bridge where stiffness can be highly variable for certain components, modal frequencies can be an identifying factor of the overall damage at predetermined locations. As revealed by the low amplitude white noise tests, it is also particularly favorable that this indicator of damage could possibly be used at a low level of response such as that from wind or traffic loading.

6.3.8.2 Comparison of Measured and Predicted Vibration Periods

In this section, the calculated periods are compared with the predicted periods from pre-test analysis that was discussed in Chapter 4. The reason that the pre-test analysis model is used in the comparison is because it utilizes a linear cracked stiffness model for the columns. The pre-test analysis model included the measured material properties making it as accurate as possible. A comparison can not be made with the computer models discussed in Chapter 7 because these models utilize fiber nonlinearity for the columns, which can not be included in modal analysis. Therefore the post-test analytical models would predict erroneously high frequencies that do not include bond-slip or elasticity at the column ends.

The calculated modal periods of the first three transverse modes from preliminary analysis were 0.40, 0.30, and 0.08 seconds, respectively. The calculated period of the first longitudinal mode was 0.41 seconds. The measured periods of these modes from free vibration testing are listed in Table 6-41. Calculated modal periods were from a cracked section linear analysis that assumed the columns were in an un-yielded state defined by the first slope of an elasto-plastic load-deflection idealization. A comparable state of damage for the bridge model would be the free vibration tests after test 11 when the concrete in the columns had cracked, but the reinforcement had not yet yielded. The measured periods of the first three transverse and the first longitudinal modes from these tests were 0.38, 0.27. 0.08, and 0.33 seconds, respectively.

The calculated periods are comparable to the measured frequencies, except that the calculated periods were generally larger. For first two transverse modes, calculated values were approximately 11 percent and 5 percent greater than measured values, respectively. The third mode prediction was a near perfect match to the measured value. For the first longitudinal mode, the calculated value was larger by approximately 24 percent.

The reason that the calculated periods of the first two transverse and the first longitudinal modes are slightly larger than the measured values is because these modes are highly dependant on column stiffness. The elasto-plastic idealized stiffness of the columns was likely lower than the low amplitude stiffness after test 11 because column stiffness is not actually linear and is larger for low forces. The prediction of the longitudinal modal period was significantly larger than the measured value because there was very little damage in the longitudinal direction since primary excitation was in the transverse direction. The prediction of the third transverse modal period was very close to measured because this mode is not dependant on column damage, only on superstructure response.

6.3.9 Achieved Shake Table Motions

Since the shake tables and bridge model are four separate systems that interact with each other, the achieved motions of the shake tables are highly dependant on the mass and stiffness of the bridge. The software that drives the shake tables modifies the target motions as testing is progressed as an attempt to compensate for the response of the payload on the tables. However, the bridge system in this experiment is highly nonlinear and relatively stiff and strong with respect to the tables, which makes compensation of the motions very difficult. This section presents the achieved shake table motions and comparisons of achieved motions with target motions as well as each other. Chapter 9 discusses this matter in further detail and describes the implications of differences between the target and achieved motions.

6.3.9.1 Target and Achieved Response Spectra

Figures 6-250 and 6-251 show comparisons of the target and the achieved response spectra of the three shake tables for tests 1 and 8. These tests are representative of the low amplitude tests. Figures 6-252 through 6-260 show the response spectra comparisons for all high amplitude tests, tests 12 through 20. On each figure, the measured transverse vibration periods, discussed in Section 6.3.8, from the most recent

free vibration test are superimposed. The location of the periods on the spectra allow for a better understanding of what frequency contents are most relevant for each motion. Table 6-42 lists the measured and target peak accelerations of the three shake tables for the same tests that are shown in Figs 6-250 through 6-260. Table 6-43 lists target and achieved comparisons of the maximum spectral accelerations.

The response spectra comparisons for tests 1 and 8, which had the same target motions, are shown in Figs. 6-250 and 6-251. As shown in the figures, frequency contents of the achieved motions for test 8 were considerably closer to the target than for test 1. The improvement in achieved motions for test 8 was a result of modified shake table drive motions to adapt for deviations in the previous tests. The modification of the drive motions was successful because there were not any significant changes in the bridge system stiffness during low amplitude testing.

The most notable difference between the target and achieved accelerations in the high amplitude testing is shown for table 3 (bent 3) in Figs. 6-255 and 6-256, which were for tests 15 and 16. It was during these tests that bent 3 had been subjected to significant yielding and damage. The achieved motion for table 3 contained a peak amplitude error of approximately 66 and 80 percent greater than the target spectral acceleration for tests 15 and 16, respectively. The peak spectral acceleration happened to occur at the frequency for the measured second transverse mode. The second transverse mode is the transverse mode of the bridge that is dominated by response of bent 3. As discussed in the pre-test analysis in Chapter 3, the failure was predicted to occur in bent 1. However, as discussed in this chapter the failure of the bridge was in bent 3. Upon review of the achieved accelerations, it appeared that the reason bent 3 failed instead of bent 1 was because of overshooting in the achieved spectral acceleration. This is further discussed in Chapter 9.

As shown in comparing the achieved response spectra of tests 16 and 17 (Figs. 6-256 and 6-257), spectral acceleration for test 17 was generally lower than test 16. The target PGA for tests 16 and 17 were 0.75 g and 1.0 g, respectively. The reason that the amplitude was reduced for test 17 was because during testing, it was observed that the achieved motion of table 3 exceeded the target motion in test 16 and that the shake table control software was not correctly adjusting the motion to compensate. As a result the drive motion for test 17 was adjusted. The result of this adjustment was discussed in Section 6.3.1 with regards to the acceleration-deflection hysteretic plots. It appeared from the hysteretic plots of the columns that the shake table motion amplitude was undershot for test 17. However, upon reviewing the target and achieved spectra, it became evident that the motions of test 16 were overshot.

6.3.9.2 Achieved Displacement History of Shake Tables

Figures 6-261 through 6-263 show displacement histories of the three shake tables for tests 13, 16, and 19, respectively. Figures 6-264 through 6-266 are the same plots, except in a larger scale having only a 5 second portion of the 25 second histories. Figures 6-267 through 6-269 show the acceleration histories. Since the target motions were the same synchronous motion for all high amplitude tests, ideally the achieved motions would be identical. However, it can be seen in Figs. 6-261 through 6-266 that the achieved displacements of these tests are significantly different among the shake tables.

Because the tests were intended to be under coherent ground motion, all target response of the bridge should have been acceleration based response. The only source of error in the achieved motions due to displacements could be from out of phase table motions causing static forces on the bridge. It is apparent that out of phase motions are present, and from the plots, is does not seem that the error is reduced as the testing amplitude is increased.

Table 6-44 lists the maximum incoherency between adjacent shake tables during testing for all low amplitude, high amplitude, and post-failure tests. The incoherency is listed between tables 1 and 2 and tables 2 and 3. For all the low amplitude tests except tests 1 and 8, incoherency was expected since the target motions were non-coherent by design. All high amplitude tests had synchronous target motions and therefore were expected to be coherent. A plot of the maximum incoherency between tables 1 and 2 vs. target PGA for the high amplitude tests 12 through 19 is shown in Fig. 6-270. Figure 6-271 shows similar results for shake tables 2 and 3. It is shown in the figures that there is a linearly increasing relationship of the incoherency error between both sets of shake tables as target PGA is increased. The error between shake tables 1 and 2 is significantly greater than for shake tables 2 and 3. A reduction of error is shown after test 16 in both plots when the shake table drive motion was adjusted as an attempt to better match the target accelerations. The significance of these displacement errors and their impact on the shake table test results are further discussed in Chapter 9.

The plots of superimposed measured transverse shake table acceleration histories are in Figs. 6-267 through 6-269. Unlike displacement incoherency, inconsistency among table acceleration histories does not relate directly to forces within the bridge. An example of this phenomenon is the application of an acceleration pulse on a structure when period of the pulse and the structure are significantly different. Although the amplitude of this pulse may be large, its period is such that the pulse would not excite the structure. Acceleration response of the bridge depends on frequency content of the shake table accelerations and on modal frequencies of the bridge. Therefore the response spectra plots in Sec. 6.3.9.1 provide the best evaluation of achieved accelerations. It can be seen in the figures that matching of the accelerations between the shake tables is generally better as the amplitude is increased.

6.3.10 Cantilever Accelerations

Although the cantilevers in the north and south end of the bridge were designed with a significant factor of safety, monitoring their damage both visually and numerically was important because there was no safety system directly beneath them. As discussed in Section 3.1.4, accelerometers were attached to the two superstructure cantilevers at the extreme ends of the bridge to measure vertical acceleration. The cantilever accelerations were measured so that the cantilevers could be monitored to make sure that they were not subjected to excessive vertical forces during testing. Since no damage was observed in the cantilevers during the tests and vertical accelerations remained low, this was not an issue.

The locations of the accelerometers on the bridge are shown in Fig. 3-8. To determine the approximate maximum forces that each cantilever was subjected to in flexure and shear from the shake table excitation, the maximum measured vertical

acceleration from high amplitude tests was multiplied by the tributary mass of the cantilever. The maximum moment and shear were then determined from the combination of force from shake table excitation and the dead load. To quantify amplitudes of the maximum moment and shear, they were compared to the cantilever capacity.

The maximum vertical accelerations in the north and south cantilevers were measured during test 19 and were 0.526 and 0.754 g, respectively. Since the cantilevers were identical, the estimated force for the south cantilever, which was subjected to the largest acceleration, was evaluated. The maximum force and moment at the support of the cantilever from the combination of vertical acceleration and dead loads are 28.0 kips (125 kN) and 524 kip-in (59.2 kN-m). When compared to the shear and moment capacity of the cantilever by conservatively excluding additional strength of the cantilever from the longitudinal post tensioning, the ratio of capacity over demand for shear and moment were 7.9 and 6.7, respectively.

6.4 Measurement of Force

Although lateral force is a defining characteristic in measuring performance of reinforced concrete columns, as discussed in Sec. 6.3.1, there was not a direct force measurement in either the individual columns or the bents. Instead, accelerations measured at the top of the bents were used as an indicator of the force. Upon completion of the shake table tests, recorded data from the pressure in the shake table actuators for select tests was reviewed to determine if it could be used to calculate force in the columns. If the force in columns could be accurately determined from actuator pressure, then it could be directly known during future bridge tests on the shake tables. Comparisons of the force approximated from accelerometers and force calculated from measured actuator pressure are further discussed in Chapter 7 where the forces based on measurements of acceleration and actuator pressure are compared with predicted forces from the experimentally verified computer model.

6.4.1 Comparison of Acceleration Estimate with Actuator Pressure Estimate of Forces

Figures 6-272 and 6-273 are comparisons of forces from measured acceleration and from measured actuator pressure for tests 15 and 18. Envelopes of the acceleration and actuator based forces are listed in Table 6-45 along with percent differences of the maximum and minimum forces for each bent and test. Tests 15 and 18 were chosen for the comparisons because Test 15 was a representative high amplitude run where the bents had yielded and test 18 was the pre-failure run. The force from acceleration was calculated assuming tributary mass for each bent which was multiplied by the measured acceleration at the top of the bents.

The force from actuator pressure for each shake table was calculated by converting measured hydraulic actuator pressure to actuator force. The friction of the shake tables, estimated as 2 kips (8.9 kN), was subtracted from the actuator force. The inertial mass of the shake table combined with the mass of the footing, spacer block if applicable, safety frames and half of the columns were multiplied by the table acceleration and then added to the reduced actuator force. This combination of actuator force, table friction, and total shake table mass multiplied by shake table acceleration was

the estimated force at the mid-height of the columns. Slight error was expected in the actuator pressure calculation of force due to error in the estimation of shake table friction, which could not be directly measured, as well as delay in the measurement of hydraulic pressure in the actuators.

As shown in the figures and when comparing the envelopes in Table 6-45, the predicted force histories of bents 1 and 3 are in good agreement for the actuator estimated and acceleration estimated forces for both tests 15 and 18. It is shown however, that for bent 2 the forces calculated from measured acceleration were greater than those from the actuator pressure. The forces estimated from the acceleration are likely greater than the actual forces because the measured acceleration at bent 2 is influenced by the stiffer bents 1 and 3. Due to the bent 1 and 3 influence, the estimate of tributary mass for bent 2 during certain instances of response was likely greater than actual tributary mass.

The agreement between the results of the two methods, and higher accuracy of force estimation for bent 2 using the actuator pressure suggests that bent force can be reliably calculated from the actuator pressure. This is further discussed in the next chapter.

6.5 Concrete Compressive Strains

The maximum measured compressive strains in the core concrete of the columns were determined utilizing both the curvature data that was discussed in Section 6.3.5 and the strain data that was discussed in Section 6.3.4. The compressive strains were determined in order to compare strains that were achieved in the confined concrete during testing with the maximum concrete strains that are predicted with the Mander model (Mander 1988) for confined concrete. This was an important comparison because the Mander model was assumed for moment curvature analysis used in the pre-test analytical models as well as in the post-test analyses that are discussed in Chapter 8. Strains from displacement transducers were calculated assuming that the column sections remained plane. These strains were the average strain that was measured in the transverse direction over each 5 in (127 mm) gauge length at the column ends. The compressive strains should not have been greatly affected by yield penetration since this is a phenomenon that is more pronounced when the reinforcement is in tension. Since the measured strains with the transducers were average strains over 5 in (127 mm), they should have been less than the maximum strains.

The maximum measured transducer compressive strains for tests 18 through 22 at each of the four column ends for the three bents are listed in Table 6-46. The values for the test having the largest displacement demand on each bent are shown in bold. The test considered for bent 3 was test 19 since this was the bent 3 failure run. The maximum displacements for bents 1 and 2 were during tests 19 and 22, respectively. Average compressive strains at the four column ends were calculated for each of the three bents during the run with maximum displacement.

Comparisons of the maximum measured concrete compressive strains from the displacement transducers with the capacity prediction of the Mander model are listed in Table 6-47. The ratio of the maximum measured compressive strains divided by the Mander's prediction was 3.0 and 2.3 for the maximum and average compressive strains

of bent 3, respectively. These ratios for bents 1 and 2 were 2.6 and 1.5, and 2.6 and 1.9, for the maximum and average compressive strains, respectively.

The maximum measured compressive strains from the longitudinal reinforcement strain gauges at the extreme compression fiber of confined concrete that were located at the column ends were also compared with the strain capacity predicted by the Mander model. This comparison was made do determine if the same compression amplitude trends were measured in the bar as were measured using the displacement transducers (discussed previously). It was assumed for the comparison that the compressive strain in the reinforcement was equal to that of the surrounding concrete. However, the compressive strain in the reinforcement was not identical to that of the surrounding concrete due to an imperfect bond. Therefore concrete compressive strains from the displacement transducers were perhaps more accurate. Because the reinforcement used for the comparison was adjacent to the extreme compression fiber and it can be assumed that the reinforcement has uniform strain, no modification was made to transfer the reinforcement strain from the center of the bar to the core edge. The reinforcement strains at each of the column ends of each bent for the run where the bent was subjected to maximum displacement are listed in Table 6-48. The strains are compared with the Mander prediction in Table 6-49. The ratio of the maximum measured compressive strains divided by the Mander prediction was 4.6 and 2.8 for the maximum and average compressive strains of bent 3, respectively. These ratios for bents 1 and 2 were 1.4 and 0.8, and 0.9 and 0.5, for the maximum and average strains respectively.

Since bent 3 is the only bent that failed and was subjected to crushing of the confined concrete, its data presents the most valid comparison for ultimate strain. The measured strains from the confined concrete using both displacement transducers and strain gauges suggest that either the maximum strain predicted from the Mander confined concrete model is conservative by a factor of at least 2, or that the displacement capacity failure occurs substantially later than crushing of the edge of the confined concrete.

6.6 Evaluation of Performance

The observed and measured response of the shake table bridge model leads to two conclusions with regards to performance. The first was that the modeling technique that was used for testing was successful. The second is that the columns, which were designed according to contemporary earthquake design code performed well.

No damage was observed in the superstructure during the tests. This included cracking of the concrete in the superstructure beams and cap beams, and slippage of the longitudinal post-tensioning. The masses and footings remained rigidly attached to the bridge deck and the shake tables throughout testing.

The shortest of the columns, which were located in bent 3 and had an aspect ratio of only 2.5, showed no signs of shear distress from the pre yield state through failure in flexure other than minor shear cracking. The confinement reinforcement in bent 3 provided adequate confinement stress on the concrete and lateral support of the longitudinal reinforcement to delay buckling of the longitudinal reinforcement, so that the bent could reach a displacement ductility of 7.6 (8.9 using pushover calculated yield displacement from Chapter 7) before failure. Further discussion of the performance of

the bridge model with respect to the design motions and column performance is presented in Chapter 8.

CH 7: Analytical Studies

7.1 Introduction

This chapter discusses the analytical models that were developed after completion of testing as an attempt duplicate the response of the bridge specimen subjected to the shake table test motions. Two analysis packages were utilized for this purpose: SAP2000 version9 (CSI 2005), and Drain-3DX (Prakash and Campbell 1994). The goal of the analytical modeling was twofold: the first was to determine the accuracy of contemporary modeling techniques for calculating the nonlinear response of this typical reinforced concrete bridge structure, the second was to develop a computer model to use for further study.

SAP2000 represents a state-of-the-art, general-purpose commercial structural analysis program for the static and dynamic analysis and design of 3D nonlinear structures, and is widely used throughout the engineering community. Drain-3DX, part of the Drain family of programs based on Drain 2D, which was developed in 1973, is a general purpose FORTRAN based program for the static and dynamic analysis of 3-dimensional nonlinear structures. Drain was written as an analysis program that was simpler than the average general structural analysis program but contained important seismic analysis features that at the time were not provided by other programs.

Because the superstructure of the bridge model was designed to remain elastic, all inelasticity in the analytical models was specified in the columns. Three parametric studies were conducted to optimize the efficiency and accuracy of the models. The first two were to determine the optimum discretization of the inelastic fiber sections and number of fiber segments in each column. The third was to determine the integration time step to converge the results.

The achieved shake table motions from tests 12 through 20 (high amplitude tests) were input to the models in sequence as an attempt to duplicate the response from low amplitude up to failure. It was determined from the comparison of calculated responses that Drain-3DX was more efficient and provided a more accurate calculated response than the SAP2000 model. The Drain-3DX model was then evaluated for accuracy in duplicating of the bridge response for the low amplitude biaxial motions. The Drain-3DX model was used for further study that is discussed in Chapters 8 through 10.

7.2 Dynamic Analytical Modeling Considerations

In this section, considerations in analytical modeling are discussed. The rate of loading for the columns was measured at the critical sections and the corresponding strain rate modification to material properties was applied for input to the analytical models. The achieved shake table motions were modified so that displacement records could be input to the computer models and produce excitation that would be comparable to that of the shake tables.

7.2.1 Strain Rate Effect on Material Properties

Previous studies have shown that compressive strength of concrete and the yield and ultimate strength of steel are influenced by strain rate (Kulkarni and Shaw, 1998)

(Zadeh and Saiidi, 2005). The measured material properties for the columns modified by the strain rate effects were calculated and used in the analyses. Concrete modifications were made according to the recommendations of Kulkarni and Shaw (Equation 7-1). The Zadeh and Saiidi recommendations were chosen for the reinforcement because unlike the Kulkarni and Shaw recommendations, which only discuss modification of the yield stress, the Zadeh and Saiidi equations include a modification for both the yield and ultimate strength for variable strain rates. Equations 7-2 and 7-3 are the Zadeh and Saiidi equations that were used for the steel reinforcement modification.

Modification factor for concrete compressive strength is:

$$y = 0.022Ln(x) + 0.9973 \quad (7\text{-}1)$$

where

x = compressive strain rate / static strain rate

static strain rate = 6.2 microstrains per second (benchmark from development of the empirical equation)

Modification factor for steel yield stress is:

$$y = (SRI/10^{-4})^{\alpha} \quad (7\text{-}2)$$

where

$SRI = K^{*}\epsilon_{ave}$

$K = (\epsilon_y / \epsilon_{0.5y})^{0.5}$

$\epsilon_{ave} = (\epsilon_y / \epsilon_{0.5y})/2$

ϵ_y = tensile strain in microstrain rate at yield strain

$\epsilon_{0.5y}$ = tensile strain rate in microstrain at one-half yield strain

$\alpha = 0.022*(\phi/\phi_8)^{0.15}-0.006*(f_y/60)$

f_y = yield stress of steel in ksi

$\alpha = 0.022*(\phi/\phi_8)^{0.15}-0.006*(f_y/414)$

f_y = yield stress of steel in MPa

ϕ = bar diameter

ϕ_8 = diameter of #8 bar

Modification factor for steel ultimate stress is:

$$y = (\epsilon_{ave} /10^{-4})^{2/3\alpha} \quad (7\text{-}3)$$

Strain rates used in these equations were the measured rates at the ends of the six columns in the plastic hinge zones and are listed in Table 7-1. The strain rates were measured from the strain gauges on longitudinal column steel at the extreme east and west sides of each column end. These locations coincided with the extreme compression fiber of the confined concrete section. Eight strain gauges were used from each bent. The gauges that are not shown in the table are gauges that did not have readings, or had errors. The compressive strain rate used in the calculation of strain rate effect for concrete was the maximum strain rate in compression before yielding of longitudinal reinforcement for each strain gauge. Both the half-yield and yield strain rates were used to calculate the effects for longitudinal reinforcement. These strain rates were the maximum rates measured within 0.01 seconds of initial yield and initial half-yield for each strain gauge that was used.

Since the average compression, half-yield, and yield strain rates for each bent were close, the average values for all three bents were used for each strain rate calculation. The strain rates used for concrete compression, steel yield and half-yield were 26800, 24100, and 42300 microstrain, respectively. For the ultimate stress variable strain rate modification (Eq. 7-3) Zadeh and Saiidi present correlation using an average strain rate of the half-yield and yield strain rates and correlation using an average strain rate from zero to ultimate strain. Their recommendation is to use the average rate from zero to ultimate because of slightly better correlation. However since good correlation can be found using the average rate from half-yield to yield and since there was limited data from the shake table test of ultimate strain rate, the average strain rate that was used for the ultimate stress modification was the average of half-yield and yield strain rate.

Figures 7-1 through 7-3 are plots of the measured and strain rate modified constitutive relationships for the longitudinal column reinforcement, unconfined concrete, and confined concrete. The measured curve for longitudinal reinforcement (Fig. 7-1) is based on the actual stress and strain from reinforcement tests. This reinforcement curve was modified directly for the yield and ultimate points. Between these points, the yield and ultimate modification factors were linearly interpolated. The curves for confined and unconfined concrete are based on the measured cylinder data that was discussed in Section 4.7.1. The Hognestad (Park and Paulay, 1975) and Mander (Mander et. al 1988) models were used to define the constitutive relationships for the unconfined and confined concrete, respectively.

Figures 7-4 through 7-9 show the strain rate modified curves superimposed on the idealized multi-linear input curves for nonlinear elements in SAP2000 and Drain-3DX. The input curves for SAP2000 and Drain-3DX are further discussed in Sections 7.3.2.3 and 7.3.3.3.

7.2.2 Stiffness Assumptions for Linear Members

Both the Drain-3DX and SAP2000 models were a 3-dimensional assemblage of linear and nonlinear elements connected at the nodes. Nonlinear column elements that were defined between nodes are discussed in Sections 7.3.2.2 and 7.3.3.2. All nonlinearity in the computer models was assumed to take place at the column ends. This was a valid assumption because the superstructure and cap beams were strong and stiff in comparison to the columns. Also, as discussed in Chapter 6, no damage was observed in these regions during testing.

The concrete stiffness for linear elements was specified as the modulus of elasticity based on the unconfined concrete strength from cylinder tests. The superstructure, which was designed to remain elastic and un-cracked using longitudinal post-tensioning, was modeled with gross section properties. The cap beams, which were designed to remain elastic and had additional strength and stiffness from the surrounding rigidly connected post-tensioned solid superstructure were also modeled using gross section properties.

As shown in the moment-curvature analysis of the column section in Fig. 4-1, the response of the columns in flexure generally remains linear after cracking of concrete in tension and until yielding of the longitudinal reinforcement. For the high amplitude tests 12 through 20, the columns were expected to have exceeded their cracking moment.

Since yielding of the reinforcement was concentrated at the column ends, and because of the intensive calculation required for fiber elements which were used to describe column nonlinearity in the computer models as discussed in Sections 7.3.2.2 and 7.3.3.2, the cracked section properties were used for linear portions of the columns. The cracked section properties were the same as those defined in Section 4.2.1 used for preliminary analysis which were from an elasto-plastic idealization of the moment curvature relationship. However, for the post-test analyses discussed in this chapter, the moment-curvature analysis was updated to include the measured material properties obtained at the time of testing.

7.2.3 Shake Table Motions

Since the achieved shake table motions were incoherent, the analytical models required displacement based input. This section describes the method that was used in order to obtain displacement records that were representative of both the acceleration and displacement response of the shake tables.

7.2.3.1 Achieved Motions and Multiple Support Excitation

The initial purpose of the analytical models was to determine the validity of analytical modeling in duplicating the response of the bridge throughout the range of damage states. The achieved shake table motions from tests 12 through 20 were input to the models in order to capture low amplitude through failure response. As discussed in Chapter 6, the target motions for these tests were synchronous for the three shake tables. However, because of the interaction between the bridge and shake tables, the achieved motions were incoherent. In order to conduct an incoherent multiple support excitation analysis, displacement records are required to satisfy the equations of motion. Accelerations are also required, but are calculated in the analysis programs internally based on time step from the displacement input. Therefore displacement records having displacements and accelerations that matched the achieved table motions were required for input to the models.

7.2.3.2 Calculation of Records for Input to Analytical Models

Two options were reviewed to obtain displacement records that were representative of both the acceleration and displacement response of each shake table. The first was to apply the achieved shake table displacements measured from shake table displacement transducers. The second was to apply displacements obtained from double integrating the measured acceleration from the accelerometers of each shake table. Both methods are discussed and their accuracy is presented in the following sections.

Displacements from the measured accelerations were used for the analyses because the accelerometers provided higher resolution than the displacement transducers. Using the integrated accelerations provided better correlation with the actual shake table response of the bridge model. This will be shown in the following sections. Another less important reason why the integrated acceleration records were used was because SAP2000 was very sensitive to abrupt changes in displacement. Since the analysis took sequential damage of each test into account, the records were spliced into one large record. Splicing of the displacement records caused finite jumps in displacement which

created significant errors in the acceleration output of all nodes in the SAP2000 model. The errors from abrupt displacement change could have been eliminated through filtration of the displacement records. However, since the displacements from the measured accelerations were determined to be more accurate in defining table response than the measured table displacements and because the measured displacements were not used, this type of filtration was not required.

7.2.2.2.1 Records from Table Displacement Transducers

The first option that was reviewed for excitation input to the computer models was the achieved displacement records measured from shake table displacement transducers. The displacement records were low pass filtered at 30 Hz with a second order filter to remove excessive noise. In order to determine what acceleration would be entered in the equations of motion for the computer models using this displacement input, the displacement records were double differentiated to obtain acceleration.

Figure 7-10 shows a comparison of the directly measured acceleration history with the acceleration that was calculated from the filtered table 1 displacement transducer measurement for tests 12, 15, and 19. These tests were chosen for the comparison because they are representative of the entire amplitude range of tests 12 through 20. Figure 7-11 contains the same plots of Fig. 7-10, except zoomed in on a 5 second window. The acceleration from the displacement records is similar to the measured acceleration, except the accelerations from displacement measurements are generally lower in amplitude at peaks and are missing some high frequency responses. Figure 7-12 shows the calculated Fourier Transforms of the directly measured acceleration and that differentiated from the measured displacement histories for table 1 during tests 12, 15 and 19. Figure 7-13 shows the same plot, except the frequency range is zoomed between 2 and 14 Hz. This range of frequencies is representative of the frequency of the first three transverse modes of the bridge. It can be seen in Fig. 7-13 that there are significant differences between the frequency content of the direct and displacement-based acceleration records. For example at 2.5 Hz (approximately the initial frequency of transverse mode 1), the differences between the two FFT responses for tests 12, 15, and 19, were 33%, 3.7%, and 7%, respectively.

7.2.3.2.2 Records from Table Accelerometers

The second option that was reviewed for shake table motion input to the computational models was displacement calculated from double integrating the acceleration that was measured by the shake table accelerometers. The displacement records from accelerometers were calculated for individual motions as well as for the spliced records from tests 12 through 20. Both calculations utilized the same method of integration. However, the spliced cumulative record was used in the analyses. The cumulative record for tests 12 through 20 was composed of nine 25 second acceleration histories having a time step of 0.01 seconds. The cumulative record was first filtered through a second order low pass filter of 30 Hz to filter out noise. Then seven seconds of zero padding were added to the ends of the record and it was filtered through a high pass filter of 0.35 Hz for baseline correction. The purpose of the zero padding was so that the ends of the acceleration record equaled zero after the double integration. The amount of

zero padding required was determined by trial and error. The high pass filter frequency was also determined by trial and error by increasing the filter frequency until the record was completely baseline corrected. The filtered and padded acceleration record was then double integrated to solve for displacement.

Two comparisons needed to be made to determine the accuracy of displacement input calculated from the accelerometers. The first was to compare the calculated displacement with the displacement measured by the shake table displacement transducers. The second was to compare the acceleration that would be calculated in the computer models (SAP 2000 or Drain 3-DX) from the displacement input with the acceleration that was measured using the table accelerometers.

Figure 7-14 shows the comparison of measured shake table displacement histories with the displacement calculated from double integrating the acceleration for table 1 during tests 12, 15, and 19. The same plots are shown in Fig. 7-15 zoomed on a five-second window. The integrated displacement history compares well with the measured displacement except that some of the peaks are slightly greater for the integrated record. Since the only structural response that is created by the displacement records is pseudo-static demand from incoherent support excitation and the calculated displacement had little deviation from the measured displacement, these differences were considered to be negligible.

Comparisons of the acceleration histories of directly measured acceleration and acceleration calculated by double integrating then double differentiating accelerometer measured acceleration of table 1 for tests 12, 15, and 19 are shown in Figs. 7-16 and 7-17. The measured and calculated accelerations are nearly identical. Figure 7-18 shows Fourier Transform of the measured acceleration from accelerometers and the acceleration that was calculated from double integration followed by double differentiation of accelerometer acceleration. The Fourier Transforms for the frequency range of the first three transverse modes are shown in Fig. 7-19. The two transforms have little deviation. The match of acceleration histories and Fourier Transforms demonstrates that only slight acceleration content was lost during the process of double integration and double differentiation. For example at 2.5 Hz (approximately the initial frequency of transverse mode 1), the difference between the two FFT responses for tests 12, 15, and 19, was 0.40%, 0.35%, and 0.35%, respectively. This shows that the acceleration that would be calculated in the computer models from the displacement input based on measured acceleration would be a very good match to the achieved shake table acceleration.

The accuracy of using displacement records from displacement transducers can be compared with the accuracy of the displacement records from accelerometers using the acceleration history comparisons in Figs. 7-11 and 7-17 and the Fourier Transform comparisons in Figs 7-13 and 7-19. These comparisons show that the accelerations from displacement records that were calculated from measured accelerations were significantly more accurate than accelerations calculated from the displacement records. This was the primary reason that displacements calculated from acceleration records were used as input for the analytical models.

7.3 Development of Computer Models of Bridge Specimen

This section describes the two analytical models and the corresponding analysis packages that were used to calculate the response of the bridge from the achieved motions of the shake tables. Each model is discussed and comparisons are made between the input material data and nonlinear column elements of the two models. Efficiency of the models is discussed including fiber discretization, the number and length of fiber segments, and integration time steps.

Both the Drain-3DX and SAP2000 models were created with the intent to use standard analytical methods to model displacement and force response for different tests. During the analytical studies it was noted that variations of the elastic stiffness and damping of the columns could be made to improve the correlation between the calculated and measured low-amplitude response. However, this was not done because identifying the best fit input parameters was not the intent of the study. The columns were also not modeled to accurately calculate complete failure. This is in part because the material models in the fiber sections were defined to have gradual strength loss at failure to aid in convergence and prevent computational instability. Furthermore fiber models describing the plastic hinge zone do not allow for direct modeling of spiral rupture.

7.3.1 Nodal Configuration and Masses

Both the SAP2000 and Drain 3DX models were composed of linear beam column elements combined with nonlinear fiber elements that connected a three-dimensional assemblage of nodes. The nodal configuration for both models is shown in Fig. 7-20. The orientation of both models is such that the global x, y, and z directions are in the longitudinal, transverse, and vertical directions of the structure, respectively. Nodes and elements were located at centerlines of the bridge components. Since footings and spacer blocks were rigidly attached to the shake tables, they were excluded from the analyses. The bottoms of the columns were assumed to be fully fixed to the shake tables.

Masses were lumped at the nodes according to tributary area. The superstructure mass was lumped at tenths of the span lengths between columns and at thirds of the total cantilever length along the length of the cantilevers. Half of the column mass was specified at the top each column. The imposed weights were modeled with nodes that were located at the center of mass of each concrete block or lead pallet. The center of mass node for each imposed load was connected with a rigid beam column element vertically to the centerline of the superstructure. Rotational inertial masses were not included.

7.3.2 SAP2000 v9 Model

SAP2000 was used to model the bridge because at the time of this research it represented state-of-the-art commercial software used in practice for nonlinear analysis of structures. Version 9, which became commercially available during this research, was utilized for the analysis because unlike version 8, which was used for the pre-test analysis, version 9 included nonlinear fiber elements that could be used to define column nonlinearity. The advantage of fiber elements over moment-rotation springs is that axial load interaction and biaxial moment interaction as well as the hysteretic relationship all implicitly defined from the fiber discretization and constitutive relationship of the

materials. This section describes the SAP2000 model including the nonlinear fiber elements that were used for the columns and the material models that were used to define individual fibers.

7.3.2.1 Description of Model

As discussed in Section 7.2.2, the bridge was modeled using a three dimensional assemblage of nodes connected by two-dimensional beam-column elements. Tributary masses were lumped at the nodes. All elements, except for portions of the columns, were assumed to behave linearly. The damping, which is further discussed in Section 7.3.6, was specified using mass and stiffness proportional coefficients that were calculated for two percent damping at the first and third transverse modes. The third transverse mode was included in the damping calculation to make sure that it was not damped out of the analysis. P-delta effects were included in the analysis

7.3.2.2 Column Element Descriptions

The linear portion of each column was modeled as a beam-column element having constant cracked section properties in both shear and flexure throughout the analyses. The flexural properties were from an elasto-plastic idealization of moment-curvature analysis. The cracked shear stiffness was specified based on the truss analogy (Park and Paulay 1975) (Eq. 7-4). The inelastic behavior in flexure was defined using a zero-length fiber discretized section (Fig. 7-21a) at each end of the column. A parametric study that was conducted to determine the optimum fiber configuration for the section is discussed in Section 7.3.5.1. Since the fiber element definition in SAP2000 is limited to zero length elements, the fiber elements are of the lumped plasticity type (Fig 7-21b). Lumped plasticity, as opposed to distributed plasticity, is when the moment-rotation relationship is defined at a single point along the element.

The constitutive relationships of the fibers were specified for confined concrete, unconfined concrete and steel using measured material properties as discussed in the next section. The material relationships, combined with the discretized section described a moment-curvature relationship at a given point which was then multiplied by a tributary length to define lumped plasticity at a finite location. The lumped plasticity was assumed to occur over the theoretical plastic hinge length (Priestley et. al 1996), and was specified at a location of half of the plastic hinge length from the column ends. A parametric study was conducted to determine the optimal number and tributary length of moment-rotation hinges is discussed in Section 7.3.5.2.

SAP2000 version 9 does not have an element to explicitly define bond slip of steel reinforcement. However, bond slip at the ends of the columns was included in the SAP2000 model by modifying the constitutive relationship strains of the inelastic steel fiber sections to include a force-slip relationship at the location of each steel fiber in the section. Since the theoretical plastic hinge length was different for each column, three constitutive models were used.

7.3.2.3 Material Input

Three stress-strain curves were used to define the fibers in the inelastic fiber sections for longitudinal column reinforcement, unconfined concrete, and confined

concrete. These constitutive relationships were specified as multi-linear curves to match the measured curves (after modification for strain rate) discussed in Section 7.2.1. There are two options in SAP2000 to specify hysteretic relationship of materials for the fiber element. The first is a Multi-Linear Kinematic Plasticity Property, which is based the kinematic hardening behavior that is commonly observed in metals (CSI 2005). The second is a Multi-Linear Takeda Plasticity Property, which is very similar to the kinematic model, but uses a degrading hysteresis loop based on the Takeda model (Takeda et al. 1970). The difference between the Takeda model and the Kinematic model is that for the Takeda model, when crossing the horizontal axis during unloading, the curve follows a secant path to the backbone force deformation relationship for the opposite loading direction (CSI 2005). The Kinematic relationship was used for the curves that defined the reinforcement. Both the confined and unconfined concrete was defined using the Takeda relationship.

The curve that was input to model the reinforcement prior to the addition of bond slip is shown in Fig. 7-7 superimposed on the measured strain rate modified curve from material tests. The specified stress-strain relationship was symmetric for tension and compression. Strength loss was specified to begin at a strain of 0.12 and reach zero at 0.18.

Tension capacity of the concrete was assumed to be zero for both the confined and unconfined concrete. The constitutive relationship that was input for unconfined concrete is shown in Figure 7-8. Strength loss of the unconfined concrete after the crushing strain of 0.004 was assumed to continue on a constant linear path until a strain of 0.01 where the stress remained at 20 percent of the stress at the crushing strain. The input for unconfined concrete is shown in Fig. 7-9. After the crushing strain of 0.0171, strength loss was assumed to be linear to a stress of 20 percent of the crushing stress at a strain of 0.02, after which the stress remained constant.

7.3.3 Drain -3DX Model

Drain-3DX was used in addition to SAP2000 to model the bridge. Drain-3DX is a FORTRAN based general purpose analysis package for the static and dynamic analysis of three-dimensional nonlinear structures. Drain-3DX, which is widely used throughout both the academic and private engineering community, was written as a somewhat simple analytical program that included important seismic analysis features that at the time were not provided by other programs. Drain-3DX contains elements that are specific to modeling nonlinear response of reinforced concrete including distributed plasticity fiber elements which have the capability of explicitly modeling reinforcement bond slip. This section describes the Drain-3DX model including the nonlinear fiber elements that were used for the columns and the material models that were used to define individual fibers.

7.3.3.1 Description of Model

The Drain-3DX computer model of the specimen was identical to the SAP2000 model except for the definition of column inelasticity in the plastic hinge regions at the ends of the columns, and the numerical integration method. Similar to the SAP2000 model, the damping was specified using mass and stiffness proportional coefficients that were calculated for two percent damping at the first and third transverse modes.

Damping is further discussed in Section 7.3.6. P-delta effects were included in the Drain analysis.

7.3.3.2 Column Element Descriptions

Columns in the Drain-3DX model were modeled using the "Fiber Beam-Column Element (Type 15)". This element allows the user to define an element with segments composed of both inelastic fiber sections and elastic sections. The entire element is assumed to be elastic in both shear and torsion. The element utilized the same fiber section discretization as that in the SAP2000 model (Fig 7-21a). However, the Drain element describes distributed plasticity, which is a moment curvature relationship that is integrated over the length of the element each time the elemental matrix is solved (Fig. 7-21c). The length for integration of curvature was defined using the theoretical plastic hinge length (Priestley et. al 1996).

Bond slip in the Drain model was directly defined in the element type 15 at the ends of each column (Fig 7-21c). The connection hinge accounted for deformation due to bar slip and crack opening, as well as compression of concrete. A fiber discretization similar to that of Fig. 7-21a was used, except instead of three layers, there were only two layers of concrete. The confined concrete layer 1 was combined with the unconfined concrete layer that is shown in Fig. 7-21a because the entire section was confined. The concrete fibers were defined using gap properties where the concrete had zero tensile stiffness, and compression stiffness that is equal to the elastic modulus of the confined concrete multiplied by a compression penetration of the column diameter divided by four. The penetration stiffness was to account for the footing and superstructure concrete compressive strain that was not accounted for in the definition of column flexural deformation. One fourth of the column diameter was used assuming a 45 degree penetration from the center of the column to the perimeter. Since at the perimeter of the column the compression was only being exerted on a half-space, the 45 degree penetration, which equals the column diameter over 2 was divided in half, which is equal to the column diameter over four. Confined concrete properties that were the same as the fiber section of the column were assumed because the reinforcement bond-slip occurred in the footing and superstructure, which were both highly confined areas. The steel fibers were defined using pullout properties based on the force-displacement bond-slip relationship.

7.3.3.3 Material Input

Figures 7-4 through 7-6 show the stress-strain curves that were used to describe the fiber properties in the inelastic fiber sections for the longitudinal column reinforcement, unconfined concrete, and confined concrete of the Drain-3DX model. These curves were the same as those discussed for the SAP2000 model, except for differences in the material strength degradation. In the Drain model, strength degradation of concrete was more gradual to avoid instability.

The stress-strain curve for longitudinal reinforcement is shown in Fig. 7-4. The curve was symmetric for tension and compression. Unlike SAP2000, in Drain it is not possible to assign a negative slope to the steel stress strain curve. Input for the reinforcement ended at ultimate strength of the steel which was at a strain of 0.12. If

fiber strains in the model exceeded the ultimate strain of 0.12, the curve continued on the final slope that was specified before 0.12, which was positive. Therefore the primary purpose of the 0.12 ultimate strain definition in the Drain-3DX model was to define the final slope of the stress-strain curve.

The stress-strain curves specified for unconfined and confined concrete in the Drain model are plotted in Figs. 7-5 and 7-6, respectively. Concrete was assumed to have zero strength in tension. The slope of strength loss for both unconfined and confined concrete after the concrete crushing strain was the same as the final slope of each curve before crushing. A stiffness degradation coefficient of 0.5 was specified to define the unloading stiffness degradation for hysteretic relationships of both confined and unconfined concrete.

7.3.4 Comparison of Models

There are two fundamental differences between the SAP2000 and Drain-3DX models. The first difference is in the nonlinear elements of the columns. The second is in the method of integration used to solve the forces and displacements. Integration methods are discussed in Section 7.3.5.3. This section summarizes the differences in the nonlinear column elements.

There are three primary differences between the nonlinear elements of the columns for SAP2000 and Drain-3DX. The first is the distribution of plasticity over the fiber element length. As shown in Figs. 7-21b and 7-21c, and discussed in previous sections, the nonlinearity in the SAP2000 model was lumped at the center of each hinge length. The moment-curvature relationship from the fiber section was multiplied by the plastic hinge length into what was essentially zero length biaxial moment-rotation spring. The nonlinearity of the Drain model was distributed, and rather than being lumped at the center, the moment-curvature relationship from the fiber section was integrated over the hinge length which had a parabolic distribution of curvature.

The second difference between the nonlinear column elements was the definition of strength degradation in the material models for the fiber sections. For fibers in the SAP2000 model, all materials were specified with strength degradation upon failure. This allowed for relatively accurate modeling of concrete crushing and fracture of longitudinal reinforcement. In the Drain-3DX model, because strength loss is not permitted in the constitutive relationship for steel, strength degradation upon material failure was only specified for the concrete. Therefore, the drain model did not account for rupture of the longitudinal reinforcement. The result from the differences in specification of strength degradation are shown and discussed for curves from pushover analyses in Section 7.4.1.

The final difference between the column elements in the two models was in how the bond slip was specified. For the SAP2000 model, bond slip was specified as part of the steel material properties by including the force-deformation relationship calculated for bond slip into the stress-strain curves for reinforcement. For the Drain-3DX model, a specific zero-length fiber element was attached to the ends of the columns. This model that explicitly defined bond slip accounted for concrete gap opening in tension, slip of the reinforcement, and compression of concrete into the connection.

7.3.5 Model Efficiency

Since inelastic modeling can be extremely computationally demanding, model efficiency was an important consideration when creating both the Drain-3DX and SAP2000 models. This included both the number and configuration of the inelastic hinges, and the method and the integration time steps. Parametric studies were conducted to determine the minimal number of fibers and fiber segments and the largest time step that could be used to obtain stable and reasonably accurate results.

7.3.5.1 Fiber Configuration

Fiber configurations and the structure setup that were used in the parametric study to determine the optimum number of fibers for analytical modeling are shown in Fig. 7-22. Figure 2-4 shows the plans of the actual column section. Increased number of fibers can drastically influence the amount of time required for analyses. Two factors were reviewed in the fiber layout: number of slices and number of layers. The goal was to specify the minimal number of slices and layers to obtain reasonably accurate results. The study was conducted in SAP2000 with a 30 in (760 mm) cantilever column having one lumped plasticity fiber section with 12 in (305 mm) tributary length located at 6 in (152 mm) from the point of fixity. A minimum of three layers were required to specify the unconfined concrete confined concrete and the longitudinal reinforcement. A minimum of four slices were required so that the section would be bi-axially symmetric and allow for defining the moment-curvature relationship about all lateral axes. Comparisons were made using lateral force-displacement curves from pushover analyses that are plotted in Fig. 7-23.

The four fiber configurations that were used in the comparison are shown in Fig. 7-22. Half of the configurations had 8 slices and half had 16 slices. Both three layer and four layer sections were investigated. The four layer sections contained an additional layer of confined concrete. One of these layers is for the reinforcement. The resulting pushover curves are shown in Fig. 7-23. The points of initiation of crushing of confined and unconfined concrete as well as rebar fracture are marked. The 8 slice, 4 layer section was chosen over the 16 slice, 4 layer section for the analytical modeling of the bridge because it provided a similar force- displacement curve and took approximately one-half the run time of the 16 slice, 4 layer section. The 8 slice, four layer section was chosen over both three layer sections because the additional layer of confined concrete in the four layer section captured the approximate location of initial confined concrete crushing that was seen in the more accurate 16 slice, 4 layer section, whereas the 3 layer sections missed that point.

7.3.5.2 Element Configuration

Once the optimum configuration of fibers was determined, a second parametric study was conducted using pushover analysis in SAP2000 to determine the optimum number of lumped plasticity hinges to use in each plastic hinge zone and still obtain reasonable load deflection results. Similar to the study for fiber configuration, the analyses were conducted using a 30 in (760 mm) cantilever column. Element configurations that were reviewed for modeling the plastic hinge zones are shown in Fig.

7-24. A comparison of pushover curves for the different configurations is shown in Fig. 7-25.

The number of the hinges varied from 1 to 4. The hinges were equally spaced when more than one was used. It was determined that the optimum configuration in the model for each plastic hinge zone was one hinge having a length of one-half the column diameter. This is the same length that is recommended in the SAP2000 manual (CSI 2005). The plastic hinge length by Paulay and Priestley (1996) was used for the columns of the bridge model because it is approximately equal to d/2 and also accounts for the variation of column heights among the three bents. This same length was used to define the distributed plasticity hinge zone in the Drain model.

7.3.5.3 Time Step and Integration Method

The integration method used for SAP2000 was the Newmark beta method using integration parameters γ=0.5 and β=0.25, which defines the average acceleration method. The relative convergence tolerance for iteration was specified as 10^{-7}. Automatic time stepping would not converge when analyzing the high amplitude tests. Therefore, a constant time-step of 0.0001 seconds was required for the model to converge on consistent displacement results. The average run time for a 25 second analysis, which was the length of one of the 9 high-amplitude tests, using a 2.8 GHz processor was approximately 12 hours.

Drain-3DX uses a more direct non-iterative method to calculate the structural response through time. Rather than iterating force for convergence, the force error is applied to the next step. If the overshoot tolerance that is specified for the material models of the fiber sections is exceeded, Drain calculates multiple events within a time step. This method of force error applied to the next step requires small time step, but is more stable than traditional iterative methods (Prakash and Campbell 1994). The time step that was required for consistent displacement results and acceptable force convergence was a constant time step of 0.0005. The average run time for a 25 second analysis using a 900 MHz processor was approximately 20 minutes.

It was observed during the analyses that the run time was proportional to the computer processor speed and inversely proportional to the time-step. If the run times for the SAP2000 and Drain 3DX models are weighted according to the time step and the inverse of computer processor speed, the Drain-3DX model would be approximately 22 times faster.

7.3.6 Damping

Damping in both the SAP2000 and Drain-3DX models was specified through mass and stiffness proportional damping. Mass and stiffness proportional damping has a greater effect on the pre-yield structural response since after yielding most of the damping comes from hysteretic energy dissipation. Therefore, the calculated modal periods for the bridge at a state of cracked stiffness were most relevant for specifying damping. The Rayleigh damping method was used to calculate the damping coefficients of the classical damping matrix based on the calculated periods of the first and third transverse modes, which were approximately 0.4 and 0.08 seconds, respectively. This range of periods was chosen because the first three modes defined 99.99 percent of the

bridge response in the transverse direction. Also, the period of the primary mode in the longitudinal direction was approximately 0.4 seconds.

The combination of mass and stiffness proportional damping that was specified in both computer models is plotted against period in Fig. 7-26. Figure 7-27 is the same plot except the x-axis is zoomed in on the range of periods for the first three calculated transverse modes. A recommended value of damping for the pre-yield response of a reinforced concrete structural system is five percent (Freeman et al. 1984). The measured damping of the bridge, discussed in Chapter 6 was an average of 4.3 percent. Both two percent and five percent damping were used in analyses. However, two percent damping was used in the final analyses for two reasons. The first is because displacement results from the analytical models for tests 12 through 14 were closer to measured response using 2 percent damping than using 5 percent damping.

The second reason that two percent damping was used instead of five percent damping is because when structures are analyzed using displacement based excitation mass proportional (viscous) damping can be greatly and unrealistically be overestimated (Wilson 2002). Typically, when earthquake analysis is conducted for a structure, uniform acceleration is applied to the analysis model. When uniform acceleration is used, nodes connected to the ground are fixed and the displacements of the mass nodes are relative displacements. Therefore the damping forces for viscous damping are proportional to relative velocity. For the analyses that were conducted on the shake table bridge model, which in practice was subjected to non-synchronous motions (even though the intent was to apply coherent motions), displacement input was required. When displacements are input to the nodes at the base of the structure, displacements of the mass nodes are absolute displacements. Therefore the damping forces for viscous damping are proportional to absolute velocity, which creates errors due to excessive damping.

7.4 Comparison of Calculated and Measured Response

To evaluate the accuracy of the Drain-3DX and SAP2000 models, their results were compared to each other as well as to the response of the shake table specimen for the achieved high amplitude test 12 through 20 motions. The direct comparisons to the specimen included pushover curves, displacement histories and acceleration-displacement hysteresis curves of the three bents. Comparisons between the two computer models included the aforementioned comparisons, as well as force-displacement hysteresis curves.

The comparisons showed that the Drain-3DX model provided more accurate results. Since the Drain model was more accurate as well as more efficient as discussed in Section 7.3.5.2 than the SAP2000 model, it was chosen for further study of the bridge. Bridge response from the Drain-3DX model was also compared to the low amplitude biaxial tests to evaluate the accuracy of the model under low amplitude incoherent and biaxial excitations.

7.4.1 Pushover Analyses

Load-deflection curves from pushover analyses of the three bents for both computer models are shown in Figs. 7-28 through 7-30. The backbone curves from the

acceleration-deflection hysteresis curves multiplied by tributary mass are superimposed on each plot. The two backbone curves shown in each figure represent the response in the positive and negative displacement ranges, although the backbone curve for the negative displacement range was converted to positive displacement to facilitate comparison with the other curves. The pushover results of the two analyses are very similar. It is shown that there is a trend for the Drain model to have a slightly greater yield displacement. This is a result of the more accurate definition of bond-slip in the Drain model.

After the peak of each SAP2000 curve, two sudden decreases in force can be observed. The first decrease is the crushing of the unconfined concrete and the second is initiation of crushing of confined concrete. The confined concrete crushing is at displacements of approximately 5.4, 8.5, and 4.0 in (137, 216, and 102 mm) for bents 1, 2, and 3. Two kinks in the curves can be seen at the location of confined concrete crushing. These kinks are from confined concrete crushing of the east and west columns which are in tension and compression due to overturning. The column in tension is subjected to crushing of confined concrete slightly after crushing in the compression column. An additional force drop is seen in bent 3 in Fig. 7-30 at a deflection of approximately 8.5 in (220 mm). This third drop is loss of capacity due to crushing of the core layer of confined concrete combined with tension rupture of reinforcement. Confined concrete crushing is not as pronounced in the pushover curves from the Drain-3DX analyses. This is because the constitutive relationship of confined concrete for the Drain-3DX model did not have as sudden of strength loss as that used in SAP2000. For this reason, the calculated ultimate displacement capacities, discussed later in this section were based on SAP2000 results.

Since the force in the "measured" backbone curves that were superimposed on the pushover curves were estimated from acceleration multiplied by tributary mass, the amplitude of backbone forces was not completely accurate. As discussed in Section 6.4.1, this is especially true for bent 2, where relatively high accelerations that were heavily influenced by response of bents 1 and 3 were recorded. However, the superimposed backbone curves do provide relatively accurate comparisons of force for bents 1 and 3 and provide a comparison of strength loss for bent 3, which was the bent that reached failure during shake table testing. In comparing the failure backbone curve and SAP2000 pushover, both plotted in Fig. 7-30, it is shown that the SAP2000 calculation for strength loss due to crushing of confined concrete is very close to measured results.

Elasto-plastic idealizations of both the SAP2000 and Drain-3DX pushovers are plotted in Fig. 7-31. The yield point was defined by passing the initial slope through the first yield displacement of longitudinal reinforcement and balancing the areas between the idealized plot and the pushover plot. Two methods were reviewed to define the ultimate displacement for the bents. One was at the displacement at crushing of confined concrete. The other was the displacement when the lateral force decreased to 85 percent of the maximum force. Results from both methods are listed in Tables 7-2 and 7-3. The first method was chosen, and the ultimate point was defined as the displacement where the confined concrete of the tension column in the SAP2000 model reached its ultimate strain in compression. Since this point was not well defined in the Drain-3DX model, the

SAP2000 displacement was used for both idealizations. The second method of failure displacement at 85 percent of the maximum force was not used because this method calculated unrealistically high failure displacements. Failure displacements using method 2 were not accurate because sudden concrete strength loss was not defined in the constitutive models.

The failure displacement ductilities calculated from the SAP2000 models for bents 1 through 3 were 8.1, 8.1, and 7.9. Failure ductilities calculated from the Drain-3DX model for bents 1 through 3 were 7.6, 7.9, and 7.4, respectively. The measured failure ductility for bent 3 is compared with pushover calculations in the next section.

7.4.1.1 Measured Ductilities Based on Pushover Analysis

In Chapter 6, the measured ductilities of each bent during each test were reported using the yield displacement from the measured elasto-plastic idealized backbone curve of the acceleration-deflection curves (Table 6-7). Since these yield displacements were based on acceleration from dynamic response, which was influenced by bent interaction, and on idealizations of incomplete curves for bents 1 and 3 which did not reach failure, they were inconsistent with each other relative to bent height and contained some error. Therefore a table similar to Table 6-7 was generated (Table 7-4), which lists the measured ductilities based on the calculated yield displacements from pushover analyses.

The measured displacement ductilities based on the calculated yield displacements, compared to those from Chapter 6 that are based on acceleration hysteresis backbone yield displacements, are 1.4 percent smaller for bent 1, 21.5 percent smaller for bent 2, and 16.6 percent larger for bent 3. The largest difference is in bent 2, which can be mostly attributed to influence of high acceleration. The only bent of the bridge model that reached failure was bent 3. The measured failure ductility for bent 3 based on yield point from the acceleration deflection hysteresis is 7.9. The failure ductility for bent 3 based on the calculated yield displacement is 9.2. Because the calculated yield displacement is more accurate than the yield displacement that was based on acceleration-deflection hysteresis, the measured failure ductility of bent 3 is considered to be 9.2. Calculated failure ductilities of this bent from the SAP2000 and Drain-3DX models respectively are 7.9 and 7.4 which are 85.9 and 80.4 percent of the measured failure ductility.

7.4.2 High Amplitude Tests

The achieved shake table displacement records of tests 12 through 20 were input to the analytical models in sequence to evaluate the accuracy of the analytical bridge response. The motions, discussed in Section 7.2.3, were displacement records calculated from the measured shake table accelerometer data. Comparisons from the two analyses are made with measured data as well as each other for top of bent displacements and accelerations in the transverse direction, which was the direction of excitation. Comparisons between the two analytical models are also made for the shear deformation hysteresis curves. Both models provided reasonable accuracy through failure of bent 3 in test 19. It was determined from the high amplitude test comparisons that the Drain-3DX model provided results that showed more consistent correlation with the measured data

for the entire range of test amplitudes. Force calculated from the Drain-3DX model is compared with the force estimated from actuator pressure in Section 7.7.

7.4.2.1 Calculated Displacement Histories

The primary direct comparisons of the computer models and the specimen response are the displacement histories of the three bents in the transverse direction. The calculated displacement responses from both models were compared for tests 12-20. Figures 7-32 through 7-40 are plots of the SAP2000 calculated displacement histories compared with measured results for the tests. Displacement history comparisons for the Drain-3DX model are plotted in Figs. 7-41 through 7-49. Peak negative and positive displacements for tests 12 through 20 are listed in Table 7-5 for SAP2000 and Table 7-6 for Drain-3DX. The tables also list the percent difference between analytical and measured peak displacements for each run and the average percent difference for each bent.

As shown in the history plots, the calculated responses from the models were most accurate for tests 12 through part of test 19 until bent 3 failed in flexure. Both models accurately calculated yielding of the three bents. The calculated responses for tests 19 and 20 are less accurate because while the analytical models were able to calculate some loss in lateral capacity as shown in the acceleration-deflection plots discussed in the next section, the models were not capable of modeling the total failure of bent 3. The average percent differences of peak displacements for all tests from the SAP2000 calculated response for bents 1 through 3 were 14.8, 12.2, and 16.1, respectively. The average percent differences of peak displacements for all tests from the Drain-3DX calculated response for bents 1 through 3 were 13.8, 11.0, and 11.5 percent respectively.

An instability that was identified with the SAP2000 model was permanent bent displacements that gradually increased as the columns were subjected to increased inelasticity. The permanent displacement was related to instability caused by the interaction of the four plastic hinges in each bent. As the permanent displacement error increased, the hinges opposed each other with spring like forces. An example of the permanent offset is shown in the bent 1 results of Figs. 7-36 and 7-37. This phenomenon was shown to decrease with small time steps and was not seen in the Drain-3DX model.

The calculated displacement responses of both the SAP2000 and Drain-3DX models were similar to the specimen response with respect to both amplitude and frequency up to failure of the model in test 19. The Drain-3DX model was more accurate in duplicating the response due to the increased accuracy from the explicitly defined Drain-3DX bond-slip model.

7.4.2.2 Calculated Acceleration-Deflection Response

Acceleration-deflection relationships for the Drain-3DX and SAP2000 models are compared with the measured values in Figs. 7-50 through 7-76. Acceleration as opposed to force was used to aid in evaluation of model accuracy because there was no direct measurement of the shear force in the columns. The calculated acceleration-deflection relationships were mostly comparable in general shape and amplitude to each other and to the measured results until failure of the bridge in test 19. However, acceleration

amplitudes from the Drain-3DX model in test 18 for bent 3 had high amplitudes that were inconsistent with the SAP2000 results and measured data. Upon comparing the forces between the two computer models, which are discussed in Section 7.4.2.3, it was concluded that the inconsistency in the acceleration values of the Drain-3DX model were indeed present, but did not affect either the force or displacement results.

7.4.2.3 Comparison of Shear-Deflection Relationships

Comparisons of the calculated force-displacement hysteresis response from the Drain-3DX and SAP2000 models for bents 1 through 3 during the high amplitude tests 12 through 20 are shown in Figs. 7-77 through 7-103. The cumulative force displacement curves for tests 12 through 19 for the three bents are shown in Figs. 7-104 through 7-106. The force-deflection curves were very similar for the two models in both amplitude and general shape for all tests. It was concluded through these force-deflection relationship comparisons that the Drain-3DX and SAP2000 models showed similar results.

7.4.3 Low Amplitude Tests

The calculated displacement responses for all full amplitude incoherent and biaxial low amplitude tests were calculated using Drain-3DX and were compared to the measured response of the shake table model. Drain-3DX was used for this comparison because it was decided from high amplitude response (test 12-19) comparisons that the Drain-3DX model was more accurate. The tests used in the comparison are tests 2 through 6, the transverse incoherent motions, and test 9, the biaxial motion. The input displacement was the double integrated shake table acceleration that was obtained using the same method as that for high amplitude motions discussed in Section 7.2.3.

7.4.3.1 Calculated Displacement Response Histories

Comparisons of the calculated and measured displacement histories of the top of bents 1 through 3 are shown in Figs. 7-107 through 7-113. Figures 7-107 through 7-111 are plots of the transverse displacement histories for low amplitude incoherent tests 2 through 6. Figures 7-112 and 7-113 are plots of the top of bent displacements for test 9, the biaxial test, in the transverse and longitudinal directions, respectively. The calculated responses from the Drain-3DX model have similar frequency contents to the experimental results. However, the amplitude of the calculated displacements at peak amplitudes is generally larger.

Table 7-7 lists the measured and calculated displacement maxima and the percent difference between the data for each test. The average percent differences between calculated and measured envelopes for bents 1, 2, and 3, were 10.2, 12.5, and 19.0 percent. The difference in the maximum displacement was generally greatest for bent 3, the shortest of the bents. This was likely due to the small aspect ratio of bent 3, which caused the bent to be subjected to the greatest amount of shear deformation.

It was observed during trial analytical runs that the low amplitude calculations could have been improved by modifying the amount of damping and the elastic stiffness of the bents. However, the purpose of comparing the measured and calculated bridge response was to evaluate the analytical models using standard modeling techniques, and not to do a system identification analysis.

7.5 Cap Beam Deformations

Measured data of cap beam bending in the bridge model was discussed in Section 6.3.6. Because cap beams in the shake table model were designed to remain elastic and were strengthened by the surrounding superstructure, they were assumed to be rigid in the analytical model of the bridge. To determine the relevance of cap beam bending to the response of the bridge, the measured deformation of the cap beams for select runs was input to the analytical models of each bent that were used for pushover analyses. The bent models for pushover analyses were identical to the bents in the analytical bridge model, except that the superstructure was not connected in the pushover models.

The measured deformation of cap beams was the difference between vertical displacement measured using displacement transducers at the extreme east and west ends of the cap beams during shake table tests. This deformation was applied to the ends of the rigid cap beams in the analytical models and column moments were determined. For the case where the cap beams are completely rigid, which is represented in analytical models, moments in the columns due to cap beam deformation would be greatest. If the cap beams had no rigidity, then the moments due to cap beam deflection would be zero. Therefore, the difference in column moments due to cap beam bending for the prototype and analytical model as well as the difference in column moments due to cap beam bending for the shake table model and analytical model are less than the moments in columns due to cap beam deformation in the analytical model with rigid cap beams.

The tests that were chosen for comparison of column moment due to cap beam deformation were tests 12, 15, and 19. These tests were chosen because they were representative of the three states of the bridge. Test 12 was before the columns had yielded, test 15 was just after the columns had yielded, and test 19 was the failure test. Table 7-8 lists the maximum column moments from the analytical models due to maximum cap beam deformations of the three bents for tests 12, 15, and 19. The percentage of these moments relative to the yield moment is tabulated for each column. For all tests, the largest moment due to cap beam deformation considering a rigid cap beam is in bent 3. The percentages of yield moment for tests 12, 15, and 19 in bent 3 are 1.15, 3.46, and 8.32, percent respectively. These moments are the maximum difference in the column moment due to cap beam deformation for rigid and completely flexible cap beams. Since the column moments are most critical before the columns have yielded, the moment from test 19 should not be viewed to be as important in this comparison. The maximum difference in column moment demands for tests 12 and 15 that is possible due to inaccurate modeling of cap beam stiffness is 3.46 percent of yield stiffness, which is negligible.

7.6 Bent 3 Shear Stiffness

Bent 3 had the smallest aspect ratio of the three bents, and was the only bent that failed. Bent 3 was therefore subjected to the largest amount of shear deformation. As discussed in Chapter 3, displacement transducers were attached to the west column of bent 3 so that the transverse shear deformation could be measured (Fig. 3-6). In this section, shear stiffness equations for cracked stiffness, and for post-yield stiffness are compared to the measured shear stiffness of bent 3. Two comparisons are made. The first is the global column stiffness which includes the entire clear height of the column.

The second is the stiffness measured from the top and bottom panel zones (Fig. 3-6) which focuses on the plastic hinge regions and therefore provides a clearer comparison for post-yield shear stiffness.

In the preliminary analyses, discussed in previous chapters, as well as the post test analyses that were discussed in this chapter, cracked shear stiffness properties were assumed for the columns. Because the response as well as failure of the columns was expected to be dominated by flexure and so that the computational models were not too complicated, special consideration was not provided for the post-yield shear stiffness. In this section, the cracked stiffness (Park and Paulay 1975) (Eq. 7-4) that was assumed in the models, as well as the post-yield stiffness that is suggested by Correal et al (2004) (Eq. 7-5) are compared to the measured shear stiffness of bent 3. The post-yield stiffness is based on a combination of the cracked stiffness and the plastic shear stiffness for plastic hinge zones as specified in Eq. 7-6.

$$K_{v\ \ cracked} = \frac{\rho_v}{1+4n\rho_v} E_s b_w d \geq 0.1 K_{v\ \ uncracked} \tag{7-4}$$

where

$K_{v\ cracked}$ = *cracked stiffness per unit length*
$K_{v\ uncracked}$ = *uncracked stiffness per unit length* = $E_c b_w d/3$
ρ_v = *tie steel ratio*
n = *modular ratio* = E_s / E_c
E_s = *elastic modulus of steel*
E_c = *elastic modulus of concrete*
b_w = *average column width*
d = *effective depth of column =0.9*column diameter*

$$K_p = \frac{9\rho_v f'_c}{9f'_c + 10E_s\rho_v} E_s b_w d \tag{7-5}$$

where

K_p = *plastic shear stiffness*
f'_c = *concrete compressive strength*

$$K_{vPY} = \frac{1}{\frac{n_{pr}d}{K_p} + \frac{L - n_{pr}d}{K_{cracked}}} \tag{7-6}$$

where

K_{vPY} = *post-yield shear stiffness*
n_{pr} = *number of potential plastic hinge regions*
L = *clear length of column*

7.6.1 Shear Stiffness of Column Clear Height

The global measured column shear deformation was calculated by subtracting flexural deformation measured from the displacement transducer panels from the total column deformation. Flexural deformation was calculated using the four pairs of

displacement transducers that measured displacements at the sides of the column over four gauge lengths (Fig. 3-6). Utilizing the displacement transducer measurements, curvature over each gauge length was determined in the same manner as for the curvature measurement discussed in Section 6.3.5. The flexural deformation was calculated using the moment area method assuming that the measured curvature was constant over each of the four gauge lengths. Total deformation was the shake table displacement transducer subtracted from the transducer measuring absolute displacement at the top of the column.

The force-shear deformation relationship was determined from the shear deformation of bent 3 and the force from the top of bent accelerometer multiplied by tributary mass, which was the bent shear. The envelopes of the positive and negative force-shear relationship for tests 12 through 19 are plotted in Fig. 7-114 with the calculated cracked stiffness and post-yield stiffness superimposed. The location where post yield stiffness begins is effective yield force from a bilinear idealization of moment-curvature analysis of the section. The calculated cracked yield stiffness correlates well with the measured shear stiffness of the bent. Although the post-yield stiffness was not included in the analytical models, it provides a slope that is similar to the measured results.

7.6.2 Shear Stiffness at Plastic Hinge Panel Zones

Another comparison of measured shear stiffness in bent 3 with shear stiffness equations was for the deformations measured with the top and bottom displacement transducer shear panels (Fig. 3-6). The purpose of this comparison was to evaluate the effectiveness of the post-yield shear stiffness equations for the local shear deformation. The shear panels at the column ends, which are approximately 14 in tall, provide a finer measurement of the post-yield stiffness in the plastic hinge regions than what was provided by the global height comparison.

The local shear deformations were calculated in a similar manner to the global deformation that was discussed previously. The shear deformation in each panel was calculated by subtracting the panel flexural deformation from the total panel deformation. Flexural deformation was determined using the curvature measurement and the moment-area method. Total panel deformation was calculated using the relative deformations of each transducer in the panels and kinematic truss equations (McGuire and Gallager 1979). Shear force was estimated from the bent accelerometer as was used for the global deformation comparison in Section 7.6.1. Figures 7-115 and 7-116 show the measured envelopes of the force-shear relationship from tests 12 through 19 for the bottom and top panel zones of bent 3, respectively, with the cracked and post-yield stiffness superimposed. Similar to the global stiffness comparison of 7.6.1, both the cracked stiffness and the post-yield stiffness have good correlation with the measured local stiffness at panel zones. The agreement of the calculated post-yield stiffness with the measured plastic hinge region panel zone stiffness suggests that the assumption of concentrated shear deformations in the plastic hinge regions after flexural column yielding in Eq. 7-6 is accurate.

As discussed in the previous section, the global shear stiffness using the local shear deformation also correlates well, which further supports that the post-yield shear stiffness equation accurately represents column deformation.

7.7 Measurement of Force

In Section 6.4, the bent shear forces obtained from acceleration multiplied by tributary mass was compared to the estimated shear force from the measured hydraulic shake table actuator pressure. Force history comparisons were made for tests 15 and 18 as shown in Figs. 6-267 and 6-268. Table 6-46 lists the maximum accelerations and actuator based forces along with percent differences of the maximum and minimum forces for each bent and test. It was determined in Section 6.4 that forces of bents 1 and 3 using actuator pressure matched the acceleration estimated forces well. Accelerations of bent 2 were greatly influenced by the response of the more stiff bents 2 and 3, which caused the acceleration estimated forces for bent 2 to be significantly greater than forces estimated from the actuator pressure. The following section presents comparisons of the Drain-3DX calculated forces with the measured forces that were estimated from actuator pressure.

7.7.1 Comparison of Drain-3DX Force with Measured Data Estimate

Figures 7-117 and 7-118 are history comparisons of the force from actuator pressure and force calculated from the Drain-3DX model for bents 1 through 3 during tests 15 and 18. Table 7-9 lists the maximum forces based on actuator pressure and those from Drain-3DX. The percent differences between these forces for each bent and test are also listed. As shown in the figures, the forces calculated from the Drain-3DX model were close in amplitude and frequency to the forces that were estimated from actuator pressure. The maximum percent difference between the maximum forces for test 15 was 13.7 percent and was in bent 3. The maximum percent difference of the peak forces for test 18 was 20.8 percent and took place in bent 2. As discussed in the previous chapter, the largest difference between the force estimated from bent acceleration and measured from actuator pressure was 51 percent.

Unlike the comparison between the measured accelerometer and actuator estimated forces for bent 2, where acceleration based estimates were much greater than the actuator estimates, bent 2 forces from the Drain-3DX analyses were close to the forces that were estimated from the actuator forces. This supports the observation that erroneously high forces from the bent 2 acceleration based force estimate are influenced by the acceleration response of bents 1 and 3, which are much stiffer. The force estimated using the measured actuator pressure was consistently accurate for all bents and could be used as a measure of force for future shake table tests when it is not possible to directly measure column shear with a load cell.

Chapter 8: Evaluation of Measured Bridge Response Compared to Target Performance

8.1 Introduction

In this chapter the performance of the bridge model, which was designed to satisfy the NCHRP 12-49 (ATC/MCEER 2002) guidelines, is evaluated with respect to the NCHRP 12-49 performance criteria. The performance criteria are presented and the measured performance indicators of shake table tests having spectral accelerations approximately equivalent to the expected and rare earthquake design motions at the design period of the bridge are assessed. Program SIMQKE (Gasparini and Vanmarcke 1976) was utilized to create synthetic ground motions that were compatible with the rare and expected earthquake design spectra. The synthetic motions were input to the experimentally calibrated Drain-3DX analytical model that was discussed in Chapter 7 and results from the analytical model are compared with the design performance criteria. Both the measured response from shake table tests, and the analytical response based on the design spectra, satisfied the performance criteria. Although the design was for an arbitrary location in the Los Angeles area and therefore the design earthquakes that are compared in this chapter are not representative of all locations, this comparison provided an experimentally verified evaluation that validates the design methodology that was used.

8.2 NCHRP Performance Criteria

The performance criteria from the NCHRP 12-49 recommendations that pertain to the bridge model are listed in Tables 8-1 through 8-3 and discussed in this section. As discussed in Chapter 2, the design using NCHRP recommendations is based on constructed response spectra of two earthquake categories at the geographic design location of the bridge: the rare and expected earthquakes. The rare earthquake is the maximum considered earthquake (MCE) and has a three percent probability of being exceeded in 75 years. The expected earthquake is the largest earthquake that is to be expected during the life of the bridge and has a fifty percent probability of being exceeded in 75 years.

Two performance levels are specified in NCHRP 12-49: life safety and operational (Table 8-1). The prototype bridge was considered to be a non-essential (not a critical lifeline) bridge. Therefore the life safety performance level is the level that was considered for the design of the bridge model and will be discussed throughout this chapter. Life safety is the minimum performance level that is allowed in the specifications and is intended to protect human life during and after a rare earthquake. For both the rare and expected design earthquakes, two performance level categories must be met for the life safety performance to be satisfied: service level and damage level. Descriptions of the service levels are listed in Table 8-2. Descriptions of the damage levels are listed in Table 8-3.

For the rare earthquake, which is the maximum considered earthquake, the expected service level is “significant disruption” and the damage level is “significant”.

For the significant disruption service level limited post-earthquake access may be possible, however, the bridge may need to be replaced. For the significant damage level, cracking, reinforcement yield, and major concrete spalling may take place. Also, replacement of the columns may be necessary. However, the bridge should not collapse.

For the expected earthquake, which is what is to be expected during the life of the bridge, the service level that must be satisfied is "immediate" use and the damage level is "minimal". Immediate use service level is where normal bridge operation can take place after post-earthquake bridge inspection. The minimal damage level permits limited damage to the columns including narrow flexural cracking and slight inelastic response. The columns should be completely repairable under non-emergency conditions.

The NCHRP 12-49 recommendations include deformation constraints in the form of plastic rotation capacities for the columns based on the performance levels discussed previously. The rotation capacities can either be calculated based on a rational analysis by the designer or the specified capacities in the NCHRP 12-49 provisions for life safety and for immediate use performance levels. The life safety rotational capacity is intended to prevent collapse due to flexural deformation in the plastic hinge zones. Life safety plastic rotational capacity can either be calculated from Equation 8-1 or can be assumed to be 0.035 radians.

$$\theta_p = \frac{L_p}{D'}(N_f)^{-0.5} \quad rad \tag{8-1}$$

where

$N_f = 3.5(T_n)^{-\frac{1}{3}}$

T_n = *natural (initial) period of vibration of the structure*

L_p = *effective plastic hinge length* $= 0.08\frac{M}{V} + 4400\varepsilon_y d_b$

M/V = *shear span of the member*

ε_y = *yield strain of longitudinal reinforcement*

d_b = *diameter of main longitudinal reinforcing bars*

D' = *pitch diameter of spiral reinforcement*

The calculated life safety plastic rotational capacities of bents 1 through 3 using Eq. 8-1 are 0.0347, 0.0400, and 0.0320 radians. The plastic rotational capacity for the immediate use performance level is 0.01 radians. Capacities that are specified by the code are compared to the measured shake table rotation demands in Section 8.4.2, as well as the calculated Drain-3DX rotation demands from synthetic motions that represented the rare and expected design spectra in Section 8.5.2.

8.3 Amplified Design Spectra

The acceleration response spectra for the rare and expected earthquakes from the column moment capacity design that is discussed in Chapter 2 are plotted in Fig. 8-1. Also plotted in the figure, are estimates of amplified response spectra of both the rare and expected design earthquakes that would be required to control the bridge design. The

amplified design spectra were constructed in the same manner as the design spectra, except that the short and long period spectral accelerations were modified so that after being reduced by response modification factors each would have a demand equal to the design capacity of the bridge. These amplified spectra are used to evaluate the performance of the bridge model in subsequent sections of this Chapter.

Because of the high R-factor that was used for the rare earthquake, the expected earthquake controlled the design. However, the bridge had additional capacity beyond the expected earthquake requirement because the capacity provided was slightly greater than the design requirements. The amplified response spectra that are plotted in the figure were determined by amplifying the short (0.2 second) and long (1.0 second) period spectral accelerations that were used to construct the rare and expected design spectra so that each spectra would have moment demand that matched the exact design capacity of the columns.

Typically as the amplitude of earthquake response spectra are increased, the spectral acceleration plateau at the top of the response spectra widens. However in comparing the rare and expected design earthquakes that were used in Chapter 2, this phenomenon is not significant since the fraction of short and long period spectral accelerations is only different by 2.3 percent between the rare and expected earthquakes. Therefore the direct scaling of short and long period spectral accelerations to construct the amplified spectra was considered to be valid for comparisons.

8.4 Measured Performance of Bridge Model during Design Earthquakes

In this section, the measured response of the bridge is evaluated for shake table tests that had acceleration response spectra that were comparable to the rare and expected design earthquakes. The measured bridge response for motions approximately equivalent to each design earthquake is compared to the performance objectives of NCHRP 12-49.

8.4.1 Shake Table Motions Comparable to Amplified Design Motions

To evaluate the measured response of the shake table bridge model with respect to the design spectra, the tests having achieved shake table accelerations that had approximately the same spectral acceleration at the calculated natural period of the bridge in the transverse direction were determined. For the response spectra comparisons, the time axes of the design spectra were compressed to account for the specimen scale.

Figures 8-2 and 8-3 show response spectra of scaled versions of the shake table input motions used for high amplitude testing superimposed on the amplified expected and rare design spectra. The shake table input motions in the figures were scaled to match the design spectra at the calculated initial period of the bridge to aid in determining what shake table tests were equivalent to the amplified design spectra. The target motion that was used for shake table tests had equivalent spectral acceleration to the expected and rare design earthquakes for scaled target motion PGA of 0.09 g and 0.61 g, respectively. As shown in the test schedule of Table 5-2, these scales are equal to the target shake table motions between tests 12 and 13 for 0.09 g, and tests 15 and 16 for 0.61g.

Since the achieved shake table motions were slightly different than the target motions as discussed in Section 6.3.9, the achieved response spectra were compared to

the rare and expected design spectra to determine which tests had spectral accelerations equivalent to the design spectra at the natural period of the bridge. The achieved spectra of the three shake tables were averaged for each of these comparisons. Response spectra for the average achieved shake table motions of tests 12 and 13 are shown with the amplified expected design earthquake spectrum superimposed in Figs. 8-4 and 8-5. The spectral acceleration for test 12 and 13 shake table motions are 73 and 142 percent of the expected earthquake design spectra at the natural period of the bridge. The spectral acceleration for tests 15 and 16 shake table motions (Figs. 8-6 and 8-7) are 86 and 151 percent of the rare earthquake design spectra at the natural period of the bridge.

The spectral accelerations of tests 13 and 16 (Figs. 8-5 and 8-7) are both larger than the spectral accelerations of the expected and rare earthquakes, respectively, at the calculated fundamental period of the bridge in the transverse direction. Tests 13 and 16 spectral accelerations are also larger than design expected and rare earthquakes, respectively, for the calculated first and second transverse modal frequencies which according to analyses defined 99.9 percent of the transverse response of the bridge model and had periods of 0.398 and 0.302 seconds (Table 4-1). However, for high frequencies such as that where superstructure bending occurs for the third transverse mode, the spectral acceleration of the design spectra is greater than that of the shake table motions.

8.4.2 Measured Bridge Performance

Table 8-4 lists the maximum measured displacement ductility demands and ratios of displacement demand over failure displacement of the 3 bents of the bridge for the motions that were close to the amplified design earthquakes at the first mode spectral acceleration. The yield and ultimate displacement values that were used to calculate the measured ductility and failure displacement demands were those from the computational analysis that was discussed in Chapter 7.

8.4.2.1 Expected Earthquake Response

For test 13, with spectral accelerations that were conservatively equivalent to the amplified expected design earthquake at the first two transverse model frequencies, the maximum displacement ductility was 0.95 in bent 1. The measured acceleration-deflection hysteresis curves for bents 1 through 3 during test 13 are plotted in Figs. 6-59, 6-68, and 6-77. As shown in the plots, no significant inelastic deformation was apparent. As listed in the descriptions of damage in Tables 6-1 through 6-6, the only measurable cracks in the bridge after test 13 were less than 0.003 in (0.08 mm) wide in bent 1. Since none of the bents reached yielding during this test and damage was negligible, the service level performance objective of the NCHRP requirements for the expected earthquake, which was “immediate” (Table 8-2), as well as the damage level performance objective for the expected earthquake, which was “minimal” (Table 8-3), were both satisfied.

Based on the curvature measurements from tests that are listed in Tables 6-30 through 6-38, the maximum rotations measured at the plastic hinge regions for bents 1 through 3 were 0.0050, 0.0022, and 0.0032 radians, respectively, for test 13. As discussed in Section 8.2, the plastic rotational capacity for the immediate use performance level is 0.01 radians. This capacity is 50 percent larger than the maximum measured rotation, for test 13, which was in bent 1.

8.4.2.2 Rare Earthquake Response

Test 16 was shown by the response spectra in Section 8.3.2 to contain spectral accelerations that are conservatively equal to that of the amplified rare design earthquake at the first two transverse modal frequencies of the bridge. As shown in Table 8-4 and the displacement-acceleration relationships of bents 1 through 3 in Figs. 6-62, 6-71, and 6-80 all of the bents underwent yielding during test 16. The maximum bent displacement ductility demand was in bent 1 and was 3.31. The failure displacement demand, which was defined as the ratio of maximum displacement over failure displacement for each bent was also the largest in bent 1 and was 0.41. As described in the damage descriptions in Tables 6-1 through 6-6, after test 16, spalling had occurred in bents 1 and 3 but it was only significant enough to expose one spiral bar, which was in bent 3. For bent 2, the middle bent, only slight flaking of concrete was observed during this test.

All of the bents yielded during test 16 and bents 2 and 3 dissipated significant hysteretic energy, however no sign of loss in lateral force capacity was seen, and the column deflections were well below failure. Therefore, life safety performance requirements of the rare event, which were a service level of "significant disruption" (Table 8-2), and a damage level of "significant" (Table 8-3), were fulfilled by a relatively high margin.

Based on the curvature measurements from tests that are listed in Tables 6-30 through 6-38, the maximum rotations measured at the plastic hinge regions for bents 1 through 3 were 0.0285, 0.0250, and 0.0260 radians, respectively, for test 16. As discussed in Section 8.2, the plastic rotational capacity for the life safety performance level can either be calculated from Equation 8-1 or can be assumed to be 0.035 radians. The largest ratio measured rotation demand over rotational capacity for the life safety requirement assuming 0.035 radians is 0.813 for bent 1. If the rotational capacities of Equation 8-1 are assumed for each bent, then the largest ratio of measured demand over rotational capacity is 0.820 for bent 1.

8.5 Bridge Performance Subjected Synthetic Earthquake Records

In the previous section, the measured bridge response was compared to the NCHRP 12-49 performance criteria to evaluate the design. However this was not a direct comparison with the design motions since the entire ranges of spectral acceleration of the achieved table motions for tests 13 and 16 were not a perfect match to the amplified expected and amplified rare design spectra. This section discusses the calculation of artificial motions that matched the amplified expected and amplified rare design spectra that were discussed in Section 8.3.1. These motions were input to the Drain-3DX model of the bridge specimen to provide a more direct comparison of the bridge response due to design motions so that the response of the bridge could be compared to the performance criteria.

8.5.1 Calculation of Synthetic Design Earthquakes

The synthetic design earthquakes were calculated to match the amplified expected and amplified rare design spectra that were discussed in Section 8.3 using program SIMQKE (Gasparini and Vanmarcke 1976). SIMQKE, a FORTRAN based program developed to simulate earthquake ground motions, has the capability to generate statistically independent baseline corrected accelerograms based on input response

spectra. The velocity response spectra was the input into SIMQKE. The response spectra of the SIMQKE generated motions that matched the amplified rare and amplified expected design spectra are plotted in Figs. 8-8 and 8-9, respectively. The spectra of the generated motions were nearly the same as the amplified design spectra.

The acceleration, velocity, and displacement histories of the amplified rare and amplified expected SIMQKE generated motions are plotted in Figs. 8-10 and 8-11, respectively. Note that these plots are for a full-scale structure with no modification of the time axis. The rise time for the intensity of the motions was specified to be 5 seconds and a constant intensity for 15 seconds was specified thereafter. The prototype scale displacement records, which had a time step of 0.02 seconds and length of 30 seconds, were time compressed by a factor of two to account for the specimen scale before using them as input to the Drain-3DX computer model of the bridge.

8.5.2 Calculated Bridge Performance

The synthetic motions equivalent to the rare and expected design motions were input to the Drain-3DX model to evaluate the response of the bridge model with regards to the NCHRP 12-49 performance objectives. The Drain-3DX results to evaluate the performance were force-displacement relationships, the maximum bent displacements, and the maximum rotations in the plastic hinges. As shown in the Drain-3DX results that are discussed subsequently, although the bridge performed well, the calculated demands from the synthetic motions were greater than the demands for shake table motions. The reason that the calculated motions were slightly more demanding is because the synthetic motions contained many high amplitude acceleration pulses for a wide range of periods.

8.5.2.1 Expected Earthquake Response

The calculated force-displacement relationships for the three bents subjected to the expected design motion are plotted in Fig. 8-12. The maximum displacements are compared to the yield and ultimate displacements in Table 8-5. As shown in the force-deformation plots, none of the bents underwent significant yielding. No significant hysteretic energy was dissipated in any of the bents. The peak displacement in bent 2 remained well below the yield value. Both bents 1 and 3 surpassed their yield displacement slightly reaching displacement ductility demands of 1.35 and 1.06, respectively. The calculated plastic hinge rotational deformation demands were 0.00590, 0.00176, and 0.00393 radians, respectively for bents 1 through 3. As discussed in Section 8.2, the plastic rotational capacity for the immediate use performance level is 0.01 radians. The largest ratio of the calculated rotational demand over immediate use performance criteria capacity is 0.59. Since the bents underwent only limited inelastic response and the calculated rotation demands at the column ends were well below the immediate use performance capacity, the bridge performed well and conformed to the requirements of Tables 8-1 through 8-3 when subjected to the expected design earthquake.

8.5.2.2 Rare Earthquake Response

The calculated force-displacement hysteretic relationships for the three bents subjected to the rare design motion are plotted in Fig. 8-13. The maximum displacements

are compared to the yield and ultimate displacements in Table 8-5. As shown in the force-displacement plots, all of bents underwent significant yielding. Bent 1 experienced the largest displacement ductility demand (Table 8-5). The maximum displacement ductility demands for bents 1 through 3 were 5.59, 2.74, and 5.09. The largest ratio of displacement demand divided by the calculated ultimate displacement capacity is 0.69 for bent 1.

The plastic hinge rotational demands for the rare earthquake were 0.01983, 0.01355, and 0.02032 radians, respectively, for bents 1 through 3. As discussed in Section 8.2, the plastic rotational capacity for the life safety performance level can be assumed to be 0.035 radians. The largest ratio of the calculated rotational demand over life safety performance criteria using the 0.035 radian capacity is 0.58 for bent 3. If the rotational capacities of Equation 8-1 are assumed, then the largest ratio of measured demand over rotational capacity is 0.64 for bent 3.

All of the bents underwent yielding when subjected to the rare design earthquake and bents 2 and 3 underwent significant hysteretic energy dissipation, however no sign of reaching the lateral force capacity was calculated, and the column deflections were well below failure displacement. Therefore, the life safety performance requirements of the rare event, which were a service level of “significant disruption” (Table 8-2), and a damage level of “significant” (Table 8-3), were satisfied.

Chapter 9: Implications of Testing on Multiple Shake Tables

9.1 Introduction

The purpose of this chapter is to present simulation issues that were identified during the testing of the bridge model on multiple shake tables. It is hoped that through future work, issues from testing a distributed system on multiple shake tables that were faced in this project can be addressed and eventually resolved. The focus in this chapter is on target vs. achieved shake table motions and their influence on the bridge response.

Preliminary RAM-Perform analysis of the bridge that was discussed in Chapter 4 predicted that the first bent failure of the bridge model would occur in bent 1 (denoted as motion 1 in Table 4-5). However, the actual failure occurred in bent 3. Through analyses of the high amplitude tests (tests 12 through 19 in Table 5-2) that are discussed in this chapter, it was determined that failure of bent 3 occurred during shake table tests because the achieved shake table motions slightly deviated from the target motions. Had the exact target motions been achieved during the shake table tests, bent 1 would have been subjected to much larger deformation, and bent 3 would have had reduced displacement demand. Two sources that caused the difference in the predicted and actual bridge response are analyzed: the spectral accelerations, and the incoherency of the actual displacements among the tables even though the target motion was coherent.

Since the bridge model was strong and stiff relative to the shake table system, the shake table actuators were highly influenced by the response of the bridge model. In particular the bridge nonlinearity had an impact on the achieved shake table motions. Some of the effects of force feedback from the bridge onto the shake tables were compensated for using iterative methods in the shake table control system that are described subsequently, but some remained. This phenomenon is discussed in further detail, and the failure of the bent using target and achieved shake table motions is analyzed and discussed utilizing results from the experimentally verified Drain-3DX model that was described in Chapter 7.

The difference in bridge response due to achieved shake table motion deviation from target motions was evident, but did not have a significant impact on this study since the global objective of the multi-university collaboration was to verify, calibrate, and integrate computer models for the study of Soil-Foundation-Structure-Interaction (SFSI), and achieved (rather than the target) motions were to be used in these analyses. However, the effect of achieved shake table motion error may be of importance in tests where matching the motions is critical, and therefore it is presented in this chapter.

9.2 Interaction of Shake Table System and Bridge Frame System

As discussed in Section 6.3.9, the achieved shake table motions slightly deviated from the target input motions. These deviations were caused by the nonlinear bridge system response and cross-coupling between shake tables. Because the bridge is strong and stiff relative to the shake tables, it causes substantial force feedback that influences table response. During the elastic bridge response, these effects can be compensated by tuning the controller of the tables. A unique disadvantage of tuning multiple tables is that to correctly measure the transfer function of each actuator (and thus determine what

control parameters must be changed) only one actuator at a time can be operated and tuned. This procedure induces undesired differential displacement among the bridge supports. To prevent large differential displacements, the actuators must be tuned at extremely low excitation levels, and hence an adequate measurement of the transfer function can not be made.

Four methods were employed during testing to improve matching between the achieved and target shake table motions. The first method was to utilize very low amplitude tuning to measure the controller transfer function and adjust the controller settings. The table motions were kept sufficiently small while monitoring column bar strains to prevent any undesired response on the bridge. The second method was to compute an inverse transfer function offline and use it to modify the shake table drive signals. This can correct for some of the errors due to the low level tuning. The third method was to add a percentage of the error between the target and achieved acceleration history records to the shake table drive signals. This error can be added to improve table tracking in both the linear and non-linear regions of bridge response. This method was effective as long as the same motions are used subsequently, such as during the high amplitude tests 12 through 20, and as long as there is not a radical change in the response of the payload during the subsequent motions. The fourth method was to change offline the controller settings and offline transfer functions to adjust for the natural frequency shift after specimen yielding. Once the structure yields, the controller settings and error measurements are no longer valid. Although this method was successfully used for this and many past tests, it can be problematic due to the difficulties in estimating the required changes for the controller settings.

All methods that were employed were to a degree successful. As discussed later in this chapter, the motions during tests 15 and 16 had errors that led to the increased damage in bent 3 rather than bent 1. However, the inconsistencies were corrected after test 16 utilizing method four that was discussed above.

9.2.1 Achieved Motion Errors

The response spectra for the achieved motions for tests 12 through 20, which were discussed in Chapter 6, are shown in Figs. 6-247 through 6-254. It can be seen in the response spectra that overshoot errors in spectral acceleration began to increase during test 14 (Fig. 6-249). During tests 15 and 16, increasing overshoot error is shown in the spectra, most notably in bent 3. The response spectra for test 17, shows improvement in matching the target motion, and tests 18 and 19 show very good correlation of target and achieved (Figs. 6-253 and 6-254). Slight increase in error can be seen in the bent 3 spectral acceleration after test 19 when bent 3 had lost significant lateral load capacity (Fig. 6-255).

It can be concluded in comparing the target and achieved response spectra of the shake tables and the maximum measured column ductilities for each test (Table 7-4) that errors in the response spectra coincide with yielding of bents 1 and 3. Effective yielding of the bents occurred during tests 14 and 15. When these tests were conducted, all of the bents had effectively yielded, which changed the force feedback of the bridge on to the shake tables. After test 16, method 2 (discussed previously) was used to adjust the input to the shake tables so that the test 17 input would have compensation for the measured

acceleration errors from test 16. As shown in the response spectra in tests 16 and 17 (Figs. 6-251 and 6-252) the compensation due to errors measured in test 16 was successful, and the acceleration error was mostly eliminated after test 16. The reason that the compensation was successful is because after test 15, the bents had all effectively yielded and therefore the bridge system had nearly constant dynamic properties thereafter until failure of bent 3 during test 19. It is shown in the table of measured modal periods in Table 6-41 that most of the frequency shifting occurred after test 14. There was not a measurement of free vibration response of the model after test 16. However, the measured frequencies after test 17 did not change appreciably until failure. No significant additional damage occurred in the bridge during test 17; hence it can be assumed that the modal properties of the bridge remained unchanged after test 16. The achieved response spectra and their impact on the bridge response including a focus on spectral error at the measured modal frequencies are further discussed in Section 9.3.

Another manifestation of error in the achieved shake table motions was the table displacement histories. Because the target motions were synchronous for high amplitude tests, as long as the displacements were synchronous they should not have had an effect on response of the bridge. As discussed in Chapter 6, however, the achieved displacements of the three tables were asynchronous, which caused pseudo-static loading on the bridge due to differential displacements. Examples of the measured displacement histories of the three shake tables are plotted in Figs. 6-256 through 6-261 for tests 13, 16, and 19. Table 6-44 lists the maximum displacement differences between adjacent shake tables for all tests. The relationships between these differences and the target PGA for the high amplitude tests are plotted in Figs. 6-265 and 6-266. The maximum differential displacement increased as high amplitude testing progressed and the peak accelerations were increased. The effect of these displacements is discussed in the next section.

9.3 Comparison of Target and Achieved Motion Responses

The results presented in Chapter 7 demonstrated that the Drain-3DX model of the bridge led to close correlation with the test data. This model was hence used to evaluate the significance of the error in the achieved shake table motions. The analysis was carried out for both the target and achieved motions. The achieved motion analysis was identical to the analysis discussed in Chapter 7 and led to results that matched the measured response well. For the target motion analysis, test 13 through 19 motions were used as input in sequence. Test 17 was not included because the achieved test 17 motions had considerably lower amplitude compared to the test 16 motion and test 17 did not induce apparent additional damage to the bridge model. The comparison began with test 13 because test 12 was of low amplitude and did not cause yielding. The comparison was concluded with test 19 because this was the failure run. Upon comparing the two analyses, it was concluded that the achieved motions caused significantly larger deflections in bent 3, and failure of bent 3 during run 19. The target motions, however, had similar displacement ductility demands in bents 1 and 3 throughout the analysis, with slightly larger demand on bent 1.

To determine the contribution of shake table differential displacement errors to the difference in the predicted and actual response of the bridge model, the achieved

shake table motions were input to the analytical model at a very long time step (100 times the actual value of 0.01 sec.) to determine forces and displacements on the columns due to pseudo-static loading. For the target motions, these forces were zero because the target motions were synchronous.

9.3.1 Results from Dynamic Analyses

Figures 9-1 through 9-6 show superimposed plots of the calculated displacement histories of bents 1 through 3 for the target and achieved high amplitude test motions. The calculated maximum displacement ductility demands for bents 1 through 3 subjected to both the target and achieved motions and the corresponding maximum achieved over target displacement ratios are listed in Tables 9-1 through 9-3.

Prior to test 15, the maximum displacements of all the bents are consistently larger for the target motions. The achieved-target ratios for test 14 ductility demands for the three bents range from 0.86 to 0.88. Although the amplitudes are undershot for the achieved motions of test 14, all bents are subjected to approximately the same relative difference from target motion amplitudes. The achieved motions for test 15 caused significantly larger demands in bent 3, and significantly smaller demands in bent 1 than the target motions. During test 15, bent 3 had an achieved/target ductility ratio of 1.33. The achieved/target ratio for bent 1 subjected to test 15 is 0.79. The difference in the achieved target ratios for bents 1 and 3 is 0.55, which is substantial considering that the target displacement ductility demands in bents 1 and 3 were 2.86 and 2.27, respectively, for test 15. Test 15 was the first test when all of the bents experienced significant yielding in the shake table tests. Therefore, the larger demands that were imposed on bent 3 during test 15 could have had a significant impact on the system response in subsequent tests.

It is shown in comparing the response histories that after test 15 that the deviation between the response from the target and achieved motions increased considerably (Figs. 9-3 through 9-6). The achieved-target maximum ductility ratios for bents 1 and 3 subjected to test 18 are 0.77 and 1.23, which shows that there is significantly more damage in bent 3 and less damage in bent 1 due to the achieved shake table motions. The same trend is shown in test 19 where the achieved-target ductility ratios are 0.76 and 1.40 for bents 1 and 3, respectively.

9.3.2 Comparison of Target and Achieved Spectra at Measured Frequencies

The errors in the response spectra for the achieved shake table motions were presented in Chapter 6 and were further discussed in Section 9.2. In Section 9.2, it was concluded that errors of the response spectra occurred because of the change in bridge response due to yielding of the bents in tests 14 and 15. The yielded bents caused the compensation of shake table input motions to be ineffective in counteracting the force feedback from the bridge on to the shake tables. This error in the motions, however, led to large error in spectral accelerations for tests 15 and 16, which affected the progression of damage in the bridge model, most notably in bent 3 as discussed in Sec. 9.3.1. In this section, the spectral accelerations for the measured modal frequencies of the bridge are compared for target and achieved motions.

The response spectra, discussed in Chapter 6, were plotted in Figs. 6-247 through 6-254 with the measured modal transverse modal frequencies of the bridge superimposed. Tables 9-4 and 9-5 list the target and achieved spectral accelerations at the measured first and second transverse modes, respectively for shake tables 1 and 3 (at bents 1 and 3). Shake table 2 is not included in the comparison because the middle bent, bent 2, did not have a significant impact on the asymmetric response of the bridge. Achieved over target spectral acceleration ratios are listed in each table along with the achieved ductilities of bents 1 and 3. The ductilities for the yield test and test immediately after yielding of each bent and the corresponding achieved-target spectral acceleration ratios are shown in bold. The spectral accelerations during these two tests have the largest impact on yielding of the bents and increased nonlinear deformations. The achieved/target spectral acceleration during and just after yield is greatest for bent 3 at mode 2 during tests 15 and 16 where the ratios are 1.66 and 1.8, respectively.

Plots showing the data from Tables 9-4 and 9-5 at measured modal frequencies are shown in Figs. 9-7 through 9-10. These plots show the target and achieved spectral accelerations vs. bent displacement ductility for bents 1 and 3. Figures 9-7 and 9-8 show the target and achieved spectral accelerations for shake tables 1 and 3, and the ductilities, respectively, at the first mode. Comparisons of second mode target and achieved spectral acceleration for motions of shake tables 1 and 3 and ductility are shown in Figs. 9-9 and 9-10, respectively. It is shown in the figures that the most significant error in the spectral acceleration is at the frequency of the second mode for shake table 3 (Fig. 9-10). The error begins when bent 3 yields and increases until the bent reached a ductility of approximately 4, which was during test 16. As discussed in the preliminary analysis in Chapter 4, the second mode shape is the mode where bent 3 has the largest displacement. This large difference in spectral acceleration supports that the deformations of bent 3 due to the achieved motions were larger than the target motion deformations of bent 3 as a result of large accelerations.

9.3.3 Bridge Response Due to Achieved Shake Table Motion Incoherency

For typical single shake table tests and in multi-table tests with highly flexible structures, the achieved displacements are not an issue as long as the achieved table accelerations are matched with target accelerations. This is because the systems are generally statically determinate and it is not possible to build up forces among shake tables. In these cases, acceleration response of the shake tables defines the structural response. However for a semi-rigid indeterminate structure such as the bridge in this study where the columns had low yield displacements and high forces can be developed with differential displacements, matching of target displacements in addition to the accelerations are critical to achieving the desired structural excitation. The measured shake table incoherency due to discrepancies in the achieved shake table motions for high amplitude tests was discussed in Section 6.3.9.2. Table 6-44 lists the maximum differential displacements between adjacent shake tables during the tests. Representative examples of the achieved shake table displacement histories are plotted for tests 13, 16, and 19 in Figs. 6-256 through 6-261

The Drain-3DX model was utilized using the achieved shake table motions at an increased time step (by a factor of 100) to determine the impact of the achieved

differential displacements on the shake table model. Except for the increased time step, this analysis was identical to that discussed in Chapter 7 and the achieved motion analysis of Section 9.3.1. Since the time step of the achieved shake table motions was increased by a large factor, the acceleration did not have any significant influence on the calculated excitation and the bent excitation was purely due to pseudo-static differential table displacement effects. The calculated effects of pseudo-static displacements cannot be directly subtracted from total excitation that was presented in 9.3.1 because both models are nonlinear. However, the calculated pseudo static displacement effects from differential shake table displacements up until yielding in the dynamic analysis can be compared, since until column yielding, both the dynamic and pseudo-static models generally respond linearly.

9.3.3.1 Increased Time-step Analysis Results

As discussed in Section 9.3.2, spectral acceleration errors in the achieved shake table motions were identified as a suspect of causing the bent 3 failure. However, it was also possible that the differential shake table motions contributed to the bent 3 failure. Therefore, the increased time step analysis was used to determine the effect on the bents from the pseudo-static loading.

Table 9-6 lists the calculated pseudo-static displacement demands due to the measured differential table displacements and the corresponding percent of static yield displacement demand for each of the three bents for the high amplitude tests 12 through 20. For comparison, the measured displacement ductility demands from the shake table tests are also shown in the table. Values are shown in bold for the tests of each bent up until the measured yield run. These values are in bold because pseudo-static forces due to differential displacements would have the largest impact on bridge response for runs up until yielding of the columns. This is because column yielding was the cause of the largest change in system response during the tests (Fig. 9-10). A parallel comparison from the same analyses is shown in Table 9-7 for the shear force demands due to differential shake table displacements compared to the effective yield force of the bents.

The largest effect of the differential displacements for bent 1 up until test 13 (when the bent reached a ductility demand of 0.95) was 2.2 percent of yield displacement and 3.6 percent of yield force, respectively. The largest effect of differential displacements for bent 3 up until test 14 (with ductility demand of 0.97) was 2.4 percent of yield displacement and 4.1 percent of yield force, respectively. For the yield runs of bents 1 and 3, the differential displacements placed demands of 3.4 and 5.8 percent of the yield displacements for bents 1 and 3, and 5.8 and 9.9 percent of the yield forces for bents 1 and 3.

The largest effects of differential displacements were on bent 2, the tallest of the bents. During the yield run of bent 2 where the bent reached a measured displacement ductility demand of 1.2, differential displacements caused demands of 30.5 percent of yield displacement and 36.2 percent of yield force. Demands from differential displacements were greatest for bent 2 because this was the most flexible part of the system and acted as a fuse. However, since bent 2 was at the center of the bridge model, it contributed only to the symmetric transverse response to the bridge. Therefore the

large displacement demands and early yielding of bent 2 did not impact the failure of the other bents.

Plots of the data from Tables 9-7 and 9-8 for pseudo-static displacement and shear demand due to differential displacements vs. dynamic displacement ductility demand for each bent are shown in Figs. 9-11 and 9-12. It is shown in the plots that no significant demands due to differential displacements were imparted on bent 1 or bent 3 prior to yielding from dynamic excitation. As discussed previously, the largest demand is for bent 2.

It was apparent from the dynamic analyses discussed in Section 9.3.1 that for bent 3, damage imposed from achieved motions was significantly greater than that from target motions. Significant acceleration error was identified on the bent 3 shake table for tests 15 and 16. The pseudo-static demands from differential displacements during these tests for the bent were 5.8 percent and 13.1 percent of the yield displacement. As shown in Figs. 9-12 and 9-13, the demand imposed on the bents from shake table differential displacement errors were comparable for bents 1 and 3 with slightly greater demand on bent 1 for a given ductility. Therefore, while the displacement errors may have had a small contribution to the achieved motions causing bent 3 to fail, it is unlikely that the demands due to shake table differential displacement errors were the only cause.

9.4 Summary and Recommendations for Future Tests

Comparisons of the calculated bridge response due to the target and achieved shake table motions were made and it was determined that the extreme ductility demands that led to bent 3 failure were caused by deviation of the achieved motions from target motions. In comparing the achieved response spectra and the bridge response, it was concluded that yielding of bent 3 had caused the overshoot in shake table accelerations of the shake table supporting bent 3 because the shake table controllers did not adequately compensate for the bent nonlinearity. The overshoot of accelerations then inflicted further damage to bent 3 contributing to its eventual failure. By the time the motion was corrected in test 17, irreversible damage to the bridge, namely bent 3, had already occurred.

Upon review of the differential shake table displacements and analyses of their effects using a reduced time step analysis, it was concluded that before yielding of bents 1 and 3, the differential displacements did not have a significant effect. For shake table motions after yielding of the bents, the impact of differential displacements increased; however, both bents 1 and 3 were subjected to approximately the same increase in demand with slight bias toward bent 1. It was therefore determined that differential displacement errors did not have a significant role in the failure of bent 3.

The global objective of the project in which this study forms a component was to verify and calibrate computer models in predicting the measured bridge response for study of SFSI. Although the achieved shake table motions in this test did cause differences in the failure progression of the bridge, the differences in the target and achieved response were not an issue because the *actual* shake table motions were used in the analyses. However, since there were significant differences in the response due to the errors in the achieved accelerations and displacements, consideration should be made for improvement of both in future tests.

Ideally in a shake table test, the actuators would have sufficient capacity so that force feedback from the specimen is not an issue. For this to occur either the specimen would have to be sufficiently small, or the shake table actuators would need to have very large capacity. Since very large actuator capacity would not be economically feasible, and significantly reducing the size of the specimen would cause the results of the experiment to be unrealistic, the most viable option is to improve the shake table controller compensation for specimen nonlinearity.

Two options could be considered for providing improvement in compensation for force feedback from the specimen. The first is an accurate analytical model of the structure integrated with shake table controllers to compensate for bridge force feedback changes when yielding occurs. If an accurate model of the specimen were developed before testing, it could be integrated with the control of the shake tables so that based on the combined movements of the shake tables, the force feedback from the bridge is known. However, this presents a problem because the purpose of experimental testing is to determine response of a structure, which is usually not already known. It is possible that pre-test models could be sufficiently accurate; however because of the variability in materials and craftsmanship and uncertainty in the response, using a preliminary analysis model might not be sufficient.

The second option to provide improvement in compensation for force feedback from the specimen is real time compensation for specimen nonlinearity. Research has been conducted for the improvement of shake table response with nonlinear payloads. Examples of iterative methods that are currently employed using adaptive inverse control and on-line iteration are discussed in Nowak et al. (2000) and Filiatrault et al. (2000). However, these approaches do not utilize real time methods and can be ineffective when sudden changes occur in the response characteristics of the specimen such as column yielding. Recent research utilizing what is called adaptive filter compensation (Dozono et al. 2004) in conjunction with the existing methods of feedback control and iterative methods (Nowak et al. 2000) has shown that it is possible to keep shake table accelerations close to target even when a large and complicated nonlinear specimen is under excitation. This experimentally proven method uses real time adaptive filter compensation (AFC) that identifies and compensates for the error in the transfer characteristics of the motion during testing. An attractive feature of AFC is that it can be easily implemented in existing control units for shake tables (Dozono et al. 2004). However, the reliability of this method and its use on a multi degree of freedom multi shake table tests for a variety of specimen is yet to be proven.

It is hoped that through future work, improvements can be made in the matching of shake table motions for nonlinear multi-degree-of-freedom (MDOF) structures supported on multiple shake tables. This is a complex issue. Since there is unpredictability in the response of the specimens tested on shake tables, there is a delay in implementing compensation of table motions due to the measured changes in the specimen, and force feedback comes not only from MDOF bridge response, but from interaction of shake tables through the bridge specimen. The off line iterative method of correcting the motion for nonlinearity after test 16 in the shake table tests was effective in compensating force feedback changes due to yielding of the bents. However, to use the method, iteration was required that used the measured response from the previous test

(test 16) and therefore the motion had acceleration errors in both tests 15 and 16 that were not compensated for until test 17. If effective compensation could be implemented in real time, a bridge response closer to that from the target motions could have been achieved.

Chapter 10: System Effects

10.1 Introduction

Past experimental studies on the seismic response of bridges have focused on the *component* performance due to a lack of available testing facilities that could accommodate large-scale *system* testing. The UNR shake table system has made it possible to address this shortcoming. One of the global objectives of the current project was to study the bridge *system* and determine the implications of piers resisting lateral forces as an integrated system of the three bents and the superstructure. To determine the system effect, the response of the complete bridge model and individual bents was studied analytically. The Drain-3DX analytical model that was discussed in Chapter 7 was used to calculate the response for test motions 13 through 19 of the complete bridge and of the individual bents having tributary mass. This provided a comparison of bent response for component testing on a single shake table, with response from system testing on multiple shake tables. Comparisons were also made between the bent and system response based on the amount of dissipated hysteretic energy and number of large displacement cycles for each bent vs. maximum displacement demand for each test motion.

Four additional systems having a constant stiffness index (sum of lateral column stiffness) were analyzed using the Drain-3DX model and compared to the system response of the shake table model. The aspect ratios of the columns were within the same range as those tested on the shake tables and discussed in Chapter 7. Both displacement ductilities and damage indices were calculated for the system and individual bent response of the models subjected to the test motions 15 and 18, and the rare and expected design motions.

To analyze the effectiveness of elastic analysis methods in predicting the difference in nonlinear system and individual bent response, two measures of irregularity were compared to the inelastic results. The first was an irregularity index that is typically used to determine whether single mode analysis is sufficient for design. The second was a comparison of the elastic response of the bents in the system subjected to a 1 g lateral load with the elastic response of individual bents having tributary mass subjected to a 1 g lateral load.

10.2 System and Bent Response Comparisons for Bridge Specimen

The nonlinear Drain-3DX analytical model of the bridge that was discussed in Chapter 7 was used to calculate both the system and individual bent response for the target shake table motions of tests 13 through 19. These were the high amplitude test motions that included first yield (test 13) through failure of bent 3 (test 19). The system response is the response of each bent within the bridge system as tested on the shake tables and as described in the Chapter 7 analytical model. The individual bent response is the response for each bent separated from the bridge system and having tributary mass lumped at the top of the bent. The individual bent response is comparable to how a bent would typically be modeled for a single shake table component test.

The amount of damage for system and individual response was calculated and compared for each test motion. A mechanistic damage model for reinforced concrete developed by Park and Ang (1985) was used to quantify damage. This model measured damage as a combination of dissipated hysteretic energy and the maximum bent displacement.

Number of half cycle post yield displacements, number of half cycles with twice the yield displacement, and the amount of hysteretic energy dissipation were compared for each bent system and individual response at a given displacement ductility level. These comparisons were to determine whether the system response impacted the amount of damage imposed on a bent for a specified displacement.

10.2.1 Results from Analyses

Figures 10-1 through 10-7 show the calculated transverse displacement histories of each bent (bents 1 through 3) in the bridge system, with the individual bent response superimposed for tests 13 through 19. Comparisons of the system and bent force-deflection relationships for each bent for tests 13 through 19 are shown in Figs. 10-8 through 10-28. Tables 10-1 through 10-3 list the displacement ductility demands and system over individual bent ratios of displacement ductility demand for bents 1 through 3, respectively.

Response of bent 1 is very similar in both amplitude and frequency for the system and individual response to all tests except test 13. The general trend of bent 1 is that there are slightly greater amplitudes for system response for all tests. For test 13, the individual response amplitude was substantially greater than the system response for bent 1 (Figs. 10-1 and 10-8). This difference is due to a slight shift in the modal frequency of the bent when it is in the bridge system compared to when it is modeled individually. The spectral acceleration for the shake table target motion peaked (Fig. 4-27) at approximately the same period as the fundamental period of bent 3, which was 0.3 seconds. For the system response, the modal frequency having large bent 3 deformation is closer to this peak of spectral acceleration and therefore the system increased the response of the bent.

The individual response of bent 2 has the largest deviation from system response of all the bents throughout the tests. For test 13, when the bent behaves elastically, the system response is larger than the individual response. This is because the individual bent response has less excitation without system influence for two reasons: The first is as an individual bent, bent 3 has a lower effective fundamental frequency because in the system the bent behavior is influenced by the stiffer bents 1 and 3. The lower frequency of bent 2 as an individual bent corresponds to a point of lower spectral acceleration on the response spectra. The second reason is because the bent 2 response is dominated by the stiff outer bents which have larger excitation. As bent 2 is subjected to more demanding motions that exceed its yield displacement, the individual bent response is substantially greater and at a completely different frequency than the system response. This is because for the individual bent response, the bent is not restrained by the rest of the system and it is allowed to reach much larger displacements. For the system response of bent 2, the bent is restrained by bents 1 and 3 and therefore has lower amplitude as well as higher frequency response.

Bent 3 has the closest correlation of all the bents between system and individual bent response. Similarly to bent 1, frequencies of the response as well as the amplitudes are comparable for both system and bent response.

10.2.2 Comparison of Damage Indices

To compare the amount of damage in the columns for system and individual bent response for the analyses that were discussed previously, a damage index was calculated for each bent and each test motion. The damage index (Equation 10-1) which was developed by Park and Ang (1985), is an empirical measure of damage based on a combination of amount of dissipated hysteretic energy and the maximum displacement demand over ultimate displacement ratio. A damage index of greater than 1 represents collapse. However, the probability of collapse at a damage index of 1 is approximately 50 percent with a standard deviation of 0.54. Increasing levels of damage index beyond one indicates a higher probability of collapse.

$$D = \frac{\delta_M}{\delta_u} + \frac{\beta}{Q_y \delta_u} \int dE \tag{10-1}$$

where

δ_M = *Maximum deformation under earthquake*

δ_u = *Ultimate deformation under monotonic loading*

Q_y = *Calculated yield strength*

dE = *Incremental absorbed hysteretic energy*

$$\beta = \left(-0.447 + 0.073 \frac{l}{d} + 0.24 n_o + 0.314 p_t \right) \times 0.7^{\rho_w}$$

$$\frac{l}{d} = \textit{Shear span ratio} \geq 1.7$$

$$n_0 = \textit{Normalized axial stress} \geq 0.2$$

$$p_t = \textit{Longitudial steel ratio}$$

$$\rho_\omega = \textit{Confinement ratio}$$

The calculated damage index, hysteretic energy dissipation, displacement ductility demand and corresponding system over individual response ratios are listed for each bent in Tables 10-1 through 10-3. The ductility ratios show the amount of maximum displacement demand that contributed to the damage for system and individual response. The hysteretic energy ratios show the difference in amount of large displacement cycles for the system and individual response. Figure 10-29 shows the variation of damage index system/individual response ratios as a function of the maximum displacement ductility demands for the three bents. Because the ductility demands were different in the system and the individual bents for each test, individual bent ductility demands were used in the plot. At low amplitudes near yielding (ductility of 1 to 2), the damage index ratios are high because at these amplitudes the comparison is at the noise level of the index and therefore slight variations in response cause large differences in the index.

Significant differences can be seen in bents 1 and 2 for the system and individual response for test 13, which were at or near yield for system response of all bents. The pre-yield differences were, as discussed in Section 10.2.1, due to slight natural frequency differences of bent 1 near a peak in the spectral acceleration and as discussed above the index was near the noise level of ductility of 1. After yielding, each of the three bents followed a general trend that is shown in the tables as well as in Fig. 10-29. The system damage index demand in bent 1 exceeded the individual demand by as much as 41 percent. In bent 2, the system damage index demand was less than the individual demand by as much as 38 percent. The damage index demands for system and individual response were approximately the same for bent 3 with a maximum system demand difference of 8.4 percent after yielding.

10.2.3 Hysteretic Energy and Displacement Cycles

The number of large displacement cycles and the amount of hysteretic energy dissipation for each of the motions from test 13 through 19 vs. achieved ductilities were plotted for the calculated system and the individual response of each bent to determine whether there is a significant difference in the damage due to repeated cycles from system response for given ductility. The maximum ductility values that were used in the comparisons corresponded with the measurements for system and individual response, respectively. Both the number of half-cycles past yield and those past twice yield displacement were used to evaluate the number of large displacement cycles.

Figures 10-30 through 10-32 show the number of half cycles past yield, half cycles past two times yield, and hysteretic energy dissipation, respectively, vs. ductility for system and individual response of bent 1. The trends in the number of large displacement cycles and hysteretic energy dissipation were generally comparable for system and individual response of the bent. However, the cycles and energy for given ductility were larger for the individual bent than for the bent in the system. The largest difference of half-cycles past yield was at a ductility of 5.4 where the individual response demanded 54 percent more cycles than the system response. The largest difference in the hysteretic energy dissipation was at a ductility of 5.0 where the individual response demanded 56 percent more energy dissipation than the system response.

Figures 10-33 through 10-35 show the system and individual bent results for bent 2. The result for bent 2 shows the same general trends as that of bent 1 for the number of large displacement cycles, which were greater for the individual response. The dissipated hysteretic energy vs. ductility was nearly the same for the system and bent response. The largest difference in half-cycles past yield was at a ductility of 1.8 where the individual response and system response demanded approximately 13 and 4 half-cycles, respectively. The largest difference in hysteretic energy dissipation was at a ductility of 4 where the system response demanded approximately 20 percent more energy dissipation.

System and individual comparison plots for large displacement cycles and hysteretic energy vs. ductility for bent 3 are in Figs. 10-36 through 10-38. The trend of the number of cycles past yield and past twice yield and hysteretic energy for given ductility is generally the same for the system and individual response of the bent. The largest difference for number of half-cycles past yield is at a ductility of 3, where the individual response demanded approximately 50 percent more cycles than the system

response. The largest difference in hysteretic energy dissipation is at a ductility of 5.9 where the system response demanded approximately 55 percent more energy dissipation than the individual response.

10.3 Parametric Study of System and Bent Responses

Five analytical systems were used to evaluate system compared to bent response including a system identical to the one tested on the shake tables. The variable that was constant for the five systems was the overall transverse stiffness index of the substructure. The stiffness index was defined as the sum of the inverse of bent heights cubed. There were two purposes to analyze the five bridge systems. The first was to evaluate the impact of varied column stiffness configurations on bridge performance. The second was to determine whether simple elastic methods could be used to estimate the difference between system and bent response.

Two sets of motions were used in the analyses. The first was the target motions of tests 15 and 18, with peak ground accelerations of 0.5 g and 1.33 g, respectively. These motions represented moderate and high intensity earthquakes. The second set was the SIMQKE design motions for the rare and expected design earthquakes that were discussed in Chapter 8. The design motions that were based on response spectra were used because unlike the shake table test motions (Figs. 4-27 and 4-28) where spectral accelerations were varied with large peaks, the design motions contained uniform acceleration response (Figs. 2-35 and 2-36) that would not be overly sensitive to slight changes in fundamental frequency of the bents due to system effects.

Tables 10-4 and 10-5 list the system and individual displacement ductility demand and the damage index (calculated from Eq. 10-1) for each column of the five systems. Data from test motions 15 and 18 are listed in Table 10-4, and for the design motions are listed in Table 10-5. The different bridge configurations and the corresponding calculated demands are compared with the response of the shake table model demands in the following section. The primary responses that are discussed and compared are the responses due the synthetic motions based on design spectra (discussed in Chapter 8) because there are no sudden variations in spectral acceleration response for slight differences in frequency. The system responses from the expected motion are close to yield for all systems that are considered. The rare motion system responses are significantly past yield and have maximum bent displacement ductility demands ranging from 4.97 to 5.86 (Table 10-5). Data from Tables 10-4 and 10-5 are used in Section 10-4 to evaluate the effectiveness of linear methods to predict variation between system and bent response.

10.3.1 Test Specimen

System and individual response of the test specimen for motions 13 through 19 was discussed in Section 10.2. Table 10-5 lists the ductility demands and damage indices for system and individual response of the test specimen subjected to the rare and expected design motions. The bridge specimen response included considerable in-plane rotation due to the flexible center bent and large variation in stiffness between the end bents (bents 1 and 3).

For the expected earthquake, which has a demand that is approximately equal to yield in bents 1 and 3, the system/individual ratio is greatest for bent 1, the medium height bent. The system/individual ratios for displacement demand and damage index for bent 1 are 1.47 and 1.57, respectively. The cause of the increased demands due to the system effect on bent 1 is the torsional irregularity particularly before yielding which causes bent 1 to pivot about the short and stiff bent 3. The system/individual ratio for bent 3 is approximately 1 for both the displacement demand and damage index. Demand on bent 2 is reduced by the system. The system/individual ratio for bent 2 is 0.67 and 0.64 for displacement demand and damage index. The reason that demand of bent 2 is reduced by the system is because of restraint provided by the other bents.

The rare earthquake demands show similar trends for all the bents as the expected earthquake except that the system effect on bent 1 is less pronounced. The system/individual ratios for displacement demand and damage index for bent 1 are 1.15 and 1.31. The system has a slightly lower effect on bent 1 after all bents have yielded because the yielding of bent 3 reduced in-plane rotation.

10.3.2 Bridge with Uniform Column Height

A bridge model with uniform column heights, labeled as "uniform" in Tables 10-4 and 10-5 was analyzed so that results could be obtained for a bridge model with no system irregularity in the transverse direction. This was to be used as a baseline for which to check the elastic methods that are discussed in Section 10.4. System irregularity was considered to be present when the bent response was different that of the system.

Each bent for the uniform system was the same column height of 70.8 in (1.80 m), and was tributary to the same amount of mass. Theoretically the bent and system response would be the same for this structure. This system was analyzed for both the two test motions and design motions. However the damage indices and comparisons with individual bent response were only calculated for the test 15 motion as reflected in Table 10-4 to show an example of results for a system with no irregularity. The displacement ductility demands for test 15 were approximately the same for all bents including for system and individual response. The system displacement ductility demand for each bent was approximately 2.82. The individual bent displacement ductility demand for each bent was approximately 2.86. The system/individual ratio for response of all the uniform system bents for test 15 is 0.99 (or nearly 1.0 as expected) for both displacement ductility demand and for damage index.

10.3.2.1 Uniform Column Height Bridge Performance

The failure of an interchange bridge at junction of I5-SR14 during the 1994 Northridge was caused by large variation among the column heights that led to high concentration of shear in one of the columns and its failure. This led to the conclusion that to avoid this type of behavior, the column heights need to be the same in the replacement bridge (Saiidi et al. 2001). Many bridge designers tend to follow adesign methodology for earthquake resistant bridges to design a bridge so that if possible it is symmetric and uniform to avoid irregular system response. Therefore it is desirable to design bridges that have uniform column height. As long as earthquake demands on the columns for this type of bridge do not fail the columns, the bridge remains intact.

However, if the columns reach their failure displacement, then the entire system will fail due to lack of substructure redundancy.

Tables 10-4 and 10-5 list the calculated ductility demands on the columns for the uniform height bridge and shake table bridge specimen for the test motions (tests 15 and 18), and the design motions (expected and rare), respectively. For the high amplitude test motion (test 18), the maximum displacement ductility demands on the columns in the specimen and the uniform system are 6.4 and 5.36, respectively. The specimen has a maximum displacement ductility demand that is 19 percent larger than that of the uniform system. For the rare design motion, the maximum displacement ductility demands on the specimen and uniform systems are 5.59 and 5.35, respectively. The specimen has a maximum displacement ductility demand that is approximately 5 percent larger than that of the uniform system.

The calculated displacement ductility capacities from the pushover analyses discussed in Chapter 7 were between and 7 and 8 for columns in both the uniform system and the specimen. Therefore the design motion demand on the columns in the bridge specimen and the uniform bridge did not reach failure, and the lack of redundancy at column failure in the uniform system was not an issue. However it should be noted that there was only a 5 percent increase in displacement ductility demand from the rare design earthquake for the non-symmetric system (in comparison to the uniform case), which was shown in tests to provide redundancy in column capacity after failure of the most critical bent. Although this study was limited it does suggest that providing redundancy by varying the column heights might be a better alternative than making the column heights the same.

10.3.3 Symmetric Bridge with Stiff Center Bent (System 1)

System 1 was a symmetric bridge with a stiff bent at the center and two flexible bents at the ends. This bent stiffness distribution is the opposite of that of the bridge specimen tested on the shake table where the center bent was the most flexible, with the exception that the bridge specimen was not symmetric. The stiff center bent was 60 in (1.52 m) tall, which was equivalent to the shortest of the bents in the bridge test specimen (bent 3). The heights of the outer bents were 80.7 in (2.05 m), which was governed by the stiffness index that was constant for all the bridge systems.

The calculated ductility demands and damage indices on each column of this system for the rare and expected motions are listed in Table 10-5. For the expected motion, response for all of the bents was larger for system response than for individual response. The flexible end bents reached approximately 80 percent of yield displacement. The stiff center bent reached a displacement ductility of 1.25 for system response. The system/individual ratios for the outer bents were 1.03 for displacement demand and 1.08 for damage index. For the center bent, the system/individual ratios were 1.17 and 1.19 for displacement demand and damage index, respectively. For this motion that led to a nearly elastic response, the system effect caused little impact on the flexible end bents but caused 19 percent increase in demand for the stiff center bent. This is to be expected because the center bent in the system is stiffer than the outer bents, and the system effect generally results in redistribution of forces from softer bents to the stiff bent.

For the rare design motion, which caused yielding in all of the bents, the system effect caused the flexible bents at the ends of the frame to have a reduced demand. The system/individual ratios of the end bents were 0.79 for both displacement ductility demand and damage index. The center bent demand was increased by the system effect. System/individual ratios for this bent were 1.28 and 1.32 for the ductility and damage index, respectively.

10.3.4 Asymmetric Bridge with Stiff Center Bent (System 2)

The column heights in System 2 are the same as those in bridge specimen except the stiff bent in the shake table model (bent 3), which has a height of 60 in (1.52 m), is moved to the center. The medium and tall bents are bents 3 and 1, with heights of 72 and 96 in (1.83 and 2.44 m), respectively. Similar to the shake table specimen, System 2 has significant coupling between bents due to asymmetry that causes significant torsional response of the superstructure. As discussed in Section 10.4, the torsional irregularity in System 2 is larger than that of the bridge model in the transverse direction due to the very large difference in stiffness between the end bents (bents 1 and 3) in System 2.

Increase in demand due to the system response of System 2 for the expected motion only occurs for bent 3, which is the stiffer of the two end bents (Table 10-5). The system/individual ratios of displacement demand and damage index for this bent are 1.2 and 1.34, respectively. The system causes reduced demands on bent 1, which has system/individual ratios of 0.56 for displacement demand and 0.54 for damage index. The demands on bent 2, which is the stiff center bent, are approximately the same for both system and individual response.

For the rare motion, the system/individual response ratios for both bents 1 and 3 are close to 1, meaning that the system effects were small. Similar to the symmetric version of this system, which is System 1, increased demands were shown on the stiff center bent from the expected motion due to system response. The system/individual ratios of bent 2, the center bent, were 1.26 for displacement demand and 1.14 for damage index.

10.3.5 Symmetric Version of Test Specimen (System 3)

System 3, which is a symmetric version of the bridge specimen, has the same height center bent as bent 2 in the specimen. The difference between System 3 and the bridge specimen is that bents 1 and 3 of System 3 are of the same height. This height was calculated by the constant lateral stiffness index and was 64.9 in (1.65 m). The combined stiffness of bents 1 and 3 in system 3 are equivalent to the combined stiffness of bents 1 and 3 in the bridge test specimen.

Response of system 3 is very similar to the response of the bridge specimen except that the symmetric end bents cause the system response to be closer to individual bent response for bents 1 and 3. The system/individual ratios of bents 1 and 3 for the expected earthquake are approximately 1.03 for both displacement demand and damage index. Similar to the test specimen, the system reduces the response of the center bent, bent 2, which in the system is restrained by the stiff end bents. The system/individual response ratios for bent 2 are 0.68 for both displacement demand and damage index.

The rare motion causes similar differences between system and individual response to the expected motion. The system causes a slight increase of demand for the end bents, which have system/individual ratios for displacement demand and damage index of 1.05 and 1.12. Similar to the response from the expected motion and the response of the bridge specimen, for the rare motion, the demand in the flexible center bent was reduced due to the system effect. The system/individual ratios for the center bent are 0.70 and 0.64 for the displacement demand and damage index, respectively.

Because System 3 is identical to the bridge specimen except that it is symmetric, the effects of torsional irregularity can be directly identified in comparing the system response of System 3 to the system response of the bridge model (Table 10-5). Under the expected motion, there were significantly larger demands on bent 1 of the specimen compared to bent 1 of system 3. The specimen ductility demand of bent 1 for the expected motion was 1.35; the displacement ductility demand on bent 1 of system 3 was only 1.07. The displacement ductility demands for bents 2 and 3 are almost identical for the bridge specimen and the symmetric version of the specimen (System 3). The largest effect of the in plane rotation caused by the difference in end bent stiffness for the specimen was on bent 1, which was the most flexible of the end bents.

For the rare motion, all the bents significantly exceeded yielding both in the system and individually. Both the test specimen and System 3 have comparable demands for the center bent, which are ductility demands of 2.74 and 2.88 for the specimen and system 3, respectively. The displacement ductility demand on bent 3 for the test specimen is 5.10, which is only slightly larger than the demand on the symmetric system 3 that is 4.97. The Bent 1 displacement ductility demand for the test specimen is 5.59, compared to 4.96 for system 3. Although there is a large torsional irregularity in the bridge specimen, the performance is very similar to that of the symmetric version (system 3) where both end bents are subjected to the same demand. This was not seen in the shake table tests because there was a significantly larger motion on bent 3 due to achieved motion discrepancies, and therefore demand on bent 3 was much larger than that of bent 1. However, for a real earthquake, as long as the site conditions between bents were similar, the motions would not be drastically different for bents 1 and 3 and they would therefore have comparable high amplitude ductility demands.

10.4 Irregularity Measures to Evaluate System Effects

The calculated data for the systems that were discussed in the previous section (Tables 10-4 and 10-5) were used to determine whether differences in the system and bent response could be correlated to simple elastic measures of system irregularity. Two methods were used in the comparisons that were made for both test motions (tests 15 and 18) and the design motions (the rare and expected design spectra compatible motions). The system irregularity measures and the corresponding maximum and minimum bent damage index system/individual ratios are listed in Table 10-6 for motions 15 and 18, and Table 10-7 for the rare and expected design motions. Damage index was used in these comparisons because the damage index includes the combined effects of both displacement as well as hysteretic energy earthquake demands. Each measure for system irregularity is discussed subsequently followed by comparisons of the irregularity measures to the system effects.

The first measure of irregularity was the irregularity index developed by Isakovic et al. (2001). Comparisons of system effects with this measure are discussed in Section 10.4.1.1. This index is typically used to determine whether single mode analysis is sufficient for design. The index is a constant value that accounts for the irregularity of the entire bridge frame. It is calculated as the percent difference in the areas between the lateral superstructure deformation from the first and second iterations of elastic multi-mode analysis. The first mode shape is estimated by a lateral load on the superstructure based on the superstructure mass. Displacements from the second iteration of the multi-mode elastic analysis are determined by re-applying lateral force based on the displacements of the first mode shape estimate. When the irregularity index is equal to zero, the shapes from the first and second iteration are equal and the system is considered to be regular.

The second measure of irregularity was a simple index that was taken as the ratio of the displacement of each bent when the system is subjected to a 1g lateral load, over the displacement of the corresponding single bents with tributary mass subjected to the 1g lateral load. For this measure, three irregularity values were determined for each system and compared to the system effect of the corresponding bent. The maximum irregularity value for the three bents in each system was also compared to the maximum bent system effect. This index was developed in the present study as a simple measure. Comparisons of system effects with this measure are discussed in Section 10.4.1.2.

10.4.1 Correlation of Irregularity Measures

The two measures of irregularity discussed previously were used to determine whether there is a correlation between the indices and the system effect. The comparisons were made for the bridge specimen as well as the four systems used in the parametric study discussed in Section 10.3. Note that the irregularity indices were based on the elastic properties of the bridge, whereas the system effect reflected the nonlinear response and the extent of damage. Tables 10-6 and 10-7 list the results for the two irregularity measures and the system/individual response ratios for the five systems subjected to motions 15 and 18 and the rare and expected design motions. The uniform system (equal column heights), listed only for motion 15 in Table 10-6, was included in the comparison to show that a uniform system where all columns have the same height and tributary mass has no system effect (no difference in the inelastic system/individual response ratios), and to show that the irregularity indices are zero for this type of system.

The measures of irregularity for each system are compared subsequently in Sections 10.4.1.1 and 10.4.1.2 with plots that show the range of damage index system/individual ratios from inelastic analysis. Since it was shown that both irregularity measures lead to expected results for the uniform system, the uniform system is excluded and the comparisons are made for the test specimen, system 1, system 2, and system 3. Figures 10-39 through 10-42 are plots of the range of system/individual damage index ratios for each of these systems, respectively for design motions and for test 15 and 18 target motions. As shown in the figures, the design motion damage index ratios, which are from motions based on the design response spectra, generally represent the largest deviation of system/individual ratios from unity. For this reason, and because the spectra for design motions are smooth and less sensitive to slight shifts in the effective structural

frequency than test motions 15 and 18, the system/individual ratios from the design motions were used for comparisons of the applicability of the measures of irregularity. Therefore, other than for a general comparison with irregularity index, system effect from test motions 15 and 18 is not included in the following comparisons.

10.4.1.1 Isakovic Irregularity Index

Figure 10-43 is a plot of the maximum system/individual damage index ratios of the four systems for the rare and expected and for test 15 and 18 motions vs. irregularity index. Figure 10-44 is a plot of the maximum system/individual damage index ratios of the four systems for the rare and expected design motions vs. irregularity index. Although there is not a direct correlation between the irregularity index and the maximum system effect for each system, a general trend is shown that as system irregularity increases, the system effect also increases.

Figures 10-45 through 10-48 are plots of the system/individual ratios of damage index for each system with the irregularity index superimposed. For comparative purposes the irregularity index is plotted as the percent irregularity divided by 100 and added to unity. The two regular systems with an irregularity index of close to zero (systems 1 and 3) have damage index system/individual ratios of up to 1.32 (Figs. 10-46 and 10-48). This demonstrates that the irregularity index does not correlate well with system/individual damage ratios for symmetric systems with a stiff superstructure and varied column heights. Although the irregularity index was shown to predict a general trend of increased maximum system/individual damage with increase of the index, it does not provide a consistent correlation and therefore can not be used to quantify either the maximum system effect in each system or the system effect for individual bents.

10.4.1.2 System/Bent Displacement Ratios (Second Measure)

Figures 10-49 through 10-52 are plots of the system/individual ratios of damage index for each system with the system/bent displacement ratios (second measure) superimposed. In comparing the maximum system/bent displacement ratio with the maximum system/individual damage ratio for each system, the measure appears to overestimate the system effect for all systems except the test model.

For individual bents in each system, the measure provides good correlation with the system effect. However, as shown in Fig. 10-51, which is for system 2 that has a stiff center bent combined with torsional irregularity, elastic displacement ratios can not be depended on as a measure to completely quantify the relative differences between the system and the bents.

10.4.1.3 Evaluation of Irregularity Measures

Significant system effects were apparent in the bridges that were analyzed. The maximum system/individual damage ratio on the five systems for the expected earthquake motion, which placed demands on the columns in the systems near column yielding, was 1.57. The maximum system/individual ratio for the rare motion, which imposed demands far greater than yielding in the columns, was 1.32.

The irregularity index by Isakovic could not be used as a measure of system effects because this index does not take into account symmetric systems with a stiff

superstructure and varied column heights. This index was not intended for the use presented in this document but was attempted to determine its applicability. The irregularity measure that used system/bent displacement ratios (the second measure) is effective as an indicator of whether there will be differences in the response due to system effects. However, due to the combination of nonlinear effects, system restraint, torsion, and variations of earthquake spectral demand, this simple elastic method can not be used to reliably quantify differences between system response and response of a bent modeled with tributary mass.

If a bent is to be tested for performance under a certain earthquake excitation level such as for design spectra, the system can have a significant effect on the amount of demand to a given bent. Prior to single bent component testing on shake tables, an elastic estimate (method 2) can be performed to determine whether there is a system effect. However in addition, nonlinear analysis should be performed to determine the severity of the system effects and whether component testing sufficiently represents the response.

Chapter 11: Summary and Conclusions

11.1 Summary

As part of a multi-university collaborative project to study soil-foundation-structure interaction (SFSI) effects, a quarter-scale, two-span bridge frame containing three, two-column bents was tested to failure on the three shake table system at the University of Nevada, Reno. The project was conducted, in part, to examine the collaborative aspects of the NSF Network for Earthquake Engineering Simulation (NEES). The research in this document was focused on the experimental testing of the shake table bridge specimen and analytical study of the linear and nonlinear response of bridge systems. This included the design of the prototype structure for the global project, development and implementation of an effective technique for experimentally testing bridges on multiple shake tables, and analytical modeling of bridge systems. The computational model that was developed and experimentally verified was used in conjunction with the measured data from testing to conduct further studies on bridge system response and shake table testing of bridges. An extended summary of this study is presented in Appendix B.

11.1.1 Experimental Studies

The bridge specimen was designed and tested with the intent to realistically model interaction among two-column bridge bents of varied heights within a system that was designed using state-of–the-art methods for earthquake resistance. The shake table tests were done in collaboration with the University of Washington. The bridge was composed of 11 major components that were constructed on and off site and were assembled on the shake tables. The columns, which were subjected to double curvature, had aspect ratios from 2.5 to 4. The tall bent was in the center and the short and medium height bents were at each end of the bridge. The superstructure of the specimen was a solid post-tensioned slab composed of six beams with moments of inertia about both bending axes that matched those of the prototype. Superimposed masses were added to the top of the specimen superstructure to account for the scaling effect. Response of the bridge specimen was documented and monitored utilizing 298 channels of accelerometers, displacement transducers, and strain gauges, four video cameras, written notes, drawings, and photographs.

The bridge frame was subjected to a set of low amplitude (pre-yield), and high amplitude acceleration record target motions that were derived from the Century City accelerogram of the 1994 Northridge, California earthquake. The low amplitude testing consisted of the following target motions: uniaxial coherent, uniaxial incoherent, biaxial coherent, and achieved centrifuge motions from the UC Davis test. High amplitude testing of the bridge consisted of uniaxial coherent target excitation with a motion that began with pre-yield amplitude and was applied at increased amplitudes in the transverse direction of the model until the first bent failure. Transverse excitation was used for high amplitude tests because the end conditions of the model were such that longitudinal response would only be accurate up to closure of the scaled prototype hinge gap.

As expected during low amplitude tests, no damage was observed in the superstructure, and the reinforcement strain in the columns remained below yield. High amplitude testing included tests 12 through 20, and ranged from target PGA of 0.075 to 1.66 g. For tests 13 and 16, which were equivalent to the expected and rare design earthquakes, the columns satisfied both the service and damage level design code life safety performance objectives. During test 13, the maximum column displacement ductility demand was 0.95 in the medium height bent. During test 16, the maximum displacement ductility demand was 3.31 which was only 40 percent of the failure displacement. The bridge was considered to have failed during test 19 when the columns of bent 3 failed in flexure at a displacement ductility of 8.9. No signs of shear distress were observed or measured throughout the tests other than minor shear cracking in bent 3, the shortest of the bents. After the bent 3 failure, the bridge was subjected to an additional test, test 20, of reduced amplitude to attempt to further damage bents 1 and 2 and measure system response after the bent 3 failure.

Although the target high amplitude motions for the three shake tables were coherent, inconsistencies in the achieved motions caused incoherency in both acceleration and displacement response, which was explored in the analytical studies. After testing, masses were removed, portions of the superstructure were shored, the superstructure was de-tensioned, and the model was disassembled utilizing the two laboratory ceiling cranes.

11.1.2 Analytical Study

Upon the completion of testing, analytical nonlinear response history modeling of the bridge for the high amplitude testing was conducted using SAP2000 (CSI 2005) and Drain-3DX (Prakash and Campbell 1994). This was conducted to determine the accuracy of contemporary modeling techniques and to develop a model to use for further study of the shake table tests and bridge system response. Fiber elements were used to define column nonlinearity in the column plastic hinge zones and the remainder of the structure was assumed to remain elastic. Parametric studies were conducted to determine the number and discretization of fibers as well as the time step to minimize the computation time yet obtain stable results. A method was developed to double integrate the measured acceleration of the tables so that the displacement input to the computer model had both acceleration and displacement content that matched the shake table motions.

The results from the analytical modeling were compared to the measured data. It was shown that both models produced reasonable results. However, the specialized reinforcement bond slip element that was utilized in the Drain-3DX model and the more refined distributed plasticity element, combined with the method of numerical integration showed that the Drain-3DX model was more accurate, required less processing time, and provided more stable results. Consequently, the Drain-3DX model was selected over the SAP2000 model to proceed with further investigation of the shake table model response, system response, and response of related bridge systems. The computer model was used to determine effects of cap beam stiffness and to aid in the verification of the force estimates from the shake table actuator pressures.

The experimentally verified Drain-3DX model was used to study three topics relating to the system response of the bridge. The first was the measured and calculated

performance of the bridge model compared to the life safety performance criteria of the NCHRP 12-49 code that was used for design. Both the measured response from shake table tests and the analytical response based on the design spectra satisfied the performance criteria.

The second topic that was studied was the effect of the achieved shake table motions on the damage progression of the bridge. Both the effect of acceleration and pseudo-static displacement inconsistencies with the target motion were investigated and it was determined that the large demand that led to the failure of bent 3 was due to acceleration overshoot from delayed compensation in adjusting the shake table controllers for the yielding of the bents. Two possibilities for solution to the achieved motion errors were presented and discussed.

The third topic that was studied using the computational models was the system and individual response of the bents (system effect). The system effects were measured using the maximum displacement demand and a mechanistic measure of damage that includes the hysteretic energy and maximum displacement.

In comparing computational model of the shake table specimen and models of the individual bents with tributary mass, it was shown that for all of the columns in this study, there was generally not an increase in hysteretic energy or large displacement cycles from system response at given displacement demand. The response of the bents for each high amplitude test motion was also compared. It was shown that there were significant differences in the bent demands for a given excitation due to system effects.

In addition to the shake table model, four bridge systems were used in a parametric study to determine the system effect. The total pier stiffness was the same in all systems. The symmetric and uniform versions of the bridge specimen were shown to be comparable in nonlinear performance to the bridge specimen for the same high amplitude demand.

The five bridge configurations were compared to two irregularity indices to evaluate the effectiveness of the measures in predicting the differences in system and individual bent response. It was determined that a simple elastic index is a good indicator of the presence of system effects.

11.2 Conclusions & Recommendations

11.2.1 Conclusions and Recommendations from Experimental Studies

1. The method used to model the post-tensioned concrete box girder bridge frame on the shake tables using longitudinal and transversely post tensioned beams connected to the bents was successful during the construction phase as well as during shake table tests. No damage was observed in the cap beams, cantilevers, or superstructure beams and slippage of post tensioning did not occur.

2. The amount of lateral reinforcement provided by the NCHRP 12-49 commentary equation that is recommended for preventing global buckling of longitudinal reinforcement in the plastic hinge zone was adequate to prevent buckling until large displacement ductility was reached.

3. The flexural failure of the column with the smallest aspect ratio (2.5) showed that the Caltrans and NCHRP 12-49 seismic detailing requirements for shear reinforcement were adequate. The column failed in flexure at a displacement ductility of 7.9 with only minimal shear cracks.

4. The bent with the shortest columns failed when the bridge was subjected to a 1.66 PGA ground motion. Although this bent had failed, the remaining two still provided sufficient redundancy and capacity to withstand a 1.0 g PGA motion that followed.

5. The measured maximum core concrete compressive strains were approximately twice those estimated using Mander's confined concrete model.

6. The measured damping factor of the bridge was approximately 4 percent.

7. Frequency shifting measured from the response of a bridge due to low amplitude vibration is an effective measure of indicating damage. Knowledge of frequencies that are dominated by certain bridge components, can allow for the location of damage to be distinguished.

8. Using top of bent acceleration as a measure of lateral force in the bents was only effective for the columns that dominated the response of the system. System irregularity and restraint prevent the acceleration from being an accurate indicator of bent shear.

9. The state-of-the-art techniques that were used to match the target motions with the shake tables were effective; however, to avoid damaging the bridge model the iterative methods for converging the shake table motions could not be implemented. Consideration should be made to attempt to improve both the achieved displacements and accelerations for future tests.

10. Actuator pressure of the shake tables can be used as an effective mean to estimate the shear force in the bents.

11.2.1 Conclusions and Recommendations from Analytical Studies

1. Incoherency in the actual shake table motions required displacement record input in the computational models. The measured displacement records did not have the resolution required to accurately define the response of the shake tables. The method that was used to double integrate the shake table accelerations provided a good match of both the shake table displacements and accelerations for displacement input to the models.

2. The available analysis tools using conventional methods were successful in estimating the nonlinear response of a concrete bridge structure with flexure dominated columns from the pre-yield state up to failure. Both the Drain-3DX and SAP2000 models provided reasonable estimates of bridge response. However, the Drain 3DX model, which explicitly modeled bond slip and incorporated a more efficient integration

method, provided a better match to the experimental results and was therefore used for further study.

3. The accuracy of response history analysis is sensitive to the time step. The time step required for accurate results in the earthquake analysis of this bridge frame was approximately 1/4000 of the fundamental period of the bridge for both the Newmark and Wilson integration methods.

4. The damping can have a significant influence on the calculated pre-yield response when conducting nonlinear computer analysis of a bridge frame or bridge system. When conducting analysis for incoherent excitation, which requires displacement input, it should be noted that the resulting velocities in the equations of motion are absolute velocities and therefore significant viscous damping can be introduced.

5. In order to model column plastic hinging of this typical reinforced concrete bridge, it was sufficient to define plastic hinge zones with a single fiber element having a length equal to the plastic hinge length and a discretized section of four layers and eight slices.

6. Explicit modeling of bond slip using an element that considers crack opening in concrete, compression strain penetration into supports, and slippage of reinforcement is important to accurately determine the bridge response.

7. The Park and Paulay cracked shear stiffness that was used in computational modeling provided a good match to the measured pre-yield shear stiffness of the bridge columns.

8. The equation for post-yield shear stiffness developed by Correal et al. provided a good match to the measured post-yield stiffness of the bent 3 column that was excited to failure during tests.

9. The assumption of rigid cap beams in the computational model and the extra rigidity of the cap beams in the shake table specimen due to the superstructure did not have a significant impact on the response of the columns.

10. The failure progression of the bridge model and computational modeling has shown that building a bridge with variable (as opposed to constant) column heights could be desirable. Analytical modeling using the design motions showed that the maximum column ductility demand for the rare design earthquake was merely 5 percent larger for the specimen than for a uniform height column system. This small increase is offset considerably by the increased redundancy of a system with variable height columns.

11. The column configuration of the model was at the border of maximum NCHRP 12-49 allowable stiffness irregularity for adjacent columns. Both the measured

response and computational modeling showed that despite the irregularity, which caused significant in-plane rotational response, the system satisfied the requirements of the design for both rare and expected design earthquakes.

12. Differential support displacement errors during shake table testing of stiff structures using multiple shake tables could cause significant structural damage. For future bridge tests, the possibility of these displacements should be considered with respect to their influence on the structure.

13. Deviations between the target and achieved motion of the shake tables affected the failure location in the bridge model. Had the achieved motions matched target motions perfectly, demands would have been significantly less in bent 3 and failure would have likely occurred in bent 1.

14. For the bridge that was tested in this study, system effects did not increase the amount of hysteretic energy dissipation or large displacement cycles on the columns for given values of achieved displacement. However, for specific motions, the system effect caused significant differences in damage to the bents. The system had effects for post yield motions on the bents that ranged from a displacement ductility decrease of 37 percent to an increase of 36 percent. The system effect on the damage indices ranged from a decrease of 39 percent to an increase of 41 percent.

15. Column response in a bridge system can vary significantly compared to the response of a single column with tributary mass. A simple irregularity index can be used as an approximate indicator to identify whether the system will have an effect on the bents. However, nonlinear analysis should be performed to determine the severity of the effects and whether single bent experimental testing leads to representative results.

References

American Association of State Highway and Transportation Officials, 1998, "AASHTO LRFD Bridge Design Specifications," AASHTO, Washington D.C.

American Association of State Highway and Transportation Officials, 2002, "AASHTO Standard Specifications for Highway Bridges," 17th ed., AASHTO, Washington D.C.

American Concrete Institute Committee 318, 2002, "Building Code Requirements for Structural Concrete (ACI318-02)," American Concrete Institute, Farmington Hills, Michigan.

American Institute of Steel Construction (AISC), 1993, "Manual of Steel Construction Load and Resistance Factor Design", AISC, Chicago, Illinois.

ATC/MCEER, 2001, "Recommended LRFD Guideline for the Seismic Design of Highway Bridges (2002) Part 1: Specifications," MCEER-02-SP01, MCEER/ATC joint venture, NCHRP 12-49 Project Team.

Caltrans (California Department of Transportation), 2004, "Caltrans Seismic Design Criteria Version 1.3." Engineering Service Center, Earthquake Engineering Branch, California.

Caltrans (California Department of Transportation), 2001, "Comparitive Bridge Costs," Division of Engineering Services, Office of Specifications and Estimates, California.

Caltrans (California Department of Transportation), 2000, "Caltrans Bridge Design Specifications," State of California, Department of Transportation.

Carden, L., Itani, A., and Buckle, I., "Displacement Based Analysis of Steel Girder Bridges with Ductile End Cross Frames," Proceedings, 2004 Asian-Pacific Network of Centers for Earthquake Engineering, July, 2004, Honolulu, HI.

Chopra, A., 2001, "*Dynamics of Structures: Theory and Applications to Earthquake Engineering*," Second Edition, Prentice-Hall, Upper Saddle River, New Jersey.

Computers and Structures, Inc., 2002, "SAP2000 NonLinear," version 8, Berkeley, CA.

Computers and Structures, Inc., 2005, "SAP2000 Linear and Nonlinear Static and Dynamic Analysis and Design of Three-Dimensional Structures," version 9.1.5. Berkeley, CA.

Correal, J., Saiidi, M. and Sanders, D., 2004, "Seismic Performance of RC Bridge Columns Reinforced with Two Interlocking Spirals," Center for Civil Engineering

Earthquake Research, Department of Civil Engineering, University of Nevada, Reno, Nevada, Report No. CCEER-04-6.

Dozono, Y., Horiuchi, T., Konno, T., and Katsumata, H., 2004, "Shaking-Table Control by Real-Time Compensation of the Reaction Force Caused by a Nonlinear Specimen." *Transactions of the ASME Journal of Pressure Vessel Technology*, Vol.126 P.1-6.

Dutta, A and Mander, J., 1998, "Capacity Design and Fatigue Analysis of Confined Concrete Column," Technical Report MCEER-98-0007, The State University of New York at Buffalo.

EduPro Civil Systems, Inc., 1999, "ProShake ground response analysis program," Redmond, Washington.

Filiatrault A., Kremmidas S., Seible F., Allan J. Clark A. J., Nowak R., and Thoen B., 2000, "Upgrade of first generation uniaxial seismic simulation system with second generation real-time three-variable digital control system." Proceedings from the 12th World Conference on Earthquake Engineering, New Zealand, Paper No. 1674.

Frankel, A., Mueller, C., Barnahard, T., Perkins, D., Leyendecker, E., Dickman, N., Hanson, S., and Hopper, M., 1996, "National seismic hazard maps: documentation", June 1996, U.S. Geological Survey Open-File Report 96-532.

Freeman, S., Nicoletti, J., and Matsumura, G., 1984, "Seismic Design Guidelines for Essential Buildings," Proceedings of Eighth World Conference on Earthquake Engineering, San Francisco, California.

French, C., and Saiidi, M., 2000, "A Comparison of Static and Dynamic Performance of Models of Flared Bridge Columns," Civil Engineering Department, University of Nevada, Reno, Report No. CCEER-00-7.

Gasparini. D. and Vanmarcke, E., 1976, "Simulated Earthquake Motions Compatible with Prescribed Response Spectra," Department of Civil Engineering, Research Report R76-4, Massachusetts Institute of Technology, Cambridge, Massachusetts.

Hoshikuma, J. and Unjoh, S., 2002, "The guidelines for testing of seismic performance of bridge columns," 18th US-Japan Bridge Engineering Workshop.

Isakovic, T. and Fischinger, M., 2001, "Analysis and design of RC viaducts in moderate seismicity regions of Europe," Proceedings of the 4th International Symposium on Earthquake Engineering for the Moderate Seismicity Regions, Seoul, Korea.

Kulkarni, S. and Shah, S., 1998, "Response of Reinforced Concrete Beams at High Strain Rates," *ACI Structural Journal*, Vol. 95, No. 6, pp. 705-715, Nov.-Dec. 1998.

Mander, J., Priestley, N., and Park, R., 1988, "Theoretical Stress-Strain Model for Confined Concrete," *Journal of Structural Engineering*, ASCE, 114(8), P. 1804-1849.

Mathsoft Engineering & Education, Inc., 2002, "MathCAD," version 11.0, Cambridge, Massachusetts.

McGuire W., and Gallagher R., 1979, "*Matrix Structural Analysis*," First Edition, John Wiley & Sons, New York.

Moustafa, K., Sanders, D., and Saiidi, M., 2004, "Impact of Aspect Ratio on Two-Column Bent Seismic Performance," Center for Civil Engineering Earthquake Research, Department of Civil Engineering, University of Nevada, Reno, Nevada, Report No. CCEER-04-3.

Nishida, H. and Unjoh, S., 2004, "Dynamic Response Characteristic of Reinforced Concrete Column Subjected to Bilateral Earthquake Ground Motions," Proceedings, 13th World Conference on Earthquake Engineering, Paper 576, Vancouver, Canada.

Nowak, R., Kusner, D., Larson, R, and Thoen, B, 2000, ''Utilizing Modern Digital Signal Processing for Improvement of Large Scale Shaking Table Performance,'' Proceedings From the 12th World Conference on Earthquake Engineering, New Zealand, Paper No. 2035.

Opensees Development Team, 2002, "OpenSees: Open System for Earthquake Engineering Simulations," Version 1.5, Berkeley, CA.

Park, R., and Paulay, T., 1975, "*Reinforced Concrete Structures*," Wiley Interscience.

Prakash, V., and Campbell, S., 1994, "Drain-3DX: Static and Dynamic Analysis of Inelastic 3D Structures", Department of Civil Engineering, University of California, Berkeley.

Priestley, N., Seible, F., and Calvi, G., 1996, "*Seismic Design and Retrofit of Bridges*," John Wiley & Sons, New York.

Pulido, C., Saiidi, M., Sanders, D., and Itani, A., 2002, "Seismic Performance and Retrofitting of Reinforced Concrete Bridge Bents," Civil Engineering Department, University of Nevada, Reno, Report No. CCEER 02-1.

Ram International, RAM Perform 3DS version2, 2003, www.ramint.com.

Ramirez, R., 1985, "*The FFT; Fundamentals and Concepts*," Prentice-Hall, Englewood Cliffs, NJ.

Saiidi, M., 1982, “Hysteresis models for reinforced concrete,” *Journal of the Structural Division*, American Society of Civil Engineers, v. 108, n. 5, p. 1077–1087.

Saiidi, M., R. Moore, and A. Itani, 2001, “Seismic Performance of Reinforced Concrete Bridges With Un-Conventional Configurations,” American Concrete Institute, *Structural Journal*, September-October 2001, pp. 717-726.

Shin, H., M. Ilankathara, P. Arduino, B. L. Kutter, and S. L. Kramer, 2005, “Experimental and Numerical Analysis of Seismic Soil-Foundation-Structure Interaction of A Two Span Bridge,” Proceedings from the Eighth National Conference on Earthquake Engineering, April 2006 (submitted for review).

Southern California Earthquake Center (SCEC), 2000, Shear Wave Velocity Calculator Java Servlet, www.scec.org.

Takeda, T., Sozen, M. and Nielsen, N., 1970, “Reinforced Concrete Response to Simulated Earthquakes,” *Journal of Structural Engineering Division*, ASCE, Vol. 96, No. 12, pp 2257-2273.

Wehbe, N. and Saiidi, M., 2003, ”User's Manual for RCMC v. 2.0, A Computer Program for Moment-Curvature Analysis of Confined and Unconfined Reinforced Concrete Sections,” Civil Engineering Department, University of Nevada, Reno, Report No. CCEER 03-2.

Wehbe, N., Saiidi, M., and Sanders, D., 1997, "Effects of Confinement and Flares on the Seismic Performance of Reinforced Concrete Bridge Columns", Civil Engineering Department, University of Nevada, Reno.

Williams, D., and Godden, W, 1975, “Seismic Response of a Curved Highway Bridge Model,” 54th Annual Meeting, Transportation Research Board, National Research Council, Washington D.C.

Wilson, E., 2002, “*Three-Dimensional Static and Dynamic Analysis of Structures. A Physical Approach with Emphasis on Earthquake Engineering*,” Computers and Structures, Inc., Berkeley, CA.

Wood, S., Anagnos, T., Arduino, A., Eberhard, M., Fenves, G., Finholt, T., Futrelle, J., Jeremic, B., Kramer, S., Kutter, B., Matamoros, A., McMullin, K., Ramirez, J., Rathje, E., Saiidi, M., Sanders, D., Stokoe, K., and Wilson, D., 2004, "Using NEES to Investigate Soil-Foundation-Structure Interaction," Proceedings, 13th World Conference on Earthquake Engineering, Paper 2344, Vancouver, Canada.

Zadeh, M., and Saiidi, M., 2005, “Effect of Constant and Variable Strain Rates on Stress-Strain Properties and Yield Propagation in Steel Reinforcing Bars,” Department of Civil Engineering, University of Nevada, Reno, pending pub.

Tables

Table 2-1: University of Nevada, Reno shake table specifications.

Table Size	14.0 ft x 14.6 ft (4.3 m x 4.5 m)
Maximum Specimen Mass	100,000 lbm (45,352 kg)
Maximum Pitch Moment	1,000,000 ft-lb (1,356 kN-m)
Maximum Yaw Moment	400,000 ft-lb (542 kN-m)
Maximum Roll Moment	400,000 ft-lb (542 kN-m)
Force Rating	165,000 lb (734 kN)
Vertical Live Load	± 150,000 lb (±667 kN)
Maximum Dynamic Displacement	± 12 inches (±300 mm)
Maximum Static Displacement	± 14 inches (±350 mm)
Maximum Velocity	± 40 in/sec (±1000 mm/sec)
Maximum Acceleration	1 g at 100,000 lbm specimen
Operating Frequency	0.1-30 Hz

Table 2-2: Lateral steel design comparison.

	NCHRP Recommended LRFD Guidelines (2001)	Caltrans Seismic Design Criteria (2003)	AASHTO Standard Specifications (2002)	AASHTO LRFD (1998)
5ft (1.52m) high column				
$\rho_{s, Required}$	0.00796	0.00853	0.01148	0.01148
Controlling Factor	Long Bar Restraint	Shear	Confinement	Confinement
Confinement	0.00280	0.00370	0.01148	0.01148
Long. Bar restraint	0.00796	N/A	N/A	N/A
Shear (Explicit)	0.00703	0.00853	0.01102	0.01129
Shear (Implicit)	0.00527	N/A	N/A	N/A
Shear crack angle (deg)	33.3	45.0	45.0	45.0
Spacing (in), (mm)	1.25 (40)	2.0 (51)	1.0 (25)	1.0 (25)
6ft (1.83m) high column				
$\rho_{s, Required}$	0.00796	0.00741	0.01148	0.01148
Controlling Factor	Long Bar Restraint	Shear	Confinement	Confinement
Confinement	0.00280	0.00480	0.01148	0.01148
Long. Bar restraint	0.00796	N/A	N/A	N/A
Shear (Explicit)	0.00569	0.00741	0.00875	0.00903
Shear (Implicit)	0.00439	N/A	N/A	N/A
Shear crack angle (deg)	33.3	45.0	45.0	45.0
Spacing (in), (mm)	1.25 (40)	2.0 (51)	1.0 (25)	1.0 (25)
8ft (2.44m) high column				
$\rho_{s, Required}$	0.00796	0.00710	0.01148	0.01148
Controlling Factor	Long Bar Restraint	Confinement	Confinement	Confinement
Confinement	0.00280	0.00710	0.01148	0.01148
Long. Bar restraint	0.00796	N/A	N/A	N/A
Shear (Explicit)	0.00401	0.00604	0.00592	0.00619
Shear (Implicit)	0.00329	N/A	N/A	N/A
Shear crack angle (deg)	33.3	45.0	45.0	45.0
Spacing (in), (mm)	1.25 (40)	2.0 (51)	1.0 (25)	1.0 (25)

Table 2-3: Shear design comparison from lateral reinforcement design.

		NCHRP 12-49		Caltrans SDC		AASHTO Standard		AASHTO LRFD	
		kip	kN	kip	kN	kip	kN	kip	kN
5ft (1.52m) high column	Vp	3.9	17.3	0.0	0.0	0.0	0.0	0.0	0.0
	Vc	3.9	17.1	14.9	66.3	6.7	29.8	6.0	26.6
	Vs	34.3	152.8	20.6	91.6	29.9	133.0	29.9	133.0
	Vn	42.1	187.2	35.5	157.9	36.6	162.8	35.9	159.6
	Vu/ϕ	34.5	153.7	35.4	157.5	35.3	157.0	35.3	157.0
	Cap. / Demand	1.22		1.00		1.04		1.02	
6ft (1.83m) high column	Vp	3.2	14.4	0.0	0.0	0.0	0.0	0.0	0.0
	Vc	3.9	17.1	11.7	52.0	6.7	29.8	6.0	26.6
	Vs	34.3	152.8	17.9	79.6	29.9	133.0	29.9	133.0
	Vn	41.4	184.3	29.6	131.7	36.6	162.8	35.9	159.6
	Vu/ϕ	28.8	128.1	29.5	131.2	29.4	130.8	29.4	130.8
	Cap. / Demand	1.44		1.00		1.24		1.22	
8ft (2.44m) high column	Vp	2.4	10.8		0.0		0.0	0.0	0.0
	Vc	3.9	17.1	10.8	48.0	6.7	29.8	6.0	26.6
	Vs	34.3	152.8	17.1	76.1	29.9	133.0	29.9	133.0
	Vn	40.6	180.7	27.9	124.1	36.6	162.8	35.9	159.6
	Vu/ϕ	21.6	96.1	22.3	99.2	22.1	98.4	22.1	98.4
	Cap. / Demand	1.88		1.25		1.65		1.62	

Table 3-1: Instrumentation summary for bridge model.

Instrument	Recorded Response	# Instruments	Notes
Displacement Transducers	Slab Displacements	25	Transverse, Longitudinal and Vertical
	Footing Slip	3	Bent 3 Slip between footing and table
	Column Curvature	68	All bents
	Column Shear	15	West column of bent 3
Accelerometers	Slab Accelerations	14	Transverse, Longitudinal and Vertical
	Support Frame Acceleration	1	Added after TEST3B
Strain Gauges	Long. Reinf. strain	104	All columns
	Trans. Reinf. Strain	56	All columns
Shake Tables	Table Responses	12	Displacement and Acceleration
Total		**298**	

Table 4-1: Bridge specimen modal mass participation factors for modes 1 through 6.

Mode	Period (s)	Long. axis disp.	Trans. axis disp.	Vert. axis disp.	Long. axis rotation	Trans. axis rotation	Vert. axis rotation
Mode 1	0.409	0.9218	0.0000	0.0002	0.0000	0.1875	0.0000
Mode 2	0.398	0.0000	0.8189	0.0000	0.8086	0.0000	0.1804
Mode 3	0.302	0.0000	0.1798	0.0000	0.1778	0.0000	0.8189
Mode 4	0.226	0.0765	0.0000	0.0008	0.0000	0.1851	0.0000
Mode 5	0.178	0.0009	0.0000	0.5158	0.0000	0.0001	0.0000
Mode 6	0.081	0.0000	0.0011	0.0000	0.0014	0.0000	0.0002

Table 4-2: Bent 1 through 3 pushover results from pre-test analyses.

Parameter		Bent 1	Bent 2	Bent 3
Yield force	(kip)	40.4	30.9	51.8
	(kN)	179.7	137.5	230.4
Yield displacement	(in)	0.60	0.99	0.47
	(mm)	15.2	25.1	11.9
Ultimate displacement	(in)	6.29	9.67	4.77
	(mm)	159.8	245.6	121.2
Displacement ductility		10.5	9.8	10.1

Table 4-3: Shake table motions used for low amplitude testing.

Test		Motion type	Motion		Bedrock depth			Bedrock PGA (g)
			Trans	Long	bent 1	bent 2	bent 3	
LowAmplitude Testing	1-a*	transverse	M-1	---	d/3	d/3	d/3	0.06
	1	transverse	M-1	---	d/3	d/3	d/3	0.06
	2-a	incoherent	M-1	---	0	d/3	2d/3	0.06
	2	incoherent	M-1	---	0	d/3	2d/3	0.06
	3-a	incoherent	M-1	---	2d/3	d/3	0	0.06
	3	incoherent	M-1	---	2d/3	d/3	0	0.06
	4	incoherent	M-1	---	0	d/2	d/2	0.06
	5	incoherent	M-1	---	d/2	0	d/2	0.06
	6	incoherent	M-1	---	d/2	d/2	0	0.06
	8	transerse	M-1	---	d/3	d/3	d/3	0.06
	9-a	biaxial	M-1	M-2	d/3	d/3	d/3	0.06
	9	biaxial	M-1	M-2	d/3	d/3	d/3	0.06
	10	centrifuge	M-1	---	UC Davis centrifuge free-field			N/A
	11	centrifuge	M-1	---	UC Davis centrifuge pile motion			N/A

* "a" after test number denotes half amplitude

Table 4-4: Shake table motions used for high amplitude testing.

Test		Motion type	Motion		Bedrock depth (and PGA scale)			Bedrock PGA (g)
			Trans	Long	bent 1	bent 2	bent 3	
High Amplitude Testing	12	transverse	M-1	---	depth=d, scaled to 0.075g			0.4
	13	transverse	M-1	---	depth=d, scaled to 0.150g			0.4
	14	transverse	M-1	---	depth=d, scaled to 0.250g			0.4
	15	transverse	M-1	---	depth=d, scaled to 0.500g			0.4
	16	transverse	M-1	---	depth=d, scaled to 0.750g			0.4
	17	transverse	M-1	---	depth=d, scaled to 1.000g			0.4
	18	transverse	M-1	---	depth=d, scaled to 1.330g			0.4
	19	transverse	M-1	---	depth=d, scaled to 1.660g			0.4
	20	transverse	M-1	---	depth=d, scaled to 1.000g			0.4
Post-Tests	21	transverse	M-1	---	depth=d, scaled to 1.000g			0.4
	22	transverse	M-1	---	depth=d, scaled to 1.500g			0.4

Table 4-5: Displacement ductility results from RAM-Perform analysis to determine shake table motion to use for high amplitude tests.

Response	PGA scale of motion	M-1 0.4g bedrock excitation	M-2 0.4g bedrock excitation	Sylmar 90	El-Centro
Bent1 μ_Δ	0.15	**1.25**	1.17	0.90	0.99
	0.25	1.70	**1.70**	1.65	1.49
	0.50	2.58	**3.34**	2.58	2.19
	1.00	**10.03**	5.89	4.71	5.17
	1.50	**11.08**	8.77	unstable	unstable
Bent2 μ_Δ	0.15	0.48	**0.54**	0.42	0.37
	0.25	**0.75**	0.68	0.70	0.53
	0.50	1.31	**1.55**	1.27	0.81
	1.00	**3.97**	3.19	2.92	2.34
	1.50	**7.68**	4.86	unstable	unstable
Bent3 μ_Δ	0.15	**1.02**	0.69	0.57	0.57
	0.25	**1.64**	1.18	0.93	0.95
	0.50	2.26	**3.32**	2.46	1.58
	1.00	**6.53**	6.17	6.52	4.34
	1.50	**24.68**	9.52	unstable	unstable

note: Bold values are most demanding motion

Table 4-6: Calculated displacement demand divided by displacement capacity from RAM-Perform analysis to determine shake table motion to use for high amplitude tests.

Response	PGA scale of motion	M-1 0.4g bedrock excitation	M-2 0.4g bedrock excitation	Sylmar 90	El-Centro
Bent1 d_{max}/d_{ult}	0.15	**0.12**	0.11	0.08	0.09
	0.25	0.16	**0.16**	0.16	0.14
	0.50	0.24	**0.32**	0.24	0.21
	1.00	**0.95**	0.56	0.44	0.49
	1.50	**1.05**	0.83	unstable	unstable
Bent2 d_{max}/d_{ult}	0.15	0.05	**0.05**	0.04	0.04
	0.25	**0.07**	0.07	0.07	0.05
	0.50	0.13	**0.16**	0.13	0.08
	1.00	**0.40**	0.32	0.29	0.23
	1.50	**0.77**	0.49	unstable	unstable
Bent3 d_{max}/d_{ult}	0.15	**0.10**	0.03	0.03	0.03
	0.25	**0.15**	0.06	0.04	0.04
	0.50	**0.21**	**0.16**	0.11	0.07
	1.00	**0.62**	0.29	0.30	0.20
	1.50	**2.34**	0.44	unstable	unstable

note: Bold values are most demanding motion

Table 4-7: Weight tributary to each shake table compared to weight limits.

	Limit		Value		SF
	(kip)	(kN)	(kip)	(kN)	
Bent 1	100.0	444.8	111.9	497.8	0.9
Bent 2	100.0	444.8	99.1	440.7	1.0
Bent 3	100.0	444.8	116.0	515.8	0.9

Table 4-8: Maximum capable yaw moment from each bent compared to table yaw moment limits.

	Limit		Value		SF
	(kip-in)	(kN-m)	(kip-in)	(kN-m)	
Bent 1	4800	542.3	1335	150.9	3.6
Bent 2	4800	542.3	1002	113.2	4.8
Bent 3	4800	542.3	1603	181.1	3.0

Note: Maximum considering both columns failing in longitudinal direction

Table 4-9: Calculated maximum pitch moment demands for each bent considering ramped motion-1 and motion-2 excitation until failure of bridge, compared to table pitch moment limits.

	PGA (g)	M-1 0.4g bedrock excitation			M-2 0.4g bedrock excitation		
		Value		SF	Value		SF
		(kip-in)	(kN-m)		(kip-in)	(kN-m)	
Bent1 (Safety Factor)	0.15	6605	746	1.82	5886	665	2.04
	0.25	7060	798	1.70	7077	800	1.70
	0.50	8343	943	1.44	8535	964	1.41
	1.00	8767	991	1.37	9720	1098	1.23
	1.50	9490	1072	1.26	10357	1170	1.16
Bent2 (Safety Factor)	0.15	2242	253	5.35	2480	280	4.84
	0.25	3355	379	3.58	3025	342	3.97
	0.50	4700	531	2.55	5199	587	2.31
	1.00	6101	689	1.97	6432	727	1.87
	1.50	6387	722	1.88	7319	827	1.64
Bent3 (Safety Factor)	0.15	6870	776	1.75	4796	542	2.50
	0.25	8216	928	1.46	7458	843	1.61
	0.50	9195	1039	1.31	9089	1027	1.32
	1.00	10782	1218	1.11	12021	1358	1.00
	1.50	11521	1302	1.04	13442	1519	0.89

Note: Moment = $2*M_{col.\ Base} + 2*Vcol*h_{footing} + Amax*m_{footing}*h_{C.G.\ footing} + (P_{max}-P_{dead})*$column spacing

Table 4-10: Displacement and velocity demands of ramped motion-1 and motion-2 compared with table limits.

	PGA (g)	M-1 0.4g bedrock excitation			M-2 0.4g bedrock excitation		
		Value		SF	Value		SF
		imperial	metric		imperial	metric	
Peak Displacement (in) (mm)	0.15	0.51	12.8	23.76	0.47	11.9	25.57
	0.25	0.84	21.4	14.25	0.78	19.9	15.34
	0.50	1.68	42.8	7.13	1.56	39.7	7.67
	1.00	3.37	85.5	3.56	3.13	79.5	3.83
	1.50	5.05	128.3	2.38	4.69	119.2	2.56
Peak Velocity (in/s) (mm/s)	0.15	3.3	85	11.99	4.2	106	9.61
	0.25	5.6	141	7.19	6.9	176	5.76
	0.50	11.1	282	3.60	13.9	353	2.88
	1.00	22.2	565	1.80	27.8	705	1.44
	1.50	33.4	847	1.20	41.6	1058	0.96

Table 4-11: Calculated maximum table actuator force demands for each bent considering ramped motion-1 and motion-2 excitation until failure of bridge, compared to table actuator limits.

	PGA (g)	M-1 0.4g bedrock excitation			M-2 0.4g bedrock excitation		
		Value		SF	Value		SF
		(kip)	(kN)		(kip)	(kN)	
Bent1 (Safety Factor)	0.15	61	272	2.69	55	243	3.03
	0.25	67	297	2.47	63	282	2.60
	0.50	90	398	1.84	83	371	1.98
	1.00	132	586	1.25	120	535	1.37
	1.50	175	781	0.94	157	699	1.05
Bent2 (Safety Factor)	0.15	26	116	6.31	30	135	5.43
	0.25	41	185	3.98	43	193	3.80
	0.50	68	303	2.42	77	344	2.13
	1.00	105	468	1.57	123	545	1.35
	1.50	142	630	1.16	167	745	0.99
Bent3 (Safety Factor)	0.15	66	293	2.51	46	204	3.60
	0.25	77	345	2.13	70	313	2.34
	0.50	101	450	1.63	89	395	1.86
	1.00	147	656	1.12	127	564	1.30
	1.50	193	857	0.86	161	717	1.02

Note: Considers max column shear*2 + (table mass+footing mass)*acceleration

Table 4-12: Summary of calculated safety factors for table limits considering ramped motion-1 and motion-2 excitation until failure of bridge.

		M-10.4g bedrock excitation		M-2 0.4g bedrock excitation	
	PGA (g)	Bent μ_Δ	Table SF	Bent μ_Δ	Table SF
Bent1	0.15	1.25	1.82	1.17	2.04
	0.25	1.70	1.70	1.70	1.70
	0.50	2.58	1.44	3.34	1.41
	1.00	10.03	1.25	5.89	1.23
	1.50	11.08	0.94	8.77	0.96
Bent2	0.15	0.48	4.79	0.54	4.79
	0.25	0.75	3.58	0.68	3.80
	0.50	1.31	2.42	1.55	2.13
	1.00	3.97	1.57	3.19	1.35
	1.50	7.68	1.16	4.86	0.96
Bent3	0.15	1.02	1.75	0.69	2.50
	0.25	1.64	1.46	1.18	1.61
	0.50	2.26	1.31	3.32	1.32
	1.00	6.53	1.11	6.17	1.00
	1.50	24.68	0.86	9.52	0.89

Table 4-13 Concrete cylinder test results for concrete used in footings, columns, and superstructure beams of bridge specimen.

Footings

Date poured: 10/5/04 Slump: 3.5 in
Max Aggregate: 3/8 in
Mix: RSRM 5000psi UNR mix

16-day

Date of Test	Age	f'c (psi)	f'c (Mpa)
10/21/04	16 days	3387	23.4
10/21/04	16 days	3559	24.5
10/21/04	16 days	3350	23.1
Average:		3432	23.7

28-day

Date of Test	Age	f'c (psi)	f'c (Mpa)
11/02/04	28 days	4009	27.6
11/02/04	28 days	4186	28.9
11/02/04	28 days	3878	26.7
Average:		4024	27.7

End of Shake Table Tests

Date of Test	Age	f'c (psi)	f'c (Mpa)
02/15/05	133 days	4832	33.3
02/15/05	133 days	4834	33.3
02/15/05	133 days	4684	32.3
Average:		4783	33.0

Columns

Date poured: 11/4/04 Slump: 2 in
Max Aggregate: 3/8 in + pl = 5 in
Mix: RSRM 5000psi UNR mix

7-day

Date of Test	Age	f'c (psi)	f'c (Mpa)
11/11/04	7 days	2530	17.4
11/11/04	7 days	2680	18.5
11/11/04	7 days	2580	17.8
Average:		2597	17.9

28-day

Date of Test	Age	f'c (psi)	f'c (Mpa)
12/03/04	28 days	4628	31.9
12/03/04	28 days	4909	33.8
12/03/04	28 days	4898	33.8
Average:		4812	33.2

End of Shake Table Tests

Date of Test	Age	f'c (psi)	f'c (Mpa)
02/15/05	103 days	5888	40.6
02/15/05	103 days	5996	41.3
02/15/05	103 days	5850	40.3
Average:		5912	40.8

Beams

Date poured: 10/22/04 Slump: 3 in
Max Aggregate: 3/8 in + pl = 5.5 in
Mix: RSRM 5000psi min mix

7-day

Date of Test	Age	f'c (psi)	f'c (Mpa)
11/02/04	11 days	5127	35.3
11/02/04	11 days	5009	34.5
11/02/04	11 days	4726	32.6
Average:		4954	34.2

28-day

Date of Test	Age	f'c (psi)	f'c (Mpa)
11/19/04	28 days	5930	40.9
11/19/04	28 days	6100	42.1
11/19/04	28 days	6126	42.2
Average:		6052	41.7

End of Shake Table Tests

Date of Test	Age	f'c (psi)	f'c (Mpa)
02/15/05	116 days	7114	49.0
02/15/05	116 days	7000	48.3
02/15/05	116 days	7549	52.1
Average:		7221	49.8

Table 4-14 Concrete cylinder test results for concrete used in spacer clocks and cap beams of bridge specimen.

Spacers			
Date poured: 11/24/04		Slump: 3.5 in	
Max Aggregate: 3/8 in		+ pl = 5.5 in	
Mix: RSRM 5000psi min mix			
7-day			
Date of Test	Age	f'c (psi)	f'c (Mpa)
12/01/04	9 days	3373	23.3
12/01/04	9 days	3355	23.1
12/01/04	9 days	3428	23.6
Average:		3385	23.3
28-day			
Date of Test	Age	f'c (psi)	f'c (Mpa)
12/22/04	28 days	5650	39.0
12/22/04	28 days	5744	39.6
12/22/04	28 days	5680	39.2
Average:		5691	39.2
End of Shake Table Tests			
Date of Test	Age	f'c (psi)	f'c (Mpa)
02/15/05	83 days	7059	48.7
02/15/05	83 days	6980	48.1
02/15/05	83 days	7007	48.3
Average:		7015	48.4

Cap Beams			
Date poured: 11/24/04		Slump: 3.5 in	
Max Aggregate: 3/8 in		+ pl = 5.5 in	
Mix: RSRM 5000psi min mix			
7-day			
Date of Test	Age	f'c (psi)	f'c (Mpa)
12/03/04	9 days	3438	23.7
12/03/04	9 days	3582	24.7
12/03/04	9 days	3258	22.5
Average:		3426	23.6
28-day			
Date of Test	Age	f'c (psi)	f'c (Mpa)
12/22/04	28 days	5596	38.6
12/22/04	28 days	5638	38.9
12/22/04	28 days	5724	39.5
Average:		5653	39.0
End of Shake Table Tests			
Date of Test	Age	f'c (psi)	f'c (Mpa)
02/15/05		6950	47.9
02/15/05		7074	48.8
02/15/05		6943	47.9
Average:		6989	48.2

Table 5-1: Event schedule for shake table setup of bridge specimen.

Start Date	End Date	# of Days	Event
13-Dec-2004	15-Dec-2004	3	begin table prep for footings
14-Dec-2004	14-Dec-2004	1	thread rods into table
15-Dec-2004	15-Dec-2004	1	place footing blocks and bent 2 on table
16-Dec-2004	16-Dec-2004	1	grout footing blocks
20-Dec-2004	20-Dec-2004	1	place bents on footing blocks
21-Dec-2004	22-Dec-2004	2	paint safety frames
22-Dec-2004	22-Dec-2004	1	grout bents on footing blocks
27-Dec-2004	27-Dec-2004	1	adjust shake table locations to fit superstructure
29-Dec-2004	30-Dec-2004	2	place beams on bent caps
3-Jan-2005	6-Jan-2005	4	attach strain gauges
4-Jan-2004	4-Jan-2004	1	pour grout at beam ends
5-Jan-2004	5-Jan-2004	1	pour hydrostone between beams
6-Jan-2004	6-Jan-2004	1	transverse post tensioning of bridge
7-Jan-2005	7-Jan-2005	1	longitudinal post tensioning of bridge
7-Jan-2005	24-Jan-2005	18	attach remaining instrumentation
10-Jan-2005	12-Jan-2005	3	place concrete blocks / lead on bridge
18-Jan-2005	19-Jan-2005	2	post-tension blocks / bolt lead on bridge
26-Jan-2005	28-Jan-2005	3	low amplitude testing (part I)
7-Feb-2005	7-Feb-2005	1	low amplitude testing (part II)
8-Feb-2005	9-Feb-2005	2	high amplitude testing
10-Feb-2005	10-Feb-2005	1	take mass off of bridge
11-Feb-2005	11-Feb-2005	1	detension bridge
12-Feb-2005	13-Feb-2005	2	take down half of superstructure and clear table 3
23-Feb-2005	23-Feb-2005	1	take down half of superstructure and clear tables 1 and 2
13-Dec-2004	23-Feb-2005	**73**	**total time using shake tables**

Table 5-2: Complete test schedule for all shake table tests.

Test	Test Type		Significance	Bedrock Motion		Bedrock Excitation (g)	Bent Bedrock Depth (Target PGA for High Amp.)		
				Trans.	Long.		1	2	3
WN0001	Low Amplitude	Jan. 27, 2005	Transverse and Longitudinal White Noise						
1A*			Uniaxial Coherent Motion	Motion-1	---	0.06	d/3	d/3	d/3
1				Motion-1	---	0.06	d/3	d/3	d/3
2A*			Incoherent Motion	Motion-1	---	0.06	0	d/3	2d/3
2				Motion-1	---	0.06	0	d/3	2d/3
3A*				Motion-1	---	0.06	2d/3	d/3	0
3				Motion-1	---	0.06	2d/3	d/3	0
WN0304A*			Transverse and Longitudinal White Noise (half-scale)						
WN0304			Transverse and Longitudinal White Noise						
4			Incoherent Motion	Motion-1	---	0.06	0	d/2	d/2
5				Motion-1	---	0.06	d/2	0	d/2
6				Motion-1	---	0.06	d/2	d/2	0
8			Uniaxial Motion	Motion-1	---	0.06	d/3	d/3	d/3
WN0809-1			Transverse and Longitudinal White Noise (End of Day)						
WN0809-2		Feb. 8, 2005	Transverse and Longitudinal White Noise (Beginning of Day)						
SQ0809-2			Transverse Square Wave (Beginning of Day)						
9A*			Biaxial Motion	Motion-1	Motion-2	0.06	d/3	d/3	d/3
9				Motion-1	Motion-2	0.06	d/3	d/3	d/3
10			Centrifuge Motion	Motion-1	---	0.10	d	d	d
11				Motion-1	---	0.10	d	d	d
WN1112-1			Transverse and Longitudinal White Noise (End of Day)						
SQ1112-1			Transverse Square Wave (End of Day)						
WN1112-2	High Amplitude	Feb. 9, 2005	Transverse and Longitudinal White Noise (Beginning of Day)						
SQ1112-2			Transverse Square Wave (Beginning of Day)						
12			Uniaxial Coherent Motion	Motion-1	---	0.40	d (0.075 g)		
13				Motion-1	---	0.40	d (0.15 g)		
14				Motion-1	---	0.40	d (0.25 g)		
WN1415			Transverse and Longitudinal White Noise						
SQ1415			Transverse Square Wave						
15			Uniaxial Coherent Motion	Motion-1	---	0.40	d (0.50 g)		
16				Motion-1	---	0.40	d (0.75 g)		
17				Motion-1	---	0.40	d (1.0 g)		
WN1718			Transverse and Longitudinal White Noise						
SQ1718			Transverse Square Wave						
18			Uniaxial Motion	Motion-1	---	0.40	d (1.33 g)		
WN1819		Feb. 10, 2005	Transverse and Longitudinal White Noise						
SQ1819			Transverse Square Wave						
19			Uniaxial Motion	Motion-1	---	0.40	d (1.66 g)		
WN1920			Transverse and Longitudinal White Noise						
SQ1920			Transverse Square Wave						
20			Uniaxial Motion	Motion-1	---	0.40	d (1.0 g)		
WN2021			Transverse and Longitudinal White Noise						
21			Uniaxial Motion	Motion-1	---	0.40	d (1.0 g)		
22				Motion-1	---	0.40	d (1.5 g)		

Notes: d = the depth from the point of column fixity to bedrock, 25.4 m.
"A" denotes half amplitude motions

Table 6-1: Description of damage progression for east column of bent 1.

Bent 1 east column, top east side

Test	Maximum crack width (in)	Maximum crack width (mm)	Maximum spall height (in)	Maximum spall height (mm)	Spall description	Exp. long. bars	Exp. lateral spirals	Extent of bar buckling or fracture
12	0.000	0.00	0.00	0	---	---	---	---
13	< 0.003	0.08	0.00	0	---	---	---	---
14	0.003	0.08	0.00	0	---	---	---	---
15	0.007	0.17	0.00	0	Flaking	---	---	---
16	0.010	0.25	3.00	76	Spall	---	---	---
17	0.010	0.25	3.50	89	Spall	---	---	---
18	0.010	0.25	3.50	89	Spall	---	---	---
19	0.030	0.75	3.50	89	Spall	---	---	---
20	0.030	0.75	3.50	89	Spall	---	---	---
21	---	---	3.50	89	Spall	---	---	---
22	---	---	3.50	89	Spall	---	---	---

Bent 1 east column, bottom east side

Test	Maximum crack width (in)	Maximum crack width (mm)	Maximum spall height (in)	Maximum spall height (mm)	Spall description	Exp. long. bars	Exp. lateral spirals	Extent of bar buckling or fracture
12	0.000	0.00	0.00	0	---	---	---	---
13	0.000	0.00	0.00	0	---	---	---	---
14	< 0.003	0.08	0.00	0	---	---	---	---
15	0.007	0.17	0.00	0	---	---	---	---
16	0.013	0.33	0.00	0	Flaking	---	---	---
17	0.013	0.33	0.00	0	Spall	---	---	---
18	0.013	0.33	2.50	64	Spall	---	2	---
19	0.013	0.33	4.50	114	Spall	---	3	---
20	0.013	0.33	5.50	140	Spall	---	3	---
21	---	---	5.50	140	Spall	---	3	---
22	---	---	5.50	140	Spall	2	3	---

Bent 1 east column, top west side

Test	Maximum crack width (in)	Maximum crack width (mm)	Maximum spall height (in)	Maximum spall height (mm)	Spall description	Exp. long. bars	Exp. lateral spirals	Extent of bar buckling or fracture
12	0.000	0.00	0.00	0	---	---	---	---
13	0.000	0.00	0.00	0	---	---	---	---
14	< 0.003	0.08	0.00	0	---	---	---	---
15	0.010	0.25	0.00	0	Flaking	---	---	---
16	0.013	0.33	5.00	127	Spall	---	---	---
17	0.013	0.33	6.00	152	Spall	---	2	---
18	0.020	0.50	6.00	152	Spall	---	2	---
19	0.020	0.50	6.00	152	Spall	1	3	---
20	0.020	0.50	6.00	152	Spall	1	3	---
21	---	---	6.00	152	Spall	1	3	---
22	---	---	6.00	152	Spall	2	3	insipient, 1 bar sep. from core

Bent 1 east column, bottom west side

Test	Maximum crack width (in)	Maximum crack width (mm)	Maximum spall height (in)	Maximum spall height (mm)	Spall description	Exp. long. bars	Exp. lateral spirals	Extent of bar buckling or fracture
12	< 0.000	0.00	0.00	0	---	---	---	---
13	0.000	0.00	0.00	0	---	---	---	---
14	0.003	0.08	0.00	0	---	---	---	---
15	0.007	0.17	0.00	0	---	---	---	---
16	0.013	0.33	0.00	0	Flaking	---	---	---
17	0.013	0.33	2.00	51	Spall	---	---	---
18	0.013	0.33	4.00	102	Spall	---	---	---
19	0.030	0.75	4.00	102	Spall	---	---	---
20	0.030	0.75	4.00	102	Spall	---	---	---
21	---	---	4.00	102	Spall	---	---	---
22	---	---	4.00	102	Spall	---	---	---

Table 6-2: Description of damage progression for west column of bent 1.

Bent 1 west column, top east side

Test	Maximum crack width (in)	Maximum crack width (mm)	Maximum spall height (in)	Maximum spall height (mm)	Spall description	Exp. long. bars	Exp. lateral spirals	Extent of bar buckling or fracture
12	0.000	0.00	0.00	0	---	---	---	---
13	0.000	0.00	0.00	0	---	---	---	---
14	0.000	0.00	0.00	0	---	---	---	---
15	0.007	0.17	0.00	0	Flaking	---	---	---
16	0.020	0.50	4.00	102	Spall	---	---	---
17	0.020	0.50	4.00	102	Spall	---	---	---
18	0.020	0.50	4.00	102	Spall	---	---	---
19	0.020	0.50	5.25	133	Spall	---	2	---
20	0.020	0.50	5.25	133	Spall	---	2	---
21	---	---	5.25	133	Spall	---	2	---
22	---	---	5.25	133	Spall	---	2	---

Bent 1 west column, bottom east side

Test	Maximum crack width (in)	Maximum crack width (mm)	Maximum spall height (in)	Maximum spall height (mm)	Spall description	Exp. long. bars	Exp. lateral spirals	Extent of bar buckling or fracture
12	0.000	0.00	0.00	0	---	---	---	---
13	0.000	0.00	0.00	0	---	---	---	---
14	0.000	0.00	0.00	0	---	---	---	---
15	0.007	0.17	0.00	0	---	---	---	---
16	0.013	0.33	0.00	0	Flaking	---	---	---
17	0.020	0.50	0.00	0	Flaking	---	---	---
18	0.020	0.50	2.50	64	Spall	---	---	---
19	0.030	0.75	3.50	89	Spall	---	---	---
20	0.030	0.75	4.00	102	Spall	---	---	---
21	---	---	4.00	102	Spall	---	---	---
22	---	---	5.00	127	Spall	---	---	---

Bent 1 west column, top west side

Test	Maximum crack width (in)	Maximum crack width (mm)	Maximum spall height (in)	Maximum spall height (mm)	Spall description	Exp. long. bars	Exp. lateral spirals	Extent of bar buckling or fracture
12	0.000	0.00	0.00	0	---	---	---	---
13	< 0.003	0.08	0.00	0	---	---	---	---
14	< 0.003	0.08	0.00	0	---	---	---	---
15	0.010	0.25	0.00	0	---	---	---	---
16	0.010	0.25	3.00	76	Spall	---	---	---
17	0.013	0.33	3.00	76	Spall	---	---	---
18	0.020	0.50	3.00	76	Spall	---	---	---
19	0.020	0.50	4.50	114	Spall	---	---	---
20	0.020	0.50	4.50	114	Spall	---	---	---
21	---	---	4.50	114	Spall	---	---	---
22	---	---	4.50	114	Spall	---	---	---

Bent 1 west column, bottom west side

Test	Maximum crack width (in)	Maximum crack width (mm)	Maximum spall height (in)	Maximum spall height (mm)	Spall description	Exp. long. bars	Exp. lateral spirals	Extent of bar buckling or fracture
12	0.000	0.00	0.00	0	---	---	---	---
13	0.000	0.00	0.00	0	---	---	---	---
14	0.000	0.00	0.00	0	---	---	---	---
15	0.007	0.17	0.00	0	---	---	---	---
16	0.020	0.50	0.00	0	Flaking	---	---	---
17	0.020	0.50	0.00	0	Flaking	---	---	---
18	0.020	0.50	4.00	102	Spall	---	1	---
19	0.020	0.50	4.00	102	Spall	---	1	---
20	0.020	0.50	4.00	102	Spall	---	1	---
21	---	---	4.00	102	Spall	2	1	---
22	---	---	4.00	102	Spall	2	2	1 bar beginning sep. from core

Table 6-3: Description of damage progression for east column of bent 2.

Bent 2 east column, top east side

Test	Maximum crack width (in)	Maximum crack width (mm)	Maximum spall height (in)	Maximum spall height (mm)	Spall description	Exp. long. bars	Exp. lateral spirals	Extent of bar buckling or fracture
12	0.000	0.00	0.00	0	---	---	---	---
13	0.000	0.00	0.00	0	---	---	---	---
14	0.000	0.00	0.00	0	---	---	---	---
15	0.003	0.08	0.00	0	---	---	---	---
16	0.007	0.17	0.00	0	---	---	---	---
17	0.007	0.17	0.00	0	---	---	---	---
18	0.013	0.33	0.00	0	Flaking	---	---	---
19	0.039	1.00	3.75	95	Spall	---	---	---
20	0.039	1.00	4.00	102	Spall	---	---	---
21	---	---	4.00	102	Spall	---	---	---
22	---	---	5.50	140	Spall	---	---	---

Bent 2 east column, bottom east side

Test	Maximum crack width (in)	Maximum crack width (mm)	Maximum spall height (in)	Maximum spall height (mm)	Spall description	Exp. long. bars	Exp. lateral spirals	Extent of bar buckling or fracture
12	0.000	0.00	0.00	0	---	---	---	---
13	0.000	0.00	0.00	0	---	---	---	---
14	0.000	0.00	0.00	0	---	---	---	---
15	0.003	0.08	0.00	0	---	---	---	---
16	0.003	0.08	0.00	0	Minor Flake	---	---	---
17	0.007	0.17	0.00	0	Minor Flake	---	---	---
18	0.020	0.50	0.00	0	Flake	---	---	---
19	0.020	0.50	3.50	89	Spall	---	---	---
20	0.020	0.50	4.00	102	Spall	---	---	---
21	---	---	4.00	102	Spall	---	---	---
22	---	---	4.00	102	Spall	---	---	---

Bent 2 east column, top west side

Test	Maximum crack width (in)	Maximum crack width (mm)	Maximum spall height (in)	Maximum spall height (mm)	Spall description	Exp. long. bars	Exp. lateral spirals	Extent of bar buckling or fracture
12	0.000	0.00	0.00	0	---	---	---	---
13	0.000	0.00	0.00	0	---	---	---	---
14	0.000	0.00	0.00	0	---	---	---	---
15	0.003	0.08	0.00	0	---	---	---	---
16	0.007	0.17	0.00	0	Minor Flake	---	---	---
17	0.010	0.25	0.00	0	Minor Flake	---	---	---
18	0.013	0.33	4.00	102	Spall	---	---	---
19	0.039	1.00	4.50	114	Spall	---	---	---
20	0.079	2.00	4.50	114	Spall	---	---	---
21	---	---	4.50	114	Spall	---	---	---
22	---	---	8.00	203	Spall	---	1	---

Bent 2 east column, bottom west side

Test	Maximum crack width (in)	Maximum crack width (mm)	Maximum spall height (in)	Maximum spall height (mm)	Spall description	Exp. long. bars	Exp. lateral spirals	Extent of bar buckling or fracture
12	0.000	0.00	0.00	0	---	---	---	---
13	0.000	0.00	0.00	0	---	---	---	---
14	0.000	0.00	0.00	0	---	---	---	---
15	0.000	0.00	0.00	0	---	---	---	---
16	0.003	0.08	0.00	0	---	---	---	---
17	0.007	0.17	0.00	0	---	---	---	---
18	0.007	0.17	0.00	0	---	---	---	---
19	0.013	0.33	4.50	114	Spall	---	---	---
20	0.013	0.33	4.50	114	Spall	---	---	---
21	---	---	4.50	114	Spall	---	---	---
22	---	---	4.50	114	Spall	---	---	---

Table 6-4: Description of damage progression for west column of bent 2.

Bent 2 west column, top east side

Test	Maximum crack width (in)	Maximum crack width (mm)	Maximum spall height (in)	Maximum spall height (mm)	Spall description	Exp. long. bars	Exp. lateral spirals	Extent of bar buckling or fracture
12	0.000	0.00	0.00	0	---	---	---	---
13	0.000	0.00	0.00	0	---	---	---	---
14	0.000	0.00	0.00	0	---	---	---	---
15	0.003	0.08	0.00	0	---	---	---	---
16	0.007	0.17	0.00	0	Minor Flake	---	---	---
17	0.007	0.17	0.00	0	Minor Flake	---	---	---
18	0.020	0.50	4.00	102	Spall	---	---	---
19	0.079	2.00	5.00	127	Spall	---	---	---
20	0.079	2.00	5.00	127	Spall	---	---	---
21	---	---	5.00	127	Spall	---	---	---
22	---	---	5.50	140	Spall	2	2	1 buckled, 1/4" sep. from core

Bent 2 west column, bottom east side

Test	Maximum crack width (in)	Maximum crack width (mm)	Maximum spall height (in)	Maximum spall height (mm)	Spall description	Exp. long. bars	Exp. lateral spirals	Extent of bar buckling or fracture
12	0.000	0.00	0.00	0	---	---	---	---
13	0.000	0.00	0.00	0	---	---	---	---
14	0.000	0.00	0.00	0	---	---	---	---
15	0.003	0.08	0.00	0	---	---	---	---
16	0.003	0.08	0.00	0	---	---	---	---
17	0.003	0.08	0.00	0	---	---	---	---
18	0.007	0.17	4.00	102	Spall	---	1	---
19	0.013	0.33	4.75	121	Spall	---	1	---
20	0.013	0.33	4.75	121	Spall	---	1	---
21	---	---	4.75	121	Spall	---	1	---
22	---	---	4.75	121	Spall	---	1	---

Bent 2 west column, top west side

Test	Maximum crack width (in)	Maximum crack width (mm)	Maximum spall height (in)	Maximum spall height (mm)	Spall description	Exp. long. bars	Exp. lateral spirals	Extent of bar buckling or fracture
12	0.000	0.00	0.00	0	---	---	---	---
13	0.000	0.00	0.00	0	---	---	---	---
14	0.000	0.00	0.00	0	---	---	---	---
15	0.000	0.00	0.00	0	---	---	---	---
16	0.003	0.08	0.00	0	---	---	---	---
17	0.007	0.17	0.00	0	---	---	---	---
18	0.010	0.25	0.00	0	Flake	---	---	---
19	> 0.079	2.00	1.00	25	Spall	---	---	---
20	> 0.079	2.00	1.00	25	Spall	---	---	---
21	---	---	1.00	25	Spall	---	---	---
22	---	---	5.00	127	Spall	---	---	---

Bent 2 west column, bottom west side

Test	Maximum crack width (in)	Maximum crack width (mm)	Maximum spall height (in)	Maximum spall height (mm)	Spall description	Exp. long. bars	Exp. lateral spirals	Extent of bar buckling or fracture
12	0.000	0.00	0.00	0	---	---	---	---
13	0.000	0.00	0.00	0	---	---	---	---
14	< 0.003	0.08	0.00	0	---	---	---	---
15	0.003	0.08	0.00	0	---	---	---	---
16	0.007	0.17	0.00	0	---	---	---	---
17	0.007	0.17	0.00	0	---	---	---	---
18	0.079	2.00	1.50	38	Spall	---	---	---
19	0.079	2.00	5.00	127	Spall	---	---	---
20	0.079	2.00	5.00	127	Spall	---	---	---
21	---	---	5.00	127	Spall	---	---	---
22	---	---	5.00	127	Spall	---	1	---

Table 6-5: Description of damage progression for east column of bent 3.

Bent 3 east column, top east side

Test	Maximum crack width (in)	Maximum crack width (mm)	Maximum spall height (in)	Maximum spall height (mm)	Spall description	Exp. long. bars	Exp. lateral spirals	Extent of bar buckling or fracture
12	0.000	0.00	0.00	0	---	---	---	---
13	0.000	0.00	0.00	0	---	---	---	---
14	< 0.003	0.08	0.00	0	---	---	---	---
15	0.007	0.17	0.00	0	Flaking	---	---	---
16	0.010	0.25	1.50	38	Spall	---	---	---
17	0.010	0.25	4.00	102	Spall	---	---	---
18	0.020	0.50	4.00	102	Spall	---	1	---
19	0.020	0.50	4.50	114	Spall	2	3	3 bars buckled
20	0.030	0.75	5.50	140	Spall	5	4	3 bars buckled
21	---	---	5.50	140	Spall	5	4	5 bars fractured
22	---	---	5.50	140	Spall	5	4	---

Bent 3 east column, bottom east side

Test	Maximum crack width (in)	Maximum crack width (mm)	Maximum spall height (in)	Maximum spall height (mm)	Spall description	Exp. long. bars	Exp. lateral spirals	Extent of bar buckling or fracture
12	0.000	0.00	0.00	0	---	---	---	---
13	0.000	0.00	0.00	0	---	---	---	---
14	0.000	0.00	0.00	0	---	---	---	---
15	0.007	0.17	0.00	0	Flake	---	---	---
16	0.010	0.25	2.25	57	Spall	---	---	---
17	0.013	0.33	2.50	64	Spall	---	---	---
18	0.013	0.33	3.50	89	Spall	---	2	---
19	---	---	6.00	152	All but 5" circ. of cover	8	4	6 bars buckled, 2 hoop fractures
20	---	---	6.00	152	All of circ.	All	4	All bars buckled
21	---	---	6.00	152	All of circ.	All	4	5 bars and 2 spirals fractured
22	---	---	4.00	102	All of circ.	All	4	---

Bent 3 east column, top west side

Test	Maximum crack width (in)	Maximum crack width (mm)	Maximum spall height (in)	Maximum spall height (mm)	Spall description	Exp. long. bars	Exp. lateral spirals	Extent of bar buckling or fracture
12	0.000	0.00	0.00	0	---	---	---	---
13	0.000	0.00	0.00	0	---	---	---	---
14	< 0.003	0.08	0.00	0	---	---	---	---
15	0.010	0.25	0.00	0	Flake	---	---	---
16	0.010	0.25	3.50	89	Spall	---	---	---
17	0.020	0.50	3.50	89	Spall	---	1	---
18	0.020	0.50	5.50	140	Spall	2	3	---
19	---	---	5.50	140	Spall	5	3	2 bars buckled
20	---	---	5.50	140	Spall	6	3	4 bars buckled, 4 bars fractured
21	---	---	5.50	140	Spall	6	4	---
22	---	---	5.50	140	Spall	6	4	---

Bent 3 east column, bottom west side

Test	Maximum crack width (in)	Maximum crack width (mm)	Maximum spall height (in)	Maximum spall height (mm)	Spall description	Exp. long. bars	Exp. lateral spirals	Extent of bar buckling or fracture
12	0.000	0.00	0.00	0	---	---	---	---
13	0.000	0.00	0.00	0	---	---	---	---
14	0.000	0.00	0.00	0	---	---	---	---
15	0.003	0.08	0.00	0	---	---	---	---
16	0.007	0.17	0.00	0	Flake	---	---	---
17	0.010	0.25	4.00	102	Spall	---	---	---
18	0.030	0.75	5.00	127	Spall	---	---	---
19	---	---	7.00	178	All but 5" circ. of cover	6	4	4 bars buckled
20	---	---	7.00	178	All of circ.	6	4	All bars buckled
21	---	---	7.00	178	All of circ.	All	4	---
22	---	---	7.00	178	All of circ.	All	4	---

Table 6-6: Description of damage progression for west column of bent 3.

Bent 3 west column, top east side

Test	Maximum crack width (in)	Maximum crack width (mm)	Maximum spall height (in)	Maximum spall height (mm)	Spall description	Exp. long. bars	Exp. lateral spirals	Extent of bar buckling or fracture
12	0.000	0.00	0.00	0	---	---	---	---
13	0.000	0.00	0.00	0	---	---	---	---
14	0.000	0.00	0.00	0	---	---	---	---
15	0.010	0.25	2.50	64	Spall	---	---	---
16	0.013	0.33	3.50	89	Spall	---	---	---
17	0.013	0.33	4.50	114	Spall	---	---	---
18	0.013	0.33	5.50	140	Spall	2	3	---
19	0.013	0.33	7.50	191	3/4 of circ.	7	6	6 bars buckled, 1 spiral fracture
20	0.013	0.33	7.50	191	3/4 of circ.	7	6	2 bars fractured, 1 spiral fractured
21	---	---	7.50	191	All of circ.	All	6	---
22	---	---	7.50	191	All of circ.	All	6	---

Bent 3 west column, bottom east side

Test	Maximum crack width (in)	Maximum crack width (mm)	Maximum spall height (in)	Maximum spall height (mm)	Spall description	Exp. long. bars	Exp. lateral spirals	Extent of bar buckling or fracture
12	0.000	0.00	0.00	0	---	---	---	---
13	0.000	0.00	0.00	0	---	---	---	---
14	0.000	0.00	0.00	0	---	---	---	---
15	0.007	0.17	0.00	0	---	---	---	---
16	0.010	0.25	0.00	0	---	---	---	---
17	0.010	0.25	0.00	0	---	---	---	---
18	0.013	0.33	2.50	64	Spall	---	---	---
19	0.013	0.33	4.50	114	3/4 of circ.	6	3	6 bars buckled
20	---	---	4.50	114	3/4 of circ.	6	3	---
21	---	---	6.00	152	All of circ.	All	3	2 bars fractured
22	---	---	6.00	152	All of circ.	All	3	---

Bent 3 west column, top west side

Test	Maximum crack width (in)	Maximum crack width (mm)	Maximum spall height (in)	Maximum spall height (mm)	Spall description	Exp. long. bars	Exp. lateral spirals	Extent of bar buckling or fracture
12	0.000	0.00	0.00	0	---	---	---	---
13	0.000	0.00	0.00	0	---	---	---	---
14	< 0.003	0.08	0.00	0	---	---	---	---
15	0.007	0.17	0.00	0	---	---	---	---
16	0.010	0.25	0.00	0	Minor Flake	---	---	---
17	0.013	0.33	0.00	0	Minor Flake	---	---	---
18	0.079	2.00	1.00	25	Spall	---	---	---
19	0.079	2.00	6.50	165	3/4 of circ.	All	4	6 bars buckled
20	---	---	6.50	165	3/4 of circ.	All	4	---
21	---	---	6.50	165	All of circ.	All	5	2 bars fractured
22	---	---	6.50	165	All of circ.	All	5	---

Bent 3 west column, bottom west side

Test	Maximum crack width (in)	Maximum crack width (mm)	Maximum spall height (in)	Maximum spall height (mm)	Spall description	Exp. long. bars	Exp. lateral spirals	Extent of bar buckling or fracture
12	0.000	0.00	0.00	0	---	---	---	---
13	0.000	0.00	0.00	0	---	---	---	---
14	< 0.003	0.08	0.00	0	---	---	---	---
15	0.007	0.17	4.00	102	Spall	---	---	---
16	0.010	0.25	4.00	102	Spall	---	1	---
17	0.010	0.25	4.00	102	Spall	---	1	---
18	0.010	0.25	4.00	102	Spall	2	2	Incipient buckling
19	0.013	0.33	8.00	203	3/4 of circ.	All	4	Several bars buckled, 1 spiral fracture
20	---	---	8.00	203	3/4 of circ.	All	4	1 bar fracture
21	---	---	8.00	203	All of circ.	All	4	All bars buckled, 1 spiral and 2 bar fractures
22	---	---	8.00	203	All of circ.	All	4	---

Table 6-7: Measured maximum transverse relative displacements and corresponding displacement ductility (using acceleration estimated yield) for all bents and all runs.

			Bent 1			Bent 2			Bent 3		
			Displacement		μ_Δ	Displacement		μ_Δ	Displacement		μ_Δ
			in	mm		in	mm		in	mm	
Low Amplitude Testing	1a	max	0.092	2.3	0.14	0.083	2.1	0.10	0.038	1.0	0.06
		min	-0.058	-1.5	0.09	-0.060	-1.5	0.07	-0.053	-1.3	0.09
	1b	max	0.151	3.8	0.23	0.138	3.5	0.17	0.071	1.8	0.12
		min	-0.097	-2.5	0.15	-0.093	-2.3	0.11	-0.089	-2.3	0.15
	2a	max	0.060	1.5	0.09	0.045	1.1	0.05	0.065	1.7	0.11
		min	-0.045	-1.1	0.07	-0.034	-0.9	0.04	-0.066	-1.7	0.11
	2b	max	0.125	3.2	0.19	0.123	3.1	0.15	0.191	4.8	0.32
		min	-0.120	-3.0	0.18	-0.108	-2.7	0.13	-0.147	-3.7	0.25
	3a	max	0.083	2.1	0.13	0.053	1.3	0.06	0.042	1.1	0.07
		min	-0.058	-1.5	0.09	-0.042	-1.1	0.05	-0.021	-0.5	0.03
	3b	max	0.192	4.9	0.29	0.154	3.9	0.19	0.047	1.2	0.08
		min	-0.157	-4.0	0.24	-0.100	-2.5	0.12	-0.061	-1.6	0.10
	4b	max	0.107	2.7	0.16	0.105	2.7	0.13	0.101	2.6	0.17
		min	-0.077	-1.9	0.12	-0.068	-1.7	0.08	-0.105	-2.7	0.18
	5b	max	0.123	3.1	0.19	0.088	2.2	0.11	0.084	2.1	0.14
		min	-0.071	-1.8	0.11	-0.056	-1.4	0.07	-0.095	-2.4	0.16
	6b	max	0.124	3.2	0.19	0.105	2.7	0.13	0.050	1.3	0.08
		min	-0.074	-1.9	0.11	-0.061	-1.5	0.07	-0.045	-1.1	0.08
	8	max	0.134	3.4	0.20	0.122	3.1	0.15	0.066	1.7	0.11
		min	-0.076	-1.9	0.11	-0.062	-1.6	0.08	-0.068	-1.7	0.11
	9a	max	0.069	1.7	0.10	0.038	1.0	0.05	0.094	2.4	0.16
		min	-0.019	-0.5	0.03	-0.030	-0.8	0.04	-0.077	-2.0	0.13
	9b	max	0.148	3.8	0.22	0.152	3.9	0.19	0.090	2.3	0.15
		min	-0.085	-2.2	0.13	-0.095	-2.4	0.12	-0.068	-1.7	0.11
	10	max	0.188	4.8	0.28	0.089	2.3	0.11	0.099	2.5	0.17
		min	-0.125	-3.2	0.19	-0.096	-2.4	0.12	-0.078	-2.0	0.13
	11	max	0.155	3.9	0.23	0.073	1.9	0.09	0.106	2.7	0.18
		min	-0.093	-2.3	0.14	-0.073	-1.9	0.09	-0.082	-2.1	0.14
High Amplitude Testing	12	max	0.232	5.9	0.35	0.170	4.3	0.21	0.124	3.1	0.21
		min	-0.188	-4.8	0.28	-0.157	-4.0	0.19	-0.123	-3.1	0.21
	13	max	0.636	16.2	0.96	0.427	10.9	0.52	0.311	7.9	0.52
		min	-0.565	-14.4	0.85	-0.368	-9.3	0.45	-0.288	-7.3	0.48
	14	max	0.753	19.1	**1.14**	0.558	14.2	0.68	0.495	12.6	0.83
		min	-0.756	-19.2	**1.14**	-0.466	-11.8	0.57	-0.474	-12.0	0.79
	15	max	1.564	39.7	**2.37**	1.248	31.7	**1.53**	1.462	37.1	**2.45**
		min	-1.133	-28.8	**1.71**	-1.114	-28.3	**1.36**	-1.056	-26.8	**1.77**
	16	max	2.217	56.3	**3.35**	1.774	45.0	**2.17**	1.598	40.6	**2.68**
		min	-2.633	-66.9	**3.98**	-2.295	-58.3	**2.81**	-1.882	-47.8	**3.16**
	17	max	1.298	33.0	**1.96**	1.421	36.1	**1.74**	1.424	36.2	**2.39**
		min	-1.979	-50.3	**2.99**	-1.946	-49.4	**2.38**	-1.331	-33.8	**2.23**
	18	max	2.778	70.6	**4.20**	2.746	69.8	**3.36**	2.909	73.9	**4.88**
		min	-2.276	-57.8	**3.44**	-3.368	-85.5	**4.12**	-3.303	-83.9	**5.54**
	19	max	2.793	70.9	**4.23**	4.268	108.4	**5.22**	4.710	119.6	**7.90**
		min	-3.522	-89.5	**5.33**	-2.989	-75.9	**3.65**	-2.443	-62.1	**4.10**
	20	max	2.245	57.0	**3.40**	3.086	78.4	**3.77**	3.479	88.4	**5.84**
		min	-1.931	-49.1	**2.92**	-2.372	-60.3	**2.90**	-1.773	-45.0	**2.97**
Post-Tests	21	max	3.012	76.5	**4.56**	3.430	87.1	**4.19**	3.834	97.4	---
		min	-2.184	-55.5	**3.30**	-2.064	-52.4	**2.52**	-3.240	-82.3	---
	22	max	1.844	46.8	**2.79**	5.242	133.1	**6.41**	6.851	174.0	---
		min	-3.261	-82.8	**4.93**	-3.714	-94.3	**4.54**	-2.839	-72.1	---

Table 6-8: Measured maximum and minimum superstructure longitudinal displacements for all runs.

			DL1		DL2		DL3		DL4	
			Relative Disp.		Relative Disp.		Relative Disp.		Relative Disp.	
			in	mm	in	mm	in	mm	in	mm
Low Amplitude Testing	1a	max	0.00	0.0	0.00	0.1	0.02	0.6	0.03	0.7
		min	-0.01	-0.2	-0.01	-0.1	-0.03	-0.9	-0.04	-1.0
	1	max	0.00	0.0	0.01	0.2	0.03	0.6	0.03	0.7
		min	-0.01	-0.4	-0.01	-0.3	-0.04	-0.9	-0.03	-0.8
	2a	max	0.00	0.0	0.01	0.1	0.02	0.6	0.03	0.7
		min	-0.01	-0.3	-0.01	-0.2	-0.04	-1.0	-0.03	-0.8
	2	max	0.00	-0.1	0.01	0.3	0.02	0.6	0.03	0.9
		min	-0.02	-0.6	-0.02	-0.5	-0.05	-1.3	-0.04	-0.9
	3a	max	0.00	-0.1	0.00	0.1	0.02	0.6	0.03	0.7
		min	-0.01	-0.3	-0.01	-0.2	-0.03	-0.9	-0.03	-0.7
	3	max	0.00	-0.1	0.00	0.0	0.02	0.5	0.03	0.7
		min	-0.01	-0.4	-0.01	-0.4	-0.04	-1.0	-0.03	-0.8
	4	max	0.00	-0.1	0.00	0.0	0.01	0.4	0.03	0.7
		min	-0.01	-0.4	-0.01	-0.3	-0.05	-1.3	-0.03	-0.8
	5	max	-0.01	-0.2	0.00	0.0	0.01	0.3	0.02	0.6
		min	-0.02	-0.4	-0.01	-0.3	-0.05	-1.2	-0.03	-0.8
	6	max	-0.01	-0.1	0.00	0.0	0.01	0.3	0.02	0.6
		min	-0.02	-0.4	-0.01	-0.3	-0.05	-1.2	-0.04	-0.9
	8	max	-0.01	-0.2	0.00	0.0	0.01	0.2	0.03	0.6
		min	-0.02	-0.5	-0.02	-0.4	-0.06	-1.5	-0.03	-0.9
	9a	max	0.12	3.1	0.12	3.1	0.06	1.5	0.09	2.2
		min	0.01	0.1	0.01	0.2	-0.06	-1.6	-0.04	-1.1
	9	max	0.18	4.5	0.19	4.8	0.11	2.8	0.15	3.7
		min	-0.08	-2.0	-0.07	-1.7	-0.14	-3.5	-0.13	-3.4
	10	max	0.07	1.8	0.08	1.9	0.03	0.7	0.04	1.1
		min	0.06	1.5	0.05	1.3	-0.03	-0.8	-0.01	-0.2
	11	max	0.07	1.8	0.08	1.9	0.03	0.9	0.04	1.1
		min	0.06	1.4	0.05	1.2	-0.03	-0.8	-0.01	-0.3
High Amplitude Testing	12	max	0.07	1.9	0.07	1.8	0.04	1.1	0.06	1.6
		min	0.06	1.5	0.03	0.9	-0.02	-0.6	-0.01	-0.1
	13	max	0.08	2.1	0.10	2.5	0.05	1.2	0.08	2.1
		min	0.03	0.6	0.00	-0.1	-0.05	-1.2	-0.03	-0.7
	14	max	0.10	2.5	0.11	2.8	0.06	1.6	0.10	2.4
		min	0.02	0.5	-0.03	-0.8	-0.05	-1.4	-0.08	-2.0
	15	max	0.14	3.5	0.12	3.0	0.10	2.6	0.10	2.6
		min	0.02	0.5	-0.05	-1.3	-0.04	-1.1	-0.09	-2.2
	16	max	0.17	4.3	0.23	5.8	0.14	3.5	0.20	5.1
		min	-0.07	-1.8	-0.10	-2.5	-0.12	-3.1	-0.11	-2.9
	17	max	0.11	2.7	0.19	4.8	0.09	2.3	0.17	4.4
		min	-0.05	-1.4	-0.07	-1.7	-0.11	-2.8	-0.10	-2.5
	18	max	0.16	4.2	0.21	5.4	0.18	4.6	0.22	5.6
		min	-0.07	-1.9	-0.21	-5.4	-0.14	-3.6	-0.18	-4.6
	19	max	0.14	3.6	0.42	10.5	0.19	4.9	0.50	12.7
		min	-0.28	-7.1	-0.16	-4.0	-0.27	-6.8	-0.13	-3.4
	20	max	0.05	1.4	0.18	4.5	0.07	1.7	0.21	5.3
		min	-0.13	-3.3	-0.07	-1.8	-0.15	-3.8	-0.07	-1.8
Post-Tests	21	max	0.16	4.1	0.32	8.2	0.20	5.1	0.40	10.3
		min	-0.25	-6.3	-0.26	-6.5	-0.26	-6.7	-0.20	-5.2
	22	max	0.12	3.0	0.43	11.0	0.13	3.4	0.64	16.3
		min	-0.28	-7.1	-0.07	-1.8	-0.24	-6.2	-0.09	-2.2

Table 6-9: Measured maximum and minimum superstructure longitudinal displacements for all runs.

			Average North		Average South		North table		South table	
			Relative Disp.		Relative Disp.		Absolute Disp.		Absolute Disp.	
			in	mm	in	mm	in	mm	in	mm
Low Amplitude Testing	1a	max	0.00	0.0	0.02	0.5	0.00	0.0	0.00	0.0
		min	-0.01	-0.1	-0.03	-0.7	0.00	0.0	0.00	-0.1
	1	max	0.00	0.0	0.01	0.3	0.00	0.0	0.00	0.1
		min	-0.01	-0.3	-0.02	-0.6	0.00	-0.1	0.00	0.0
	2a	max	0.00	0.1	0.02	0.5	0.00	0.0	0.00	0.1
		min	-0.01	-0.2	-0.03	-0.7	0.00	-0.1	0.00	0.0
	2	max	0.00	0.0	0.01	0.4	0.00	0.0	0.01	0.1
		min	-0.02	-0.4	-0.03	-0.7	0.00	-0.1	0.00	0.0
	3a	max	0.00	0.0	0.01	0.4	0.00	0.0	0.01	0.2
		min	-0.01	-0.2	-0.02	-0.6	0.00	-0.1	0.00	0.1
	3	max	0.00	0.0	0.02	0.4	0.00	0.0	0.01	0.1
		min	-0.01	-0.3	-0.03	-0.7	0.00	0.0	0.00	0.0
	4	max	0.00	-0.1	0.01	0.3	0.00	0.1	0.00	0.1
		min	-0.01	-0.3	-0.03	-0.8	0.00	0.0	0.00	0.0
	5	max	0.00	-0.1	0.01	0.3	0.00	0.1	0.00	0.1
		min	-0.01	-0.4	-0.03	-0.8	0.00	0.0	0.00	0.0
	6	max	0.00	-0.1	0.01	0.2	0.00	0.1	0.00	0.1
		min	-0.01	-0.3	-0.03	-0.9	0.00	0.0	0.00	0.0
	8	max	-0.01	-0.2	0.01	0.2	0.00	0.1	0.00	0.1
		min	-0.02	-0.4	-0.04	-1.1	0.00	0.0	0.00	0.0
	9a	max	0.12	3.0	0.06	1.6	0.08	2.0	0.05	1.4
		min	0.01	0.2	-0.05	-1.2	0.00	0.1	0.00	-0.1
	9	max	0.18	4.6	0.12	3.0	0.12	3.0	0.08	2.1
		min	-0.07	-1.8	-0.13	-3.3	-0.05	-1.3	-0.05	-1.2
	10	max	0.07	1.8	0.03	0.8	0.04	1.1	0.03	0.7
		min	0.06	1.5	-0.01	-0.3	0.04	1.0	0.03	0.7
	11	max	0.07	1.8	0.03	0.8	0.04	1.0	0.03	0.8
		min	0.05	1.4	-0.01	-0.3	0.04	1.0	0.03	0.7
High Amplitude Testing	12	max	0.07	1.8	0.04	1.0	0.06	1.6	0.05	1.2
		min	0.05	1.3	0.00	-0.1	0.06	1.4	0.04	1.1
	13	max	0.08	2.1	0.04	1.0	0.06	1.5	0.05	1.2
		min	0.03	0.8	-0.01	-0.2	0.06	1.4	0.04	1.0
	14	max	0.08	2.2	0.05	1.3	0.06	1.5	0.05	1.4
		min	0.02	0.4	-0.03	-0.8	0.05	1.4	0.04	1.1
	15	max	0.09	2.2	0.06	1.5	0.06	1.6	0.06	1.4
		min	0.01	0.2	-0.03	-0.8	0.05	1.4	0.04	1.1
	16	max	0.10	2.5	0.07	1.7	0.06	1.5	0.06	1.4
		min	-0.01	-0.4	-0.04	-1.1	0.05	1.2	0.04	1.0
	17	max	0.08	2.1	0.06	1.6	0.06	1.6	0.06	1.5
		min	-0.01	-0.2	-0.05	-1.3	0.05	1.3	0.05	1.2
	18	max	0.08	2.1	0.08	2.2	0.06	1.6	0.07	1.8
		min	-0.06	-1.5	-0.04	-1.1	0.05	1.2	0.05	1.2
	19	max	0.10	2.6	0.21	5.3	0.08	2.1	0.10	2.6
		min	-0.07	-1.7	-0.06	-1.5	0.07	1.7	0.08	2.0
	20	max	0.09	2.2	0.08	2.1	0.08	2.1	0.11	2.7
		min	-0.07	-1.7	-0.06	-1.6	0.07	1.8	0.09	2.2
Post-Tests	21	max	0.08	2.0	0.16	4.1	0.08	2.1	0.10	2.6
		min	-0.09	-2.3	-0.06	-1.5	0.06	1.6	0.08	2.1
	22	max	0.10	2.6	0.29	7.2	0.08	2.1	0.10	2.7
		min	-0.03	-0.8	-0.04	-1.1	0.06	1.5	0.08	2.0

Table 6-10: Maximum and minimum strains for all tests (microstrain).

	Strain Gauge		1WTSL1	1WTSL2	1WTSL3	1WTSL4	1WTSL5	1WTSL6	1WTSL7	1WTSL8
Low Amplitude Testing	1a	ϵ_{max}	60	45	181	385	257	204	400	302
		ϵ_{min}	-38	-53	-204	-136	-317	-128	-204	-415
	1	ϵ_{max}	68	75	339	619	460	415	664	558
		ϵ_{min}	-60	-75	-294	-234	-483	-173	-340	-611
	2a	ϵ_{max}	38	45	166	249	219	158	264	249
		ϵ_{min}	-38	-38	-158	-106	-211	-106	-158	-287
	2	ϵ_{max}	53	75	483	506	626	317	506	702
		ϵ_{min}	-60	-68	-264	-264	-385	-226	-400	-498
	3a	ϵ_{max}	38	45	234	332	309	204	332	340
		ϵ_{min}	-38	-38	-151	-143	-249	-121	-219	-324
	3	ϵ_{max}	91	98	687	792	1026	535	815	951
		ϵ_{min}	-68	-98	-332	-355	-566	-264	-528	-724
	4	ϵ_{max}	53	60	377	415	513	256	445	505
		ϵ_{min}	-38	-53	-166	-196	-302	-181	-279	-377
	5	ϵ_{max}	60	60	355	506	468	324	528	453
		ϵ_{min}	-30	-60	-189	-158	-355	-158	-241	-445
	6	ϵ_{max}	68	60	324	536	453	347	543	445
		ϵ_{min}	-30	-75	-204	-174	-385	-158	-249	-468
	8	ϵ_{max}	60	75	347	558	506	369	558	483
		ϵ_{min}	-45	-53	-219	-189	-400	-158	-264	-498
	9a	ϵ_{max}	-23	0	204	204	106	106	226	113
		ϵ_{min}	-83	-83	-234	-158	-272	-226	-181	-332
	9	ϵ_{max}	15	23	679	543	566	452	551	505
		ϵ_{min}	-106	-121	-475	-294	-498	-407	-408	-604
	10	ϵ_{max}	23	38	551	672	823	445	672	732
		ϵ_{min}	-113	-136	-370	-370	-619	-332	-536	-747
	11	ϵ_{max}	15	23	438	536	611	347	551	551
		ϵ_{min}	-106	-113	-324	-317	-513	-294	-423	-634
High Amplitude Testing	12	ϵ_{max}	45	75	815	906	1215	724	913	1086
		ϵ_{min}	-128	-151	-475	-483	-777	-385	-687	-920
	13	ϵ_{max}	498	505	**2912**	**2777**	**4068**	**3054**	**2536**	**4036**
		ϵ_{min}	-204	-294	-800	-1117	-1902	-679	-1487	-2331
	14	ϵ_{max}	694	747	**5017**	**3230**	**6785**	**3875**	**2958**	**6782**
		ϵ_{min}	-257	-355	-920	-1328	-2211	-769	-1834	**-2716**
	15	ϵ_{max}	973	1034	**13866**	**9772**	**15124**	**10465**	**9116**	**12350**
		ϵ_{min}	-362	-596	-468	-1690	**-3207**	-543	**-2913**	**-4700**
	16	ϵ_{max}	1230	1328	**33896**	**14323**	**35818**	**3430**	**14716**	**34395**
		ϵ_{min}	-589	-656	1343	-2053	**-4687**	**-6092**	**-5803**	**-7062**
	17	ϵ_{max}	1139	1260	**24557**	**8784**	**27041**	1086	**8029**	**25229**
		ϵ_{min}	-543	-634	2158	-1298	-2151	-422	**-4724**	**-3252**
	18	ϵ_{max}	1441	1335	**29958**	**17152**	**33916**	935	**21734**	**30359**
		ϵ_{min}	-611	-815	2112	-1426	**-4234**	-573	**-4475**	**-7031**
	19	ϵ_{max}	1509	1494	**50660**	**15024**	**56059**	829	**23741**	**49824**
		ϵ_{min}	-724	-845	**4240**	-2030	-1019	-581	**-5056**	**-4202**
	20	ϵ_{max}	1441	1313	**29415**	**11855**	**34625**	694	**19176**	**29039**
		ϵ_{min}	-649	-807	**10034**	-143	**4906**	-249	-2022	-1011
Post-Tests	21	ϵ_{max}	1539	1366	**34191**	**11176**	**39304**	739	**26465**	**32637**
		ϵ_{min}	-702	-883	**9702**	-589	**4090**	-452	-2090	**-4210**
	22	ϵ_{max}	1426	1501	**49588**	**8331**	**57878**	656	**16821**	**48828**
		ϵ_{min}	-777	-800	**10917**	**-2996**	**9079**	-188	**-2709**	1260

Table 6-11: Maximum and minimum strains for all tests (microstrain).

	Strain Gauge		1WBSL 1	1WBSL 2	1WBSL 3	1WBSL 4	1WBSL 5	1WBSL 6	1WBSL 7	1WBSL 8
Low Amplitude Testing	1a	ϵ_{max}	294	287	60	385	392	724	362	83
		ϵ_{min}	-347	-143	-38	-166	-430	-257	-294	-23
	1	ϵ_{max}	498	491	128	739	800	1185	709	136
		ϵ_{min}	-551	-257	-60	-226	-588	-377	-437	-30
	2a	ϵ_{max}	249	211	45	211	287	347	272	75
		ϵ_{min}	-242	-136	-53	-151	-272	-211	-181	-30
	2	ϵ_{max}	626	400	113	543	988	845	980	279
		ϵ_{min}	-423	-325	-75	-302	-475	-453	-377	-45
	3a	ϵ_{max}	362	257	60	272	422	453	385	83
		ϵ_{min}	-287	-166	-38	-166	-332	-272	-241	-23
	3	ϵ_{max}	936	649	249	867	1298	1373	1260	400
		ϵ_{min}	-634	-408	-60	-324	-679	-558	-513	-15
	4	ϵ_{max}	491	347	60	309	528	543	551	189
		ϵ_{min}	-347	-219	-68	-249	-400	-347	-264	0
	5	ϵ_{max}	453	430	60	407	468	702	483	166
		ϵ_{min}	-392	-181	-68	-219	-445	-302	-294	15
	6	ϵ_{max}	453	445	75	445	483	732	475	166
		ϵ_{min}	-423	-204	-68	-219	-475	-309	-332	15
	8	ϵ_{max}	475	445	91	475	528	815	535	174
		ϵ_{min}	-430	-204	-75	-226	-483	-324	-332	-8
	9a	ϵ_{max}	143	143	317	234	121	189	211	196
		ϵ_{min}	-317	-151	-302	-347	-324	-257	-249	-241
	9	ϵ_{max}	506	430	792	958	619	822	928	868
		ϵ_{min}	-589	-355	-505	-649	-604	-468	-551	-438
	10	ϵ_{max}	740	551	121	649	996	1117	965	272
		ϵ_{min}	-649	-438	-106	-355	-671	-558	-513	-68
	11	ϵ_{max}	566	445	75	483	687	785	649	181
		ϵ_{min}	-536	-355	-113	-332	-558	-460	-437	-83
High Amplitude Testing	12	ϵ_{max}	1079	785	234	950	1381	1494	1365	483
		ϵ_{min}	-792	-543	-121	-407	-792	-671	-649	-83
	13	ϵ_{max}	**3608**	**2649**	1162	**3176**	**4587**	**4655**	**3613**	1735
		ϵ_{min}	-1789	-1291	-181	-611	-1328	-1064	-1169	-128
	14	ϵ_{max}	**5517**	**3215**	1720	**4481**	**8532**	**5832**	**7618**	**2626**
		ϵ_{min}	-2038	-1691	-143	-256	-1531	-1086	-1267	-166
	15	ϵ_{max}	**9902**	**7246**	**5983**	**17795**	**13233**	**19413**	**14564**	**7386**
		ϵ_{min}	**-2966**	-2196	-15	649	**-3704**	-1532	-45	-60
	16	ϵ_{max}	**25253**	**13450**	**13648**	**25414**	**29083**	**29492**	**37507**	**24355**
		ϵ_{min}	**-3781**	**-3170**	**2482**	**4971**	**-5296**	-2248	890	**2829**
	17	ϵ_{max}	**18498**	**7925**	**10532**	**15155**	**17291**	**16410**	**28072**	**17934**
		ϵ_{min}	**-3253**	-2385	**5688**	**6110**	822	-498	**2904**	**9431**
	18	ϵ_{max}	**22536**	**20206**	**13701**	**34405**	**17827**	**30352**	**34301**	**21367**
		ϵ_{min}	**-4777**	-2166	**5885**	**6140**	588	**-18485**	792	**9642**
	19	ϵ_{max}	**243197**	**21549**	**18680**	**36872**	**19260**	**241423**	**40999**	**37234**
		ϵ_{min}	**-10808**	-2068	**7424**	**3915**	566	**-24641**	**2708**	**11015**
	20	ϵ_{max}	**243197**	**17511**	**13384**	**29396**	**9581**	**241423**	**21699**	**21903**
		ϵ_{min}	**-10030**	-98	**9378**	**5801**	2173	**-8835**	**4156**	**16199**
Post-Tests	21	ϵ_{max}	**243197**	**23617**	**16854**	**41519**	**15247**	**241423**	**22815**	**23653**
		ϵ_{min}	**-14785**	-181	**8917**	**3191**	**2648**	**-13912**	-701	**14826**
	22	ϵ_{max}	**243197**	**15043**	**18755**	**24199**	**10434**	**241423**	**27121**	**31537**
		ϵ_{min}	-1215	-189	**8352**	**2572**	**3516**	**-18673**	1908	**14886**

Table 6-12: Maximum and minimum strains for all tests (microstrain).

	Strain Gauge		1WBSL 9	1WBSL 10	1ETSL1	1ETSL2	1ETSL3	1ETSL4	1ETSL6	1ETSL7
Low Amplitude Testing	1a	ϵ_{max}	53	90	53	30	324	347	189	498
		ϵ_{min}	-83	-45	-75	-38	-143	-173	-211	-249
	1	ϵ_{max}	83	121	91	45	611	664	324	852
		ϵ_{min}	-143	-60	-98	-45	-226	-264	-294	-370
	2a	ϵ_{max}	45	60	38	23	211	181	158	279
		ϵ_{min}	-53	-38	-53	-30	-121	-143	-166	-196
	2	ϵ_{max}	98	106	75	45	475	475	438	626
		ϵ_{min}	-106	-83	-106	-45	-309	-339	-264	-437
	3a	ϵ_{max}	53	75	60	30	264	272	226	377
		ϵ_{min}	-68	-53	-60	-38	-158	-189	-174	-264
	3	ϵ_{max}	128	151	106	60	807	845	626	1041
		ϵ_{min}	-151	-106	-128	-60	-347	-437	-347	-566
	4	ϵ_{max}	83	90	60	38	392	355	324	483
		ϵ_{min}	-83	-60	-75	-30	-196	-234	-219	-332
	5	ϵ_{max}	75	106	75	45	498	445	287	611
		ϵ_{min}	-106	-53	-68	-45	-181	-211	-234	-294
	6	ϵ_{max}	75	113	75	45	528	475	294	634
		ϵ_{min}	-113	-53	-68	-30	-181	-219	-249	-302
	8	ϵ_{max}	90	113	75	53	543	520	324	686
		ϵ_{min}	-106	-60	-75	-30	-189	-234	-257	-317
	9a	ϵ_{max}	-23	0	-15	-23	173	113	68	173
		ϵ_{min}	-113	-83	-91	-83	-211	-181	-241	-249
	9	ϵ_{max}	38	60	30	-15	641	513	355	634
		ϵ_{min}	-173	-128	-136	-106	-385	-377	-400	-483
	10	ϵ_{max}	68	83	45	0	701	671	475	845
		ϵ_{min}	-181	-151	-159	-106	-392	-445	-407	-603
	11	ϵ_{max}	53	75	38	0	551	490	355	641
		ϵ_{min}	-166	-128	-136	-98	-339	-385	-355	-498
High Amplitude Testing	12	ϵ_{max}	143	143	83	23	943	928	702	1154
		ϵ_{min}	-226	-158	-196	-113	-498	-603	-483	-762
	13	ϵ_{max}	852	980	906	279	**2474**	**3002**	2060	**3454**
		ϵ_{min}	-596	-422	-377	-166	-1109	-1275	-936	-1689
	14	ϵ_{max}	1071	1320	1125	505	**3198**	**3922**	**2875**	**4246**
		ϵ_{min}	-747	-483	-491	-174	-1395	-1463	-1139	-2142
	15	ϵ_{max}	1290	2074	1480	717	**7761**	**10688**	**5840**	**15258**
		ϵ_{min}	-1011	-520	-672	-279	-1682	-2195	-928	**-2693**
	16	ϵ_{max}	1614	2383	1616	1026	**8070**	**18683**	**19058**	**22287**
		ϵ_{min}	-1086	-694	-989	-332	-573	**-5581**	-611	**-3643**
	17	ϵ_{max}	1516	1976	1502	981	2165	**12045**	**14026**	**13750**
		ϵ_{min}	-1071	-618	-936	-332	-272	**-3696**	1532	-1991
	18	ϵ_{max}	1629	**2549**	1759	1034	**2466**	**29846**	**16440**	**30222**
		ϵ_{min}	-1259	-709	-1034	-453	-241	**-3258**	679	-1486
	19	ϵ_{max}	1825	**2609**	1819	1252	**2738**	**35035**	**20876**	**32688**
		ϵ_{min}	-1342	-769	-1117	-490	347	**-5310**	868	-2285
	20	ϵ_{max}	1621	**2466**	1774	1109	**2542**	**28443**	**5674**	**26549**
		ϵ_{min}	-1297	-679	-1027	-498	528	-166	**2671**	928
Post-Tests	21	ϵ_{max}	1689	**2670**	1850	1147	**2791**	**37901**	**6013**	**29747**
		ϵ_{min}	-1372	-724	-1064	-528	362	-536	1728	**-3009**
	22	ϵ_{max}	1863	2330	1759	1252	**2776**	**28435**	**6036**	**21858**
		ϵ_{min}	-1297	-799	-1170	-498	415	-1297	1230	**-3228**

Table 6-13: Maximum and minimum strains for all tests (microstrain).

	Strain Gauge		1ETSL8	1EBSL1	1EBSL2	1EBSL3	1EBSL4	1EBSL5	1EBSL6	1EBSL7
Low Amplitude Testing	1a	ϵ_{max}	279	189	423	151	249	332	717	498
		ϵ_{min}	-430	-279	-234	-53	-234	-355	-287	-189
	1	ϵ_{max}	513	332	724	287	536	725	1169	882
		ϵ_{min}	-611	-415	-362	-60	-294	-491	-460	-279
	2a	ϵ_{max}	234	174	287	60	234	272	340	279
		ϵ_{min}	-279	-189	-189	-68	-196	-249	-226	-166
	2	ϵ_{max}	641	423	551	196	815	921	822	656
		ϵ_{min}	-498	-324	-438	-83	-294	-408	-543	-370
	3a	ϵ_{max}	332	234	355	113	332	377	453	339
		ϵ_{min}	-347	-211	-241	-23	-181	-294	-302	-204
	3	ϵ_{max}	860	581	898	370	996	1162	1350	1041
		ϵ_{min}	-694	-468	-566	-83	-332	-536	-687	-422
	4	ϵ_{max}	452	340	460	98	430	475	551	453
		ϵ_{min}	-392	-241	-302	-83	-257	-340	-370	-241
	5	ϵ_{max}	430	317	543	174	392	415	732	558
		ϵ_{min}	-460	-287	-294	-75	-257	-377	-340	-219
	6	ϵ_{max}	422	309	581	181	385	415	770	603
		ϵ_{min}	-483	-287	-294	-60	-264	-385	-340	-211
	8	ϵ_{max}	468	332	619	226	430	468	830	626
		ϵ_{min}	-490	-309	-294	-75	-249	-400	-377	-234
	9a	ϵ_{max}	98	83	189	498	332	83	219	219
		ϵ_{min}	-317	-226	-241	-347	-332	-309	-226	-204
	9	ϵ_{max}	468	302	611	1170	777	498	807	784
		ϵ_{min}	-588	-430	-460	-641	-566	-498	-505	-370
	10	ϵ_{max}	671	445	755	226	792	853	1109	845
		ϵ_{min}	-724	-490	-566	-113	-370	-551	-641	-453
	11	ϵ_{max}	505	347	589	121	566	574	807	641
		ϵ_{min}	-603	-423	-460	-106	-332	-475	-513	-377
High Amplitude Testing	12	ϵ_{max}	958	732	1049	423	1124	1208	1471	1056
		ϵ_{min}	-860	-588	-724	-113	-430	-642	-830	-536
	13	ϵ_{max}	**2526**	**2445**	**3267**	1728	**4285**	**4483**	**4761**	**3115**
		ϵ_{min}	-1735	-1139	-1720	-204	-460	-891	-2007	-996
	14	ϵ_{max}	**3552**	**3033**	**3992**	**2467**	**7854**	**10717**	**6941**	**4269**
		ϵ_{min}	-1999	-1268	-2173	-91	543	-642	**-3040**	-807
	15	ϵ_{max}	**6712**	**4089**	**10564**	**14269**	**13747**	**18944**	**18929**	**14195**
		ϵ_{min}	**-2828**	-2082	**-2966**	445	**2618**	1517	**-5523**	-754
	16	ϵ_{max}	**24050**	**19322**	**16360**	**14925**	**20515**	**22634**	**92950**	**21383**
		ϵ_{min}	**-3462**	-2354	**-4339**	-2369	**5289**	1902	**-24445**	830
	17	ϵ_{max}	**17067**	**14139**	**9364**	**2513**	**8307**	**7389**	**125988**	**13441**
		ϵ_{min}	-596	-1667	**-2935**	423	**4489**	**2989**	**-20401**	1531
	18	ϵ_{max}	**20928**	**17806**	**22864**	2286	**8511**	**7449**	**95832**	**30366**
		ϵ_{min}	**-3062**	**-2777**	**-2724**	-241	**4202**	2068	**-19269**	1539
	19	ϵ_{max}	**26976**	**30594**	**24728**	2256	**7952**	**9261**	**124924**	**31445**
		ϵ_{min}	-1863	-1848	**-2513**	-257	2354	2249	**-18379**	898
	20	ϵ_{max}	**18386**	**16961**	**19974**	1720	**4957**	**6770**	**16983**	**25683**
		ϵ_{min}	-1275	-234	-106	-143	1705	1728	**-2829**	**4993**
Post-Tests	21	ϵ_{max}	**19435**	**19496**	**26848**	1607	**5236**	**7215**	**17571**	**35292**
		ϵ_{min}	-1863	-211	91	**-6263**	1230	528	**-5032**	**4465**
	22	ϵ_{max}	**22421**	**30579**	**17771**	**159902**	**5364**	**7540**	**14727**	**23910**
		ϵ_{min}	339	1418	143	**-25648**	**-4836**	287	**-10977**	**4148**

Table 6-14: Maximum and minimum strains for all tests (microstrain).

	Strain Gauge		1EBSL8	1EBSL9	1EBSL10	2WTSL1	2WTSL2	2WTSL3	2WTSL4	2WTSL5
Low Amplitude Testing	1a	ϵ_{max}	204	60	53	58	45	95	149	189
		ϵ_{min}	-83	-90	-68	-25	-14	-24	-149	-108
	1	ϵ_{max}	430	90	83	76	63	155	226	379
		ϵ_{min}	-98	-121	-98	-49	-32	-42	-256	-150
	2a	ϵ_{max}	121	45	38	46	33	77	95	136
		ϵ_{min}	-68	-53	-53	-1	-20	0	-77	-49
	2	ϵ_{max}	317	98	75	94	63	149	273	362
		ϵ_{min}	-128	-98	-106	-37	-26	-42	-232	-156
	3a	ϵ_{max}	143	60	38	58	33	89	125	159
		ϵ_{min}	-68	-60	-75	-1	-8	-6	-95	-72
	3	ϵ_{max}	619	136	113	70	39	202	256	445
		ϵ_{min}	-75	-121	-136	-67	-62	-24	-279	-156
	4	ϵ_{max}	241	98	53	64	21	155	214	302
		ϵ_{min}	-45	-75	-75	-31	-44	-12	-172	-114
	5	ϵ_{max}	294	83	68	64	10	125	178	237
		ϵ_{min}	-45	-83	-68	-19	-44	-6	-137	-96
	6	ϵ_{max}	324	75	75	64	27	143	208	296
		ϵ_{min}	-53	-83	-75	-31	-32	-12	-161	-96
	8	ϵ_{max}	347	90	68	64	39	155	220	326
		ϵ_{min}	-53	-83	-75	-37	-32	-24	-172	-108
	9a	ϵ_{max}	128	0	-8	22	10	166	101	94
		ϵ_{min}	-256	-98	-91	-43	-32	-172	-101	-150
	9	ϵ_{max}	634	53	38	46	39	392	315	332
		ϵ_{min}	-347	-143	-143	-79	-56	-291	-250	-269
	10	ϵ_{max}	460	83	53	46	27	77	273	207
		ϵ_{min}	-158	-151	-151	-55	-44	-89	-172	-227
	11	ϵ_{max}	317	60	30	34	27	59	220	148
		ϵ_{min}	-174	-136	-136	-49	-32	-77	-131	-185
High Amplitude Testing	12	ϵ_{max}	656	121	91	70	45	190	476	480
		ϵ_{min}	-174	-173	-189	-91	-62	-101	-339	-304
	13	ϵ_{max}	1909	837	687	141	87	713	1219	1414
		ϵ_{min}	-189	-505	-460	-174	-97	-167	-785	-578
	14	ϵ_{max}	2210	1078	906	302	200	951	1581	1836
		ϵ_{min}	-287	-694	-566	-192	-109	-220	-969	-679
	15	ϵ_{max}	**6065**	1478	1366	1295	848	2039	**4690**	**6277**
		ϵ_{min}	-181	-973	-694	-424	-282	-291	-2099	-1059
	16	ϵ_{max}	**7054**	2149	1539	1734	1133	**2758**	**17287**	**12566**
		ϵ_{min}	38	-988	-921	-638	-454	-636	**-3638**	-417
	17	ϵ_{max}	2226	1991	1336	1681	1008	2188	**13465**	**9451**
		ϵ_{min}	415	-875	-860	-649	-525	-523	-1843	-203
	18	ϵ_{max}	2301	2073	1675	2026	1246	**3923**	**25972**	**19545**
		ϵ_{min}	415	-1018	-943	-857	-739	-850	**-4637**	-691
	19	ϵ_{max}	2233	**2450**	1758	2050	1395	**5071**	**23071**	**30900**
		ϵ_{min}	241	-1048	-1185	-1036	-888	-921	**-6408**	-625
	20	ϵ_{max}	2105	2043	1653	2032	1323	**3733**	**19879**	**22072**
		ϵ_{min}	392	-988	-913	-970	-912	-779	**-3228**	647
Post-Tests	21	ϵ_{max}	2082	2149	1781	2008	1353	**4435**	**17745**	**26423**
		ϵ_{min}	158	-1116	-1004	-976	-912	-369	**-3692**	**2466**
	22	ϵ_{max}	2090	**2413**	1615	2317	1478	**6070**	**34509**	**40239**
		ϵ_{min}	611	-1078	-1094	-1048	-1043	-357	**-5963**	968

Table 6-15: Maximum and minimum strains for all tests (microstrain).

	Strain Gauge		2WTSL6	2WTSL7	2WTSL8	2WBSL 1	2WBSL 2	2WBSL 3	2WBSL 5	2WBSL 7
Low Amplitude Testing	1a	ϵ_{max}	75	215	232	173	143	0	362	226
		ϵ_{min}	-86	-219	-148	-130	-128	-60	-211	-75
	1	ϵ_{max}	116	334	422	298	196	15	626	422
		ϵ_{min}	-133	-362	-220	-190	-219	-60	-302	-143
	2a	ϵ_{max}	33	126	161	114	91	0	173	158
		ϵ_{min}	-62	-124	-71	-65	-68	-60	-128	-23
	2	ϵ_{max}	122	381	393	292	226	53	558	385
		ϵ_{min}	-116	-332	-238	-219	-189	-68	-332	-121
	3a	ϵ_{max}	63	179	185	131	121	-8	204	166
		ϵ_{min}	-62	-136	-101	-83	-68	-68	-166	-45
	3	ϵ_{max}	116	381	500	322	226	53	709	498
		ϵ_{min}	-163	-397	-238	-231	-242	-53	-317	-121
	4	ϵ_{max}	87	292	339	209	189	23	407	309
		ϵ_{min}	-98	-255	-166	-178	-143	-53	-241	-75
	5	ϵ_{max}	87	256	262	173	174	23	302	226
		ϵ_{min}	-74	-183	-142	-142	-98	-45	-204	-75
	6	ϵ_{max}	99	280	333	209	181	30	407	302
		ϵ_{min}	-98	-243	-166	-148	-136	-38	-219	-90
	8	ϵ_{max}	104	304	375	244	196	60	460	317
		ϵ_{min}	-92	-273	-166	-154	-158	-23	-219	-106
	9a	ϵ_{max}	122	96	137	30	38	143	68	234
		ϵ_{min}	-246	-207	-166	-148	-136	-249	-211	-234
	9	ϵ_{max}	372	399	369	244	166	475	520	573
		ϵ_{min}	-431	-380	-356	-291	-272	-355	-377	-415
	10	ϵ_{max}	93	346	250	143	174	-23	234	143
		ϵ_{min}	-133	-296	-297	-273	-196	-128	-362	-211
	11	ϵ_{max}	57	251	185	102	136	-45	158	90
		ϵ_{min}	-121	-243	-238	-225	-158	-128	-317	-173
High Amplitude Testing	12	ϵ_{max}	206	554	541	345	317	30	686	452
		ϵ_{min}	-217	-516	-410	-380	-355	-136	-475	-256
	13	ϵ_{max}	871	1410	1498	1207	1200	468	1599	1131
		ϵ_{min}	-335	-992	-707	-671	-755	-151	-626	-354
	14	ϵ_{max}	1270	1772	1938	1570	1442	717	2120	1365
		ϵ_{min}	-395	-1176	-826	-790	-928	-181	-634	-392
	15	ϵ_{max}	**2994**	**4352**	**6581**	**3080**	**2928**	1796	**7000**	**2971**
		ϵ_{min}	-383	-2151	-1421	-1438	-1630	-166	-883	-475
	16	ϵ_{max}	**14015**	**11106**	**12579**	**4495**	**6378**	**5146**	**12823**	**5746**
		ϵ_{min}	-288	**-3275**	-808	-2342	-2008	-98	128	-370
	17	ϵ_{max}	**10365**	**9370**	**9322**	**3674**	**5366**	**3946**	**10160**	**4766**
		ϵ_{min}	1668	**-2633**	-178	-2128	-1751	634	505	860
	18	ϵ_{max}	**19829**	**18507**	**20735**	**10148**	**10151**	**7915**	**18993**	**9155**
		ϵ_{min}	2019	**-5748**	434	**-3109**	-2393	702	-1456	935
	19	ϵ_{max}	**18450**	**16807**	**33855**	**21087**	**7042**	**13340**	**241443**	**14848**
		ϵ_{min}	**2756**	**-13048**	1272	**-2799**	**-3291**	1517	**-12393**	1742
	20	ϵ_{max}	**14437**	**12990**	**24582**	**14381**	**5389**	**8172**	**241443**	**11100**
		ϵ_{min}	**3291**	**-9737**	**4489**	-1830	**-2868**	**3199**	1524	**3069**
Post-Tests	21	ϵ_{max}	**10323**	**10874**	**28909**	**17579**	**4732**	**9356**	**241443**	**12819**
		ϵ_{min}	2167	**-10652**	**6064**	-754	**-3004**	**3237**	**4714**	**3386**
	22	ϵ_{max}	**25732**	**23691**	**43361**	**29528**	**8491**	**16457**	**241443**	**19184**
		ϵ_{min}	**2673**	**-15557**	**5624**	-1402	**-5796**	**3539**	**5763**	**3356**

Table 6-16: Maximum and minimum strains for all tests (microstrain).

	Strain Gauge		2WBSL 9	2WBSL 10	2ETSL1	2ETSL2	2ETSL3	2ETSL4	2ETSL5	2ETSL6
Low Amplitude Testing	1a	ϵ_{max}	40	68	187	107	259	205	232	152
		ϵ_{min}	-25	-38	-36	-134	-45	-178	-152	-169
	1	ϵ_{max}	58	83	187	116	348	285	375	259
		ϵ_{min}	-43	-53	-18	-134	-134	-214	-232	-250
	2a	ϵ_{max}	40	45	196	125	241	143	169	116
		ϵ_{min}	-13	-15	-18	-116	0	-107	-98	-161
	2	ϵ_{max}	82	91	205	152	348	268	339	223
		ϵ_{min}	-37	-53	-36	-107	-45	-232	-232	-268
	3a	ϵ_{max}	46	53	196	116	268	143	152	98
		ϵ_{min}	-19	-15	-18	-107	9	-125	-125	-161
	3	ϵ_{max}	70	75	196	107	357	294	410	276
		ϵ_{min}	-49	-60	-18	-125	-161	-250	-223	-250
	4	ϵ_{max}	58	68	223	116	366	214	312	196
		ϵ_{min}	-25	-38	-36	-107	-36	-187	-196	-196
	5	ϵ_{max}	52	75	205	116	294	223	214	169
		ϵ_{min}	-25	-23	-18	-134	-36	-152	-178	-187
	6	ϵ_{max}	58	75	214	152	321	214	294	205
		ϵ_{min}	-25	-30	0	-107	-36	-143	-161	-214
	8	ϵ_{max}	70	75	214	116	339	223	348	232
		ϵ_{min}	-25	-38	-9	-107	-45	-178	-152	-187
	9a	ϵ_{max}	-25	-8	152	62	241	98	54	-27
		ϵ_{min}	-73	-68	-71	-169	-98	-161	-196	-294
	9	ϵ_{max}	16	23	161	71	428	232	294	294
		ϵ_{min}	-91	-113	-89	-178	-241	-285	-348	-437
	10	ϵ_{max}	-2	23	152	98	375	232	161	71
		ϵ_{min}	-91	-91	-80	-169	-107	-232	-330	-383
	11	ϵ_{max}	-7	8	178	80	321	205	152	27
		ϵ_{min}	-79	-83	-80	-178	-98	-232	-268	-357
High Amplitude Testing	12	ϵ_{max}	34	60	161	71	499	383	437	312
		ϵ_{min}	-103	-113	-80	-161	-187	-339	-410	-446
	13	ϵ_{max}	189	121	169	143	1168	1088	1347	1159
		ϵ_{min}	-370	-181	-80	-205	-348	-642	-758	-758
	14	ϵ_{max}	331	158	205	169	1507	1454	1730	1578
		ϵ_{min}	-465	-226	-80	-223	-428	-767	-910	-892
	15	ϵ_{max}	1033	709	455	1079	**3398**	**3746**	**5021**	**4548**
		ϵ_{min}	-846	-701	-98	-312	-731	-1480	-2069	-1650
	16	ϵ_{max}	1241	1071	820	1249	**7687**	**14750**	**8436**	**9774**
		ϵ_{min}	-1173	-898	-178	-490	-1356	-1882	**-5547**	**-3389**
	17	ϵ_{max}	1187	1048	874	1195	**6617**	**11415**	**6733**	**7295**
		ϵ_{min}	-1143	-913	-169	-490	-1275	-1596	**-4727**	**-3023**
	18	ϵ_{max}	1437	1328	990	1471	**11638**	**21153**	**17702**	**19834**
		ϵ_{min}	-1315	-1026	-250	-651	-1445	**-2497**	**-7411**	**-3585**
	19	ϵ_{max}	1675	1350	1079	1668	**9970**	**19040**	**26959**	**34049**
		ϵ_{min}	-1399	-1101	-330	-669	-1364	-2140	**-6136**	**-3157**
	20	ϵ_{max}	1562	1328	1124	1534	**8222**	**17051**	**5021**	**23436**
		ϵ_{min}	-1381	-1041	-366	-669	-963	-339	**2747**	0
Post-Tests	21	ϵ_{max}	1621	1297	1106	1587	**7830**	**15687**	**5003**	**27895**
		ϵ_{min}	-1375	-1041	-321	-633	-580	-98	**3273**	1445
	22	ϵ_{max}	1829	1509	1195	1757	**10104**	**256883**	**5574**	**43930**
		ϵ_{min}	-1422	-1056	-357	-740	-348	27	2328	214

Table 6-17: Maximum and minimum strains for all tests (microstrain).

	Strain Gauge		2ETSL7	2ETSL8	2EBSL1	2EBSL2	2EBSL3	2EBSL4	2EBSL5	2EBSL6
Low Amplitude Testing	1a	ϵ_{max}	303	241	294	223	71	241	410	375
		ϵ_{min}	-178	-259	-143	-134	-250	-214	-214	-178
	1	ϵ_{max}	339	437	490	285	0	517	758	544
		ϵ_{min}	-303	-348	-259	-232	-223	-312	-276	-303
	2a	ϵ_{max}	205	152	223	169	36	125	178	259
		ϵ_{min}	-143	-169	-125	-98	-223	-187	-161	-107
	2	ϵ_{max}	410	419	455	321	9	437	633	669
		ϵ_{min}	-250	-348	-241	-214	-205	-276	-303	-241
	3a	ϵ_{max}	214	196	259	178	18	143	232	294
		ϵ_{min}	-116	-196	-116	-98	-241	-187	-187	-80
	3	ϵ_{max}	410	464	553	303	107	678	856	606
		ϵ_{min}	-312	-312	-223	-285	-196	-259	-285	-312
	4	ϵ_{max}	321	276	401	259	27	294	490	490
		ϵ_{min}	-205	-285	-205	-169	-205	-223	-232	-223
	5	ϵ_{max}	303	285	348	232	27	259	366	401
		ϵ_{min}	-187	-241	-134	-143	-178	-196	-232	-161
	6	ϵ_{max}	312	321	383	214	45	330	473	437
		ϵ_{min}	-205	-241	-161	-169	-187	-223	-241	-178
	8	ϵ_{max}	312	392	446	241	45	410	553	455
		ϵ_{min}	-250	-250	-196	-169	-178	-196	-250	-205
	9a	ϵ_{max}	161	62	107	98	134	62	116	205
		ϵ_{min}	-169	-268	-223	-169	-348	-285	-223	-89
	9	ϵ_{max}	383	375	410	214	339	660	660	544
		ϵ_{min}	-339	-428	-339	-339	-428	-357	-357	-348
	10	ϵ_{max}	375	223	285	205	36	223	321	544
		ϵ_{min}	-268	-446	-348	-214	-268	-357	-366	-232
	11	ϵ_{max}	294	161	196	169	-18	107	223	437
		ϵ_{min}	-268	-357	-303	-205	-232	-303	-312	-178
High Amplitude Testing	12	ϵ_{max}	535	508	553	357	27	589	874	803
		ϵ_{min}	-446	-544	-428	-366	-232	-392	-437	-366
	13	ϵ_{max}	1329	1400	1721	1249	553	1400	1757	1489
		ϵ_{min}	-838	-901	-856	-722	-250	-660	-776	-598
	14	ϵ_{max}	1730	1775	2221	1712	660	1712	2256	1846
		ϵ_{min}	-963	-1142	-990	-812	-276	-740	-838	-696
	15	ϵ_{max}	**4138**	**4361**	**8847**	**4022**	1864	**3986**	**8285**	**5708**
		ϵ_{min}	-1641	**-2836**	-1784	-1195	-214	-1195	-1391	-722
	16	ϵ_{max}	**8918**	**7643**	**14911**	**13056**	**6207**	**7482**	**12681**	**10051**
		ϵ_{min}	-2158	**-5868**	-1614	-1552	-143	-678	-1311	**-5128**
	17	ϵ_{max}	**7259**	**5904**	**11477**	**10577**	**5083**	**6305**	**10345**	1677
		ϵ_{min}	-2301	**-4905**	-972	125	**2488**	223	-678	**-7036**
	18	ϵ_{max}	**8312**	**16810**	**21367**	**20003**	**10407**	**12806**	**21929**	1204
		ϵ_{min}	**-4584**	**-6769**	**-3710**	-562	**2542**	473	-963	**-2907**
	19	ϵ_{max}	**7027**	**28546**	**33014**	**5467**	**14617**	**24373**	**32158**	1115
		ϵ_{min}	**-7750**	**-5529**	**-2872**	-2265	**5440**	1347	321	**-4031**
	20	ϵ_{max}	**7170**	**20181**	**23106**	**4120**	**10916**	**259478**	**20975**	785
		ϵ_{min}	**-6635**	**-3228**	-1641	-1632	**6216**	**3398**	1685	**-3861**
Post-Tests	21	ϵ_{max}	**7946**	**24239**	**27369**	**3906**	**12227**	**259549**	**19129**	705
		ϵ_{min}	**-3969**	-731	490	-1677	**6323**	**4691**	1142	**-3121**
	22	ϵ_{max}	**10862**	**38080**	**41246**	**4994**	**18728**	**259701**	**17568**	1070
		ϵ_{min}	**-9515**	-2149	-1962	-1864	**7161**	**4013**	**-2533**	**-6162**

Table 6-18: Maximum and minimum strains for all tests (microstrain).

	Strain Gauge		2EBSL7	2EBSL8	2EBSL9	2EBSL10	3WTSL1	3WTSL2	3WTSL3	3WTSL4
Low Amplitude Testing	1a	ϵ_{max}	259	-18	169	134	60	15	215	360
		ϵ_{min}	-116	-232	-80	-89	-71	-121	-243	-276
	1	ϵ_{max}	410	-18	161	152	60	15	476	693
		ϵ_{min}	-205	-250	-89	-80	-77	-169	-362	-461
	2a	ϵ_{max}	232	0	196	161	60	15	262	645
		ϵ_{min}	-71	-223	-89	-80	-77	-163	-326	-336
	2	ϵ_{max}	410	0	187	161	60	15	887	1489
		ϵ_{min}	-152	-250	-89	-107	-118	-240	-564	-639
	3a	ϵ_{max}	285	9	178	134	60	15	72	45
		ϵ_{min}	-45	-205	-71	-89	-65	-110	-136	-152
	3	ϵ_{max}	490	36	178	152	60	15	262	229
		ϵ_{min}	-205	-205	-98	-116	-77	-110	-243	-318
	4	ϵ_{max}	330	9	196	169	60	21	631	764
		ϵ_{min}	-107	-214	-80	-71	-77	-151	-362	-538
	5	ϵ_{max}	285	0	161	161	60	15	631	627
		ϵ_{min}	-89	-223	-62	-80	-77	-121	-326	-496
	6	ϵ_{max}	375	18	187	152	60	15	203	294
		ϵ_{min}	-134	-187	-71	-71	-77	-110	-249	-265
	8	ϵ_{max}	357	9	205	152	60	15	447	383
		ϵ_{min}	-116	-214	-45	-89	-77	-121	-296	-419
	9a	ϵ_{max}	250	241	98	71	13	-32	203	140
		ϵ_{min}	-169	-410	-161	-152	-77	-169	-368	-282
	9	ϵ_{max}	508	598	116	89	54	15	780	592
		ϵ_{min}	-339	-499	-161	-152	-136	-193	-707	-514
	10	ϵ_{max}	321	-62	89	89	60	15	447	556
		ϵ_{min}	-169	-285	-178	-143	-124	-193	-439	-514
	11	ϵ_{max}	232	-71	125	71	60	15	447	615
		ϵ_{min}	-161	-285	-143	-169	-124	-193	-445	-508
High Amplitude Testing	12	ϵ_{max}	544	9	178	125	60	15	643	907
		ϵ_{min}	-241	-285	-134	-169	-136	-234	-516	-586
	13	ϵ_{max}	1257	455	178	187	250	206	1618	2333
		ϵ_{min}	-383	-241	-259	-259	-148	-353	-1010	-1097
	14	ϵ_{max}	1534	687	259	294	631	955	**3110**	**3712**
		ϵ_{min}	-357	-268	-294	-401	-196	-431	-1075	-1590
	15	ϵ_{max}	**4557**	2033	883	990	964	1478	**17145**	**14377**
		ϵ_{min}	-339	-339	-499	-678	-326	-870	-1390	**-2506**
	16	ϵ_{max}	**20485**	**10809**	1168	1463	1005	1727	**35443**	**16488**
		ϵ_{min}	535	-98	-794	-838	-451	-948	1766	**-4182**
	17	ϵ_{max}	**16070**	**9061**	1124	1364	1011	1543	**23459**	**15114**
		ϵ_{min}	**5734**	**5422**	-767	-865	-386	-954	**4394**	**-2470**
	18	ϵ_{max}	**25541**	**14688**	1427	1659	1201	1918	**33927**	**37015**
		ϵ_{min}	**5806**	**5663**	-919	-954	-576	-1067	1986	**-7630**
	19	ϵ_{max}	**13056**	**20190**	1712	1685	1344	1727	**9714**	**83729**
		ϵ_{min}	**5262**	**7634**	-865	-1079	-576	-1138	**-29093**	-1002
	20	ϵ_{max}	**7785**	**14296**	1534	1578	958	776	**12568**	**147783**
		ϵ_{min}	**5110**	**9239**	-883	-990	-308	-425	**-19385**	**19668**
Post-Tests	21	ϵ_{max}	**7357**	**16079**	1578	1570	946	158	**191635**	**93341**
		ϵ_{min}	**5164**	**9944**	-874	-999	-267	-110	**-15907**	**3100**
	22	ϵ_{max}	**8071**	**25933**	1793	1801	441	146	**191635**	**53060**
		ϵ_{min}	**4967**	**11112**	-963	-999	-190	-3	**191635**	**12493**

Table 6-19: Maximum and minimum strains for all tests (microstrain).

	Strain Gauge		3WTSL5	3WTSL6	3WTSL7	3WTSL8	3WBSL 1	3WBSL 2	3WBSL 3	3WBSL 4
Low Amplitude Testing	1a	ϵ_{max}	343	210	195	259	225	122	85	189
		ϵ_{min}	-239	-123	-192	-192	-191	-169	-34	-138
	1	ϵ_{max}	777	436	361	503	433	229	263	415
		ϵ_{min}	-430	-171	-364	-341	-339	-288	-52	-221
	2a	ϵ_{max}	391	376	355	420	279	229	126	356
		ϵ_{min}	-382	-141	-227	-335	-322	-193	-40	-138
	2	ϵ_{max}	1146	1095	1033	991	766	847	489	1194
		ϵ_{min}	-864	-212	-513	-769	-744	-371	-64	-251
	3a	ϵ_{max}	159	49	129	200	124	92	55	82
		ϵ_{min}	-103	-82	-61	-74	-66	-33	1	-31
	3	ϵ_{max}	349	222	272	390	291	241	90	213
		ϵ_{min}	-239	-159	-192	-198	-209	-110	-34	-90
	4	ϵ_{max}	777	602	611	771	606	544	334	594
		ϵ_{min}	-543	-165	-394	-496	-458	-270	-22	-155
	5	ϵ_{max}	771	507	534	628	552	467	281	493
		ϵ_{min}	-430	-159	-358	-389	-399	-235	-17	-155
	6	ϵ_{max}	206	263	308	247	231	276	79	249
		ϵ_{min}	-239	-105	-132	-264	-238	-80	-11	-48
	8	ϵ_{max}	521	352	385	574	433	336	197	332
		ϵ_{min}	-346	-135	-275	-329	-292	-181	-5	-102
	9a	ϵ_{max}	195	287	177	236	136	104	221	201
		ϵ_{min}	-234	-307	-186	-198	-262	-140	-189	-215
	9	ϵ_{max}	593	977	462	503	463	330	804	885
		ϵ_{min}	-430	-569	-412	-460	-488	-282	-355	-411
	10	ϵ_{max}	599	400	450	628	445	378	239	362
		ϵ_{min}	-424	-236	-400	-442	-464	-330	-70	-209
	11	ϵ_{max}	599	424	480	616	445	389	233	386
		ϵ_{min}	-495	-230	-394	-502	-476	-318	-70	-203
High Amplitude Testing	12	ϵ_{max}	920	590	664	806	594	544	352	606
		ϵ_{min}	-608	-302	-477	-573	-595	-389	-82	-268
	13	ϵ_{max}	2245	1904	1740	1775	1557	1596	1155	2050
		ϵ_{min}	-1327	-462	-923	-1340	-1231	-734	-141	-381
	14	ϵ_{max}	**3809**	**3414**	**2590**	**3475**	**2776**	**2488**	2040	**3423**
		ϵ_{min}	-1755	-420	-1309	-2041	-1849	-1031	-94	-387
	15	ϵ_{max}	**4374**	**21658**	**10800**	**11982**	**10028**	**8647**	**8972**	**23778**
		ϵ_{min}	**-8972**	174	-1844	**-3813**	**-2628**	-1507	61	5
	16	ϵ_{max}	967	**22936**	**11900**	**27813**	**24307**	**10014**	**21599**	**26287**
		ϵ_{min}	**-11582**	**7189**	-2088	**-3759**	**-2497**	-1352	**-42052**	**6521**
	17	ϵ_{max}	777	**20041**	**10711**	**18646**	**17911**	**9057**	**14590**	**23386**
		ϵ_{min}	**-8229**	**9067**	-1208	-1102	326	-538	**-19212**	**9451**
	18	ϵ_{max}	**3387**	**42447**	**23046**	**34501**	**188495**	**21035**	**26592**	**49519**
		ϵ_{min}	**-13128**	**9579**	**-6362**	**-3302**	**-24148**	-1204	**-78237**	**9766**
	19	ϵ_{max}	2293	**63396**	**35762**	**14877**	**188495**	**28050**	**7141**	**69255**
		ϵ_{min}	**-23388**	**15060**	**-4609**	**4754**	2336	716	**3045**	172
	20	ϵ_{max}	-566	**53891**	**26952**	**12993**	**188495**	**24989**	**4941**	**47242**
		ϵ_{min}	**-11005**	**40783**	**14212**	**10645**	**188495**	**21416**	**2908**	-60
Post-Tests	21	ϵ_{max}	-1506	**54075**	**23379**	**12042**	**188495**	**25161**	**187587**	**60909**
		ϵ_{min}	**-8865**	**41300**	**11181**	**10383**	**188495**	**20067**	**-202001**	**3524**
	22	ϵ_{max}	**-2701**	**61131**	**188827**	**11661**	**188495**	**23455**	**61434**	**189945**
		ϵ_{min}	**-3473**	**42227**	**-7492**	**11269**	**188495**	**22100**	**-202001**	**13624**

Table 6-20: Maximum and minimum strains for all tests (microstrain).

	Strain Gauge		3WBSL 5	3WBSL 6	3WBSL 7	3WBSL 8	3WBSL 9	3WBSL 10	3ETSL1	3ETSL2
Low Amplitude Testing	1a	ϵ_{max}	506	305	318	67	60	48	65	18
		ϵ_{min}	-213	-230	-175	-52	-47	-30	-24	-23
	1	ϵ_{max}	1065	661	740	180	102	77	101	137
		ϵ_{min}	-397	-397	-288	-100	-88	-65	-65	-59
	2a	ϵ_{max}	560	608	384	120	66	71	107	119
		ϵ_{min}	-373	-272	-246	-52	-82	-48	-42	-59
	2	ϵ_{max}	1321	1404	1038	590	155	238	178	137
		ϵ_{min}	-778	-492	-449	-76	-189	-196	-107	-71
	3a	ϵ_{max}	179	79	92	61	13	-48	59	12
		ϵ_{min}	-76	-64	-92	-29	-35	-95	6	-23
	3	ϵ_{max}	370	215	289	114	48	24	48	119
		ϵ_{min}	-195	-153	-187	-88	-82	-149	-48	-23
	4	ϵ_{max}	946	673	740	257	108	149	101	137
		ϵ_{min}	-451	-337	-282	-52	-136	-196	-95	-65
	5	ϵ_{max}	887	542	657	209	102	131	101	137
		ϵ_{min}	-373	-296	-258	-64	-112	-190	-77	-53
	6	ϵ_{max}	364	251	199	78	37	54	65	119
		ϵ_{min}	-219	-106	-175	-58	-82	-149	-36	-23
	8	ϵ_{max}	685	328	449	114	84	89	65	131
		ϵ_{min}	-266	-230	-235	-82	-94	-178	-59	-23
	9a	ϵ_{max}	191	79	402	572	1	-48	18	-5
		ϵ_{min}	-260	-159	-348	-379	-100	-166	-59	-89
	9	ϵ_{max}	744	382	1139	1226	66	107	54	-5
		ϵ_{min}	-451	-308	-686	-647	-148	-196	-107	-124
	10	ϵ_{max}	750	435	497	126	60	119	65	-5
		ϵ_{min}	-445	-349	-306	-153	-142	-220	-107	-130
	11	ϵ_{max}	738	483	503	162	66	125	65	-5
		ϵ_{min}	-457	-343	-282	-141	-142	-214	-107	-130
High Amplitude Testing	12	ϵ_{max}	958	756	770	287	120	196	107	-5
		ϵ_{min}	-528	-415	-359	-189	-160	-214	-107	-142
	13	ϵ_{max}	2266	2040	1757	994	459	553	541	185
		ϵ_{min}	-1146	-718	-728	-314	-498	-369	-214	-202
	14	ϵ_{max}	**4680**	**3812**	**4420**	2159	1023	1070	1100	750
		ϵ_{min}	-1015	-1045	-556	-213	-707	-493	-416	-213
	15	ϵ_{max}	**15035**	**23679**	**20947**	**19458**	1564	1783	1676	1136
		ϵ_{min}	**-2811**	-748	598	174	-1045	-969	-660	-451
	16	ϵ_{max}	**19910**	**26788**	**39102**	**24398**	1897	1867	1861	1510
		ϵ_{min}	**-4957**	964	**8576**	**12402**	-1087	-1112	-951	-630
	17	ϵ_{max}	**9257**	**24625**	**28360**	**19809**	1737	1819	1849	1344
		ϵ_{min}	**-4023**	**3295**	**12404**	**13971**	-1075	-1082	-880	-641
	18	ϵ_{max}	**9293**	**54818**	**62328**	**41596**	2177	2170	2176	1695
		ϵ_{min}	**-13892**	**-4570**	**10525**	**14584**	-1152	-1296	-1201	-766
	19	ϵ_{max}	**188509**	**190393**	**40035**	**51399**	1975	2366	**2491**	1689
		ϵ_{min}	**-58977**	**-78992**	**-23829**	**10024**	-1259	-1272	-1076	-903
	20	ϵ_{max}	**188509**	**190393**	**29025**	**21860**	946	1225	1058	1344
		ϵ_{min}	**188509**	**190393**	-865	**5726**	-344	-410	-589	-743
Post-Tests	21	ϵ_{max}	**188509**	**190393**	**48322**	**25986**	280	1308	458	1510
		ϵ_{min}	**188509**	**190393**	**3154**	**7824**	1	-273	-273	-636
	22	ϵ_{max}	**188509**	**190393**	**44179**	**45092**	262	250	428	185
		ϵ_{min}	**188509**	**190393**	**10615**	**20742**	66	131	-178	-392

Table 6-21: Maximum and minimum strains for all tests (microstrain).

	Strain Gauge		3ETSL3	3ETSL4	3ETSL5	3ETSL6	3ETSL7	3ETSL8	3EBSL1	3EBSL2
Low Amplitude Testing	1a	ϵ_{max}	201	384	275	434	348	240	173	228
		ϵ_{min}	-186	-240	-171	-196	-294	-194	-130	-248
	1	ϵ_{max}	516	717	572	809	693	626	452	490
		ϵ_{min}	-376	-425	-314	-326	-550	-331	-225	-420
	2a	ϵ_{max}	397	717	352	440	657	436	327	484
		ϵ_{min}	-233	-300	-302	-309	-365	-319	-219	-277
	2	ϵ_{max}	1336	1710	940	1183	1680	947	910	1369
		ϵ_{min}	-501	-627	-700	-576	-758	-682	-505	-610
	3a	ϵ_{max}	153	200	84	191	146	192	173	79
		ϵ_{min}	-55	-56	-100	-77	-92	-75	-17	-123
	3	ϵ_{max}	207	390	281	440	348	388	351	270
		ϵ_{min}	-198	-246	-225	-196	-276	-200	-136	-265
	4	ϵ_{max}	766	943	709	952	919	751	702	769
		ϵ_{min}	-388	-496	-463	-380	-591	-462	-309	-485
	5	ϵ_{max}	593	764	631	815	770	626	637	638
		ϵ_{min}	-376	-430	-403	-368	-526	-379	-267	-444
	6	ϵ_{max}	337	533	185	387	419	246	256	329
		ϵ_{min}	-192	-193	-266	-196	-193	-272	-160	-206
	8	ϵ_{max}	391	580	477	637	532	561	500	436
		ϵ_{min}	-310	-377	-314	-261	-407	-313	-196	-366
	9a	ϵ_{max}	**18790**	372	84	250	247	234	185	121
		ϵ_{min}	**16353**	-234	-243	-267	-258	-194	-184	-259
	9	ϵ_{max}	**21441**	764	500	755	699	507	595	484
		ϵ_{min}	**15401**	-490	-439	-511	-567	-379	-350	-444
	10	ϵ_{max}	**19598**	753	530	773	681	626	559	549
		ϵ_{min}	**14528**	-490	-469	-374	-561	-390	-326	-491
	11	ϵ_{max}	**20359**	764	530	773	746	626	565	603
		ϵ_{min}	**14450**	-496	-486	-374	-579	-390	-344	-497
High Amplitude Testing	12	ϵ_{max}	754	1103	726	999	1014	810	720	840
		ϵ_{min}	-744	-567	-581	-523	-698	-521	-422	-592
	13	ϵ_{max}	**2436**	**2863**	1820	2135	**2756**	1750	1802	2124
		ϵ_{min}	-1339	-1067	-1146	-951	-1382	-1027	-808	-1074
	14	ϵ_{max}	**5848**	**6222**	**3253**	**3692**	**5782**	**3277**	**4067**	**3676**
		ϵ_{min}	-1749	-1940	-1693	-1087	-2202	-1151	-766	-1573
	15	ϵ_{max}	**32534**	**22076**	**13401**	**11218**	**26939**	**11107**	**12752**	**12789**
		ϵ_{min}	**-3229**	**-4378**	**-3274**	-2229	**-5175**	-1330	-873	**-2774**
	16	ϵ_{max}	**80163**	**24181**	**189157**	**190291**	**29792**	**19834**	**24344**	**15375**
		ϵ_{min}	-2254	**-7273**	**-25751**	**-3418**	**-4747**	305	1178	**-4112**
	17	ϵ_{max}	**62543**	**22635**	**189157**	**190291**	**27741**	**13693**	**16782**	**14293**
		ϵ_{min}	**7037**	**-3278**	**-22458**	**-16490**	-573	1446	**2705**	-2019
	18	ϵ_{max}	**191383**	**47698**	**189157**	**190291**	**54499**	**20856**	**37993**	**33138**
		ϵ_{min}	534	**-7279**	**-30804**	**-11978**	**-8533**	234	1992	**-3321**
	19	ϵ_{max}	**191383**	**82695**	**189157**	**190291**	**32985**	**9882**	**26817**	**49034**
		ϵ_{min}	**19396**	**2809**	**-200431**	**-33795**	**9426**	**3034**	1873	1803
	20	ϵ_{max}	**191383**	**73005**	**189157**	**190291**	**13670**	**7790**	**23262**	**39184**
		ϵ_{min}	**191383**	**61008**	**-200431**	**-5142**	**13236**	**4567**	**13013**	**26331**
Post-Tests	21	ϵ_{max}	**191383**	**70520**	**189157**	**190291**	**13658**	**190287**	**28785**	**32098**
		ϵ_{min}	**191383**	**61335**	**-200431**	**10695**	**13254**	**4990**	**11462**	**27170**
	22	ϵ_{max}	**191383**	**69997**	**189157**	**190291**	**13688**	**190287**	**27756**	**189336**
		ϵ_{min}	**191383**	**63303**	**189157**	**4227**	**13308**	**190287**	**10808**	**30505**

Table 6-22: Maximum and minimum strains for all tests (microstrain).

	Strain Gauge		3EBSL3	3EBSL4	3EBSL5	3EBSL6	3EBSL7	3EBSL8	3EBSL9	3EBSL10
Low Amplitude Testing	1a	ϵ_{max}	17	311	412	19	388	160	52	56
		ϵ_{min}	-42	-153	-224	-29	-314	-55	-25	-68
	1	ϵ_{max}	107	721	864	31	875	326	88	92
		ϵ_{min}	-48	-254	-343	-29	-551	-84	-49	-128
	2a	ϵ_{max}	53	376	466	31	804	249	70	92
		ϵ_{min}	-36	-218	-319	-29	-355	-43	-49	-86
	2	ϵ_{max}	416	1096	1179	72	1856	724	159	235
		ϵ_{min}	-48	-373	-563	-29	-724	-66	-210	-181
	3a	ϵ_{max}	17	115	73	31	114	76	4	15
		ϵ_{min}	-30	-46	-99	-5	-94	-43	-67	-45
	3	ϵ_{max}	53	287	275	37	334	189	58	39
		ϵ_{min}	-36	-123	-165	-5	-248	-96	-132	-98
	4	ϵ_{max}	160	775	840	66	929	385	123	140
		ϵ_{min}	-6	-242	-325	1	-545	-72	-174	-169
	5	ϵ_{max}	148	697	727	60	768	320	111	128
		ϵ_{min}	-6	-224	-289	1	-486	-96	-162	-152
	6	ϵ_{max}	59	228	162	48	370	100	46	56
		ϵ_{min}	0	-123	-182	1	-183	-96	-138	-92
	8	ϵ_{max}	118	507	501	54	483	189	88	80
		ϵ_{min}	5	-159	-224	1	-385	-120	-150	-134
	9a	ϵ_{max}	219	139	73	-17	186	486	16	-45
		ϵ_{min}	-244	-206	-236	-59	-195	-370	-162	-140
	9	ϵ_{max}	856	531	584	-11	602	1021	76	50
		ϵ_{min}	-387	-367	-385	-64	-433	-613	-216	-193
	10	ϵ_{max}	71	555	549	-5	643	142	76	68
		ϵ_{min}	-90	-266	-373	-53	-510	-167	-198	-211
	11	ϵ_{max}	107	543	561	1	703	142	88	80
		ϵ_{min}	-90	-266	-385	-59	-504	-162	-210	-217
High Amplitude Testing	12	ϵ_{max}	148	787	822	13	1071	385	117	134
		ϵ_{min}	-107	-337	-444	-47	-623	-167	-228	-241
	13	ϵ_{max}	772	1863	1964	54	**3223**	1283	385	544
		ϵ_{min}	-155	-557	-795	-47	-1069	-328	-364	-538
	14	ϵ_{max}	1509	**3759**	**3527**	108	**8419**	2103	765	1091
		ϵ_{min}	-173	-498	-759	-35	-1895	-286	-531	-746
	15	ϵ_{max}	**6658**	**19833**	**9496**	352	**30754**	**11353**	1187	1733
		ϵ_{min}	-107	-236	-1128	-35	**-4790**	-173	-834	-966
	16	ϵ_{max}	**39693**	**24030**	**18347**	768	**34190**	**12959**	1413	1852
		ϵ_{min}	**-200195**	691	**-12393**	108	**-13422**	**3726**	-899	-1174
	17	ϵ_{max}	**59269**	**5257**	1559	708	**30878**	**11015**	1300	1810
		ϵ_{min}	**-200195**	341	**-10098**	150	**-5557**	**5088**	-899	-1133
	18	ϵ_{max}	**57640**	**15654**	**2944**	1428	**49658**	**24699**	1615	2232
		ϵ_{min}	**-200195**	-1021	**-15484**	54	**-41885**	**5082**	-977	-1454
	19	ϵ_{max}	**189393**	**10257**	**6547**	756	**191594**	**17619**	1496	**2678**
		ϵ_{min}	**-200195**	**-3399**	**-2489**	-2145	**-48050**	1283	-1089	-1358
	20	ϵ_{max}	**189393**	**6690**	**5007**	-1497	**191594**	**42956**	950	1317
		ϵ_{min}	**-200195**	**-10776**	168	**-3263**	**191594**	**-200606**	-679	-389
Post-Tests	21	ϵ_{max}	**189393**	**189793**	**7623**	-1355	**191594**	**188982**	1294	550
		ϵ_{min}	**-200195**	**-24021**	**-3286**	**-3756**	**191594**	**-200606**	-650	3
	22	ϵ_{max}	**189393**	**189793**	**5554**	**189578**	**191594**	**188982**	908	336
		ϵ_{min}	**-200195**	**-136257**	**-3850**	**-3394**	**191594**	**188982**	-519	128

Table 6-23: Maximum and minimum strains for all tests (microstrain).

	Strain Gauge		1WTSH 1	1WTSH 2	1WTSH 3	1WTSH 4	1WBSH 1	1WBSH 2	1WBSH 3	1WBSH 4
Low Amplitude Testing	1a	ϵ_{max}	45	30	30	38	30	15	30	23
		ϵ_{min}	-23	-23	-30	-23	-23	-38	-23	-30
	1	ϵ_{max}	45	38	38	38	38	23	30	30
		ϵ_{min}	-23	-15	-30	-15	-23	-30	-15	-23
	2a	ϵ_{max}	38	38	30	45	38	23	38	23
		ϵ_{min}	-15	-15	-23	-15	-23	-30	-15	-30
	2	ϵ_{max}	53	38	45	45	38	23	38	30
		ϵ_{min}	-30	-15	-23	-8	-23	-38	-15	-30
	3a	ϵ_{max}	45	45	38	53	30	23	38	30
		ϵ_{min}	-23	-8	-15	-15	-23	-30	-15	-23
	3	ϵ_{max}	68	45	45	60	38	30	45	45
		ϵ_{min}	-23	-8	-23	0	-15	-23	-8	-23
	4	ϵ_{max}	60	53	45	53	45	30	45	38
		ϵ_{min}	-15	0	-8	0	-15	-23	-8	-15
	5	ϵ_{max}	68	53	53	60	45	38	45	38
		ϵ_{min}	-15	0	-8	0	-15	-15	-15	-15
	6	ϵ_{max}	68	53	45	60	38	38	45	38
		ϵ_{min}	-15	0	-8	0	-8	-15	-8	-23
	8	ϵ_{max}	68	60	53	53	45	30	45	45
		ϵ_{min}	-8	0	0	8	-15	-15	0	-15
	9a	ϵ_{max}	23	8	-8	8	-8	-23	-8	-23
		ϵ_{min}	-45	-45	-68	-53	-68	-83	-60	-75
	9	ϵ_{max}	30	30	0	23	15	-15	8	-8
		ϵ_{min}	-60	-38	-68	-53	-68	-83	-53	-75
	10	ϵ_{max}	45	23	15	15	8	-15	8	-15
		ϵ_{min}	-53	-38	-60	-45	-53	-75	-53	-75
	11	ϵ_{max}	45	23	8	15	0	-15	8	-8
		ϵ_{min}	-45	-38	-60	-38	-68	-75	-45	-68
High Amplitude Testing	12	ϵ_{max}	60	38	23	30	23	-23	8	0
		ϵ_{min}	-53	-30	-75	-38	-60	-83	-45	-68
	13	ϵ_{max}	68	75	136	60	68	121	53	106
		ϵ_{min}	-45	-30	-75	-45	-53	-83	-45	-60
	14	ϵ_{max}	98	53	136	76	174	181	75	189
		ϵ_{min}	-38	-45	-30	-38	-15	-60	0	-23
	15	ϵ_{max}	158	83	166	76	506	279	317	340
		ϵ_{min}	-68	-75	8	-15	38	-23	15	23
	16	ϵ_{max}	226	151	490	68	800	498	385	875
		ϵ_{min}	-174	-174	-136	-53	68	60	45	189
	17	ϵ_{max}	0	106	302	45	491	332	302	717
		ϵ_{min}	-189	-174	-151	-45	91	91	38	204
	18	ϵ_{max}	189	143	324	76	1155	649	626	898
		ϵ_{min}	-204	-242	-158	-60	60	15	60	196
	19	ϵ_{max}	196	347	702	174	1079	694	717	1155
		ϵ_{min}	-279	-287	-204	-83	23	-15	-8	189
	20	ϵ_{max}	30	234	324	121	845	603	513	762
		ϵ_{min}	-272	-249	-196	-60	23	8	-8	211
Post-Tests	21	ϵ_{max}	174	332	438	166	1162	717	981	921
		ϵ_{min}	-302	-249	-219	-53	38	23	0	219
	22	ϵ_{max}	143	430	604	295	642	520	619	1230
		ϵ_{min}	-279	-317	-211	-45	15	8	-15	219

Table 6-24: Maximum and minimum strains for all tests (microstrain).

	Strain Gauge		1WBSH5	1WBSH6	1ETSH3	1ETSH4	1EBSH1	1EBSH2	1EBSH3	1EBSH4
Low Amplitude Testing	1a	ϵ_{max}	15	45	23	15	30	30	15	30
		ϵ_{min}	-30	-15	-38	-45	-23	-30	-45	-23
	1	ϵ_{max}	23	53	23	15	38	38	15	45
		ϵ_{min}	-30	-23	-30	-38	-23	-23	-38	-8
	2a	ϵ_{max}	15	38	30	15	38	38	15	45
		ϵ_{min}	-30	-8	-30	-30	-15	-23	-38	-8
	2	ϵ_{max}	23	53	30	23	45	38	23	45
		ϵ_{min}	-30	-15	-30	-30	-23	-15	-38	-8
	3a	ϵ_{max}	23	45	23	23	38	38	15	45
		ϵ_{min}	-30	-8	-23	-23	-15	-15	-30	-8
	3	ϵ_{max}	30	68	38	30	53	53	23	60
		ϵ_{min}	-30	-8	-15	-30	-23	-15	-38	8
	4	ϵ_{max}	30	68	38	38	53	45	30	60
		ϵ_{min}	-23	8	-15	-23	-8	-8	-30	8
	5	ϵ_{max}	30	60	45	30	45	53	23	60
		ϵ_{min}	-23	8	-15	-15	-8	0	-23	8
	6	ϵ_{max}	38	68	45	30	53	53	30	68
		ϵ_{min}	-23	8	-8	-23	-8	0	-23	15
	8	ϵ_{max}	30	68	38	30	53	53	30	60
		ϵ_{min}	-23	8	-15	-15	-8	0	-30	8
	9a	ϵ_{max}	-15	8	-15	-23	8	-8	-30	15
		ϵ_{min}	-75	-53	-68	-83	-60	-60	-83	-45
	9	ϵ_{max}	-8	23	-15	-8	45	0	15	15
		ϵ_{min}	-68	-45	-68	-91	-75	-60	-75	-38
	10	ϵ_{max}	-8	23	-8	-23	23	0	-8	23
		ϵ_{min}	-60	-38	-60	-75	-45	-60	-60	-38
	11	ϵ_{max}	0	15	-8	-23	23	0	-8	23
		ϵ_{min}	-60	-38	-60	-75	-53	-53	-60	-38
High Amplitude Testing	12	ϵ_{max}	0	38	-8	-23	53	8	0	53
		ϵ_{min}	-60	-30	-60	-75	-60	-60	-68	-23
	13	ϵ_{max}	189	113	91	53	151	30	68	128
		ϵ_{min}	-53	-30	-53	-75	-75	-45	-53	-23
	14	ϵ_{max}	204	151	173	106	151	121	143	158
		ϵ_{min}	0	-8	-23	-38	-83	-8	-15	0
	15	ϵ_{max}	189	392	279	309	256	196	294	249
		ϵ_{min}	23	-15	-8	0	-53	23	15	23
	16	ϵ_{max}	166	724	362	445	611	362	1071	777
		ϵ_{min}	-166	-91	-23	8	-60	-15	38	-15
	17	ϵ_{max}	106	468	226	362	513	294	709	634
		ϵ_{min}	-128	-53	-30	91	-68	-8	83	60
	18	ϵ_{max}	151	1343	219	460	648	385	754	769
		ϵ_{min}	-204	-38	-60	98	-90	-91	75	-38
	19	ϵ_{max}	166	1471	415	513	1146	535	837	1418
		ϵ_{min}	-340	-83	-60	68	-128	-106	-38	-8
	20	ϵ_{max}	113	1207	219	385	603	430	679	762
		ϵ_{min}	-196	23	-60	75	-90	-106	-38	38
Post-Tests	21	ϵ_{max}	121	1592	249	438	791	566	965	965
		ϵ_{min}	-226	-8	-106	106	-98	-91	-38	30
	22	ϵ_{max}	98	1117	385	528	1146	460	988	1395
		ϵ_{min}	-332	-23	-68	91	-83	-113	-30	8

Table 6-25: Maximum and minimum strains for all tests (microstrain).

	Strain Gauge		1EBSH5	1EBSH6	2WTSH 1	2WTSH 2	2WTSH 3	2WBSH 1	2WBSH 2	2WBSH 3
Low Amplitude Testing	1a	ϵ_{max}	8	30	25	25	40	31	45	36
		ϵ_{min}	-53	-38	-4	-17	5	-11	0	0
	1	ϵ_{max}	15	38	25	25	46	37	53	42
		ϵ_{min}	-60	-45	-10	-17	5	1	0	6
	2a	ϵ_{max}	15	30	31	25	40	37	60	42
		ϵ_{min}	-45	-30	-4	-17	5	1	0	6
	2	ϵ_{max}	15	45	25	31	46	37	53	48
		ϵ_{min}	-68	-30	-4	-17	11	1	8	0
	3a	ϵ_{max}	23	38	25	31	46	43	60	48
		ϵ_{min}	-45	-23	-10	-11	11	1	15	12
	3	ϵ_{max}	23	68	43	31	58	43	60	42
		ϵ_{min}	-60	-15	7	-11	17	7	15	6
	4	ϵ_{max}	23	60	43	37	58	49	68	48
		ϵ_{min}	-45	-8	7	1	22	13	8	12
	5	ϵ_{max}	30	60	43	42	58	49	75	48
		ϵ_{min}	-38	-8	7	1	22	13	15	12
	6	ϵ_{max}	30	60	43	37	58	49	68	54
		ϵ_{min}	-38	-8	7	7	17	19	15	12
	8	ϵ_{max}	23	68	43	37	58	55	75	48
		ϵ_{min}	-45	-8	13	1	22	19	23	12
	9a	ϵ_{max}	-23	8	7	13	11	-17	8	-6
		ϵ_{min}	-90	-53	-34	-65	-25	-52	-38	-41
	9	ϵ_{max}	-15	15	7	54	22	-11	15	6
		ϵ_{min}	-106	-60	-28	-76	-19	-46	-45	-35
	10	ϵ_{max}	-23	15	13	1	22	-5	15	12
		ϵ_{min}	-90	-53	-28	-47	-19	-40	-38	-29
	11	ϵ_{max}	-23	23	13	7	22	-5	23	12
		ϵ_{min}	-98	-60	-28	-47	-19	-40	-45	-29
High Amplitude Testing	12	ϵ_{max}	-8	30	13	19	-1	1	23	12
		ϵ_{min}	-113	-53	-22	-47	-37	-34	-30	-23
	13	ϵ_{max}	45	189	13	78	22	1	30	54
		ϵ_{min}	-90	-38	-28	-65	-37	-34	-38	-23
	14	ϵ_{max}	121	272	25	120	34	13	38	60
		ϵ_{min}	-45	-38	-22	-71	-25	-28	-30	12
	15	ϵ_{max}	181	309	67	155	88	37	98	131
		ϵ_{min}	-8	-23	-10	-76	-1	-17	-23	24
	16	ϵ_{max}	302	551	156	144	106	67	143	137
		ϵ_{min}	-38	83	13	-53	-85	1	-15	-1730
	17	ϵ_{max}	219	498	91	102	94	84	166	-41
		ϵ_{min}	15	189	-10	-5	-61	25	8	-1854
	18	ϵ_{max}	249	649	144	209	100	275	340	84
		ϵ_{min}	-181	121	-177	-47	-221	25	-8	-1866
	19	ϵ_{max}	317	528	162	245	52	661	453	-101
		ϵ_{min}	-234	-294	-195	-23	-209	-17	-23	-1522
	20	ϵ_{max}	173	294	114	173	11	530	332	-166
		ϵ_{min}	-136	-173	-177	-11	-203	1	-15	-1474
Post-Tests	21	ϵ_{max}	241	332	103	185	22	536	324	-95
		ϵ_{min}	-256	-106	-189	-23	-209	25	-8	-1468
	22	ϵ_{max}	309	324	221	304	22	899	672	-77
		ϵ_{min}	-166	-302	-320	-35	-465	-58	15	-1420

Table 6-26: Maximum and minimum strains for all tests (microstrain).

	Strain Gauge		2ETSH1	2ETSH2	2ETSH3	2EBSH1	2EBSH2	2EBSH3	3WTSH 1	3WTSH 2
Low Amplitude Testing	1a	ϵ_{max}	134	80	89	134	125	143	30	-154
		ϵ_{min}	-107	-125	-125	-71	-89	-98	-6	-219
	1	ϵ_{max}	134	89	98	134	134	152	30	-154
		ϵ_{min}	-107	-125	-143	-71	-98	-80	-12	-219
	2a	ϵ_{max}	107	98	116	143	116	161	30	-154
		ϵ_{min}	-116	-134	-116	-80	-89	-98	-6	-219
	2	ϵ_{max}	125	125	98	161	116	134	42	25
		ϵ_{min}	-89	-134	-107	-71	-98	-89	-6	-290
	3a	ϵ_{max}	125	125	116	152	107	152	30	-171
		ϵ_{min}	-98	-125	-125	-89	-98	-89	-6	-290
	3	ϵ_{max}	125	98	107	143	143	143	36	-154
		ϵ_{min}	-89	-116	-134	-62	-107	-80	-6	-290
	4	ϵ_{max}	134	98	125	152	134	161	36	-154
		ϵ_{min}	-80	-116	-125	-62	-71	-89	-6	-290
	5	ϵ_{max}	125	134	107	134	125	161	42	-154
		ϵ_{min}	-80	-107	-107	-45	-89	-80	-6	-290
	6	ϵ_{max}	125	107	107	152	134	161	30	-166
		ϵ_{min}	-89	-125	-107	-80	-80	-89	-6	-290
	8	ϵ_{max}	134	116	116	178	125	169	36	-154
		ϵ_{min}	-80	-125	-107	-71	-71	-62	-6	-290
	9a	ϵ_{max}	98	80	80	89	80	98	0	-201
		ϵ_{min}	-134	-152	-125	-134	-125	-169	-42	-320
	9	ϵ_{max}	89	80	89	71	80	125	12	-154
		ϵ_{min}	-116	-169	-143	-125	-143	-116	-54	-290
	10	ϵ_{max}	98	80	80	107	125	116	12	-154
		ϵ_{min}	-125	-143	-143	-125	-134	-125	-30	-290
	11	ϵ_{max}	107	80	98	98	98	116	6	-154
		ϵ_{min}	-116	-152	-125	-125	-107	-134	-30	-290
High Amplitude Testing	12	ϵ_{max}	107	107	98	107	134	107	18	417
		ϵ_{min}	-116	-152	-125	-134	-116	-116	-30	-219
	13	ϵ_{max}	116	98	107	98	107	116	48	**2884**
		ϵ_{min}	-125	-152	-161	-125	-134	-125	-36	-219
	14	ϵ_{max}	125	98	116	98	80	125	59	**4418**
		ϵ_{min}	-125	-178	-125	-116	-143	-98	-12	-219
	15	ϵ_{max}	152	89	152	134	107	178	297	1683
		ϵ_{min}	-98	-152	-98	-98	-125	-80	-77	-219
	16	ϵ_{max}	214	80	161	214	98	303	589	1160
		ϵ_{min}	-54	-178	-80	-62	-1400	-54	-196	-142
	17	ϵ_{max}	223	80	143	223	-589	232	369	554
		ϵ_{min}	9	-161	-107	-71	-1409	-18	-214	-160
	18	ϵ_{max}	205	125	125	473	-624	303	868	1505
		ϵ_{min}	-80	-196	-134	-125	**-5306**	-54	-226	-273
	19	ϵ_{max}	152	241	143	339	-71	250	1034	**4792**
		ϵ_{min}	-285	-232	-169	-178	**-4236**	-98	-279	-1842
	20	ϵ_{max}	18	187	107	223	285	187	755	**19428**
		ϵ_{min}	-276	-276	-152	-169	**-2658**	-107	-375	**-5926**
Post-Tests	21	ϵ_{max}	18	161	98	241	259	205	654	**22662**
		ϵ_{min}	-285	-214	-152	-187	**-2559**	-89	-577	-1360
	22	ϵ_{max}	36	606	**255188**	259	312	285	-42	**187415**
		ϵ_{min}	-428	-187	-223	-223	**-2881**	-125	-1153	**-11425**

Table 6-27: Maximum and minimum strains for all tests (microstrain).

	Strain Gauge		3WTSH 3	3WTSH 4	3WTSH 6	3WTSH 7	3WBSH 1	3WBSH 2	3WBSH 3	3WBSH 4
Low Amplitude Testing	1a	ϵ_{max}	28	43	56	45	29	20	-1	27
		ϵ_{min}	-14	8	-4	9	-6	-16	-36	-3
	1	ϵ_{max}	28	49	56	45	24	20	-1	27
		ϵ_{min}	-14	8	-4	3	-6	-16	-36	-9
	2a	ϵ_{max}	34	43	56	45	24	20	-1	27
		ϵ_{min}	-14	8	-4	3	-6	-16	-36	-9
	2	ϵ_{max}	28	55	62	45	29	20	-1	21
		ϵ_{min}	-14	14	-4	3	-6	-21	-36	-15
	3a	ϵ_{max}	34	49	56	45	35	20	-1	27
		ϵ_{min}	-8	20	-4	9	-6	-16	-36	-9
	3	ϵ_{max}	34	26	44	27	18	32	23	27
		ϵ_{min}	-8	-10	-4	-15	-18	-10	-13	-9
	4	ϵ_{max}	40	32	50	27	24	32	23	27
		ϵ_{min}	-2	-4	-4	-9	-18	-4	-7	-3
	5	ϵ_{max}	40	32	50	27	24	38	29	33
		ϵ_{min}	4	-4	-4	-3	-6	-4	-7	-3
	6	ϵ_{max}	40	32	50	33	24	32	23	27
		ϵ_{min}	-2	-4	-4	-3	-18	-4	-7	-3
	8	ϵ_{max}	40	32	50	33	24	38	29	27
		ϵ_{min}	4	2	-4	-3	-12	-4	-7	-3
	9a	ϵ_{max}	4	20	62	15	0	-16	-36	21
		ϵ_{min}	-37	-22	-4	-26	-36	-51	-84	-21
	9	ϵ_{max}	4	20	62	27	6	2	-30	27
		ϵ_{min}	-37	-22	-4	-26	-36	-45	-78	-27
	10	ϵ_{max}	16	20	14	27	6	-4	-36	27
		ϵ_{min}	-26	-16	-4	-15	-30	-39	-66	-3
	11	ϵ_{max}	16	26	44	21	12	-4	-36	27
		ϵ_{min}	-20	-10	-4	-9	-24	-45	-66	-3
High Amplitude Testing	12	ϵ_{max}	16	49	50	63	12	2	-19	-9
		ϵ_{min}	-26	8	-4	21	-24	-39	-54	-45
	13	ϵ_{max}	22	61	73	63	12	14	-19	3
		ϵ_{min}	-32	20	-4	21	-24	-45	-60	-68
	14	ϵ_{max}	34	91	192	176	107	62	71	39
		ϵ_{min}	-37	26	-4	33	-18	-63	-54	-51
	15	ϵ_{max}	28	323	204	306	362	198	326	122
		ϵ_{min}	-251	49	-75	15	12	-87	-143	-74
	16	ϵ_{max}	-91	531	817	408	452	549	392	318
		ϵ_{min}	-513	67	-123	-68	0	-230	-239	-193
	17	ϵ_{max}	-144	507	834	390	452	424	350	193
		ϵ_{min}	-489	49	-75	-62	12	-230	-244	-152
	18	ϵ_{max}	248	1137	2154	544	624	1780	1141	377
		ϵ_{min}	-727	-64	-63	-98	-101	-265	-292	-294
	19	ϵ_{max}	**188256**	709	1595	544	582	1506	1075	805
		ϵ_{min}	**-201332**	-1526	127	-199	-137	151	-203	-2167
	20	ϵ_{max}	**188256**	-807	**188771**	259	178	823	404	**189313**
		ϵ_{min}	**-201332**	-2031	**-20656**	-104	-83	335	-114	**-25001**
Post-Tests	21	ϵ_{max}	**188256**	-670	**188771**	140	214	953	368	**189313**
		ϵ_{min}	**188256**	-1835	**-41225**	-145	-89	216	-137	**189313**
	22	ϵ_{max}	**188256**	376	**188771**	122	184	769	190	**189313**
		ϵ_{min}	**188256**	**-2780**	**188771**	-110	-54	222	-78	**189313**

Table 6-28: Maximum and minimum strains for all tests (microstrain).

	Strain Gauge		3WBSH 5	3WBSH 6	3WBSH 7	3ETSH1	3ETSH2	3ETSH3	3ETSH4	3ETSH5
Low Amplitude Testing	1a	ϵ_{max}	-56	29	17	9	32	34	47	55
		ϵ_{min}	-103	-6	-19	-98	-28	-8	-90	14
	1	ϵ_{max}	-61	29	23	9	61	51	-54	61
		ϵ_{min}	-145	-1	-13	-80	-28	-8	-90	2
	2a	ϵ_{max}	-73	35	23	9	32	51	-54	61
		ϵ_{min}	-145	-6	-13	-80	-28	-8	-96	8
	2	ϵ_{max}	-61	53	41	9	55	75	-54	61
		ϵ_{min}	-180	-18	-13	-80	-40	-8	-96	2
	3a	ϵ_{max}	-97	29	29	9	20	40	-54	61
		ϵ_{min}	-133	-1	-7	-80	-22	4	-96	26
	3	ϵ_{max}	28	17	35	39	32	34	65	32
		ϵ_{min}	-26	-18	-1	-80	-28	-8	-66	-16
	4	ϵ_{max}	16	29	41	39	43	57	65	32
		ϵ_{min}	-50	-18	11	-80	-34	-2	-60	-16
	5	ϵ_{max}	10	29	47	39	55	51	65	38
		ϵ_{min}	-56	-12	11	-80	-28	-2	-66	-22
	6	ϵ_{max}	-8	23	41	39	32	45	65	32
		ϵ_{min}	-56	-12	11	-80	-28	-2	-60	-10
	8	ϵ_{max}	-2	23	47	39	38	51	65	38
		ϵ_{min}	-61	-12	11	-80	-28	-2	-60	-16
	9a	ϵ_{max}	10	-6	-13	-3	-28	4	-78	26
		ϵ_{min}	-26	-36	-42	-134	-69	-44	-132	-10
	9	ϵ_{max}	4	5	-7	-3	-4	22	-72	44
		ϵ_{min}	-50	-30	-42	-140	-87	-38	-144	-10
	10	ϵ_{max}	-2	11	-1	3	8	22	-78	38
		ϵ_{min}	-56	-30	-42	-128	-75	-38	-126	-10
	11	ϵ_{max}	-8	11	5	3	8	28	-78	44
		ϵ_{min}	-73	-30	-36	-128	-75	-32	-126	-10
High Amplitude Testing	12	ϵ_{max}	-14	29	11	9	8	45	-78	67
		ϵ_{min}	-91	-24	-36	-116	-87	-20	-138	2
	13	ϵ_{max}	-2	47	23	9	55	87	47	145
		ϵ_{min}	-91	-36	-36	-116	-99	-20	-144	14
	14	ϵ_{max}	-2	89	88	56	85	242	100	234
		ϵ_{min}	-103	-36	-19	-92	-99	-2	-144	55
	15	ϵ_{max}	99	630	433	247	269	432	94	412
		ϵ_{min}	-127	17	11	-152	-46	51	-334	55
	16	ϵ_{max}	206	695	719	639	460	468	59	632
		ϵ_{min}	-79	-6	106	-140	61	-50	-476	-4
	17	ϵ_{max}	141	665	659	431	347	313	-84	489
		ϵ_{min}	-61	17	118	-104	91	-56	-405	-4
	18	ϵ_{max}	890	1022	1129	1002	662	1032	-90	935
		ϵ_{min}	-56	-6	136	-104	55	-525	-887	-46
	19	ϵ_{max}	1460	**6408**	1057	1953	798	343	493	947
		ϵ_{min}	-983	-298	-1564	-9	-200	**-3111**	-1083	-34
	20	ϵ_{max}	164	**4654**	-357	2149	222	-977	-453	620
		ϵ_{min}	-1363	**3971**	**-2664**	-265	-254	**-3545**	-1095	-10
Post-Tests	21	ϵ_{max}	2126	**4446**	-381	**2910**	204	-1304	-506	656
		ϵ_{min}	-1435	**3661**	**-3193**	270	-515	**-3284**	-1606	-46
	22	ϵ_{max}	**188071**	**4060**	-506	**3879**	257	**188006**	53	531
		ϵ_{min}	-1821	**3376**	**-3930**	574	-438	**-3278**	**-2426**	-10

Table 6-29: Maximum and minimum strains for all tests (microstrain).

	Strain Gauge		3ETSH6	3ETSH7	3EBSH2	3EBSH3	3EBSH4	3EBSH5	3EBSH6	3EBSH7
Low Amplitude Testing	1a	ϵ_{max}	32	49	37	18	-9	301	60	27
		ϵ_{min}	-4	8	2	-17	-50	-264	-71	-14
	1	ϵ_{max}	32	49	43	24	-9	735	60	45
		ϵ_{min}	-4	8	8	-11	-50	-436	-71	-9
	2a	ϵ_{max}	32	49	43	24	-15	640	60	51
		ϵ_{min}	-4	20	8	-11	-50	-270	-71	-3
	2	ϵ_{max}	32	61	43	30	-15	1544	60	104
		ϵ_{min}	-4	8	2	-5	-62	-537	-71	-3
	3a	ϵ_{max}	32	49	43	36	-15	69	60	75
		ϵ_{min}	-4	20	14	1	-50	-127	-71	39
	3	ϵ_{max}	20	37	20	30	3	277	102	81
		ϵ_{min}	-16	-4	-16	-5	-32	-204	-23	39
	4	ϵ_{max}	26	37	20	36	3	812	102	110
		ϵ_{min}	-10	2	-10	-5	-32	-406	-23	45
	5	ϵ_{max}	26	37	26	30	-3	640	102	98
		ϵ_{min}	-10	-4	-10	1	-38	-377	-23	45
	6	ϵ_{max}	26	37	26	36	-3	260	102	81
		ϵ_{min}	-10	-4	-4	1	-32	-186	-23	45
	8	ϵ_{max}	32	49	26	36	-3	372	102	87
		ϵ_{min}	-10	8	-10	1	-32	-317	-23	51
	9a	ϵ_{max}	-10	2	-4	-23	-38	236	-59	39
		ϵ_{min}	-52	-40	-40	-53	-74	-281	-95	3
	9	ϵ_{max}	-4	8	8	1	-20	717	42	63
		ϵ_{min}	-46	-28	-46	-47	-80	-489	-95	3
	10	ϵ_{max}	-4	14	8	1	-38	474	42	69
		ϵ_{min}	-40	-28	-34	-35	-74	-424	-95	15
	11	ϵ_{max}	-4	14	8	6	-38	515	42	63
		ϵ_{min}	-40	-28	-28	-29	-74	-406	-95	15
High Amplitude Testing	12	ϵ_{max}	2	25	8	6	-38	884	-59	93
		ϵ_{min}	-28	-16	-40	-35	-74	-460	-95	21
	13	ϵ_{max}	20	37	14	12	9	**2524**	42	229
		ϵ_{min}	-22	-16	-52	-35	-74	-763	-95	21
	14	ϵ_{max}	192	121	67	90	87	**5039**	60	241
		ϵ_{min}	-16	-4	-28	-11	-62	-1072	-95	39
	15	ϵ_{max}	412	418	353	161	390	**17095**	108	598
		ϵ_{min}	8	14	20	-35	-50	-602	-71	69
	16	ϵ_{max}	477	465	412	226	396	**19604**	286	758
		ϵ_{min}	-64	-4	-147	-190	-217	**-4062**	-142	75
	17	ϵ_{max}	471	453	234	179	253	**16548**	108	592
		ϵ_{min}	-70	-4	-177	-178	-199	**-3242**	-148	69
	18	ϵ_{max}	763	644	662	250	562	**190069**	429	830
		ϵ_{min}	-295	-40	-266	-451	-401	**-24780**	-481	-240
	19	ϵ_{max}	929	691	971	333	**187667**	**190069**	1053	592
		ϵ_{min}	-373	-76	-248	-606	**-33584**	**-18347**	-517	**-3629**
	20	ϵ_{max}	192	370	424	84	**187667**	**190069**	476	**188029**
		ϵ_{min}	-301	-46	-46	-356	**-201921**	**190069**	-659	-234
Post-Tests	21	ϵ_{max}	198	335	347	36	**187667**	**190069**	863	**188029**
		ϵ_{min}	-325	-46	-183	-475	**-201921**	**190069**	-1860	**188029**
	22	ϵ_{max}	168	287	412	42	**187667**	**190069**	**188247**	**188029**
		ϵ_{min}	-307	-22	-105	-439	**-201921**	**190069**	**188247**	**188029**

Table 6-30: Column curvature envelopes.

	Location		Bent 1 top west column, trans. direction at 2.5in (64mm) from fixity		Bent 1 top west column, trans. direction at 8.5in (216mm) from fixity		Bent 1 top west column, long. direction at 2.5in (64mm) from fixity		Bent 1 bottom west column, trans. direction at 2.5in (64mm) from fixity	
	Gauge length		5in	127mm	7in	178mm	5in	127mm	5in	127mm
	Unit		rad/in	rad/mm	rad/in	rad/mm	rad/in	rad/mm	rad/in	rad/mm
Low Amplitude Testing	1a	max	1.3E-04	5.1E-06	3.7E-05	1.5E-06	1.4E-05	5.6E-07	8.7E-05	3.4E-06
		min	-6.2E-05	-2.5E-06	-4.6E-05	-1.8E-06	1.7E-06	6.6E-08	-1.4E-04	-5.5E-06
	1b	max	2.1E-04	8.4E-06	7.6E-05	3.0E-06	2.1E-05	8.3E-07	1.5E-04	6.0E-06
		min	-1.1E-04	-4.2E-06	-7.5E-05	-2.9E-06	-3.2E-06	-1.2E-07	-2.3E-04	-8.9E-06
	2a	max	9.0E-05	3.5E-06	2.5E-05	9.8E-07	1.6E-05	6.4E-07	7.1E-05	2.8E-06
		min	-5.1E-05	-2.0E-06	-3.7E-05	-1.5E-06	7.4E-07	2.9E-08	-8.9E-05	-3.5E-06
	2b	max	1.7E-04	6.5E-06	5.3E-05	2.1E-06	2.4E-05	9.4E-07	1.8E-04	7.2E-06
		min	-1.3E-04	-5.1E-06	-9.2E-05	-3.6E-06	-8.0E-06	-3.1E-07	-1.8E-04	-7.0E-06
	3a	max	1.0E-04	4.1E-06	3.3E-05	1.3E-06	1.4E-05	5.6E-07	9.5E-05	3.7E-06
		min	-7.1E-05	-2.8E-06	-4.9E-05	-1.9E-06	3.6E-06	1.4E-07	-1.2E-04	-4.7E-06
	3b	max	2.5E-04	9.8E-06	9.7E-05	3.8E-06	2.7E-05	1.1E-06	2.5E-04	9.8E-06
		min	-2.1E-04	-8.1E-06	-1.2E-04	-4.9E-06	-2.1E-06	-8.3E-08	-2.7E-04	-1.1E-05
	4b	max	1.3E-04	5.1E-06	4.2E-05	1.6E-06	2.9E-05	1.1E-06	1.3E-04	5.1E-06
		min	-1.0E-04	-4.1E-06	-6.4E-05	-2.5E-06	8.4E-06	3.3E-07	-1.4E-04	-5.6E-06
	5b	max	1.6E-04	6.4E-06	5.3E-05	2.1E-06	2.6E-05	1.0E-06	1.2E-04	4.6E-06
		min	-9.5E-05	-3.7E-06	-5.7E-05	-2.3E-06	7.5E-06	2.9E-07	-1.8E-04	-6.9E-06
	6b	max	1.7E-04	6.6E-06	5.7E-05	2.2E-06	2.4E-05	9.5E-07	1.2E-04	4.6E-06
		min	-9.4E-05	-3.7E-06	-5.5E-05	-2.2E-06	9.5E-06	3.7E-07	-1.8E-04	-7.3E-06
	8	max	1.8E-04	7.0E-06	5.8E-05	2.3E-06	2.6E-05	1.0E-06	1.3E-04	5.0E-06
		min	-1.0E-04	-4.0E-06	-6.0E-05	-2.3E-06	6.5E-06	2.6E-07	-1.9E-04	-7.5E-06
	9a	max	8.3E-05	3.3E-06	2.2E-05	8.5E-07	8.4E-05	3.3E-06	7.5E-05	2.9E-06
		min	-4.2E-05	-1.7E-06	-3.1E-05	-1.2E-06	-3.3E-05	-1.3E-06	-5.5E-05	-2.2E-06
	9b	max	1.9E-04	7.5E-06	6.6E-05	2.6E-06	1.7E-04	6.6E-06	1.8E-04	7.0E-06
		min	-1.2E-04	-4.7E-06	-7.3E-05	-2.9E-06	-9.8E-05	-3.9E-06	-1.8E-04	-6.9E-06
	10	max	2.2E-04	8.8E-06	9.1E-05	3.6E-06	3.5E-05	1.4E-06	2.5E-04	9.8E-06
		min	-1.8E-04	-7.2E-06	-1.0E-04	-4.0E-06	7.6E-06	3.0E-07	-2.2E-04	-8.8E-06
	11	max	1.9E-04	7.3E-06	7.1E-05	2.8E-06	3.9E-05	1.5E-06	1.9E-04	7.6E-06
		min	-1.4E-04	-5.5E-06	-8.5E-05	-3.4E-06	7.5E-06	2.9E-07	-1.8E-04	-7.3E-06
High Amplitude Testing	12	max	3.2E-04	1.3E-05	1.2E-04	4.5E-06	3.4E-05	1.3E-06	3.5E-04	1.4E-05
		min	-2.5E-04	-9.7E-06	-1.5E-04	-5.7E-06	-1.8E-05	-7.0E-07	-2.8E-04	-1.1E-05
	13	max	9.4E-04	3.7E-05	3.6E-04	1.4E-05	9.4E-05	3.7E-06	8.5E-04	3.3E-05
		min	-7.7E-04	-3.0E-05	-3.1E-04	-1.2E-05	-5.3E-05	-2.1E-06	-1.0E-03	-4.0E-05
	14	max	1.2E-03	4.5E-05	4.4E-04	1.7E-05	1.9E-04	7.4E-06	1.2E-03	4.6E-05
		min	-1.1E-03	-4.2E-05	-3.9E-04	-1.5E-05	-1.1E-04	-4.2E-06	-1.2E-03	-4.9E-05
	15	max	2.9E-03	1.2E-04	8.1E-04	3.2E-05	3.2E-04	1.3E-05	1.9E-03	7.4E-05
		min	-1.8E-03	-7.0E-05	-5.6E-04	-2.2E-05	-1.4E-04	-5.5E-06	-2.9E-03	-1.2E-04
	16	max	4.6E-03	1.8E-04	1.0E-03	4.0E-05	5.8E-04	2.3E-05	5.2E-03	2.1E-04
		min	-5.1E-03	-2.0E-04	-1.1E-03	-4.4E-05	-1.8E-04	-7.1E-06	-3.8E-03	-1.5E-04
	17	max	2.6E-03	1.0E-04	6.0E-04	2.4E-05	5.8E-04	2.3E-05	3.9E-03	1.5E-04
		min	-3.8E-03	-1.5E-04	-7.8E-04	-3.1E-05	1.7E-06	6.6E-08	-2.0E-03	-7.8E-05
	18	max	5.8E-03	2.3E-04	1.4E-03	5.3E-05	7.1E-04	2.8E-05	4.6E-03	1.8E-04
		min	-4.3E-03	-1.7E-04	-8.4E-04	-3.3E-05	-2.8E-04	-1.1E-05	-4.6E-03	-1.8E-04
	19	max	5.5E-03	2.2E-04	1.5E-03	5.8E-05	1.0E-03	4.0E-05	7.6E-03	3.0E-04
		min	-7.2E-03	-2.9E-04	-1.3E-03	-5.0E-05	-1.5E-04	-5.8E-06	-4.6E-03	-1.8E-04
	20	max	4.2E-03	1.7E-04	1.2E-03	4.9E-05	5.3E-04	2.1E-05	4.1E-03	1.6E-04
		min	-3.8E-03	-1.5E-04	-6.7E-04	-2.6E-05	1.7E-05	6.8E-07	-3.6E-03	-1.4E-04
Post-Tests	21	max	5.8E-03	2.3E-04	1.7E-03	6.6E-05	8.7E-04	3.4E-05	4.7E-03	1.8E-04
		min	-4.2E-03	-1.7E-04	-7.9E-04	-3.1E-05	-1.9E-04	-7.4E-06	-5.3E-03	-2.1E-04
	22	max	3.4E-03	1.4E-04	1.1E-03	4.4E-05	1.2E-03	4.6E-05	7.2E-03	2.9E-04
		min	-6.7E-03	-2.6E-04	-1.1E-03	-4.4E-05	3.9E-05	1.5E-06	-3.0E-03	-1.2E-04

Table 6-31: Column curvature envelopes.

	Location		Bent 1 bottom west column, trans. direction at 8.5in (216mm) from fixity		Bent 1 bottom west column, long. direction at 2.5in (64mm) from fixity		Bent 1 top east column, trans. direction at 2.5in (64mm) from fixity		Bent 1 top east column, trans. direction at 8.5in (216mm) from fixity	
	Gauge length		7in	178mm	5in	127mm	5in	127mm	7in	178mm
	Unit		rad/in	rad/mm	rad/in	rad/mm	rad/in	rad/mm	rad/in	rad/mm
Low Amplitude Testing	1a	max	1.9E-05	7.6E-07	1.5E-05	5.8E-07	1.1E-04	4.5E-06	6.5E-05	2.6E-06
		min	-4.2E-05	-1.7E-06	-6.3E-06	-2.5E-07	-7.7E-05	-3.0E-06	-3.1E-05	-1.2E-06
	1b	max	3.5E-05	1.4E-06	2.1E-05	8.1E-07	1.8E-04	6.9E-06	1.1E-04	4.5E-06
		min	-7.8E-05	-3.1E-06	-1.1E-05	-4.3E-07	-1.4E-04	-5.5E-06	-5.3E-05	-2.1E-06
	2a	max	1.6E-05	6.2E-07	8.1E-06	3.2E-07	6.9E-05	2.7E-06	4.6E-05	1.8E-06
		min	-2.3E-05	-9.2E-07	-3.8E-06	-1.5E-07	-6.7E-05	-2.7E-06	-2.6E-05	-1.0E-06
	2b	max	4.7E-05	1.8E-06	2.3E-05	8.9E-07	1.6E-04	6.2E-06	9.1E-05	3.6E-06
		min	-5.6E-05	-2.2E-06	-1.3E-05	-5.1E-07	-1.5E-04	-6.0E-06	-7.6E-05	-3.0E-06
	3a	max	2.2E-05	8.7E-07	1.2E-05	4.7E-07	1.1E-04	4.2E-06	5.4E-05	2.1E-06
		min	-3.0E-05	-1.2E-06	-3.1E-06	-1.2E-07	-9.1E-05	-3.6E-06	-3.7E-05	-1.5E-06
	3b	max	6.7E-05	2.6E-06	1.3E-05	5.0E-07	2.2E-04	8.6E-06	1.5E-04	5.8E-06
		min	-9.3E-05	-3.7E-06	-1.6E-05	-6.4E-07	-2.3E-04	-9.1E-06	-9.8E-05	-3.8E-06
	4b	max	2.8E-05	1.1E-06	-4.2E-07	-1.7E-08	1.1E-04	4.3E-06	7.8E-05	3.1E-06
		min	-4.2E-05	-1.7E-06	-1.7E-05	-6.9E-07	-1.4E-04	-5.4E-06	-4.4E-05	-1.7E-06
	5b	max	2.7E-05	1.1E-06	4.2E-06	1.7E-07	1.2E-04	4.8E-06	9.6E-05	3.8E-06
		min	-5.6E-05	-2.2E-06	-1.7E-05	-6.6E-07	-1.4E-04	-5.3E-06	-4.0E-05	-1.6E-06
	6b	max	2.7E-05	1.1E-06	2.1E-07	8.3E-09	1.3E-04	4.9E-06	9.7E-05	3.8E-06
		min	-6.0E-05	-2.3E-06	-1.7E-05	-6.6E-07	-1.4E-04	-5.3E-06	-3.8E-05	-1.5E-06
	8	max	2.8E-05	1.1E-06	8.1E-06	3.2E-07	1.6E-04	6.2E-06	1.0E-04	4.0E-06
		min	-6.3E-05	-2.5E-06	-1.8E-05	-7.2E-07	-1.4E-04	-5.4E-06	-4.2E-05	-1.7E-06
	9a	max	-2.3E-05	-9.2E-07	8.2E-05	3.2E-06	6.0E-05	2.3E-06	5.3E-05	2.1E-06
		min	-6.2E-05	-2.4E-06	-5.9E-05	-2.3E-06	-6.7E-05	-2.7E-06	-1.1E-05	-4.4E-07
	9b	max	6.5E-06	2.5E-07	1.8E-04	7.2E-06	1.6E-04	6.2E-06	1.1E-04	4.4E-06
		min	-1.0E-04	-4.0E-06	-1.6E-04	-6.4E-06	-1.5E-04	-5.9E-06	-5.2E-05	-2.0E-06
	10	max	2.6E-05	1.0E-06	1.6E-05	6.3E-07	2.1E-04	8.1E-06	1.4E-04	5.5E-06
		min	-1.2E-04	-4.6E-06	-1.2E-05	-4.6E-07	-2.2E-04	-8.8E-06	-8.4E-05	-3.3E-06
	11	max	1.0E-05	4.1E-07	1.5E-05	5.8E-07	1.6E-04	6.1E-06	1.1E-04	4.4E-06
		min	-1.0E-04	-4.0E-06	-1.0E-05	-4.1E-07	-1.6E-04	-6.3E-06	-5.9E-05	-2.3E-06
High Amplitude Testing	12	max	4.4E-05	1.7E-06	3.8E-05	1.5E-06	2.5E-04	9.9E-06	2.0E-04	7.7E-06
		min	-1.4E-04	-5.7E-06	-7.1E-06	-2.8E-07	-2.9E-04	-1.1E-05	-1.1E-04	-4.5E-06
	13	max	2.1E-04	8.1E-06	7.5E-05	3.0E-06	7.1E-04	2.8E-05	6.1E-04	2.4E-05
		min	-3.5E-04	-1.4E-05	-3.8E-05	-1.5E-06	-8.0E-04	-3.2E-05	-3.7E-04	-1.4E-05
	14	max	3.0E-04	1.2E-05	1.3E-04	5.1E-06	9.0E-04	3.5E-05	7.0E-04	2.7E-05
		min	-3.8E-04	-1.5E-05	-7.6E-05	-3.0E-06	-1.1E-03	-4.4E-05	-4.8E-04	-1.9E-05
	15	max	5.5E-04	2.1E-05	2.4E-04	9.3E-06	2.5E-03	9.9E-05	1.1E-03	4.4E-05
		min	-6.8E-04	-2.7E-05	-1.1E-04	-4.2E-06	-1.8E-03	-6.9E-05	-7.6E-04	-3.0E-05
	16	max	1.2E-03	4.8E-05	3.7E-04	1.5E-05	3.9E-03	1.5E-04	1.5E-03	5.7E-05
		min	-1.3E-03	-5.0E-05	-2.5E-04	-9.8E-06	-4.7E-03	-1.8E-04	-1.8E-03	-7.1E-05
	17	max	7.9E-04	3.1E-05	3.6E-04	1.4E-05	2.3E-03	8.9E-05	6.6E-04	2.6E-05
		min	-8.0E-04	-3.2E-05	-1.5E-04	-5.9E-06	-3.5E-03	-1.4E-04	-1.3E-03	-5.2E-05
	18	max	8.5E-04	3.3E-05	8.1E-04	3.2E-05	5.4E-03	2.1E-04	1.4E-03	5.4E-05
		min	-1.8E-03	-7.0E-05	-2.2E-05	-8.7E-07	-4.2E-03	-1.6E-04	-1.4E-03	-5.5E-05
	19	max	1.2E-03	4.6E-05	7.3E-04	2.9E-05	5.5E-03	2.2E-04	1.1E-03	4.5E-05
		min	-1.7E-03	-6.8E-05	-3.5E-04	-1.4E-05	-6.9E-03	-2.7E-04	-2.0E-03	-7.7E-05
	20	max	5.2E-04	2.0E-05	7.6E-04	3.0E-05	4.4E-03	1.7E-04	8.6E-04	3.4E-05
		min	-1.4E-03	-5.5E-05	2.8E-04	1.1E-05	-3.7E-03	-1.4E-04	-1.1E-03	-4.5E-05
Post-Tests	21	max	5.7E-04	2.3E-05	1.0E-03	4.1E-05	6.0E-03	2.4E-04	1.1E-03	4.5E-05
		min	-1.8E-03	-6.9E-05	-1.7E-05	-6.6E-07	-4.2E-03	-1.6E-04	-1.3E-03	-5.0E-05
	22	max	9.0E-04	3.5E-05	7.8E-04	3.1E-05	3.7E-03	1.4E-04	6.1E-04	2.4E-05
		min	-1.2E-03	-4.6E-05	-3.3E-04	-1.3E-05	-6.5E-03	-2.6E-04	-1.7E-03	-6.8E-05

Table 6-32: Column curvature envelopes.

	Location		Bent 1 top east column, long. direction at 2.5in (64mm) from fixity		Bent 1 bottom east column, trans. direction at 2.5in (64mm) from fixity		Bent 1 bottom east column, trans. direction at 8.5in (216mm) from fixity		Bent 1 bottom east column, long direction at 2.5in (64mm) from fixity	
	Gauge length		5in	127mm	5in	127mm	7in	178mm	5in	127mm
	Unit		rad/in	rad/mm	rad/in	rad/mm	rad/in	rad/mm	rad/in	rad/mm
Low Amplitude Testing	1a	max	9.7E-06	3.8E-07	7.3E-05	2.9E-06	2.8E-05	1.1E-06	8.9E-06	3.5E-07
		min	-2.7E-06	-1.1E-07	-1.5E-04	-6.0E-06	-4.9E-05	-1.9E-06	-7.5E-06	-2.9E-07
	1b	max	1.5E-05	5.8E-07	1.4E-04	5.7E-06	4.8E-05	1.9E-06	1.7E-05	6.6E-07
		min	-6.0E-06	-2.4E-07	-2.2E-04	-8.8E-06	-8.1E-05	-3.2E-06	-1.1E-05	-4.5E-07
	2a	max	1.2E-05	4.8E-07	6.0E-05	2.4E-06	2.2E-05	8.9E-07	9.6E-06	3.8E-07
		min	-5.5E-06	-2.2E-07	-9.9E-05	-3.9E-06	-2.9E-05	-1.2E-06	-7.5E-06	-2.9E-07
	2b	max	2.0E-05	7.9E-07	1.8E-04	7.0E-06	5.9E-05	2.3E-06	3.4E-05	1.3E-06
		min	-1.7E-05	-6.8E-07	-1.8E-04	-7.1E-06	-5.9E-05	-2.3E-06	-1.8E-05	-7.1E-07
	3a	max	7.7E-06	3.0E-07	9.4E-05	3.7E-06	3.3E-05	1.3E-06	1.1E-05	4.3E-07
		min	-2.1E-07	-8.3E-09	-1.2E-04	-4.7E-06	-3.8E-05	-1.5E-06	-4.8E-06	-1.9E-07
	3b	max	2.1E-05	8.5E-07	2.5E-04	9.7E-06	9.3E-05	3.6E-06	1.4E-05	5.6E-07
		min	-5.4E-06	-2.1E-07	-2.7E-04	-1.1E-05	-1.0E-04	-3.9E-06	-1.8E-05	-7.1E-07
	4b	max	2.1E-05	8.2E-07	1.2E-04	4.9E-06	4.4E-05	1.7E-06	-8.4E-07	-3.3E-08
		min	4.3E-06	1.7E-07	-1.5E-04	-5.8E-06	-5.1E-05	-2.0E-06	-2.4E-05	-9.4E-07
	5b	max	2.0E-05	8.0E-07	1.1E-04	4.4E-06	4.0E-05	1.6E-06	-8.4E-07	-3.3E-08
		min	4.3E-06	1.7E-07	-1.8E-04	-7.0E-06	-6.0E-05	-2.4E-06	-2.1E-05	-8.4E-07
	6b	max	1.9E-05	7.7E-07	1.1E-04	4.4E-06	4.1E-05	1.6E-06	-1.6E-06	-6.2E-08
		min	4.4E-06	1.7E-07	-1.9E-04	-7.3E-06	-6.3E-05	-2.5E-06	-2.0E-05	-7.8E-07
	8	max	2.0E-05	8.0E-07	1.2E-04	4.8E-06	4.3E-05	1.7E-06	2.4E-06	9.5E-08
		min	1.2E-06	4.6E-08	-1.9E-04	-7.5E-06	-6.8E-05	-2.7E-06	-2.0E-05	-7.8E-07
	9a	max	6.9E-05	2.7E-06	1.7E-05	6.8E-07	2.3E-06	9.2E-08	9.2E-05	3.6E-06
		min	-4.8E-05	-1.9E-06	-1.1E-04	-4.4E-06	-4.6E-05	-1.8E-06	-6.1E-05	-2.4E-06
	9b	max	1.7E-04	6.5E-06	1.2E-04	4.8E-06	3.5E-05	1.4E-06	2.0E-04	8.0E-06
		min	-1.1E-04	-4.5E-06	-2.2E-04	-8.8E-06	-9.0E-05	-3.6E-06	-1.5E-04	-5.7E-06
	10	max	2.3E-05	9.0E-07	1.9E-04	7.6E-06	5.9E-05	2.3E-06	2.3E-05	9.2E-07
		min	-8.4E-07	-3.3E-08	-2.7E-04	-1.1E-05	-1.1E-04	-4.3E-06	-3.2E-07	-1.2E-08
	11	max	2.1E-05	8.5E-07	1.3E-04	5.2E-06	4.1E-05	1.6E-06	2.2E-05	8.7E-07
		min	-2.1E-07	-8.3E-09	-2.3E-04	-8.9E-06	-9.2E-05	-3.6E-06	4.2E-07	1.7E-08
High Amplitude Testing	12	max	3.4E-05	1.3E-06	2.7E-04	1.1E-05	1.0E-04	4.0E-06	2.9E-05	1.1E-06
		min	-1.3E-05	-5.2E-07	-3.3E-04	-1.3E-05	-1.5E-04	-6.0E-06	-1.7E-05	-6.5E-07
	13	max	9.3E-05	3.7E-06	8.8E-04	3.5E-05	3.1E-04	1.2E-05	6.9E-05	2.7E-06
		min	-4.5E-05	-1.8E-06	-9.1E-04	-3.6E-05	-3.2E-04	-1.3E-05	-4.2E-05	-1.7E-06
	14	max	2.1E-04	8.2E-06	1.3E-03	5.0E-05	4.0E-04	1.6E-05	1.4E-04	5.6E-06
		min	-5.1E-05	-2.0E-06	-1.1E-03	-4.3E-05	-3.6E-04	-1.4E-05	-4.9E-05	-1.9E-06
	15	max	3.5E-04	1.4E-05	2.1E-03	8.1E-05	5.4E-04	2.1E-05	2.8E-04	1.1E-05
		min	-7.7E-05	-3.0E-06	-2.6E-03	-1.0E-04	-7.1E-04	-2.8E-05	-7.0E-05	-2.7E-06
	16	max	5.2E-04	2.1E-05	5.7E-03	2.2E-04	1.0E-03	4.1E-05	4.8E-04	1.9E-05
		min	-2.5E-04	-9.8E-06	-3.9E-03	-1.5E-04	-1.1E-03	-4.1E-05	-9.5E-05	-3.7E-06
	17	max	3.6E-04	1.4E-05	4.2E-03	1.7E-04	7.3E-04	2.9E-05	4.4E-04	1.8E-05
		min	-2.2E-04	-8.6E-06	-2.2E-03	-8.6E-05	-5.6E-04	-2.2E-05	1.2E-04	4.8E-06
	18	max	5.4E-04	2.1E-05	4.8E-03	1.9E-04	7.6E-04	3.0E-05	4.8E-04	1.9E-05
		min	-4.0E-04	-1.6E-05	-5.3E-03	-2.1E-04	-1.3E-03	-5.0E-05	-2.7E-05	-1.0E-06
	19	max	4.1E-04	1.6E-05	8.0E-03	3.2E-04	1.1E-03	4.3E-05	7.7E-04	3.0E-05
		min	-7.9E-04	-3.1E-05	-5.3E-03	-2.1E-04	-1.2E-03	-4.9E-05	1.9E-04	7.5E-06
	20	max	2.3E-04	9.2E-06	4.1E-03	1.6E-04	5.0E-04	2.0E-05	7.3E-04	2.9E-05
		min	-6.0E-04	-2.4E-05	-4.3E-03	-1.7E-04	-9.8E-04	-3.9E-05	2.8E-04	1.1E-05
Post-Tests	21	max	6.1E-04	2.4E-05	4.7E-03	1.9E-04	5.8E-04	2.3E-05	8.4E-04	3.3E-05
		min	-6.0E-04	-2.4E-05	-6.0E-03	-2.4E-04	-1.3E-03	-5.2E-05	1.5E-04	6.1E-06
	22	max	3.6E-04	1.4E-05	7.4E-03	2.9E-04	8.4E-04	3.3E-05	1.0E-03	4.0E-05
		min	-6.5E-04	-2.6E-05	-3.7E-03	-1.4E-04	-8.3E-04	-3.3E-05	3.1E-04	1.2E-05

Table 6-33: Column curvature envelopes.

	Location		Bent 2 top west column, trans. direction at 2.5in (64mm) from fixity		Bent 2 top west column, trans. direction at 8.5in (216mm) from fixity		Bent 2 bottom west column, trans. direction at 2.5in (64mm) from fixity		Bent 2 bottom west column, trans. direction at 8.5in (216mm) from fixity	
	Gauge length		5in	127mm	7in	178mm	5in	127mm	7in	178mm
	Unit		rad/in	rad/mm	rad/in	rad/mm	rad/in	rad/mm	rad/in	rad/mm
Low Amplitude Testing	1a	max	6.9E-05	2.7E-06	1.2E-05	4.7E-07	6.2E-05	2.5E-06	2.1E-05	8.1E-07
		min	-4.1E-05	-1.6E-06	-5.2E-05	-2.0E-06	-6.9E-05	-2.7E-06	-1.2E-04	-4.6E-06
	1b	max	1.4E-04	5.5E-06	2.5E-05	9.7E-07	1.0E-04	4.0E-06	1.3E-05	5.0E-07
		min	-5.1E-05	-2.0E-06	-7.5E-05	-3.0E-06	-1.0E-04	-4.0E-06	-1.0E-04	-4.1E-06
	2a	max	3.8E-05	1.5E-06	8.1E-06	3.2E-07	4.8E-05	1.9E-06	2.5E-05	9.8E-07
		min	-2.9E-05	-1.1E-06	-3.5E-05	-1.4E-06	-2.5E-05	-9.8E-07	-5.7E-05	-2.2E-06
	2b	max	9.7E-05	3.8E-06	1.6E-03	6.4E-05	1.2E-04	4.6E-06	1.5E-05	5.7E-07
		min	-8.9E-05	-3.5E-06	-8.4E-05	-3.3E-06	-1.0E-04	-3.9E-06	-1.1E-04	-4.5E-06
	3a	max	6.8E-05	2.7E-06	1.5E-05	5.9E-07	5.8E-05	2.3E-06	1.3E-05	5.0E-07
		min	-3.6E-06	-1.4E-07	-3.5E-05	-1.4E-06	-2.3E-05	-9.0E-07	-6.8E-05	-2.7E-06
	3b	max	1.5E-04	5.7E-06	4.8E-05	1.9E-06	1.0E-04	4.1E-06	1.5E-05	5.7E-07
		min	-7.1E-05	-2.8E-06	-6.5E-05	-2.6E-06	-1.2E-04	-4.8E-06	-1.1E-04	-4.3E-06
	4b	max	1.1E-04	4.5E-06	1.5E-05	5.7E-07	8.0E-05	3.1E-06	1.4E-05	5.4E-07
		min	-4.8E-05	-1.9E-06	-6.4E-05	-2.5E-06	-8.6E-05	-3.4E-06	-1.0E-04	-4.0E-06
	5b	max	9.8E-05	3.9E-06	2.6E-05	1.0E-06	7.2E-05	2.8E-06	1.5E-05	5.9E-07
		min	-2.4E-05	-9.4E-07	-3.7E-05	-1.4E-06	-5.8E-05	-2.3E-06	-8.2E-05	-3.2E-06
	6b	max	1.0E-04	4.0E-06	2.9E-05	1.1E-06	7.4E-05	2.9E-06	1.9E-05	7.4E-07
		min	-5.0E-05	-2.0E-06	-4.6E-05	-1.8E-06	-7.8E-05	-3.1E-06	-9.8E-05	-3.9E-06
	8	max	1.0E-04	3.9E-06	2.8E-05	1.1E-06	8.1E-05	3.2E-06	1.9E-05	7.5E-07
		min	-6.3E-05	-2.5E-06	-5.2E-05	-2.0E-06	-8.3E-05	-3.3E-06	-9.9E-05	-3.9E-06
	9a	max	3.9E-04	1.5E-05	7.0E-06	2.8E-07	7.6E-05	3.0E-06	2.1E-05	8.1E-07
		min	-3.6E-05	-1.4E-06	-3.5E-05	-1.4E-06	1.6E-05	6.3E-07	-9.7E-05	-3.8E-06
	9b	max	1.3E-04	5.2E-06	4.8E-05	1.9E-06	1.3E-04	5.2E-06	1.5E-05	6.1E-07
		min	-7.5E-05	-3.0E-06	-6.3E-05	-2.5E-06	-8.4E-05	-3.3E-06	-2.1E-04	-8.1E-06
	10	max	9.8E-05	3.9E-06	3.2E-05	1.3E-06	1.3E-04	5.0E-06	1.9E-05	7.4E-07
		min	-6.9E-05	-2.7E-06	-6.3E-05	-2.5E-06	-4.7E-05	-1.9E-06	-1.3E-04	-5.2E-06
	11	max	8.6E-05	3.4E-06	2.4E-05	9.5E-07	1.2E-04	4.7E-06	2.1E-05	8.3E-07
		min	-3.6E-05	-1.4E-06	-7.3E-05	-2.9E-06	-2.3E-05	-8.9E-07	-1.3E-04	-5.0E-06
High Amplitude Testing	12	max	1.5E-04	6.0E-06	5.8E-05	2.3E-06	1.9E-04	7.4E-06	8.9E-06	3.5E-07
		min	-1.3E-04	-5.0E-06	-9.8E-05	-3.9E-06	-1.2E-04	-4.5E-06	-2.1E-04	-8.3E-06
	13	max	4.0E-04	1.6E-05	1.7E-04	6.8E-06	4.4E-04	1.7E-05	2.3E-05	9.2E-07
		min	-3.1E-04	-1.2E-05	-2.1E-04	-8.4E-06	-4.0E-04	-1.6E-05	-2.4E-04	-9.6E-06
	14	max	5.3E-04	2.1E-05	2.3E-04	9.0E-06	5.4E-04	2.1E-05	3.4E-05	1.3E-06
		min	-3.8E-04	-1.5E-05	-2.7E-04	-1.0E-05	-5.3E-04	-2.1E-05	-2.2E-04	-8.8E-06
	15	max	1.2E-03	4.8E-05	5.2E-04	2.0E-05	1.4E-03	5.3E-05	1.2E-04	4.6E-06
		min	-8.0E-04	-3.1E-05	-6.1E-04	-2.4E-05	-1.3E-03	-5.1E-05	-3.7E-04	-1.5E-05
	16	max	1.9E-03	7.6E-05	7.5E-04	3.0E-05	3.2E-03	1.3E-04	2.3E-04	9.1E-06
		min	-2.1E-03	-8.2E-05	-1.2E-03	-4.6E-05	-2.0E-03	-7.9E-05	-4.7E-04	-1.9E-05
	17	max	1.5E-03	6.1E-05	6.2E-04	2.4E-05	2.6E-03	1.0E-04	1.9E-04	7.4E-06
		min	-1.9E-03	-7.4E-05	-8.7E-04	-3.4E-05	-1.7E-03	-6.6E-05	-4.5E-04	-1.8E-05
	18	max	3.4E-03	1.3E-04	1.2E-03	4.7E-05	4.8E-03	1.9E-04	2.9E-04	1.2E-05
		min	-3.6E-03	-1.4E-04	-1.5E-03	-6.0E-05	-3.6E-03	-1.4E-04	-7.5E-04	-2.9E-05
	19	max	6.2E-03	2.4E-04	1.5E-03	5.9E-05	4.3E-03	1.7E-04	2.6E-04	1.0E-05
		min	-3.4E-03	-1.3E-04	-1.3E-03	-5.0E-05	-6.3E-03	-2.5E-04	-1.3E-03	-5.0E-05
	20	max	4.4E-03	1.7E-04	9.6E-04	3.8E-05	3.3E-03	1.3E-04	7.8E-05	3.1E-06
		min	-2.7E-03	-1.1E-04	-9.4E-04	-3.7E-05	-4.4E-03	-1.7E-04	-1.0E-03	-3.9E-05
Post-Tests	21	max	4.9E-03	1.9E-04	1.1E-03	4.3E-05	2.7E-03	1.1E-04	6.6E-05	2.6E-06
		min	-2.4E-03	-9.3E-05	-8.0E-04	-3.2E-05	-5.1E-03	-2.0E-04	-1.1E-03	-4.4E-05
	22	max	7.6E-03	3.0E-04	1.6E-03	6.4E-05	5.2E-03	2.1E-04	1.6E-04	6.1E-06
		min	-4.6E-03	-1.8E-04	-1.4E-03	-5.6E-05	-8.3E-03	-3.2E-04	-1.6E-03	-6.1E-05

Table 6-34: Column curvature envelopes.

	Location		Bent 2 top east column, trans. direction at 2.5in (64mm) from fixity		Bent 2 top east column, trans. direction at 8.5in (216mm) from fixity		Bent 2 top east column, long. direction at 2.5in (64mm) from fixity		Bent 2 bottom east column, trans. direction at 2.5in (64mm) from fixity	
	Gauge length		5in	127mm	7in	178mm	5in	127mm	5in	127mm
	Unit		rad/in	rad/mm	rad/in	rad/mm	rad/in	rad/mm	rad/in	rad/mm
Low Amplitude Testing	1a	max	5.0E-05	2.0E-06	1.4E-05	5.5E-07	2.1E-05	8.3E-07	5.9E-05	2.3E-06
		min	-5.9E-05	-2.3E-06	-6.8E-05	-2.7E-06	8.5E-06	3.4E-07	-6.1E-05	-2.4E-06
	1b	max	1.2E-04	4.7E-06	5.7E-05	2.2E-06	-9.1E-06	-3.6E-07	9.7E-05	3.8E-06
		min	-6.2E-05	-2.4E-06	-6.0E-05	-2.4E-06	-3.0E-05	-1.2E-06	-1.3E-04	-5.0E-06
	2a	max	2.2E-05	8.8E-07	2.0E-05	7.8E-07	2.1E-05	8.4E-07	4.5E-05	1.8E-06
		min	-4.4E-05	-1.7E-06	-3.7E-05	-1.5E-06	2.6E-06	1.0E-07	-3.7E-05	-1.5E-06
	2b	max	9.1E-05	3.6E-06	5.4E-05	2.1E-06	3.7E-05	1.4E-06	1.3E-04	4.9E-06
		min	-8.8E-05	-3.5E-06	-7.1E-05	-2.8E-06	-6.6E-06	-2.6E-07	-1.2E-04	-4.6E-06
	3a	max	3.7E-05	1.5E-06	3.3E-06	1.3E-07	6.3E-07	2.5E-08	4.1E-05	1.6E-06
		min	-3.8E-05	-1.5E-06	-5.8E-05	-2.3E-06	-1.6E-05	-6.1E-07	-4.1E-05	-1.6E-06
	3b	max	1.2E-04	4.7E-06	5.8E-05	2.3E-06	2.7E-05	1.1E-06	1.3E-04	5.1E-06
		min	-8.1E-05	-3.2E-06	-7.5E-05	-2.9E-06	6.6E-06	2.6E-07	-1.2E-04	-4.9E-06
	4b	max	9.1E-05	3.6E-06	2.0E-05	7.8E-07	2.3E-05	8.9E-07	1.0E-04	4.1E-06
		min	-5.1E-05	-2.0E-06	-7.6E-05	-3.0E-06	-1.7E-05	-6.6E-07	-6.1E-05	-2.4E-06
	5b	max	5.7E-05	2.3E-06	1.7E-05	6.7E-07	7.2E-06	2.8E-07	6.5E-05	2.6E-06
		min	-5.6E-05	-2.2E-06	-6.9E-05	-2.7E-06	-1.7E-05	-6.6E-07	-5.9E-05	-2.3E-06
	6b	max	8.5E-05	3.4E-06	3.6E-05	1.4E-06	-3.9E-06	-1.5E-07	8.6E-05	3.4E-06
		min	-4.8E-05	-1.9E-06	-5.6E-05	-2.2E-06	-1.8E-05	-7.1E-07	-6.7E-05	-2.6E-06
	8	max	8.2E-05	3.2E-06	5.6E-05	2.2E-06	-1.2E-05	-4.8E-07	8.2E-05	3.2E-06
		min	-6.0E-05	-2.4E-06	-4.3E-05	-1.7E-06	-2.9E-05	-1.2E-06	-9.4E-05	-3.7E-06
	9a	max	2.0E-05	8.0E-07	9.8E-07	3.8E-08	6.9E-05	2.7E-06	5.5E-05	2.2E-06
		min	-4.7E-05	-1.8E-06	-5.9E-05	-2.3E-06	-5.7E-05	-2.2E-06	-9.3E-06	-3.6E-07
	9b	max	1.1E-04	4.5E-06	5.3E-05	2.1E-06	1.5E-04	5.8E-06	1.4E-04	5.6E-06
		min	-8.1E-05	-3.2E-06	-7.9E-05	-3.1E-06	-9.1E-05	-3.6E-06	-1.1E-04	-4.3E-06
	10	max	6.7E-05	2.6E-06	3.1E-05	1.2E-06	2.3E-05	9.2E-07	1.4E-04	5.4E-06
		min	-8.1E-05	-3.2E-06	-9.2E-05	-3.6E-06	-2.0E-05	-7.9E-07	-4.7E-05	-1.9E-06
	11	max	5.2E-05	2.1E-06	2.7E-05	1.0E-06	6.3E-07	2.5E-08	1.0E-04	4.1E-06
		min	-6.5E-05	-2.6E-06	-7.7E-05	-3.0E-06	-2.7E-05	-1.1E-06	-3.8E-05	-1.5E-06
High Amplitude Testing	12	max	1.4E-04	5.4E-06	7.0E-05	2.8E-06	2.8E-05	1.1E-06	2.2E-04	8.8E-06
		min	-1.2E-04	-4.7E-06	-1.2E-04	-4.8E-06	-8.4E-07	-3.3E-08	-1.1E-04	-4.5E-06
	13	max	3.2E-04	1.2E-05	2.2E-04	8.7E-06	5.1E-05	2.0E-06	5.0E-04	2.0E-05
		min	-3.0E-04	-1.2E-05	-2.7E-04	-1.0E-05	-2.5E-05	-9.7E-07	-3.4E-04	-1.3E-05
	14	max	4.3E-04	1.7E-05	2.6E-04	1.0E-05	7.7E-05	3.0E-06	6.1E-04	2.4E-05
		min	-3.7E-04	-1.5E-05	-3.6E-04	-1.4E-05	-4.7E-05	-1.8E-06	-4.5E-04	-1.8E-05
	15	max	9.7E-04	3.8E-05	5.4E-04	2.1E-05	5.3E-05	2.1E-06	1.3E-03	5.2E-05
		min	-1.1E-03	-4.2E-05	-7.4E-04	-2.9E-05	-7.8E-05	-3.1E-06	-1.1E-03	-4.4E-05
	16	max	1.5E-03	6.0E-05	8.0E-04	3.1E-05	2.8E-04	1.1E-05	2.8E-03	1.1E-04
		min	-3.0E-03	-1.2E-04	-1.1E-03	-4.3E-05	-9.1E-05	-3.6E-06	-1.8E-03	-6.9E-05
	17	max	1.2E-03	4.6E-05	6.9E-04	2.7E-05	2.2E-04	8.7E-06	2.3E-03	9.0E-05
		min	-2.6E-03	-1.0E-04	-9.2E-04	-3.6E-05	-9.6E-06	-3.8E-07	-1.4E-03	-5.6E-05
	18	max	2.8E-03	1.1E-04	1.3E-03	5.3E-05	3.1E-04	1.2E-05	4.4E-03	1.7E-04
		min	-5.0E-03	-2.0E-04	-1.4E-03	-5.6E-05	-9.1E-05	-3.6E-06	-3.1E-03	-1.2E-04
	19	max	5.3E-03	2.1E-04	1.8E-03	7.0E-05	5.4E-04	2.1E-05	3.8E-03	1.5E-04
		min	-4.5E-03	-1.8E-04	-1.2E-03	-4.9E-05	-7.5E-05	-2.9E-06	-5.6E-03	-2.2E-04
	20	max	3.7E-03	1.5E-04	1.3E-03	5.0E-05	3.3E-04	1.3E-05	2.9E-03	1.2E-04
		min	-3.5E-03	-1.4E-04	-1.0E-03	-4.0E-05	5.4E-05	2.1E-06	-4.0E-03	-1.6E-04
Post-Tests	21	max	4.3E-03	1.7E-04	1.4E-03	5.5E-05	7.1E-04	2.8E-05	2.5E-03	9.9E-05
		min	-2.9E-03	-1.2E-04	-9.5E-04	-3.7E-05	9.6E-05	3.8E-06	-4.5E-03	-1.8E-04
	22	max	7.0E-03	2.8E-04	1.9E-03	7.6E-05	8.8E-04	3.4E-05	5.1E-03	2.0E-04
		min	-5.6E-03	-2.2E-04	-1.5E-03	-6.0E-05	2.1E-04	8.4E-06	-6.2E-03	-2.5E-04

Table 6-35: Column curvature envelopes.

	Location		Bent 2 bottom east column, trans. direction at 8.5in (216mm) from fixity		Bent 2 bottom east column, long. direction at 2.5in (64mm) from fixity		Bent 3 top west column, trans direction at 2.5in (64mm) from fixity		Bent 3 top west column, trans. direction at 8.5in (216mm) from fixity	
	Gauge length		7in	178mm	5in	127mm	5in	127mm	7in	178mm
	Unit		rad/in	rad/mm	rad/in	rad/mm	rad/in	rad/mm	rad/in	rad/mm
Low Amplitude Testing	1a	max	2.3E-05	9.0E-07	0.0E+00	0.0E+00	7.8E-05	3.1E-06	2.0E-05	7.7E-07
		min	-3.3E-05	-1.3E-06	-1.3E-05	-4.9E-07	-6.6E-05	-2.6E-06	-2.6E-05	-1.0E-06
	1b	max	4.4E-05	1.7E-06	-5.8E-06	-2.3E-07	1.3E-04	5.1E-06	3.9E-05	1.5E-06
		min	-5.6E-05	-2.2E-06	-2.4E-05	-9.5E-07	-1.0E-04	-4.0E-06	-5.4E-05	-2.1E-06
	2a	max	1.1E-05	4.4E-07	-6.3E-07	-2.5E-08	1.0E-04	4.0E-06	3.6E-05	1.4E-06
		min	-2.4E-05	-9.6E-07	-1.4E-05	-5.7E-07	-8.1E-05	-3.2E-06	-3.2E-05	-1.3E-06
	2b	max	3.9E-05	1.5E-06	1.3E-05	5.1E-07	2.8E-04	1.1E-05	1.3E-04	5.3E-06
		min	-5.8E-05	-2.3E-06	-1.5E-05	-6.0E-07	-2.1E-04	-8.4E-06	-8.5E-05	-3.3E-06
	3a	max	2.4E-05	9.4E-07	-1.0E-05	-4.1E-07	1.8E-05	7.3E-07	1.9E-05	7.4E-07
		min	-1.6E-05	-6.2E-07	-1.9E-05	-7.5E-07	-7.9E-05	-3.1E-06	-2.3E-06	-9.2E-08
	3b	max	3.1E-05	1.2E-06	8.4E-06	3.3E-07	5.5E-05	2.2E-06	3.3E-05	1.3E-06
		min	-6.9E-05	-2.7E-06	-8.6E-06	-3.4E-07	-1.1E-04	-4.4E-06	-2.7E-05	-1.1E-06
	4b	max	2.2E-05	8.7E-07	2.0E-06	7.9E-08	1.4E-04	5.5E-06	8.3E-05	3.3E-06
		min	-4.7E-05	-1.9E-06	-1.5E-05	-5.9E-07	-1.5E-04	-5.8E-06	-6.4E-05	-2.5E-06
	5b	max	2.6E-05	1.0E-06	-5.1E-06	-2.0E-07	1.1E-04	4.5E-06	6.8E-05	2.7E-06
		min	-2.6E-05	-1.0E-06	-1.8E-05	-7.2E-07	-1.4E-04	-5.5E-06	-6.1E-05	-2.4E-06
	6b	max	2.3E-05	9.0E-07	-6.4E-06	-2.5E-07	6.4E-05	2.5E-06	3.9E-05	1.5E-06
		min	-4.4E-05	-1.7E-06	-1.9E-05	-7.5E-07	-1.6E-04	-6.1E-06	-1.8E-05	-7.0E-07
	8	max	2.8E-05	1.1E-06	-2.4E-06	-9.5E-08	7.8E-05	3.1E-06	5.0E-05	2.0E-06
		min	-4.3E-05	-1.7E-06	-1.8E-05	-6.9E-07	-1.2E-04	-4.7E-06	-4.5E-05	-1.8E-06
	9a	max	2.2E-05	8.6E-07	2.0E-05	8.0E-07	1.0E-04	4.0E-06	-7.5E-06	-3.0E-07
		min	-5.2E-06	-2.0E-07	-8.1E-05	-3.2E-06	5.9E-06	2.3E-07	-4.9E-05	-1.9E-06
	9b	max	3.5E-05	1.4E-06	8.2E-05	3.2E-06	1.7E-04	6.6E-06	2.4E-05	9.6E-07
		min	-6.5E-05	-2.5E-06	-1.2E-04	-4.9E-06	-6.0E-05	-2.4E-06	-8.2E-05	-3.2E-06
	10	max	2.7E-05	1.1E-06	-8.8E-06	-3.5E-07	1.7E-04	6.7E-06	3.1E-05	1.2E-06
		min	-4.3E-05	-1.7E-06	-2.8E-05	-1.1E-06	-7.3E-05	-2.9E-06	-9.5E-05	-3.8E-06
	11	max	3.2E-05	1.3E-06	-2.0E-05	-8.0E-07	1.9E-04	7.3E-06	4.2E-05	1.6E-06
		min	-2.7E-05	-1.1E-06	-3.2E-05	-1.3E-06	-7.5E-05	-2.9E-06	-9.5E-05	-3.7E-06
High Amplitude Testing	12	max	3.9E-05	1.5E-06	-1.4E-05	-5.7E-07	2.3E-04	9.0E-06	6.8E-05	2.7E-06
		min	-9.2E-05	-3.6E-06	-2.7E-05	-1.1E-06	-1.1E-04	-4.2E-06	-1.0E-04	-4.1E-06
	13	max	5.9E-05	2.3E-06	-6.2E-06	-2.4E-07	4.9E-04	1.9E-05	2.0E-04	7.8E-06
		min	-2.5E-04	-1.0E-05	-5.1E-05	-2.0E-06	-3.5E-04	-1.4E-05	-2.7E-04	-1.1E-05
	14	max	7.8E-05	3.1E-06	-2.4E-06	-9.5E-08	7.7E-04	3.0E-05	2.9E-04	1.1E-05
		min	-3.2E-04	-1.3E-05	-8.8E-05	-3.4E-06	-6.7E-04	-2.6E-05	-4.4E-04	-1.7E-05
	15	max	2.5E-04	9.9E-06	2.0E-06	7.9E-08	1.7E-03	6.5E-05	3.6E-04	1.4E-05
		min	-6.5E-04	-2.5E-05	-2.3E-04	-9.1E-06	-1.9E-03	-7.3E-05	-7.5E-04	-2.9E-05
	16	max	7.8E-04	3.1E-05	-3.4E-06	-1.3E-07	3.0E-03	1.2E-04	3.4E-04	1.3E-05
		min	-9.2E-04	-3.6E-05	-3.1E-04	-1.2E-05	-3.8E-03	-1.5E-04	-1.0E-03	-4.1E-05
	17	max	7.1E-04	2.8E-05	-2.0E-05	-8.0E-07	2.5E-03	9.9E-05	2.8E-04	1.1E-05
		min	-7.2E-04	-2.8E-05	-2.9E-04	-1.1E-05	-2.6E-03	-1.0E-04	-6.6E-04	-2.6E-05
	18	max	1.4E-03	5.4E-05	1.2E-04	4.6E-06	6.4E-03	2.5E-04	3.5E-04	1.4E-05
		min	-1.4E-03	-5.4E-05	-6.2E-04	-2.5E-05	-6.6E-03	-2.6E-04	-1.7E-03	-6.5E-05
	19	max	1.2E-03	4.7E-05	-1.9E-05	-7.6E-07	1.2E-02	4.6E-04	9.3E-04	3.7E-05
		min	-1.8E-03	-7.2E-05	-1.0E-03	-4.0E-05	-5.5E-03	-2.2E-04	-7.8E-04	-3.1E-05
	20	max	9.5E-04	3.8E-05	-8.6E-05	-3.4E-06	9.7E-03	3.8E-04	1.9E-04	7.4E-06
		min	-1.3E-03	-5.0E-05	-7.6E-04	-3.0E-05	-4.1E-03	-1.6E-04	-5.4E-04	-2.1E-05
Post-Tests	21	max	8.3E-04	3.3E-05	-1.5E-05	-6.0E-07	1.1E-02	4.1E-04	4.1E-04	1.6E-05
		min	-1.4E-03	-5.6E-05	-7.9E-04	-3.1E-05	-7.3E-03	-2.9E-04	-2.0E-04	-8.0E-06
	22	max	1.4E-03	5.5E-05	-1.4E-04	-5.4E-06	---	---	---	---
		min	-2.1E-03	-8.1E-05	-1.3E-03	-5.0E-05	---	---	---	---

Table 6-36: Column curvature envelopes.

	Location		Bent 3 top west column, long. direction at 2.5in (64mm) from fixity		Bent 3 bottom west column, trans direction at 2.5in (64mm) from fixity		Bent 3 bottom west column, trans direction at 8.5in (216mm) from fixity		Bent 3 bottom west column, long. direction at 2.5in (64mm) from fixity	
	Gauge length		5in	127mm	5in	127mm	7in	178mm	5in	127mm
	Unit		rad/in	rad/mm	rad/in	rad/mm	rad/in	rad/mm	rad/in	rad/mm
Low Amplitude Testing	1a	max	1.1E-05	4.1E-07	1.2E-04	4.7E-06	1.9E-05	7.4E-07	2.4E-05	9.3E-07
		min	-2.0E-05	-8.0E-07	-5.4E-05	-2.1E-06	-3.7E-05	-1.5E-06	1.3E-06	5.0E-08
	1b	max	2.4E-05	9.3E-07	2.2E-04	8.6E-06	4.5E-05	1.8E-06	4.5E-05	1.8E-06
		min	-3.2E-05	-1.3E-06	-1.2E-04	-4.8E-06	-5.9E-05	-2.3E-06	-4.6E-06	-1.8E-07
	2a	max	1.1E-05	4.4E-07	1.5E-04	5.8E-06	2.8E-05	1.1E-06	3.3E-05	1.3E-06
		min	-2.4E-05	-9.6E-07	-1.2E-04	-4.7E-06	-5.6E-05	-2.2E-06	1.9E-06	7.5E-08
	2b	max	3.6E-05	1.4E-06	3.3E-04	1.3E-05	8.1E-05	3.2E-06	8.1E-05	3.2E-06
		min	-4.8E-05	-1.9E-06	-3.7E-04	-1.5E-05	-1.2E-04	-4.7E-06	-2.0E-05	-8.0E-07
	3a	max	2.0E-06	7.9E-08	7.2E-05	2.8E-06	4.7E-06	1.8E-07	2.6E-05	1.0E-06
		min	-2.4E-05	-9.3E-07	-5.7E-06	-2.2E-07	-2.3E-05	-9.0E-07	1.5E-05	5.9E-07
	3b	max	1.3E-05	5.1E-07	1.3E-04	5.3E-06	2.8E-05	1.1E-06	3.1E-05	1.2E-06
		min	-3.2E-05	-1.3E-06	-6.4E-05	-2.5E-06	-4.1E-05	-1.6E-06	-1.3E-06	-5.0E-08
	4b	max	2.6E-05	1.0E-06	2.6E-04	1.0E-05	6.3E-05	2.5E-06	4.6E-05	1.8E-06
		min	-2.5E-05	-9.8E-07	-2.0E-04	-7.8E-06	-7.3E-05	-2.9E-06	-9.3E-06	-3.6E-07
	5b	max	2.4E-05	9.3E-07	2.4E-04	9.5E-06	5.7E-05	2.2E-06	4.0E-05	1.6E-06
		min	-2.7E-05	-1.1E-06	-1.6E-04	-6.5E-06	-6.5E-05	-2.6E-06	-2.6E-06	-1.0E-07
	6b	max	9.9E-06	3.9E-07	1.2E-04	4.6E-06	2.2E-05	8.5E-07	2.6E-05	1.0E-06
		min	-1.8E-05	-7.0E-07	-7.9E-05	-3.1E-06	-4.8E-05	-1.9E-06	-2.6E-06	-1.0E-07
	8	max	2.1E-05	8.3E-07	2.0E-04	7.7E-06	4.1E-05	1.6E-06	2.6E-05	1.0E-06
		min	-2.0E-05	-7.7E-07	-1.0E-04	-4.1E-06	-5.3E-05	-2.1E-06	-5.9E-06	-2.3E-07
	9a	max	5.4E-05	2.1E-06	1.2E-04	4.8E-06	-2.0E-05	-7.9E-07	1.2E-04	4.6E-06
		min	-1.1E-04	-4.4E-06	-5.5E-06	-2.2E-07	-7.8E-05	-3.1E-06	-8.1E-05	-3.2E-06
	9b	max	1.7E-04	6.5E-06	2.3E-04	9.2E-06	1.2E-05	4.6E-07	2.5E-04	9.6E-06
		min	-2.2E-04	-8.5E-06	-1.1E-04	-4.4E-06	-1.1E-04	-4.3E-06	-2.0E-04	-7.9E-06
	10	max	1.5E-05	5.9E-07	2.5E-04	9.8E-06	1.3E-05	5.0E-07	4.8E-05	1.9E-06
		min	-4.8E-05	-1.9E-06	-1.3E-04	-5.3E-06	-1.0E-04	-4.1E-06	-1.3E-05	-5.2E-07
	11	max	1.9E-05	7.5E-07	2.5E-04	9.9E-06	1.4E-05	5.3E-07	5.1E-05	2.0E-06
		min	-4.9E-05	-1.9E-06	-1.5E-04	-5.7E-06	-1.1E-04	-4.2E-06	-1.6E-05	-6.4E-07
High Amplitude Testing	12	max	3.7E-05	1.4E-06	2.9E-04	1.1E-05	4.8E-05	1.9E-06	5.9E-05	2.3E-06
		min	-7.1E-05	-2.8E-06	-2.3E-04	-8.9E-06	-1.1E-04	-4.3E-06	-3.7E-05	-1.4E-06
	13	max	1.4E-04	5.3E-06	6.1E-04	2.4E-05	1.7E-04	6.6E-06	1.5E-04	5.8E-06
		min	-1.4E-04	-5.6E-06	-6.4E-04	-2.5E-05	-1.9E-04	-7.6E-06	-1.3E-04	-4.9E-06
	14	max	2.8E-04	1.1E-05	1.0E-03	4.0E-05	2.4E-04	9.5E-06	2.4E-04	9.5E-06
		min	-1.8E-04	-7.0E-06	-1.0E-03	-4.0E-05	-2.7E-04	-1.1E-05	-2.1E-04	-8.5E-06
	15	max	4.3E-04	1.7E-05	2.6E-03	1.0E-04	4.9E-04	1.9E-05	7.5E-04	3.0E-05
		min	-2.1E-04	-8.4E-06	-3.7E-03	-1.5E-04	-5.1E-04	-2.0E-05	-2.8E-04	-1.1E-05
	16	max	7.2E-04	2.8E-05	5.2E-03	2.0E-04	7.3E-04	2.9E-05	1.1E-03	4.4E-05
		min	-5.0E-04	-2.0E-05	-4.1E-03	-1.6E-04	-5.5E-04	-2.2E-05	-4.8E-04	-1.9E-05
	17	max	6.3E-04	2.5E-05	3.5E-03	1.4E-04	4.1E-04	1.6E-05	1.0E-03	3.9E-05
		min	-4.4E-04	-1.7E-05	-3.6E-03	-1.4E-04	-4.7E-04	-1.8E-05	-3.3E-04	-1.3E-05
	18	max	1.4E-03	5.7E-05	8.6E-03	3.4E-04	1.1E-03	4.2E-05	1.7E-03	6.8E-05
		min	-7.6E-04	-3.0E-05	-8.1E-03	-3.2E-04	-8.8E-04	-3.5E-05	-1.0E-03	-4.0E-05
	19	max	1.2E-03	4.6E-05	6.7E-03	2.6E-04	3.4E-04	1.4E-05	2.8E-03	1.1E-04
		min	-1.6E-03	-6.4E-05	-1.5E-02	-5.9E-04	-9.0E-04	-3.5E-05	-6.7E-04	-2.6E-05
	20	max	2.1E-04	8.4E-06	4.9E-03	1.9E-04	1.7E-04	6.5E-06	2.3E-03	9.0E-05
		min	-1.4E-03	-5.6E-05	-1.2E-02	-4.6E-04	-2.8E-04	-1.1E-05	-2.1E-04	-8.4E-06
Post-Tests	21	max	4.6E-04	1.8E-05	7.6E-03	3.0E-04	1.4E-04	5.4E-06	2.9E-03	1.1E-04
		min	-2.5E-03	-9.8E-05	-1.3E-02	-5.1E-04	-2.8E-04	-1.1E-05	-6.1E-04	-2.4E-05
	22	max	---	---	---	---	---	---	---	---
		min	---	---	---	---	---	---	---	---

Table 6-37: Column curvature envelopes.

	Location		Bent 3 top east column, trans. direction at 2.5in (64mm) from fixity		Bent 3 top east column, trans direction at 8.5in (216mm) from fixity		Bent 3 top east column, long. direction at 2.5in (64mm) from fixity		Bent 3 bottom east column, trans. direction at 2.5in (64mm) from fixity	
	Gauge length		5in	127mm	7in	178mm	5in	127mm	5in	127mm
	Unit		rad/in	rad/mm	rad/in	rad/mm	rad/in	rad/mm	rad/in	rad/mm
Low Amplitude Testing	1a	max	8.4E-05	3.3E-06	2.3E-06	9.2E-08	1.4E-05	5.7E-07	8.7E-05	3.4E-06
		min	-8.6E-05	-3.4E-06	-3.6E-05	-1.4E-06	-2.2E-05	-8.5E-07	-7.8E-05	-3.1E-06
	1b	max	1.5E-04	5.8E-06	1.9E-05	7.4E-07	1.8E-05	7.2E-07	1.9E-04	7.4E-06
		min	-1.7E-04	-6.8E-06	-6.5E-05	-2.5E-06	-2.4E-05	-9.3E-07	-1.6E-04	-6.3E-06
	2a	max	1.3E-04	5.2E-06	1.6E-05	6.5E-07	1.6E-05	6.4E-07	1.1E-04	4.4E-06
		min	-1.1E-04	-4.2E-06	-4.7E-05	-1.8E-06	-2.3E-05	-9.0E-07	-1.5E-04	-6.0E-06
	2b	max	3.5E-04	1.4E-05	1.4E-04	5.3E-06	4.1E-05	1.6E-06	2.8E-04	1.1E-05
		min	-2.6E-04	-1.0E-05	-9.4E-05	-3.7E-06	-3.5E-05	-1.4E-06	-3.8E-04	-1.5E-05
	3a	max	4.7E-05	1.8E-06	3.3E-06	1.3E-07	1.1E-05	4.1E-07	3.3E-05	1.3E-06
		min	-3.9E-05	-1.5E-06	-1.6E-05	-6.5E-07	-2.2E-05	-8.5E-07	-4.2E-05	-1.6E-06
	3b	max	1.0E-04	4.1E-06	1.1E-05	4.2E-07	1.8E-05	7.0E-07	9.1E-05	3.6E-06
		min	-8.2E-05	-3.2E-06	-4.0E-05	-1.6E-06	-2.8E-05	-1.1E-06	-8.5E-05	-3.4E-06
	4b	max	2.1E-04	8.4E-06	6.7E-05	2.6E-06	2.5E-05	9.8E-07	2.2E-04	8.6E-06
		min	-2.0E-04	-7.7E-06	-7.6E-05	-3.0E-06	-1.5E-05	-5.9E-07	-2.3E-04	-9.1E-06
	5b	max	2.0E-04	7.8E-06	5.3E-05	2.1E-06	2.4E-05	9.3E-07	2.0E-04	7.7E-06
		min	-1.8E-04	-7.1E-06	-7.3E-05	-2.9E-06	-1.7E-05	-6.7E-07	-1.9E-04	-7.4E-06
	6b	max	1.2E-04	4.6E-06	1.6E-05	6.5E-07	2.2E-05	8.7E-07	8.3E-05	3.2E-06
		min	-7.9E-05	-3.1E-06	-3.4E-05	-1.3E-06	-1.4E-05	-5.7E-07	-1.1E-04	-4.3E-06
	8	max	1.3E-04	5.0E-06	2.4E-05	9.4E-07	2.6E-05	1.0E-06	1.6E-04	6.1E-06
		min	-1.6E-04	-6.2E-06	-5.7E-05	-2.2E-06	-9.8E-06	-3.9E-07	-1.3E-04	-5.2E-06
	9a	max	6.4E-05	2.5E-06	4.5E-07	1.8E-08	8.8E-05	3.5E-06	5.8E-05	2.3E-06
		min	-7.1E-05	-2.8E-06	-3.2E-05	-1.3E-06	-7.6E-05	-3.0E-06	-6.5E-05	-2.6E-06
	9b	max	1.4E-04	5.7E-06	3.8E-05	1.5E-06	1.8E-04	7.0E-06	1.6E-04	6.3E-06
		min	-1.5E-04	-5.9E-06	-6.0E-05	-2.4E-06	-1.6E-04	-6.2E-06	-1.6E-04	-6.3E-06
	10	max	1.7E-04	6.5E-06	4.8E-05	1.9E-06	3.1E-05	1.2E-06	1.8E-04	7.1E-06
		min	-1.8E-04	-7.2E-06	-7.6E-05	-3.0E-06	-3.1E-05	-1.2E-06	-1.9E-04	-7.5E-06
	11	max	1.8E-04	7.0E-06	5.5E-05	2.2E-06	3.3E-05	1.3E-06	1.8E-04	6.9E-06
		min	-1.9E-04	-7.3E-06	-7.7E-05	-3.0E-06	-2.9E-05	-1.2E-06	-2.0E-04	-8.1E-06
High Amplitude Testing	12	max	2.5E-04	9.8E-06	8.7E-05	3.4E-06	2.9E-05	1.1E-06	2.3E-04	9.2E-06
		min	-2.1E-04	-8.4E-06	-9.0E-05	-3.6E-06	-5.4E-05	-2.1E-06	-2.7E-04	-1.0E-05
	13	max	5.7E-04	2.3E-05	2.3E-04	8.9E-06	1.1E-04	4.3E-06	5.4E-04	2.1E-05
		min	-4.9E-04	-1.9E-05	-2.5E-04	-9.8E-06	-1.1E-04	-4.3E-06	-6.4E-04	-2.5E-05
	14	max	9.9E-04	3.9E-05	3.0E-04	1.2E-05	1.3E-04	5.3E-06	9.4E-04	3.7E-05
		min	-8.3E-04	-3.3E-05	-4.2E-04	-1.6E-05	-1.6E-04	-6.2E-06	-1.0E-03	-4.0E-05
	15	max	3.2E-03	1.3E-04	8.0E-04	3.2E-05	5.1E-04	2.0E-05	2.4E-03	9.6E-05
		min	-2.3E-03	-9.2E-05	-7.0E-04	-2.8E-05	-6.2E-05	-2.4E-06	-3.5E-03	-1.4E-04
	16	max	3.6E-03	1.4E-04	8.8E-04	3.4E-05	6.9E-04	2.7E-05	5.0E-03	2.0E-04
		min	-4.8E-03	-1.9E-04	-9.3E-04	-3.6E-05	-1.7E-04	-6.5E-06	-3.8E-03	-1.5E-04
	17	max	3.0E-03	1.2E-04	7.5E-04	3.0E-05	6.5E-04	2.5E-05	3.5E-03	1.4E-04
		min	-3.3E-03	-1.3E-04	-6.3E-04	-2.5E-05	-4.6E-06	-1.8E-07	-3.1E-03	-1.2E-04
	18	max	7.0E-03	2.8E-04	1.6E-03	6.3E-05	7.3E-04	2.9E-05	9.3E-03	3.7E-04
		min	-8.7E-03	-3.4E-04	-1.6E-03	-6.1E-05	-2.4E-04	-9.3E-06	-6.8E-03	-2.7E-04
	19	max	1.4E-02	5.3E-04	2.1E-03	8.2E-05	8.8E-04	3.4E-05	7.5E-03	2.9E-04
		min	-6.0E-03	-2.4E-04	-1.1E-03	-4.3E-05	-3.3E-04	-1.3E-05	-1.3E-02	-5.0E-04
	20	max	1.1E-02	4.5E-04	-1.3E-04	-5.1E-06	6.7E-04	2.6E-05	5.8E-03	2.3E-04
		min	-5.1E-03	-2.0E-04	-6.7E-04	-2.6E-05	6.9E-05	2.7E-06	-1.1E-02	-4.2E-04
Post-Tests	21	max	1.3E-02	5.1E-04	-4.1E-05	-1.6E-06	4.2E-04	1.7E-05	1.0E-02	4.0E-04
		min	-9.8E-03	-3.9E-04	-5.0E-04	-2.0E-05	-6.1E-04	-2.4E-05	-1.2E-02	-4.8E-04
	22	max	---	---	---	---	---	---	---	---
		min	---	---	---	---	---	---	---	---

Table 6-38: Column curvature envelopes.

	Location		Bent 3 bottom east column, trans. direction at 8.5in (216mm) from fixity		Bent 3 bottom east column, long. direction at 2.5in (64mm) from fixity	
	Gauge length		7in	178mm	5in	127mm
	Unit		rad/in	rad/mm	rad/in	rad/mm
Low Amplitude Testing	1a	max	2.0E-05	7.9E-07	1.8E-05	7.2E-07
		min	-2.0E-05	-7.9E-07	-7.2E-06	-2.8E-07
	1b	max	4.1E-05	1.6E-06	3.5E-05	1.4E-06
		min	-4.0E-05	-1.6E-06	-1.7E-05	-6.8E-07
	2a	max	2.4E-05	9.6E-07	1.8E-05	6.9E-07
		min	-4.0E-05	-1.6E-06	-4.7E-06	-1.9E-07
	2b	max	6.7E-05	2.6E-06	3.3E-05	1.3E-06
		min	-1.2E-04	-4.7E-06	-1.5E-05	-5.9E-07
	3a	max	-6.9E-06	-2.7E-07	1.5E-05	5.9E-07
		min	-2.4E-05	-9.3E-07	-3.5E-06	-1.4E-07
	3b	max	1.2E-05	4.6E-07	2.9E-05	1.1E-06
		min	-4.0E-05	-1.6E-06	-1.9E-05	-7.5E-07
	4b	max	4.7E-05	1.9E-06	2.8E-05	1.1E-06
		min	-8.2E-05	-3.2E-06	-1.6E-05	-6.2E-07
	5b	max	4.2E-05	1.6E-06	2.4E-05	9.4E-07
		min	-7.1E-05	-2.8E-06	-2.2E-05	-8.6E-07
	6b	max	6.9E-06	2.7E-07	9.3E-06	3.6E-07
		min	-4.7E-05	-1.9E-06	-2.2E-05	-8.8E-07
	8	max	3.0E-05	1.2E-06	1.9E-05	7.5E-07
		min	-5.7E-05	-2.2E-06	-2.9E-05	-1.2E-06
	9a	max	4.9E-06	1.9E-07	1.1E-04	4.4E-06
		min	-3.3E-05	-1.3E-06	-1.1E-04	-4.2E-06
	9b	max	3.3E-05	1.3E-06	2.3E-04	9.2E-06
		min	-6.5E-05	-2.5E-06	-2.5E-04	-9.9E-06
	10	max	3.7E-05	1.4E-06	3.4E-05	1.3E-06
		min	-7.1E-05	-2.8E-06	-1.3E-05	-5.1E-07
	11	max	3.5E-05	1.4E-06	2.9E-05	1.1E-06
		min	-7.3E-05	-2.9E-06	-1.4E-05	-5.6E-07
High Amplitude Testing	12	max	4.9E-05	1.9E-06	7.2E-05	2.8E-06
		min	-1.0E-04	-3.9E-06	1.2E-05	4.6E-07
	13	max	1.4E-04	5.5E-06	1.2E-04	4.6E-06
		min	-2.2E-04	-8.6E-06	-6.1E-05	-2.4E-06
	14	max	2.5E-04	9.7E-06	1.6E-04	6.5E-06
		min	-3.1E-04	-1.2E-05	-7.6E-05	-3.0E-06
	15	max	4.9E-04	1.9E-05	4.7E-04	1.8E-05
		min	-7.2E-04	-2.8E-05	-1.2E-04	-4.7E-06
	16	max	8.0E-04	3.2E-05	5.6E-04	2.2E-05
		min	-8.1E-04	-3.2E-05	-3.5E-04	-1.4E-05
	17	max	4.8E-04	1.9E-05	3.4E-04	1.3E-05
		min	-7.0E-04	-2.8E-05	-3.0E-04	-1.2E-05
	18	max	9.4E-04	3.7E-05	7.4E-04	2.9E-05
		min	-1.7E-03	-6.8E-05	-6.2E-04	-2.4E-05
	19	max	1.6E-04	6.1E-06	1.6E-03	6.4E-05
		min	-2.0E-03	-7.9E-05	-7.9E-04	-3.1E-05
	20	max	-3.9E-05	-1.5E-06	1.4E-03	5.6E-05
		min	-4.5E-04	-1.8E-05	-5.1E-04	-2.0E-05
Post-Tests	21	max	6.2E-05	2.4E-06	1.7E-03	6.9E-05
		min	-3.5E-04	-1.4E-05	-2.6E-04	-1.0E-05
	22	max	---	---	---	---
		min	---	---	---	---

Table 6-39: Damping calculated at each bent during square wave tests using log decrement method.

Test Number	Bent 1	Bent 2	Bent 3	Average
SQ0809-2	0.0419	0.0406	0.0442	0.0422
SQ1112-1	0.0361	0.0427	0.0501	0.0430
SQ1112-2	0.0382	0.0427	0.0497	0.0435
SQ1415	0.0399	0.0452	0.0445	0.0432
SQ1718	0.0391	0.0408	0.0521	0.0440
SQ1819	0.0393	0.0435	0.0562	0.0463
SQ1920	0.0384	0.0385	0.0433	0.0400
Average	0.0390	0.0420	0.0486	**0.0432**

Table 6-40: Modal frequencies (Hz) recorded from superstructure accelerometers during progression of tests.

		Transverse Modes					Longitudinal Modes	
WN#	event timing	1	2	3	4	5	1	2
0001	before testing	3.03	4.25	12.94	16.02	18.51	3.08	5.22
0304	after test 3b	2.73	3.76	12.60	16.02	18.26	3.03	5.13
0809-1	after test 8	2.73	3.76	12.60	16.02	18.26	3.03	5.13
0809-2	after test 8	2.64	3.76	12.60	16.21	18.26	3.03	5.03
1112-1	after test 11	2.64	3.76	12.60	16.02	17.87	3.03	4.98
1112-2	after test 11	2.64	3.76	12.60	16.02	17.87	3.03	4.98
1415	after test 14	2.29	3.37	12.26	15.63	17.87	2.73	4.88
1718	after test 17	1.51	1.76	12.11	14.26	15.28	2.00	4.49
1819	after test 18	1.37	1.61	11.91	14.16	14.99	1.76	4.39
1920	after test 19	1.37	1.51	11.77	13.92	14.50	2.00	4.39
2021	after test 20	1.37	2.00	13.77	13.77	14.65	2.00	4.74

Table 6-41: Modal periods (seconds) recorded from superstructure accelerometers during progression of tests.

		Transverse Modes					Longitudinal Modes	
WN#	event timing	1	2	3	4	5	1	2
0001	before testing	0.33	0.24	0.08	0.06	0.05	0.33	0.19
0304	after test 3b	0.37	0.27	0.08	0.06	0.05	0.33	0.20
0809-1	after test 8	0.37	0.27	0.08	0.06	0.05	0.33	0.20
0809-2	after test 8	0.38	0.27	0.08	0.06	0.05	0.33	0.20
1011-1	after test 11	0.38	0.27	0.08	0.06	0.06	0.33	0.20
1011-2	after test 11	0.38	0.27	0.08	0.06	0.06	0.33	0.20
1415	after test 14	0.44	0.30	0.08	0.06	0.06	0.37	0.20
1718	after test 17	0.66	0.57	0.08	0.07	0.07	0.50	0.22
1819	after test 18	0.73	0.62	0.08	0.07	0.07	0.57	0.23
1920	after test 19	0.73	0.66	0.08	0.07	0.07	0.50	0.23
2021	after test 20	0.73	0.50	0.07	0.07	0.07	0.50	0.21

Table 6-42: Target and achieved maximum earthquake accelerations for tables 1 through 3 during high amplitude tests (12-20) and select low amplitude tests (1 and 8).

Table motion	Table 1 (bent1)			Table 2 (bent2)			Table 3 (bent3)		
	Target (g)	Achieved (g)	Achieved /target	Target (g)	Achieved (g)	Achieved /target	Target (g)	Achieved (g)	Achieved /target
test 1	0.15	0.21	1.34	0.15	0.32	2.09	0.15	0.25	1.63
test 8	0.15	0.16	1.07	0.15	0.22	1.41	0.15	0.21	1.38
test 12	0.08	0.07	0.94	0.08	0.10	1.29	0.08	0.08	1.09
test 13	0.15	0.18	1.18	0.15	0.18	1.19	0.15	0.17	1.15
test 14	0.25	0.35	1.39	0.25	0.31	1.25	0.25	0.28	1.12
test 15	0.50	0.67	1.34	0.50	0.64	1.29	0.50	0.72	1.45
test 16	0.75	0.98	1.31	0.75	0.94	1.25	0.75	1.25	1.67
test 17	1.00	1.20	1.20	1.00	1.50	1.50	1.00	1.09	1.09
test 18	1.33	1.56	1.17	1.33	1.81	1.36	1.33	1.59	1.19
test 19	1.66	2.00	1.20	1.66	2.13	1.28	1.66	2.20	1.33
test 20	1.00	1.26	1.26	1.00	1.30	1.30	1.00	1.43	1.43

Table 6-43: Target and achieved maximum spectral accelerations (2% damping) for tables 1 through 3 during high amplitude tests (12-20) and select low amplitude tests (1 and 8).

Table motion	Table 1 (bent1)			Table 2 (bent2)			Table 3 (bent3)		
	Target (g)	Achieved (g)	Achieved /target	Target (g)	Achieved (g)	Achieved /target	Target (g)	Achieved (g)	Achieved /target
test 1	1.84	2.38	1.29	2.38	2.67	1.12	2.38	3.36	1.41
test 8	1.84	1.78	0.96	1.78	1.53	0.86	1.78	2.20	1.24
test 12	0.58	0.47	0.80	0.58	0.49	0.84	0.58	0.48	0.83
test 13	1.16	1.15	0.99	1.16	1.04	0.90	1.16	1.01	0.87
test 14	1.93	2.37	1.22	1.93	1.94	1.00	1.93	1.82	0.94
test 15	3.86	5.07	1.31	3.86	4.60	1.19	3.86	6.43	1.66
test 16	5.80	7.01	1.21	5.80	6.88	1.19	5.80	10.42	1.80
test 17	7.73	7.66	0.99	7.73	8.98	1.16	7.73	7.78	1.01
test 18	10.28	10.65	1.04	10.28	11.29	1.10	10.28	10.81	1.05
test 19	12.83	13.09	1.02	12.83	13.17	1.03	12.83	14.39	1.12
test 20	7.73	8.30	1.07	7.73	8.30	1.07	7.73	9.73	1.26

Table 6-44: Maximum displacement incoherency of achieved shake table motions between adjacent tables for all tests.

Test			Maximum displacement difference in table motions			
			Shake tables 1 and 2		Shake tables 2 and 3	
			(in)	(mm)	(in)	(mm)
Coherent and Incoherent Target Motions	Low Amplitude Testing	1a	0.029	0.73	0.024	0.62
		1	0.073	1.87	0.040	1.02
		2a	0.032	0.82	0.029	0.74
		2	0.105	2.67	0.077	1.96
		3a	0.058	1.47	0.021	0.52
		3	0.138	3.49	0.065	1.65
		4	0.065	1.64	0.032	0.81
		5	0.079	2.00	0.054	1.37
		6	0.063	1.61	0.050	1.28
		8	0.060	1.52	0.042	1.07
		9a	0.045	1.15	0.022	0.56
		9	0.096	2.44	0.050	1.27
		10	0.071	1.81	0.032	0.80
		11	0.067	1.70	0.039	0.99
Coherent Target Motions	High Amplitude Testing	12	0.079	2.00	0.031	0.79
		13	0.162	4.12	0.077	1.95
		14	0.255	6.48	0.139	3.54
		15	0.561	14.26	0.320	8.12
		16	1.219	30.95	0.519	13.18
		17	0.579	14.72	0.357	9.06
		18	1.392	35.37	0.483	12.26
		19	2.271	57.69	0.516	13.11
		20	1.588	40.35	0.371	9.43
	Post-Tests	21	1.882	47.81	0.418	10.61
		22	2.755	69.97	0.654	16.61

Table 6-45: Comparison of bent 1-3 lateral force envelopes for tests 15 and 18 for measured from actuator pressure and estimated from bent acceleration.

		From actuator pressure		Estimate from acceleration		
		kip	kN	kip	kN	% diff
Test 15	bent 1 max	42.0	186.7	43.2	192.2	-2.9
	bent 1 min	-42.9	-191.0	-36.3	-161.6	16.6
	bent 2 max	27.9	124.2	46.8	208.2	-50.6
	bent 2 min	-28.6	-127.2	-40.0	-178.0	-33.3
	bent 3 max	49.8	221.3	49.0	217.8	1.6
	bent 3 min	-50.8	-226.0	-52.1	-232.0	-2.6
Test 18	bent 1 max	52.1	232.0	43.7	194.4	17.6
	bent 1 min	-46.3	-206.0	-40.7	-181.0	12.9
	bent 2 max	42.6	189.7	43.8	194.7	-2.6
	bent 2 min	-41.1	-182.9	-48.8	-217.0	-17.1
	bent 3 max	51.8	230.5	55.0	244.5	-5.9
	bent 3 min	-51.2	-227.6	-56.9	-253.1	-10.6

Table 6-46: Maximum transducer measured compressive strains at extreme fiber of core concrete for bents 1-3 during tests 18 through 22.

	Test number				
Location	18	19	20	21	22
bent 1 top west	-0.0200	**-0.0229**	-0.0186	-0.0258	-0.0227
bent 1 bottom west	-0.0199	**-0.0212**	-0.0161	-0.0232	-0.0220
bent 1 top east	-0.0277	**-0.0447**	-0.0264	-0.0306	-0.0441
bent 1 bottom east	-0.0116	**-0.0161**	-0.0070	-0.0127	-0.0139
bent 1 average	-0.0198	**-0.0262**	-0.0170	-0.0231	-0.0257
bent 2 top west	-0.0147	-0.0359	-0.0276	-0.0297	**-0.0451**
bent 2 bottom west	-0.0088	-0.0189	-0.0137	-0.0151	**-0.0274**
bent 2 top east	-0.0184	-0.0207	-0.0158	-0.0177	**-0.0289**
bent 2 bottom east	-0.0149	-0.0168	-0.0130	-0.0141	**-0.0254**
bent 2 average	-0.0142	-0.0231	-0.0175	-0.0191	**-0.0317**
bent 3 top west	-0.0300	**-0.0352**	-0.0325	N/A	N/A
bent 3 bottom west	-0.0204	**-0.0545**	-0.0519	N/A	N/A
bent 3 top east	-0.0399	**-0.0406**	-0.0275	N/A	N/A
bent 3 bottom east	-0.0247	**-0.0416**	-0.0454	N/A	N/A
bent 3 average	-0.0287	**-0.0430**	-0.0393		

note: bold values denote table test with largest displacement demand

Table 6-47: Comparison of maxumum novotechnic measured compressive strain on core concrete with Manders confined concrete strain capacity.

		Bent 1	Bent 2	**Bent 3**
Maximum displacement run		19	22	**19**
Ductility Demand		5.33	6.41	**7.90**
measured core concrete compressive strain (at four joints)	maximum	-0.0447	-0.0451	**-0.0519**
	average	-0.0262	-0.0317	**-0.0393**
Capacity using Mander's model		-0.0171	-0.0171	**-0.0171**
measured strain / Mander's capacity (at four joints)	maximum	2.62	2.64	**3.04**
	average	1.53	1.85	**2.30**

note: bold values show bent that reached failure ductility

Table 6-48: Maximum strain gauge measured compressive strains at extreme fiber of core concrete for bents 1-3 during tests 18-22.

Bent	Bent 1	Bent 2	**Bent 3**
test run	19	22	19
top west	-0.0051	-0.0156	-0.0291
bottom west	-0.0246	-0.0014	-0.0790
top east	-0.0053	-0.0095	-0.0338
bottom east	-0.0184	-0.0062	-0.0481
average	-0.0133	-0.0082	-0.0475

Table 6-49: Comparison of maximum strain gauge measured compressive strain on core concrete with Mander confined concrete strain capacity.

		Bent 1	Bent 2	**Bent 3**
Maximum displacement run		19	22	**19**
Ductility Demand		5.33	6.41	**7.90**
measured core concrete compressive strain (at four joints)	maximum	-0.0246	-0.0156	**-0.0790**
	average	-0.0133	-0.0082	**-0.0475**
Capacity using Mander's model		-0.0171	-0.0171	**-0.0171**
measured strain / Mander's capacity (at four joints)	maximum	1.44	0.91	**4.62**
	average	0.78	0.48	**2.78**

note: bold values show bent that reached failure ductility

Table 7-1: Measured strain rates used to modify material properties for analyses.

BENT 1	TOP				BOTTOM				
location	ww	we	ew	ee	ww	we	ew	ee	
name	1WTSL4	1WTSL5	1ETSL4	1ETSL5	1WBSL5	1WBSL6	1EBSL5	1EBSL6	Average
ten half yield run	13	12	13	--	12	12	12	12	
ten yield run	13	13	13	--	13	13	13	13	
half yield ten rate	29430	11320	39976	--	22633	24143	10566	20370	22634
yield ten rate	30185	33961	30925	--	28668	38478	30189	33951	32337
comp rate	-30939	-33207	-30170	--	-33949	-15844	-31699	-18107	-27702

BENT 2	TOP				BOTTOM				
location	ww	we	ew	ee	ww	we	ew	ee	
name	2WTSL5	2WTSL4	2ETSL5	2ETSL4	2WBSL6	2WBSL5	2EBSL6	2EBSL5	Average
ten half yield run	13	13	13	14	--	13	13	13	
ten yield run	15	15	15	15	--	15	15	15	
half yield ten rate	8323	10106	24079	20511	--	18103	11593	28538	17322
yield ten rate	34479	36263	34780	41023	--	21120	49941	25862	34781
comp rate	-46369	-21996	-46374	-30321	--	-12823	-24079	-16944	-28415

BENT 3	TOP				BOTTOM				
location	ww	we	ew	ee	ww	we	ew	ee	
name	3WTSL4	3WTSL5	3ETSL4	3ETSL5	3WBSL5	3WBSL6	3EBSL5	3EBSL6	Average
ten half yield run	13	13	13	13	13	13	13	--	
ten yield run	14	14	13	14	14	14	14	--	
half yield ten rate	13673	42208	23779	23184	50530	33291	39235	--	32271
yield ten rate	62420	75498	44585	50530	70148	55286	59447	--	59702
comp rate	-35074	-29724	-20212	-20212	-26157	-26751	-12484	--	-24373

Table 7-2: Comparison of SAP 2000 and Drain-3DX elasto-plastic pushover analyses for bents 1-3 considering failure as crushing of confined concrete.

		SAP2000 pushover					Drain-3DX pushover					SAP2000 /D3DX ratio	
		Force (kip)	Force (kN)	Disp. (in)	Disp. (mm)	μ_Δ	Force (kip)	Force (kN)	Disp. (in)	Disp. (mm)	μ_Δ	force	displ.
Bent 1	yield	42.9	191	0.67	17.0	8.1	43.0	191	0.71	18.0	7.6	1.00	0.94
	ult.	42.9	191	5.40	137.2		43.0	191	5.40	137.2		1.00	1.00
Bent 2	yield	30.0	134	1.04	26.5	8.1	30.3	135	1.08	27.4	7.9	0.99	0.97
	ult.	30.0	134	8.47	215.1		30.3	135	8.47	215.1		0.99	1.00
Bent 3	yield	53.0	236	0.51	13.0	7.9	53.0	236	0.54	13.8	7.4	1.00	0.94
	ult.	53.0	236	4.02	102.1		53.0	236	4.02	102.1		1.00	1.00

Table 7-3: Comparison of SAP 2000 and Drain-3DX elasto-plastic pushover analyses for bents 1-3 considering failure as 85 percent of maximum force.

		SAP2000 pushover					Drain-3DX pushover					SAP2000 /D3DX ratio	
		Force (kip)	Force (kN)	Disp. (in)	Disp. (mm)	μ_Δ	Force (kip)	Force (kN)	Disp. (in)	Disp. (mm)	μ_Δ	force	displ.
Bent 1	yield	41.5	185	0.65	16.5	10.0	42.4	189	0.70	17.8	9.3	0.98	0.93
	ult.	41.5	185	6.50	165.1		42.4	189	6.50	165.1		0.98	1.00
Bent 2	yield	29.9	133	1.04	26.4	7.3	30.2	134	1.07	27.3	7.0	0.99	0.97
	ult.	29.9	133	7.56	191.9		30.2	134	7.56	191.9		0.99	1.00
Bent 3	yield	50.6	225	0.49	12.4	15.8	51.4	229	0.50	12.6	15.5	0.98	0.98
	ult.	50.6	225	7.69	195.4		51.4	229	7.69	195.4		0.98	1.00

Table 7-4: Measured maximum transverse relative displacements and corresponding displacement ductility (using pushover calculated yield) for all bents and all runs.

			Bent 1			Bent 2			Bent 3		
			Displacement		μ_Δ	Displacement		μ_Δ	Displacement		μ_Δ
			in	mm		in	mm		in	mm	
Low Amplitude Testing	1a	max	0.092	2.3	0.14	0.083	2.1	0.08	0.038	1.0	0.07
		min	-0.058	-1.5	0.09	-0.060	-1.5	0.06	-0.053	-1.3	0.10
	1	max	0.151	3.8	0.23	0.138	3.5	0.13	0.071	1.8	0.14
		min	-0.097	-2.5	0.14	-0.093	-2.3	0.09	-0.089	-2.3	0.17
	2a	max	0.060	1.5	0.09	0.045	1.1	0.04	0.065	1.7	0.13
		min	-0.045	-1.1	0.07	-0.034	-0.9	0.03	-0.066	-1.7	0.13
	2	max	0.125	3.2	0.19	0.123	3.1	0.12	0.191	4.8	0.37
		min	-0.120	-3.0	0.18	-0.108	-2.7	0.10	-0.147	-3.7	0.29
	3a	max	0.083	2.1	0.12	0.053	1.3	0.05	0.042	1.1	0.08
		min	-0.058	-1.5	0.09	-0.042	-1.1	0.04	-0.021	-0.5	0.04
	3	max	0.192	4.9	0.29	0.154	3.9	0.15	0.047	1.2	0.09
		min	-0.157	-4.0	0.23	-0.100	-2.5	0.10	-0.061	-1.6	0.12
	4	max	0.107	2.7	0.16	0.105	2.7	0.10	0.101	2.6	0.20
		min	-0.077	-1.9	0.11	-0.068	-1.7	0.07	-0.105	-2.7	0.21
	5	max	0.123	3.1	0.18	0.088	2.2	0.08	0.084	2.1	0.16
		min	-0.071	-1.8	0.11	-0.056	-1.4	0.05	-0.095	-2.4	0.19
	6	max	0.124	3.2	0.19	0.105	2.7	0.10	0.050	1.3	0.10
		min	-0.074	-1.9	0.11	-0.061	-1.5	0.06	-0.045	-1.1	0.09
	8	max	0.134	3.4	0.20	0.122	3.1	0.12	0.066	1.7	0.13
		min	-0.076	-1.9	0.11	-0.062	-1.6	0.06	-0.068	-1.7	0.13
	9a	max	0.069	1.7	0.10	0.038	1.0	0.04	0.094	2.4	0.18
		min	-0.019	-0.5	0.03	-0.030	-0.8	0.03	-0.077	-2.0	0.15
	9	max	0.148	3.8	0.22	0.152	3.9	0.15	0.090	2.3	0.18
		min	-0.085	-2.2	0.13	-0.095	-2.4	0.09	-0.068	-1.7	0.13
	10	max	0.188	4.8	0.28	0.089	2.3	0.09	0.099	2.5	0.19
		min	-0.125	-3.2	0.19	-0.096	-2.4	0.09	-0.078	-2.0	0.15
	11	max	0.155	3.9	0.23	0.073	1.9	0.07	0.106	2.7	0.21
		min	-0.093	-2.3	0.14	-0.073	-1.9	0.07	-0.082	-2.1	0.16
High Amplitude Testing	12	max	0.232	5.9	0.35	0.170	4.3	0.16	0.124	3.1	0.24
		min	-0.188	-4.8	0.28	-0.157	-4.0	0.15	-0.123	-3.1	0.24
	13	max	0.636	16.2	0.95	0.427	10.9	0.41	0.311	7.9	0.61
		min	-0.565	-14.4	0.84	-0.368	-9.3	0.35	-0.288	-7.3	0.56
	14	max	0.753	19.1	**1.12**	0.558	14.2	0.54	0.495	12.6	0.97
		min	-0.756	-19.2	**1.13**	-0.466	-11.8	0.45	-0.474	-12.0	0.93
	15	max	1.564	39.7	**2.33**	1.248	31.7	**1.20**	1.462	37.1	**2.86**
		min	-1.133	-28.8	**1.69**	-1.114	-28.3	**1.07**	-1.056	-26.8	**2.07**
	16	max	2.217	56.3	**3.31**	1.774	45.0	**1.70**	1.598	40.6	**3.13**
		min	-2.633	-66.9	**3.93**	-2.295	-58.3	**2.20**	-1.882	-47.8	**3.68**
	17	max	1.298	33.0	**1.94**	1.421	36.1	**1.36**	1.424	36.2	**2.79**
		min	-1.979	-50.3	**2.95**	-1.946	-49.4	**1.87**	-1.331	-33.8	**2.61**
	18	max	2.778	70.6	**4.14**	2.746	69.8	**2.64**	2.909	73.9	**5.69**
		min	-2.276	-57.8	**3.40**	-3.368	-85.5	**3.23**	-3.303	-83.9	**6.46**
	19	max	2.793	70.9	**4.17**	4.268	108.4	**4.10**	4.710	119.6	**9.22**
		min	-3.522	-89.5	**5.25**	-2.989	-75.9	**2.87**	-2.443	-62.1	**4.78**
	20	max	2.245	57.0	**3.35**	3.086	78.4	**2.96**	3.479	88.4	**6.81**
		min	-1.931	-49.1	**2.88**	-2.372	-60.3	**2.28**	-1.773	-45.0	**3.47**
Post-Tests	21	max	3.012	76.5	**4.49**	3.430	87.1	**3.29**	3.834	97.4	---
		min	-2.184	-55.5	**3.26**	-2.064	-52.4	**1.98**	-3.240	-82.3	---
	22	max	1.844	46.8	**2.75**	5.242	133.1	**5.03**	6.851	174.0	---
		min	-3.261	-82.8	**4.86**	-3.714	-94.3	**3.56**	-2.839	-72.1	---

Table 7-5: Comparison of bent 1-3 peak displacements of measured and SAP2000 predicted for high amplitude tests.

		Bent 1				Bent 2				Bent 3				Bent 1	Bent 2	Bent 3
Test		Measured		SAP2000		Measured		SAP2000		Measured		SAP2000		Percent	Percent	Percent
		(in)	(mm)	(in)	(mm)	(in)	(mm)	(in)	(mm)	(in)	(mm)	(in)	(mm)	difference	difference	difference
12	max	0.23	5.9	0.23	5.7	0.17	4.3	0.17	4.3	0.12	3.1	0.12	3.2	2.6	0.3	0.8
	min	-0.19	-4.8	-0.21	-5.4	-0.16	-4.0	-0.15	-3.8	-0.12	-3.1	-0.13	-3.2	12.9	3.9	3.2
13	max	0.64	16.2	0.57	14.4	0.43	10.9	0.35	9.0	0.31	7.9	0.32	8.0	11.5	19.2	1.3
	min	-0.56	-14.4	-0.60	-15.3	-0.37	-9.3	-0.39	-9.9	-0.29	-7.3	-0.32	-8.2	6.2	6.1	11.1
14	max	0.75	19.1	0.80	20.3	0.56	14.2	0.63	16.1	0.49	12.6	0.74	18.9	6.3	12.9	40.2
	min	-0.76	-19.2	-0.82	-20.9	-0.47	-11.8	-0.61	-15.6	-0.47	-12.0	-0.60	-15.3	8.6	27.2	24.2
15	max	1.56	39.7	1.46	37.2	1.25	31.7	1.15	29.2	1.46	37.1	1.27	32.3	6.7	8.3	13.8
	min	-1.13	-28.8	-1.21	-30.7	-1.11	-28.3	-1.35	-34.3	-1.06	-26.8	-1.39	-35.3	6.5	19.2	27.2
16	max	2.22	56.3	2.01	51.0	1.77	45.0	1.74	44.3	1.60	40.6	1.71	43.5	9.9	1.8	6.9
	min	-2.63	-66.9	-2.82	-71.6	-2.30	-58.3	-2.41	-61.3	-1.88	-47.8	-2.07	-52.6	6.8	5.0	9.6
17	max	1.30	33.0	1.64	41.5	1.42	36.1	1.79	45.5	1.42	36.2	1.54	39.1	23.0	23.0	7.7
	min	-1.98	-50.3	-1.45	-36.7	-1.95	-49.4	-1.61	-40.9	-1.33	-33.8	-1.36	-34.6	31.1	18.8	2.3
18	max	2.78	70.6	2.29	58.1	2.75	69.8	3.00	76.2	2.91	73.9	2.97	75.4	19.4	8.8	2.1
	min	-2.28	-57.8	-2.70	-68.5	-3.37	-85.5	-3.73	-94.7	-3.30	-83.9	-3.72	-94.5	17.0	10.1	11.8
19	max	2.79	70.9	3.79	96.2	4.27	108.4	3.84	97.6	4.71	119.6	4.11	104.4	30.2	10.5	13.6
	min	-3.52	-89.5	-2.47	-62.8	-2.99	-75.9	-3.82	-97.0	-2.44	-62.1	-4.69	-119.2	35.0	24.4	63.1
20	max	2.25	57.0	2.83	71.8	3.09	78.4	2.80	71.1	3.48	88.4	3.31	84.1	23.0	9.7	4.9
	min	-1.93	-49.1	-2.14	-54.5	-2.37	-60.3	-2.64	-66.9	-1.77	-45.0	-2.82	-71.6	10.5	10.5	45.6
Average														**14.8**	**12.2**	**16.1**

Table 7-6: Comparison of bent 1-3 peak displacements of measured and Drain-3DX predicted for high amplitude tests.

Test		Bent 1				Bent 2				Bent 3				Bent 1	Bent 2	Bent 3
		Measured		Drain-3DX		Measured		Drain-3DX		Measured		Drain-3DX		Percent	Percent	Percent
		(in)	(mm)	(in)	(mm)	(in)	(mm)	(in)	(mm)	(in)	(mm)	(in)	(mm)	difference	difference	difference
12	max	0.23	5.9	0.30	7.6	0.17	4.3	0.18	4.5	0.11	2.7	0.12	3.2	24.8	4.1	15.8
	min	-0.19	-4.8	-0.27	-6.8	-0.16	-4.0	-0.18	-4.6	-0.09	-2.3	-0.13	-3.2	34.6	14.9	31.7
13	max	0.64	16.2	0.56	14.3	0.43	10.9	0.40	10.1	0.29	7.4	0.32	8.0	12.3	7.2	7.3
	min	-0.56	-14.4	-0.66	-16.8	-0.37	-9.3	-0.40	-10.0	-0.30	-7.6	-0.32	-8.2	15.9	7.2	7.3
14	max	0.75	19.1	0.79	20.0	0.56	14.2	0.62	15.6	0.65	16.4	0.74	18.9	4.4	9.8	13.9
	min	-0.76	-19.2	-0.86	-21.8	-0.47	-11.8	-0.58	-14.6	-0.55	-14.0	-0.60	-15.3	12.9	21.0	8.8
15	max	1.56	39.7	1.61	40.8	1.25	31.7	1.38	35.0	1.62	41.2	1.27	32.3	2.8	9.9	24.1
	min	-1.13	-28.8	-1.25	-31.7	-1.11	-28.3	-1.16	-29.3	-1.23	-31.1	-1.39	-35.3	9.7	3.6	12.5
16	max	2.22	56.3	2.28	58.0	1.77	45.0	1.92	48.7	1.71	43.5	1.71	43.5	3.0	7.8	0.1
	min	-2.63	-66.9	-2.70	-68.6	-2.30	-58.3	-2.34	-59.5	-2.07	-52.5	-2.07	-52.6	2.5	2.1	0.2
17	max	1.30	33.0	1.30	33.1	1.42	36.1	1.64	41.7	1.48	37.5	1.54	39.1	0.3	14.4	4.1
	min	-1.98	-50.3	-1.91	-48.4	-1.95	-49.4	-2.19	-55.6	-1.78	-45.2	-1.36	-34.6	3.8	11.7	26.7
18	max	2.78	70.6	2.50	63.5	2.75	69.8	3.07	77.9	3.24	82.2	2.97	75.4	10.5	11.0	8.6
	min	-2.28	-57.8	-3.06	-77.7	-3.37	-85.5	-3.71	-94.3	-3.36	-85.4	-3.72	-94.5	29.3	9.8	10.1
19	max	2.79	70.9	3.73	94.8	4.27	108.4	3.96	100.7	3.93	99.8	4.11	104.4	28.8	7.4	4.5
	min	-3.52	-89.5	-2.78	-70.7	-2.99	-75.9	-3.56	-90.5	-4.63	-117.6	-4.69	-119.2	23.4	17.5	1.4
20	max	2.25	57.0	2.83	72.0	3.09	78.4	2.68	68.1	3.14	79.7	3.31	84.1	23.2	14.0	5.4
	min	-1.93	-49.1	-2.06	-52.4	-2.37	-60.3	-3.03	-76.9	-3.59	-91.1	-2.82	-71.6	6.5	24.3	23.9
Average														**13.8**	**11.0**	**11.5**

Table 7-7: Comparison of bent 1-3 displacement envelopes of measured and D3DX predicted for select low amplitude tests.

	Test	Direction	Sign	Measured (in)	Measured (mm)	D3DX predicted (in)	D3DX predicted (mm)	Percent difference
Bent 1	2	Transverse	max	0.117	2.96	0.132	3.36	12.6
			min	-0.128	-3.24	-0.156	-3.95	19.9
	3	Transverse	max	0.181	4.60	0.214	5.43	16.6
			min	-0.168	-4.27	-0.181	-4.59	7.2
	4	Transverse	max	0.091	2.31	0.102	2.60	12.0
			min	-0.092	-2.35	-0.097	-2.46	4.7
	5	Transverse	max	0.107	2.71	0.117	2.97	9.2
			min	-0.086	-2.20	-0.087	-2.20	0.3
	6	Transverse	max	0.108	2.74	0.116	2.94	7.1
			min	-0.090	-2.28	-0.087	-2.20	3.6
	9	Transverse	max	0.126	3.20	0.131	3.32	3.5
			min	-0.108	-2.74	-0.118	-3.00	9.3
	9	Longitudinal	max	0.112	2.85	0.148	3.75	27.3
			min	-0.143	-3.63	-0.156	-3.97	8.9
	Average							**10.2**

	Test	Direction	Sign	Measured (in)	Measured (mm)	D3DX predicted (in)	D3DX predicted (mm)	Percent difference
Bent 2	2	Transverse	max	0.121	3.07	0.152	3.86	22.7
			min	-0.110	-2.80	-0.145	-3.69	27.5
	3	Transverse	max	0.152	3.87	0.170	4.33	11.2
			min	-0.101	-2.58	-0.140	-3.55	31.9
	4	Transverse	max	0.098	2.48	0.112	2.84	13.2
			min	-0.075	-1.90	-0.079	-2.00	5.2
	5	Transverse	max	0.079	2.01	0.085	2.16	7.2
			min	-0.065	-1.65	-0.069	-1.76	6.7
	6	Transverse	max	0.095	2.42	0.108	2.73	12.1
			min	-0.071	-1.80	-0.071	-1.79	0.3
	9	Transverse	max	0.144	3.65	0.166	4.21	14.3
			min	-0.104	-2.63	-0.103	-2.60	1.1
	9	Longitudinal	max	0.108	2.74	0.128	3.26	17.4
			min	-0.132	-3.36	-0.138	-3.50	4.1
	Average							**12.5**

	Test	Direction	Sign	Measured (in)	Measured (mm)	D3DX predicted (in)	D3DX predicted (mm)	Percent difference
Bent 3	2	Transverse	max	0.187	4.75	0.223	5.66	17.5
			min	-0.151	-3.84	-0.194	-4.93	24.9
	3	Transverse	max	0.033	0.84	0.052	1.33	44.3
			min	-0.075	-1.90	-0.055	-1.39	30.6
	4	Transverse	max	0.094	2.39	0.076	1.94	21.1
			min	-0.112	-2.84	-0.114	-2.91	2.2
	5	Transverse	max	0.067	1.70	0.069	1.74	2.5
			min	-0.112	-2.84	-0.093	-2.36	18.6
	6	Transverse	max	0.043	1.09	0.048	1.22	10.8
			min	-0.052	-1.32	-0.036	-0.91	37.1
	9	Transverse	max	0.069	1.76	0.062	1.58	11.2
			min	-0.088	-2.24	-0.072	-1.83	20.3
	9	Longitudinal	max	0.106	2.70	0.133	3.37	22.1
			min	-0.138	-3.50	-0.142	-3.60	2.9
	Average							**19.0**

Table 7-8: Analytical moment induced on columns from measured displacements due to rigid cap beams compared to yield moment.

	Bent	Measured deflection (in)	(mm)	Maximum Column Moment (kip-in)	(kN-m)	Max. Moment / Yield Moment
Test 12	bent 1	0.014	0.35	3.4	0.38	0.52%
	bent 2	0.013	0.32	1.8	0.21	0.29%
	bent 3	0.031	0.80	7.4	0.83	1.15%
Test 15	bent 1	0.057	1.44	13.7	1.55	2.14%
	bent 2	0.060	1.53	8.8	0.99	1.37%
	bent 3	0.095	2.40	22.2	2.51	3.46%
Test 19	bent 1	0.119	3.03	28.8	3.26	4.50%
	bent 2	0.158	4.02	23.1	2.61	3.60%
	bent 3	0.227	5.76	53.3	6.02	8.32%

Table 7-9: Comparison of bent 1-3 lateral force envelopes for tests 15 and 18 for measured from actuator pressure and calculated from Drain-3DX.

		From actuator pressure kip	kN	Calculated from Drain-3DX kip	kN	% diff
Test 15	bent 1 max	42.0	186.7	44.8	199.1	-6.4
	bent 1 min	-42.9	-191.0	-43.8	-194.6	-1.9
	bent 2 max	27.9	124.2	29.4	130.9	-5.3
	bent 2 min	-28.6	-127.2	-28.3	-126.0	0.9
	bent 3 max	49.8	221.3	57.1	253.8	-13.7
	bent 3 min	-50.8	-226.0	-56.4	-250.9	-10.4
Test 18	bent 1 max	52.1	232.0	44.8	199.1	15.3
	bent 1 min	-46.3	-206.0	-45.9	-204.1	0.9
	bent 2 max	42.6	189.7	34.6	153.9	20.8
	bent 2 min	-41.1	-182.9	-34.1	-151.9	18.5
	bent 3 max	51.8	230.5	58.2	259.0	-11.6
	bent 3 min	-51.2	-227.6	-59.5	-264.5	-15.0

Table 8-1: NCHRP 12-49 design earthquakes and performance objectives (ATC/MCEER 2001).

Probability of Exceedance for Design Earthquake Motions		Performance Level	
		Life Safety	Operational
Rare Earthquake 3% PE in 75 Years	Service Level Damage Level	**Significant Disruption** **Significant**	Immediate Minimal
Expected 50% PE in 75 Years	Service Level Damage Level	**Immediate** **Minimal**	Immediate Minimal to None

Table 8-2: NCHRP 12-49 service levels for performance objectives (ATC/MCEER 2001).

Service Levels	
Immediate	Full access to normal traffic shall be available following an inspection of the bridge.
Significant Disruption	Limited access (Reduced lanes, light emergency traffic) may be possible after shoring, however the bridge may need to be replaced

Table 8-3: NCHRP 12-49 damage levels for performance objectives (ATC/MCEER 2001).

Damage Levels	
None	Evidence of movement may be present but no noticable damage
Minimal	Some visable signs of damage. Minor inelastic respose may occur, but post-earthquake damage is limited to narrow flexural cracking in concrete and the onset of yielding in steel. Permanent deformations are not apparent, and any repairs could be made under non-emergency conditions with the exception of superstructure joints.
Significant	Although there is no collapse, permanent offsets may occur and damage consisting of cracking, reinforcement yield, and major spalling of concrete on the seismic load path is possible. These conditions may require closure to repair the damage. Partial or complete replacement of the columns and piles may be necessary if significant lateral soil flow occurs.

Table 8-4: Measured displacement demands for table motions equivalent to amplified design earthquakes at first mode spectral acceleration.

	Event	Measure	Bent 1	Bent 2	Bent 3
Expected event	measured from test 12	ductility demand (Δ_{max}/Δ_y)	0.35	0.16	0.24
		failure demand ($\Delta_{max}/\Delta_{ult}$)	0.04	0.02	0.03
	measured from test 13	ductility demand (Δ_{max}/Δ_y)	0.95	0.41	0.61
		failure demand ($\Delta_{max}/\Delta_{ult}$)	0.12	0.05	0.08
Rare event	measured from test 15	ductility demand (Δ_{max}/Δ_y)	2.33	1.20	2.86
		failure demand ($\Delta_{max}/\Delta_{ult}$)	0.29	0.15	0.36
	measured from test 16	ductility demand (Δ_{max}/Δ_y)	3.31	1.70	3.13
		failure demand ($\Delta_{max}/\Delta_{ult}$)	0.41	0.21	0.40

Table 8-5: Drain-3DX calculated displacement demands for synthetic motions equivalent to amplified design earthquake spectra.

Event	Measure	Bent 1	Bent 2	Bent 3
Drain-3DX from amplified 50%PE in 75 year design spectrum	ductility demand (Δ_{max}/Δ_y)	1.35	0.62	1.06
	failure demand ($\Delta_{max}/\Delta_{ult}$)	0.17	0.08	0.13
Drain-3DX from amplified 3%PE in 75 year design spectrum	ductility demand (Δ_{max}/Δ_y)	5.59	2.74	5.09
	failure demand ($\Delta_{max}/\Delta_{ult}$)	0.69	0.34	0.65

Table 9-1: Comparison of calculated bent 1 displacement ductility demands for tests 13-19 in sequence (except test 17) using target and achieved shake table motions.

	Displacement ductility demands		Achieved/target ratio
	Bent 1 target	Bent 1 achieved	
test 13	1.53	0.93	0.61
test 14	1.41	1.21	0.86
test 15	2.86	2.26	0.79
test 16	3.78	3.80	1.01
test 18	5.57	4.31	0.77
test 19	6.95	5.26	0.76

Table 9-2: Comparison of calculated bent 2 displacement ductility demands for tests 13-19 in sequence (except test 17) using target and achieved shake table motions.

	displacement ductility demands		Achieved/target ratio
	Bent 2 target	Bent 2 achieved	
test 13	0.56	0.37	0.65
test 14	0.65	0.57	0.88
test 15	1.44	1.28	0.89
test 16	2.29	2.17	0.95
test 18	3.01	3.44	1.14
test 19	3.67	3.67	1.00

Table 9-3: Comparison of calculated bent 3 displacement ductility demands for tests 13-19 in sequence (except test 17) using target and achieved shake table motions.

	displacement ductility demands		Achieved/target ratio
	Bent 3 target	Bent 3 achieved	
test 13	1.15	0.55	0.48
test 14	1.37	1.20	0.88
test 15	2.27	3.01	1.33
test 16	4.35	3.83	0.88
test 18	5.05	6.22	1.23
test 19	6.14	8.58	1.40

Table 9-4: Target and achieved spectral accelerations for shake tables 1 and 3 at measured first transverse modal periods for tests 12 through 19.

Test	Measured displacement ductility		Mode 1 period	Spectral acceleration			Achieved/target spectral acceleration	
				Target	Table 1	Table 3		
	bent 1	bent 3	(s)	(g)	(g)	(g)	Table 1	Table 3
test 12	0.35	0.24	0.379	0.251	0.216	0.273	0.86	1.08
test 13	0.95	0.61	0.379	0.502	0.312	0.585	0.62	1.17
test 14	***1.13***	0.97	0.379	0.838	0.720	0.822	***0.86***	0.98
test 15	***2.33***	**2.86**	0.436	1.651	1.928	1.395	***1.17***	**0.84**
test 16	3.93	**3.68**	0.436	2.477	3.562	2.567	1.44	**1.04**
test 17	2.95	2.79	0.436	3.303	2.436	2.587	0.74	0.78
test 18	4.14	6.46	0.661	1.323	0.894	1.368	0.68	1.03
test 19	5.25	9.22	0.661	1.609	1.162	1.913	0.72	1.19

Table 9-5: Target and achieved spectral accelerations for shake tables 1 and 3 at measured second transverse modal periods for tests 12 through 19.

Test	Measured displacement ductility		Mode 1 period	Spectral acceleration			Achieved/target spectral acceleration	
				Target	Table 1	Table 3		
	bent 1	bent 3	(s)	(g)	(g)	(g)	Table 1	Table 3
test 12	0.35	0.24	0.266	0.415	0.383	0.221	0.92	0.53
test 13	0.95	0.61	0.266	0.830	0.727	0.536	0.88	0.65
test 14	**1.13**	0.97	0.266	1.383	1.624	1.270	**1.17**	0.92
test 15	**2.33**	***2.86***	0.297	3.864	5.067	6.426	**1.31**	***1.66***
test 16	3.93	***3.68***	0.297	5.795	7.015	10.420	1.21	***1.80***
test 17	2.95	2.79	0.297	7.727	7.662	5.726	0.99	0.74
test 18	4.14	6.46	0.569	1.756	1.260	1.596	0.72	0.91
test 19	5.25	9.22	0.621	2.166	1.633	2.008	0.75	0.93

Table 9-6: Calculated transverse pseudo-static displacement demands on bents 1-3 from achieved high amplitude test shake table motions compared to yield deflections.

		Pseudo-static displacement demand (in)	(mm)	Pseudo-static displacement demand / yield displacement	Measured displacement ductility demand
Bent 1	**test 12**	**0.007**	**0.19**	**1.0%**	**0.35**
	test 13	**0.015**	**0.39**	**2.2%**	**0.95**
	test 14	**0.024**	**0.62**	**3.4%**	**1.13**
	test 15	0.058	1.48	8.2%	2.33
	test 16	0.139	3.54	19.6%	3.93
	test 17	0.063	1.60	8.9%	2.95
	test 18	0.137	3.49	19.3%	4.14
	test 19	0.224	5.68	31.5%	5.25
	test 20	0.154	3.91	21.7%	3.35
Bent 2	**test 12**	**0.033**	**0.84**	**3.1%**	**0.16**
	test 13	**0.068**	**1.72**	**6.3%**	**0.41**
	test 14	**0.105**	**2.65**	**9.7%**	**0.54**
	test 15	**0.330**	**8.37**	**30.5%**	**1.20**
	test 16	0.738	18.74	68.3%	2.20
	test 17	0.368	9.35	34.1%	1.87
	test 18	0.691	17.54	63.9%	3.23
	test 19	1.180	29.96	109.2%	4.10
	test 20	0.886	22.51	82.0%	2.96
Bent 3	**test 12**	**0.004**	**0.11**	**0.8%**	**0.24**
	test 13	**0.009**	**0.23**	**1.7%**	**0.61**
	test 14	**0.013**	**0.33**	**2.4%**	**0.97**
	test 15	**0.032**	**0.80**	**5.8%**	**2.86**
	test 16	0.071	1.79	13.1%	3.68
	test 17	0.036	0.93	6.7%	2.79
	test 18	0.067	1.70	12.4%	6.46
	test 19	0.112	2.83	20.7%	9.22
	test 20	0.077	1.96	14.3%	6.81

Table 9-7: Calculated transverse pseudo-static shear demands on bents 1-3 from achieved high amplitude test shake table motions compared to yield forces.

		Pseudo-static force demand (kip)	Pseudo-static force demand (kN)	Pseudo-static force demand / yield force	Measured displacement ductility demand
Bent 1	**test 12**	**0.75**	**3.34**	**1.7%**	**0.35**
	test 13	**1.56**	**6.92**	**3.6%**	**0.95**
	test 14	**2.49**	**11.06**	**5.8%**	**1.13**
	test 15	5.72	25.46	13.3%	2.33
	test 16	11.09	49.35	25.8%	3.93
	test 17	6.18	27.48	14.4%	2.95
	test 18	10.87	48.37	25.3%	4.14
	test 19	15.57	69.28	36.2%	5.25
	test 20	11.96	53.21	27.8%	3.35
Bent 2	**test 12**	**1.48**	**6.57**	**4.9%**	**0.16**
	test 13	**3.03**	**13.47**	**10.0%**	**0.41**
	test 14	**4.55**	**20.25**	**15.0%**	**0.54**
	test 15	**10.97**	**48.78**	**36.2%**	**1.20**
	test 16	21.11	93.91	69.7%	2.20
	test 17	12.03	53.51	39.7%	1.87
	test 18	20.03	89.11	66.1%	3.23
	test 19	28.65	127.45	94.6%	4.10
	test 20	22.13	98.43	73.0%	2.96
Bent 3	**test 12**	**0.725**	**3.23**	**1.4%**	**0.24**
	test 13	**1.520**	**6.76**	**2.9%**	**0.61**
	test 14	**2.174**	**9.67**	**4.1%**	**0.97**
	test 15	**5.246**	**23.34**	**9.9%**	**2.86**
	test 16	9.968	44.34	18.8%	3.68
	test 17	6.034	26.84	11.4%	2.79
	test 18	9.462	42.09	17.9%	6.46
	test 19	13.130	58.41	24.8%	9.22
	test 20	10.165	45.22	19.2%	6.81

Table 10-1: Comparison of calculated system and individual damage states for bent 1 subjected to target motions of tests 13-19.

motion	item compared	system		individual		sys./indiv.
		US	SI	US	SI	ratio
test 13	Displacement ductility demand	1.62		1.04		1.56
motion	hysteretic energy, (k-in, kN-mm)	37.9	4284	10.6	1203	3.56
response	Damage Index (1=failure)	0.24		0.14		1.71
test 14	Displacement ductility demand	1.87		1.70		1.10
motion	hysteretic energy, (k-in, kN-mm)	51.3	5795	38.6	4363	1.33
response	Damage Index (1=failure)	0.28		0.25		1.13
test 15	Displacement ductility demand	3.01		2.61		1.15
motion	hysteretic energy, (k-in, kN-mm)	123.0	13897	90.5	10230	1.36
response	Damage Index (1=failure)	0.49		0.41		1.20
test 16	Displacement ductility demand	3.90		3.91		1.00
motion	hysteretic energy, (k-in, kN-mm)	256.6	28986	208.1	23516	1.23
response	Damage Index (1=failure)	0.73		0.69		1.07
test 17	Displacement ductility demand	5.43		4.06		1.34
motion	hysteretic energy, (k-in, kN-mm)	534.9	60430	355.3	40145	1.51
response	Damage Index (1=failure)	1.19		0.85		1.41
test 18	Displacement ductility demand	6.40		4.72		1.36
motion	hysteretic energy, (k-in, kN-mm)	859.7	97137	680.8	76916	1.26
response	Damage Index (1=failure)	1.63		1.25		1.31
test 19	Displacement ductility demand	7.72		6.56		1.18
motion	hysteretic energy, (k-in, kN-mm)	1233.9	139411	986.6	111474	1.25
response	Damage Index (1=failure)	2.15		1.77		1.22

Table 10-2: Comparison of calculated system and individual damage states for bent 2 subjected to target motions of tests 13-19.

motion	item compared	system		individual		sys./indiv.
		US	SI	US	SI	ratio
test 13	Displacement ductility demand	0.58		0.41		1.41
motion	hysteretic energy, (k-in, kN-mm)	2.8	317	0.8	91	3.49
response	Damage Index (1=failure)	0.12		0.08		1.43
test 14	Displacement ductility demand	0.72		0.66		1.10
motion	hysteretic energy, (k-in, kN-mm)	3.3	368	1.9	212	1.73
response	Damage Index (1=failure)	0.14		0.13		1.11
test 15	Displacement ductility demand	1.84		1.85		0.99
motion	hysteretic energy, (k-in, kN-mm)	29.0	3277	44.1	4978	0.66
response	Damage Index (1=failure)	0.38		0.40		0.96
test 16	Displacement ductility demand	2.39		2.73		0.87
motion	hysteretic energy, (k-in, kN-mm)	60.3	6815	132.8	15004	0.45
response	Damage Index (1=failure)	0.52		0.65		0.79
test 17	Displacement ductility demand	2.59		3.27		0.79
motion	hysteretic energy, (k-in, kN-mm)	109.5	12375	261.6	29560	0.42
response	Damage Index (1=failure)	0.61		0.88		0.69
test 18	Displacement ductility demand	3.24		5.14		0.63
motion	hysteretic energy, (k-in, kN-mm)	239.7	27079	417.8	47210	0.57
response	Damage Index (1=failure)	0.86		1.40		0.61
test 19	Displacement ductility demand	4.03		5.82		0.69
motion	hysteretic energy, (k-in, kN-mm)	383.8	43369	611.1	69045	0.63
response	Damage Index (1=failure)	1.15		1.71		0.67

Table 10-3: Comparison of calculated system and individual damage states for bent 3 subjected to target motions of tests 13-19.

motion	item compared	system		individual		sys./indiv.
		US	SI	US	SI	ratio
test 13	Displacement ductility demand	1.22		1.26		0.96
motion	hysteretic energy, (k-in, kN-mm)	23.8	2684	29.5	3334	0.81
response	Damage Index (1=failure)	0.14		0.15		0.93
test 14	Displacement ductility demand	1.42		1.91		0.75
motion	hysteretic energy, (k-in, kN-mm)	42.2	4772	53.0	5991	0.80
response	Damage Index (1=failure)	0.18		0.23		0.76
test 15	Displacement ductility demand	3.47		2.96		1.17
motion	hysteretic energy, (k-in, kN-mm)	167.7	18953	190.6	21529	0.88
response	Damage Index (1=failure)	0.49		0.46		1.06
test 16	Displacement ductility demand	4.66		4.31		1.08
motion	hysteretic energy, (k-in, kN-mm)	285.5	32259	287.3	32460	0.99
response	Damage Index (1=failure)	0.72		0.69		1.05
test 17	Displacement ductility demand	5.21		6.17		0.84
motion	hysteretic energy, (k-in, kN-mm)	510.1	57628	510.3	57654	1.00
response	Damage Index (1=failure)	0.99		1.08		0.92
test 18	Displacement ductility demand	5.96		5.82		1.02
motion	hysteretic energy, (k-in, kN-mm)	845.0	95468	867.1	97968	0.97
response	Damage Index (1=failure)	1.38		1.39		0.99
test 19	Displacement ductility demand	6.71		6.98		0.96
motion	hysteretic energy, (k-in, kN-mm)	1271.2	143627	1281.9	144837	0.99
response	Damage Index (1=failure)	1.87		1.90		0.98

Table 10-4: Comparison of system and individual response using ductility demand and damage index for lab bridge model with constant stiffness index and varied column configurations (test 15 and 18 target motions).

	Motion	Bent heights Bent1	Bent2	Bent3		Bent 1 System	Bent 1 Individual	Bent 2 System	Bent 2 Individual	Bent 3 System	Bent 3 Individual	system/individual ratio Bent1	Bent2	Bent3
Test Specimen	test 15 (0.5g)	72.0 in (183 mm)	96.0 in (244 mm)	60.0 in (152 mm)	μ_Δ	3.01	2.61	1.84	1.85	3.47	2.96	1.15	0.99	1.17
					D_i	0.49	0.41	0.38	0.40	0.49	0.46	1.20	0.96	1.06
	test 18 (1.33g)				μ_Δ	6.40	4.72	3.24	5.14	5.96	5.82	1.36	0.63	1.02
					D_i	1.63	1.25	0.86	1.40	1.38	1.39	1.31	0.61	0.99
Uniform	test 15 (0.5g)	70.8 in (180 mm)	70.8 in (180 mm)	70.8 in (180 mm)	μ_Δ	2.81	2.86	2.82	2.86	2.82	2.86	0.98	0.99	0.99
					D_i	0.47	0.48	0.48	0.48	0.48	0.48	0.98	0.99	0.99
	test 18 (1.33g)				μ_Δ	5.35		5.36		5.35				
System 1	test 15 (0.5g)	80.7 in (205 mm)	60.0 in (152 mm)	80.7 in (205 mm)	μ_Δ	2.04	2.59	3.15	2.96	2.04	2.59	0.79	1.07	0.79
					D_i	0.31	0.40	0.55	0.55	0.31	0.40	0.79	0.99	0.79
	test 18 (1.33g)				μ_Δ	4.03	5.05	6.25	5.82	4.03	5.05	0.80	1.07	0.80
					D_i	0.98	1.23	1.78	1.55	0.98	1.23	0.80	1.15	0.80
System 2	test 15 (0.5g)	96.0 in (244 mm)	60.0 in (152 mm)	72.0 in (183 mm)	μ_Δ	1.56	1.85	2.86	2.96	2.25	2.61	0.84	0.97	0.86
					D_i	0.21	0.28	0.48	0.55	0.38	0.41	0.77	0.87	0.92
	test 18 (1.33g)				μ_Δ	4.20	5.14	6.60	5.82	5.32	4.72	0.82	1.13	1.13
					D_i	0.88	1.09	1.74	1.55	1.26	1.25	0.81	1.13	1.01
System 3	test 15 (0.5g)	64.9 in (165 mm)	96.0 in (244 mm)	64.9 in (165 mm)	μ_Δ	2.74	2.38	1.61	1.85	2.75	2.38	1.15	0.87	1.15
					D_i	0.47	0.43	0.23	0.28	0.47	0.43	1.09	0.82	1.10
	test 18 (1.33g)				μ_Δ	5.53	5.20	3.20	5.14	5.52	5.20	1.06	0.62	1.06
					D_i	1.52	1.37	0.66	1.09	1.52	1.37	1.10	0.61	1.10

Table 10-5: Comparison of system and individual response using ductility demand and damage index for lab bridge model with constant stiffness index and varied column configurations (rare and expected synthetic motions).

	Motion	Bent heights Bent1	Bent2	Bent3		Bent 1 System	Bent 1 Individual	Bent 2 System	Bent 2 Individual	Bent 3 System	Bent 3 Individual	system/individual ratio Bent1	Bent2	Bent3
Test Specimen	expected	72.0 in (183 mm)	96.0 in (244 mm)	60.0 in (152 mm)	μ_Δ	1.35	0.91	0.63	0.94	1.06	1.08	1.47	0.67	0.99
					D_i	0.19	0.12	0.08	0.12	0.15	0.16	1.57	0.64	0.98
	rare				μ_Δ	5.59	4.84	2.74	4.13	5.10	4.59	1.15	0.66	1.11
					D_i	1.81	1.38	0.56	1.04	1.46	1.45	1.31	0.54	1.01
Uniform	expected	70.8 in (180 mm)	70.8 in (180 mm)	70.8 in (180 mm)	μ_Δ	0.99		0.99		0.98				
	rare				μ_Δ	5.34		5.35		5.34				
System 1	expected	80.7 in (205 mm)	60.0 in (152 mm)	80.7 in (205 mm)	μ_Δ	0.82	0.80	1.25	1.08	0.82	0.80	1.02	1.17	1.03
					D_i	0.11	0.11	0.19	0.16	0.11	0.11	1.08	1.19	1.08
	rare				μ_Δ	3.78	4.79	5.86	4.59	3.78	4.79	0.79	1.28	0.79
					D_i	1.04	1.32	1.91	1.45	1.05	1.32	0.79	1.32	0.79
System 2	expected	96.0 in (244 mm)	60.0 in (152 mm)	72.0 in (183 mm)	μ_Δ	0.52	0.94	1.04	1.08	1.12	0.91	0.56	0.96	1.22
					D_i	0.07	0.12	0.14	0.16	0.17	0.12	0.54	0.93	1.34
	rare				μ_Δ	4.10	4.13	5.78	4.59	5.02	4.84	0.99	1.26	1.04
					D_i	1.00	1.04	1.65	1.45	1.42	1.38	0.96	1.14	1.03
System 3	expected	64.9 in (165 mm)	96.0 in (244 mm)	64.9 in (165 mm)	μ_Δ	1.07	1.02	0.64	0.94	1.06	1.02	1.04	0.68	1.03
					D_i	0.16	0.15	0.08	0.12	0.15	0.15	1.04	0.68	1.02
	rare				μ_Δ	4.96	4.75	2.88	4.13	4.97	4.75	1.05	0.70	1.05
					D_i	1.62	1.44	0.66	1.04	1.62	1.44	1.12	0.64	1.12

Table 10-6: Comparison of system and individual damage index and displacement ductility with iregularity indices for lab bridge model with constant stiffness index and varied column configurations (test 15 and 18 target motions).

						Elastic Irregularity Indices		Inelastic Response Ratios	
	Motion	Bent heights Bent1	Bent2	Bent3	Max bent disp. ductility	SM Regularity Index (%)	Maximum elastic bent system /system SDOF elastic displacement ratio	Maximum bent damage index system /individual ratio	Minimum bent damage index system /individual ratio
Specimen	test 15 (0.5g)	72.0 in (183 mm)	96.0 in (244 mm)	60.0 in (152 mm)	3.47	10.66	1.27	1.20	0.96
	test 18 (1.33g)				6.40	10.66	1.27	1.31	0.61
Uniform	test 15 (0.5g)	70.8 in (180 mm)	70.8 in (180 mm)	70.8 in (180 mm)	2.86	0.10	1.01	0.99	0.98
System 1	test 15 (0.5g)	80.7 in (205 mm)	60.0 in (152 mm)	80.7 in (205 mm)	3.15	0.03	1.59	0.99	0.79
	test 18 (1.33g)				6.25	0.03	1.59	1.15	0.80
System 2	test 15 (0.5g)	96.0 in (244 mm)	96.0 in (152 mm)	72.0 in (183 mm)	2.96	29.85	1.66	0.92	0.77
	test 18 (1.33g)				6.60	29.85	1.66	1.13	0.81
System 3	test 15 (0.5g)	64.9 in (165 mm)	60.0 in (244 mm)	64.9 in (165 mm)	2.75	0.15	1.27	1.10	0.82
	test 18 (1.33g)				5.53	0.15	1.27	1.10	0.61

Table 10-7: Comparison of system and individual damage index and displacement ductility with irregularity indices for lab bridge model with constant stiffness index and varied column configurations (rare and expected synthetic motions).

						Elastic Irregularity Indices		Inelastic Response Ratios	
	Motion	Bent heights Bent1	Bent2	Bent3	Max bent disp. ductility	SM Regularity Index (%)	Maximum elastic bent system /system SDOF elastic displacement ratio	Maximum bent damage index system /individual ratio	Minimum bent damage index system /individual ratio
Specimen	expected	72.0 in (183 mm)	96.0 in (244 mm)	60.0 in (152 mm)	1.35	10.66	1.27	1.57	0.64
	rare				5.59	10.66	1.27	1.31	0.54
System 1	expected	80.7 in (205 mm)	60.0 in (152 mm)	80.7 in (205 mm)	1.25	0.03	1.59	1.19	1.08
	rare				5.86	0.03	1.59	1.32	0.79
System 2	expected	96.0 in (244 mm)	60.0 in (152 mm)	72.0 in (183 mm)	1.10	29.85	1.66	1.34	0.54
	rare				5.74	29.85	1.66	1.14	0.96
System 3	expected	64.9 in (165 mm)	96.0 in (244 mm)	64.9 in (165 mm)	1.07	0.15	1.27	1.04	0.68
	rare				4.97	0.15	1.27	1.12	0.64

Figures

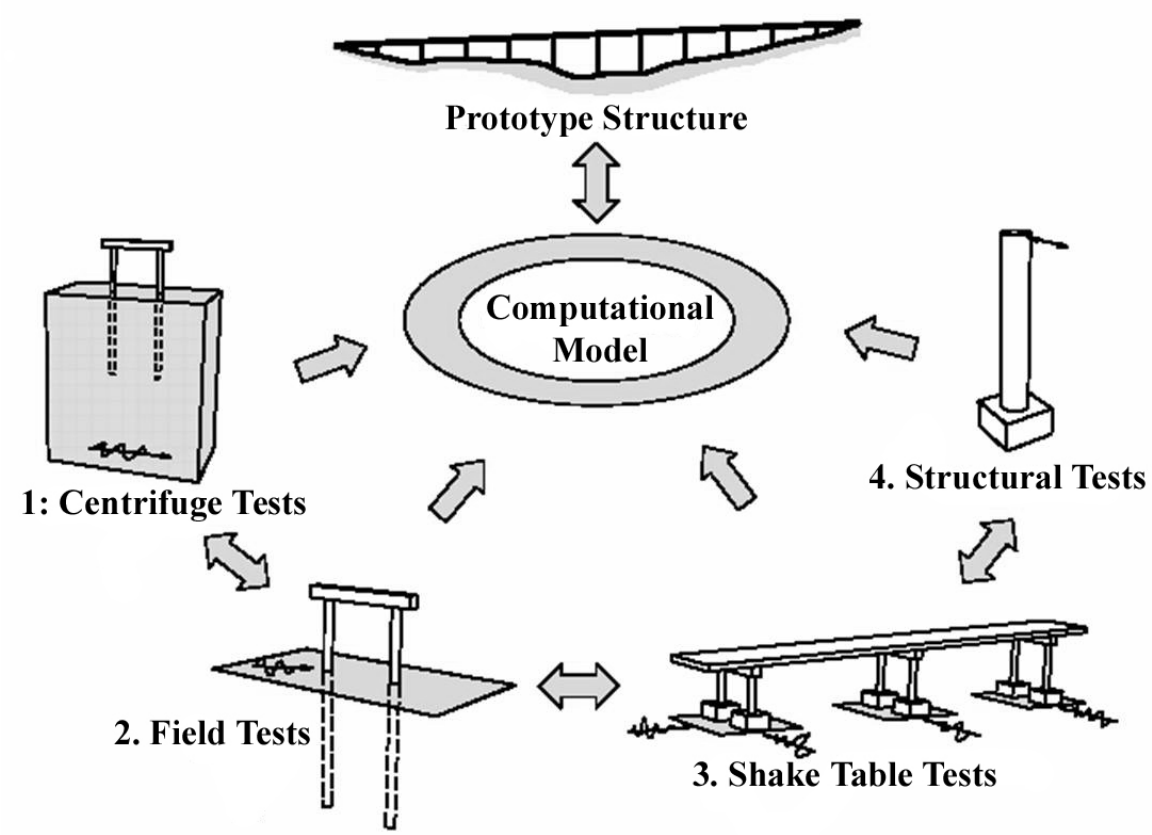

Figure 1-1: Experimental tests that are part of the Pre-NEES test to study soil-foundation-structure-interaction.

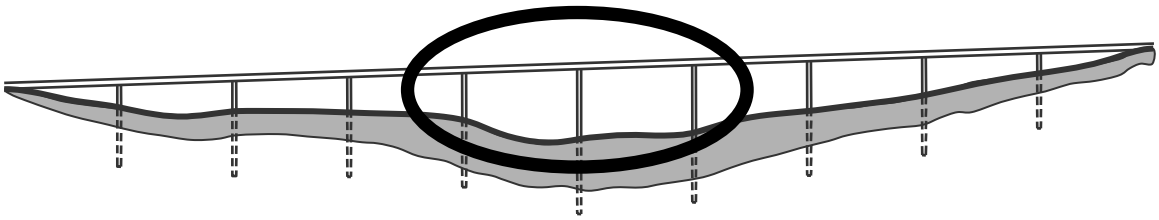

Figure 1-2: Example of prototype location in a multi-span bridge.

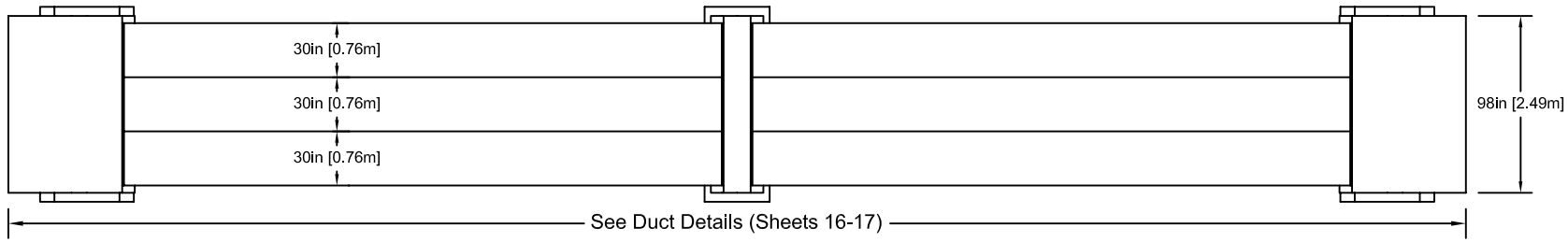

Top View

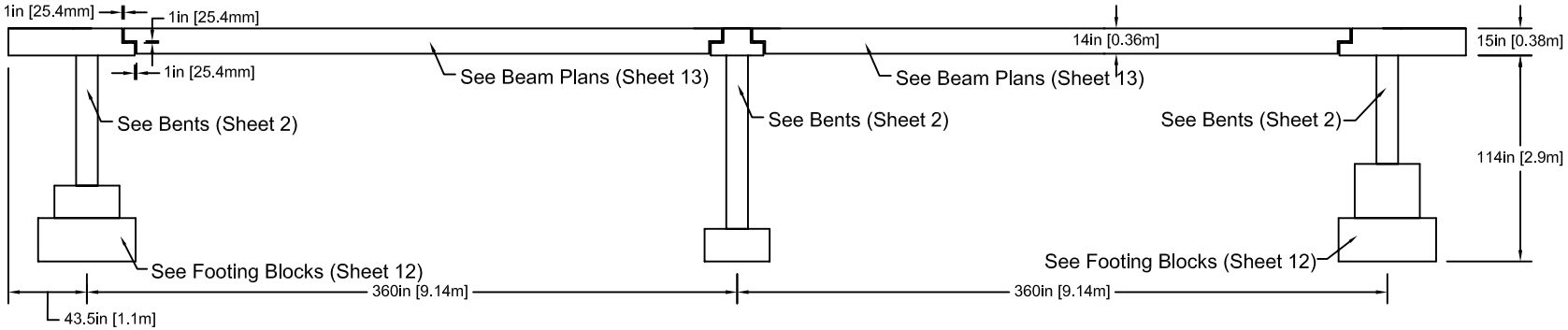

Elevation View

NOTES:

- Concrete is $\frac{3}{8}$in (9.5 mm) agg.; 28-day comp strength = 5000psi (35 MPa)
- Reinforcement is ASTM A706 Grade 60

Figure 2-1: Bridge Plans Sheet 1; Span.

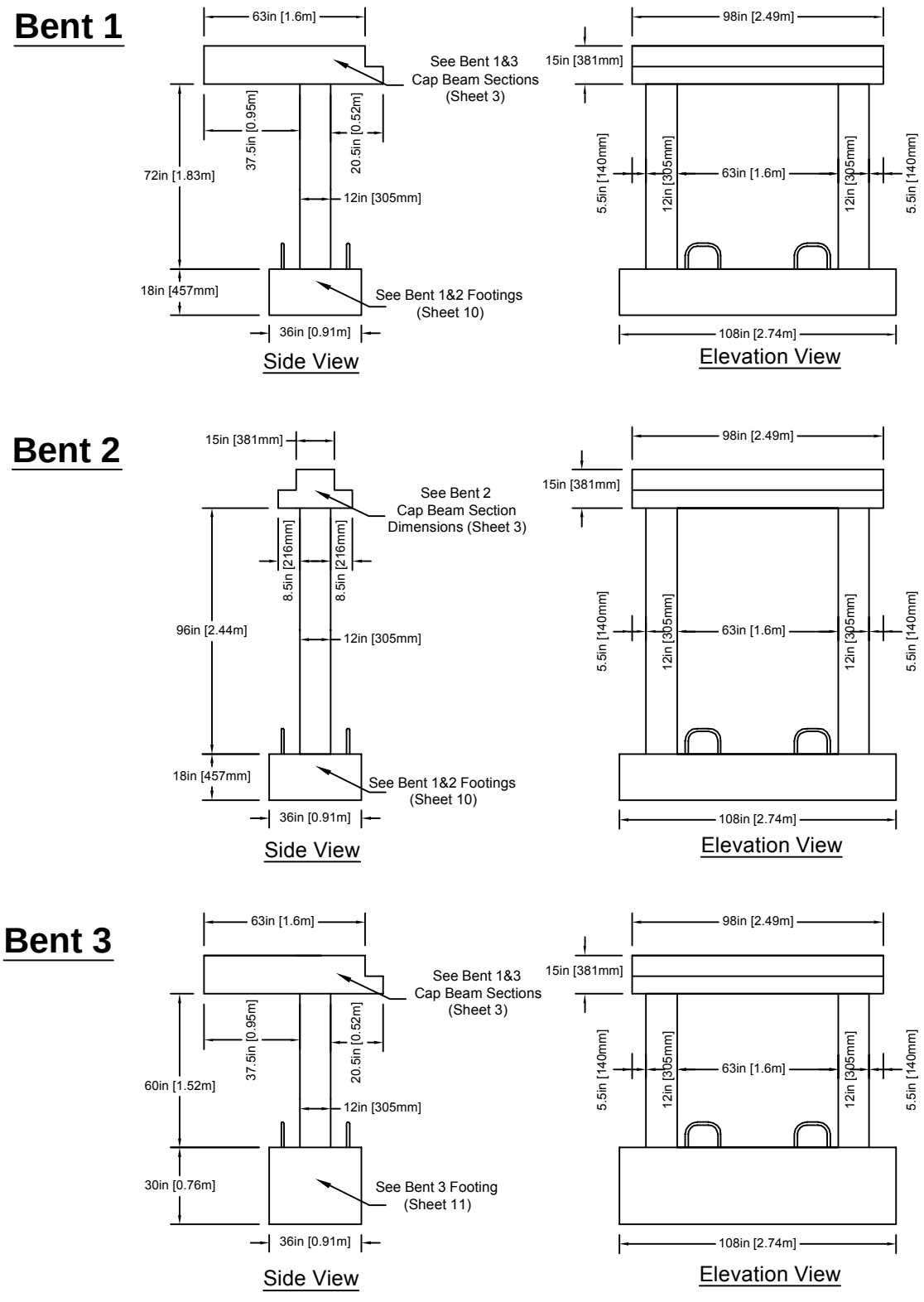

Figure 2-2: Bridge Plans Sheet 2; Bents.

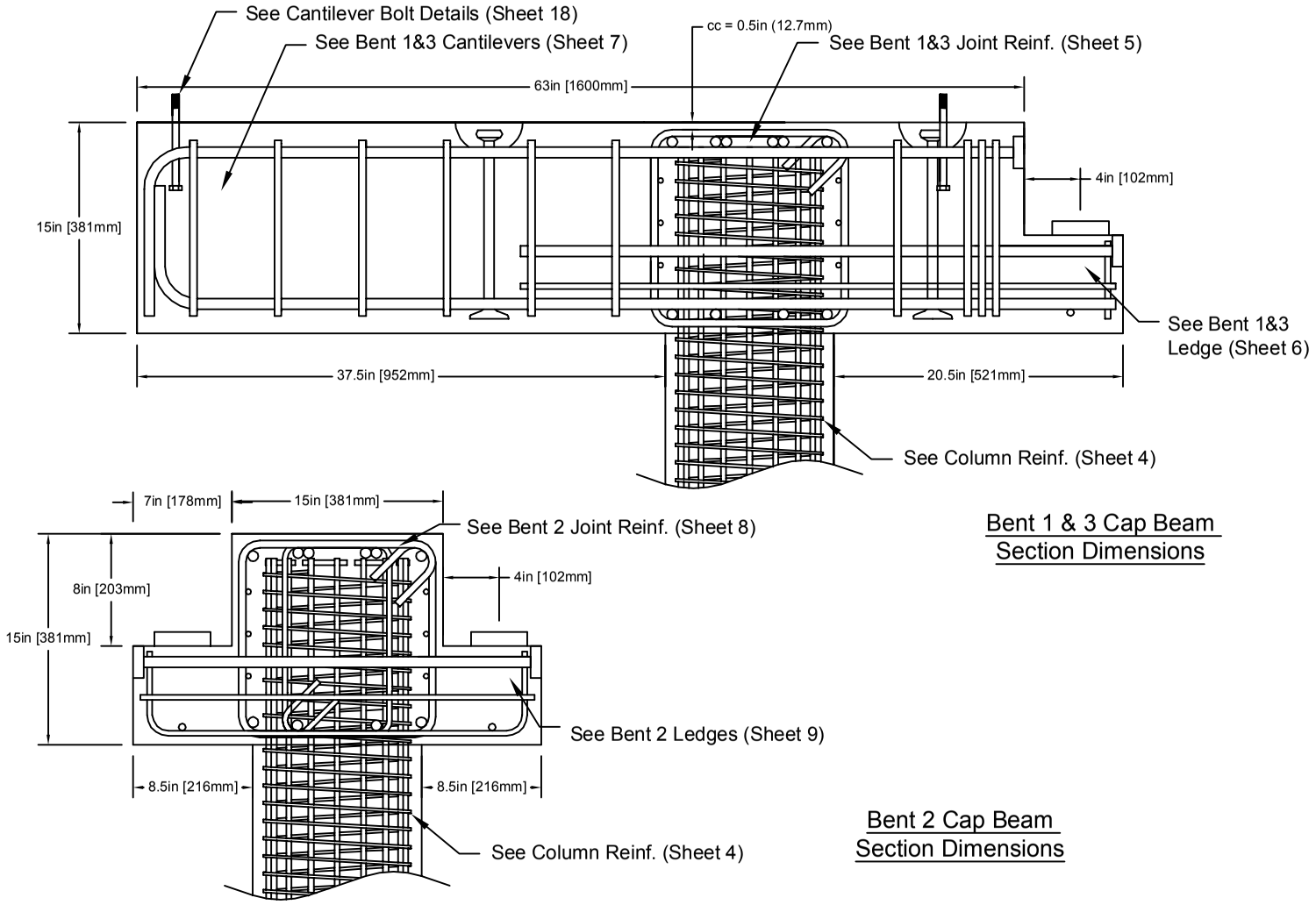

Figure 2-3: Bridge Plans Sheet 3; Bent Sections.

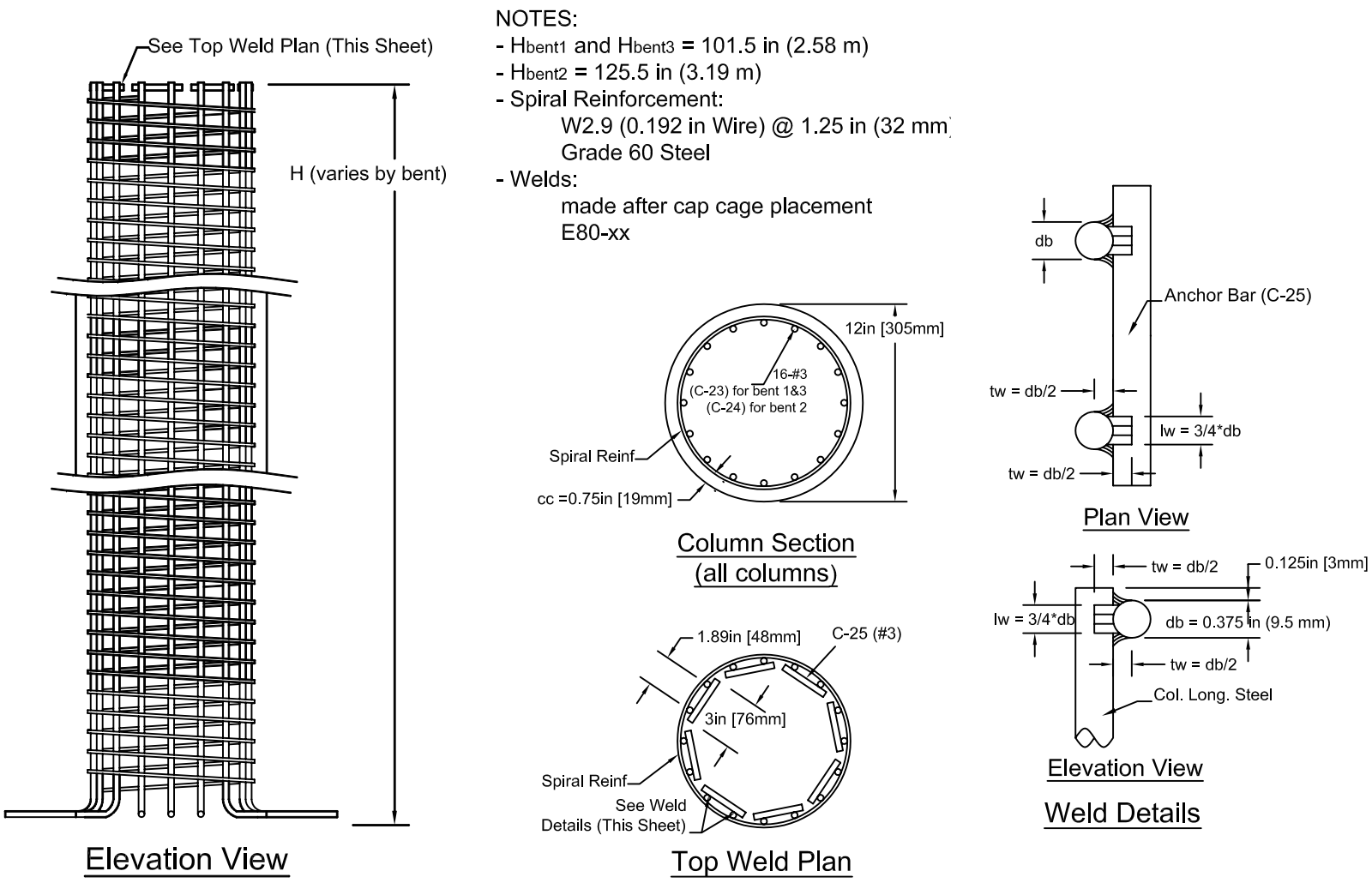

Figure 2-4: Bridge Plans Sheet 4; Column Reinforcement.

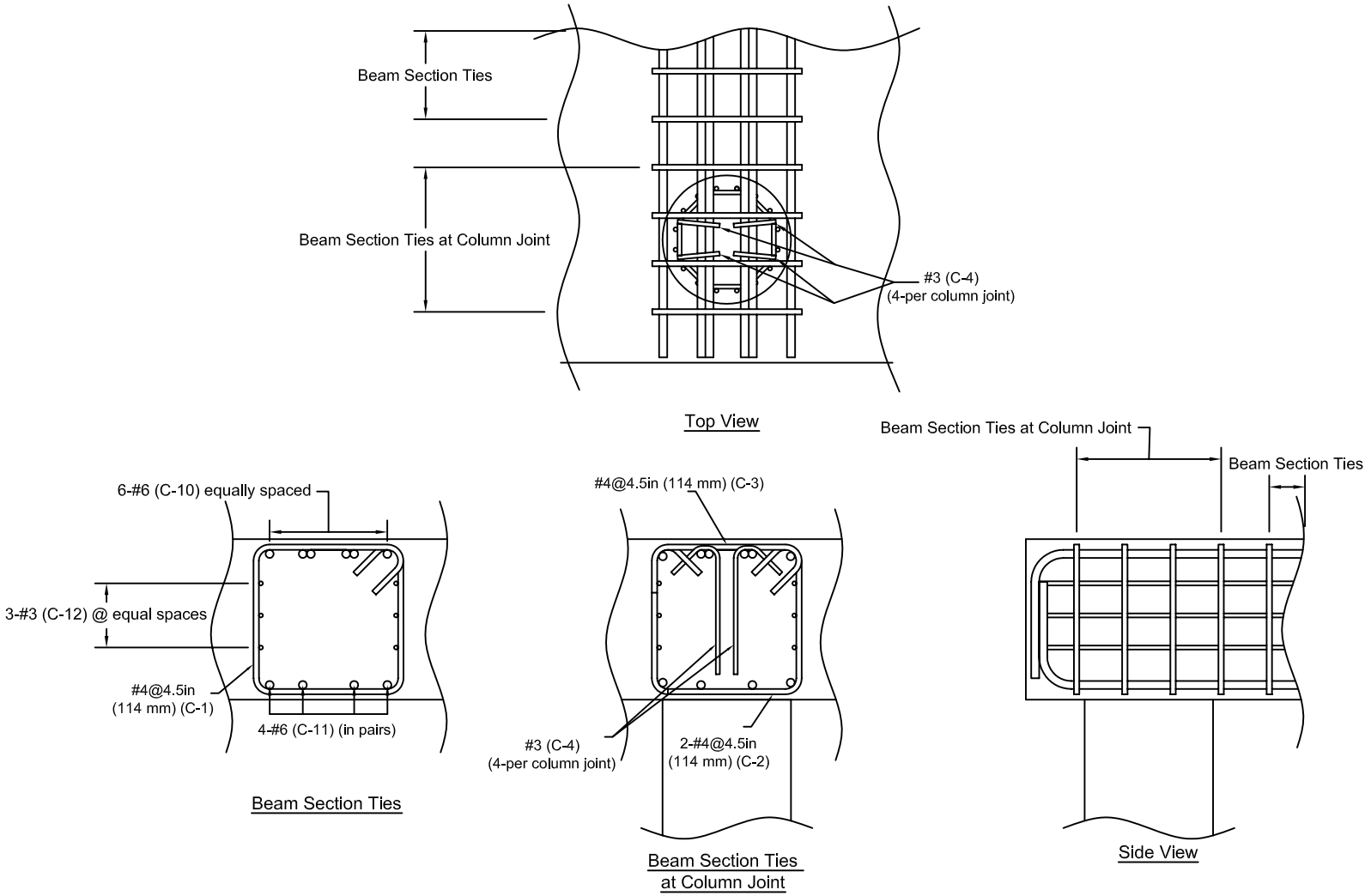

Figure 2-5: Bridge Plans Sheet 5; Bent 1&3 Joint Reinforcement.

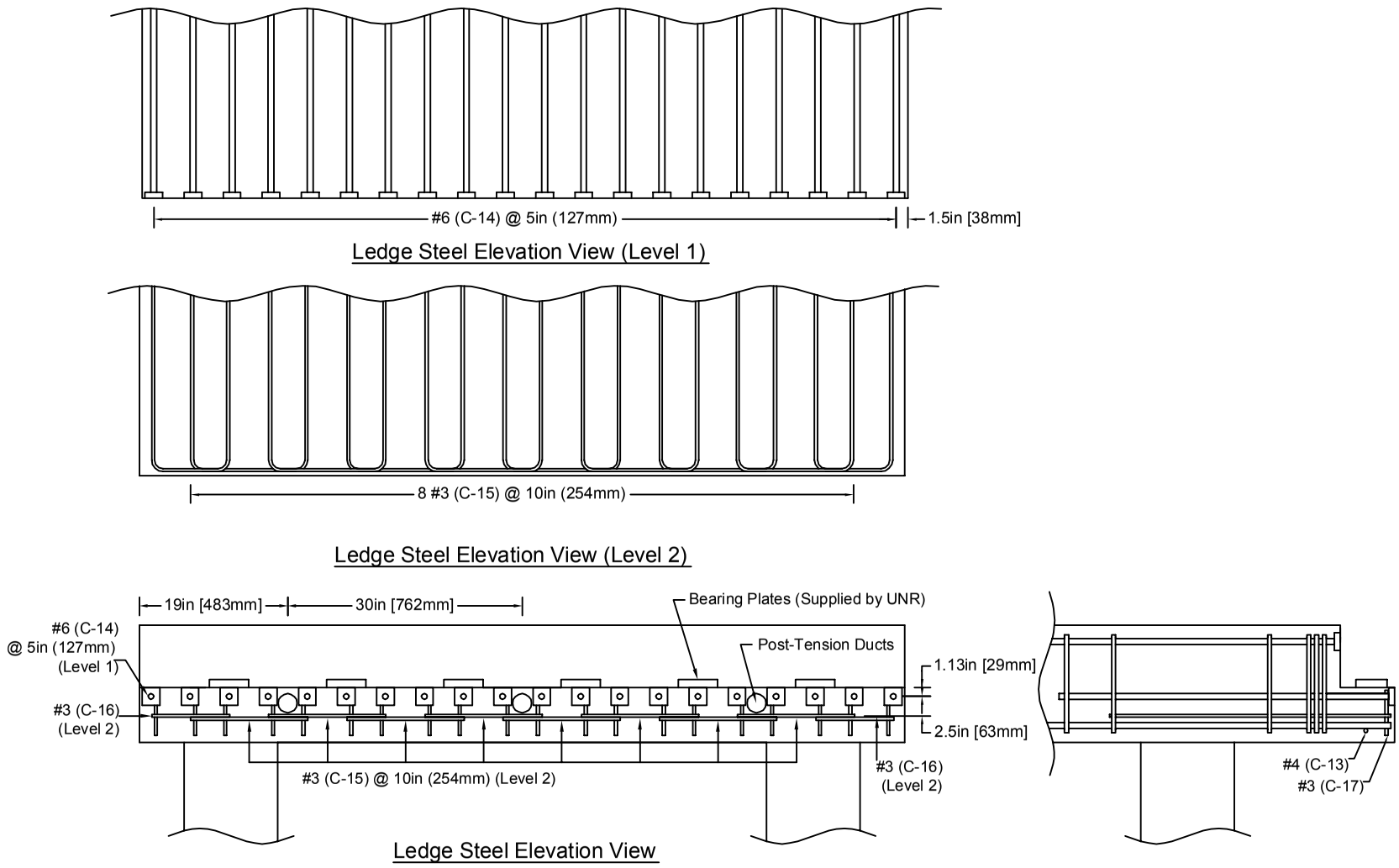

Figure 2-6: Bridge Plans Sheet 6; Bent 1&3 Ledge Reinforcement.

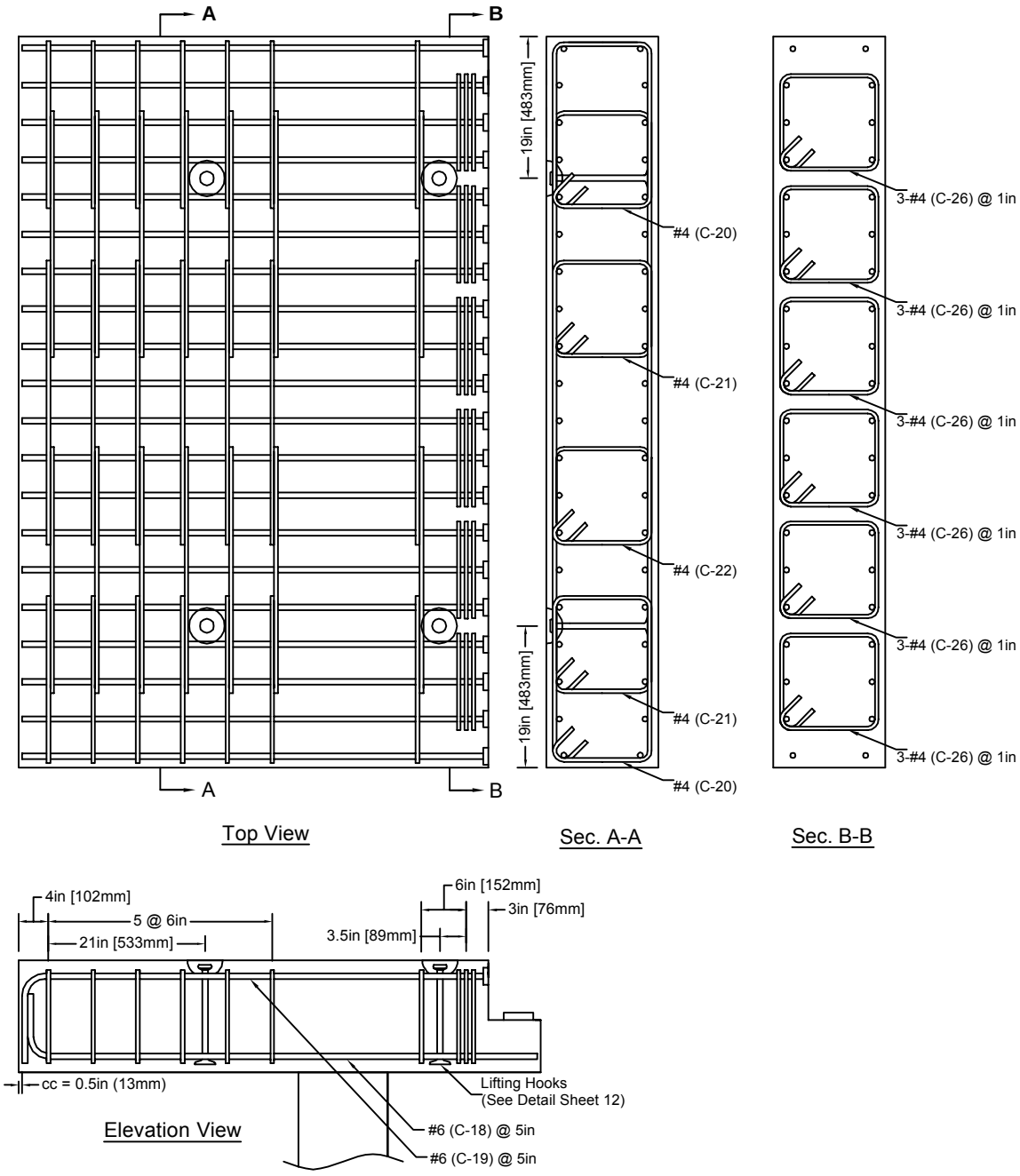

Figure 2-7: Bridge Plans Sheet 7; Bent 1&3 Cantilever Reinforcement.

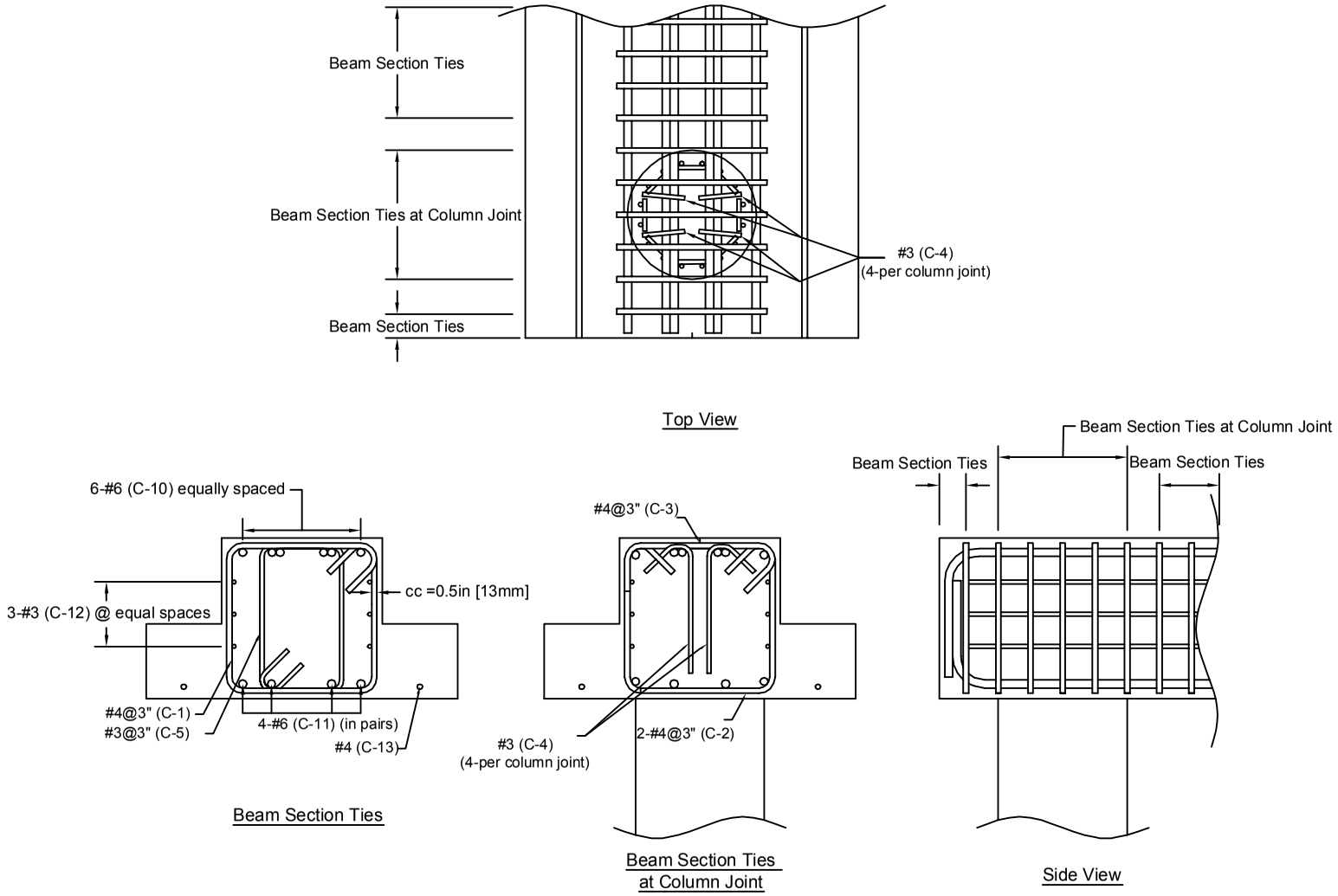

Figure 2-8: Bridge Plans Sheet 8; Bent 2 Joint Reinforcement.

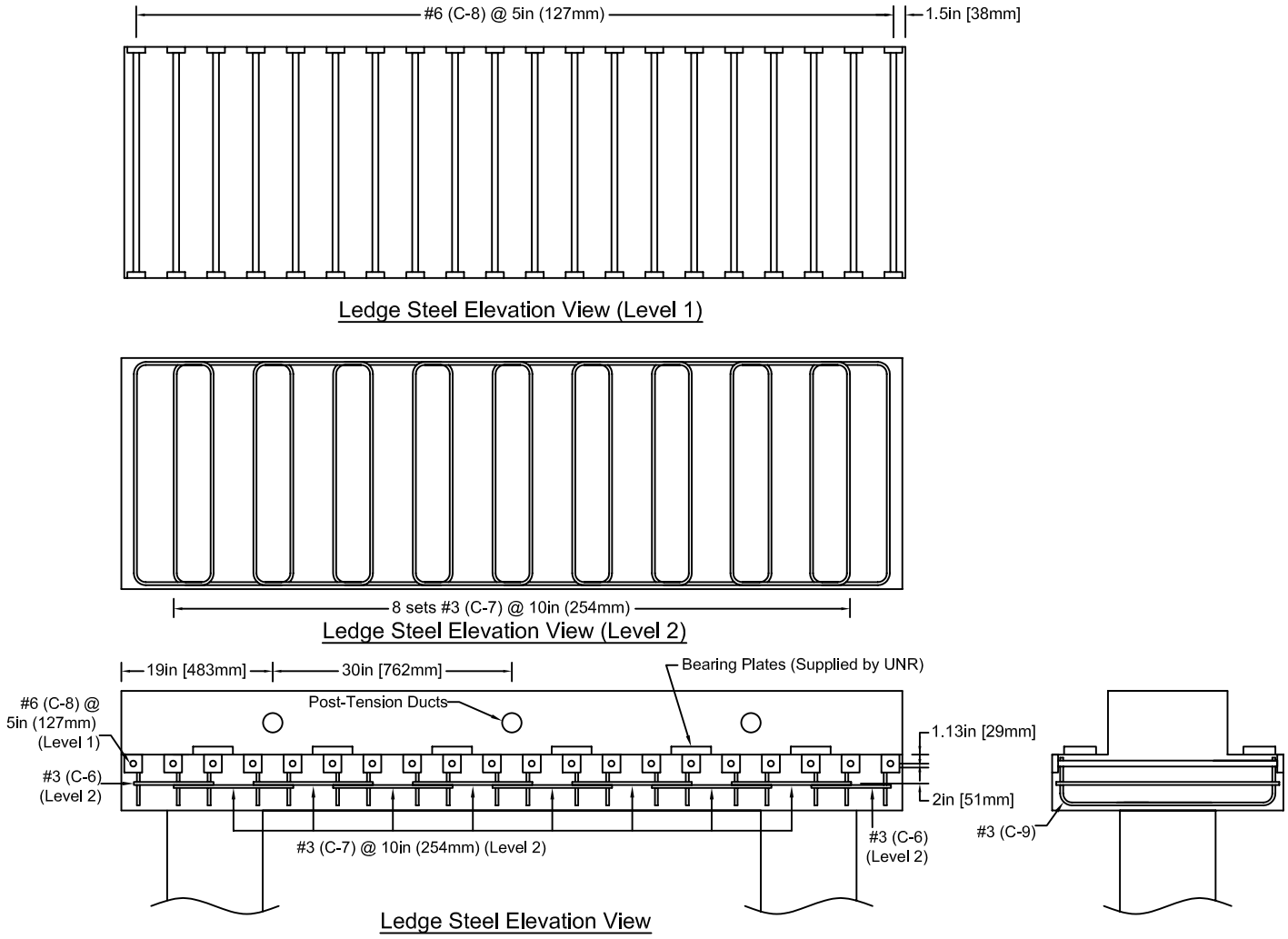

Figure 2-9: Bridge Plans Sheet 9; Bent 2 Ledge Reinforcement.

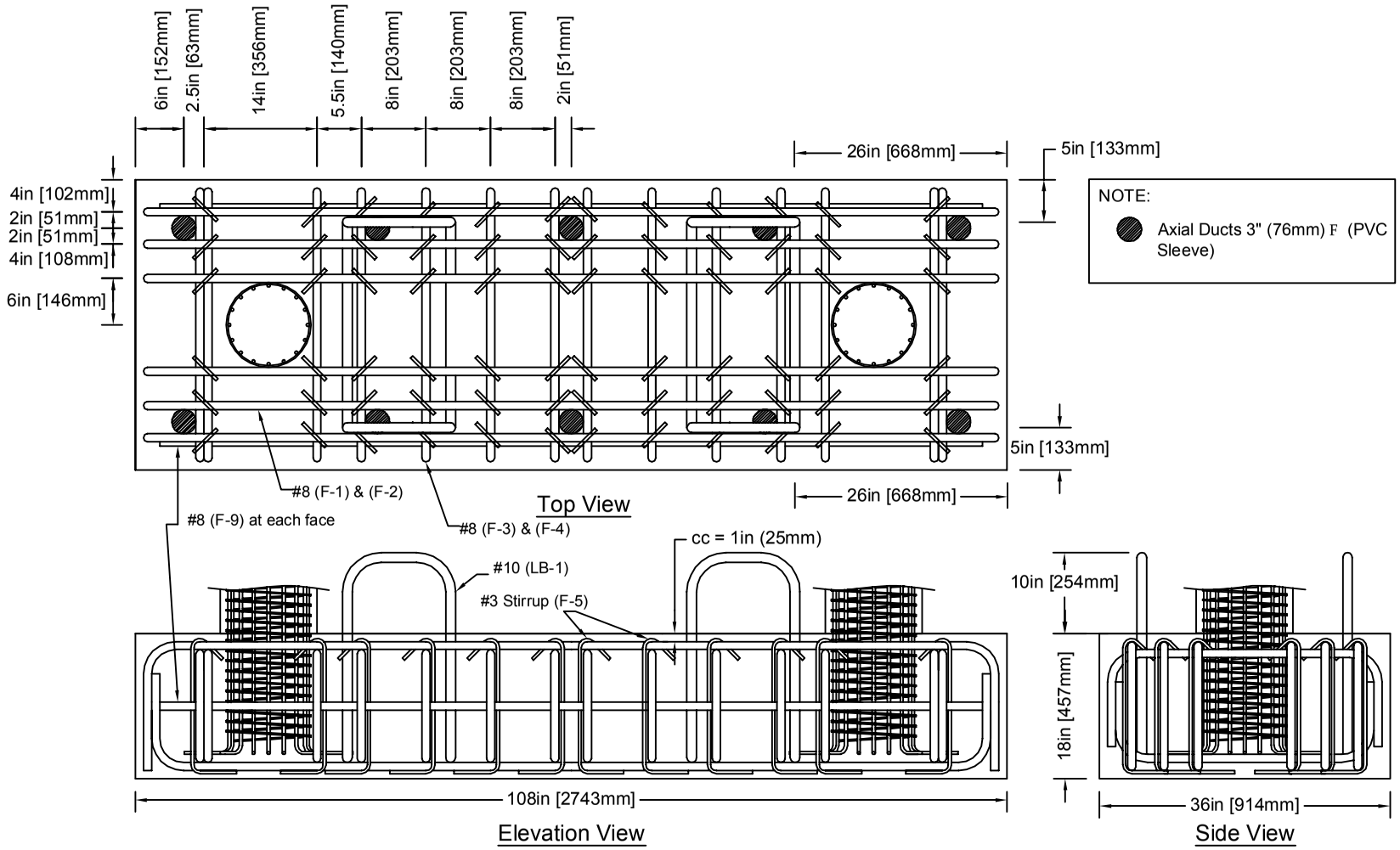

Figure 2-10: Bridge Plans Sheet 10; Bent 1&2 Footings.

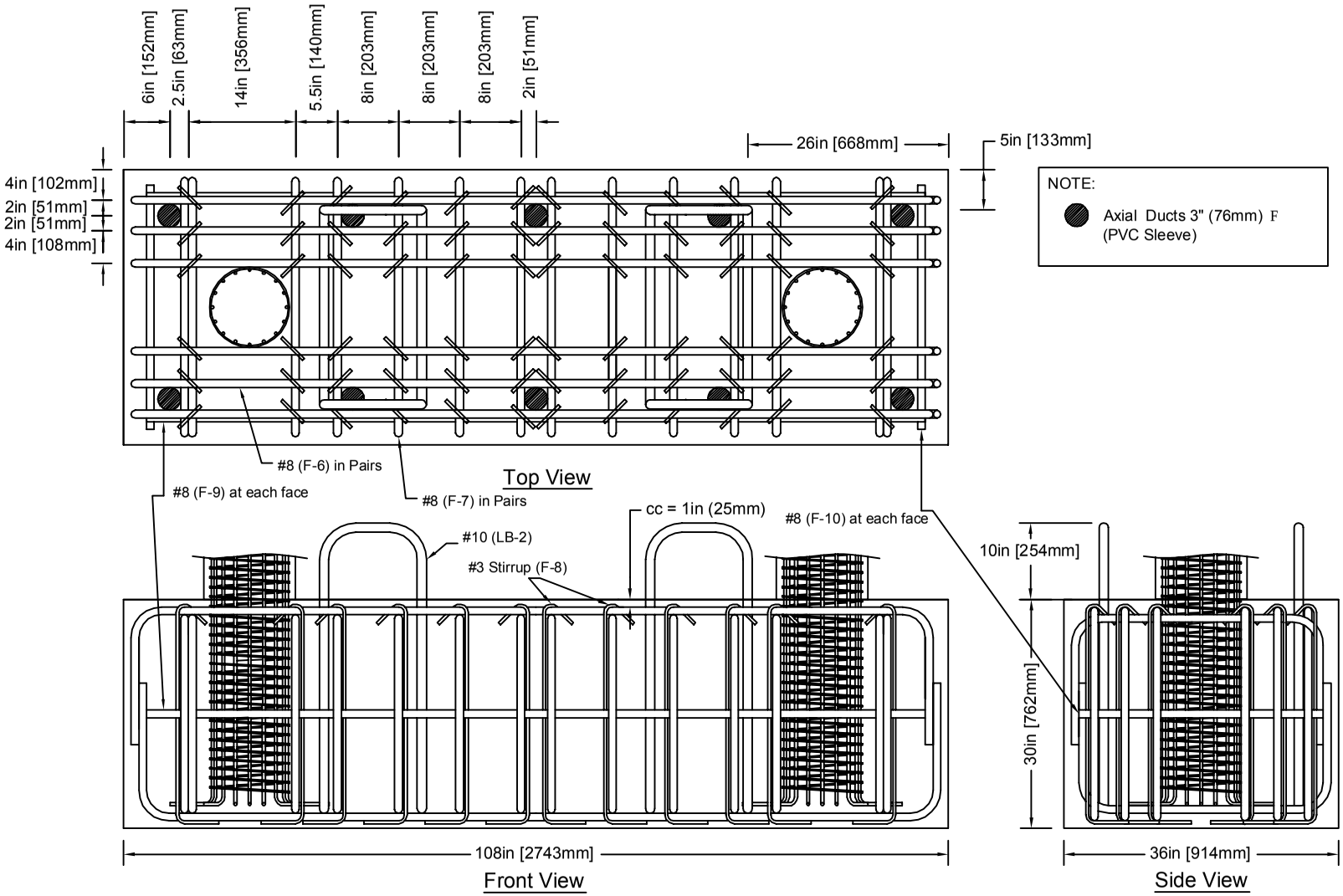

Figure 2-11: Bridge Plans Sheet 11; Bent 3 Footings.

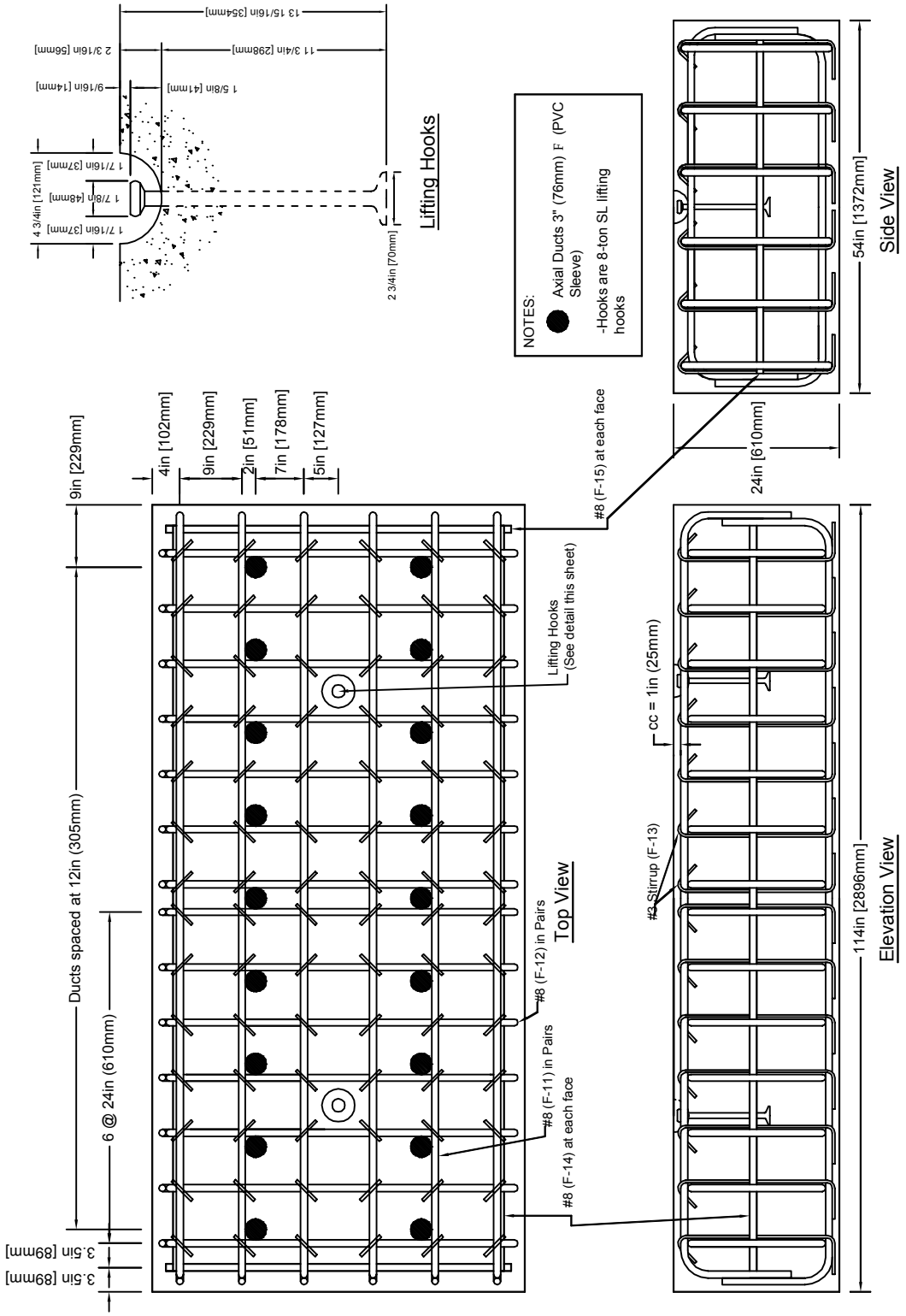

Figure 2-12: Bridge Plans Sheet 12; Footing Blocks.

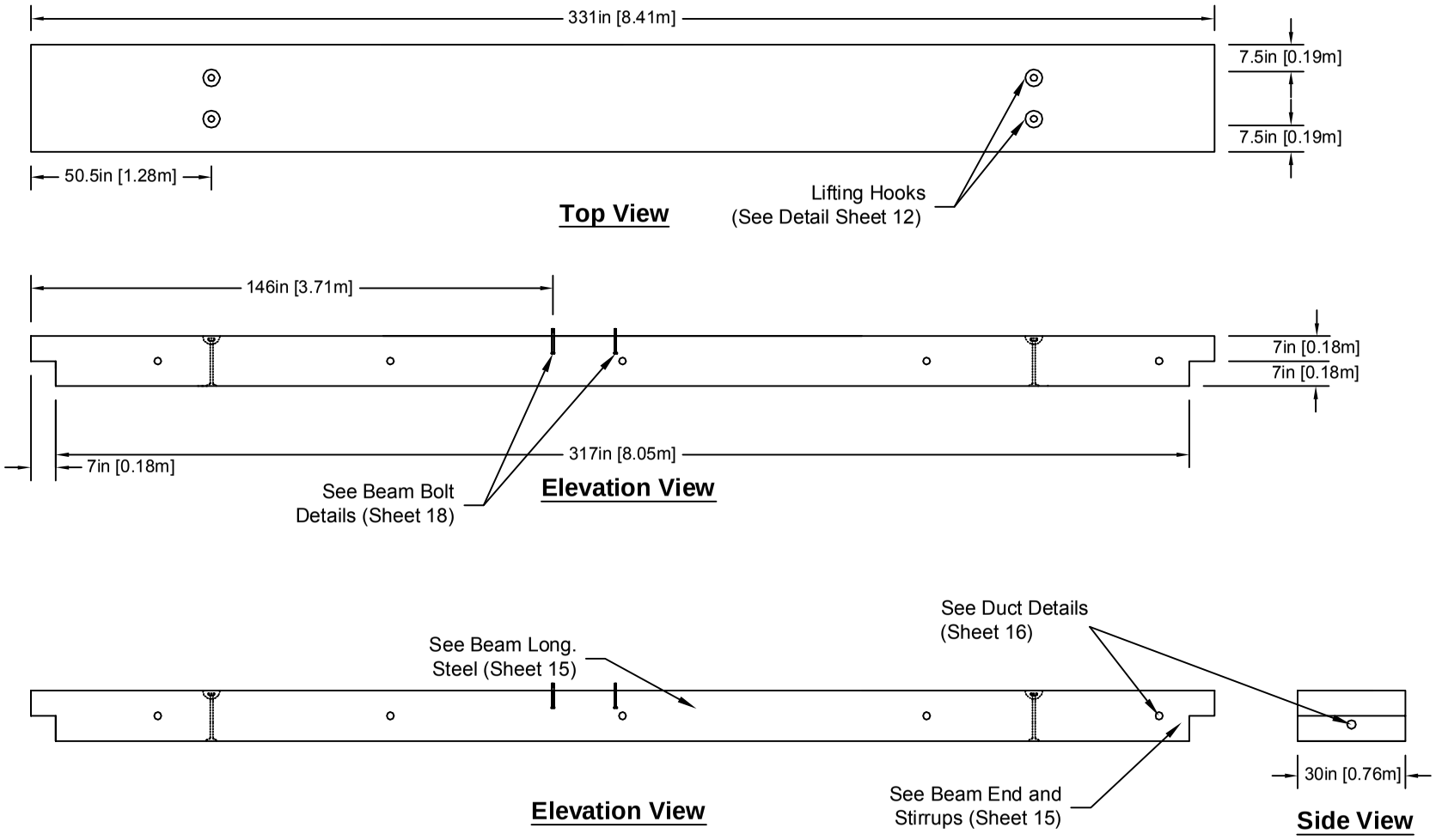

Figure 2-13: Bridge Plans Sheet 13; Beam Plans.

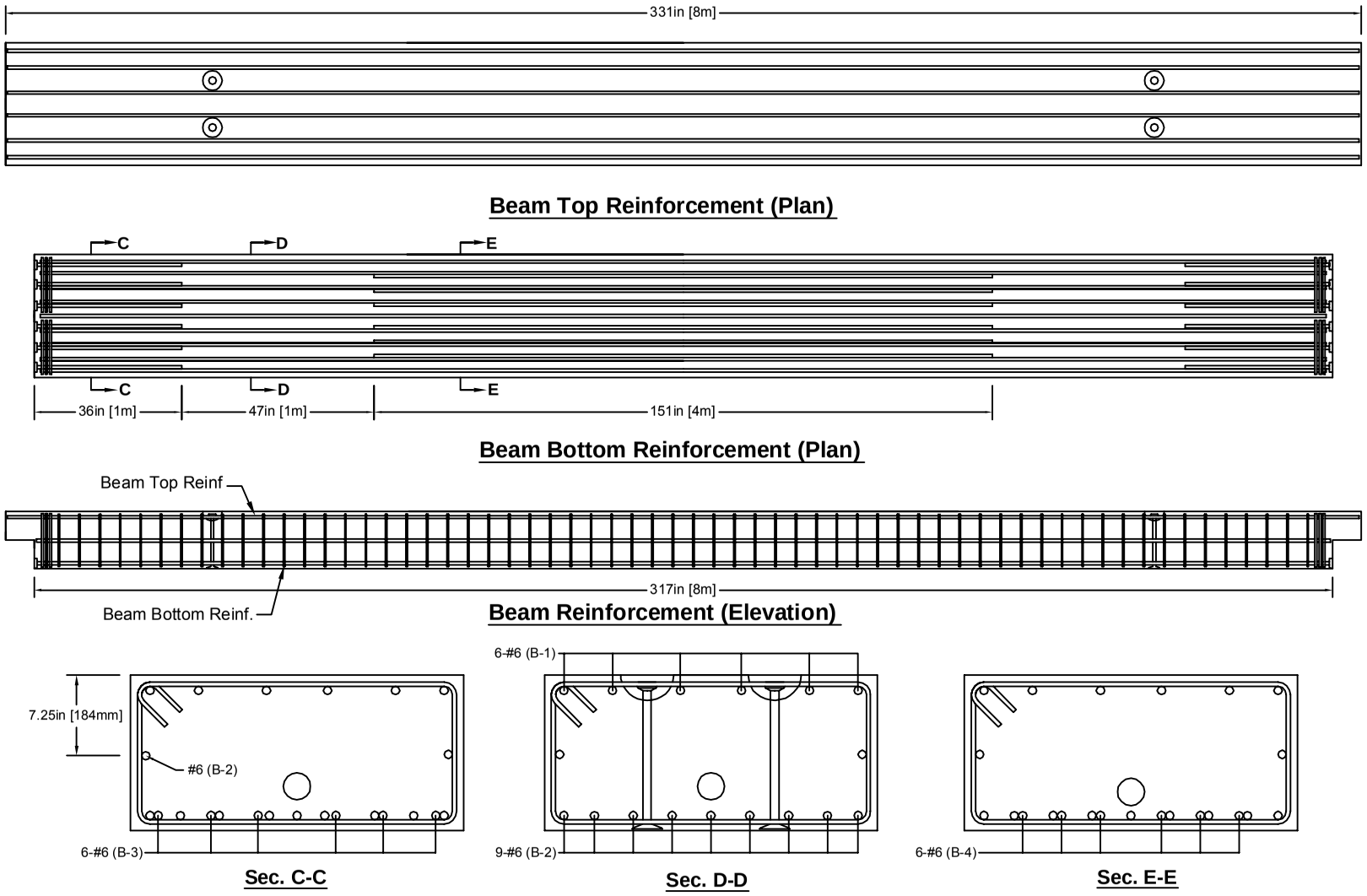

Figure 2-14: Bridge Plans Sheet 14; Beam Longitudinal Steel.

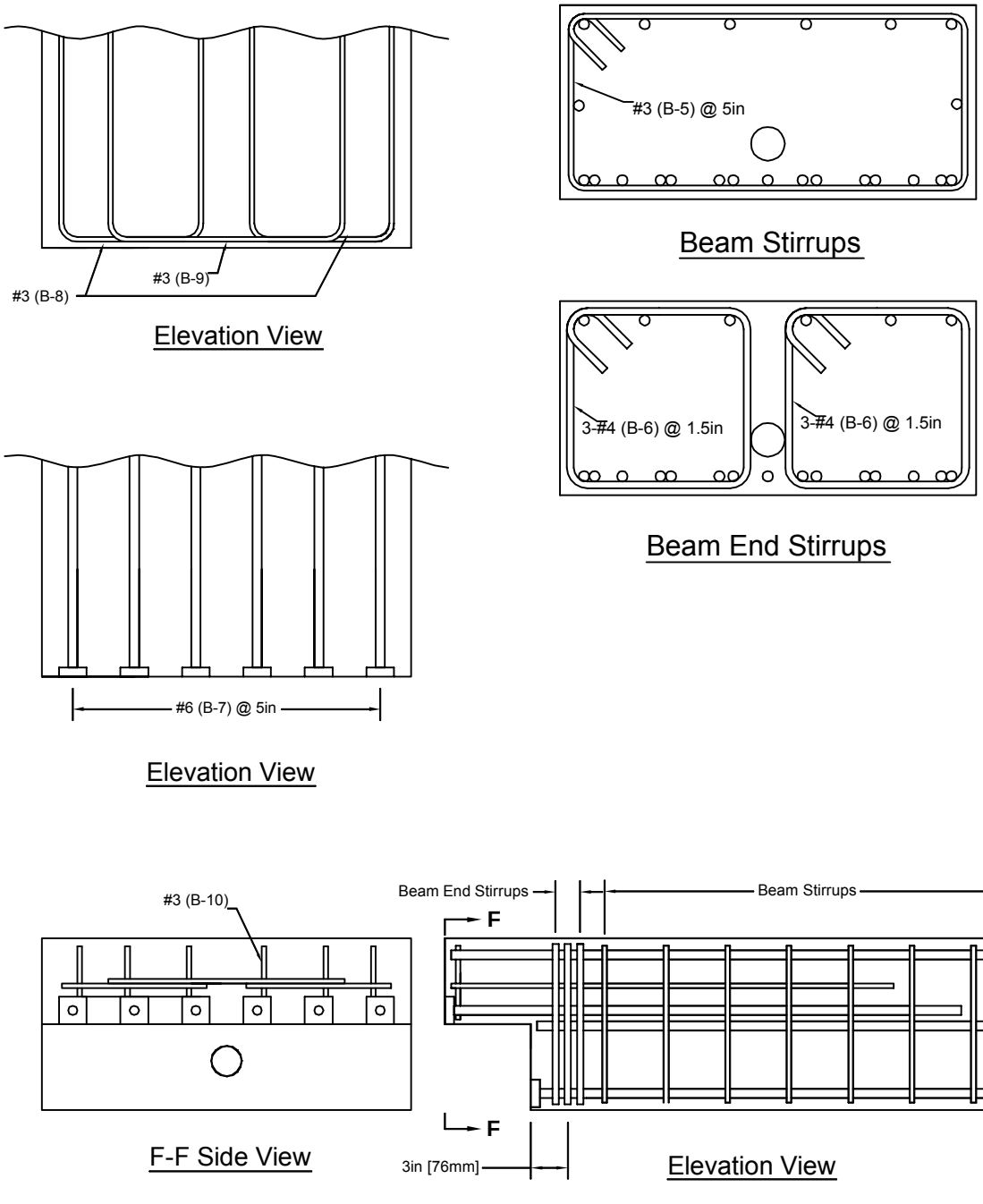

Figure 2-15: Bridge Plans Sheet 15; Beam End and Stirrups.

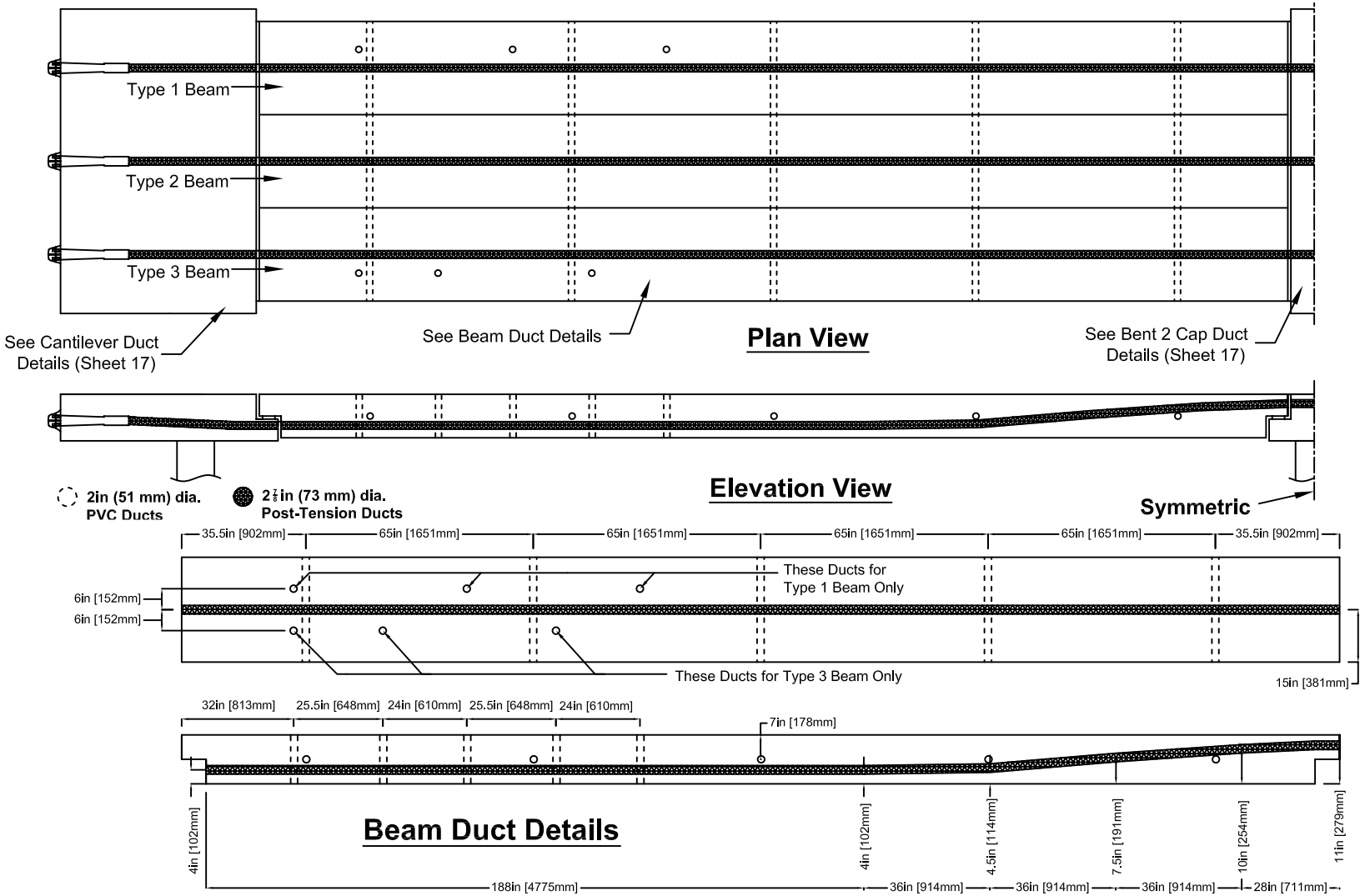

Figure 2-16: Bridge Plans Sheet 16; Duct Details.

Post Tension NOTES:

-Strand Post-Tensioning System w/ 9-0.5" 270 ksi (1860 MPa) tendons
-Each Duct Effective Post Tension Force = 230 kip (137 kN)
-Post-Tension Duct Diameter 2 $\frac{7}{8}$ in (73 mm)
-Anchors Located in Cantilevers

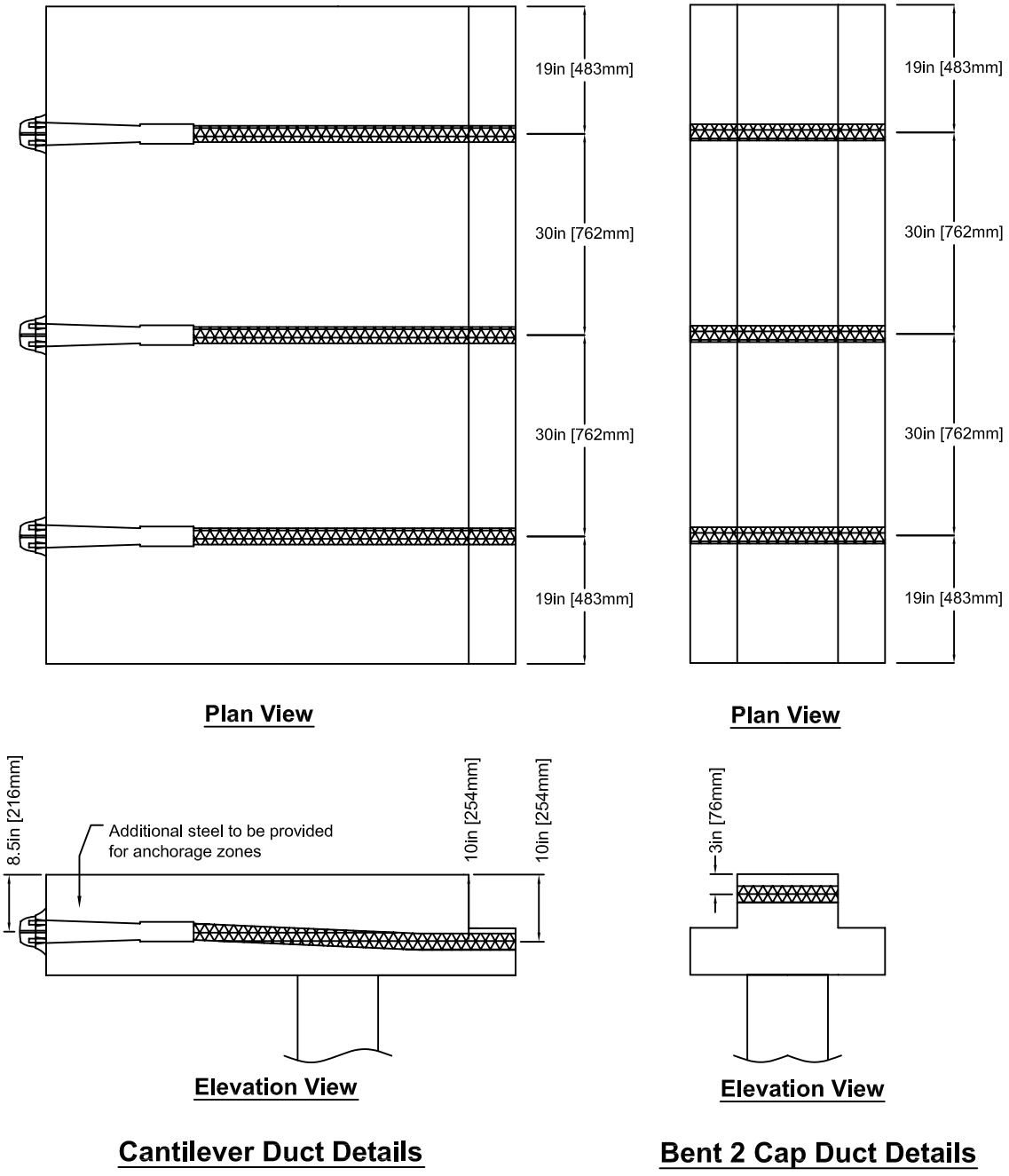

Figure 2-17: Bridge Plans Sheet 17; Duct Details 2.

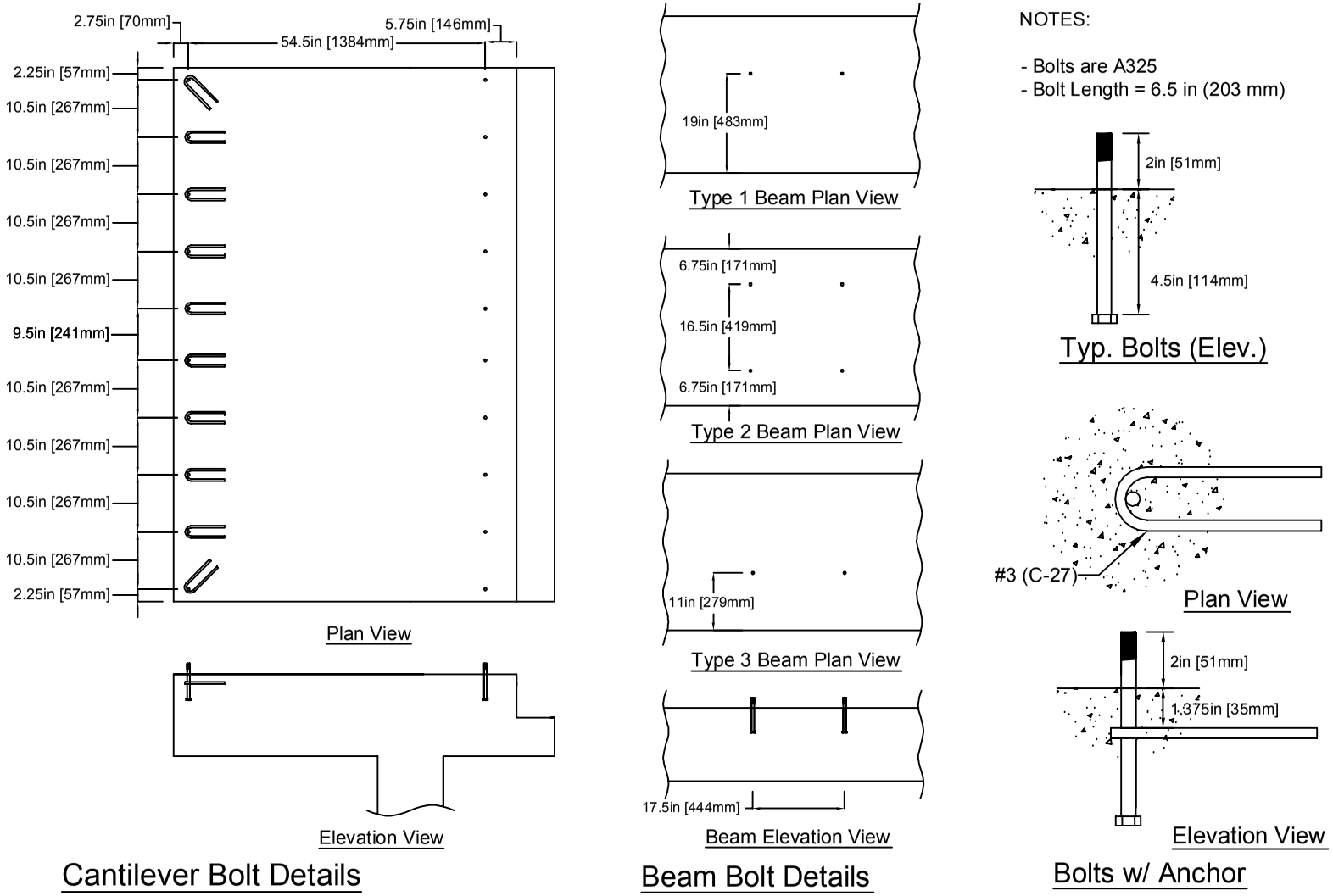

Figure 2-18: Bridge Plans Sheet 18; Bolt Details.

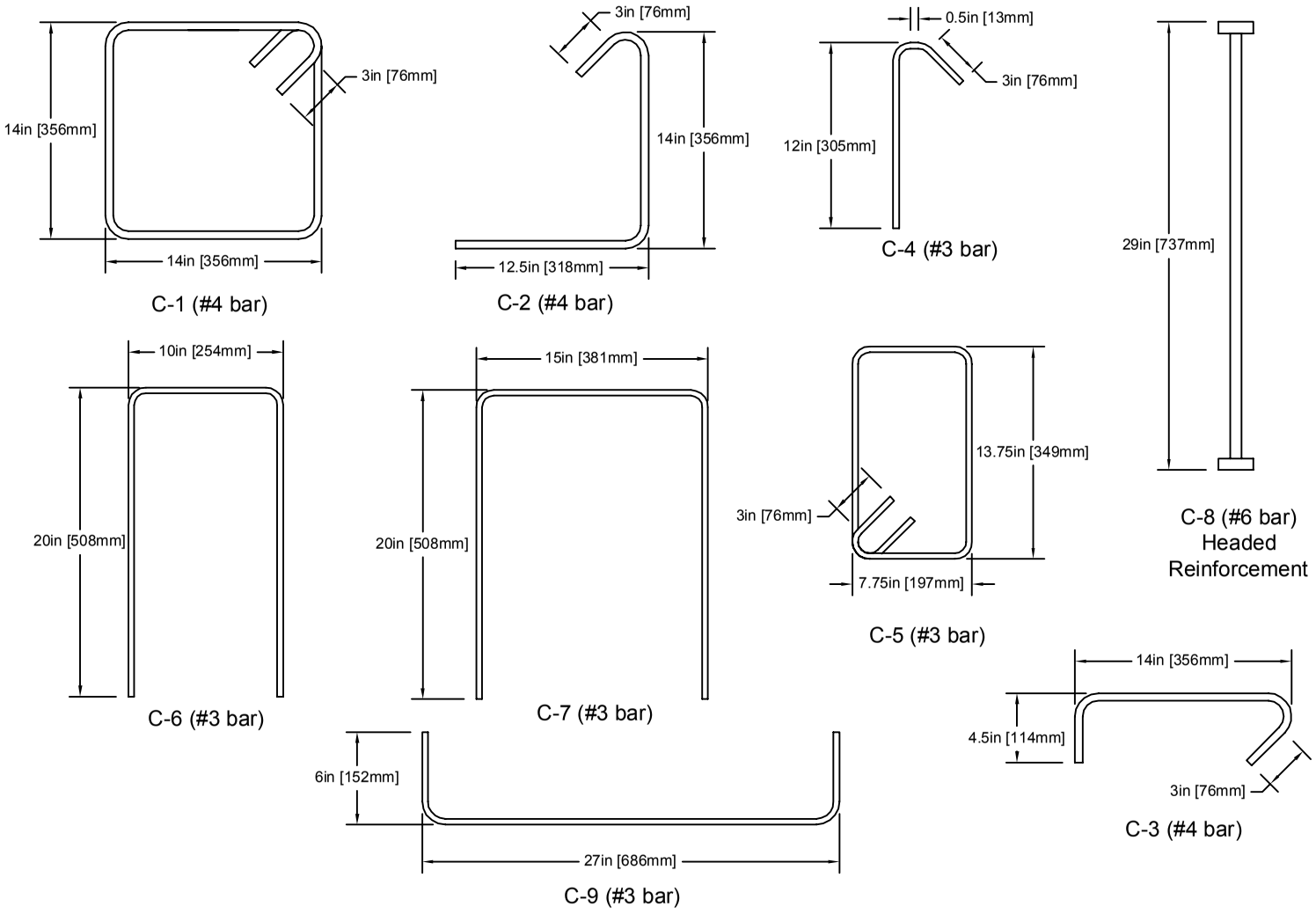

Figure 2-19: Bridge Plans Sheet 19; Steel Details 1.

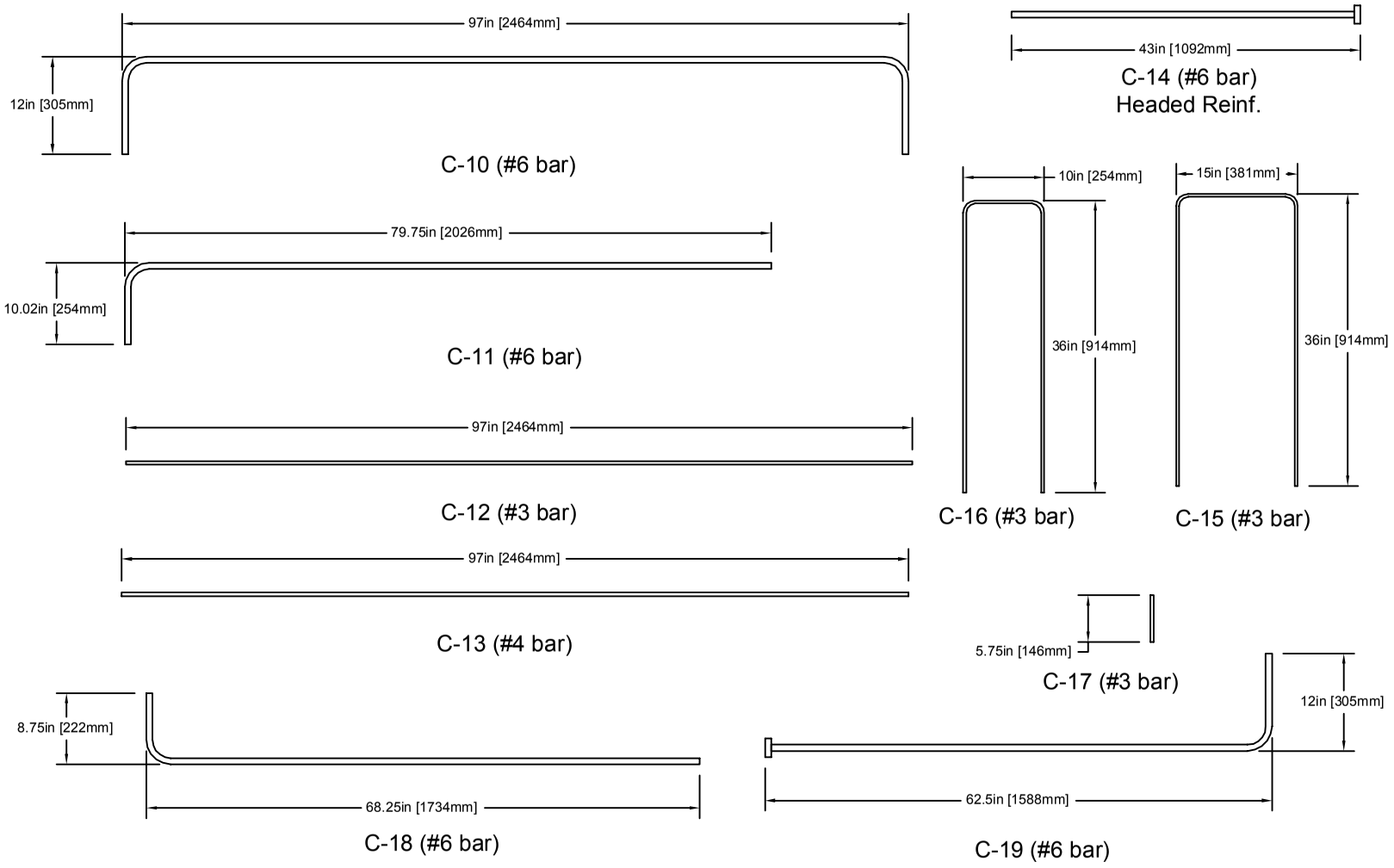

Figure 2-20: Bridge Plans Sheet 20; Steel Details 2.

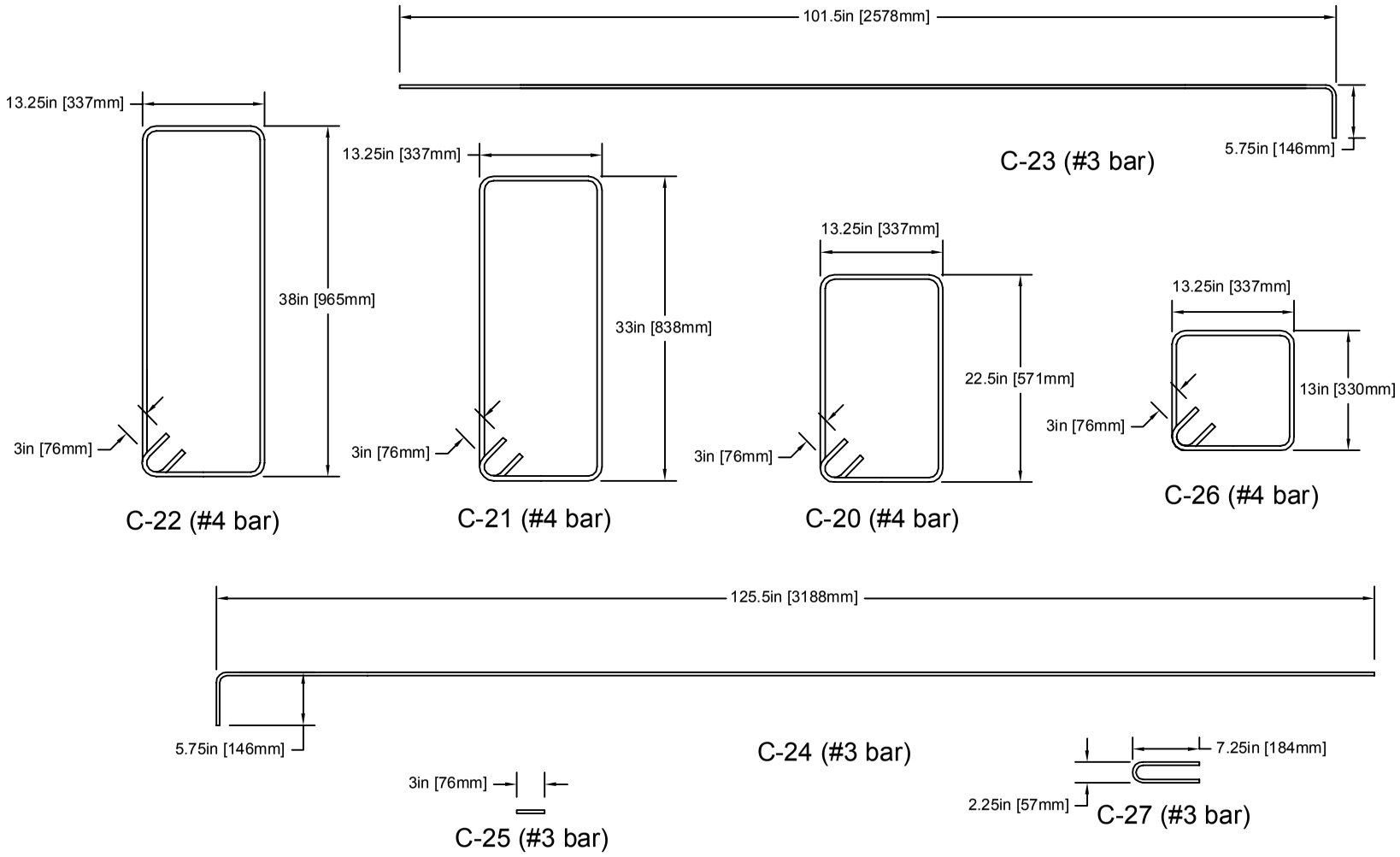

Figure 2-21: Bridge Plans Sheet 21; Steel Details 3.

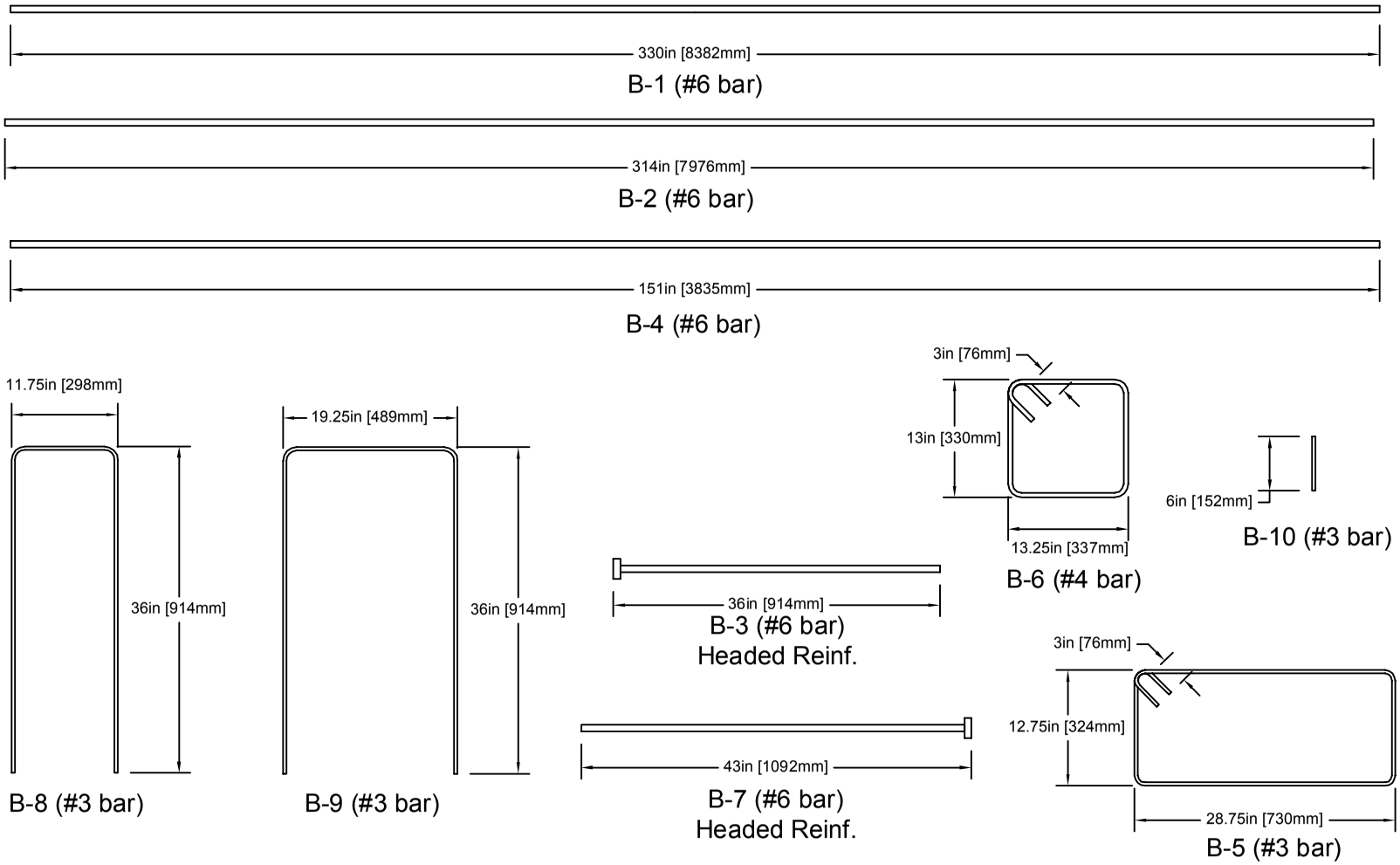

Figure 2-22: Bridge Plans Sheet 22; Steel Details 4.

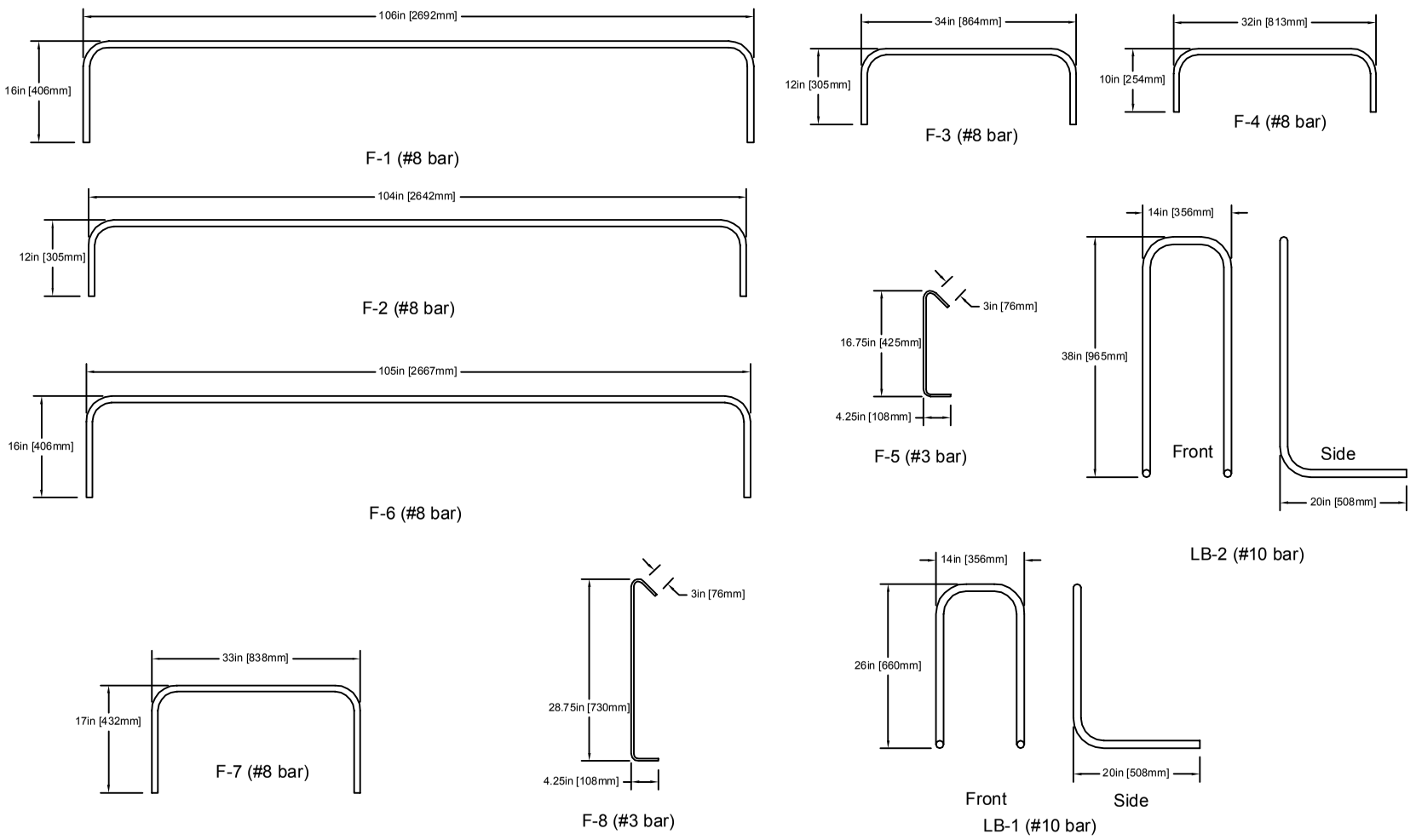

Figure 2-23: Bridge Plans Sheet 23; Steel Details 5.

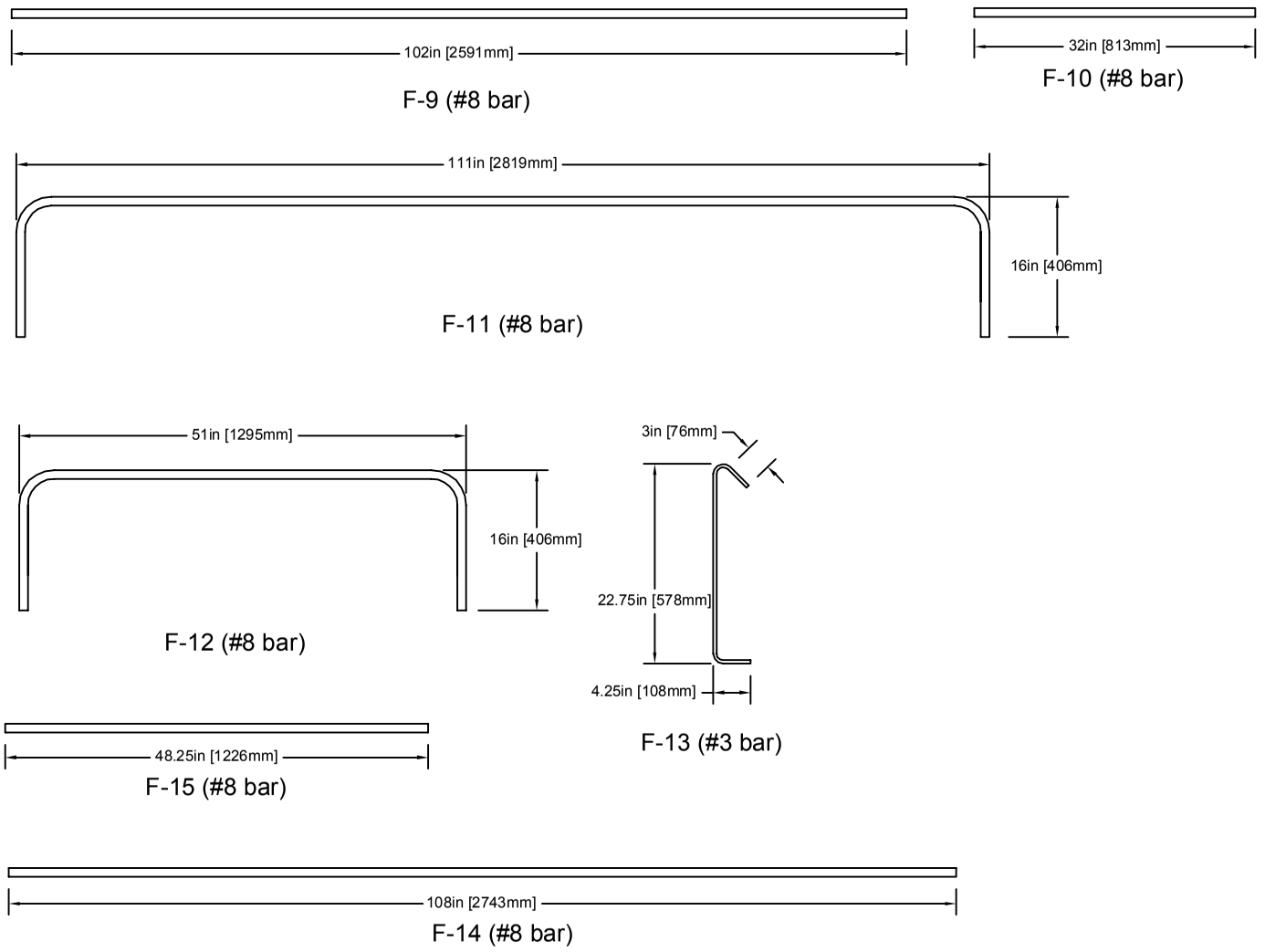

Figure 2-24: Bridge Plans Sheet 24; Steel Details 6.

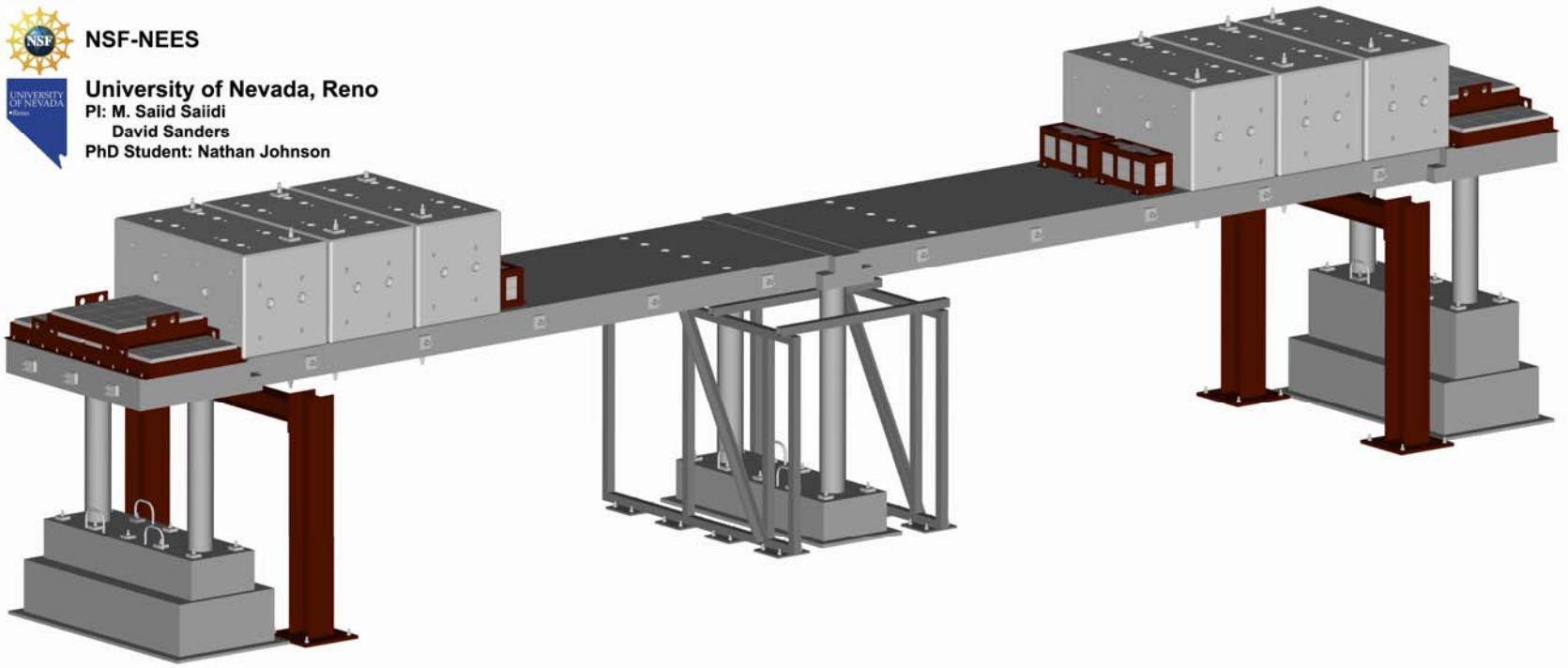

Figure 2-25: Rendering of bridge specimen.

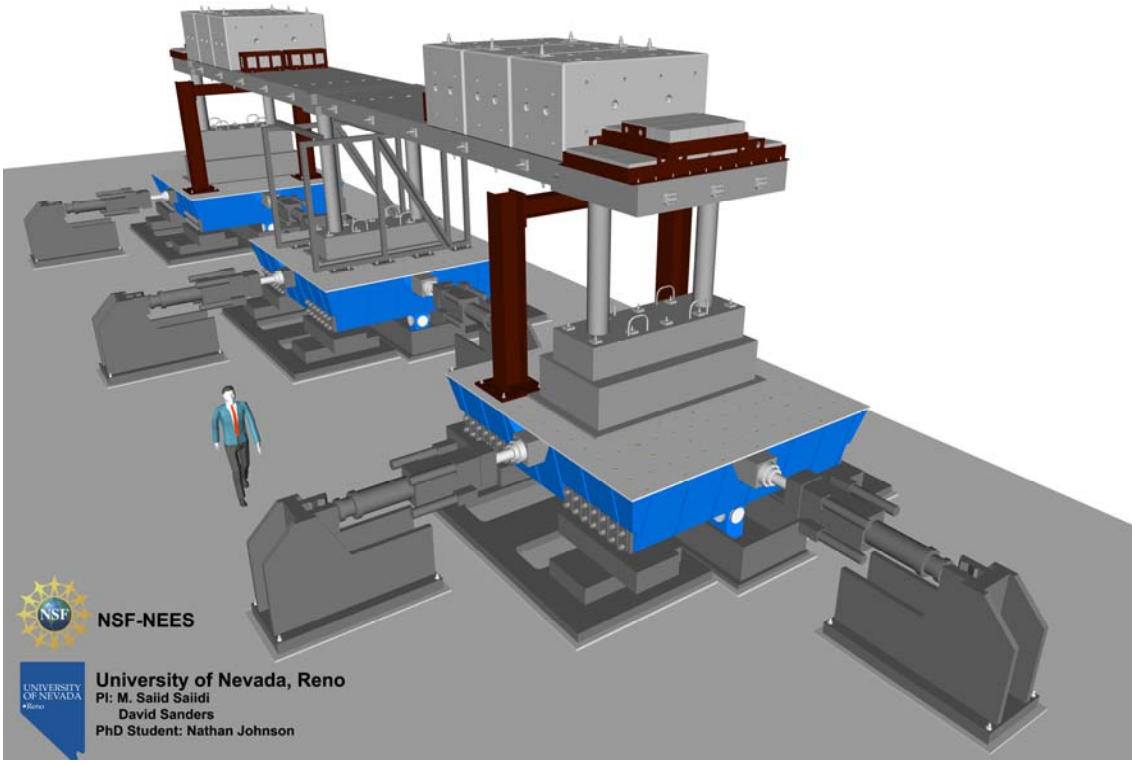

Figure 2-26: Rendering of bridge specimen on shake tables.

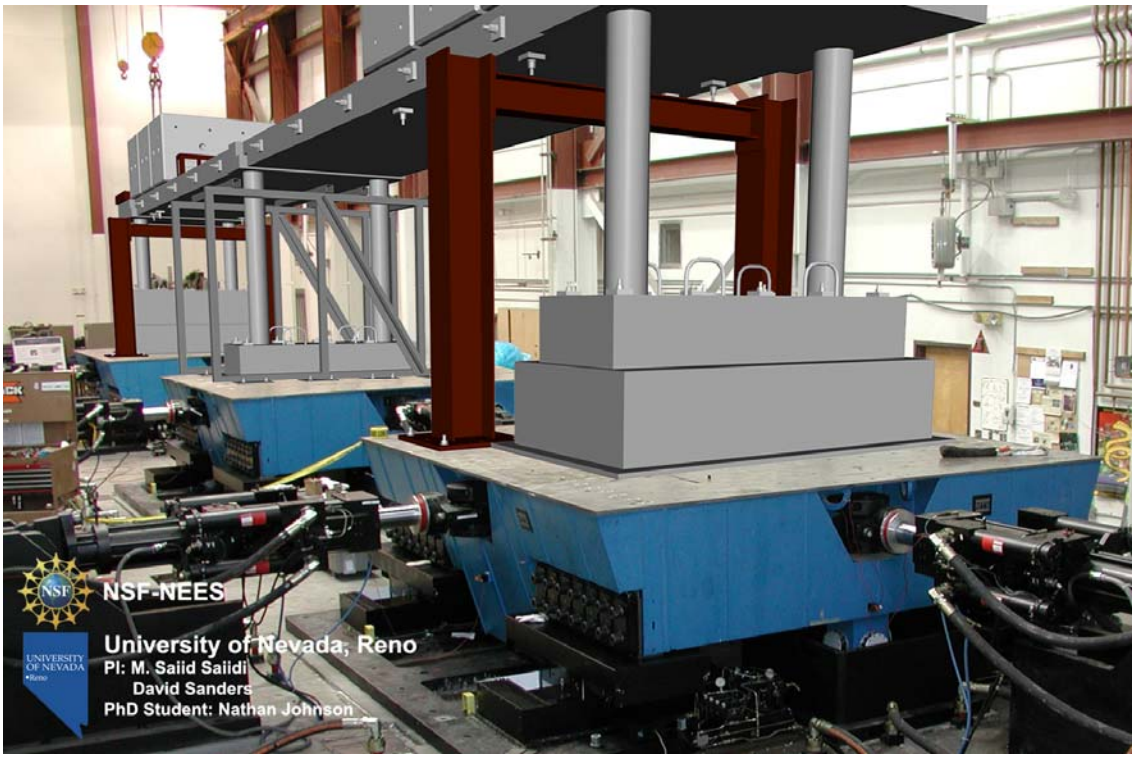

Figure 2-27: Rendering of bridge specimen superimposed on shake tables.

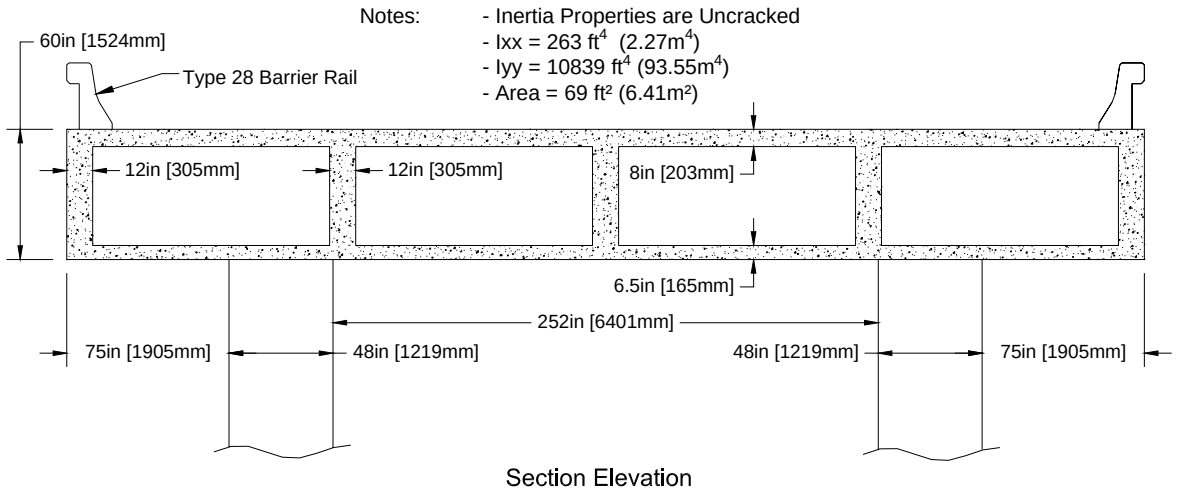

Figure 2-28: Dimensions of idealized prototype section.

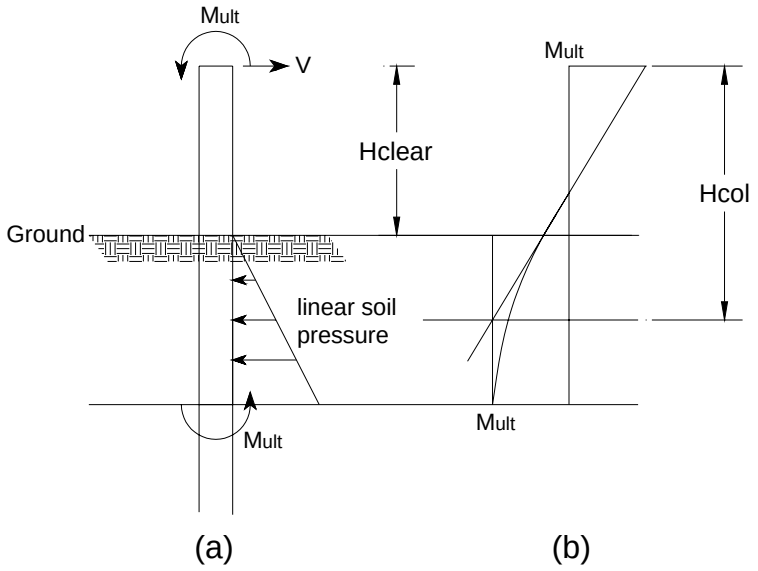

Figure 2-29: Location of column point of maximum curvature.

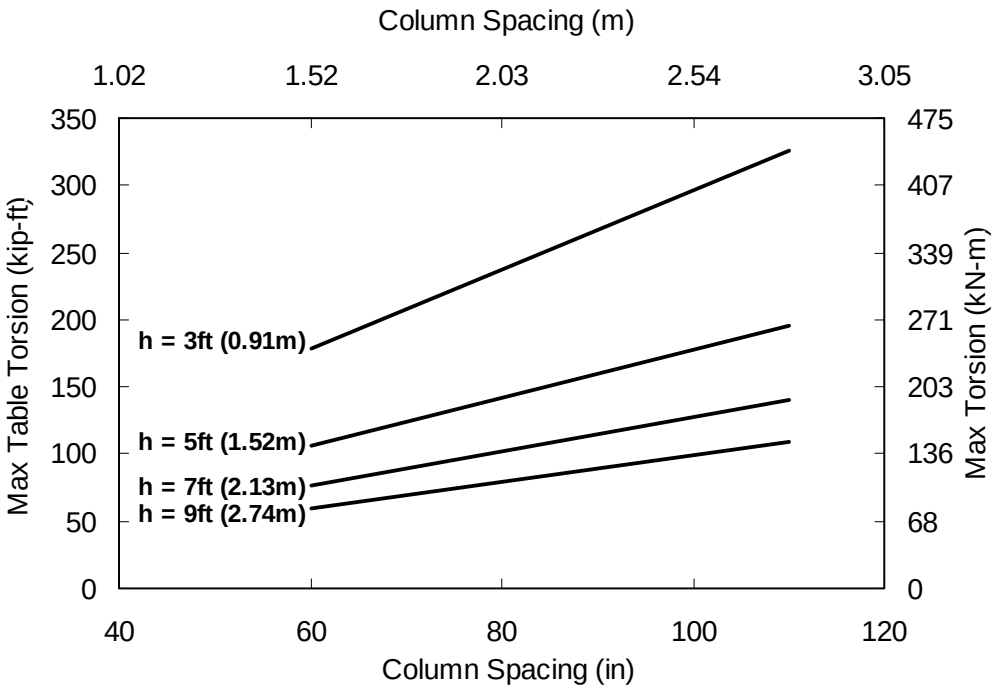

Figure 2-30: Maximum table torsion considering M-ϕ analysis for 12 in (305 mm) diameter columns having 1.5% longitudinal steel ratio.

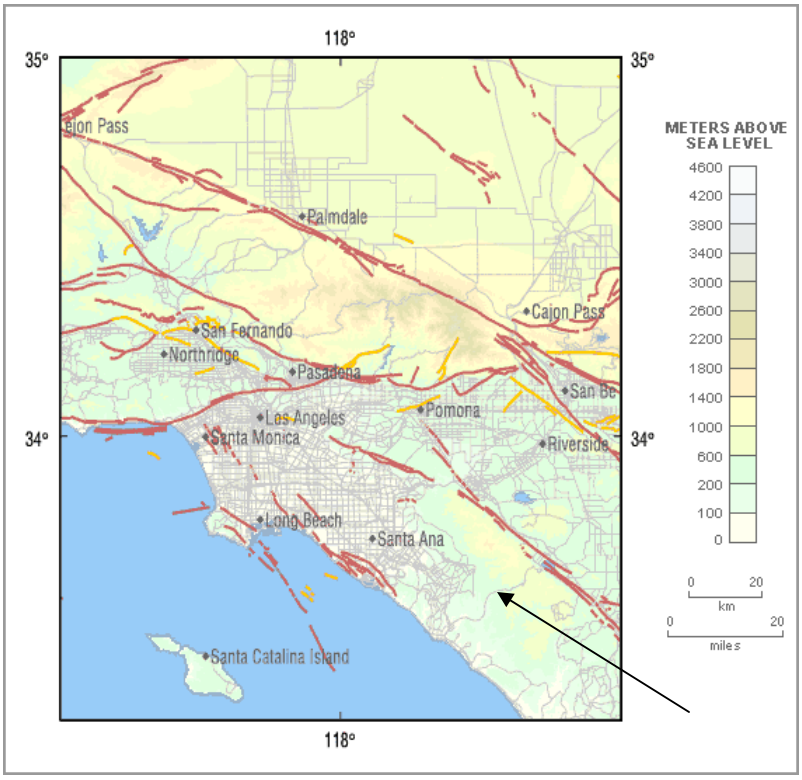

Figure 2-31: Map of Los Angeles area showing acceptable location of prototype.

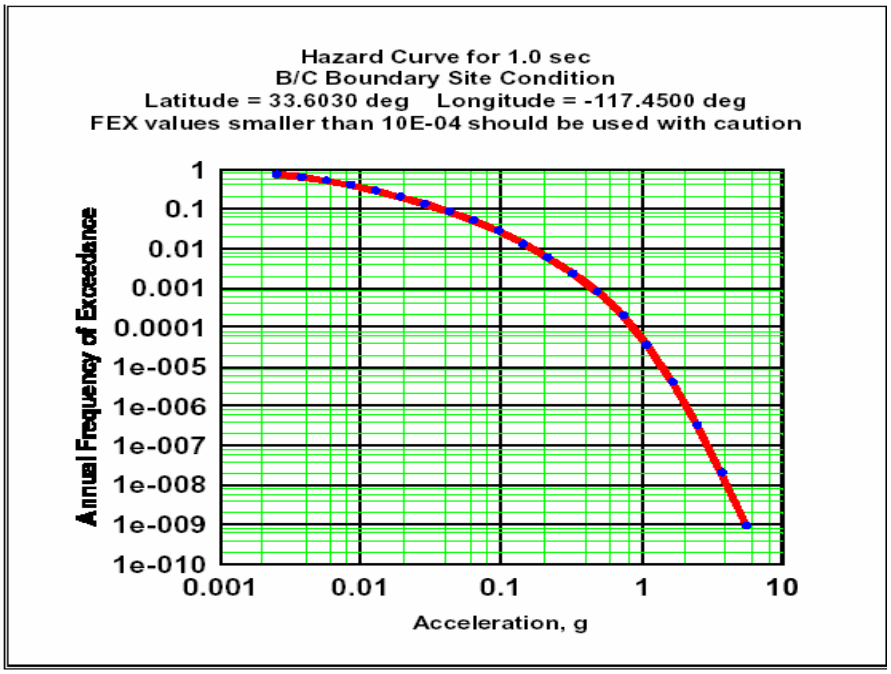

Figure 2-32: Hazard curve for 1.0 second spectral acceleration.

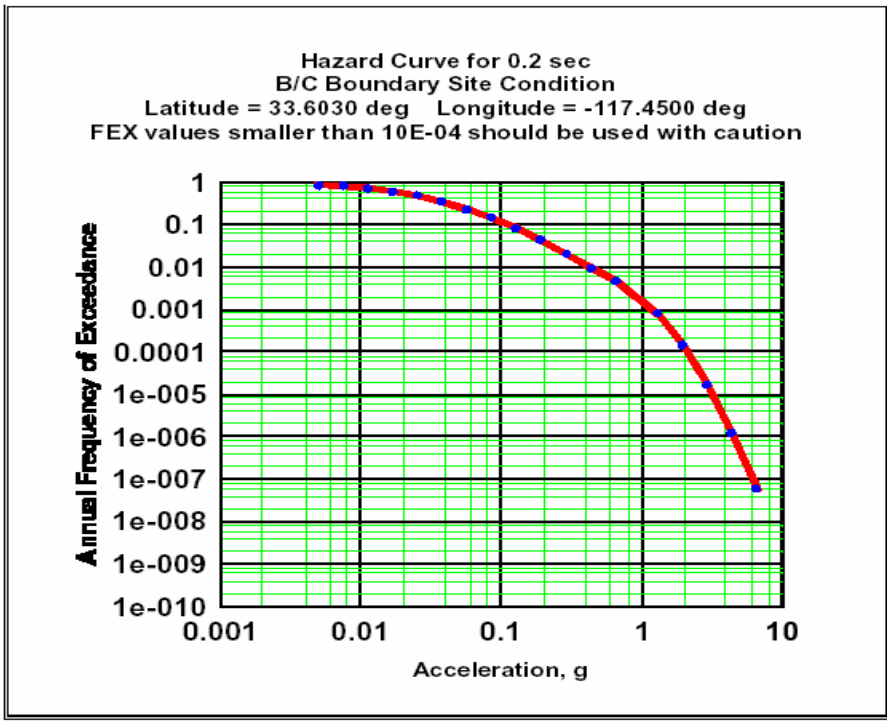

Figure 2-33: Hazard curve for 0.2 second spectral acceleration.

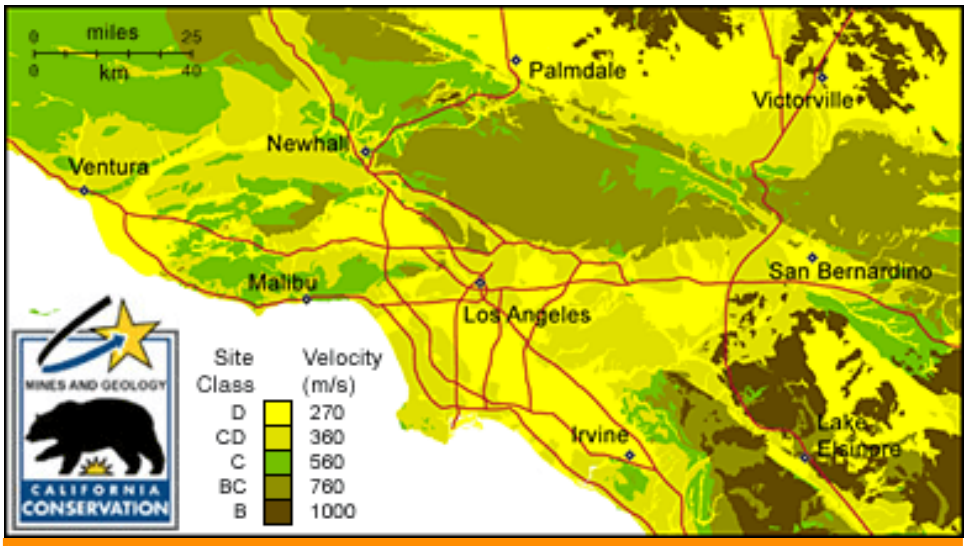

Shear-Wave Velocity Calculator

Note: The velocity (V_s) results are in meters per second (m/s), calculated using bilinear interpolation on a grid of data points spaced 400 meters apart. "Min. V_s" and "Max. V_s"are the minimum and maximum velocities among the four grid points surrounding each requested location

Site				adjacent points	
Longitude	Latitude	Category	V_s (m/s)	Min. V_s	Max. V_s
-117.45	33.6	B	1000.0	1000.0	1000.0

Figure 2-34: Map and data from shear wave velocity calculator.

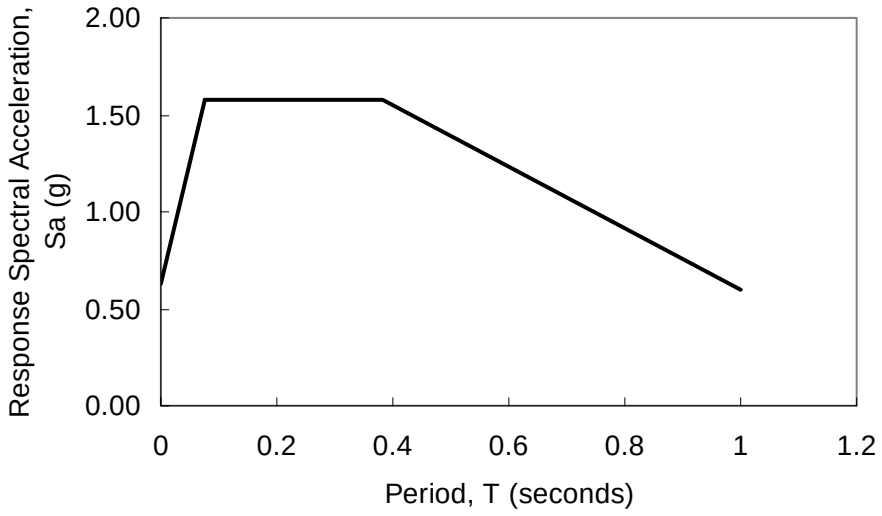

Figure 2-35: Design response spectrum constructed for rare earthquake (3% PE in 75 years).

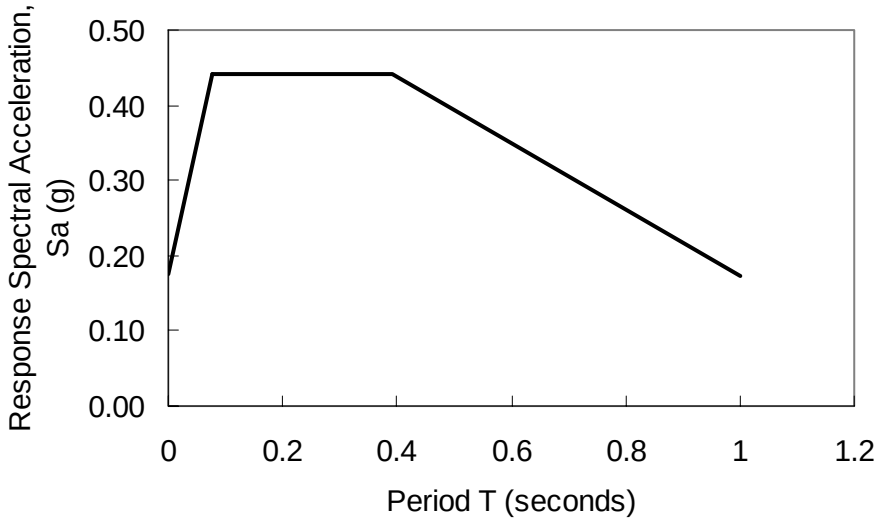

Figure 2-36: Design response spectrum constructed for expected earthquake (50% PE in 75 years).

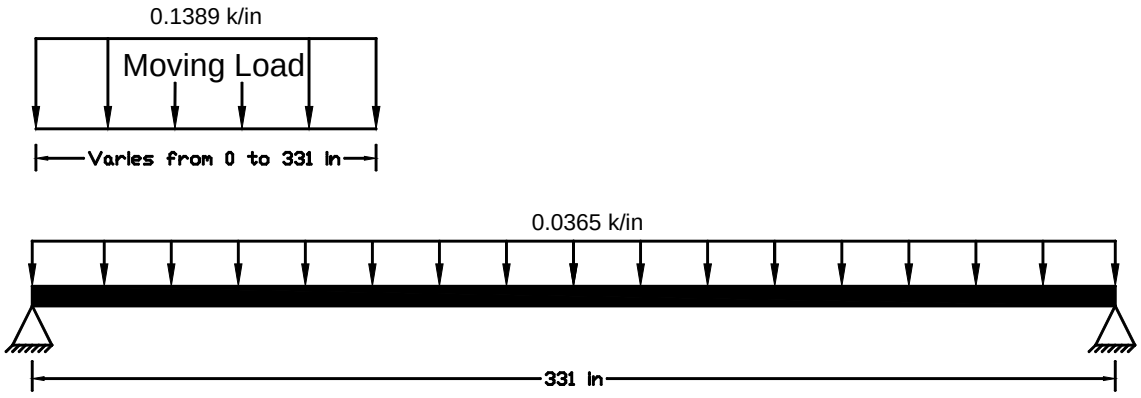

Figure 2-37: Pinned end loading condition for design of a typical superstructure beam.

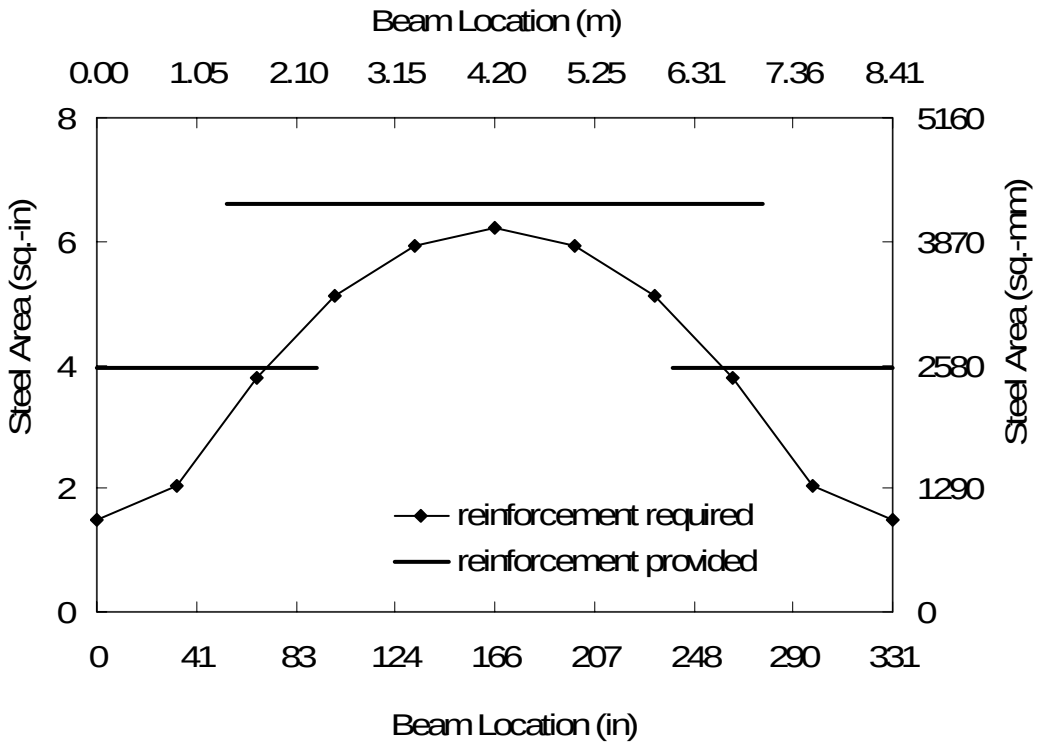

Figure 2-38: Positive moment reinforcement design for superstructure beams.

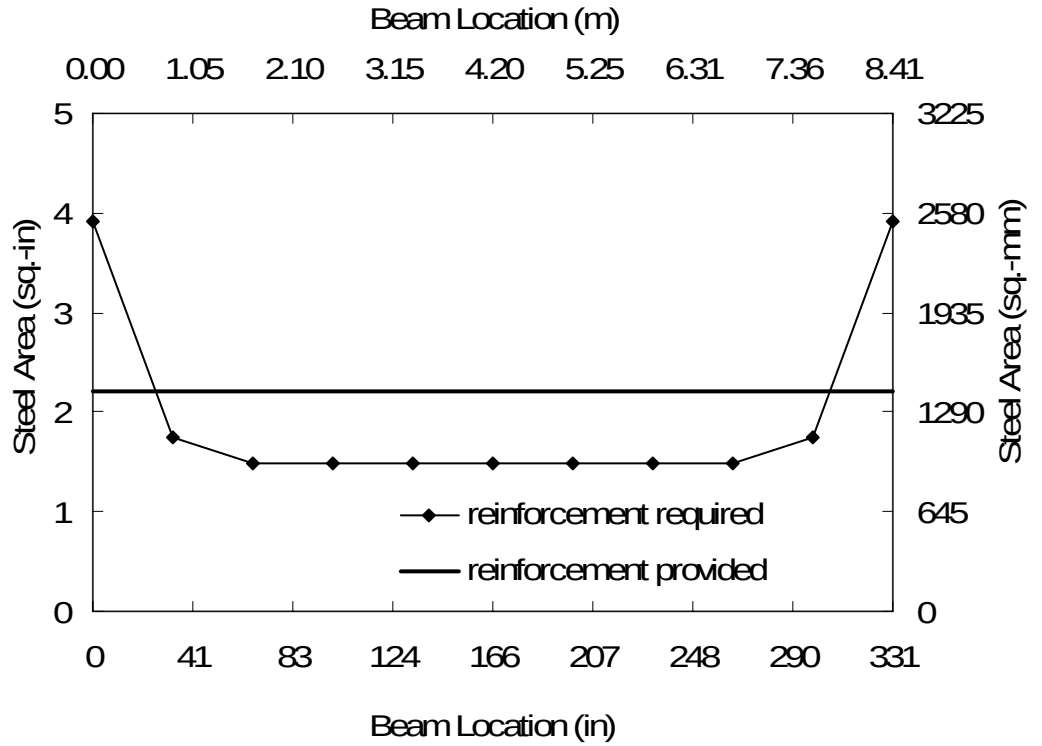

Figure 2-39: Negative moment reinforcement design for superstructure beams.

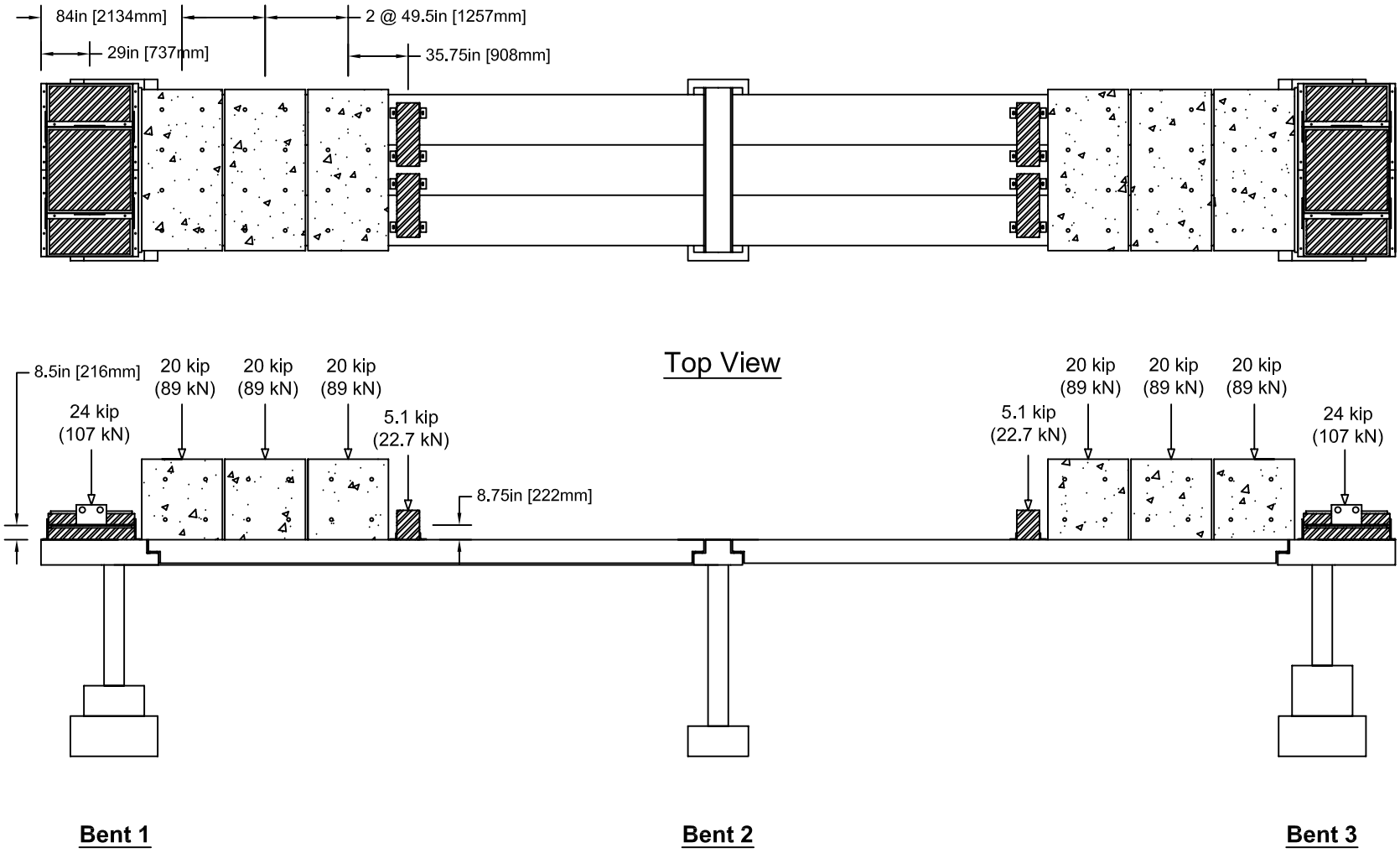

Figure 2-40: Distribution of masses on shake table model.

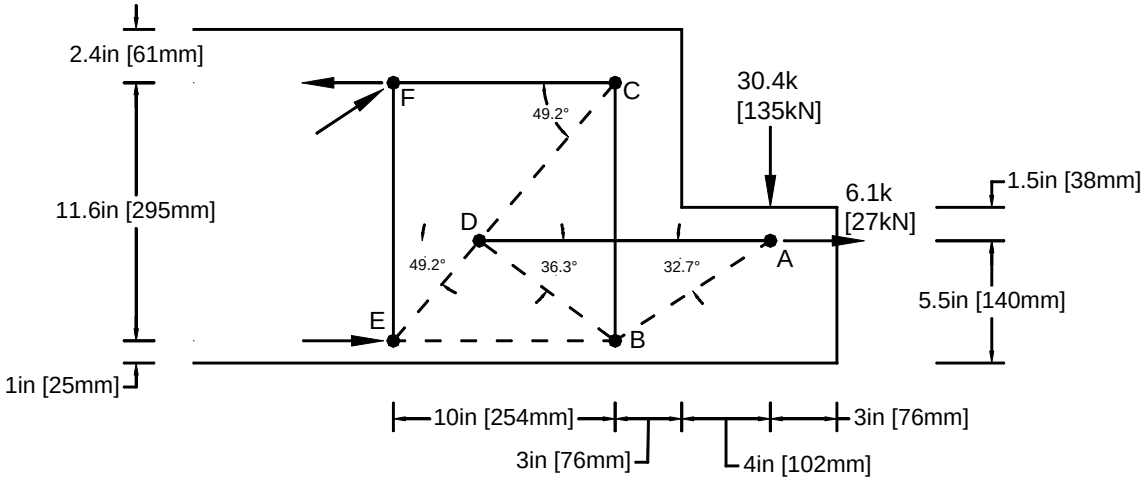

Cantilever strut-and-tie Model
(Per Bearing Plate)

Figure 2-41: Strut-and-Tie model used for typical ledge design.

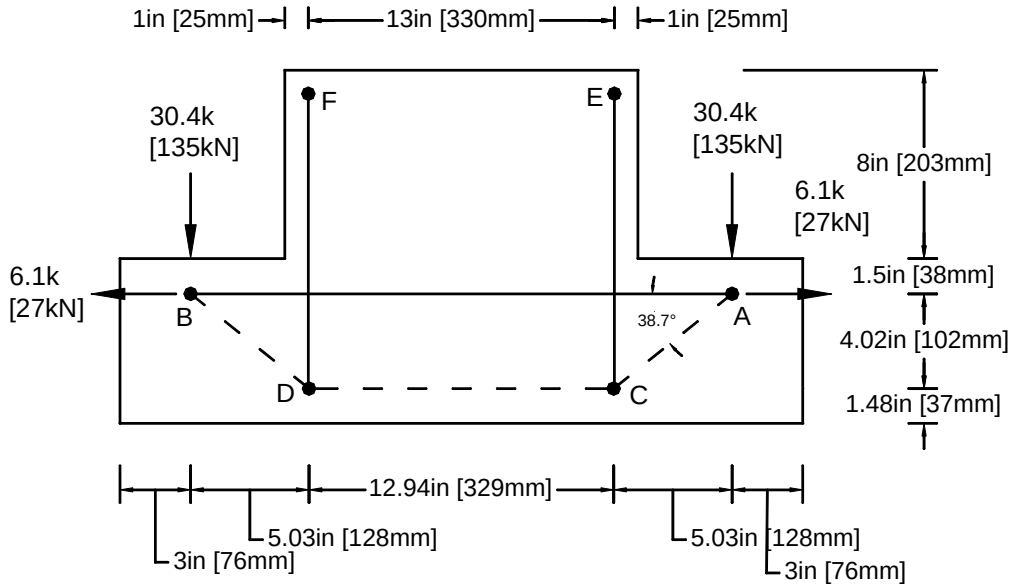

T-beam strut-and-tie Model
(Per Bearing Plate)

Figure 2-42: Strut-and-Tie model used for T-beam ledge design.

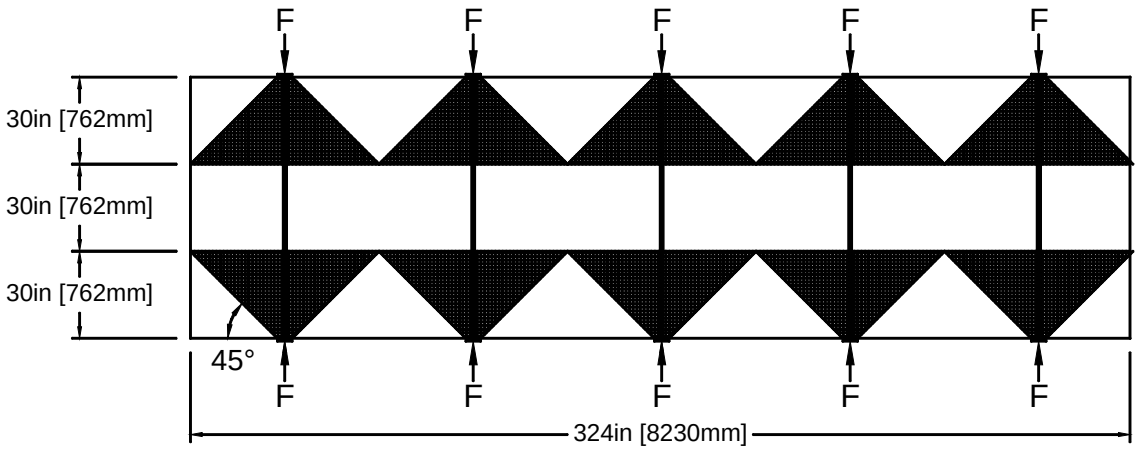

Figure 2-43: Assumption of transverse clamping force spreading for a three-beam span (plan view).

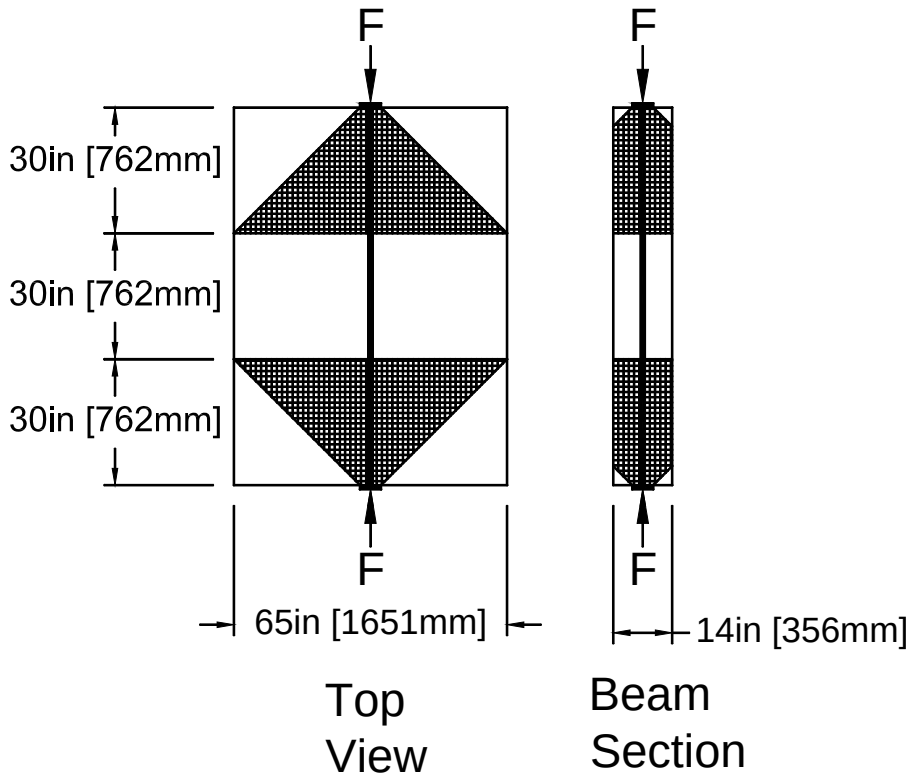

Figure 2-44: Transverse clamping force tributary to one transverse post-tension rod.

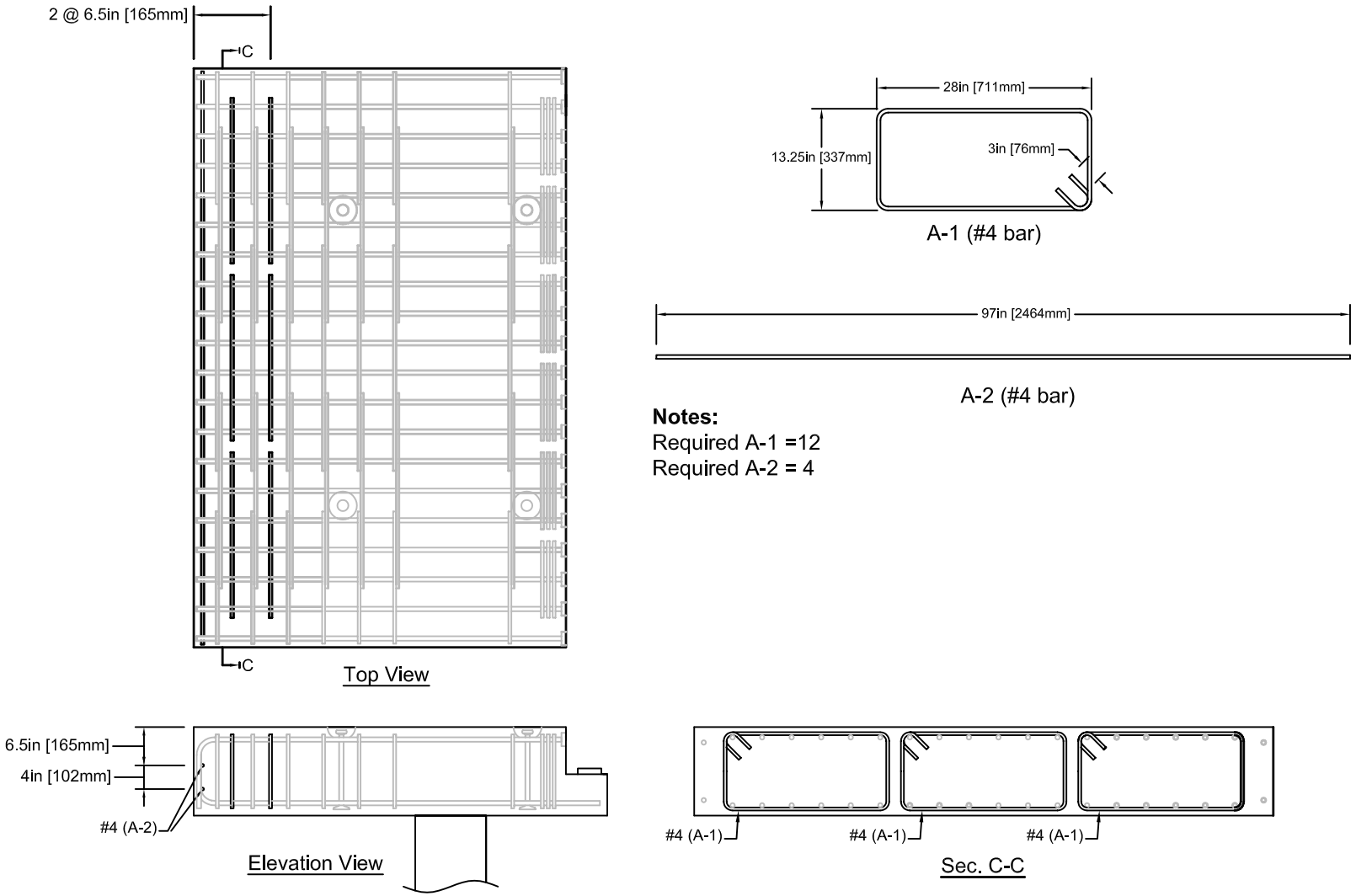

Figure 2-45: Additional reinforcement required in cantilevers for anchorage zones.

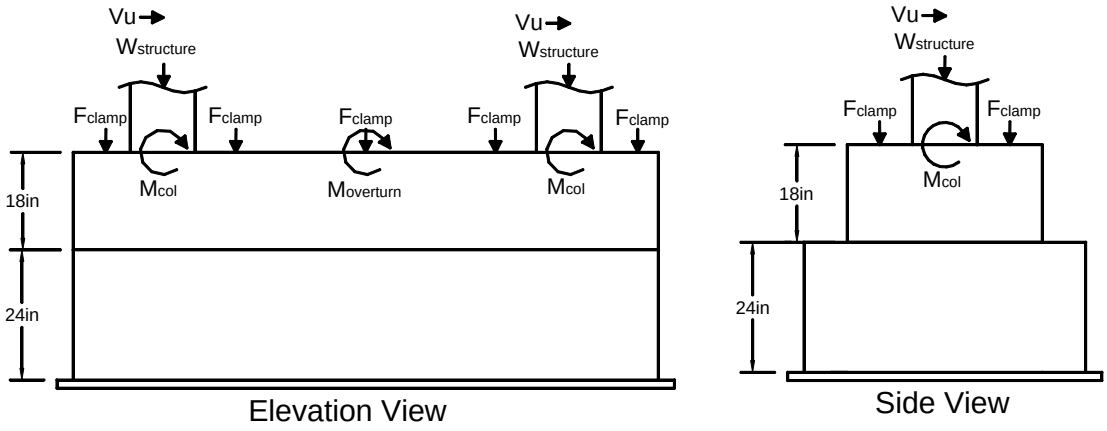

Figure 2-46: Forces used to calculate design loads for footing of bent 1.

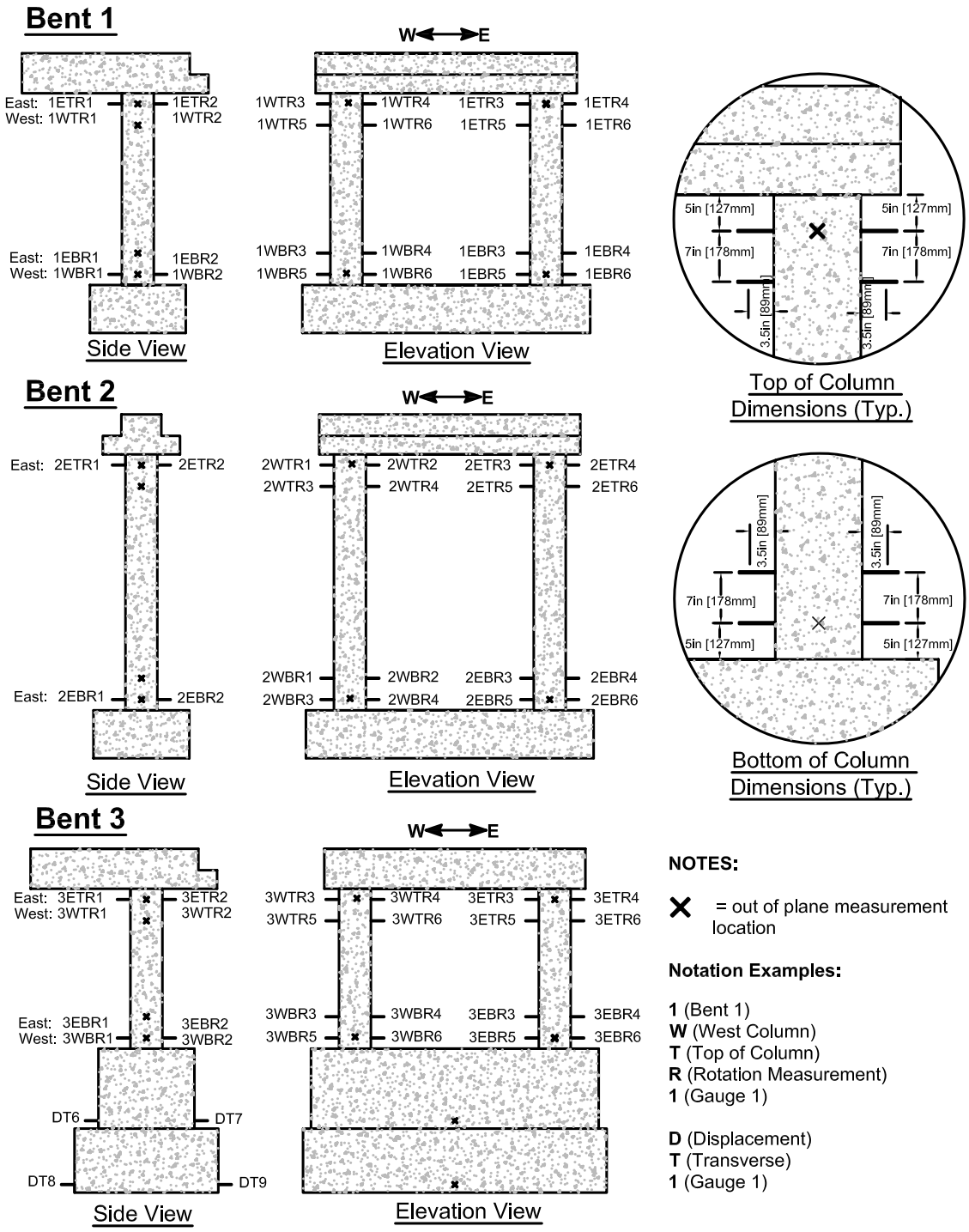

Figure 3-1: Instrumentation plans sheet 1 of 8; Column curvature gauges.

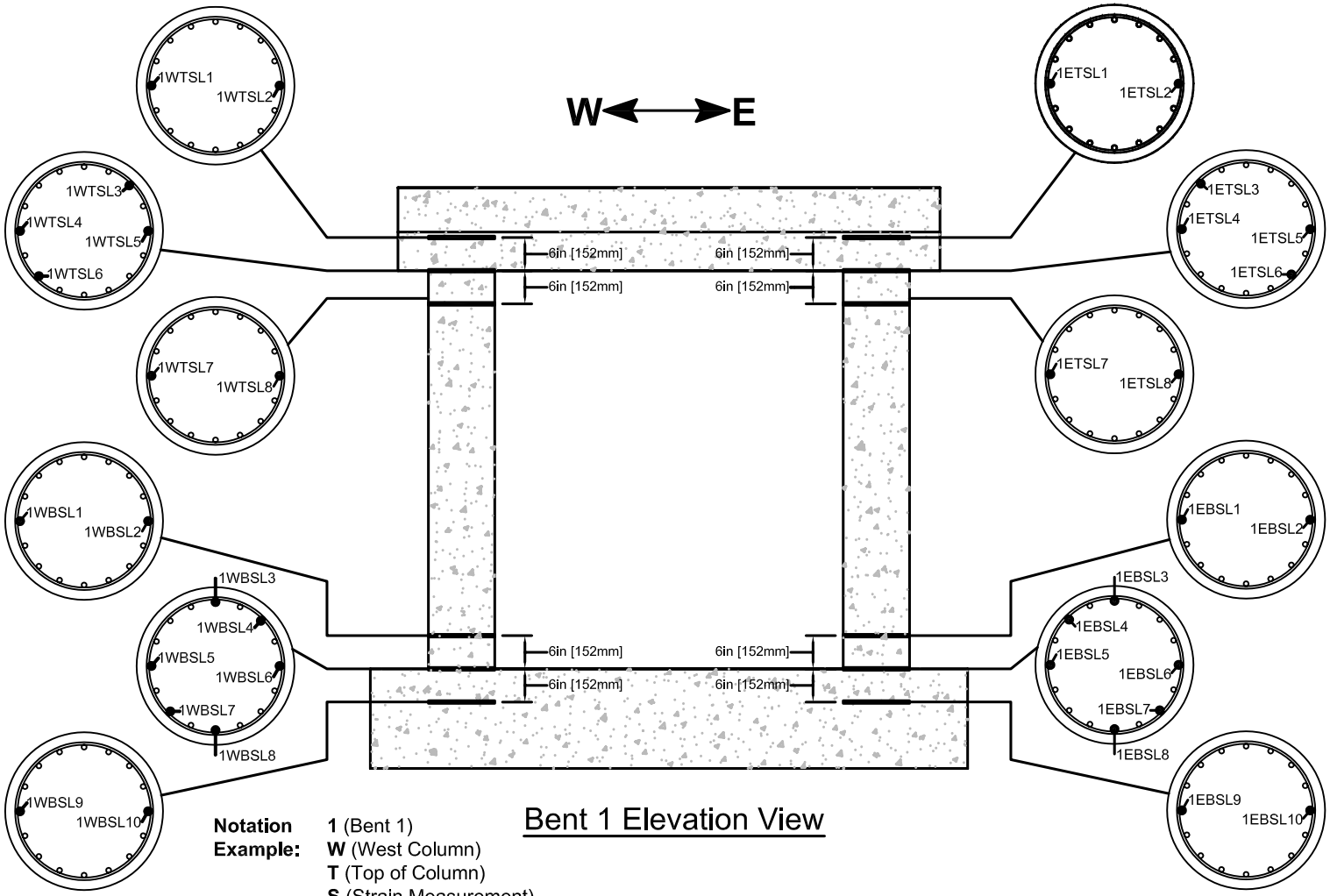

Figure 3-2: Instrumentation sheet 2 of 8; Bent 1 longitudinal strain gauges.

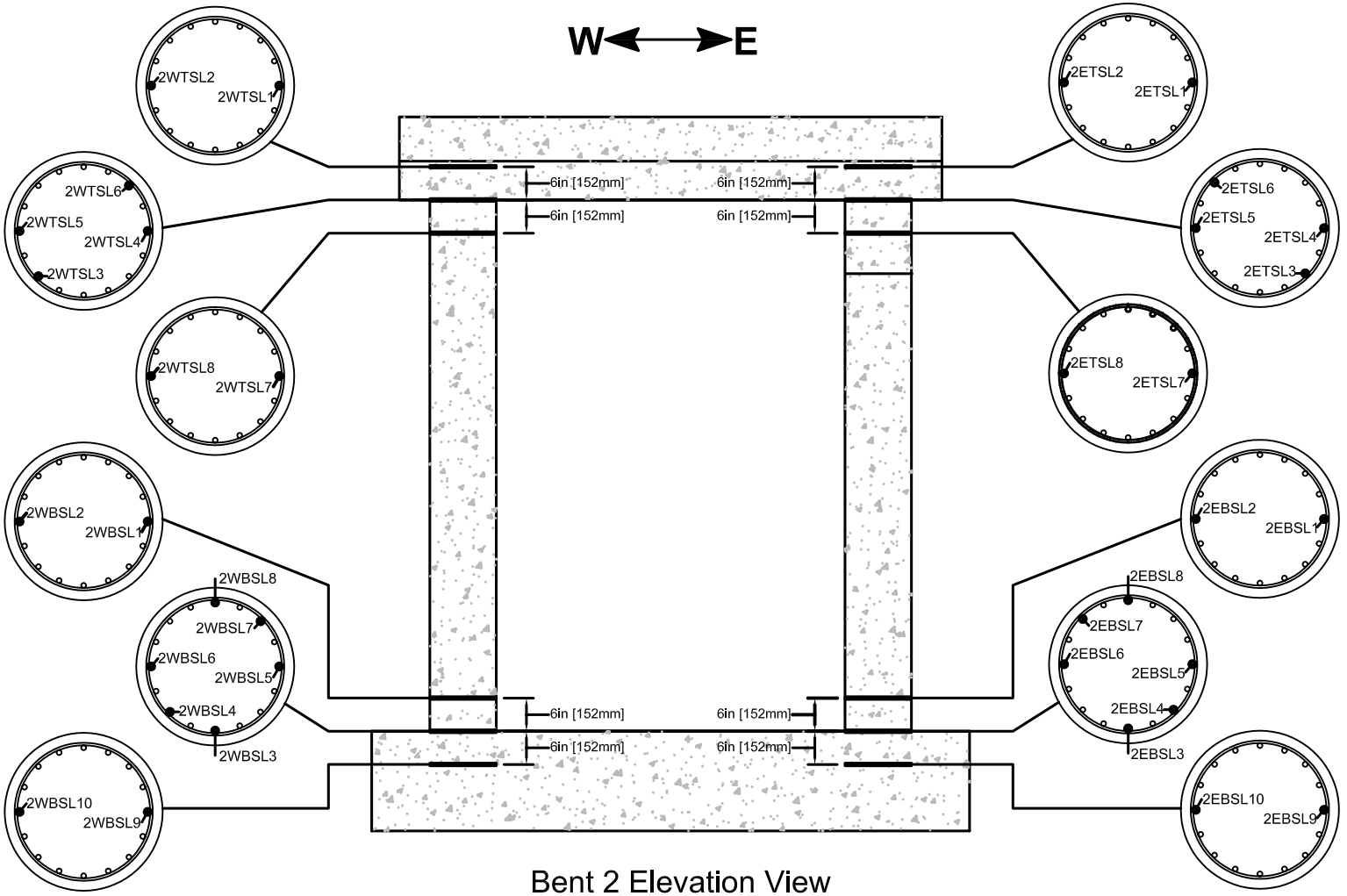

Figure 3-3: Instrumentation sheet 3 of 8; Bent 2 longitudinal strain gauges.

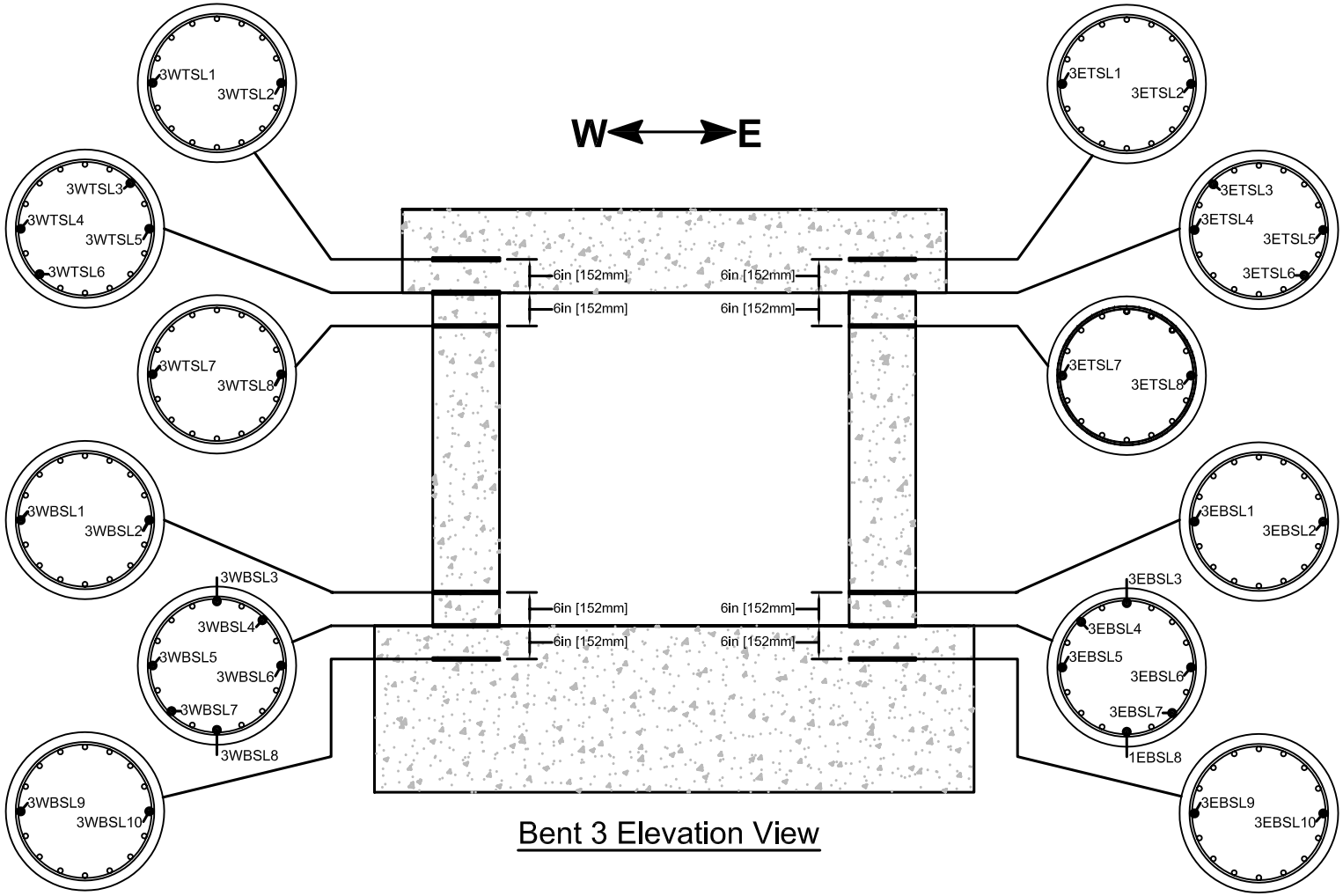

Figure 3-4: Instrumentation sheet 4 of 8; Bent 3 longitudinal strain gauges.

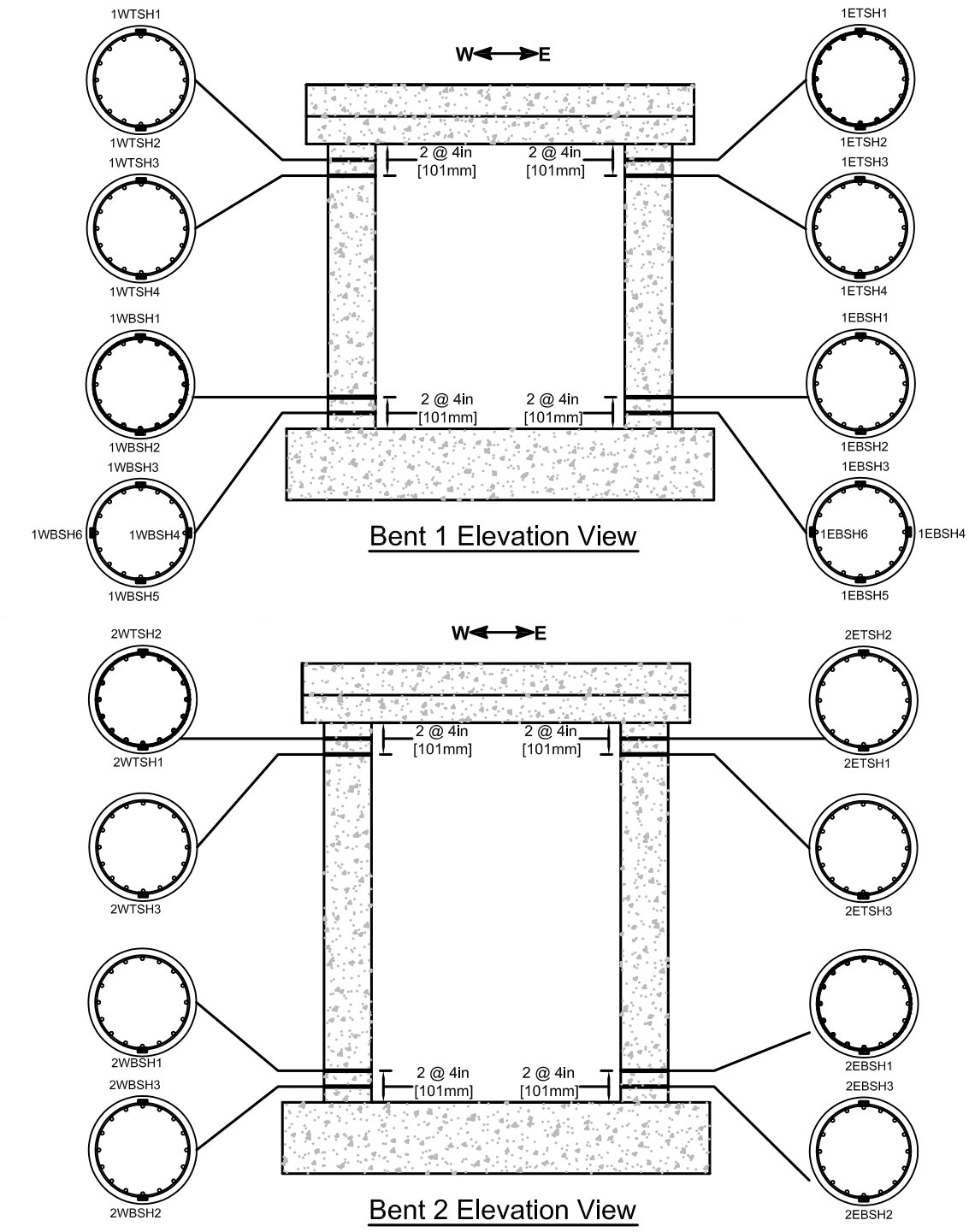

Figure 3-5: Instrumentation plans sheet 5 of 8; Bent 1 & 2 transverse strain gauges.

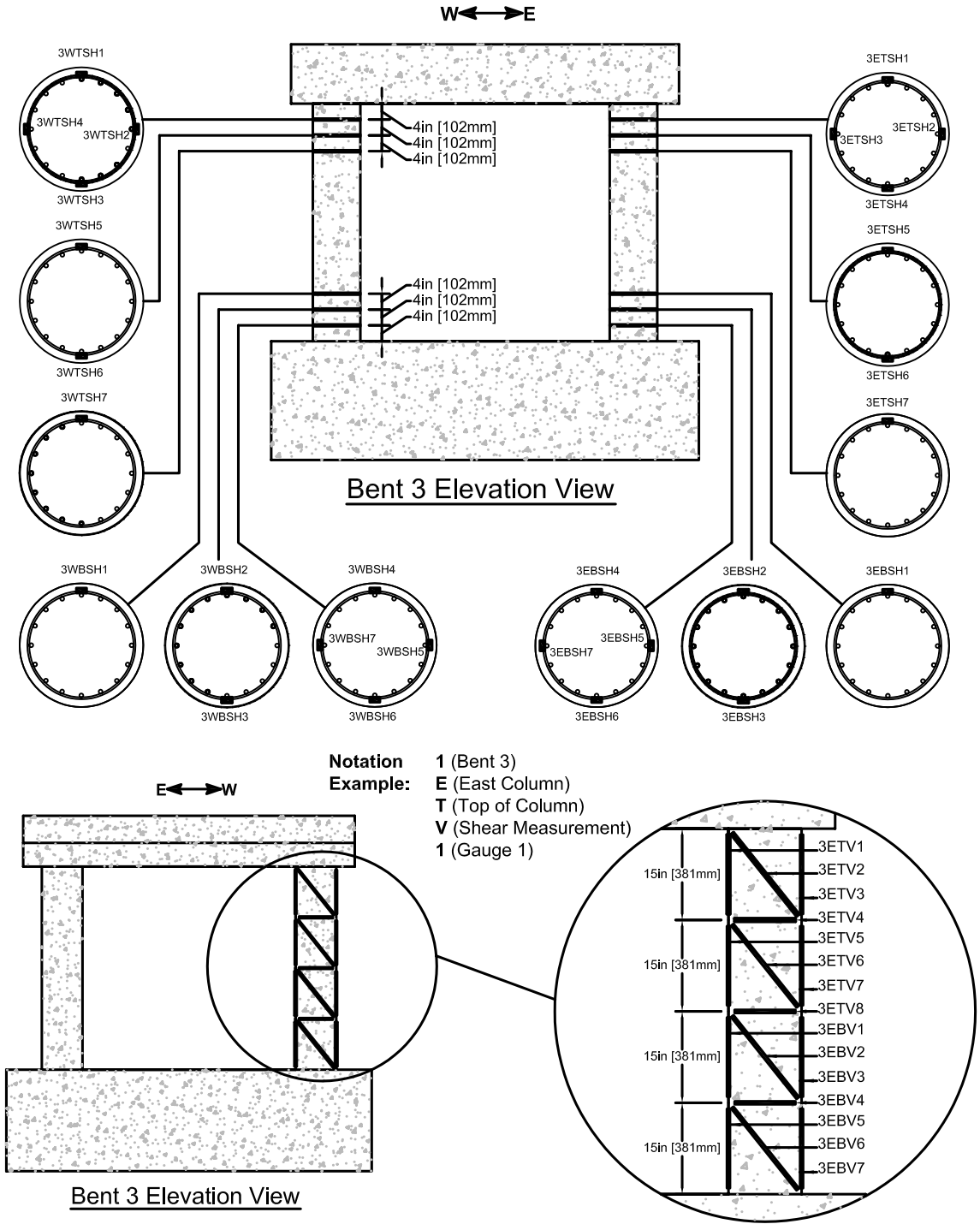

Figure 3-6: Instrumentation plans sheet 6 of 8; Bent 3 transverse strain gauges and west column shear transducers.

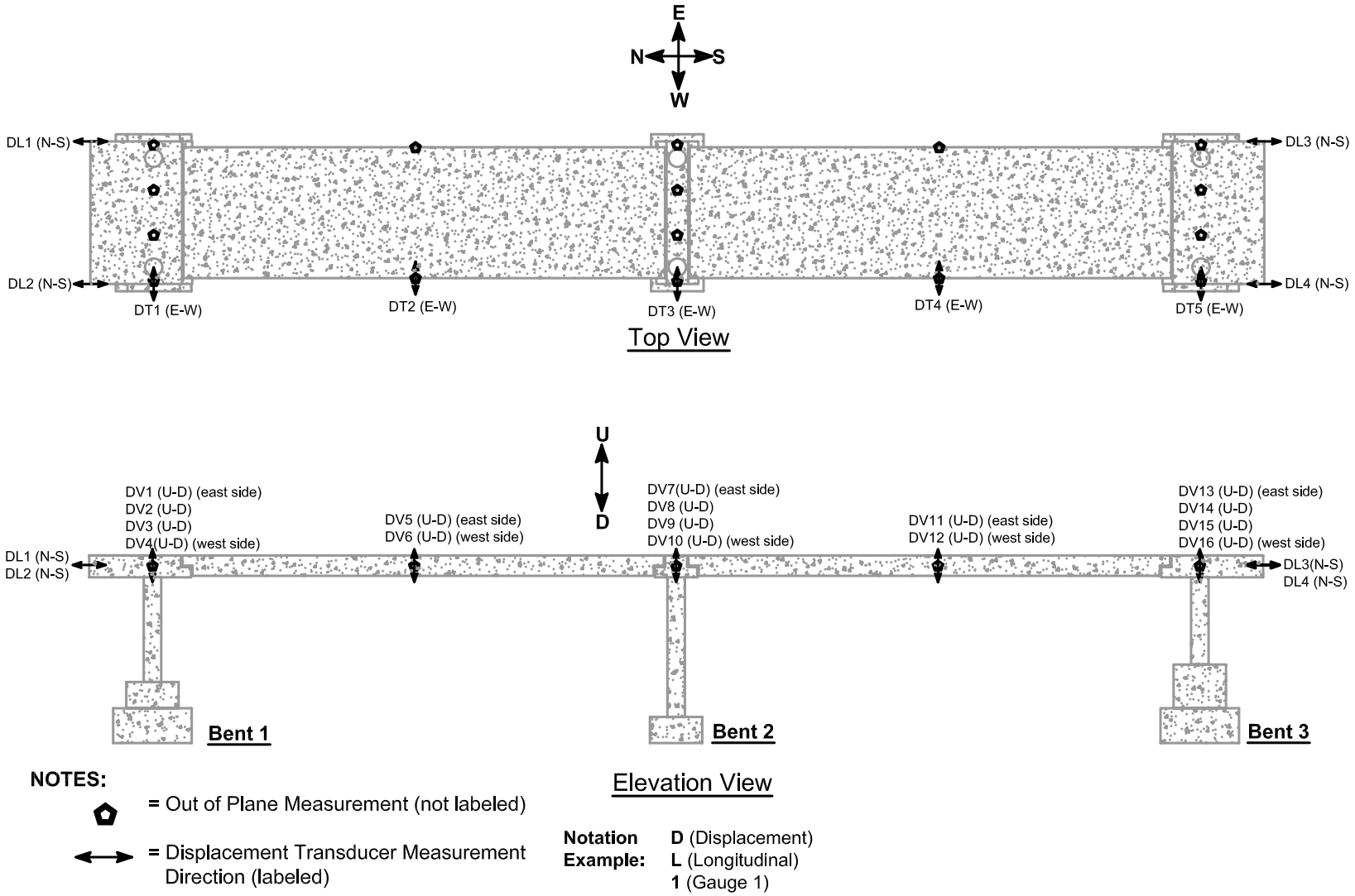

Figure 2-40: Distribution of masses on shake table model.

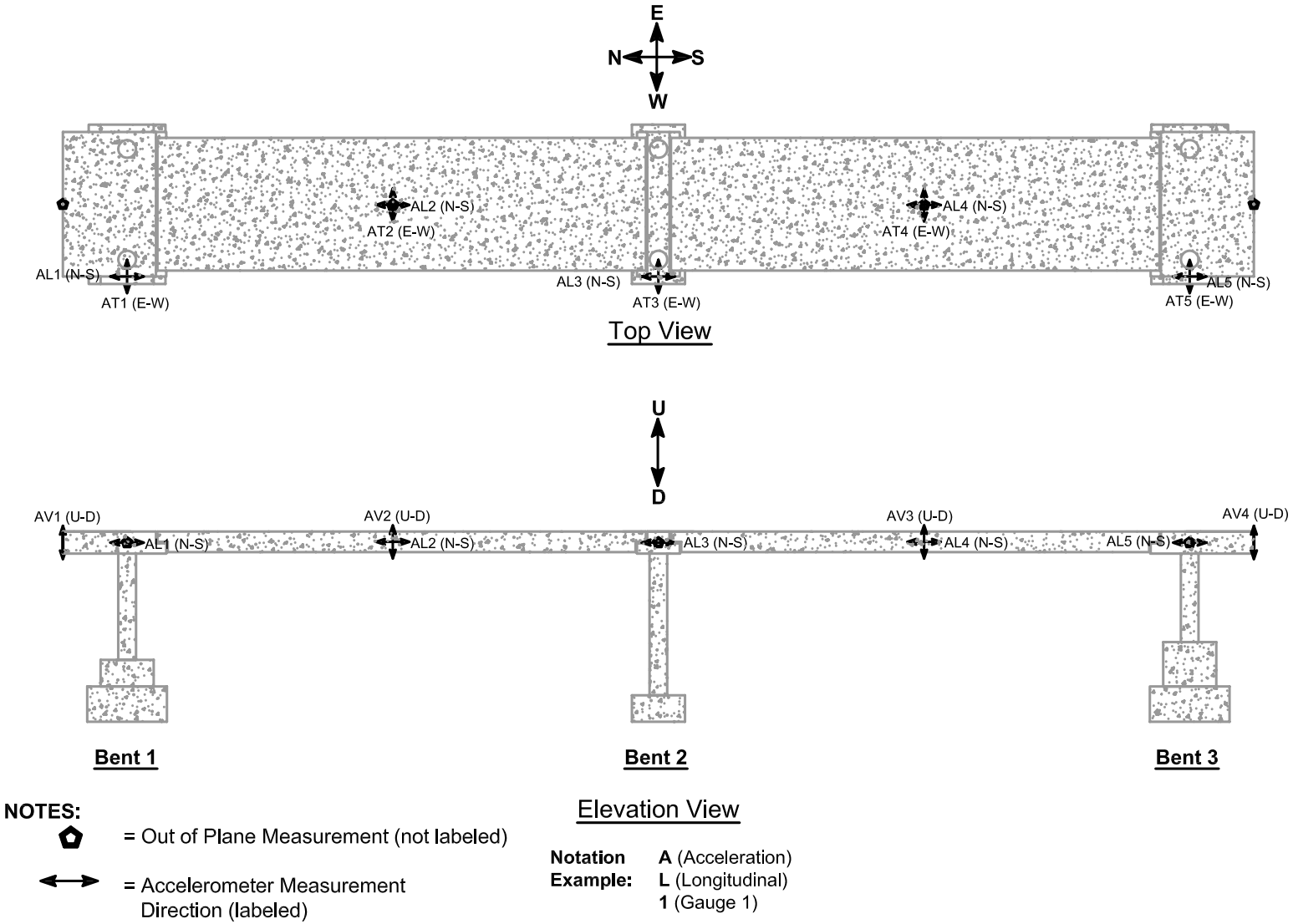

Figure 3-8: Instrumentation sheet 8 of 8; Accelerometers.

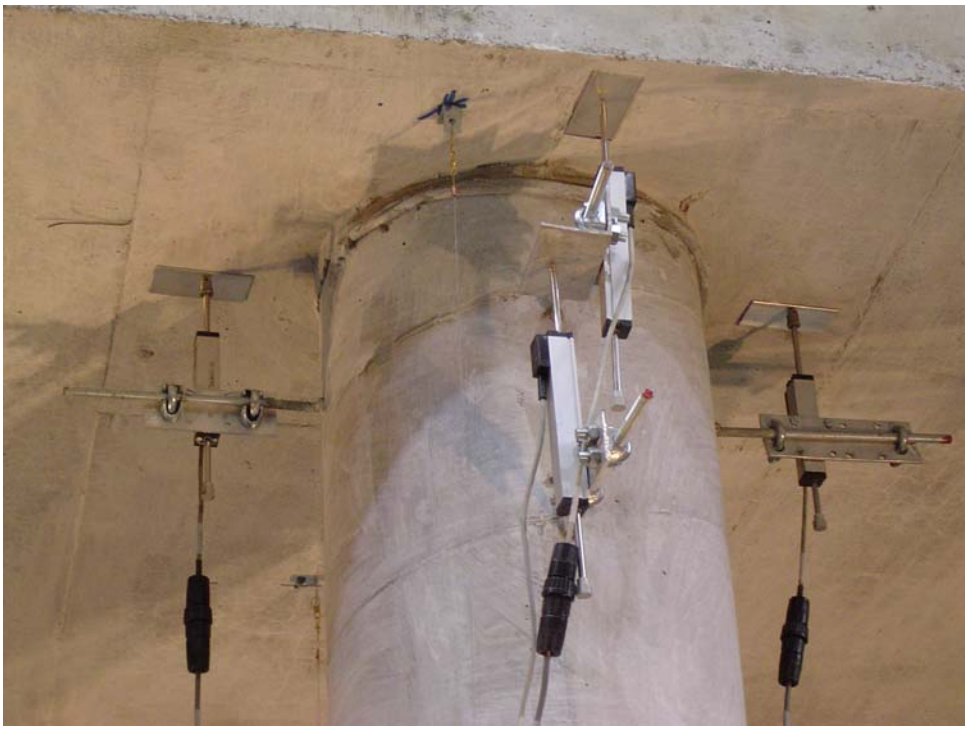

Figure 3-9: Photograph of typical curvature measurement in plastic hinge region.

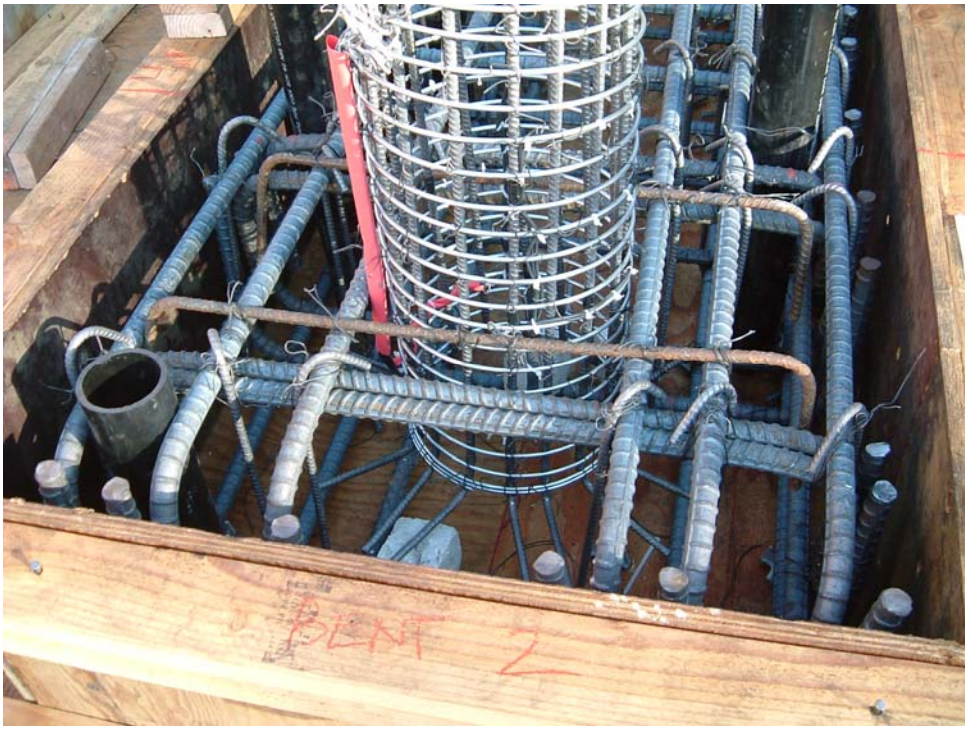

Figure 3-10: Photograph of strain gauges on column cage at the base of a bent 2 column

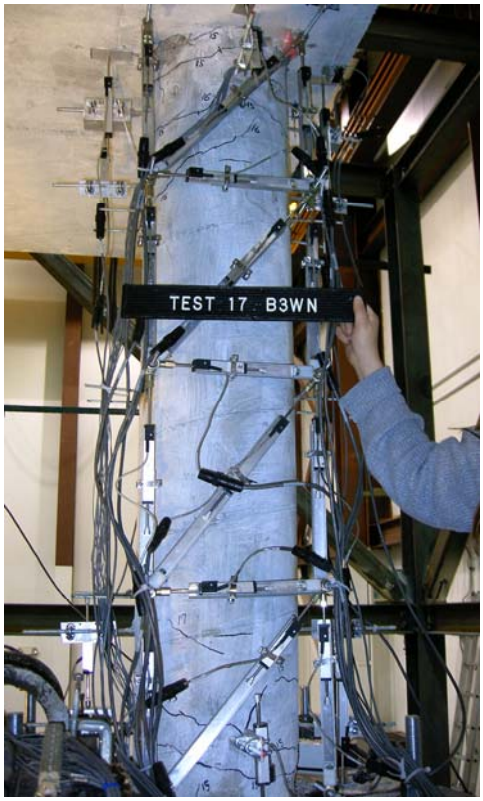

Figure 3-11: Photograph of shear measurement on west column of bent 3.

Figure 3-12: Photograph of shear bent 1 safety frame with timber on top.

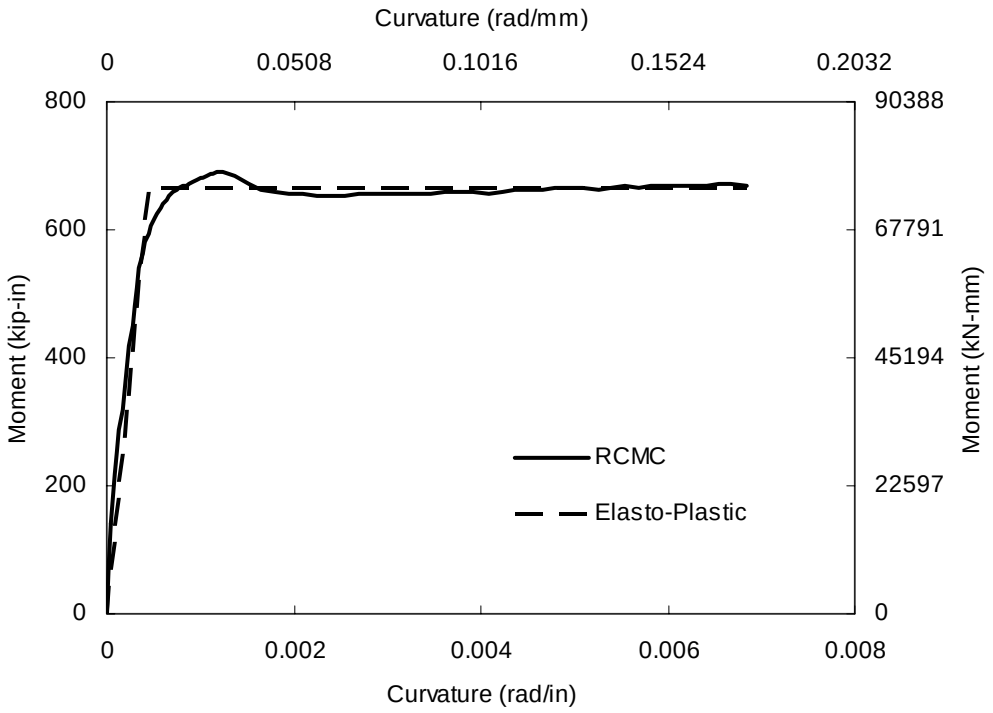

Figure 4-1: Moment curvature relationship for columns of bridge model.

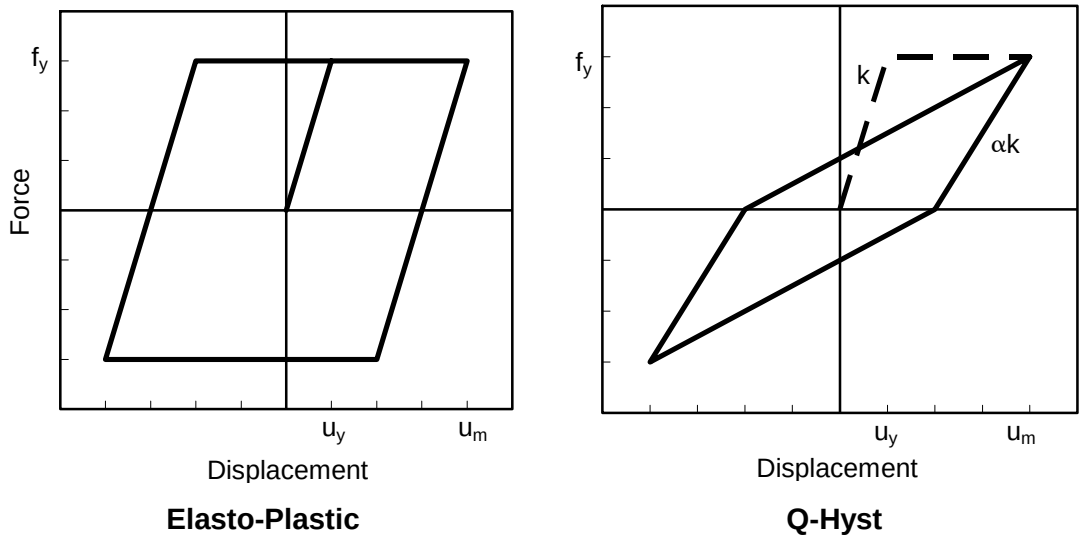

Figure 4-2: Elasto-plastic model with no unloading stiffness degradation compared to Q-hyst model.

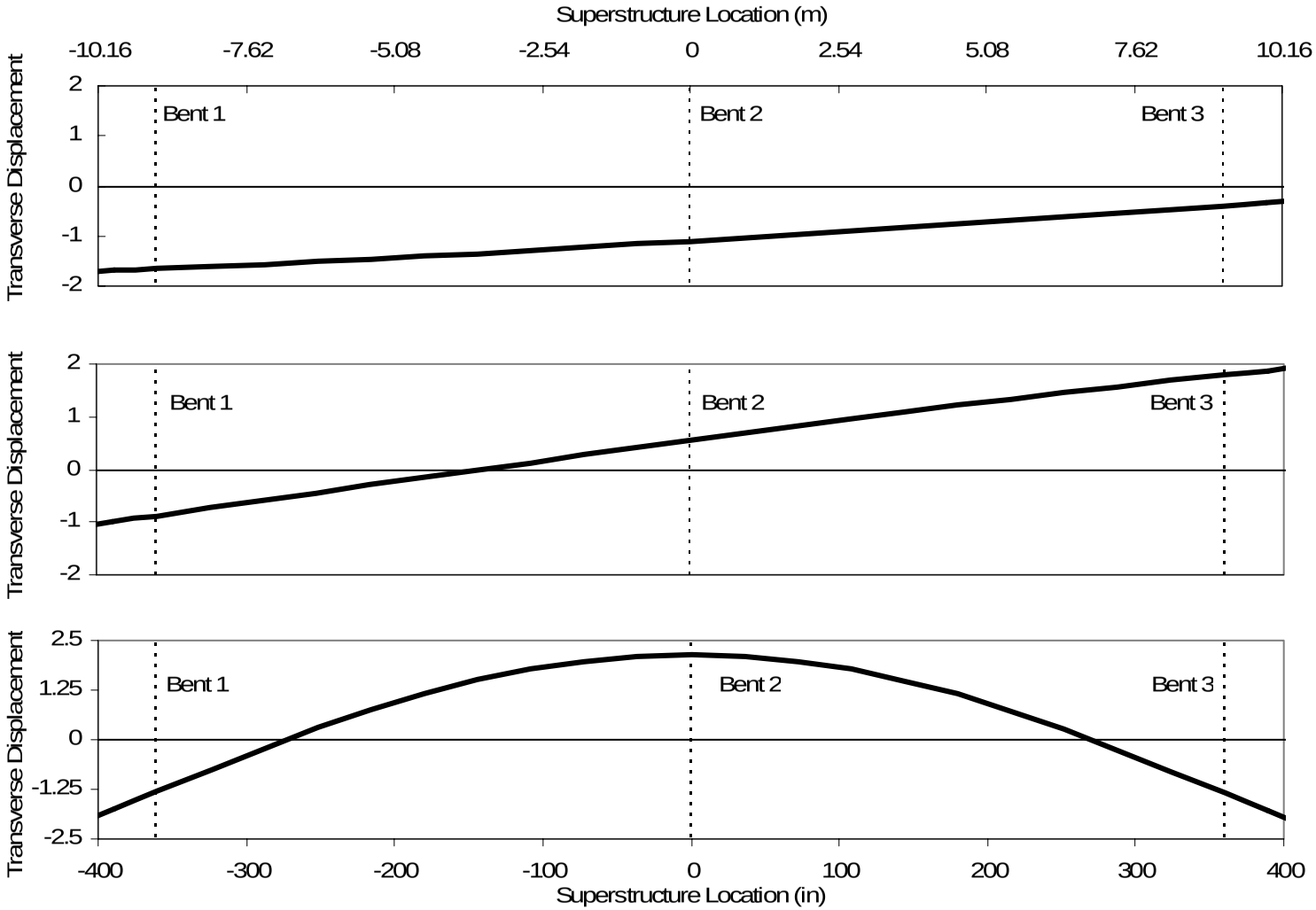

Figure 4-3: Elastic transverse mode shapes of shake table bridge specimen: from top to bottom, mode 2, mode 3, mode 6.

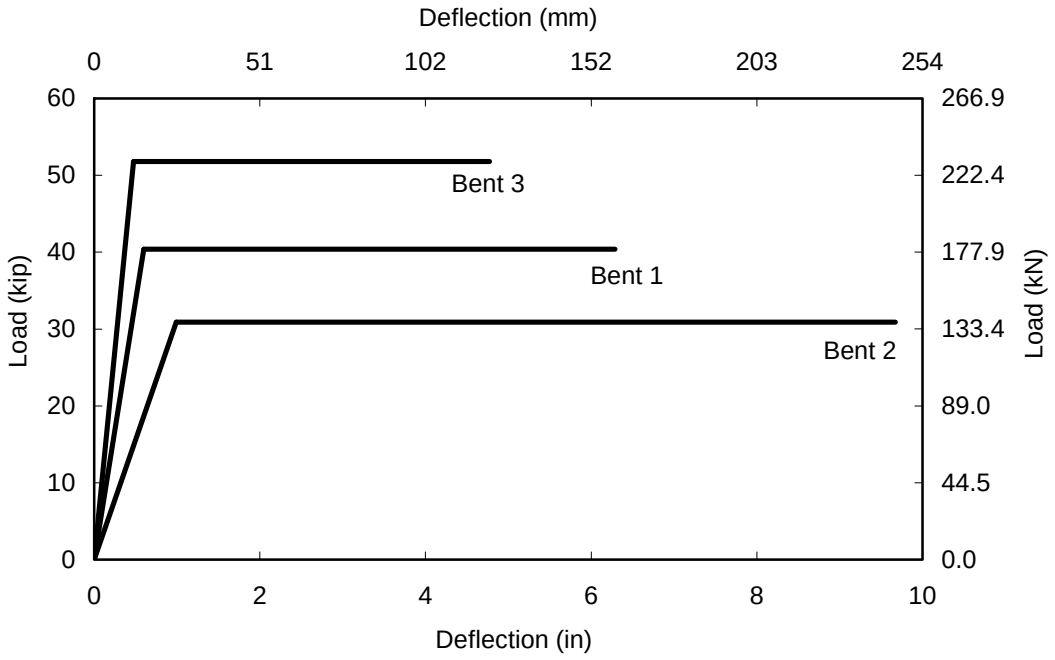

Figure 4-4: Elasto-plastic idealized pre-test pushover analyses of bents 1 through 3

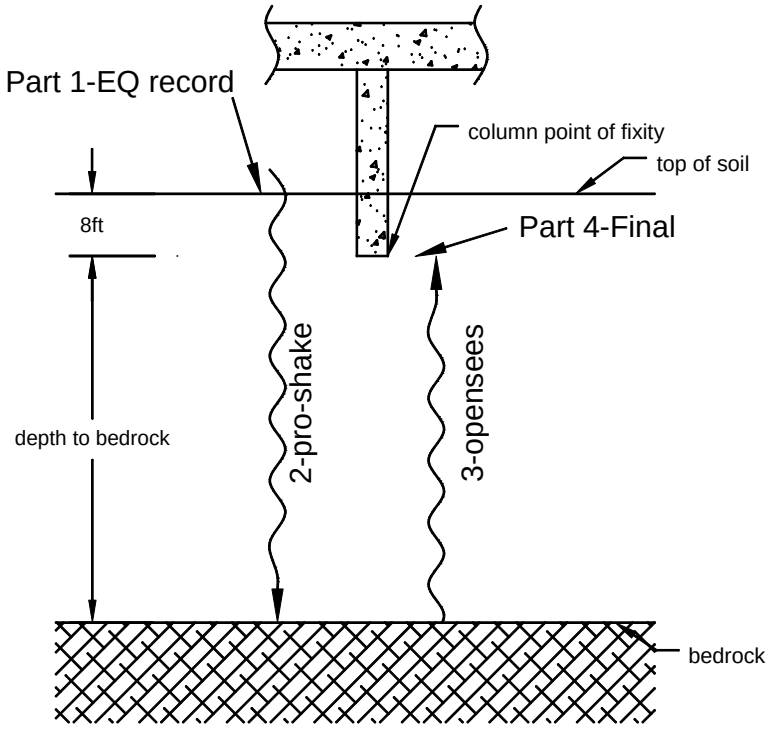

Figure 4-5: Schematic of steps taken to obtain calculated earthquake motions.

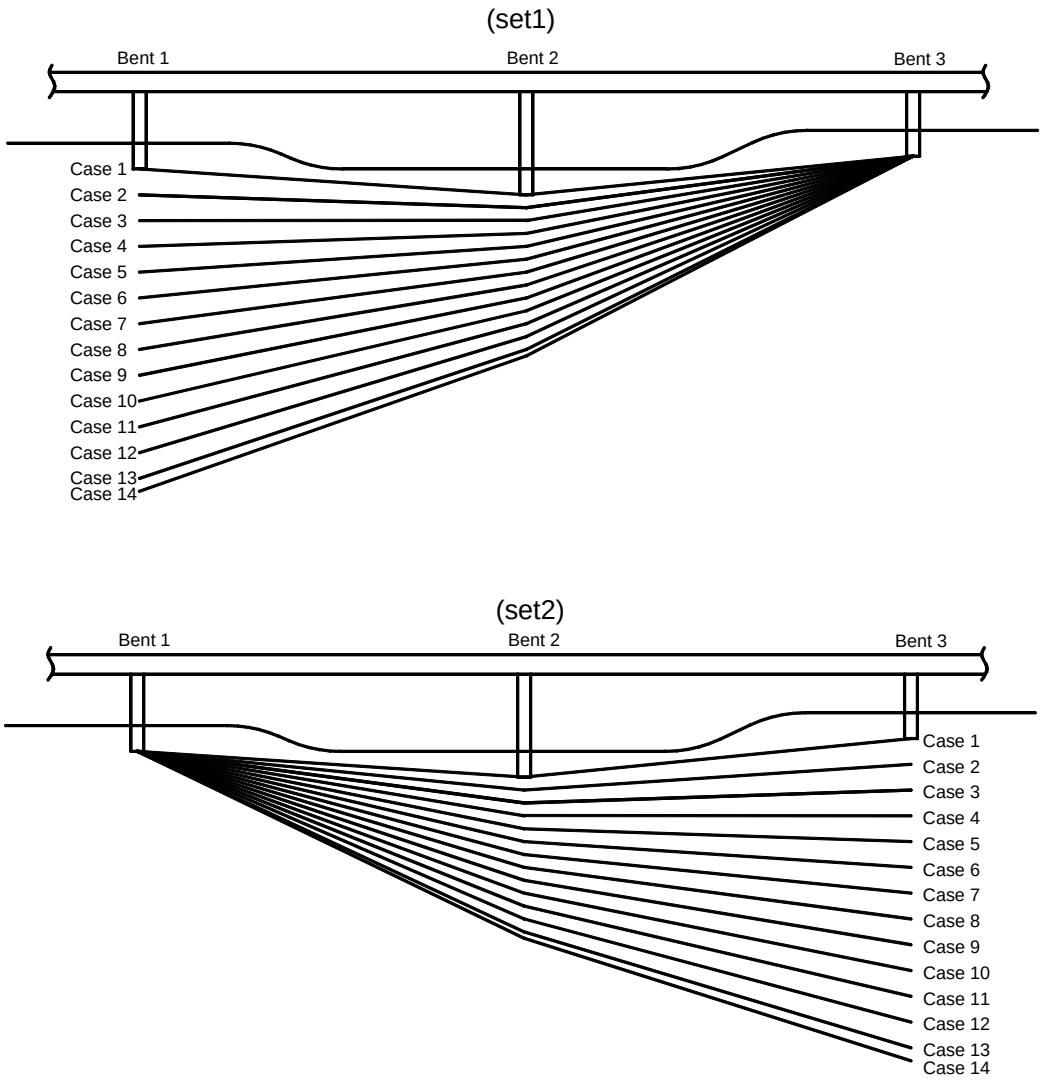

Figure 4-6: Bedrock depth configurations of methodology 1 for incoherent ground motion part of low amplitude testing.

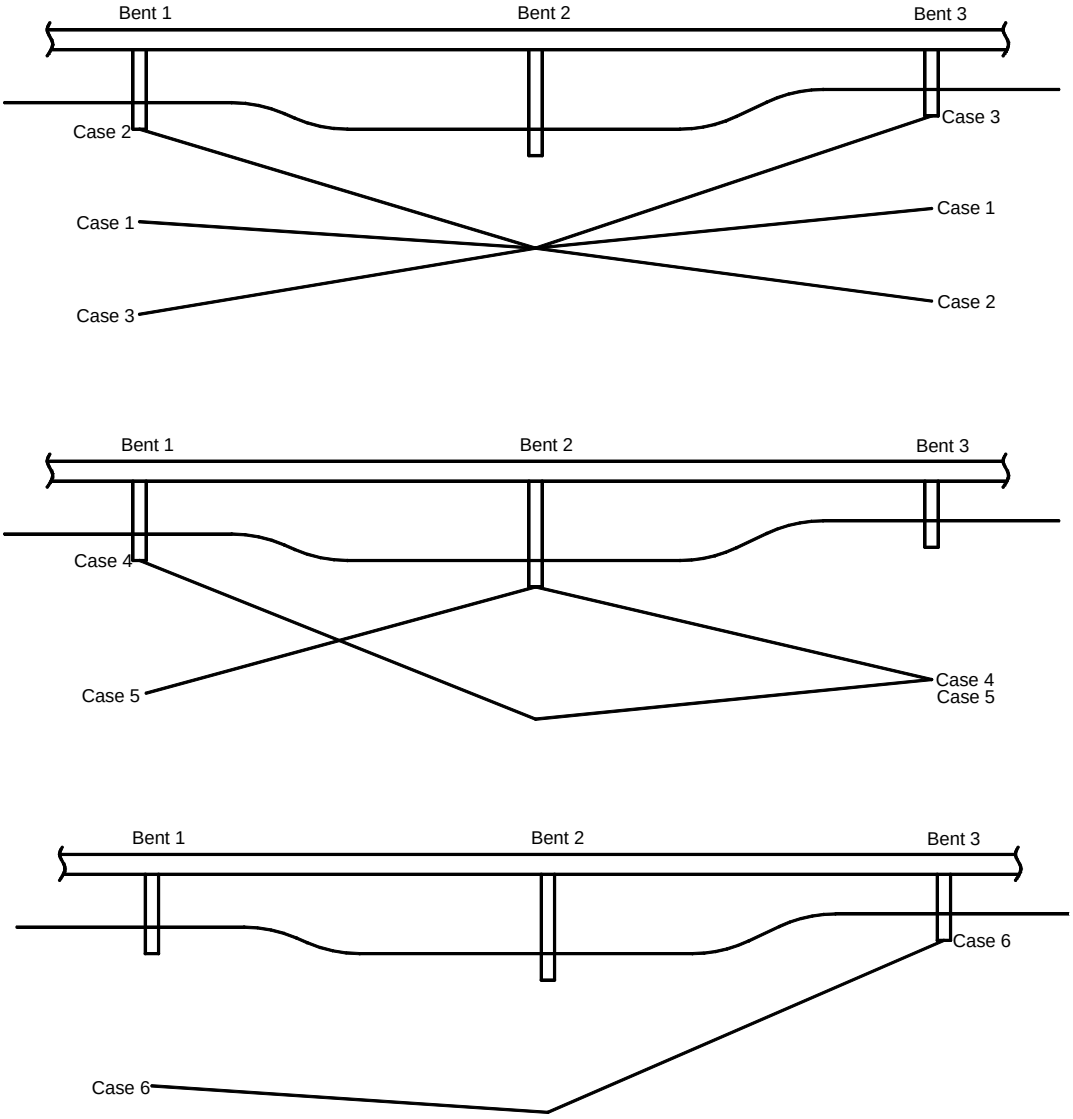

Figure 4-7: Bedrock depth configurations of methodology 2 for incoherent ground motion part of low amplitude testing.

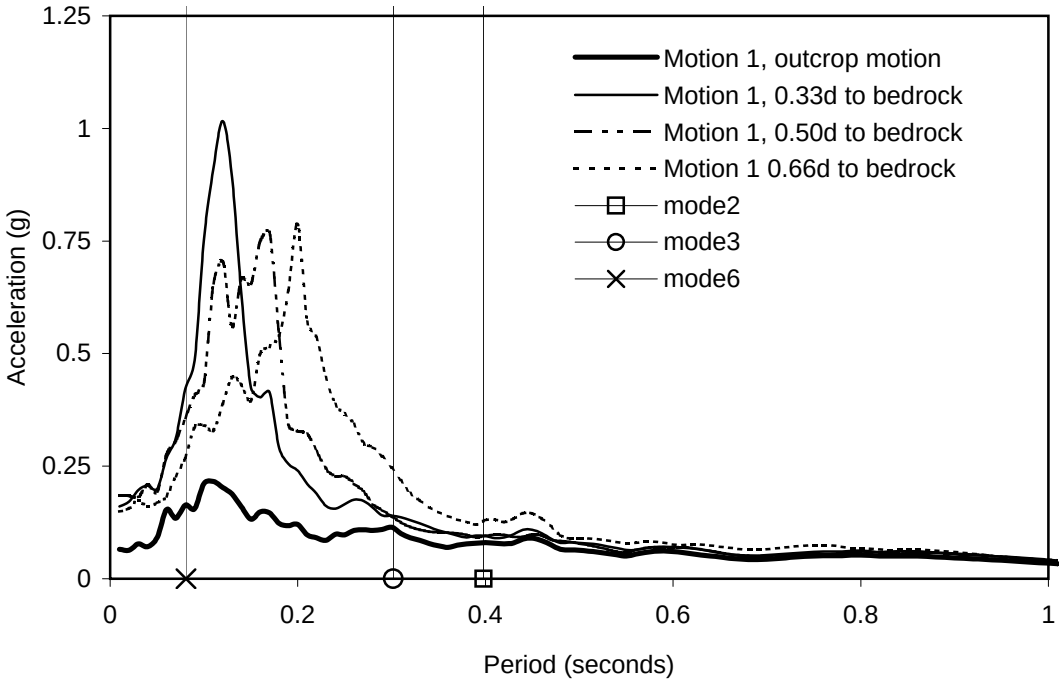

Figure 4-8: Response spectra of target shake table motions used for low-amplitude incoherent excitation with superimposed transverse modal periods.

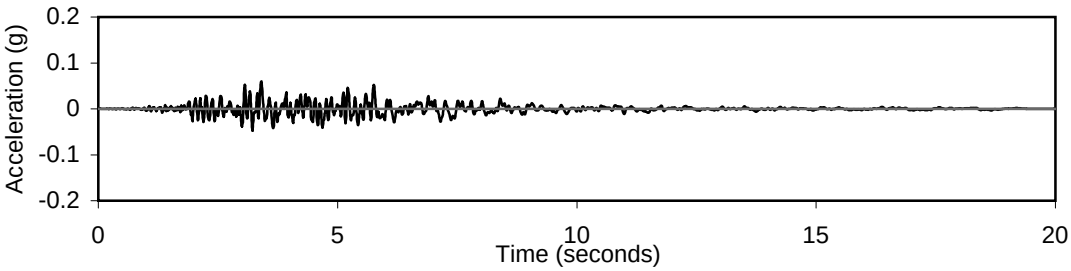

Figure 4-9: Acceleration history of motion 1 outcrop motion (0d to bedrock) having 0.06 PGA bedrock excitation

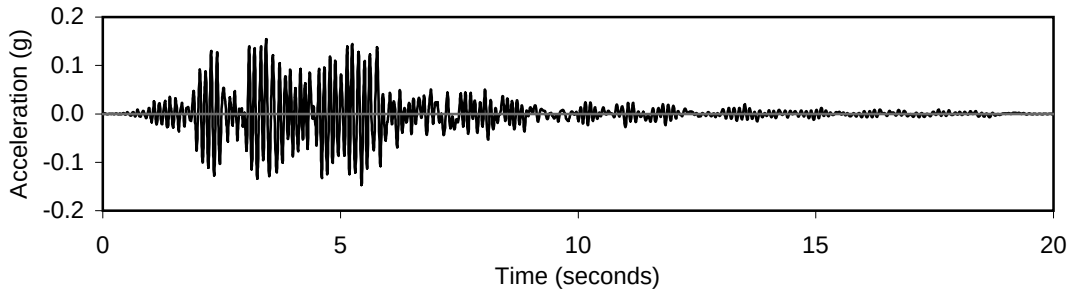

Figure 4-10: Acceleration history of motion 1, 0.33d to bedrock motion having 0.06 PGA bedrock excitation.

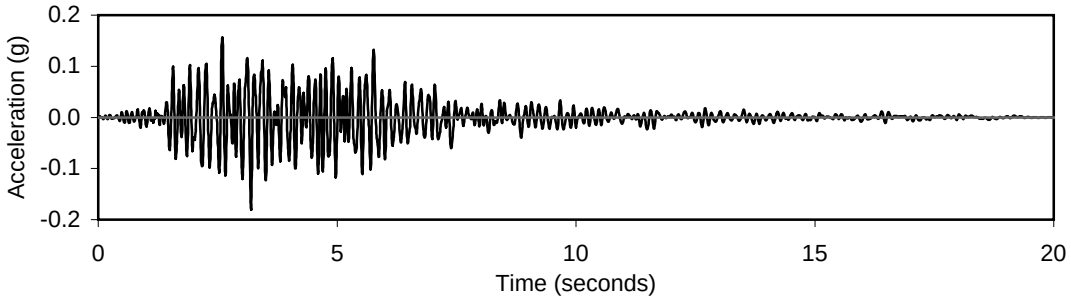

Figure 4-11: Acceleration history of motion 1, 0.50d to bedrock motion having 0.06 PGA bedrock excitation.

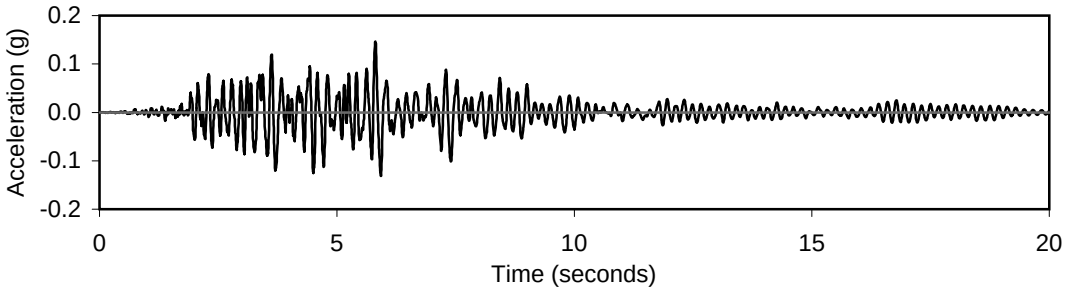

Figure 4-12: Acceleration history of motion 1, 0.66d to bedrock motion having 0.06 PGA bedrock excitation.

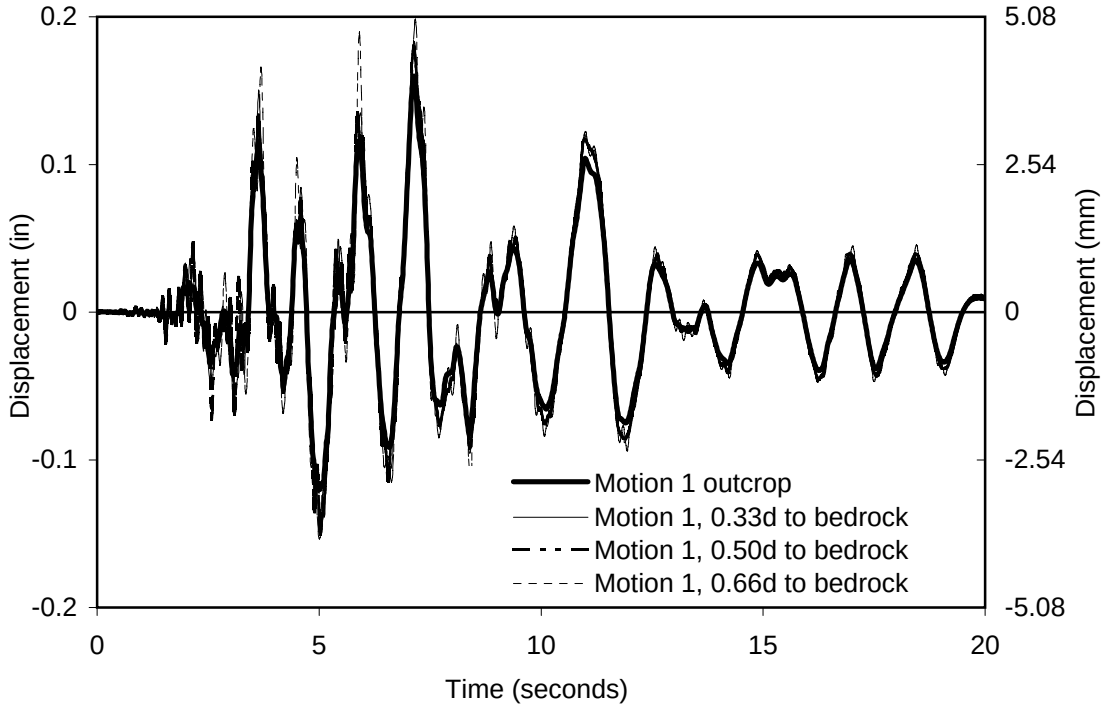

Figure 4-13: Displacement histories of target shake table motions used for low-amplitude incoherent excitation, based on motion 1 with 0.06 PGA bedrock excitation.

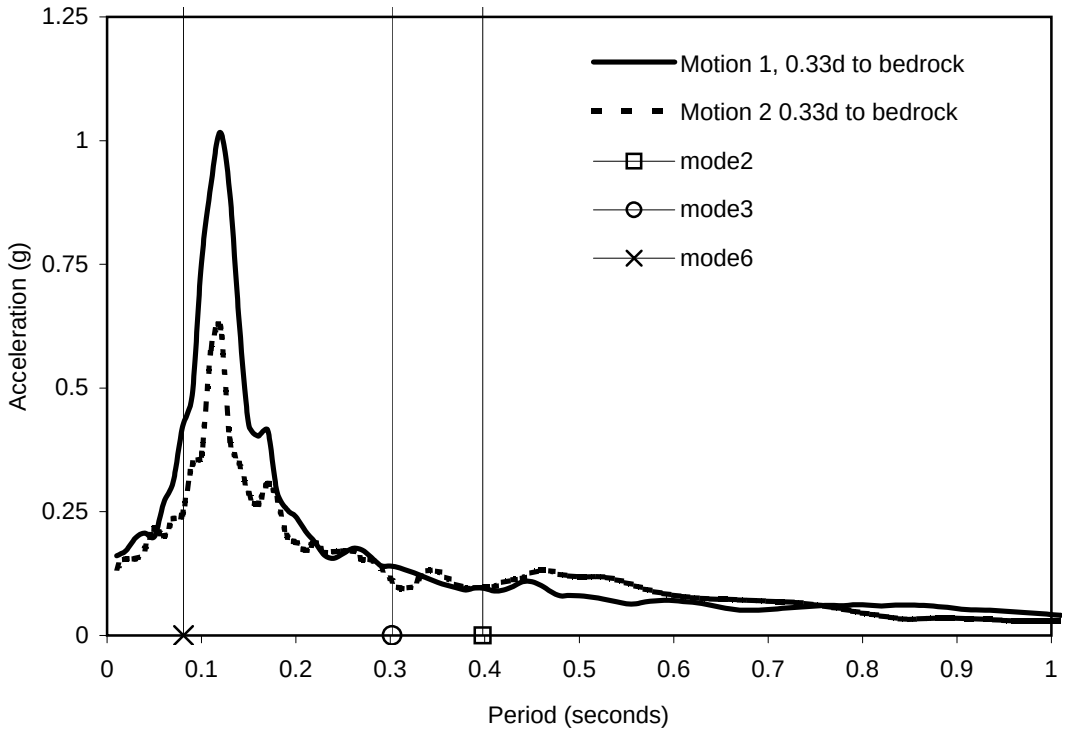

Figure 4-14: Response spectra of target shake table motions used for low-amplitude biaxial excitation with superimposed transverse modal periods.

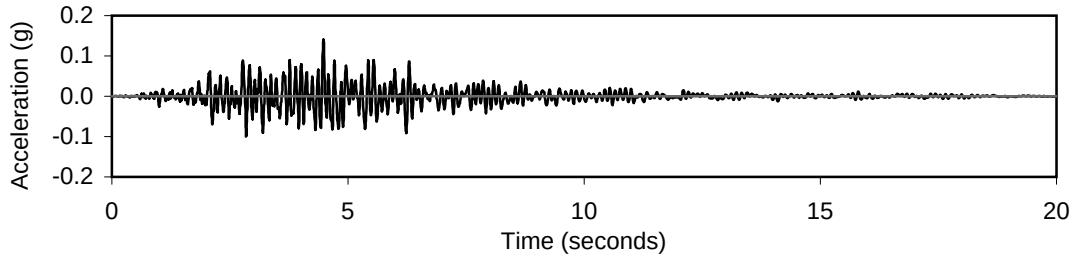

Figure 4-15: Acceleration history of motion 2, 0.33d to bedrock motion having 0.06 PGA bedrock excitation.

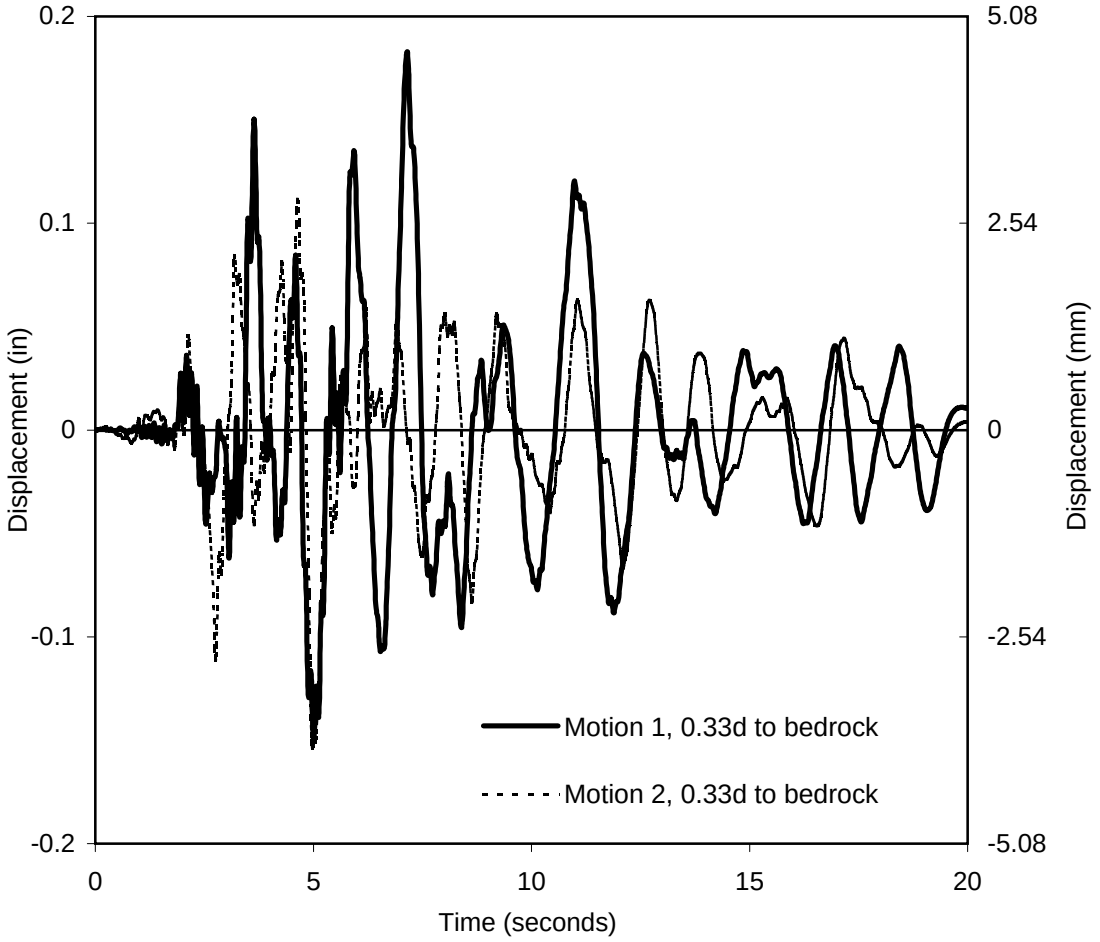

Figure 4-16: Displacement histories of target table motions used for low-amplitude biaxial excitation, based on motion 1 and motion 2 with 0.06 PGA bedrock excitation.

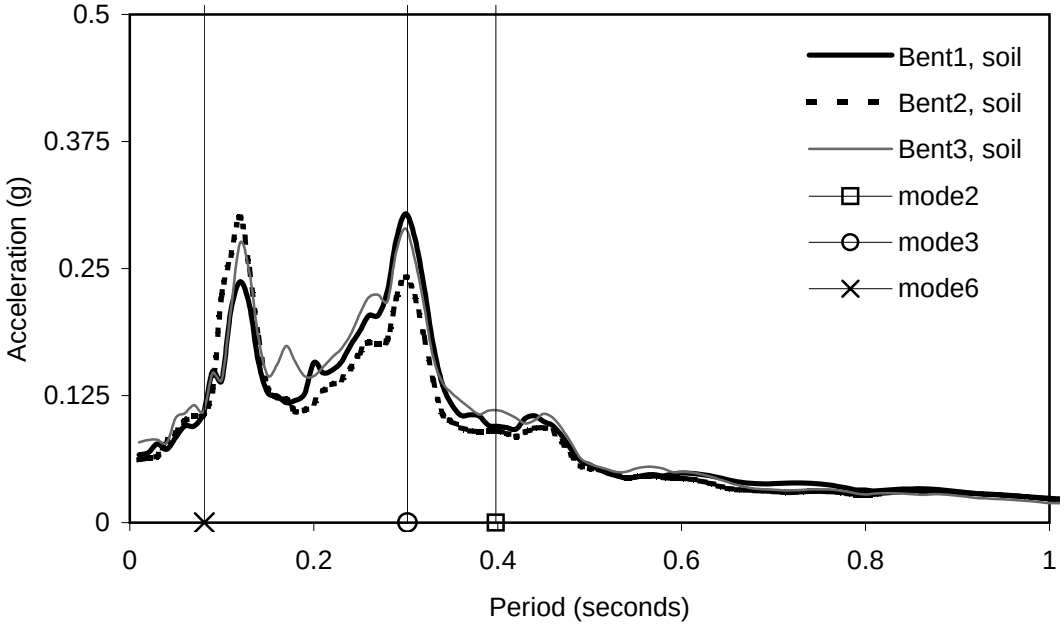

Figure 4-17: Response spectra of achieved centrifuge soil motions for each bent with superimposed transverse modal periods of the shake table specimen.

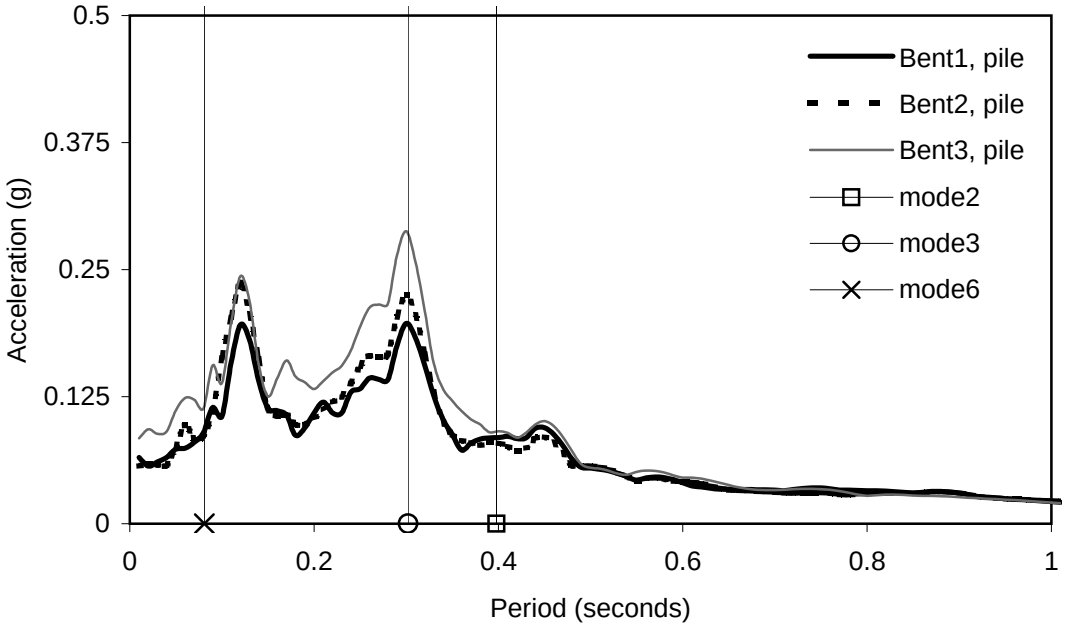

Figure 4-18: Response spectra of achieved centrifuge pile motions for each bent with superimposed transverse modal periods of the shake table specimen.

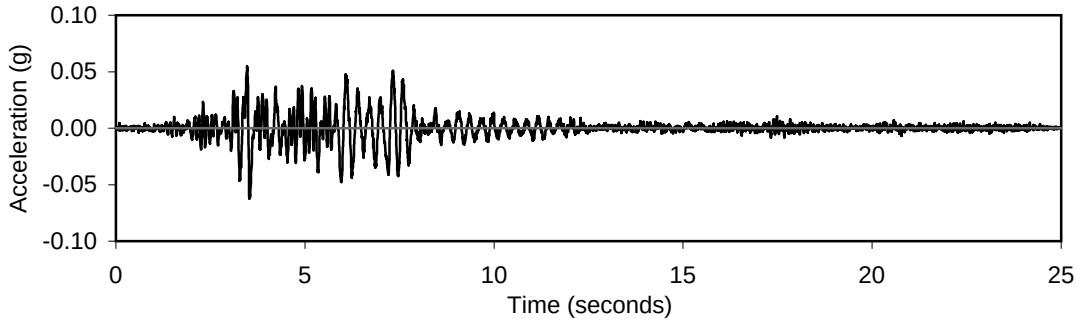

Figure 4-19: Acceleration history of achieved centrifuge bent 1 soil motion, with 0.1g PGA motion-1 target.

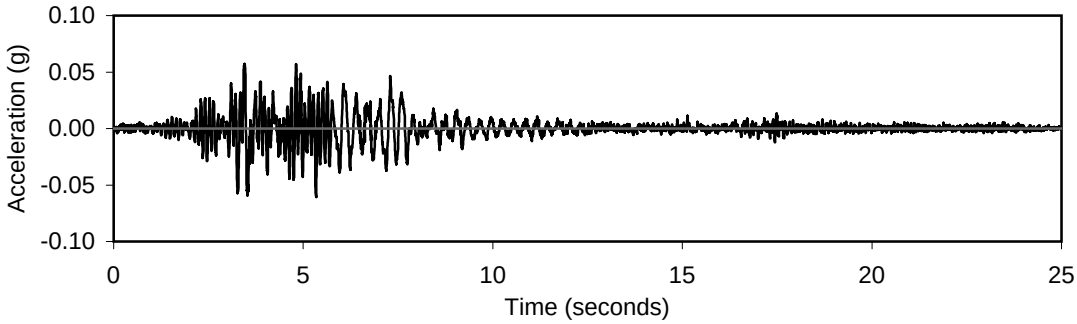

Figure 4-20: Acceleration history of achieved centrifuge bent 2 soil motion, with 0.1g PGA motion-1 target.

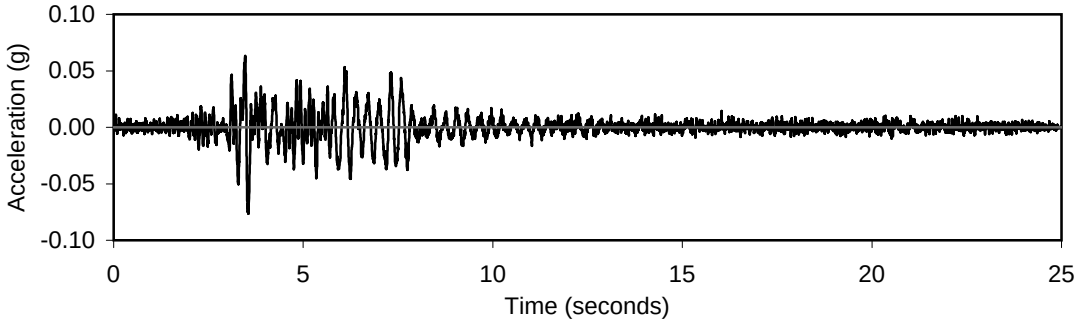

Figure 4-21: Acceleration history of achieved centrifuge bent 3 soil motion, with 0.1g PGA motion-1 target.

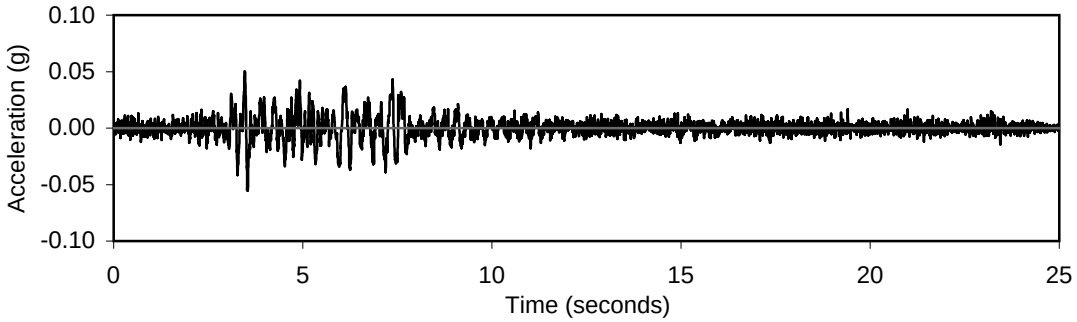

Figure 4-22: Acceleration history of achieved centrifuge bent 1 pile motion, with 0.1g PGA motion-1 target.

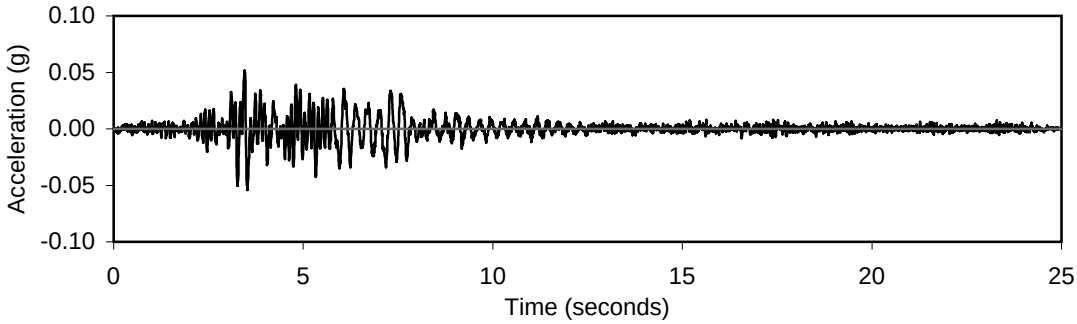

Figure 4-23: Acceleration history of achieved centrifuge bent 2 pile motion, with 0.1g PGA motion-1 target.

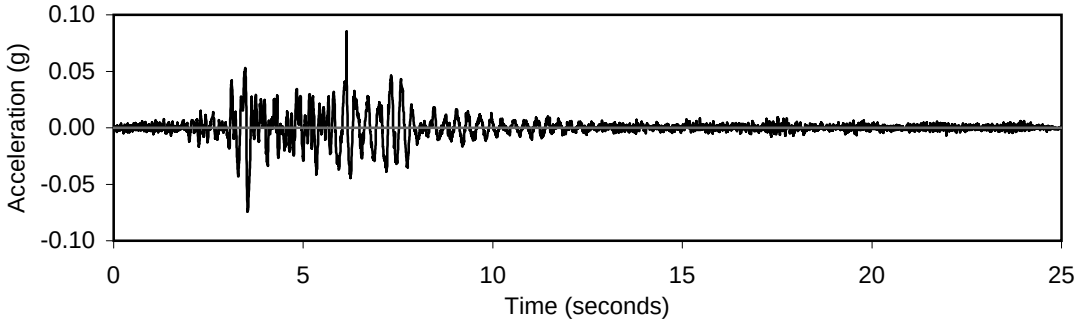

Figure 4-24: Acceleration history of achieved centrifuge bent 3 pile motion, with 0.1g PGA motion-1 target.

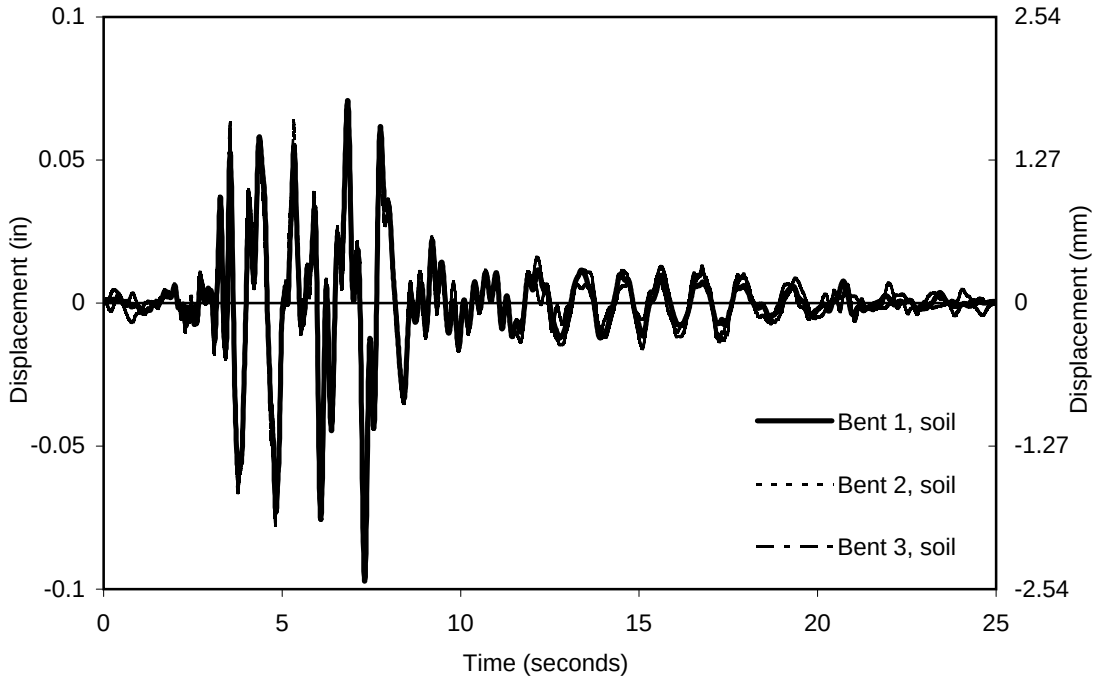

Figure 4-25: Displacement histories of achieved centrifuge soil motions for bents 1-3, with 0.1g PGA motion-1 target.

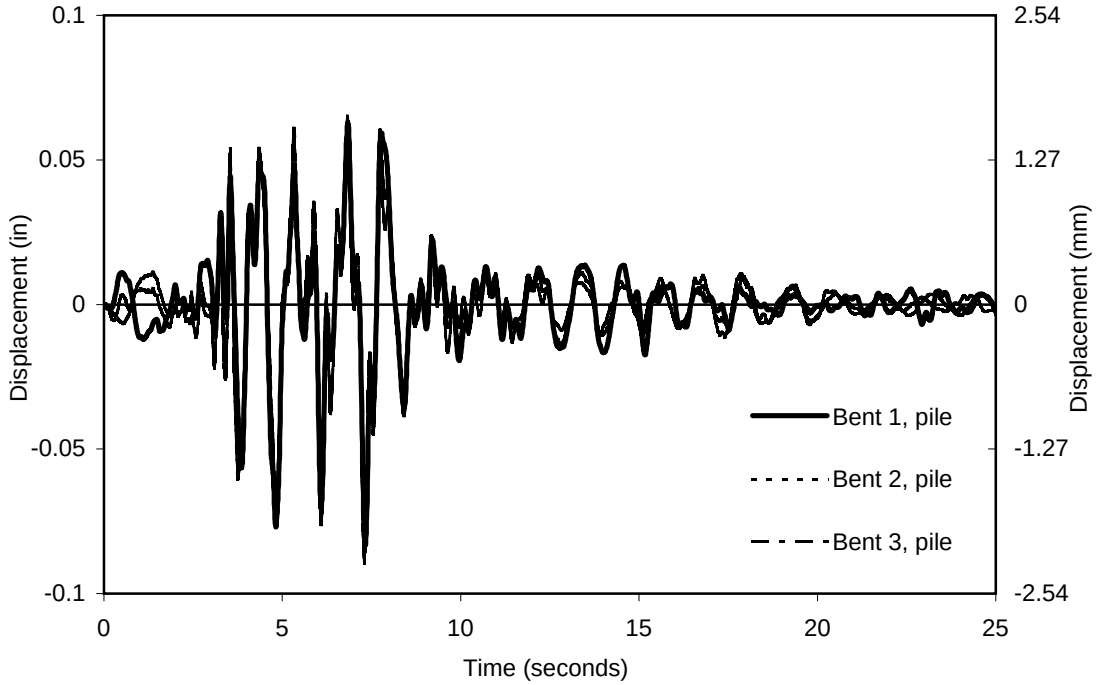

Figure 4-26: Displacement histories of achieved centrifuge pile motions for bents 1-3, with 0.1g PGA motion-1 target.

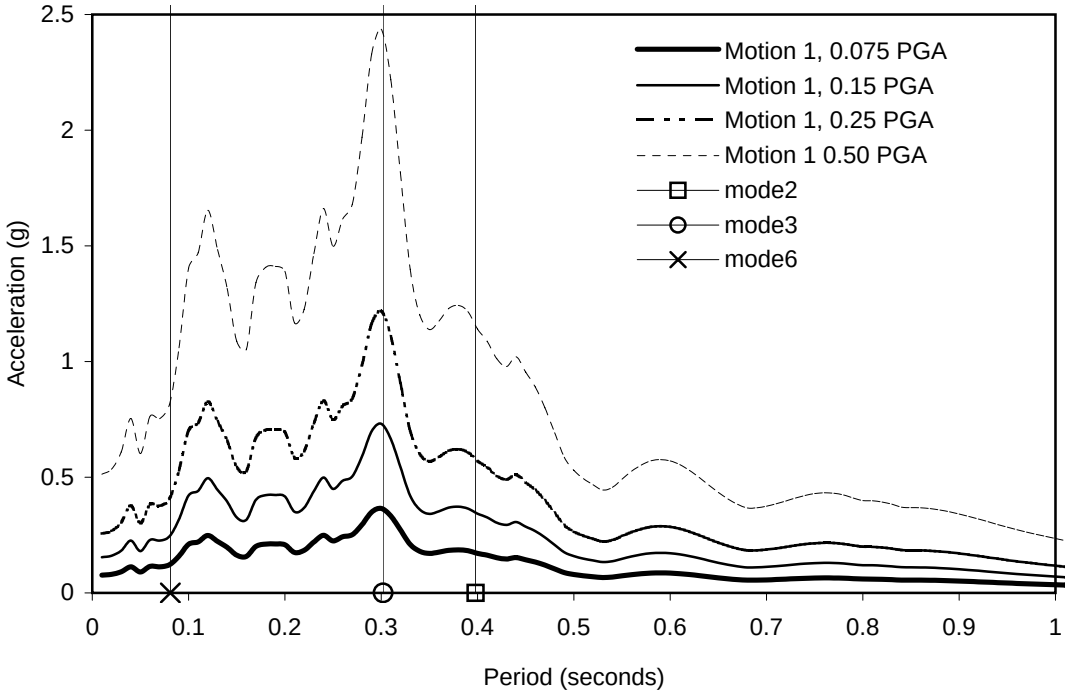

Figure 4-27: Response spectra of ramped input motion for high amplitude tests with superimposed transverse modal periods, 5% damping (from 0.075 to 0.5 PGA).

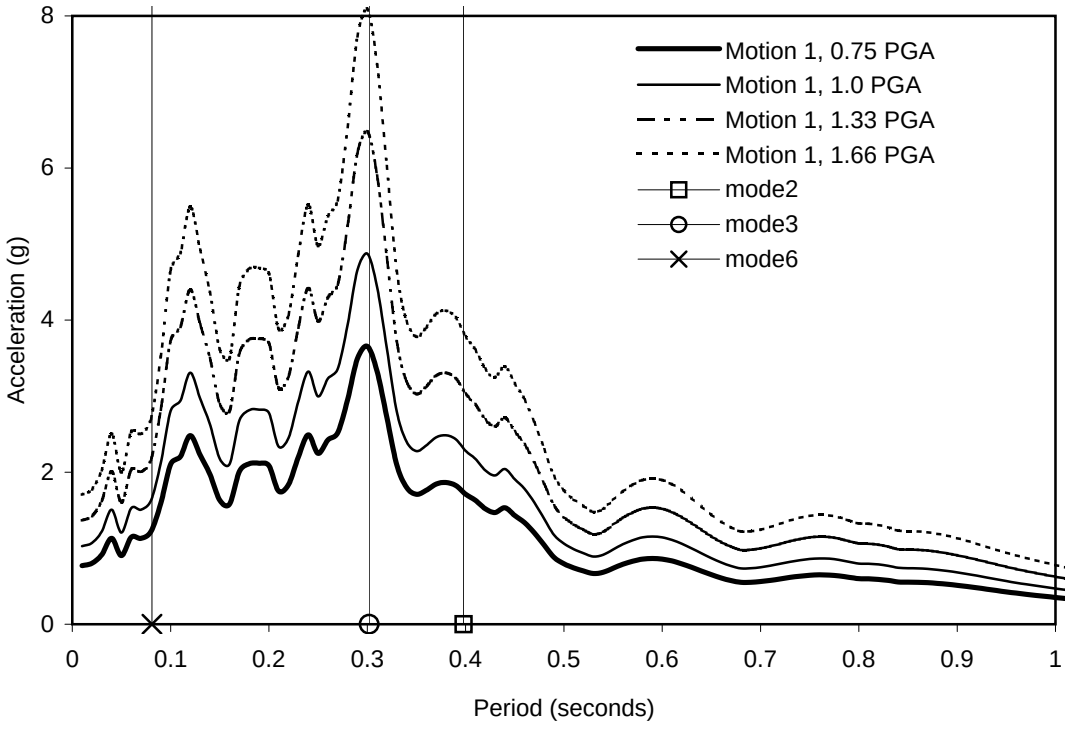

Figure 4-28: Response spectra of ramped input motion for high amplitude tests with superimposed transverse modal periods, 5% damping (from 0.75 to 1.66 PGA).

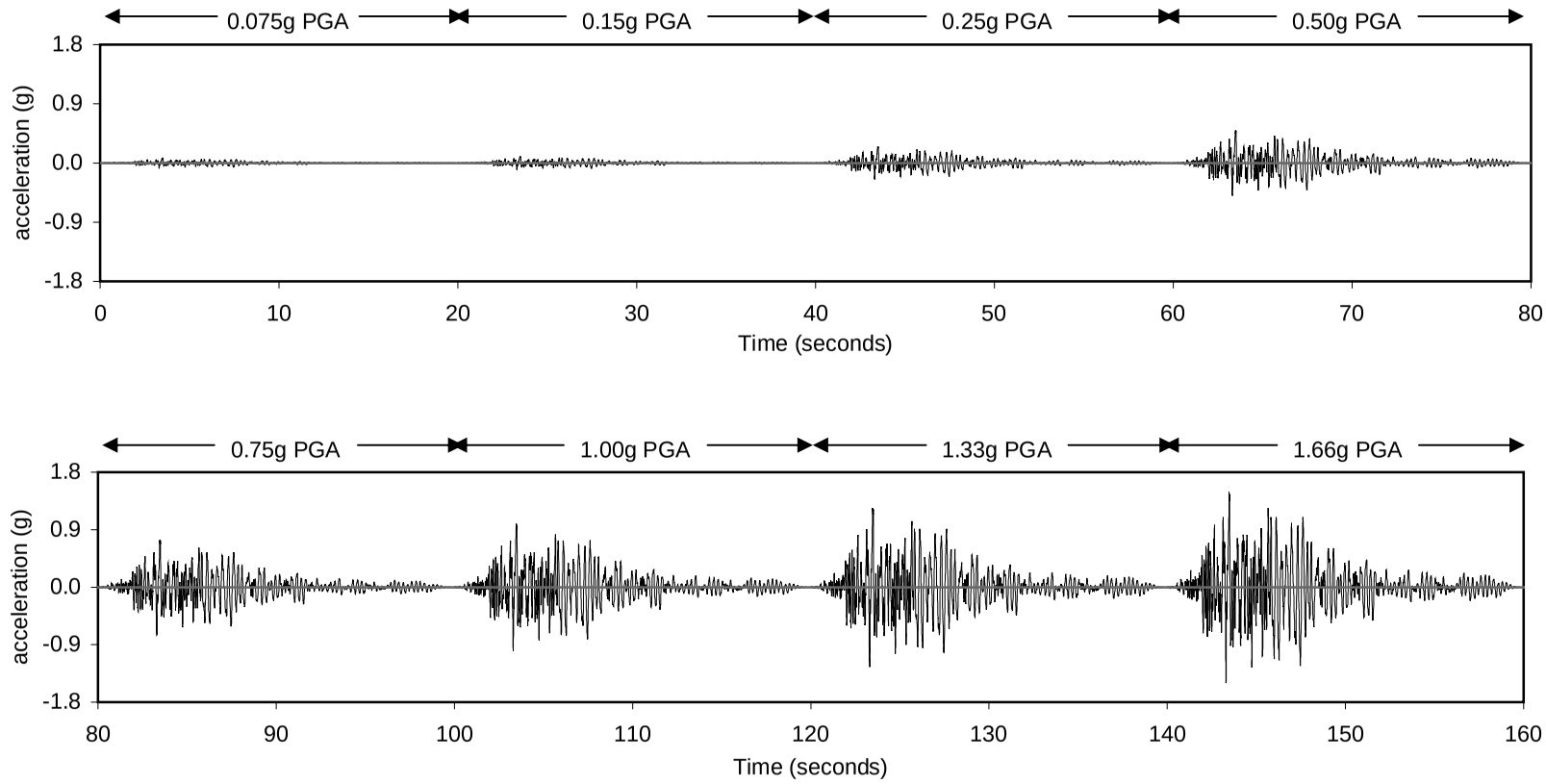

Figure 4-29: Table acceleration input history of ramped transverse coherent motion for high amplitude tests, based on motion-1 0.4g bedrock excitation and depth of d (83.3 ft [25.4 m]) to bedrock, scaled from 0.075 to 1.66 g PGA.

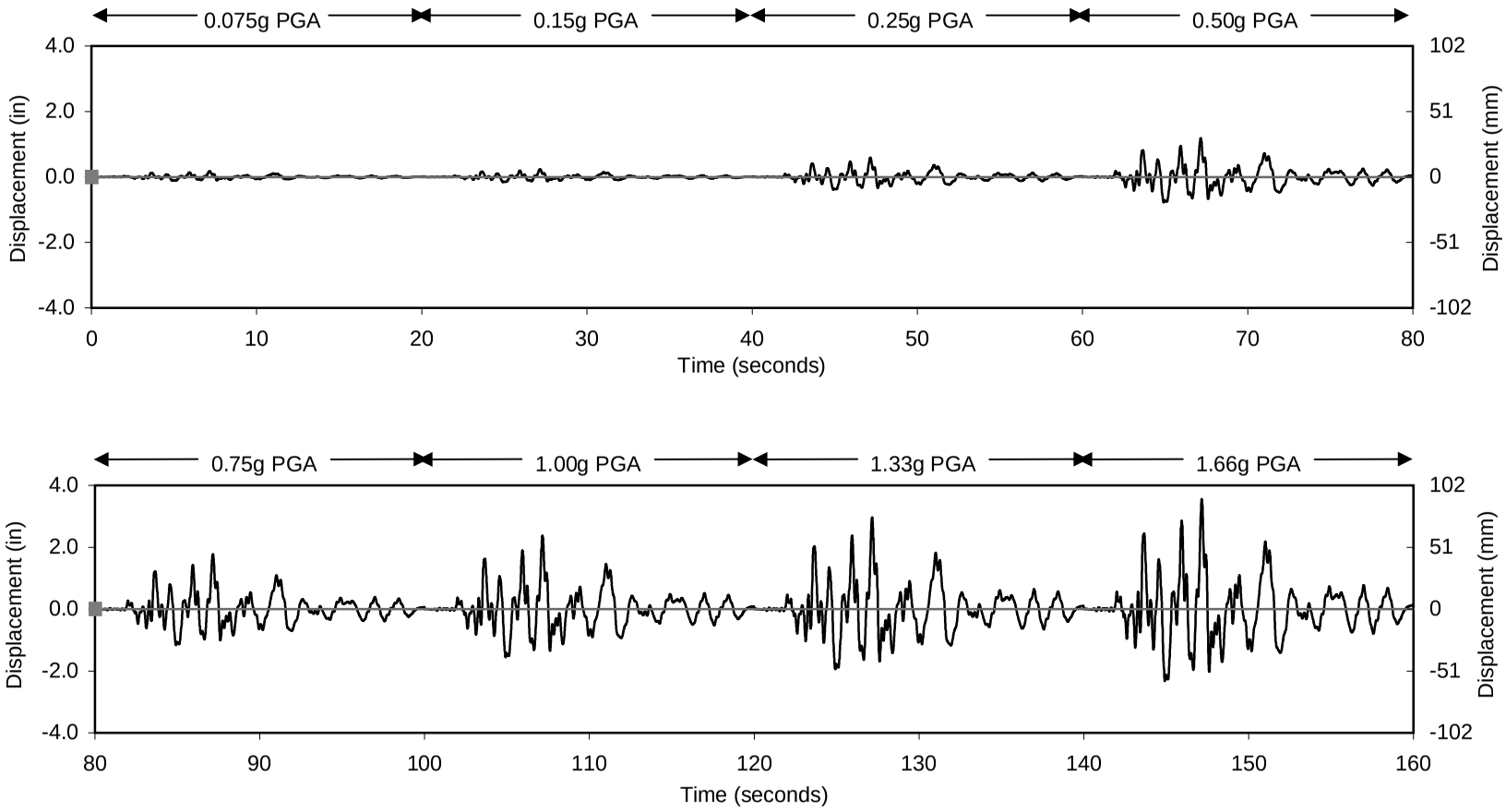

Figure 4-30: Table displacement input history of ramped transverse coherent motion for high amplitude tests, based on motion-1 0.4g bedrock excitation and depth of d (83.3ft [25.4 m]) to bedrock, scaled from 0.075 to 1.66 g PGA.

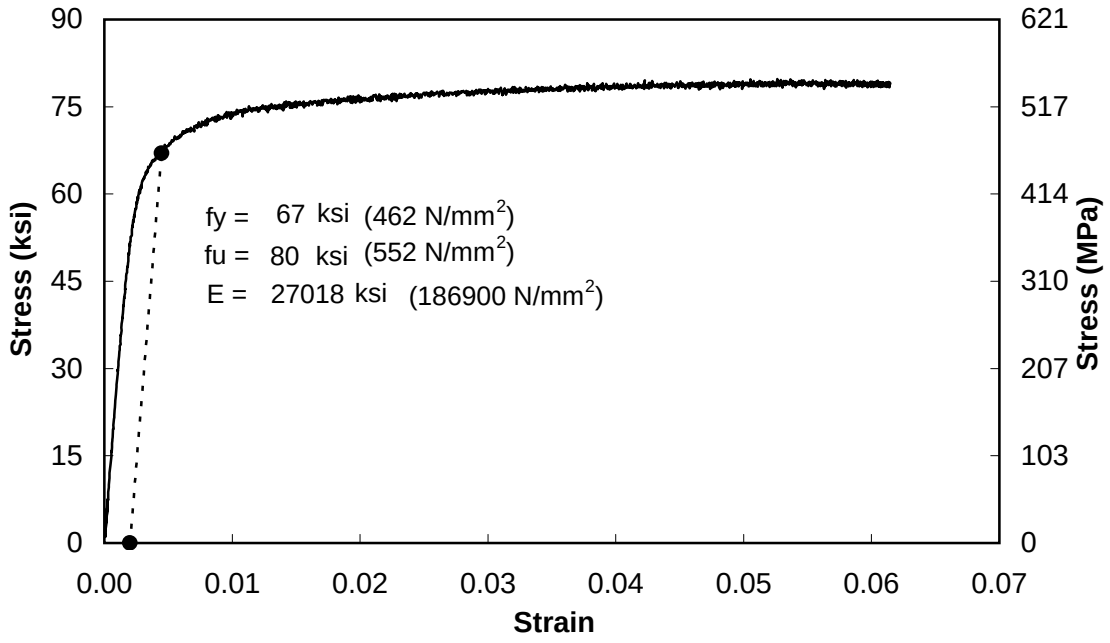

Figure 4-31: Measured stress-strain curve from test of W2.9 steel used for column lateral reinforcement (dual strain gauge test).

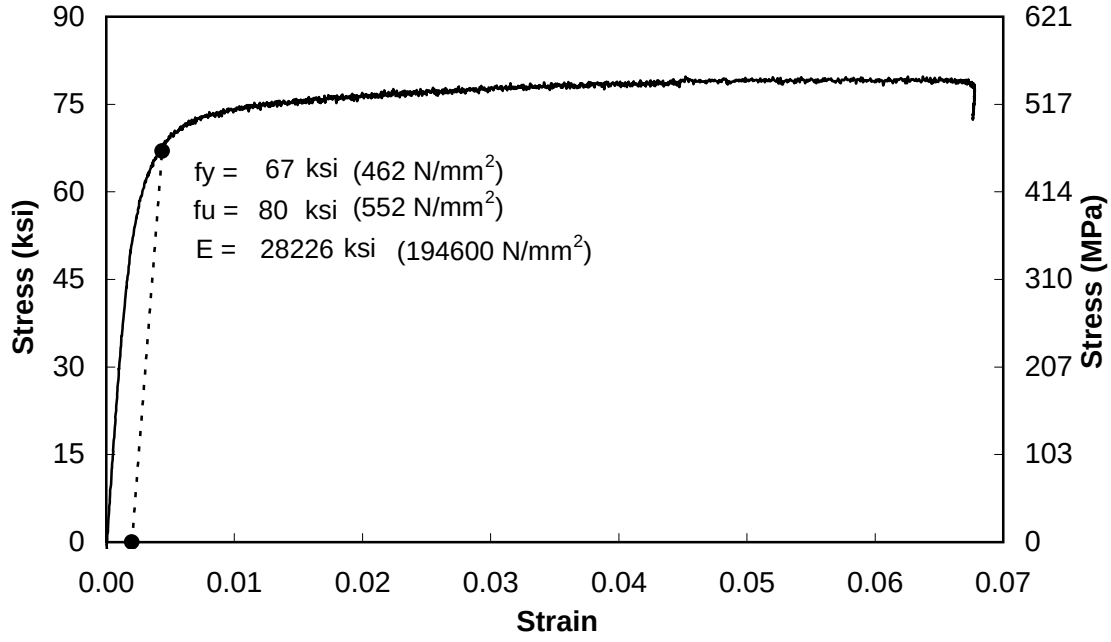

Figure 4-32: Measured stress-strain curve from test of W2.9 steel used for column lateral reinforcement (dual strain gauge test).

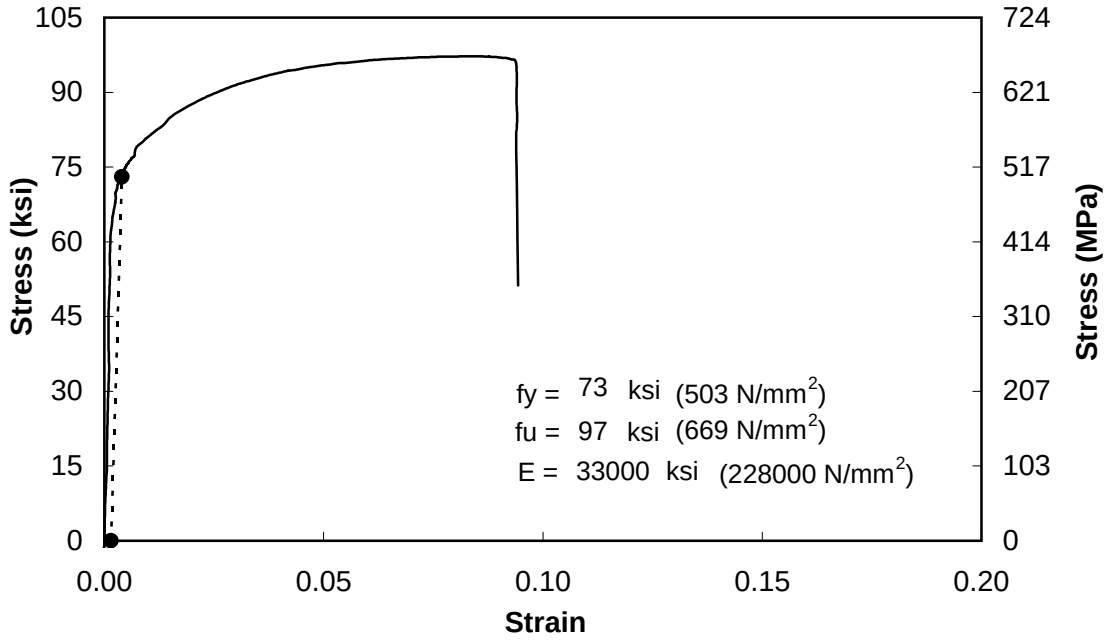

Figure 4-33: Measured stress-strain curve 1 from test of #3 rebar used for longitudinal column reinforcement.

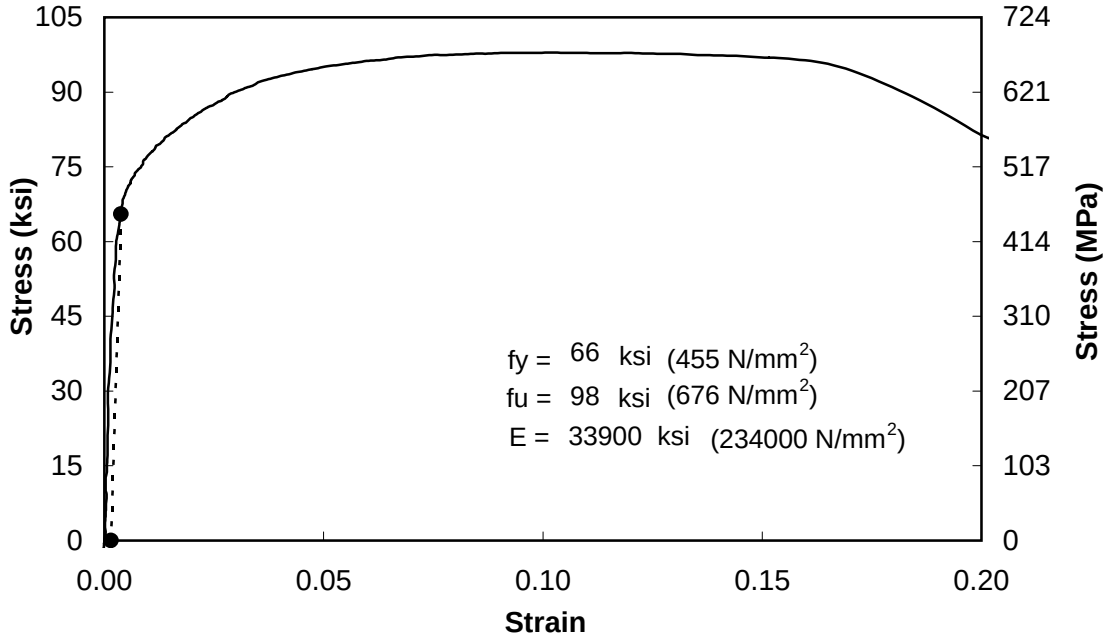

Figure 4-34: Measured stress-strain curve 2 from test of #3 rebar used for longitudinal column reinforcement.

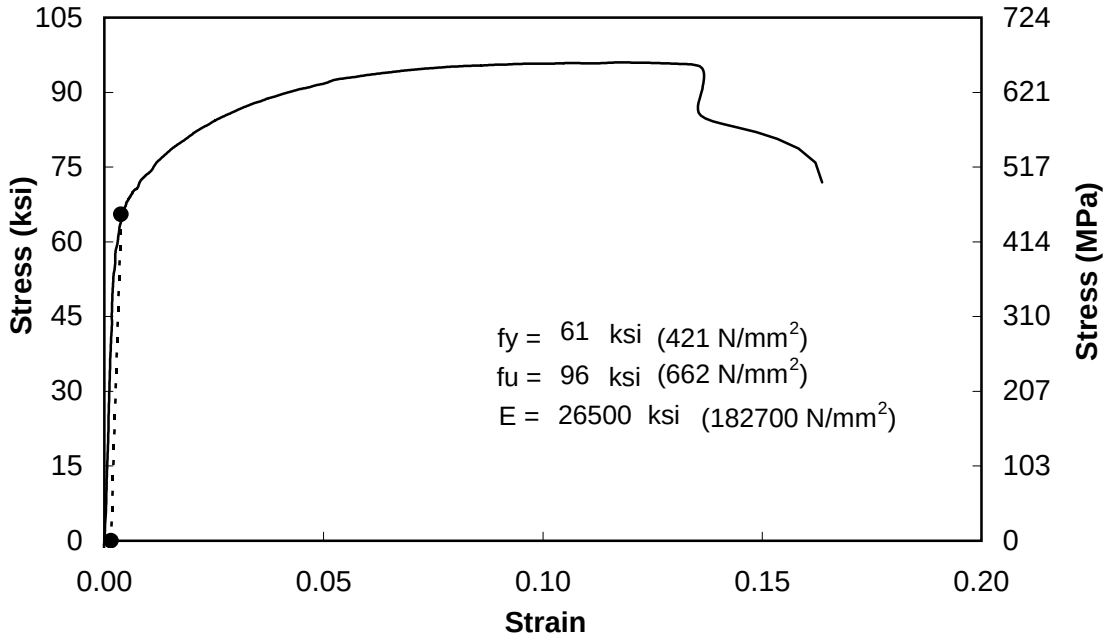

Figure 4-35: Measured stress-strain curve 3 from test of #3 rebar used for longitudinal column reinforcement.

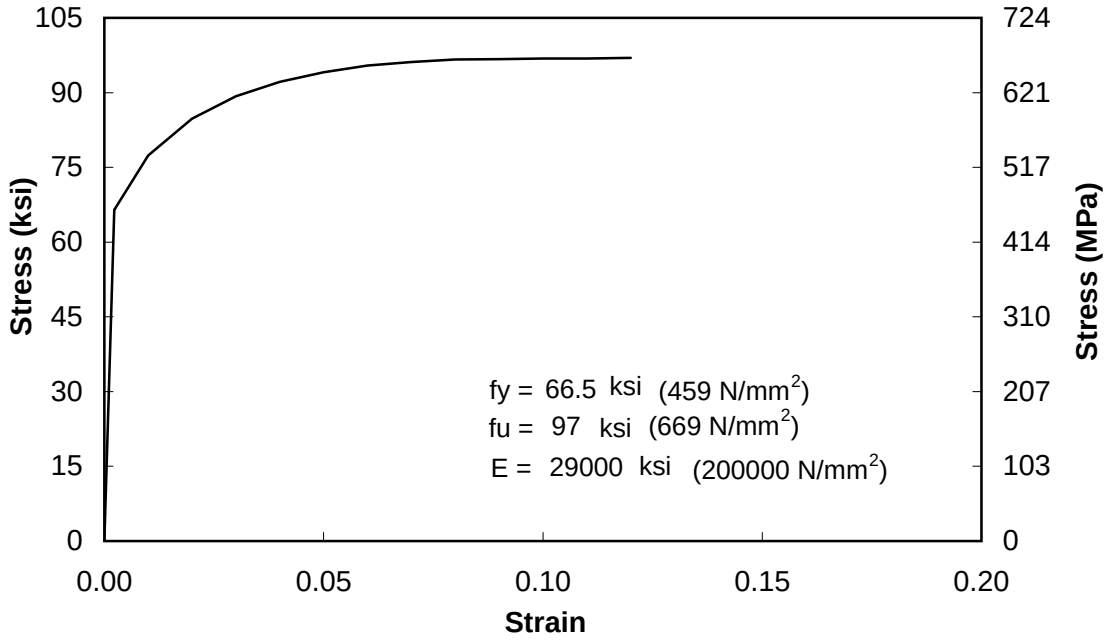

Figure 4-36: Average of stress-strain curves from tests of #3 rebar used for longitudinal column reinforcement.

Figure 5-1: Off-site formwork for superstructure beams.

Figure 5-2: Check of longitudinal post-tension duct path prior to placement of reinforcement cages.

Figure 5-3: Superstructure beams prior to placement of concrete

Figure 5-4: Placement of concrete for superstructure beams.

Figure 5-5: Superstructure beams after transportation to UNR laboratory.

Figure 5-6: Column steel cages prior to placement in footing cages.

Figure 5-7: Column reinforcement cages after placement in footings.

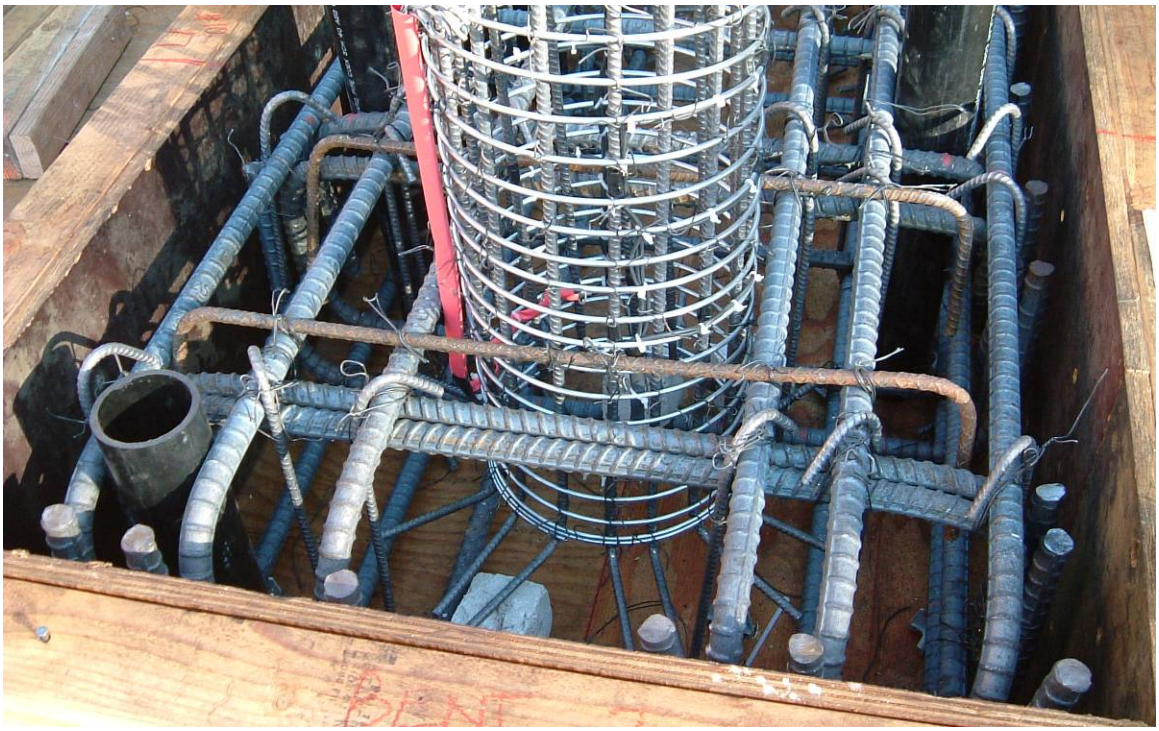

Figure 5-8: Close-up of column cage attachment to footing cage prior to pour of footing concrete.

Figure 5-9: Bents after casting of footing concrete and during construction of working platform.

Figure 5-10: Completed working platform and installed sono-tubes.

Figure 5-11: Top of working platform prior to pour of concrete for columns.

Figure 5-12: Attachment and embedment of curvature rods in columns prior to column concrete pour.

Figure 5-13: Assembly of reinforcement cage for cap beam of bent-2.

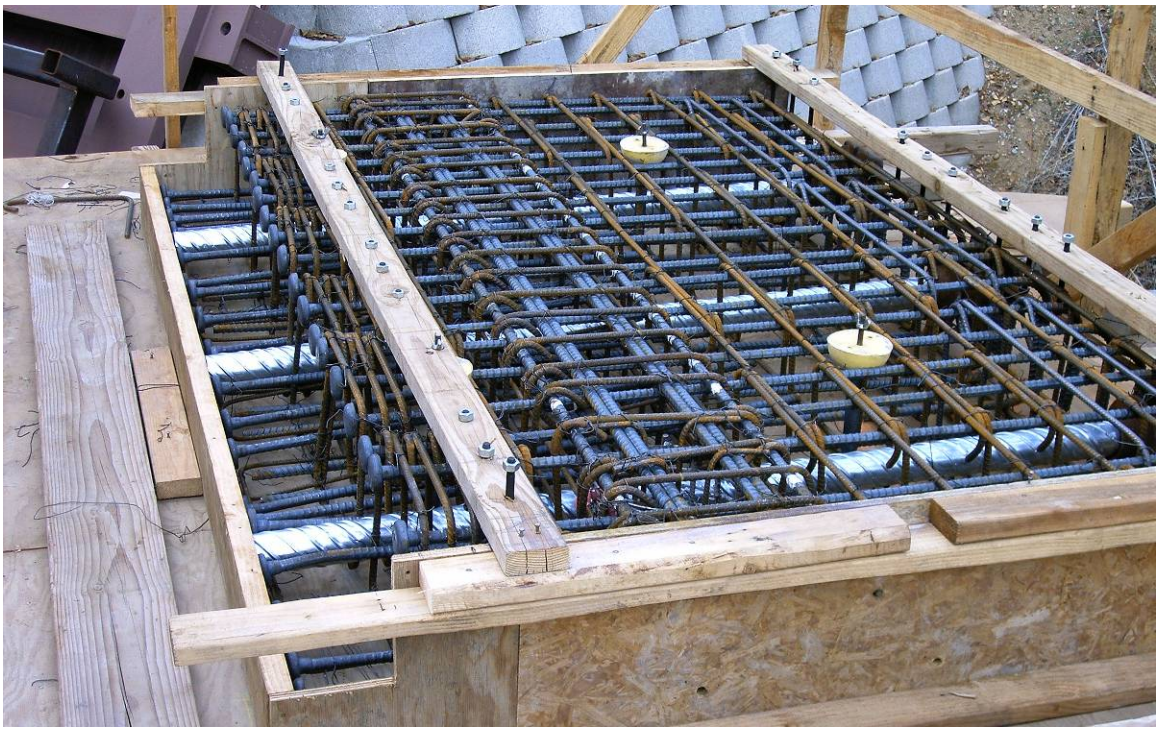

Figure 5-14: Assembly of reinforcement cages and formwork for cantilever cap beams of bents 1 and 3.

Figure 5-15: Installation of anchor and rebar spiral for post-tension anchorage.

Figure 5-16: Formwork for bent-2 cap beam after assembly of cages.

Figure 5-17: Placement of concrete for cap beams/cantilevers.

Figure 5-18: Completed bents 1 through 3 after removal of formwork.

Figure 5-19: Reinforcement cages for spacer blocks.

Figure 5-20: Completed formwork for spacer blocks prior to placement of concrete.

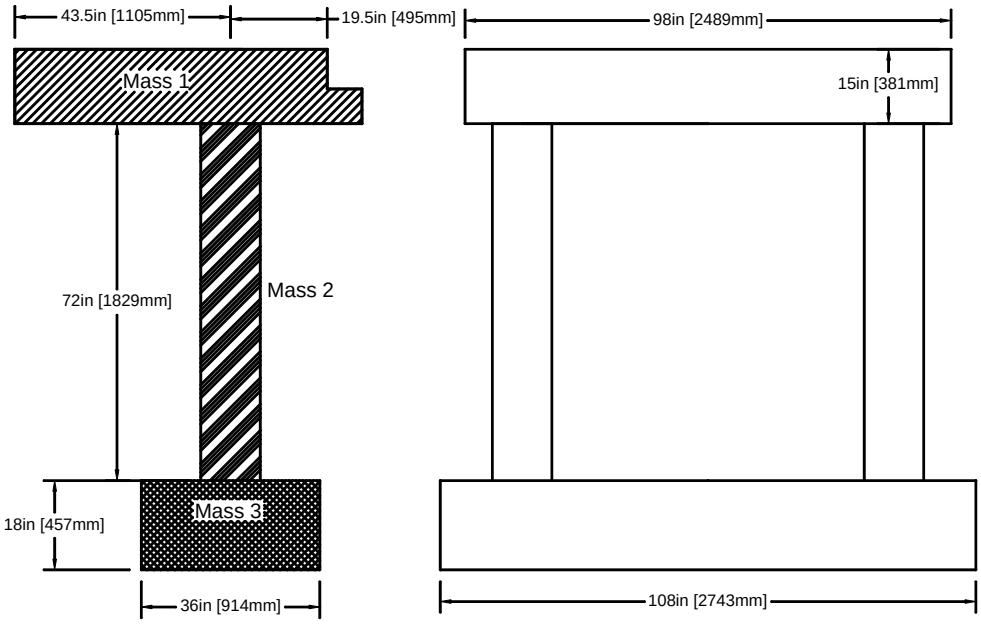

Figure 5-21: Masses considered for bent stability of bent-1.

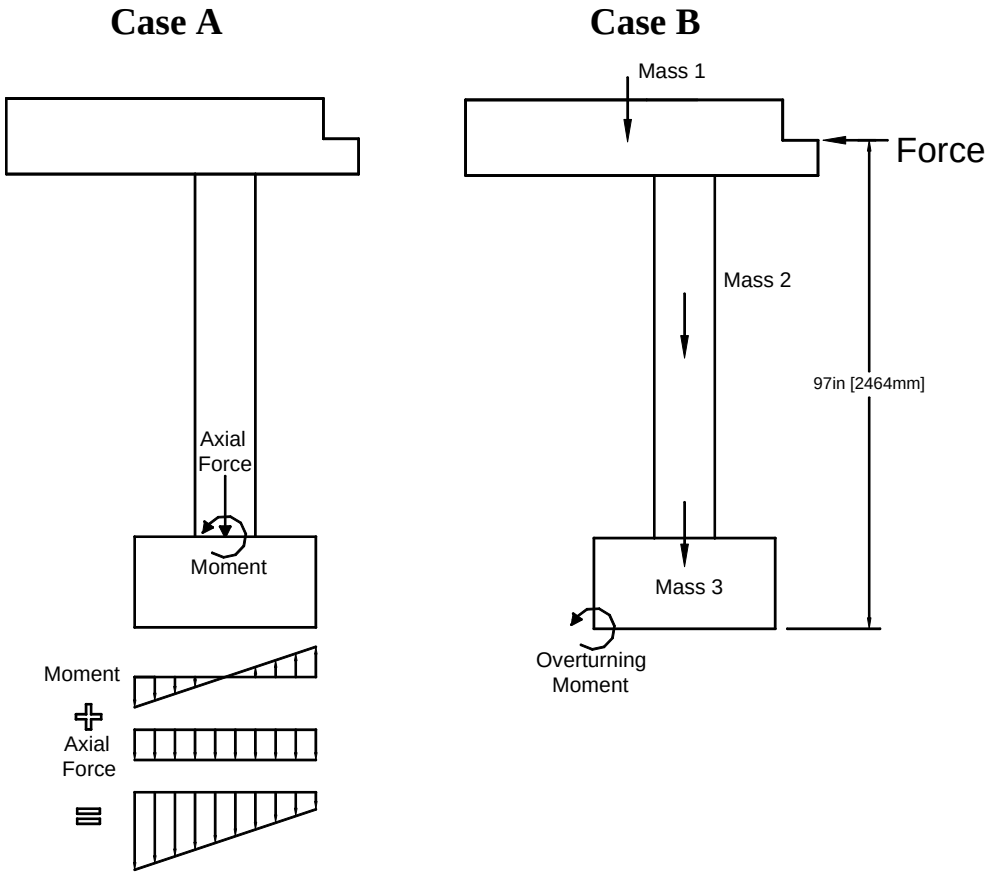

Figure 5-22: Two cases that were considered for bent stability analysis of bent 1, Case-A: uplift under self weight, Case-B force required for overturning.

Figure 5-23: Bracing of cantilevers of bents 1 and 3.

Figure 5-24: Bare shake tables prior to assembly of bridge.

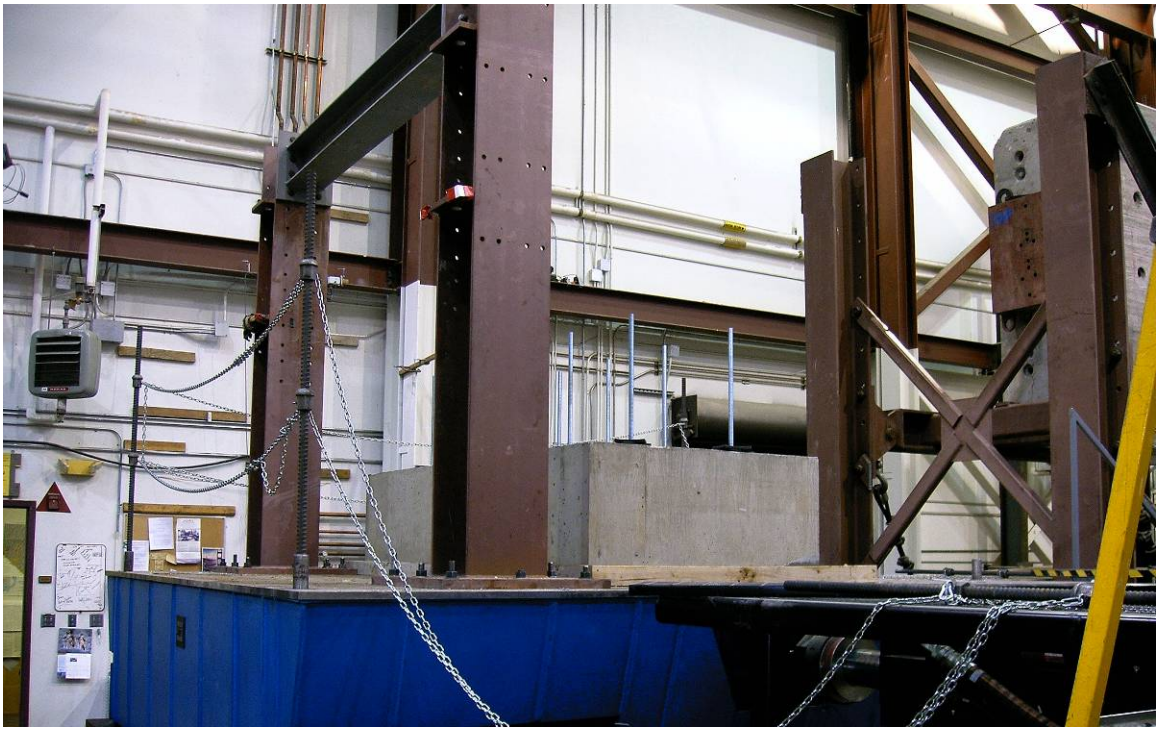

Figure 5-25: Attachment of spacer blocks and safety frames to table 1.

Figure 5-26: Placement and grouting of bent 2 on middle shake table.

Figure 5-27: Transportation of bents to shake tables using crane in laboratory.

Figure 5-28: Placement of bent 3 on end shake table.

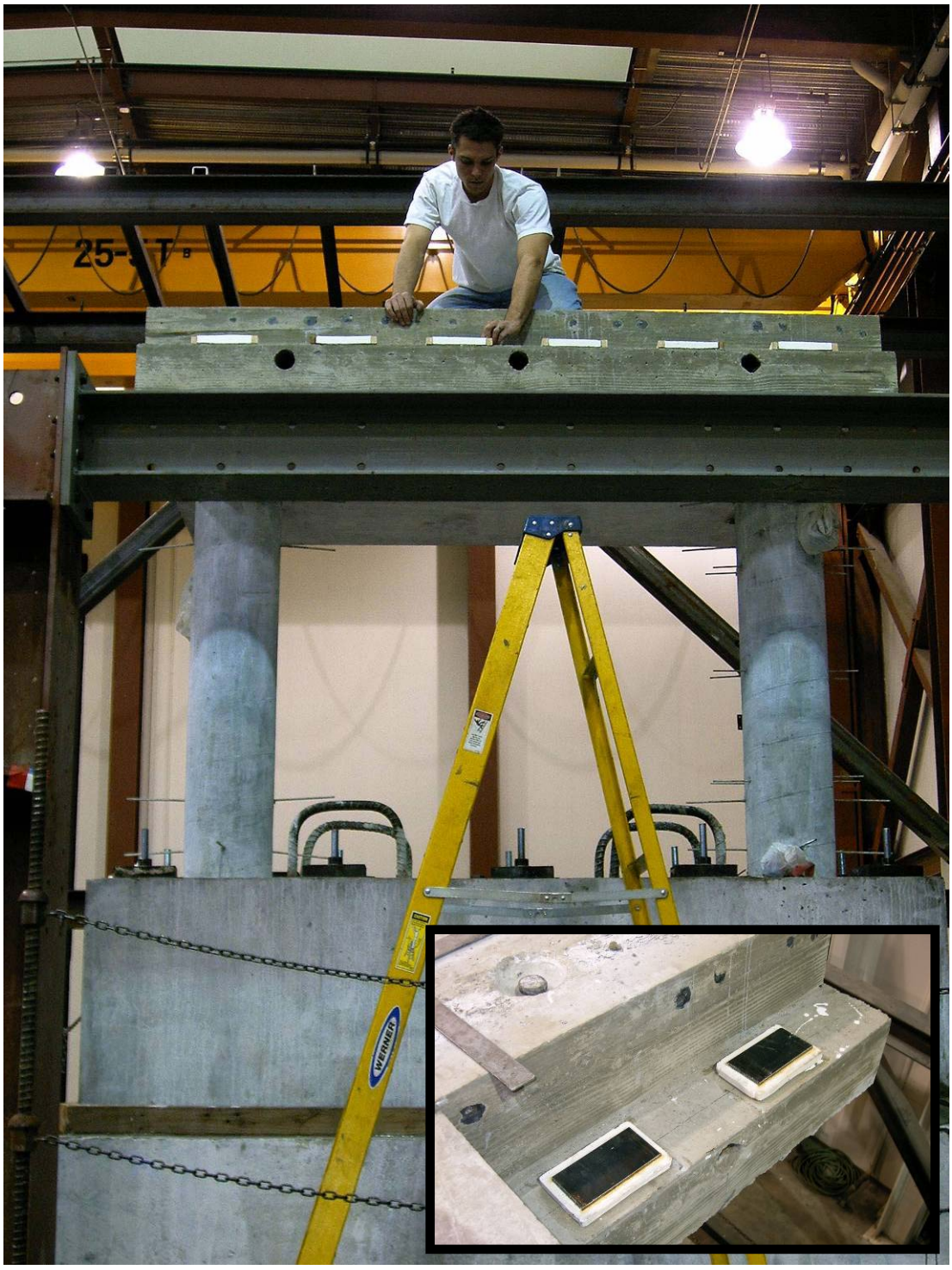

Figure 5-29: Installation of bearing plates on ledges for superstructure beams.

Figure 5-30: Lowering superstructure beams on to ledges.

Figure 5-31: Placement of superstructure beams.

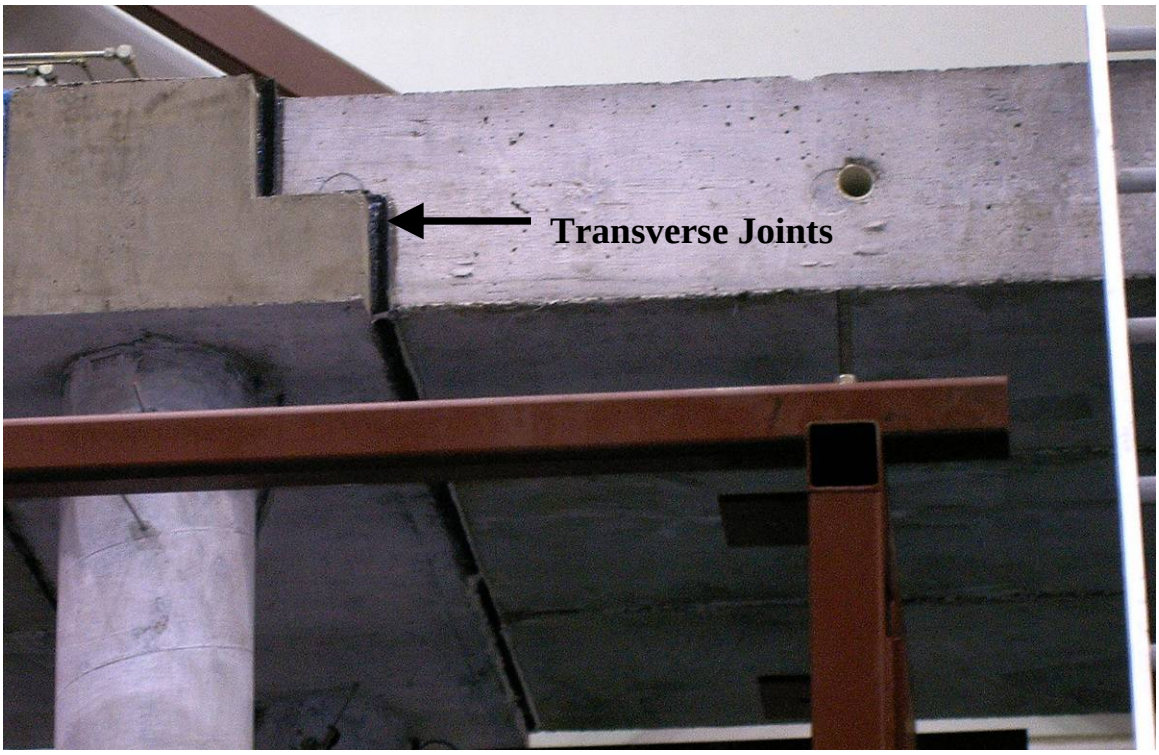

Figure 5-32: Sealing of transverse superstructure joints between bent caps and superstructure beams prior to pouring grout.

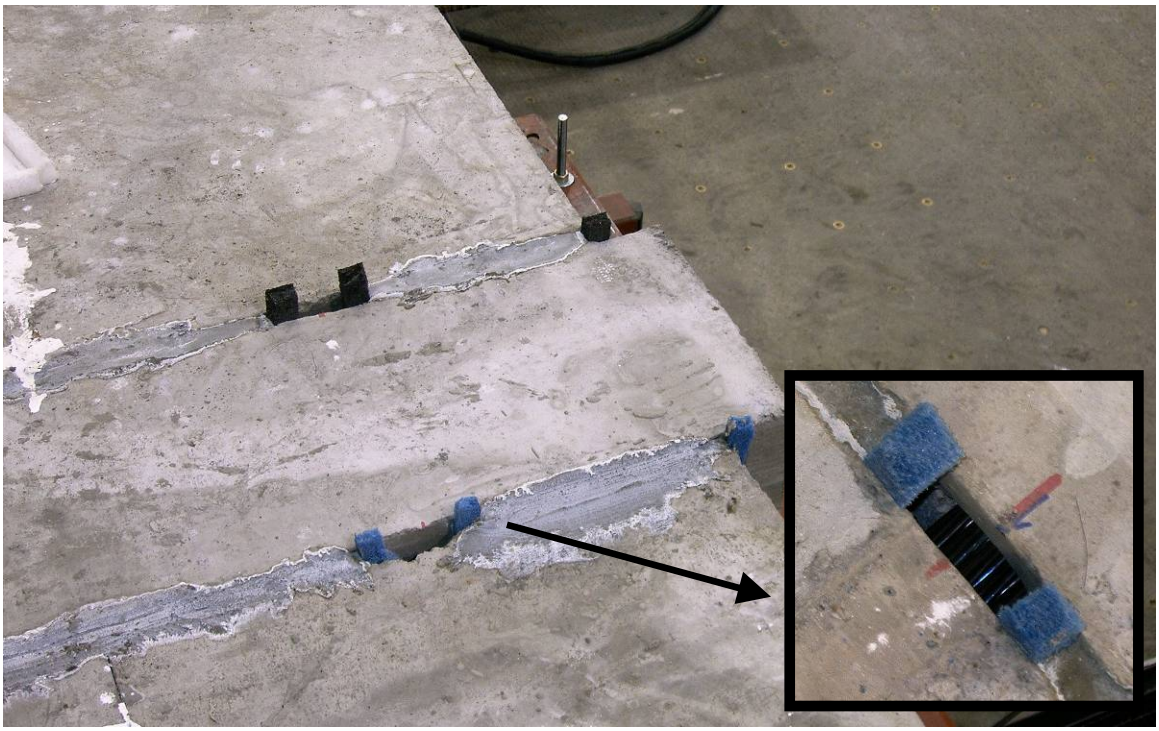

Figure 5-33: Sealing ducts for longitudinal post-tensioning prior to grout pour (top view).

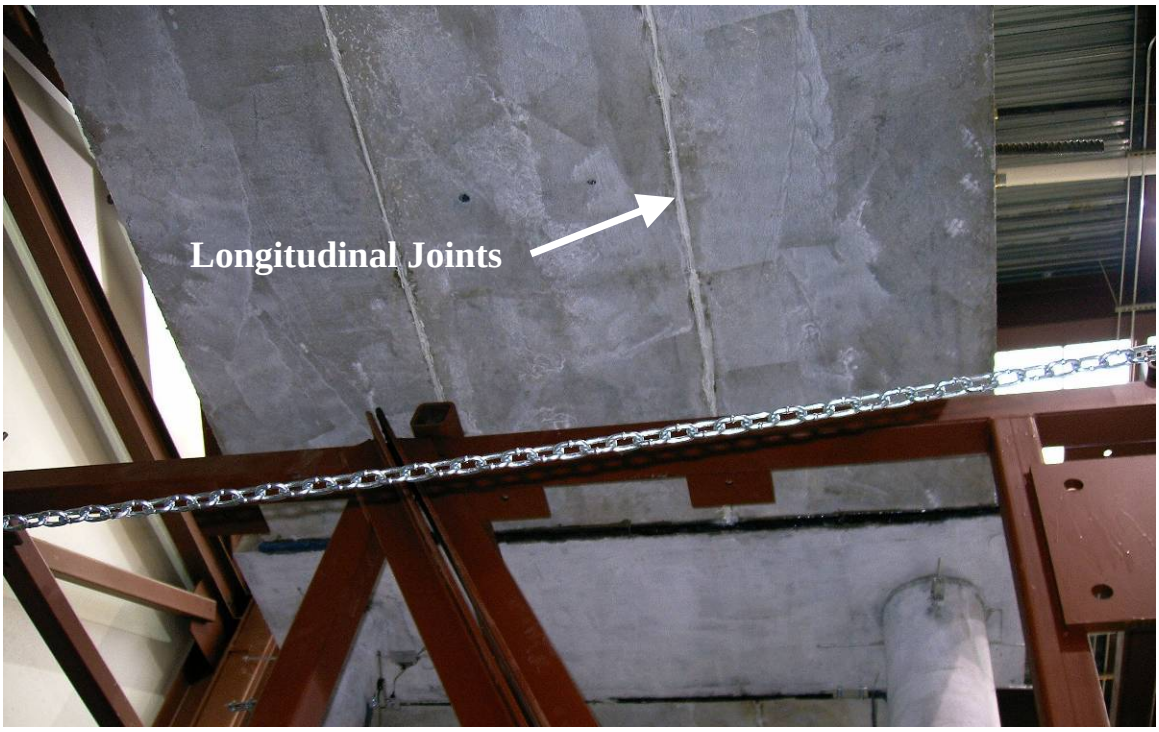

Figure 5-34: Sealing longitudinal superstructure beams prior to pouring hydrostone.

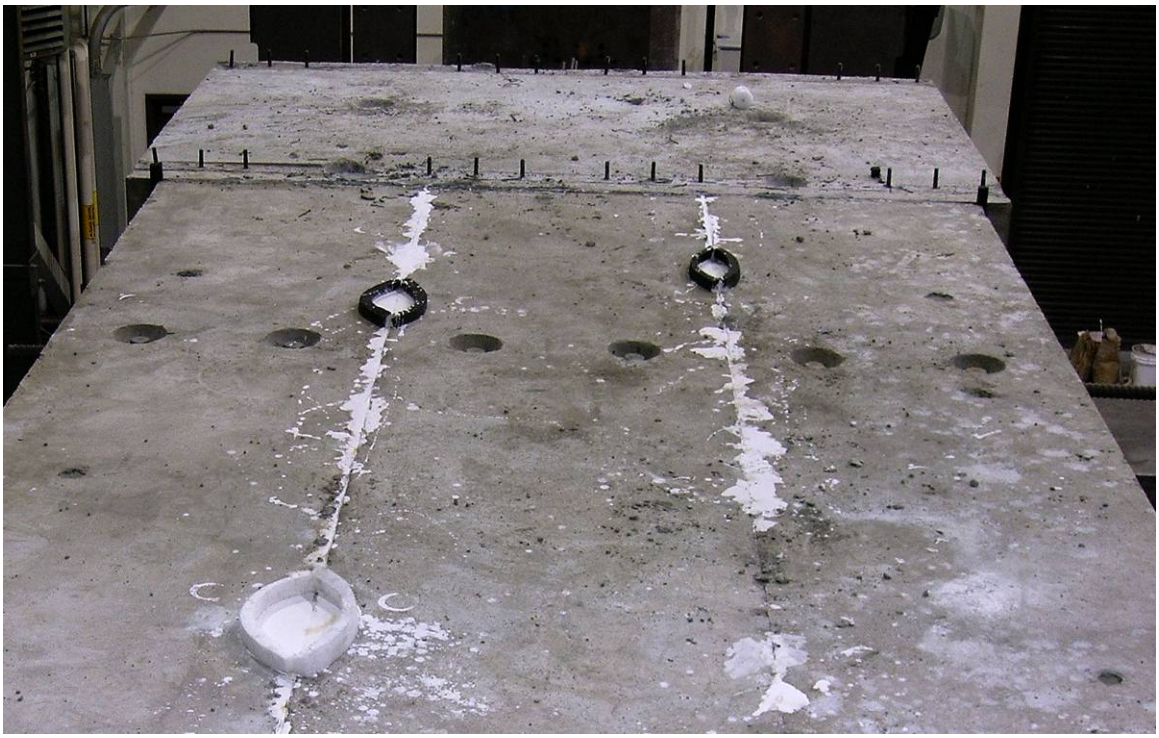

Figure 5-35: Locations used to pour hydrostone between superstructure beams.

Figure 5-36: Superstructure after pouring of grout and hydrostone.

Figure 5-37: Transverse post-tensioning of superstructure beams.

Figure 5-38: Longitudinal post-tensioning of superstructure beams.

Figure 5-39: Collars and post-tension strands after longitudinal post-tensioning.

Figure 5-40: Post-tensioned bridge model prior to placement of masses.

Figure 5-41: Placement of masses on top of bridge superstructure.

Figure 5-42: Completed bridge before shake table testing.

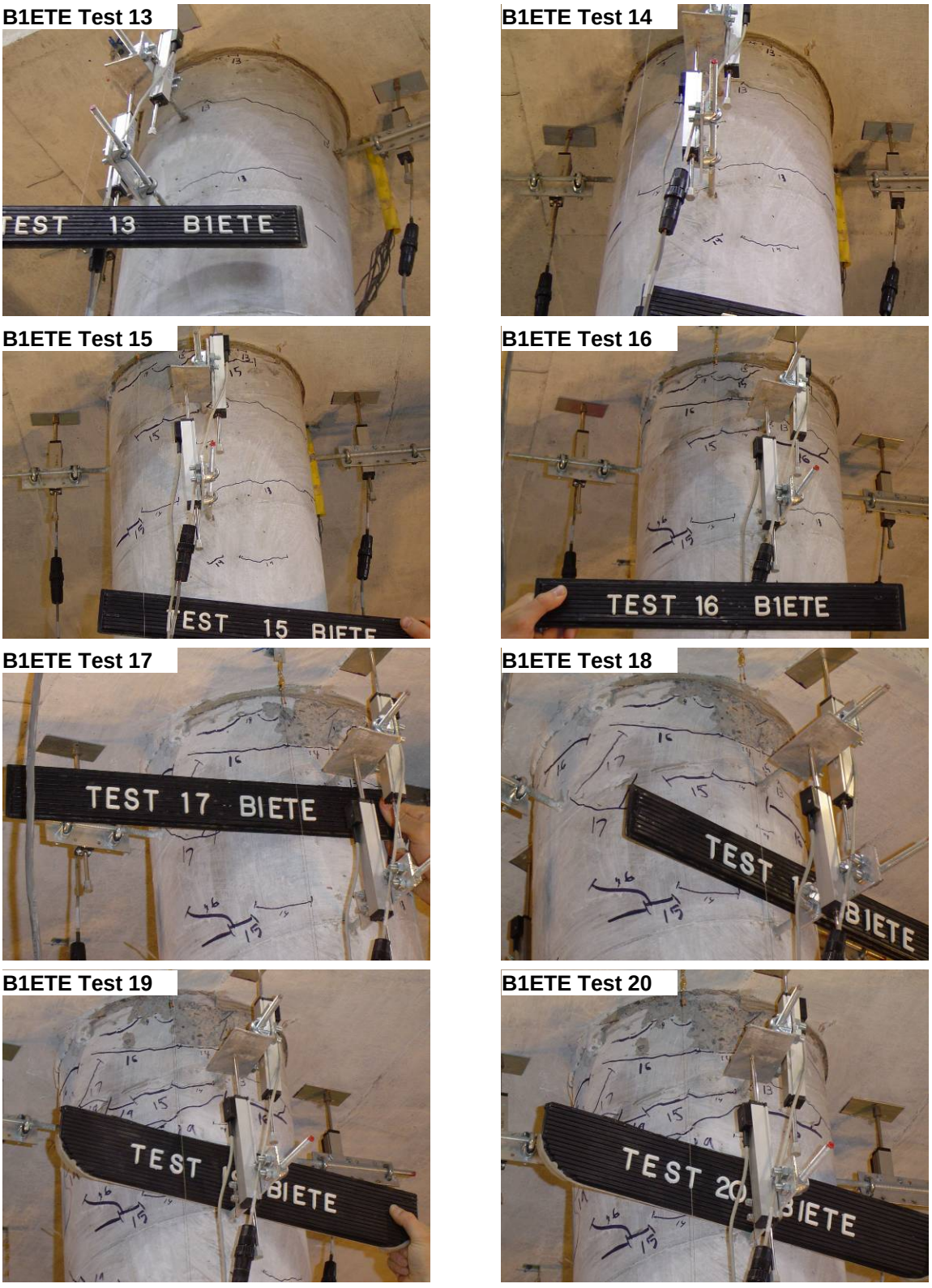

Figure 6-1: Photographs of damage progression for bent 1, east column top east side, through test 20.

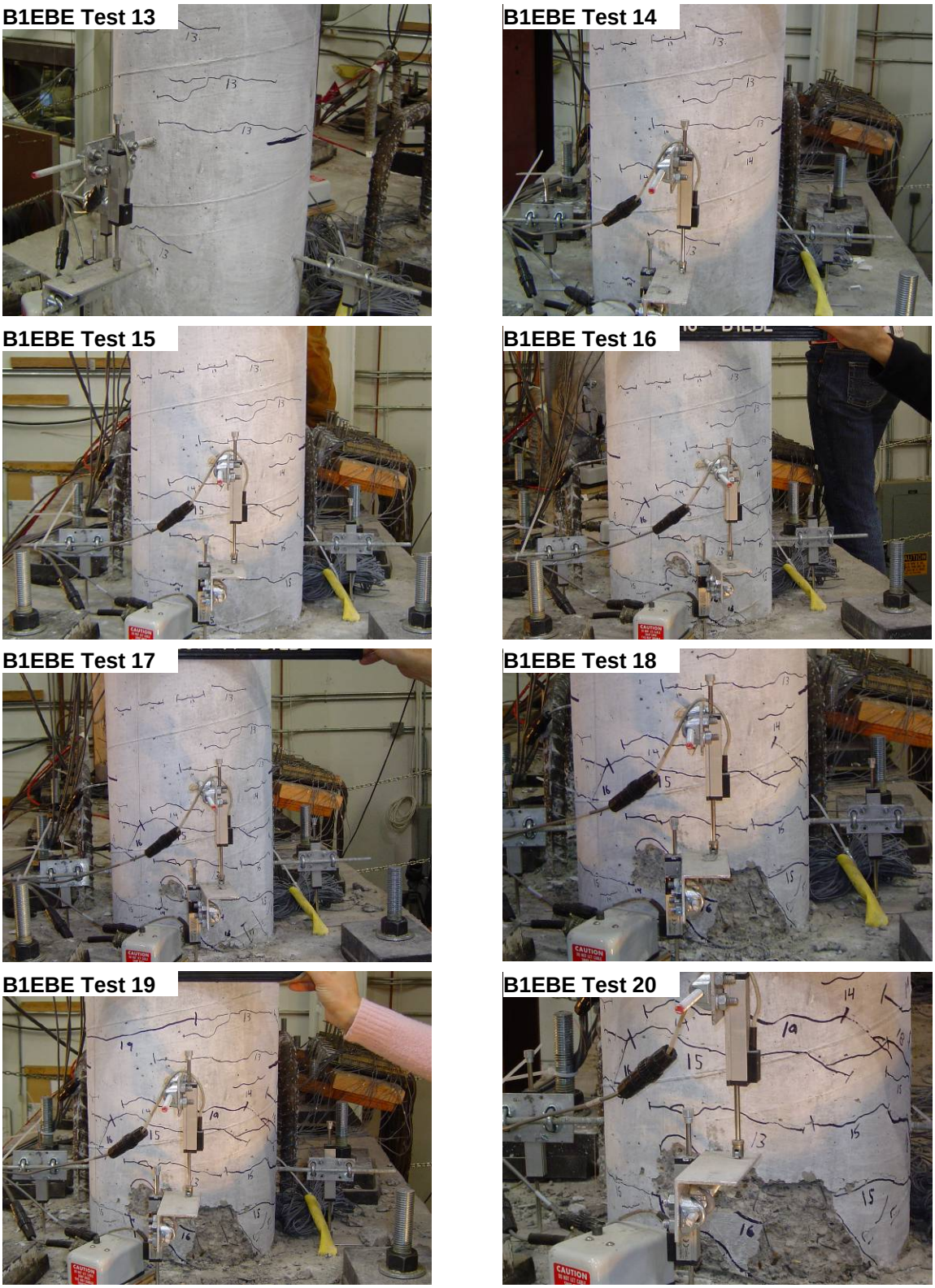

Figure 6-2: Photographs of damage progression for bent 1, east column bottom east side, through test 20.

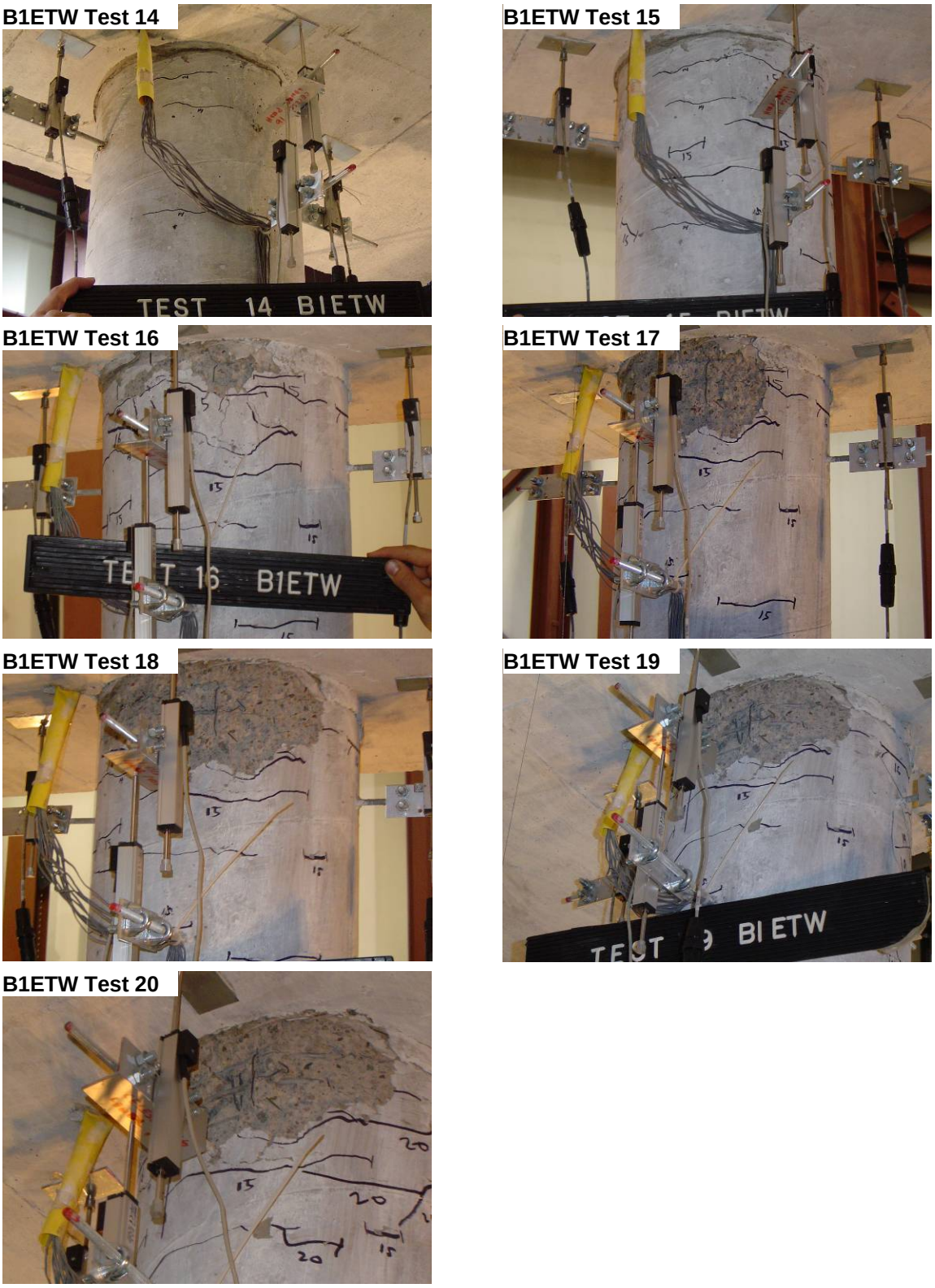

Figure 6-3: Photographs of damage progression for bent 1, east column top west side, through test 20.

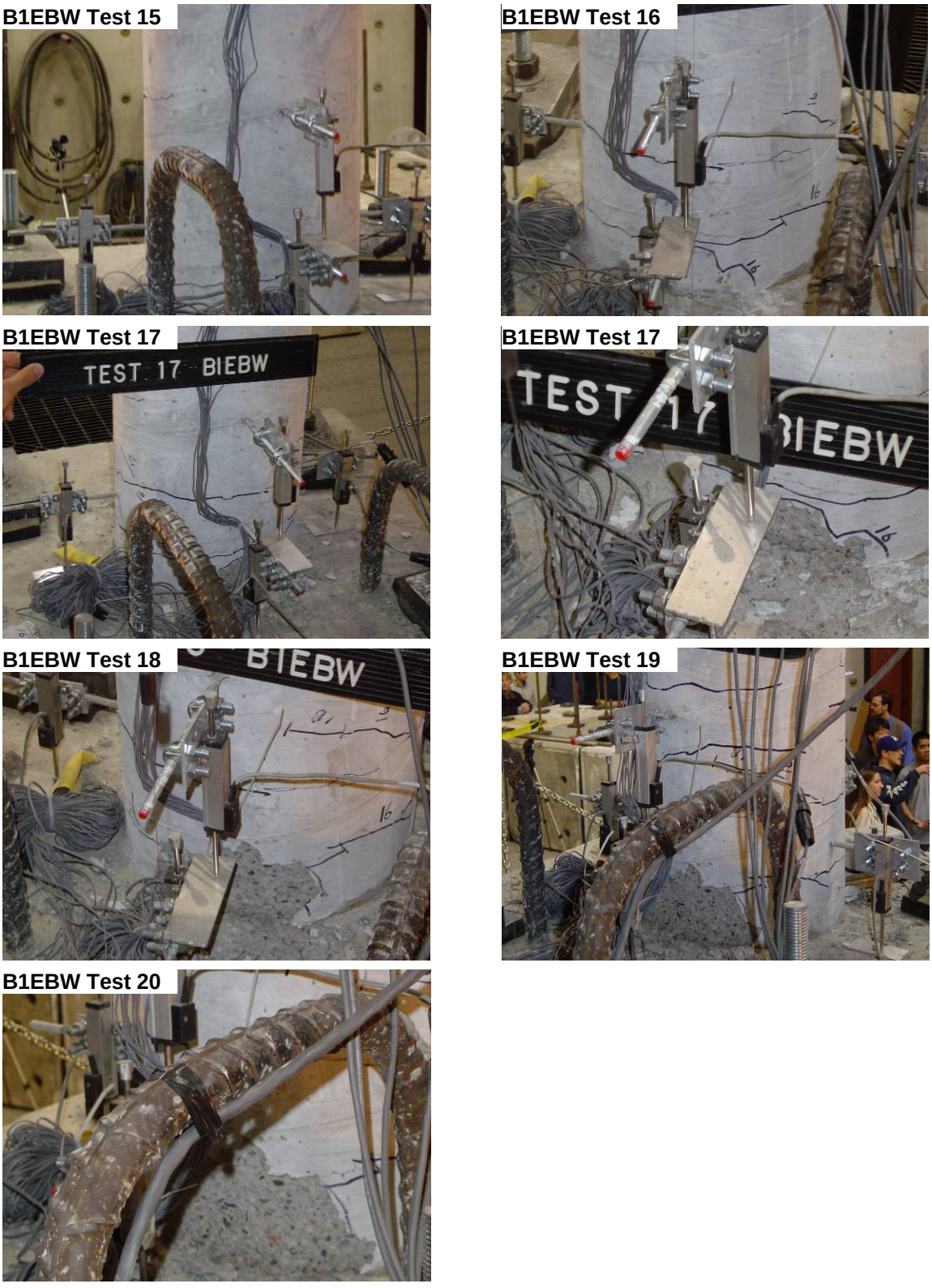

Figure 6-4: Photographs of damage progression for bent 1, east column bottom west side, through test 20.

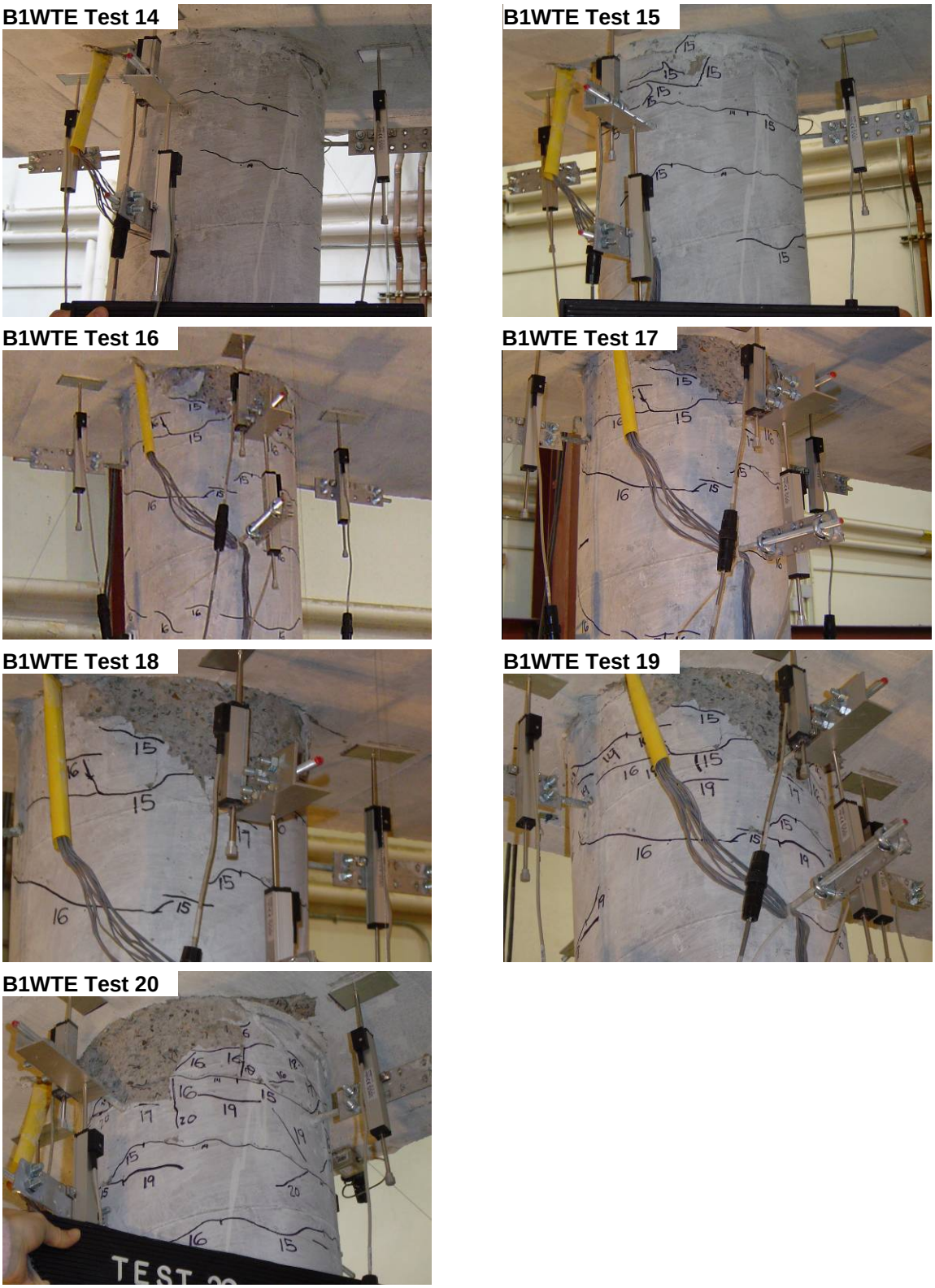

Figure 6-5: Photographs of damage progression for bent 1, west column top east side, through test 20.

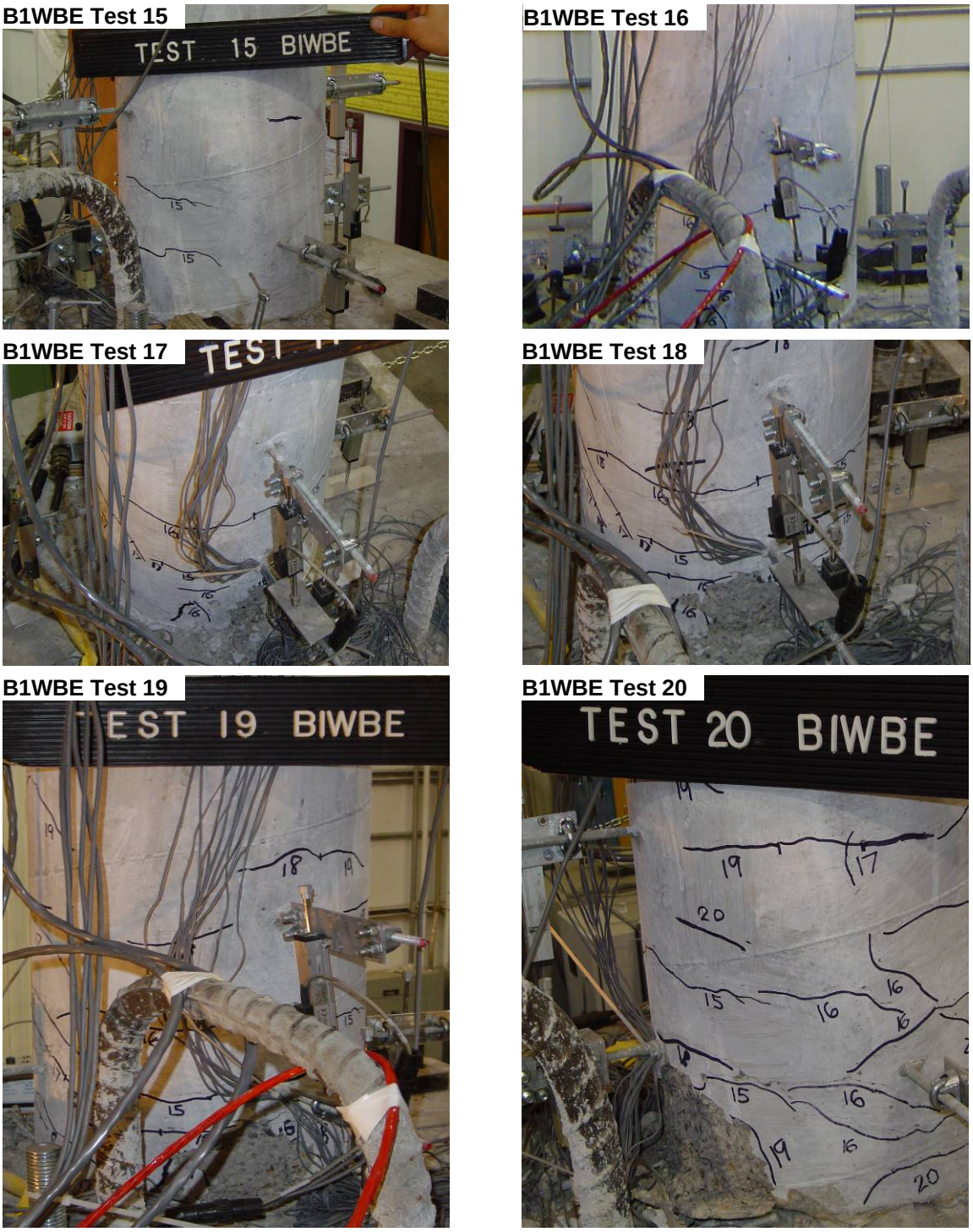

Figure 6-6: Photographs of damage progression for bent 1, west column bottom east side, through test 20.

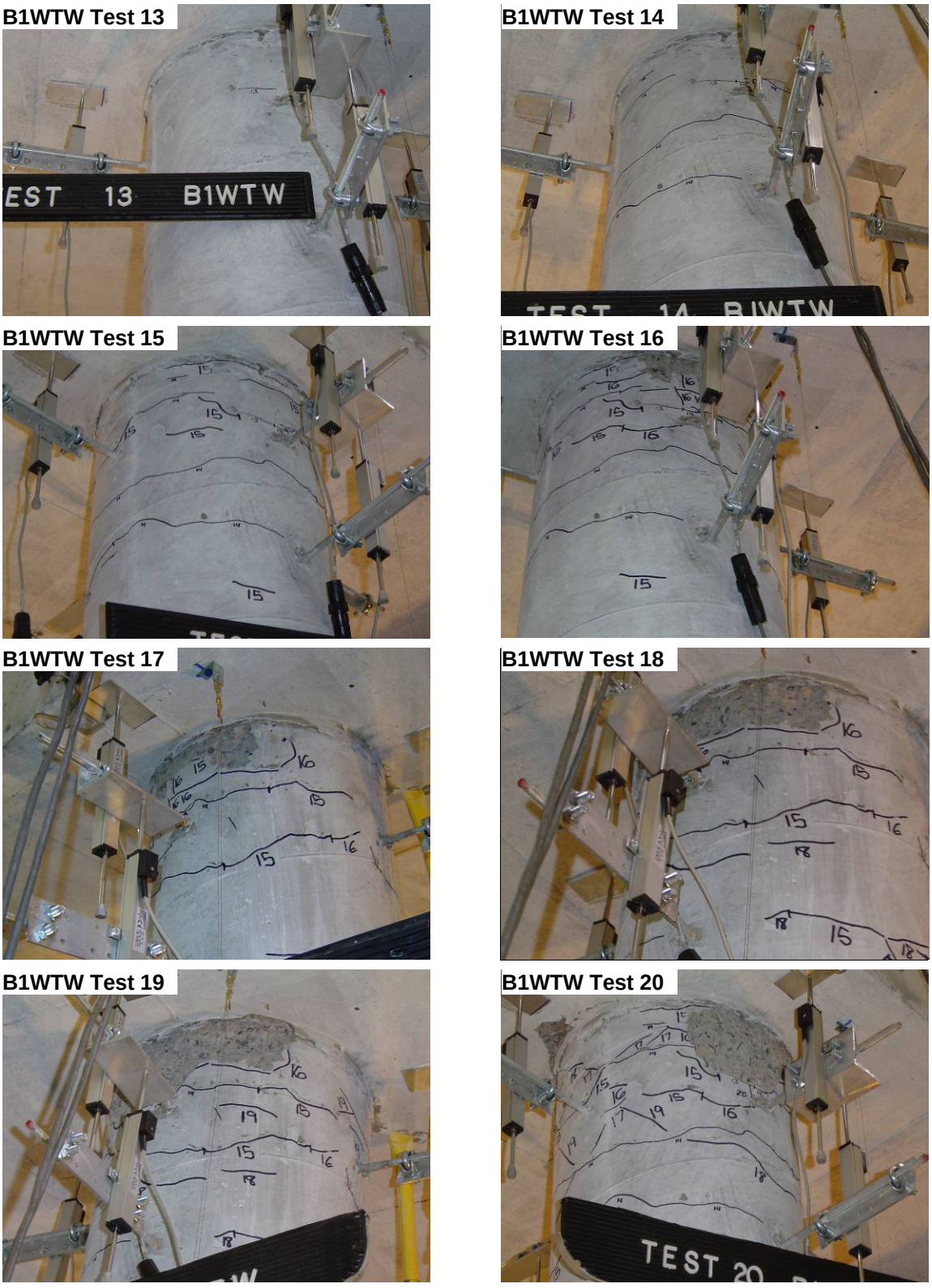

Figure 6-7: Photographs of damage progression for bent 1, west column top west side, through test 20.

B1WBW Test 14

B1WBW Test 15

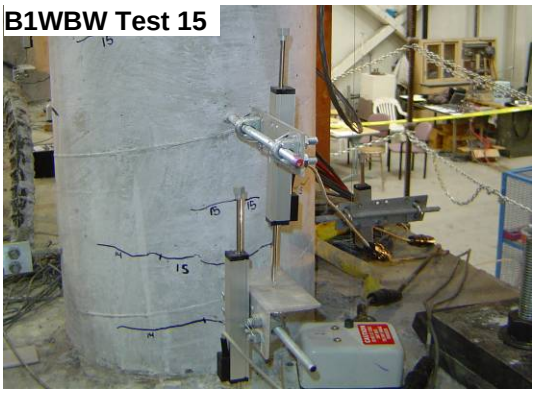

B1WBW Test 16

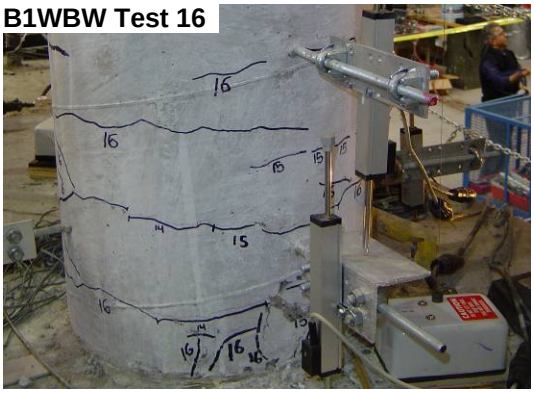

B1WBW Test 17

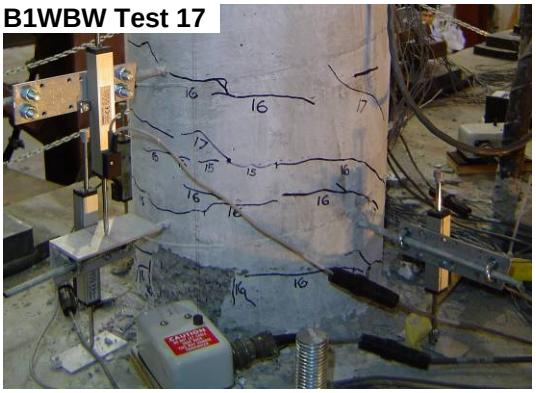

B1WBW Test 18

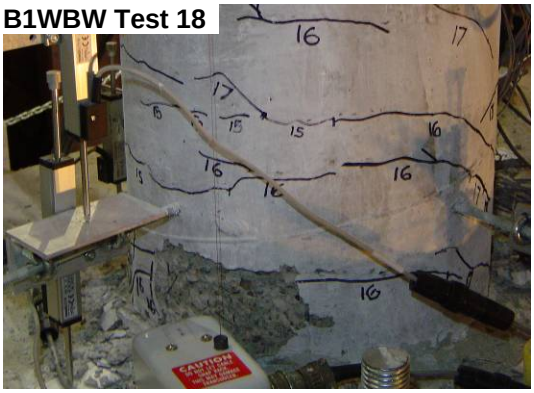

B1WBW Test 19

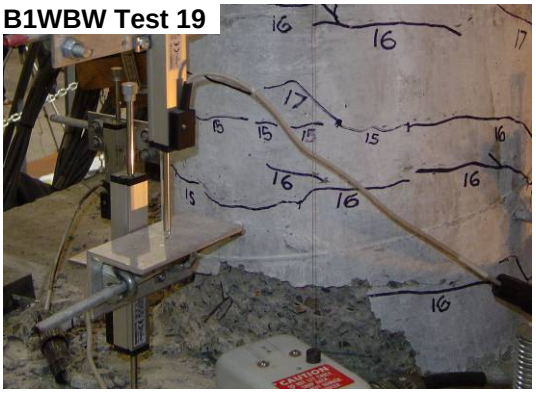

B1WBW Test 20

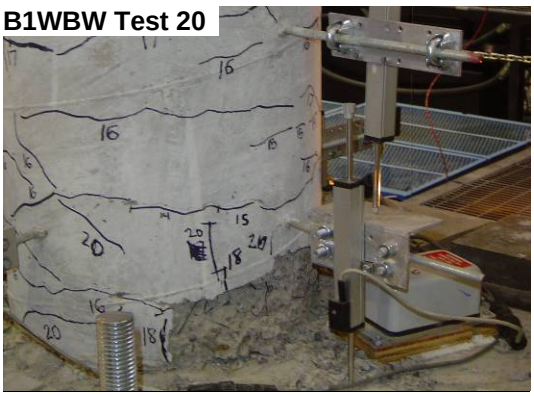

Figure 6-8: Photographs of damage progression for bent 1, west column bottom west side, through test 20.

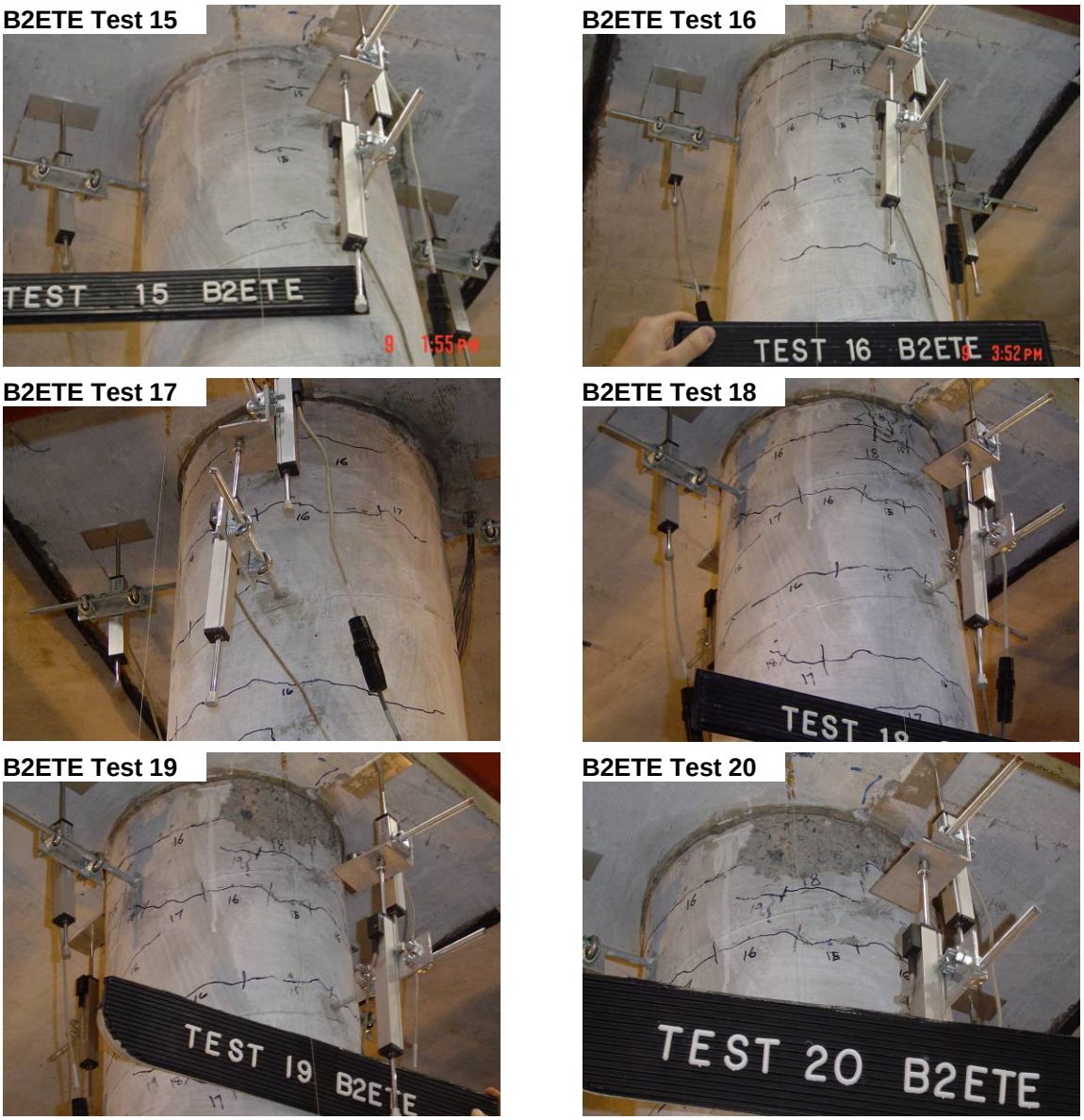

Figure 6-9: Photographs of damage progression for bent 2, east column top east side, through test 20.

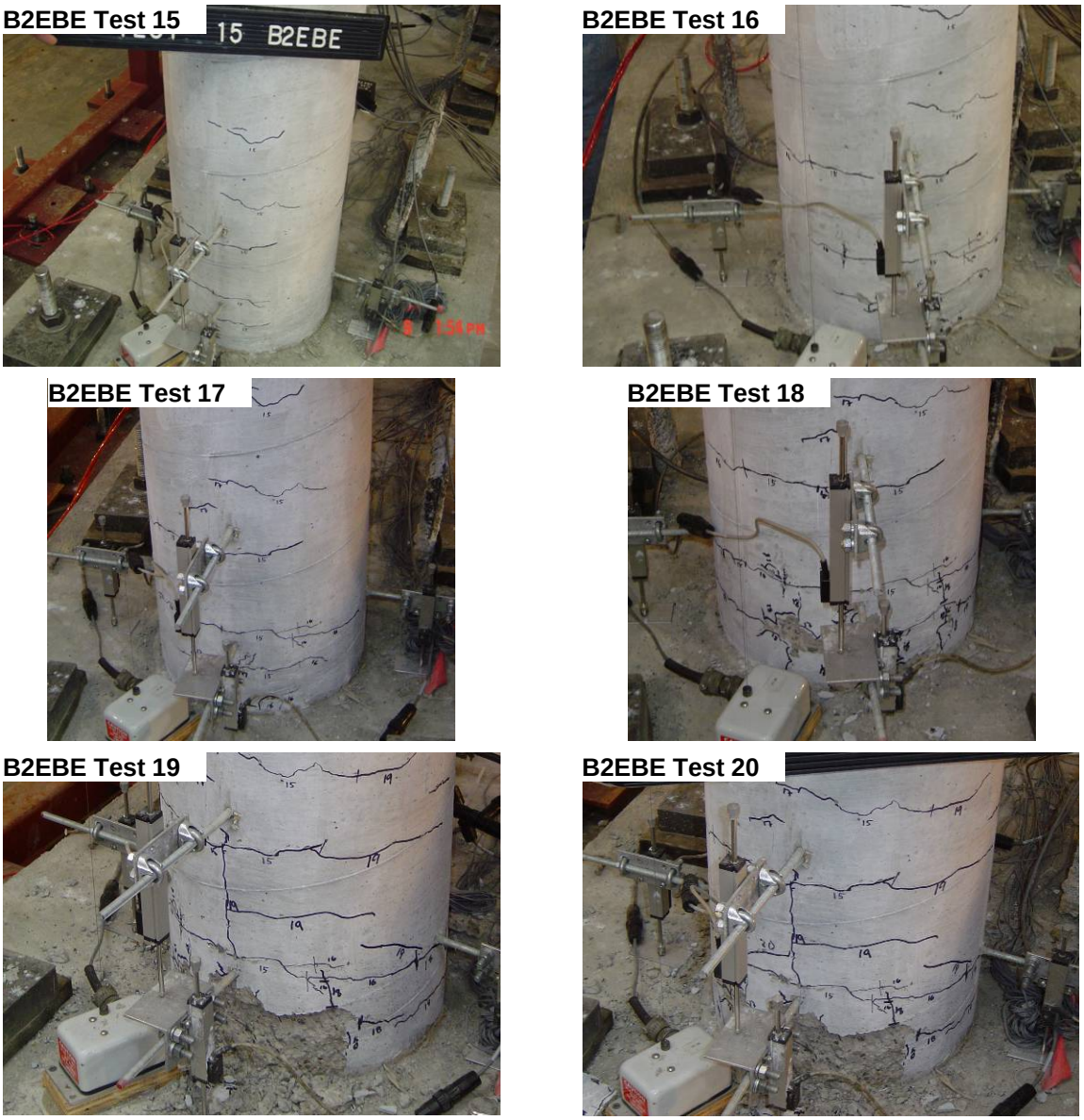

Figure 6-10: Photographs of damage progression for bent 2, east column bottom east side, through test 20.

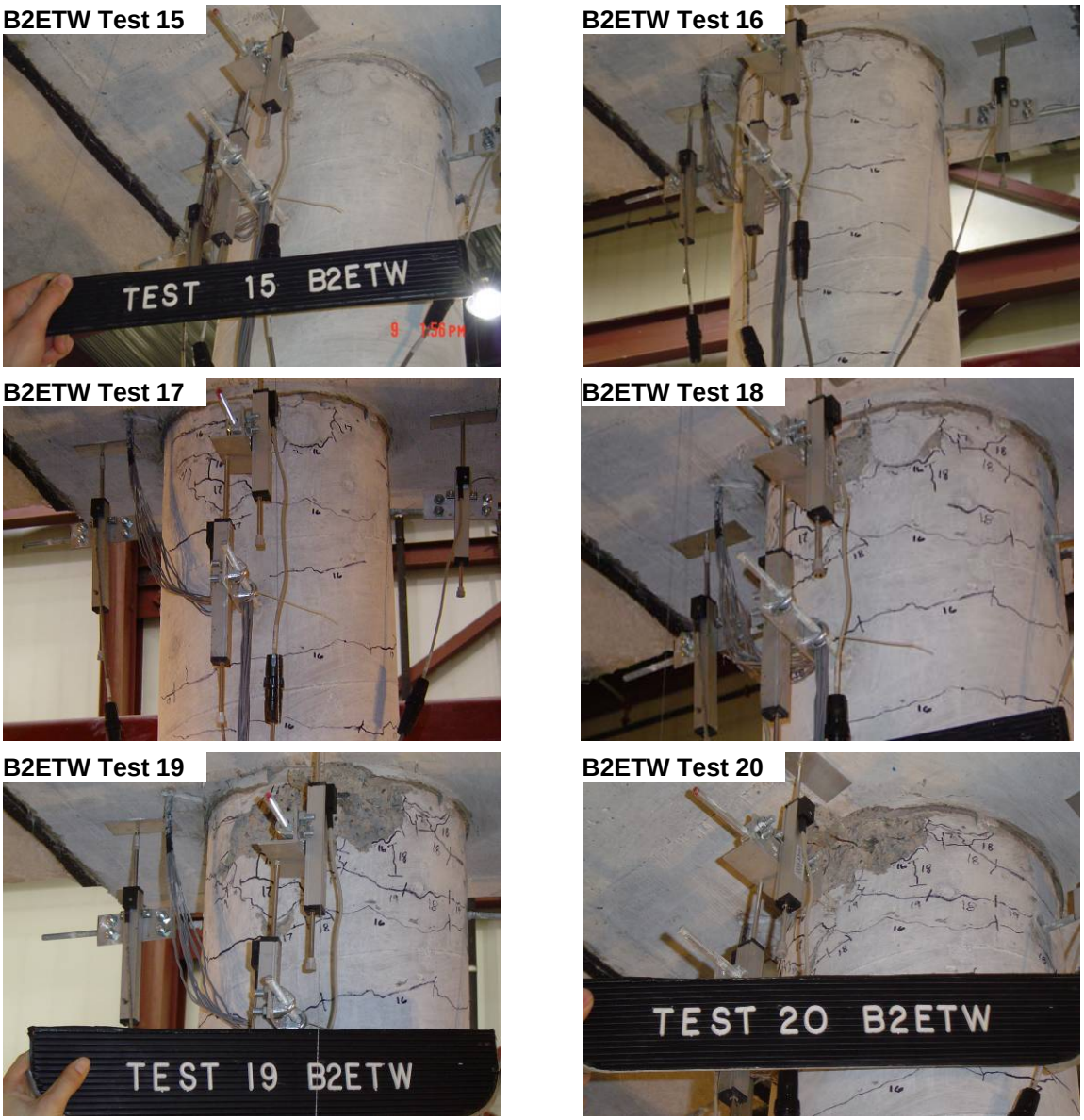

Figure 6-11: Photographs of damage progression for bent 2, east column top west side, through test 20.

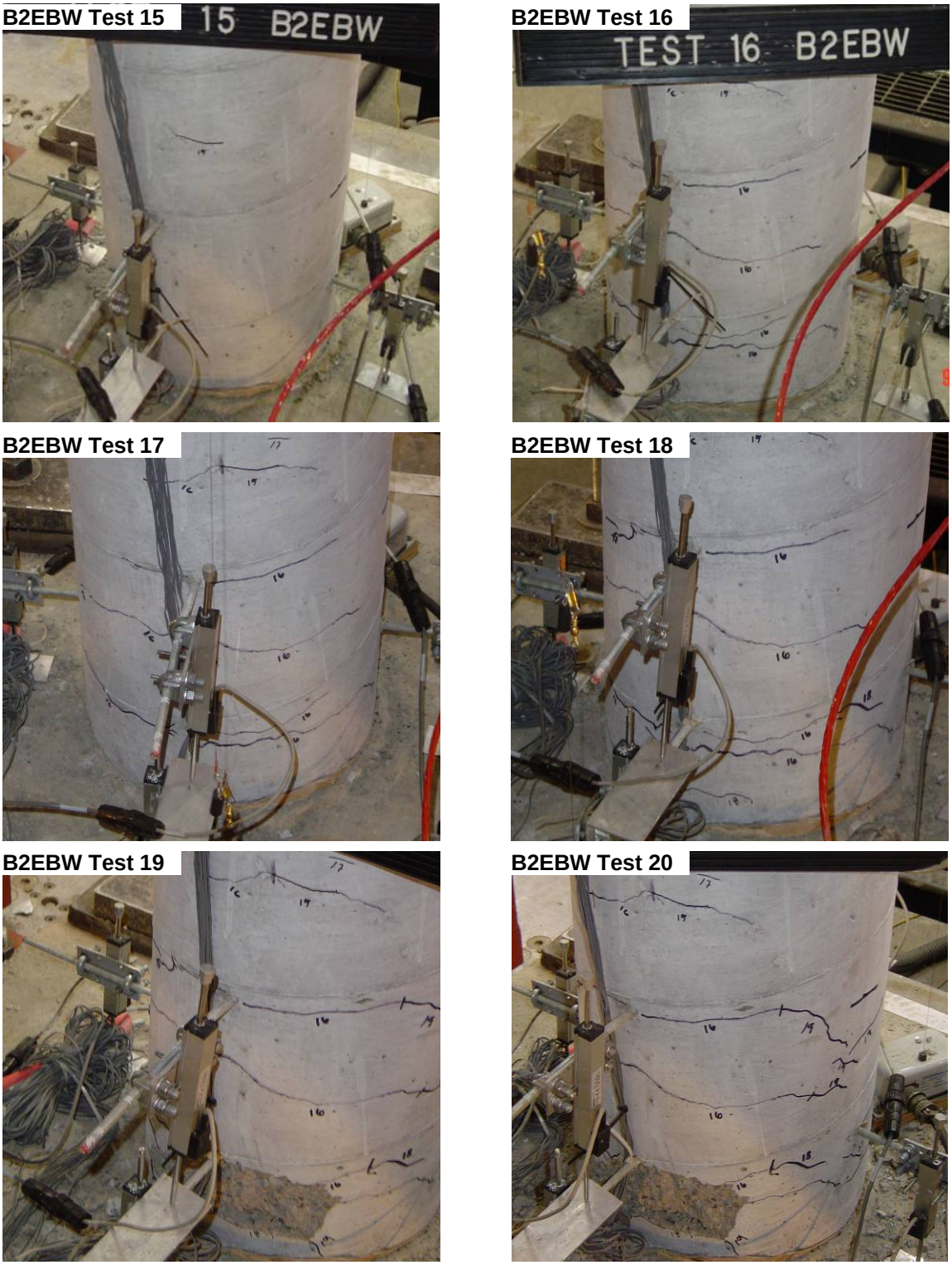

Figure 6-12: Photographs of damage progression for bent 2, east column bottom west side, through test 20.

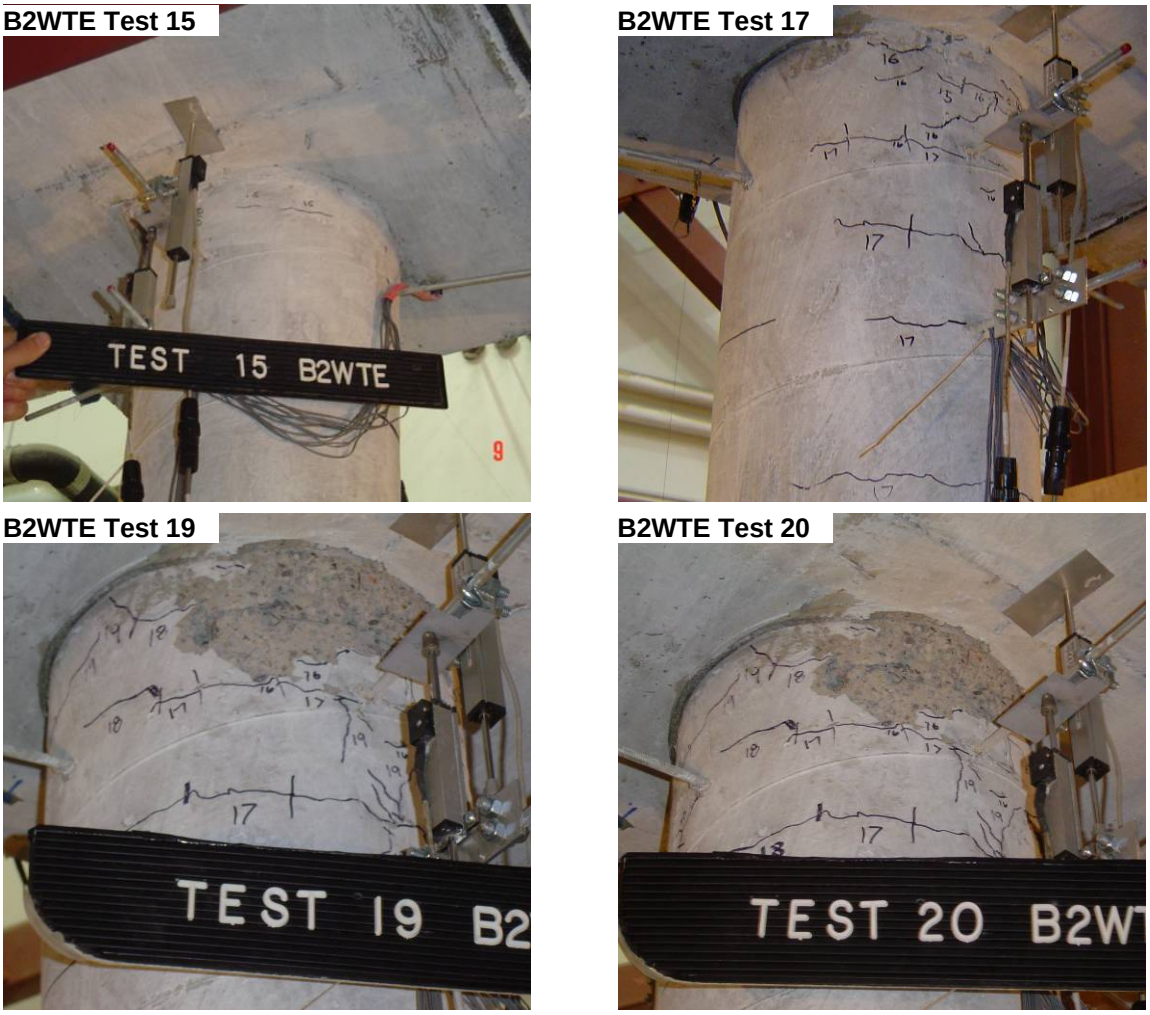

Figure 6-13: Photographs of damage progression for bent 2, west column top east side, through test 20.

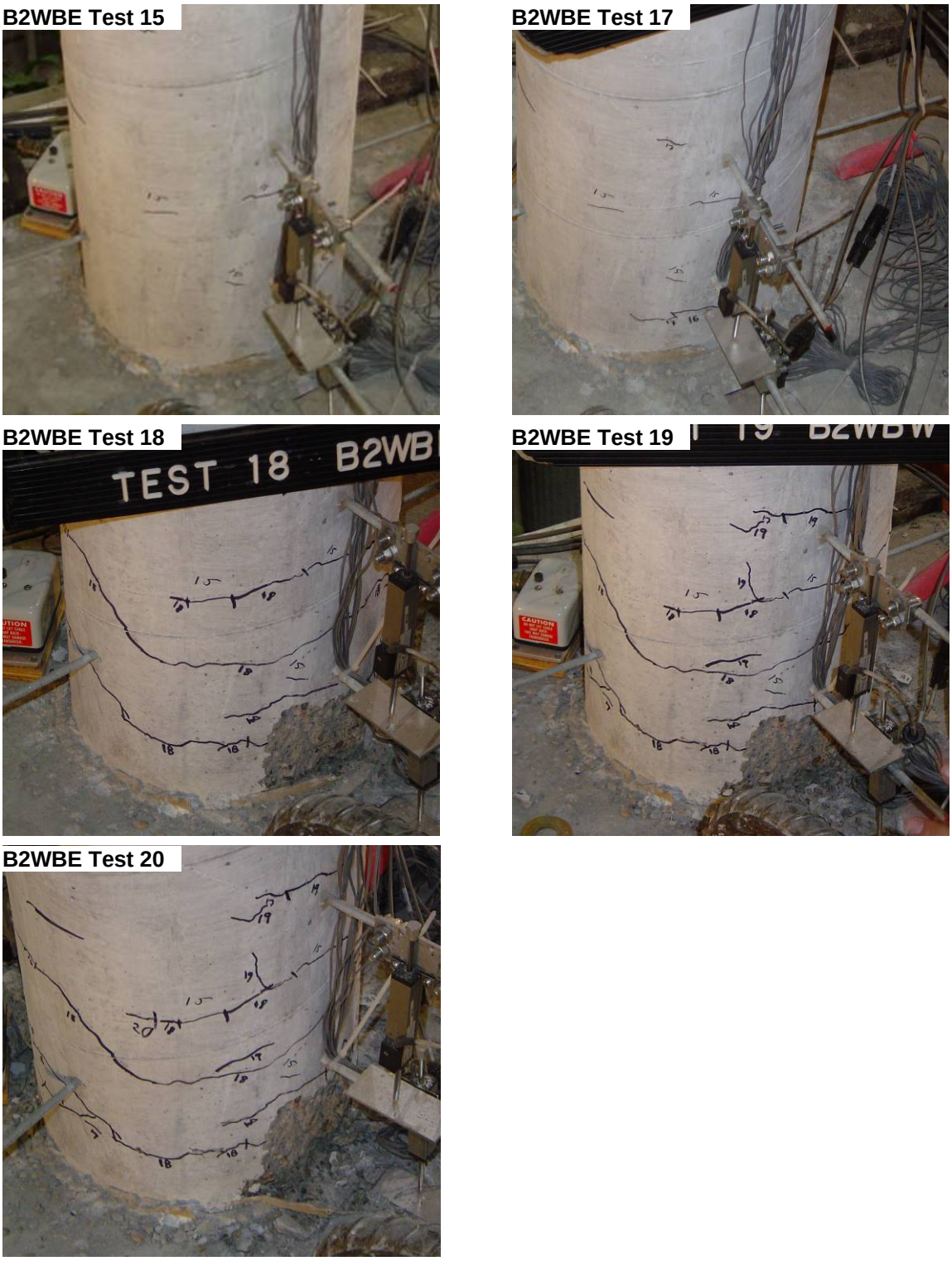

Figure 6-14: Photographs of damage progression for bent 2, west column bottom east side, through test 20.

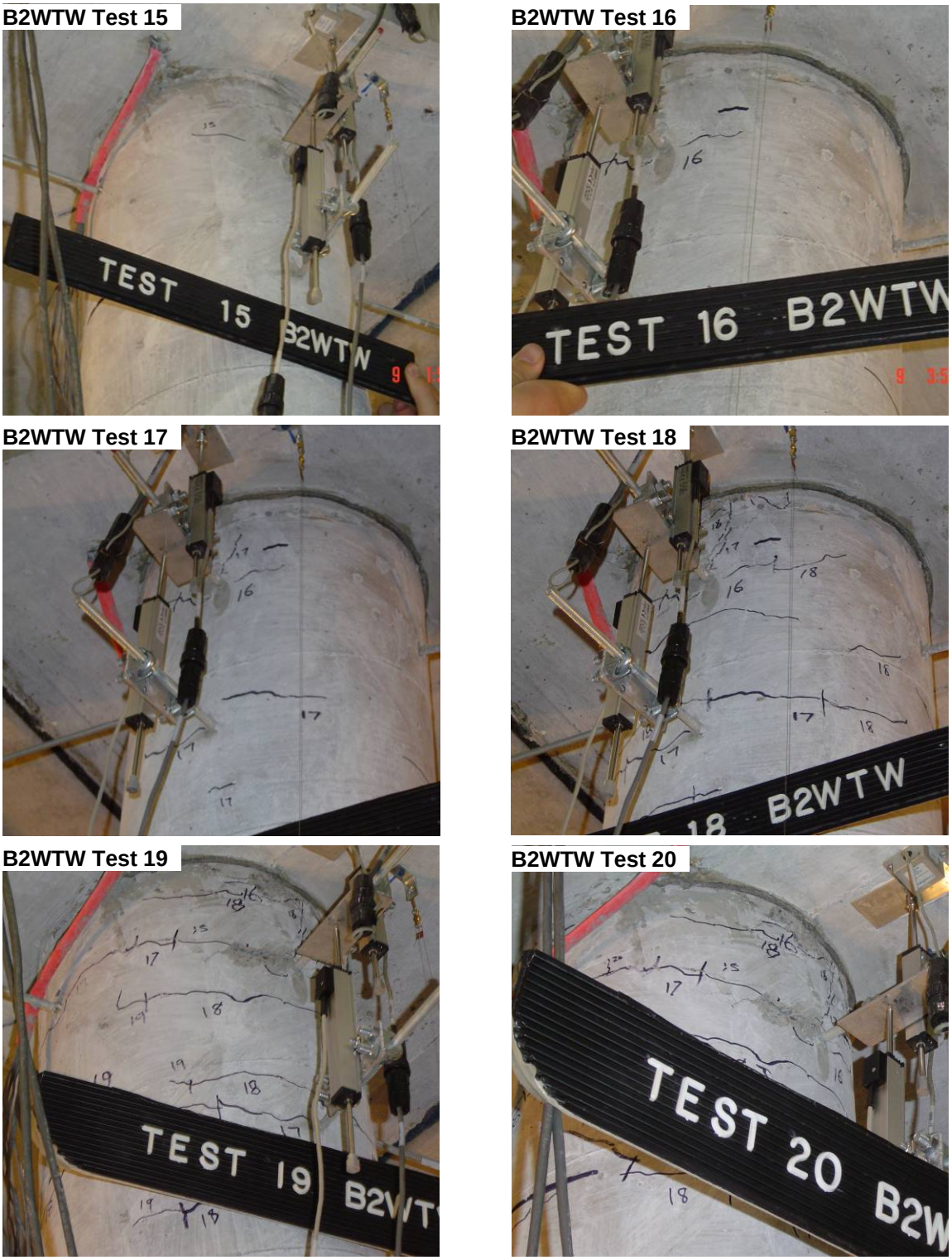

Figure 6-15: Photographs of damage progression for bent 2, west column top west side, through test 20.

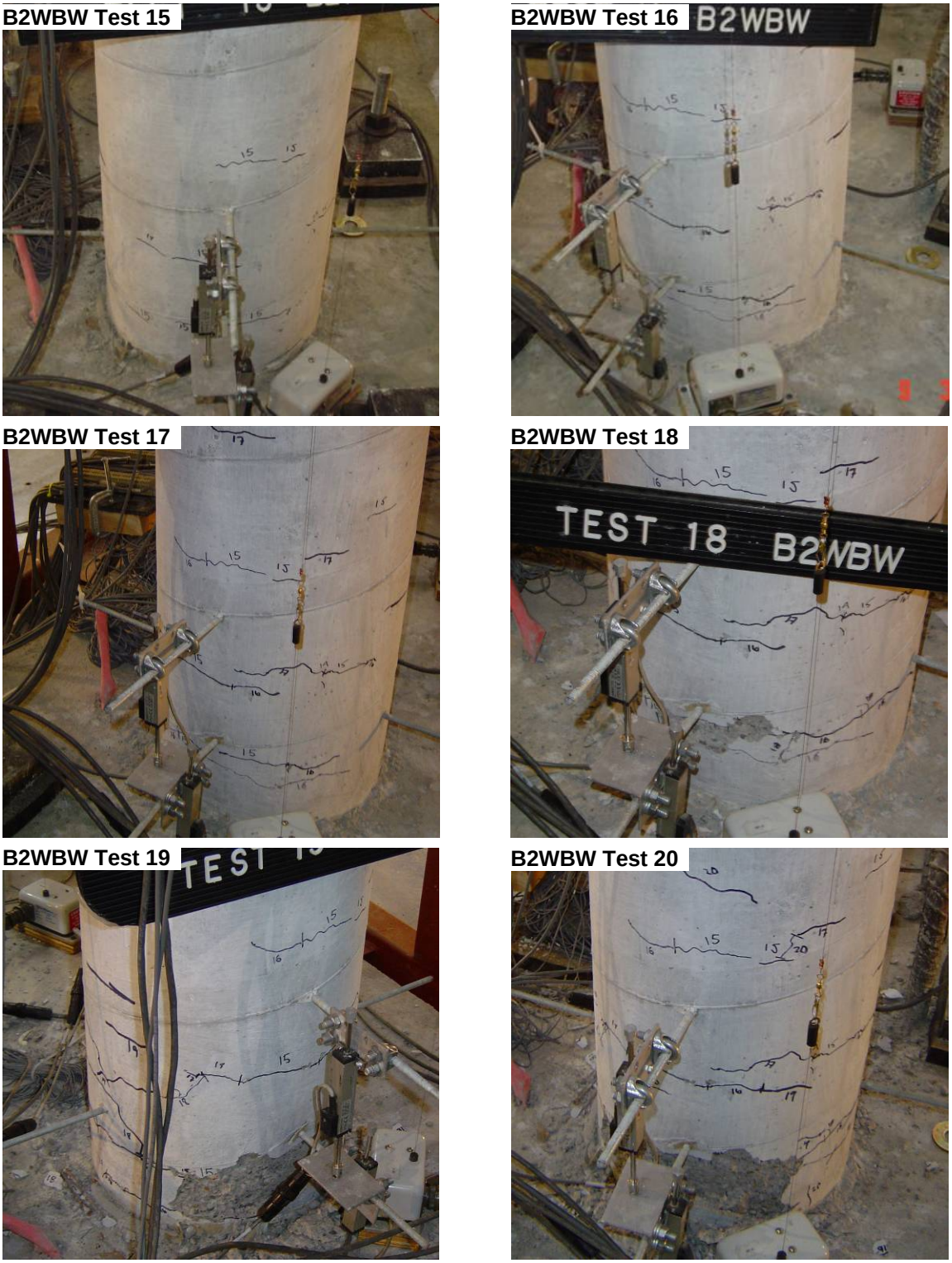

Figure 6-16: Photographs of damage progression for bent 2, west column bottom west side, through test 20.

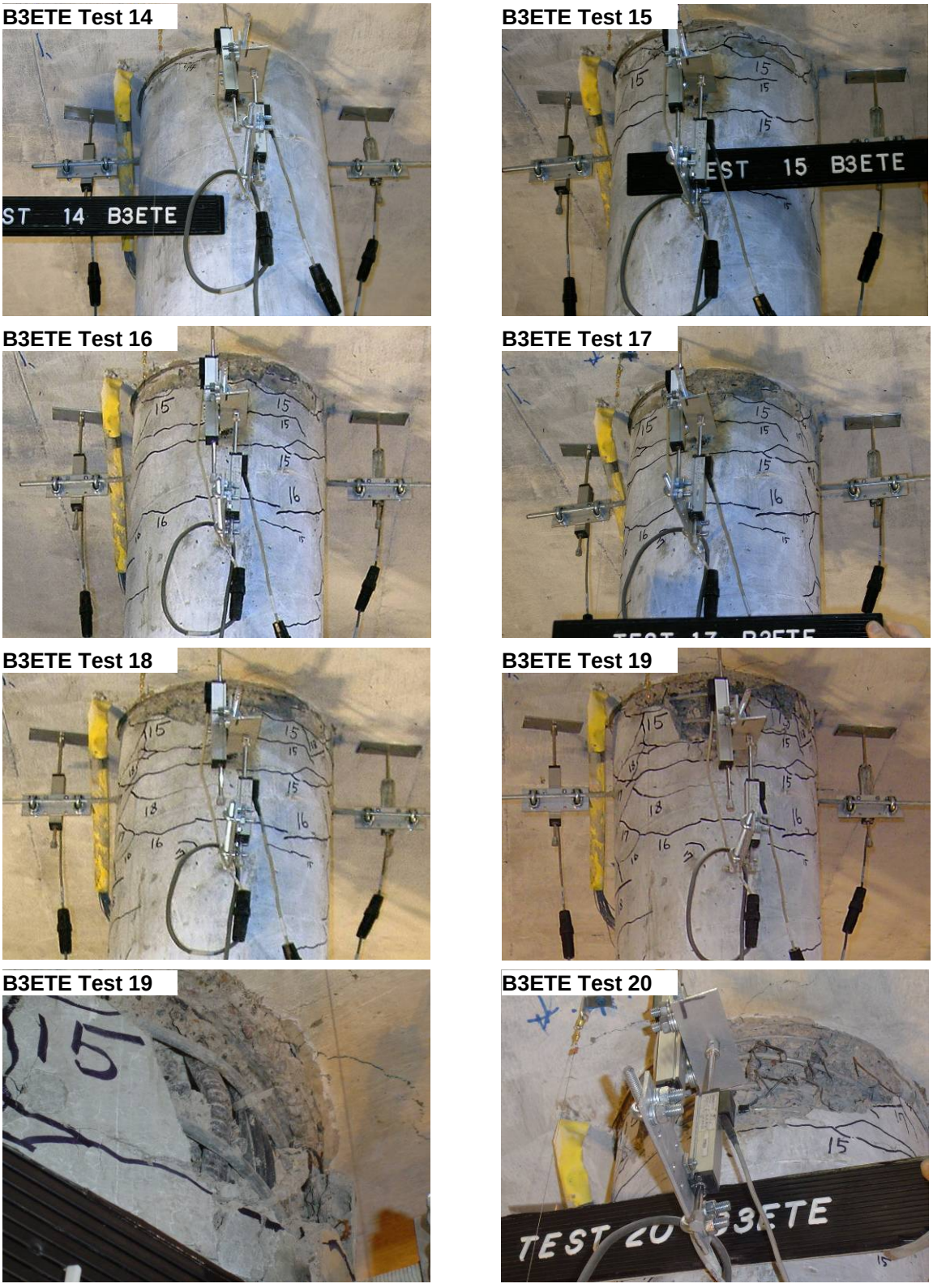

Figure 6-17: Photographs of damage progression for bent 3, east column top east side, through test 20.

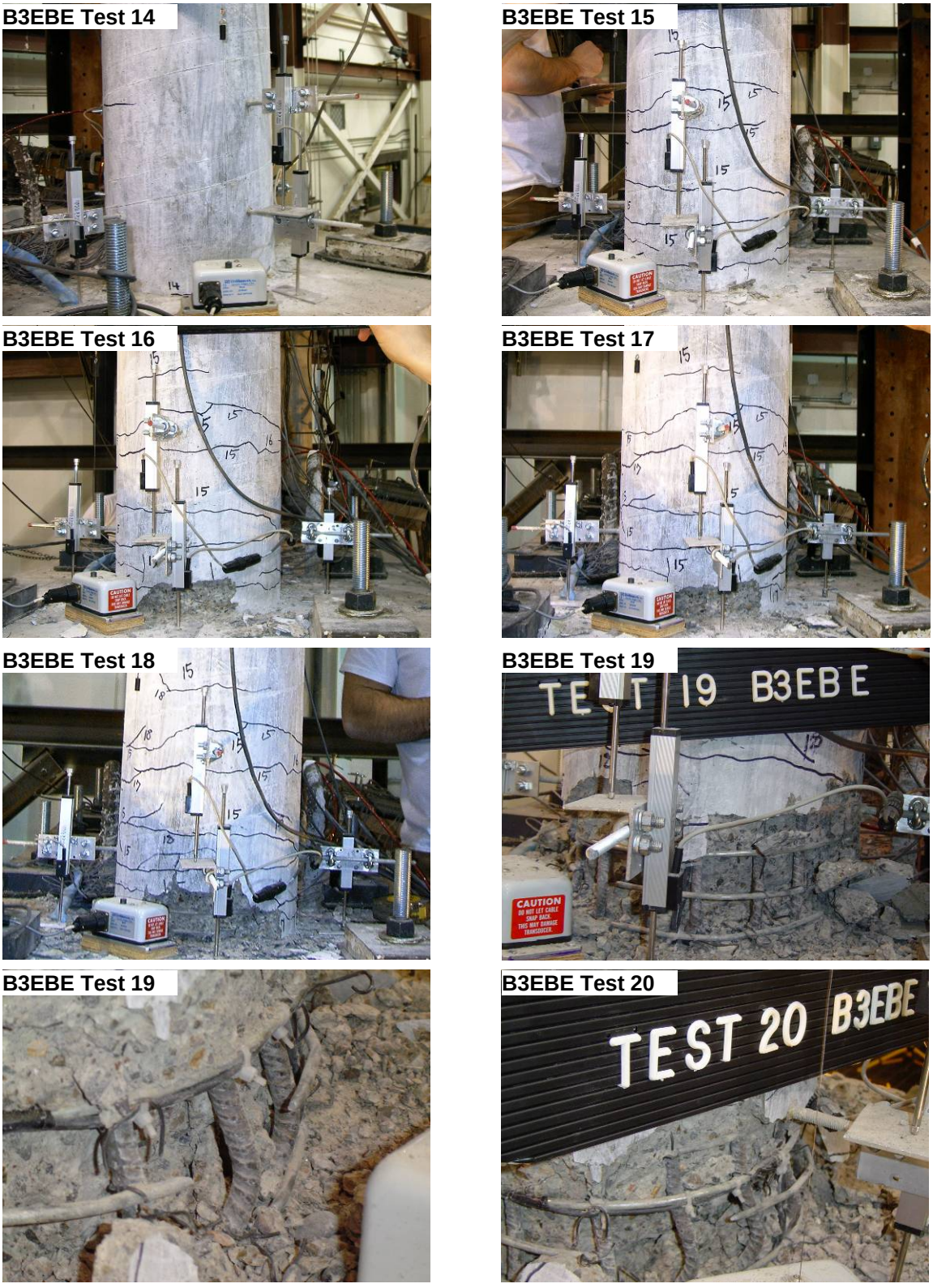

Figure 6-18: Photographs of damage progression for bent 3, east column bottom east side, through test 20.

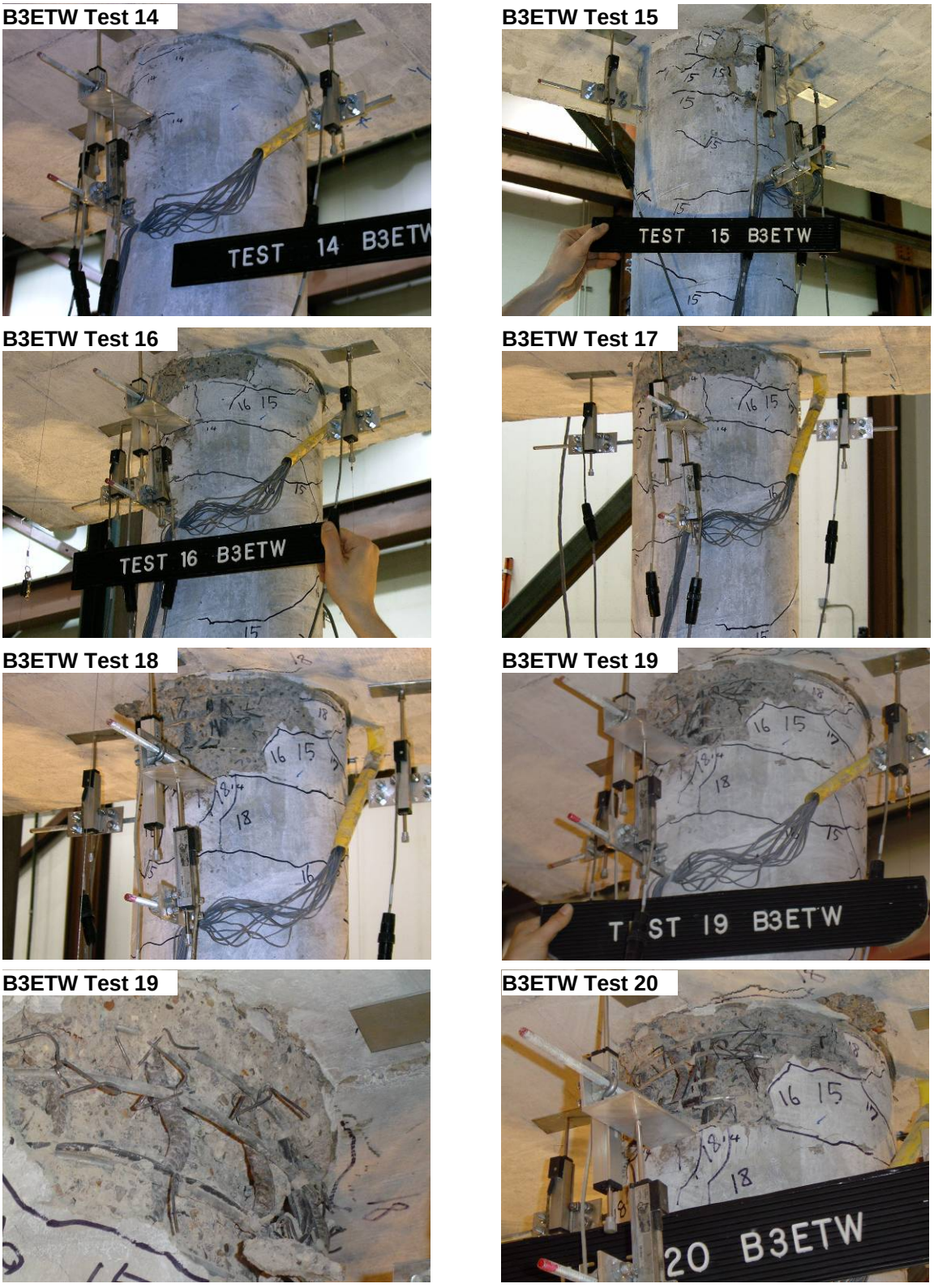

Figure 6-19: Photographs of damage progression for bent 3, east column top west side, through test 20.

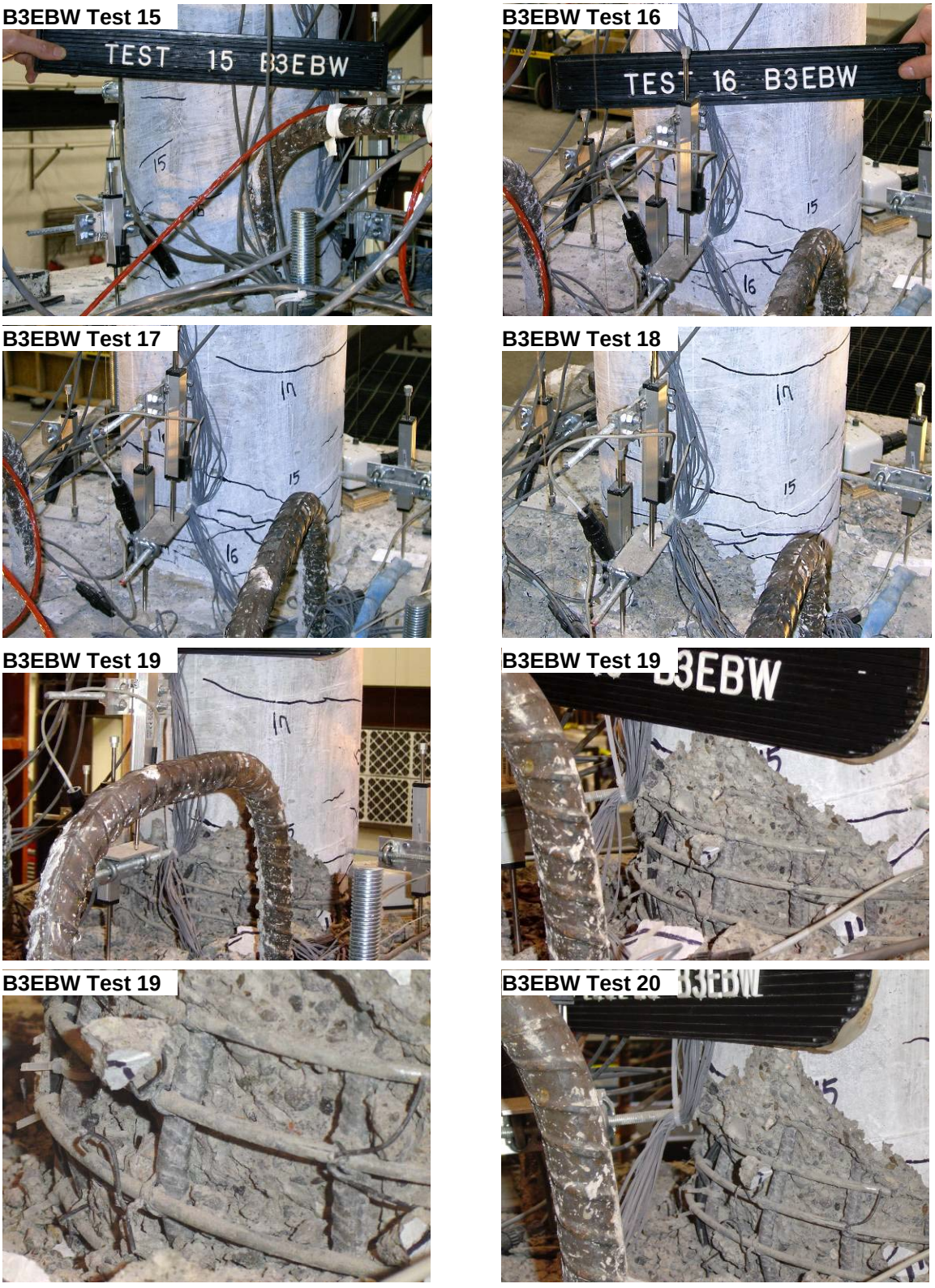

Figure 6-20: Photographs of damage progression for bent 3, east column bottom west side, through test 20.

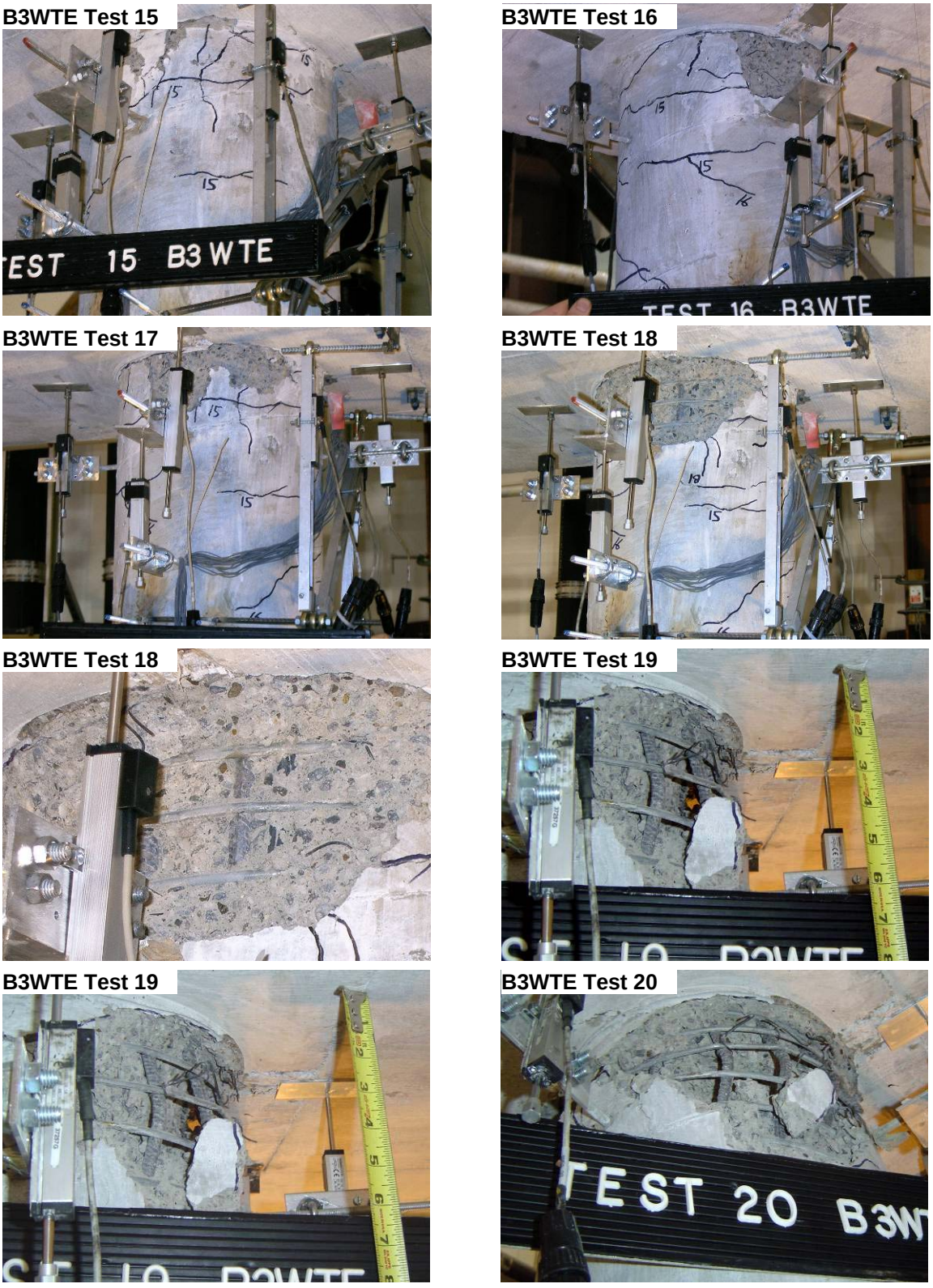

Figure 6-21: Photographs of damage progression for bent 3, west column top east side, through test 20.

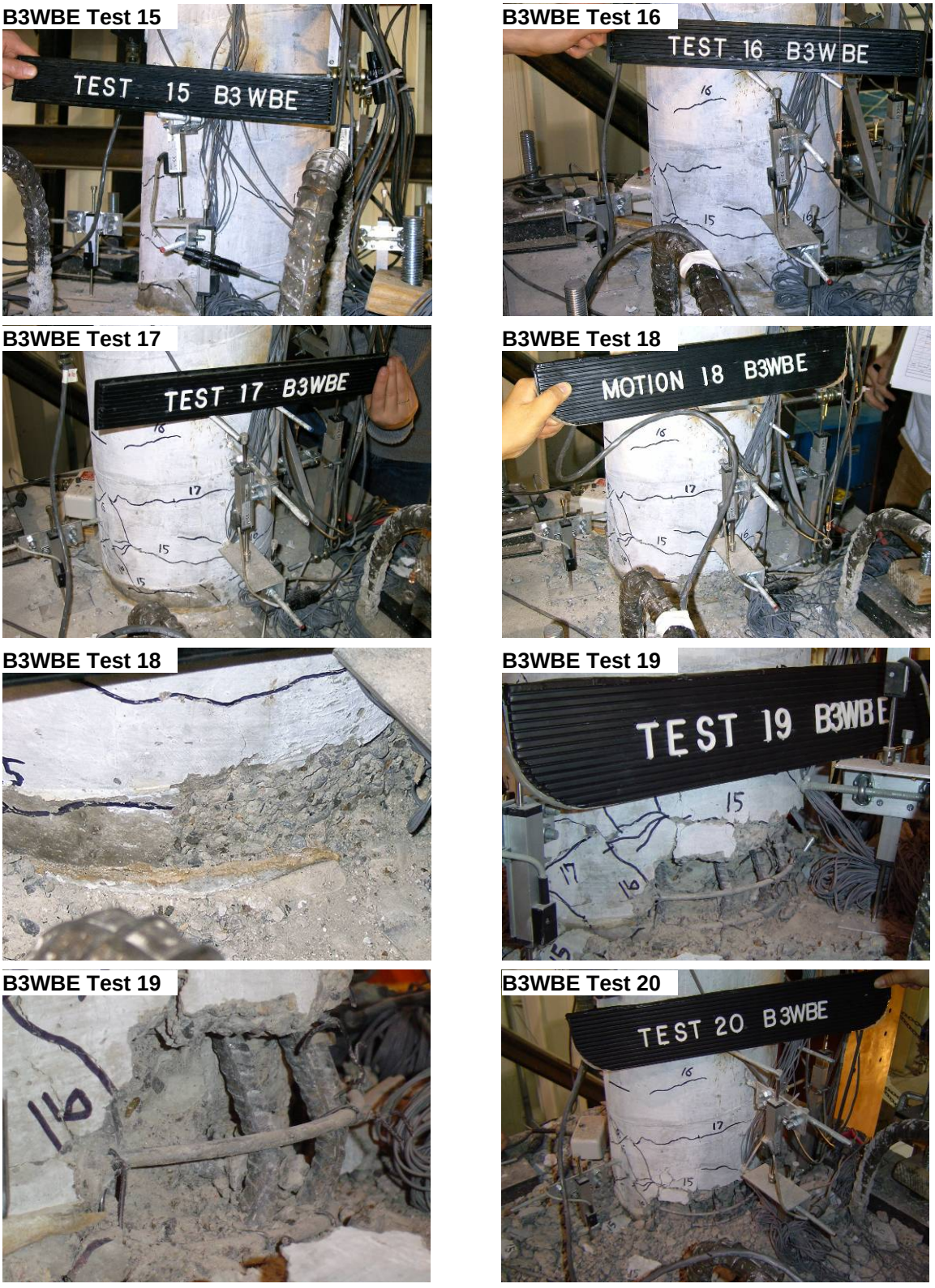

Figure 6-22: Photographs of damage progression for bent 3, west column bottom east side, through test 20.

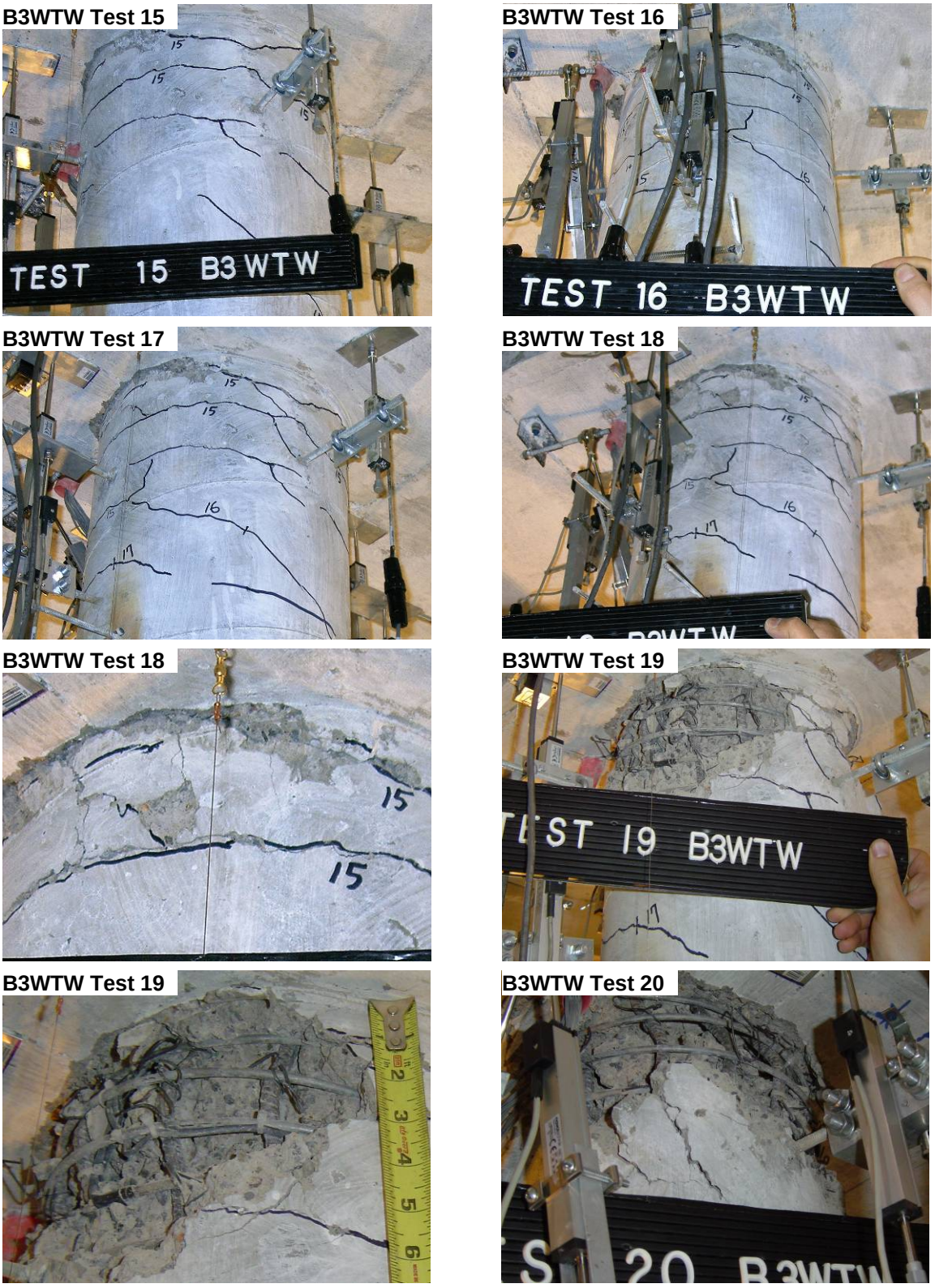

Figure 6-23: Photographs of damage progression for bent 3, west column top west side, through test 20.

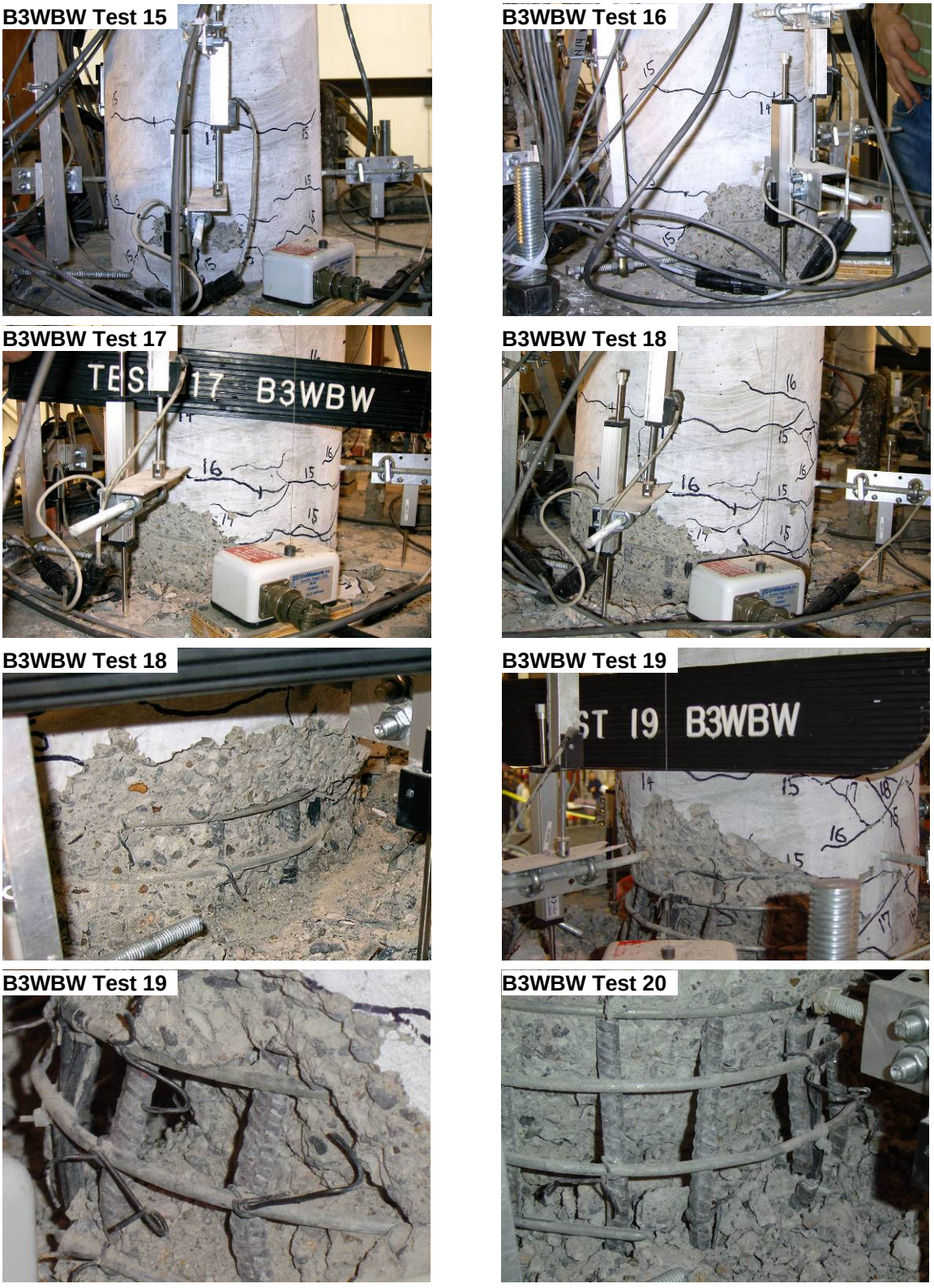

Figure 6-24: Photographs of damage progression for bent 3, west column bottom west side, through test 20.

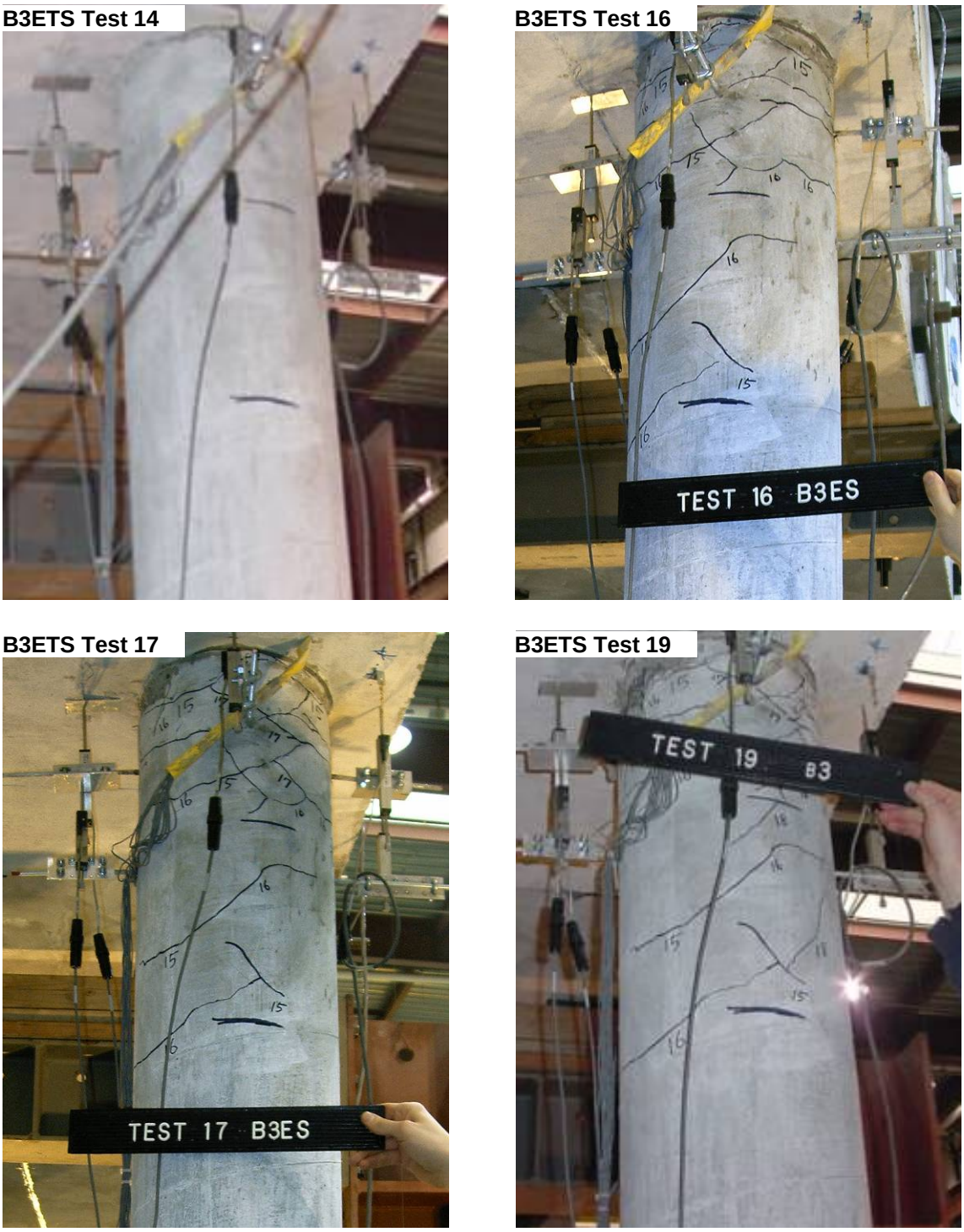

Figure 6-25: Photographs of shear crack progression for bent 3, east column top south side, through test 19.

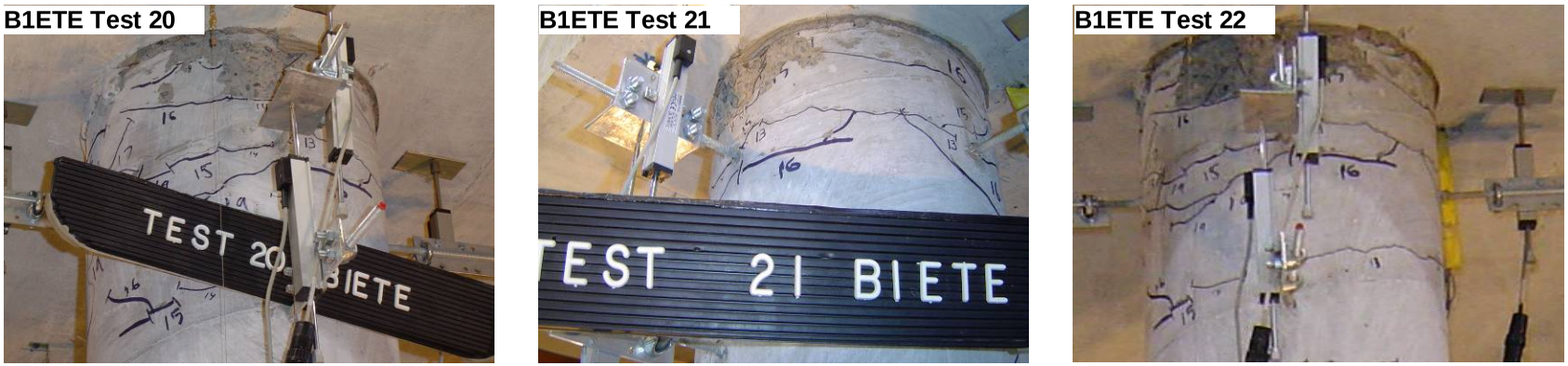

Figure 6-26: Photographs damage progression for bent 1, east column top east side, for tests 20-22.

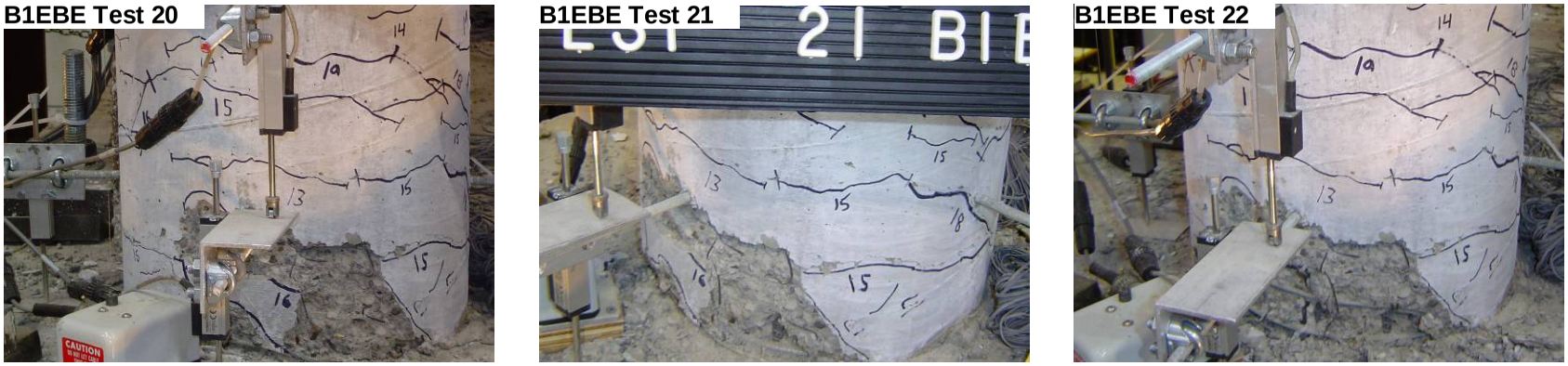

Figure 6-27: Photographs damage progression for bent 1, east column bottom east side, for tests 20-22.

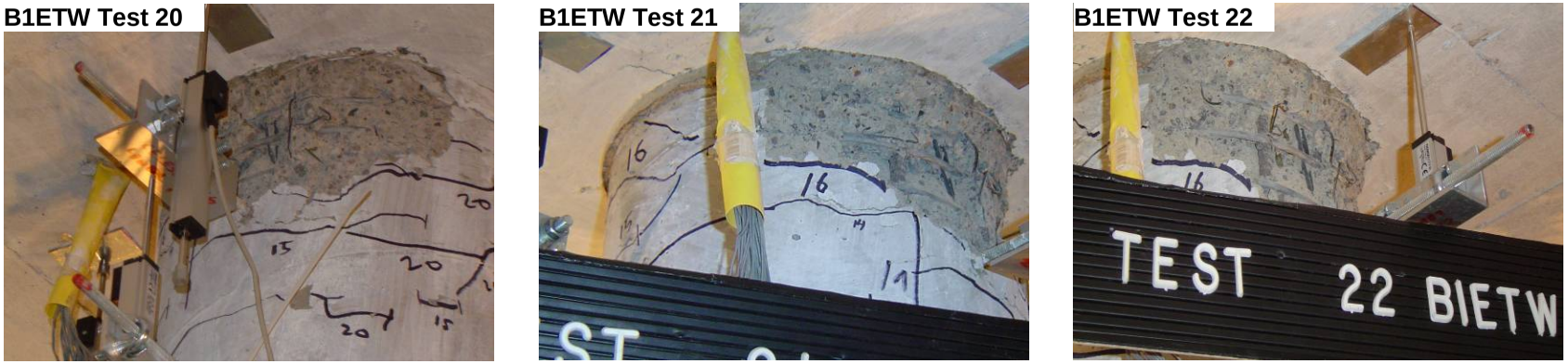

Figure 6-28: Photographs damage progression for bent 1, east column top west side, for tests 20-22.

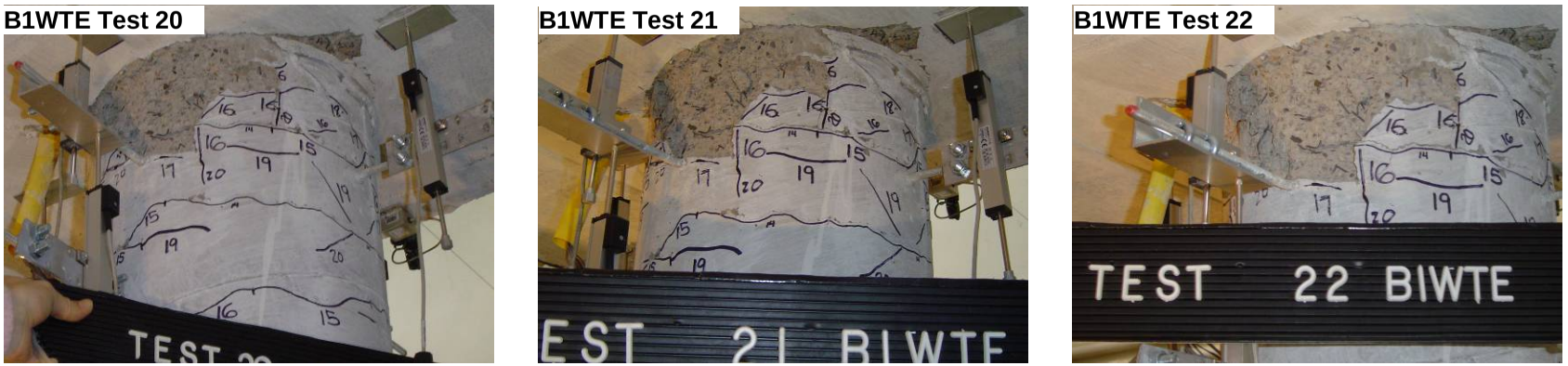

Figure 6-29: Photographs damage progression for bent 1, west column top east side, for tests 20-22.

Figure 6-30: Photographs damage progression for bent 2, east column top east side, for tests 20-22.

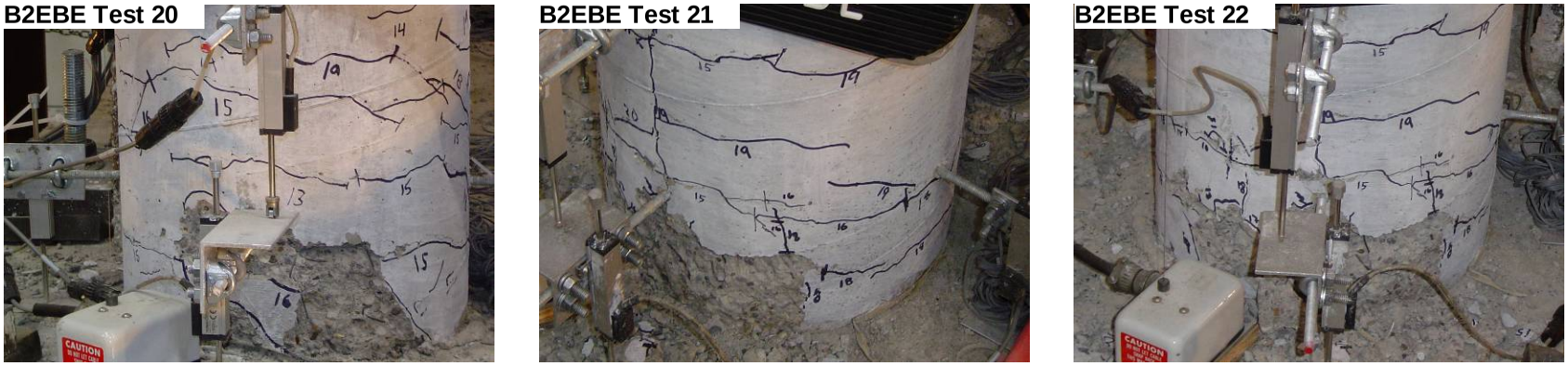

Figure 6-31: Photographs damage progression for bent 2, east column bottom east side, for tests 20-22.

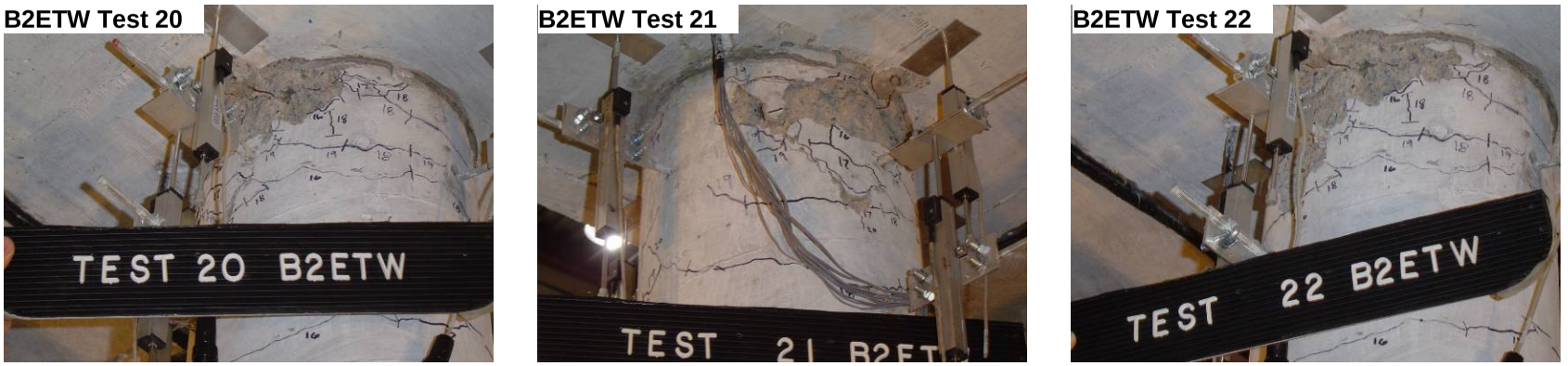

Figure 6-32: Photographs damage progression for bent 2, east column top west side, for tests 20-22.

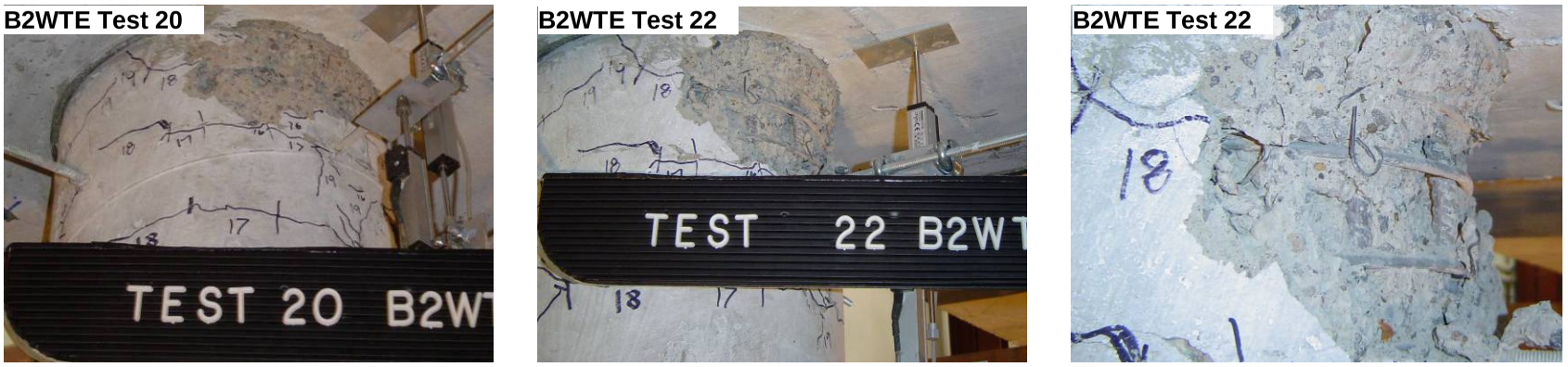

Figure 6-33: Photographs damage progression for bent 2, west column top east side, for tests 20-22.

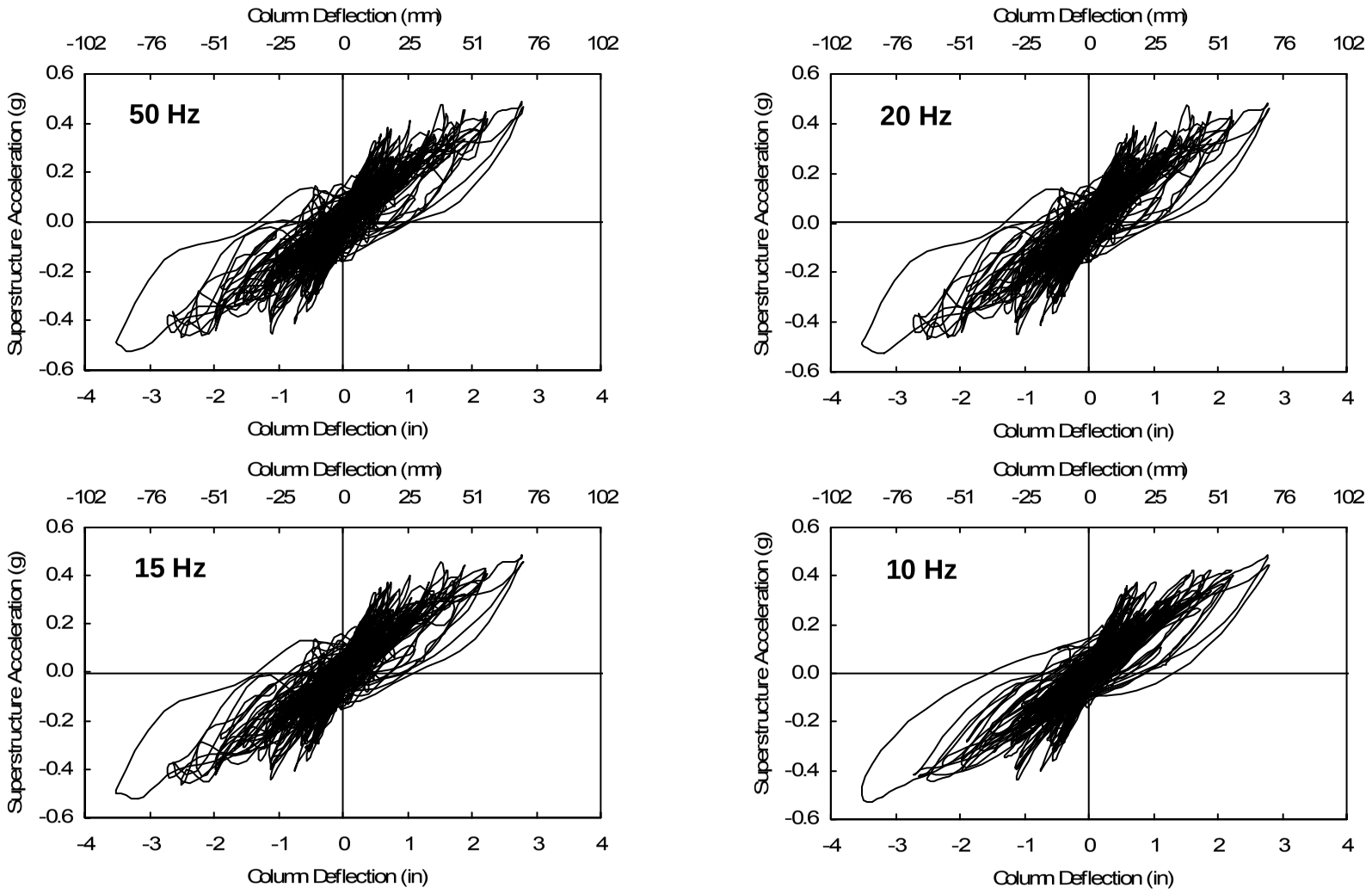

Figure 6-34: Bent 1 cumulative lateral acceleration vs. deflection hysteresis for high amplitude tests filtered at 50Hz, 20Hz, 15Hz, and 10Hz.

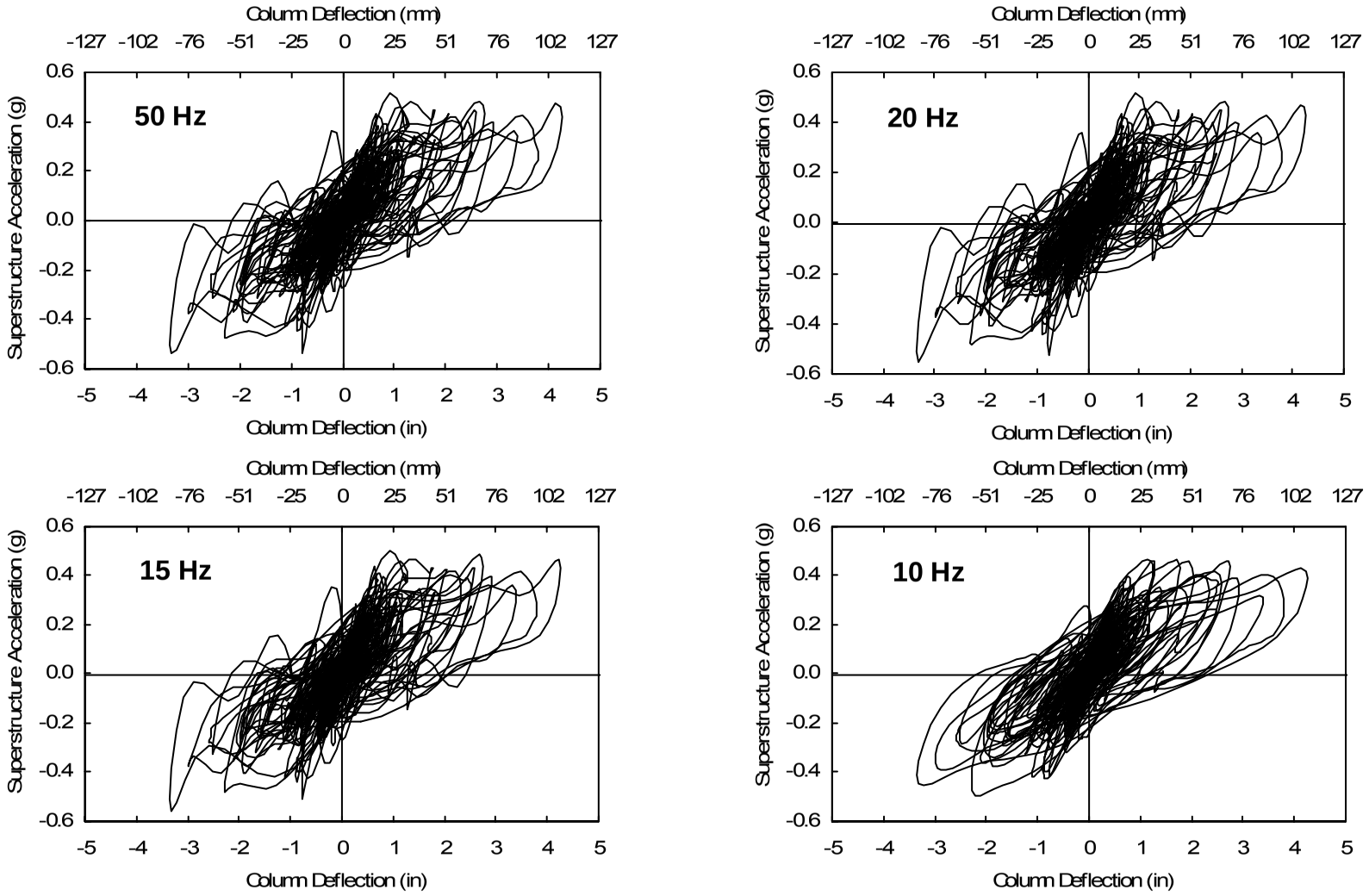

Figure 6-35: Bent 2 cumulative lateral acceleration vs. deflection hysteresis for high amplitude tests filtered at 50Hz, 20Hz, 15Hz, and 10Hz.

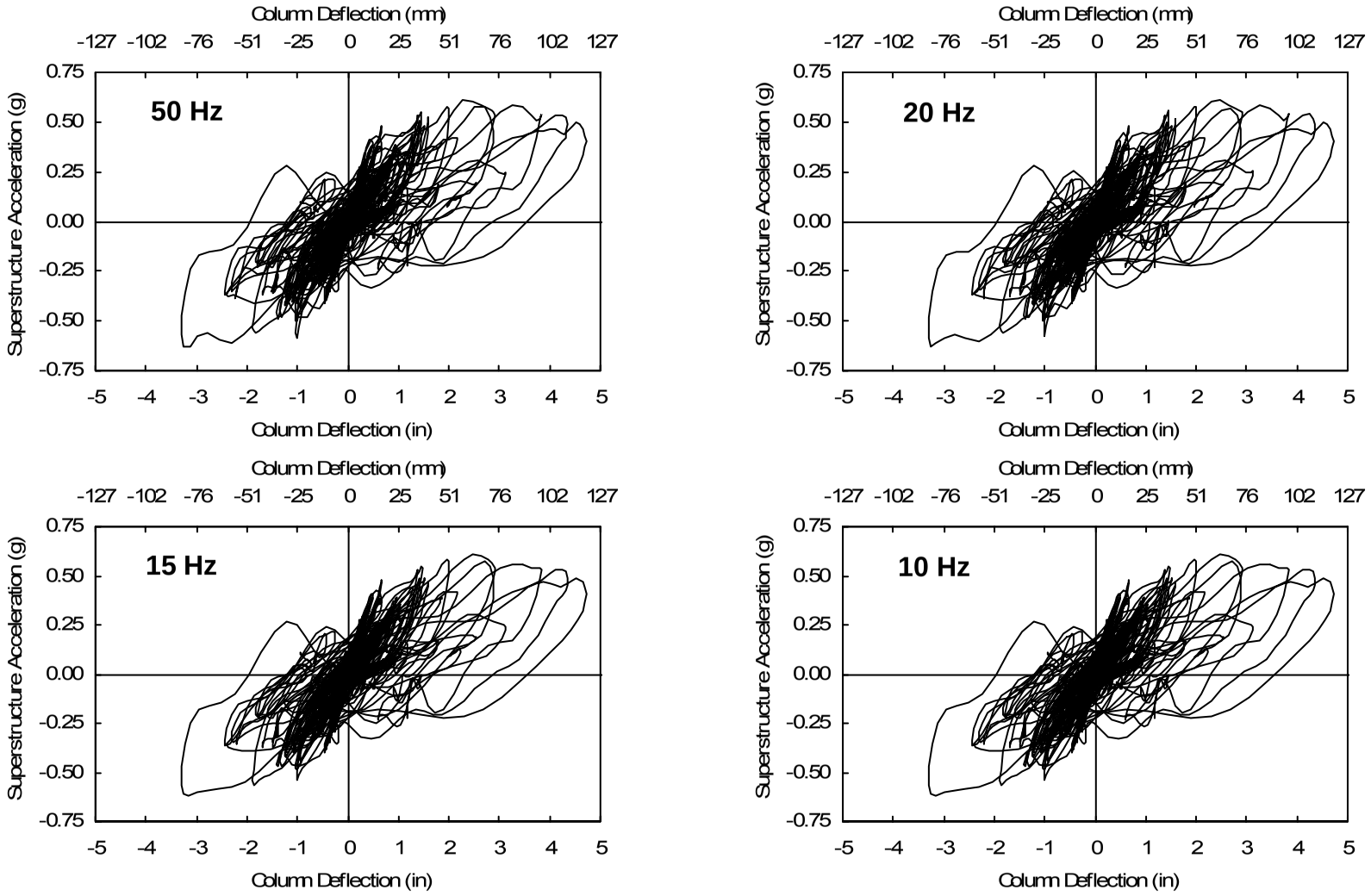

Figure 6-36: Bent 3 cumulative lateral acceleration vs. deflection hysteresis for high amplitude tests filtered at 50Hz, 20Hz, 15Hz, and 10Hz.

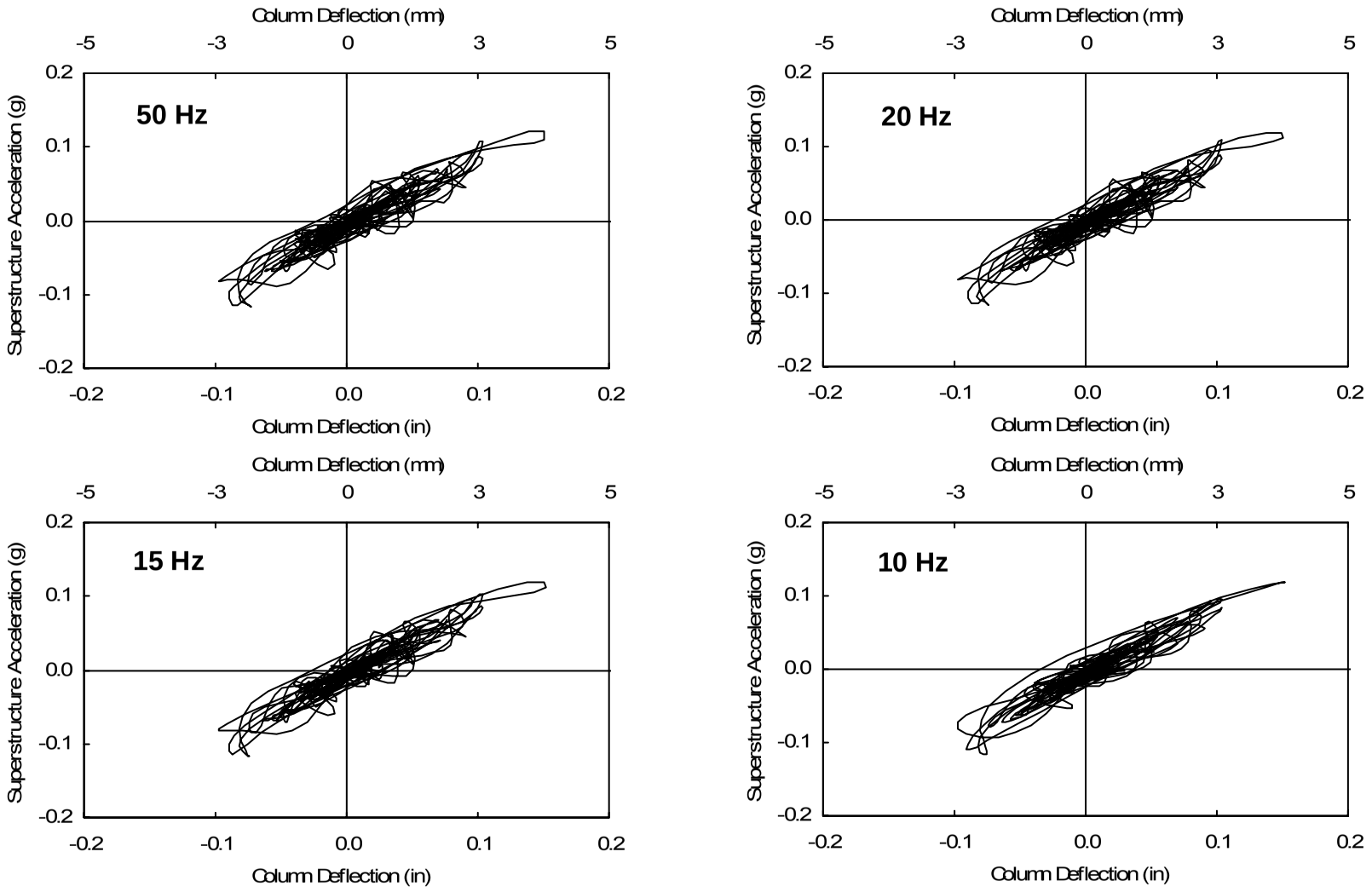

Figure 6-37: Bent 1 cumulative lateral acceleration vs. deflection hysteresis for test 1 filtered at 50Hz, 20Hz, 15Hz, and 10Hz.

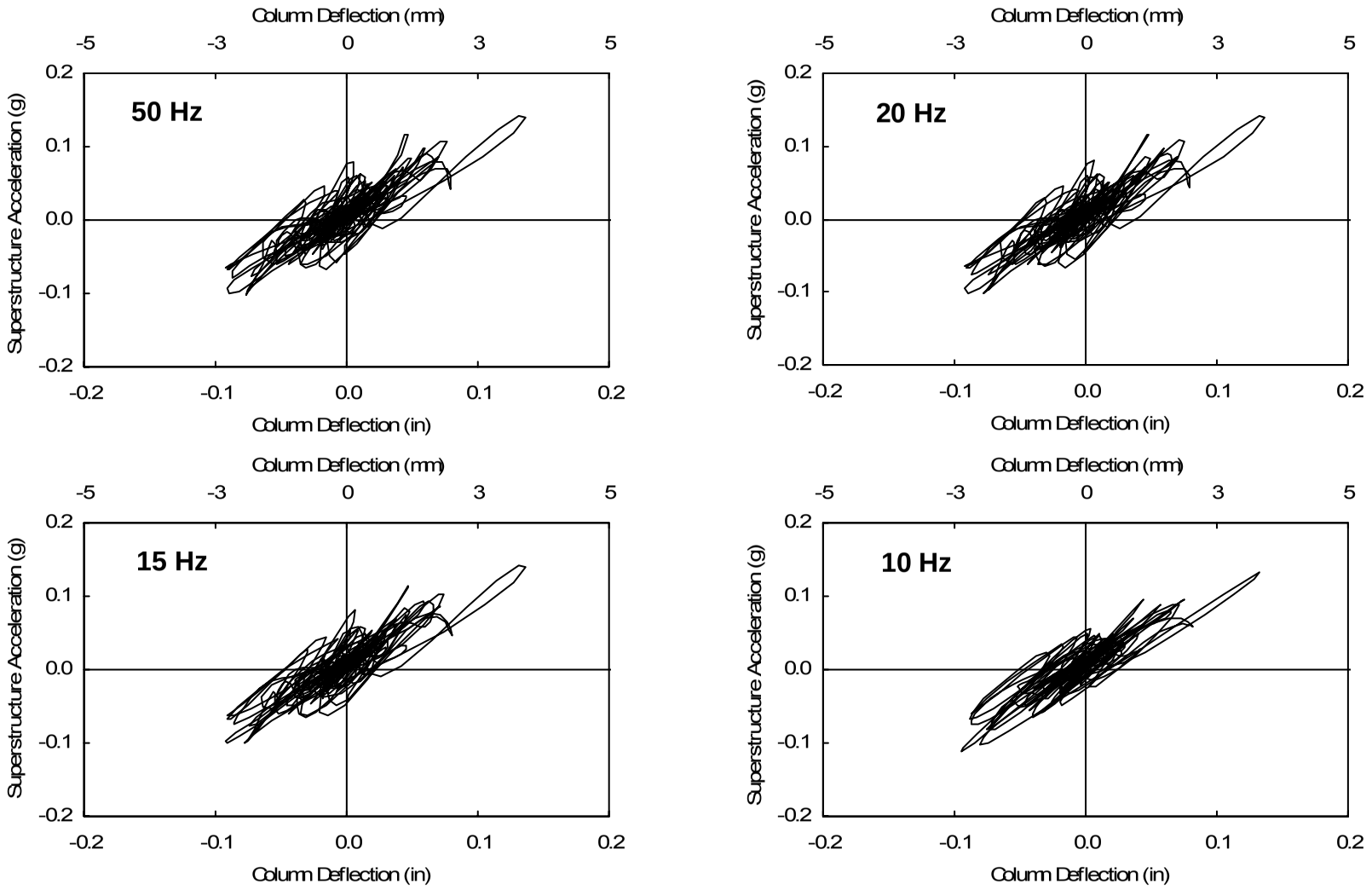

Figure 6-38: Bent 2 cumulative lateral acceleration vs. deflection hysteresis for test 1 filtered at 50Hz, 20Hz, 15Hz, and 10Hz.

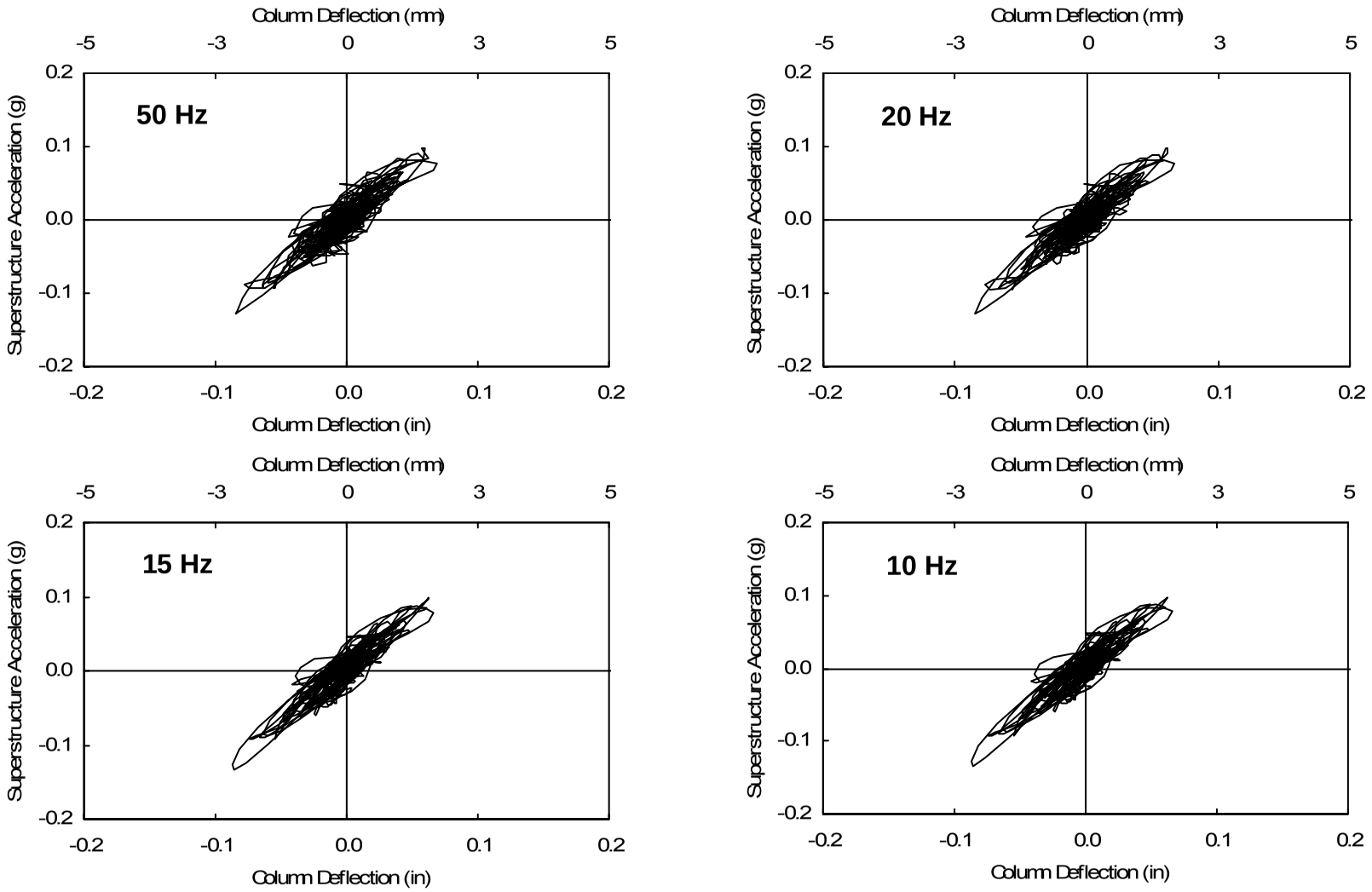

Figure 6-39: Bent 3 cumulative lateral acceleration vs. deflection hysteresis for test 1 filtered at 50Hz, 20Hz, 15Hz, and 10Hz.

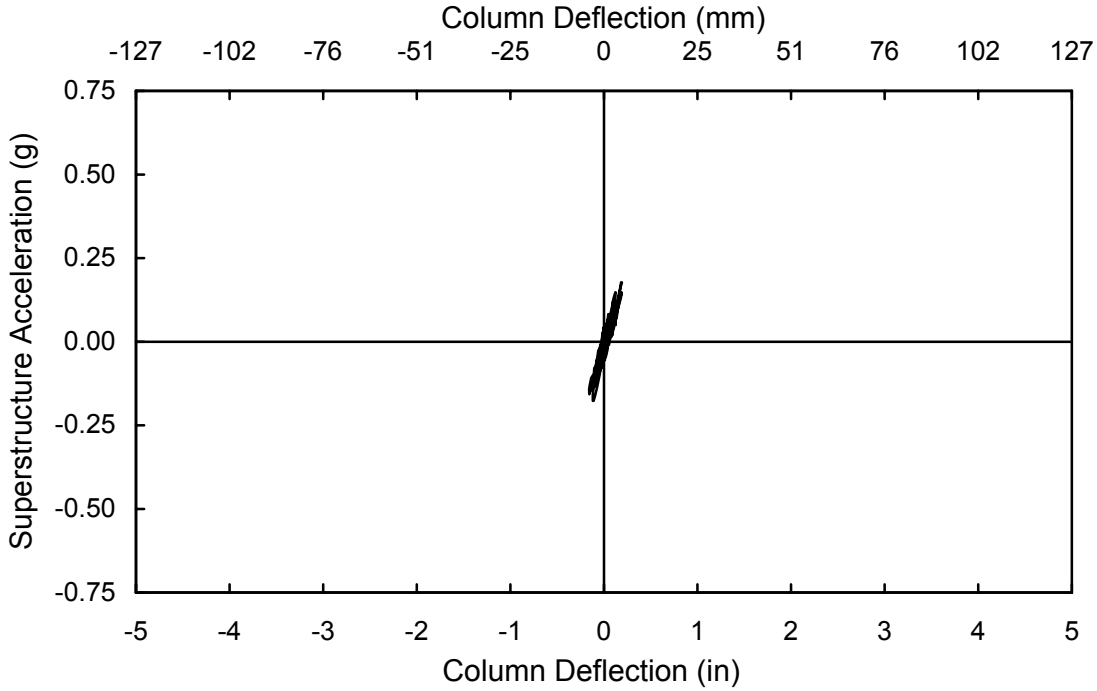

Figure 6-40: Bent 1 cumulative lateral acceleration vs. deflection hysteresis for low amplitude testing (tests 1-11).

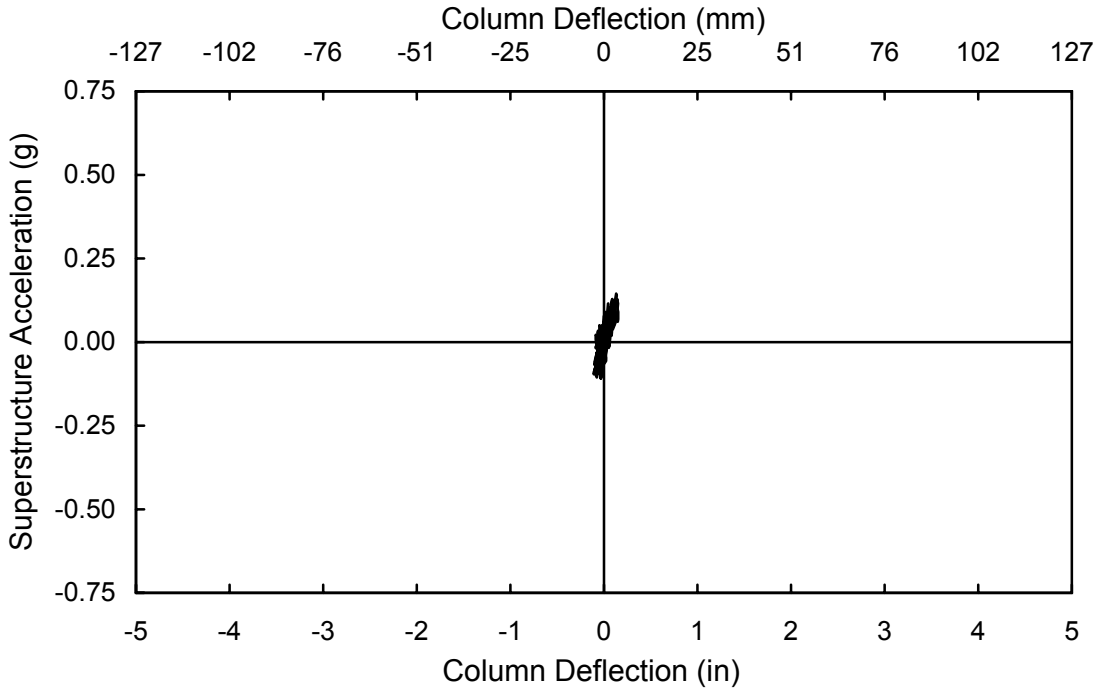

Figure 6-41: Bent 2 cumulative lateral acceleration vs. deflection hysteresis for low amplitude testing (tests 1-11)

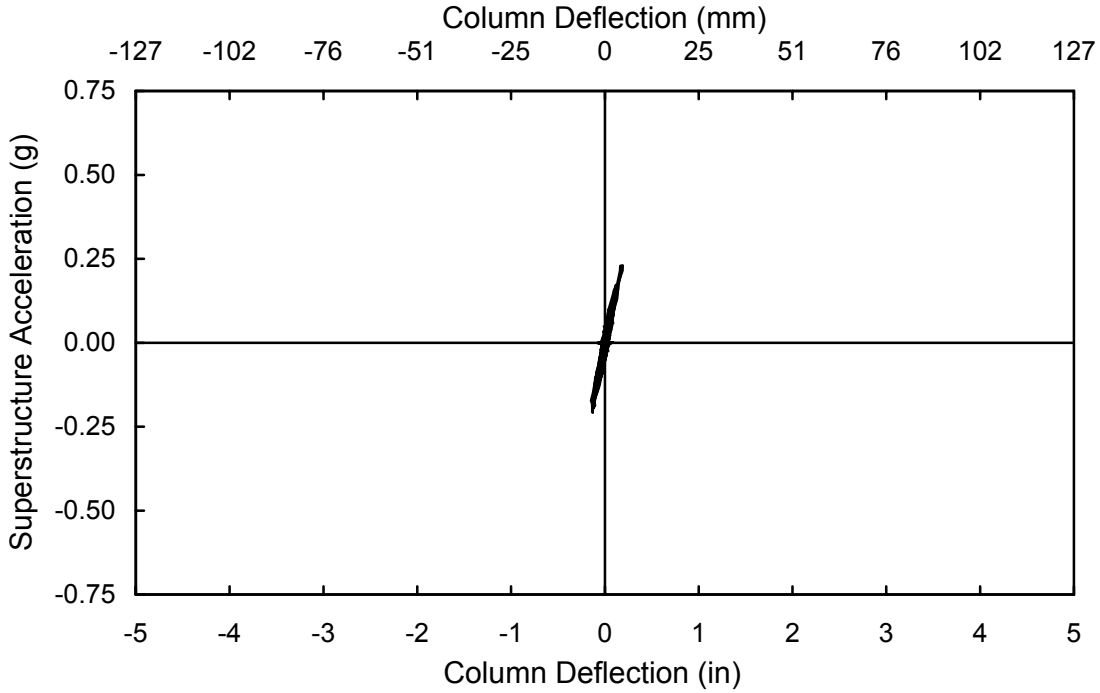

Figure 6-42: Bent 3 cumulative lateral acceleration vs. deflection hysteresis for low amplitude testing (tests 1-11).

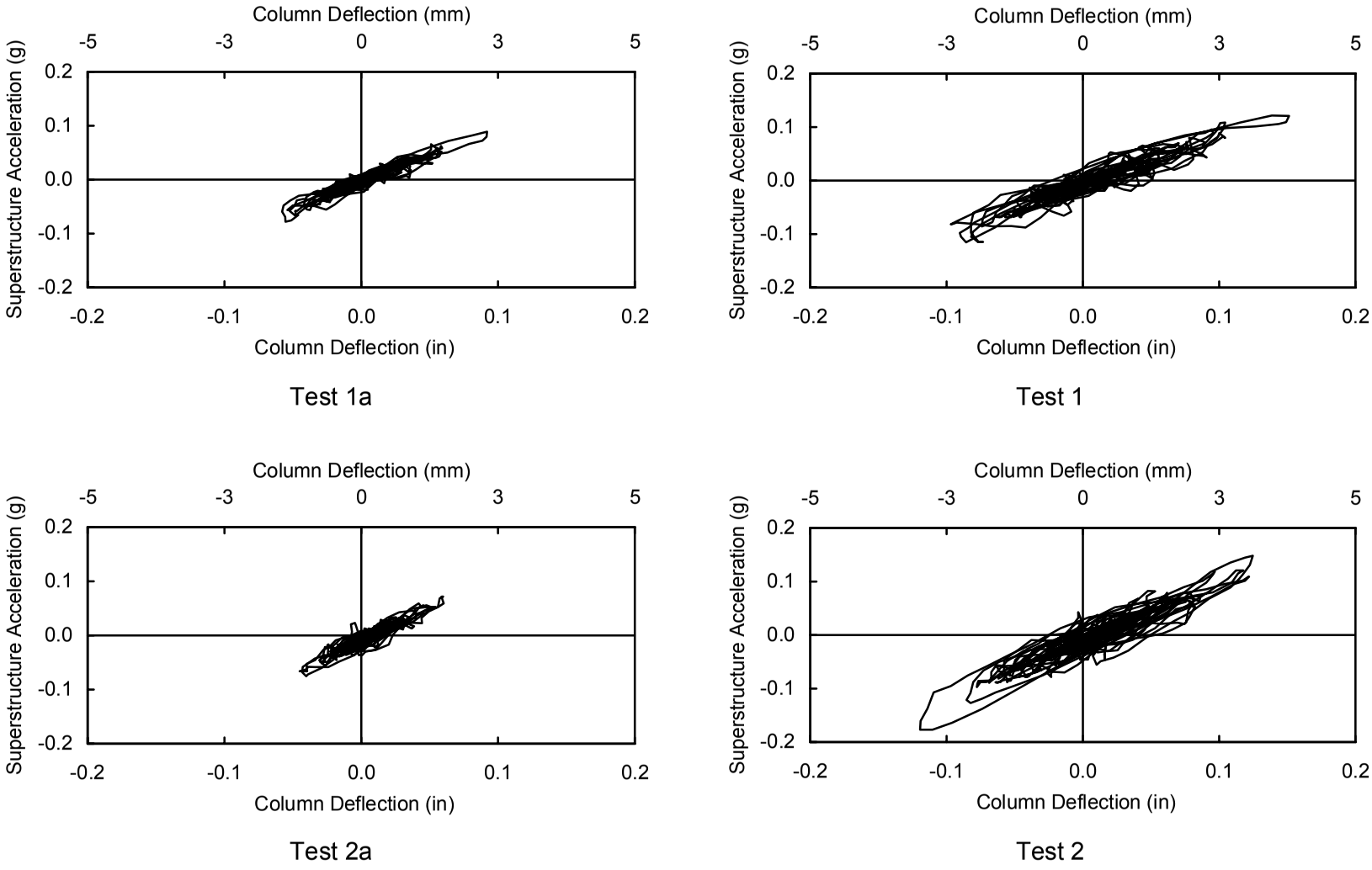

Figure 6-43: Bent 1 lateral acceleration vs. deflection hysteresis for tests 1a through 2

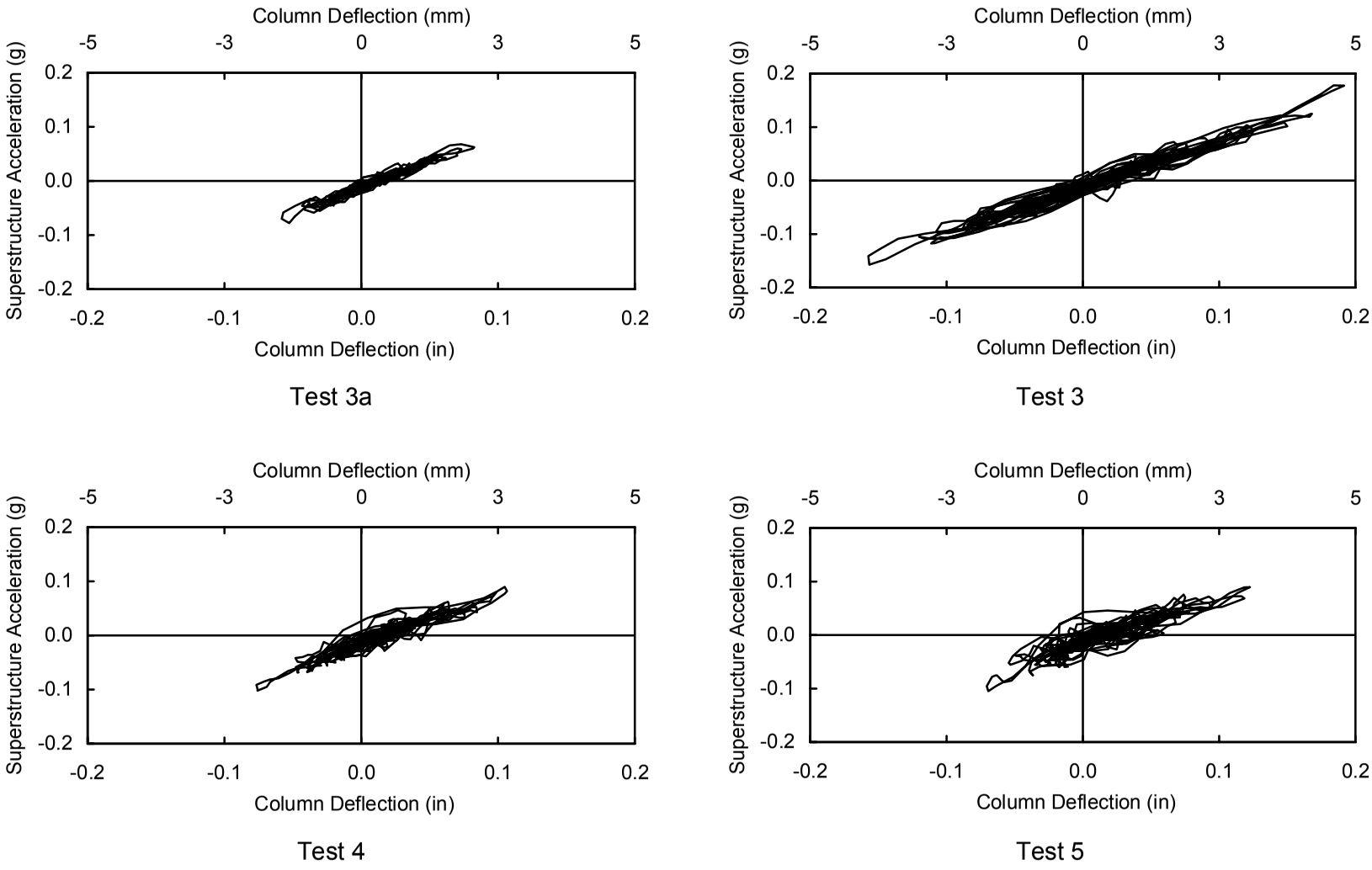

Figure 6-44: Bent 1 lateral acceleration vs. deflection hysteresis for tests 3a through 5.

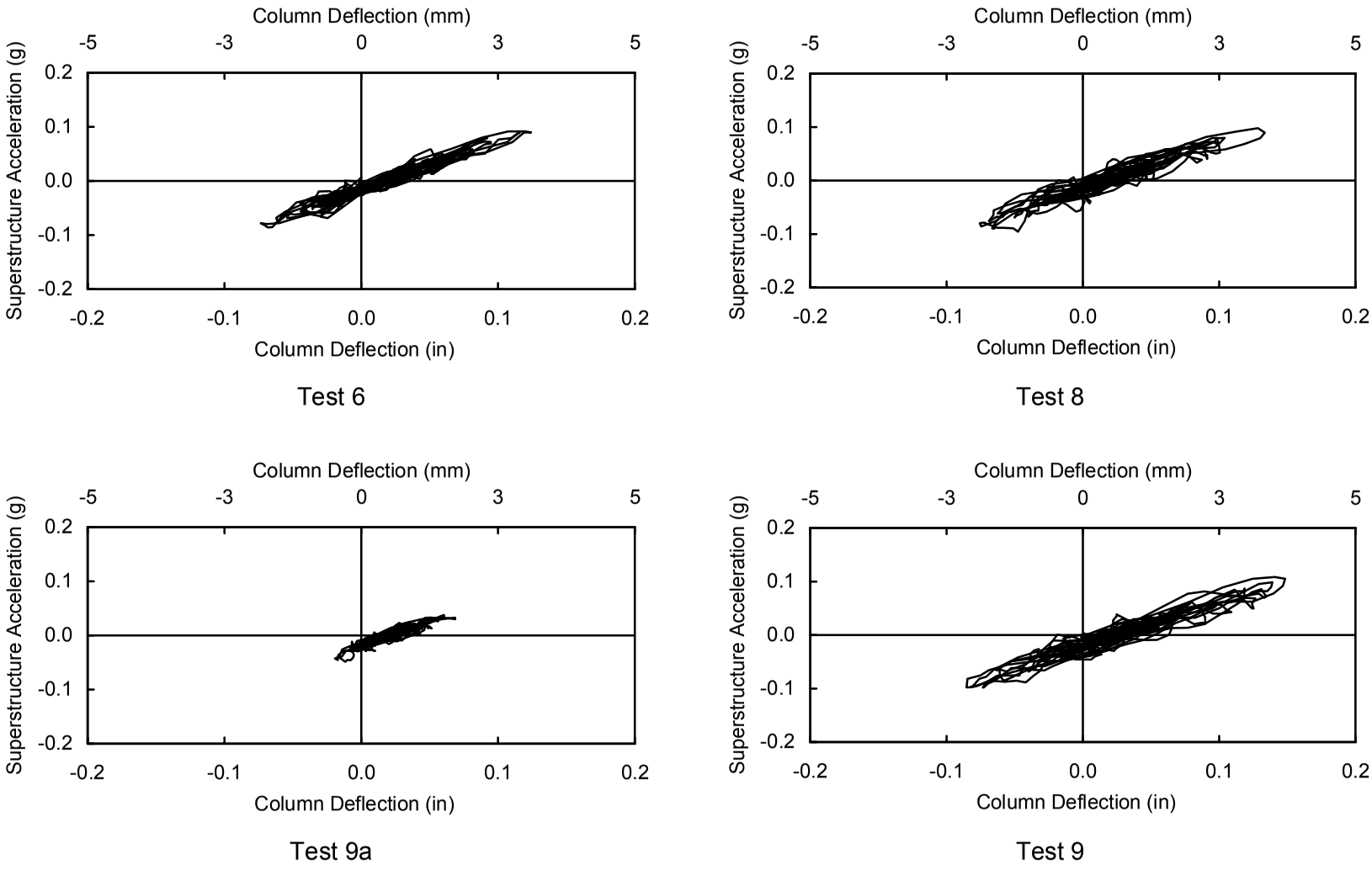

Figure 6-45: Bent 1 lateral acceleration vs. deflection hysteresis for tests 6 through 9.

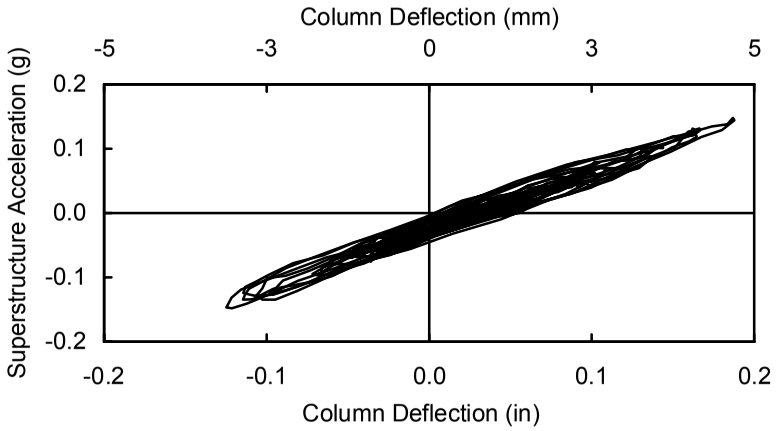

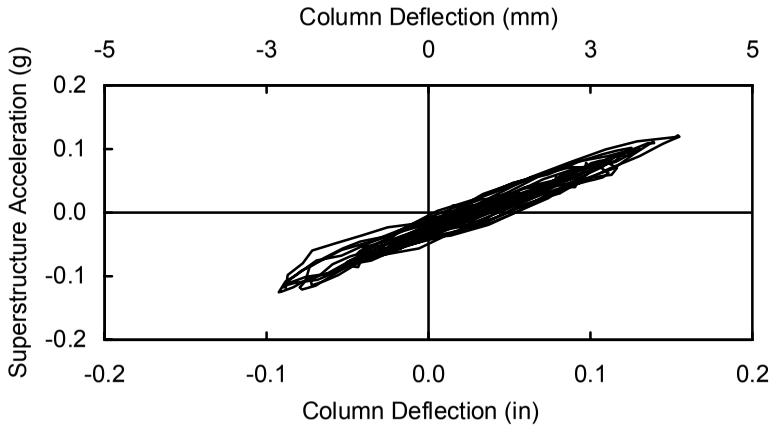

Figure 6-46: Bent 1 lateral acceleration vs. deflection hysteresis for tests 10 and 11.

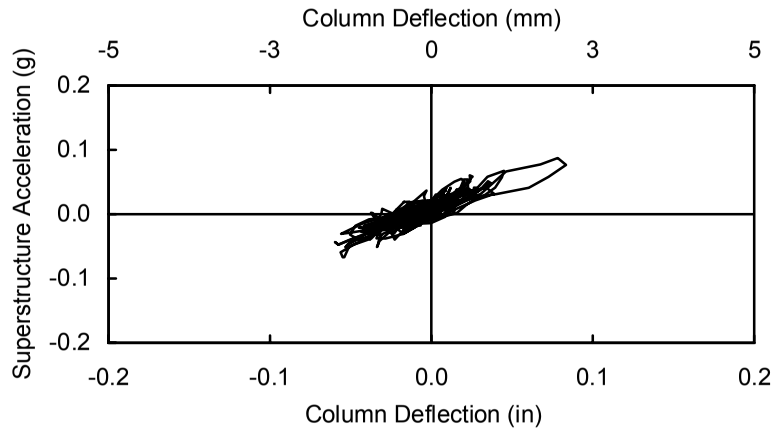

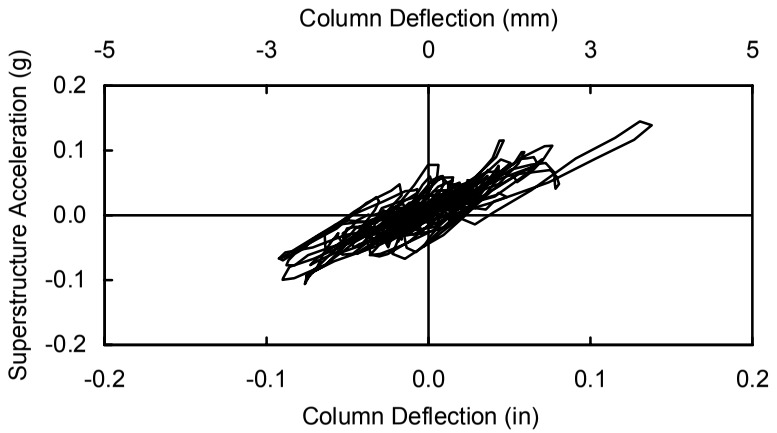

Figure 6-47: Bent 2 lateral acceleration vs. deflection hysteresis for tests 1a through 1.

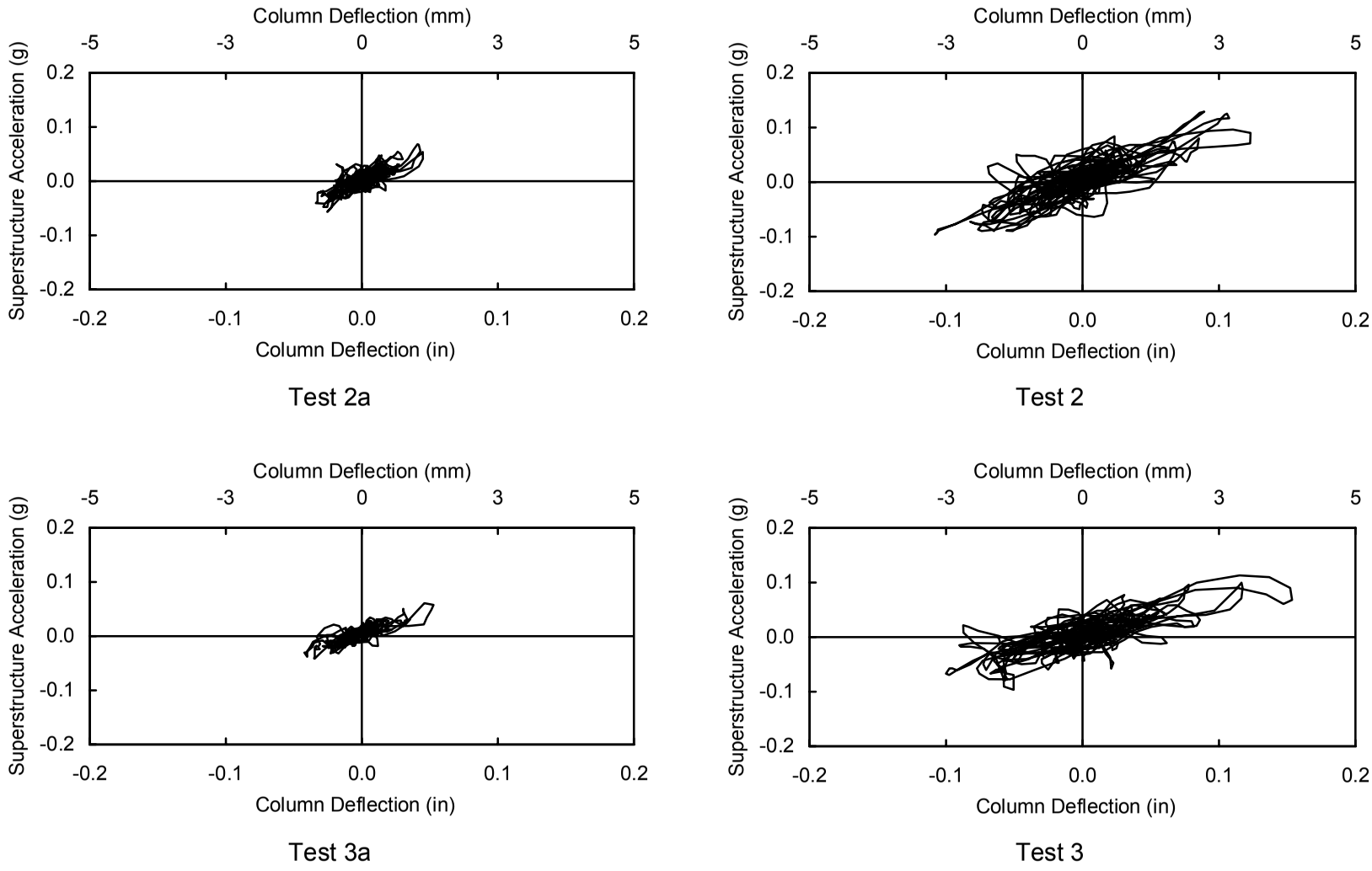

Figure 6-48: Bent 2 lateral acceleration vs. deflection hysteresis for tests 2a through 3.

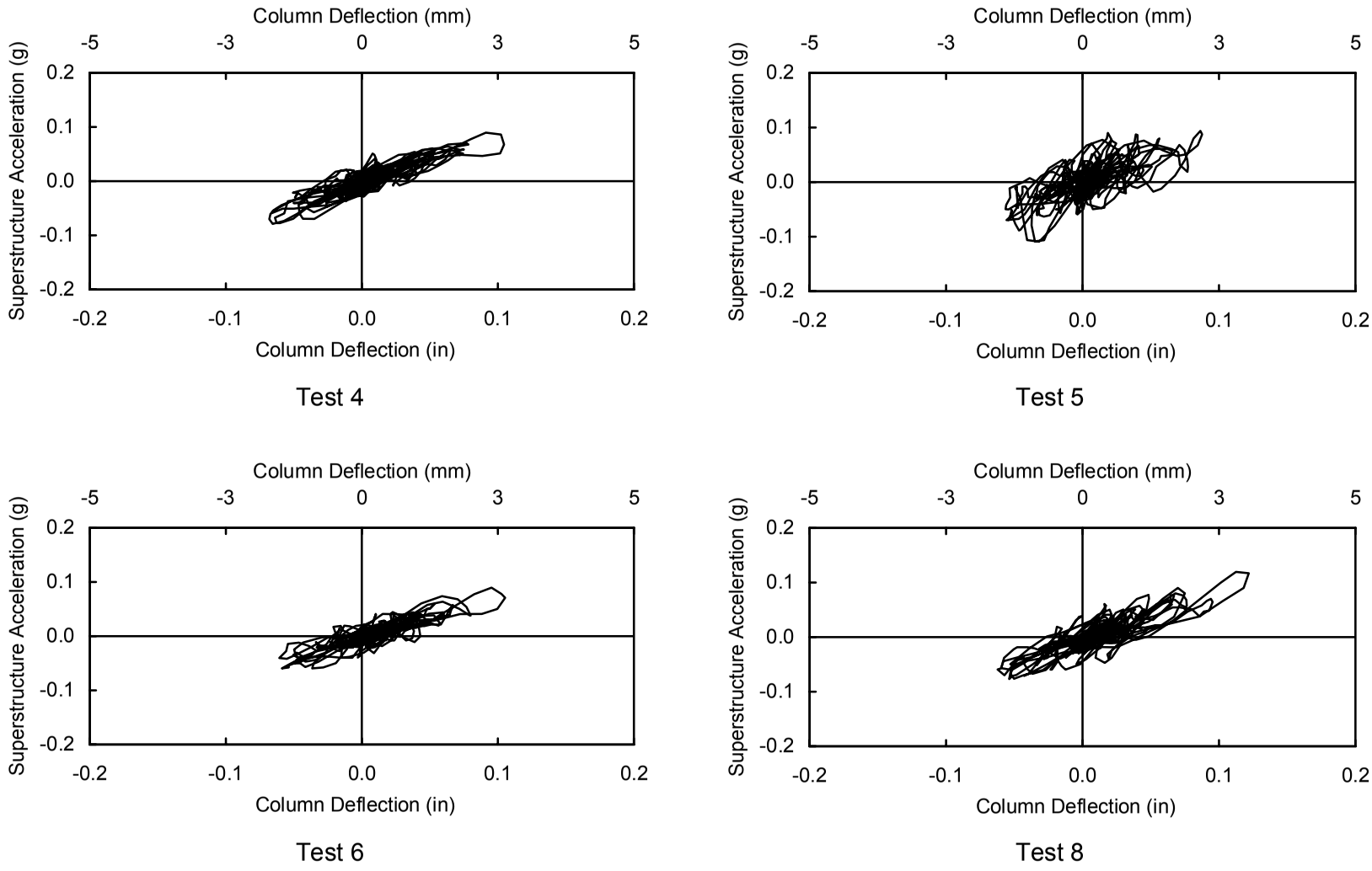

Figure 6-49: Bent 2 lateral acceleration vs. deflection hysteresis for tests 4 through 8.

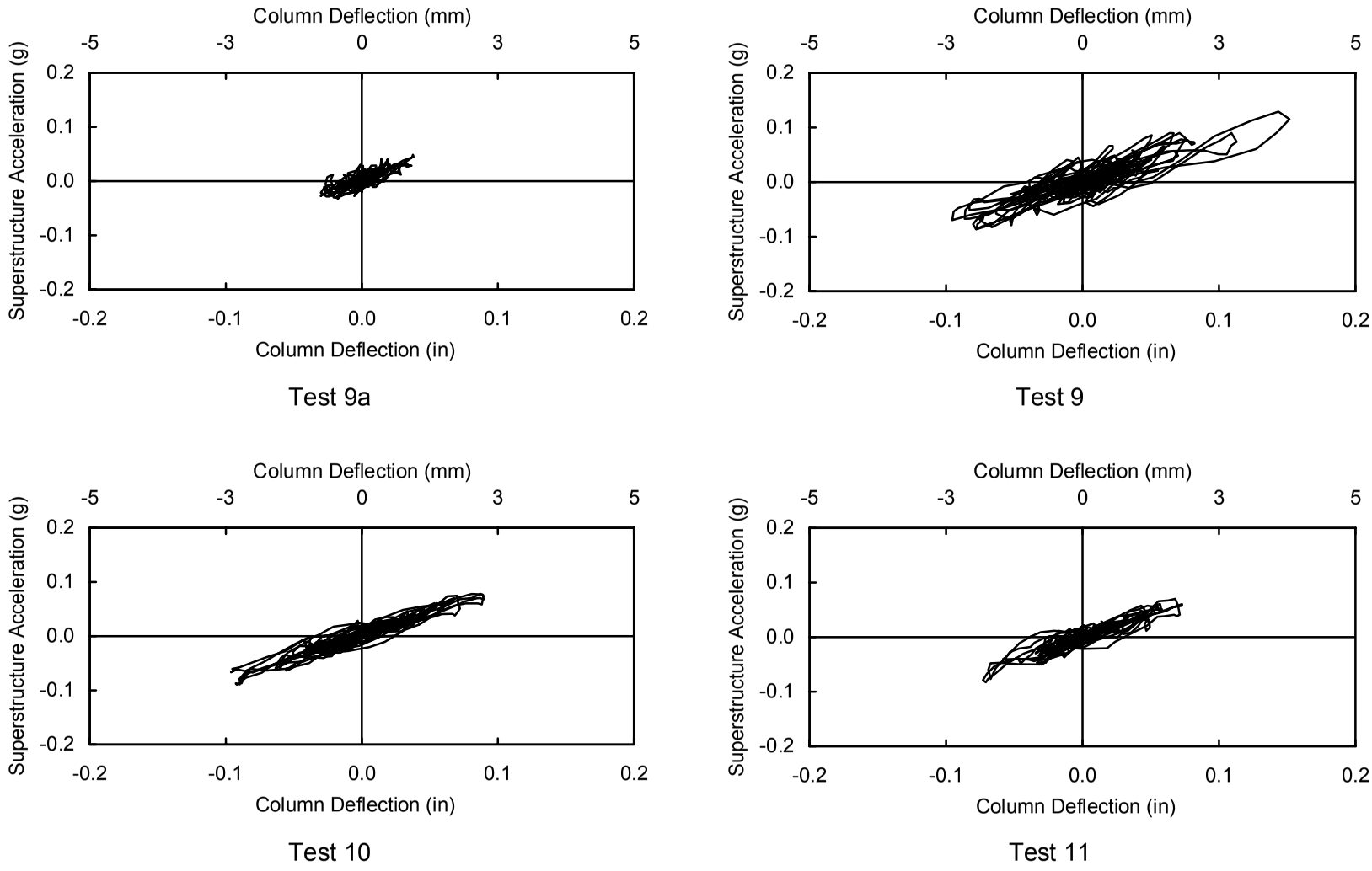

Figure 6-50: Bent 2 lateral acceleration vs. deflection hysteresis for tests 9a through 11.

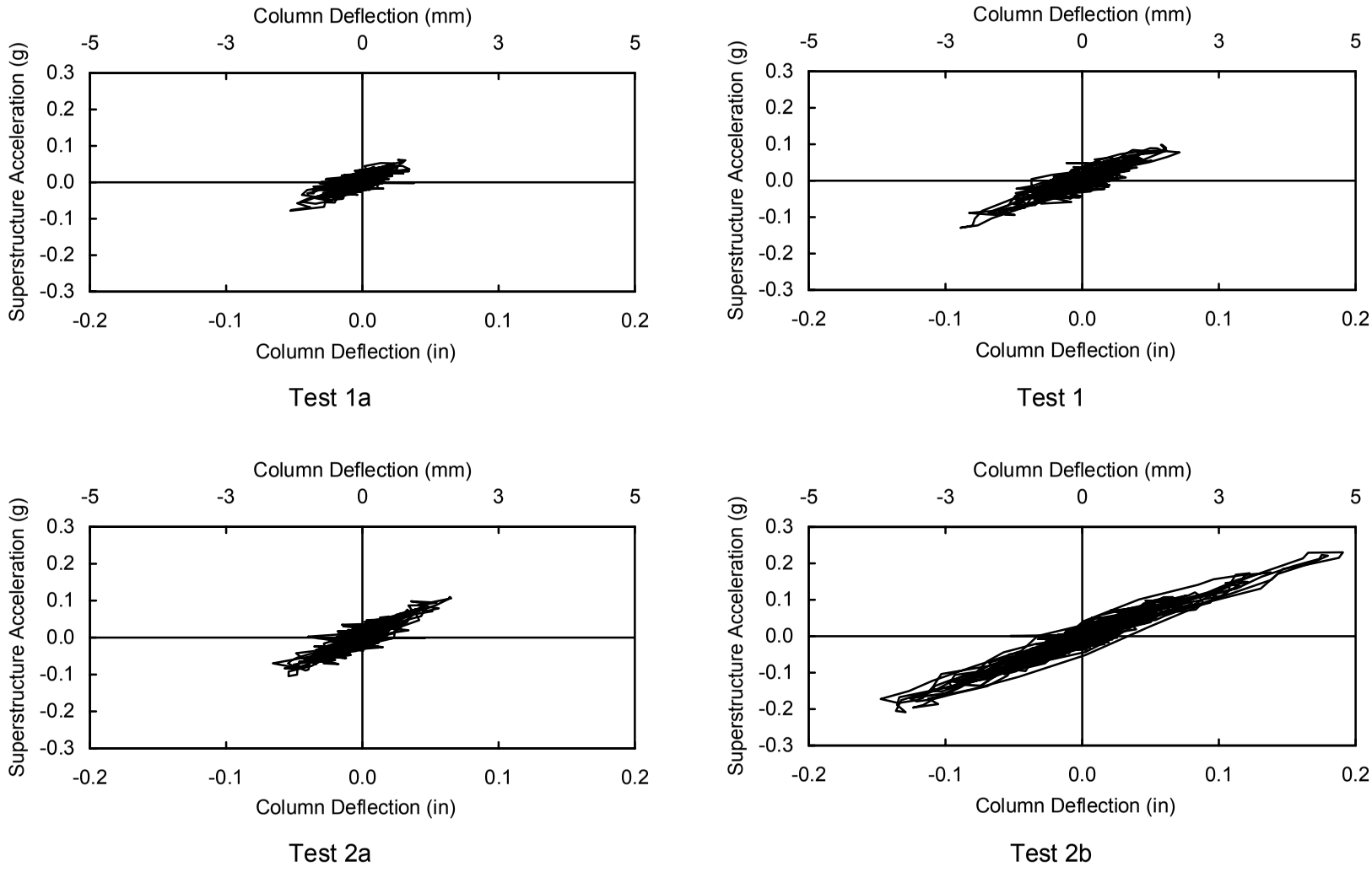

Figure 6-51: Bent 3 lateral acceleration vs. deflection hysteresis for tests 1a through 2.

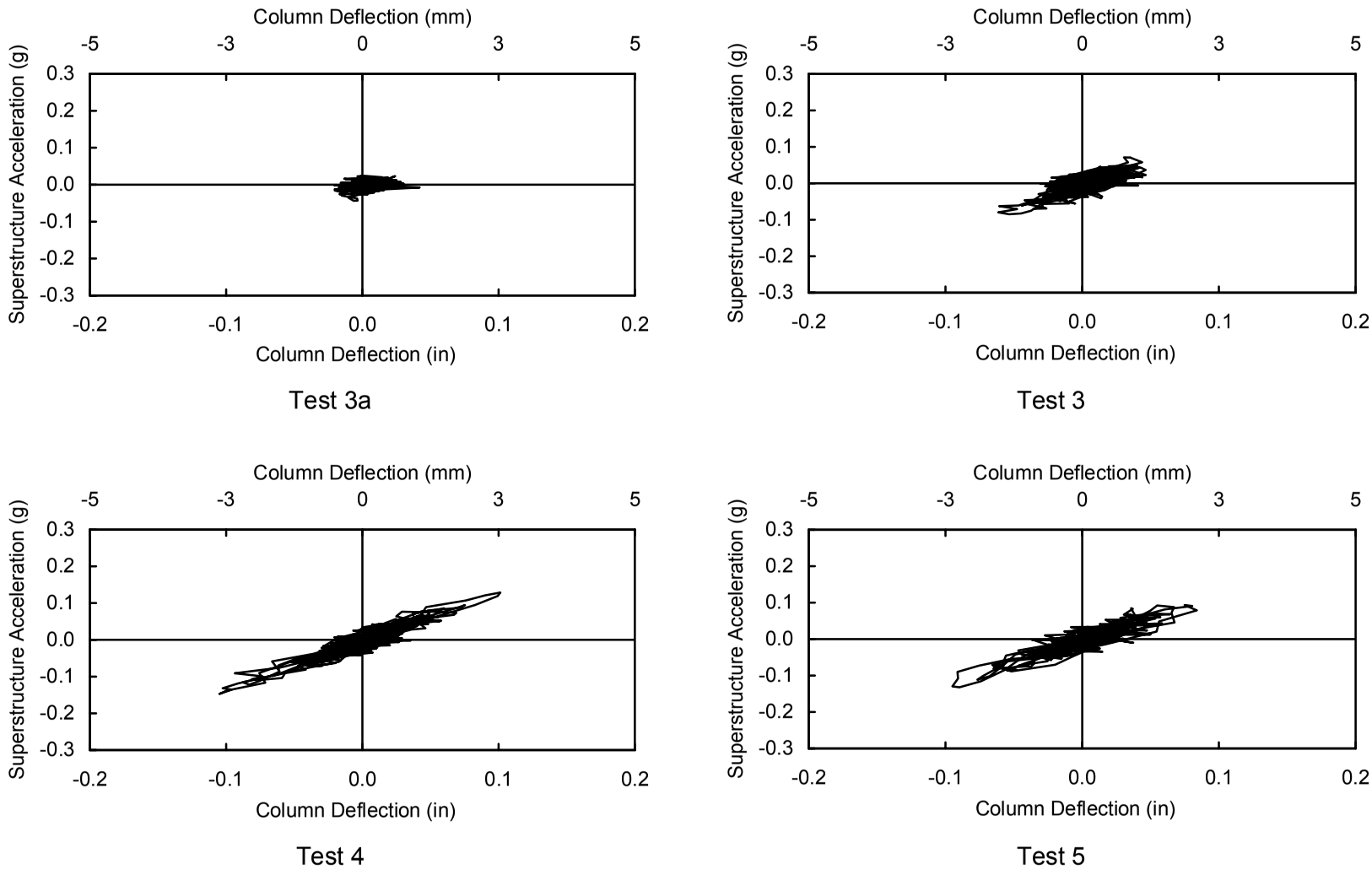

Figure 6-52: Bent 3 lateral acceleration vs. deflection hysteresis for tests 3a through 5.

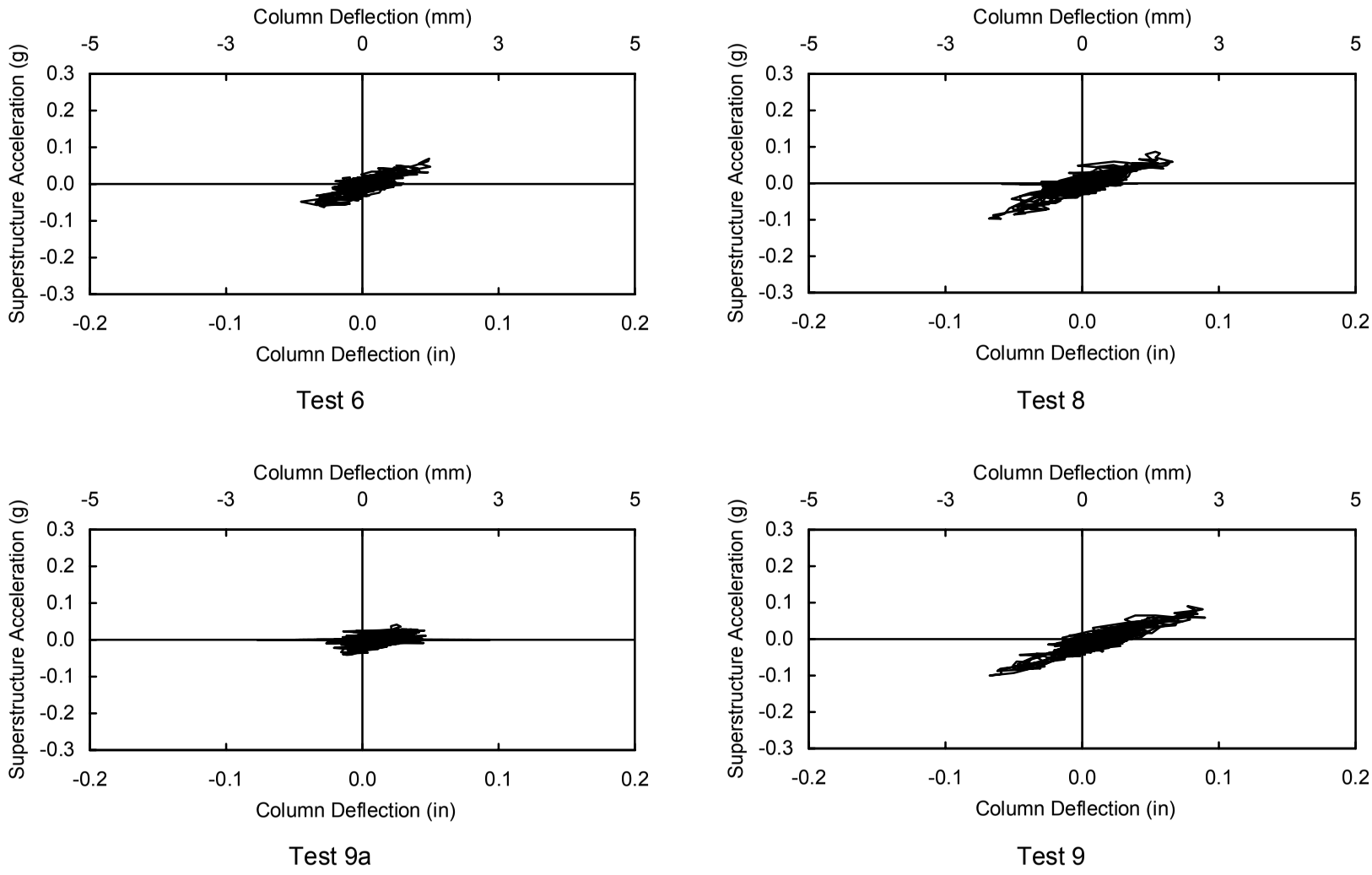

Figure 6-53: Bent 3 lateral acceleration vs. deflection hysteresis for tests 6 through 9.

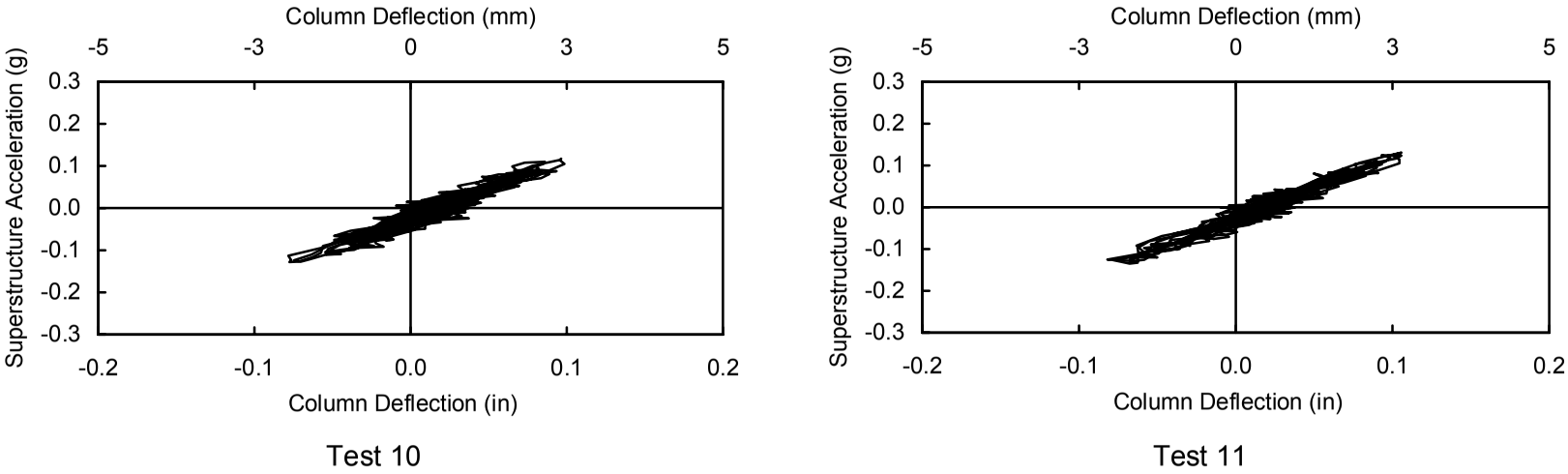

Figure 6-54: Bent 3 lateral acceleration vs. deflection hysteresis for tests 10 and 11.

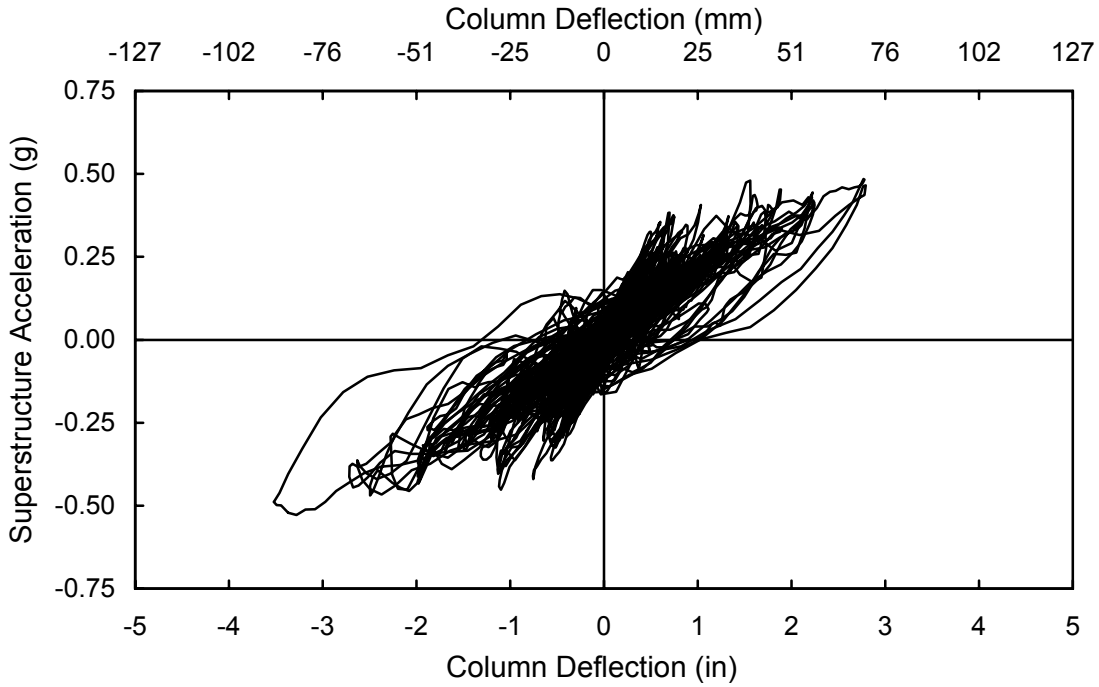

Figure 6-55: Bent 1 cumulative lateral acceleration vs. deflection hysteresis for high amplitude testing (tests 12-20).

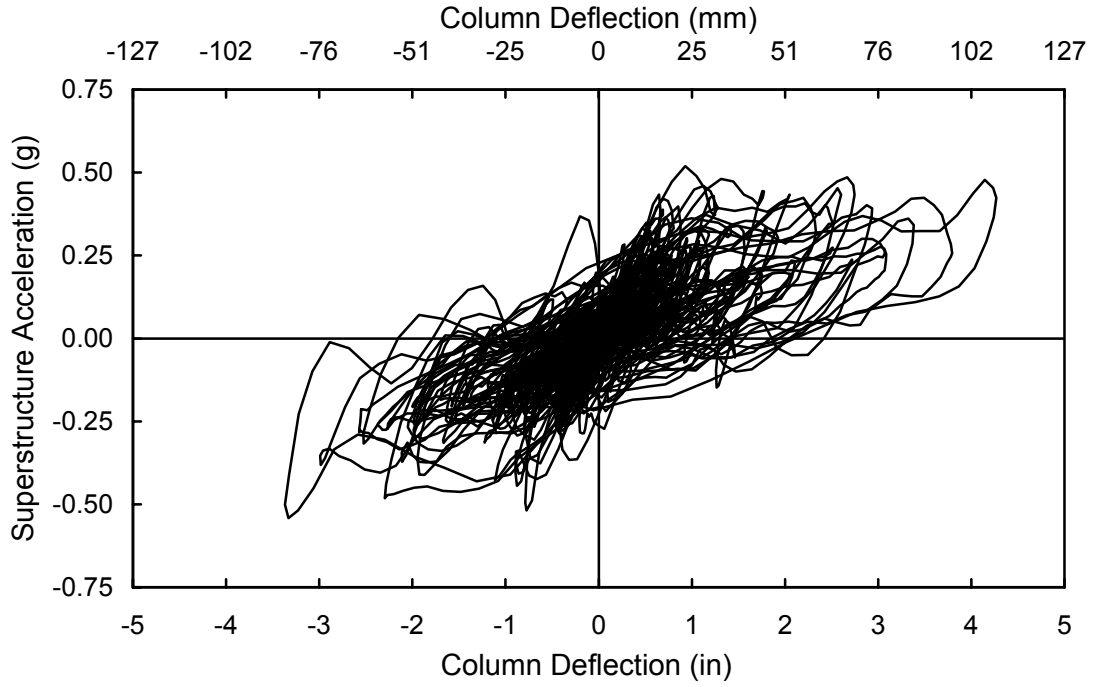

Figure 6-56: Bent 2 cumulative lateral acceleration vs. deflection hysteresis for high amplitude testing (tests 12-20)

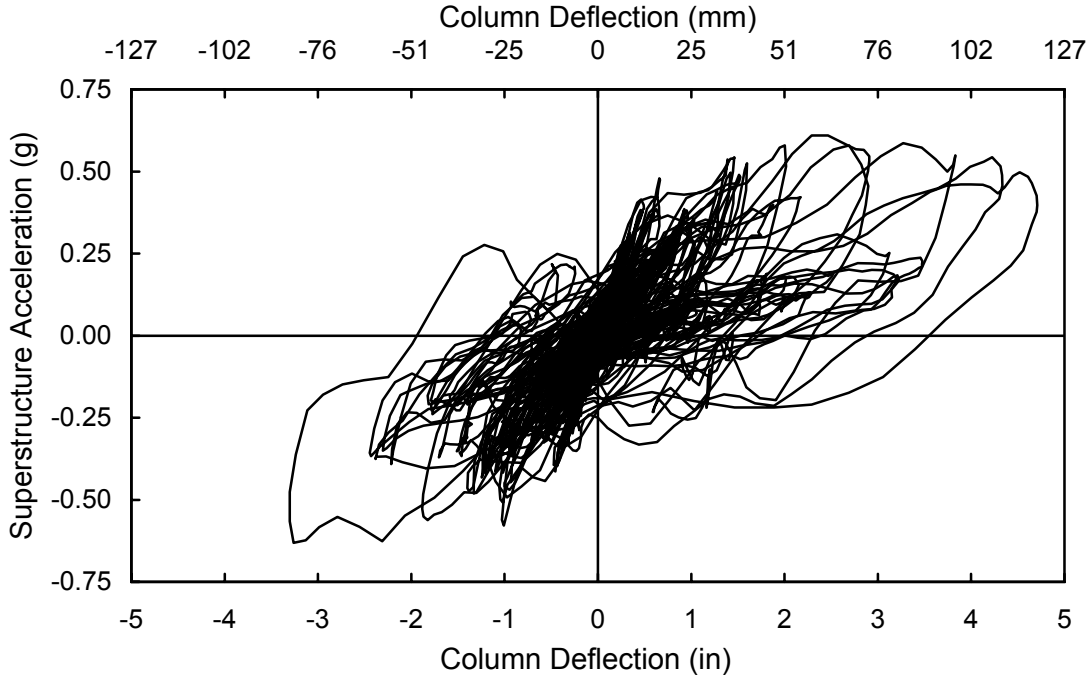

Figure 6-57: Bent 3 cumulative lateral acceleration vs. deflection hysteresis for high amplitude testing (tests 12-20).

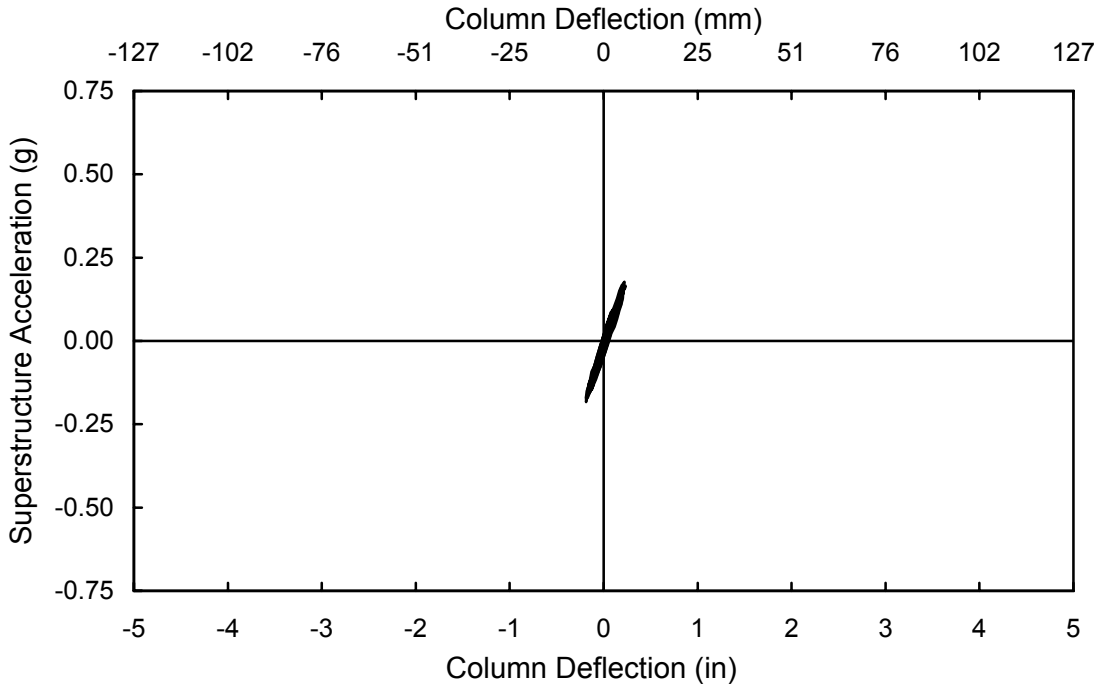

Figure 6-58: Bent 1 lateral acceleration vs. deflection hysteresis for test 12.

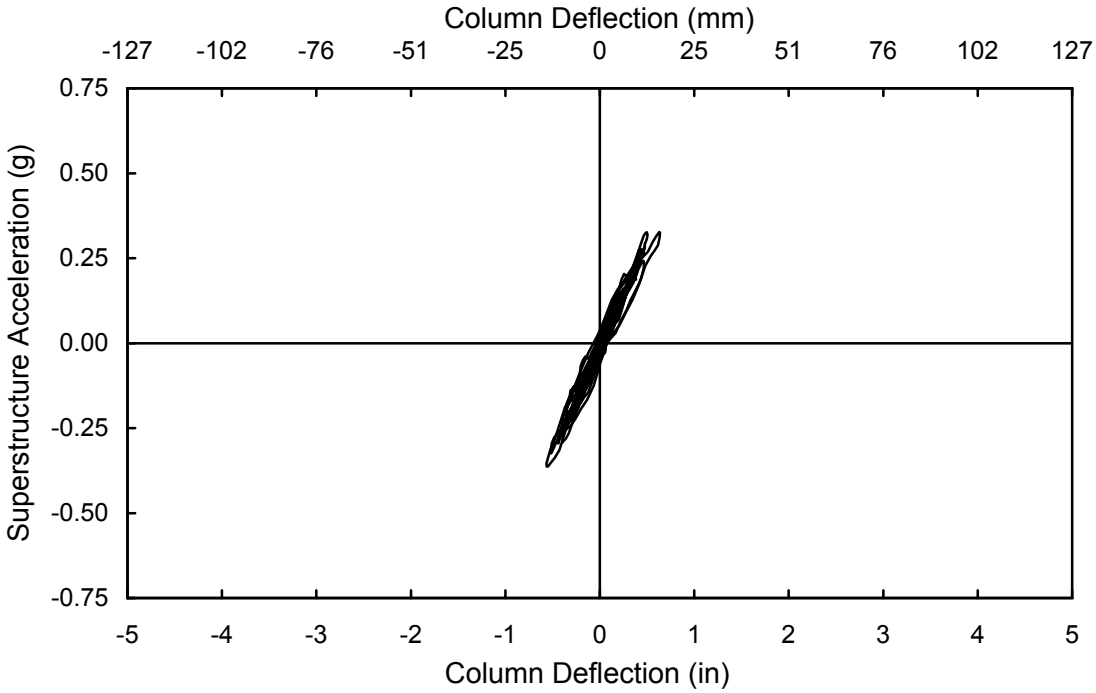

Figure 6-59: Bent 1 lateral acceleration vs. deflection hysteresis for test 13.

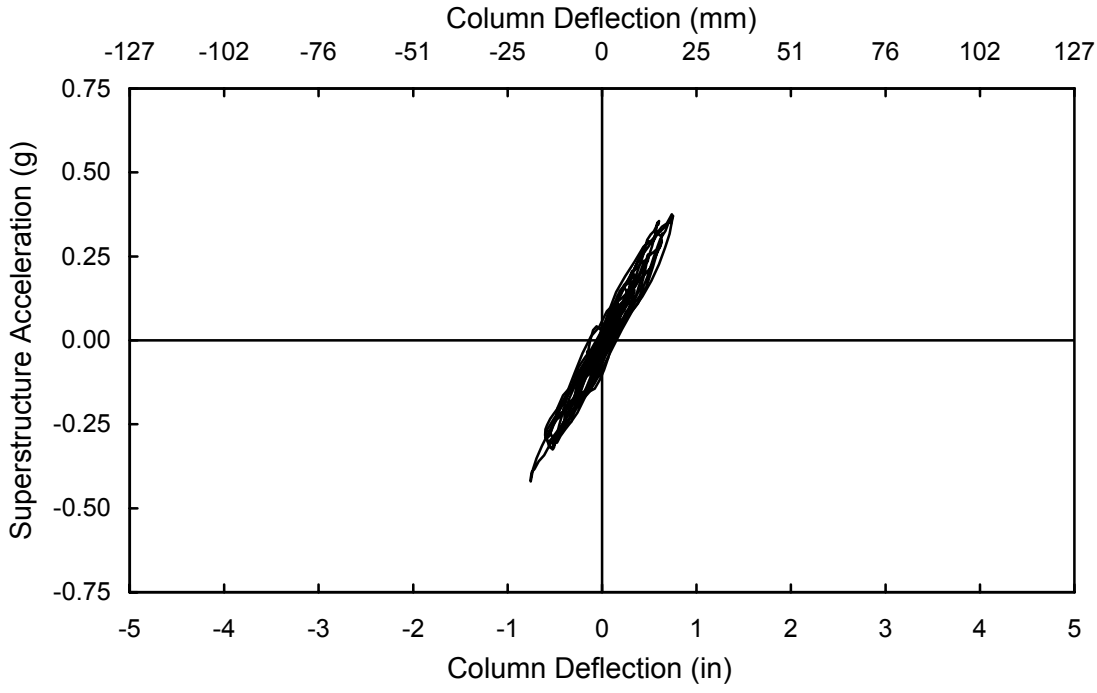

Figure 6-60: Bent 1 lateral acceleration vs. deflection hysteresis for test 14.

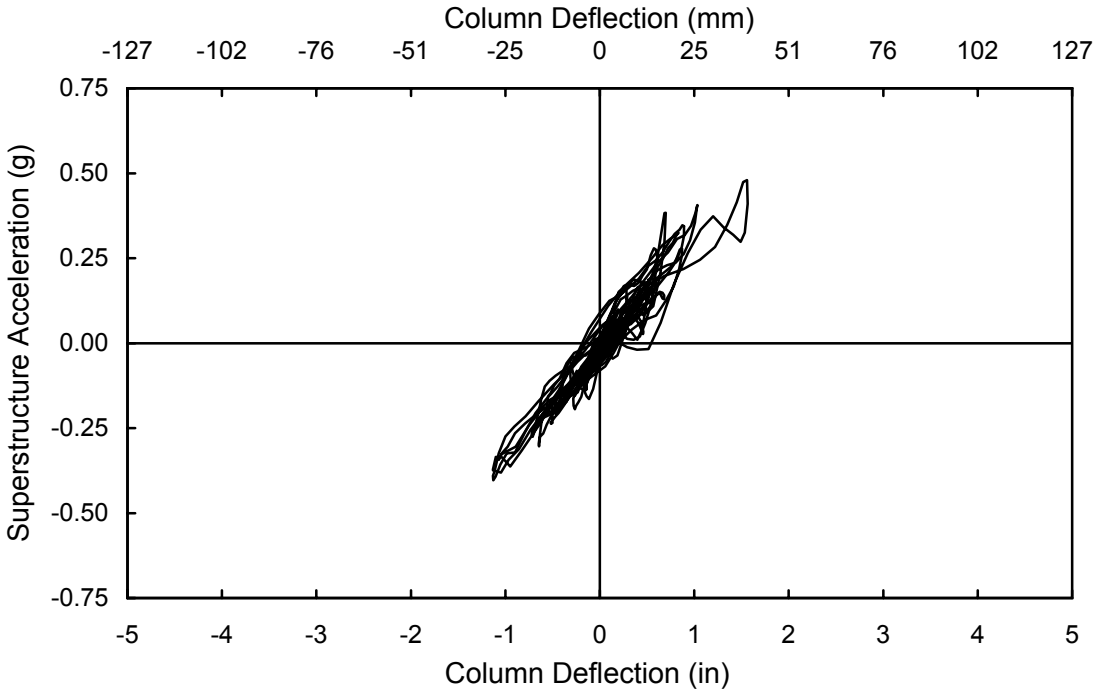

Figure 6-61: Bent 1 lateral acceleration vs. deflection hysteresis for test 15.

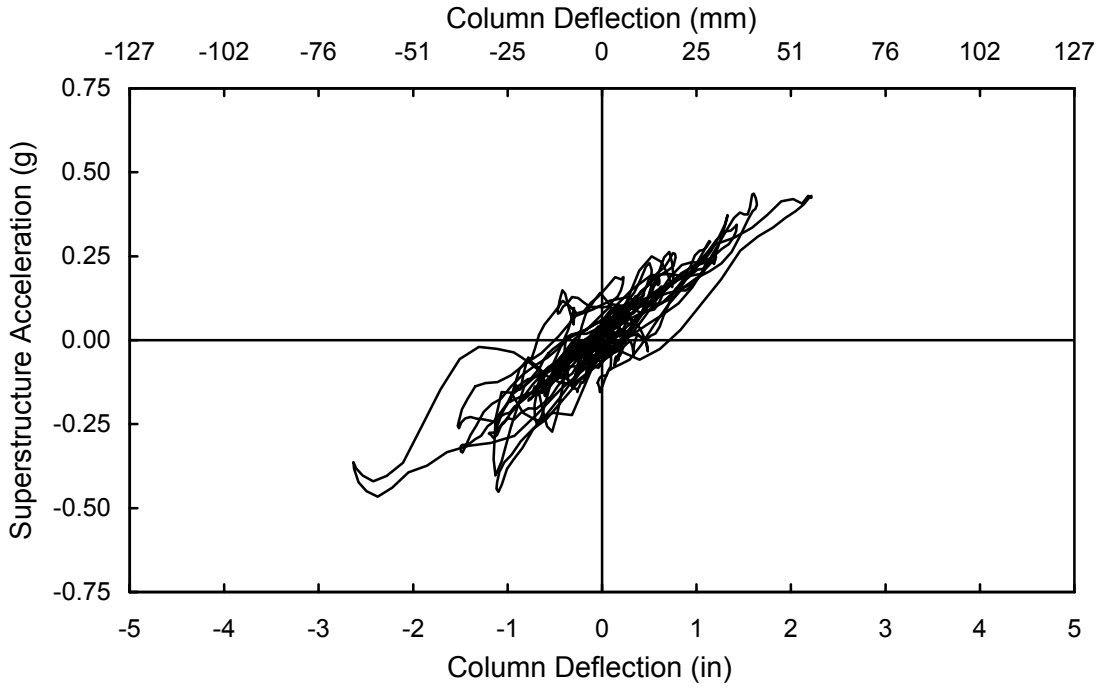

Figure 6-62: Bent 1 lateral acceleration vs. deflection hysteresis for test 16.

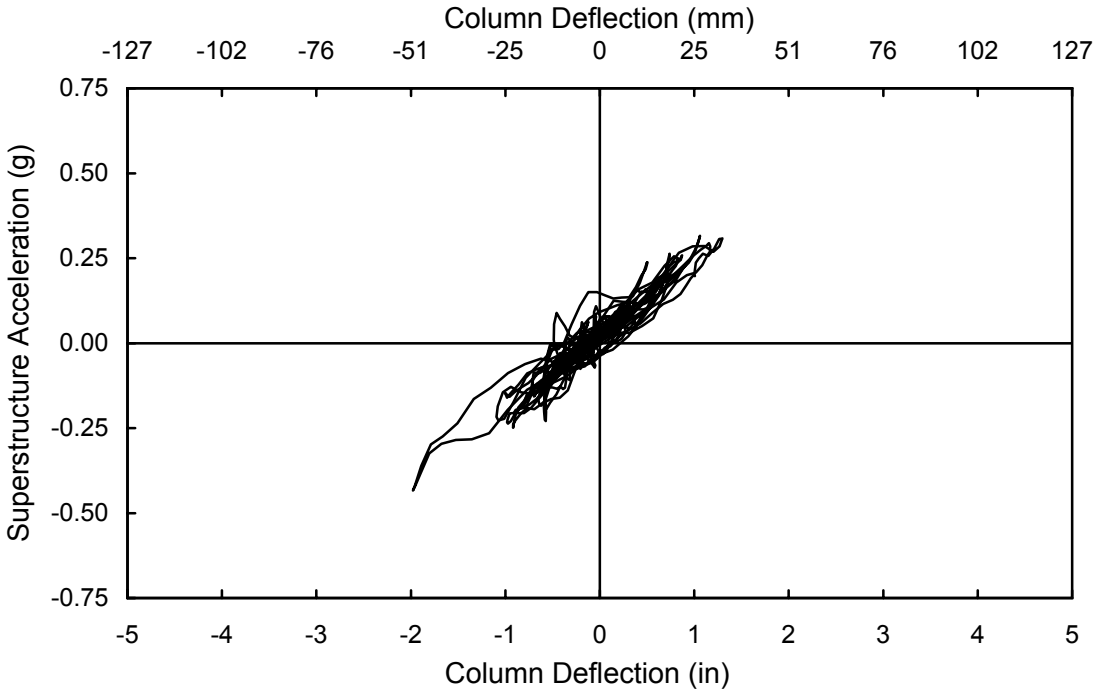

Figure 6-63: Bent 1 lateral acceleration vs. deflection hysteresis for test 17.

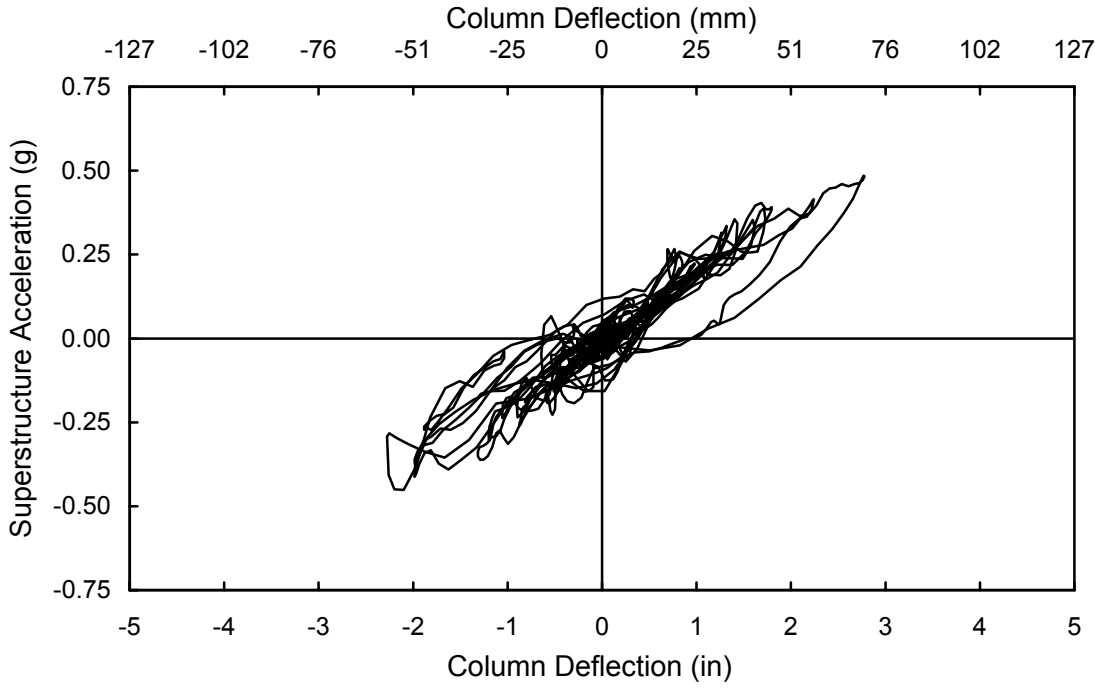

Figure 6-64: Bent 1 lateral acceleration vs. deflection hysteresis for test 18.

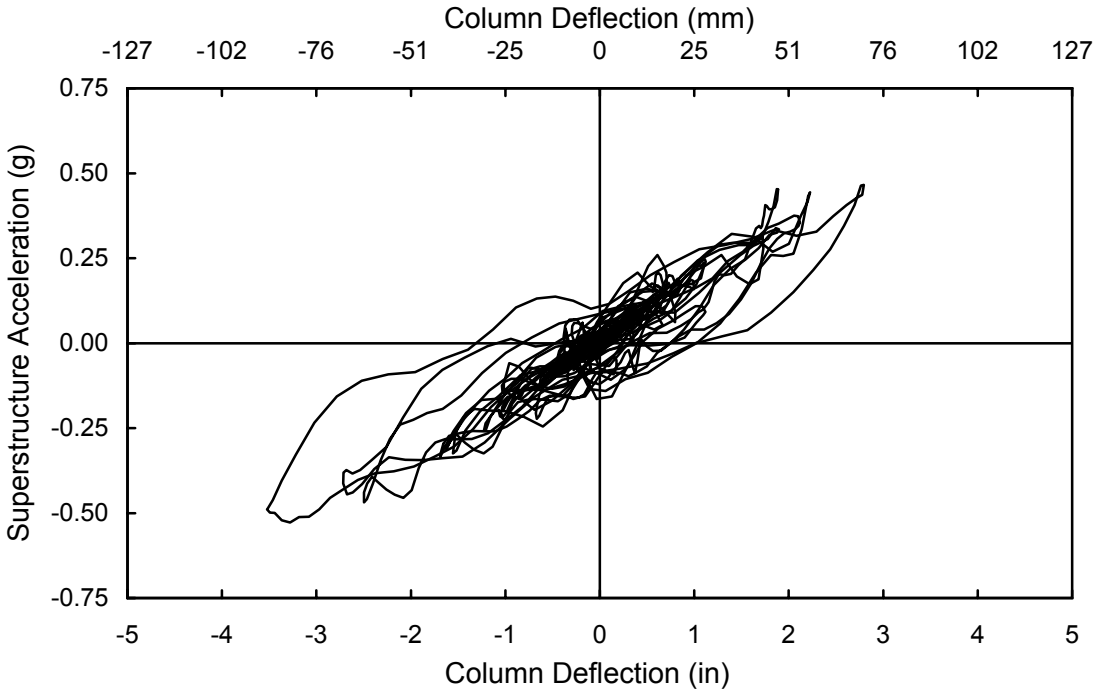

Figure 6-65: Bent 1 lateral acceleration vs. deflection hysteresis for test 19.

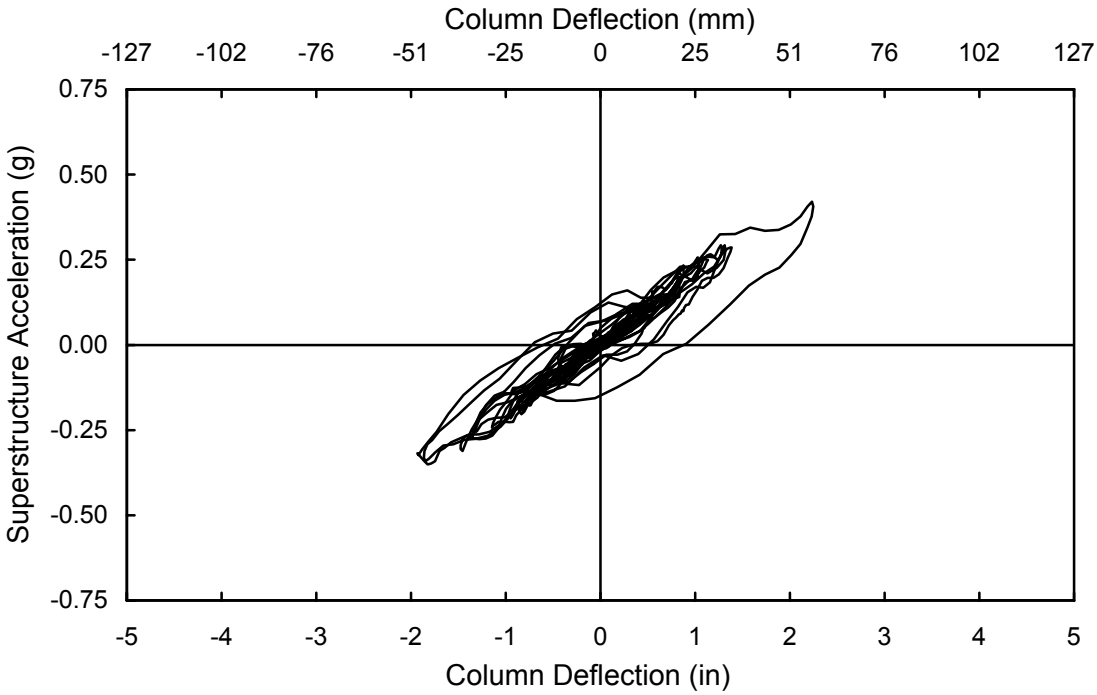

Figure 6-66: Bent 1 lateral acceleration vs. deflection hysteresis for test 20.

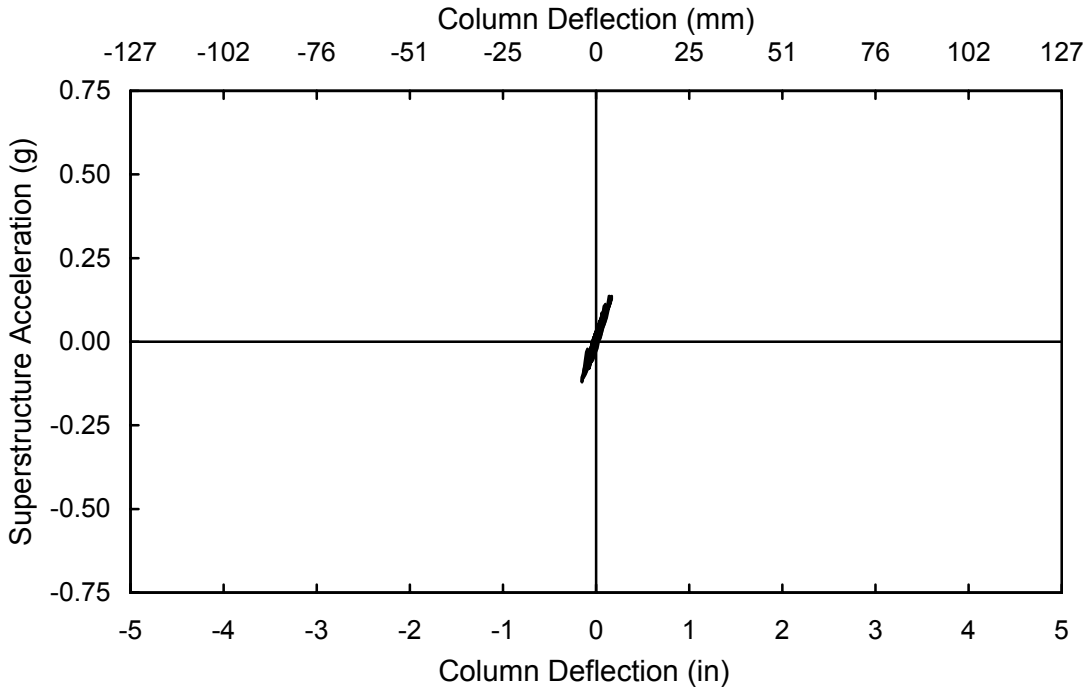

Figure 6-67: Bent 2 lateral acceleration vs. deflection hysteresis for test 12.

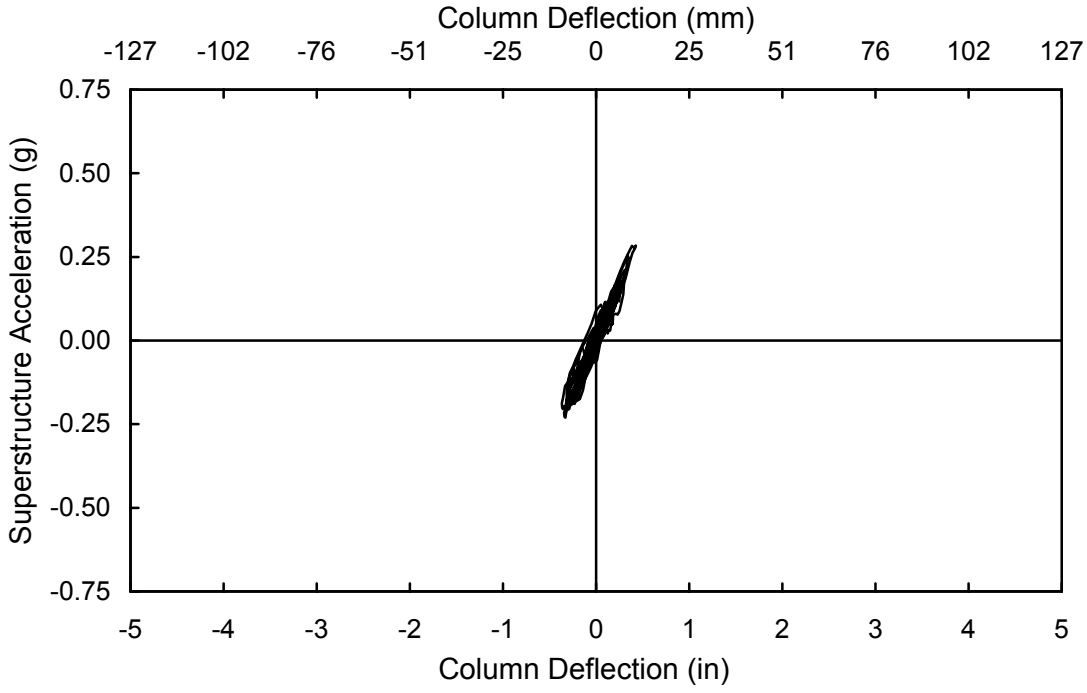

Figure 6-68: Bent 2 lateral acceleration vs. deflection hysteresis for test 13.

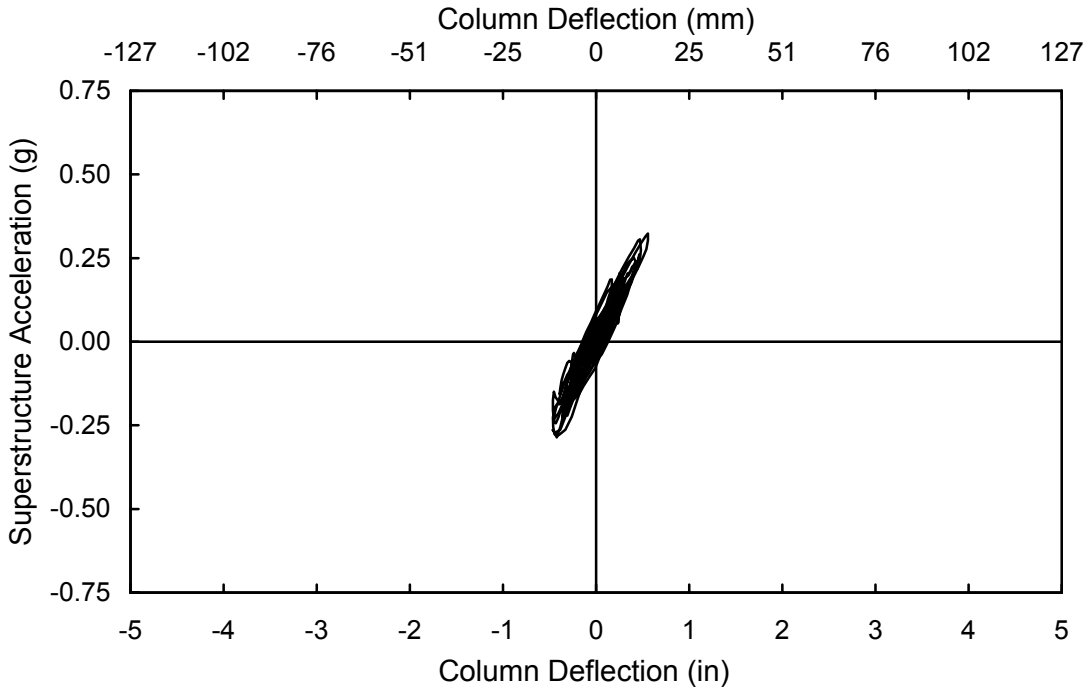

Figure 6-69: Bent 2 lateral acceleration vs. deflection hysteresis for test 14.

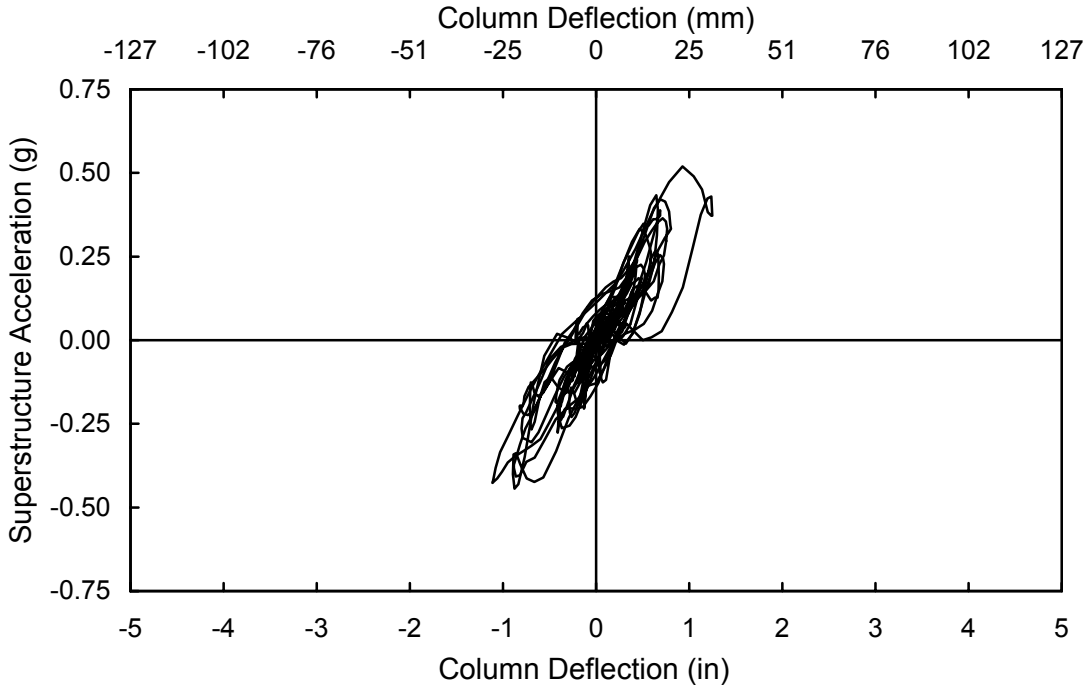

Figure 6-70: Bent 2 lateral acceleration vs. deflection hysteresis for test 15.

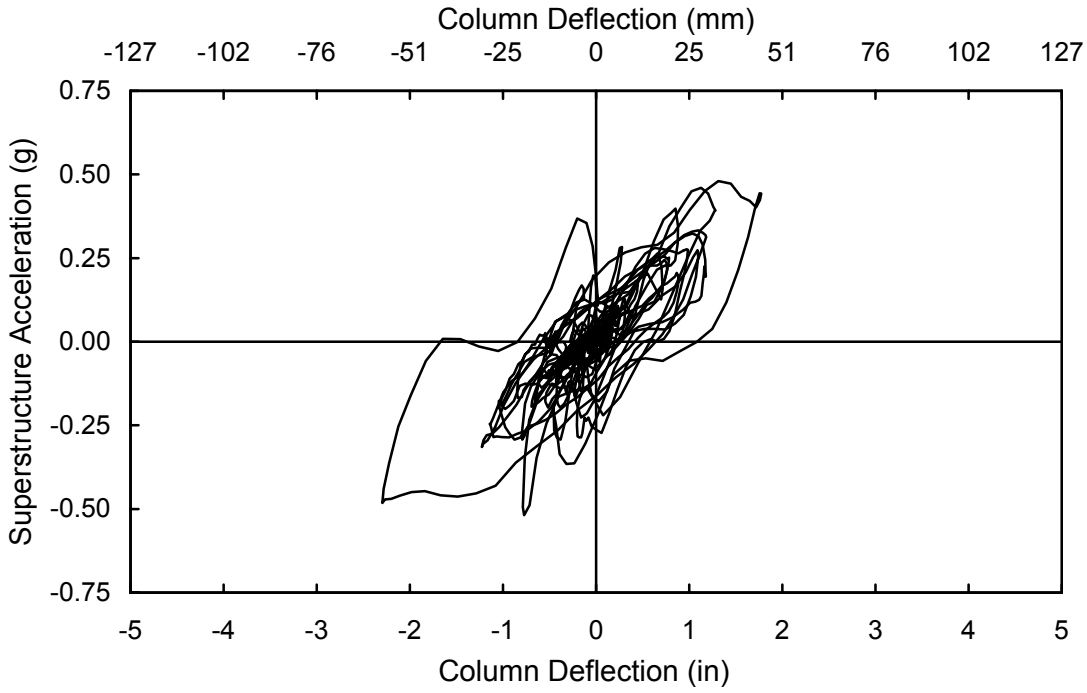

Figure 6-71: Bent 2 lateral acceleration vs. deflection hysteresis for test 16.

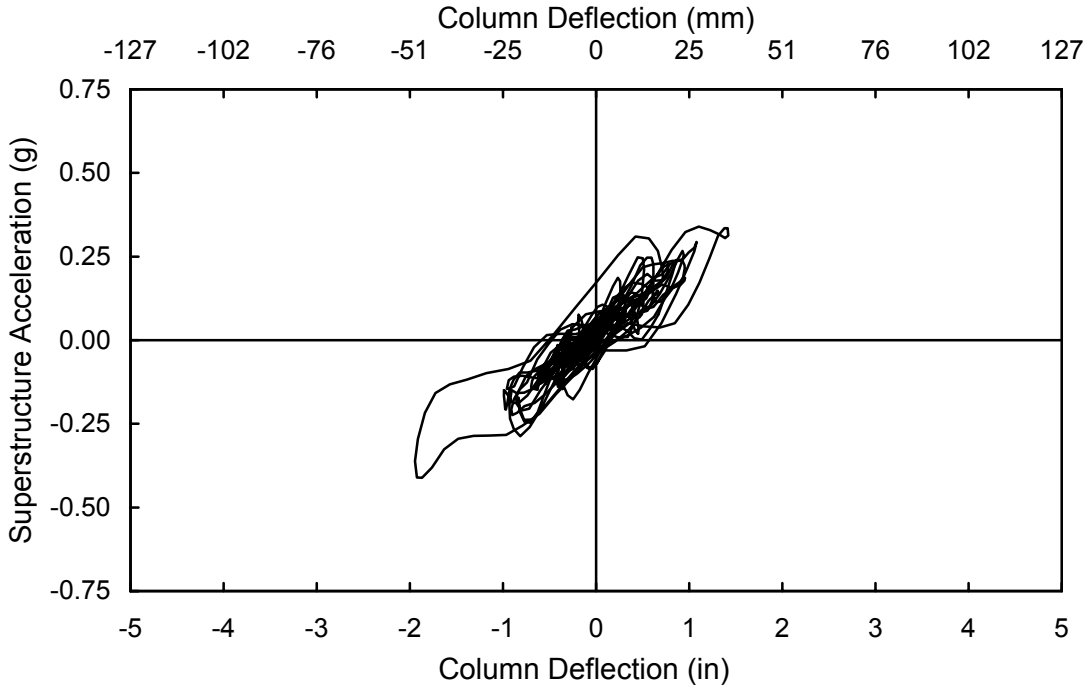

Figure 6-72: Bent 2 lateral acceleration vs. deflection hysteresis for test 17.

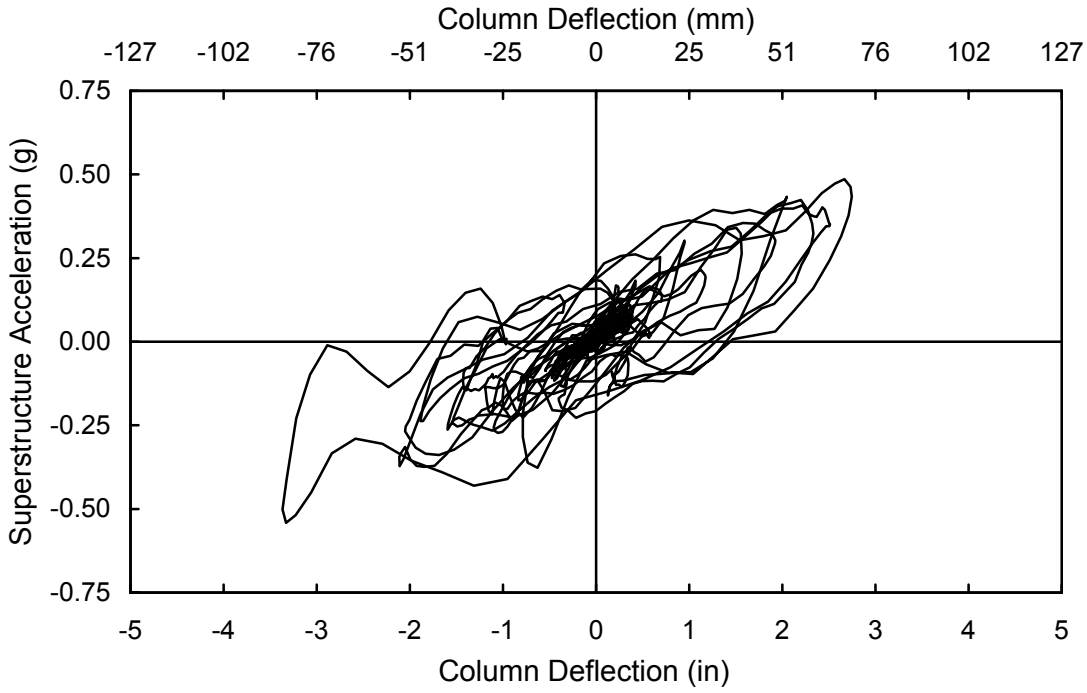

Figure 6-73: Bent 2 lateral acceleration vs. deflection hysteresis for test 18.

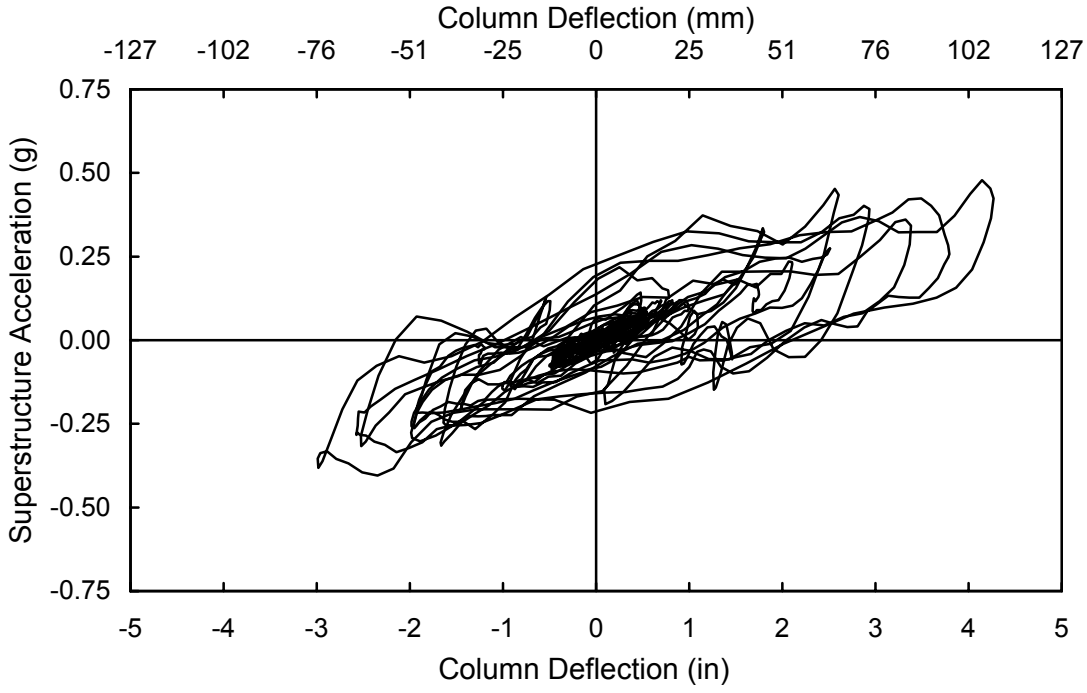

Figure 6-74: Bent 2 lateral acceleration vs. deflection hysteresis for test 19.

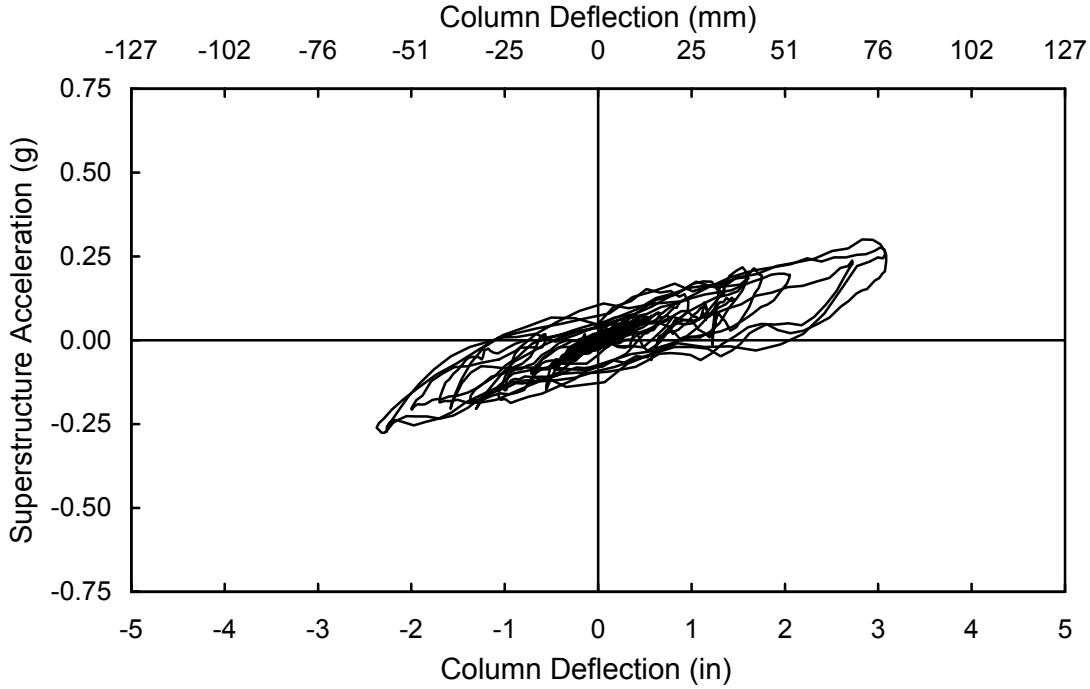

Figure 6-75: Bent 2 lateral acceleration vs. deflection hysteresis for test 20.

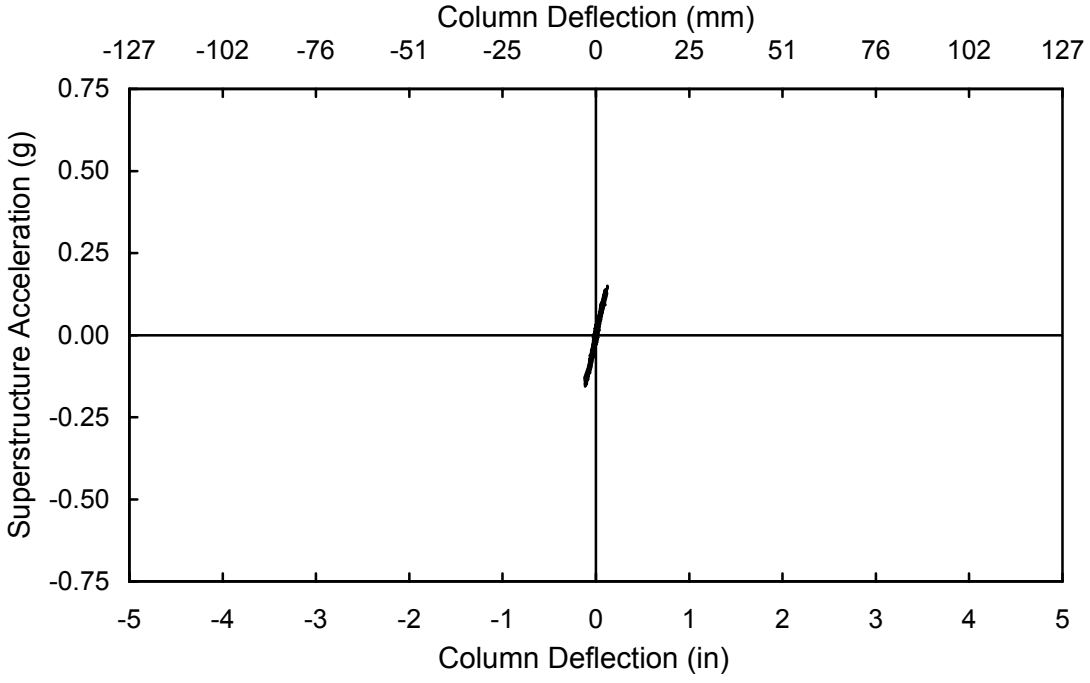

Figure 6-76: Bent 3 lateral acceleration vs. deflection hysteresis for test 12.

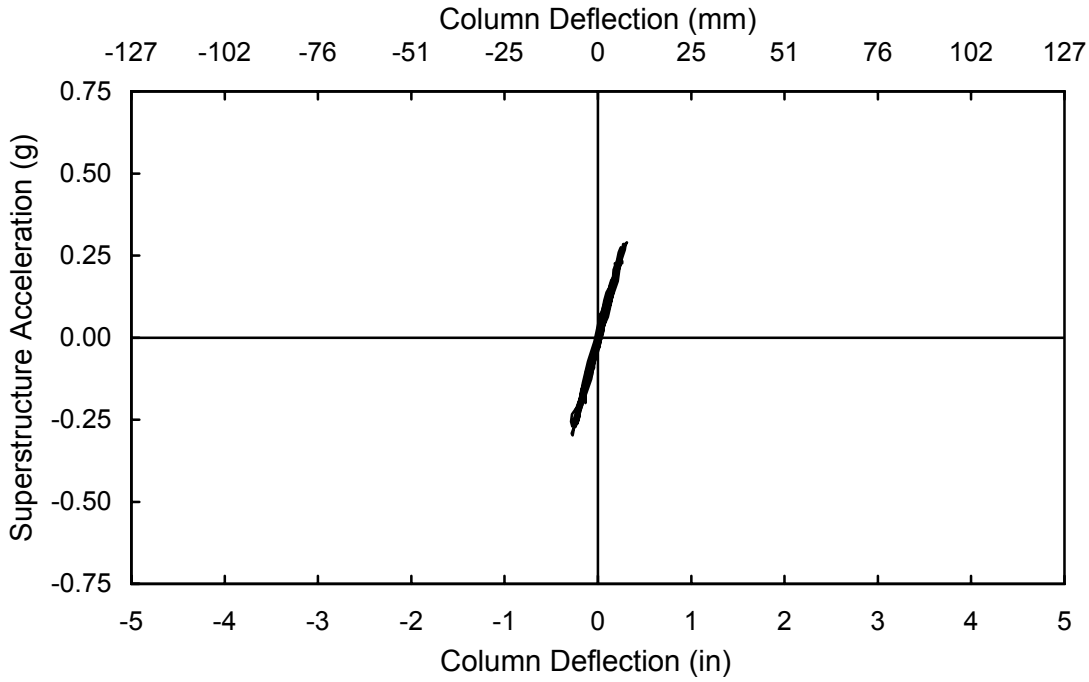

Figure 6-77: Bent 3 lateral acceleration vs. deflection hysteresis for test 13.

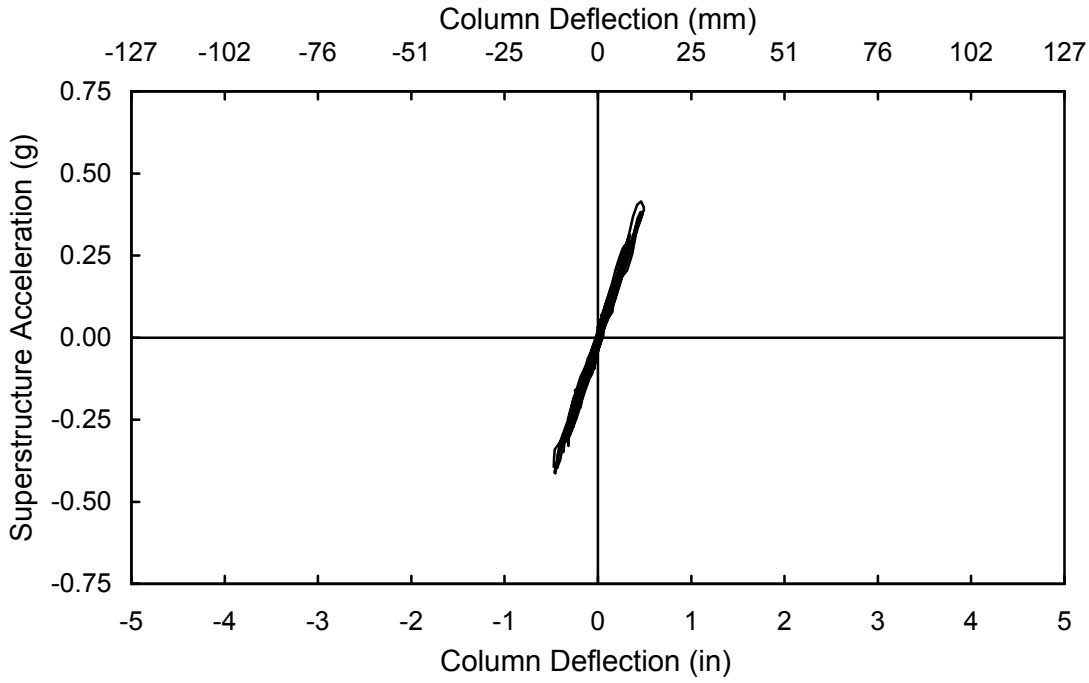

Figure 6-78: Bent 3 lateral acceleration vs. deflection hysteresis for test 14.

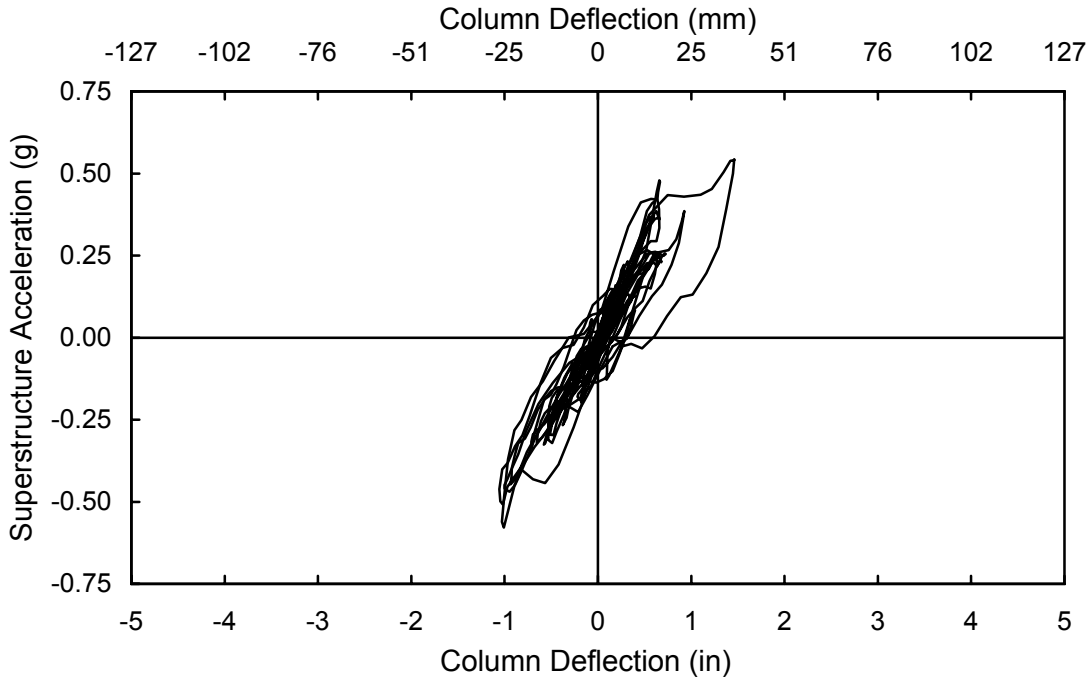

Figure 6-79: Bent 3 lateral acceleration vs. deflection hysteresis for test 15.

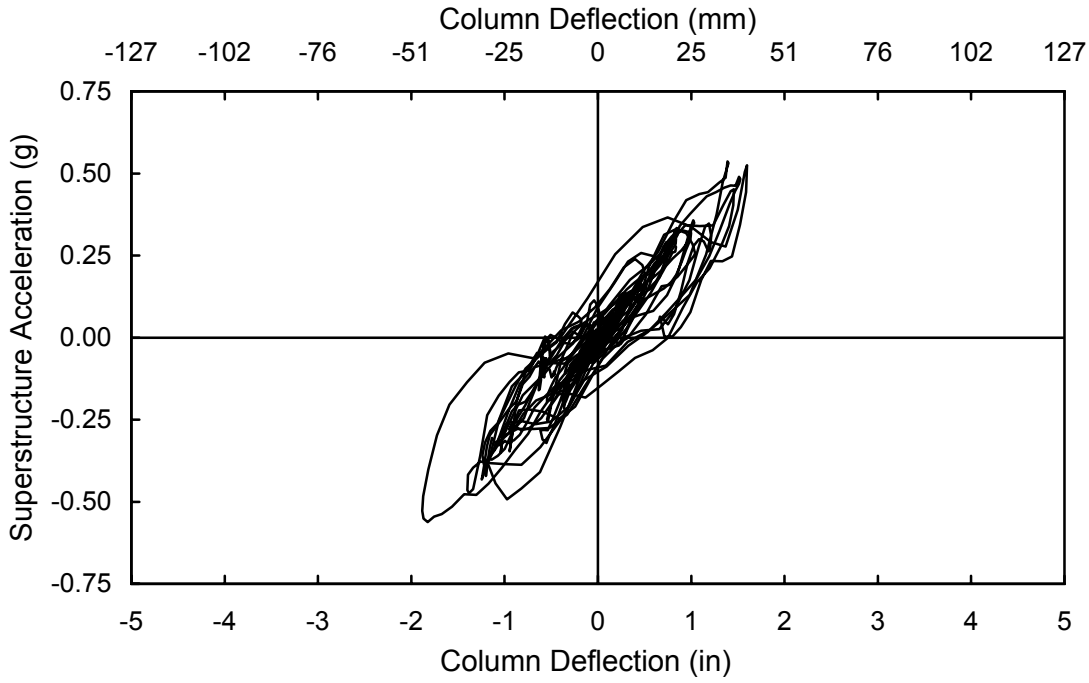

Figure 6-80: Bent 3 lateral acceleration vs. deflection hysteresis for test 16.

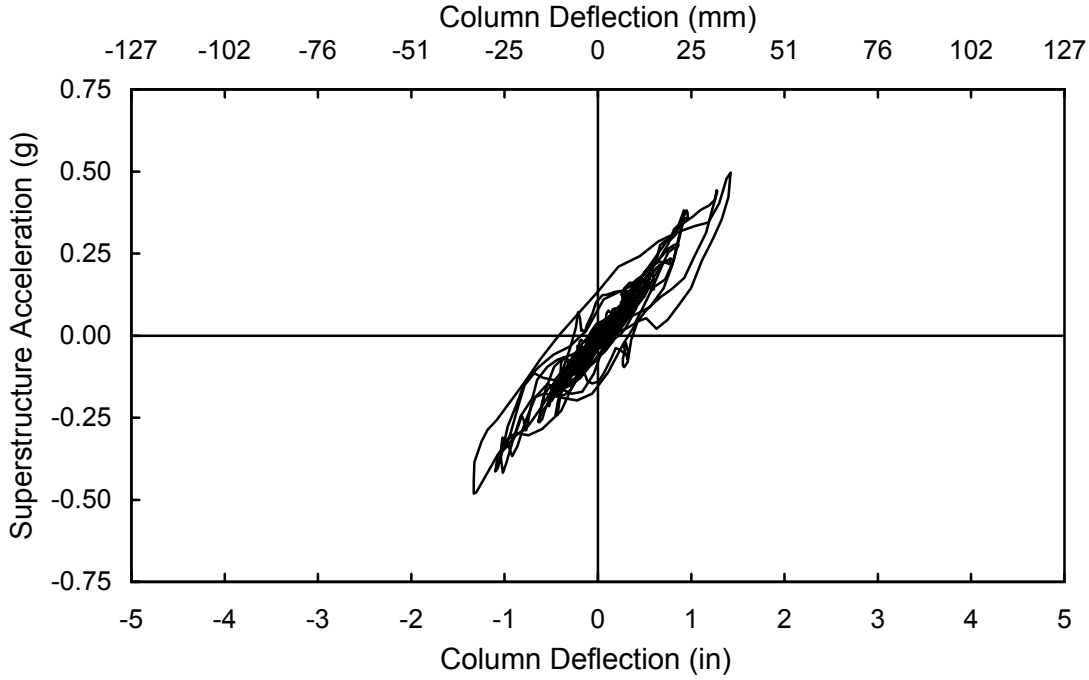

Figure 6-81: Bent 3 lateral acceleration vs. deflection hysteresis for test 17.

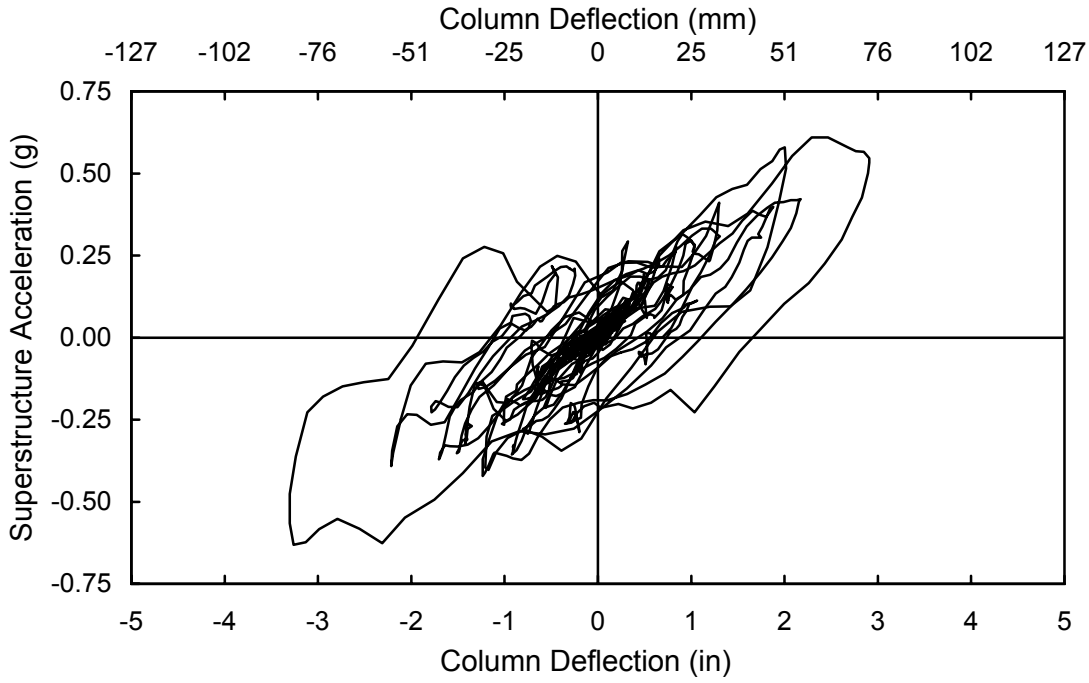

Figure 6-82: Bent 3 lateral acceleration vs. deflection hysteresis for test 18.

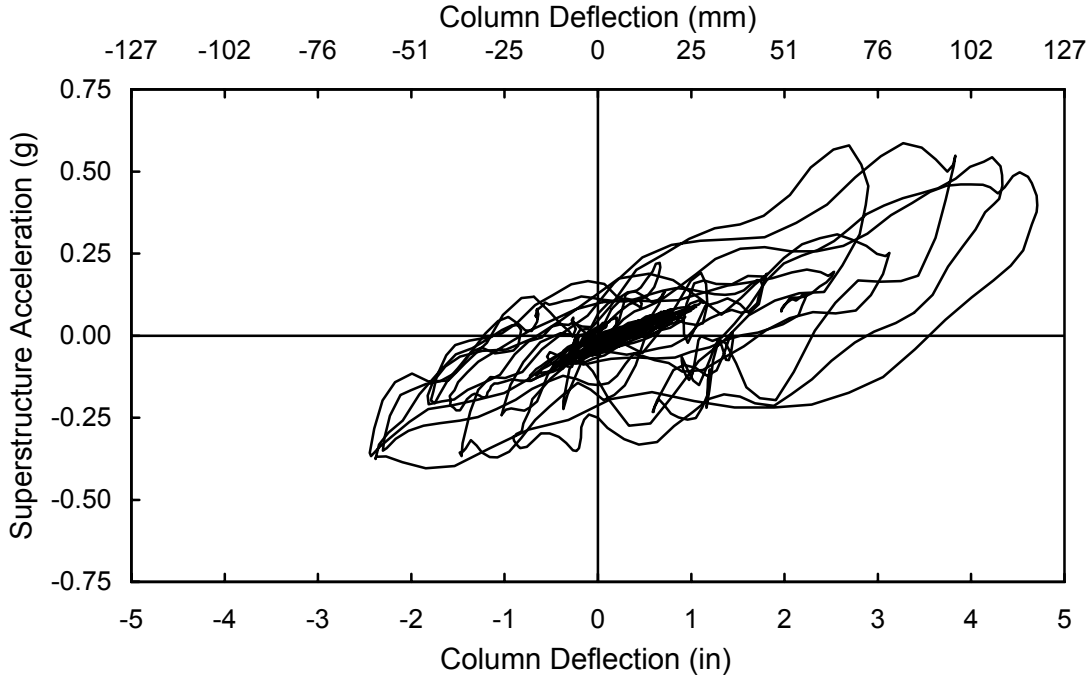

Figure 6-83: Bent 3 lateral acceleration vs. deflection hysteresis for test 19.

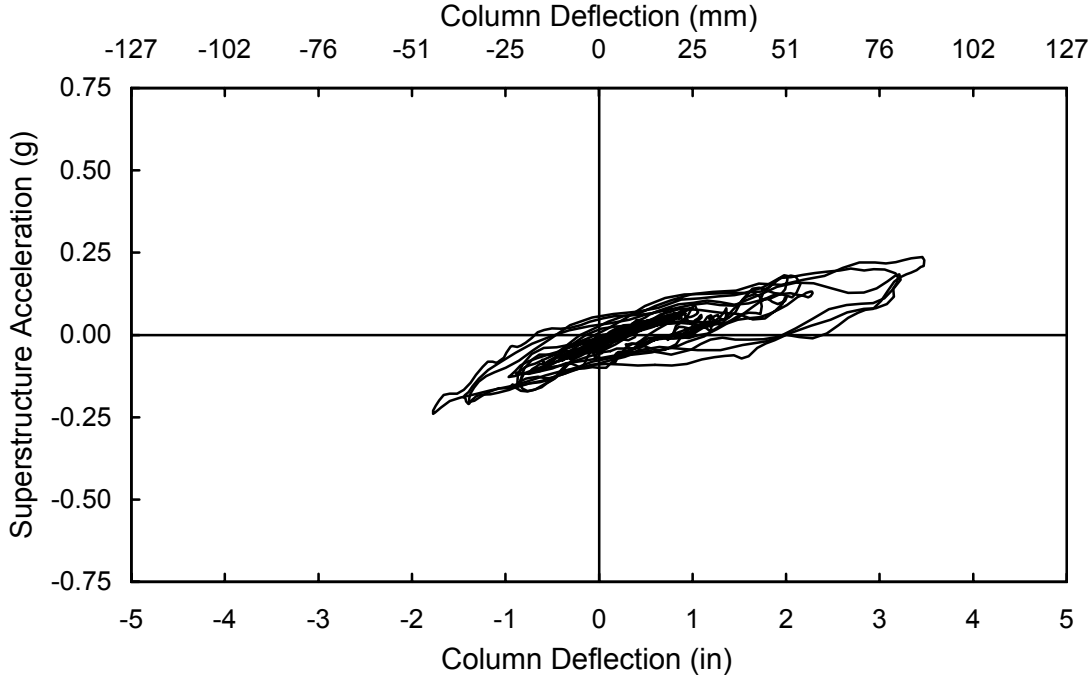

Figure 6-84: Bent 3 lateral acceleration vs. deflection hysteresis for test 20.

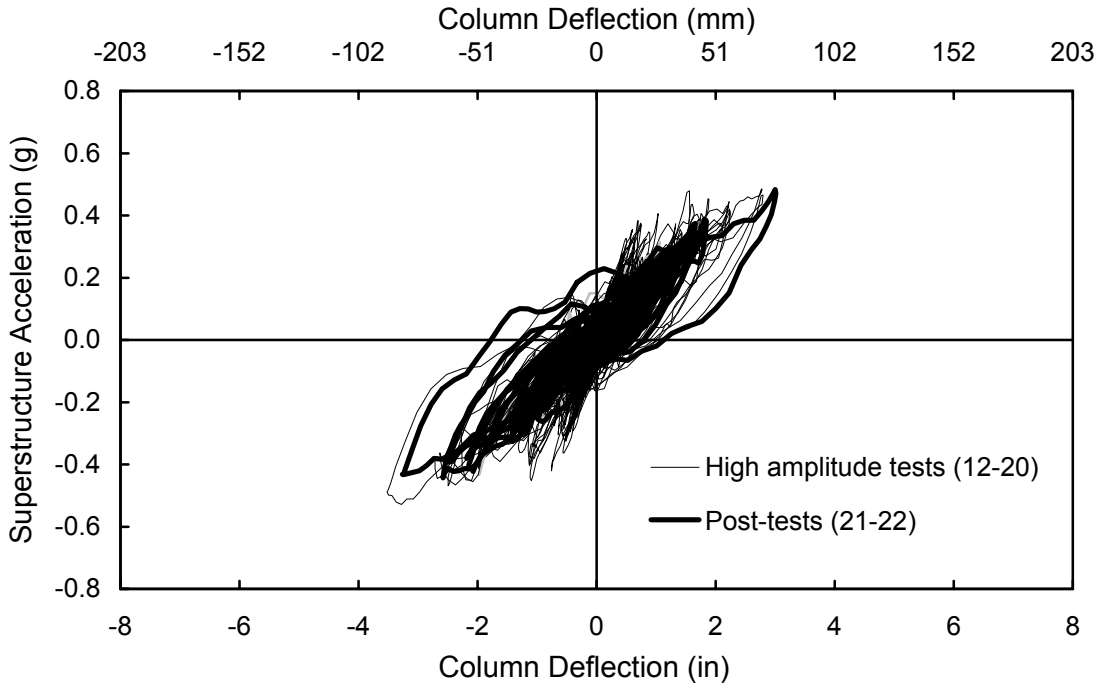

Figure 6-85: Bent 1 cumulative lateral acceleration vs. deflection hysteresis for post-tests (tests 21-22)

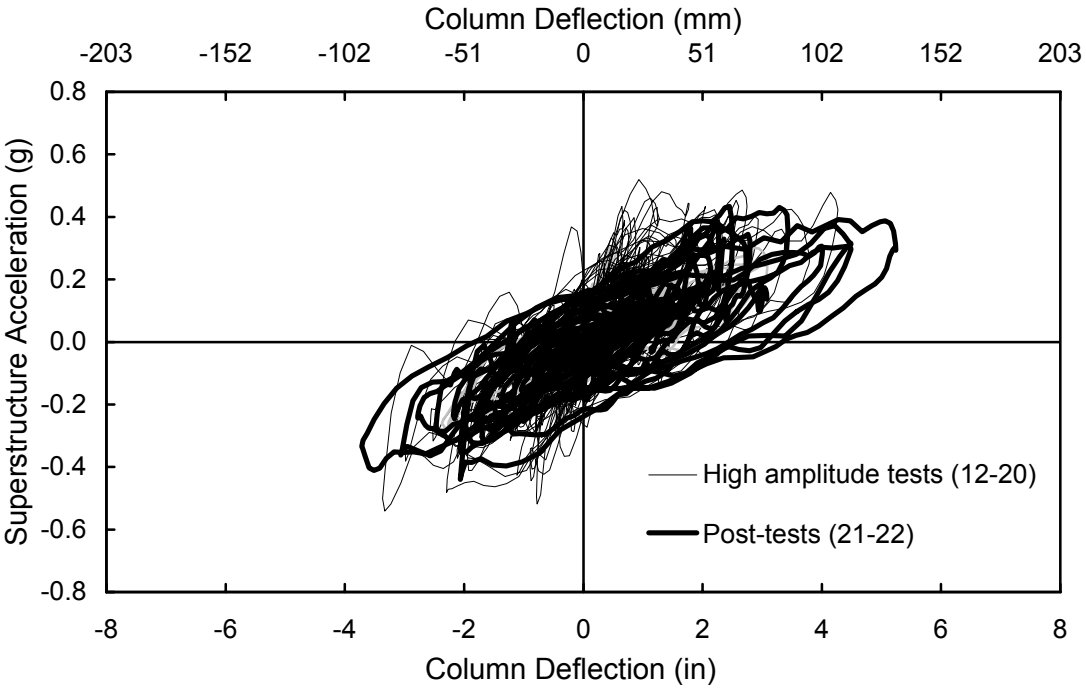

Figure 6-86: Bent 2 cumulative lateral acceleration vs. deflection hysteresis for post-tests (tests 21-22).

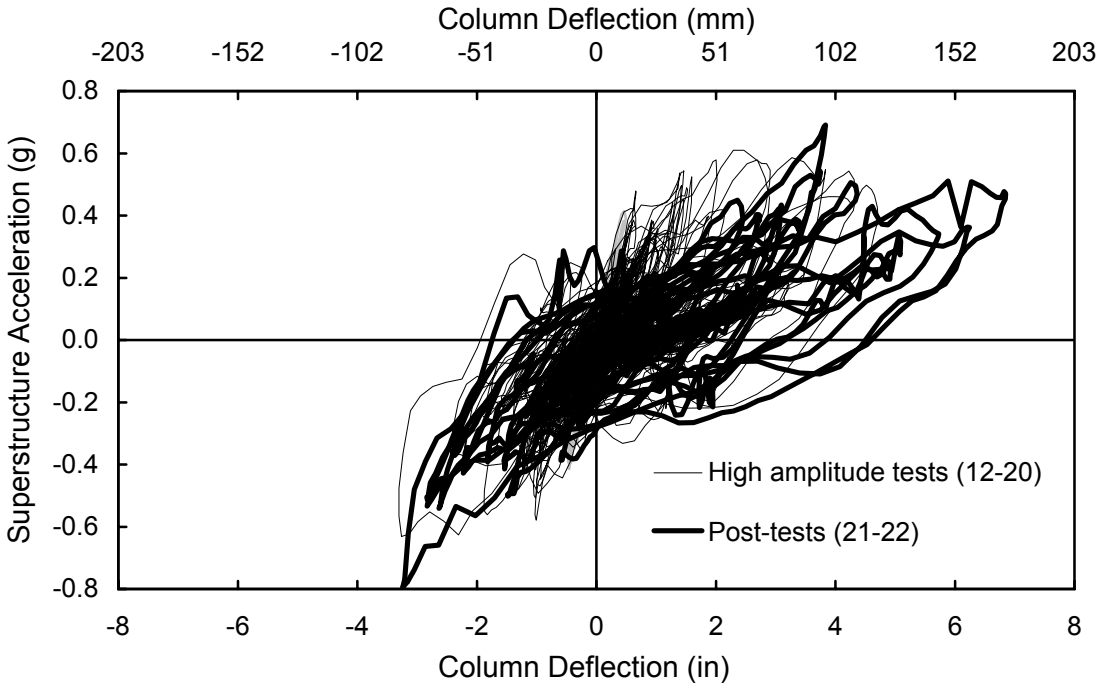

Figure 6-87: Bent 3 cumulative lateral acceleration vs. deflection hysteresis for post-tests (tests 21-22).

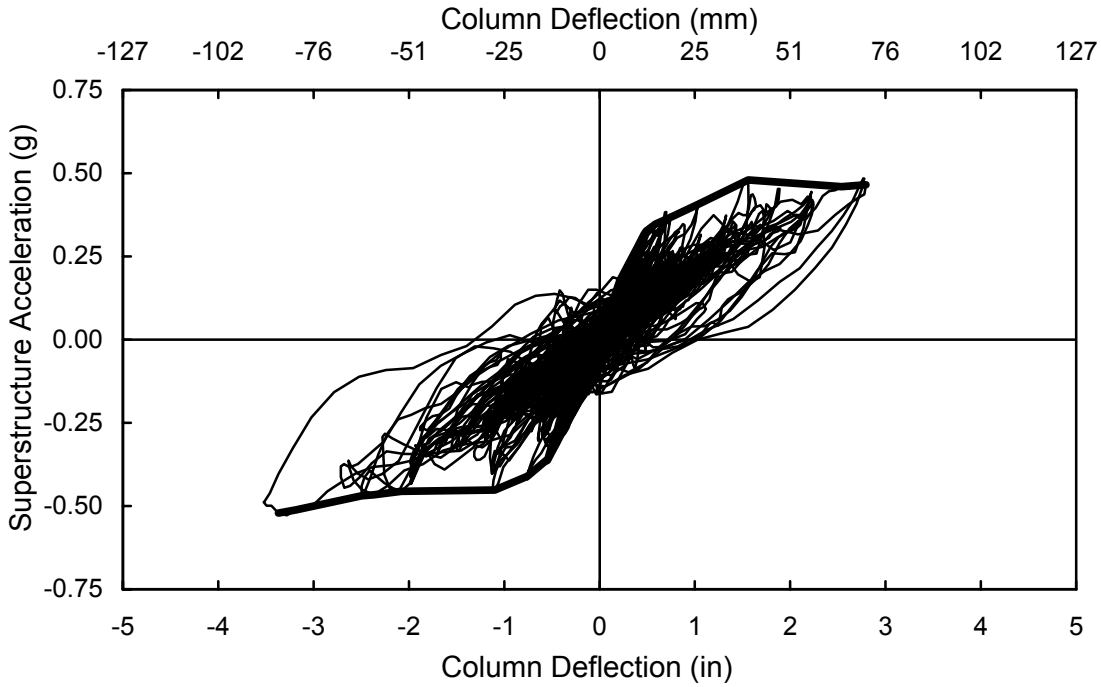

Figure 6-88: Bent 1 backbone curve from acceleration-deflection hysteresis.

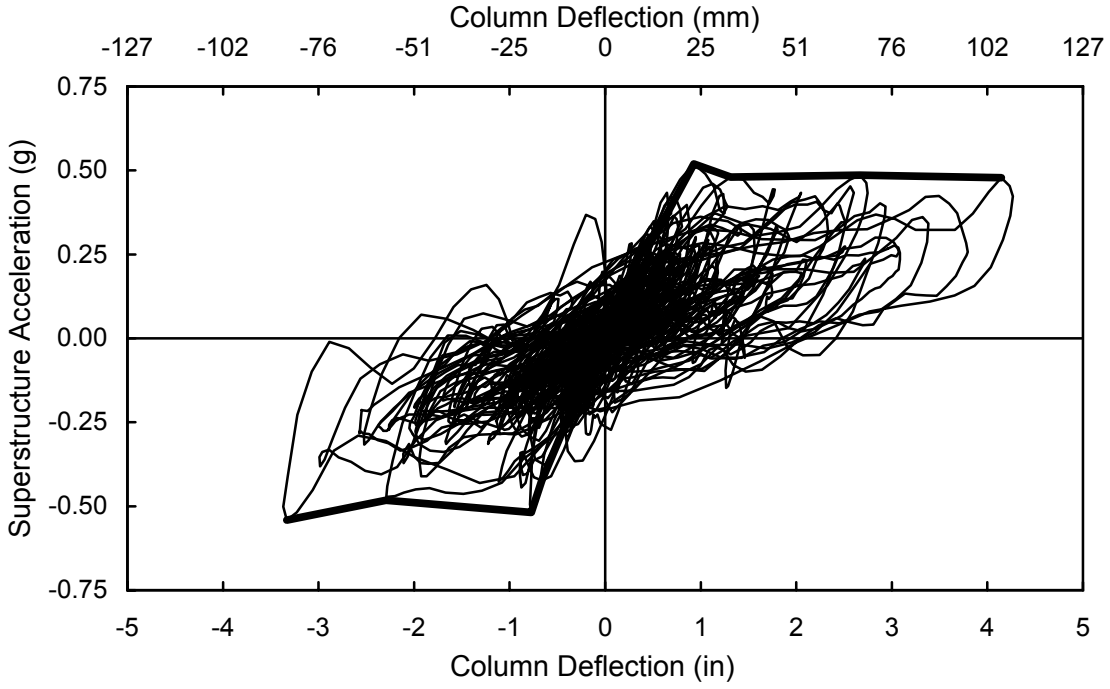

Figure 6-89: Bent 2 backbone curve from acceleration-deflection hysteresis.

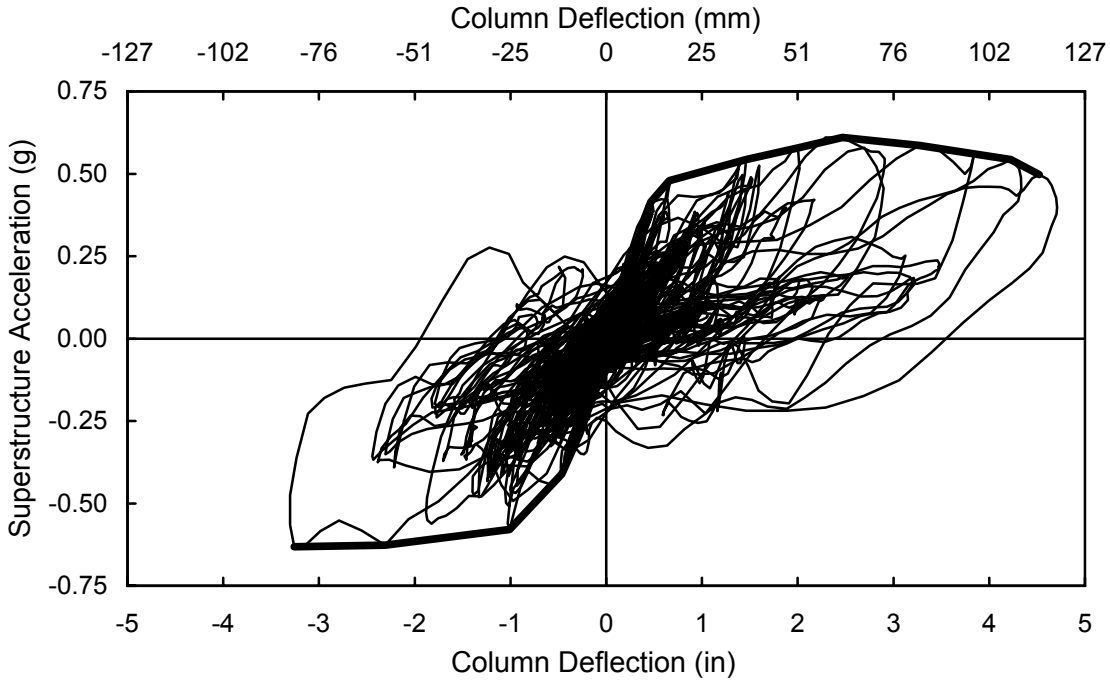

Figure 6-90: Bent 3 backbone curve from acceleration-deflection hysteresis.

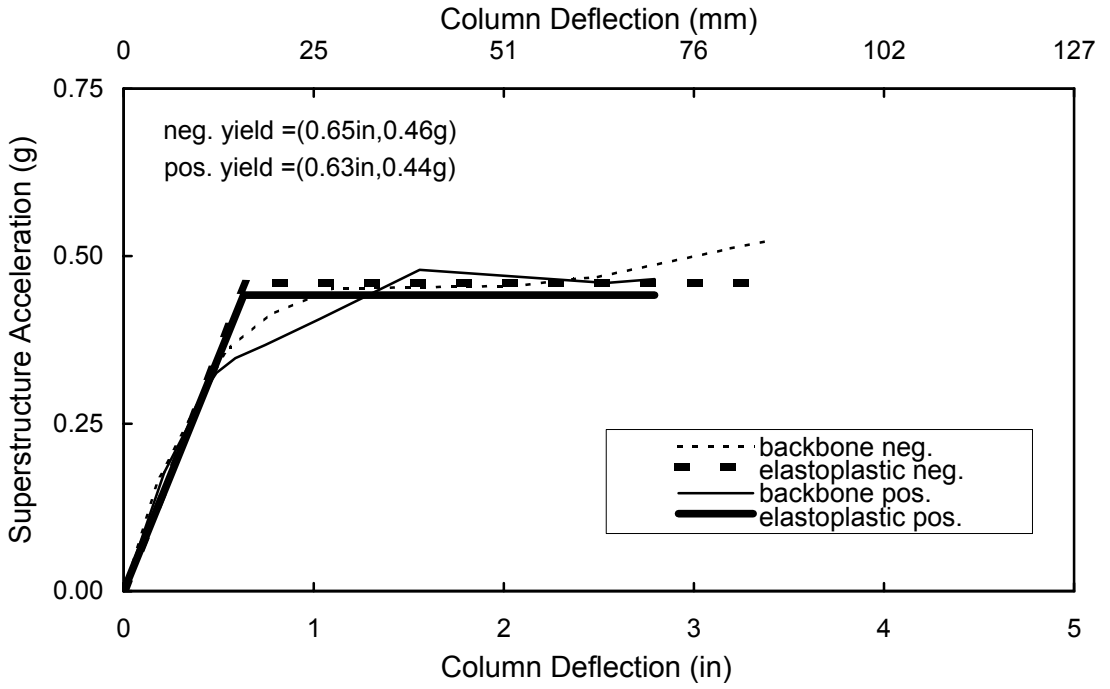

Figure 6-91: Bent 1 elastoplastic idealization from acceleration-deflection hysteresis.

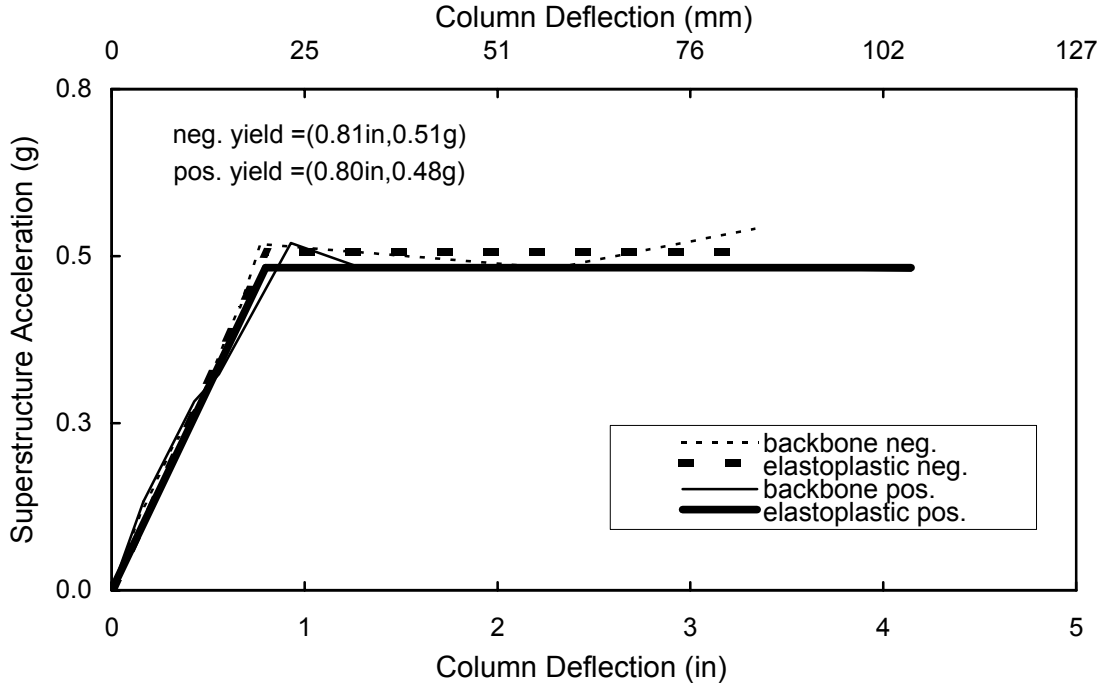

Figure 6-92: Bent 2 elastoplastic idealization from acceleration-deflection hysteresis.

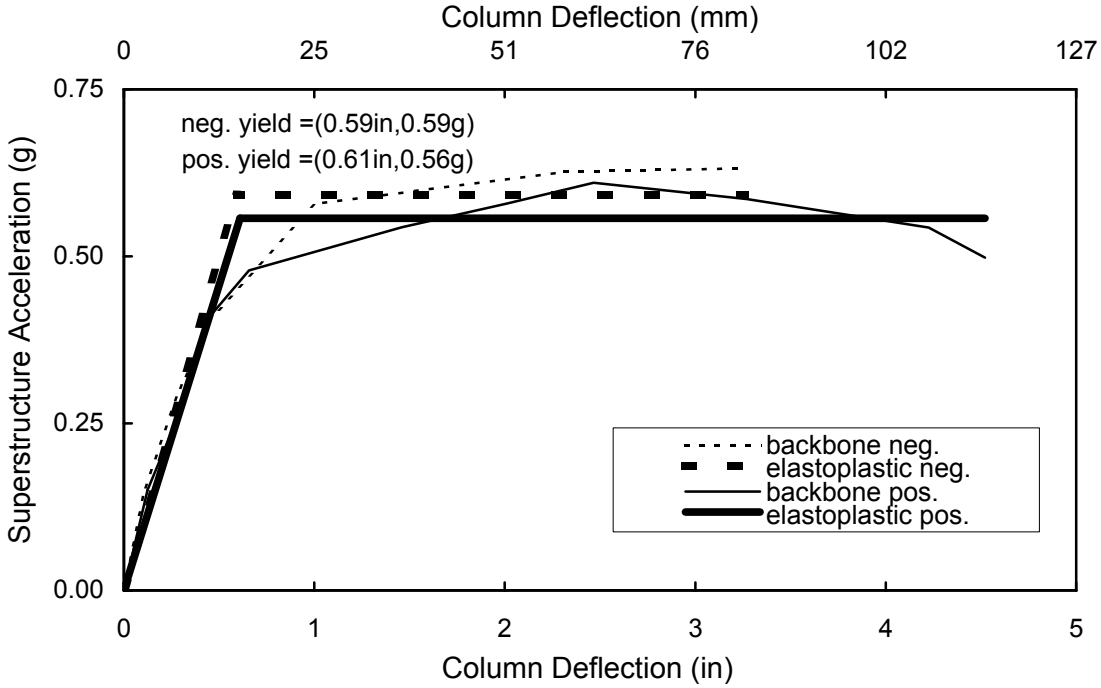

Figure 6-93: Bent 3 elastoplastic idealization from acceleration-deflection hysteresis.

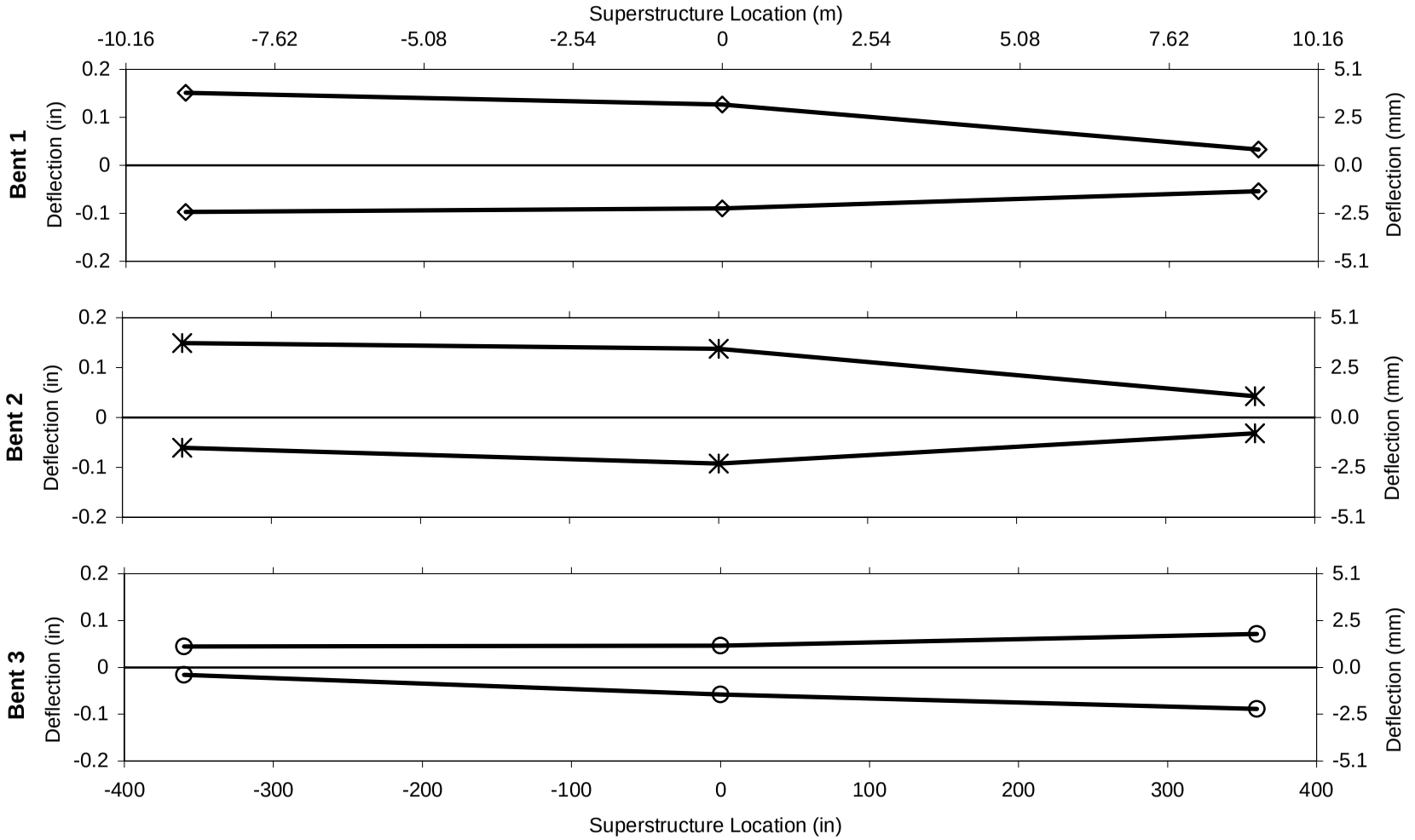

Figure 6-94: Test 1 transverse deflection plot of superstructure at instant of maximum deflections for each bent.

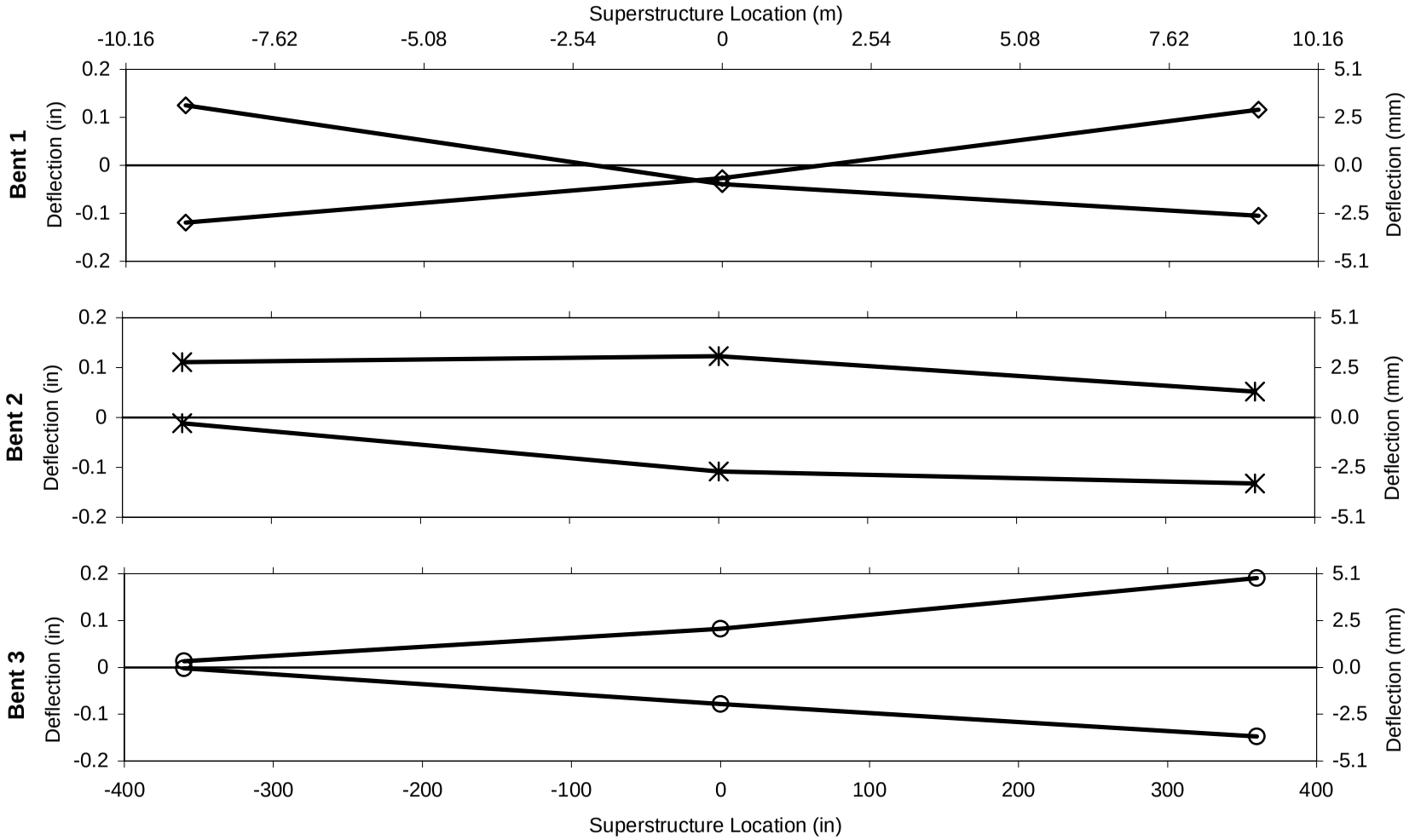

Figure 6-95: Test 2 transverse deflection plot of superstructure at instant of maximum deflections for each bent.

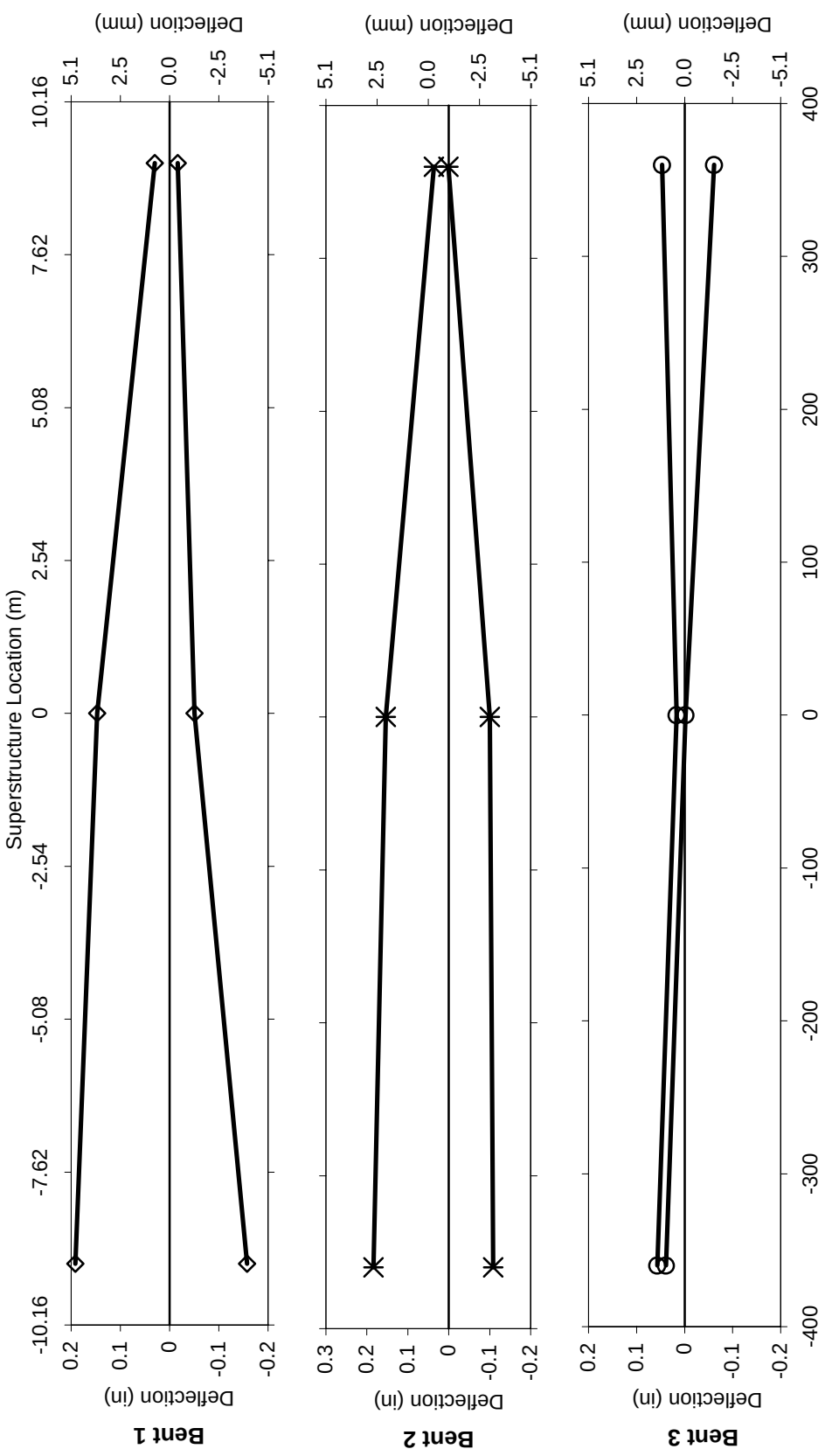

Figure 6-96: Test 3 transverse deflection plot of superstructure at instant of maximum deflections for each bent.

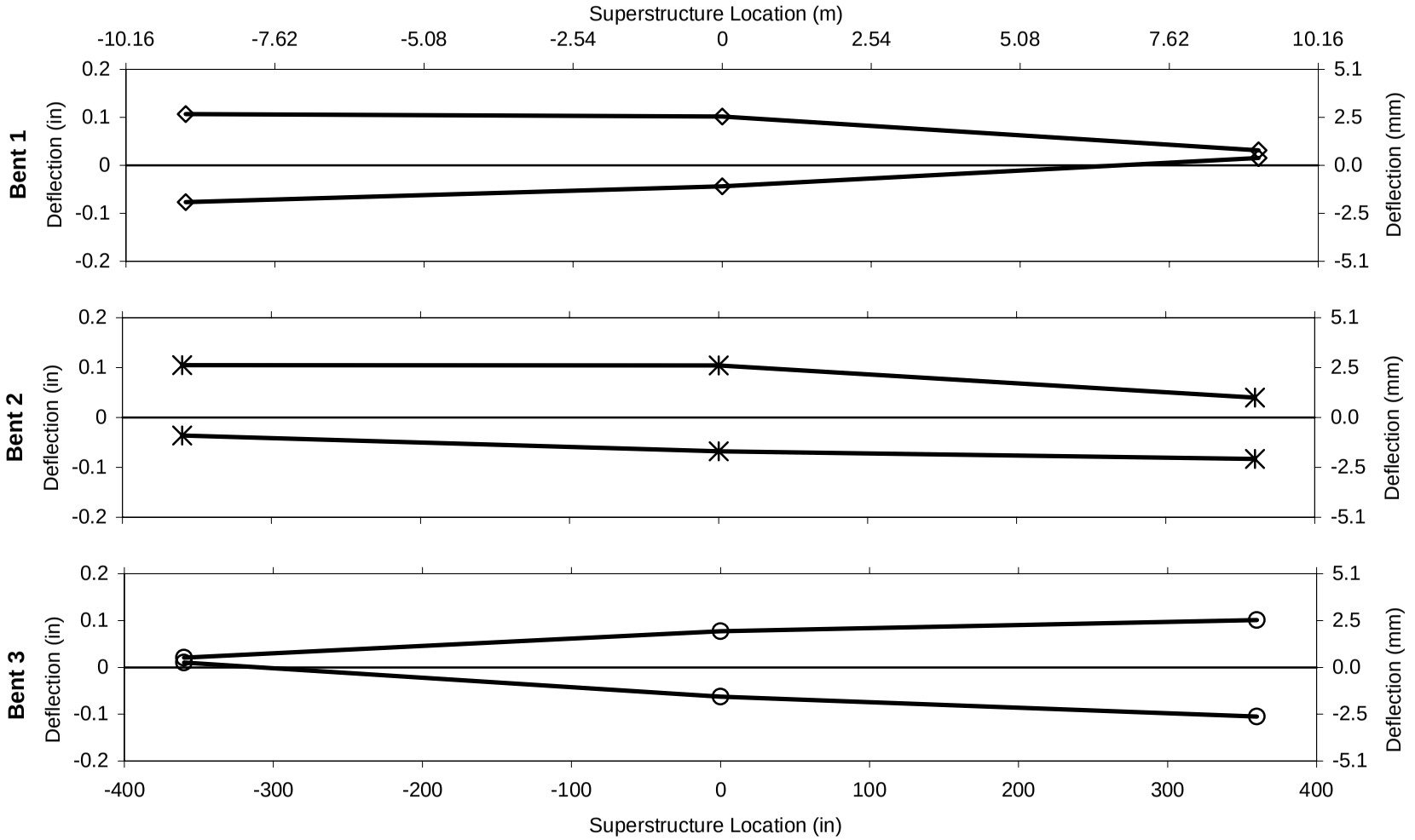

Figure 6-97: Test 4 transverse deflection plot of superstructure at instant of maximum deflections for each bent.

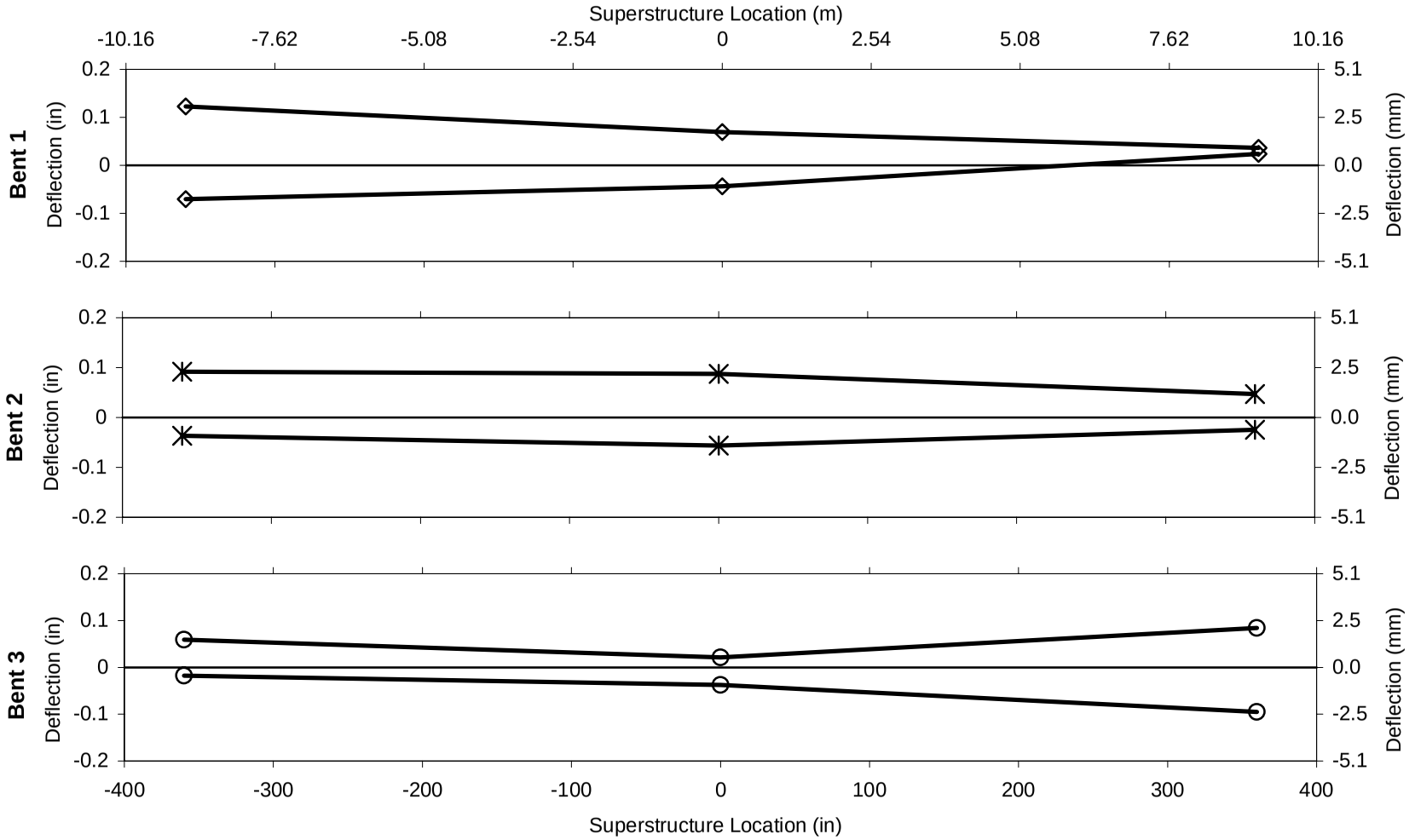

Figure 6-98: Test 5 transverse deflection plot of superstructure at instant of maximum deflections for each bent.

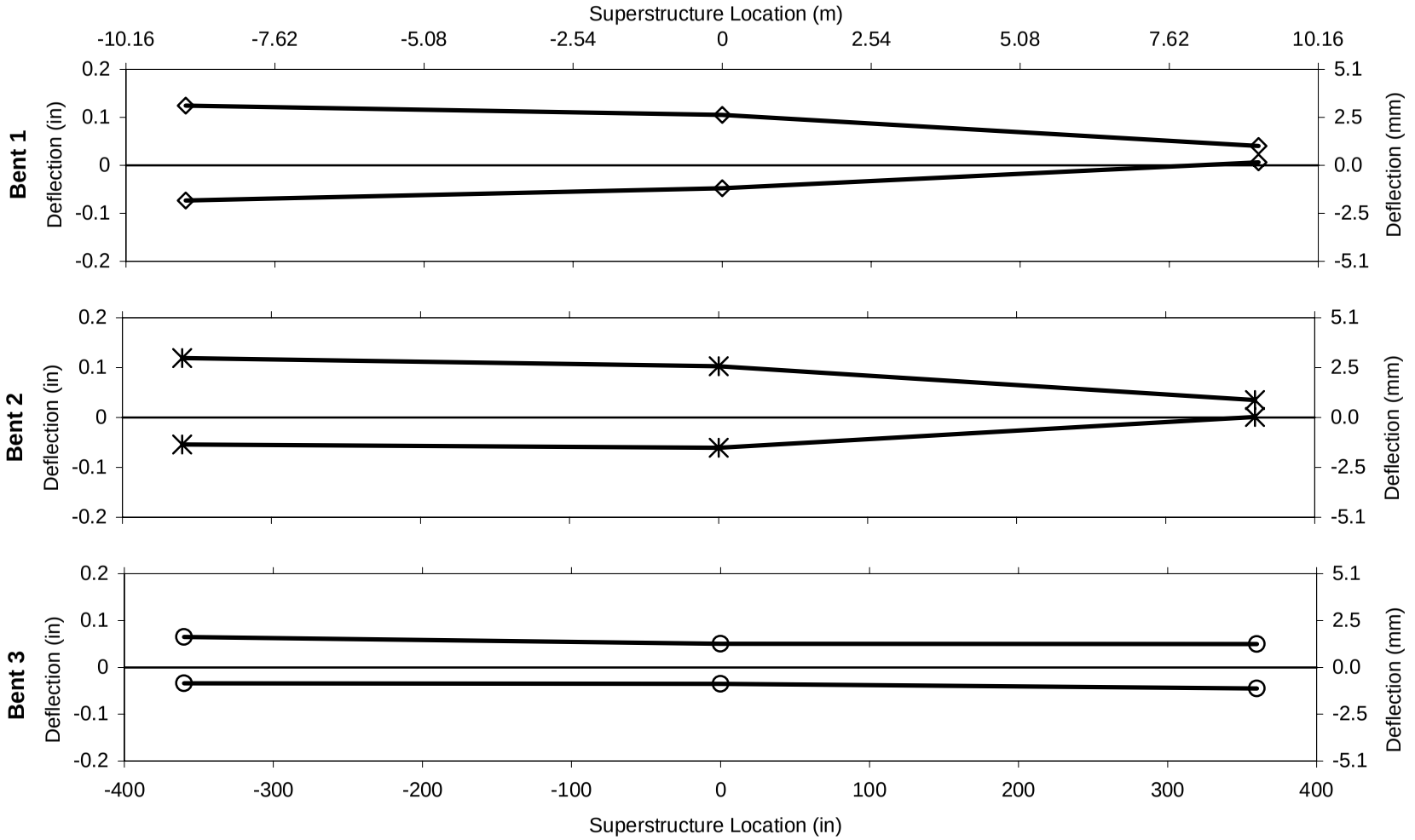

Figure 6-99: Test 6 transverse deflection plot of superstructure at instant of maximum deflections for each bent.

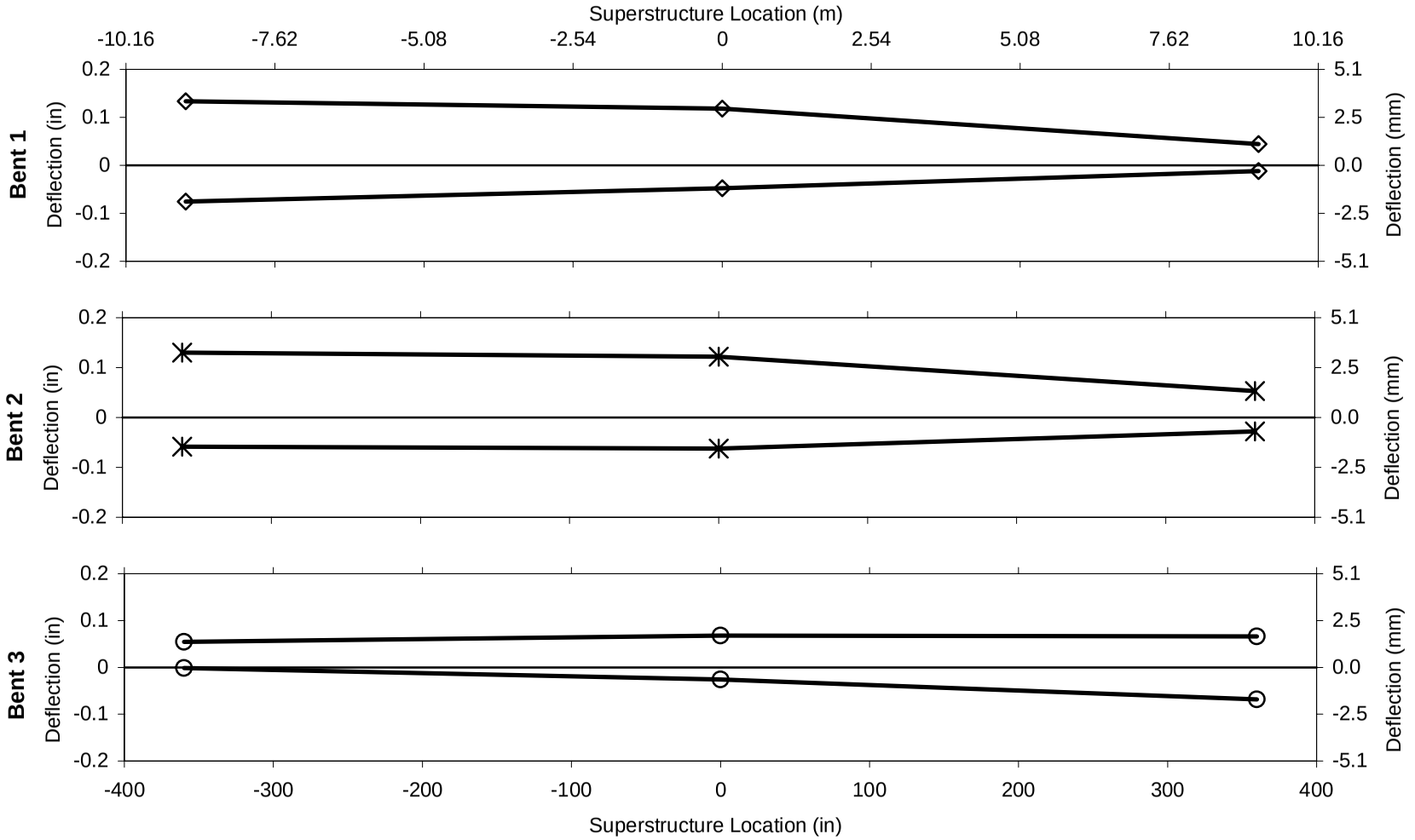

Figure 6-100: Test 8 transverse deflection plot of superstructure at instant of maximum deflections for each bent.

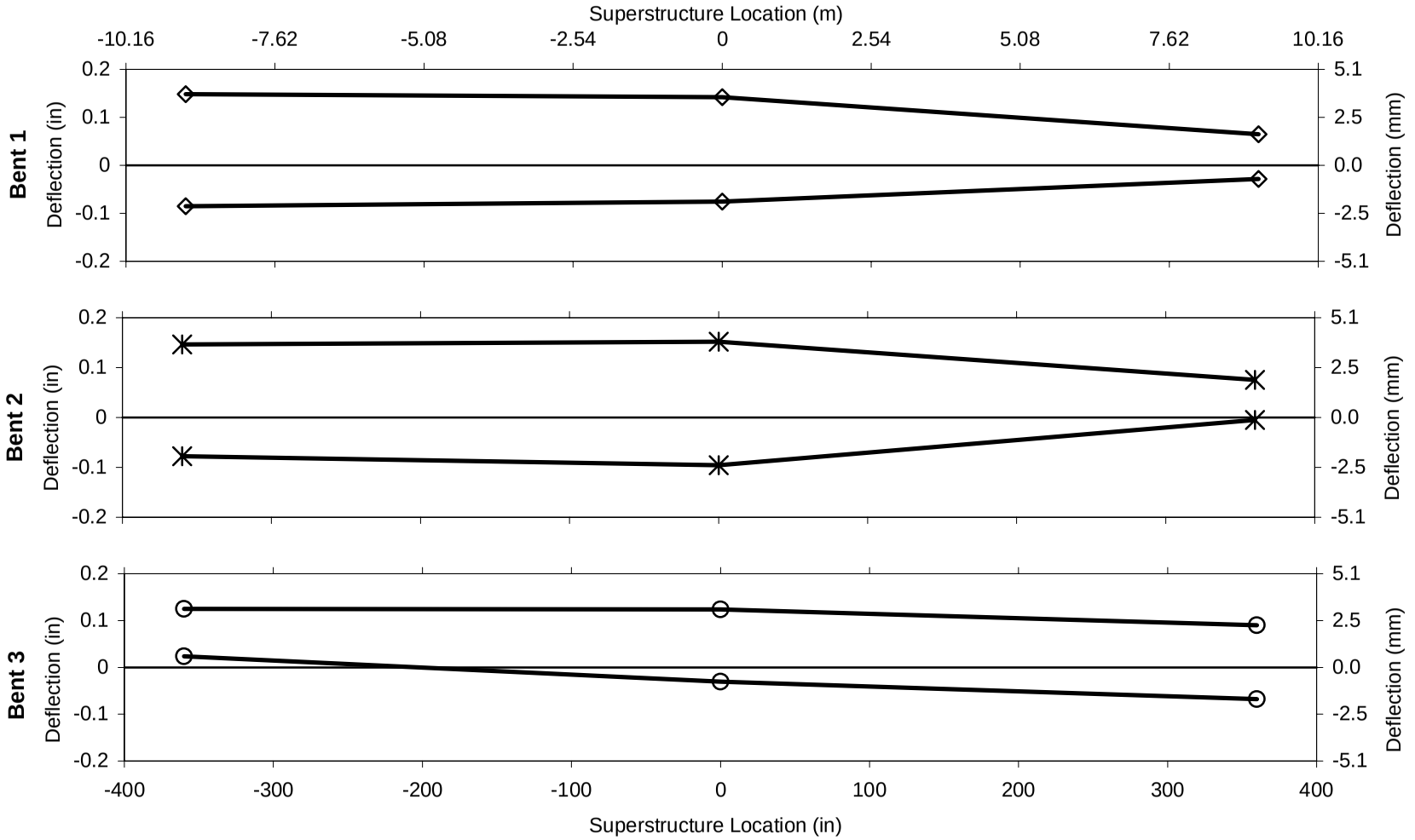

Figure 6-101: Test 9 transverse deflection plot of superstructure at instant of maximum deflections for each bent.

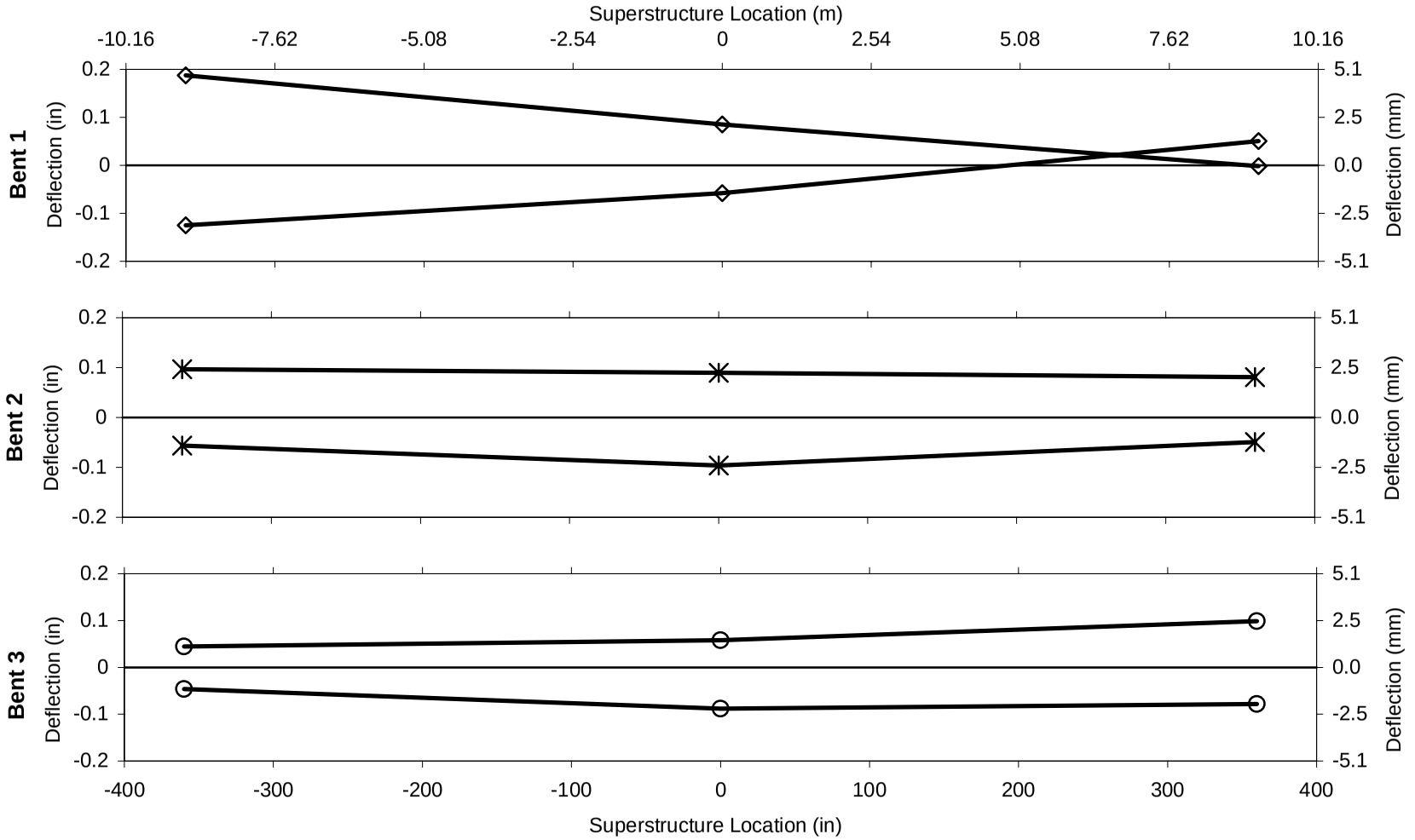

Figure 6-102: Test 10 transverse deflection plot of superstructure at instant of maximum deflections for each bent.

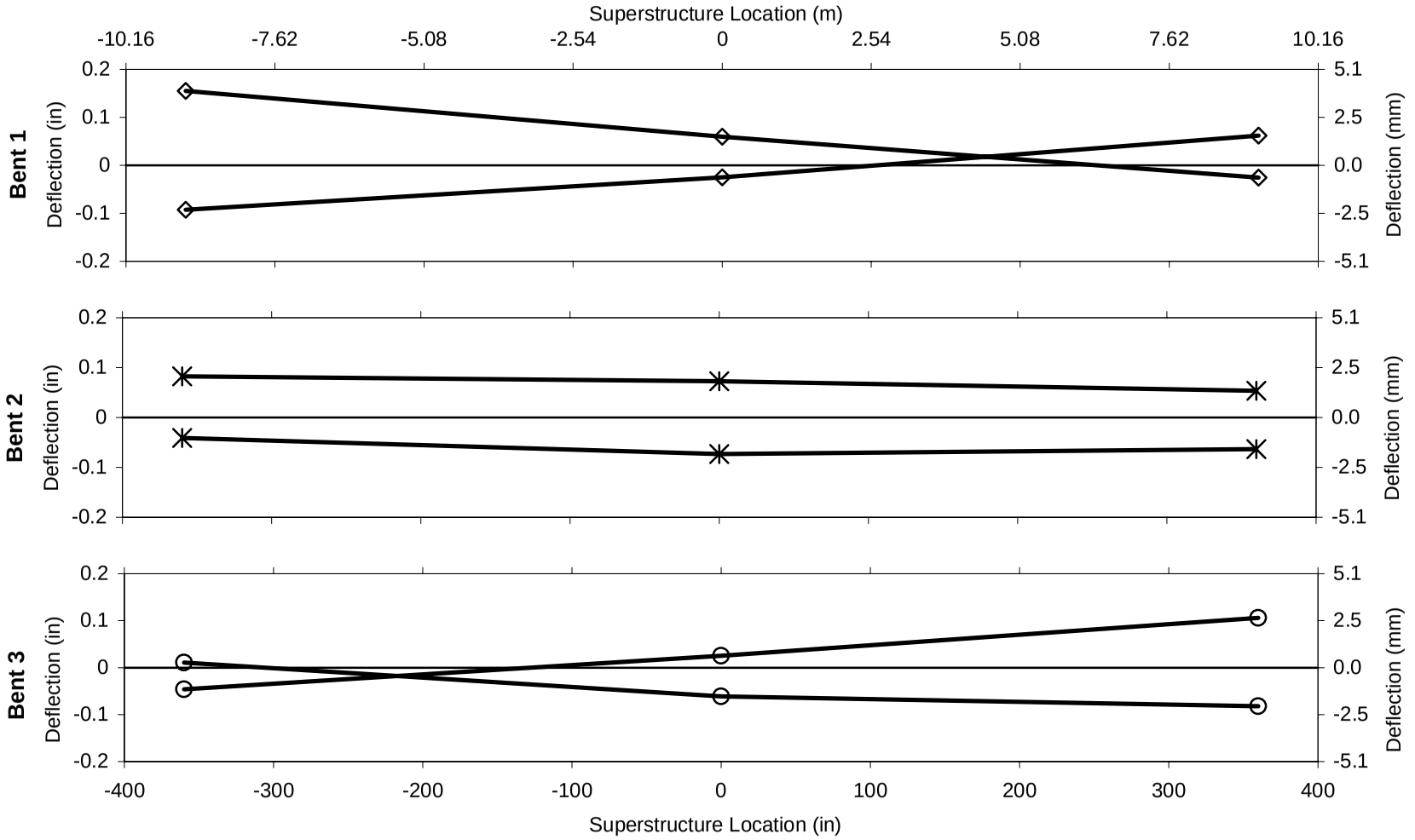

Figure 6-103: Test 11 transverse deflection plot of superstructure at instant of maximum deflections for each bent.

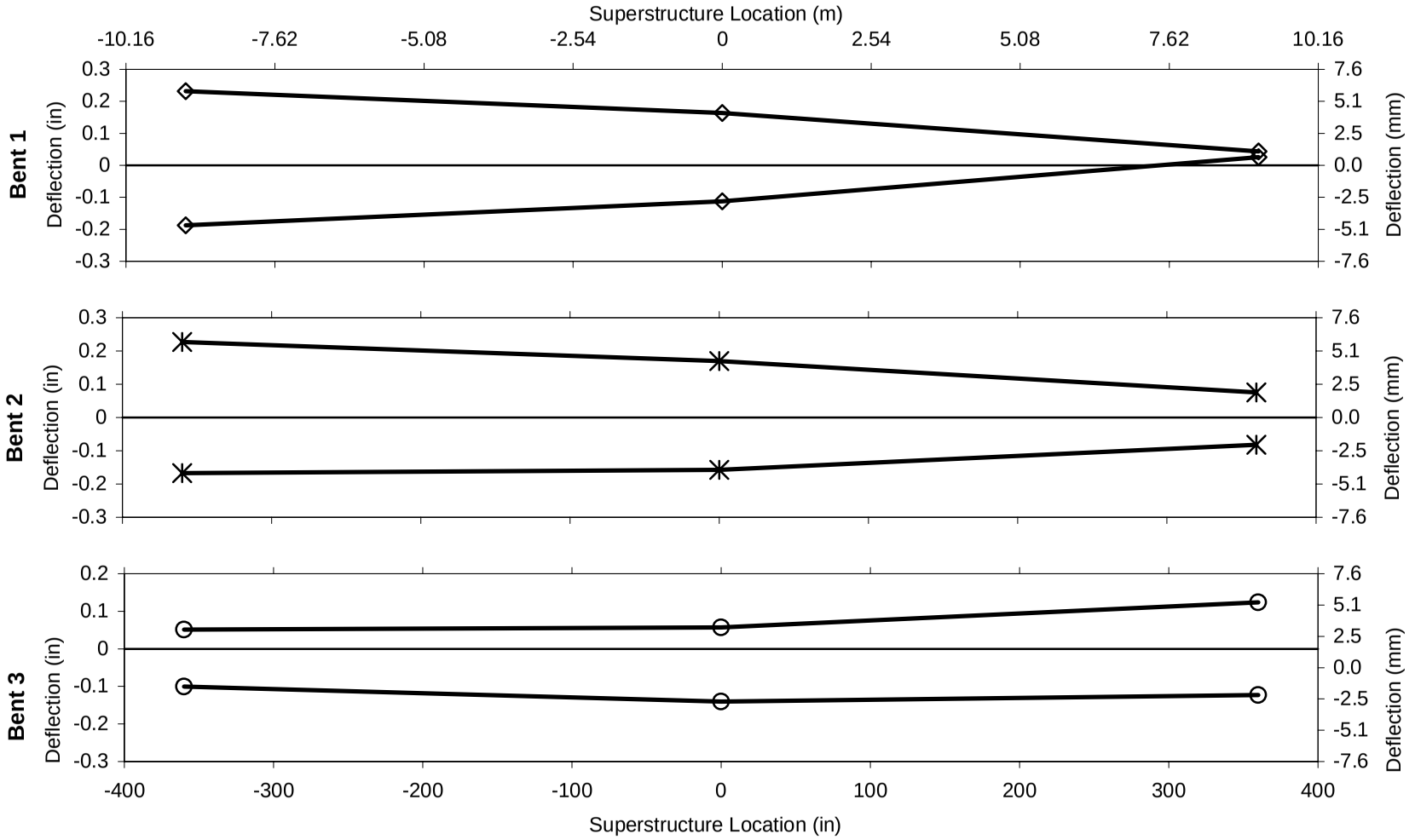

Figure 6-104: Test 12 transverse deflection plot of superstructure at instant of maximum deflections for each bent.

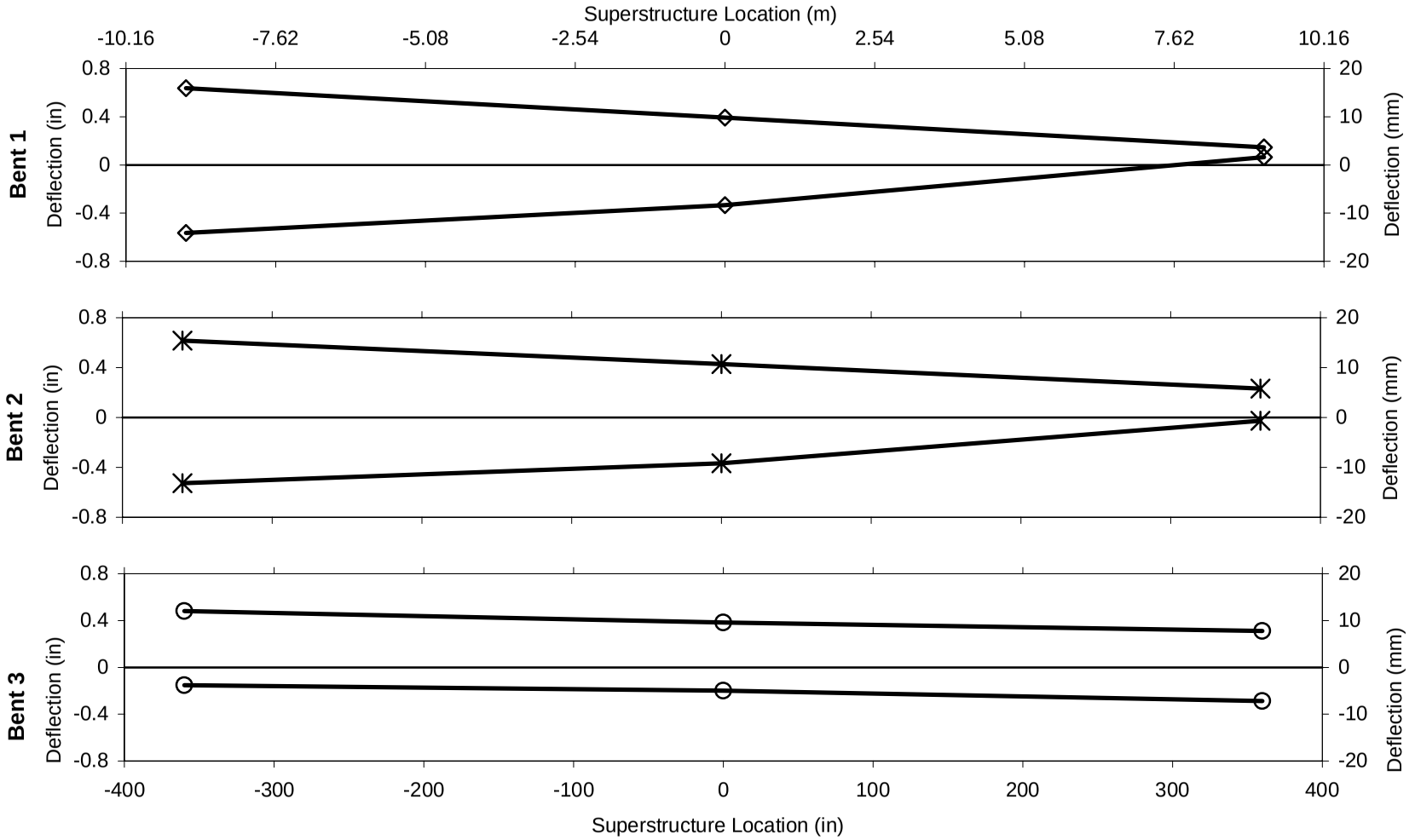

Figure 6-105: Test 13 transverse deflection plot of superstructure at instant of maximum deflections for each bent.

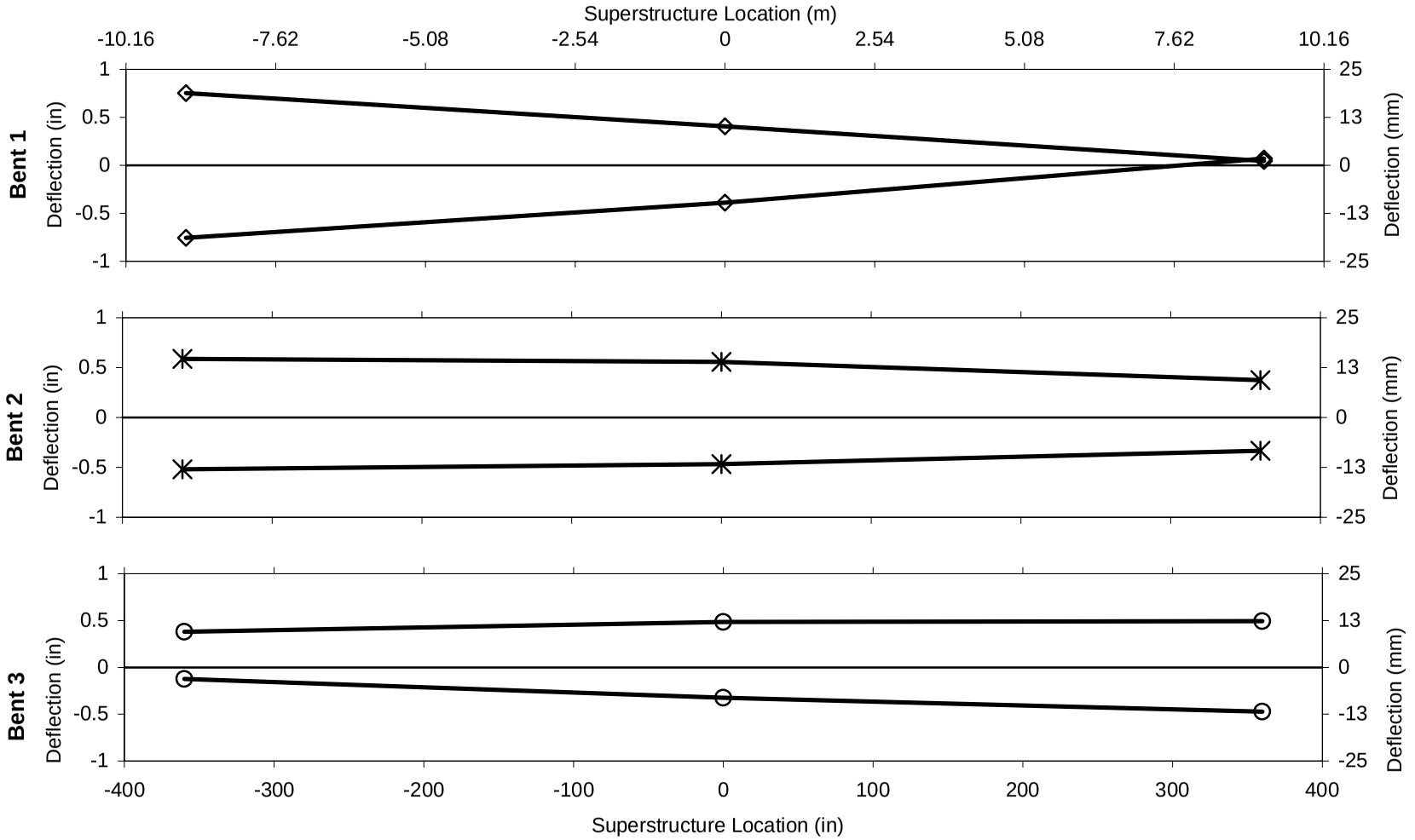

Figure 6-106: Test 14 transverse deflection plot of superstructure at instant of maximum deflections for each bent.

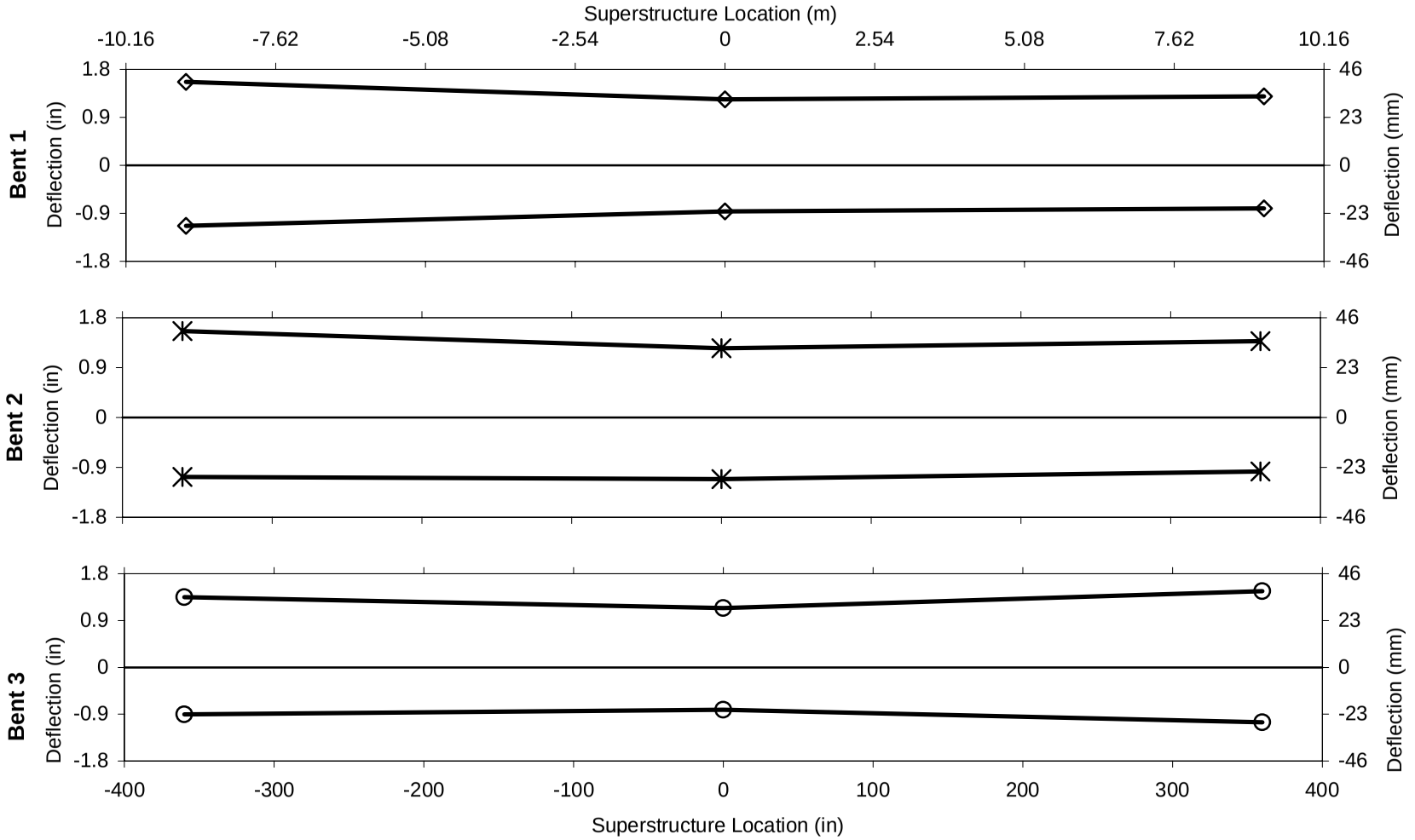

Figure 6-107: Test 15 transverse deflection plot of superstructure at instant of maximum deflections for each bent.

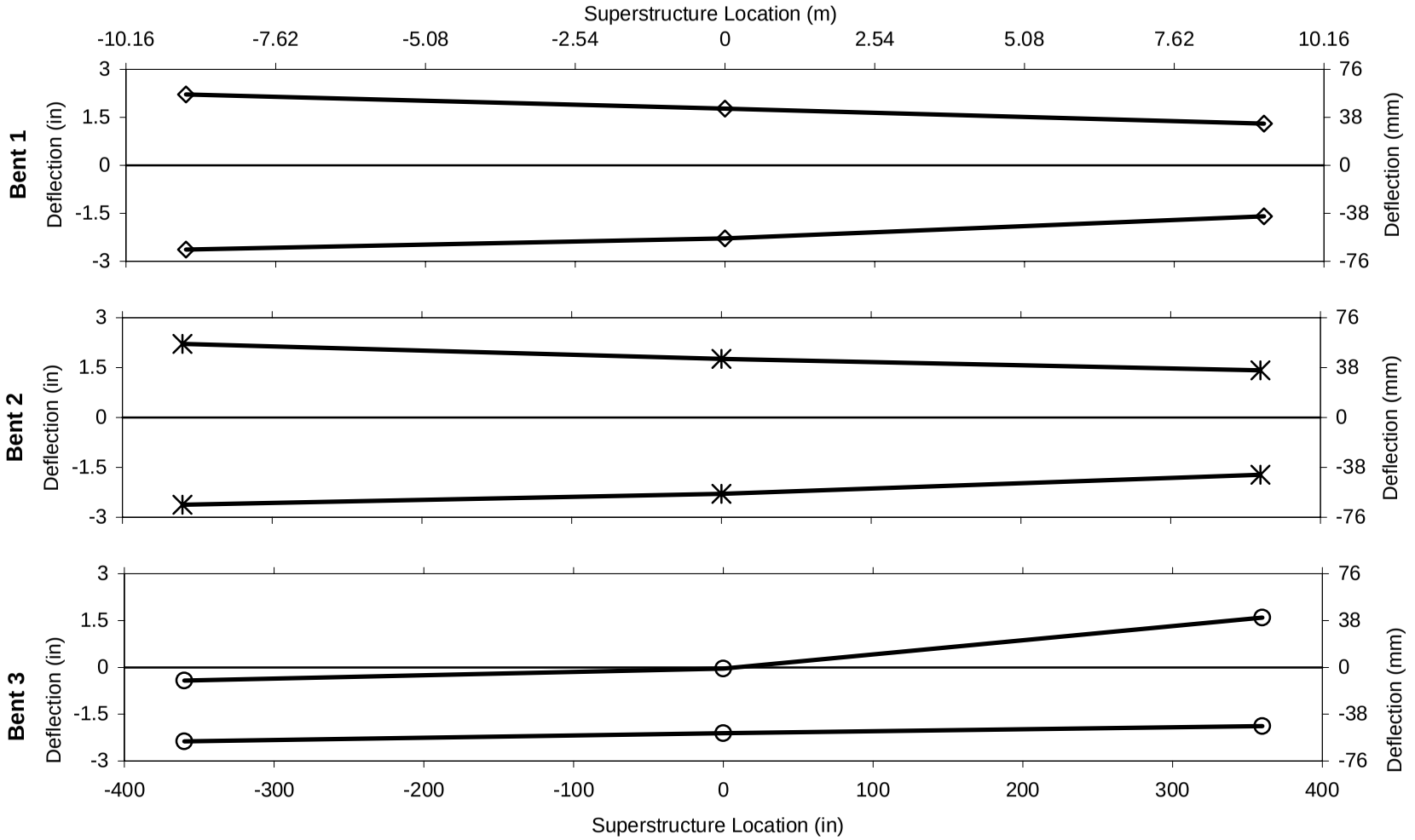

Figure 6-108: Test 16 transverse deflection plot of superstructure at instant of maximum deflections for each bent.

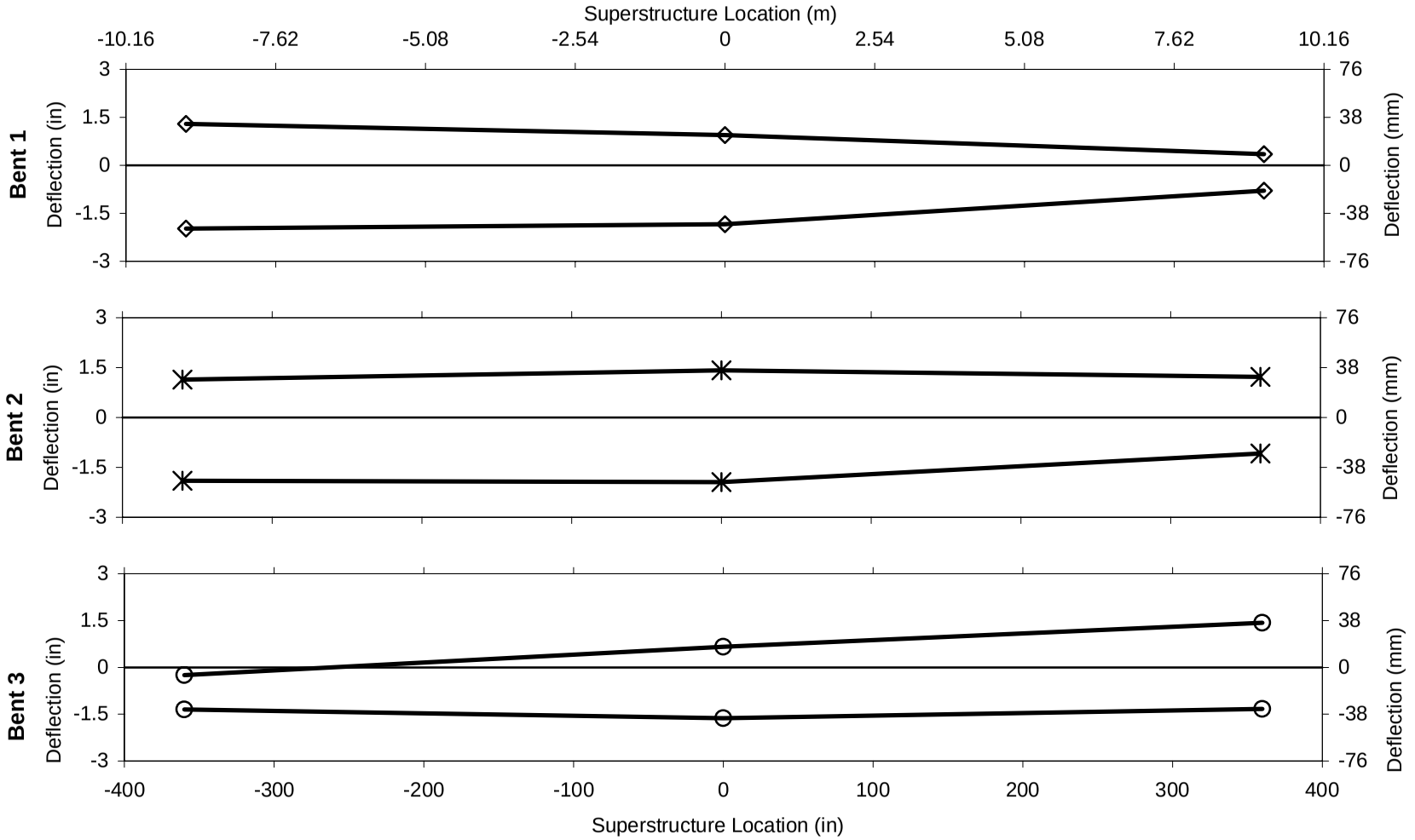

Figure 6-109: Test 17 transverse deflection plot of superstructure at instant of maximum deflections for each bent.

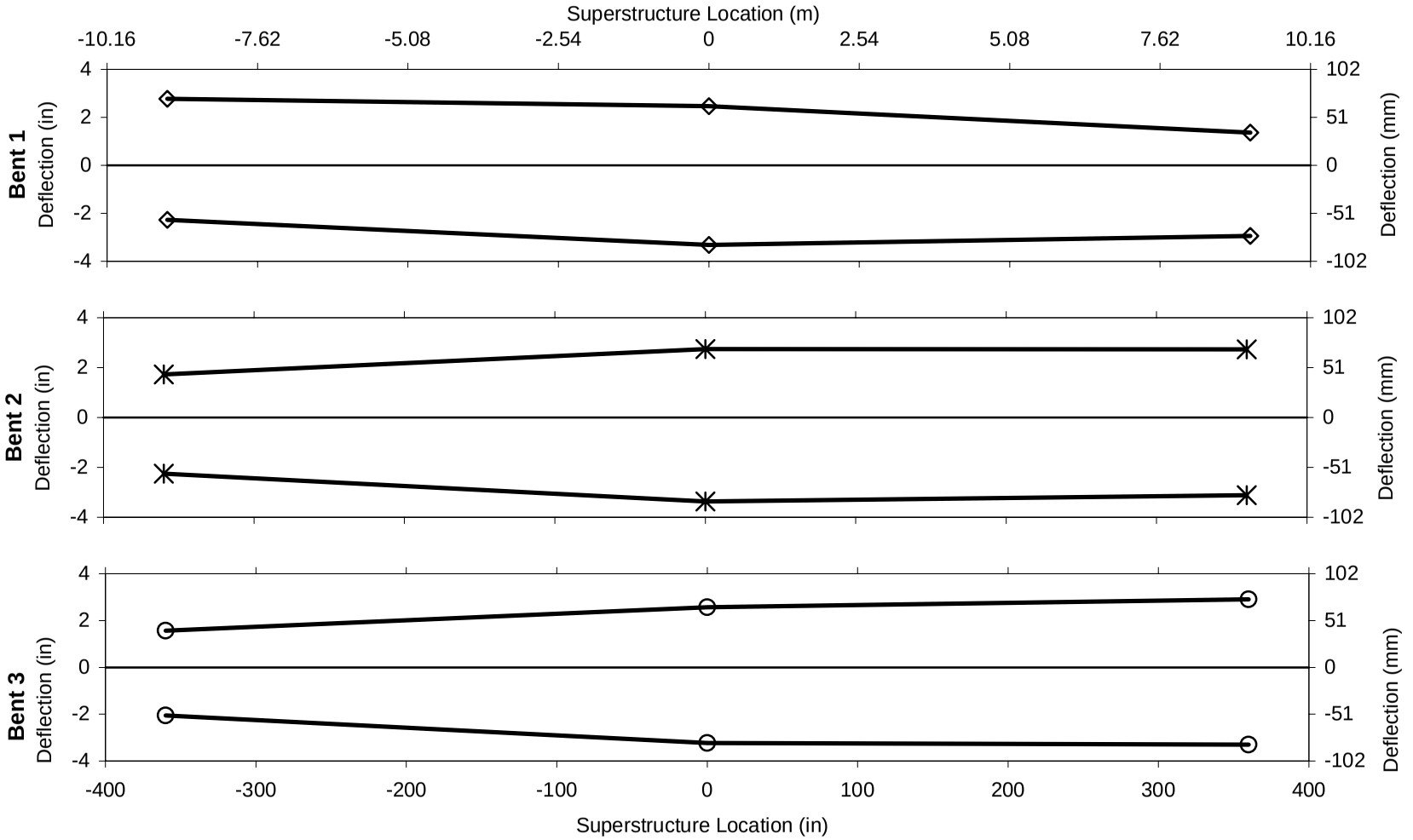

Figure 6-110: Test 18 transverse deflection plot of superstructure at instant of maximum deflections for each bent.

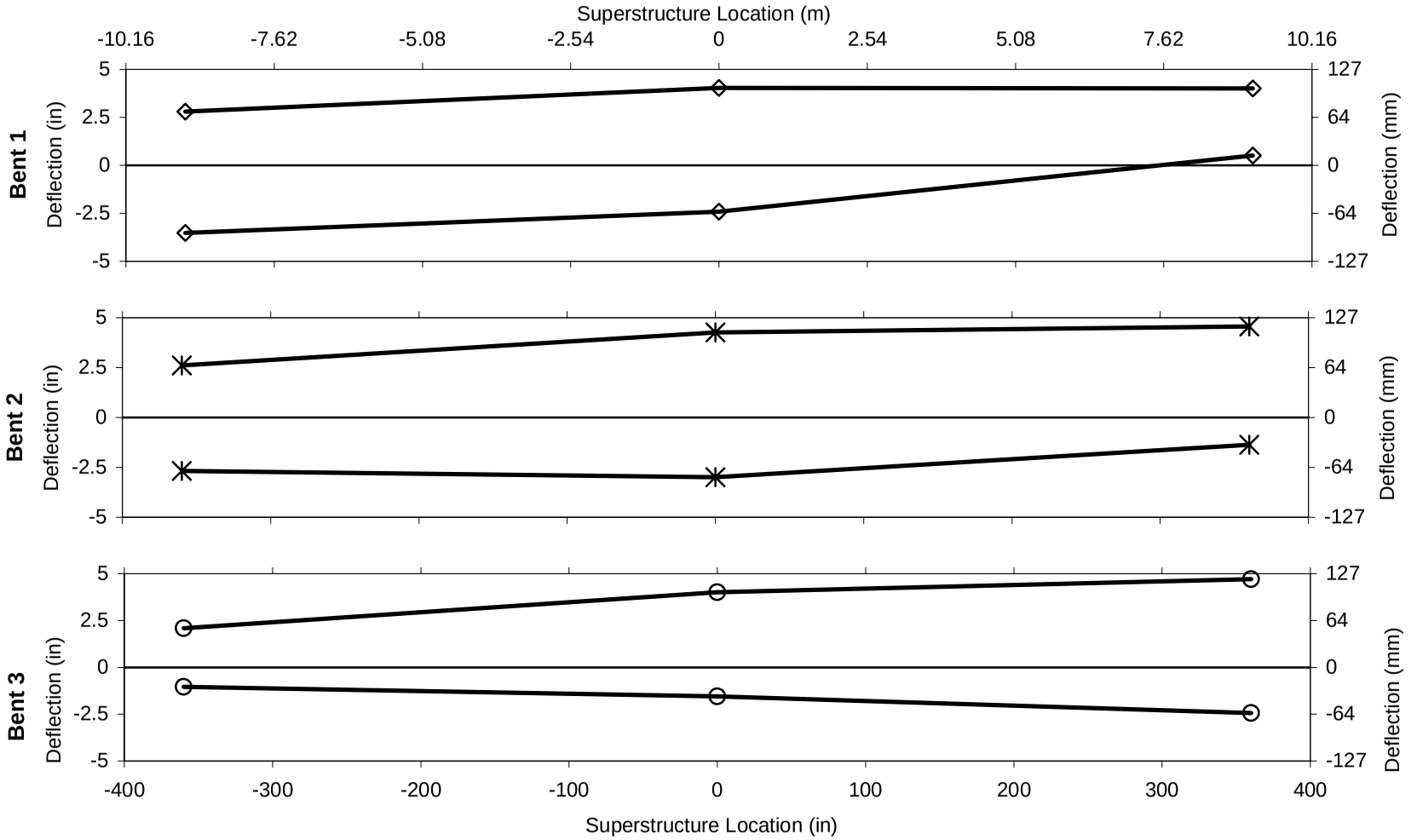

Figure 6-111: Test 19 transverse deflection plot of superstructure at instant of maximum deflections for each bent.

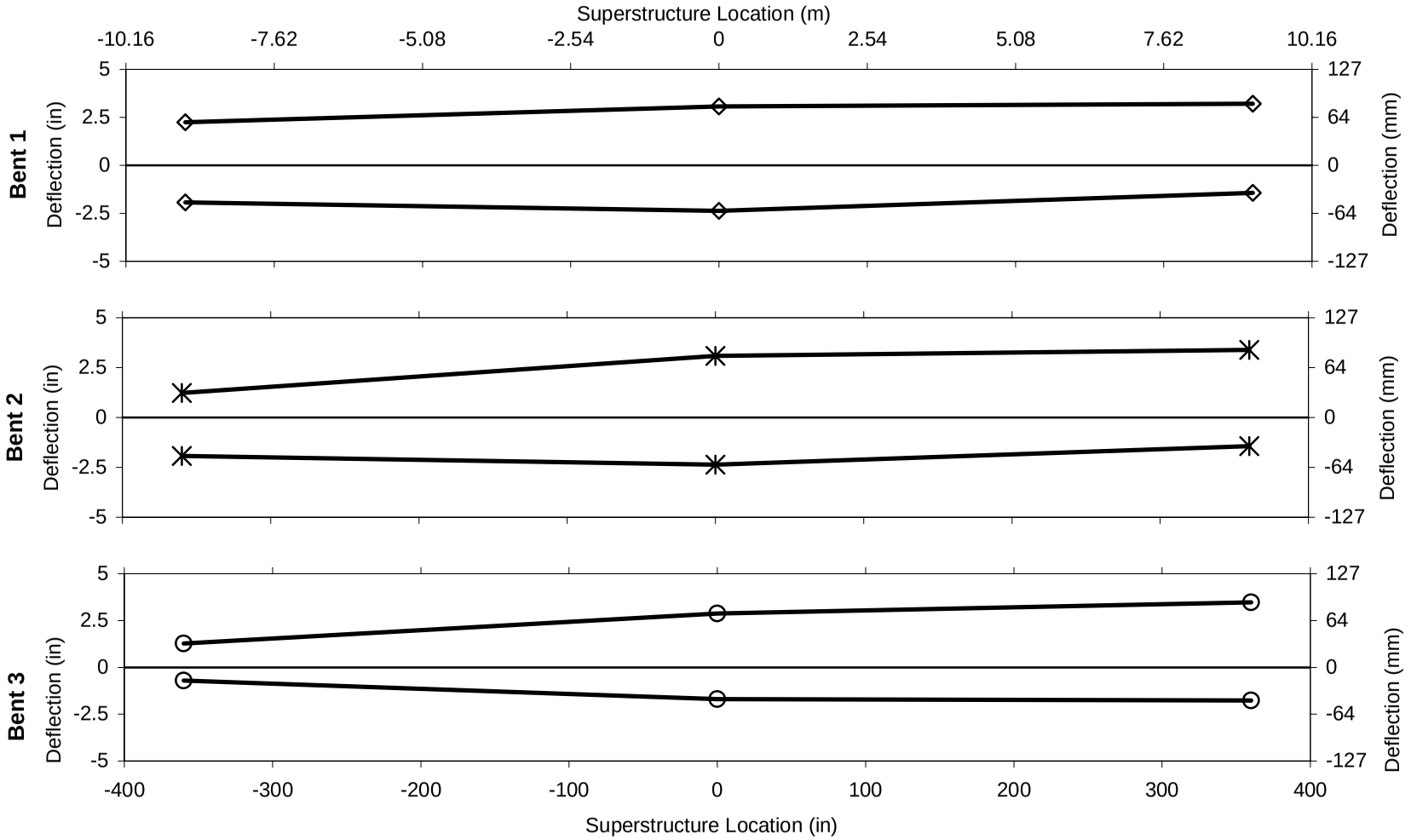

Figure 6-112: Test 20 transverse deflection plot of superstructure at instant of maximum deflections for each bent.

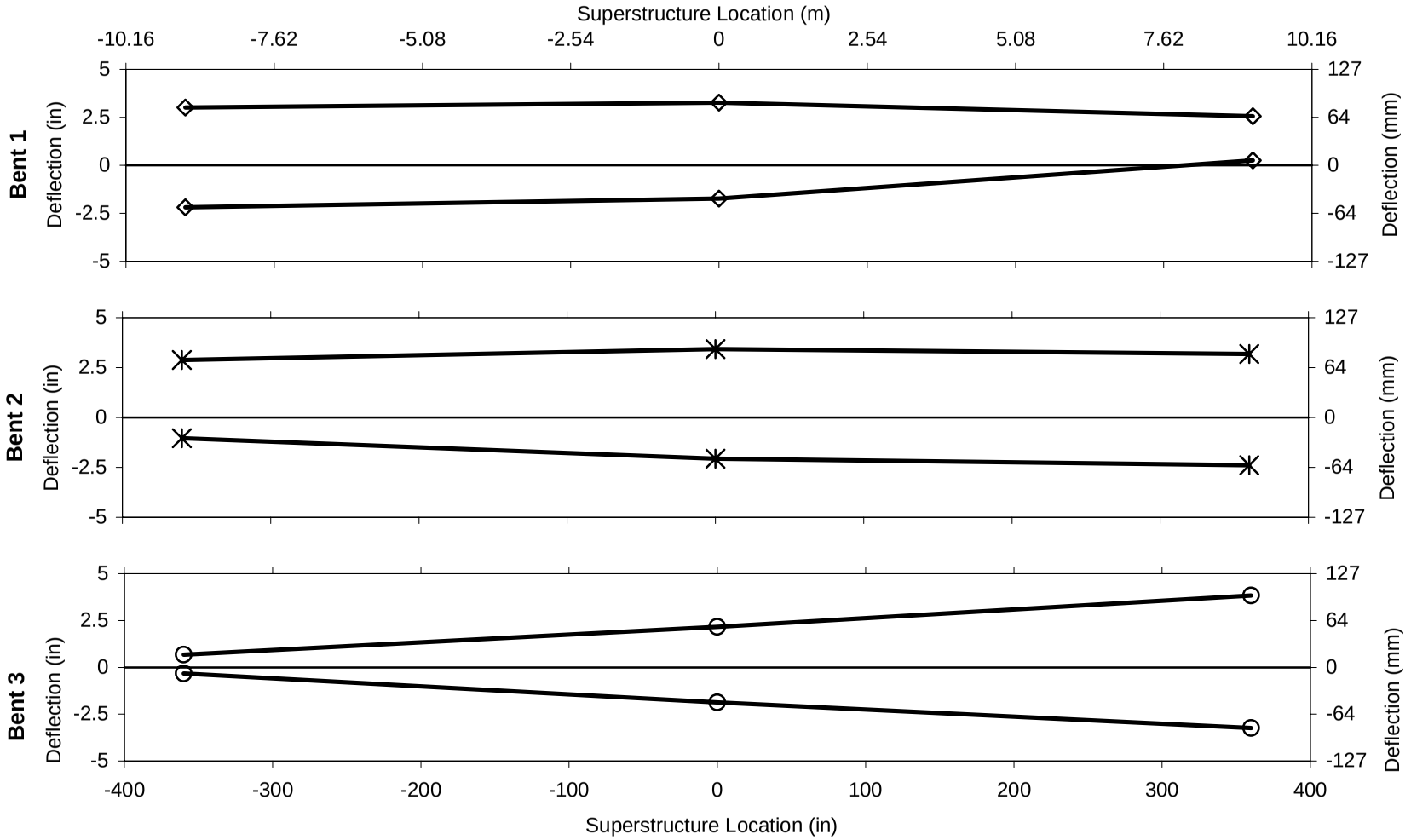

Figure 6-113: Test 21 transverse deflection plot of superstructure at instant of maximum deflections for each bent (test 21 was after removal of bent 3 mass).

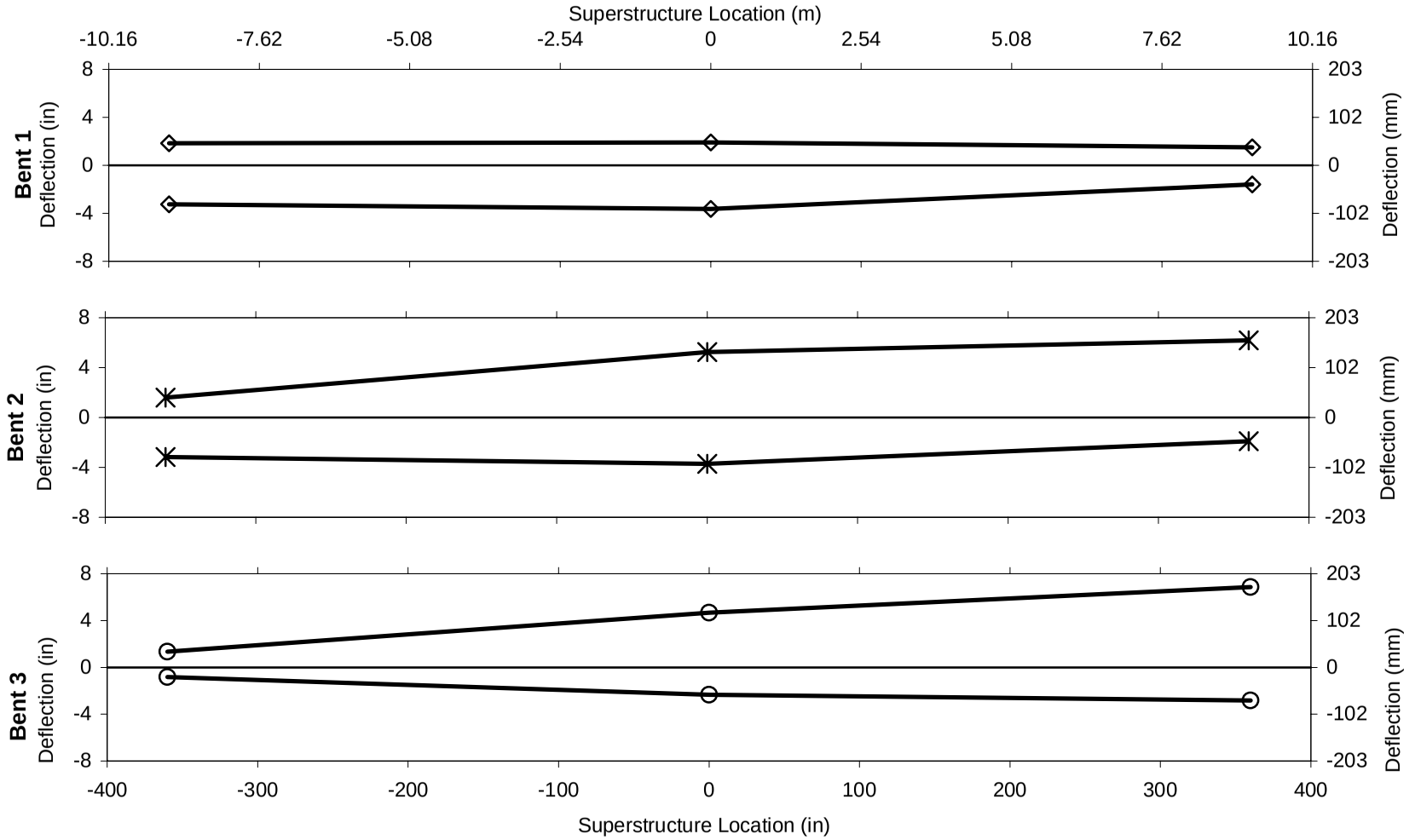

Figure 6-114: Test 22 transverse deflection plot of superstructure at instant of maximum deflections for each bent (test 21 was after removal of bent 3 mass).

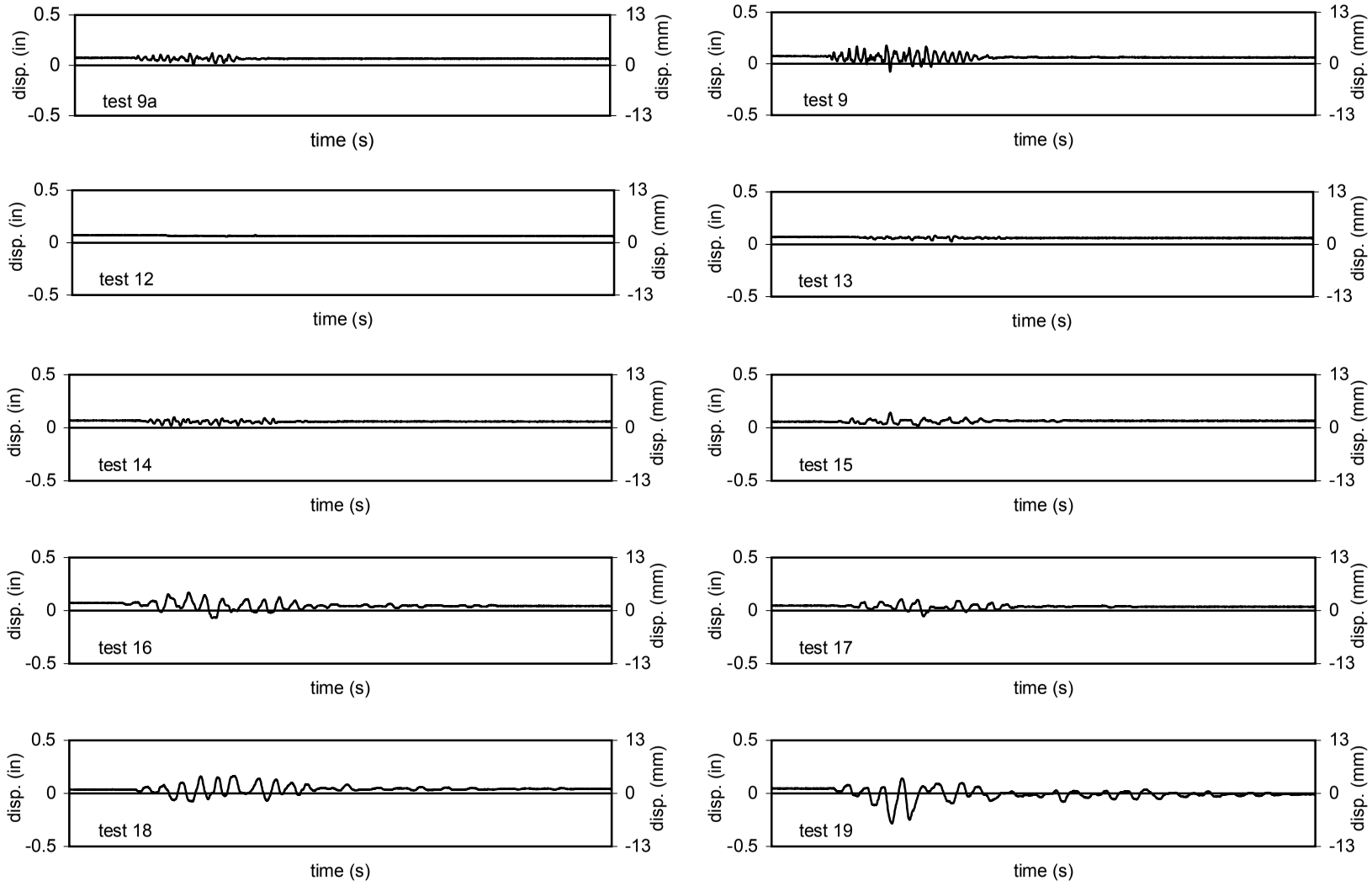

Figure 6-115: Relative displacement histories of DL1 (northeast corner of superstructure) for biaxial tests and tests 12-19.

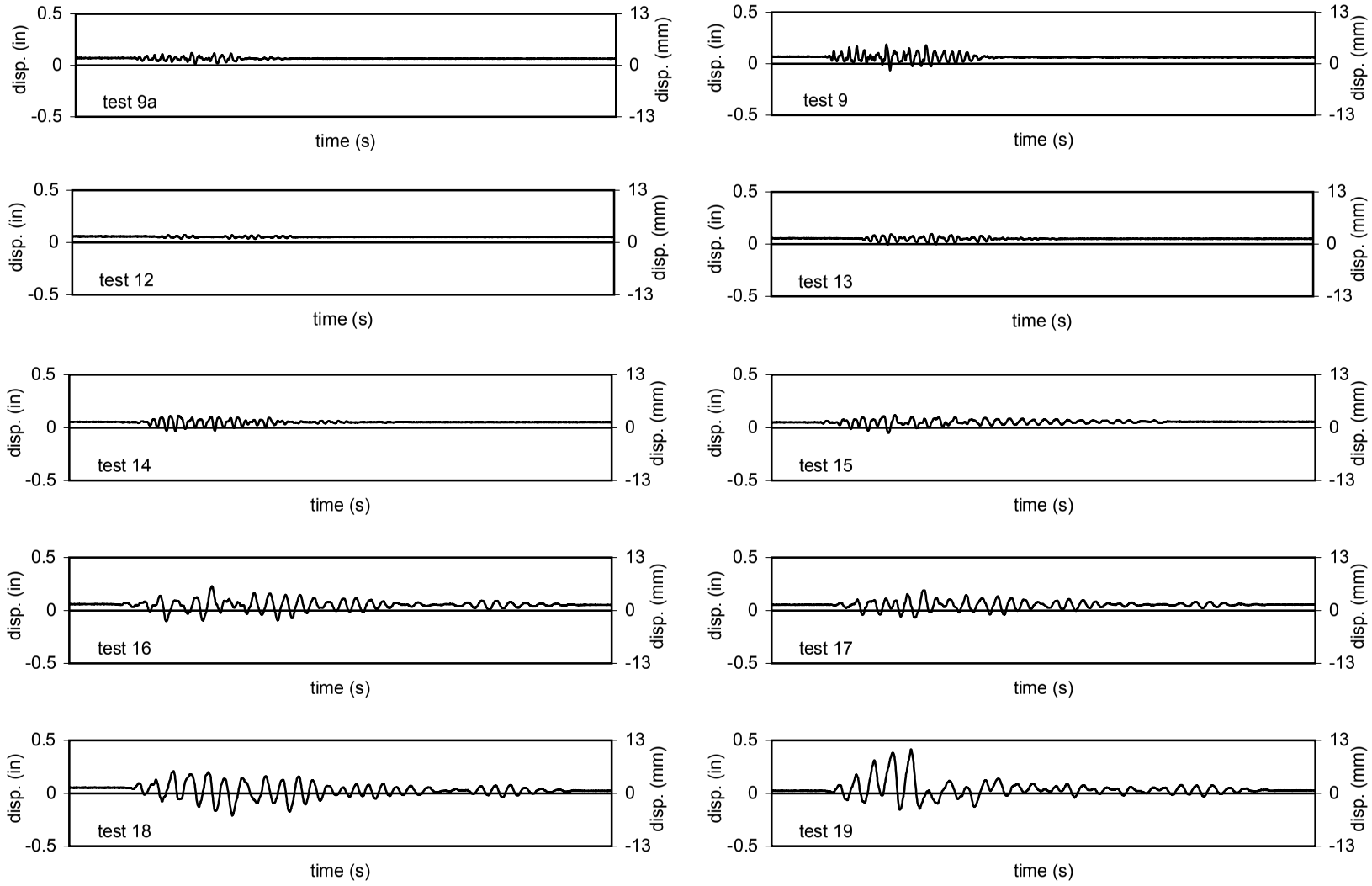

Figure 6-116: Relative displacement histories of DL2 (northwest corner of superstructure) for biaxial tests and tests 12-19.

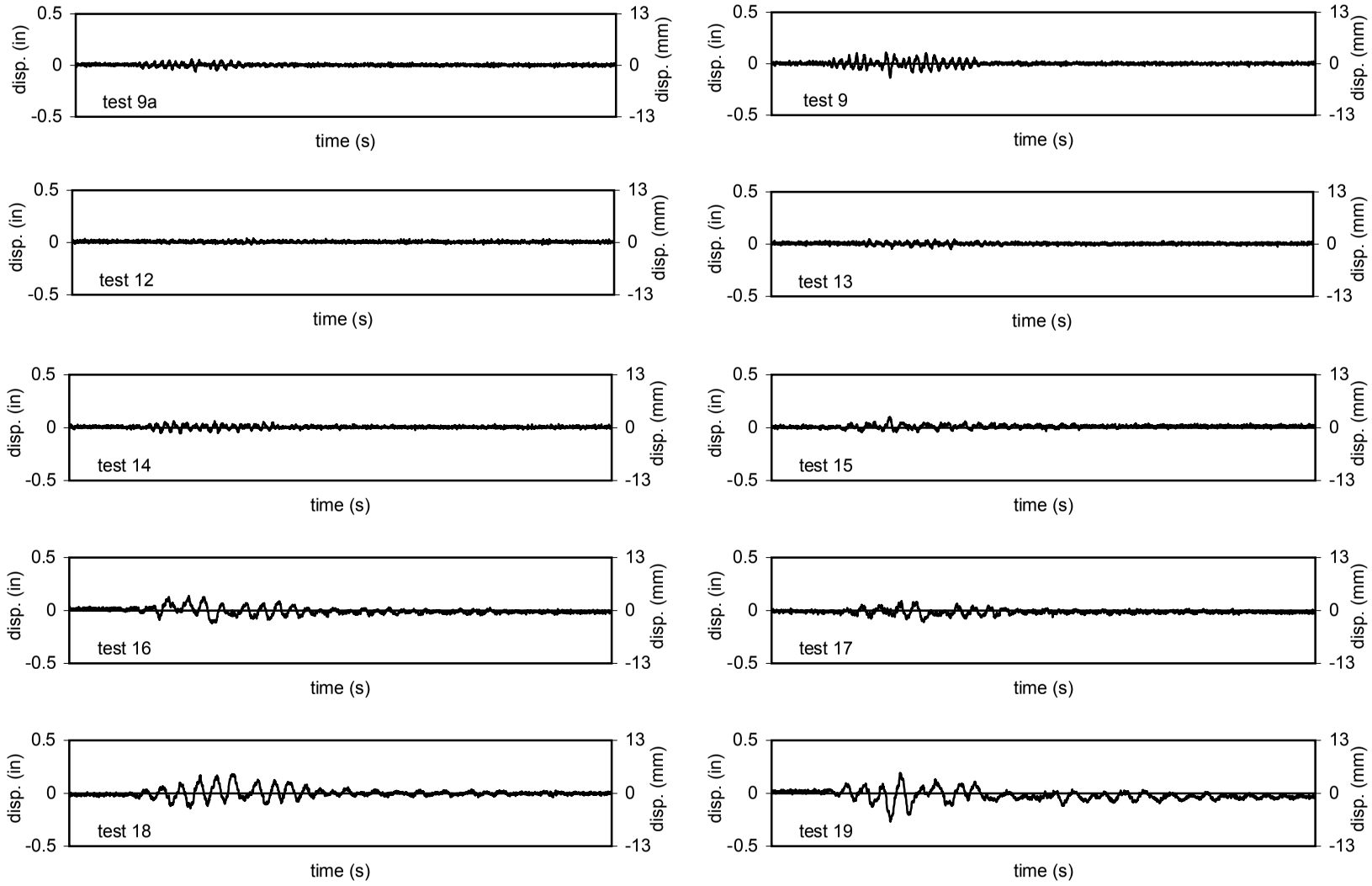

Figure 6-117: Relative displacement histories of DL3 (southeast corner of superstructure) for biaxial tests and tests 12-19.

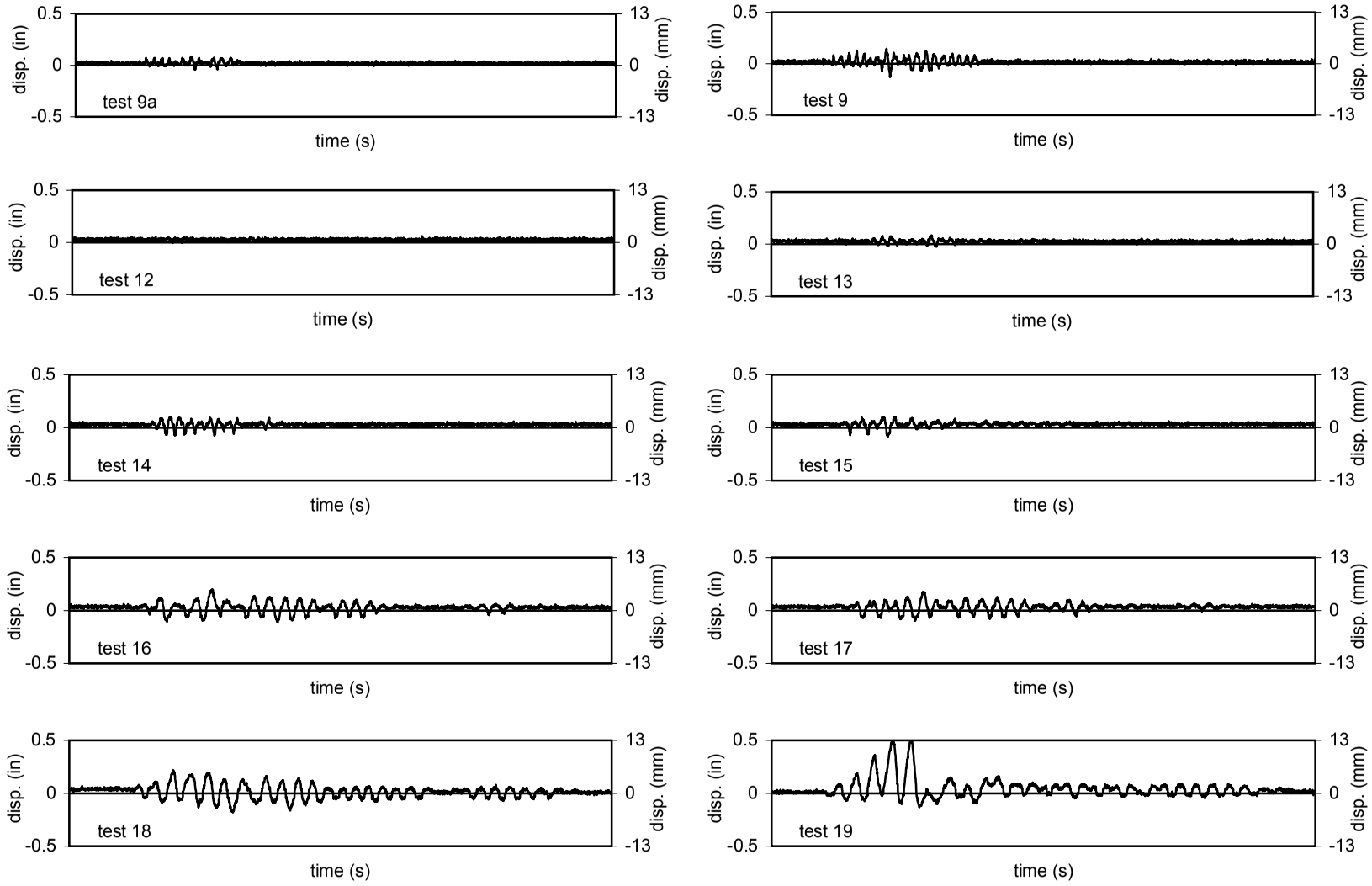

Figure 6-118: Relative displacement histories of DL4 (southwest corner of superstructure) for biaxial tests and tests 12-19.

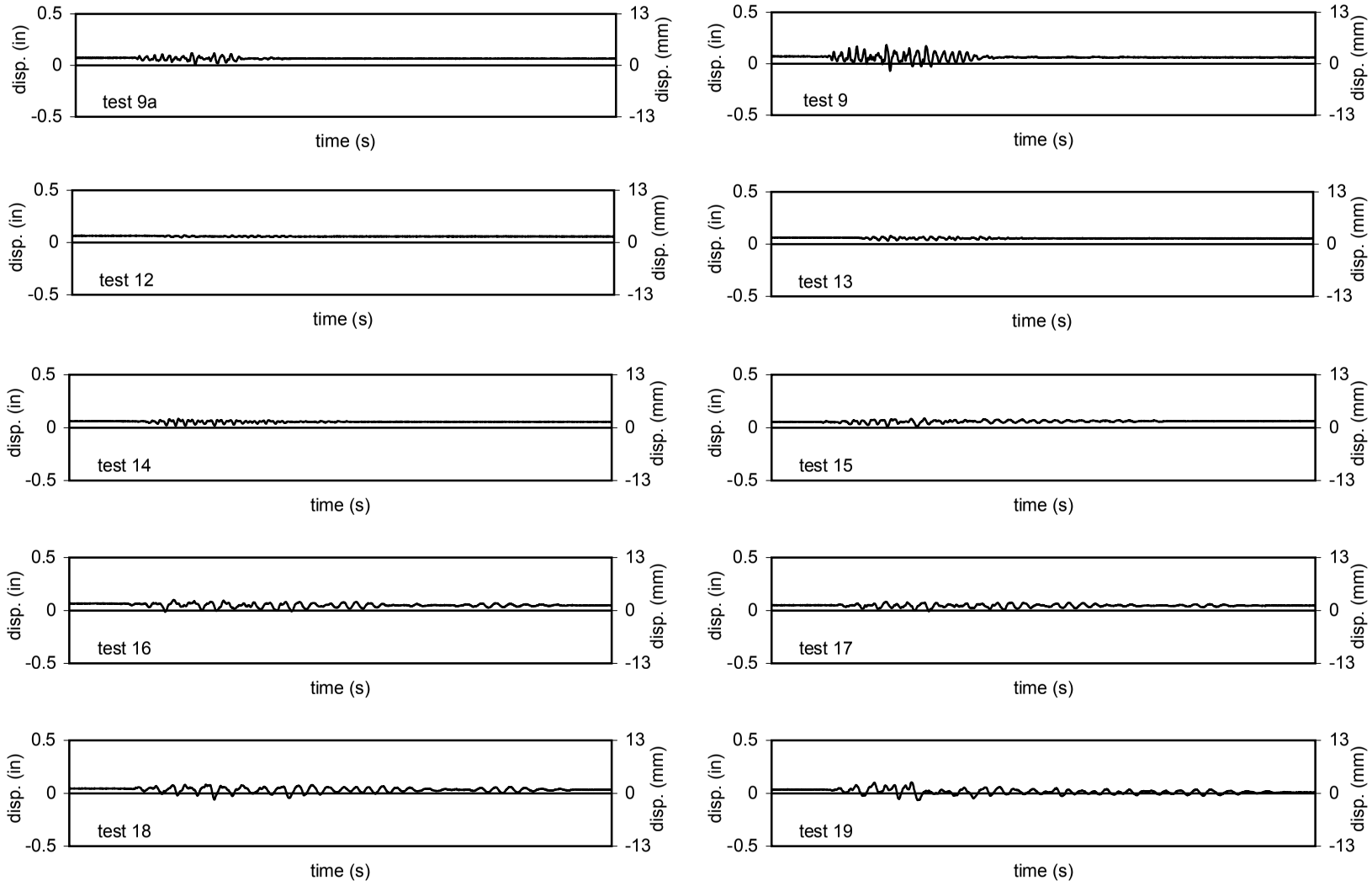

Figure 6-119: Relative displacement histories of north end of superstructure (average) for biaxial tests and tests 12-19.

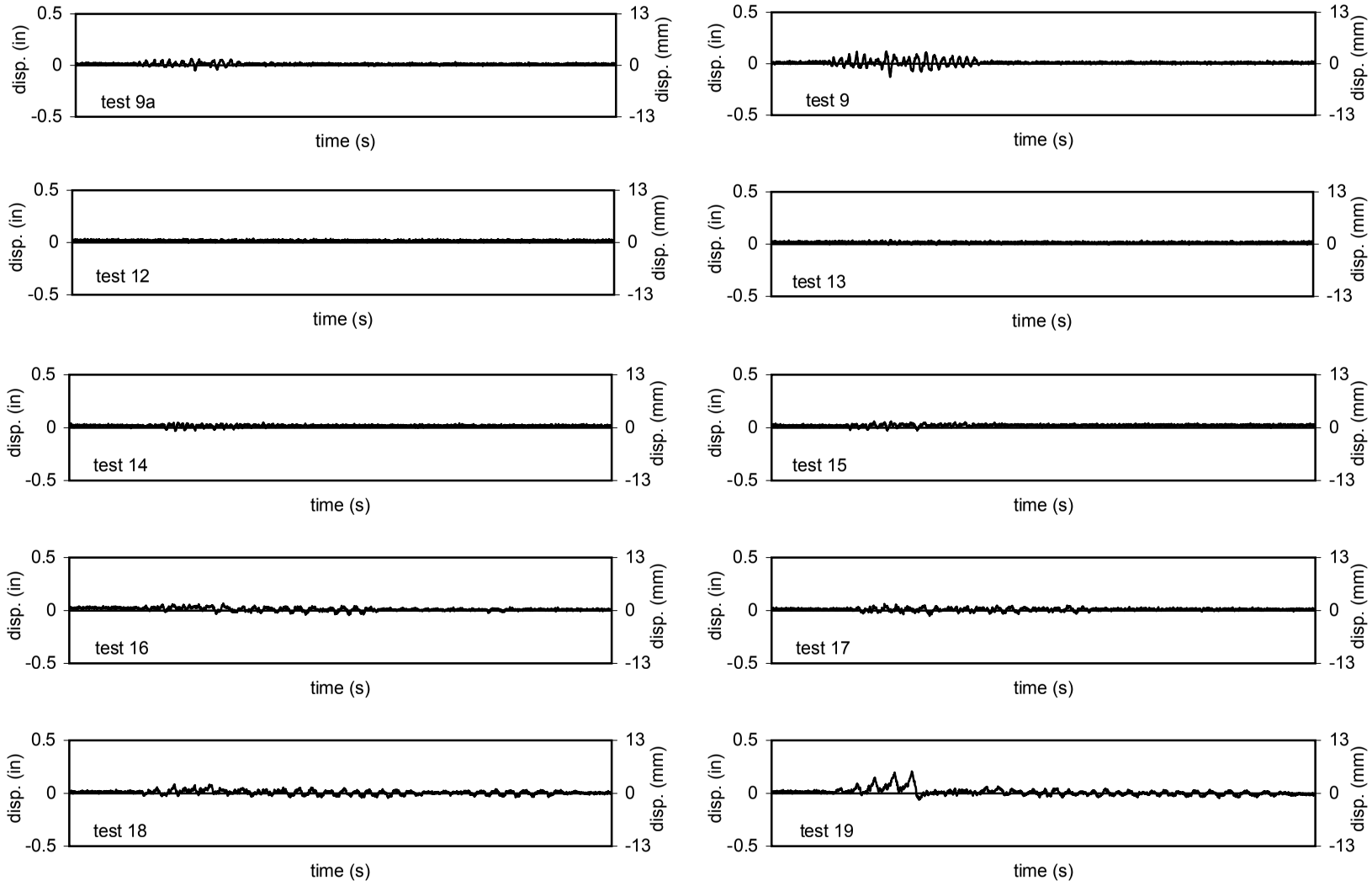

Figure 6-120: Relative displacement histories of south end of superstructure (average) for biaxial tests and tests 12-19.

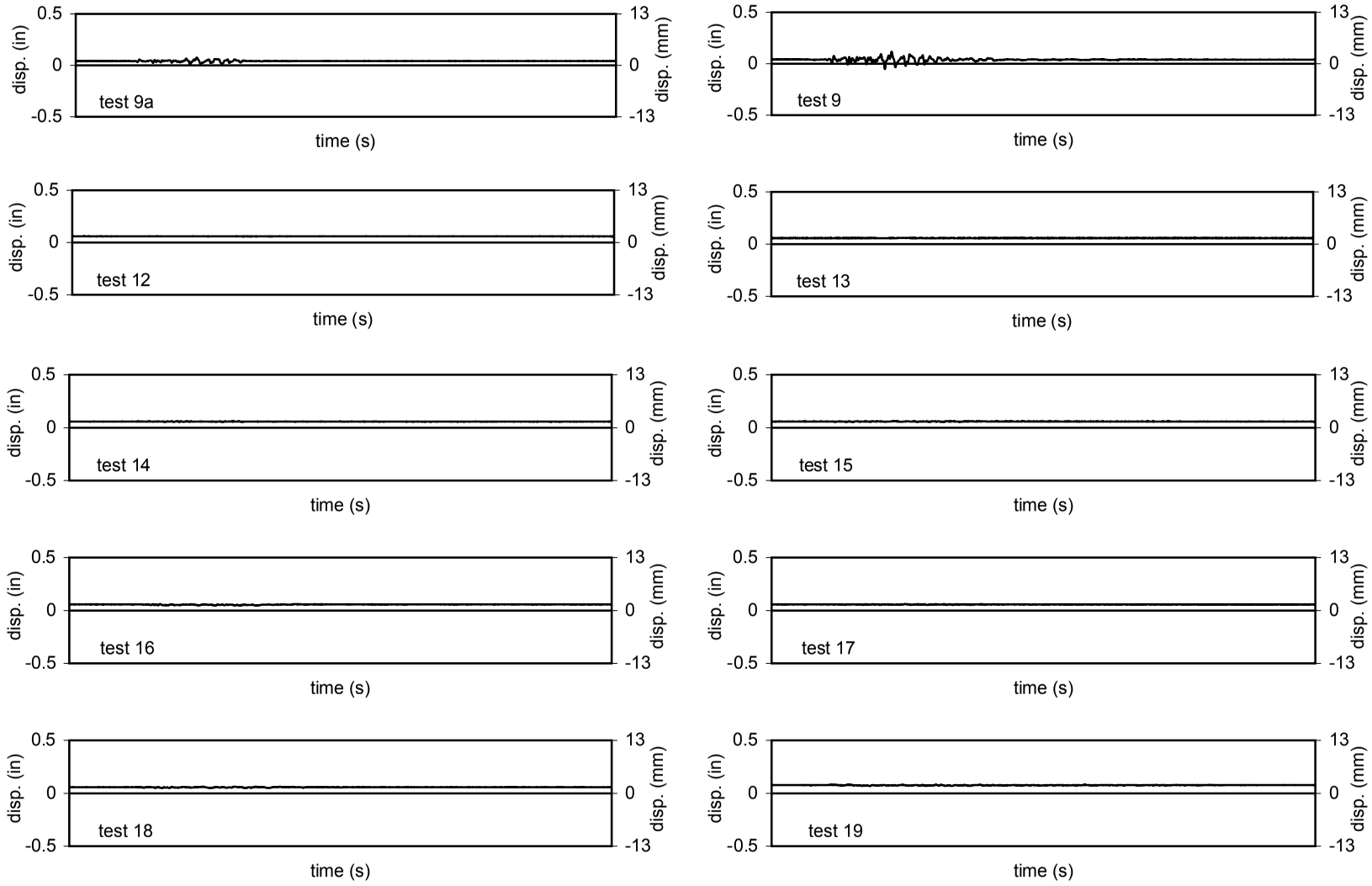

Figure 6-121: Longitudinal displacement histories (N-S) of Table 1 (north table) for biaxial tests and tests 12-19.

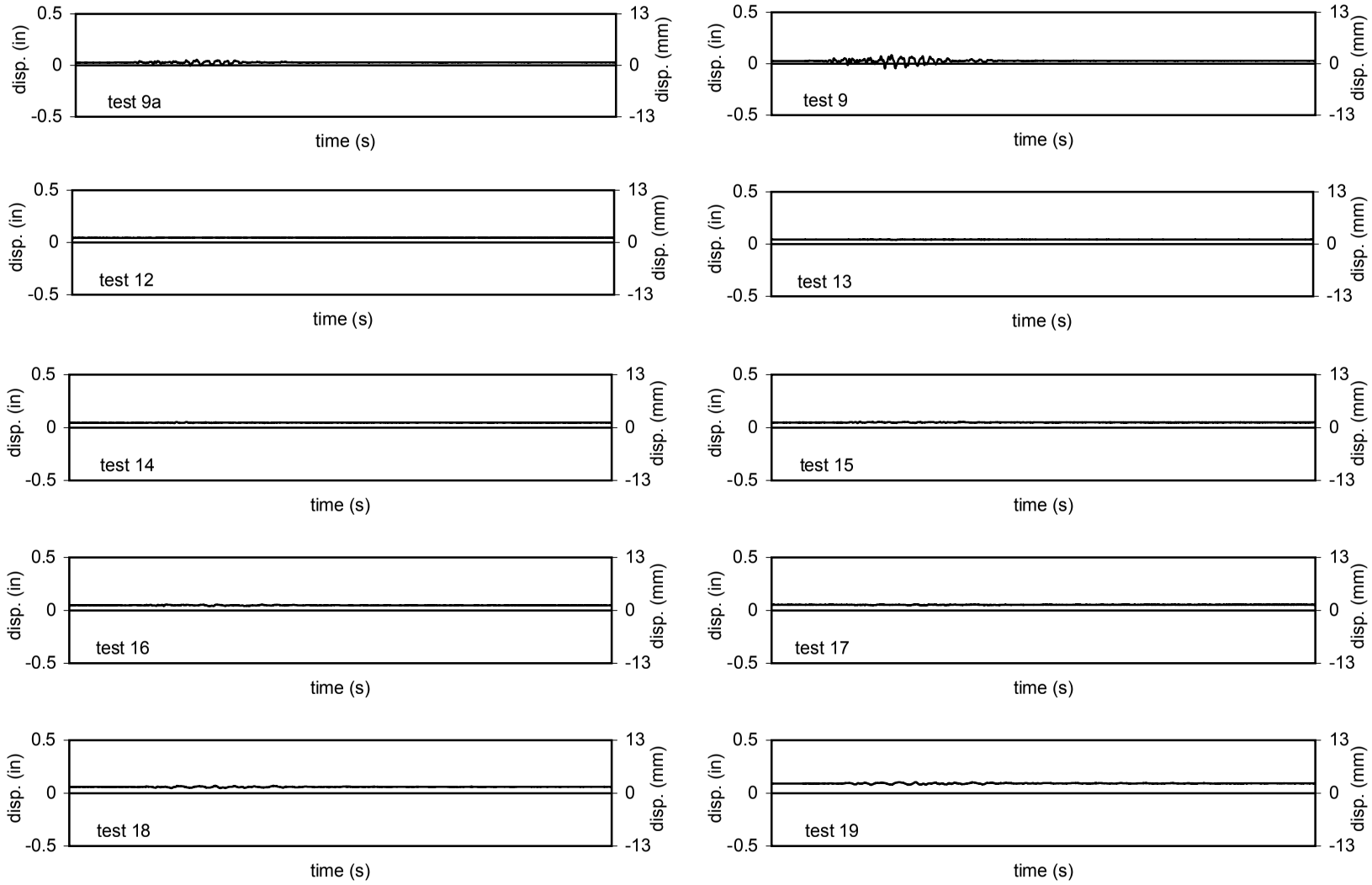

Figure 6-122: Longitudinal displacement histories (N-S) of Table 3 (south table) for biaxial tests and tests 12-19.

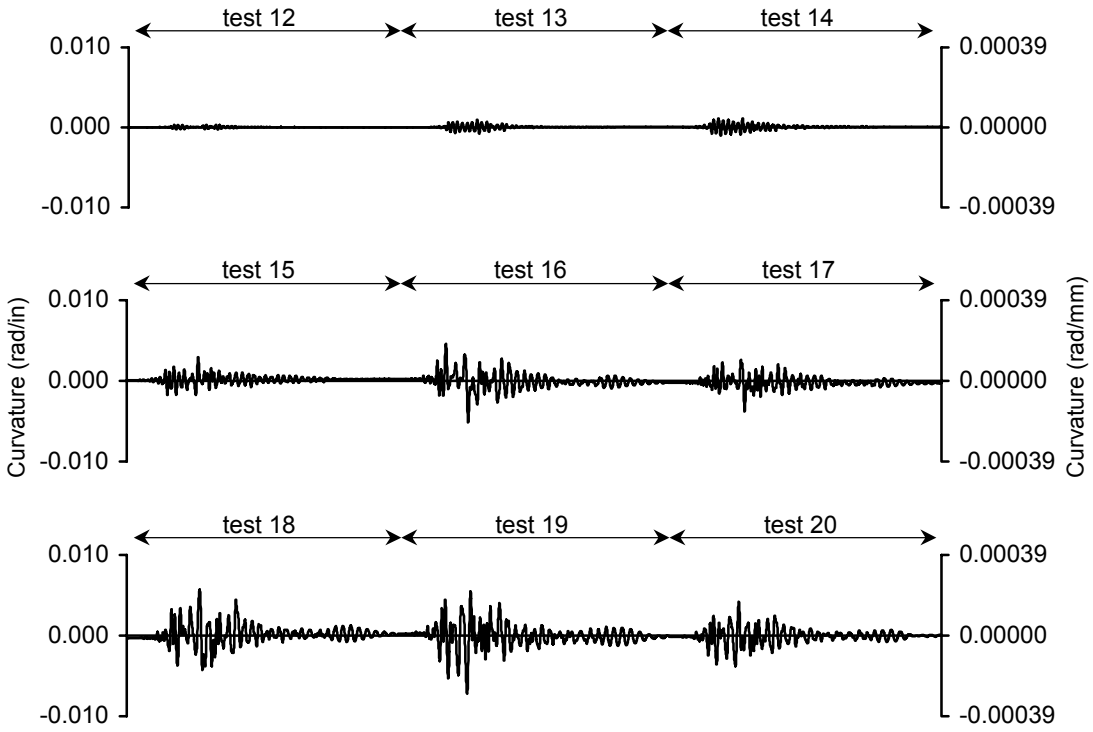

Figure 6-123: Curvature history for bent 1 top west column, trans. direction at 2.5 in (64mm) from fixity, during high amplitude tests

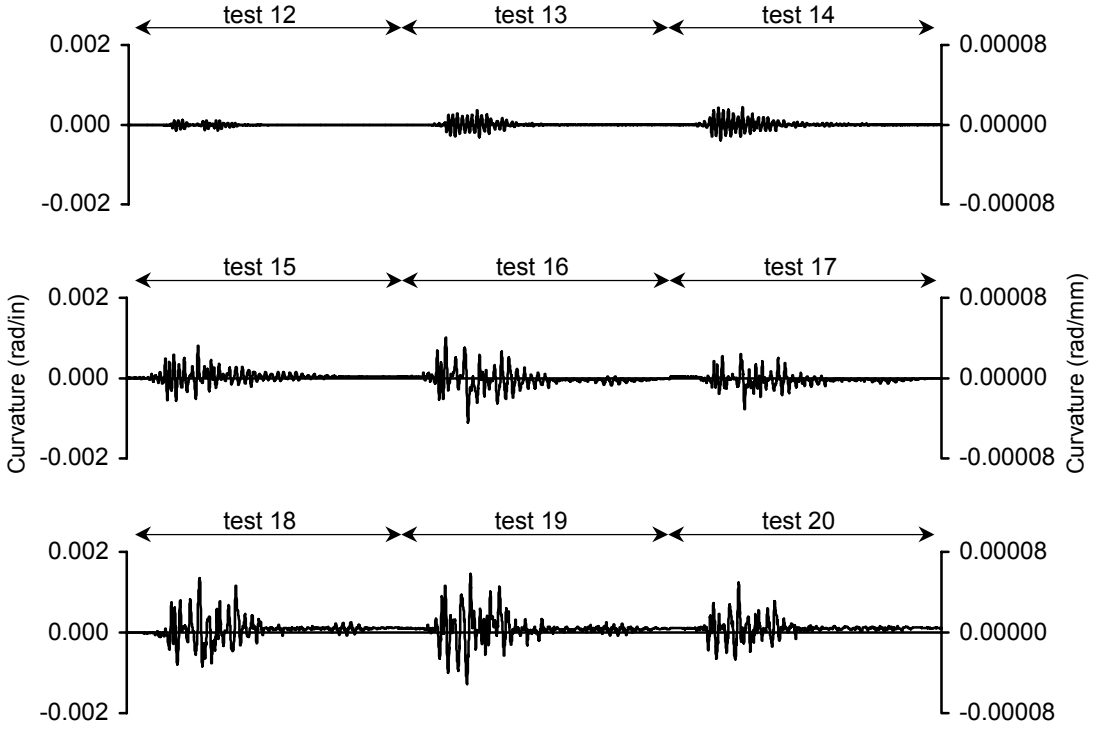

Figure 6-124: Curvature history for bent 1 top west column, trans. direction at 8.5 in (216mm) from fixity, during high amplitude tests.

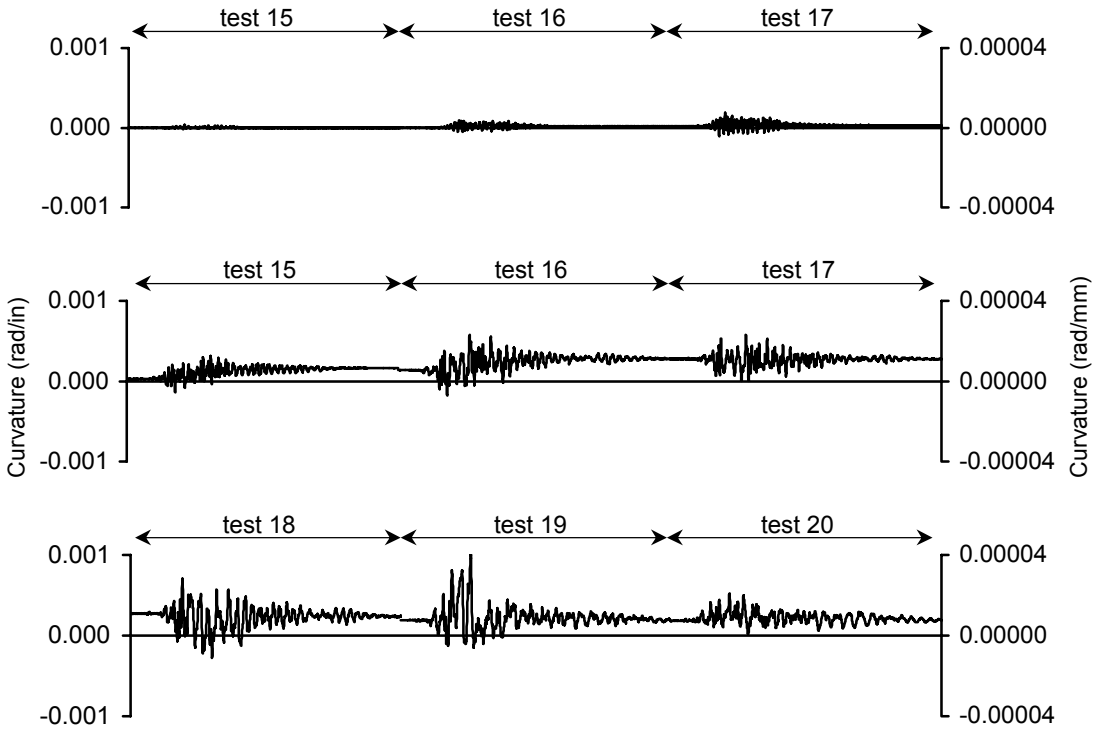

Figure 6-125: Curvature history for bent 1 top west column, long. direction at 2.5 in (64mm) from fixity, during high amplitude tests.

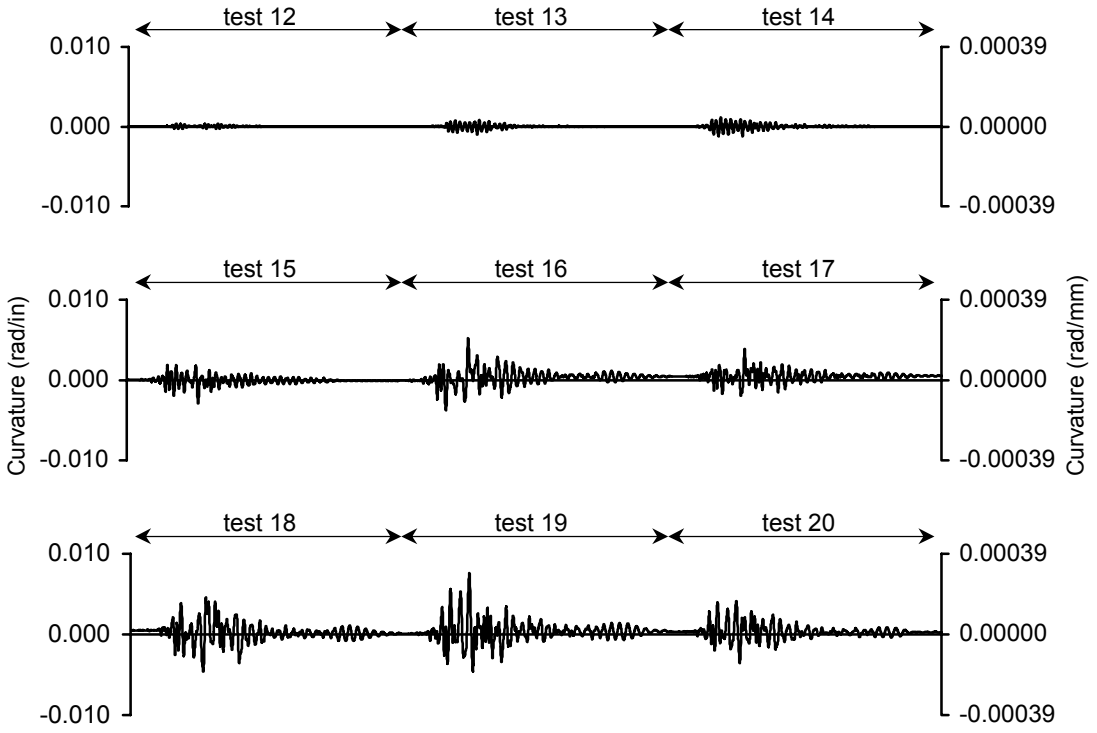

Figure 6-126: Curvature history for bent 1 bottom west column, trans. direction at 2.5 in (64mm) from fixity, during high amplitude tests.

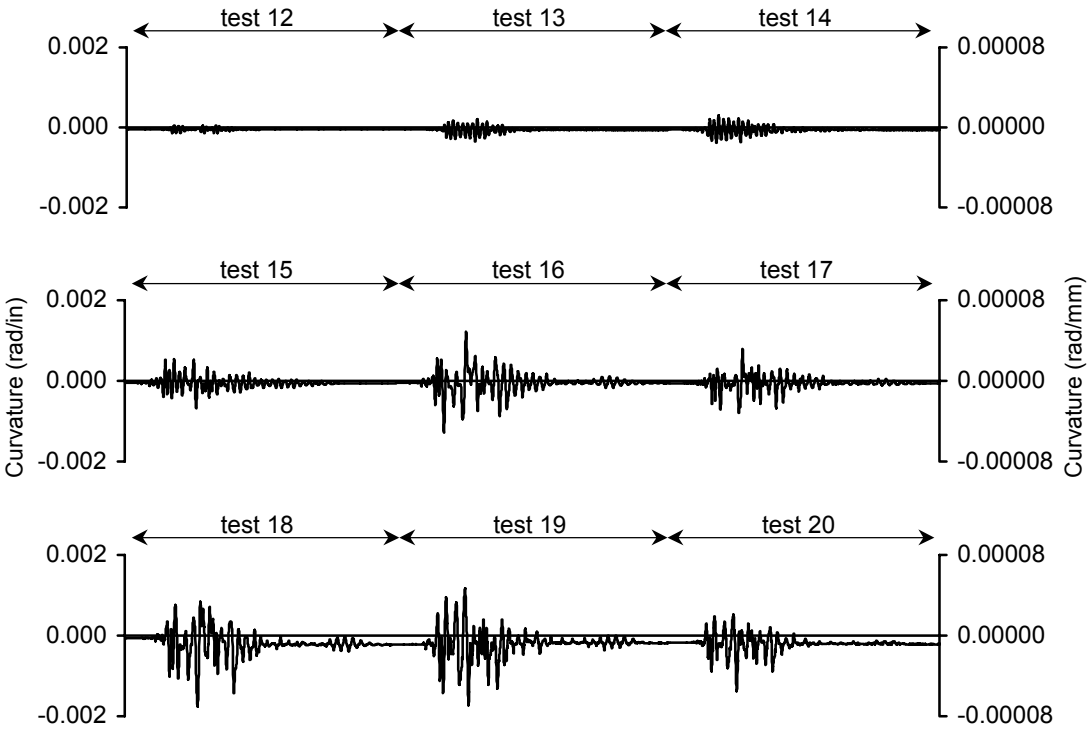

Figure 6-127: Curvature history for bent 1 bottom west column, trans. direction at 8.5 in (216mm) from fixity, during high amplitude tests

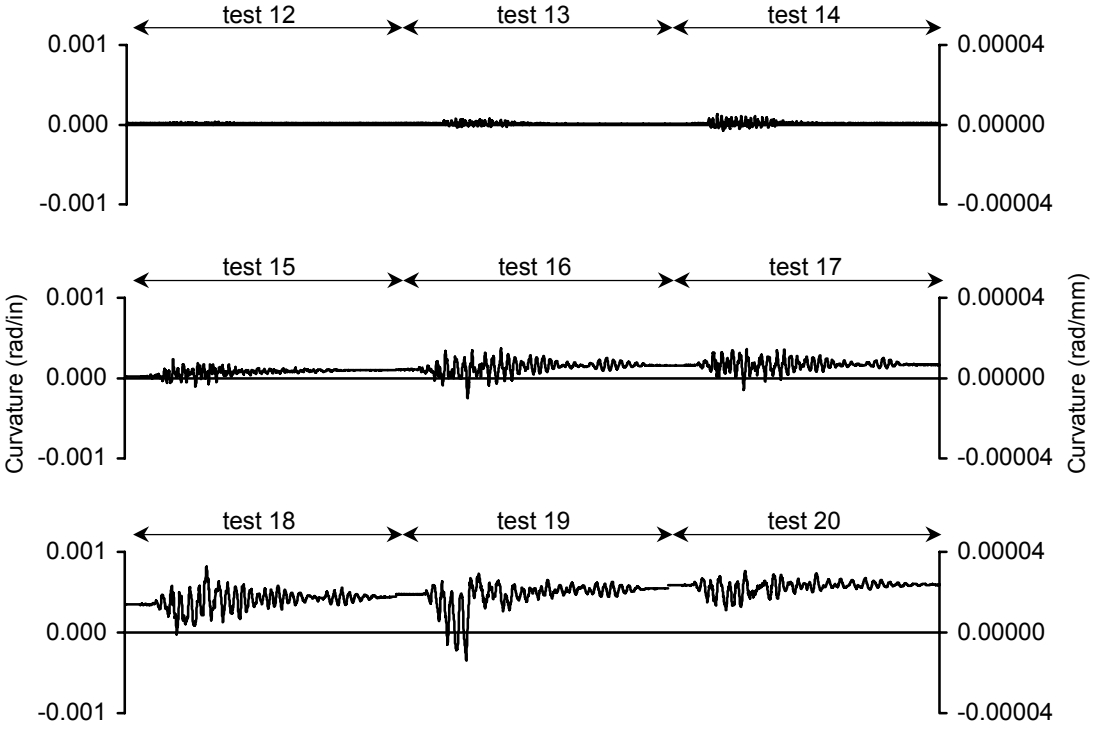

Figure 6-128: Curvature history for bent 1 bottom west column, long. direction at 2.5 in (64mm) from fixity, during high amplitude tests.

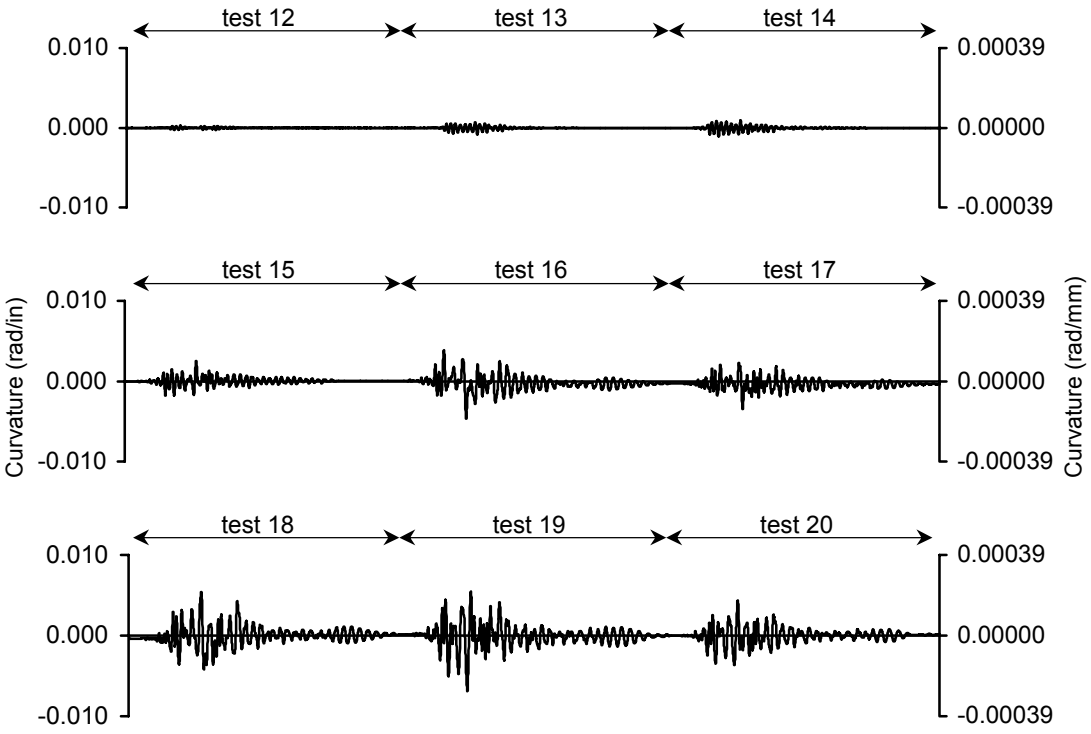

Figure 6-129: Curvature history for bent 1 top east column, trans. direction at 2.5 in (64mm) from fixity, during high amplitude tests.

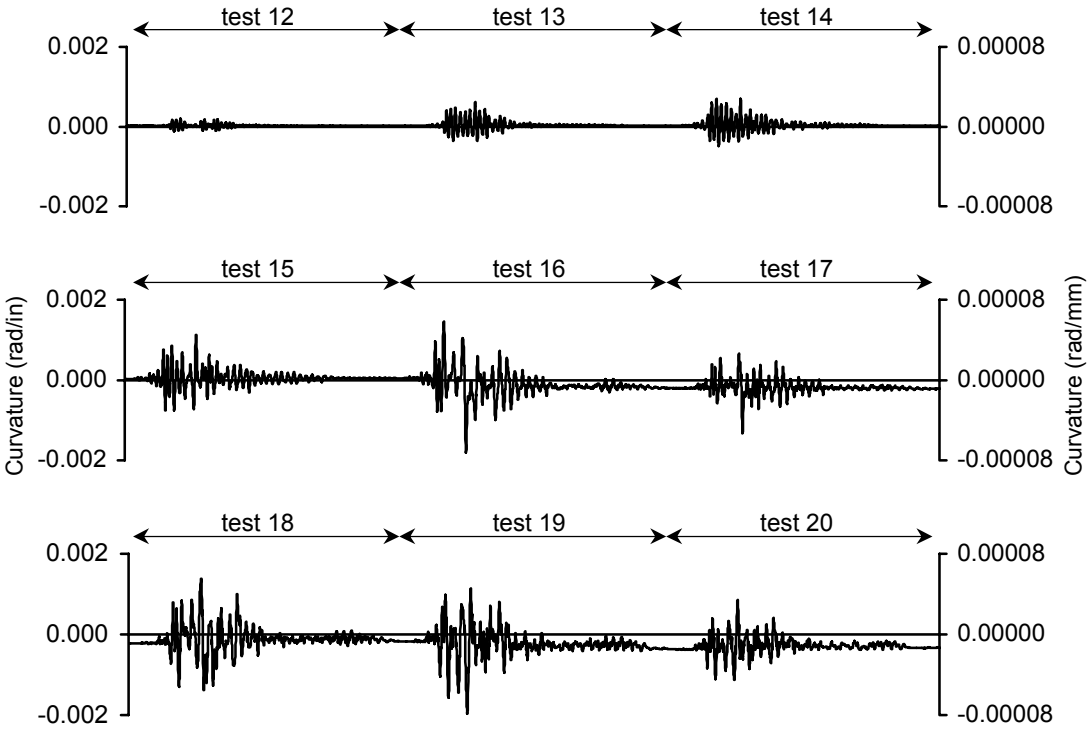

Figure 6-130: Curvature history for bent 1 top east column, trans. direction at 8.5 in (216mm) from fixity, during high amplitude tests.

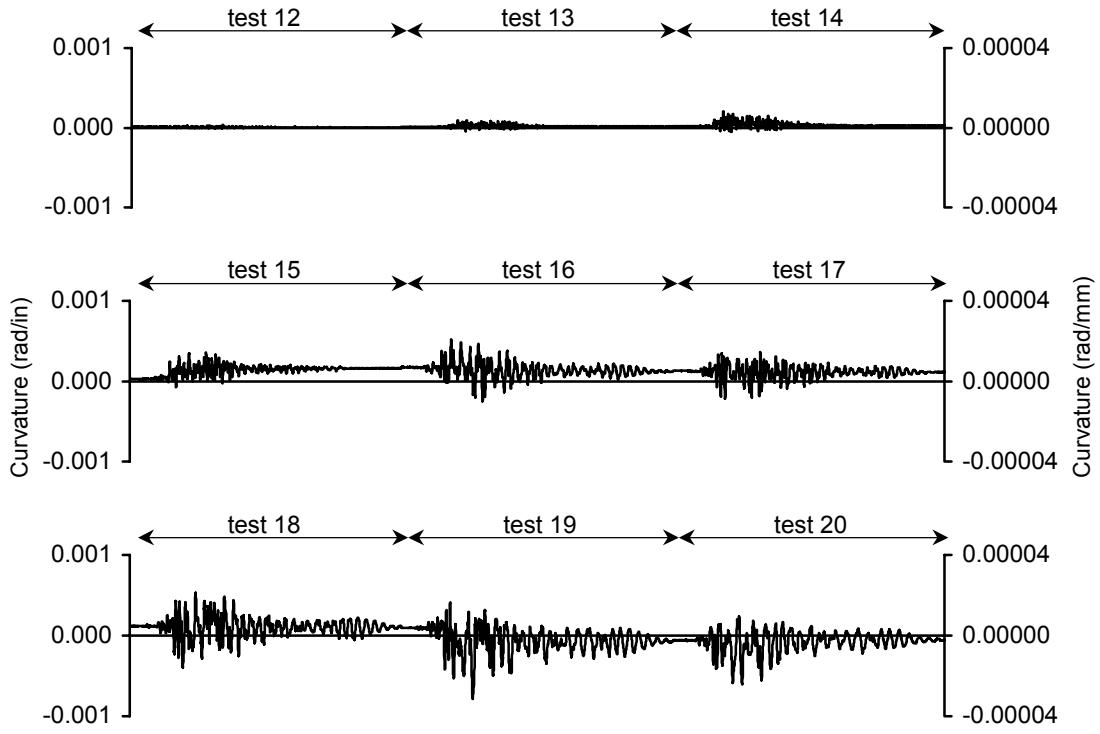

Figure 6-131: Curvature history for bent 1 top east column, long. direction at 2.5 in (64mm) from fixity, during high amplitude tests

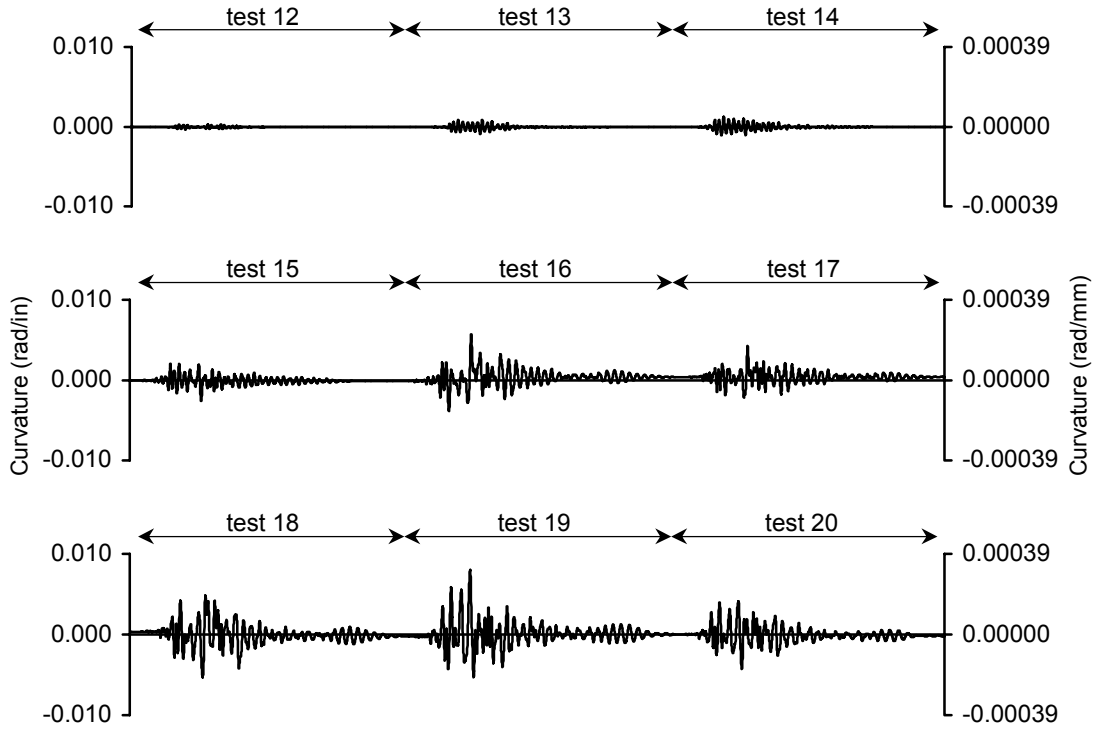

Figure 6-132: Curvature history for bent 1 bottom east column, trans. direction at 2.5 in (64mm) from fixity, during high amplitude tests.

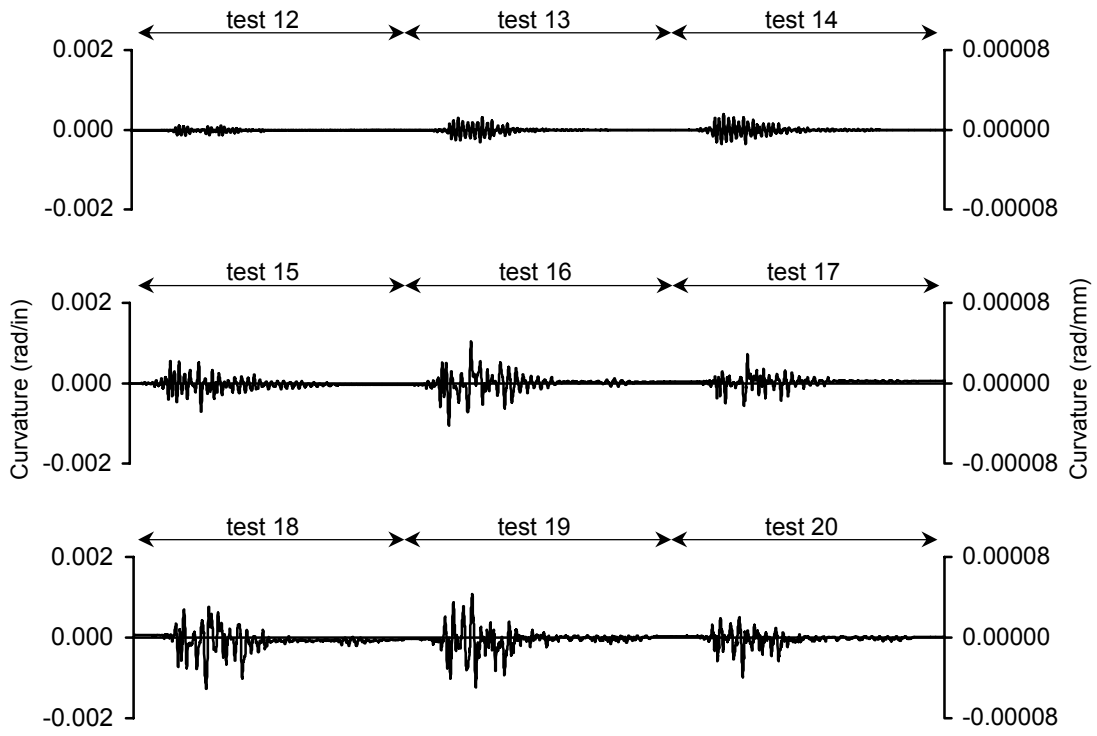

Figure 6-133: Curvature history for bent 1 bottom east column, trans. direction at 8.5 in (216mm) from fixity, during high amplitude tests.

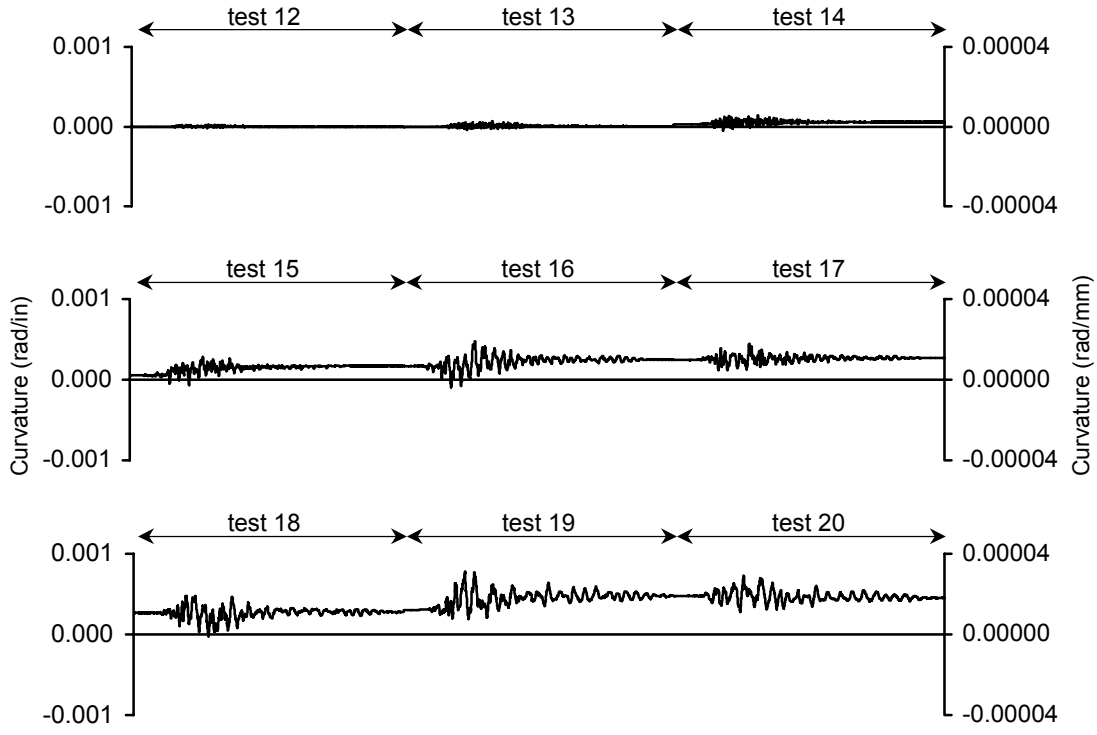

Figure 6-134: Curvature history for bent 1 bottom east column, long direction at 2.5 in (64mm) from fixity, during high amplitude tests.

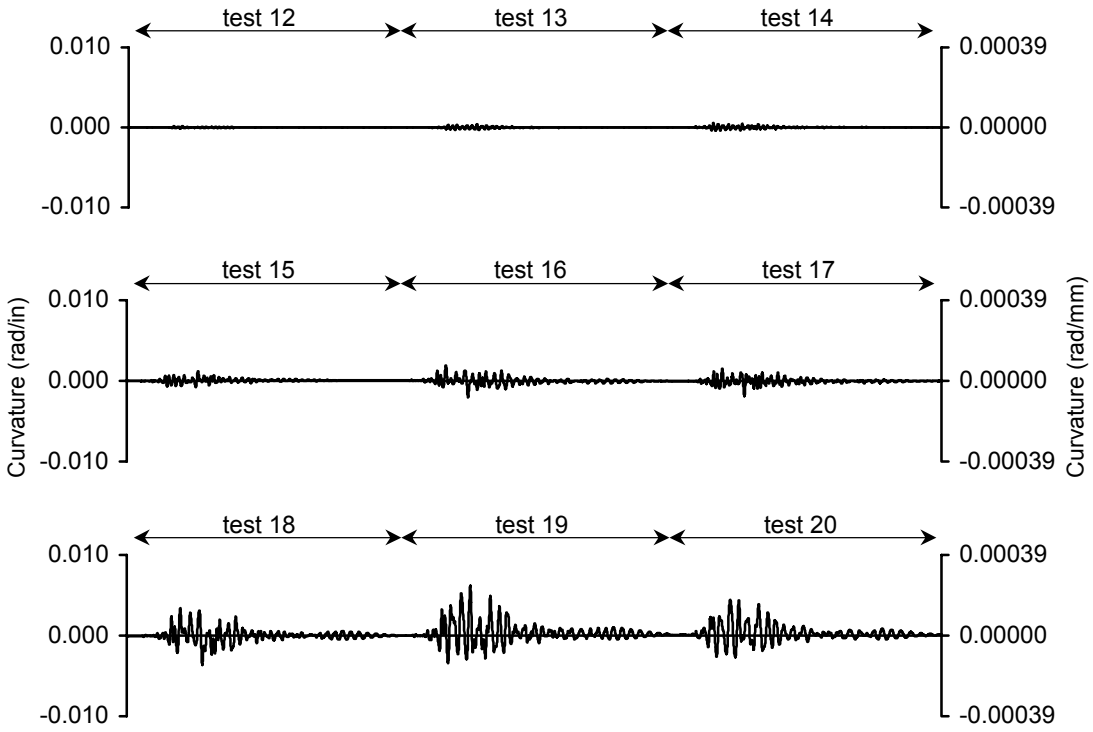

Figure 6-135: Curvature history for bent 2 top west column, trans. direction at 2.5 in (64mm) from fixity, during high amplitude tests

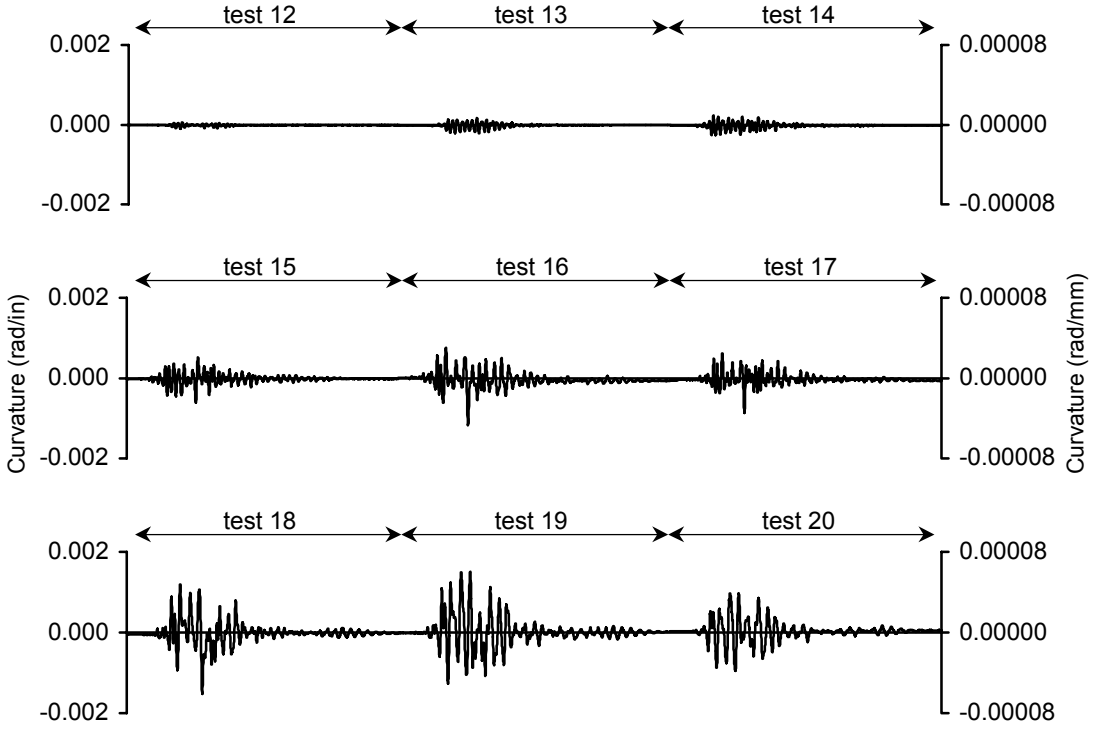

Figure 6-136: Curvature history for bent 2 top west column, trans. direction at 8.5 in (216mm) from fixity, during high amplitude tests.

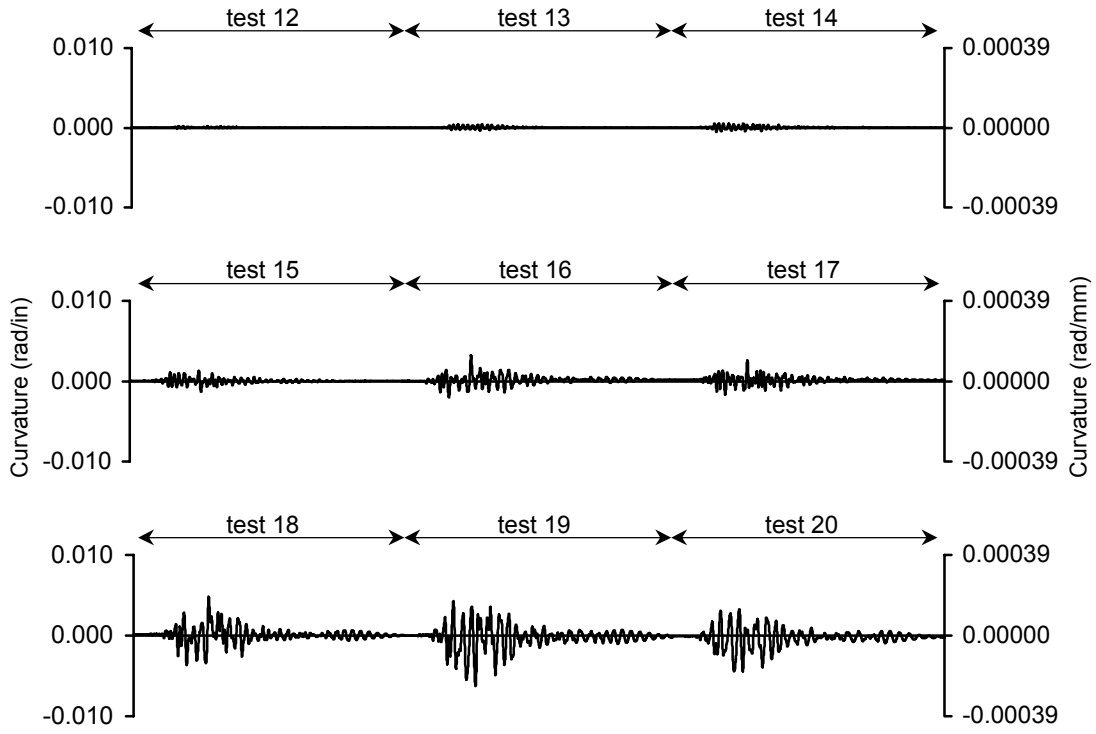

Figure 6-137: Curvature history for bent 2 bottom west column, trans. direction at 2.5 in (64mm) from fixity, during high amplitude tests

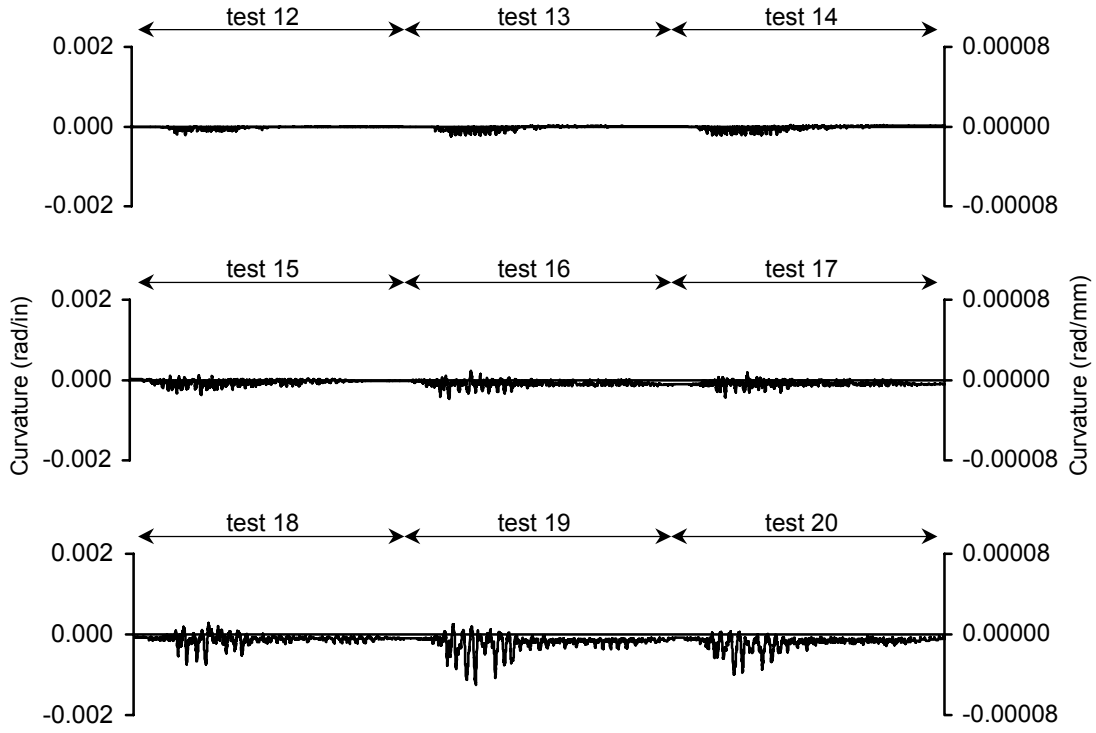

Figure 6-138: Curvature history for bent 2 bottom west column, trans. direction at 8.5 in (216mm) from fixity, during high amplitude tests.

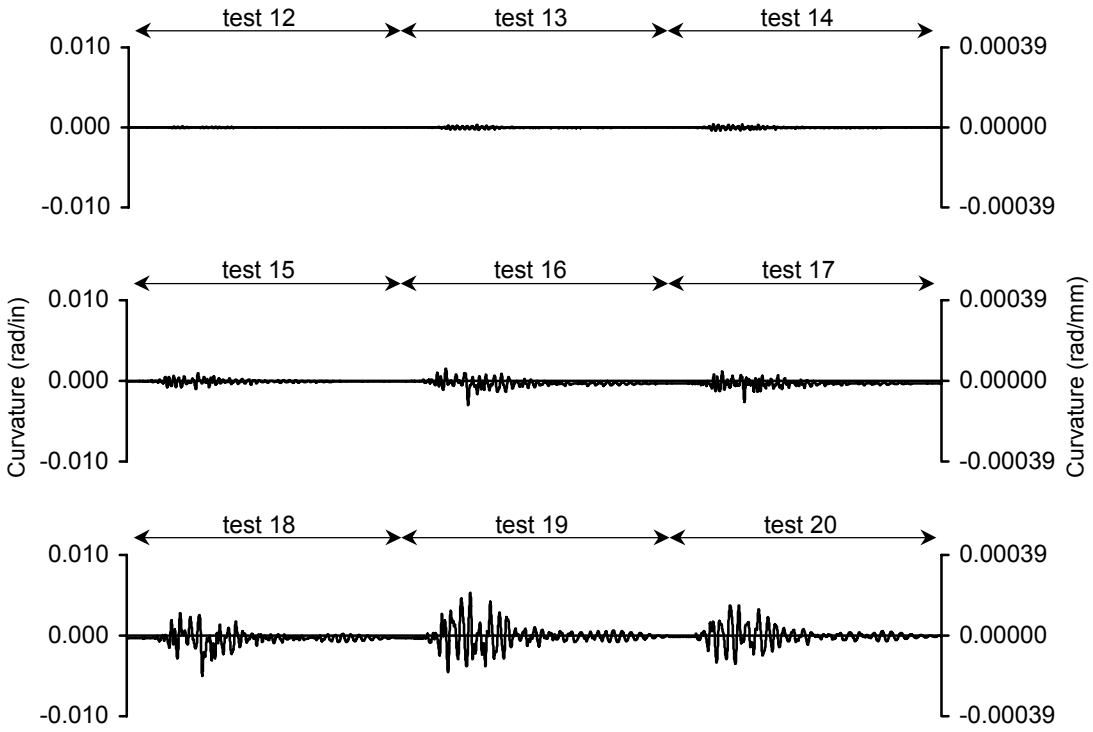

Figure 6-139: Curvature history for bent 2 top east column, trans. direction at 2.5 in (64mm) from fixity, during high amplitude tests

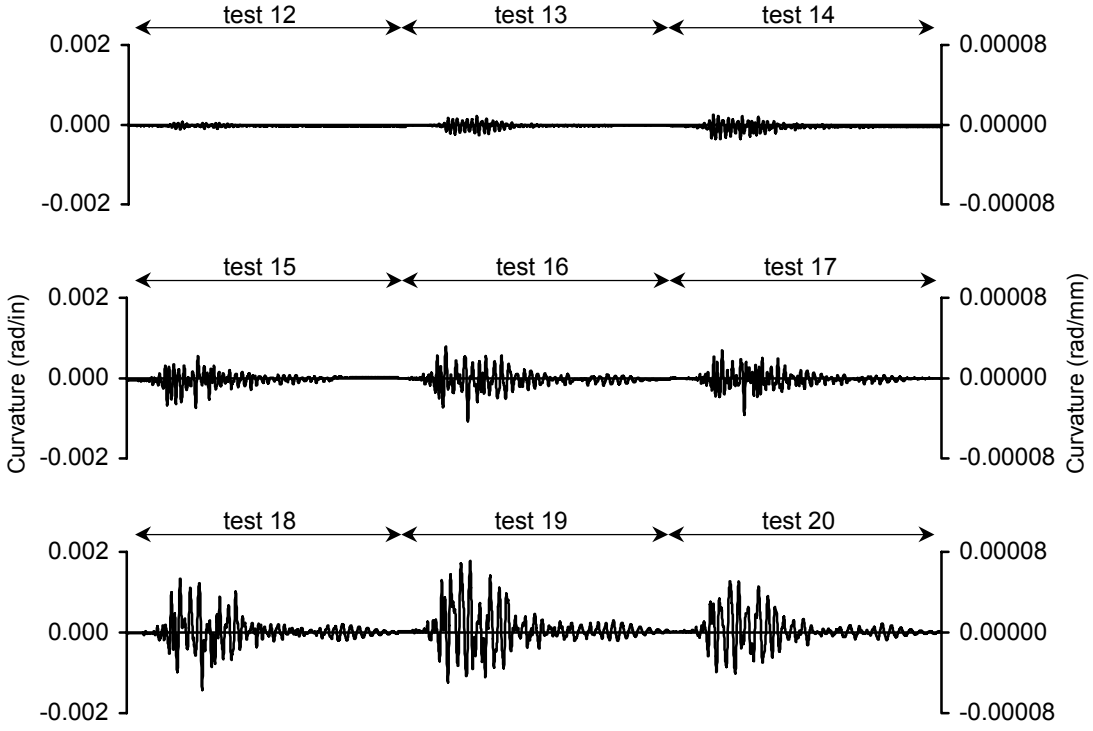

Figure 6-140: Curvature history for bent 2 top east column, trans. direction at 8.5 in (216mm) from fixity, during high amplitude tests.

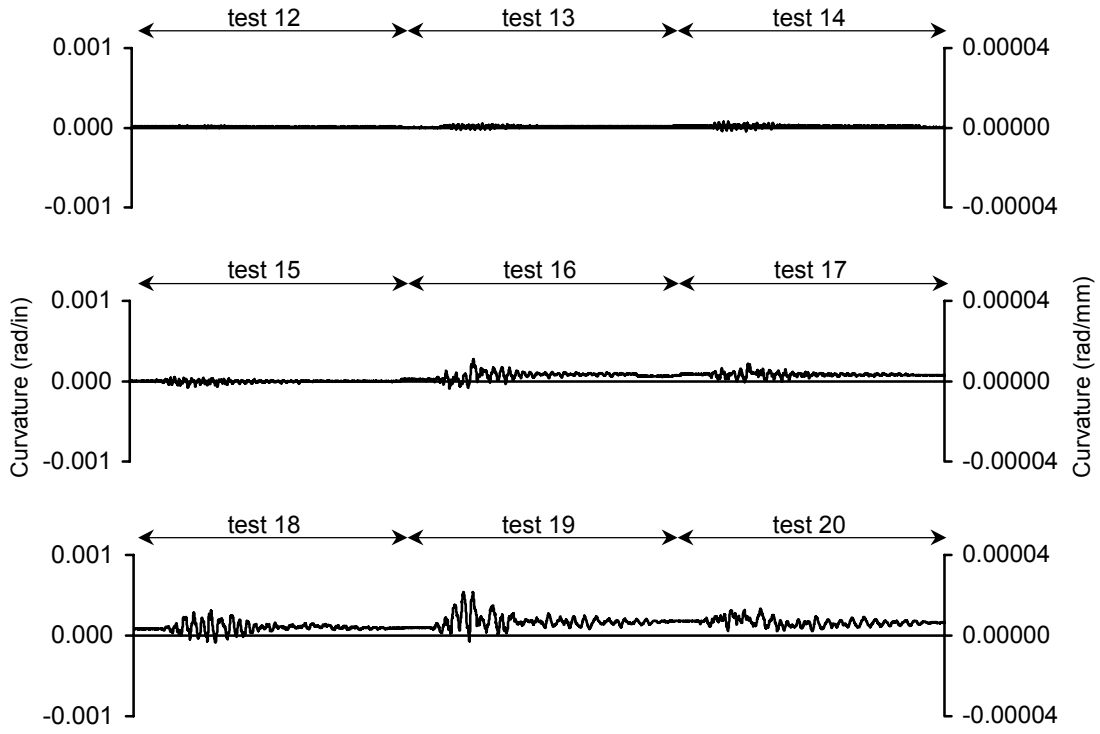

Figure 6-141: Curvature history for bent 2 top east column, long. direction at 2.5 in (64mm) from fixity, during high amplitude tests.

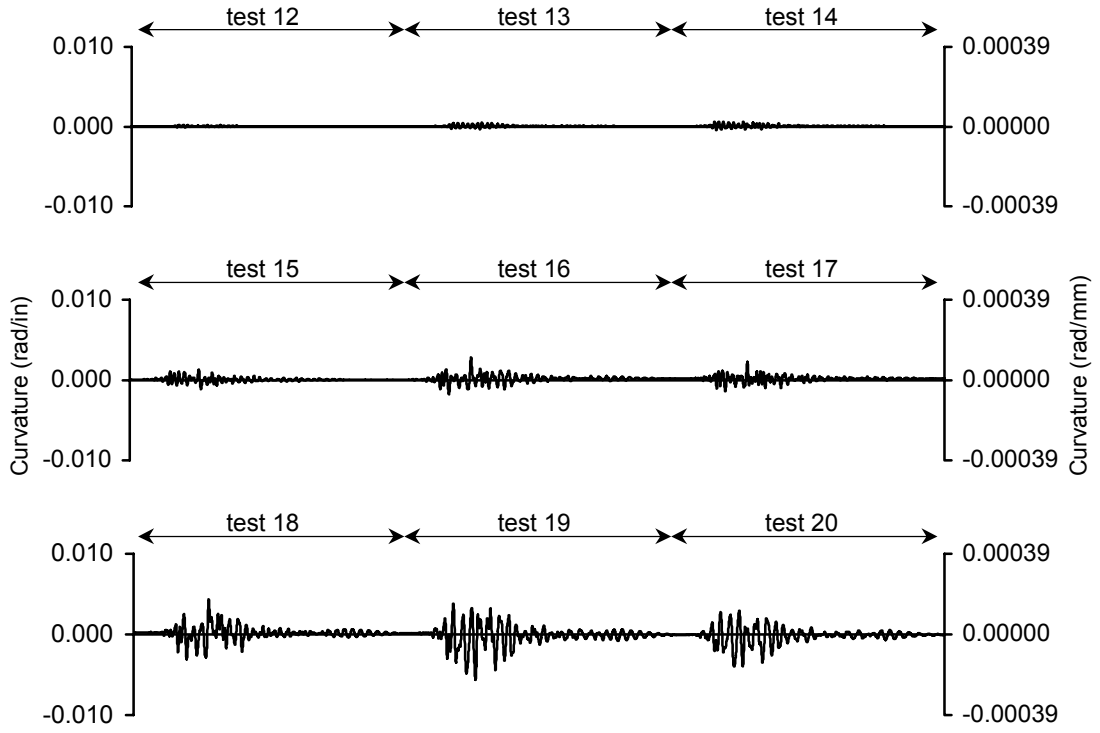

Figure 6-142: Curvature history for bent 2 bottom east column, trans. direction at 2.5 in (64mm) from fixity, during high amplitude tests.

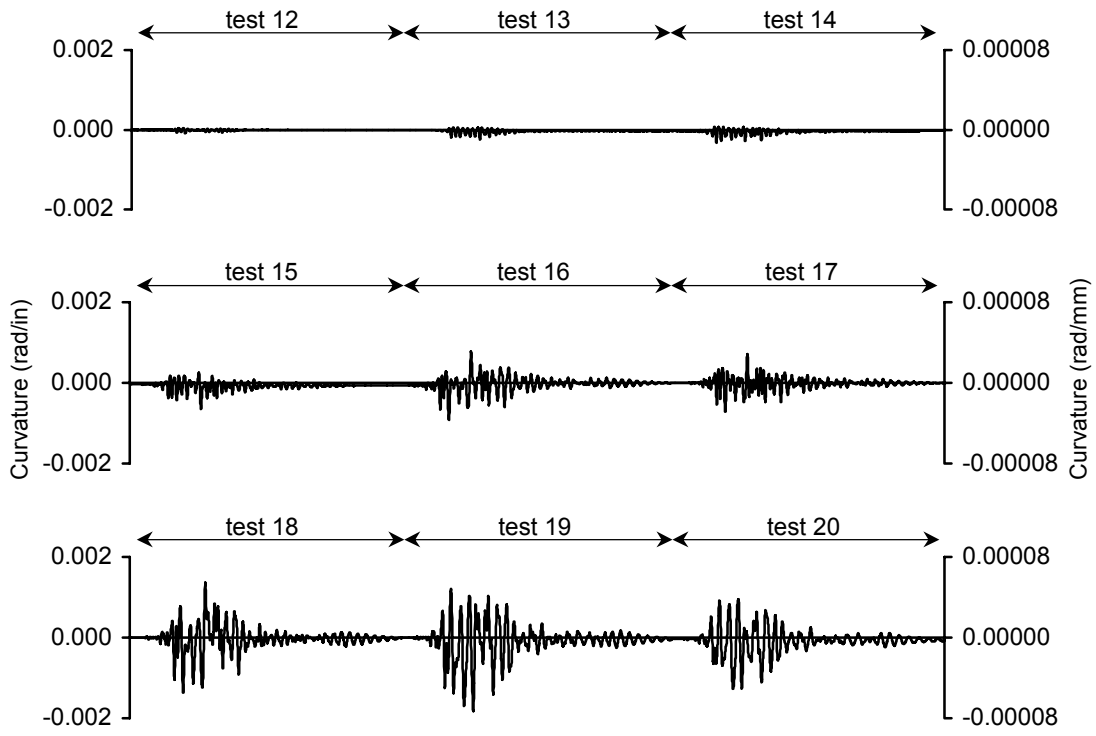

Figure 6-143: Curvature history for bent 2 bottom east column, trans. direction at 8.5 in (216mm) from fixity, during high amplitude tests

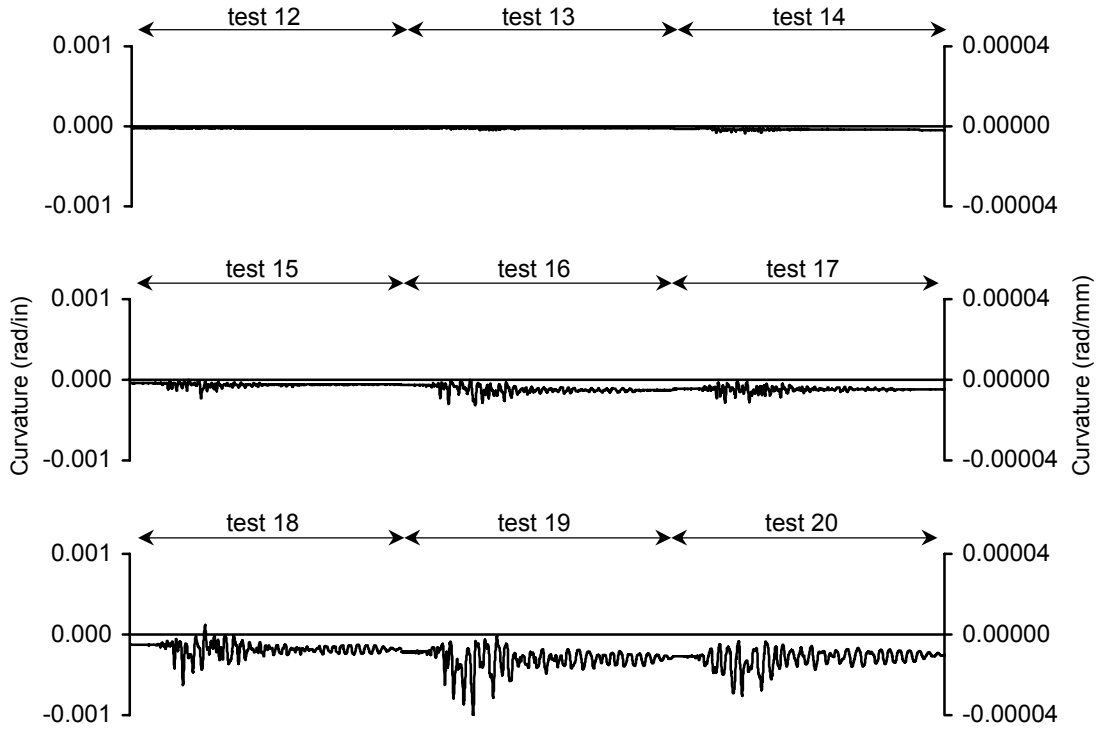

Figure 6-144: Curvature history for bent 2 bottom east column, long. direction at 2.5 in (64mm) from fixity, during high amplitude tests.

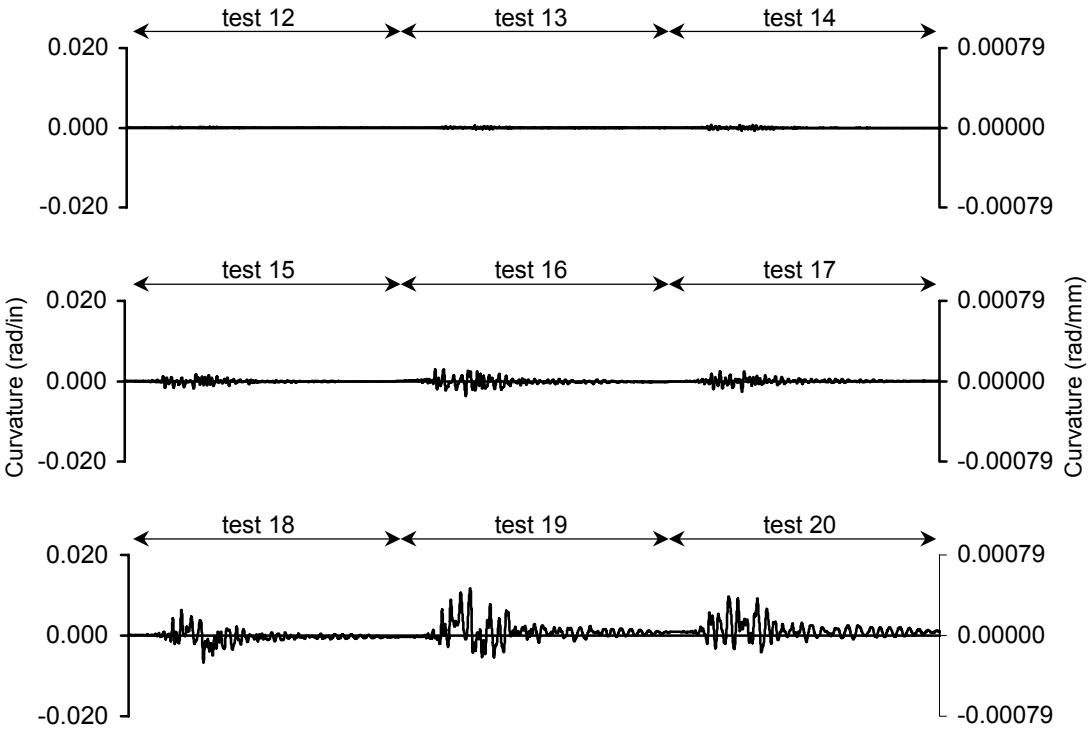

Figure 6-145: Curvature history for bent 3 top west column, trans direction at 2.5 in (64mm) from fixity, during high amplitude tests.

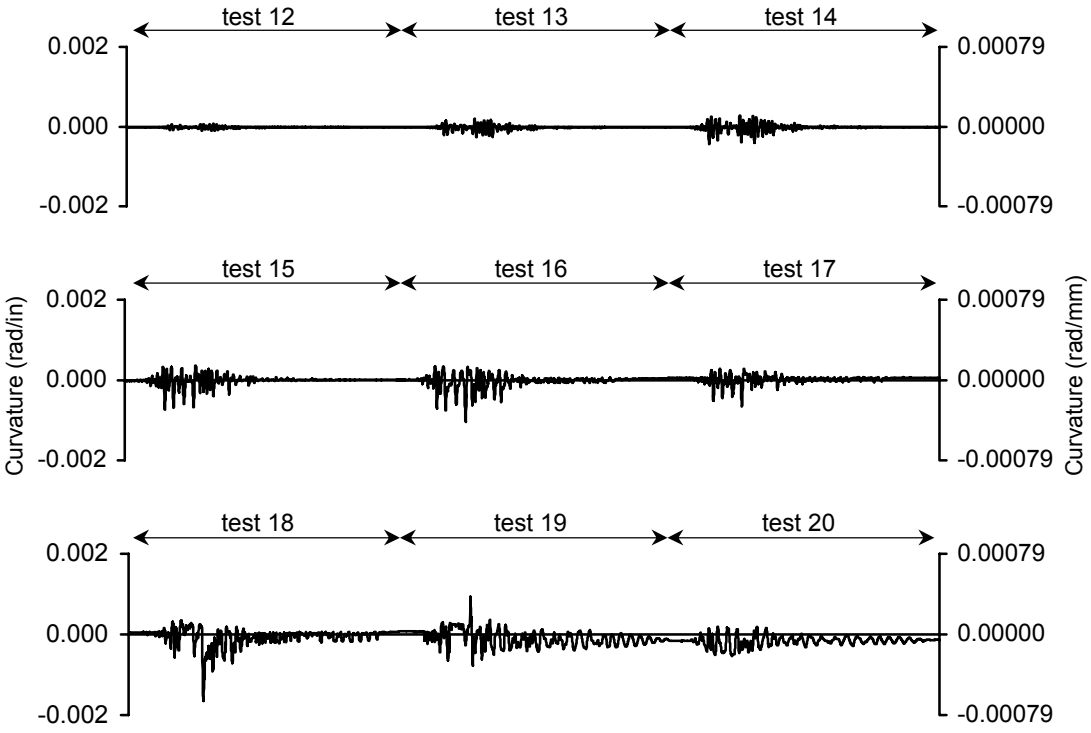

Figure 6-146: Curvature history for bent 3 top west column, trans. direction at 8.5 in (216mm) from fixity, during high amplitude tests.

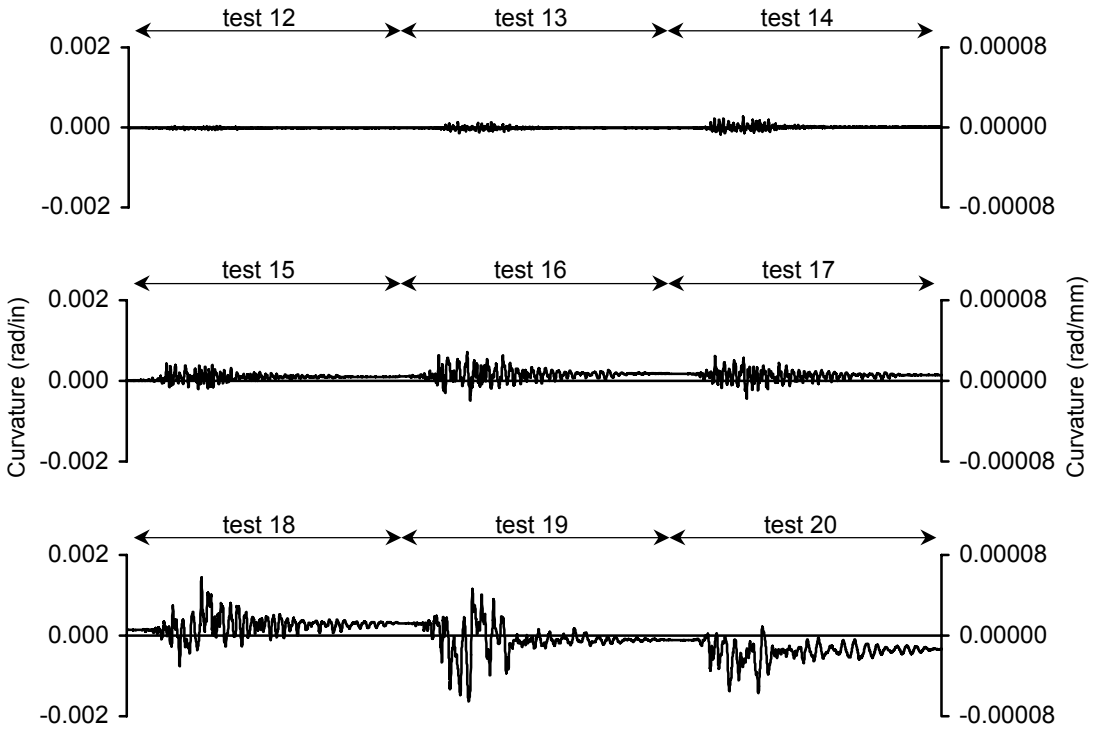

Figure 6-147: Curvature history for bent 3 top west column, long. direction at 2.5 in (64mm) from fixity, during high amplitude tests

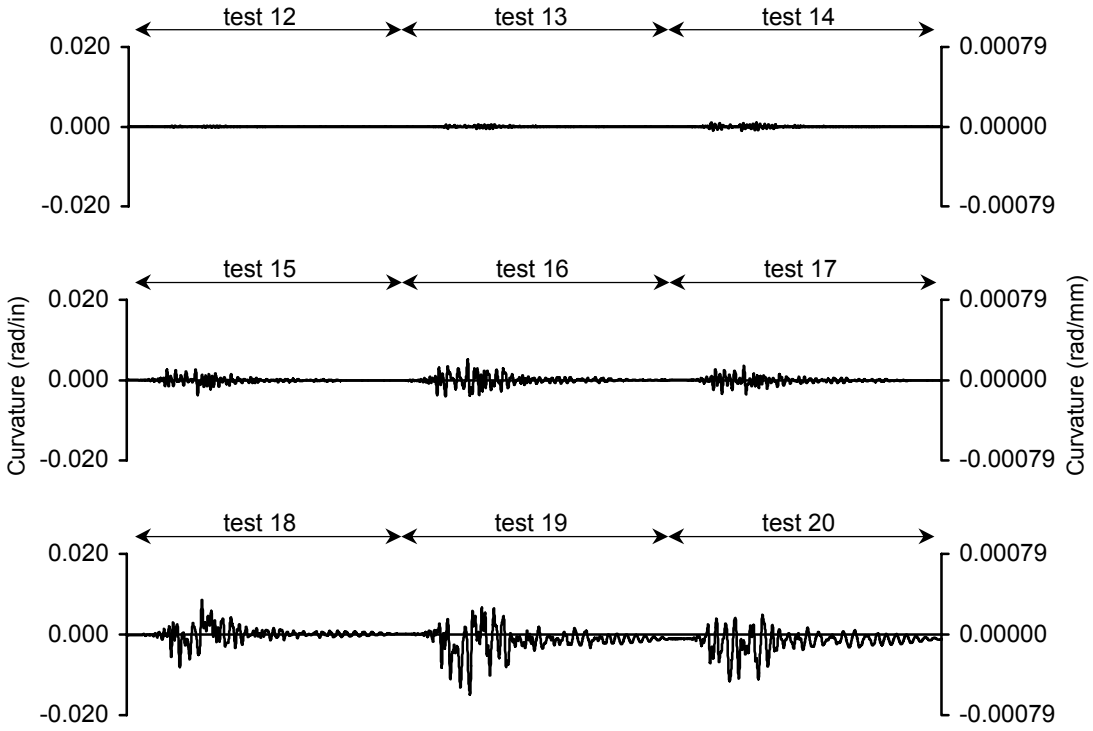

Figure 6-148: Curvature history for bent 3 bottom west column, trans direction at 2.5 in (64mm) from fixity, during high amplitude tests.

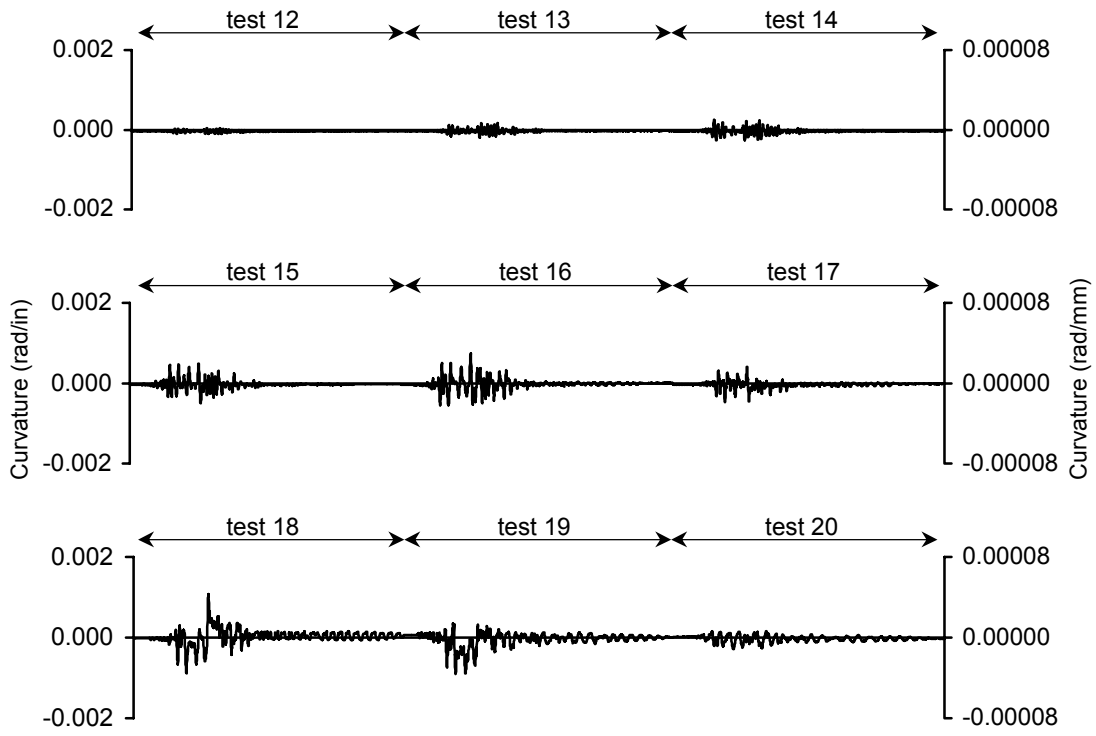

Figure 6-149: Curvature history for bent 3 bottom west column, trans direction at 8.5 in (216mm from fixity, during high amplitude tests.

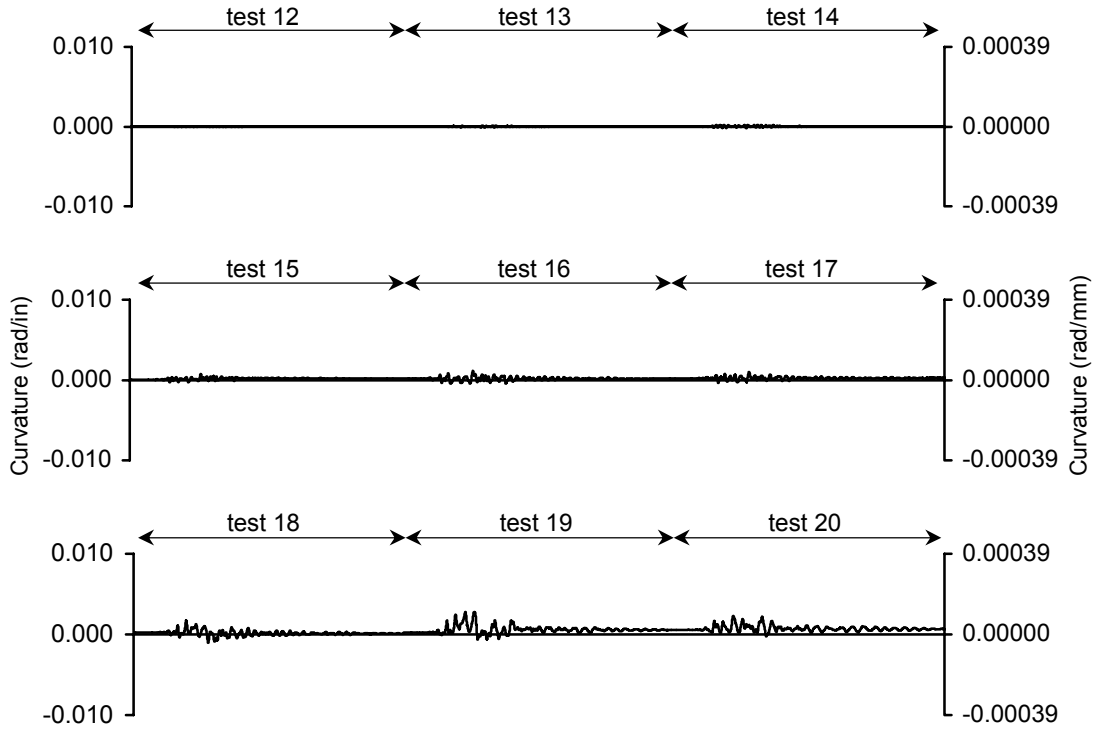

Figure 6-150: Curvature history for bent 3 bottom west column, long. direction at 2.5 in (64mm) from fixity, during high amplitude tests.

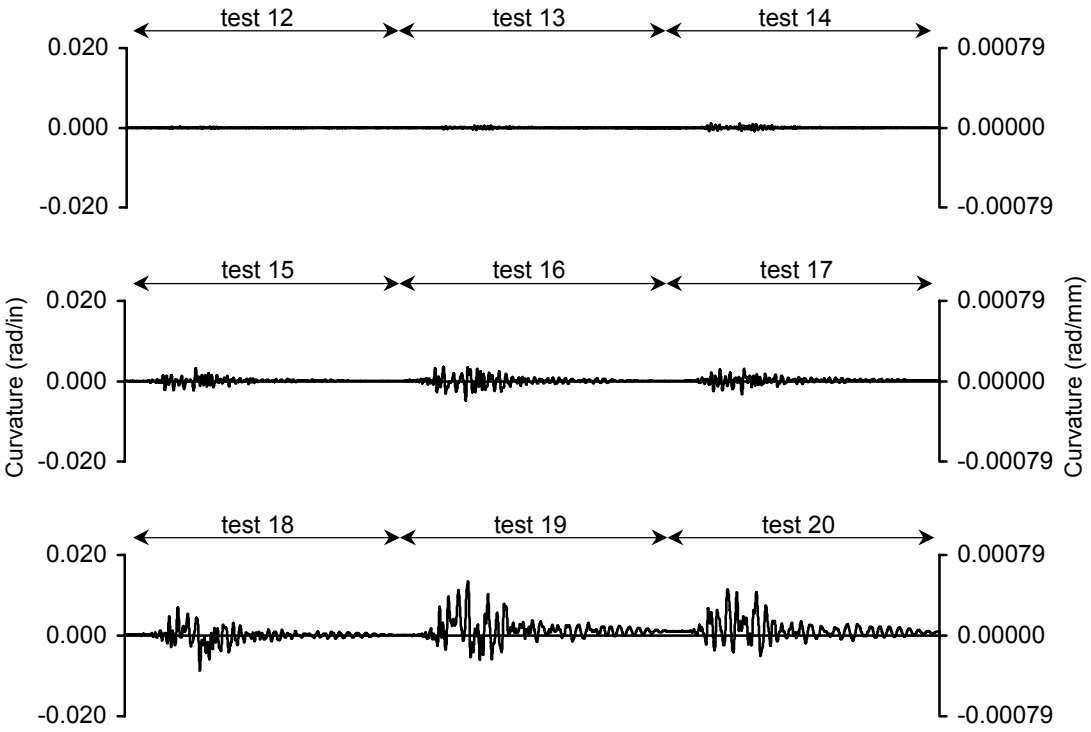

Figure 6-151: Curvature history for bent 3 top east column, trans. direction at 2.5 in (64mm) from fixity, during high amplitude tests

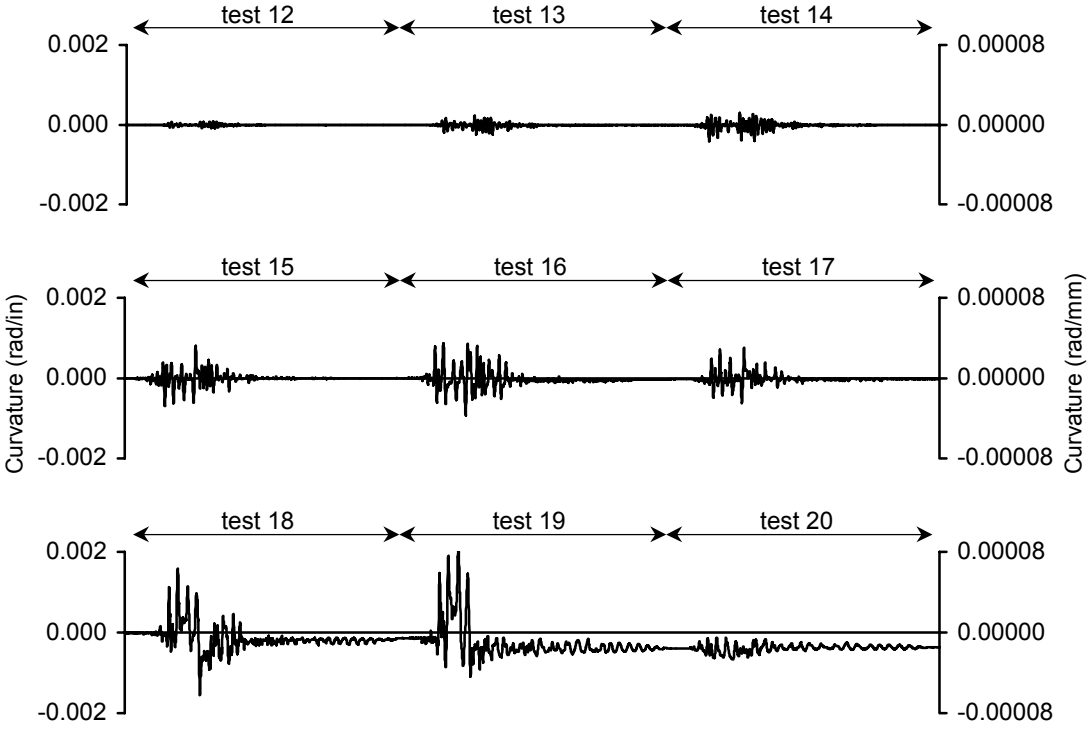

Figure 6-152: Curvature history for bent 3 top east column, trans direction at 8.5 in (216mm) from fixity, during high amplitude tests.

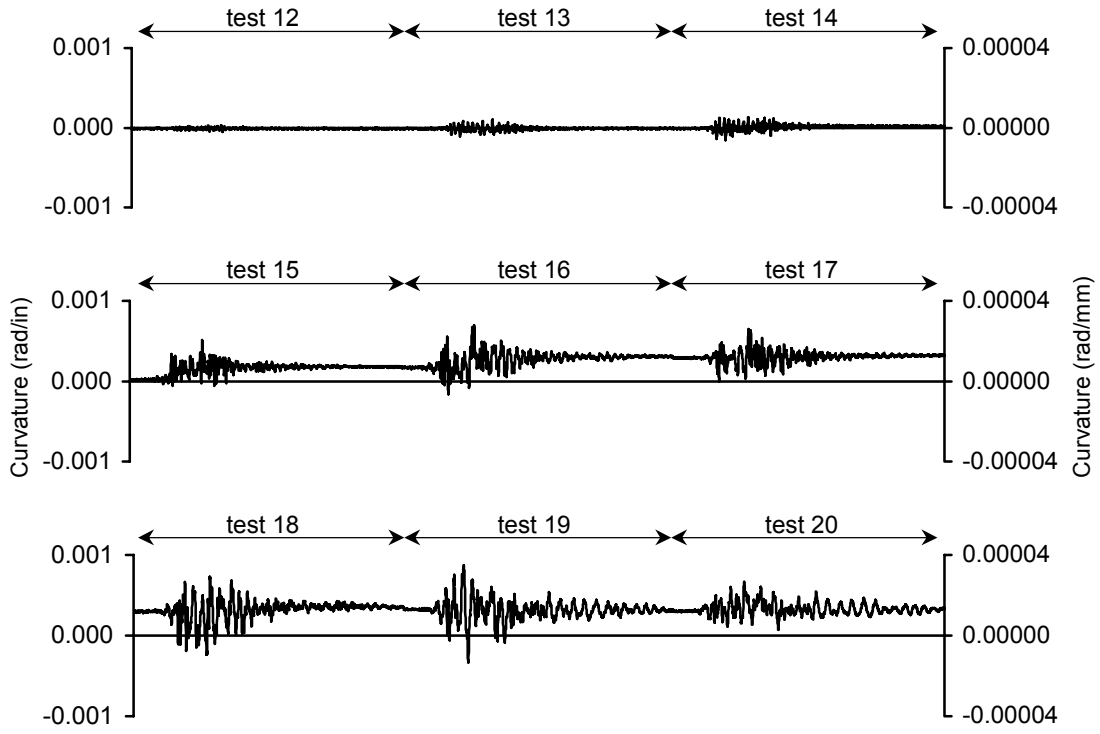

Figure 6-153: Curvature history for bent 3 top east column, long. direction at 2.5 in (64mm) from fixity, during high amplitude tests.

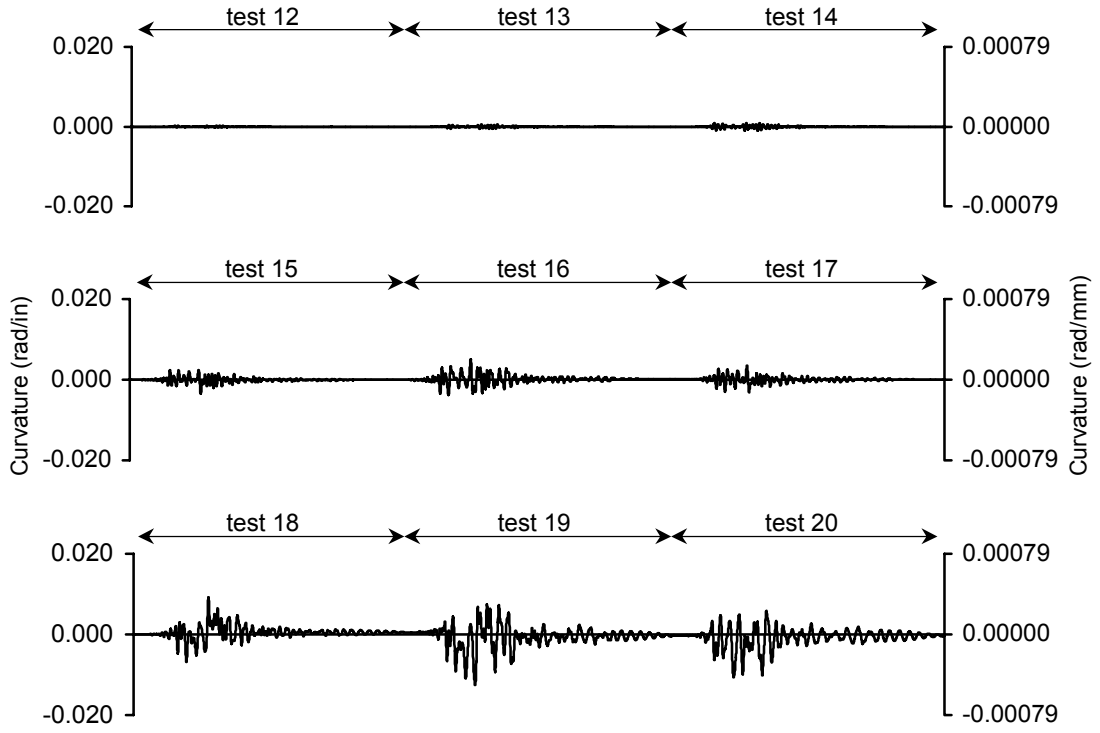

Figure 6-154: Curvature history for bent 3 bottom east column, trans. direction at 2.5 in (64mm) from fixity, during high amplitude tests.

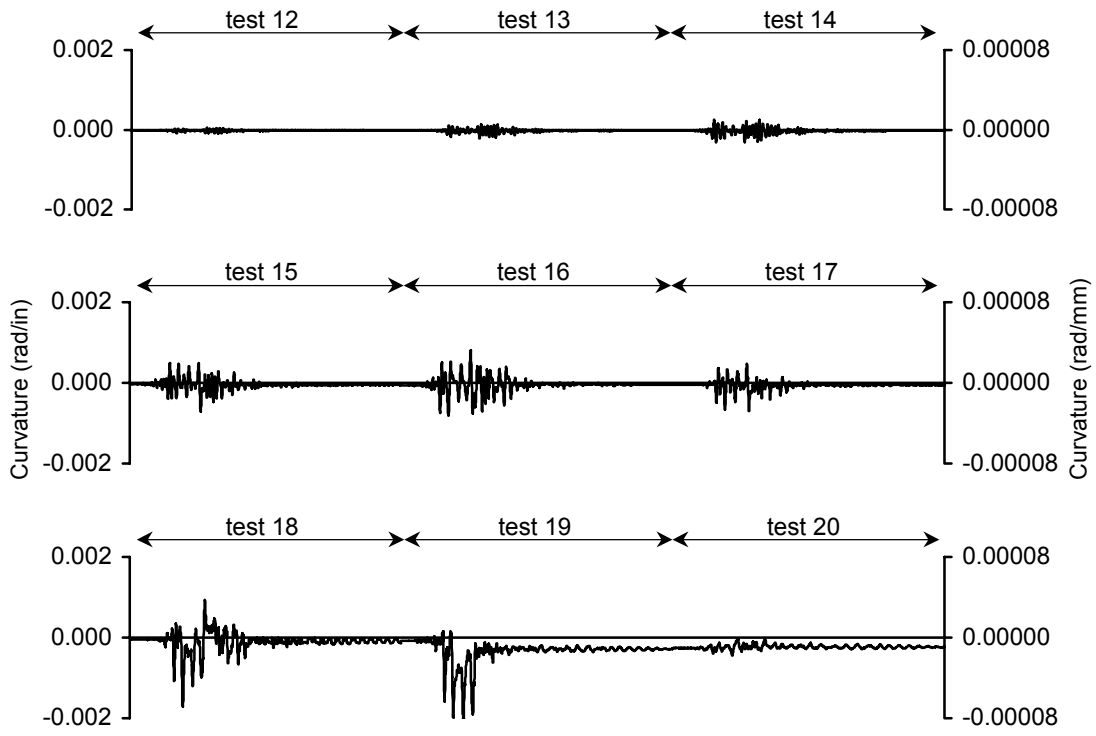

Figure 6-155: Curvature history for bent 3 bottom east column, trans. direction at 8.5 in (216mm) from fixity, during high amplitude tests

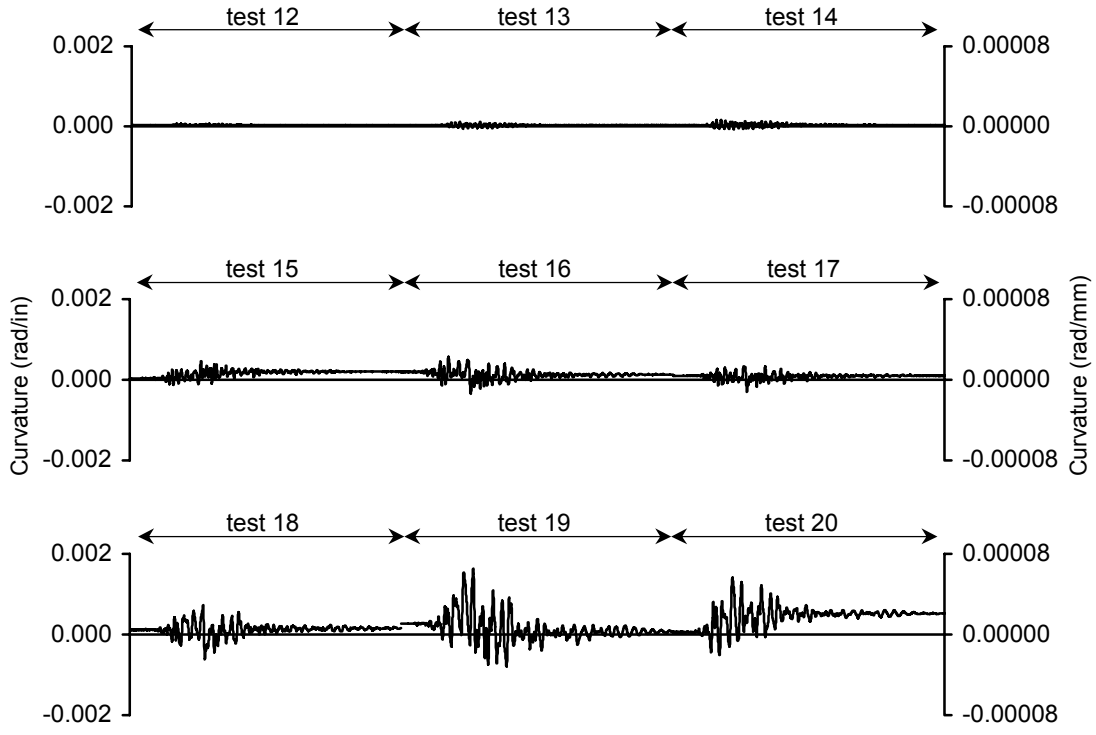

Figure 6-156: Curvature history for bent 3 bottom east column, long. direction at 2.5 in (64mm) from fixity, during high amplitude tests.

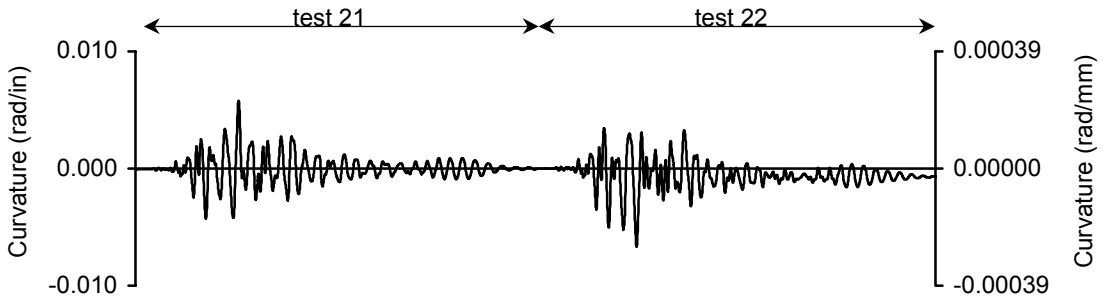

Figure 6-157: Curvature history for bent 1 top west column, trans. direction at 2.5 in (64mm) from fixity, during post tests.

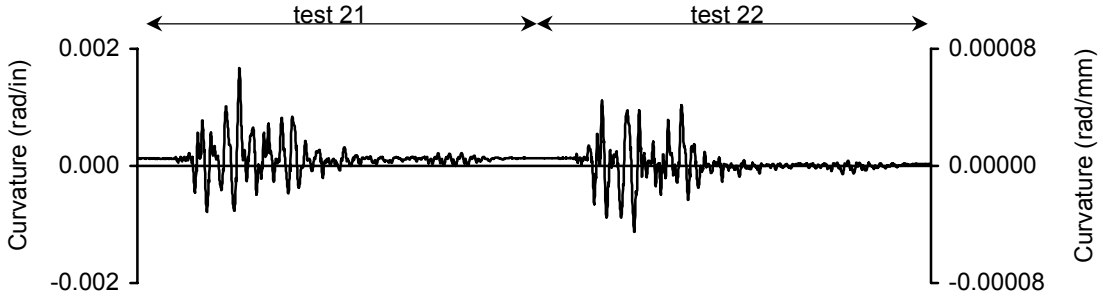

Figure 6-158: Curvature history for bent 1 top west column, trans. direction at 8.5 in (216mm) from fixity, during post tests.

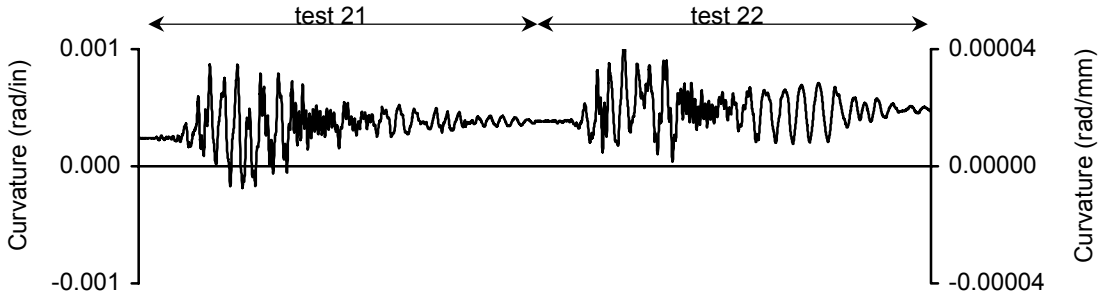

Figure 6-159: Curvature history for bent 1 top west column, long. direction at 2.5 in (64mm) from fixity, during post tests.

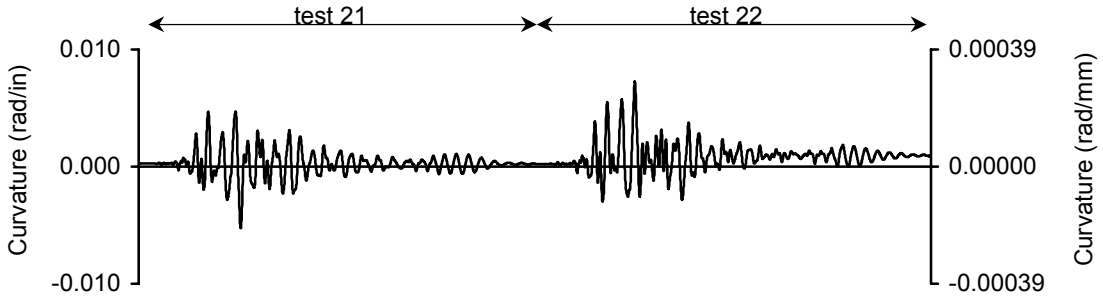

Figure 6-160: Curvature history for bent 1 bottom west column, trans. direction at 2.5 in (64mm) from fixity, during post tests.

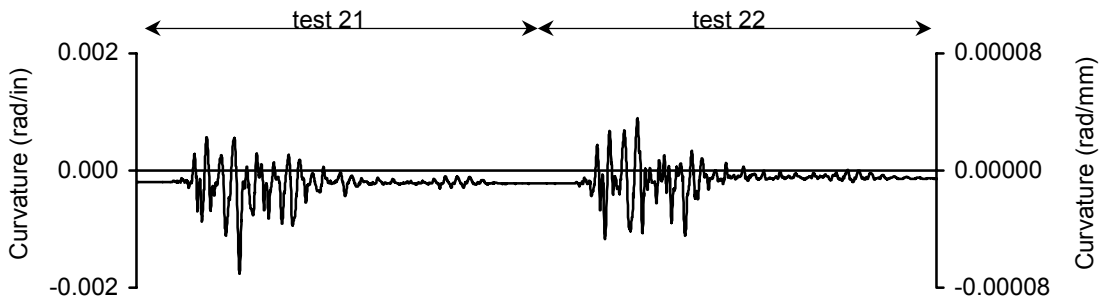

Figure 6-161: Curvature history for bent 1 bottom west column, trans. direction at 8.5 in (216mm) from fixity, during post tests.

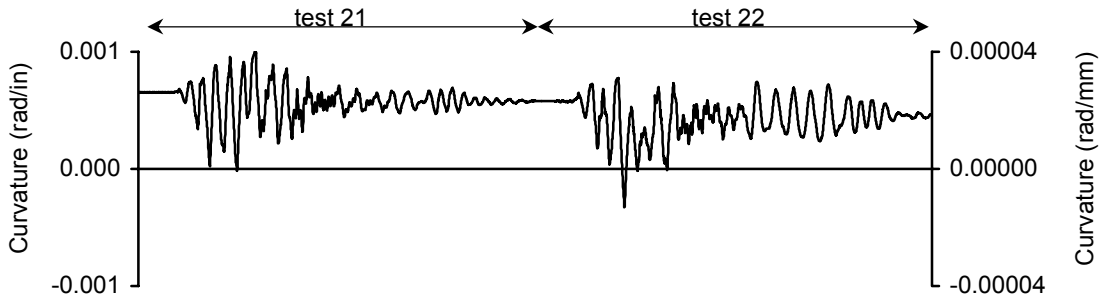

Figure 6-162: Curvature history for bent 1 bottom west column, long. direction at 2.5 in (64mm) from fixity, during post tests.

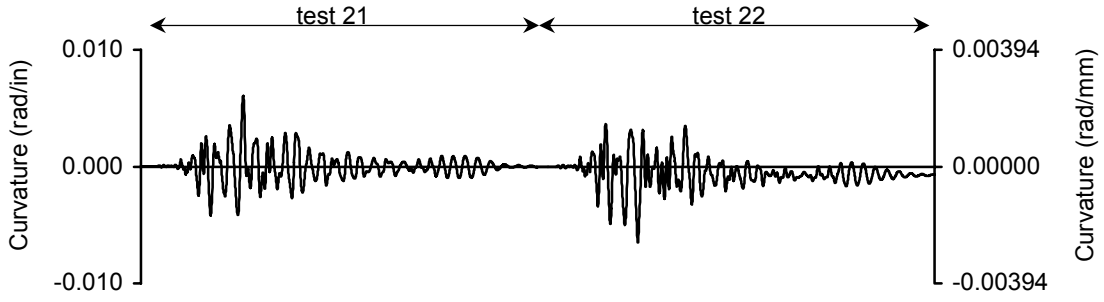

Figure 6-163: Curvature history for bent 1 top east column, trans. direction at 2.5 in (64mm) from fixity, during post tests.

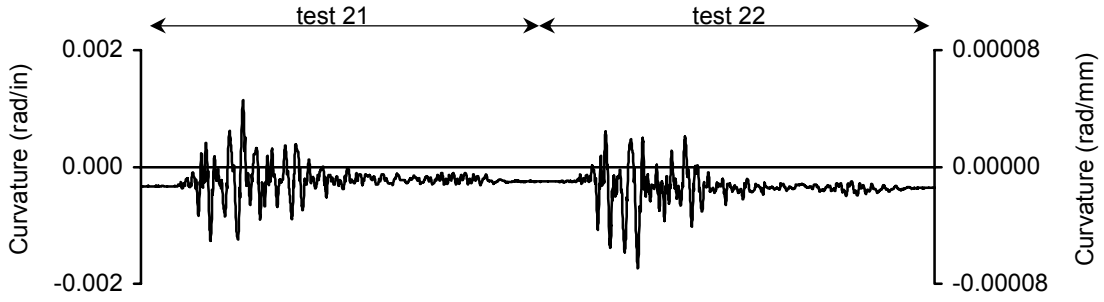

Figure 6-164: Curvature history for bent 1 top east column, trans. direction at 8.5 in (216mm) from fixity, during post tests.

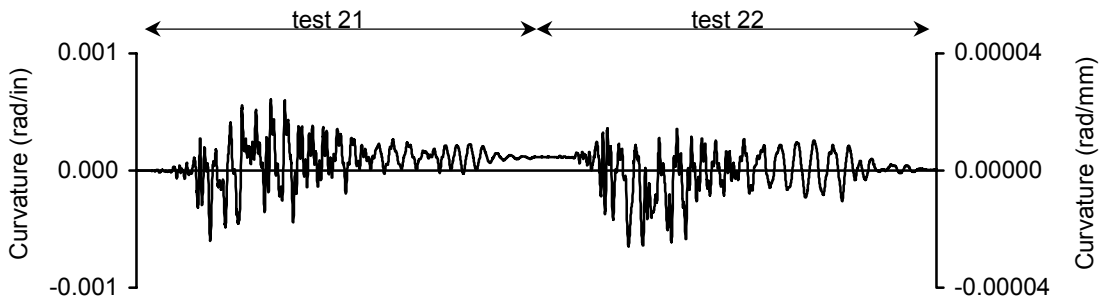

Figure 6-165: Curvature history for bent 1 top east column, long. direction at 2.5 in (64mm) from fixity, during post tests.

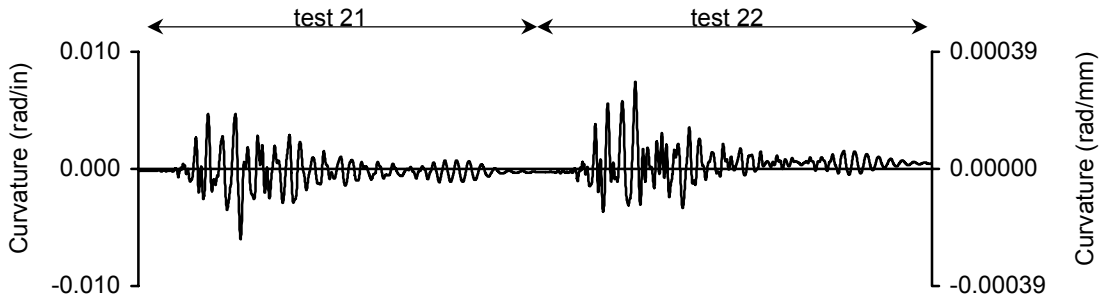

Figure 6-166: Curvature history for bent 1 bottom east column, trans. direction at 2.5 in (64mm) from fixity, during post tests.

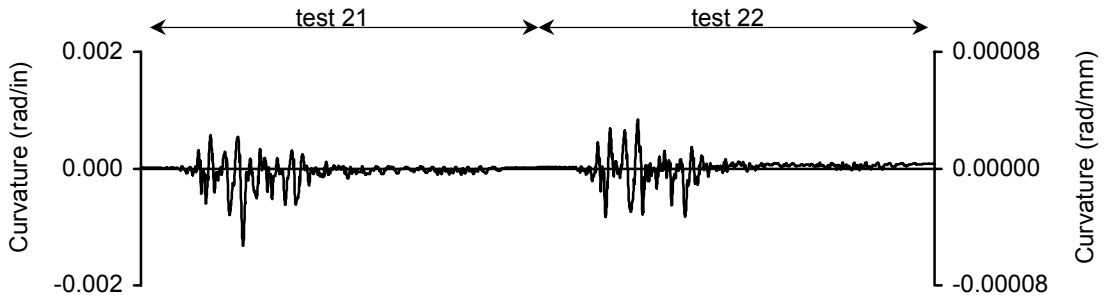

Figure 6-167: Curvature history for bent 1 bottom east column, trans. direction at 8.5 in (216mm) from fixity, during post tests.

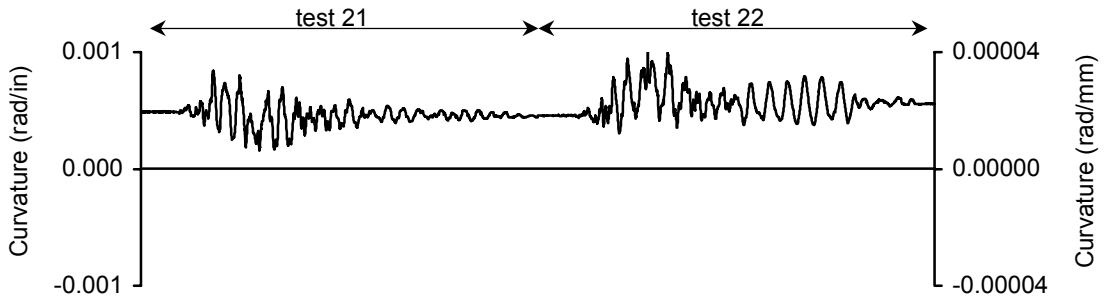

Figure 6-168: Curvature history for bent 1 bottom east column, long direction at 2.5 in (64mm) from fixity, during post tests.

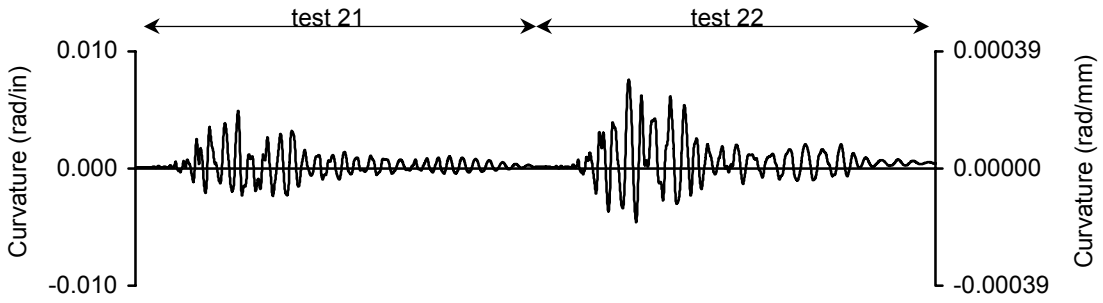

Figure 6-169: Curvature history for bent 2 top west column, trans. direction at 2.5 in (64mm) from fixity, during post tests.

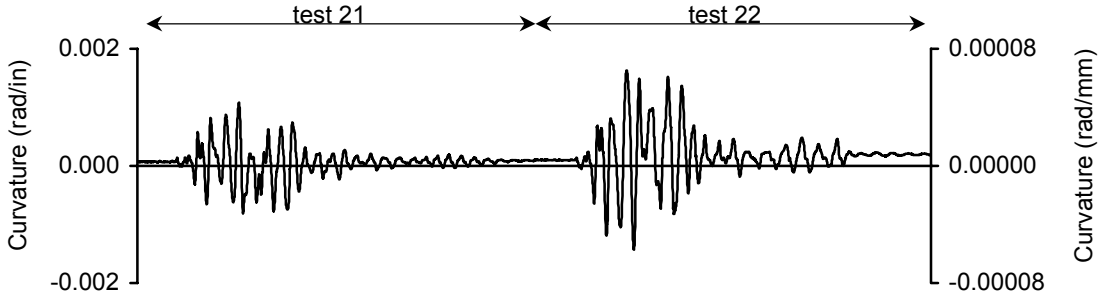

Figure 6-170: Curvature history for bent 2 top west column, trans. direction at 8.5 in (216mm) from fixity, during post tests.

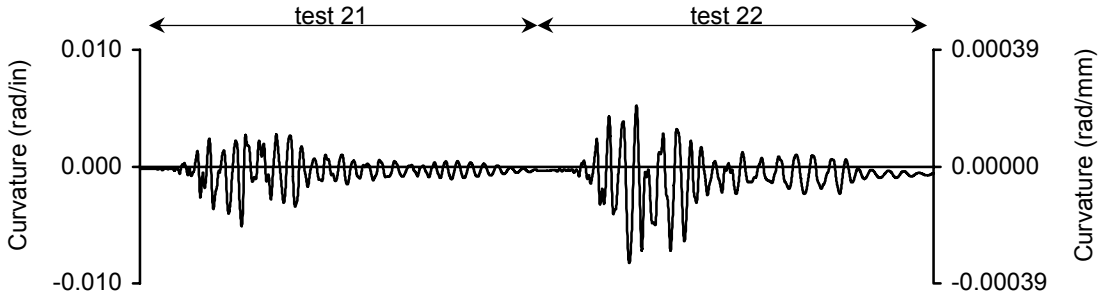

Figure 6-171: Curvature history for bent 2 bottom west column, trans. direction at 2.5 in (64mm) from fixity, during post tests.

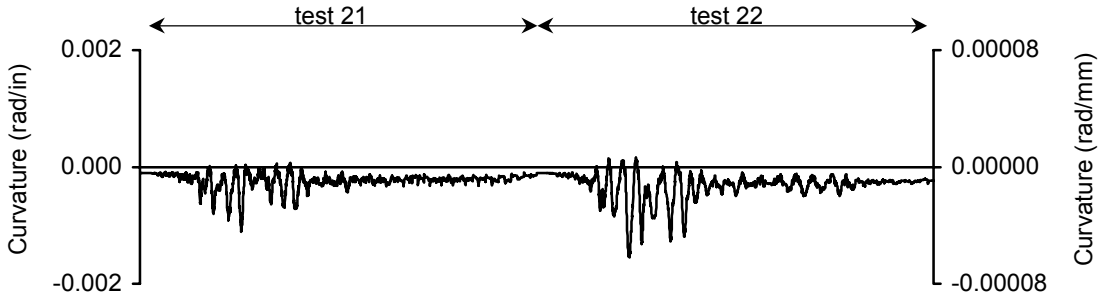

Figure 6-172: Curvature history for bent 2 bottom west column, trans. direction at 8.5 in (216mm) from fixity, during post tests.

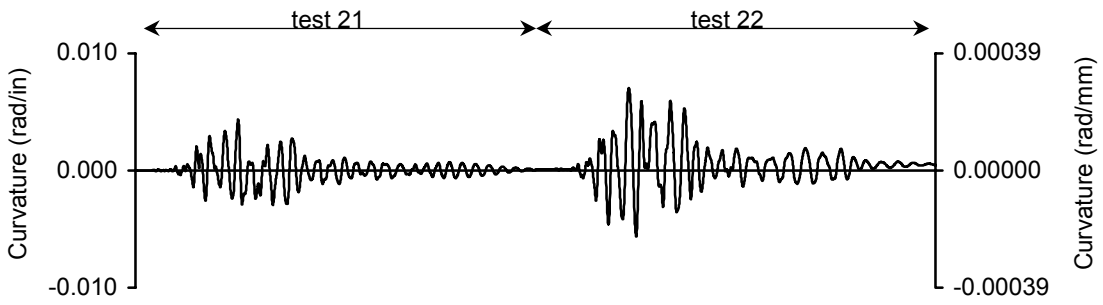

Figure 6-173: Curvature history for bent 2 top east column, trans. direction at 2.5 in (64mm) from fixity, during post tests.

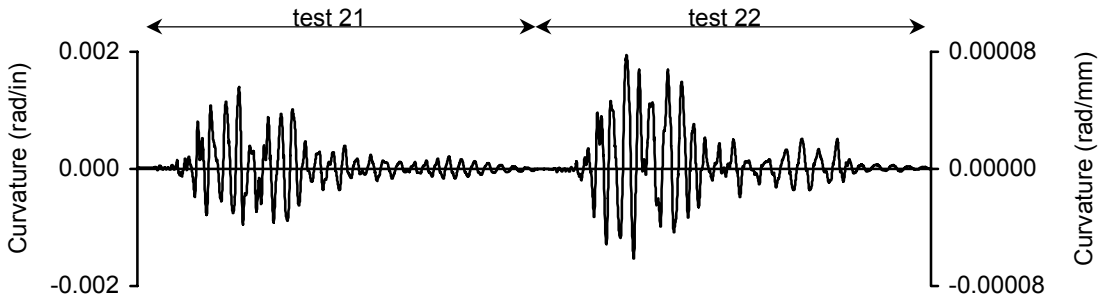

Figure 6-174: Curvature history for bent 2 top east column, trans. direction at 8.5 in (216mm) from fixity, during post tests.

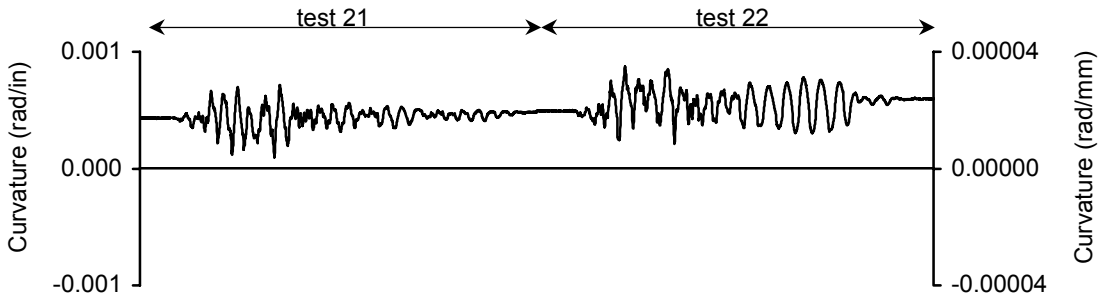

Figure 6-175: Curvature history for bent 2 top east column, long. direction at 2.5 in (64mm) from fixity, during post tests.

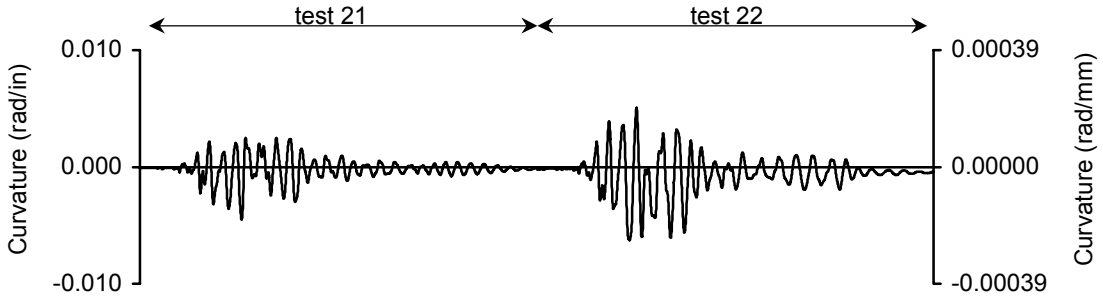

Figure 6-176: Curvature history for bent 2 bottom east column, trans. direction at 2.5 in (64mm) from fixity, during post tests.

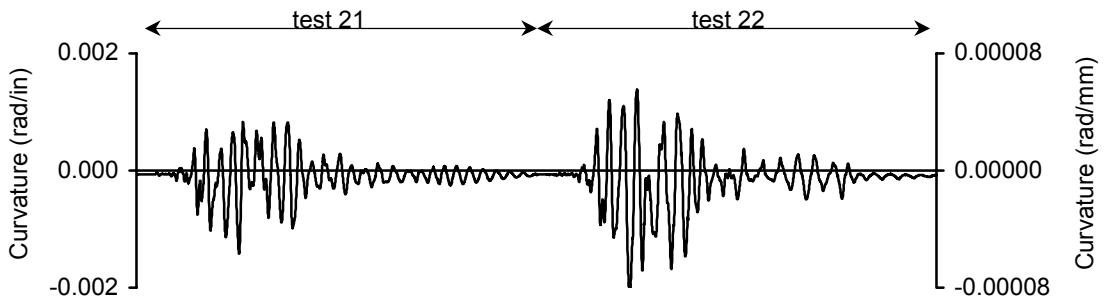

Figure 6-177: Curvature history for bent 2 bottom east column, trans. direction at 8.5 in (216mm) from fixity, during post tests.

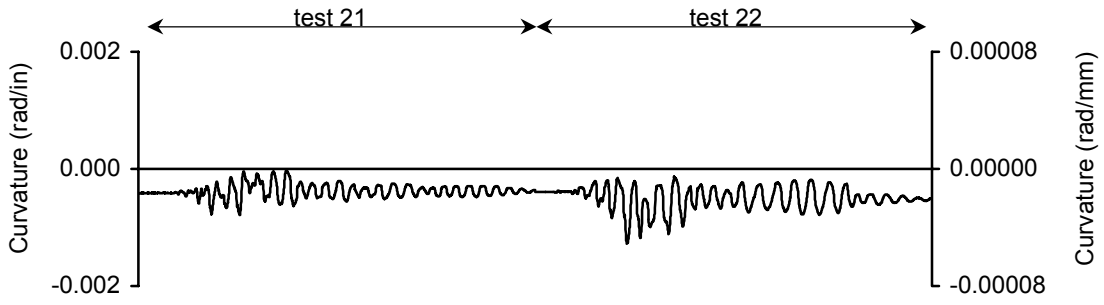

Figure 6-178: Curvature history for bent 2 bottom east column, long. direction at 2.5 in (64mm) from fixity, during post tests.

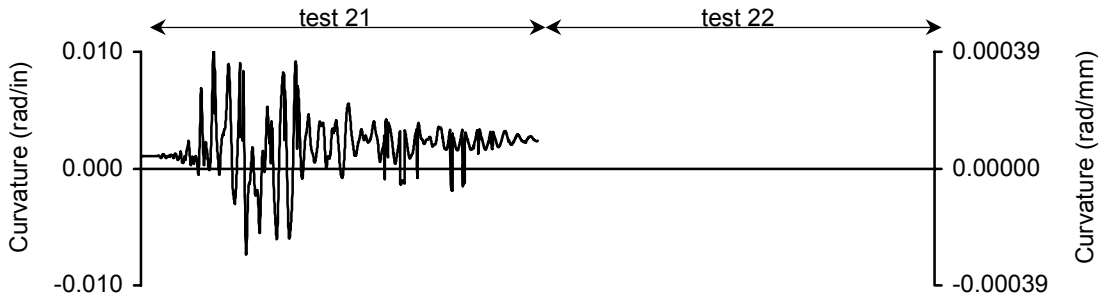

Figure 6-179: Curvature history for bent 3 top west column, trans direction at 2.5 in (64mm) from fixity, during post tests.

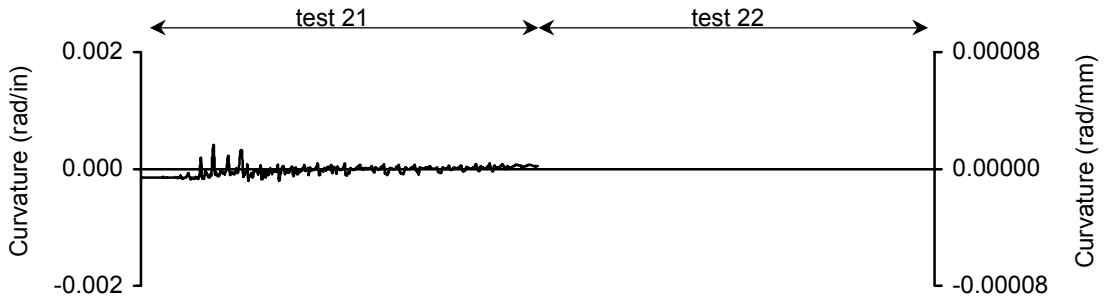

Figure 6-180: Curvature history for bent 3 top west column, trans. direction at 8.5 in (216mm) from fixity, during post tests.

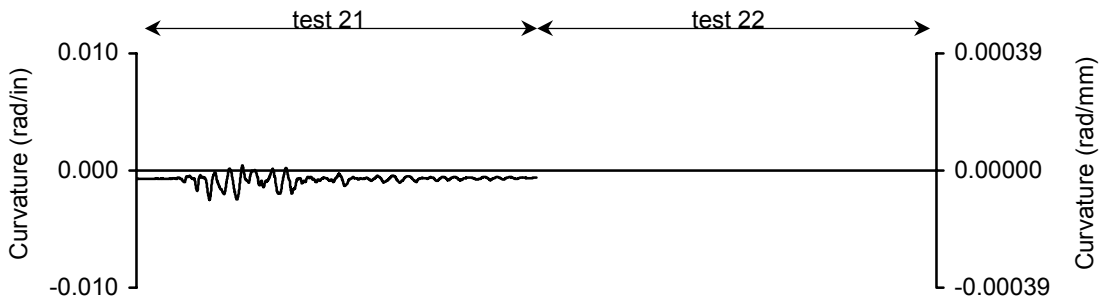

Figure 6-181: Curvature history for bent 3 top west column, long. direction at 2.5 in (64mm) from fixity, during post tests.

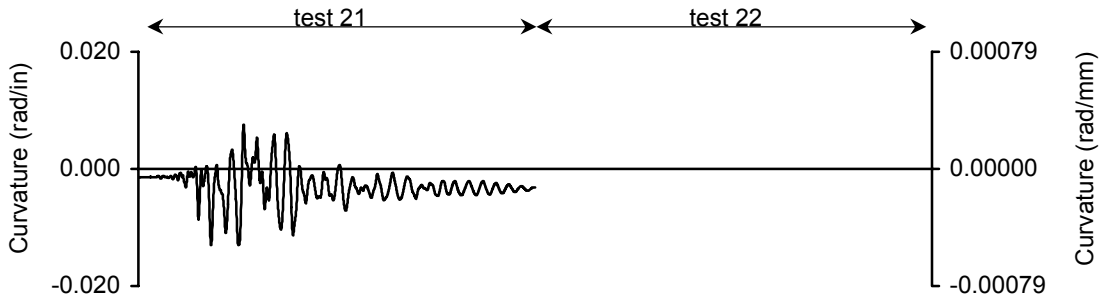

Figure 6-182: Curvature history for bent 3 bottom west column, trans direction at 2.5 in (64mm) from fixity, during post tests.

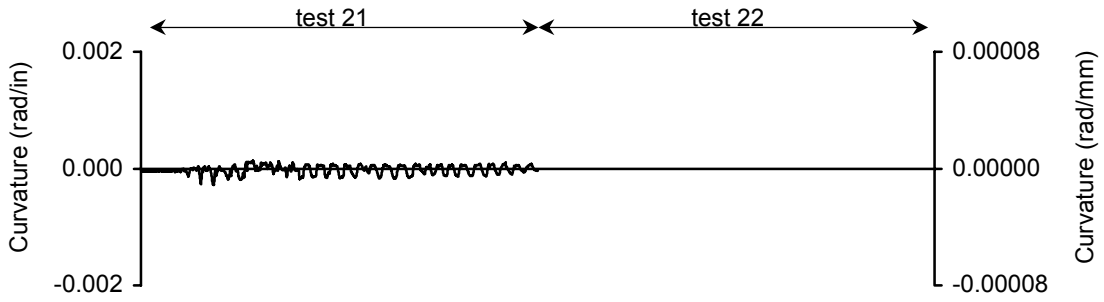

Figure 6-183: Curvature history for bent 3 bottom west column, trans direction at 8.5 in (216mm) from fixity, during post tests.

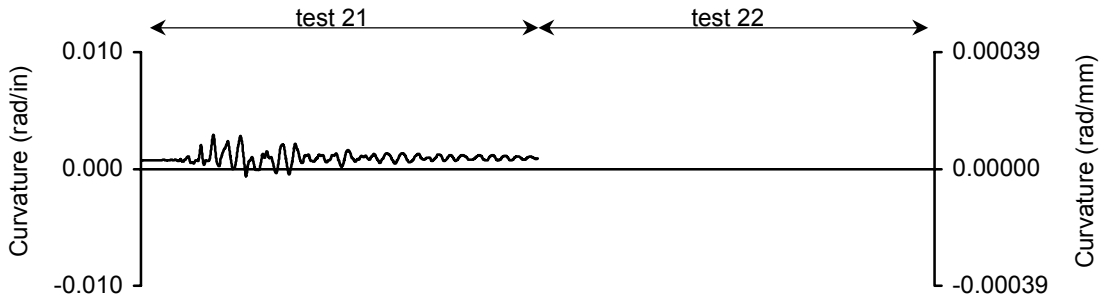

Figure 6-184: Curvature history for bent 3 bottom west column, long. direction at 2.5 in (64mm) from fixity, during post tests.

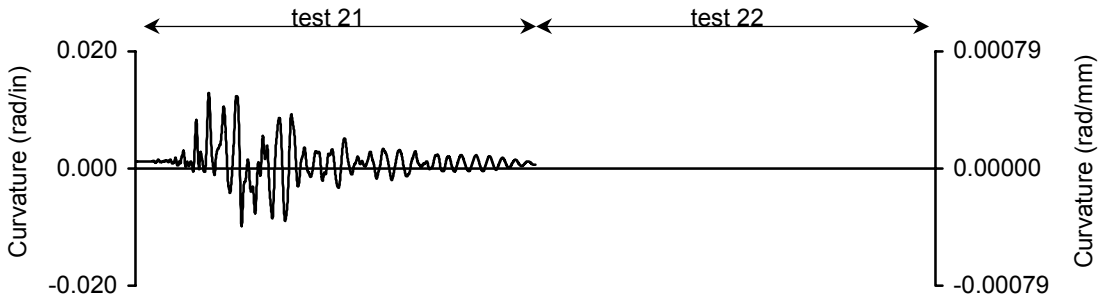

Figure 6-185: Curvature history for bent 3 top east column, trans. direction at 2.5 in (64mm) from fixity, during post tests.

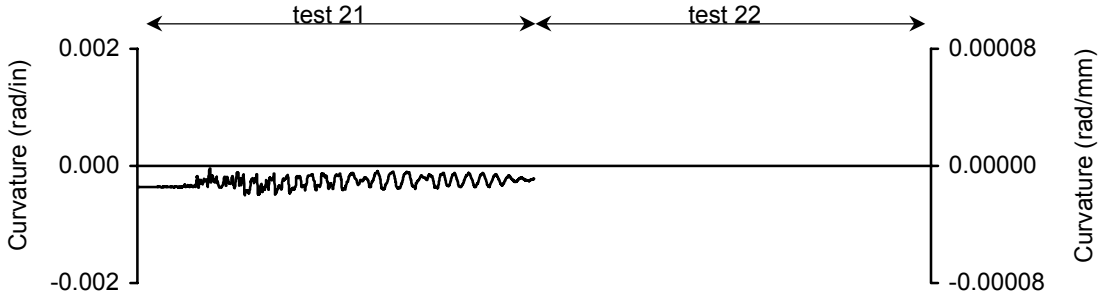

Figure 6-186: Curvature history for bent 3 top east column, trans direction at 8.5 in (216mm) from fixity, during post tests.

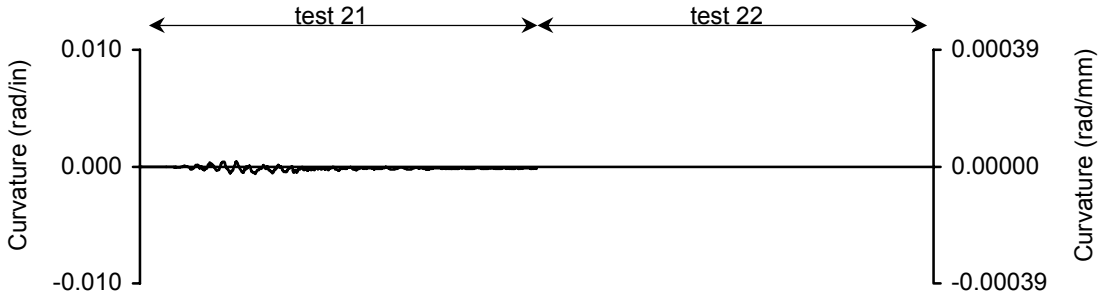

Figure 6-187: Curvature history for bent 3 top east column, long. direction at 2.5 in (64mm) from fixity, during post tests.

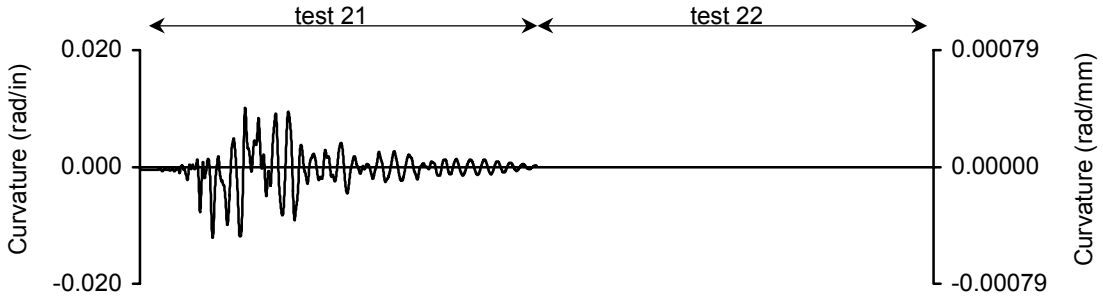

Figure 6-188: Curvature history for bent 3 bottom east column, trans. direction at 2.5 in (64mm) from fixity, during post tests.

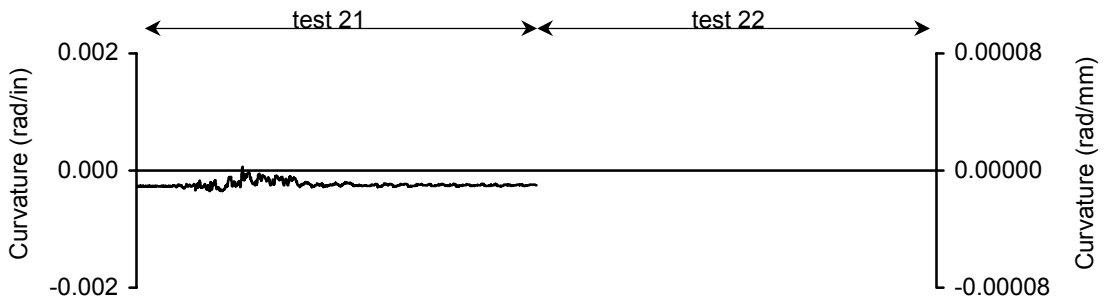

Figure 6-189: Curvature history for bent 3 bottom east column, trans. direction at 8.5 in (216mm) from fixity, during post tests.

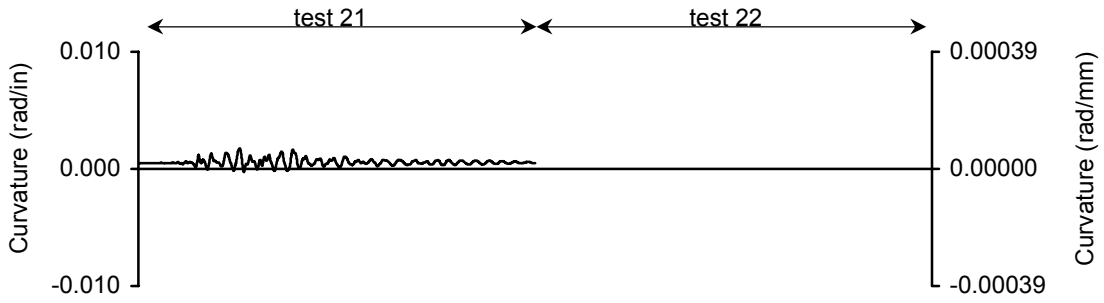

Figure 6-190: Curvature history for bent 3 bottom east column, long. direction at 2.5 in (64mm) from fixity, during post tests.

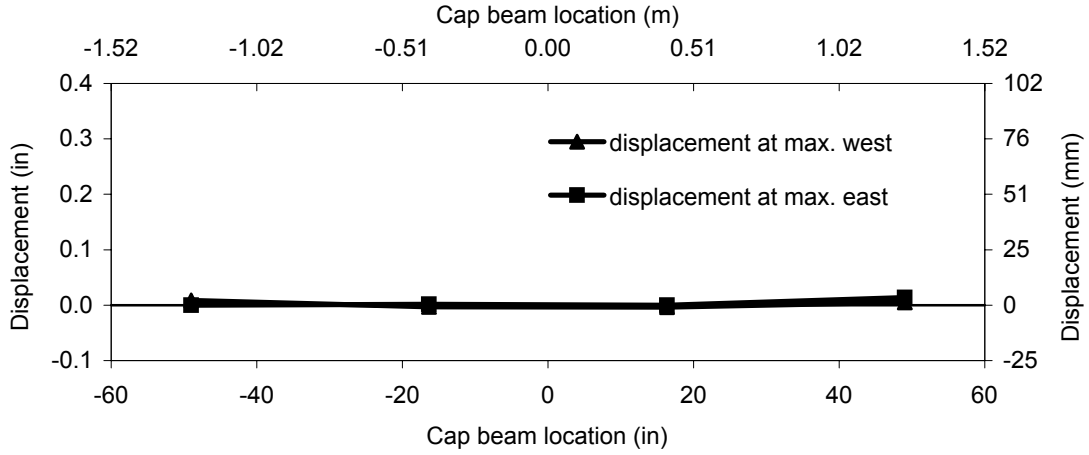

Figure 6-191: Plots of vertical bent displacements of bent 1 for test 12.

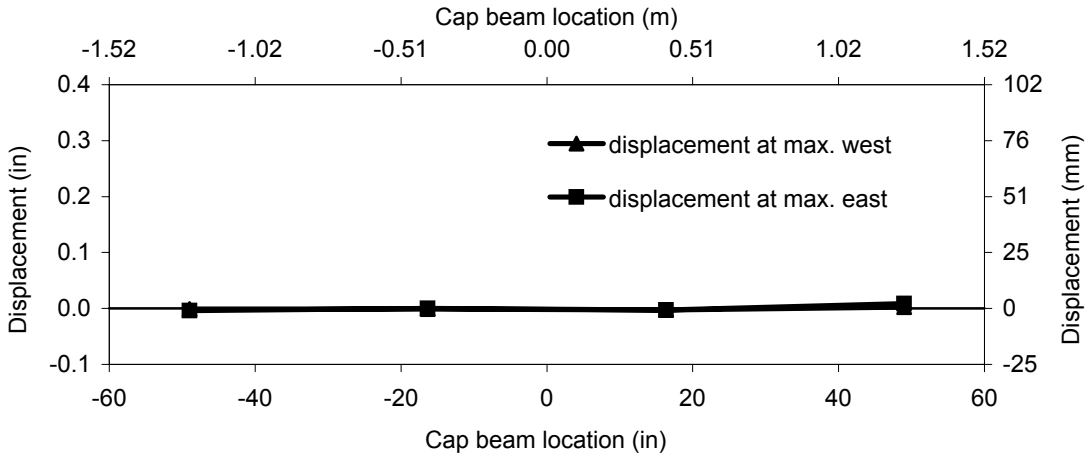

Figure 6-192: Plots of vertical bent displacements of bent 2 for test 12.

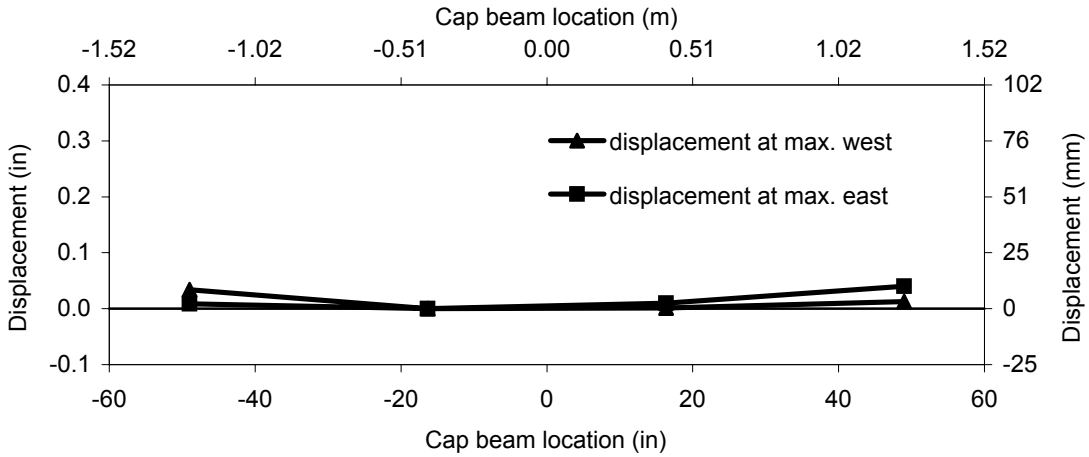

Figure 6-193: Plots of vertical bent displacements of bent 3 for test 12.

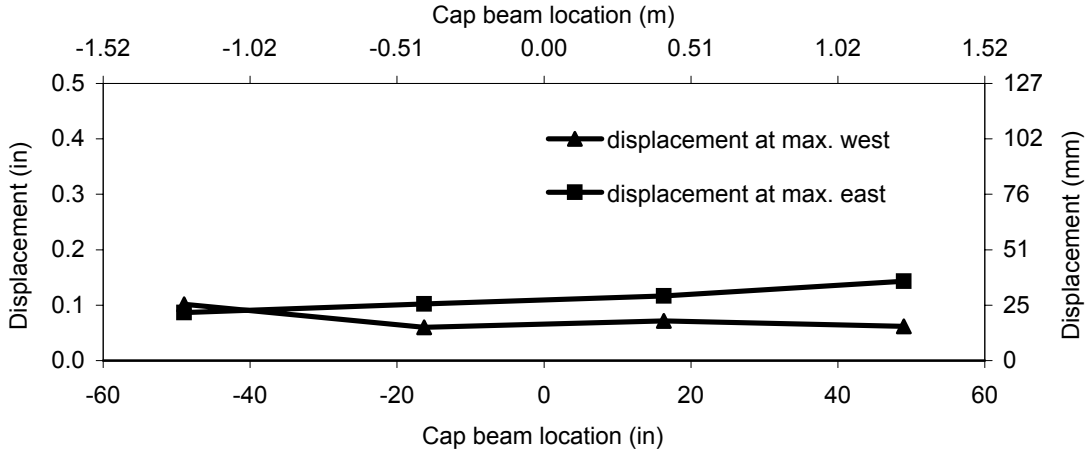

Figure 6-194: Plots of vertical bent displacements of bent 1 for test 15.

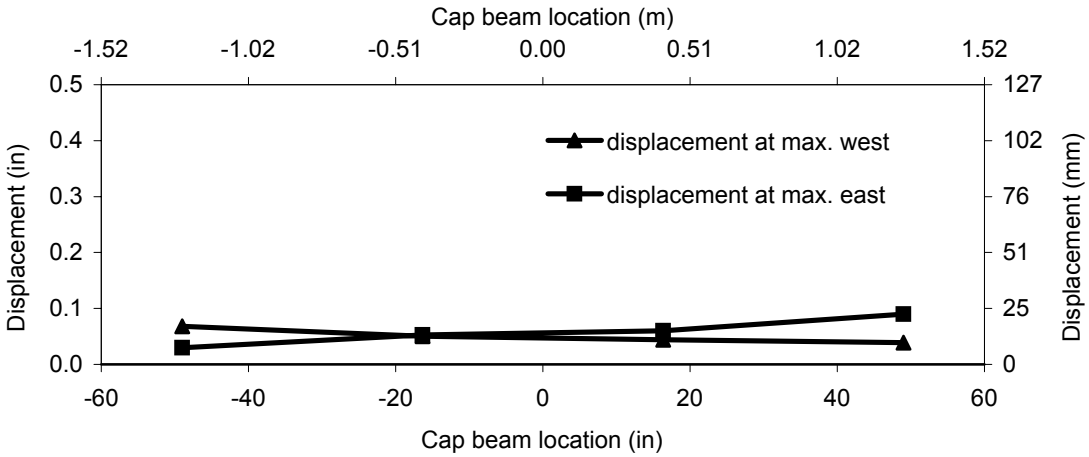

Figure 6-195: Plots of vertical bent displacements of bent 2 for test 15.

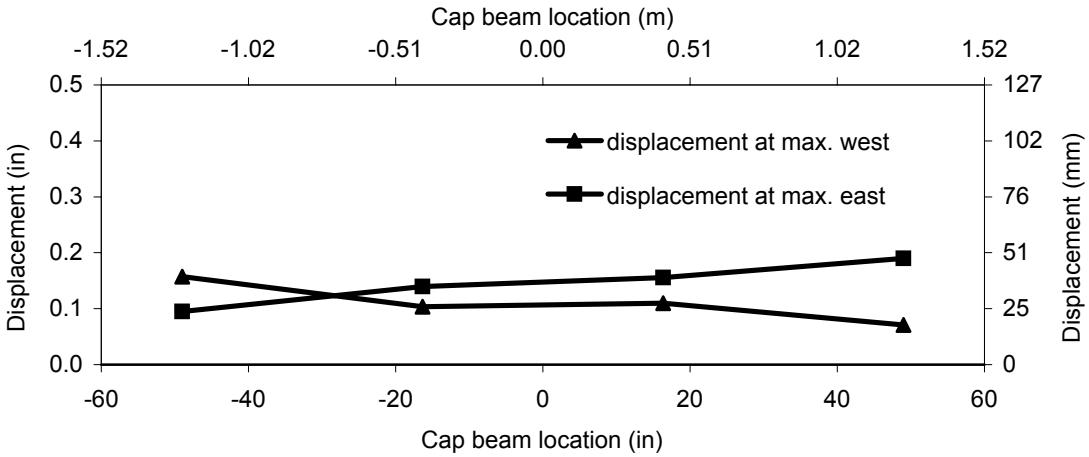

Figure 6-196: Plots of vertical bent displacements of bent 3 for test 15.

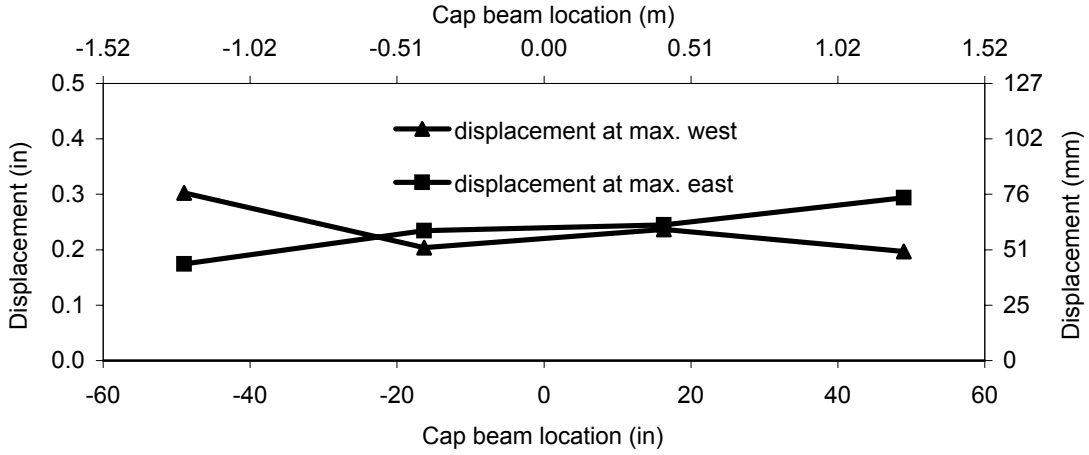

Figure 6-197: Plots of vertical bent displacements of bent 1 for test 19.

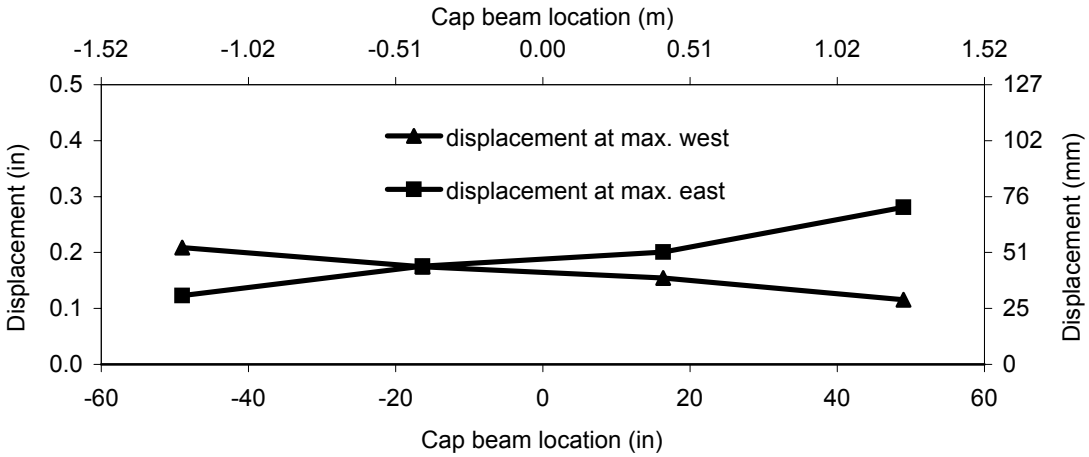

Figure 6-198: Plots of vertical bent displacements of bent 2 for test 19.

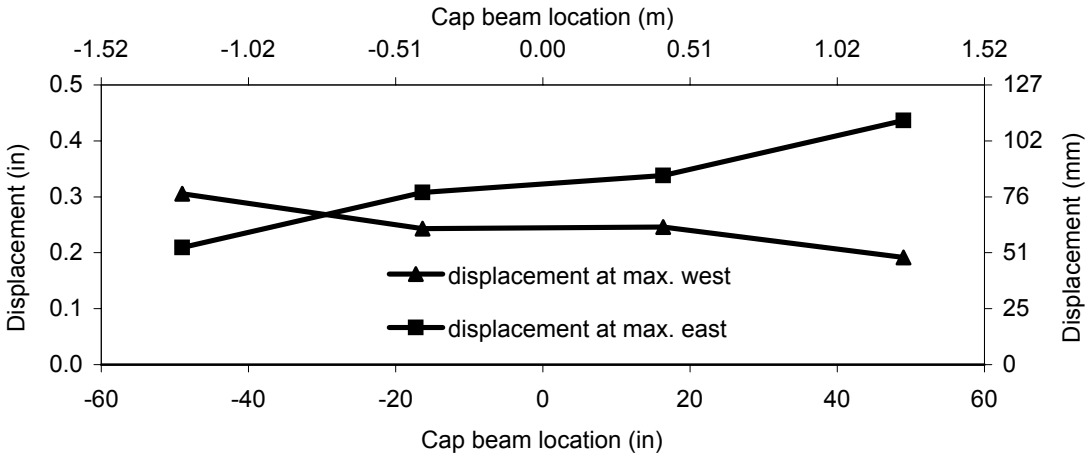

Figure 6-199: Plots of vertical bent displacements of bent 3 for test 19.

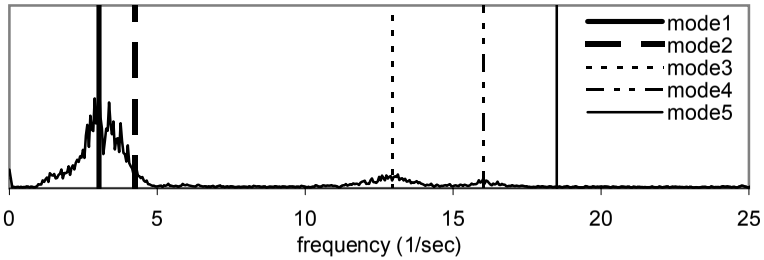

Figure 6-200: FFT plot for bent 1 transverse acceleration during WN0001

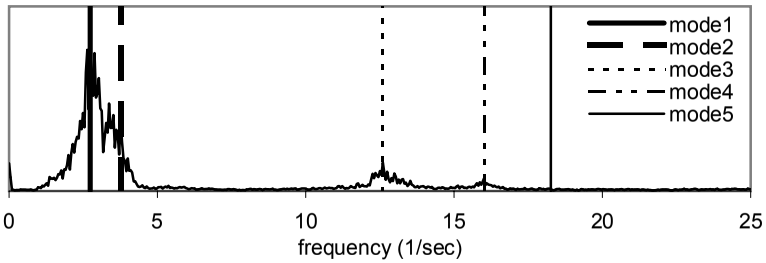

Figure 6-201: FFT plot for bent 1 transverse acceleration during WN0304

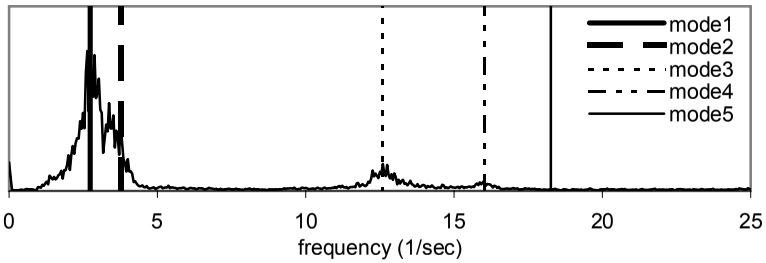

Figure 6-202: FFT plot for bent 1 transverse acceleration during WN0809-1

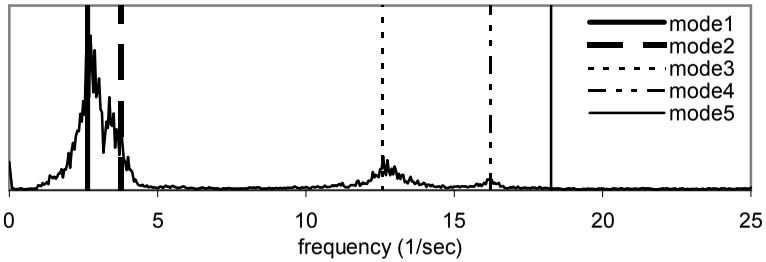

Figure 6-203: FFT plot for bent 1 transverse acceleration during WN0809-2

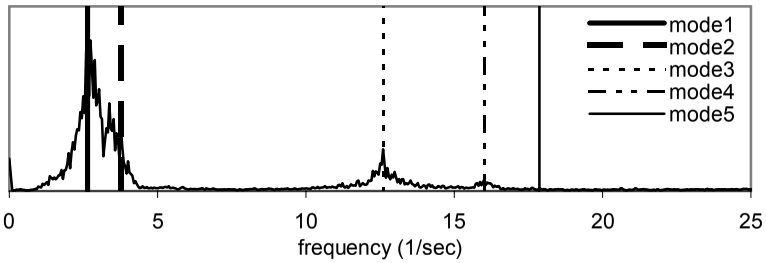

Figure 6-204: FFT plot for bent 1 transverse acceleration during WN1112-1

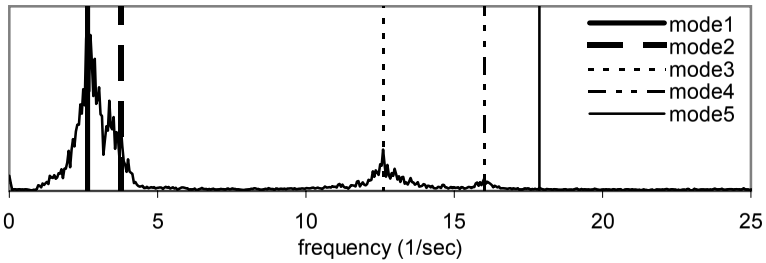

Figure 6-205: FFT plot for bent 1 transverse acceleration during WN1112-2

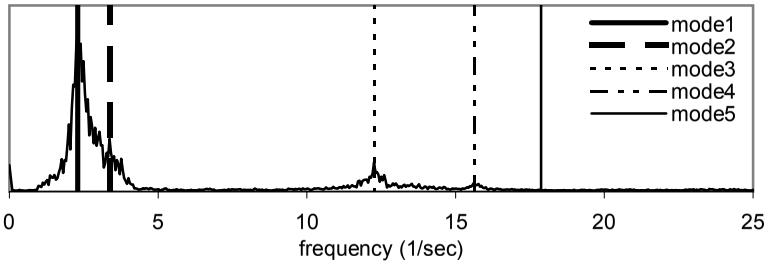

Figure 6-206: FFT plot for bent 1 transverse acceleration during WN1415

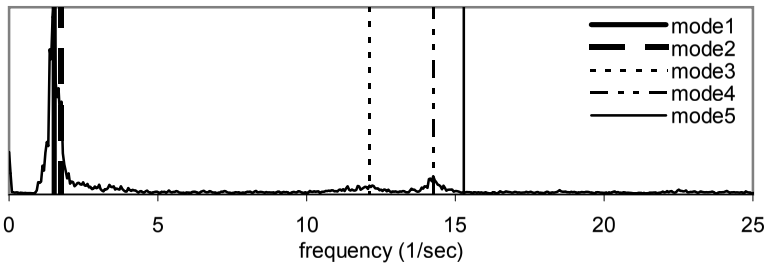

Figure 6-207: FFT plot for bent 1 transverse acceleration during WN1718

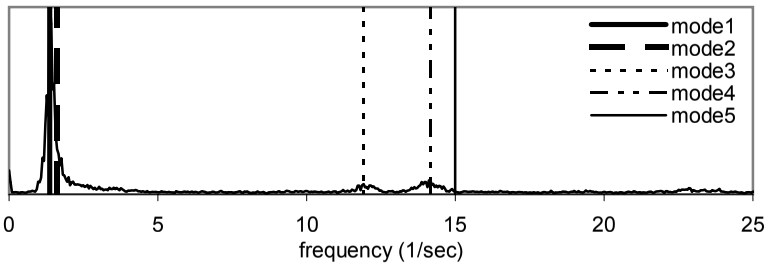

Figure 6-208: FFT plot for bent 1 transverse acceleration during WN1819

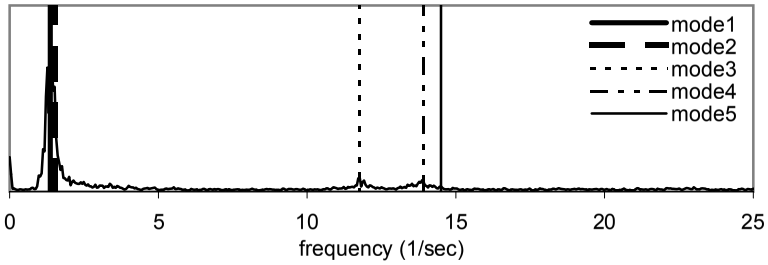

Figure 6-209: FFT plot for bent 1 transverse acceleration during WN1920

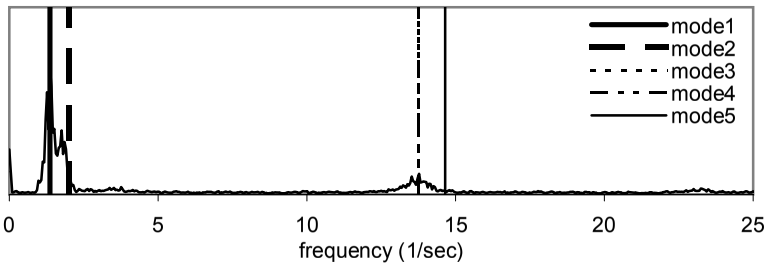

Figure 6-210: FFT plot for bent 1 transverse acceleration during WN2021

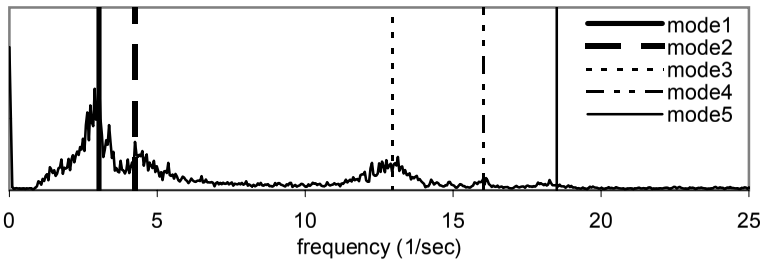

Figure 6-211: FFT plot for bent 2 transverse acceleration during WN0001

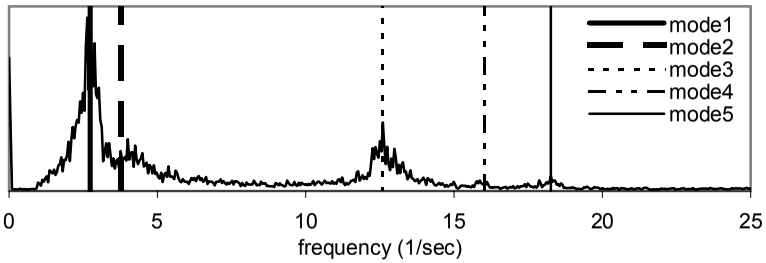

Figure 6-212: FFT plot for bent 2 transverse acceleration during WN0304

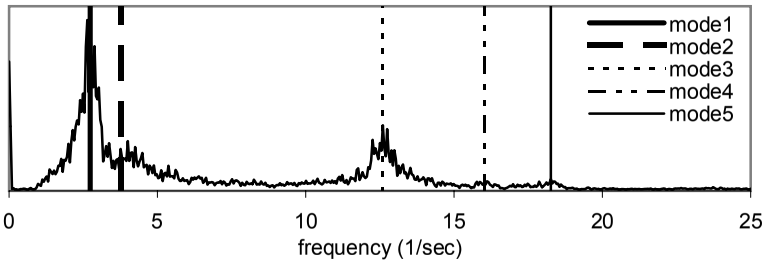

Figure 6-213: FFT plot for bent 2 transverse acceleration during WN0809-1

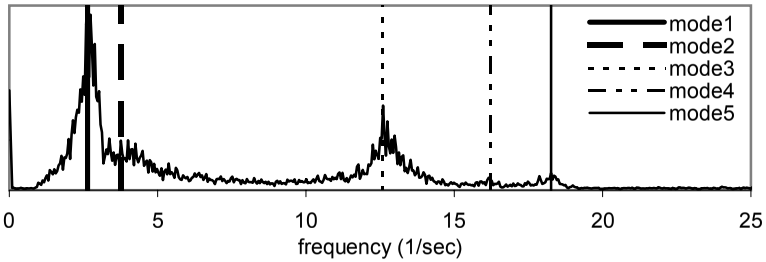

Figure 6-214: FFT plot for bent 2 transverse acceleration during WN0809-2

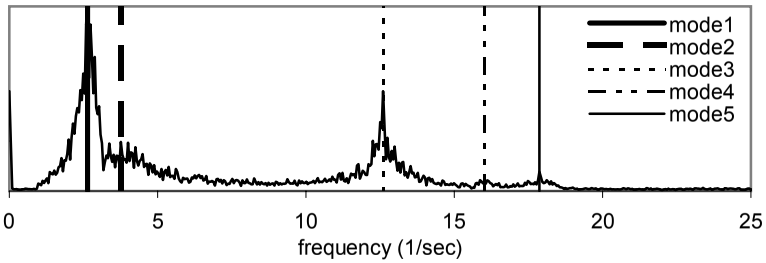

Figure 6-215: FFT plot for bent 2 transverse acceleration during WN1112-1

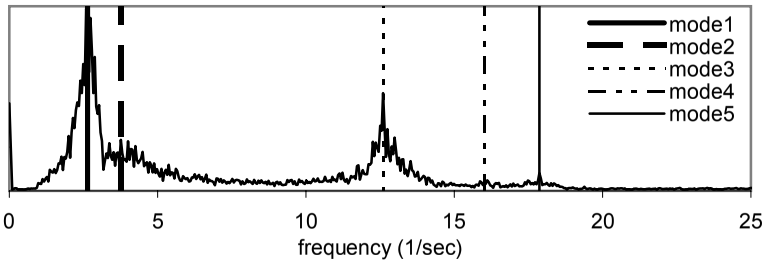

Figure 6-216: FFT plot for bent 2 transverse acceleration during WN1112-2

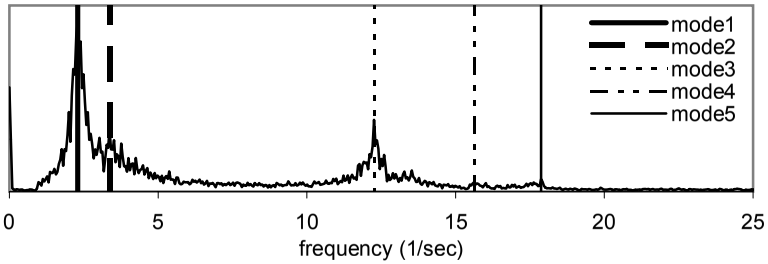

Figure 6-217: FFT plot for bent 2 transverse acceleration during WN1415

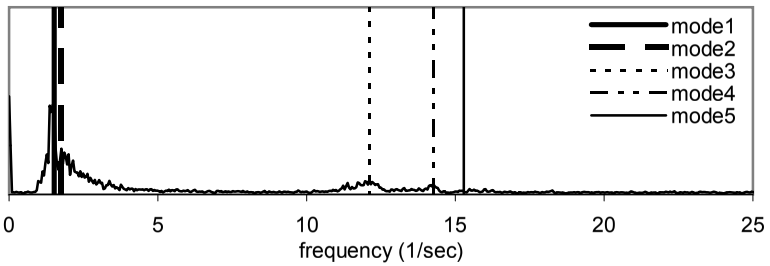

Figure 6-218: FFT plot for bent 2 transverse acceleration during WN1718

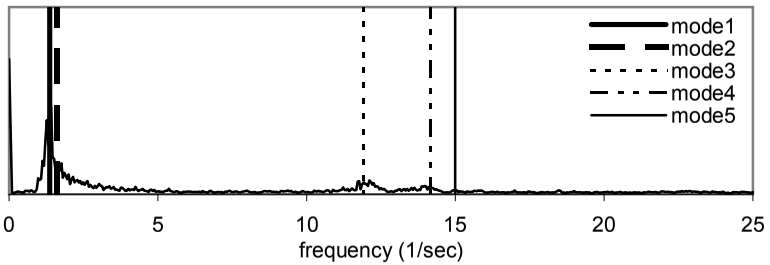

Figure 6-219: FFT plot for bent 2 transverse acceleration during WN1819

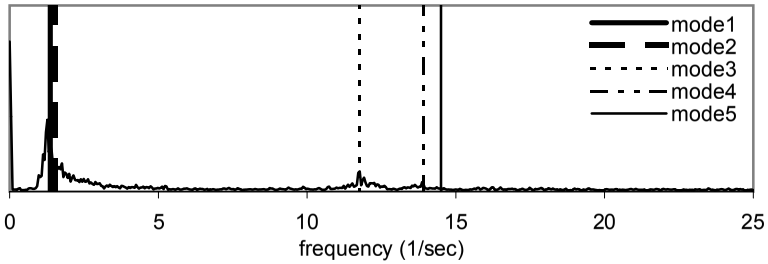

Figure 6-220: FFT plot for bent 2 transverse acceleration during WN1920

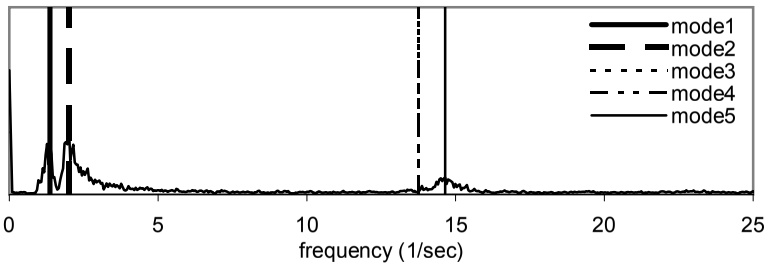

Figure 6-221: FFT plot for bent 2 transverse acceleration during WN2021

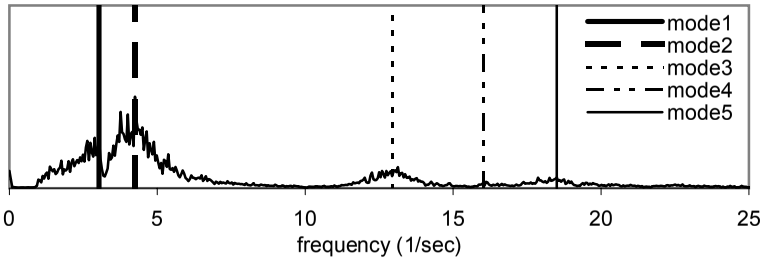

Figure 6-222: FFT plot for bent 3 transverse acceleration during WN0001

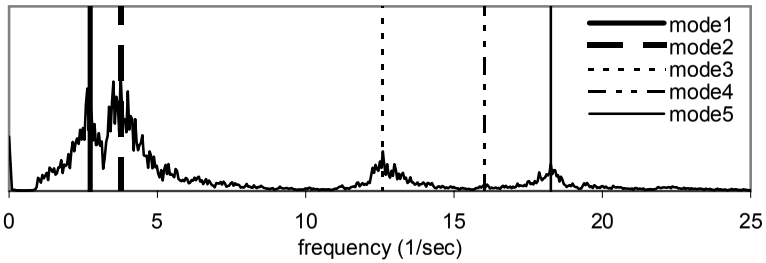

Figure 6-223: FFT plot for bent 3 transverse acceleration during WN0304

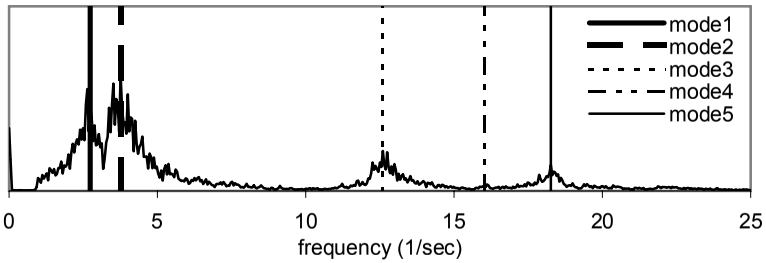

Figure 6-224: FFT plot for bent 3 transverse acceleration during WN0809-1

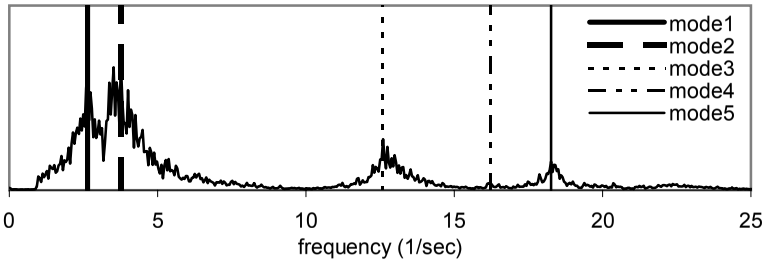

Figure 6-225: FFT plot for bent 3 transverse acceleration during WN0809-2

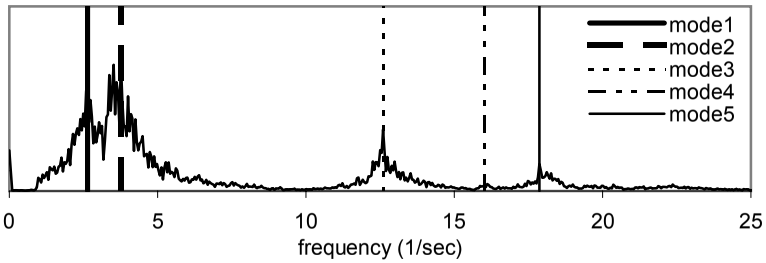

Figure 6-226: FFT plot for bent 3 transverse acceleration during WN1112-1

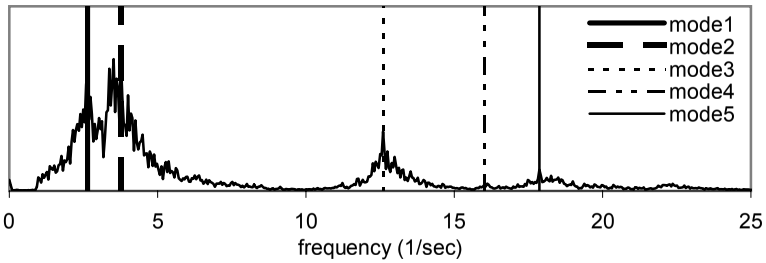

Figure 6-227: FFT plot for bent 3 transverse acceleration during WN1112-2

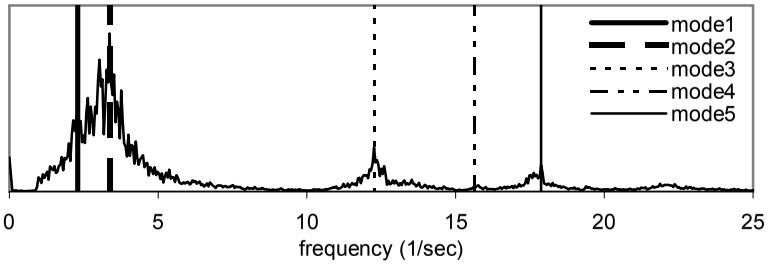

Figure 6-228: FFT plot for bent 3 transverse acceleration during WN1415

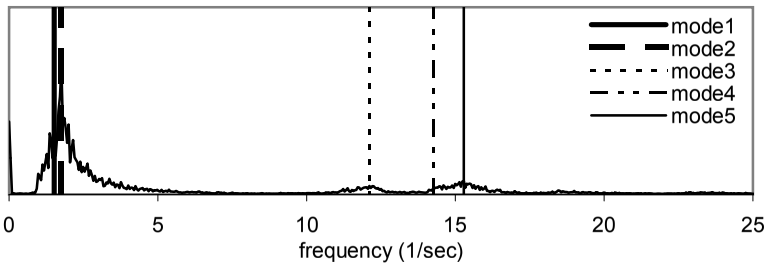

Figure 6-229: FFT plot for bent 3 transverse acceleration during WN1718

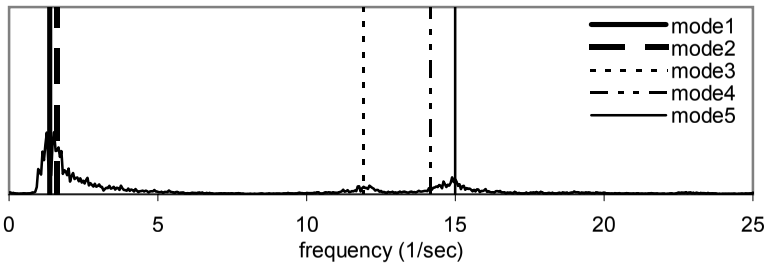

Figure 6-230: FFT plot for bent 3 transverse acceleration during WN1819

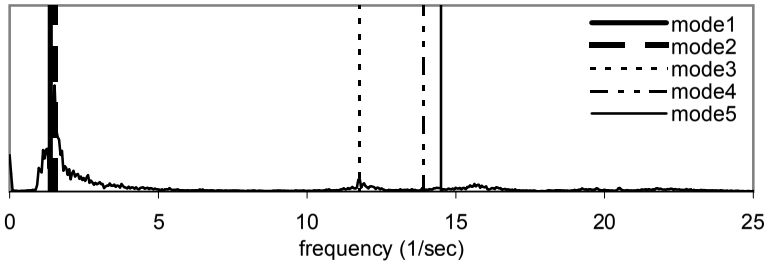

Figure 6-231: FFT plot for bent 3 transverse acceleration during WN1920

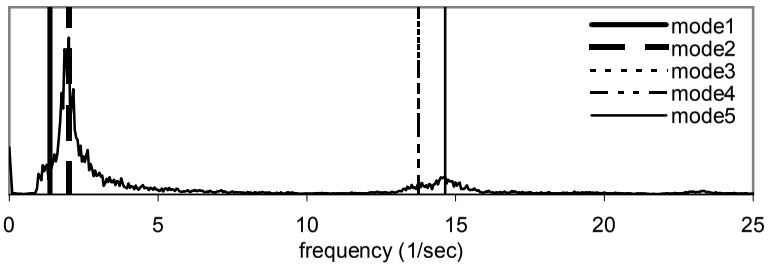

Figure 6-232: FFT plot for bent 3 transverse acceleration during WN2021

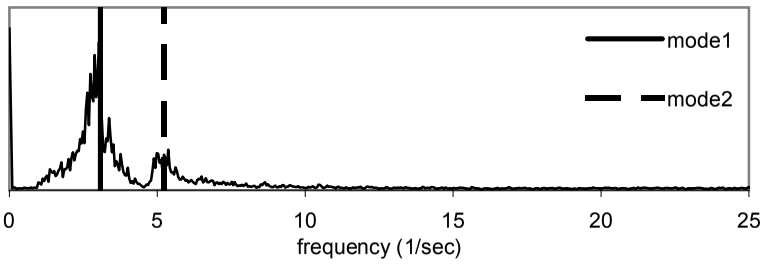

Figure 6-233: FFT plot for superstructure longitudinal acceleration during WN0001

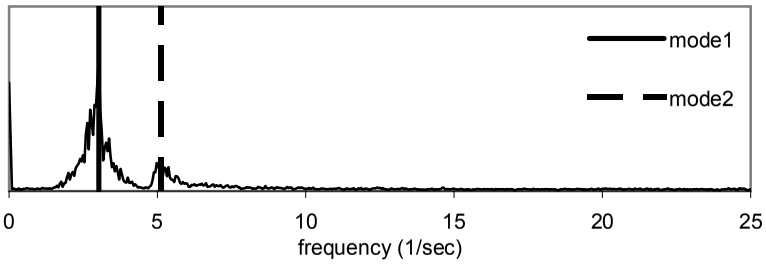

Figure 6-234: FFT plot for superstructure longitudinal acceleration during WN0304

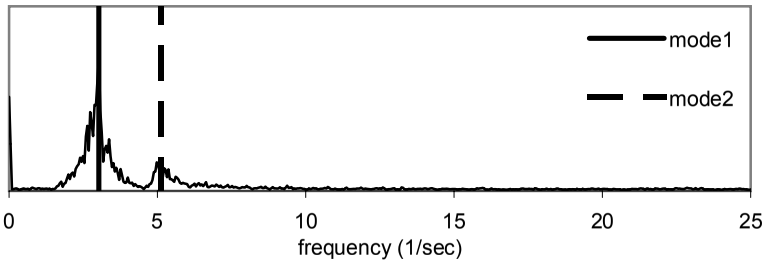

Figure 6-235: FFT plot for superstructure longitudinal acceleration during WN0809-1

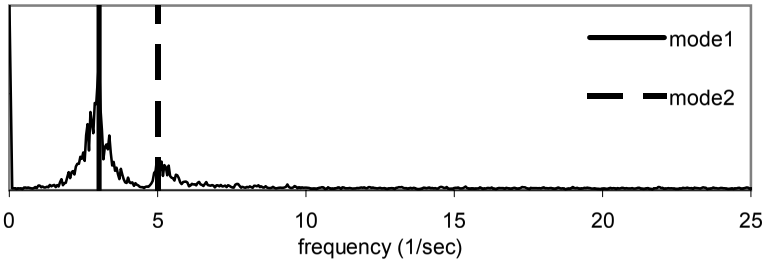

Figure 6-236: FFT plot for superstructure longitudinal acceleration during WN0809-2

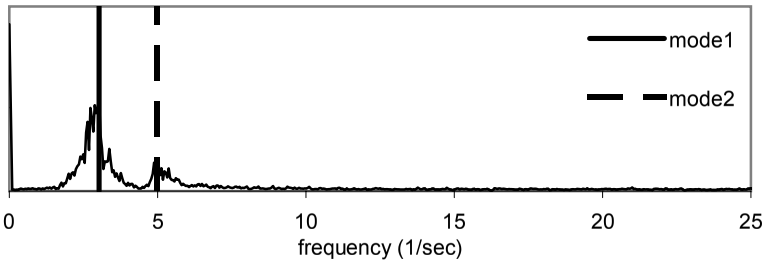

Figure 6-237: FFT plot for superstructure longitudinal acceleration during WN1112-1

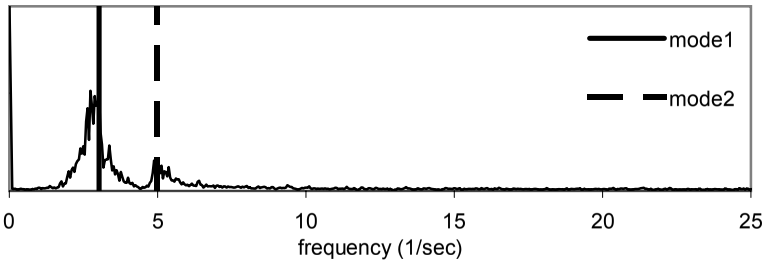

Figure 6-238: FFT plot for superstructure longitudinal acceleration during WN1112-2

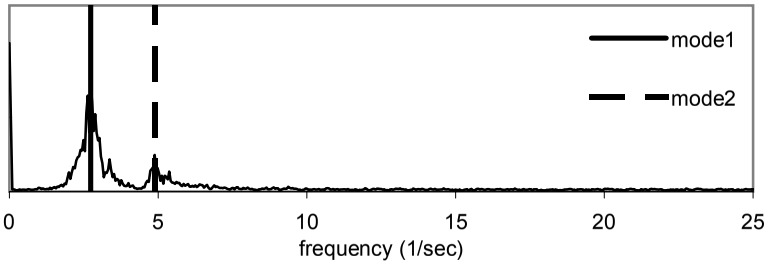

Figure 6-239: FFT plot for superstructure longitudinal acceleration during WN1415

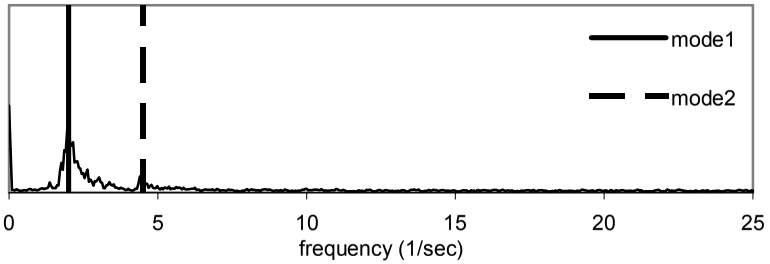

Figure 6-240: FFT plot for superstructure longitudinal acceleration during WN1718

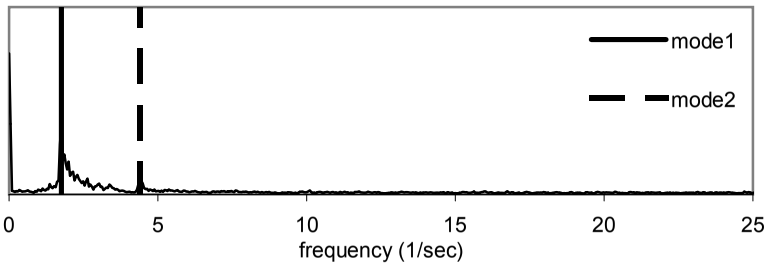

Figure 6-241: FFT plot for superstructure longitudinal acceleration during WN1819

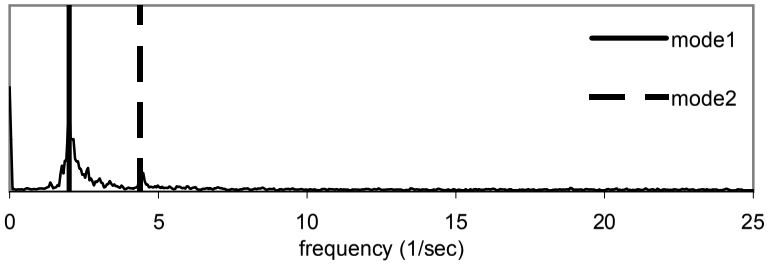

Figure 6-242: FFT plot for superstructure longitudinal acceleration during WN1920

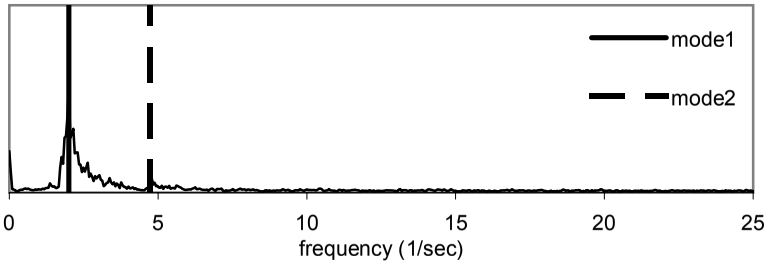

Figure 6-243: FFT plot for superstructure longitudinal acceleration during WN2021

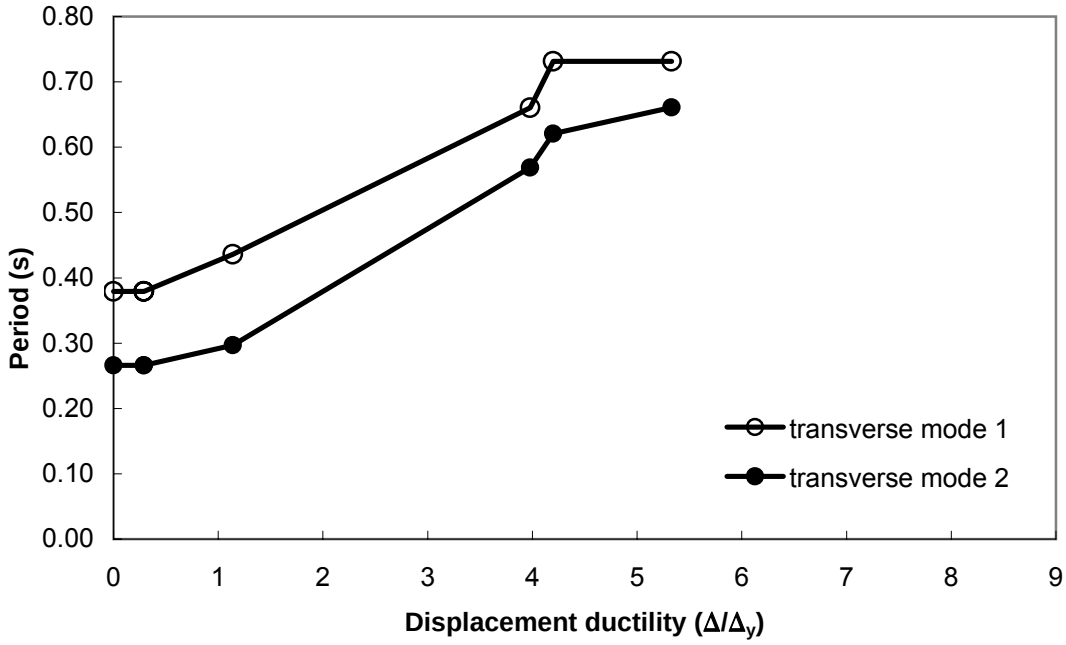

Figure 6-244: Period from FFT vs. achieved bent 1 displacement ductility for transverse modes 1 and 2.

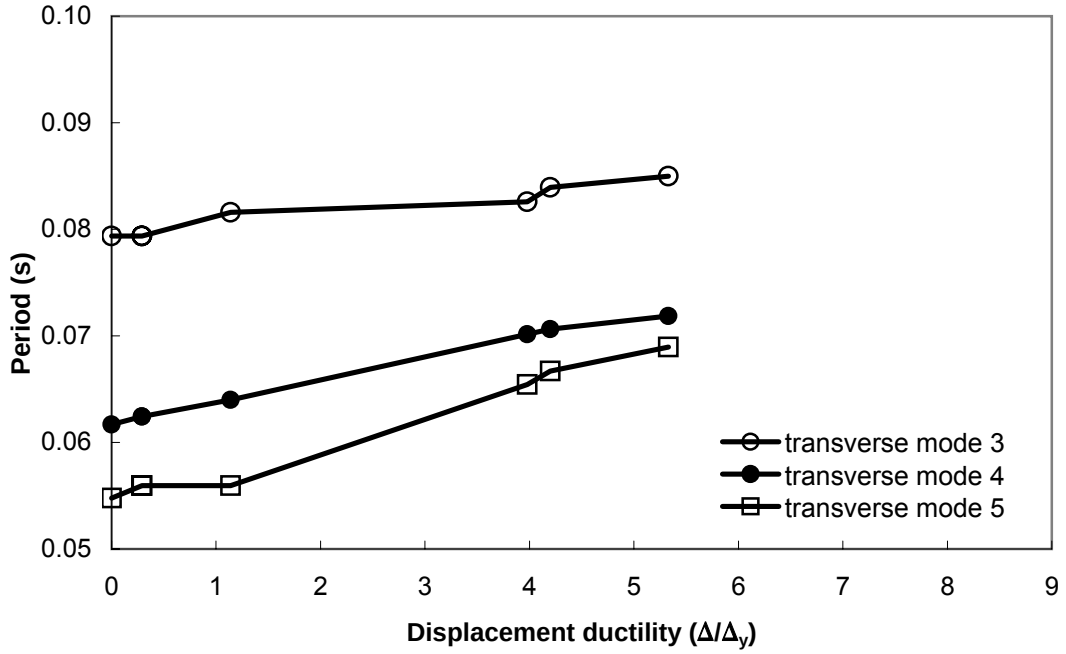

Figure 6-245: Period from FFT vs. achieved bent 1 displacement ductility for transverse modes 3 through 5.

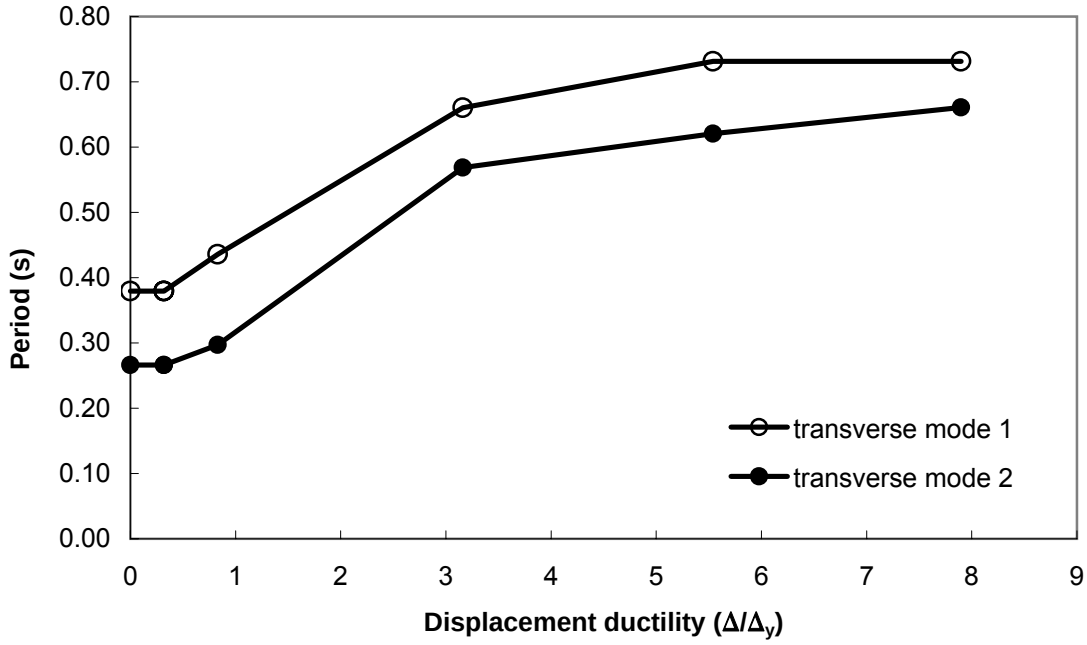

Figure 6-246: Period from FFT vs. achieved bent 3 displacement ductility for transverse modes 1 and 2.

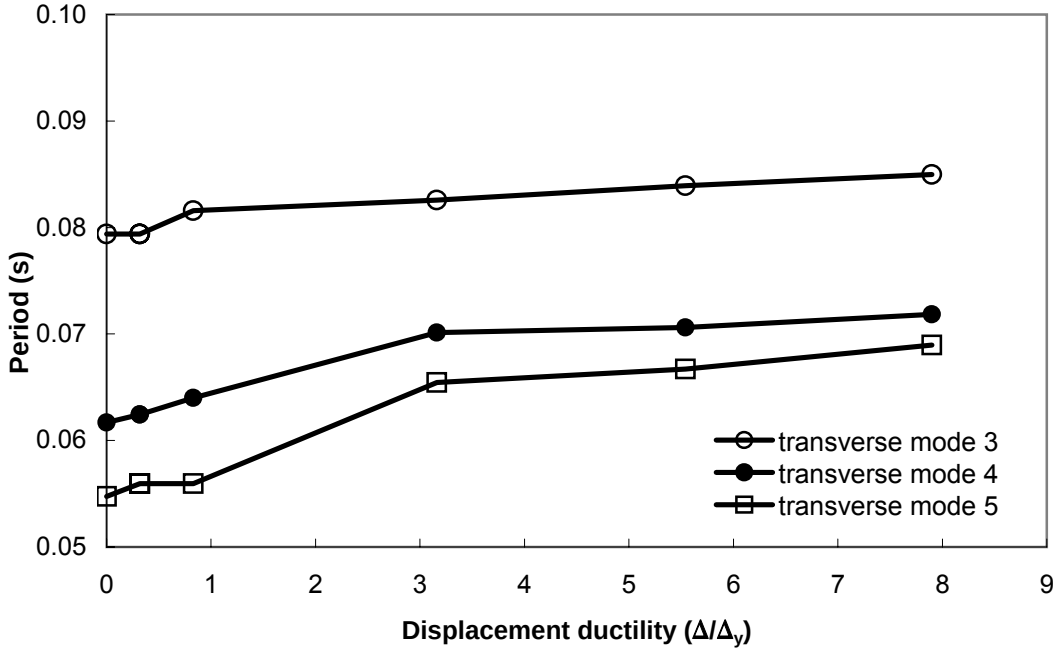

Figure 6-247: Period from FFT vs. achieved bent 3 displacement ductility for transverse modes 3 through 5.

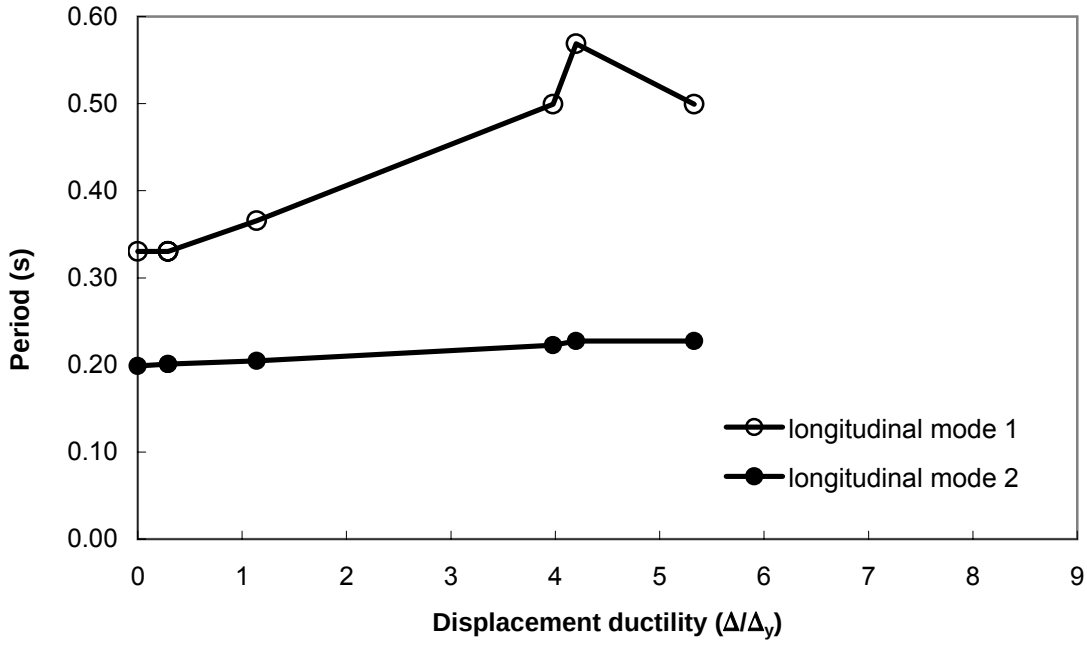

Figure 6-248: Period from FFT vs. achieved bent 1 displacement ductility for longitudinal modes 1 and 2.

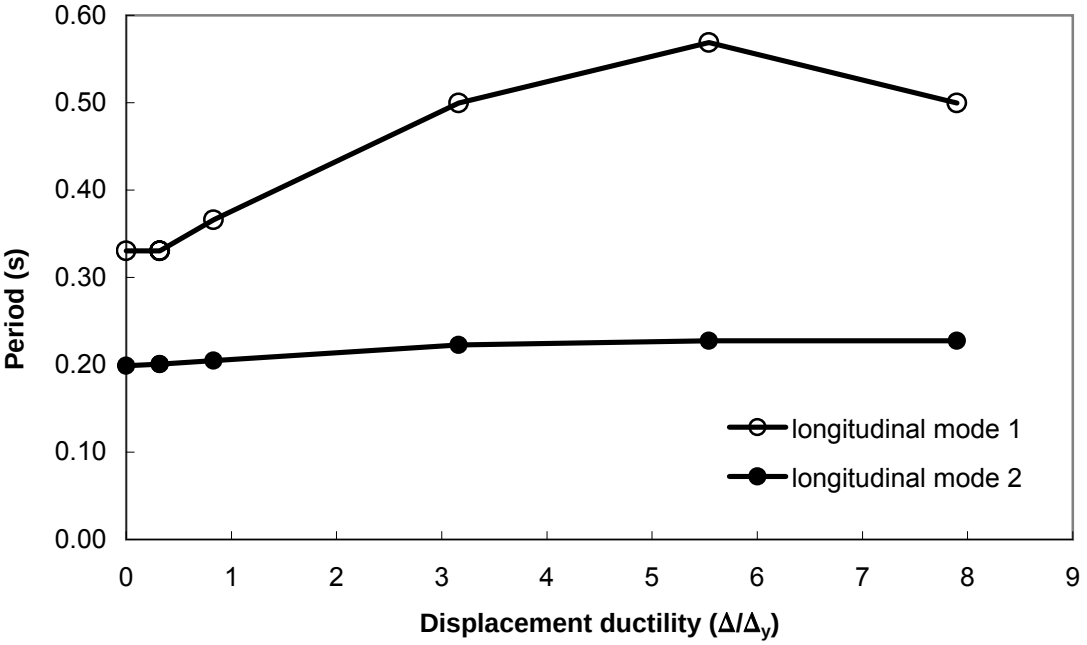

Figure 6-249: Period from FFT vs. achieved bent 3 displacement ductility for longitudinal modes 1 and 2.

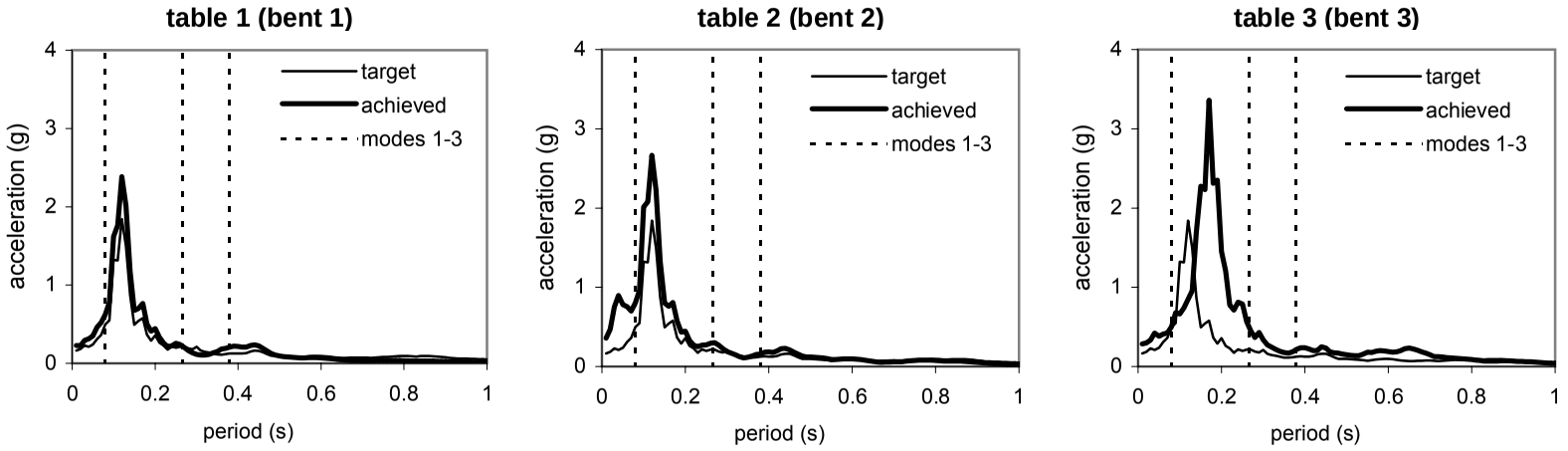

Figure 6-250: Target vs achieved response spectrum (2% damping) plots for test 1b tables 1-3 with superimposed measured transverse modes 1-3 from free vibration after test 3b

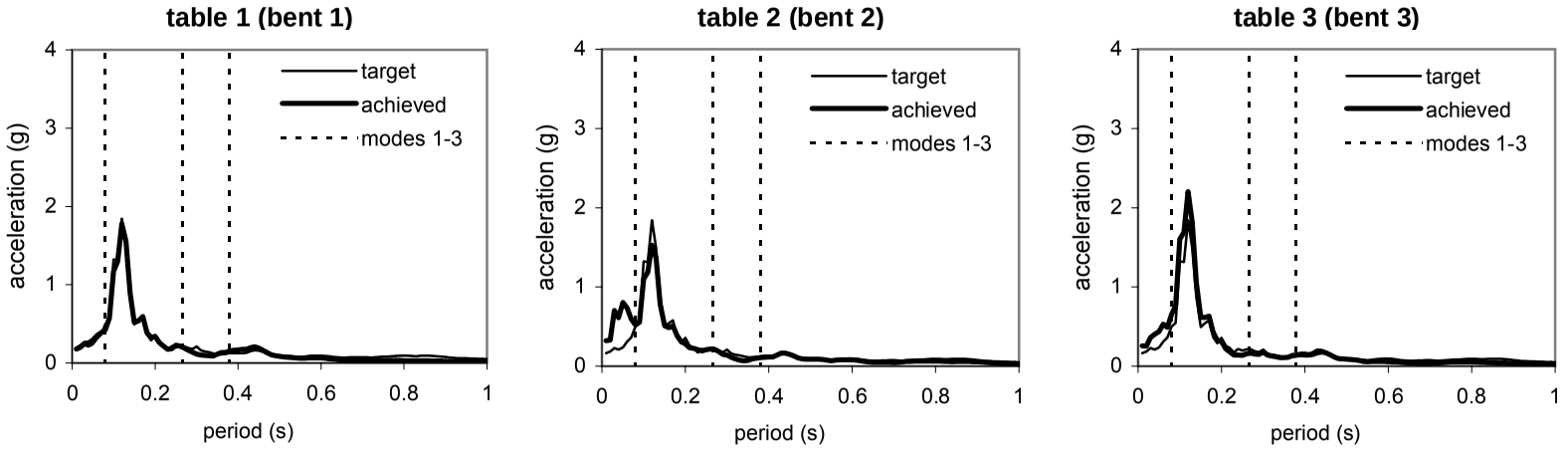

Figure 6-251: Target vs achieved response spectrum (2% damping) plots for test 8 tables 1-3 with superimposed measured transverse modes 1-3 from free vibration after test 3b.

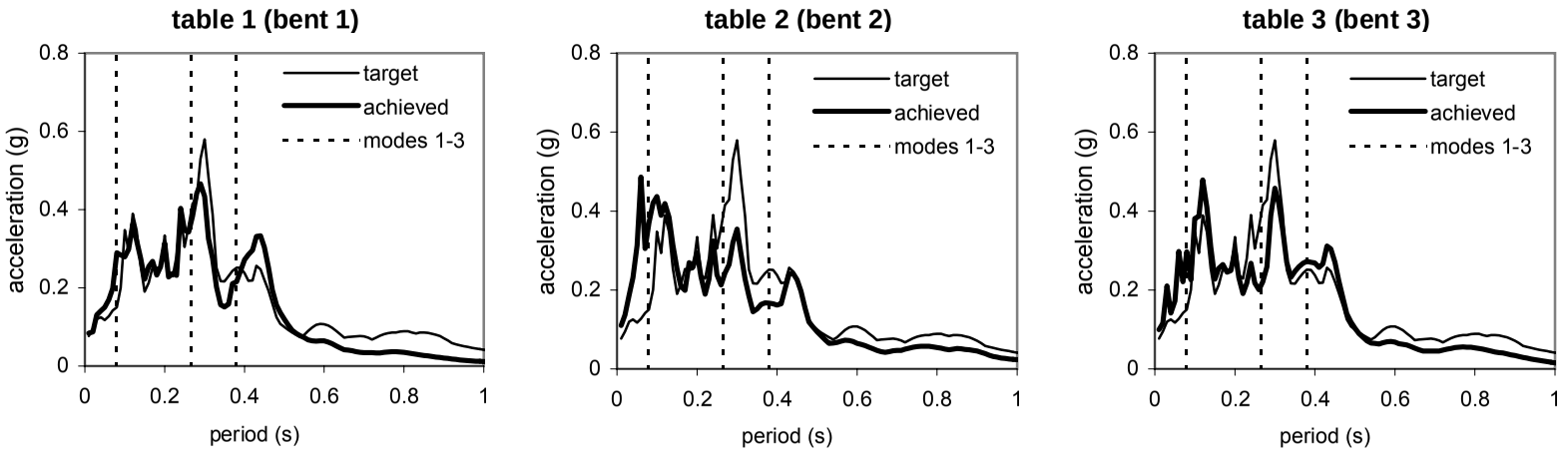

Figure 6-252: Target vs achieved response spectrum (2% damping) plots for test 12 tables 1-3 with superimposed measured transverse modes 1-3 from free vibration after test 11.

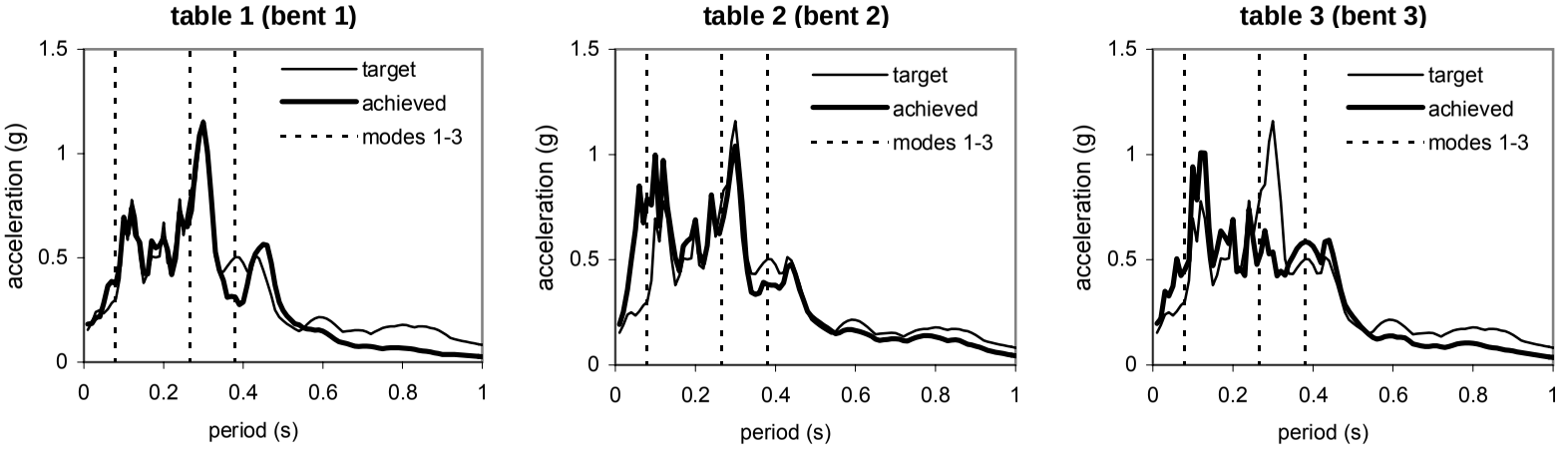

Figure 6-253: Target vs achieved response spectrum (2% damping) plots for test 13 tables 1-3 with superimposed measured transverse modes 1-3 from free vibration after test 11.

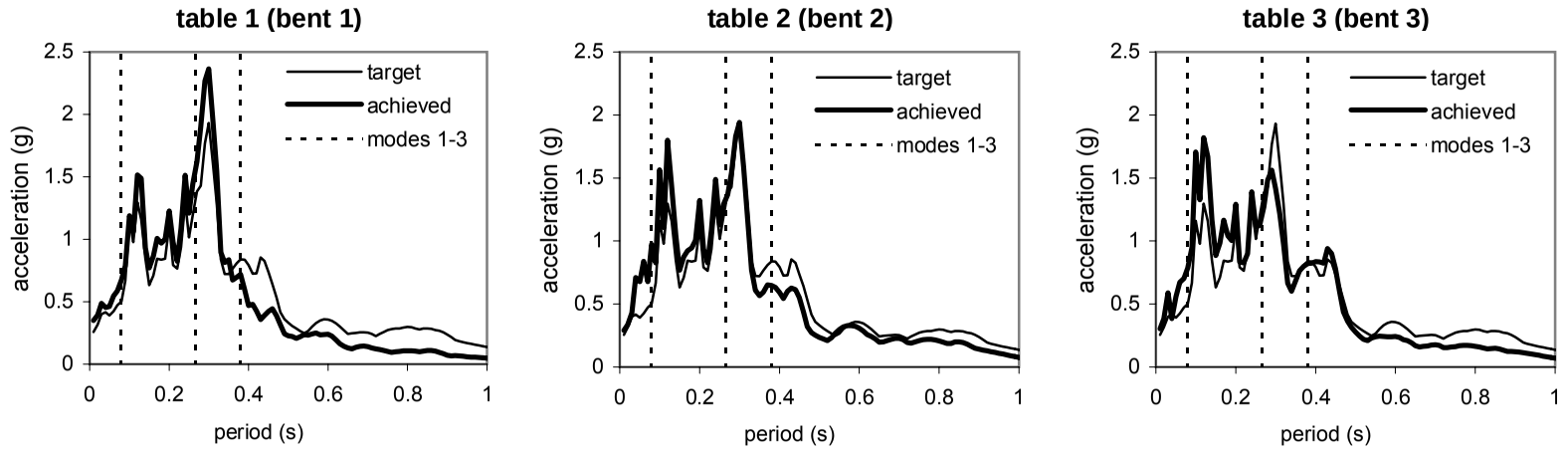

Figure 6-254: Target vs achieved response spectrum (2% damping) plots for test 14 tables 1-3 with superimposed measured transverse modes 1-3 from free vibration after test 11.

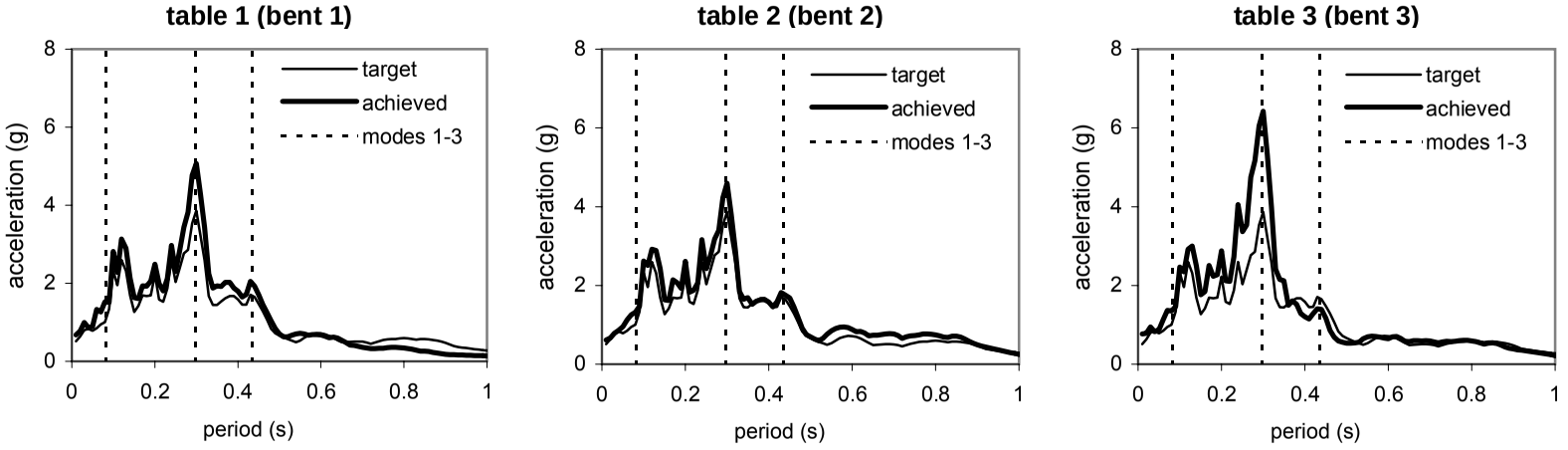

Figure 6-255: Target vs achieved response spectrum (2% damping) plots for test 15 tables 1-3 with superimposed measured transverse modes 1-3 from free vibration after test 14.

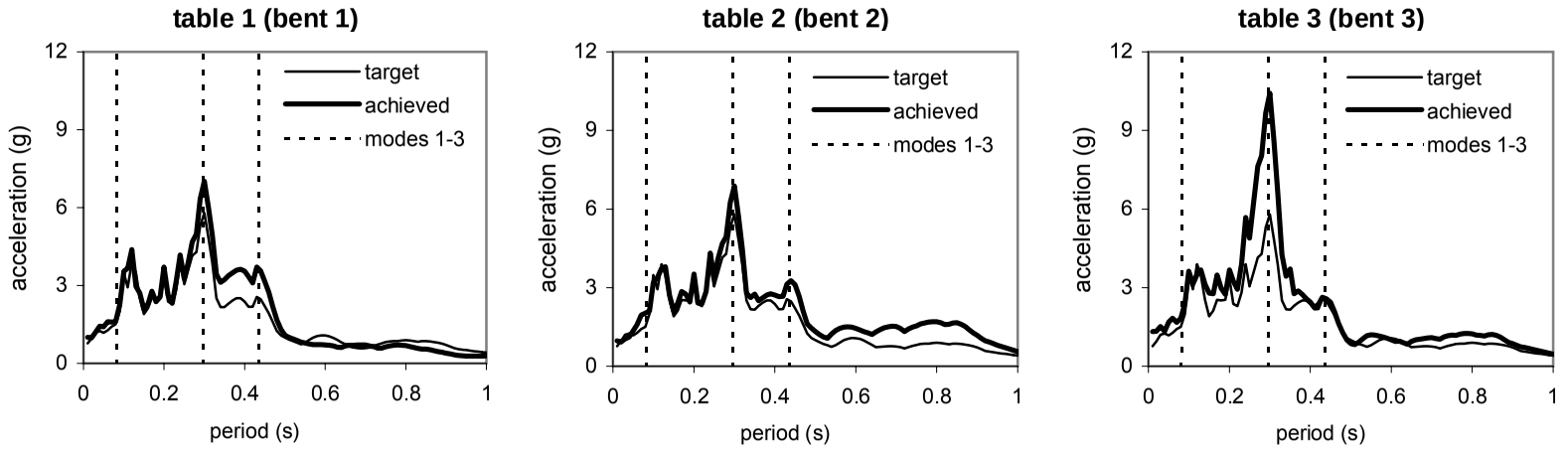

Figure 6-256: Target vs achieved response spectrum (2% damping) plots for test 16 tables 1-3 with superimposed measured transverse modes 1-3 from free vibration after test 14.

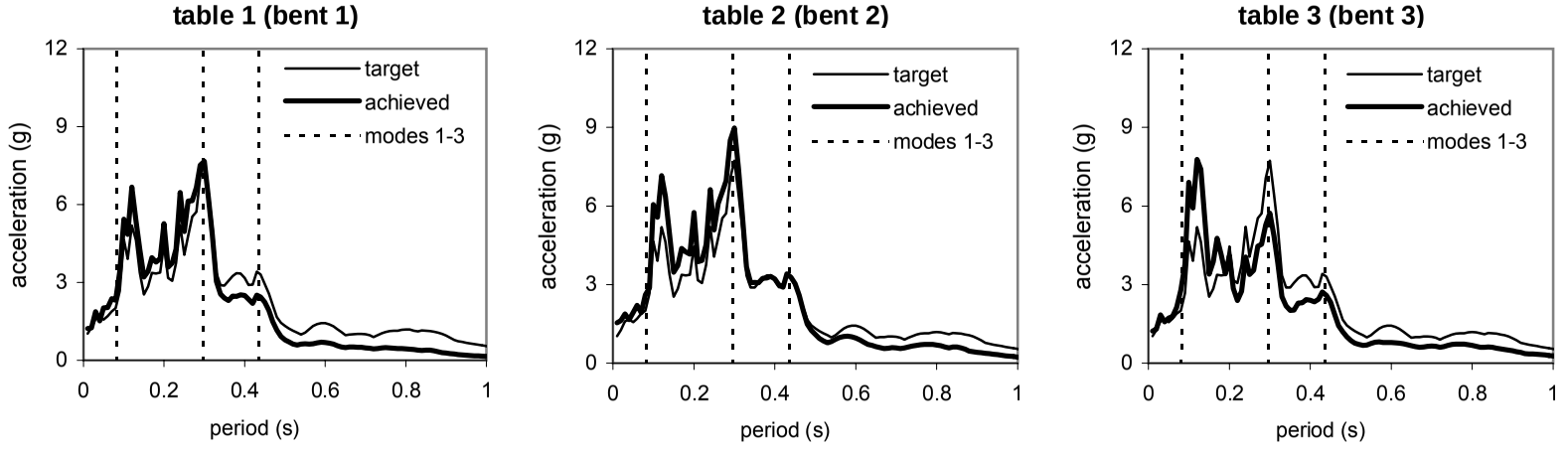

Figure 6-257: Target vs achieved response spectrum (2% damping) plots for test 17 tables 1-3 with superimposed measured transverse modes 1-3 from free vibration after test 14.

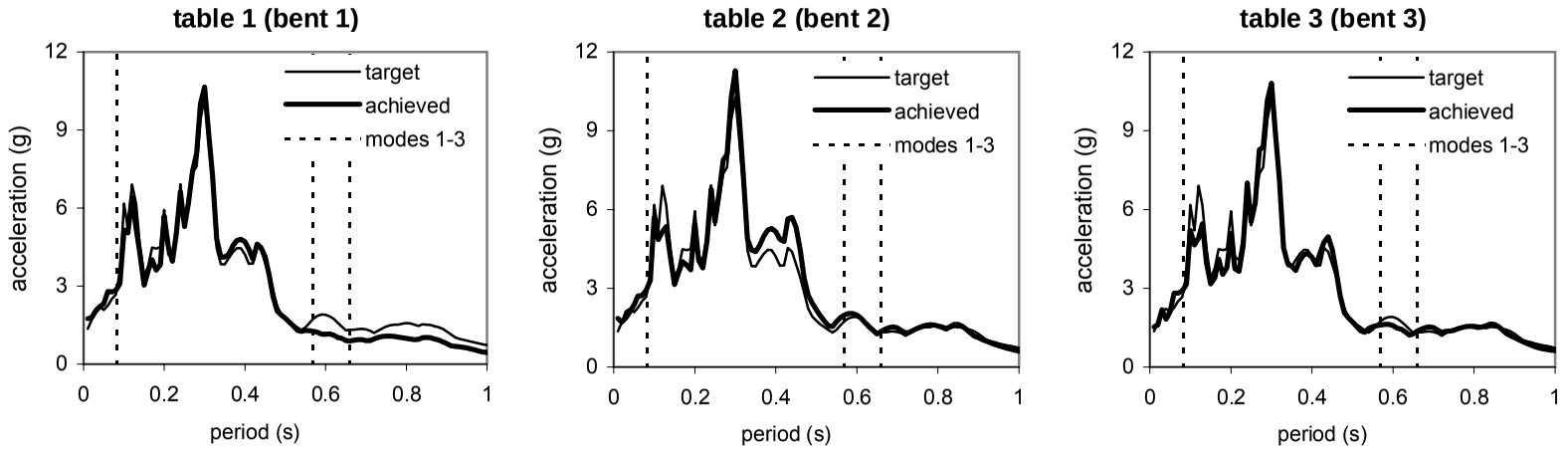

Figure 6-258: Target vs achieved response spectrum (2% damping) plots for test 18 tables 1-3 with superimposed measured transverse modes 1-3 from free vibration after test 17.

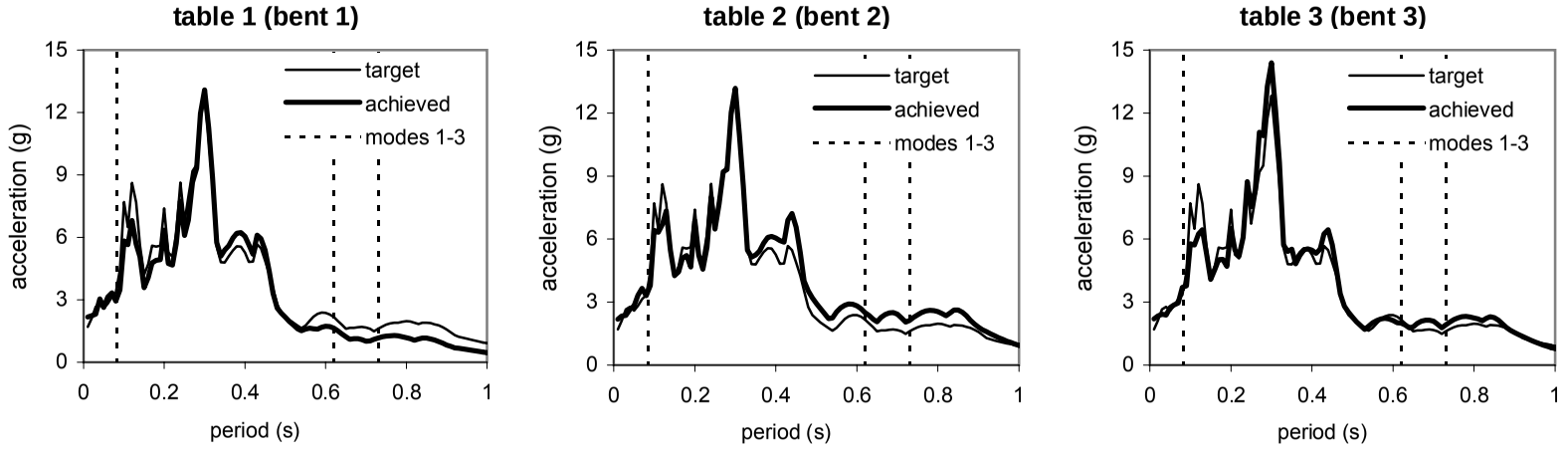

Figure 6-259: Target vs achieved response spectrum (2% damping) plots for test 19 tables 1-3 with superimposed measured transverse modes 1-3 from free vibration after test 18.

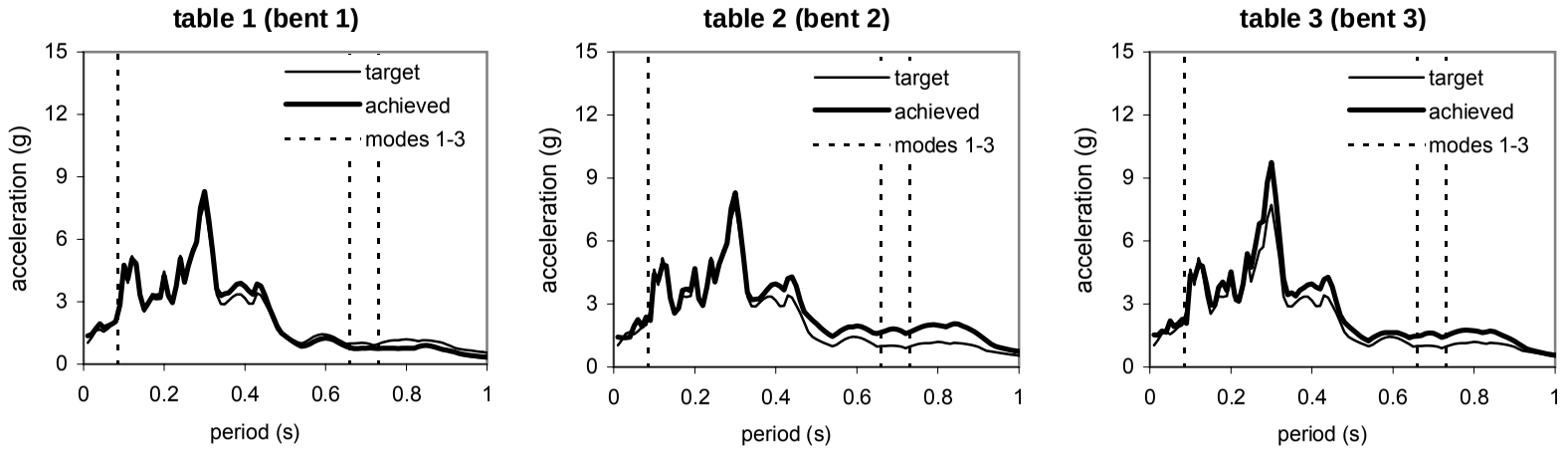

Figure 6-260: Target vs achieved response spectrum (2% damping) plots for test 20 tables 1-3 with superimposed measured transverse modes 1-3 from free vibration after test 19.

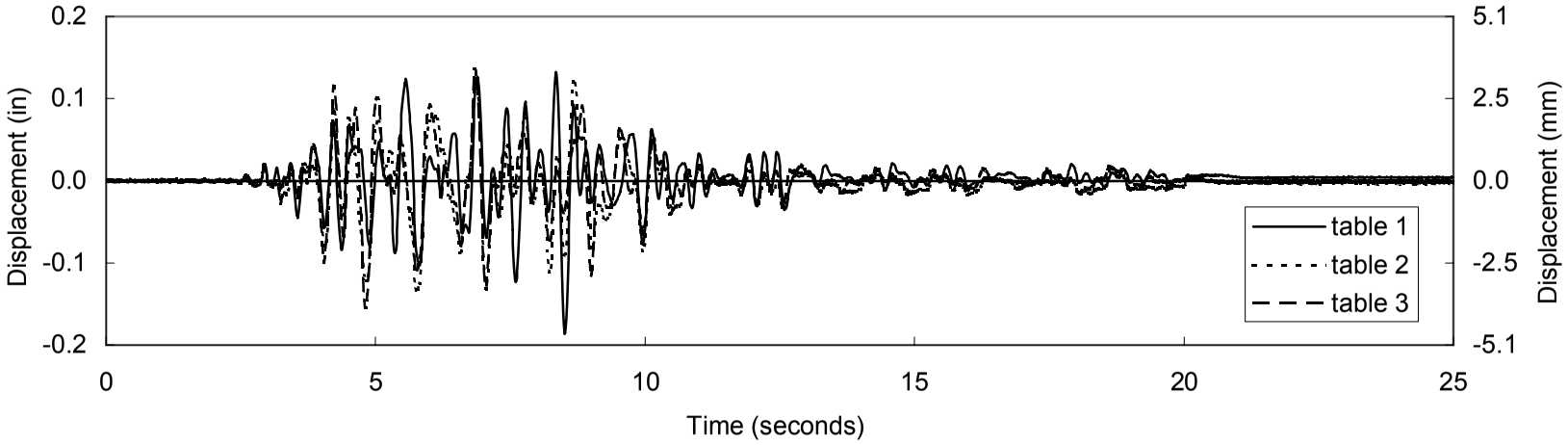

Figure 6-261: Achieved transverse table displacement history comparison for test 13.

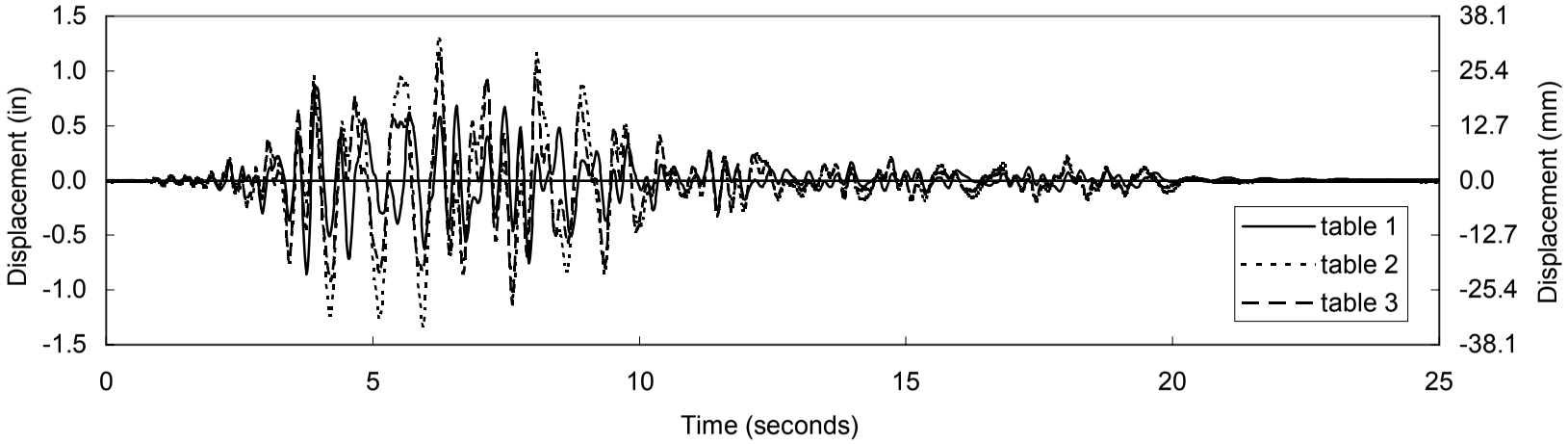

Figure 6-262: Achieved transverse table displacement history comparison for test 16.

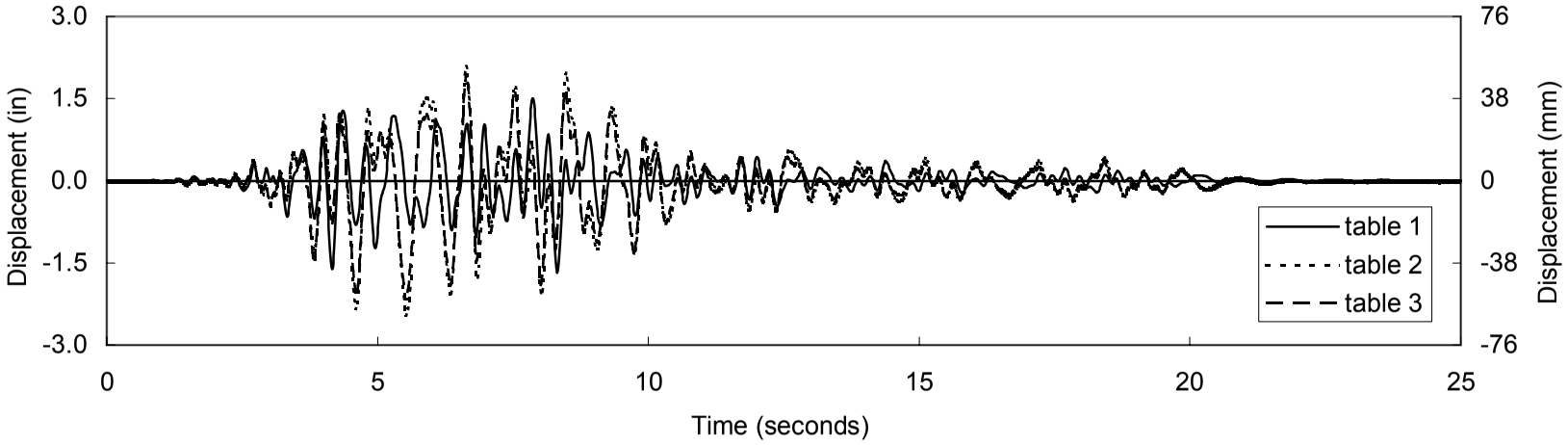

Figure 6-263: Achieved transverse table displacement history comparison for test 19.

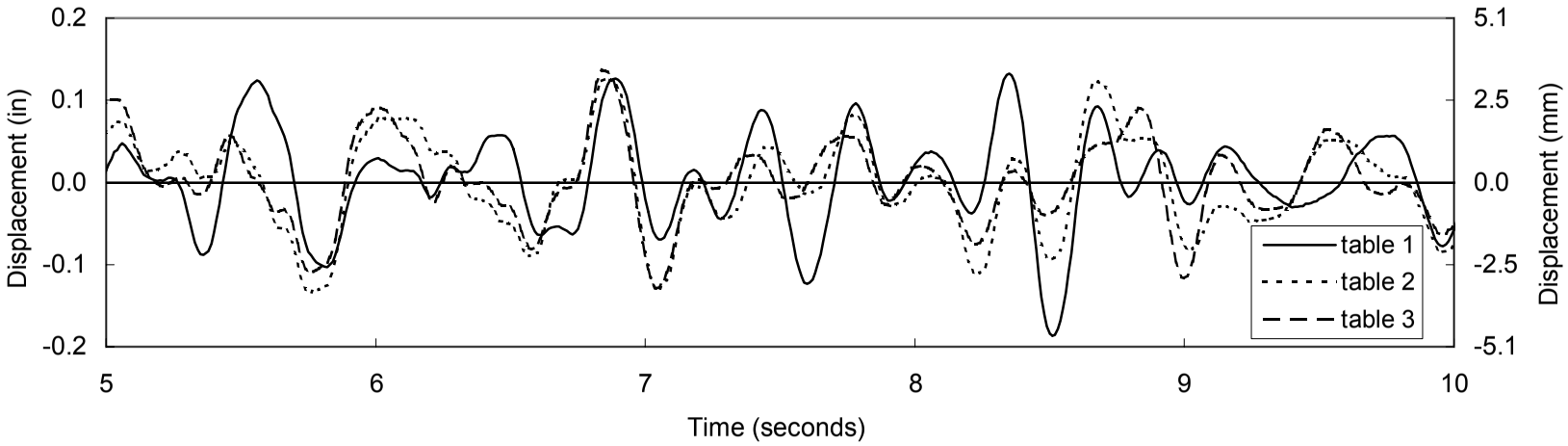

Figure 6-264: Achieved transverse table displacement history comparison for test 13 (t=5 to t=10 seconds).

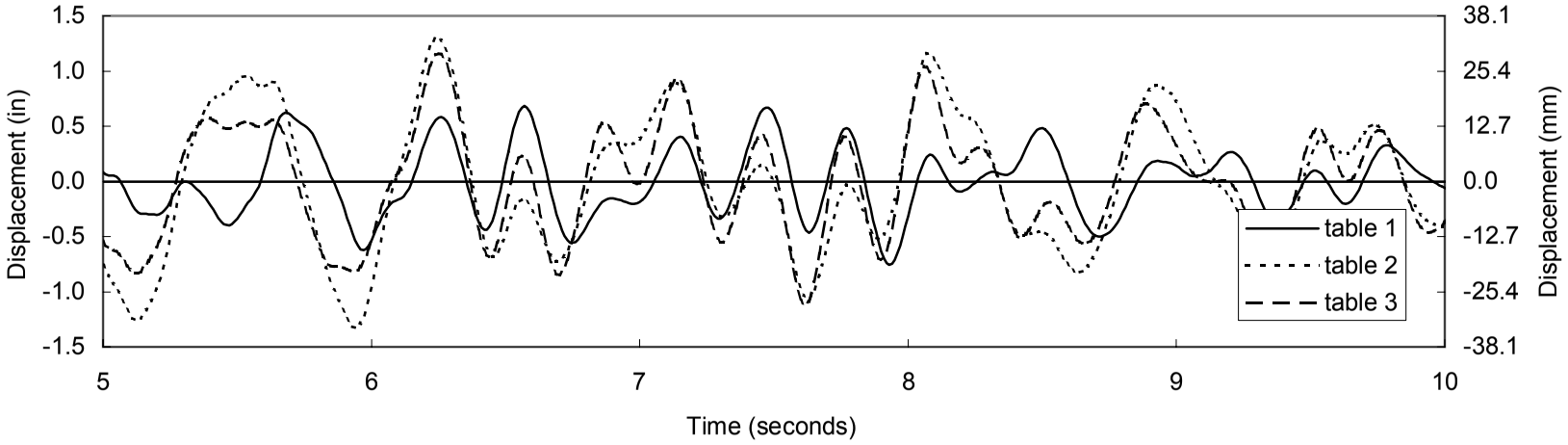

Figure 6-265: Achieved transverse table displacement history comparison for test 16 (t=5 to t=10 seconds).

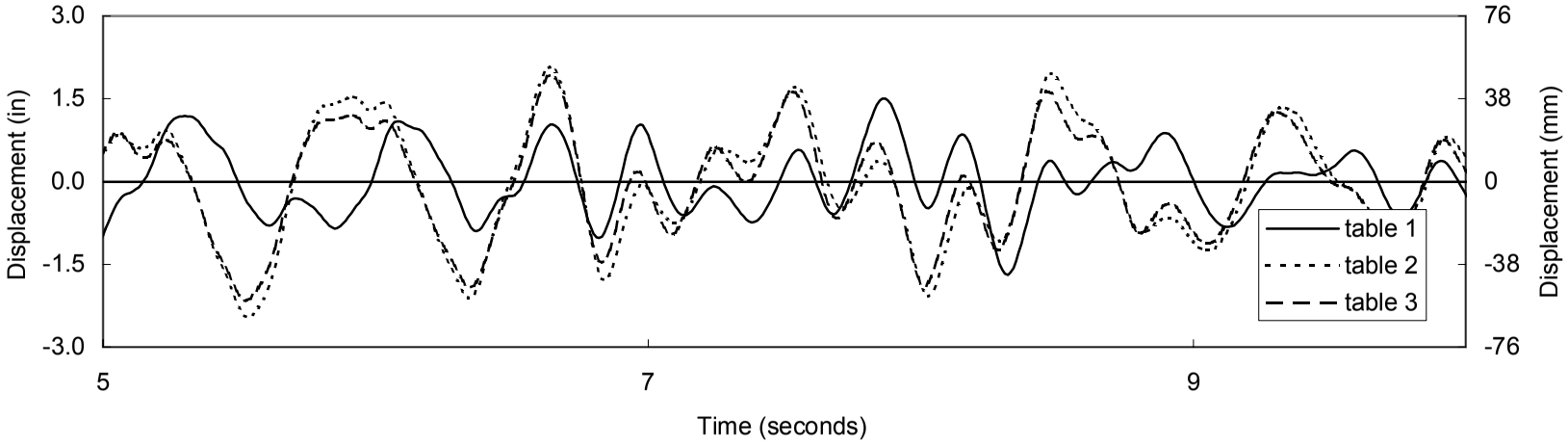

Figure 6-266: Achieved transverse table displacement history comparison for test 19 (t=5 to t=10 seconds)

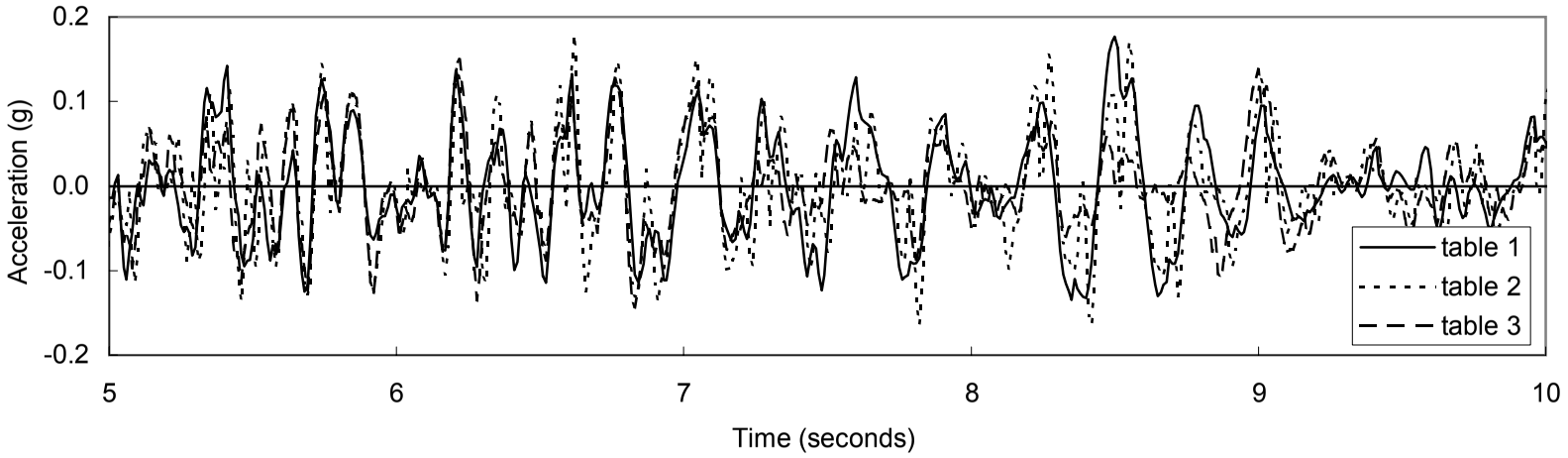

Figure 6-267: Achieved transverse table acceleration history comparison for test 13 (t=5 to t=10 seconds).

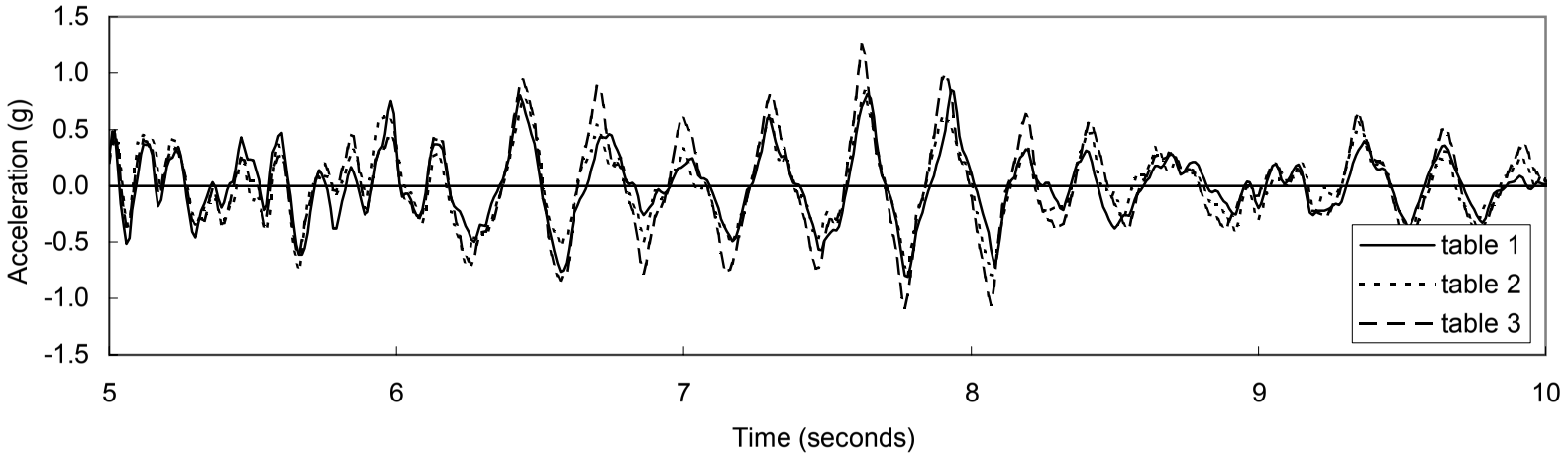

Figure 6-268: Achieved transverse table acceleration history comparison for test 16 (t=5 to t=10 seconds).

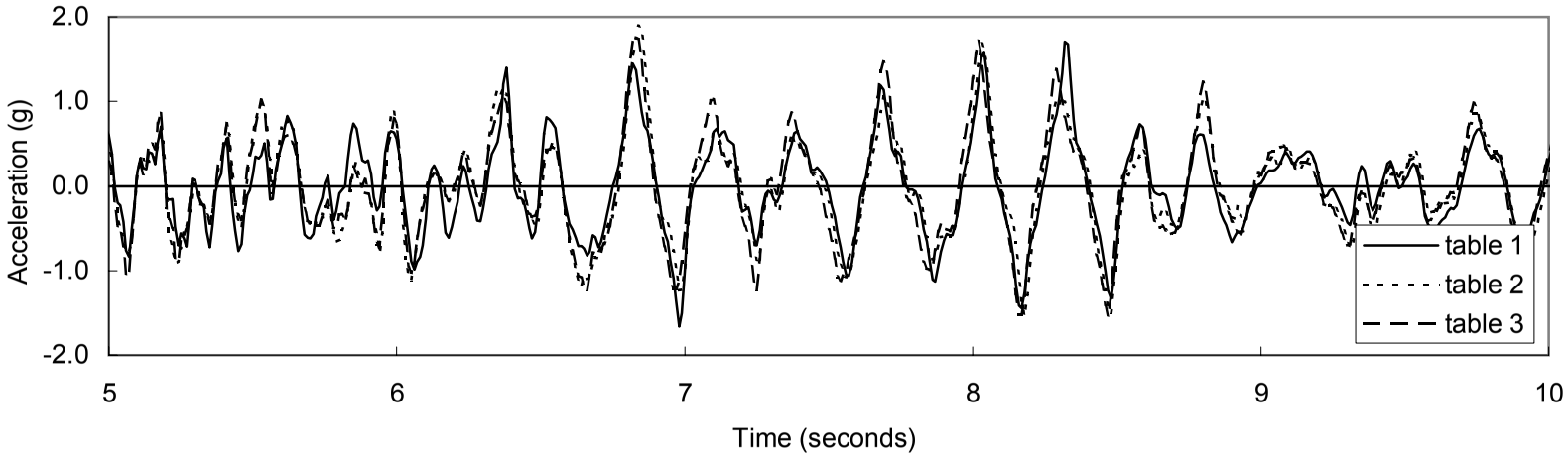

Figure 2-269: Achieved transverse table acceleration history comparison for test 19 (t=5 to t=10 seconds).

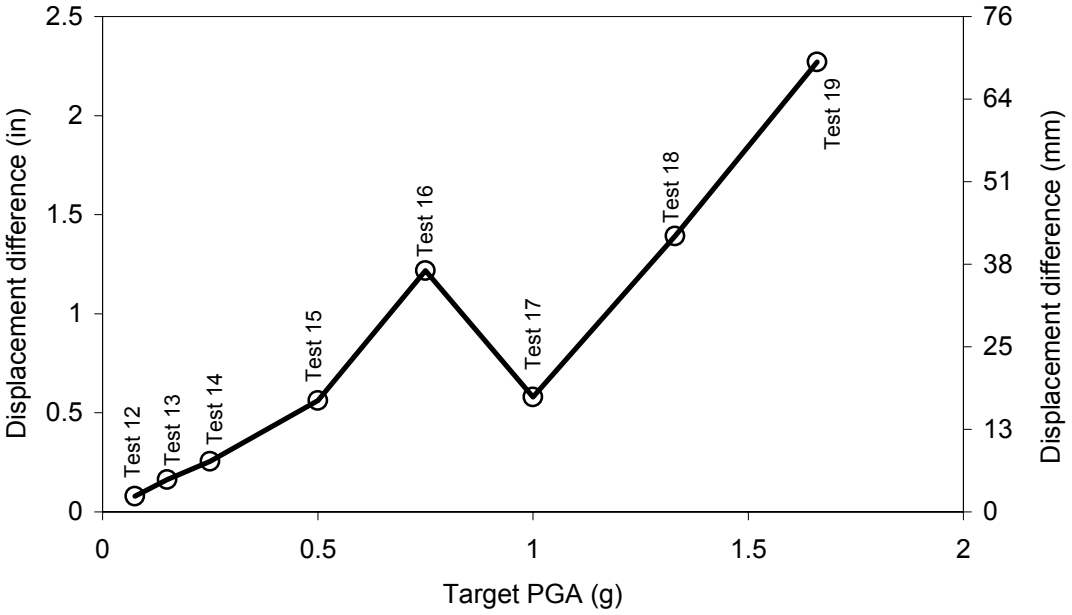

Figure 6-270: Maximum displacement incoherency between shake tables 1 and 2 (bents 1 and 2) compared with target PGA for tests 12-19.

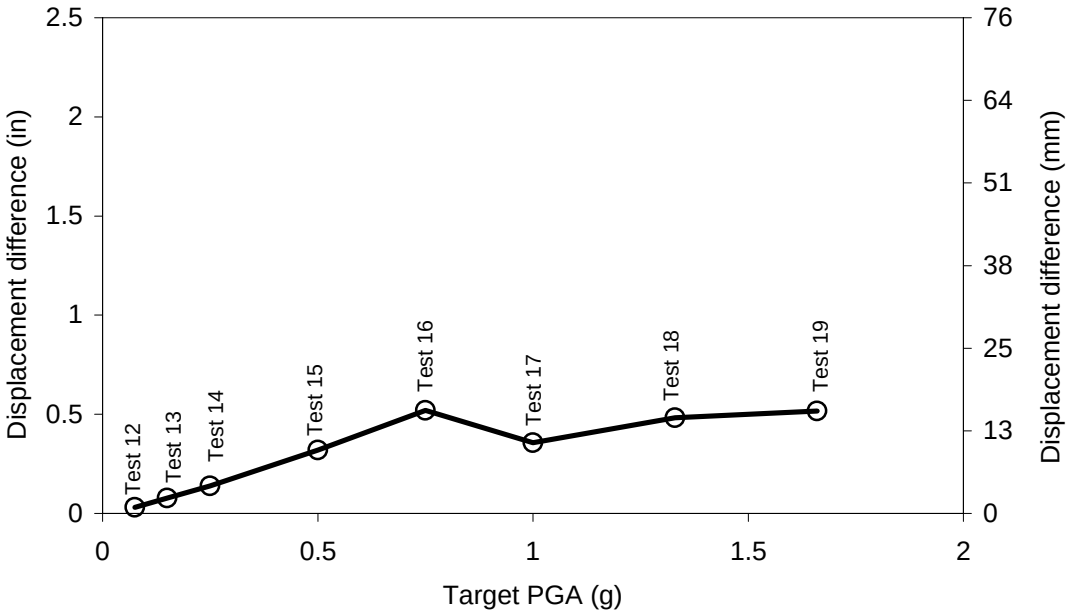

Figure 6-271: Maximum displacement incoherency between shake tables 2 and 3 (bents 2 and 3) compared with target PGA for tests 12-19.

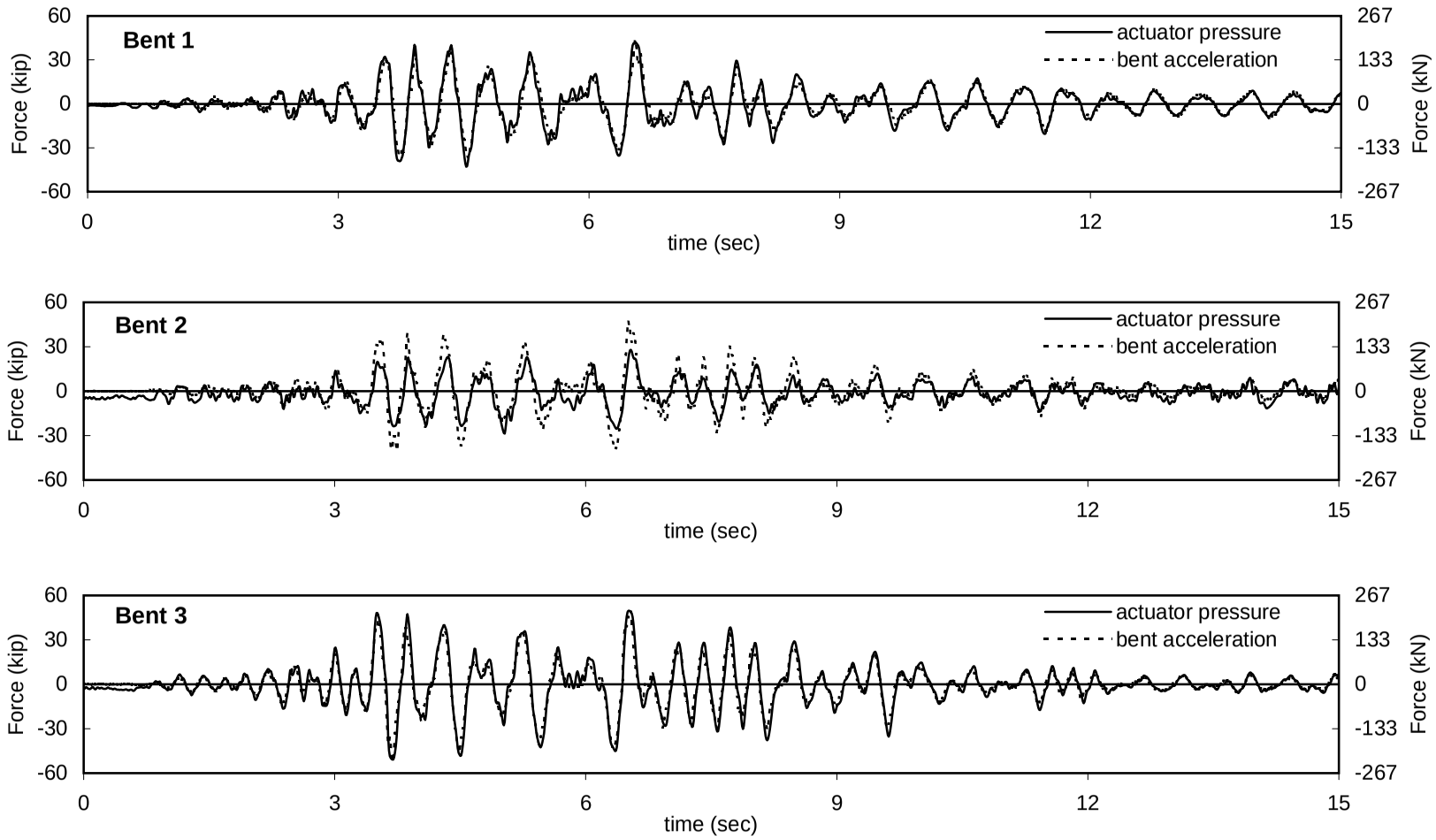

Figure 6-272: Test 15 force history comparison for bents 1-3 comparing force (calculated from actuator pressure), and force estimated from measured bent acceleration and tributary mass.

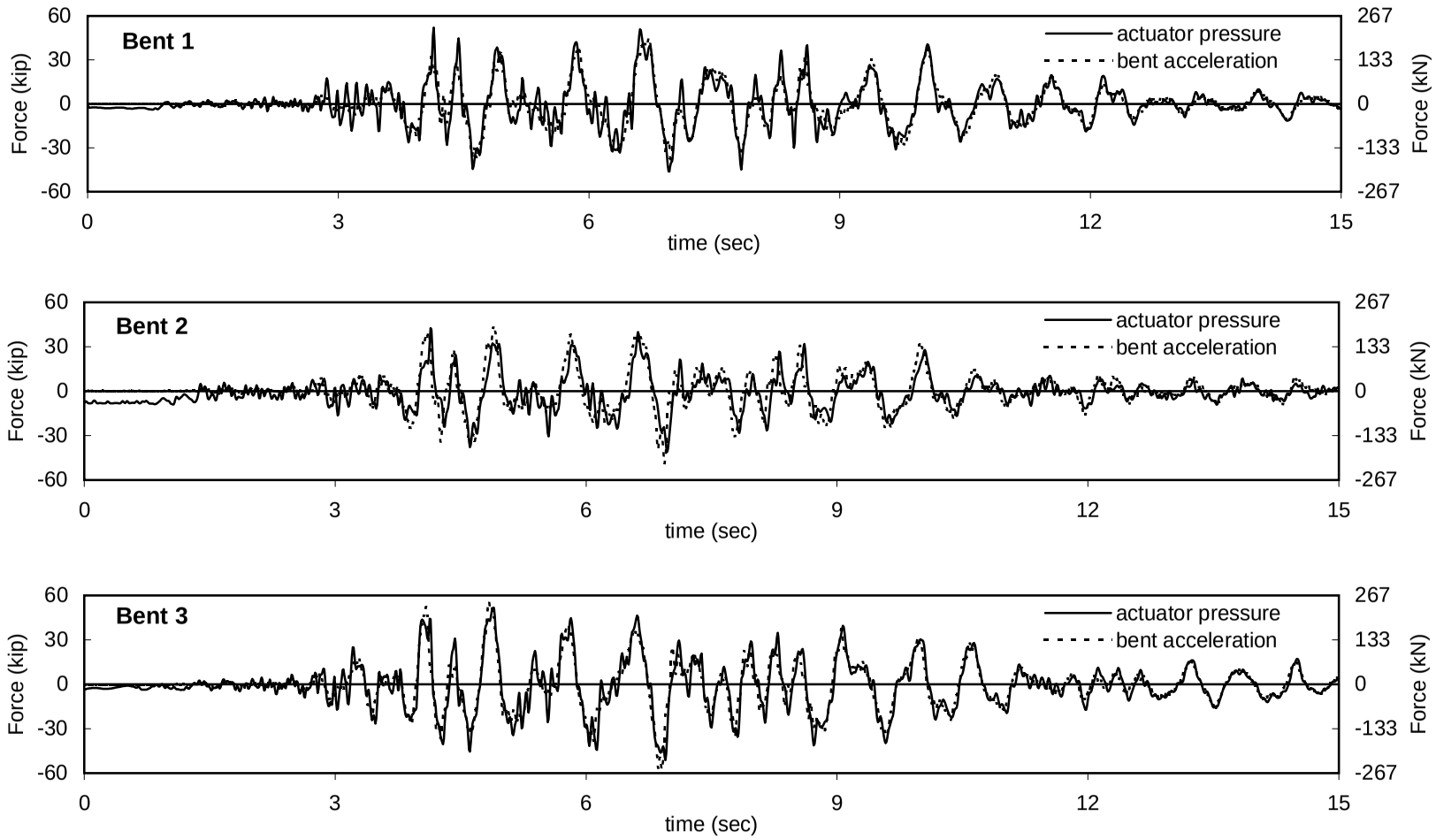

Figure 6-273: Test 18 force history comparison for bents 1-3 comparing force (calculated from actuator pressure), and force estimated from measured bent acceleration and tributary mass.

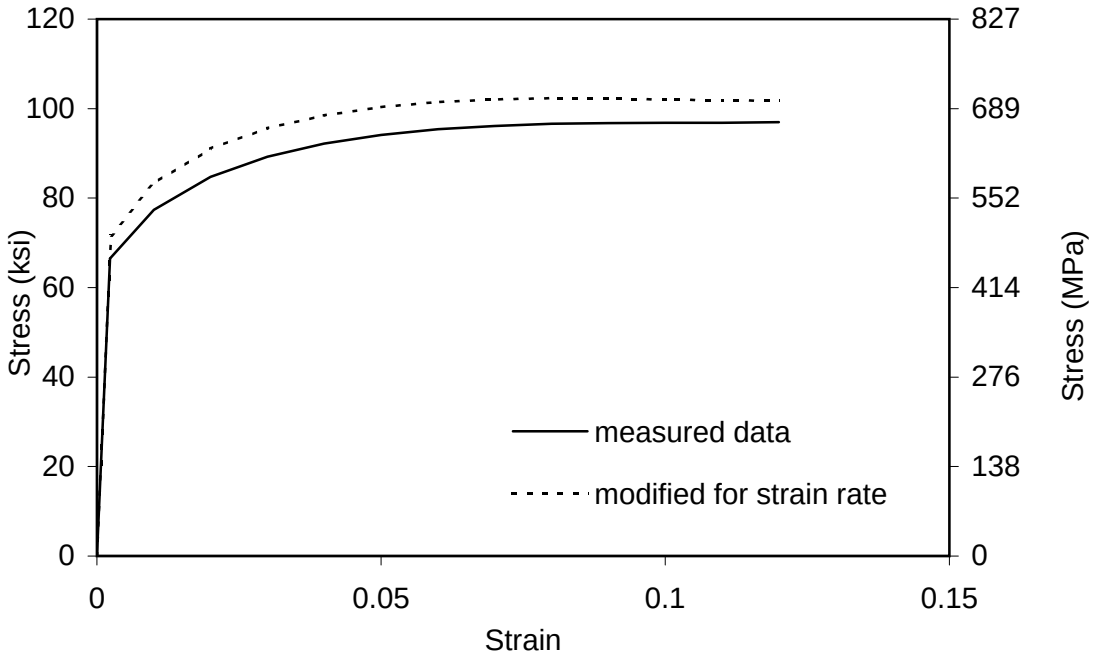

Figure 7-1: Measured and rate modified stress-strain curve for longitudinal column reinforcement.

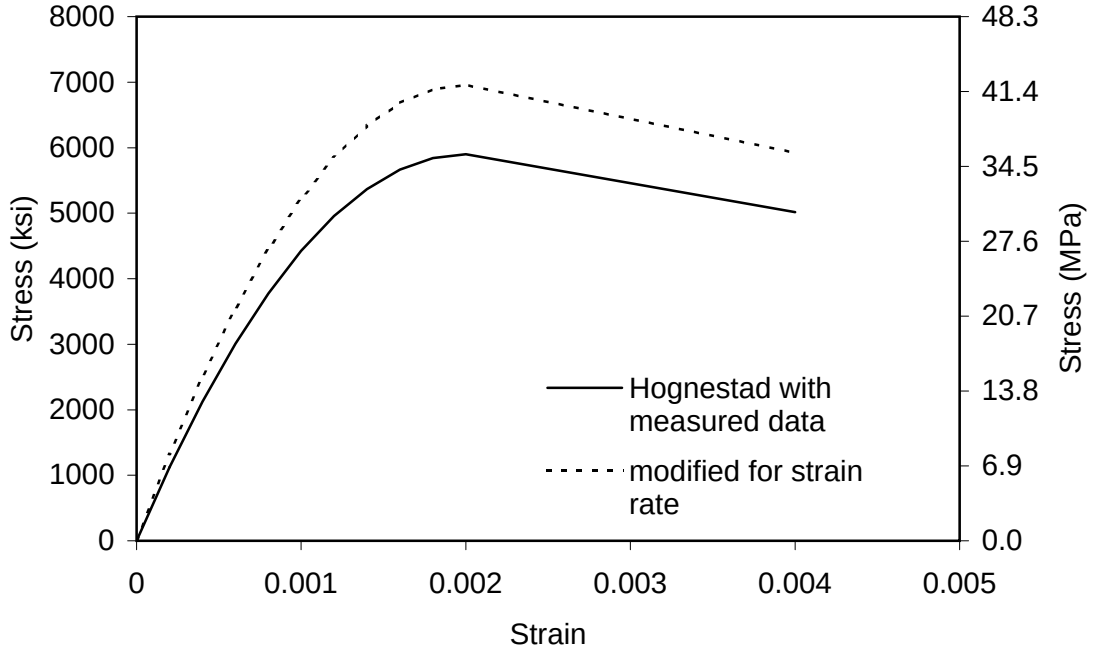

Figure 7-2: Measured and rate modified stress-strain curve for unconfined concrete in columns.

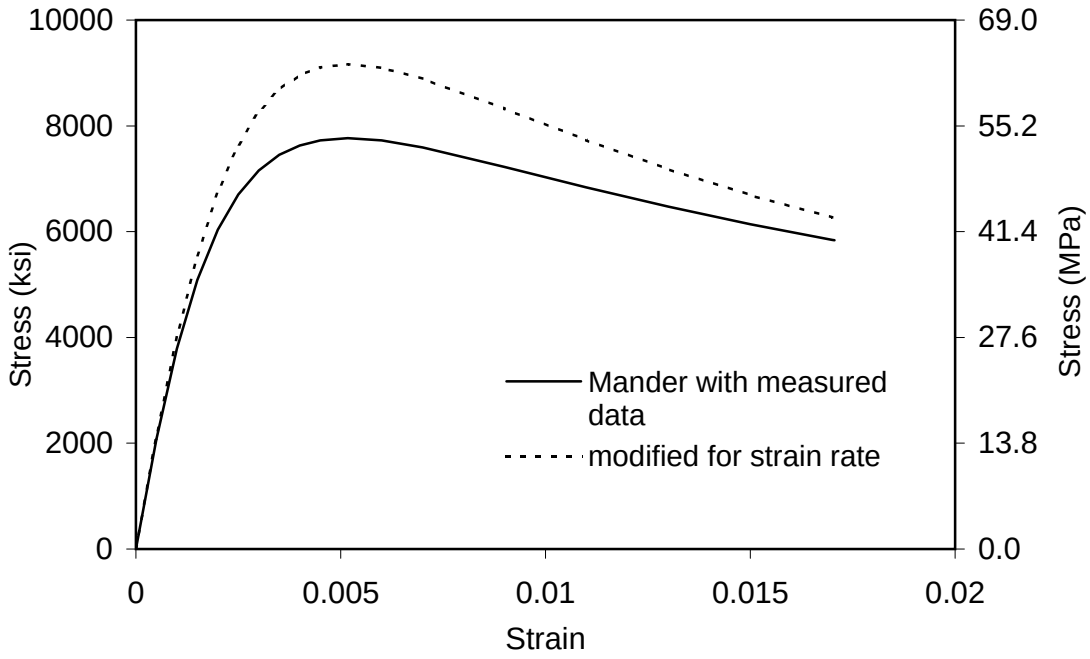

Figure 7-3: Measured and rate modified stress-strain curve for confined concrete in columns.

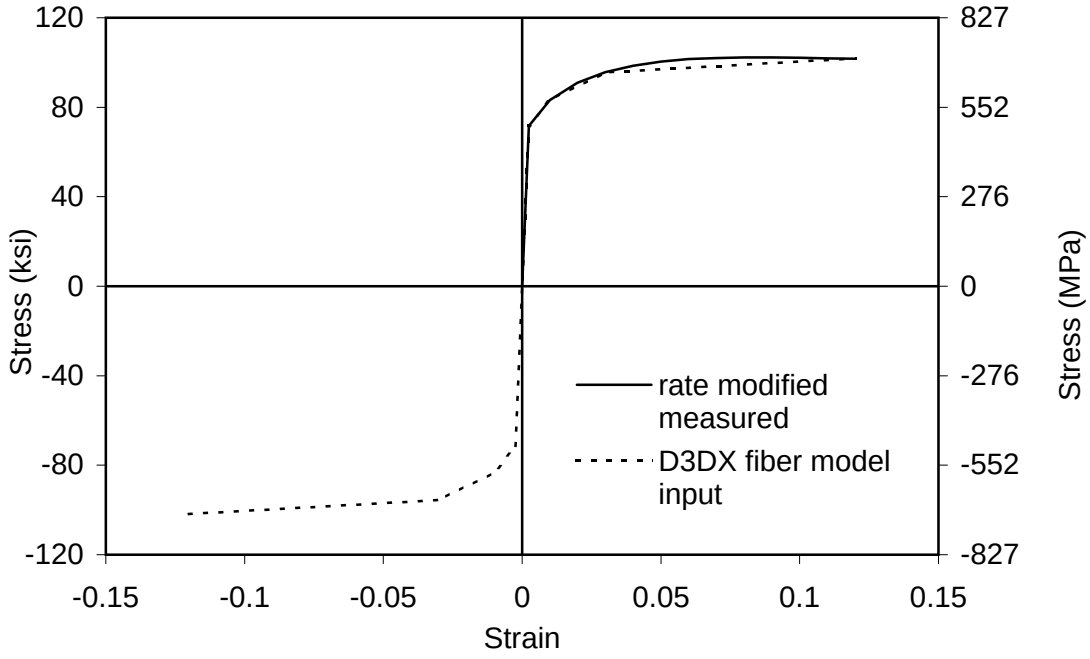

Figure 7-4: Drain-3DX fber element stress-strain curve for longitudinal column reinforcement.

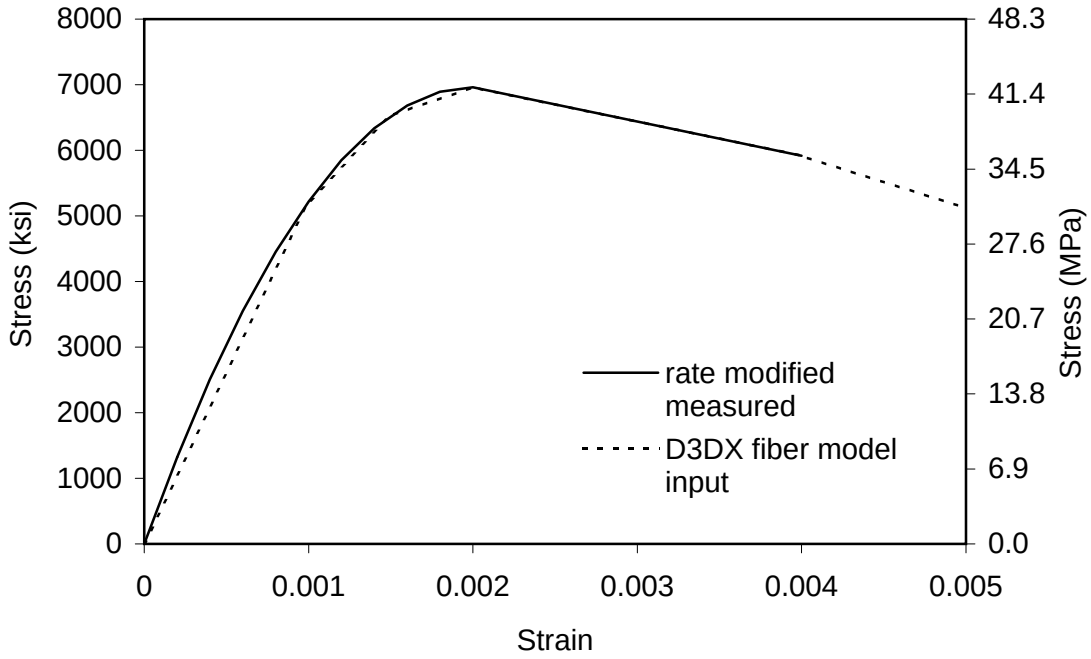

Figure 7-5: Drain-3DX fiber element stress-strain curve for unconfined concrete in columns.

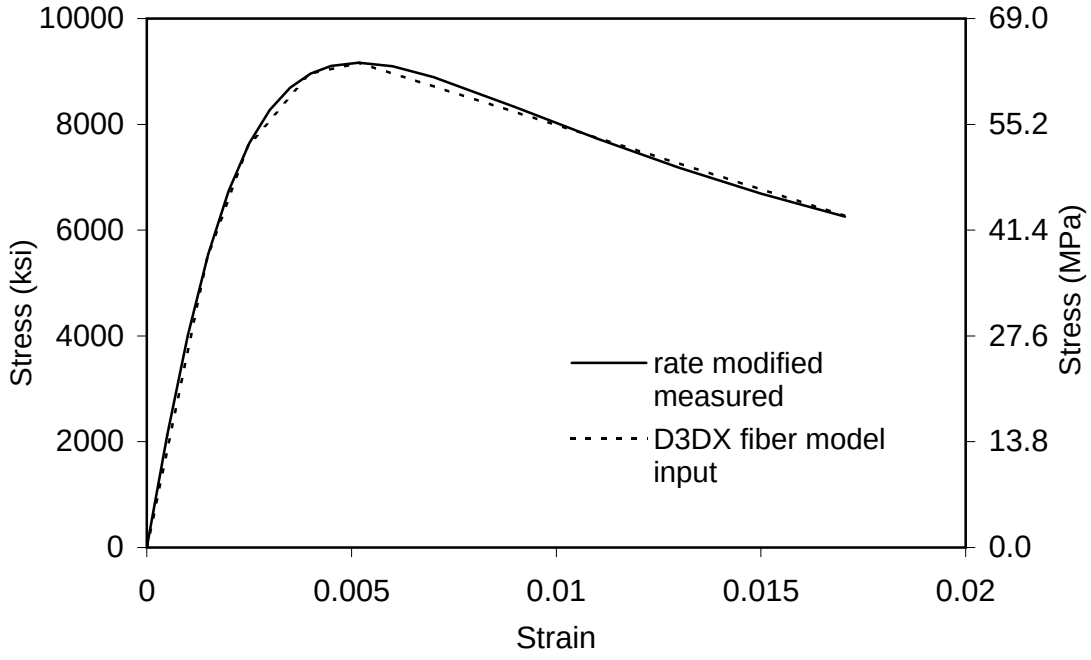

Figure 7-6: Drain-3DX fiber element stress-strain curve for confined concrete in columns.

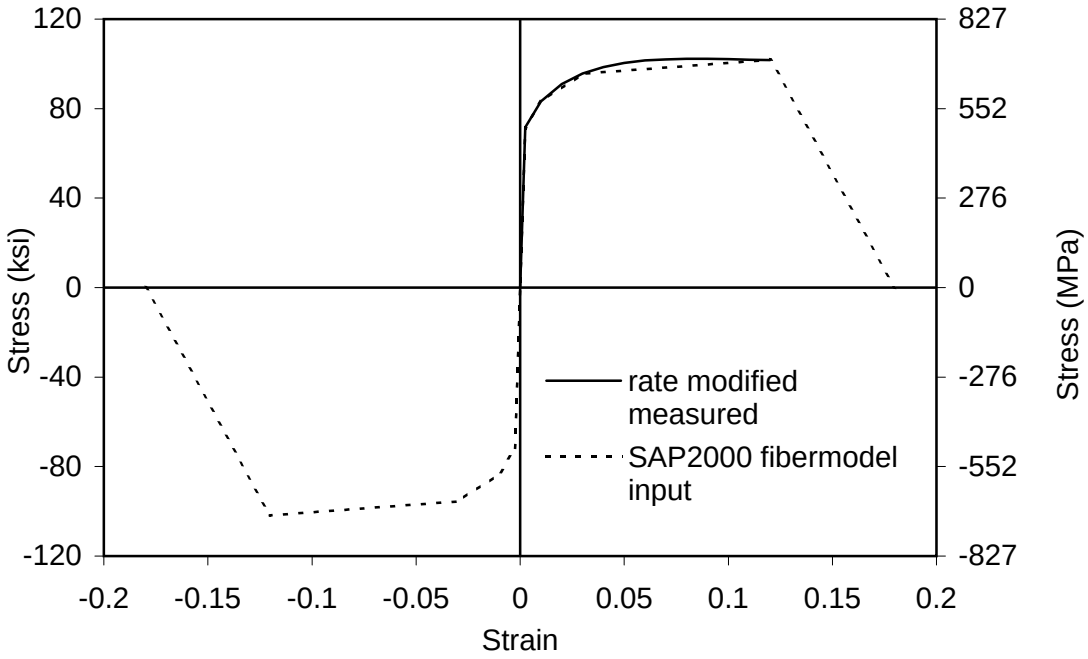

Figure 7-7: SAP2000 fiber element stress-strain curve for longitudinal column reinforcement.

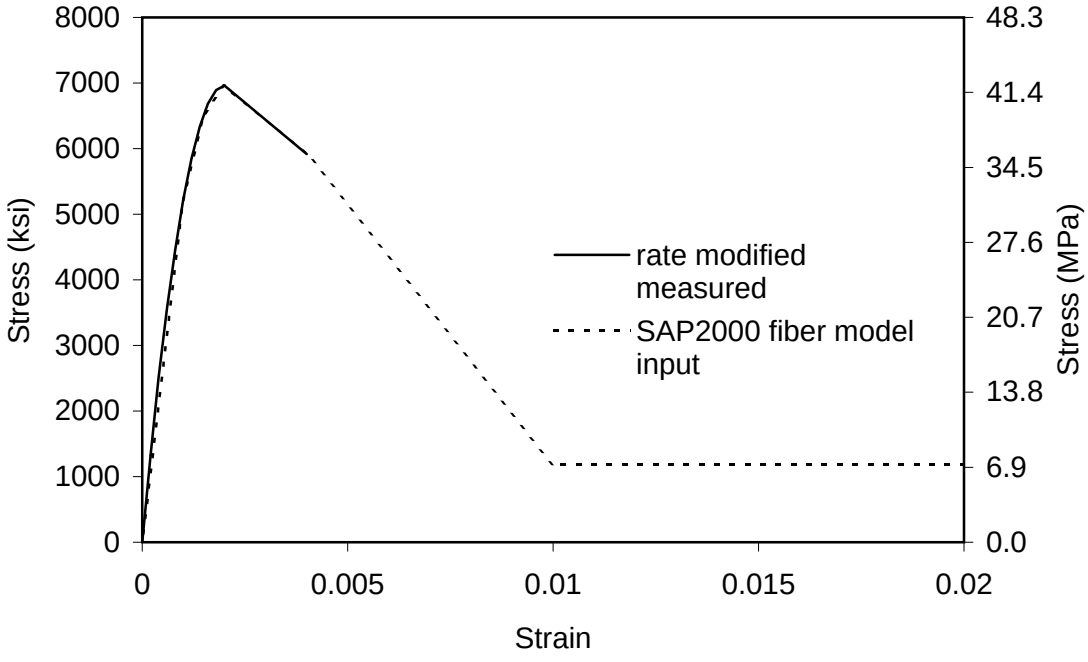

Figure 7-8: SAP2000 fiber element stress-strain curve for unconfined concrete in columns.

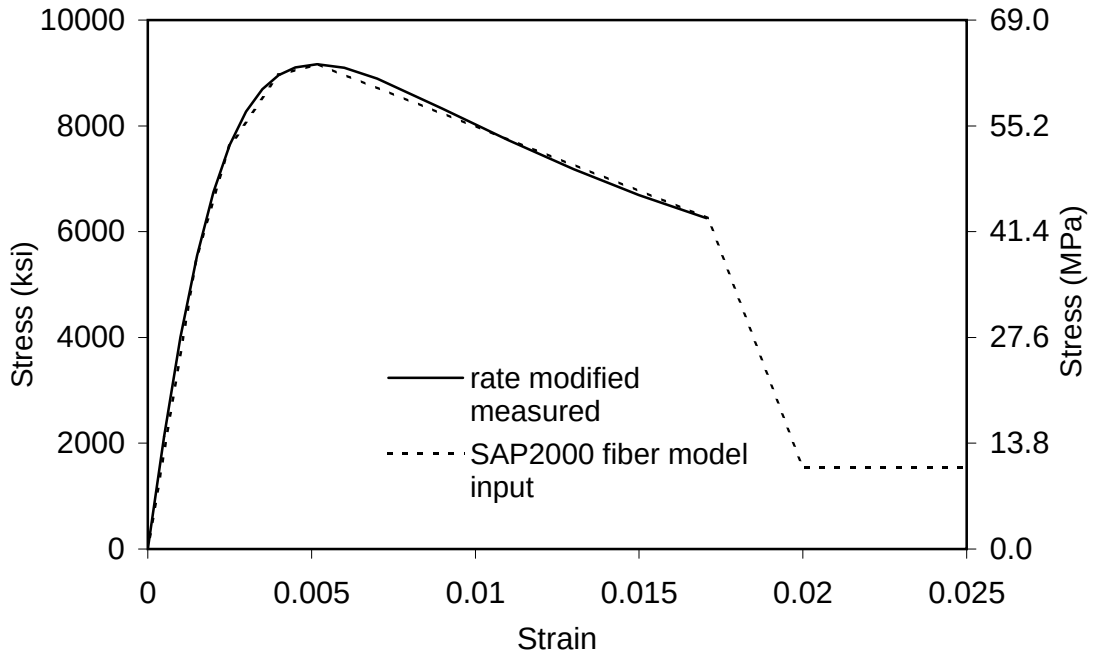

Figure 7-9: SAP2000 fiber element stress-strain curve for confined concrete in columns.

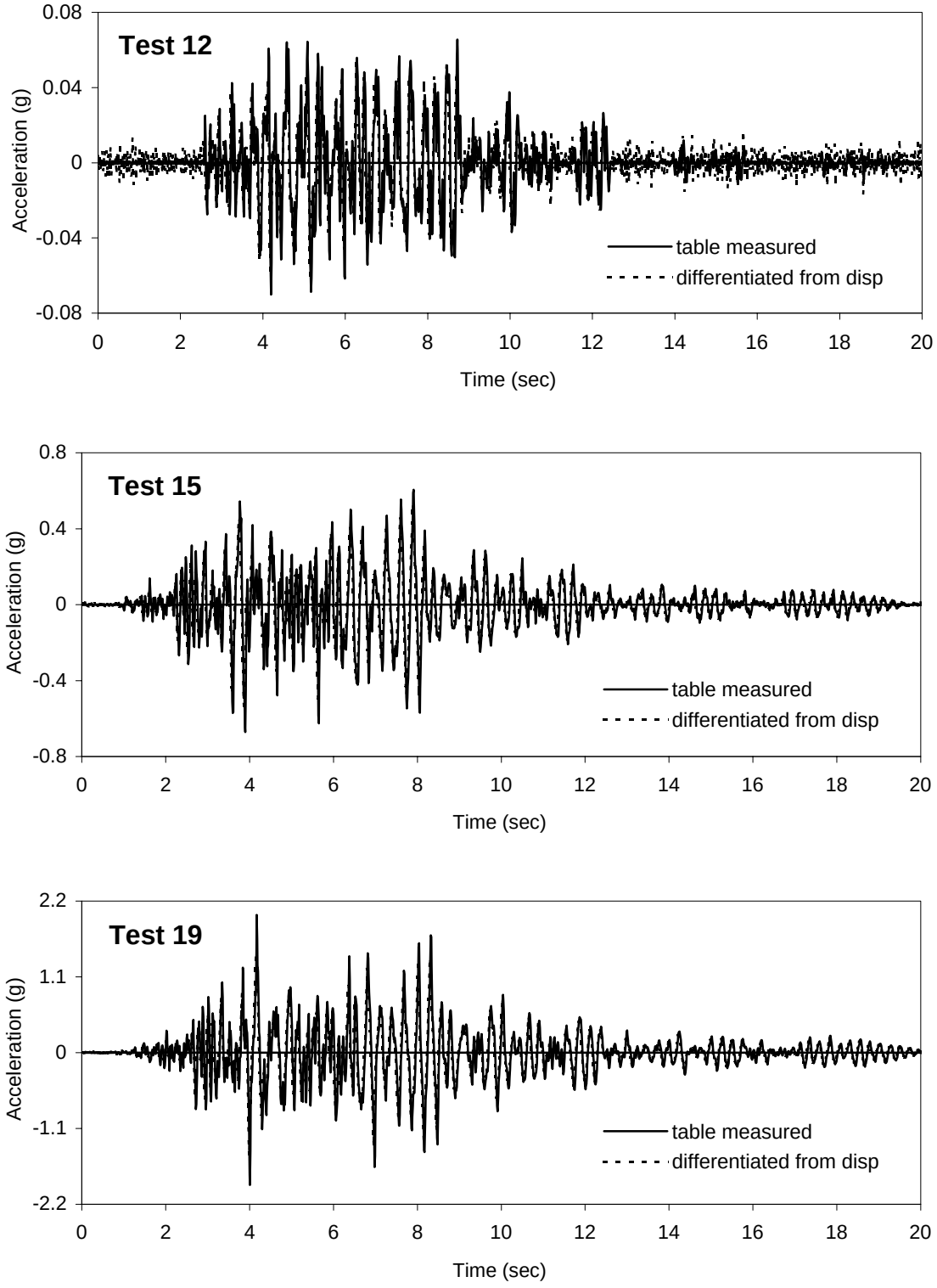

Figure 7-10: Comparison of measured shake table 1 acceleration history with acceleration from double differentiated filtered displacement.

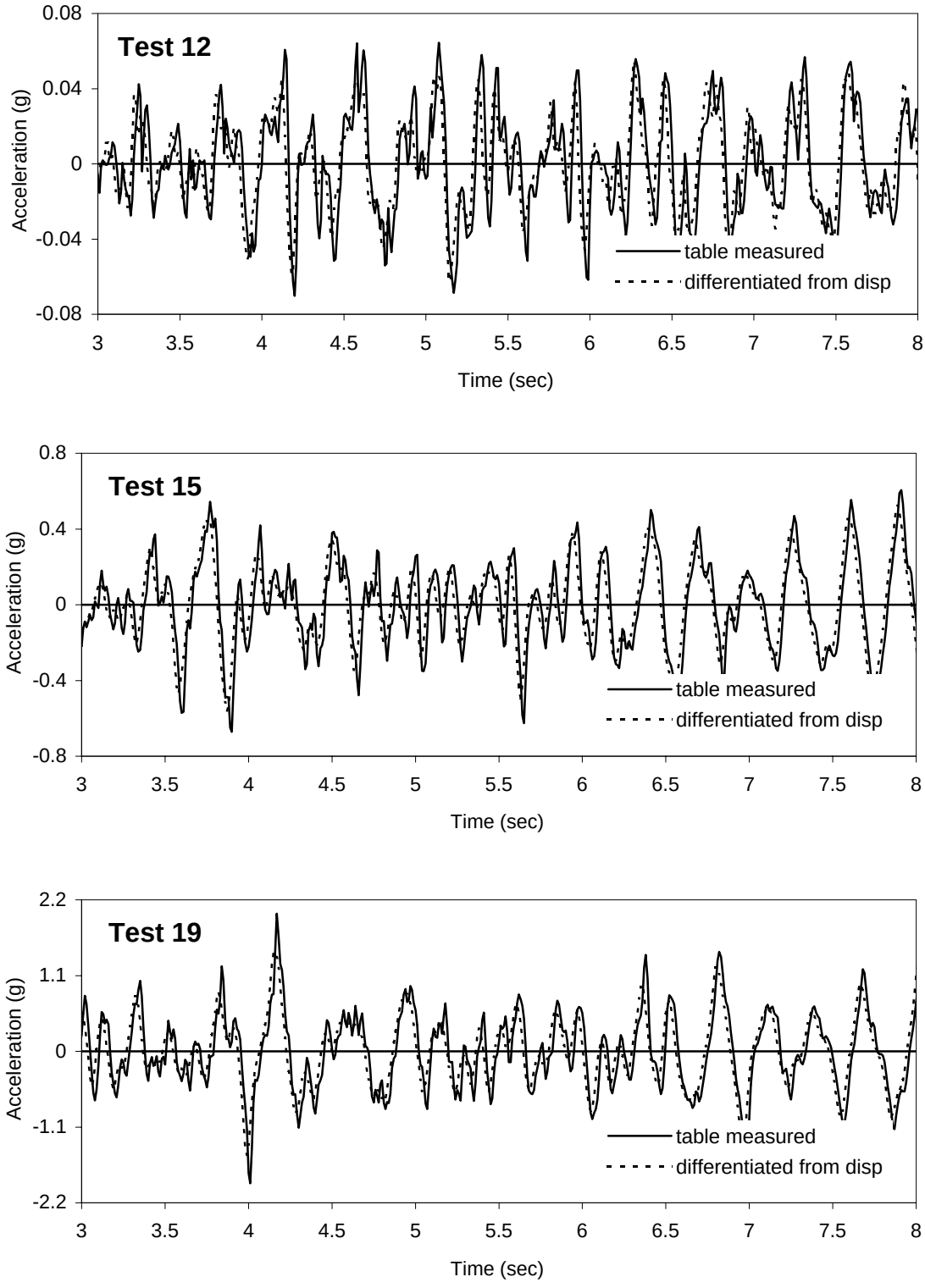

Figure 7-11: Comparison of measured shake table 1 acceleration with acceleration history from double differentiated filtered displacement (3 to 8 seconds).

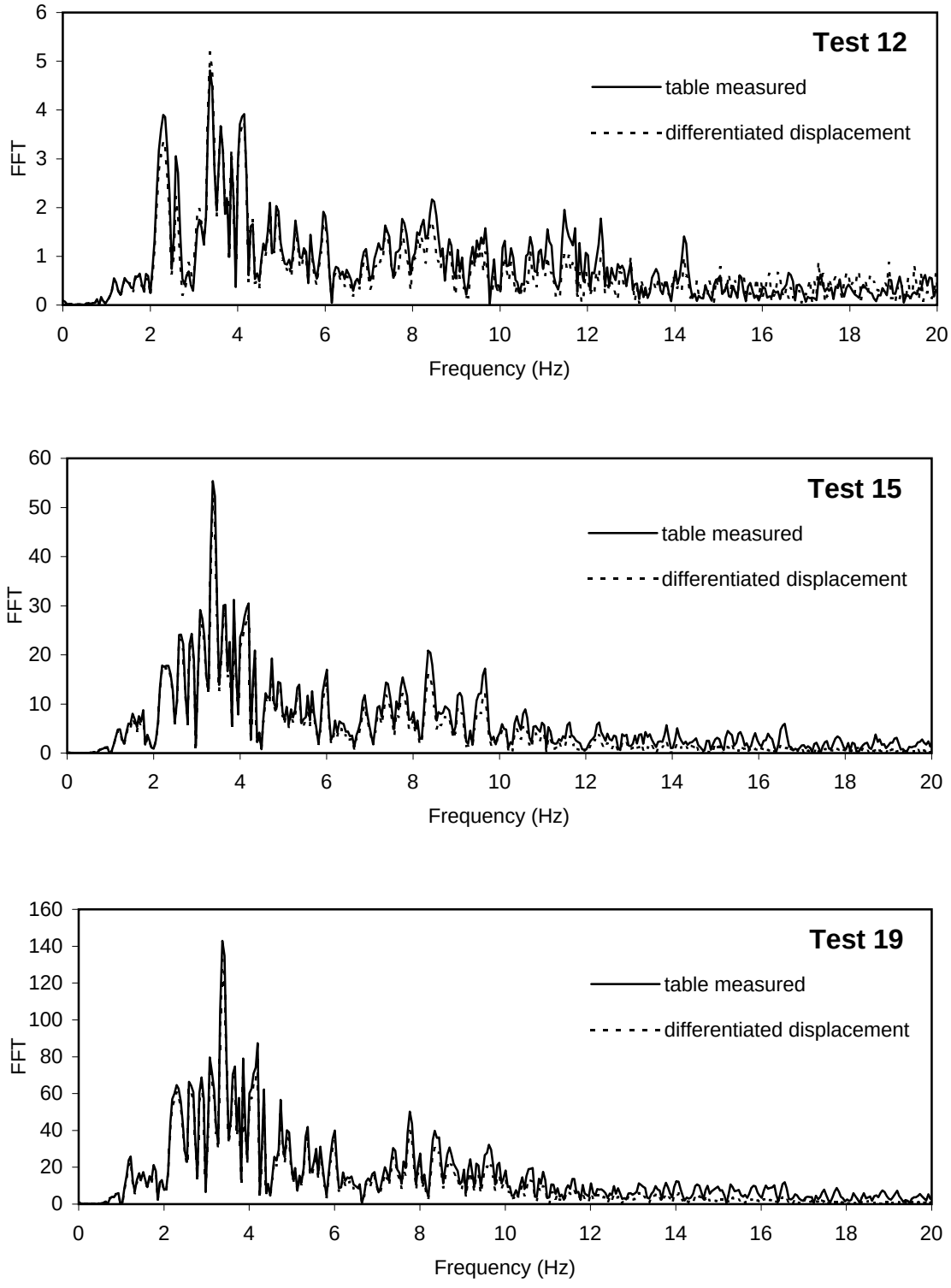

Figure 7-12: Comparison FFT for measured shake table 1 acceleration history with acceleration from double differentiated filtered displacement.

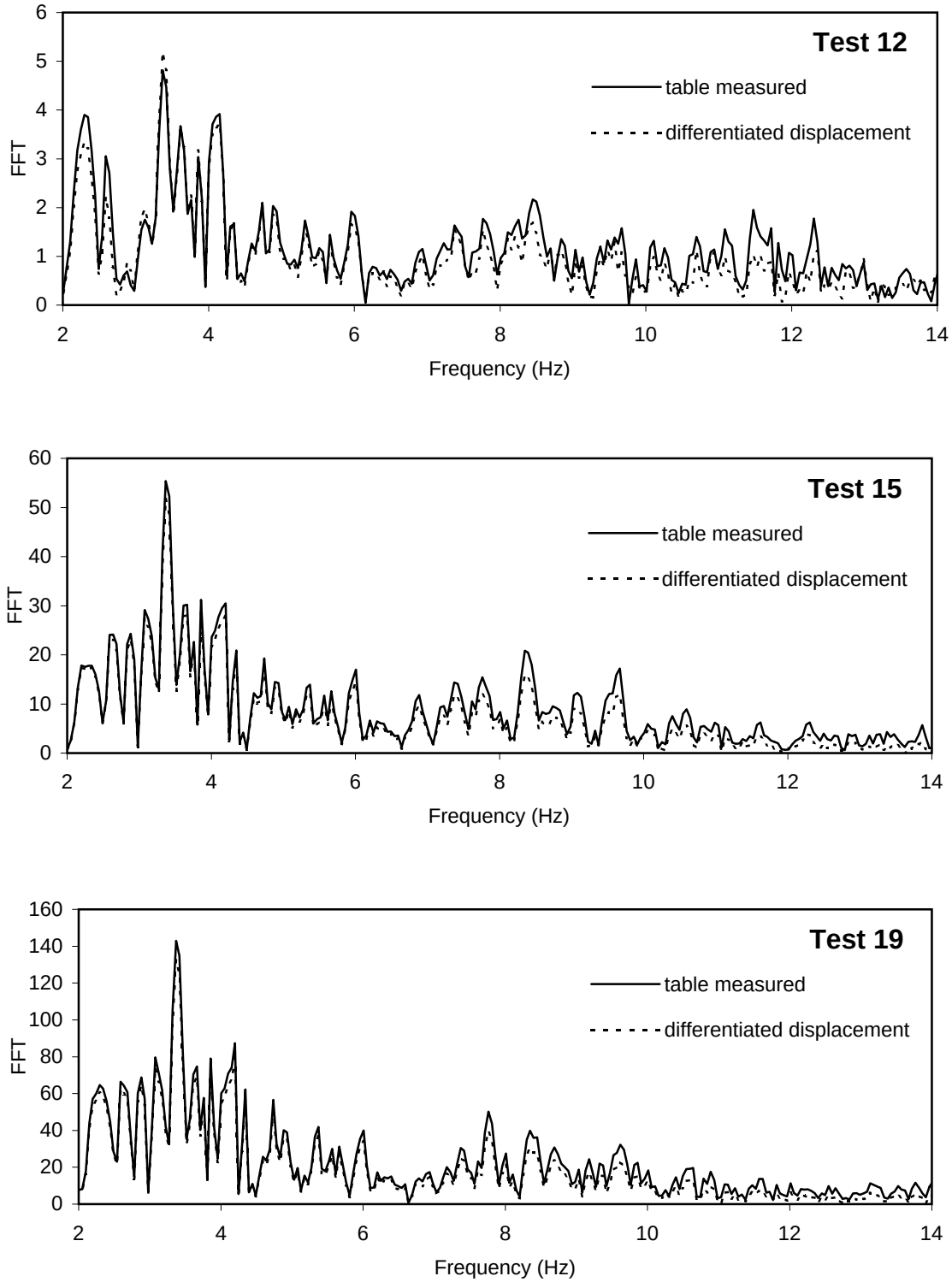

Figure 7-13: Comparison FFT for measured shake table 1 acceleration history with acceleration from double differentiated filtered displacement (2 to 14 Hz).

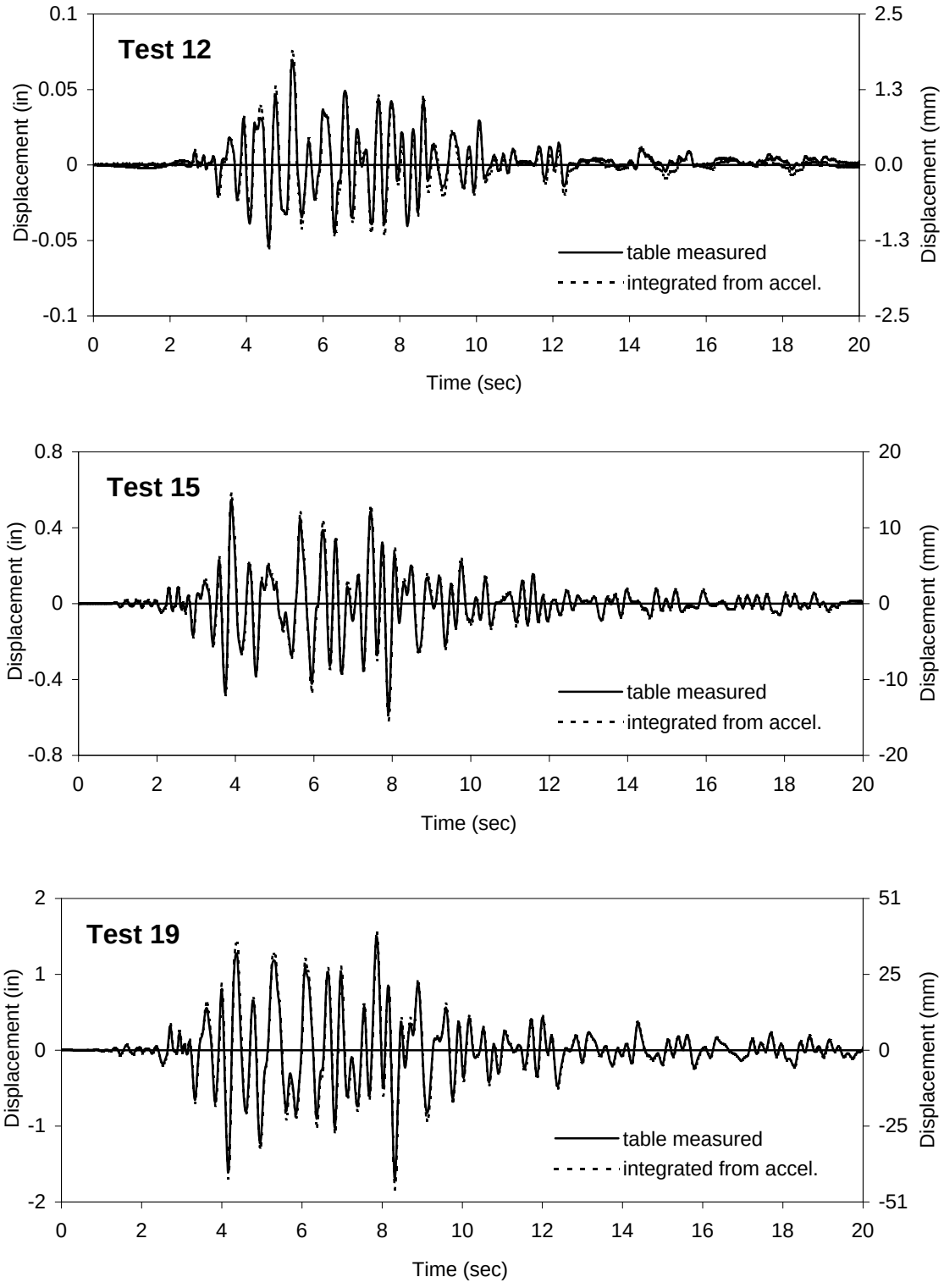

Figure 7-14: Comparison of measured shake table 1 displacement history with displacement from filtered and integrated acceleration.

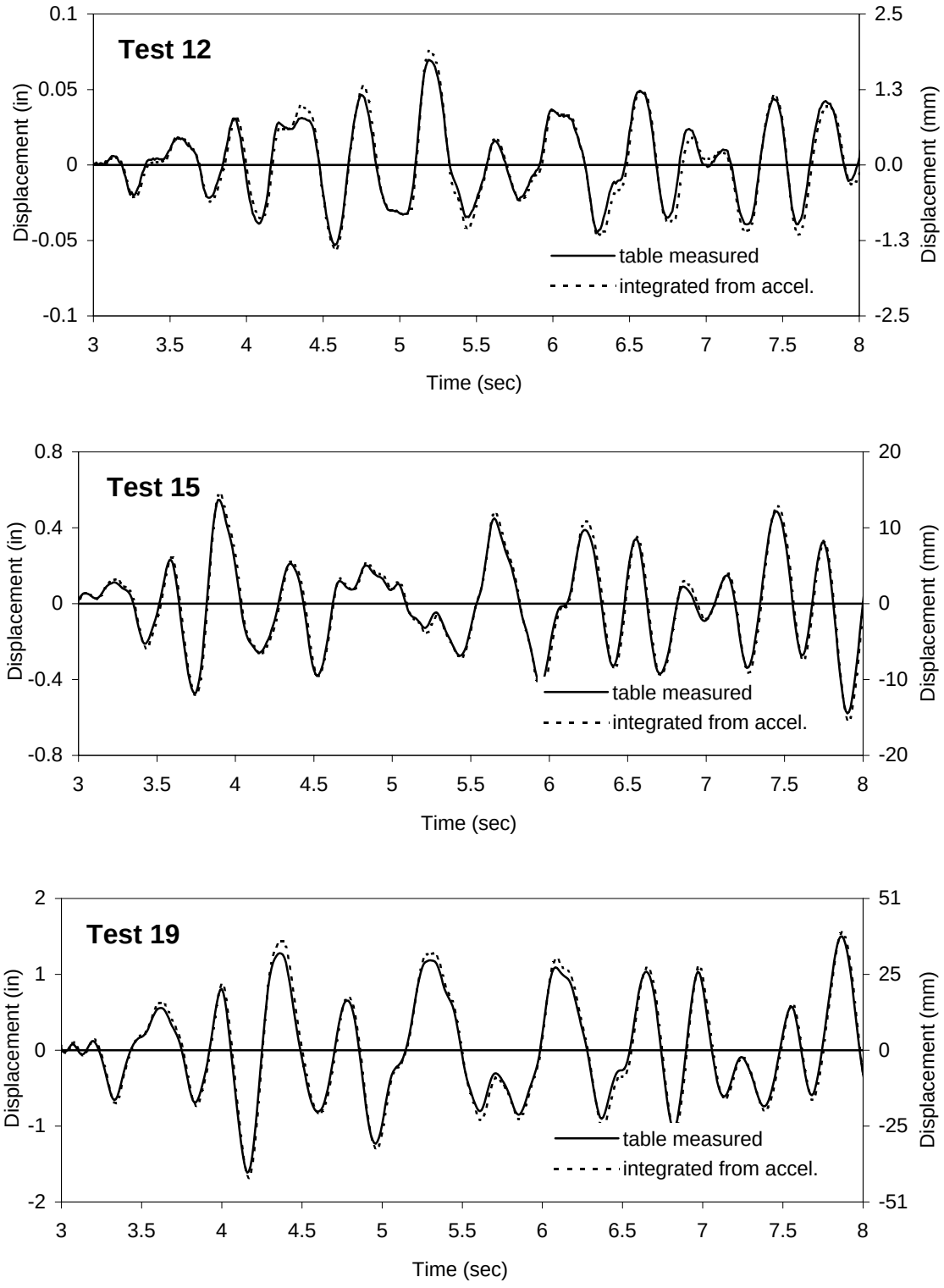

Figure 7-15: Comparison of measured shake table 1 displacement history with displacement from filtered and integrated acceleration (3 to 8 seconds).

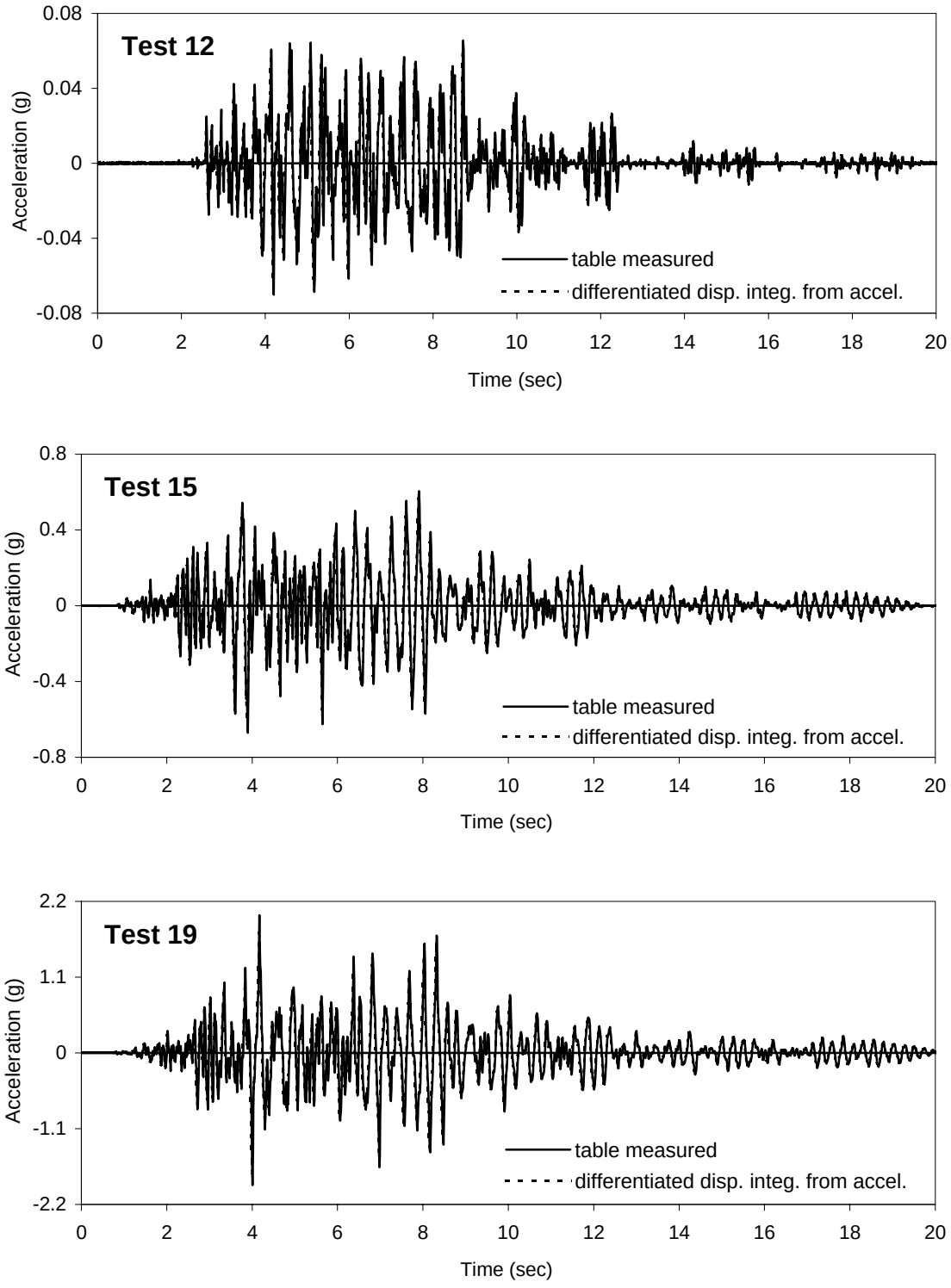

Figure 7-16: Comparison of measured shake table 1 acceleration history with acceleration from double differentiated displacement from double integrated acceleration..

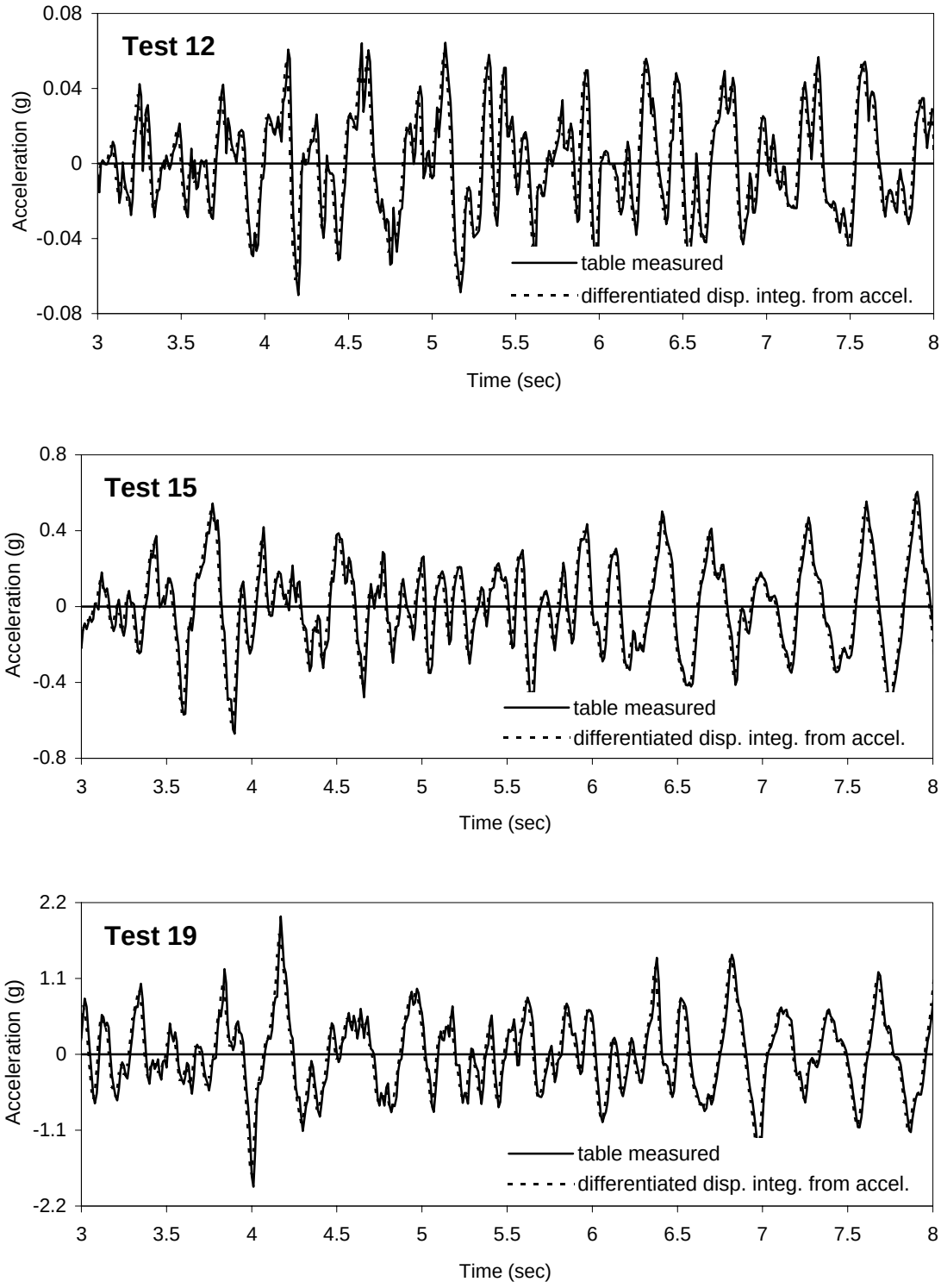

Figure 7-17: Comparison of measured shake table 1 acceleration history with acceleration from double differentiated displacement from double integrated acceleration (3 to 8 sec).

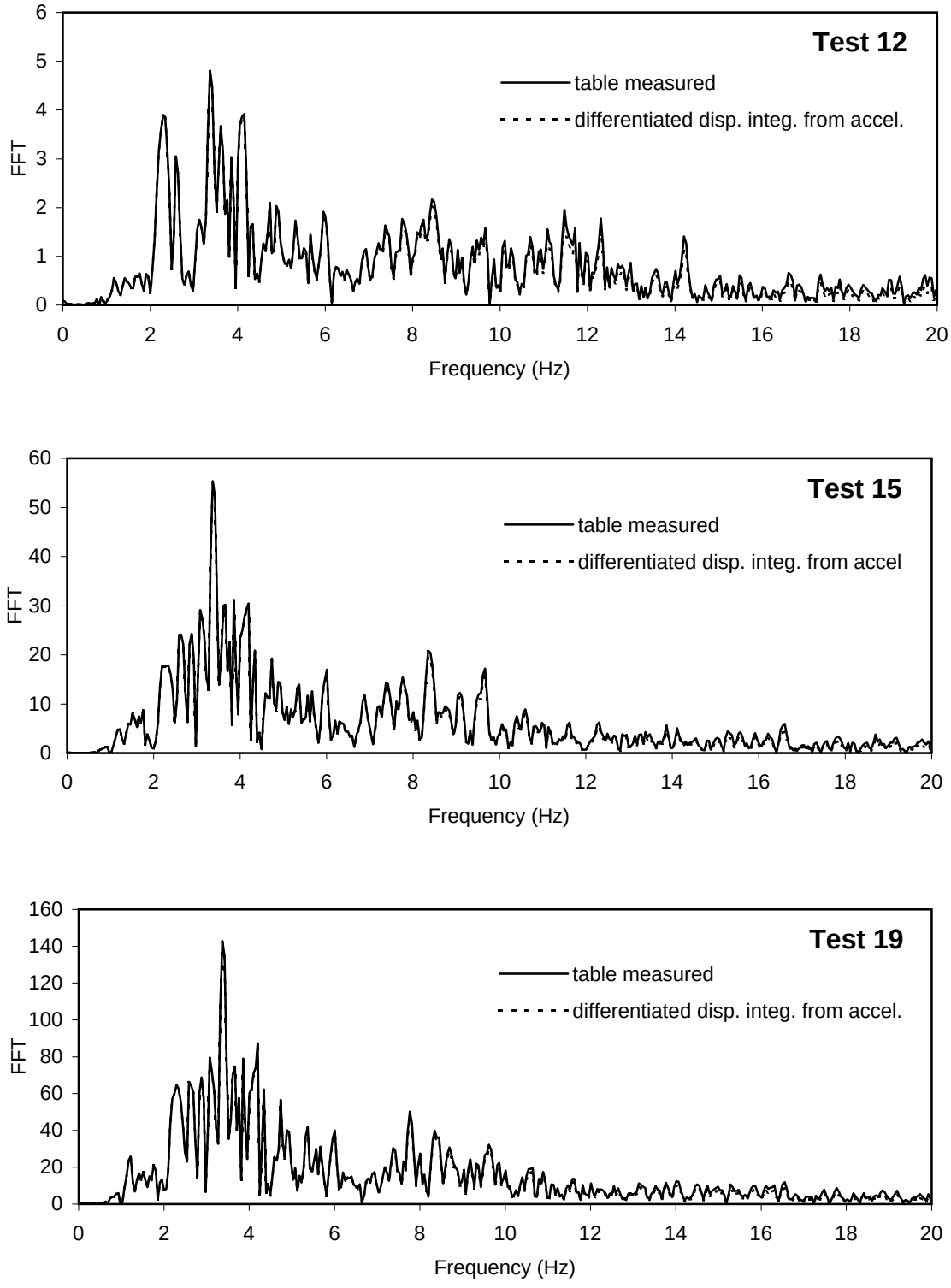

Figure 7-18: Comparison FFT for measured shake table 1 acceleration history with acceleration from double differentiated, double integrated acceleration..

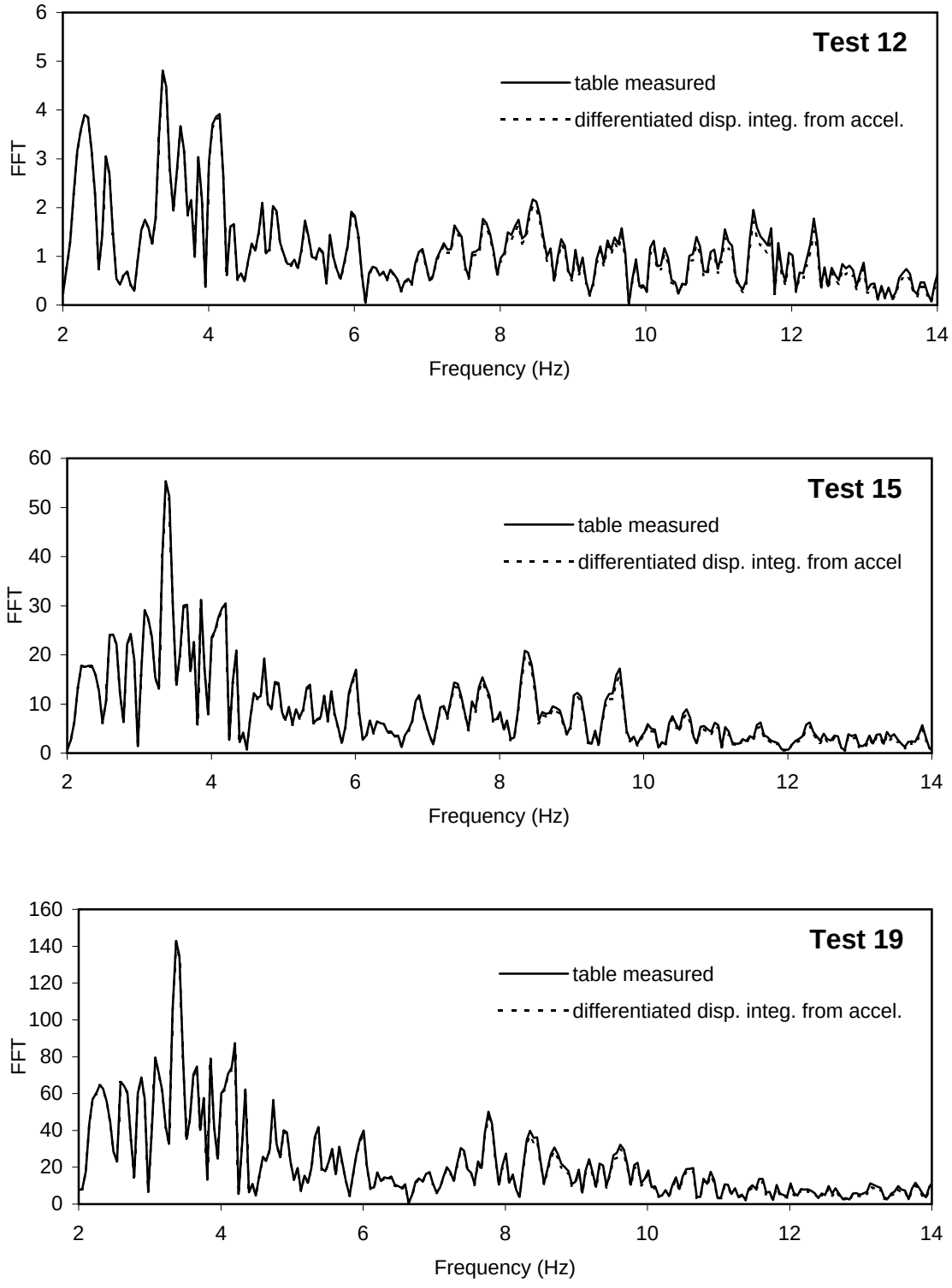

Figure 7-19: Comparison FFT for measured shake table 1 acceleration history with acceleration from double differentiated, double integrated acceleration (2-14 Hz).

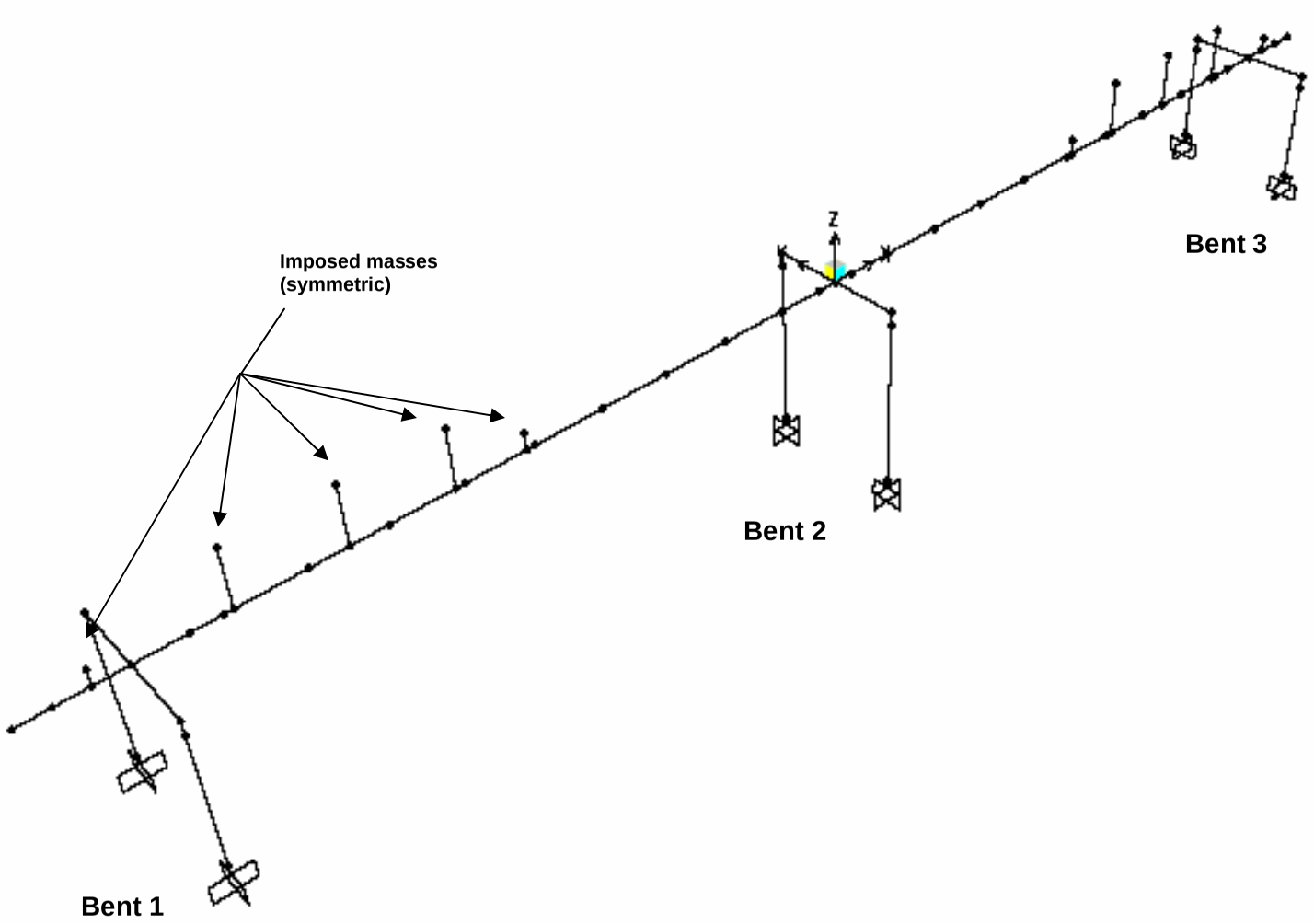

Figure 7-20: Nodal configuration of computer models.

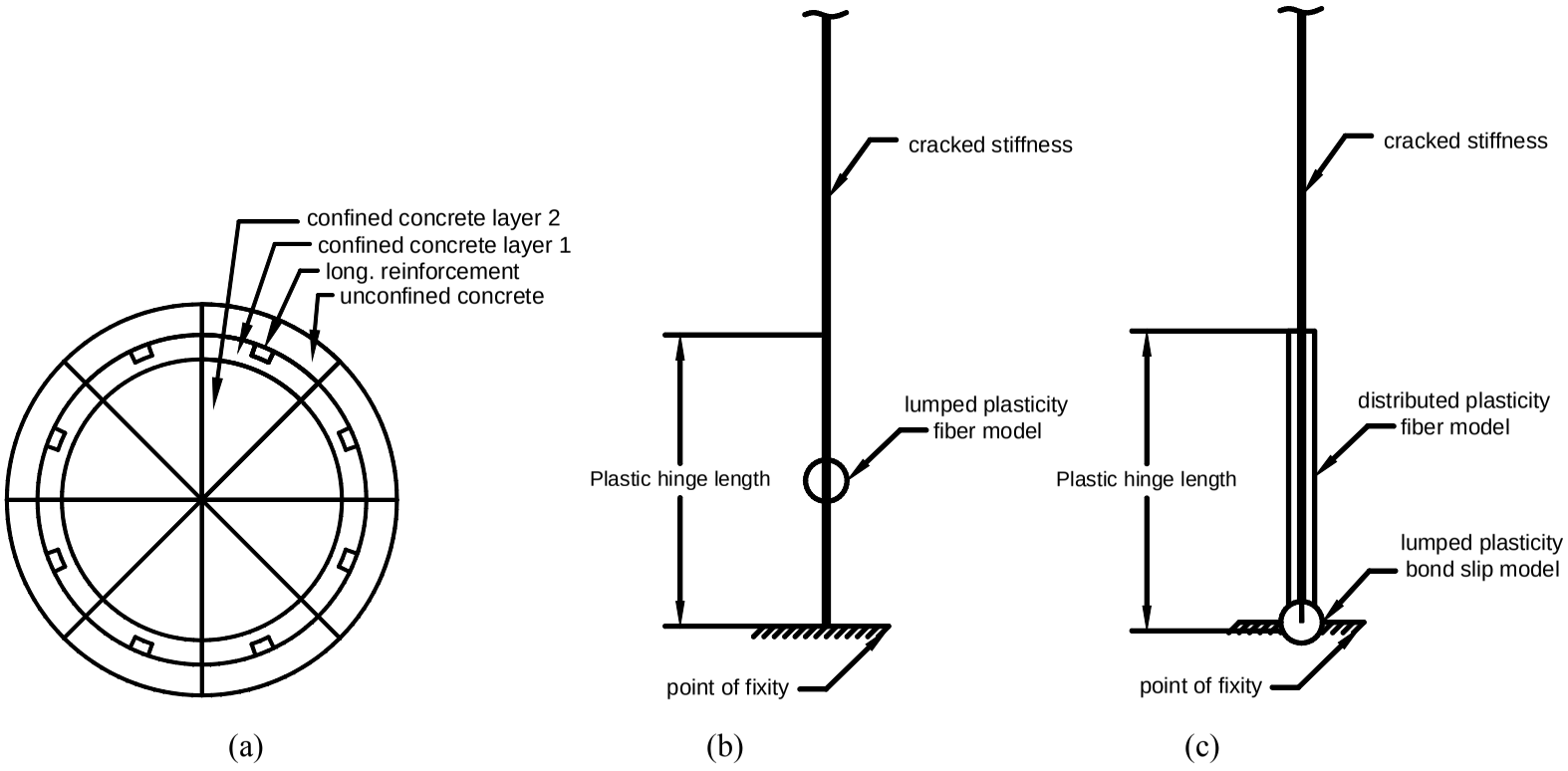

Figure 7-21: (a) fiber discretization of hinge models, (b) hinge zone configuration of SAP 2000 model, (c) hinge zone configuration of Drain-3DX model.

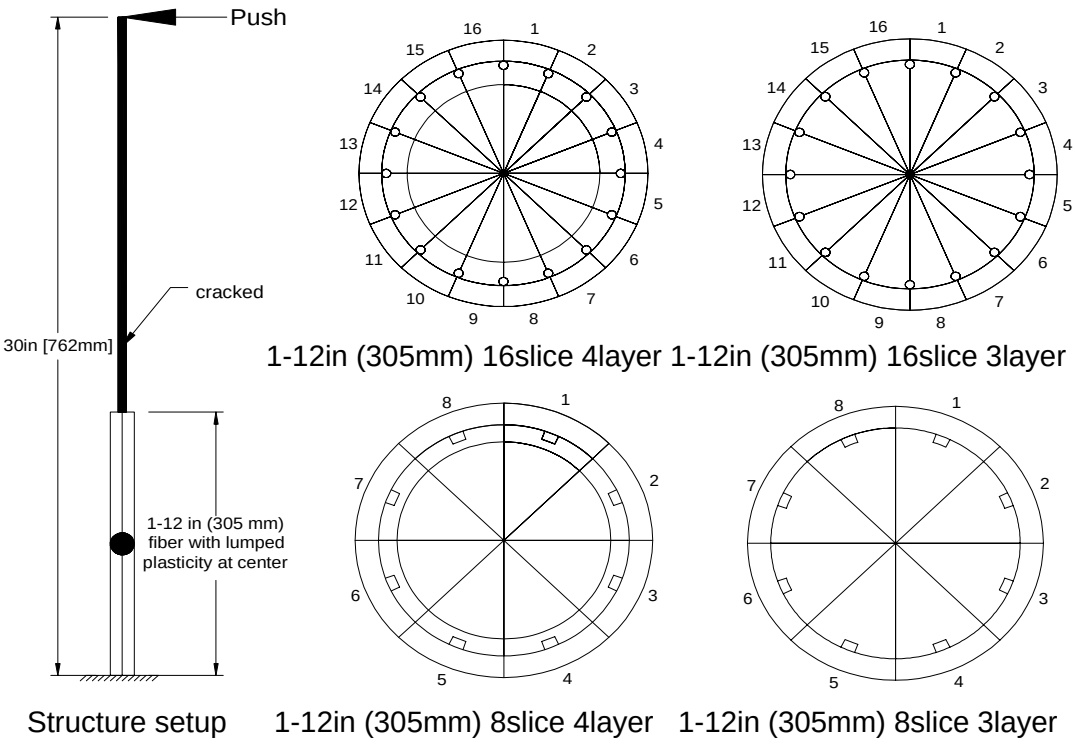

Figure 7-22: Fiber configurations considered for load-deflection comparison.

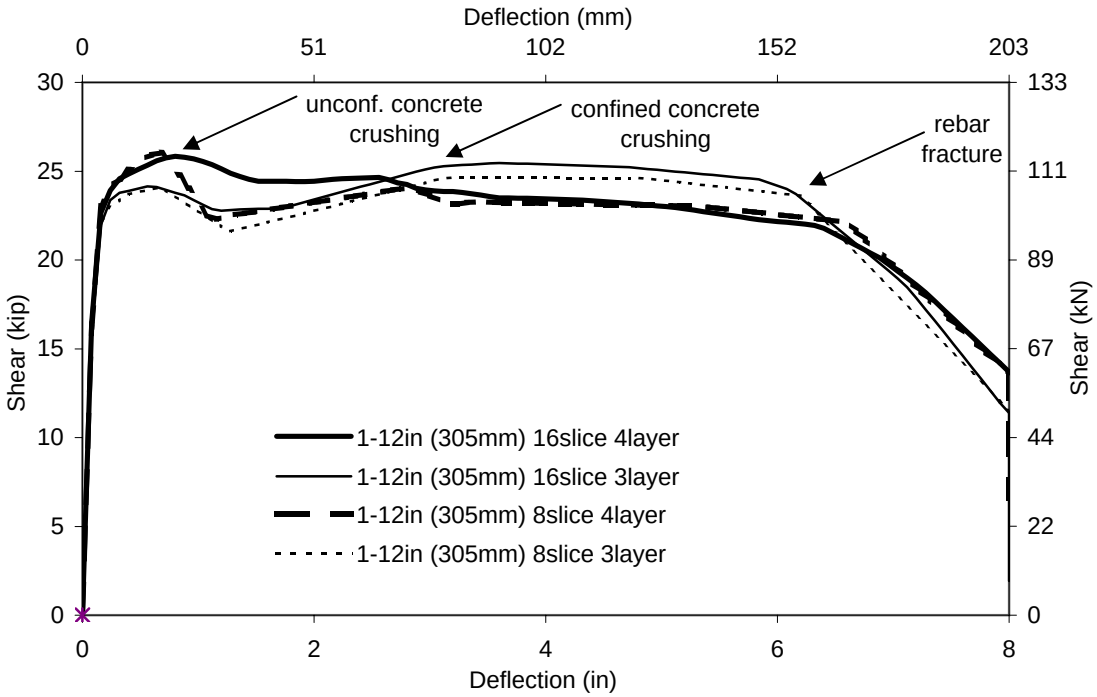

Figure 7-23: Load-deflection comparison of different fiber configurations.

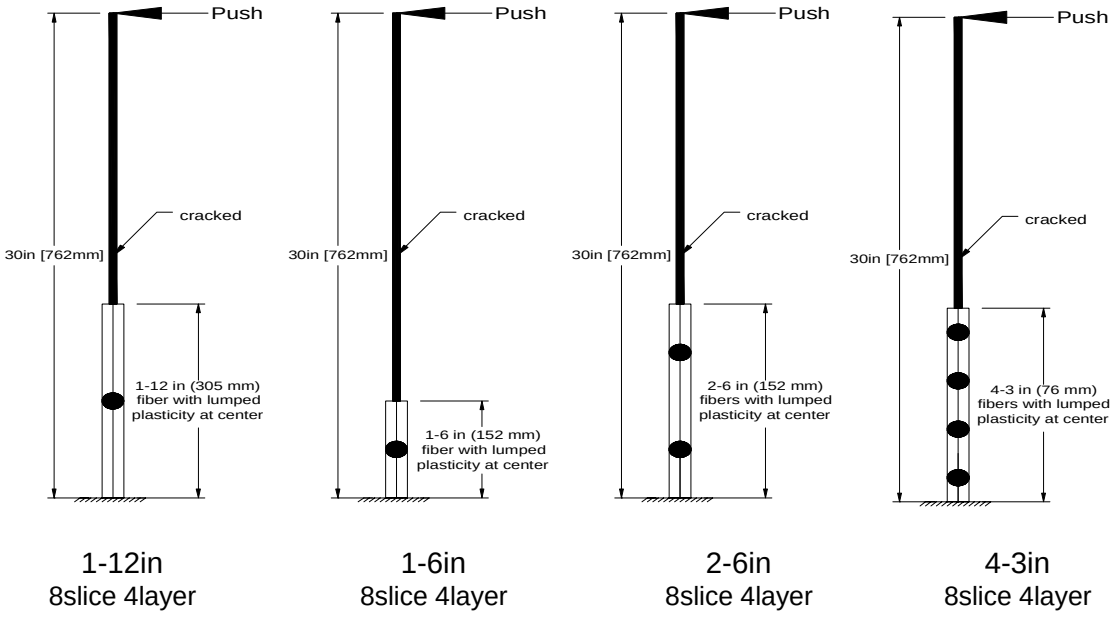

Figure 7-24: Element configurations considered for load-deflection comparison.

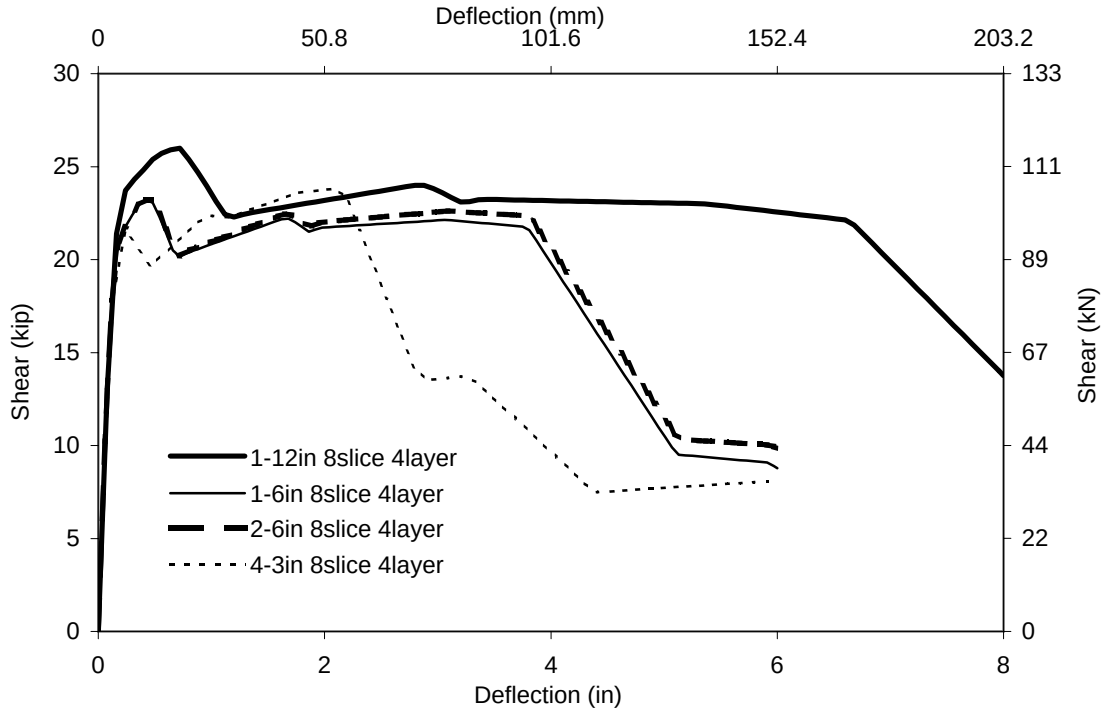

Figure 7-25: Cantilever load-deflection comparison of different element configurations.

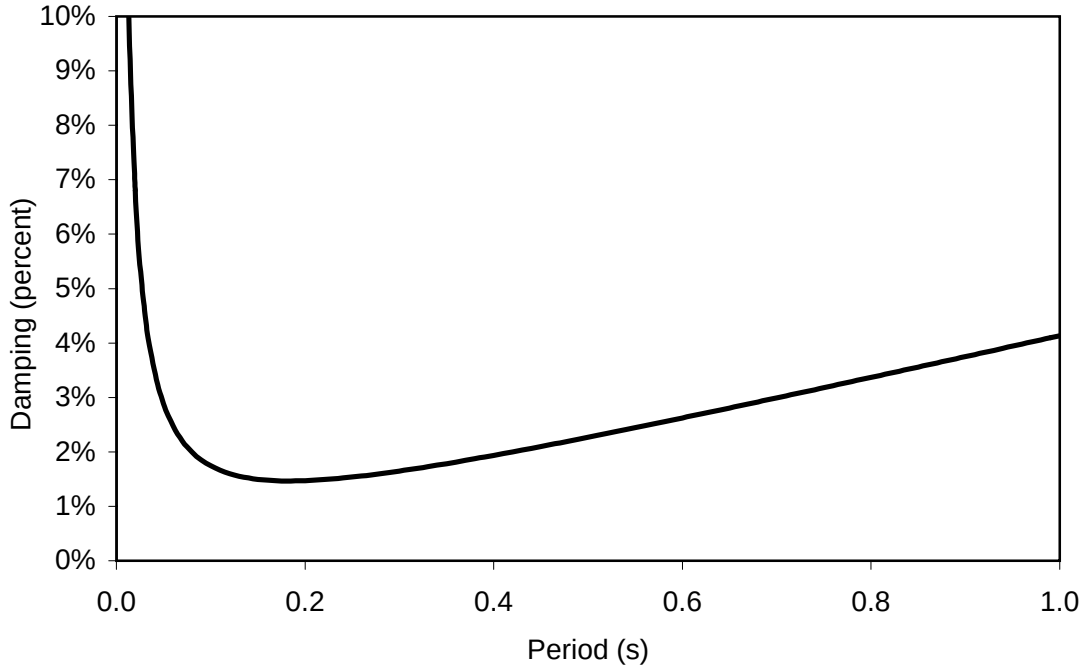

Figure 7-26: Combination of mass and stiffness proportional damping used in analyses.

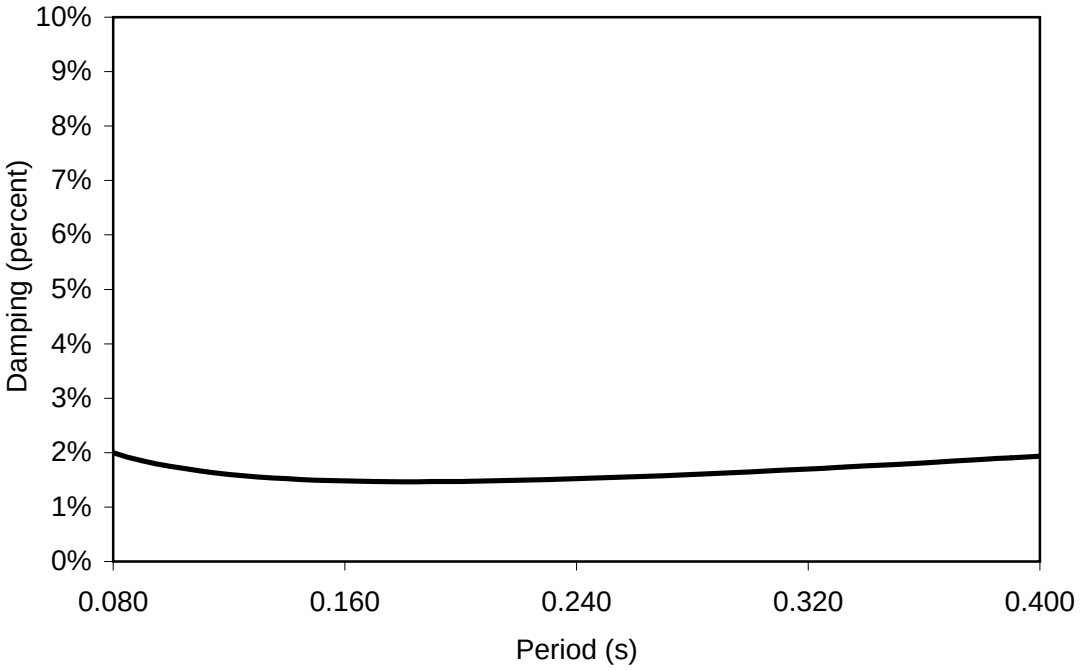

Figure 7-27: Combination of mass and stiffness proportional damping used in analyses (between first and third transverse modes).

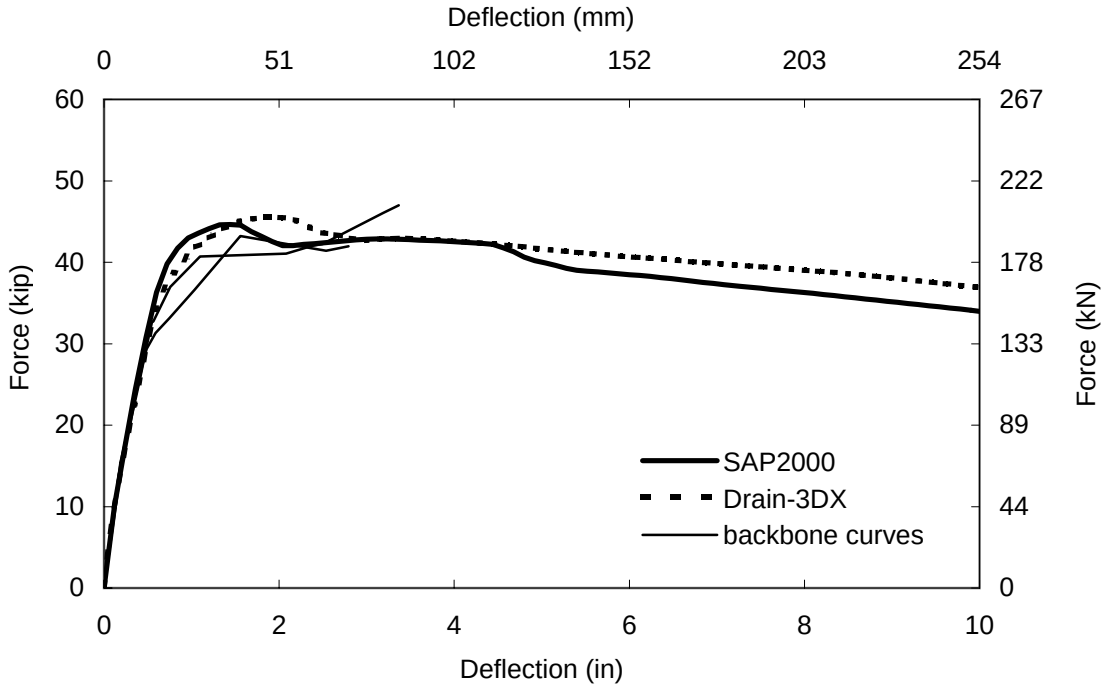

Figure 7-28: Comparison of bent-1 pushover analyses using SAP2000 and Drain-3DX with superimposed acceleration backbone curves multiplied by tributary mass.

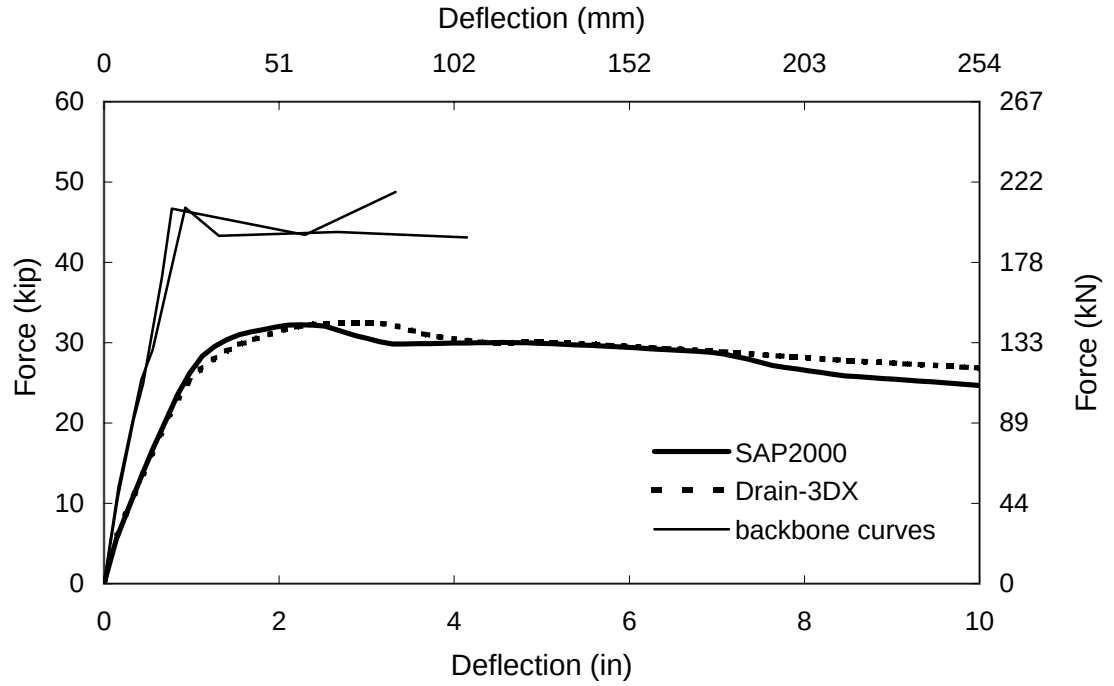

Figure 7-29: Comparison of bent-2 pushover analyses using SAP2000 and Drain-3DX with superimposed acceleration backbone curves multiplied by tributary mass.

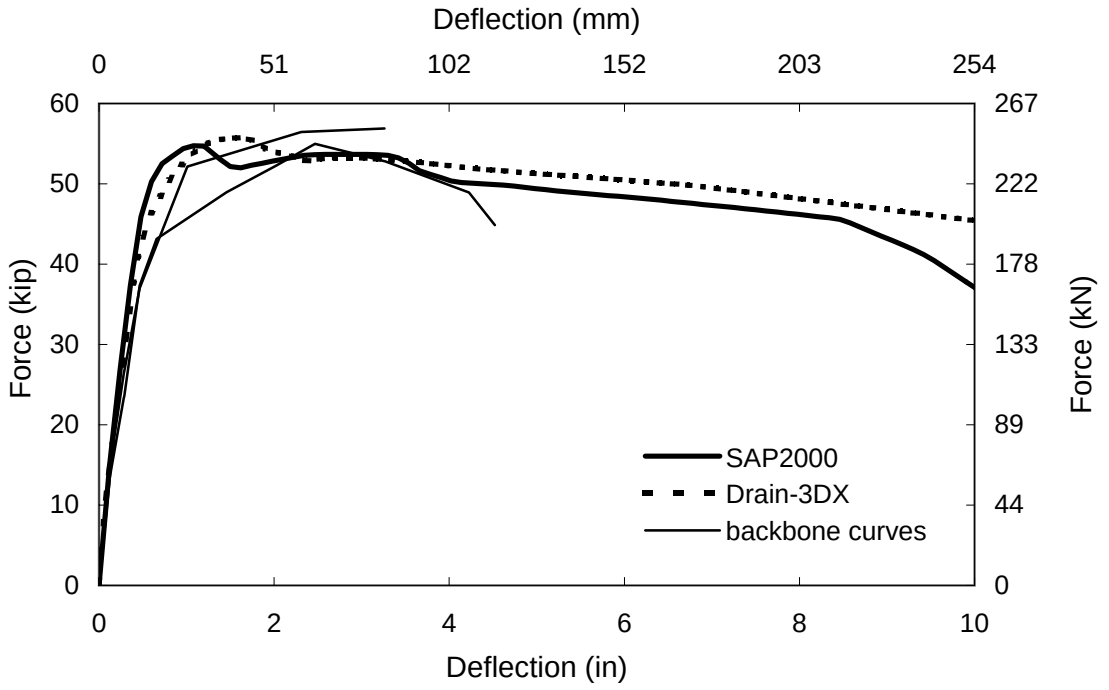

Figure 7-30: Comparison of bent-3 pushover analyses using SAP2000 and Drain-3DX with superimposed acceleration backbone curves multiplied by tributary mass.

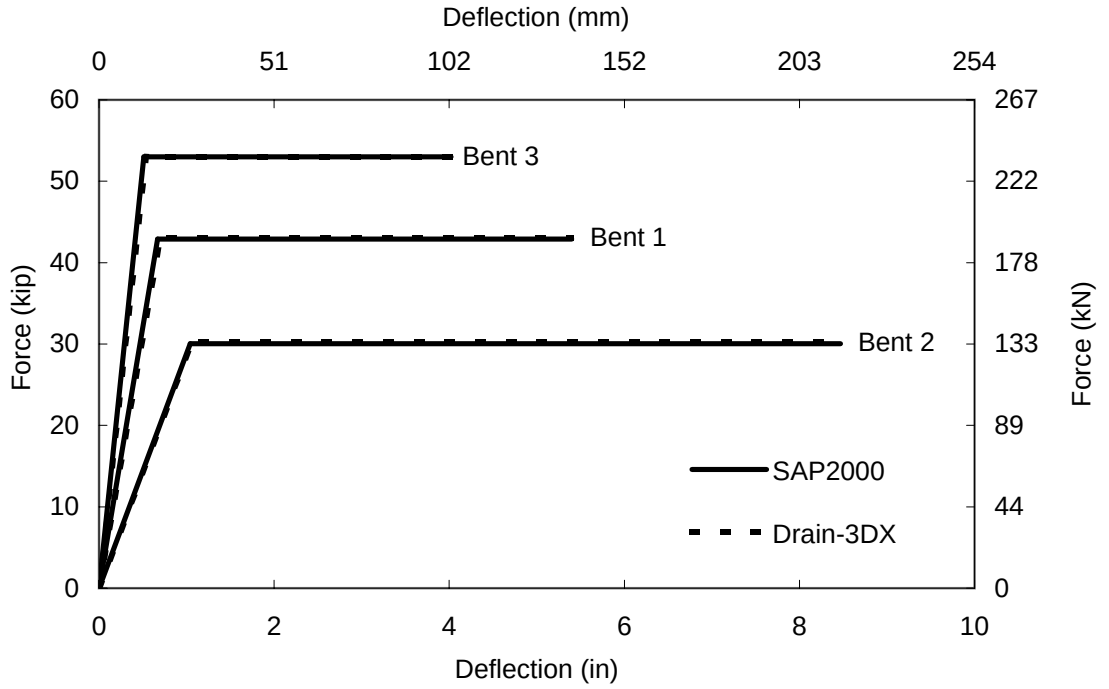

Figure 7-31: Comparison of bents 1-3 idealized elasto-plastic pushover analyses using SAP2000 and Drain-3DX.

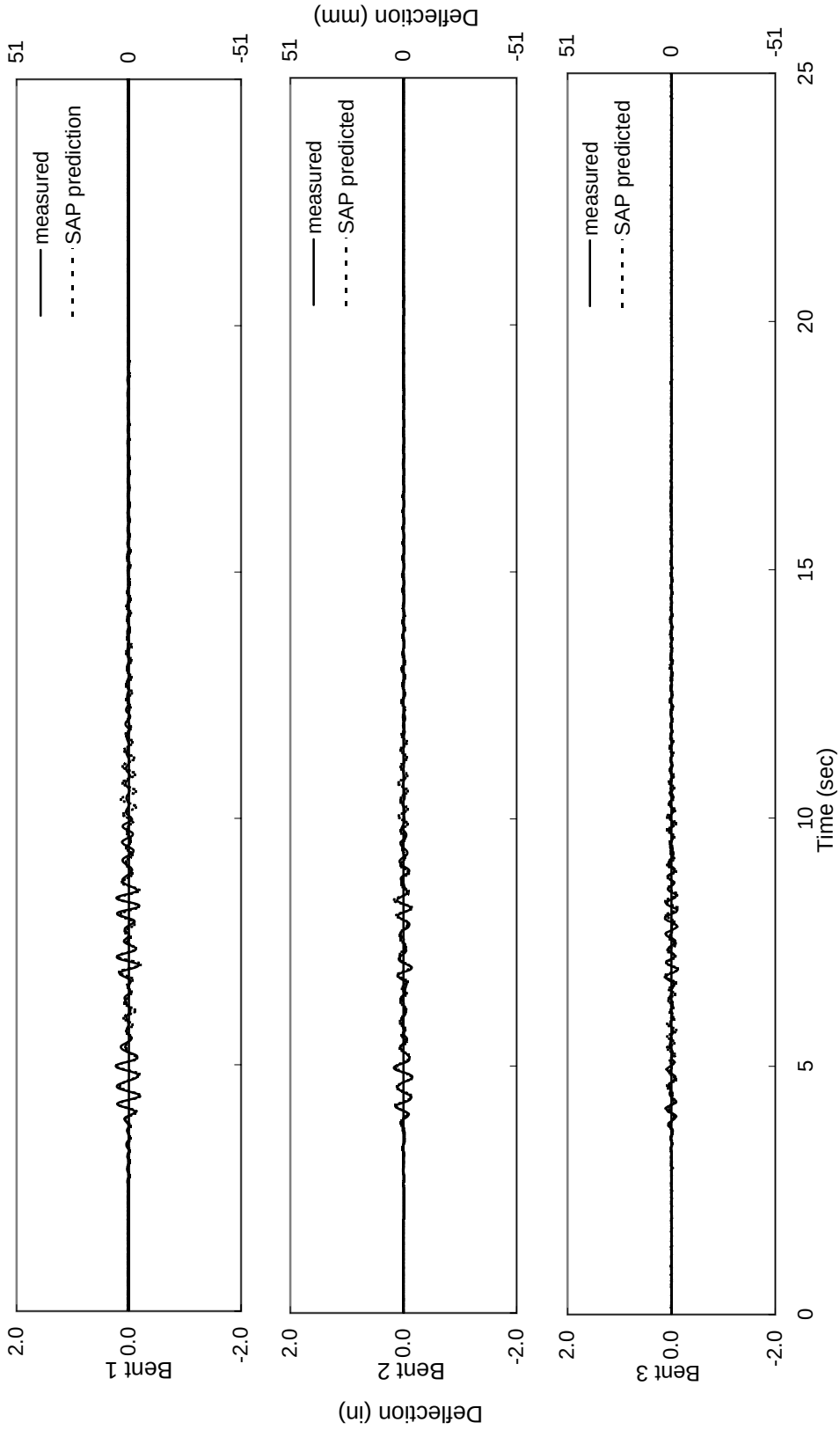

Figure 7-32: SAP2000 column deflection predictions for test 12.

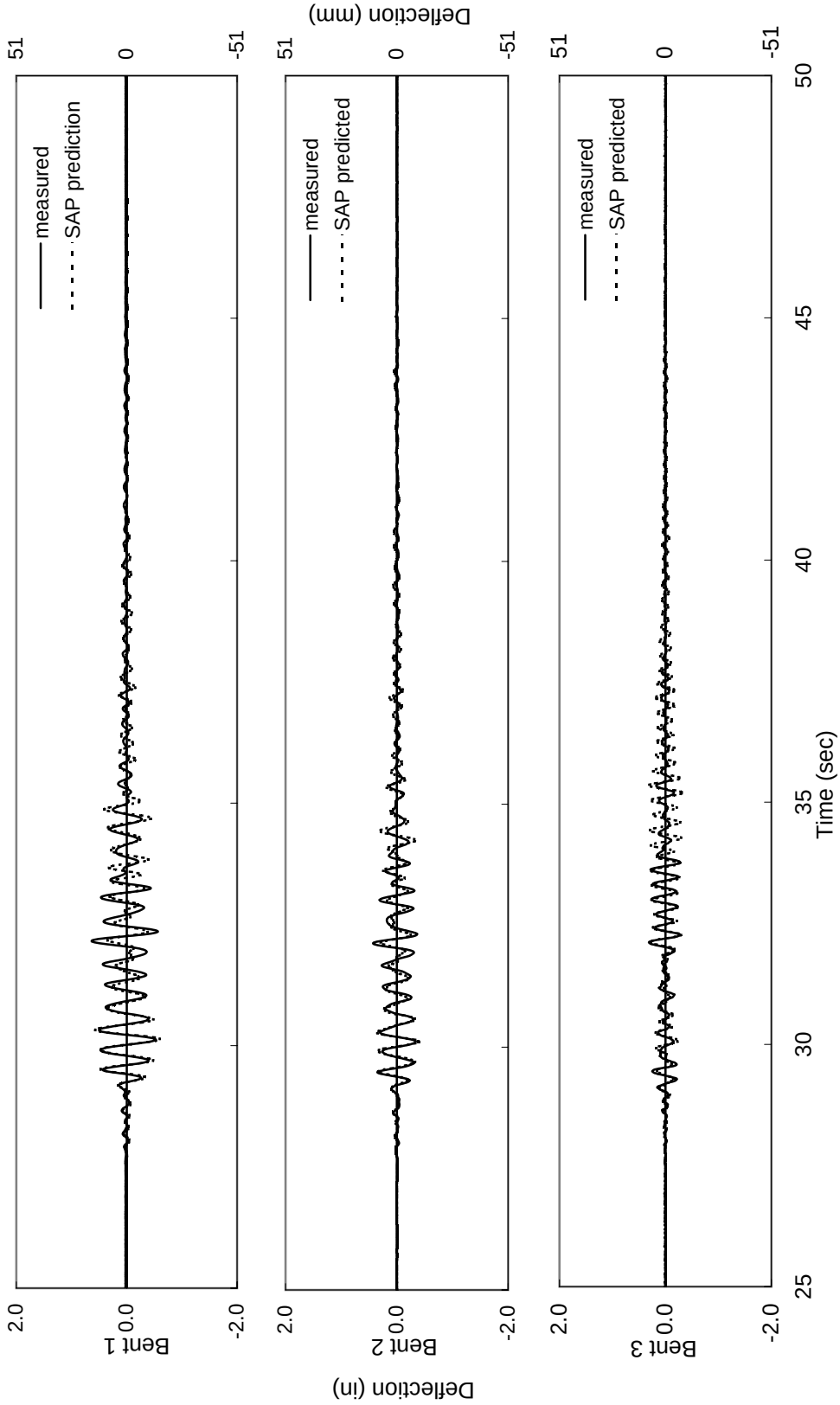

Figure 7-33: SAP2000 column deflection predictions for test 13.

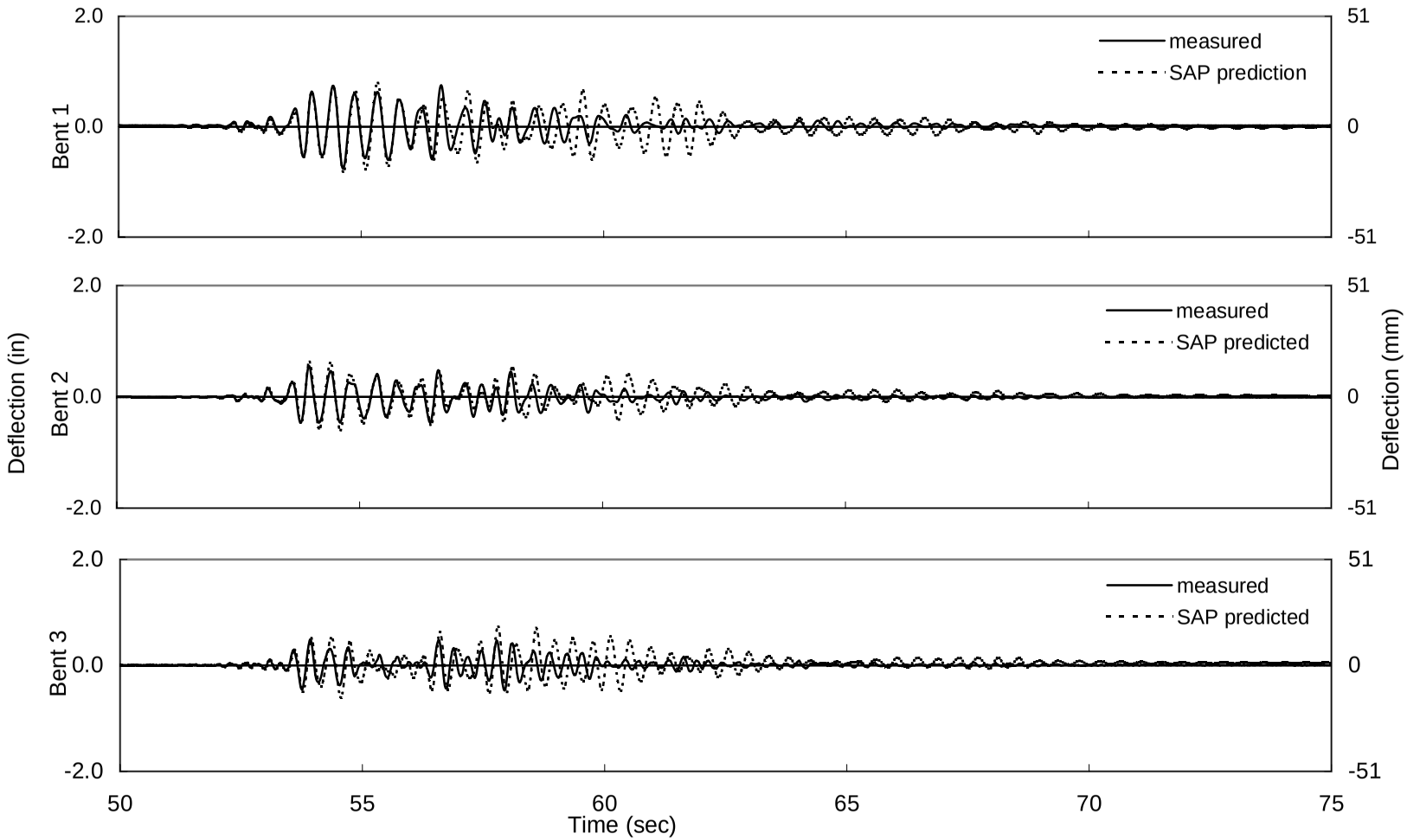

Figure 7-34: SAP2000 column deflection predictions for test 14.

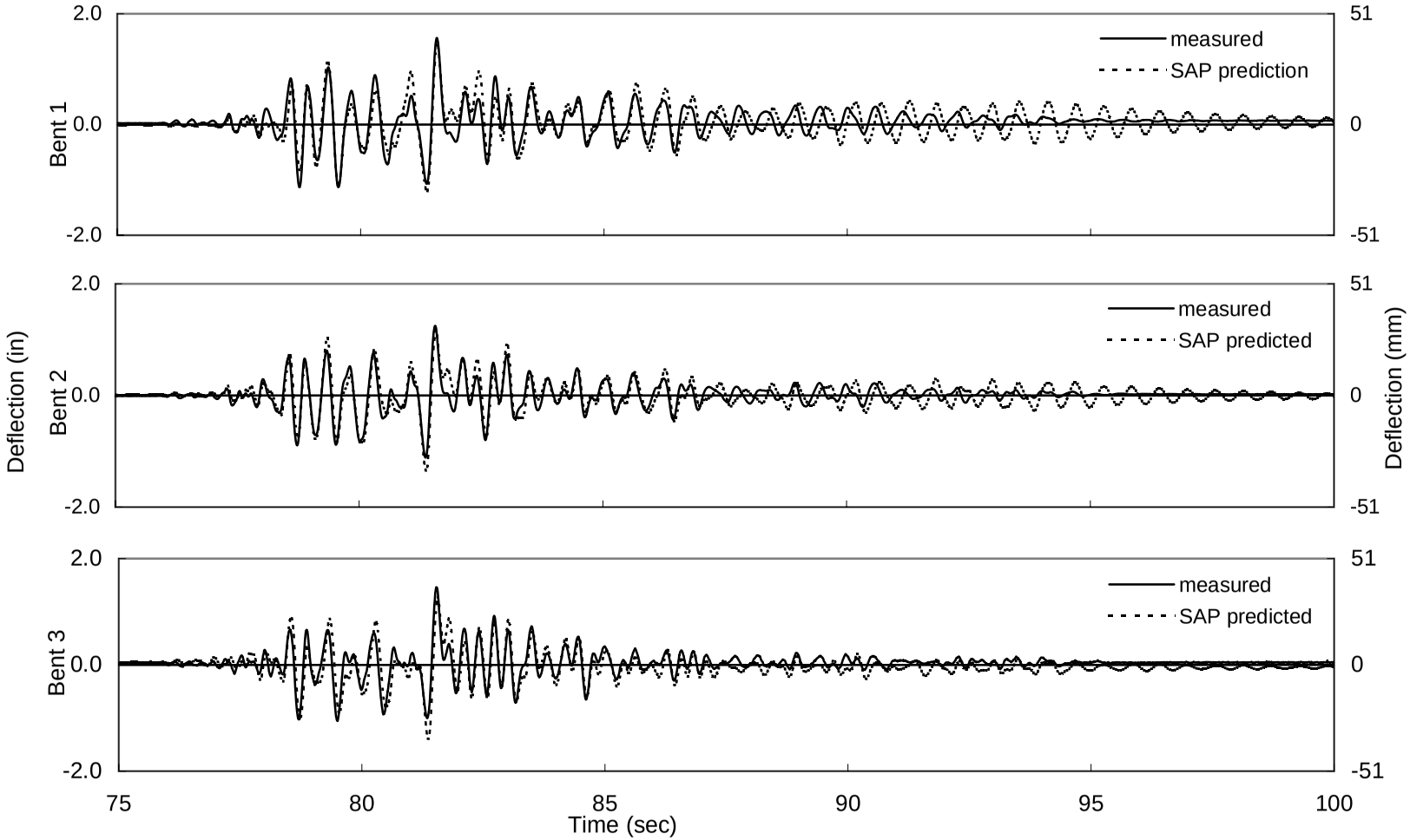

Figure 7-35: SAP2000 column deflection predictions for test 15.

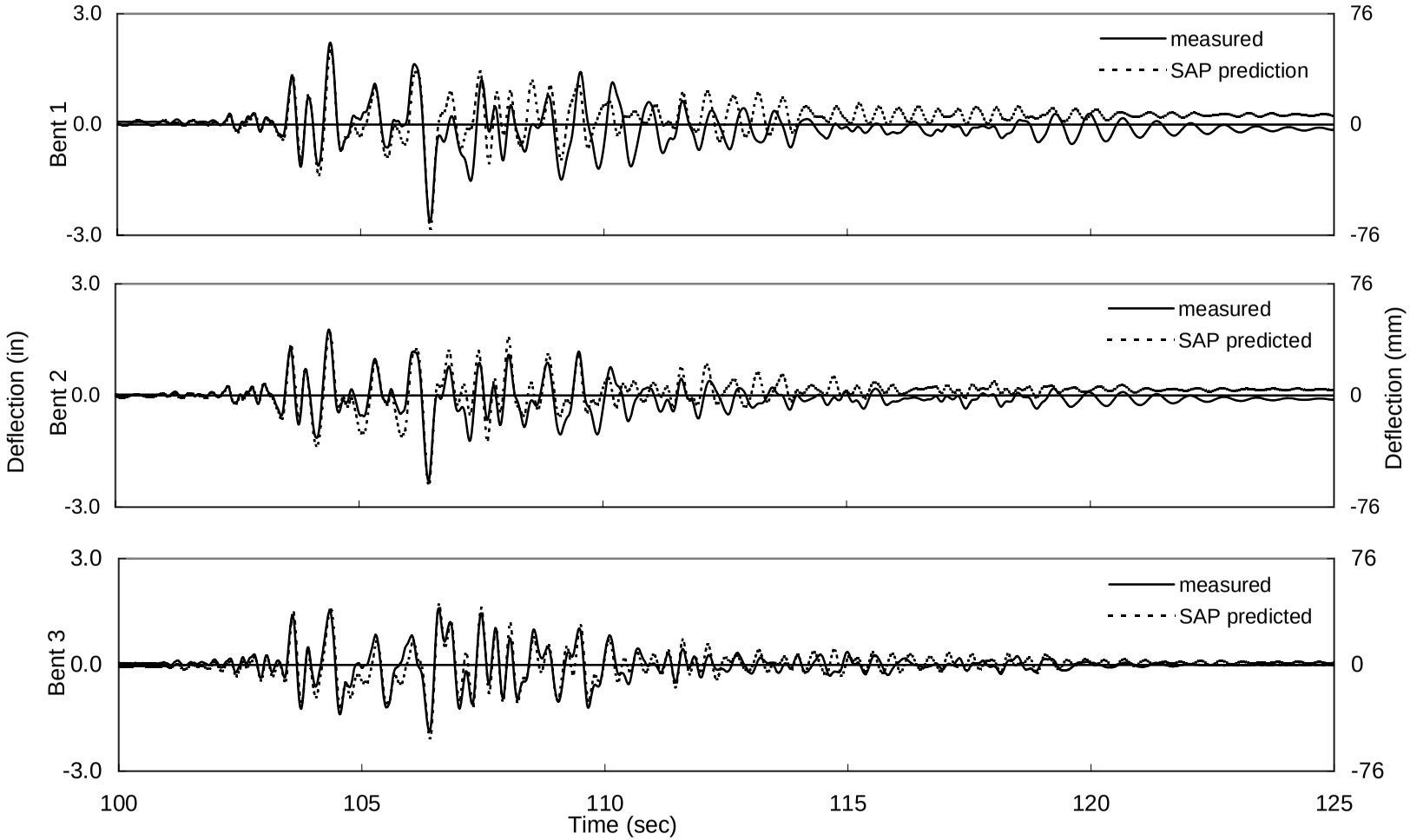

Figure 7-36: SAP2000 column deflection predictions for test 16.

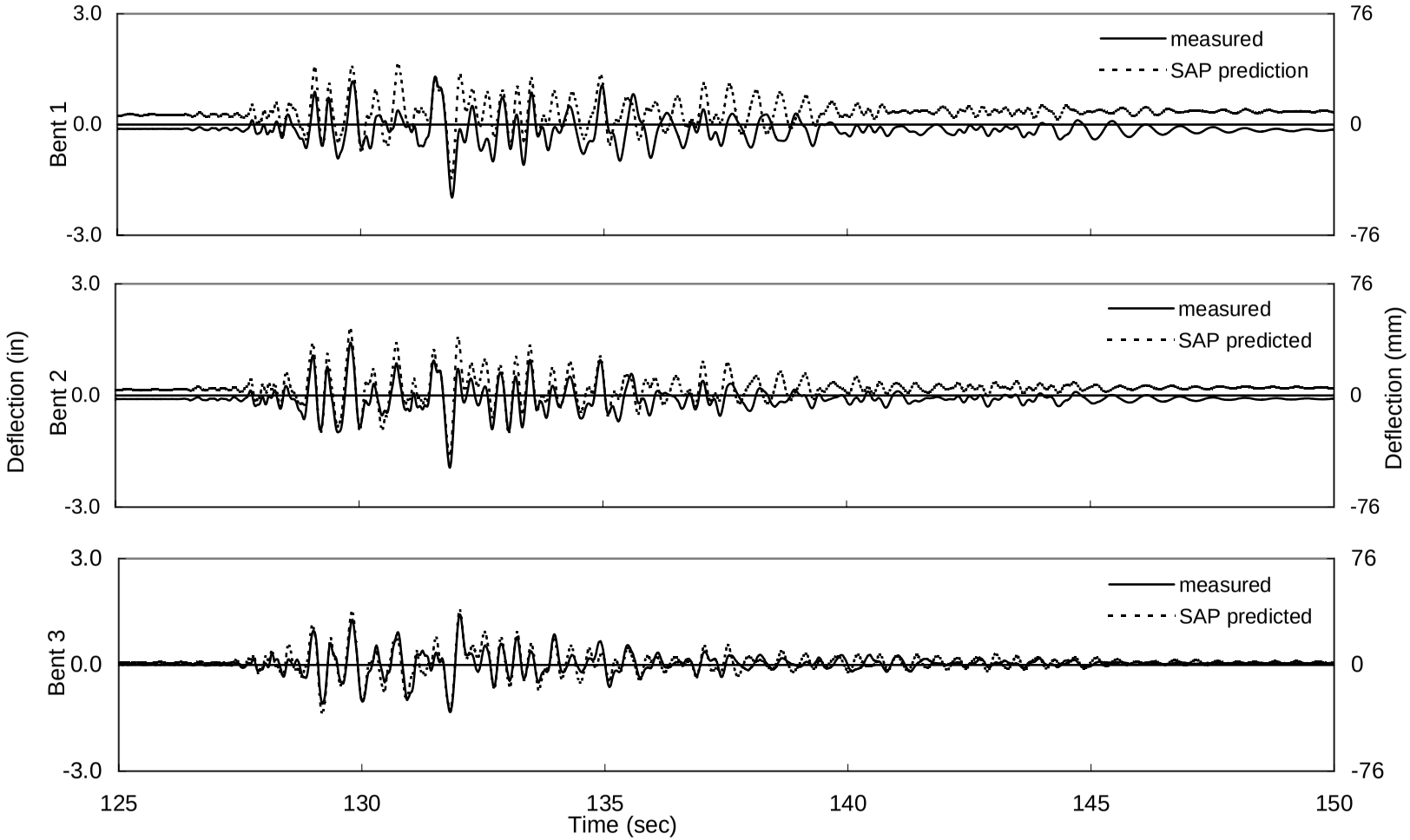

Figure 7-37: SAP2000 column deflection predictions for test 17.

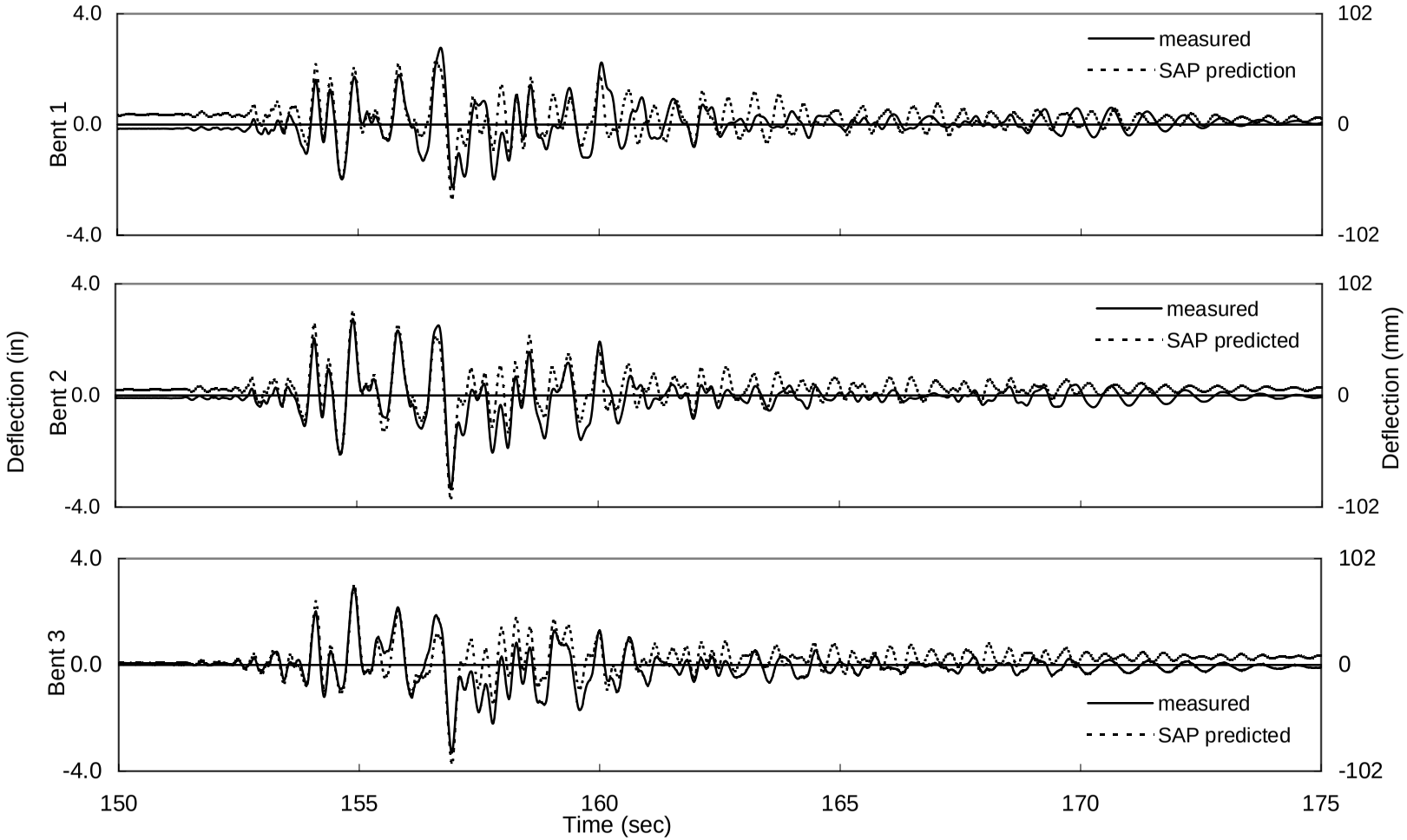

Figure 7-38: SAP2000 column deflection predictions for test 18.

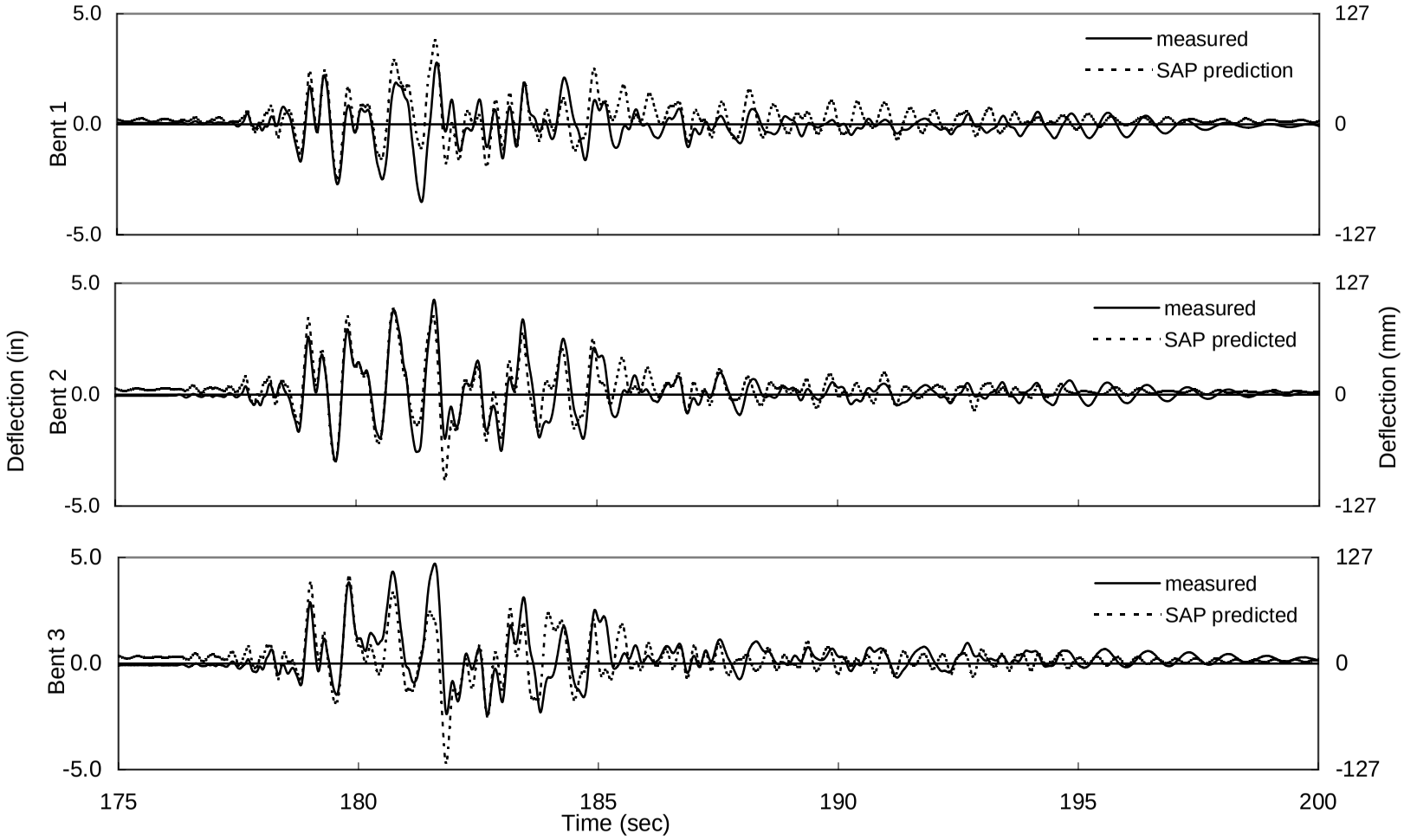

Figure 7-39: SAP2000 column deflection predictions for test 19.

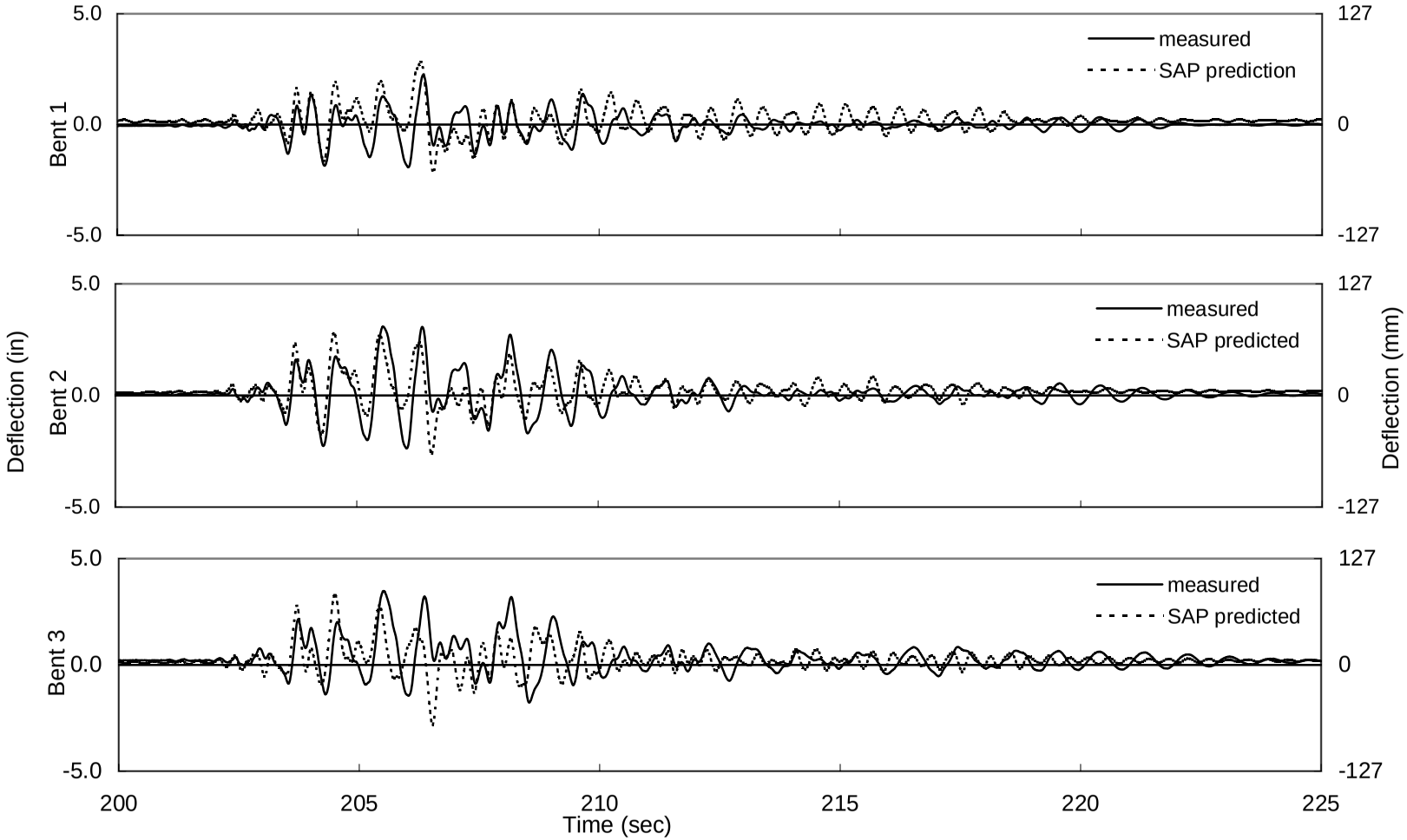

Figure 7-40: SAP2000 column deflection predictions for test 20.

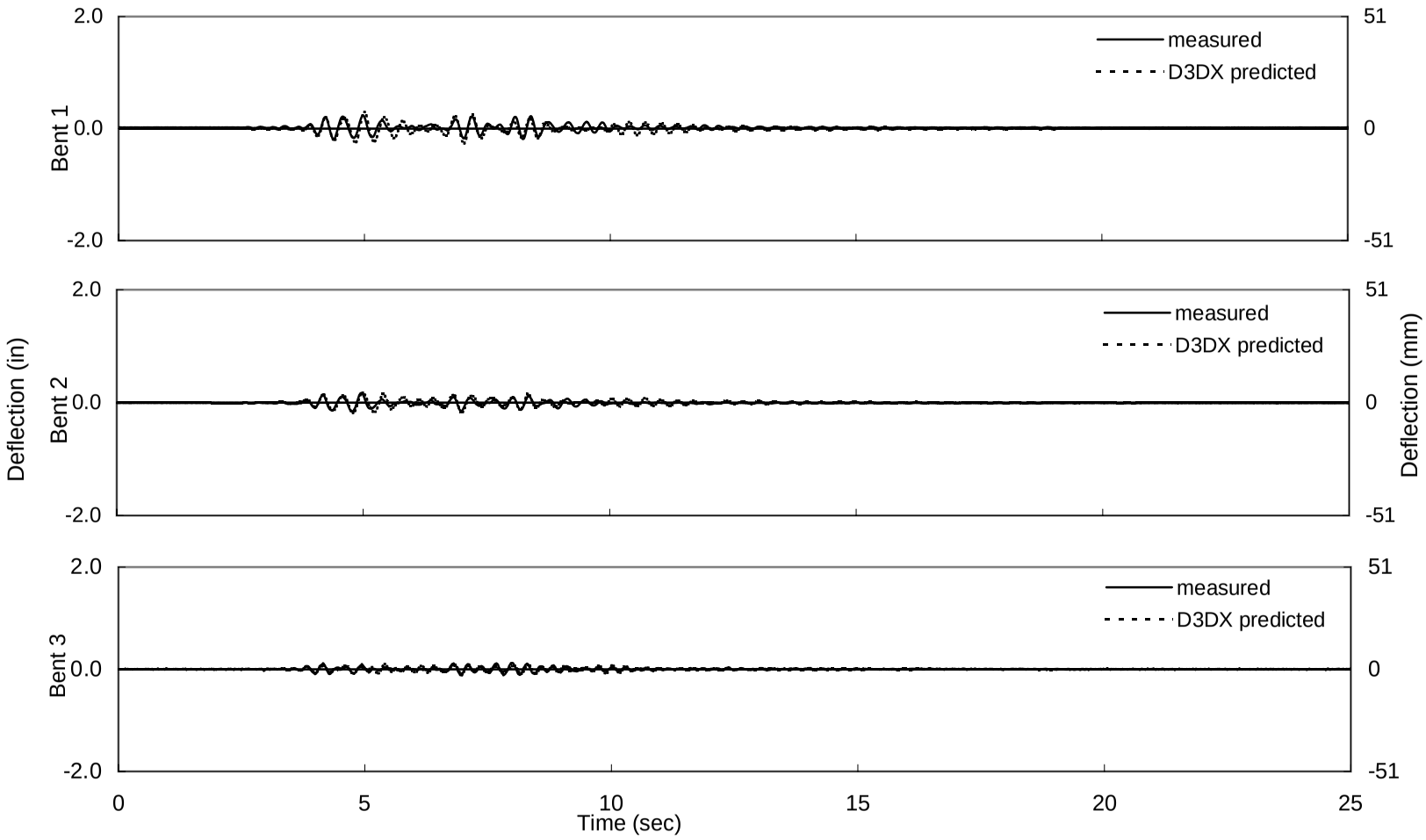

Figure 7-41: Drain-3DX column deflection predictions for test 12.

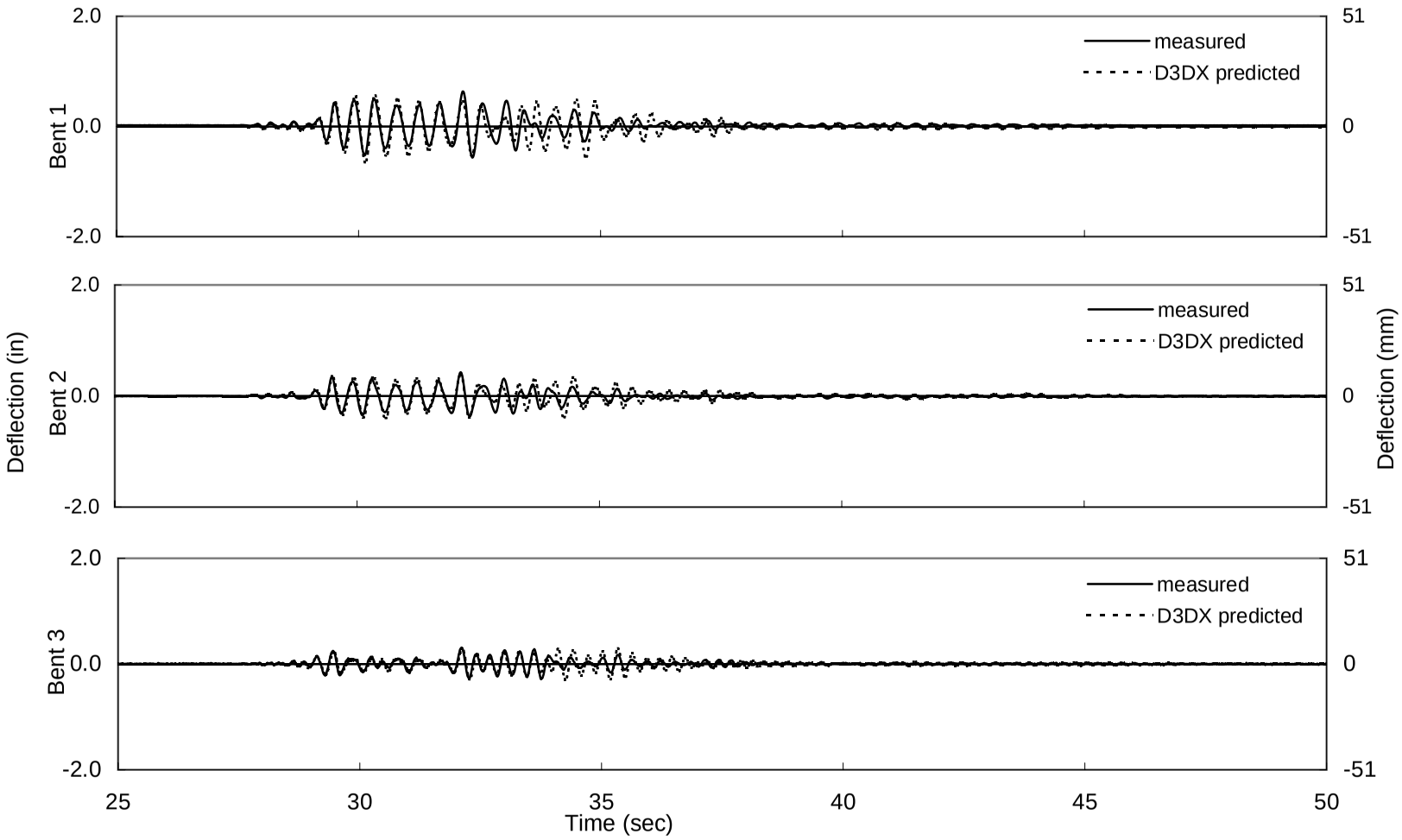

Figure 7-42: Drain-3DX column deflection predictions for test 13.

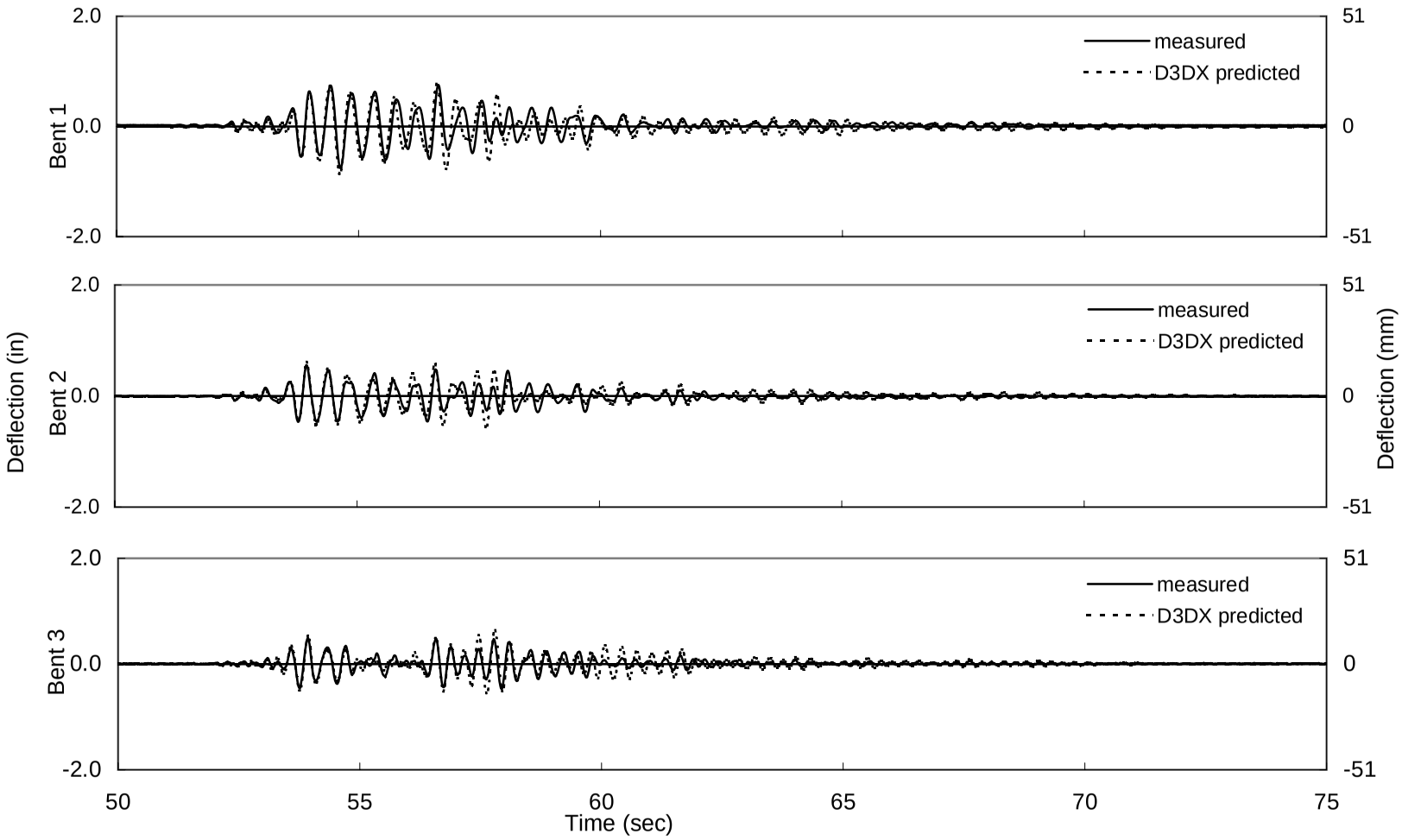

Figure 7-43: Drain-3DX column deflection predictions for test 14.

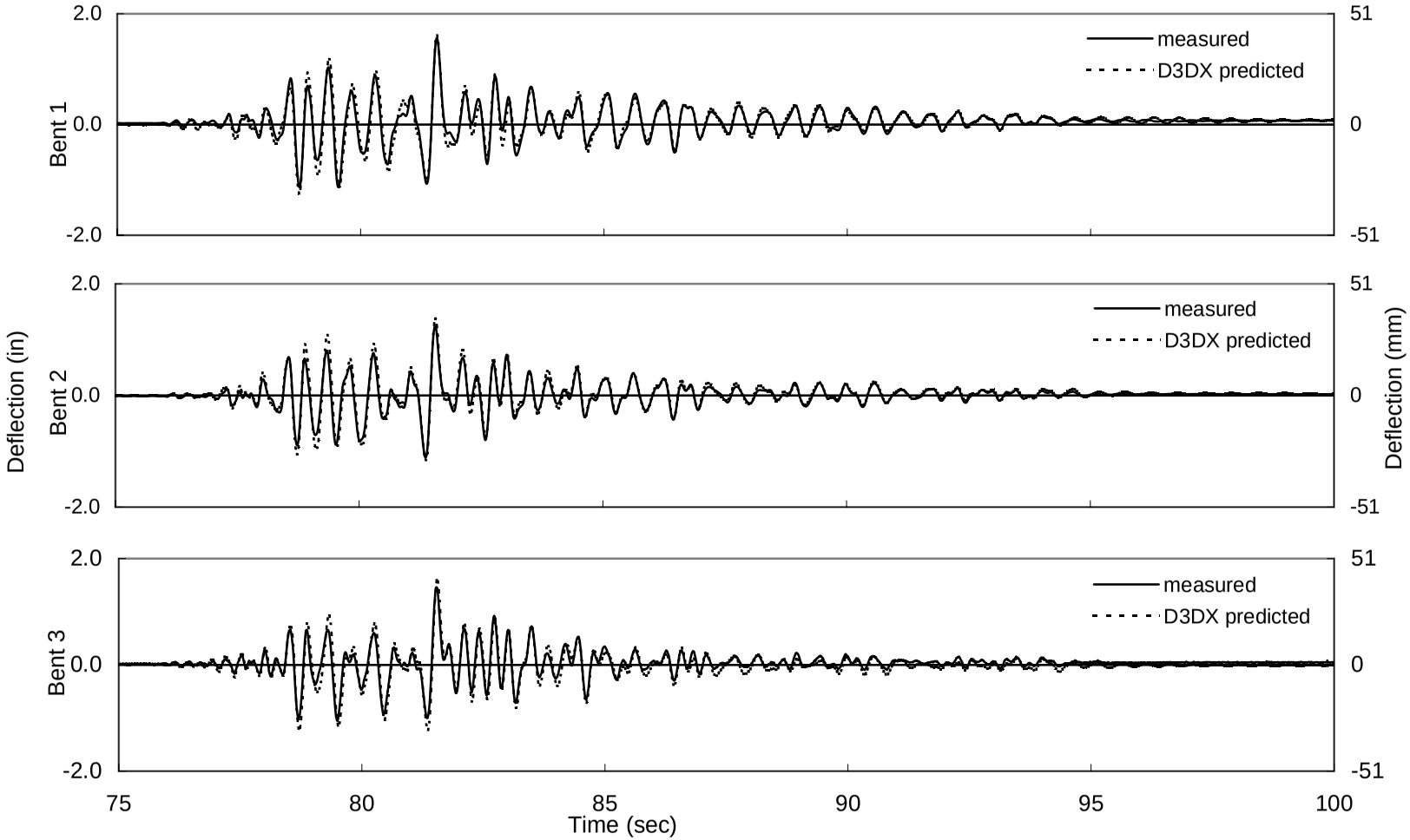

Figure 7-44: Drain-3DX column deflection predictions for test 15.

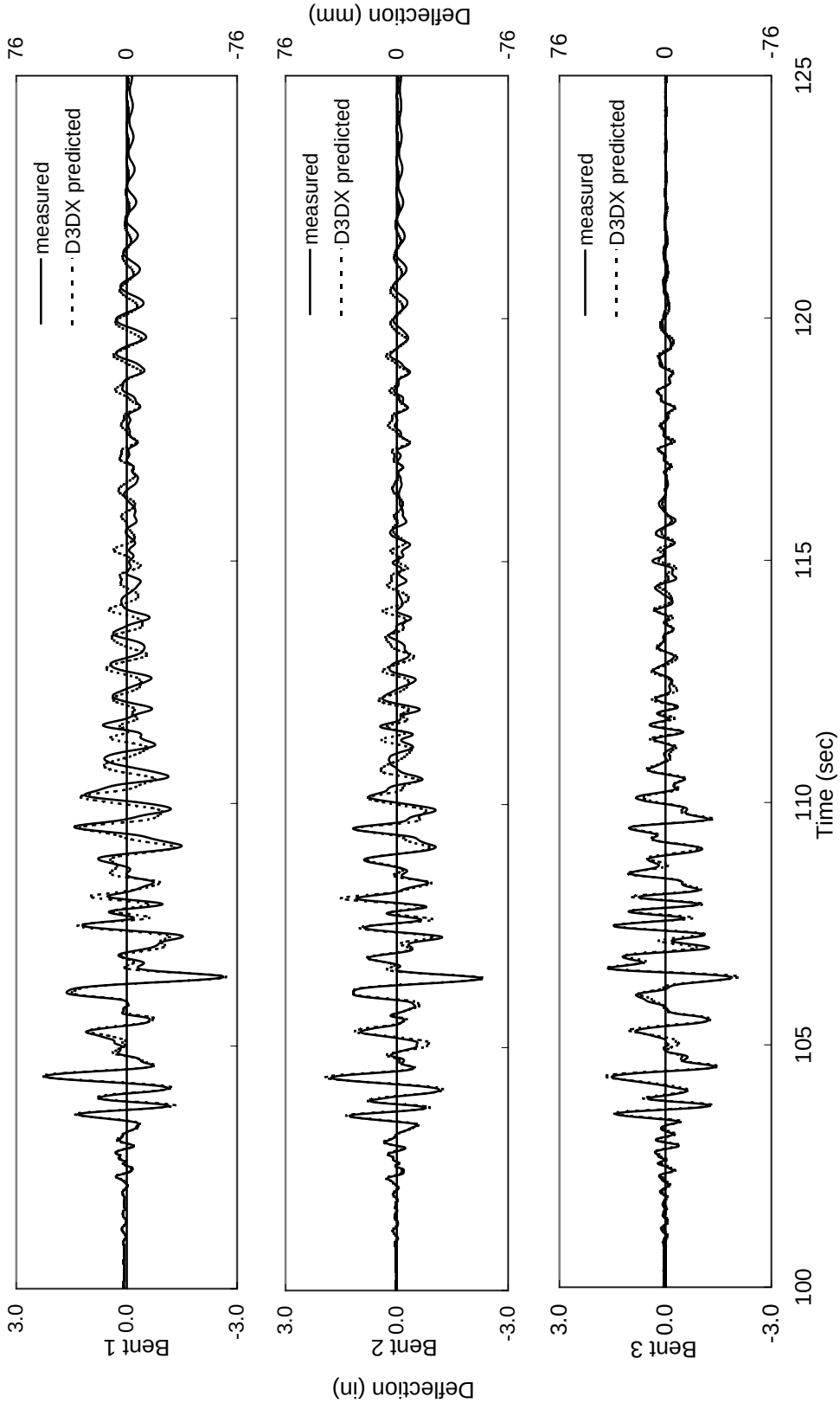

Figure 7-45: Drain-3DX column deflection predictions for test 16.

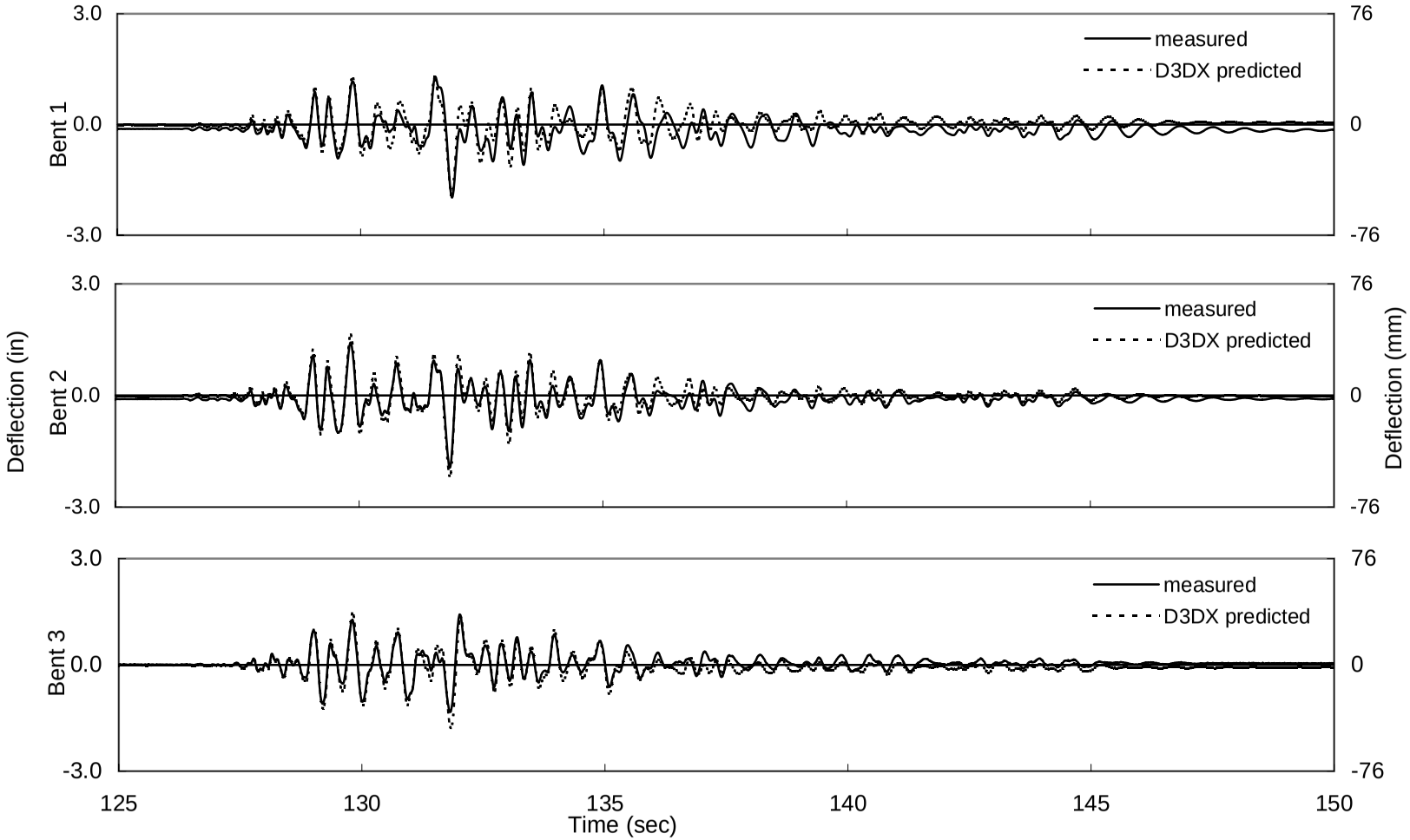

Figure 7-46: Drain-3DX column deflection predictions for test 17.

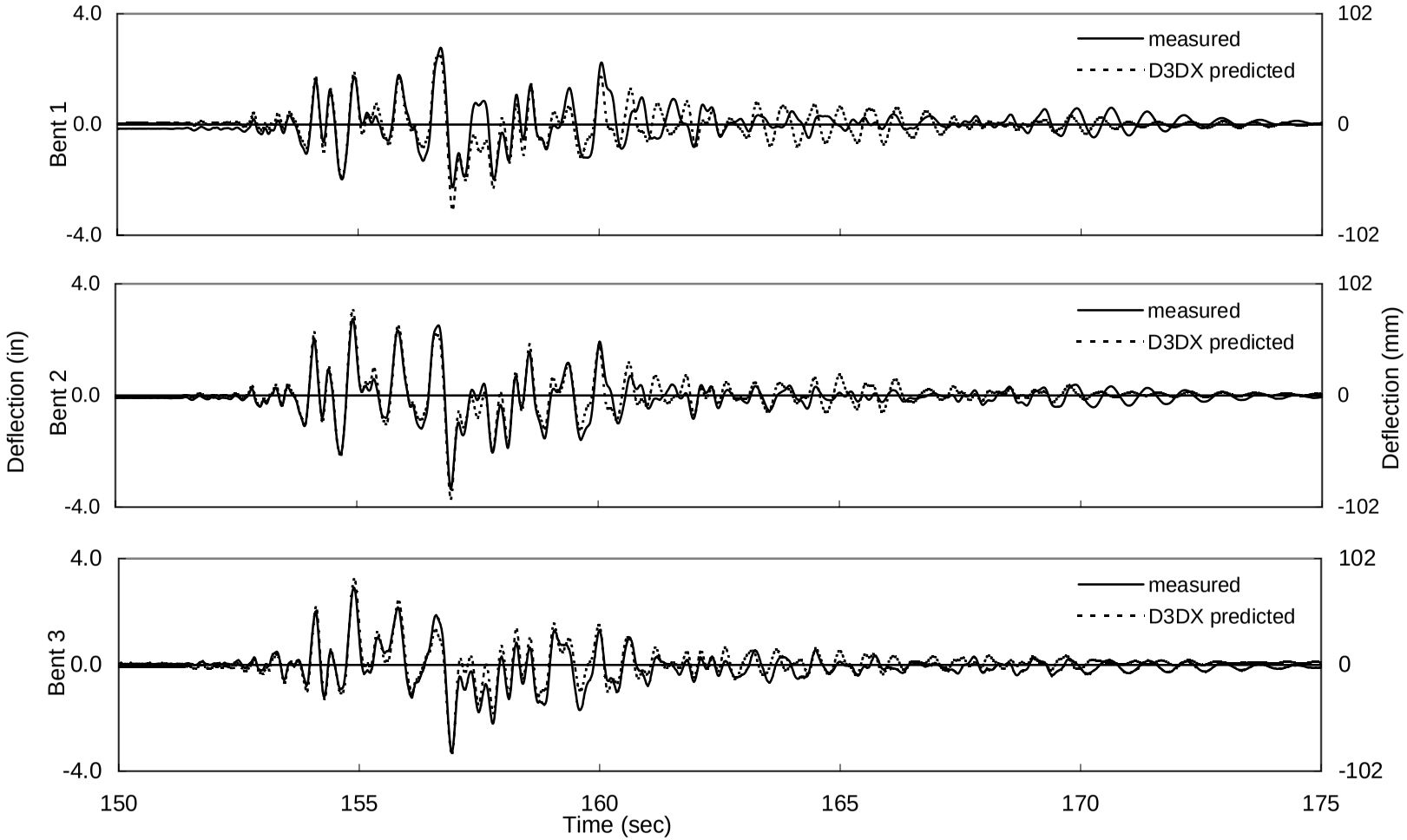

Figure 7-47: Drain-3DX column deflection predictions for test 18.

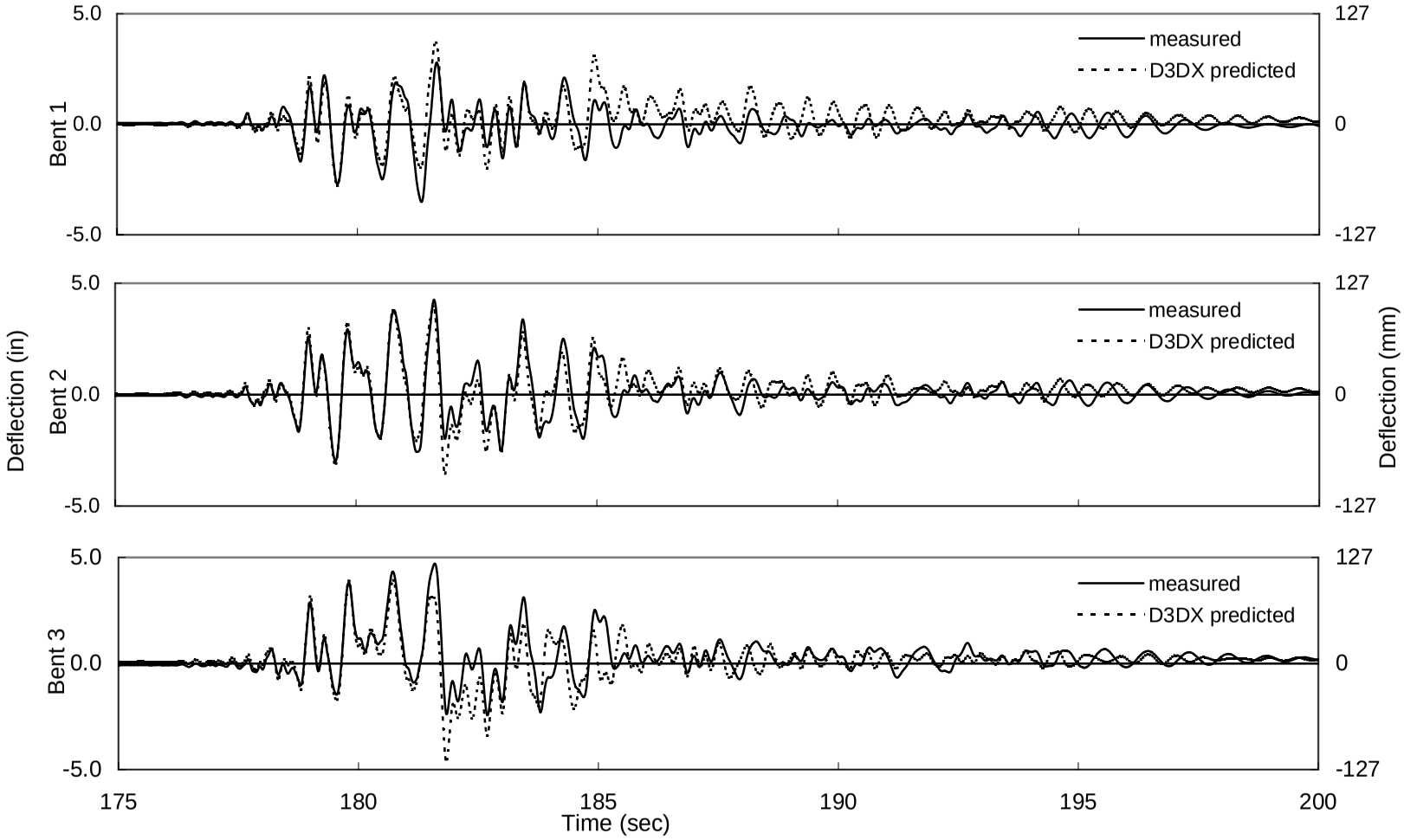

Figure 7-48: Drain-3DX column deflection predictions for test 19.

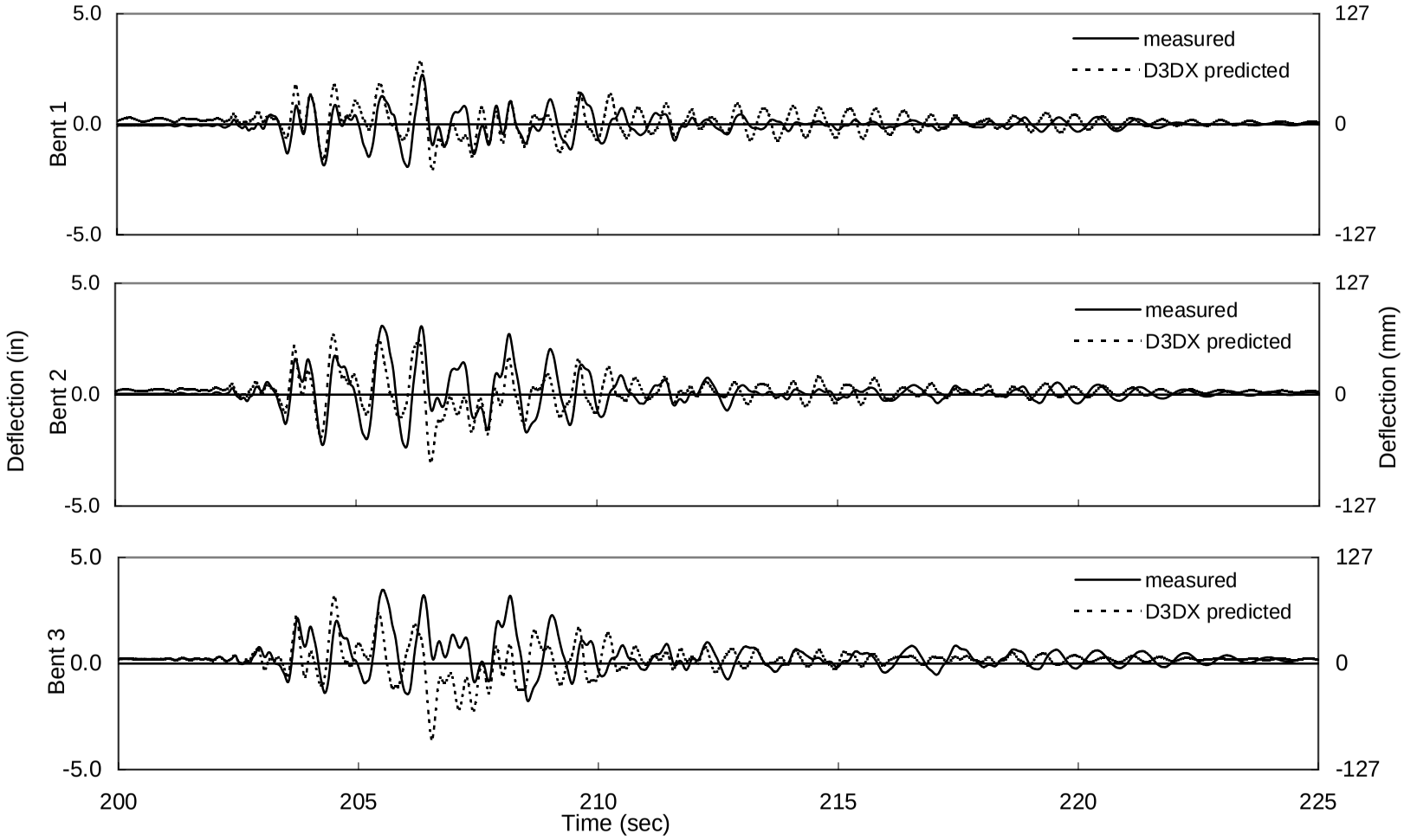

Figure 7-49: Drain-3DX column deflection predictions for test 20.

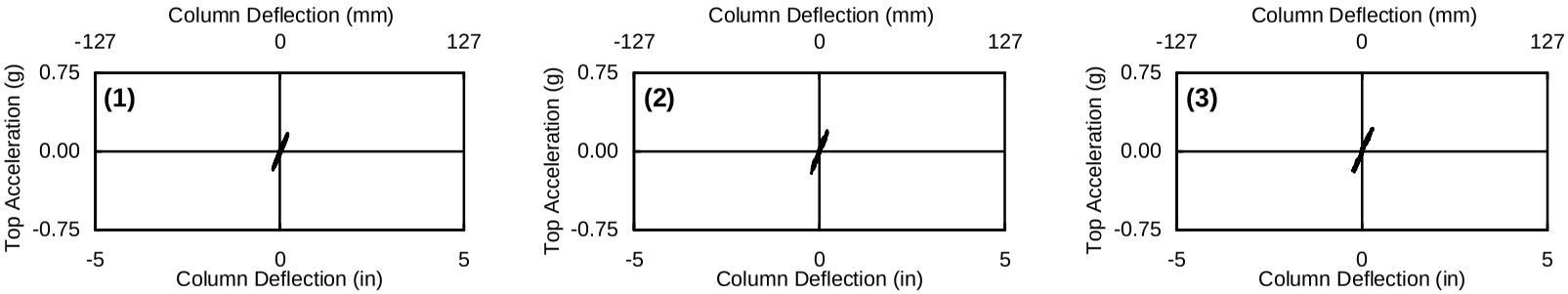

Figure 7-50: Bent1 run 12 acceleration-deflection comparison of measured data (1) with SAP2000 (2) and Drain-3DX (3).

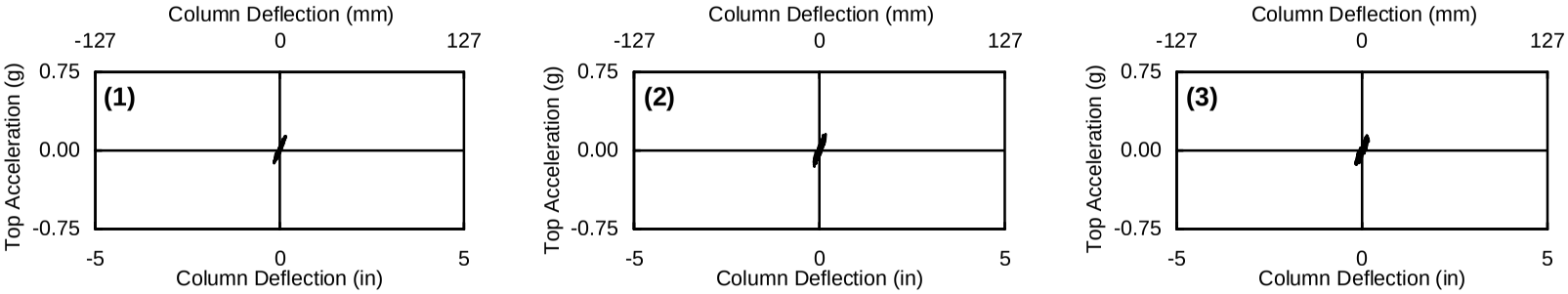

Figure 7-51: Bent2 run 12 acceleration-deflection comparison of measured data (1) with SAP2000 (2) and Drain-3DX (3).

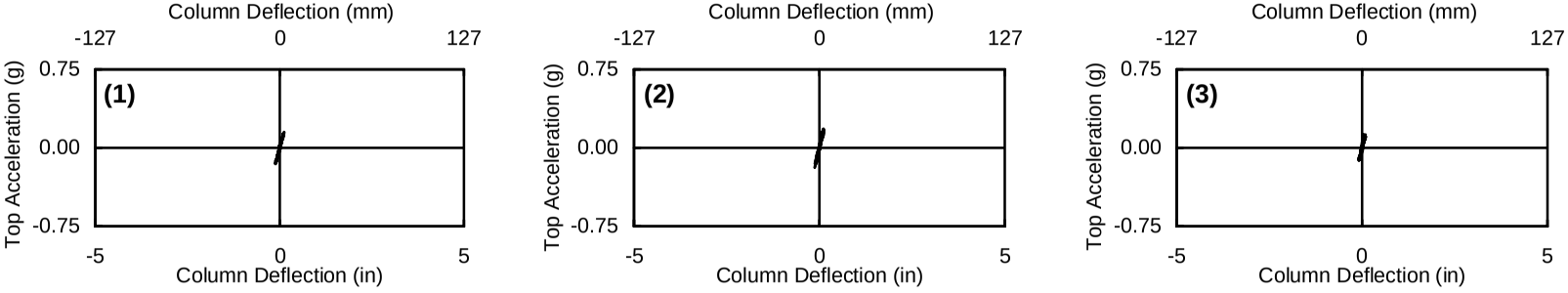

Figure 7-52: Bent3 run 12 acceleration-deflection comparison of measured data (1) with SAP2000 (2) and Drain-3DX (3).

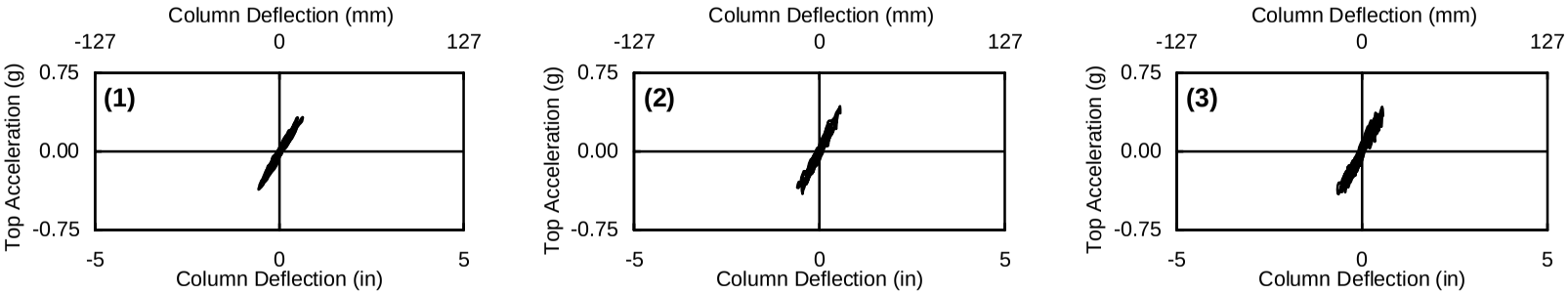

Figure 7-53: Bent1 run 13 acceleration-deflection comparison of measured data (1) with SAP2000 (2) and Drain-3DX (3).

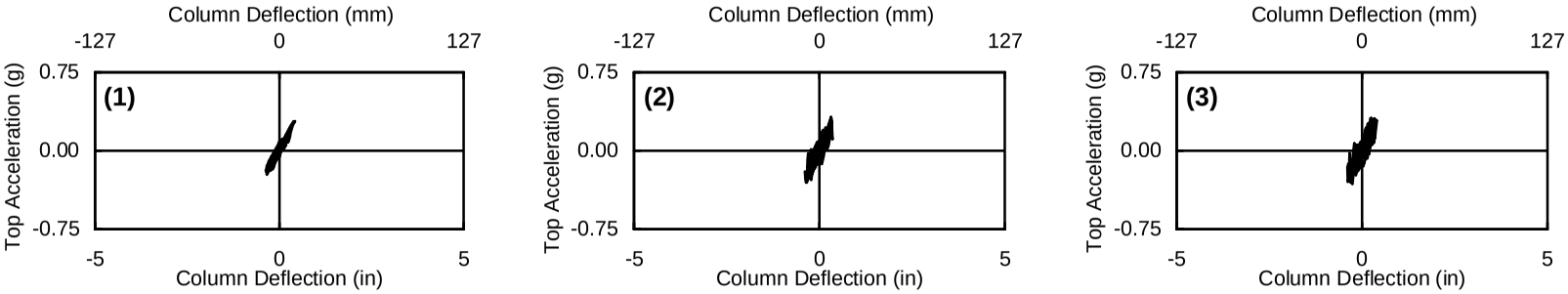

Figure 7-54: Bent2 run 13 acceleration-deflection comparison of measured data (1) with SAP2000 (2) and Drain-3DX (3).

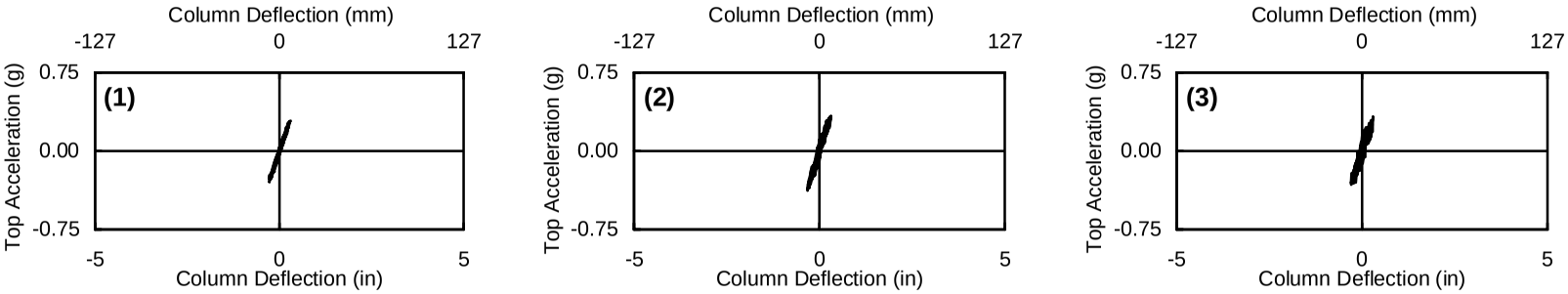

Figure 7-55: Bent3 run 13 acceleration-deflection comparison of measured data (1) with SAP2000 (2) and Drain-3DX (3).

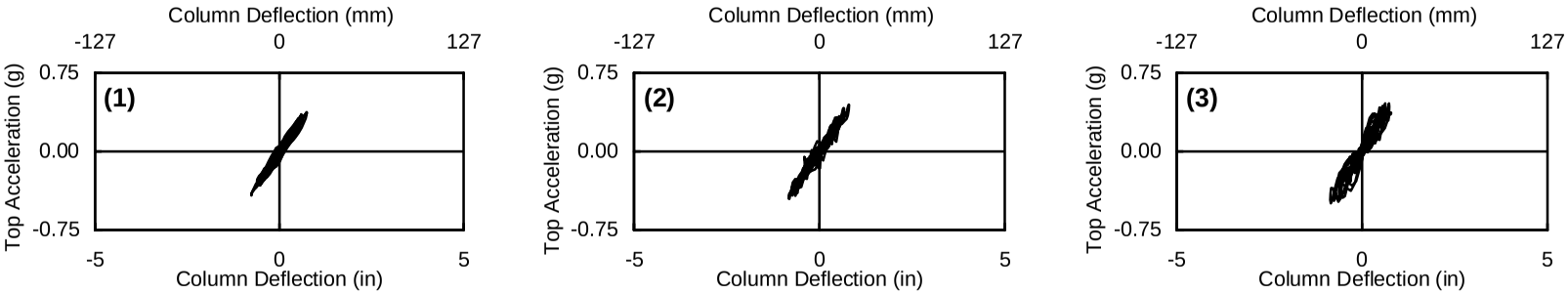

Figure 7-56: Bent1 run 14 acceleration-deflection comparison of measured data (1) with SAP2000 (2) and Drain-3DX (3).

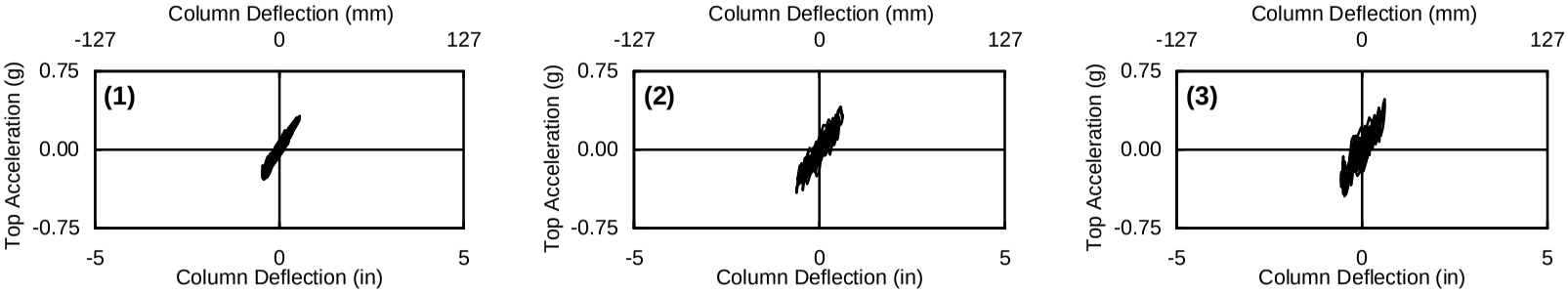

Figure 7-57: Bent2 run 14 acceleration-deflection comparison of measured data (1) with SAP2000 (2) and Drain-3DX (3).

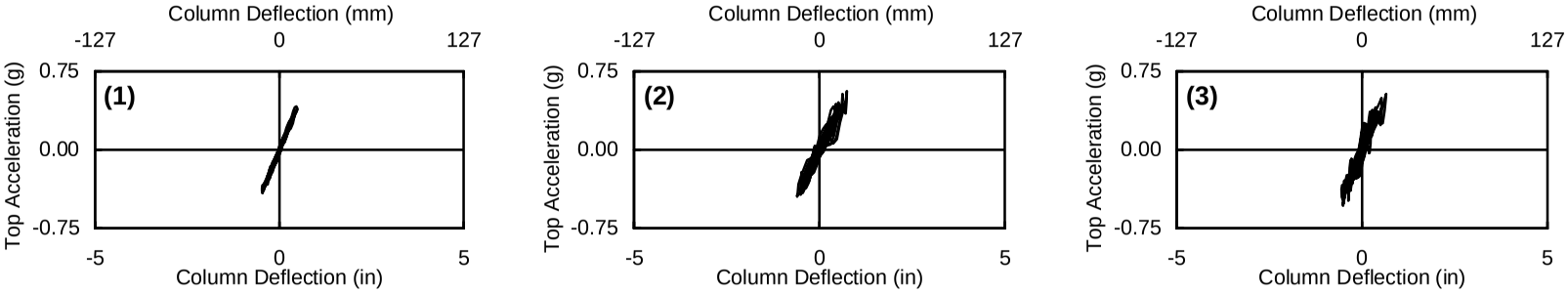

Figure 7-58: Bent3 run 14 acceleration-deflection comparison of measured data (1) with SAP2000 (2) and Drain-3DX (3).

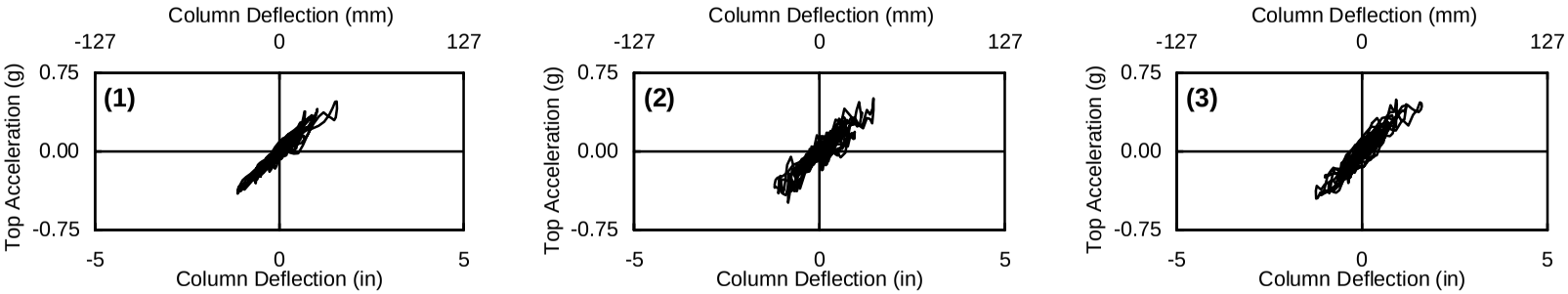

Figure 7-59: Bent1 run 15 acceleration-deflection comparison of measured data (1) with SAP2000 (2) and Drain-3DX (3).

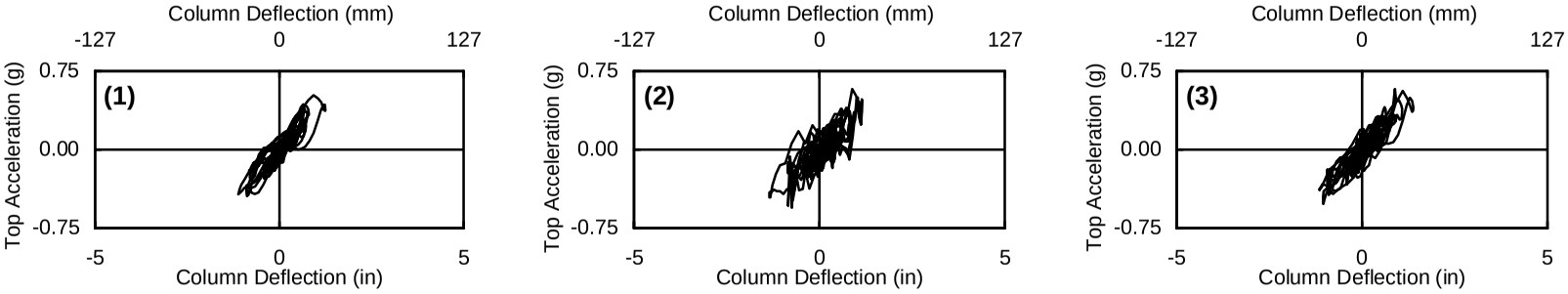

Figure 7-60: Bent2 run 15 acceleration-deflection comparison of measured data (1) with SAP2000 (2) and Drain-3DX (3).

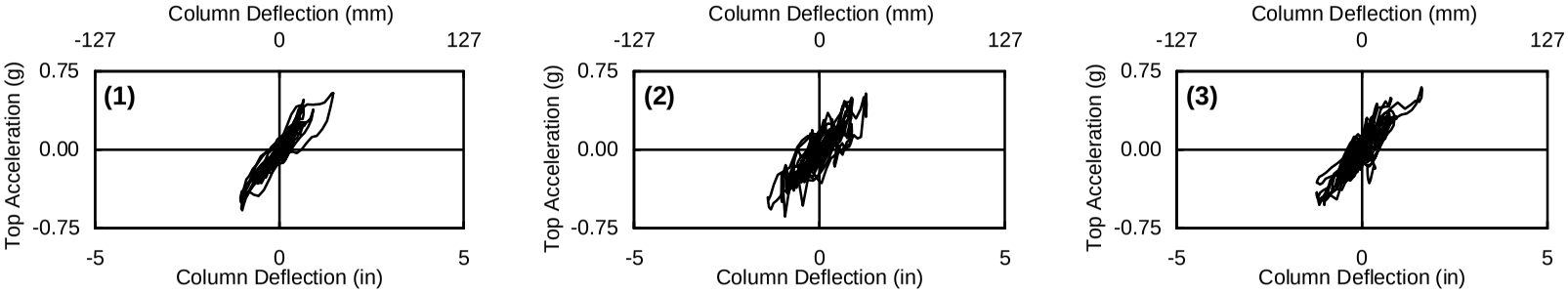

Figure 7-61: Bent3 run 15 acceleration-deflection comparison of measured data (1) with SAP2000 (2) and Drain-3DX (3).

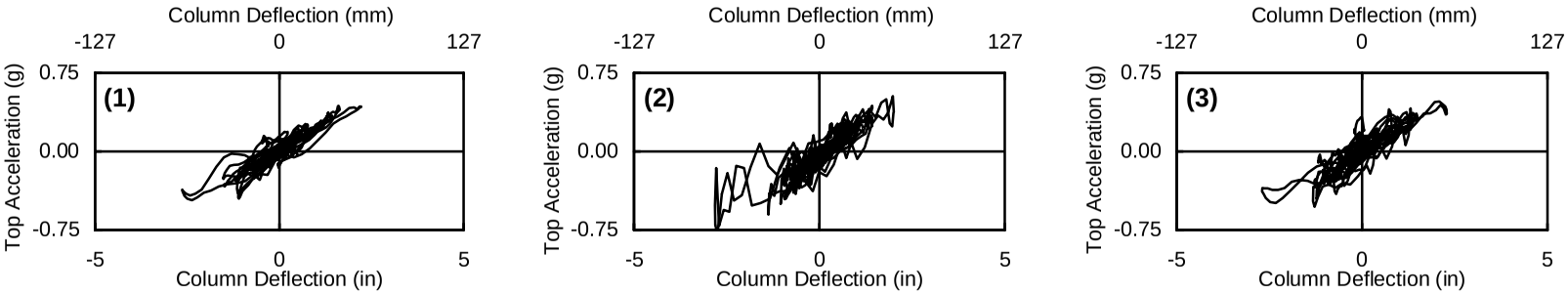

Figure 7-62: Bent1 run 16 acceleration-deflection comparison of measured data (1) with SAP2000 (2) and Drain-3DX (3).

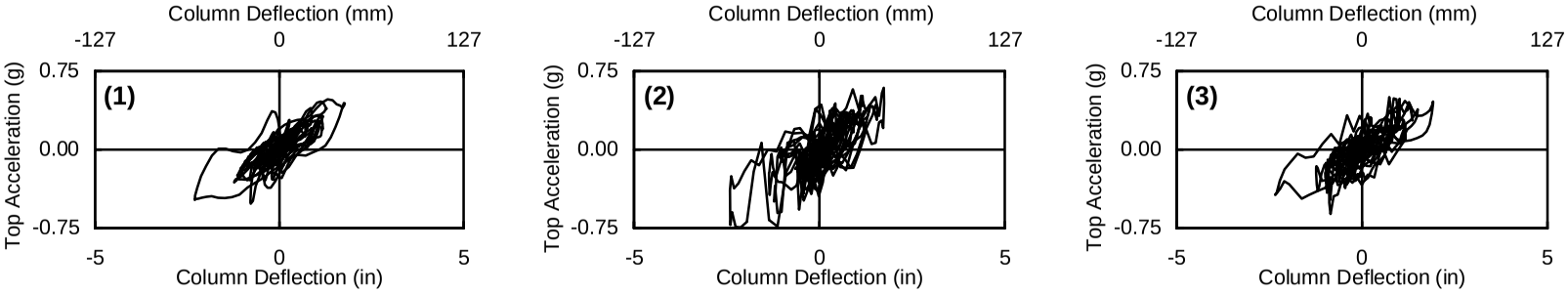

Figure 7-63: Bent2 run 16 acceleration-deflection comparison of measured data (1) with SAP2000 (2) and Drain-3DX (3).

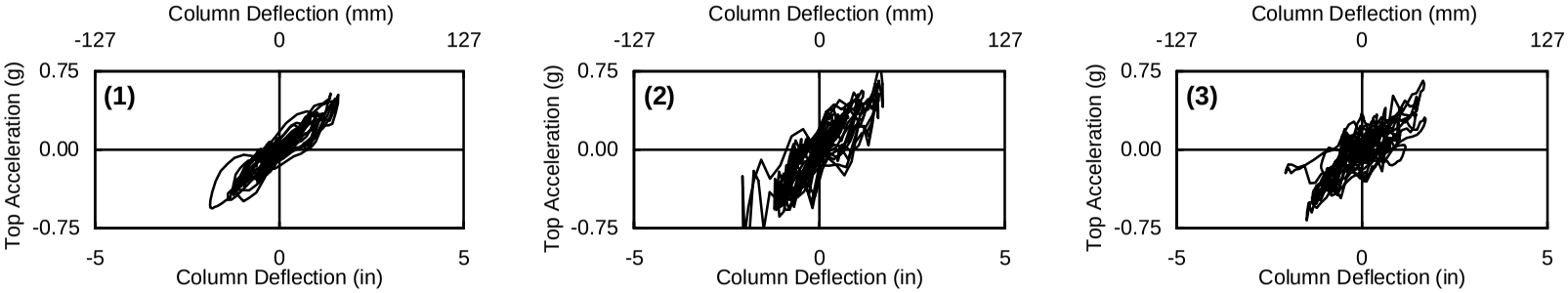

Figure 7-64: Bent3 run 16 acceleration-deflection comparison of measured data (1) with SAP2000 (2) and Drain-3DX (3).

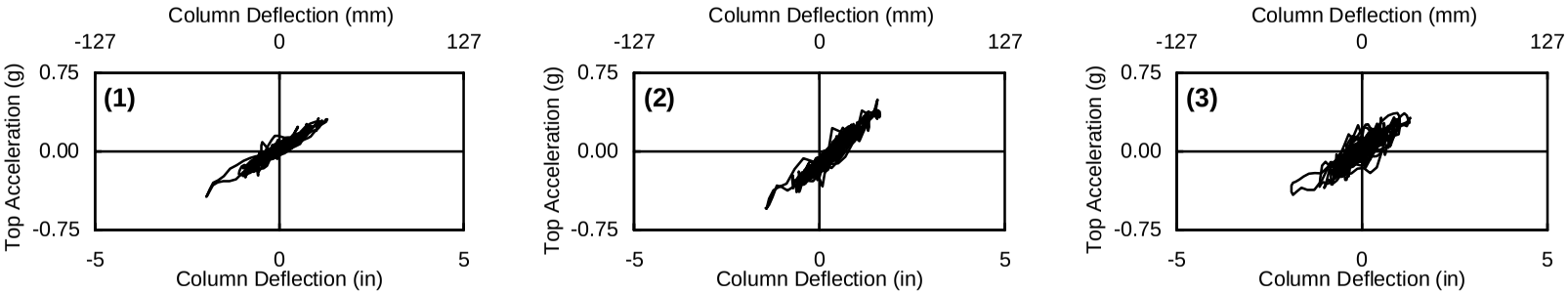

Figure 7-65: Bent1 run 17 acceleration-deflection comparison of measured data (1) with SAP2000 (2) and Drain-3DX (3).

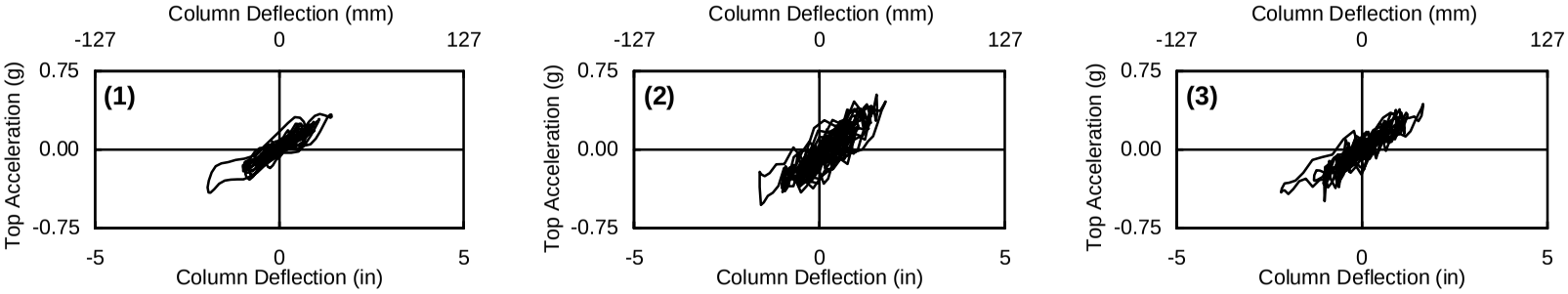

Figure 7-66: Bent2 run 17 acceleration-deflection comparison of measured data (1) with SAP2000 (2) and Drain-3DX (3).

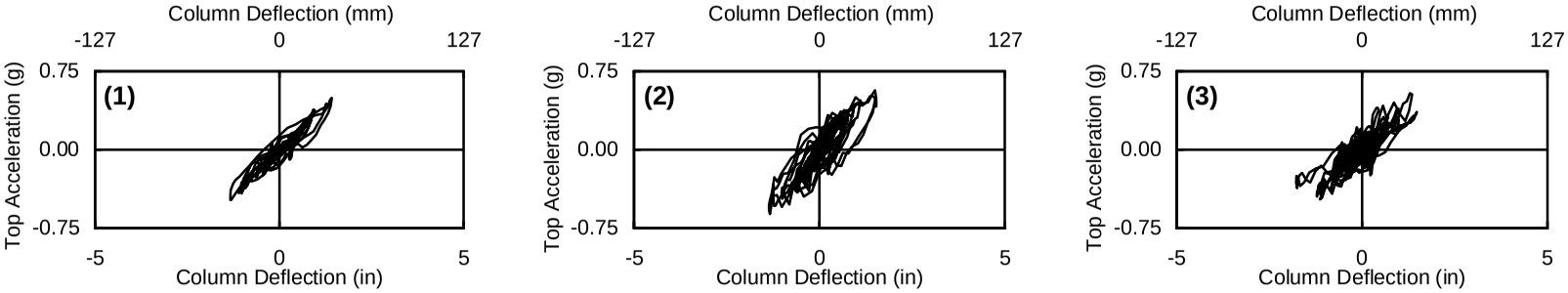

Figure 7-67: Bent3 run 17 acceleration-deflection comparison of measured data (1) with SAP2000 (2) and Drain-3DX (3).

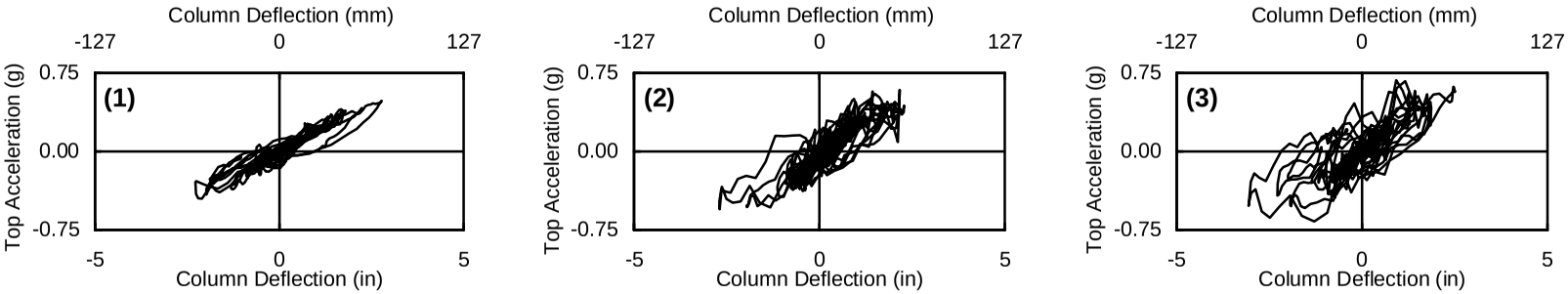

Figure 7-68: Bent1 run 18 acceleration-deflection comparison of measured data (1) with SAP2000 (2) and Drain-3DX (3).

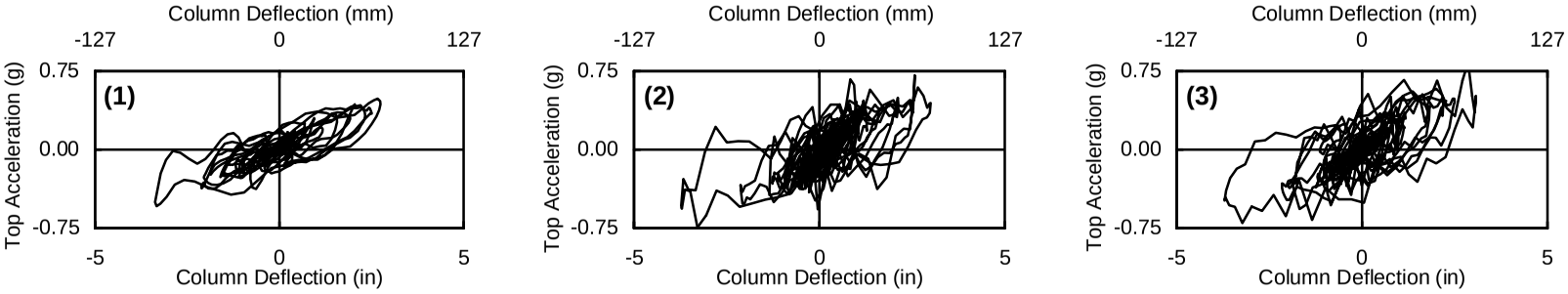

Figure 7-69: Bent2 run 18 acceleration-deflection comparison of measured data (1) with SAP2000 (2) and Drain-3DX (3).

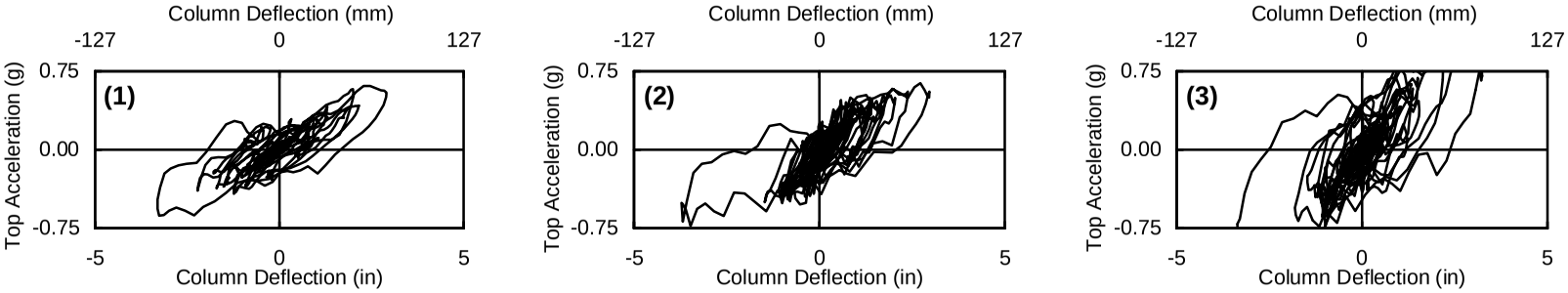

Figure 7-70: Bent3 run 18 acceleration-deflection comparison of measured data (1) with SAP2000 (2) and Drain-3DX (3).

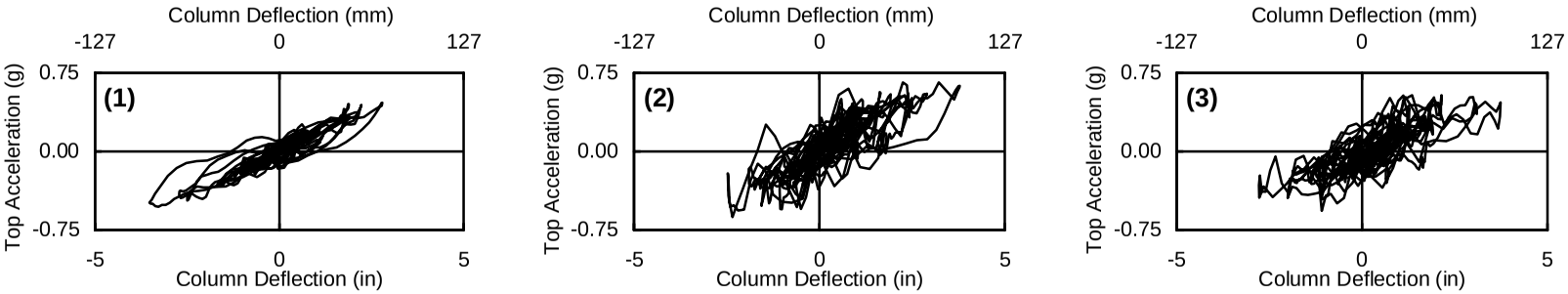

Figure 7-71: Bent1 run 19 acceleration-deflection comparison of measured data (1) with SAP2000 (2) and Drain-3DX (3).

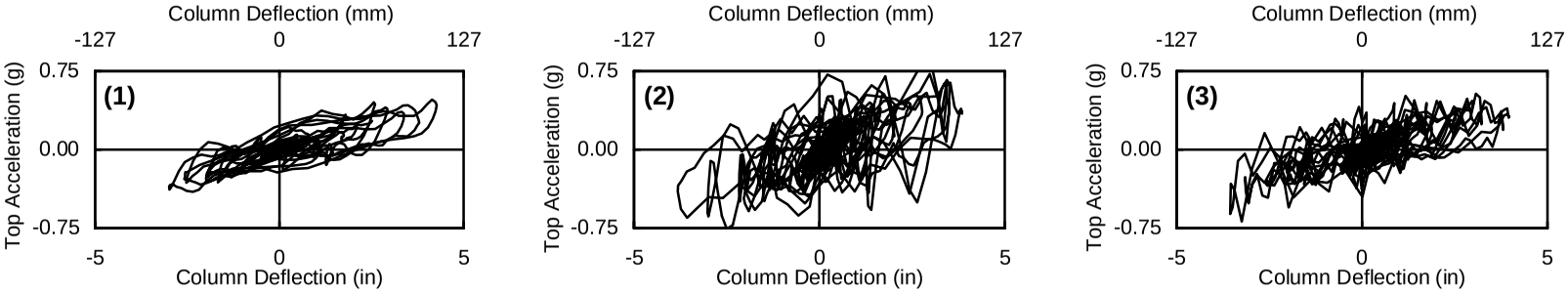

Figure 7-72: Bent2 run 19 acceleration-deflection comparison of measured data (1) with SAP2000 (2) and Drain-3DX (3).

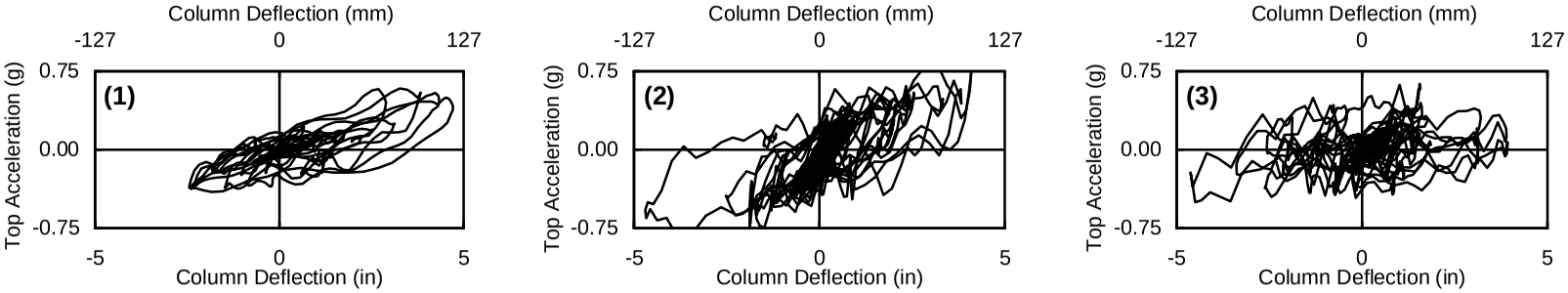

Figure 7-73: Bent3 run 19 acceleration-deflection comparison of measured data (1) with SAP2000 (2) and Drain-3DX (3).

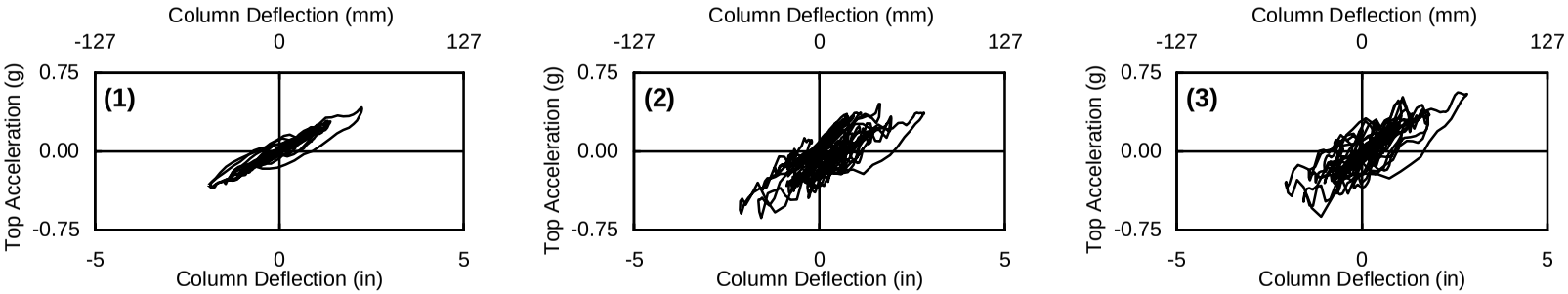

Figure 7-74: Bent1 run 20 acceleration-deflection comparison of measured data (1) with SAP2000 (2) and Drain-3DX (3).

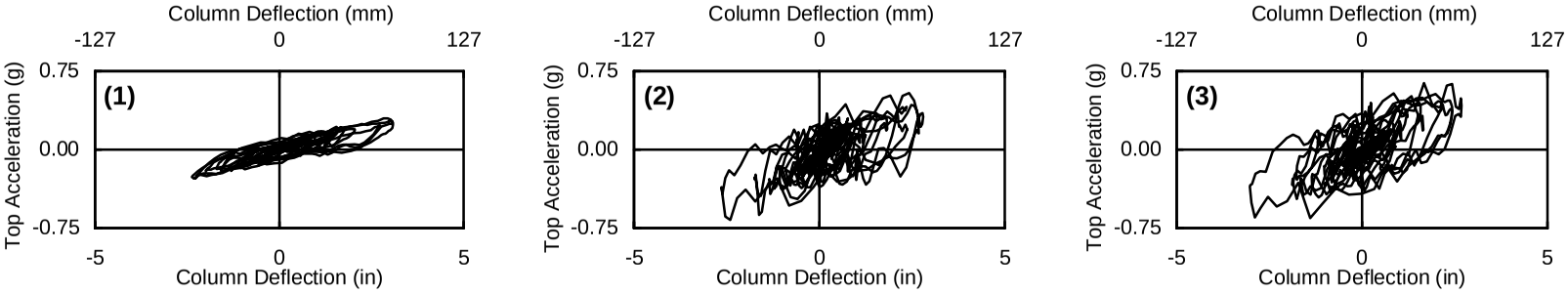

Figure 7-75: Bent2 run 20 acceleration-deflection comparison of measured data (1) with SAP2000 (2) and Drain-3DX (3).

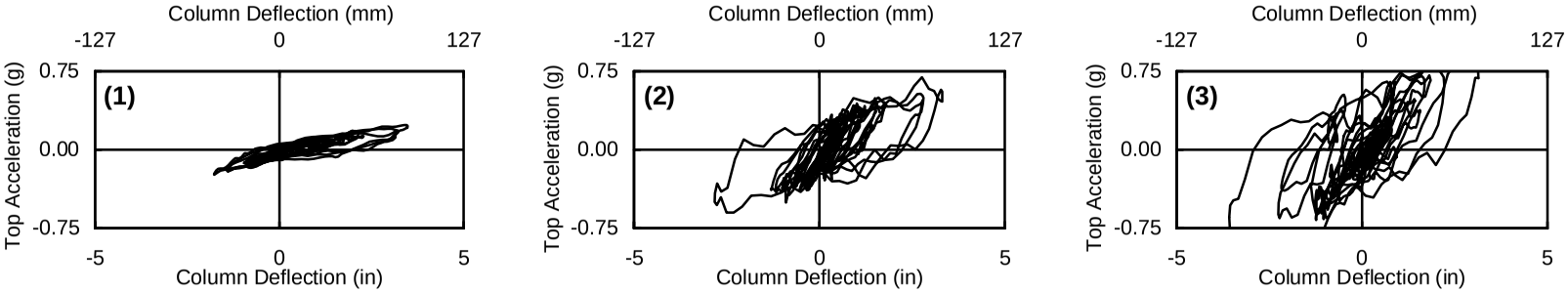

Figure 7-76: Bent3 run 20 acceleration-deflection comparison of measured data (1) with SAP2000 (2) and Drain-3DX (3).

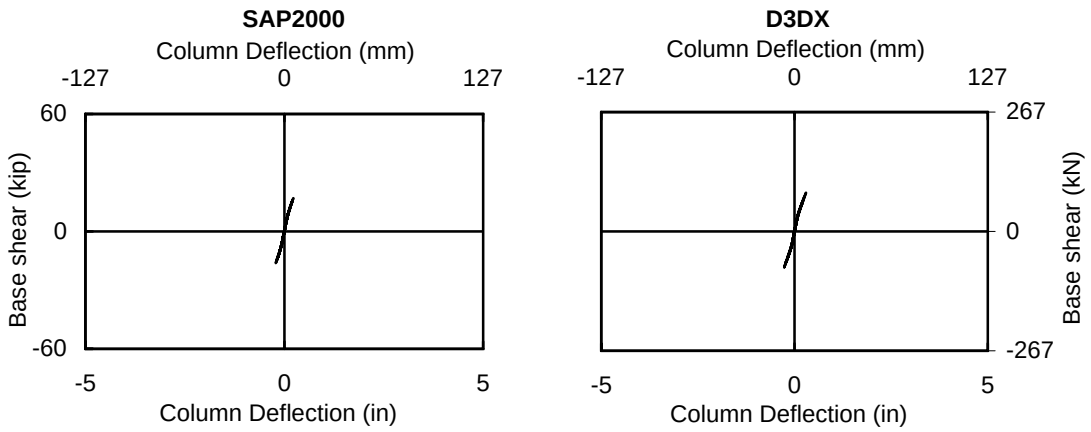

Figure 7-77: Bent 1 run 12 Force-deflection comparison of SAP2000 and Drain-3DX results.

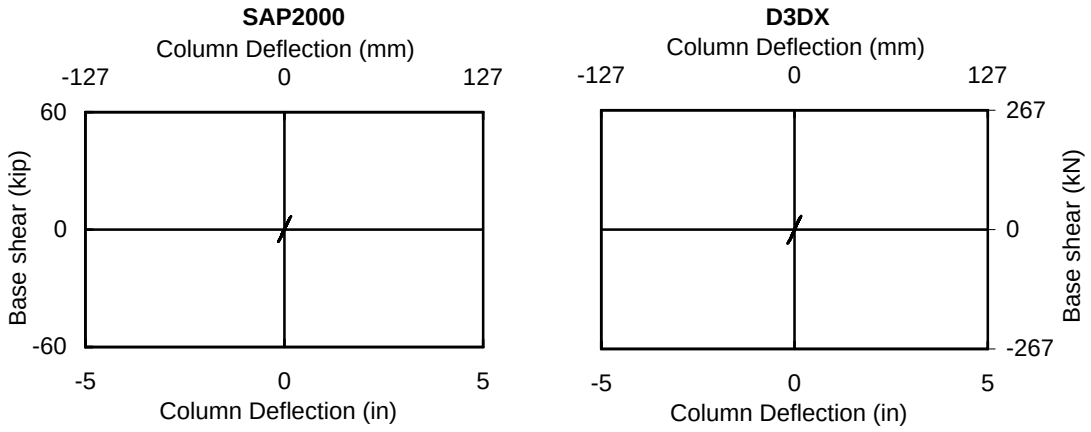

Figure 7-78: Bent 2 run 12 Force-deflection comparison of SAP2000 and Drain-3DX results.

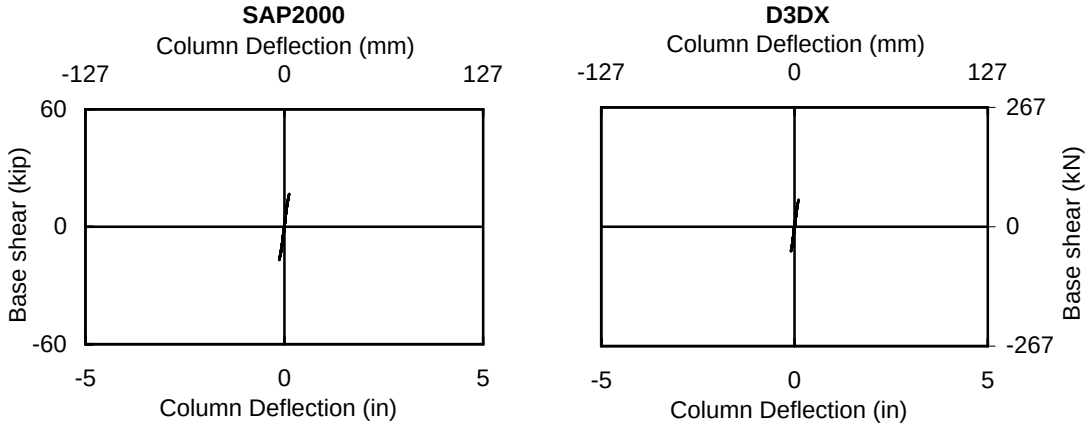

Figure 7-79: Bent 3 run 12 Force-deflection comparison of SAP2000 and Drain-3DX results.

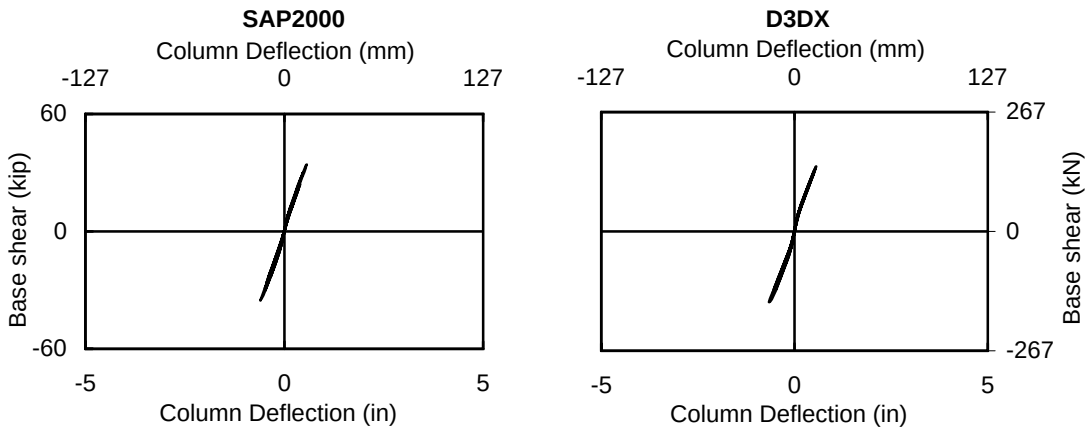

Figure 7-80: Bent 1 run 13 Force-deflection comparison of SAP2000 and Drain-3DX results.

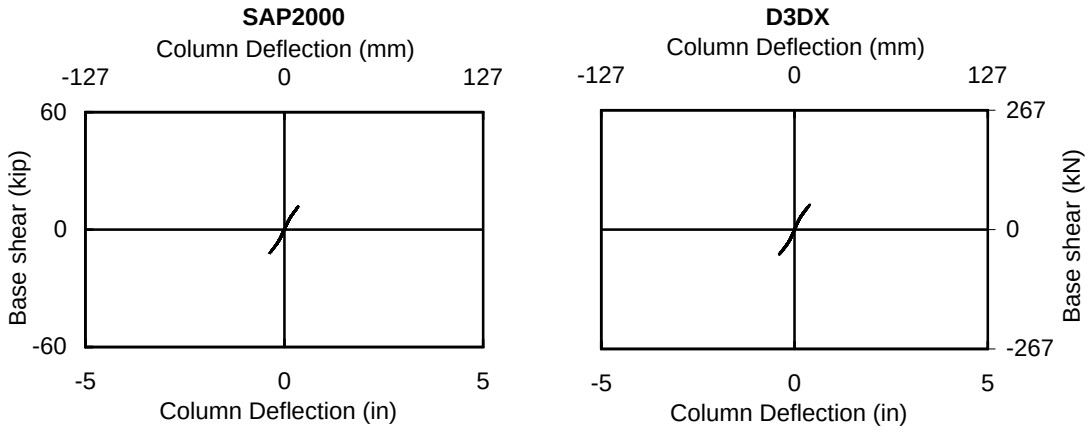

Figure 7-81: Bent 2 run 13 Force-deflection comparison of SAP2000 and Drain-3DX results.

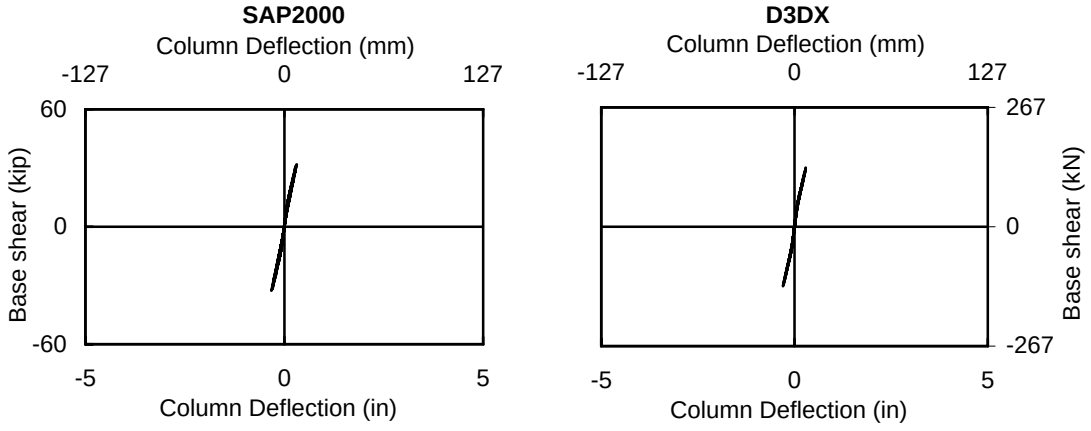

Figure 7-82: Bent 3 run 13 Force-deflection comparison of SAP2000 and Drain-3DX results.

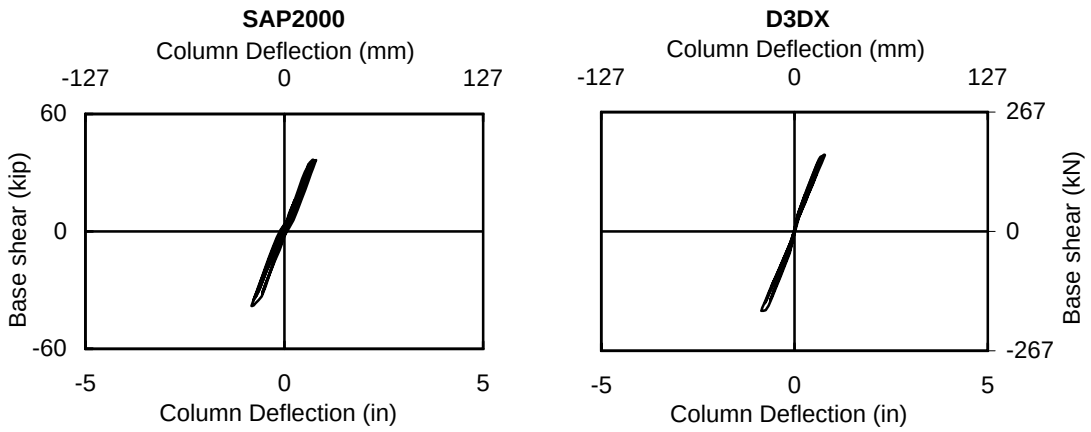

Figure 7-83: Bent 1 run 14 Force-deflection comparison of SAP2000 and Drain-3DX results.

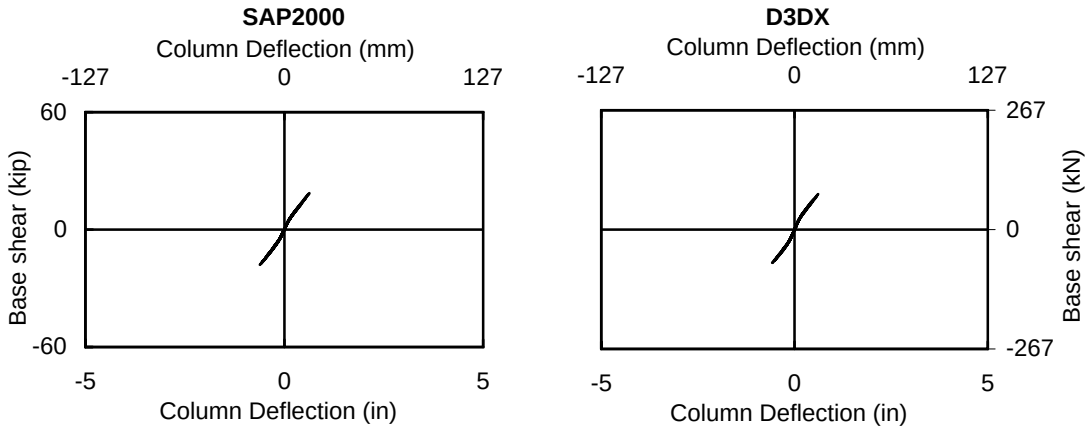

Figure 7-84: Bent 2 run 14 Force-deflection comparison of SAP2000 and Drain-3DX results.

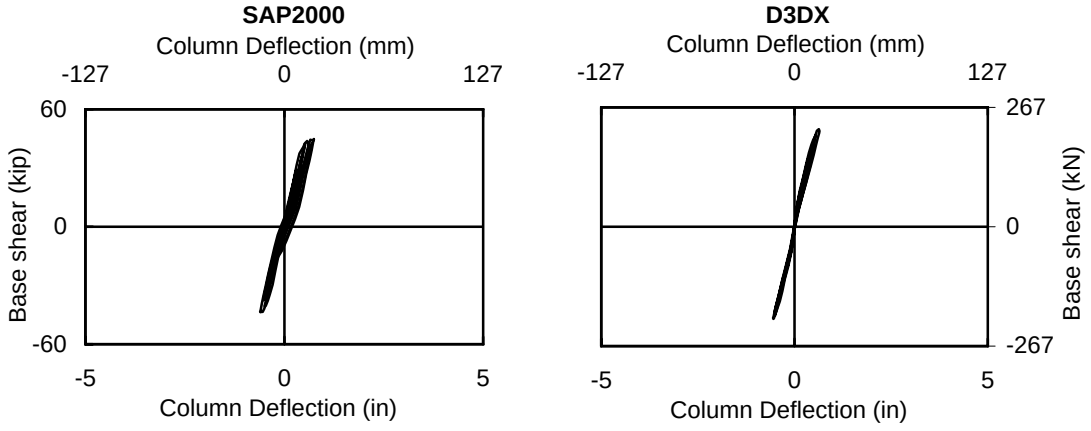

Figure 7-85: Bent 3 run 14 Force-deflection comparison of SAP2000 and Drain-3DX results.

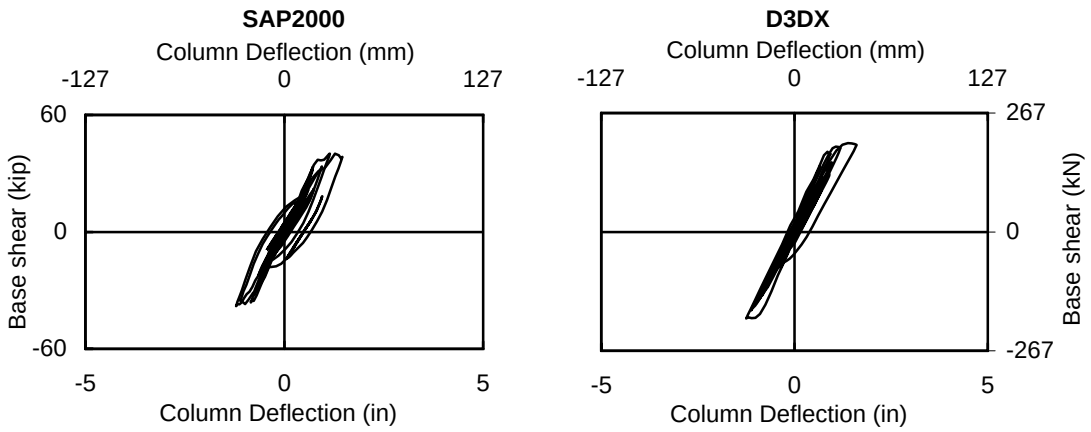

Figure 7-86: Bent 1 run 15 Force-deflection comparison of SAP2000 and Drain-3DX results.

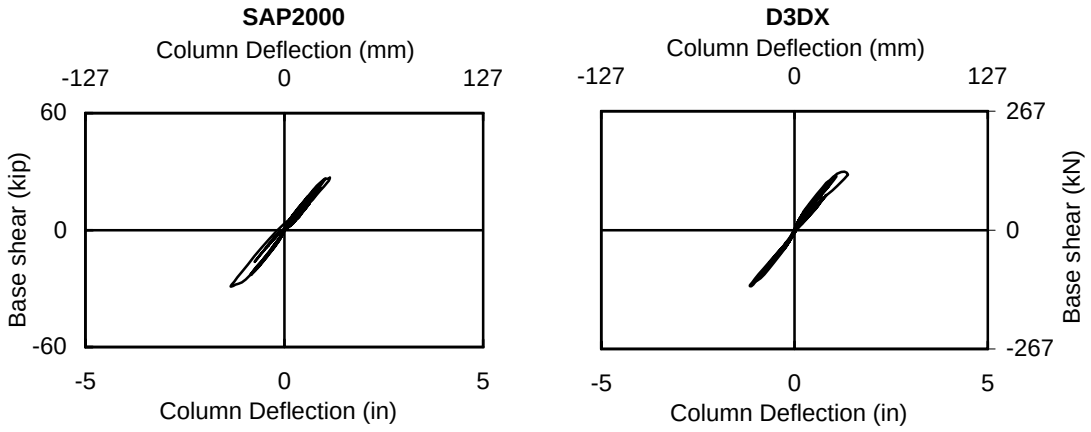

Figure 7-87: Bent 2 run 15 Force-deflection comparison of SAP2000 and Drain-3DX results.

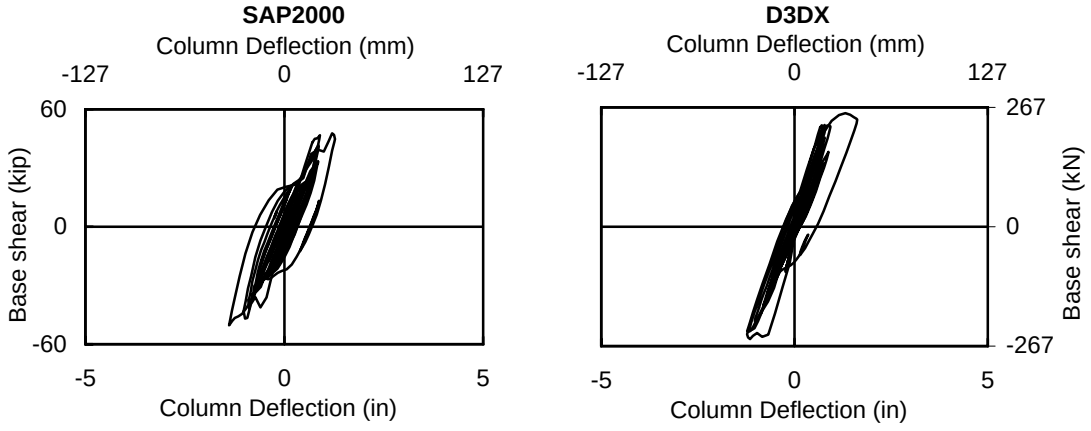

Figure 7-88: Bent 3 run 15 Force-deflection comparison of SAP2000 and Drain-3DX results.

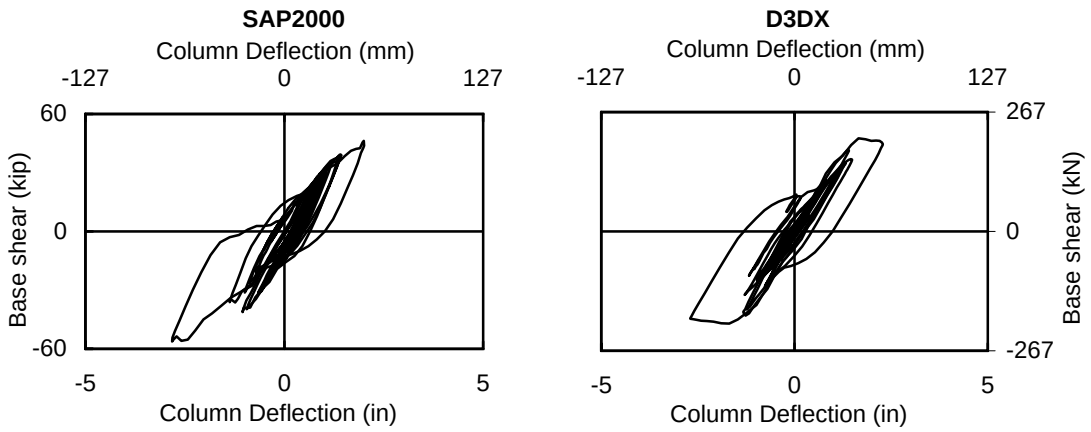

Figure 7-89: Bent 1 run 16 Force-deflection comparison of SAP2000 and Drain-3DX results.

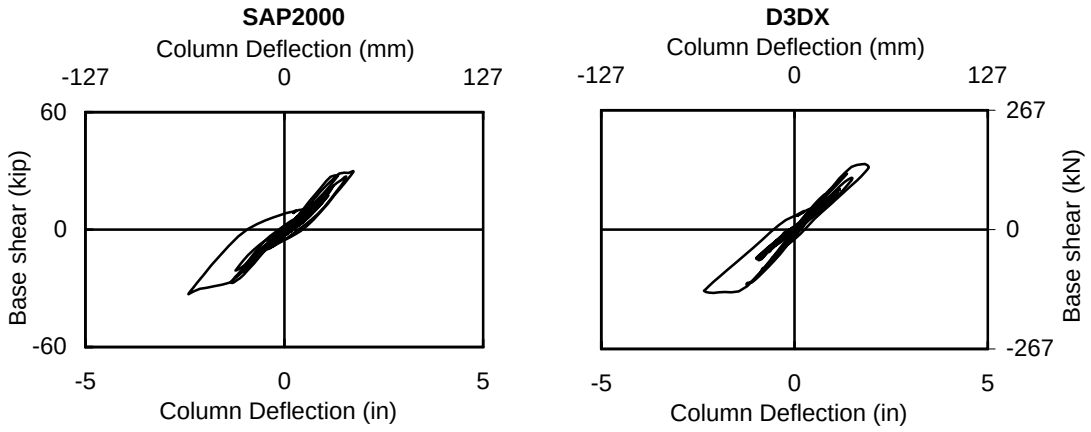

Figure 7-90: Bent 2 run 16 Force-deflection comparison of SAP2000 and Drain-3DX results.

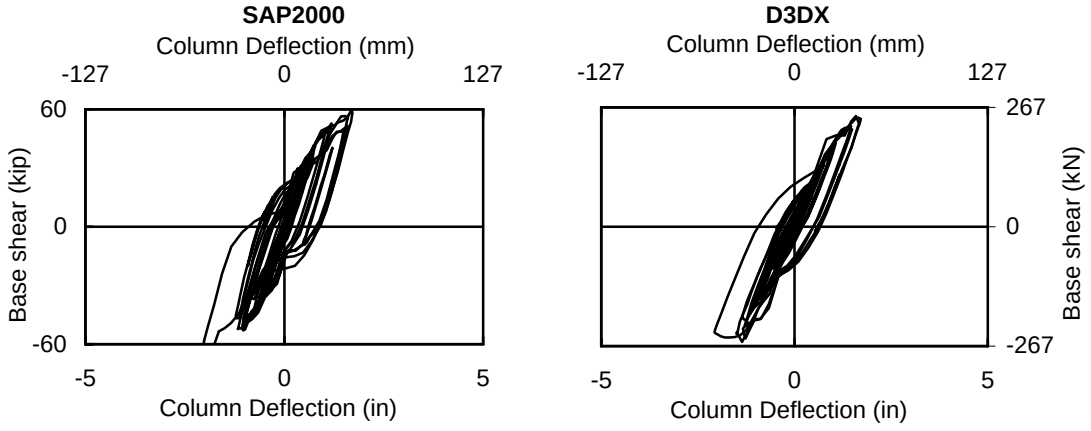

Figure 7-91: Bent 3 run 16 Force-deflection comparison of SAP2000 and Drain-3DX results.

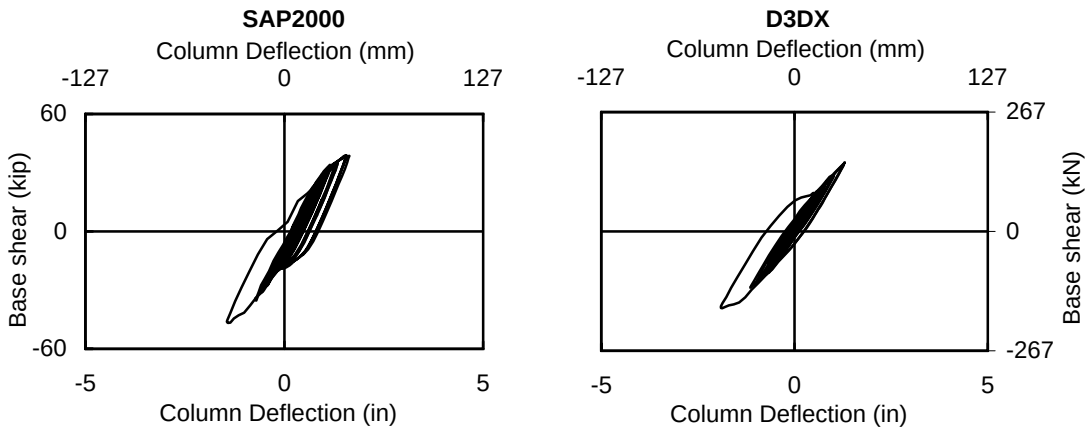

Figure 7-92: Bent 1 run 17 Force-deflection comparison of SAP2000 and Drain-3DX results.

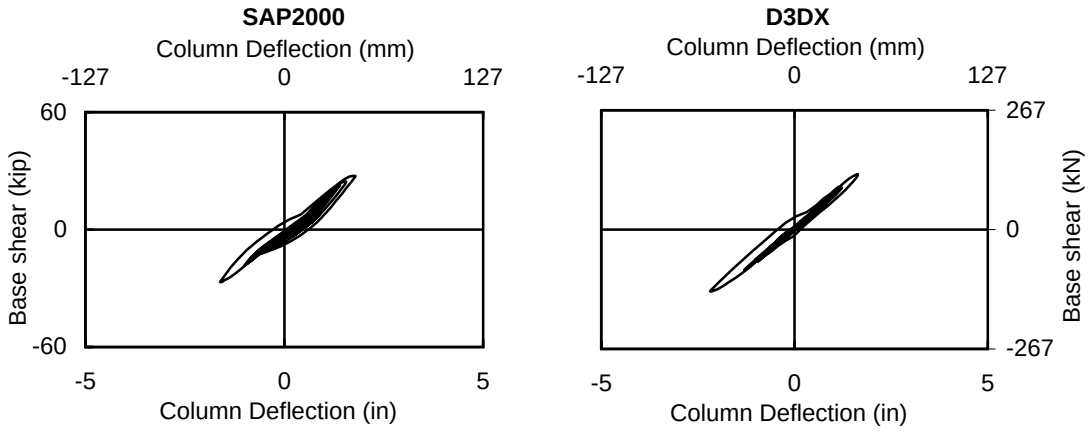

Figure 7-93: Bent 2 run 17 Force-deflection comparison of SAP2000 and Drain-3DX results.

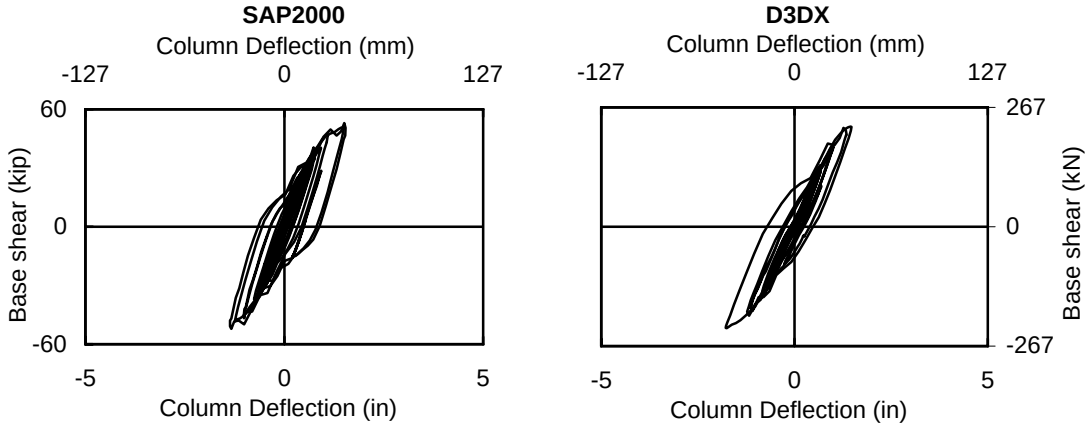

Figure 7-94: Bent 3 run 17 Force-deflection comparison of SAP2000 and Drain-3DX results.

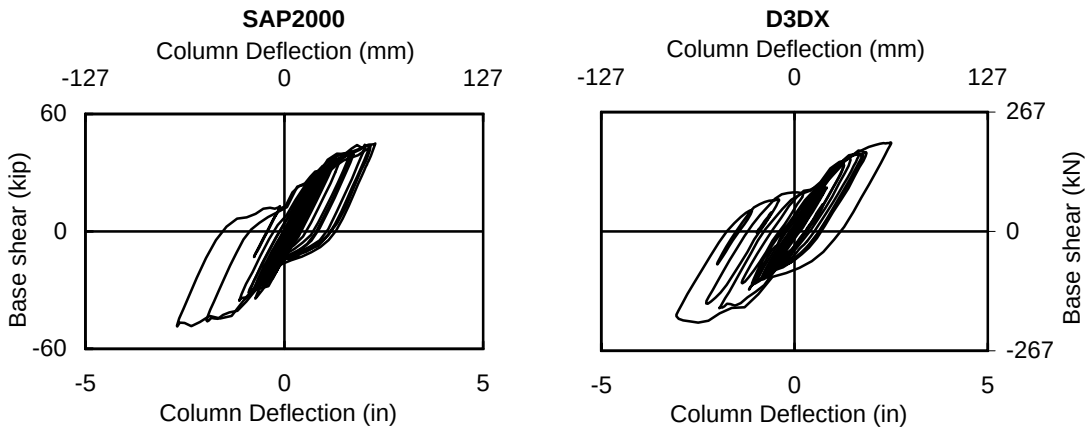

Figure 7-95: Bent 1 run 18 Force-deflection comparison of SAP2000 and Drain-3DX results.

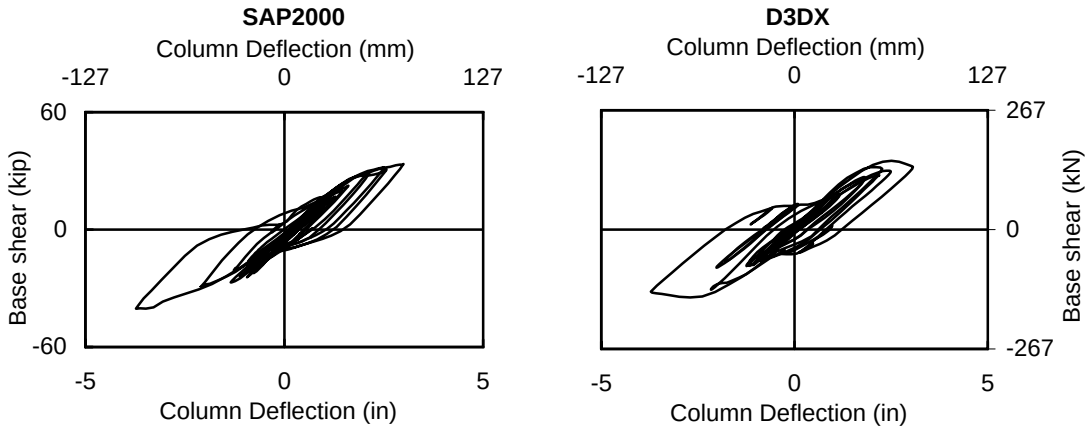

Figure 7-96: Bent 2 run 18 Force-deflection comparison of SAP2000 and Drain-3DX results.

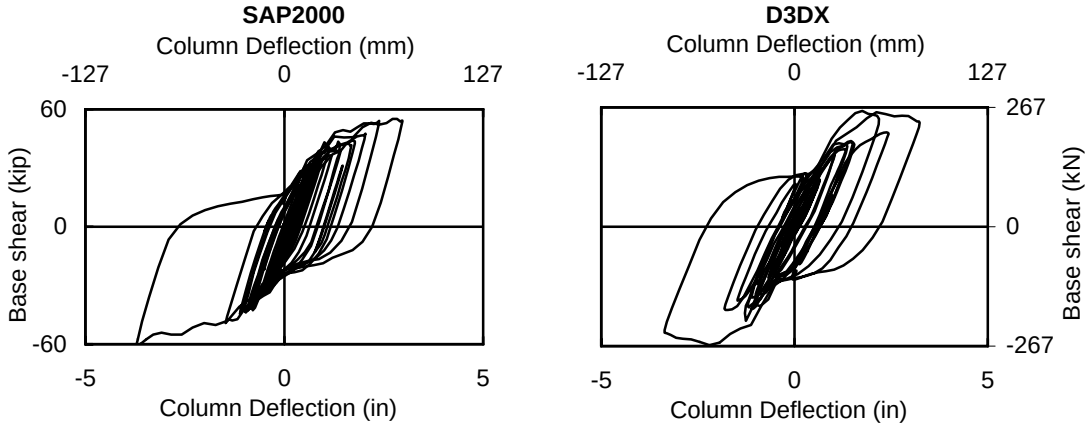

Figure 7-97: Bent 3 run 18 Force-deflection comparison of SAP2000 and Drain-3DX results.

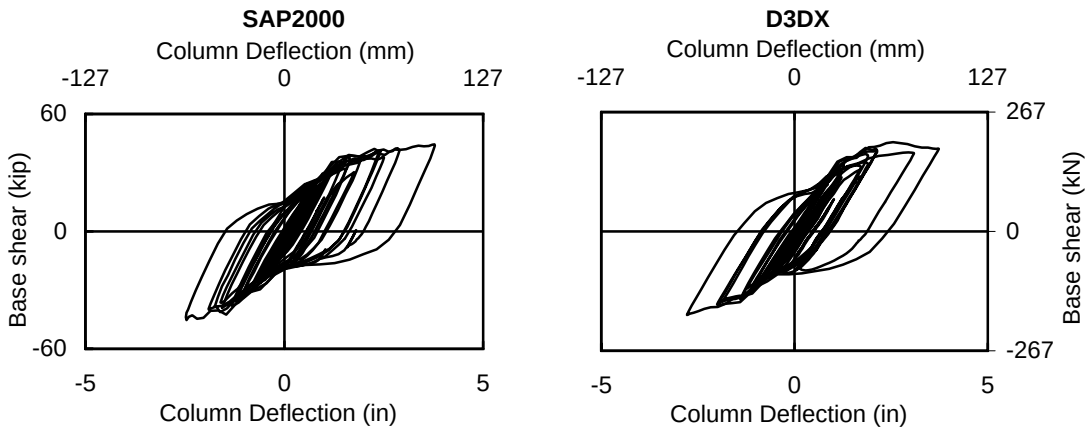

Figure 7-98: Bent 1 run 19 Force-deflection comparison of SAP2000 and Drain-3DX results.

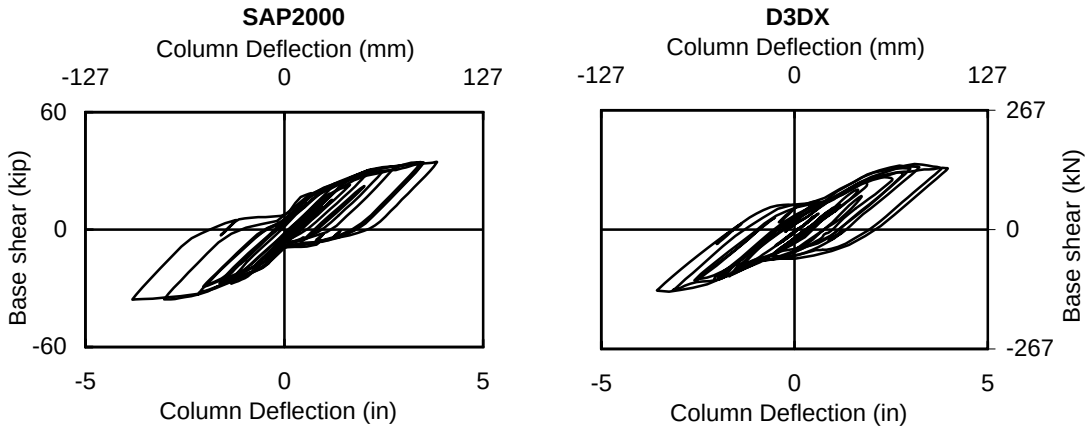

Figure 7-99: Bent 2 run 19 Force-deflection comparison of SAP2000 and Drain-3DX results.

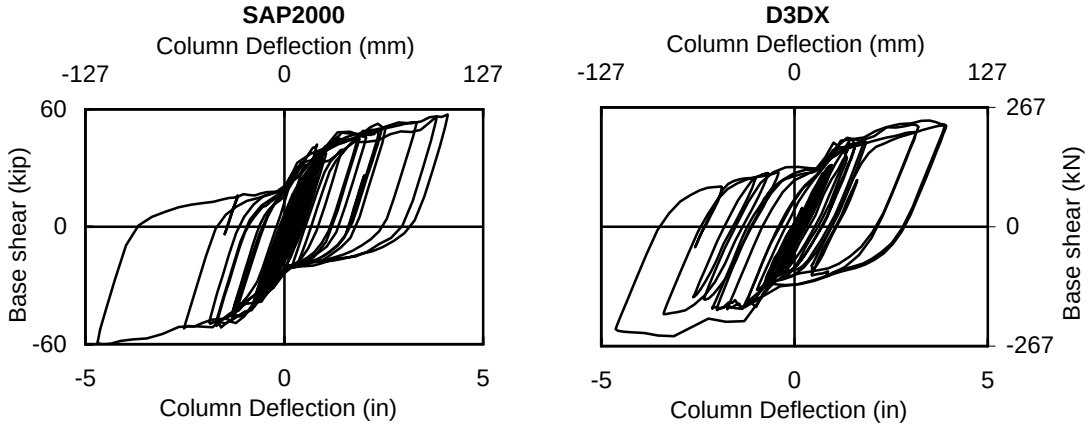

Figure 7-100: Bent 3 run 19 Force-deflection comparison of SAP2000 and Drain-3DX results.

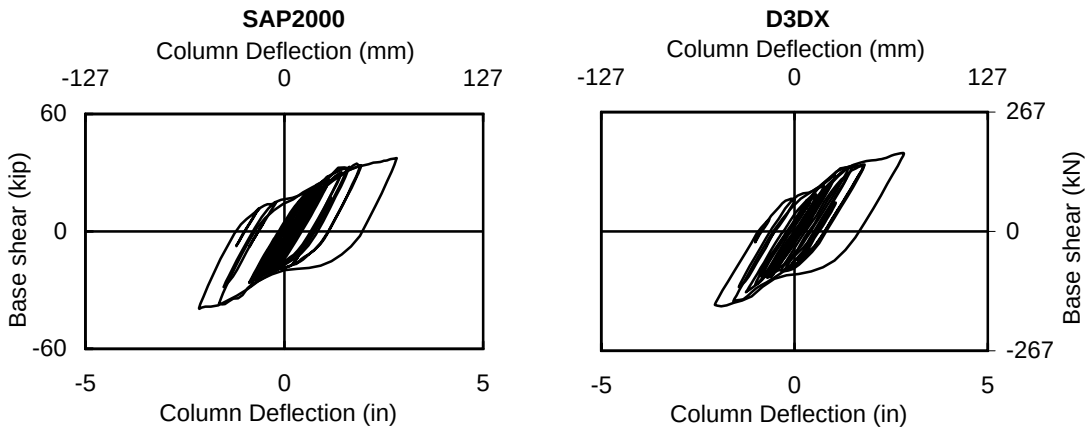

Figure 7-101: Bent 1 run 20 Force-deflection comparison of SAP2000 and Drain-3DX results.

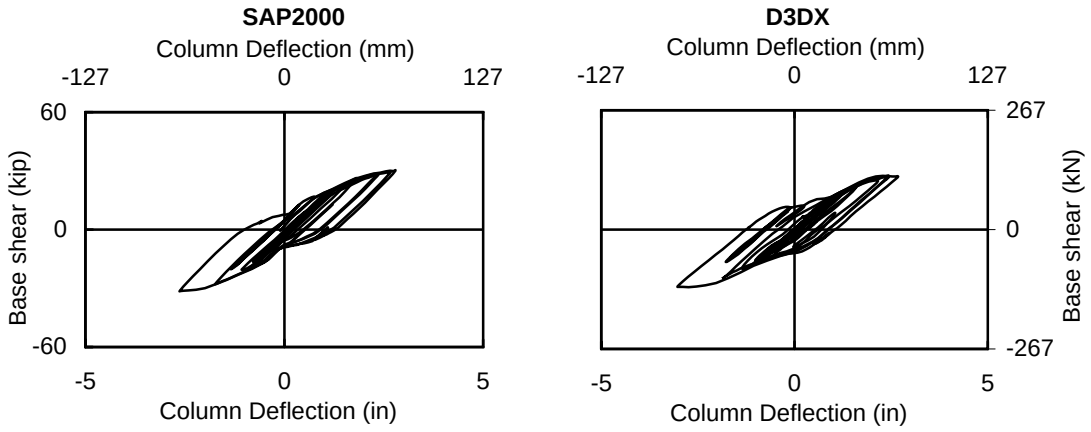

Figure 7-102: Bent 2 run 20 Force-deflection comparison of SAP2000 and Drain-3DX results.

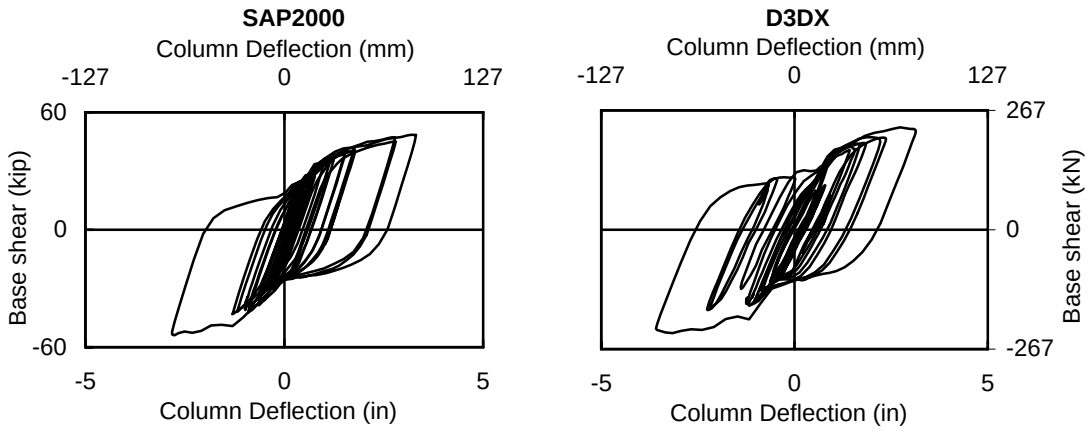

Figure 7-103: Bent 3 run 20 Force-deflection comparison of SAP2000 and Drain-3DX results.

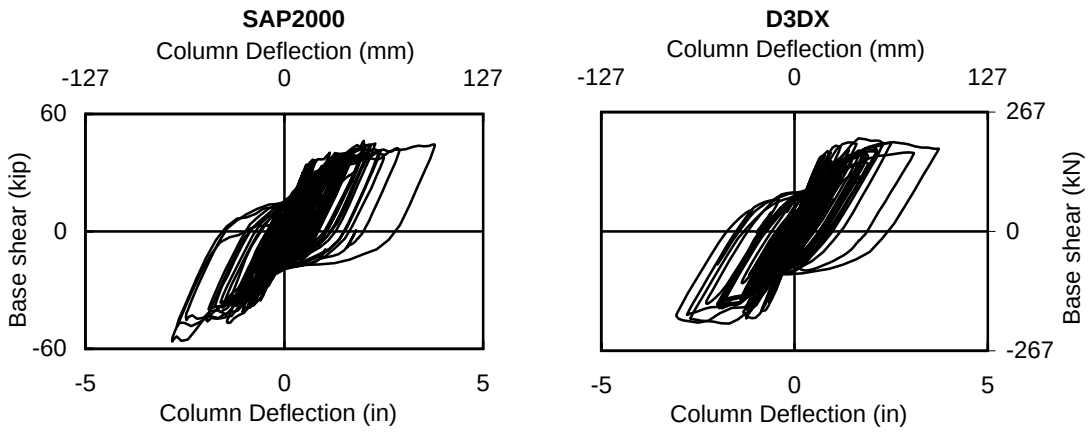

Figure 7-104: Bent 1 run 12-19 Force-deflection comparison of SAP2000 and Drain-3DX results.

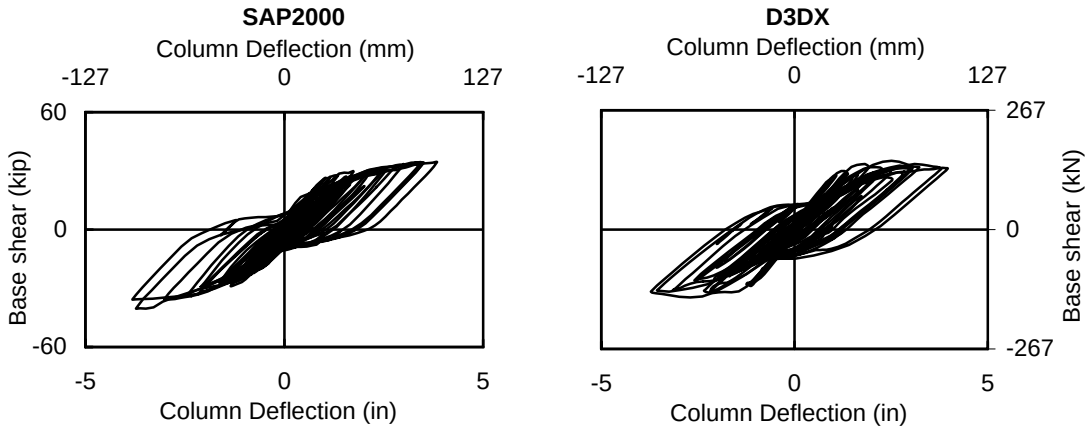

Figure 7-105: Bent 2 run 12-19 Force-deflection comparison of SAP2000 and Drain-3DX results.

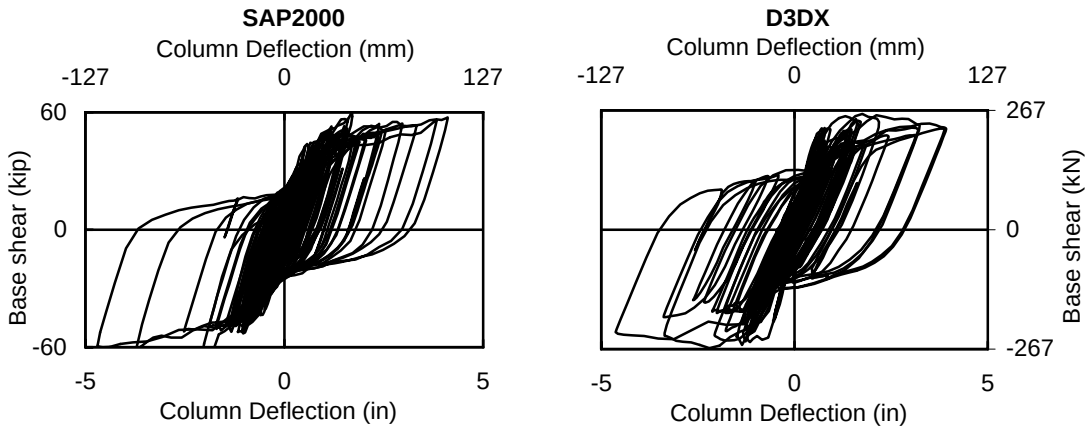

Figure 7-106: Bent 3 run 12-19 Force-deflection comparison of SAP2000 and Drain-3DX results.

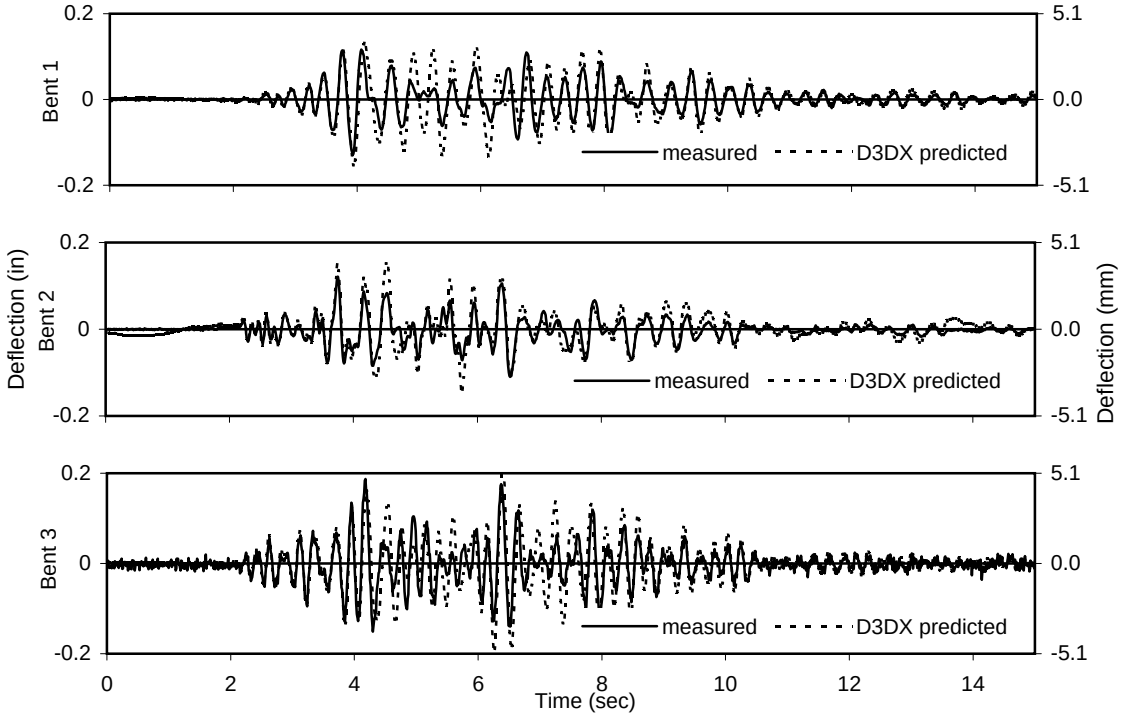

Figure 7-107: Test 2 measured and Drain-3DX predicted transverse displacement histories for bents 1 through 3.

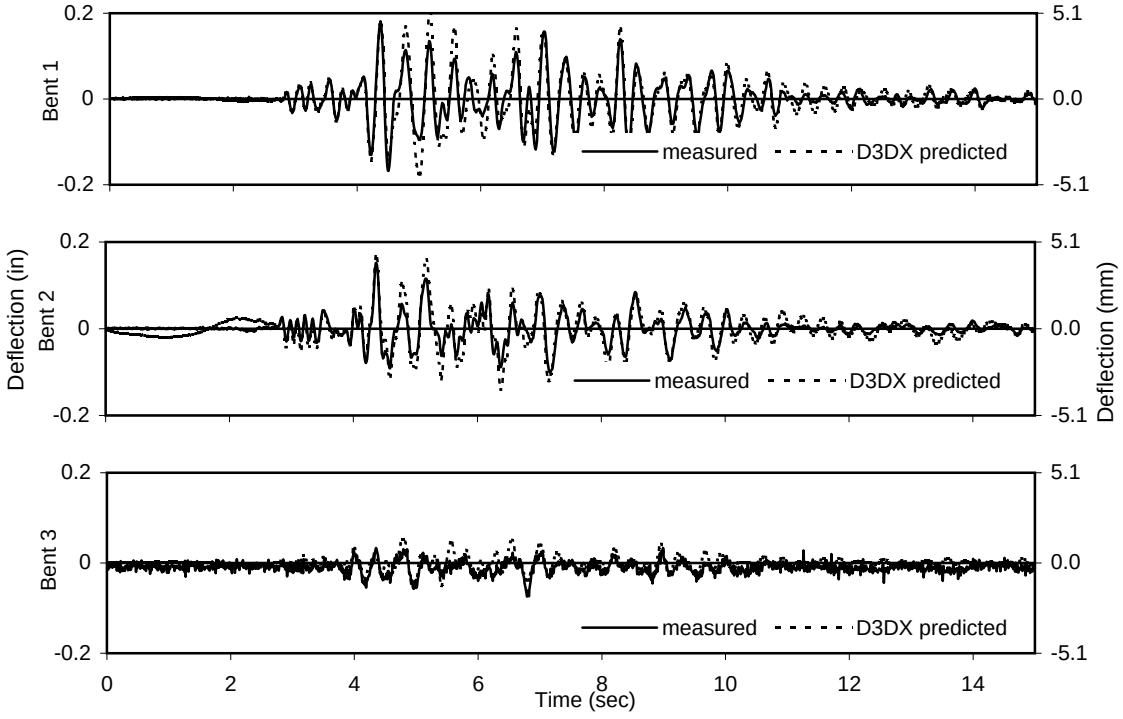

Figure 7-108: Test 3 measured and Drain-3DX predicted transverse displacement histories for bents 1 through 3.

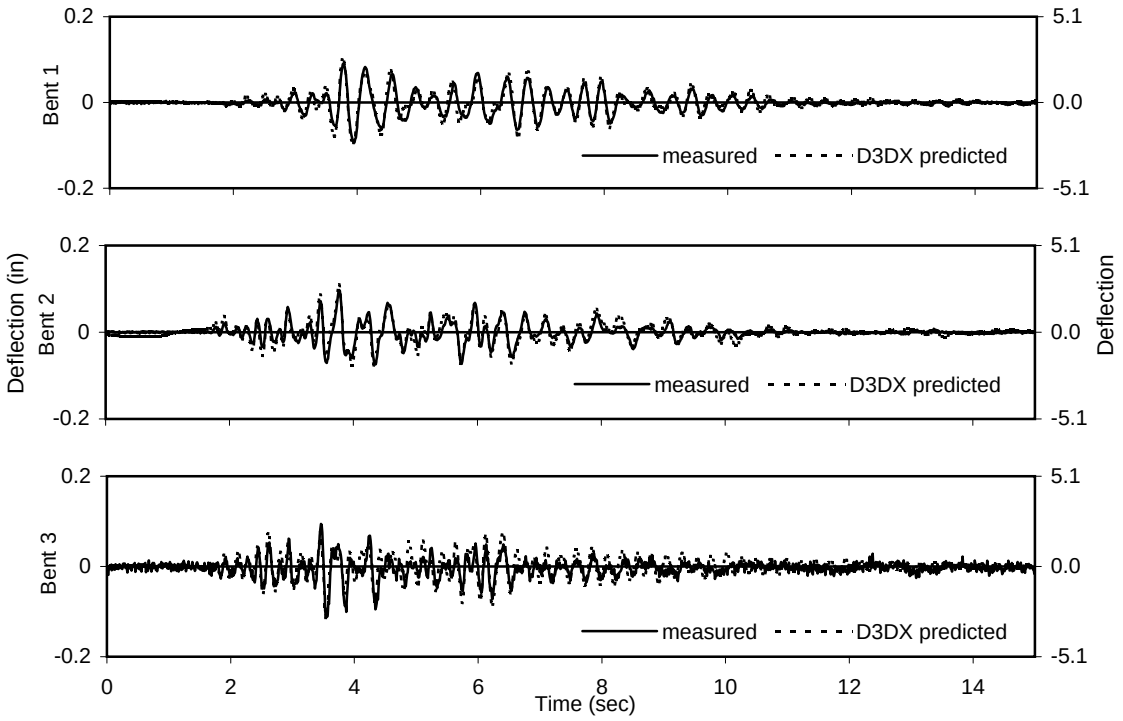

Figure 7-109: Test 4 measured and Drain-3DX predicted transverse displacement histories for bents 1 through 3.

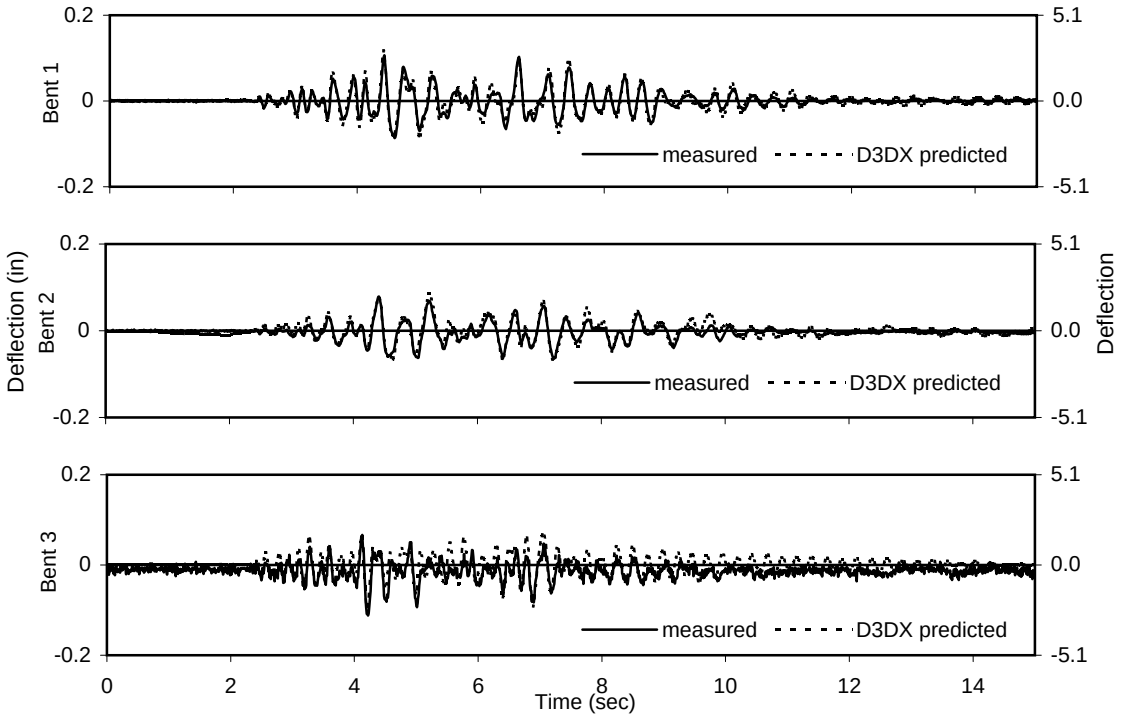

Figure 7-110: Test 5 measured and Drain-3DX predicted transverse displacement histories for bents 1 through 3.

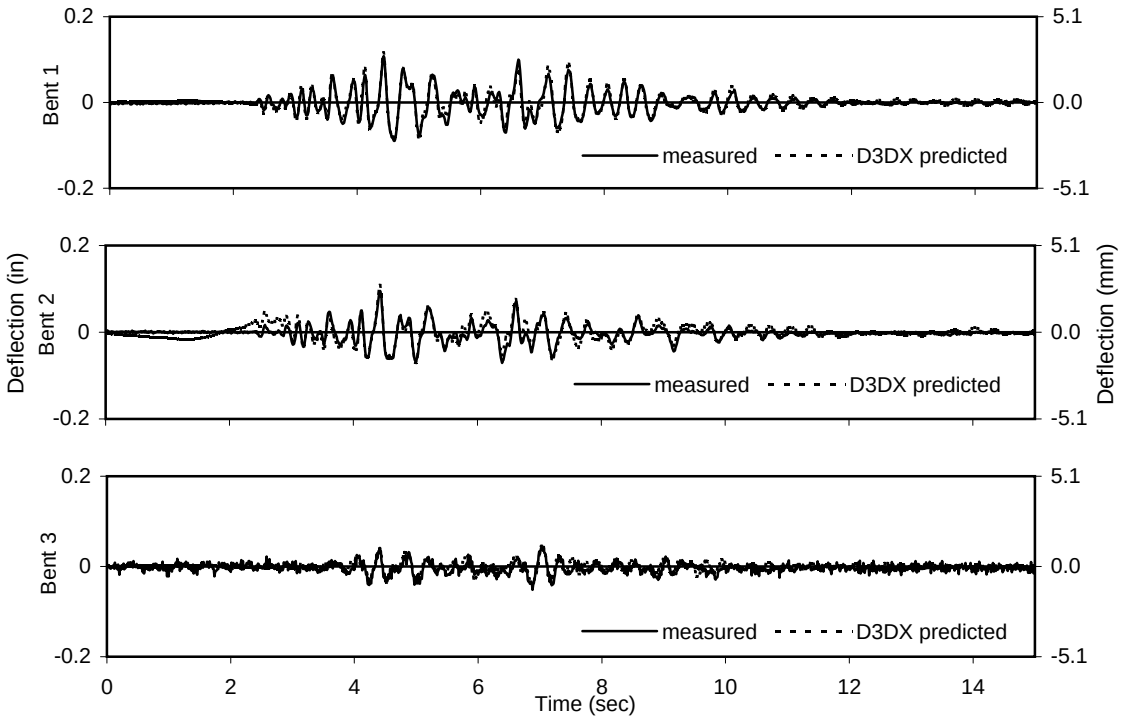

Figure 7-111: Test 6 measured and Drain-3DX predicted transverse displacement histories for bents 1 through 3.

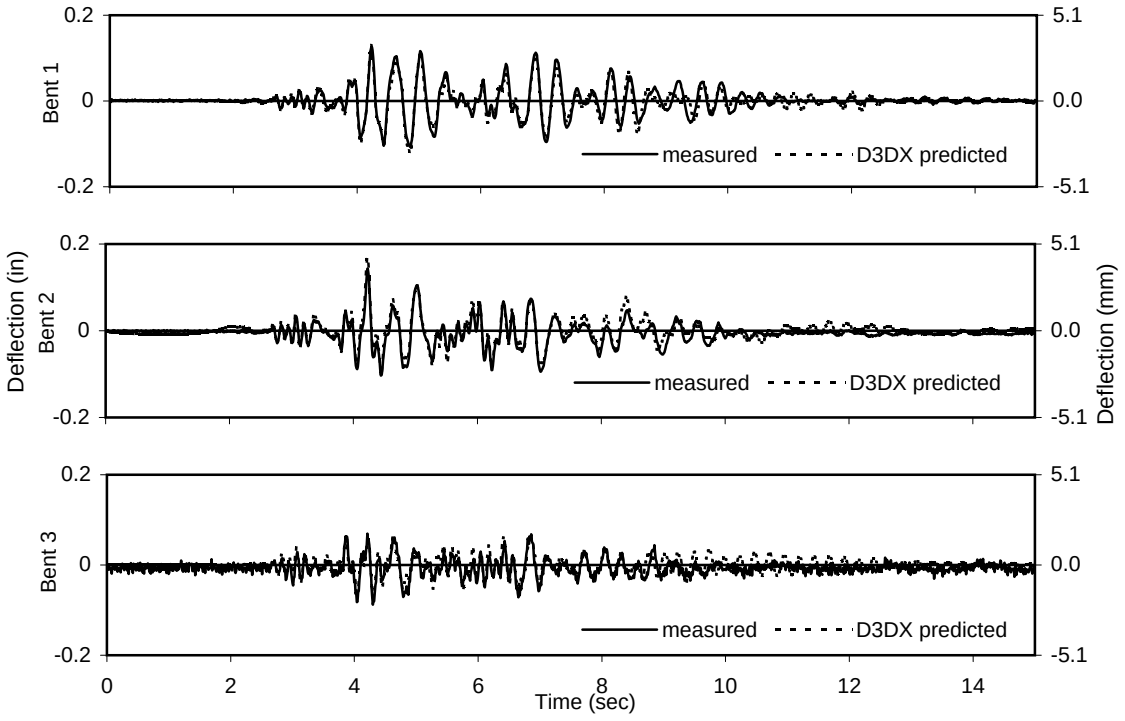

Figure 7-112: Test 9 measured and Drain-3DX predicted transverse displacement histories for bents 1 through 3.

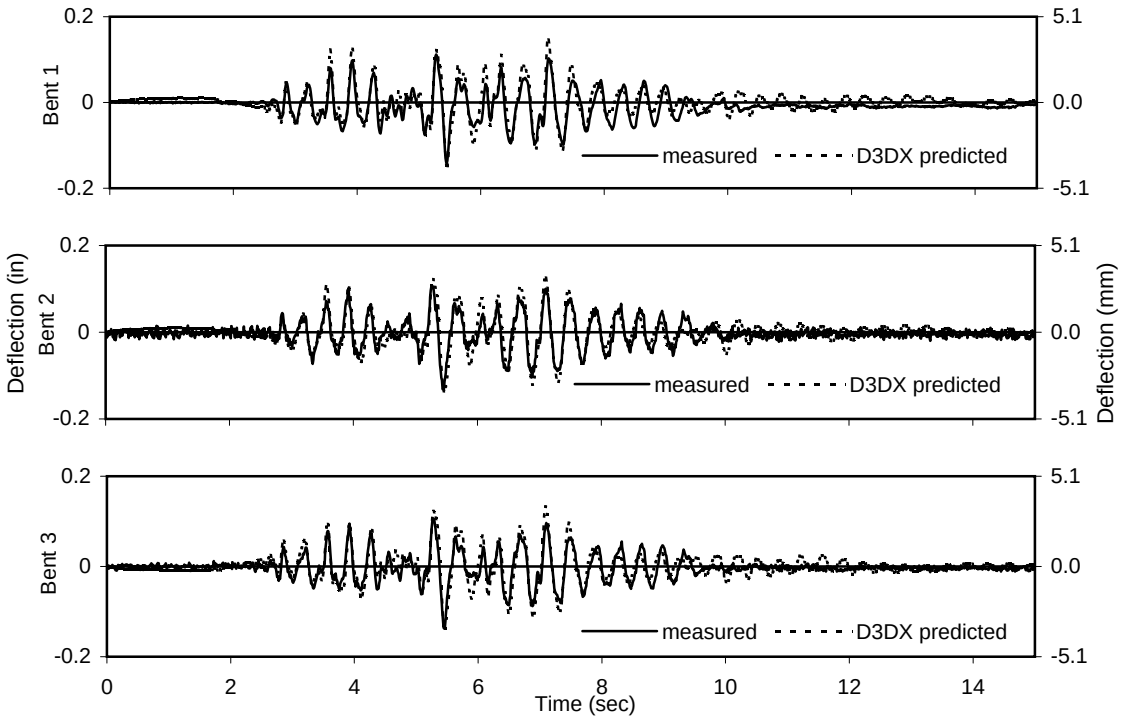

Figure 7-113: Test 9 measured and Drain-3DX predicted longitudinal displacement histories for bents 1 through 3.

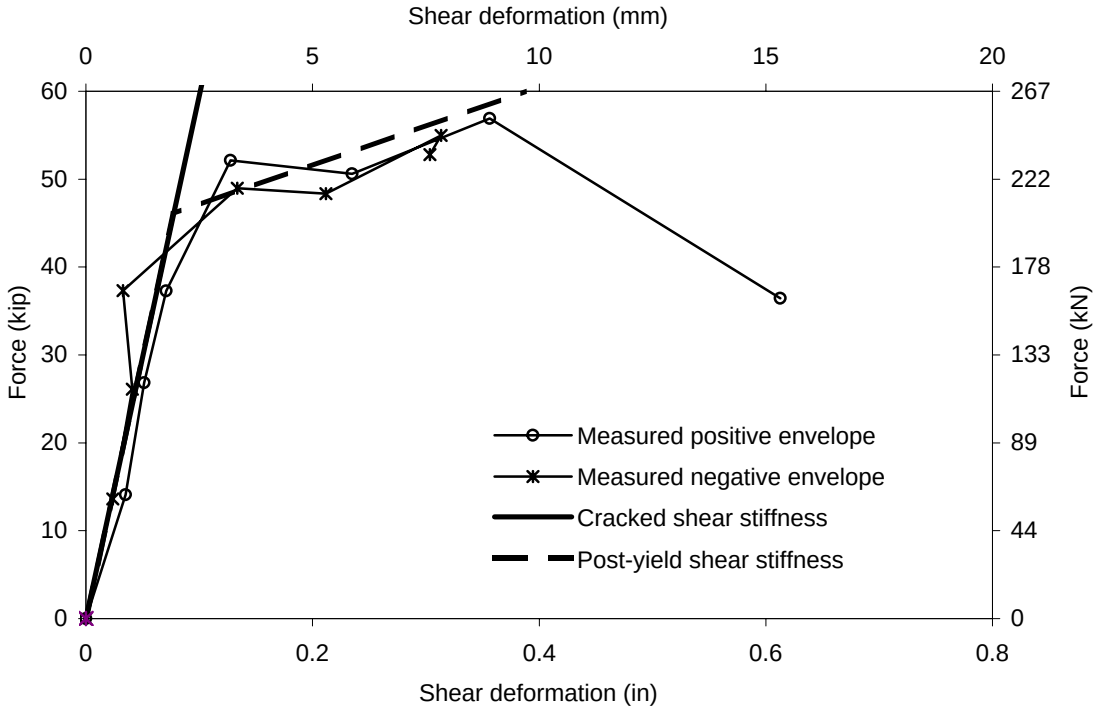

Figure 7-114: Measured test 12-19 bent 3 global force-shear deformation envelope compared to calculated cracked and post-yield shear stiffness.

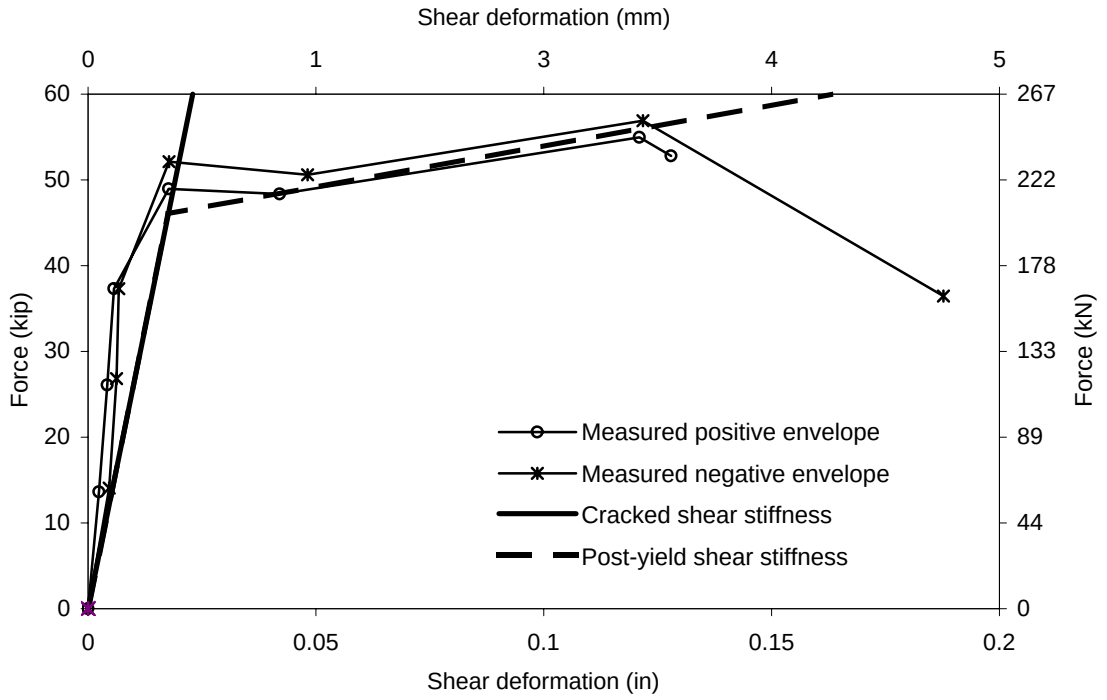

Figure 7-115: Measured test 12-19 bent 3 force-shear deformation envelope compared to calculated cracked and post-yield shear stiffness for bottom panel zone.

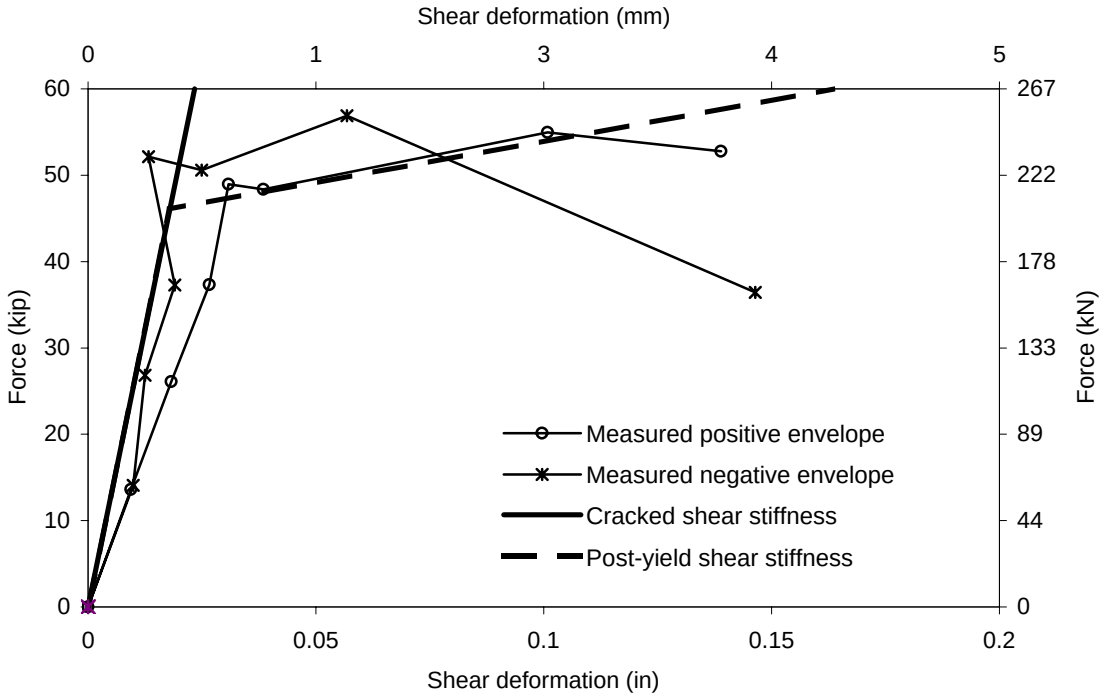

Figure 7-116: Measured test 12-19 bent 3 force-shear deformation envelope compared to calculated cracked and post-yield shear stiffness for top panel zone.

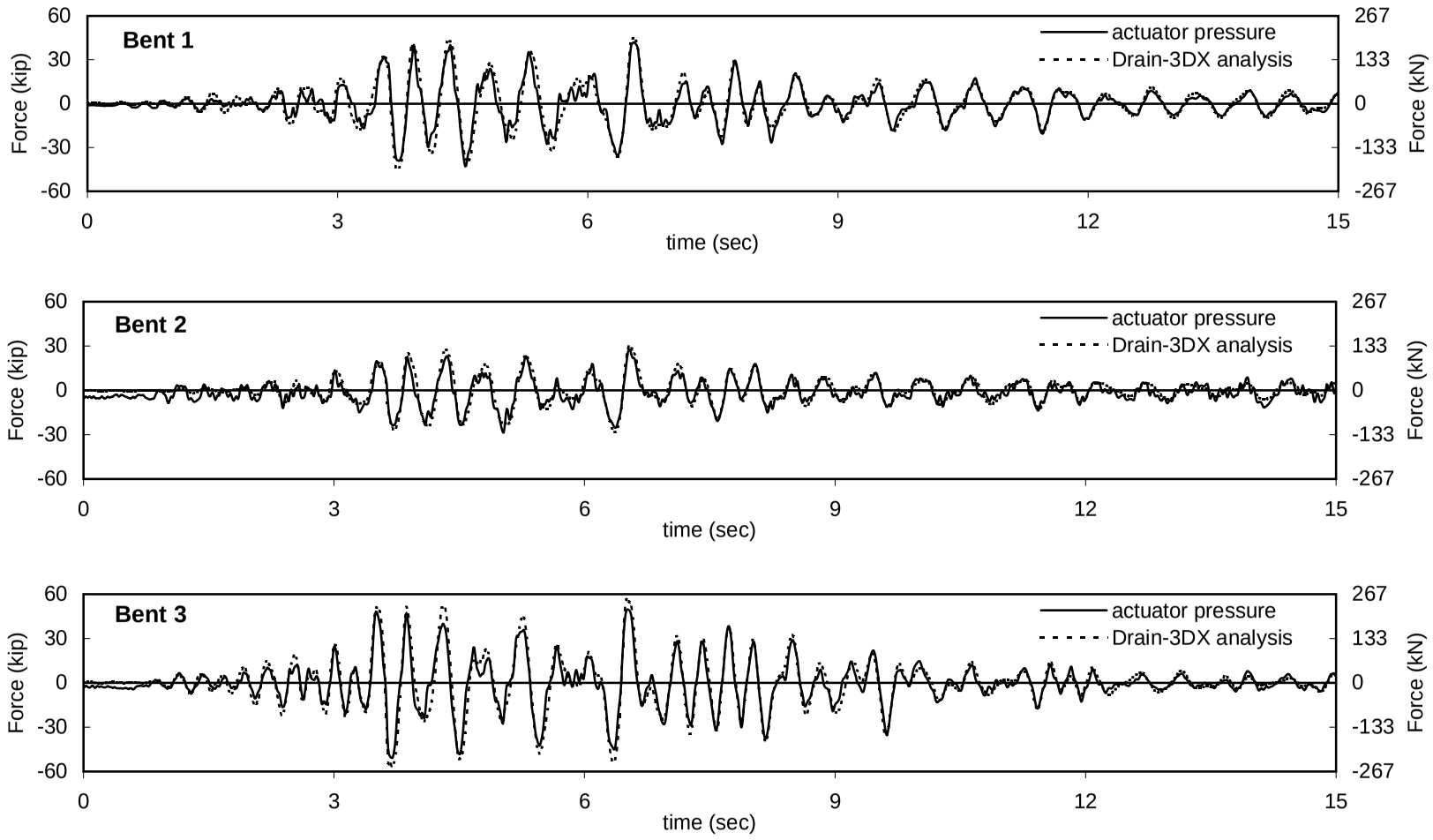

Figure 7-117: Test 15 force history comparison for bents 1-3 comparing force (calculated from actuator pressure), and force calculated using Drain-3DX.

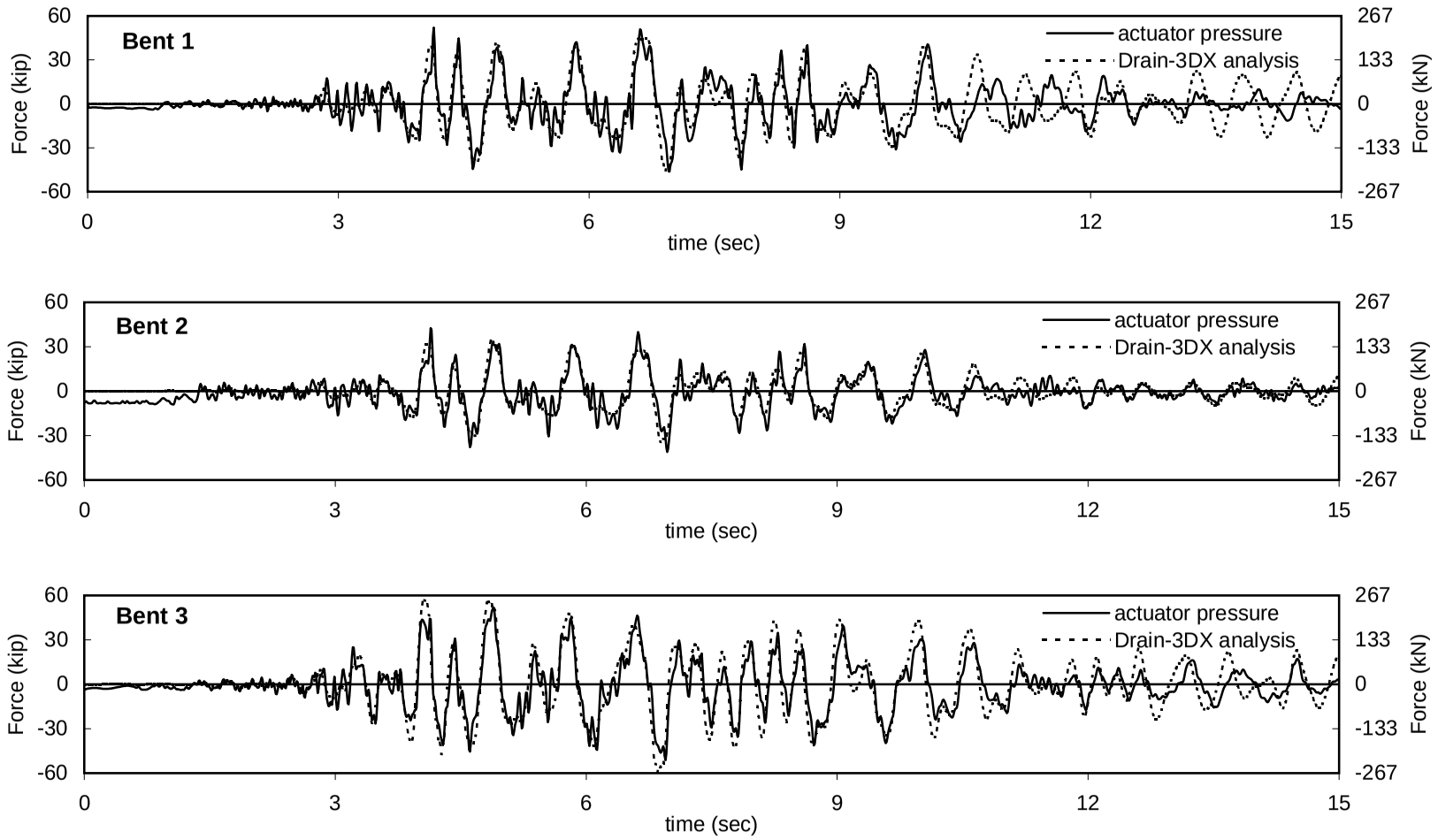

Figure 7-118: Test 18 force history comparison for bents 1-3 comparing force (calculated from actuator pressure), and force calculated using Drain-3DX.

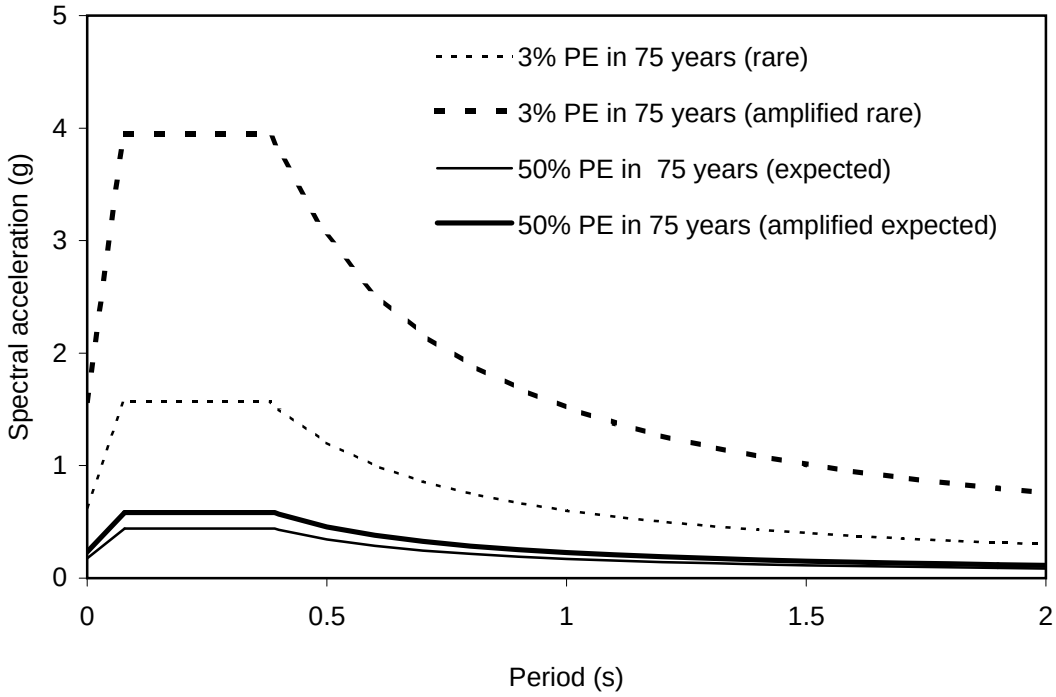

Figure 8-1: NCHRP 12-49 prototype response spectra for expected and rare earthquakes and corresponding amplified spectra to control design.

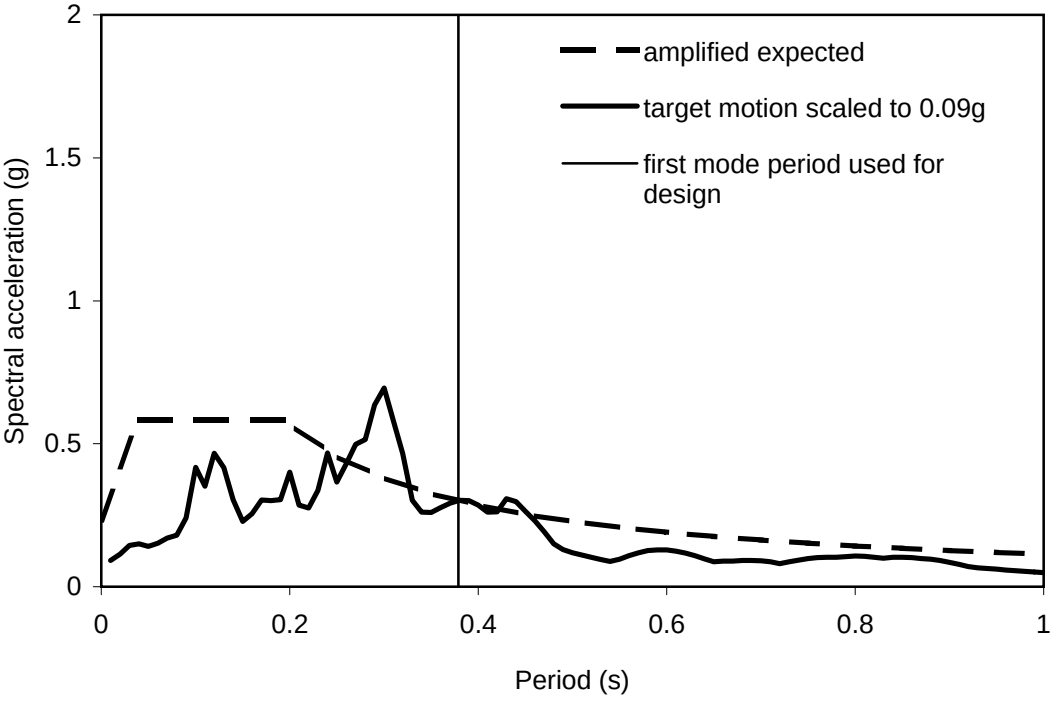

Figure 8-2: Specimen NCHRP amplified expected earthquake design spectrum compared with target motion scaled to match design SA at first mode.

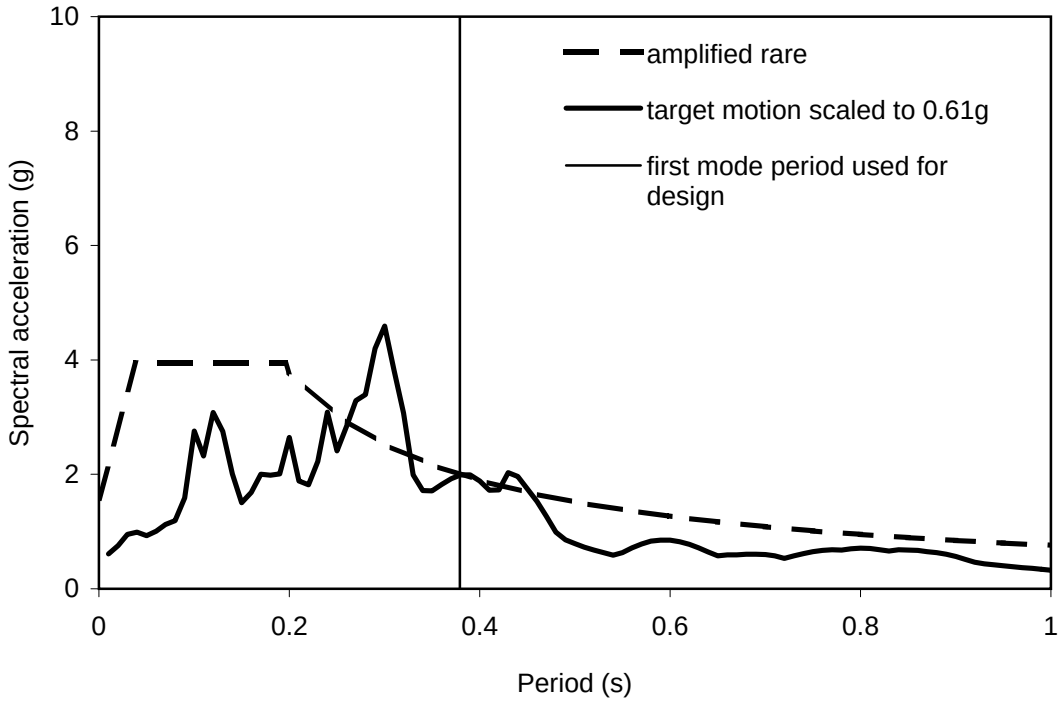

Figure 8-3: Specimen NCHRP amplified rare earthquake design spectrum compared with target motion scaled to match design SA at first mode.

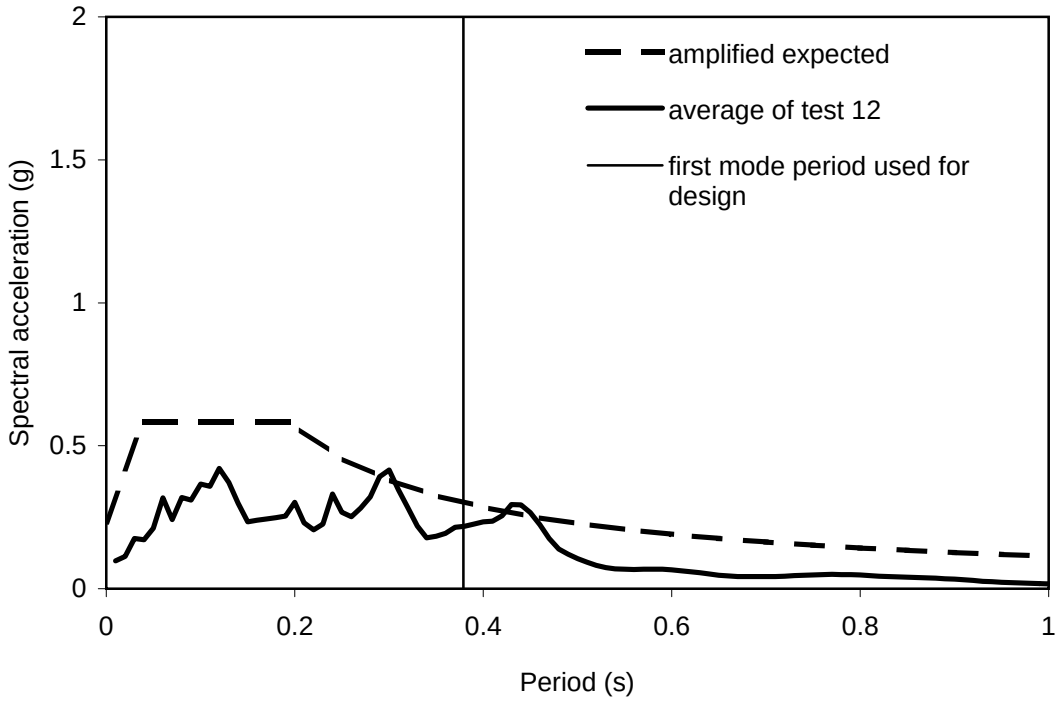

Figure 8-4: Specimen NCHRP amplified expected earthquake design spectrum compared with average achieved motion spectrum for test 12.

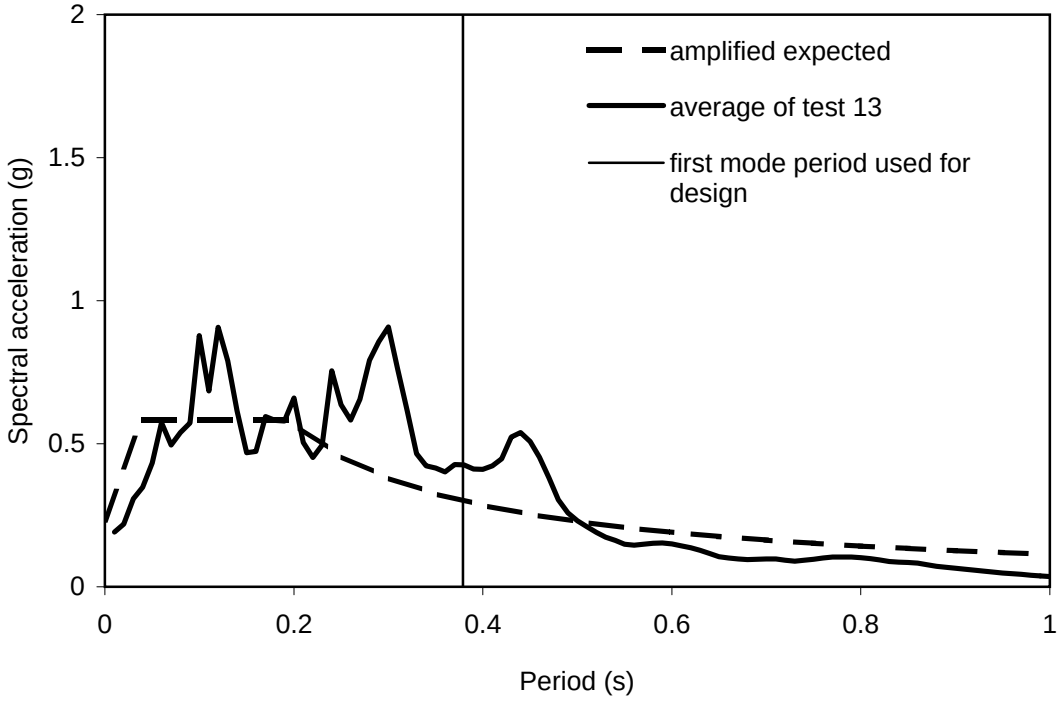

Figure 8-5: Specimen NCHRP amplified expected earthquake design spectrum compared with average achieved motion spectrum for test 13.

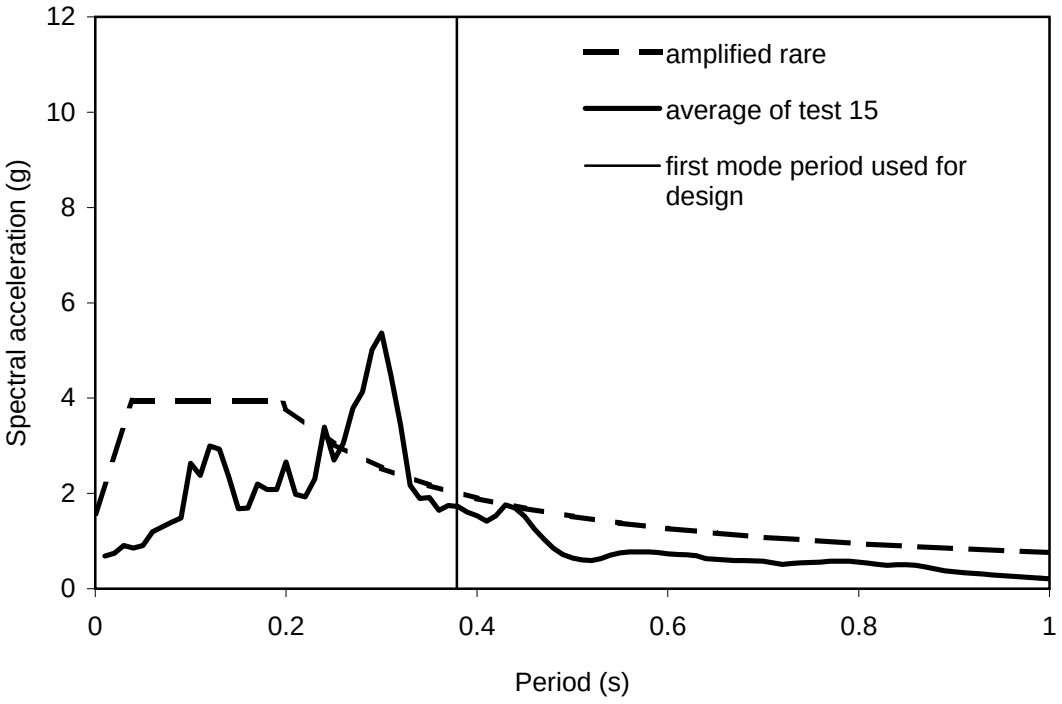

Figure 8-6: Specimen NCHRP amplified rare earthquake design spectrum compared with average achieved motion spectrum for test 15.

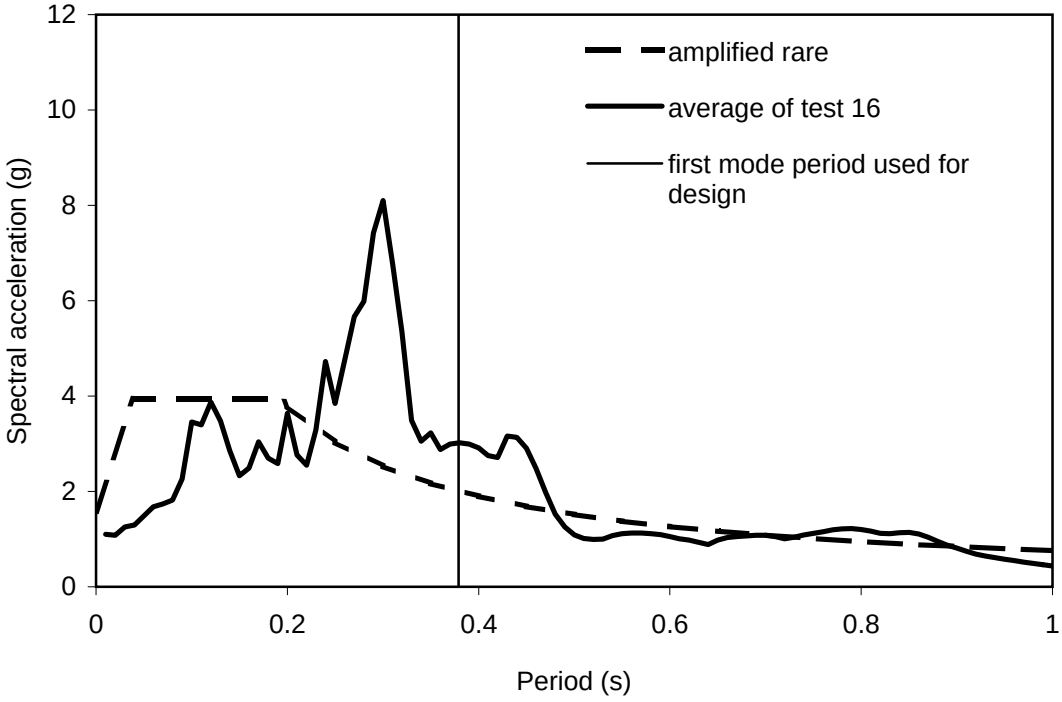

Figure 8-7: Specimen NCHRP amplified rare earthquake design spectrum compared with average achieved motion spectrum for test 16.

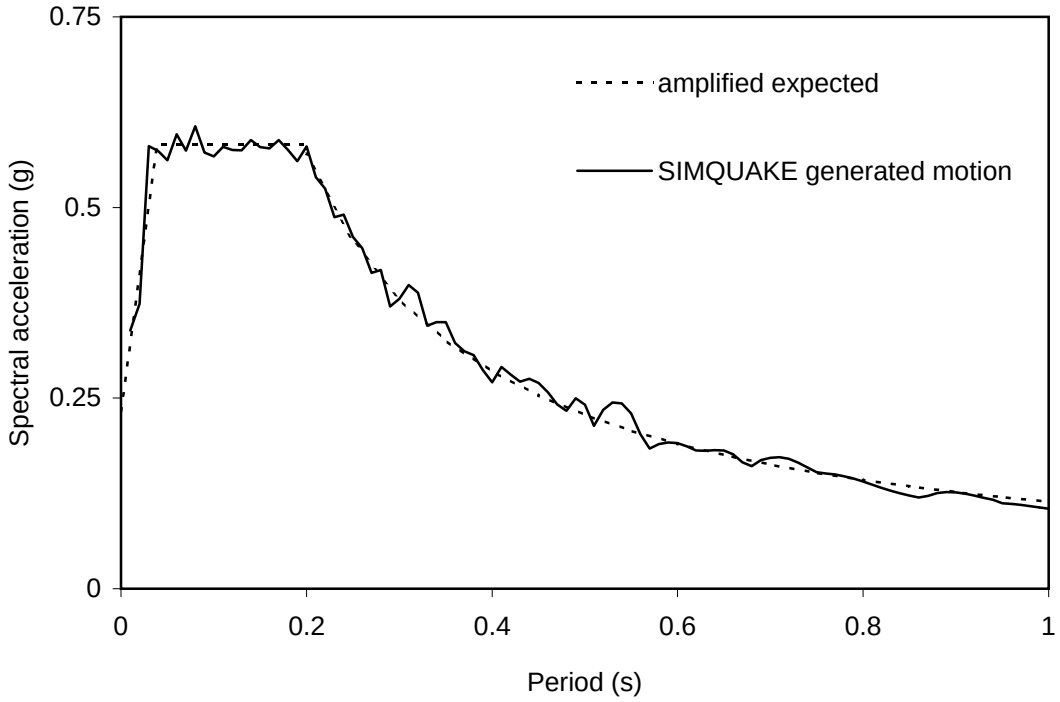

Figure 8-8: Specimen NCHRP amplified expected earthquake design spectrum compared with spectrum from SIMQUAKE generated motion.

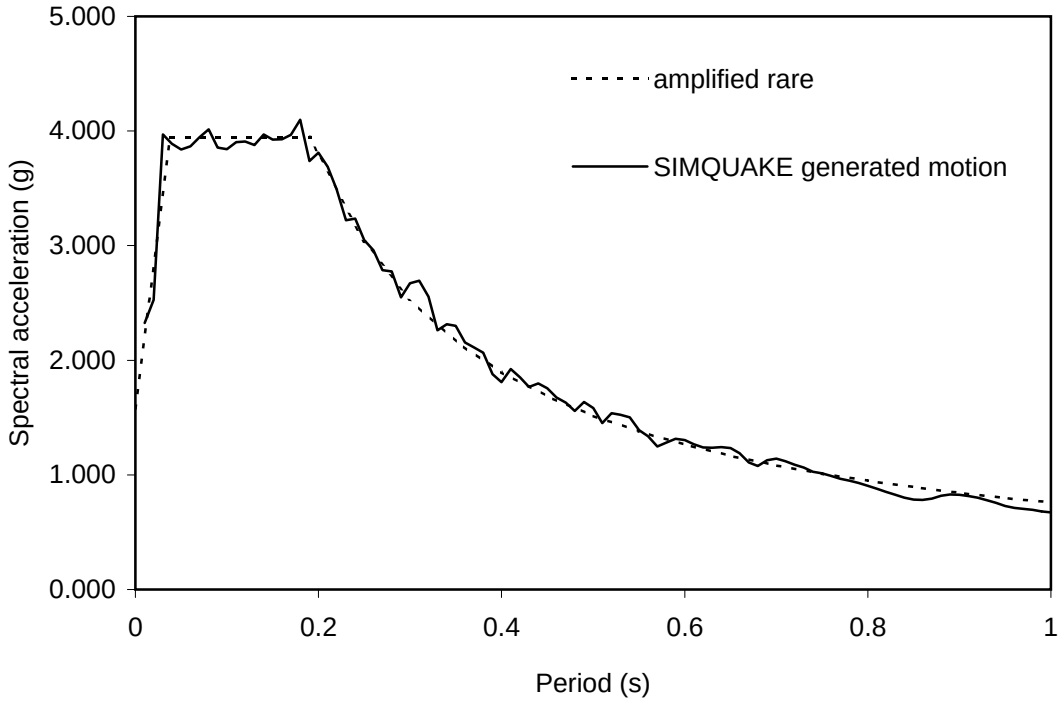

Figure 8-9: Specimen NCHRP amplified rare earthquake design spectrum compared with spectrum from SIMQUAKE generated motion.

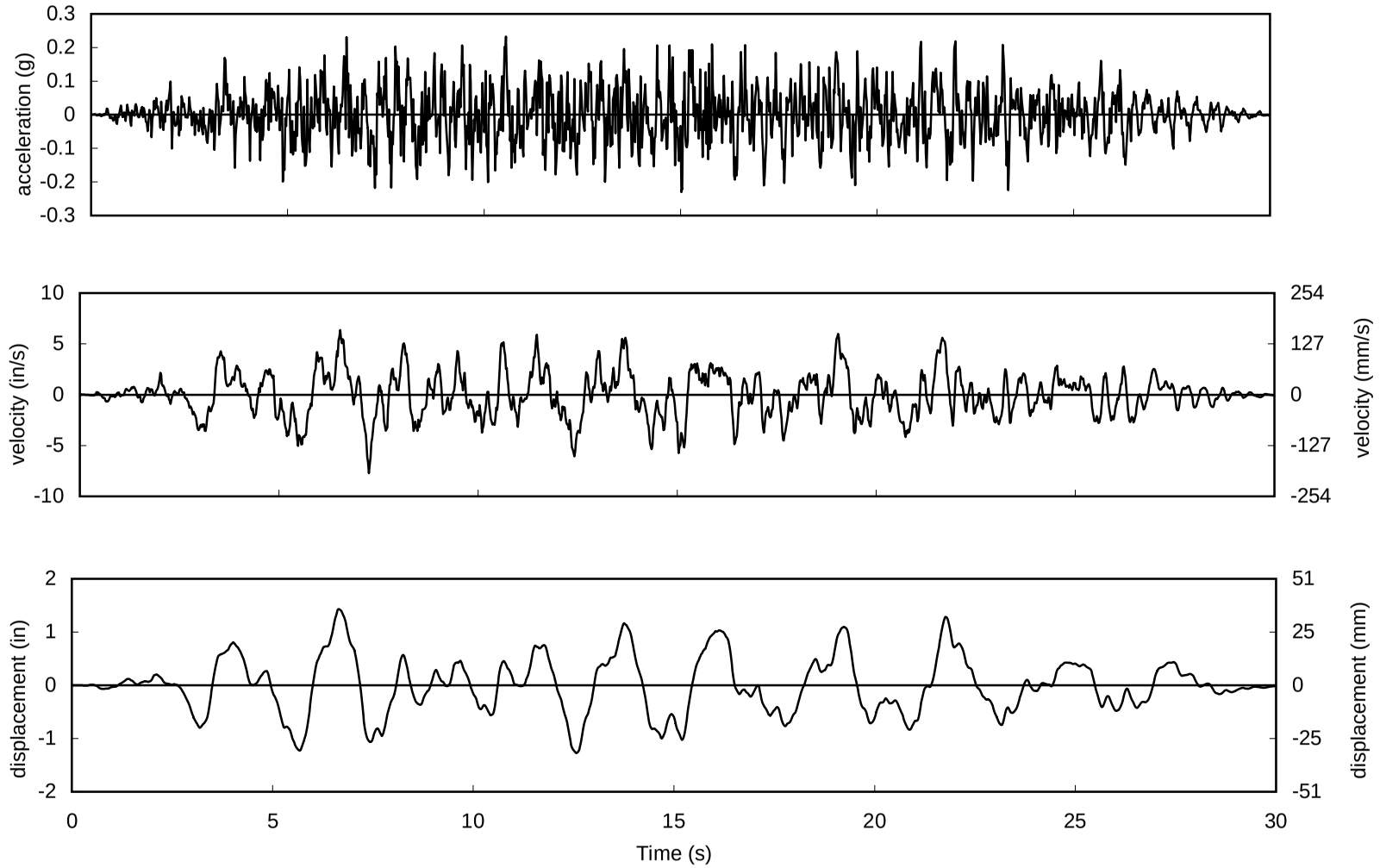

Figure 8-10: Prototype scale acceleration, velocity, and displacement histories from SIMQKE generated earthquake motion based on "amplified expected" earthquake.

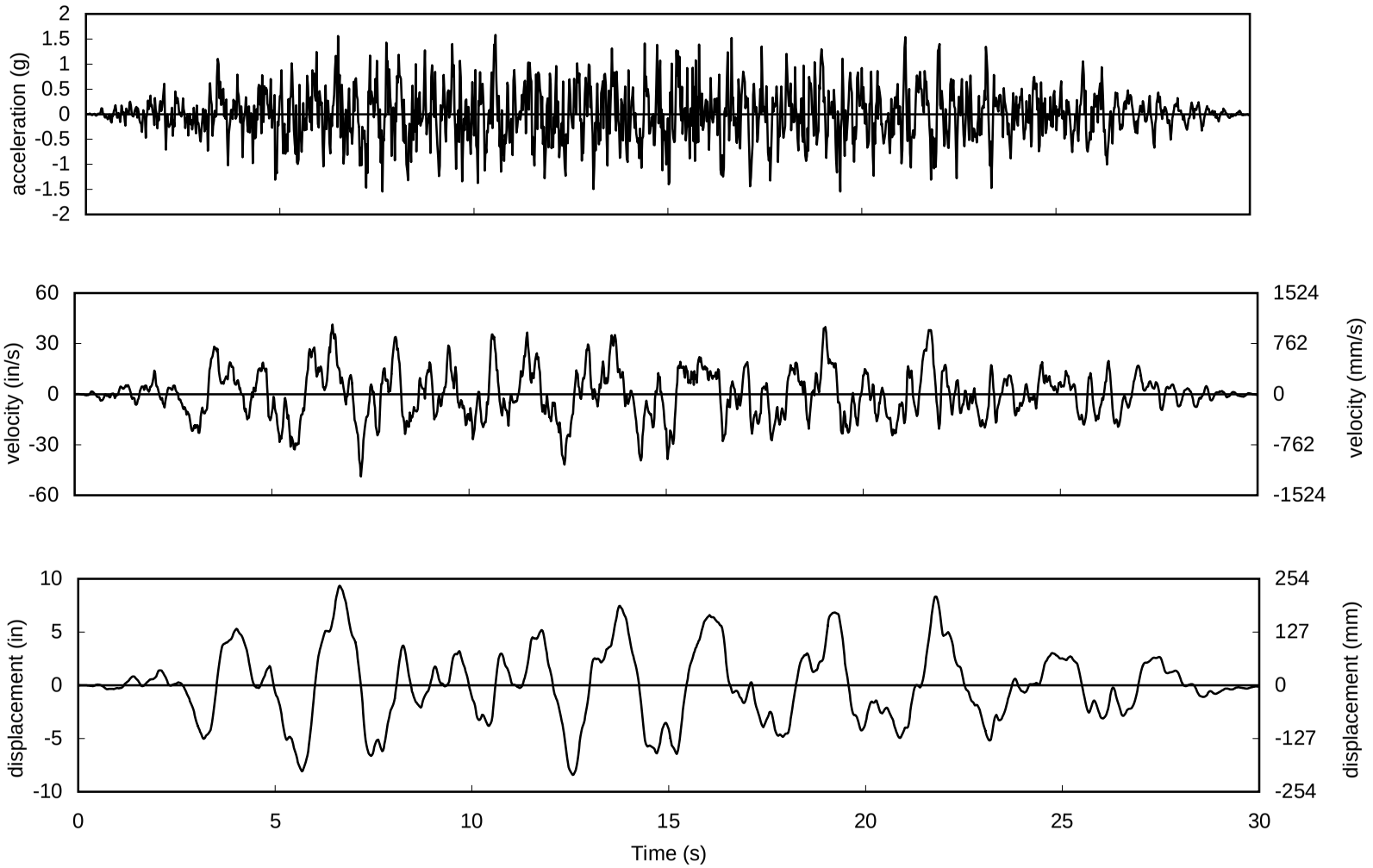

Figure 8-11: Prototype scale acceleration, velocity, and displacement histories from SIMQKE generated earthquake motion based on "amplified rare" earthquake.

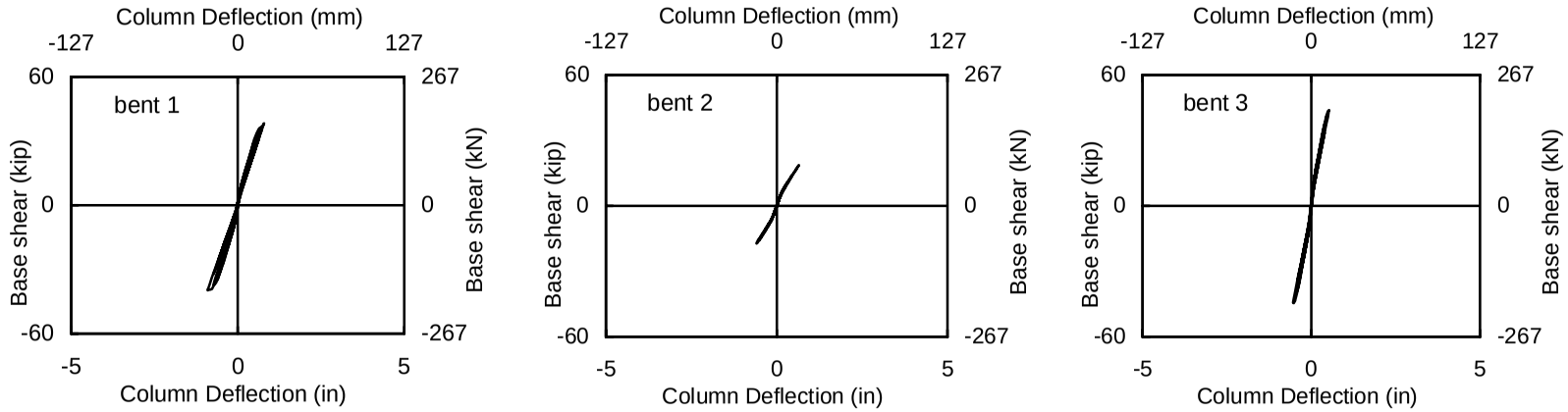

Figure 8-12: Drain-3DX calculated shear-deflection hysteresis for bents 1-3 when subjected to synthetic motion based on amplified expected (50% PE in 75 year) earthquake design spectrum.

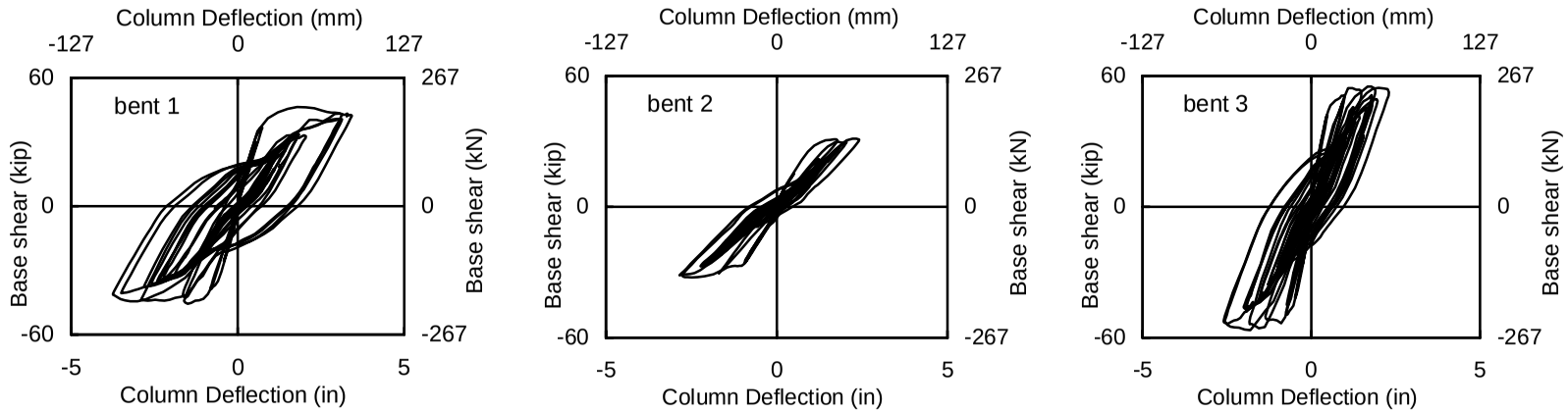

Figure 8-13: Drain-3DX calculated shear-deflection hysteresis for bents 1-3 when subjected to synthetic motion based on amplified rare (3% PE in 75 year) earthquake design spectrum.

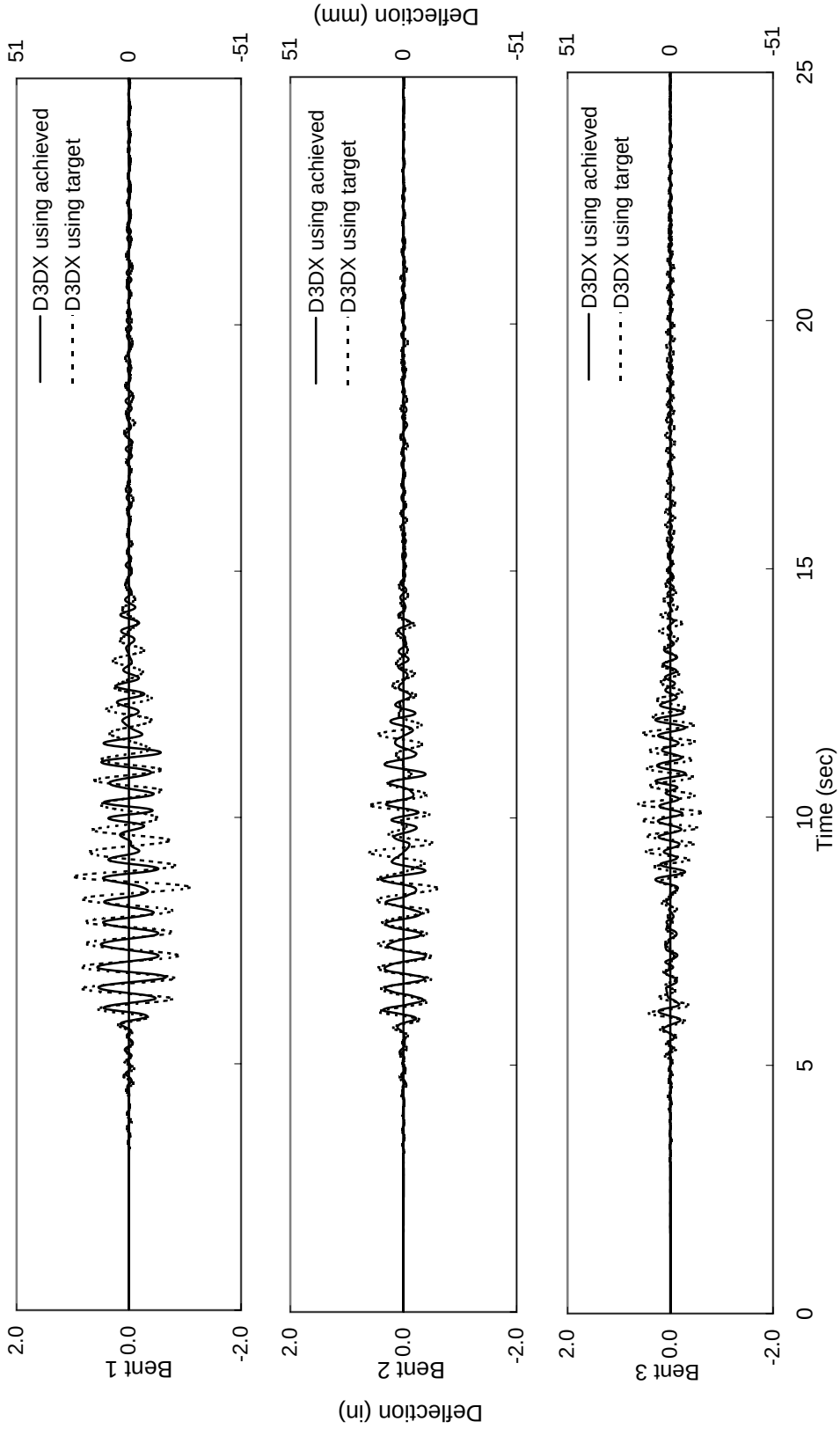

Figure 9-1: D3DX column deflection predictions for test 13 using target and achieved shake table motions.

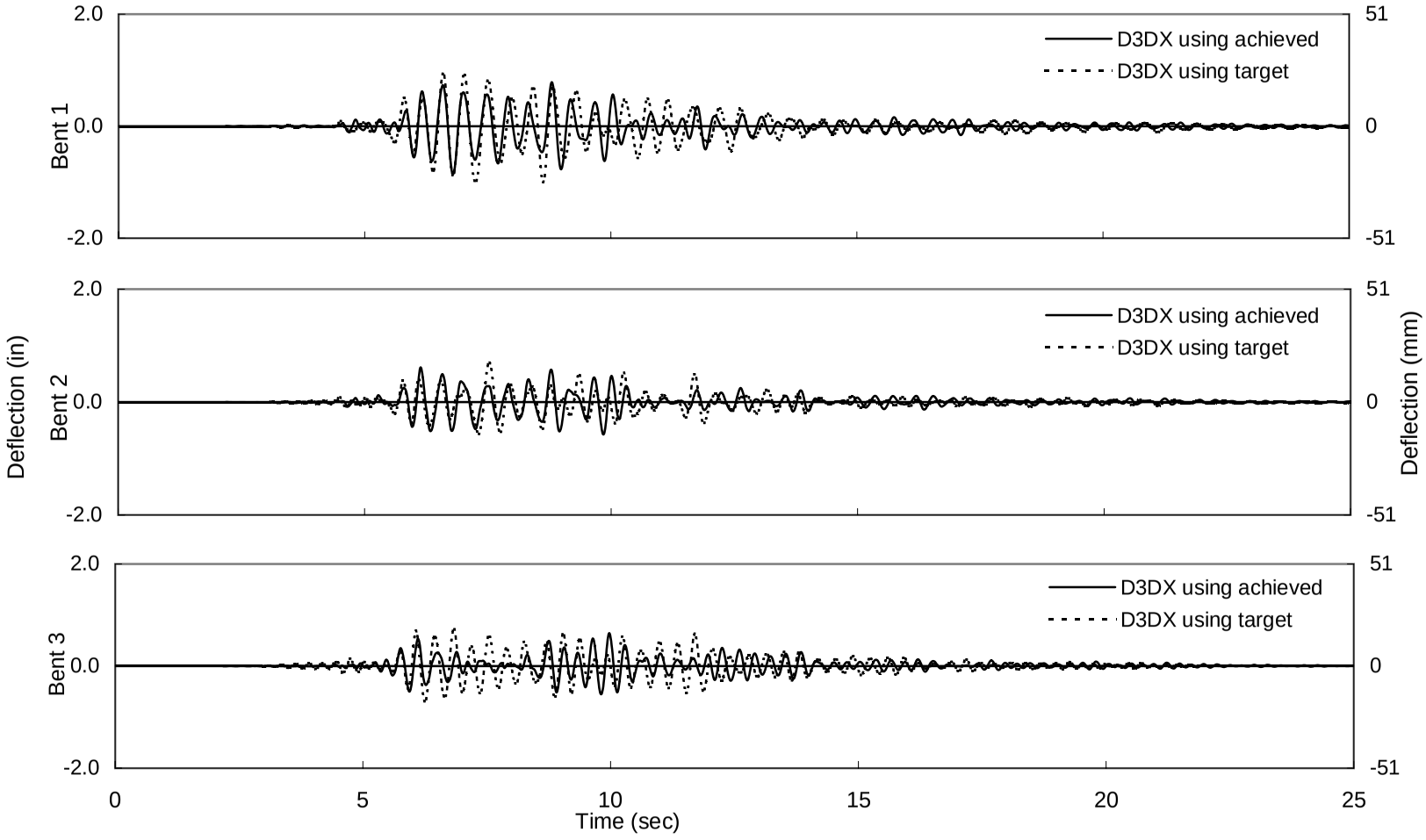

Figure 9-2: D3DX column deflection predictions for test 14 using target and achieved shake table motions.

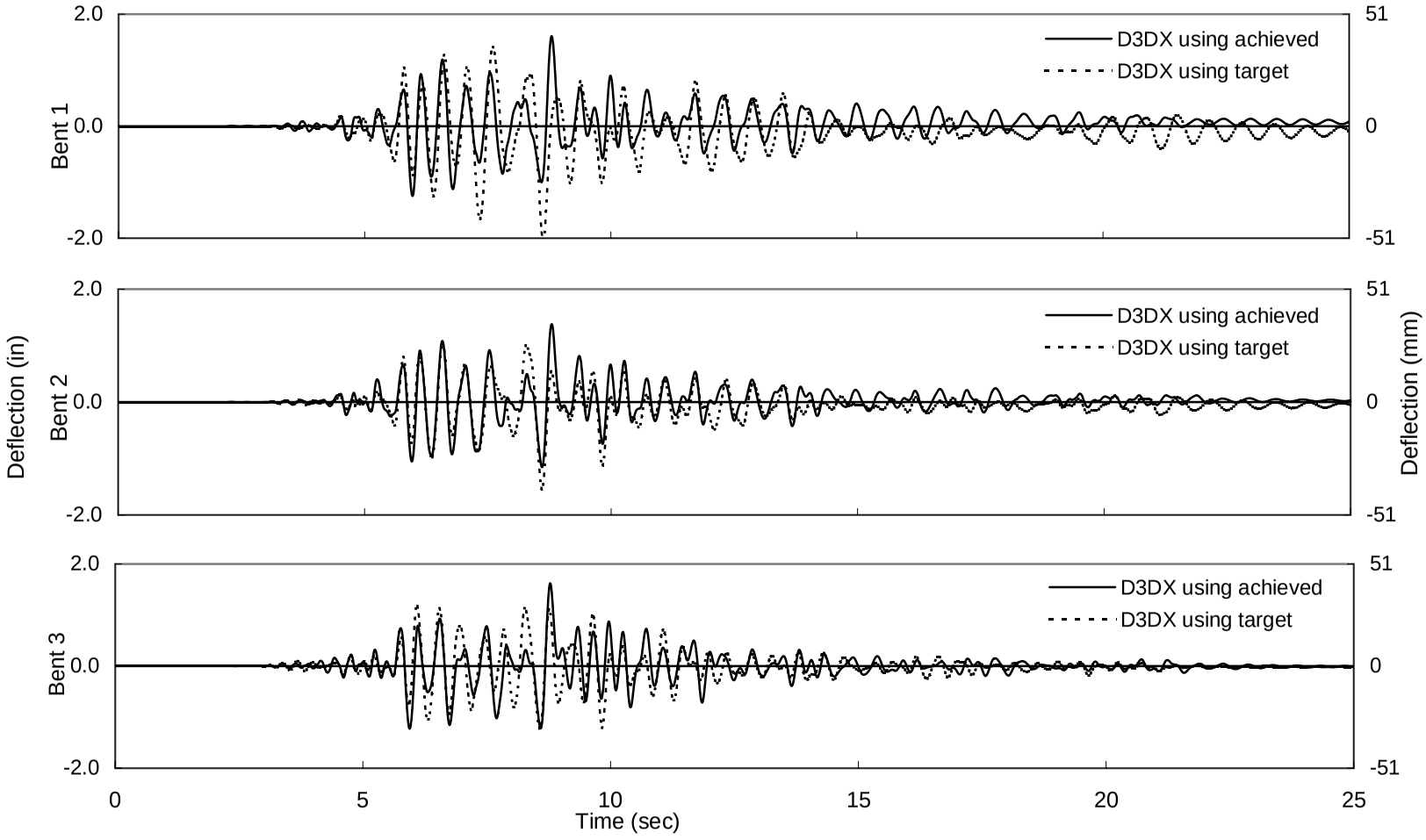

Figure 9-3: D3DX column deflection predictions for test 15 using target and achieved shake table motions.

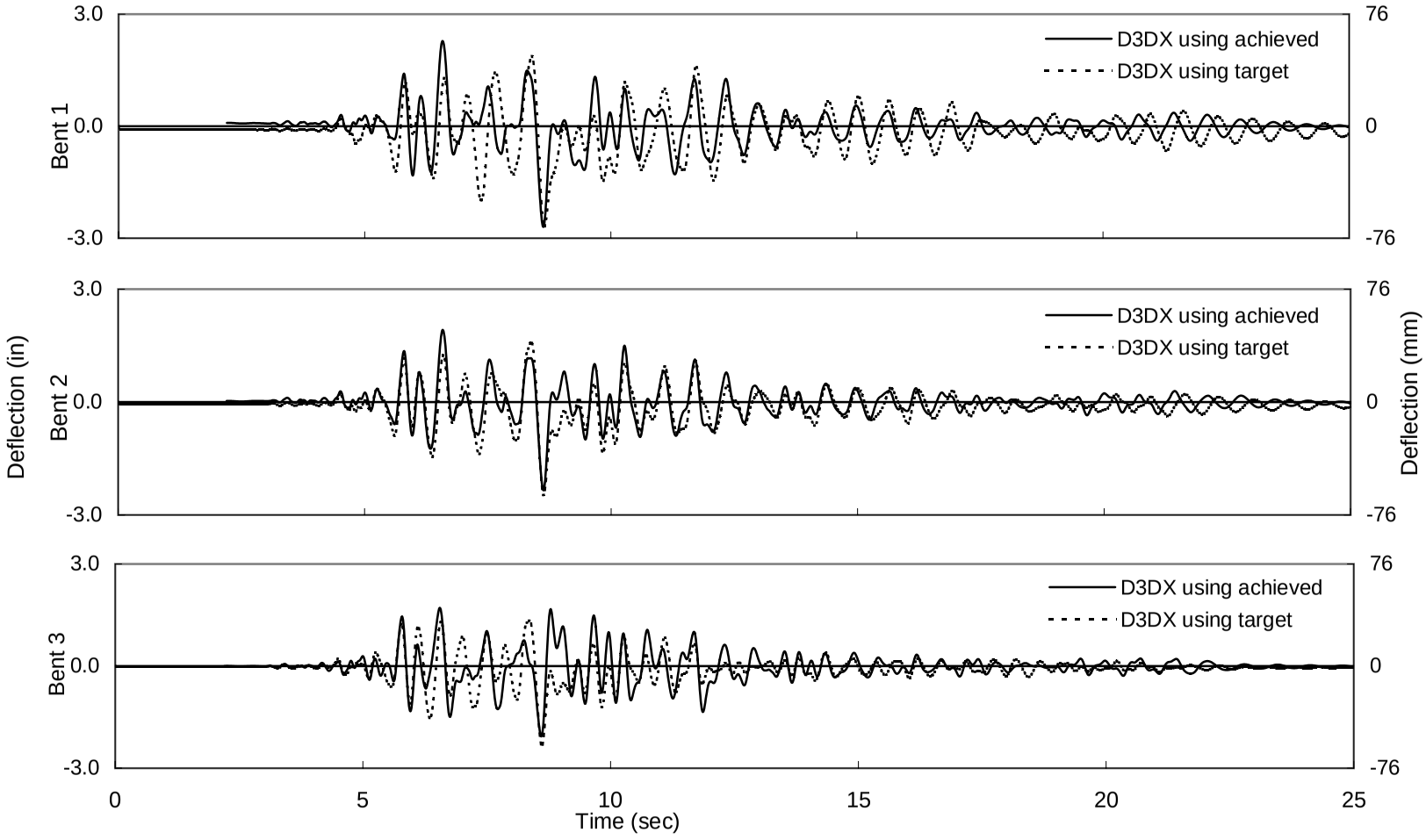

Figure 9-4: D3DX column deflection predictions for test 16 using target and achieved shake table motions.

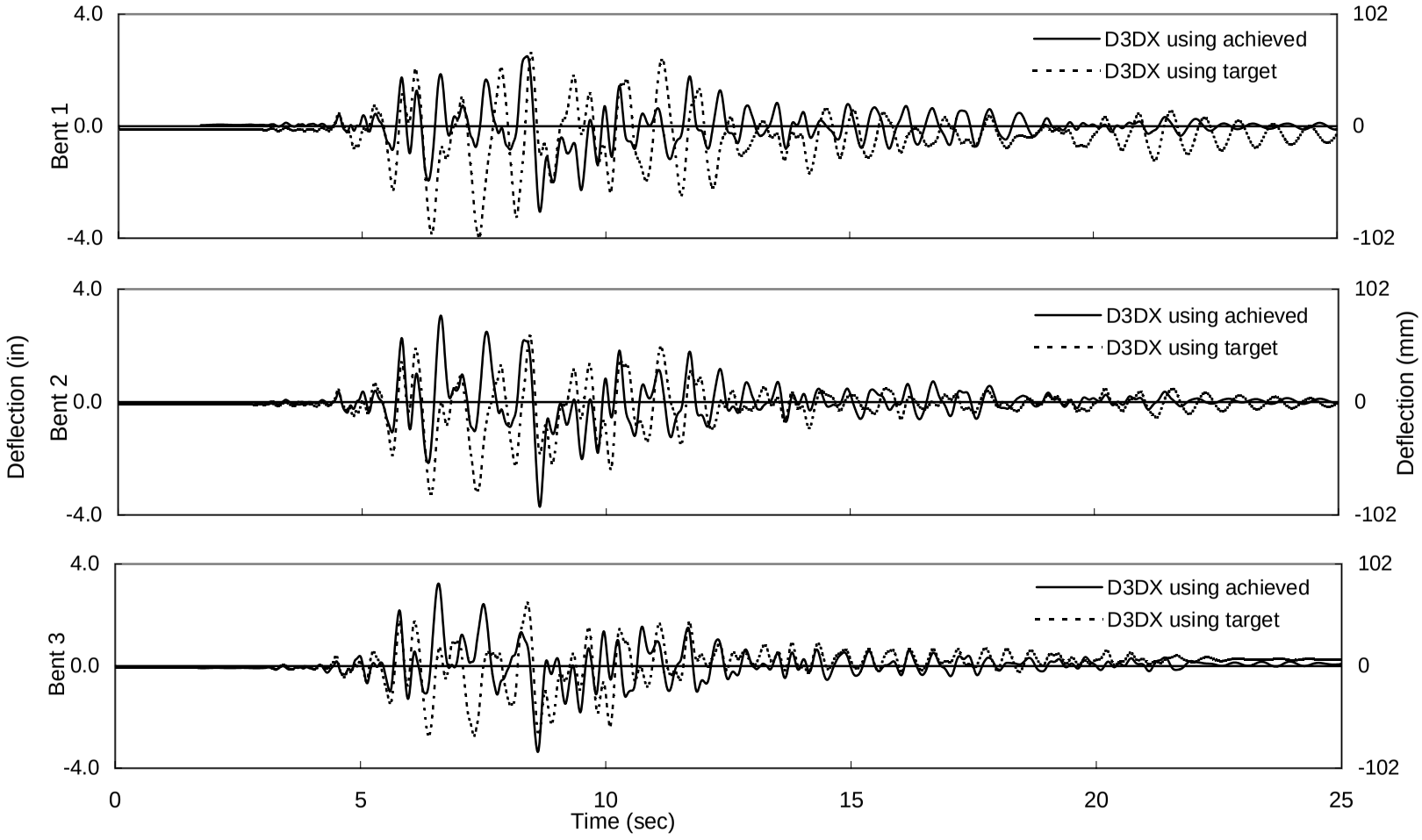

Figure 9-5: D3DX column deflection predictions for test 18 using target and achieved shake table motions.

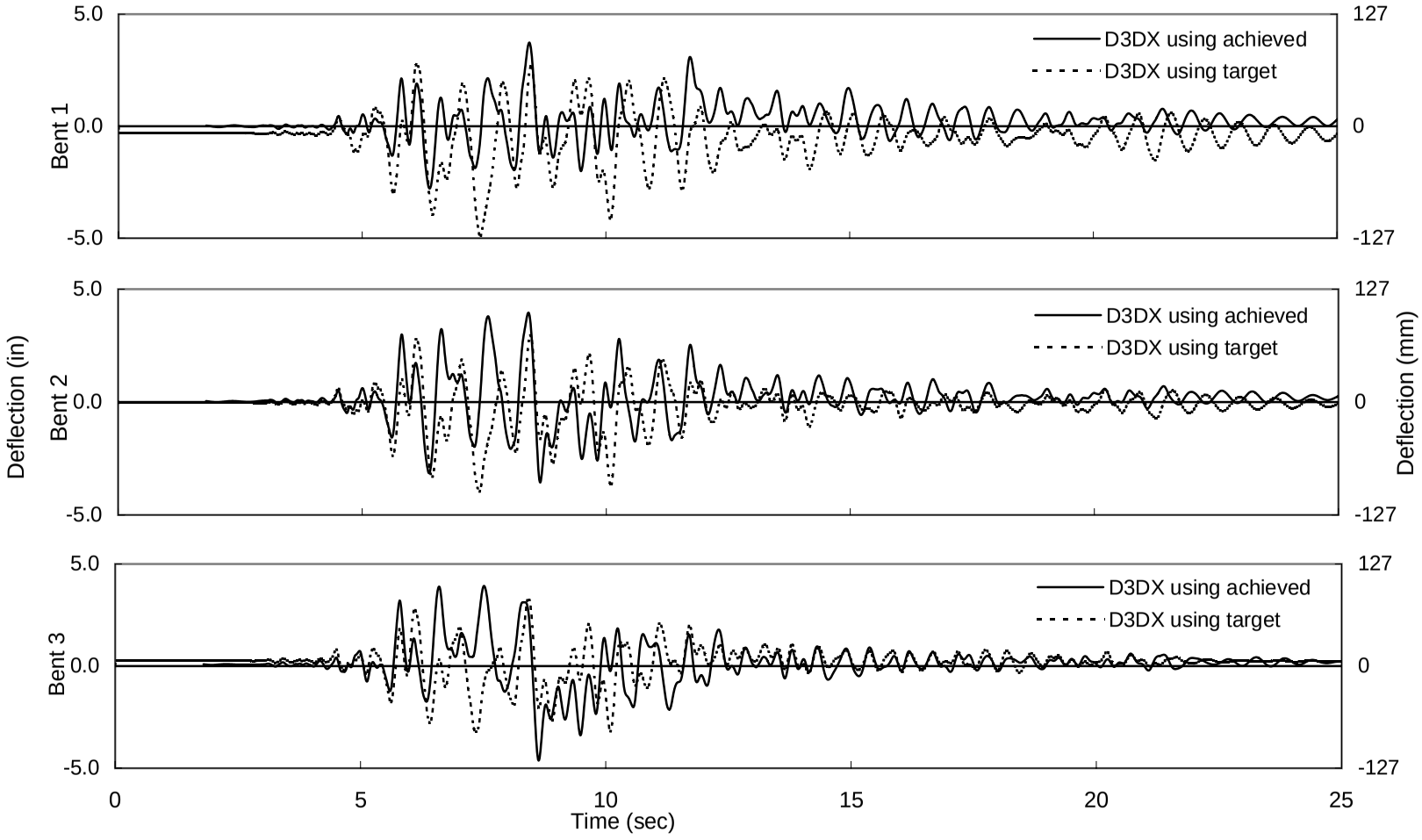

Figure 9-6: D3DX column deflection predictions for test 19 using target and achieved shake table motions.

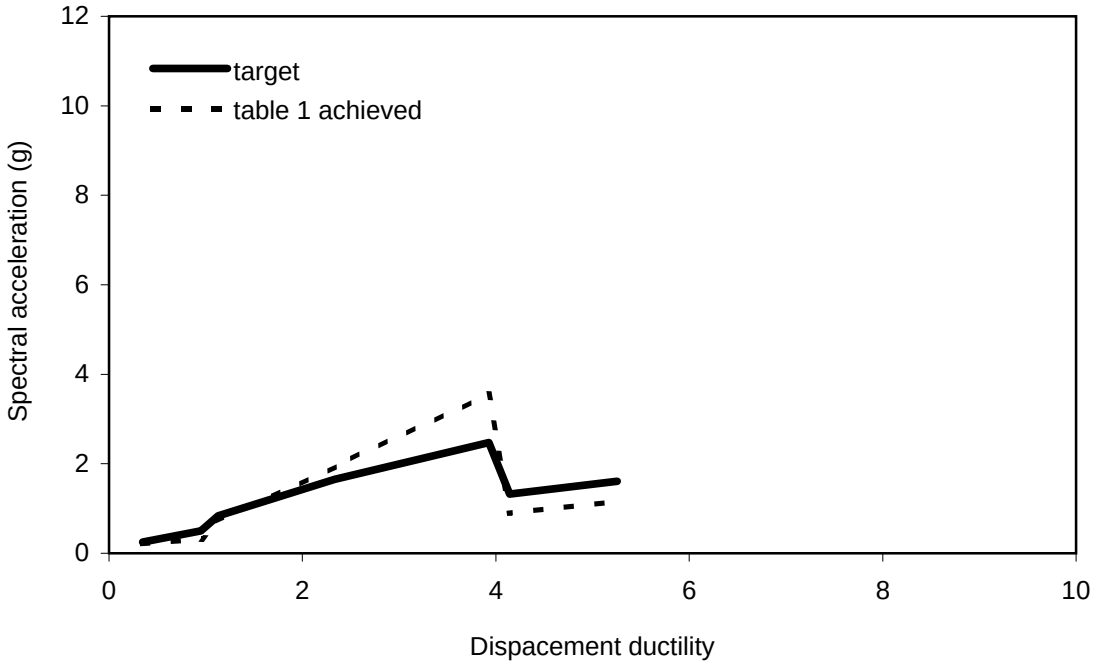

Figure 9-7: Target and table 1 achieved spectral accelerations at measured transverse mode 1 frequencies for tests 12 through 19 vs. displacement ductility of bent 1.

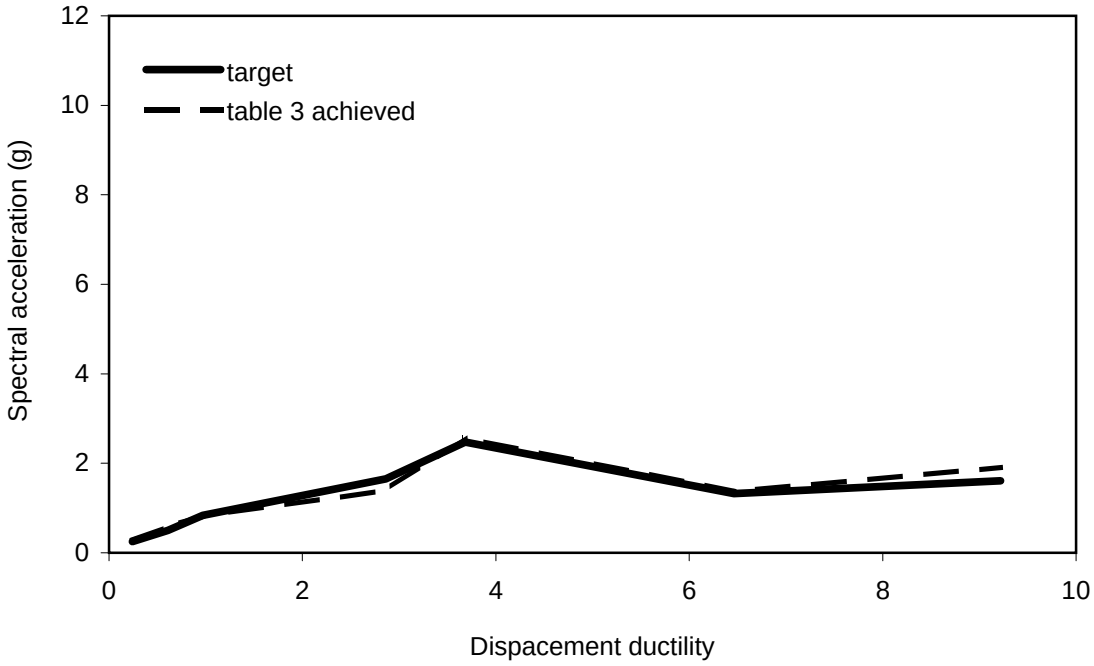

Figure 9-8: Target and table 3 achieved spectral accelerations at measured transverse mode 1 frequencies for tests 12 through 19 vs. displacement ductility of bent 3.

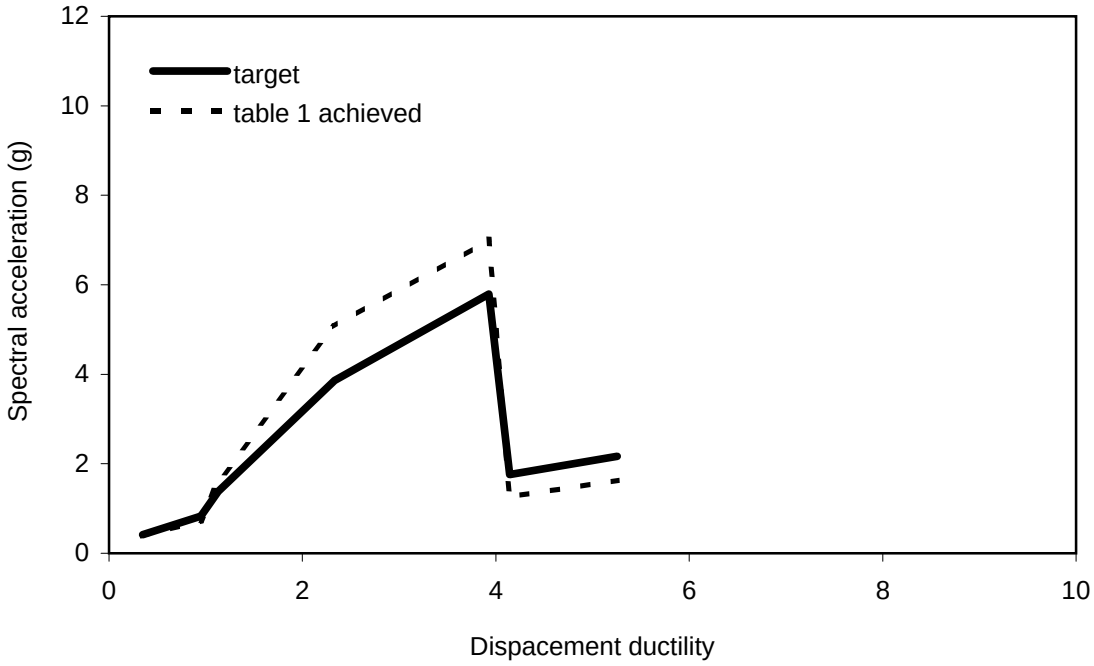

Figure 9-9: Target and table 1 achieved spectral accelerations at measured transverse mode 2 frequencies for tests 12 through 19 vs. displacement ductility of bent 1.

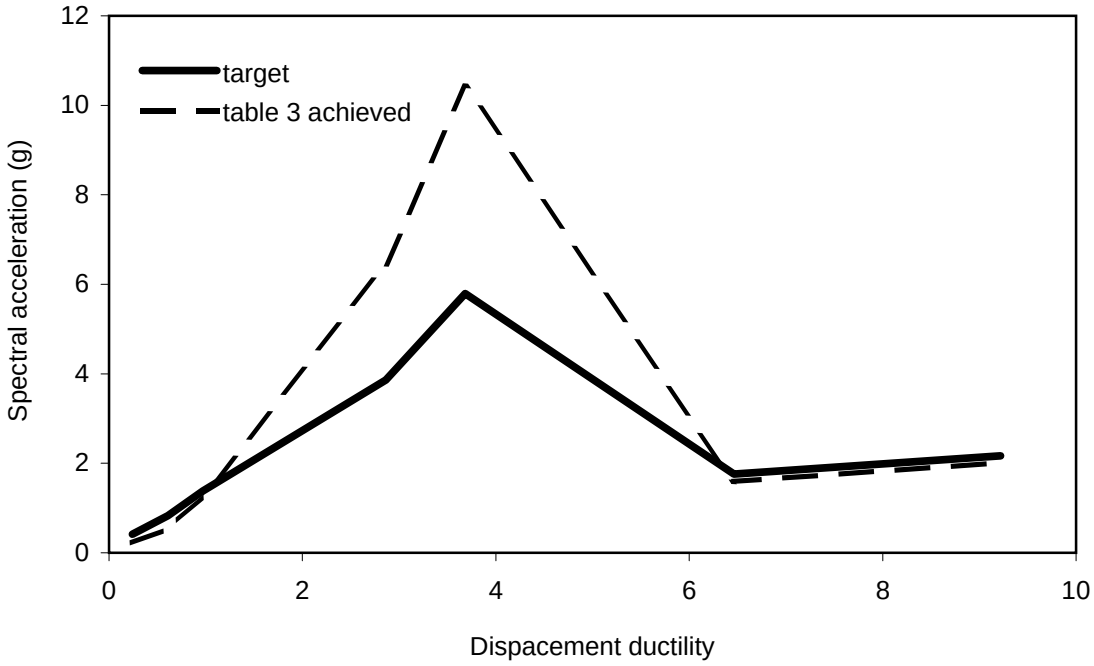

Figure 9-10: Target and table 3 achieved spectral accelerations at measured transverse mode 2 frequencies for tests 12 through 19 vs. displacement ductility of bent 3.

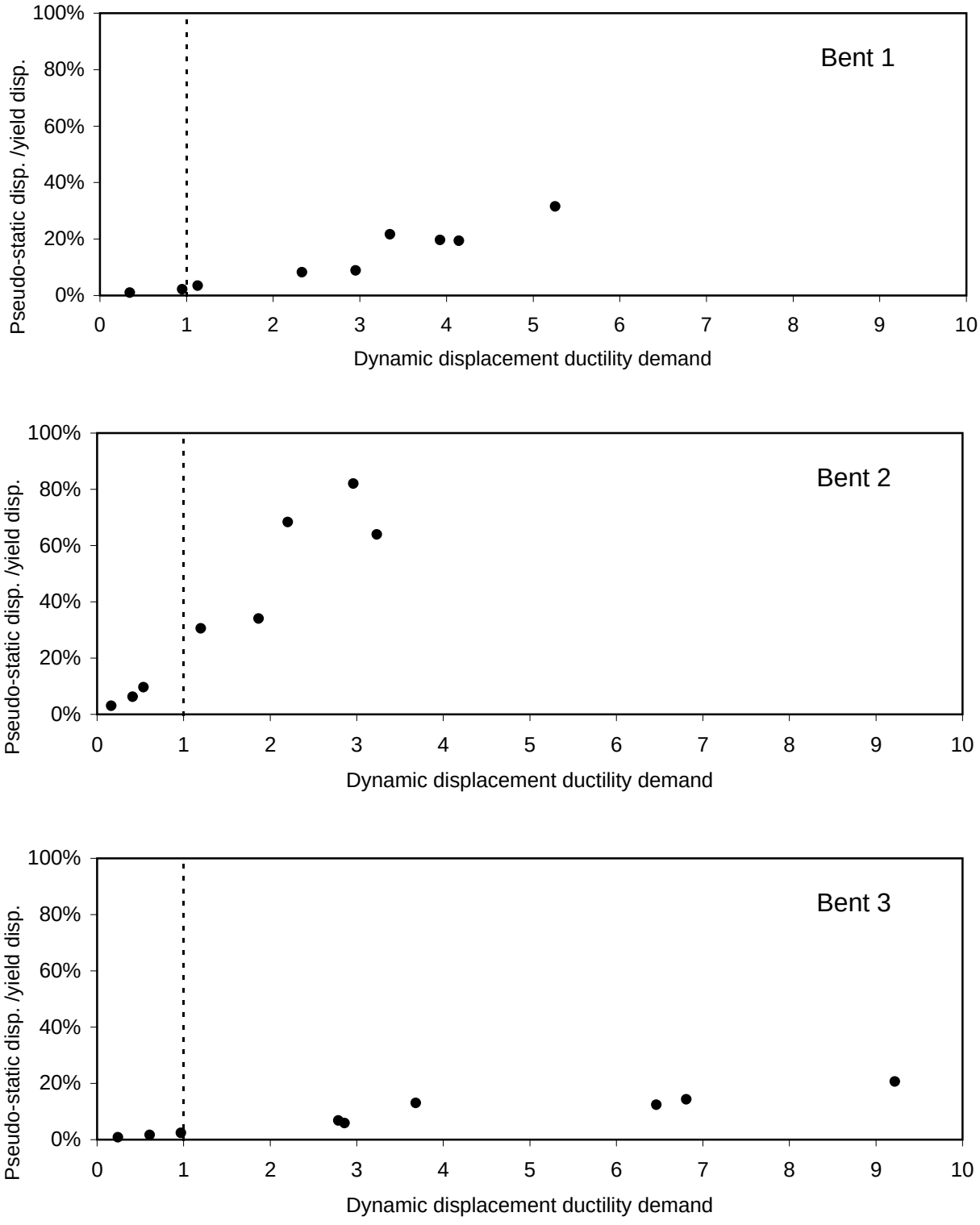

Figure 9-11: Calculated bent 1-3 pseudo-static displacement demand divided by yield displacement vs. calculated dynamic displacement ductility demand for tests 12 through 20.

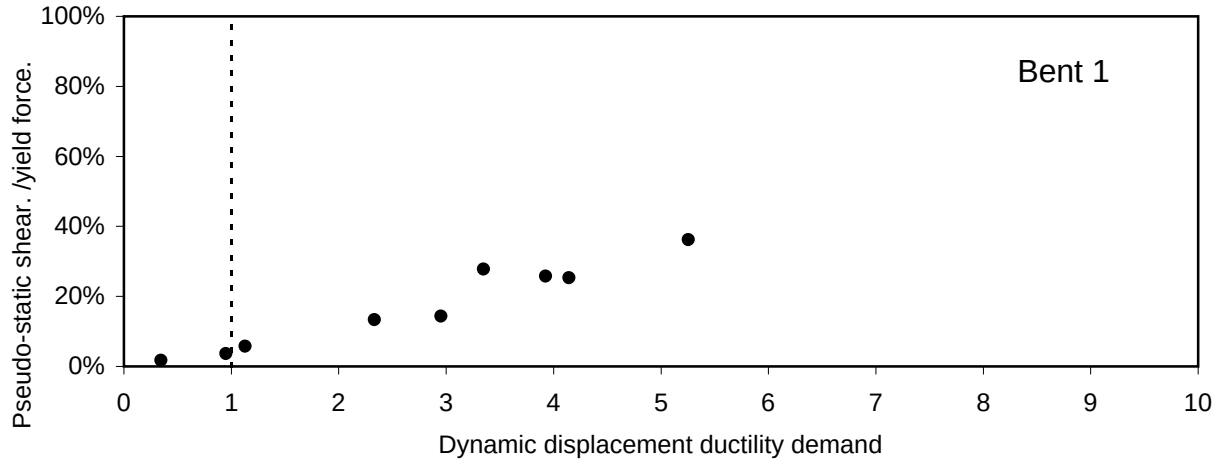

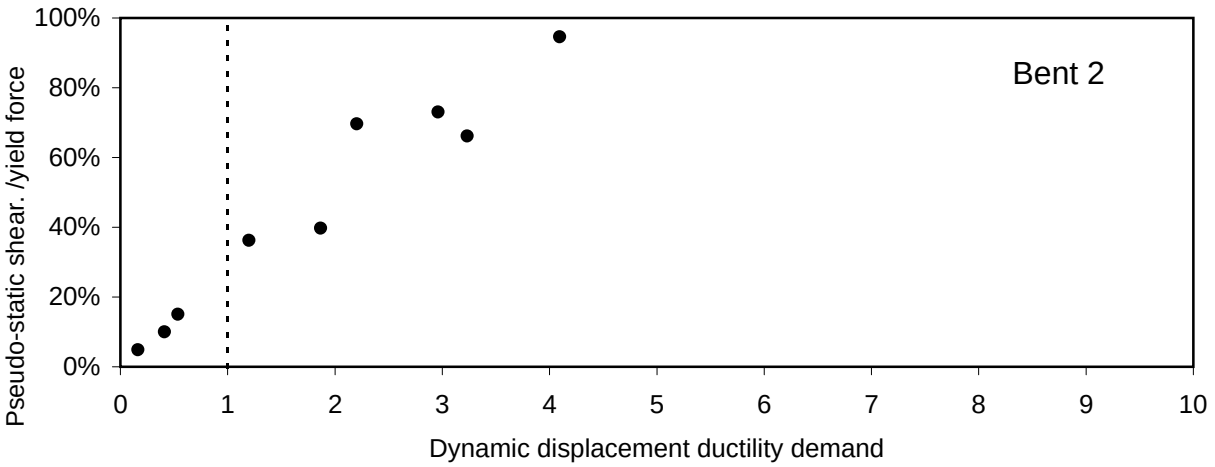

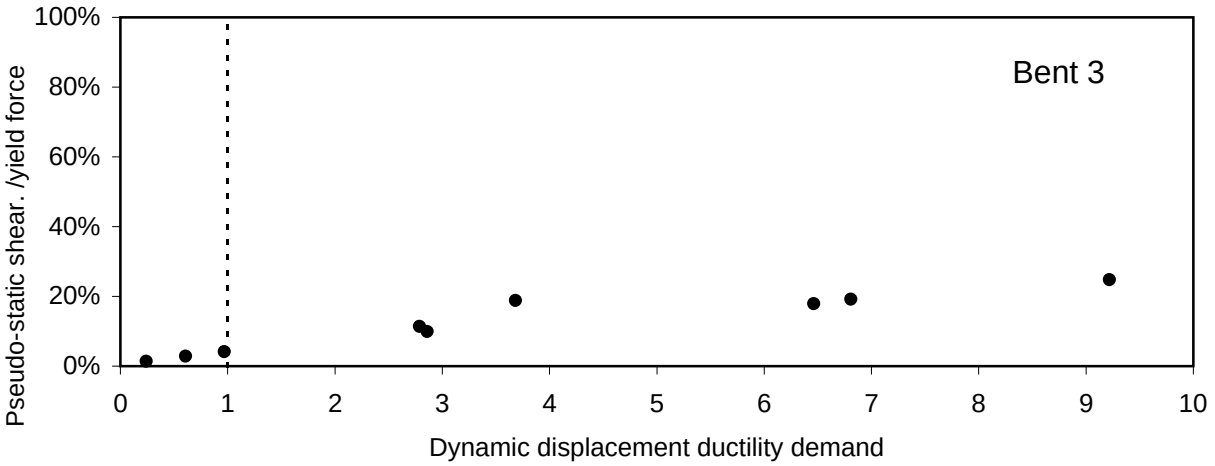

Figure 9-12: Calculated bent 1-3 pseudo-static shear demand divided by yield force vs. calculated dynamic displacement ductility demand for tests 12 through 20.

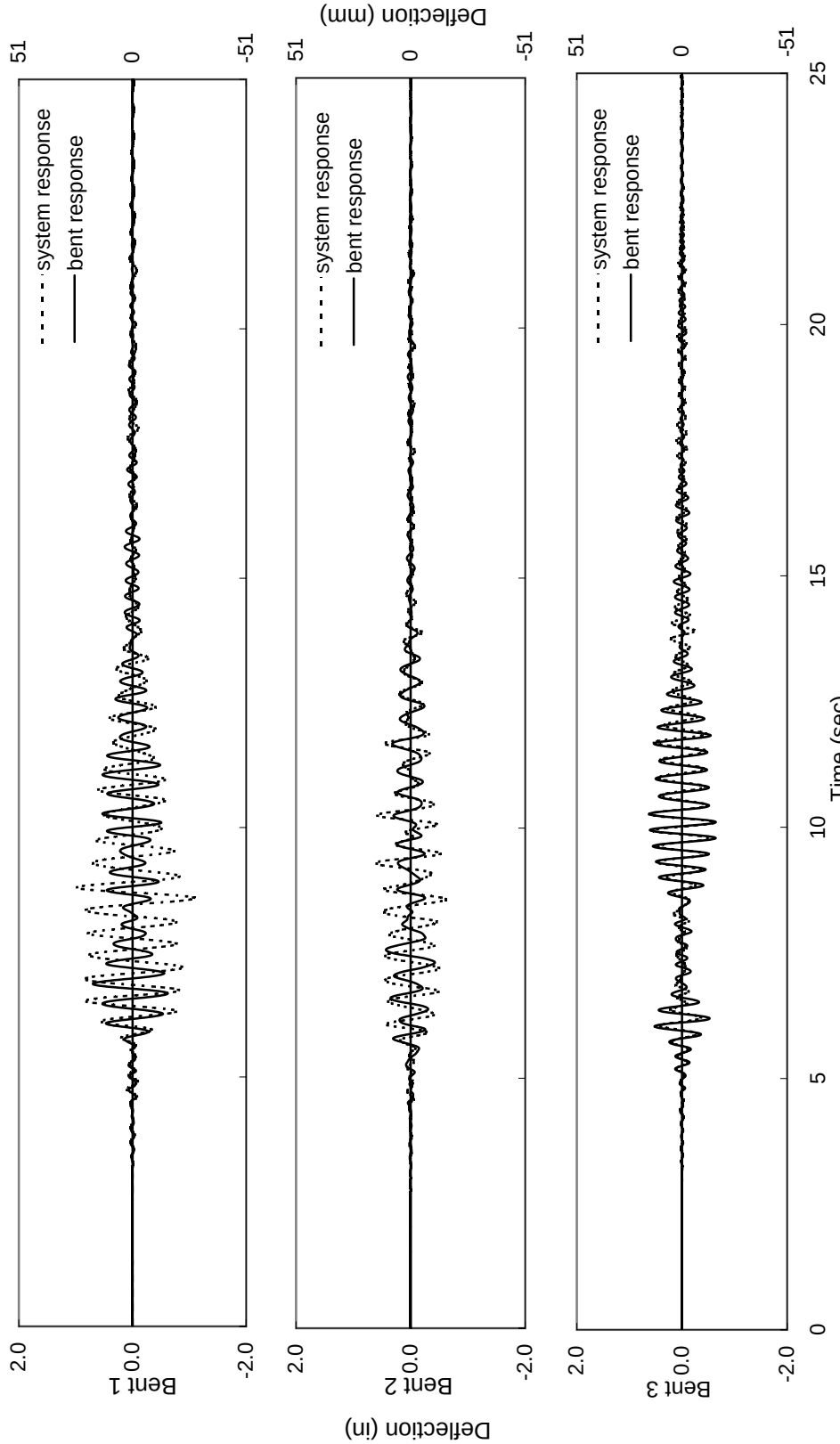

Figure 10-1: Comparison of calculated system and individual bent displacement response for bents 1-3 subjected to target motion of test 13.

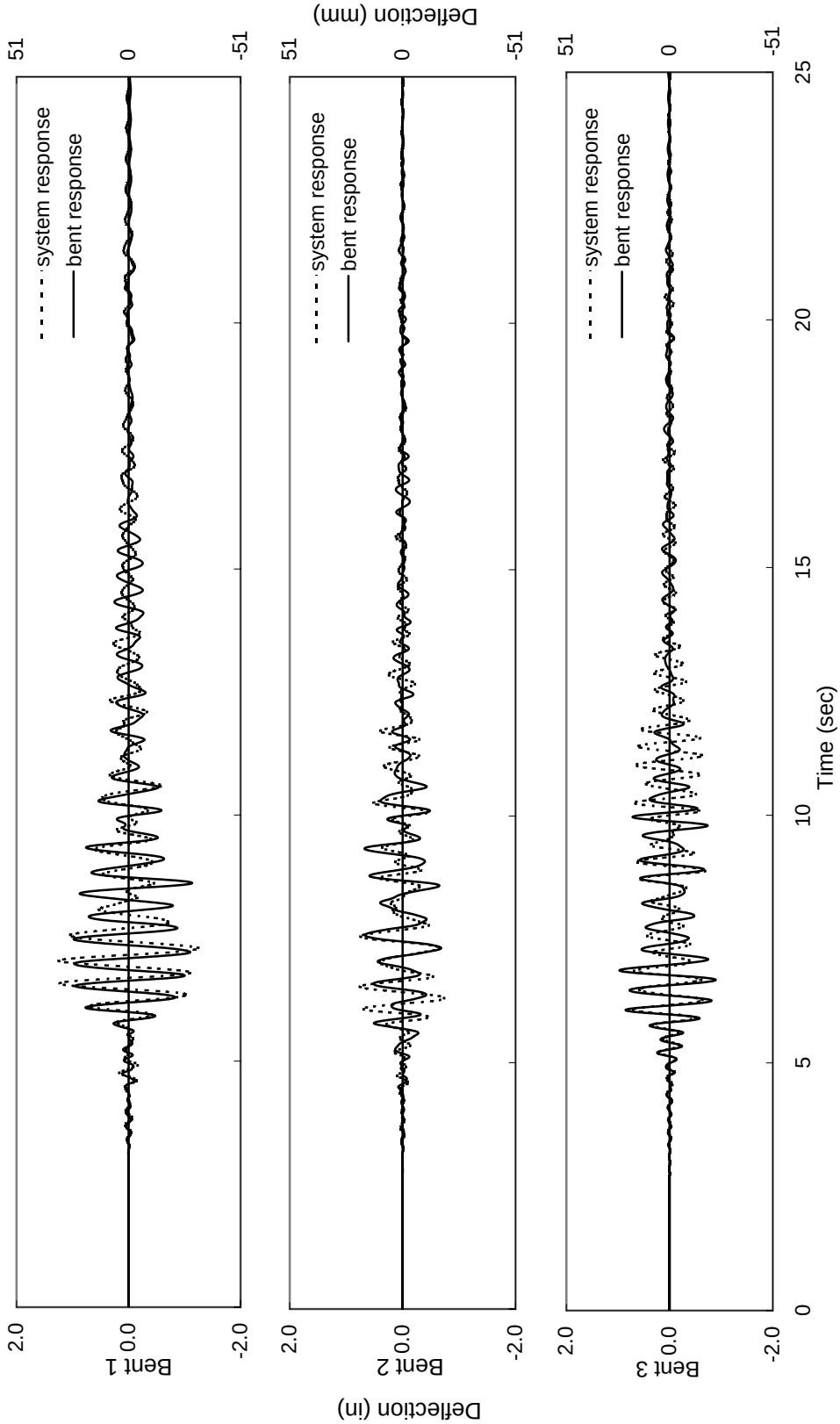

Figure 10-2: Comparison of calculated system and individual bent displacement response for bents 1-3 subjected to target motion of test 14.

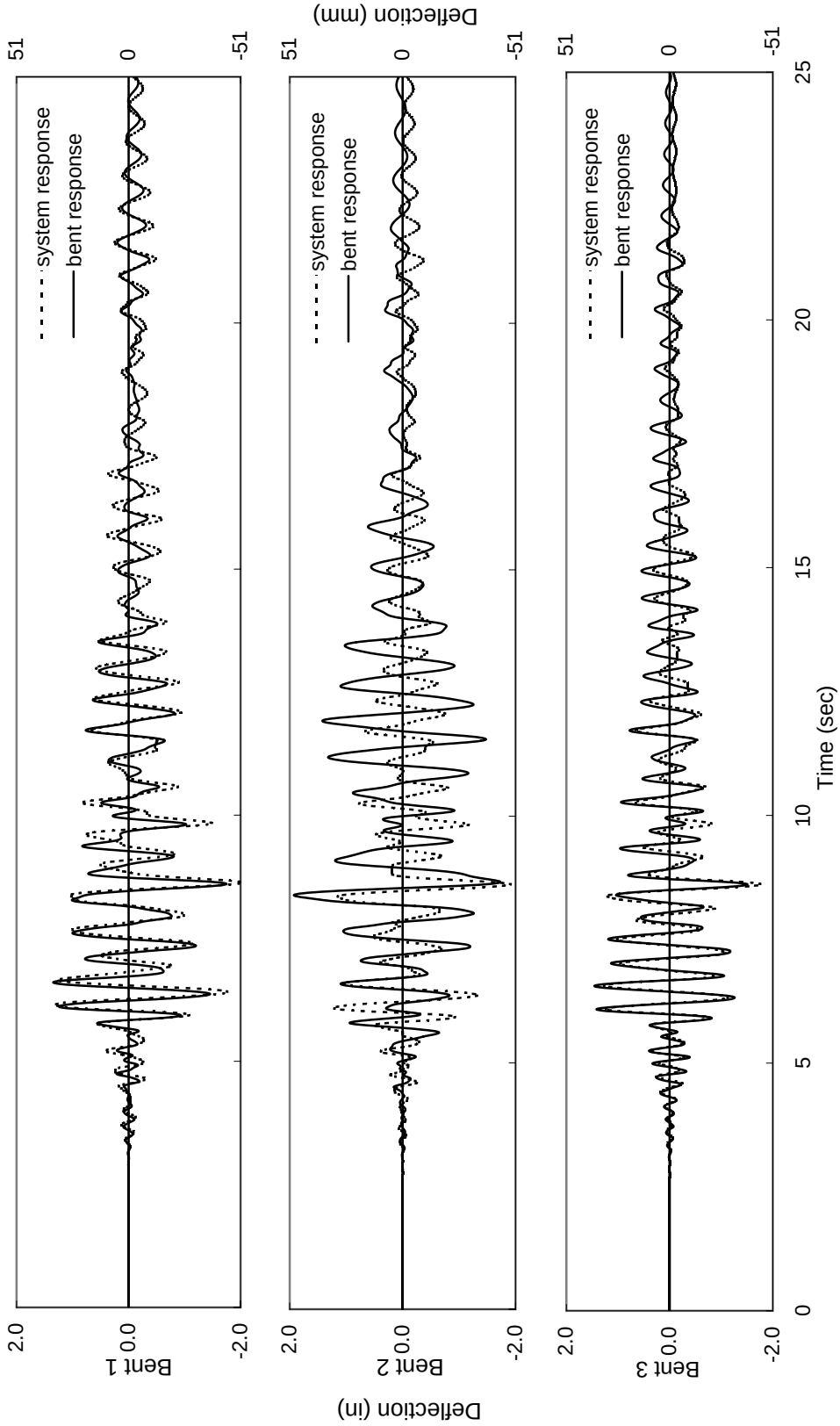

Figure 10-3: Comparison of calculated system and individual bent displacement response for bents 1-3 subjected to target motion of test 15.

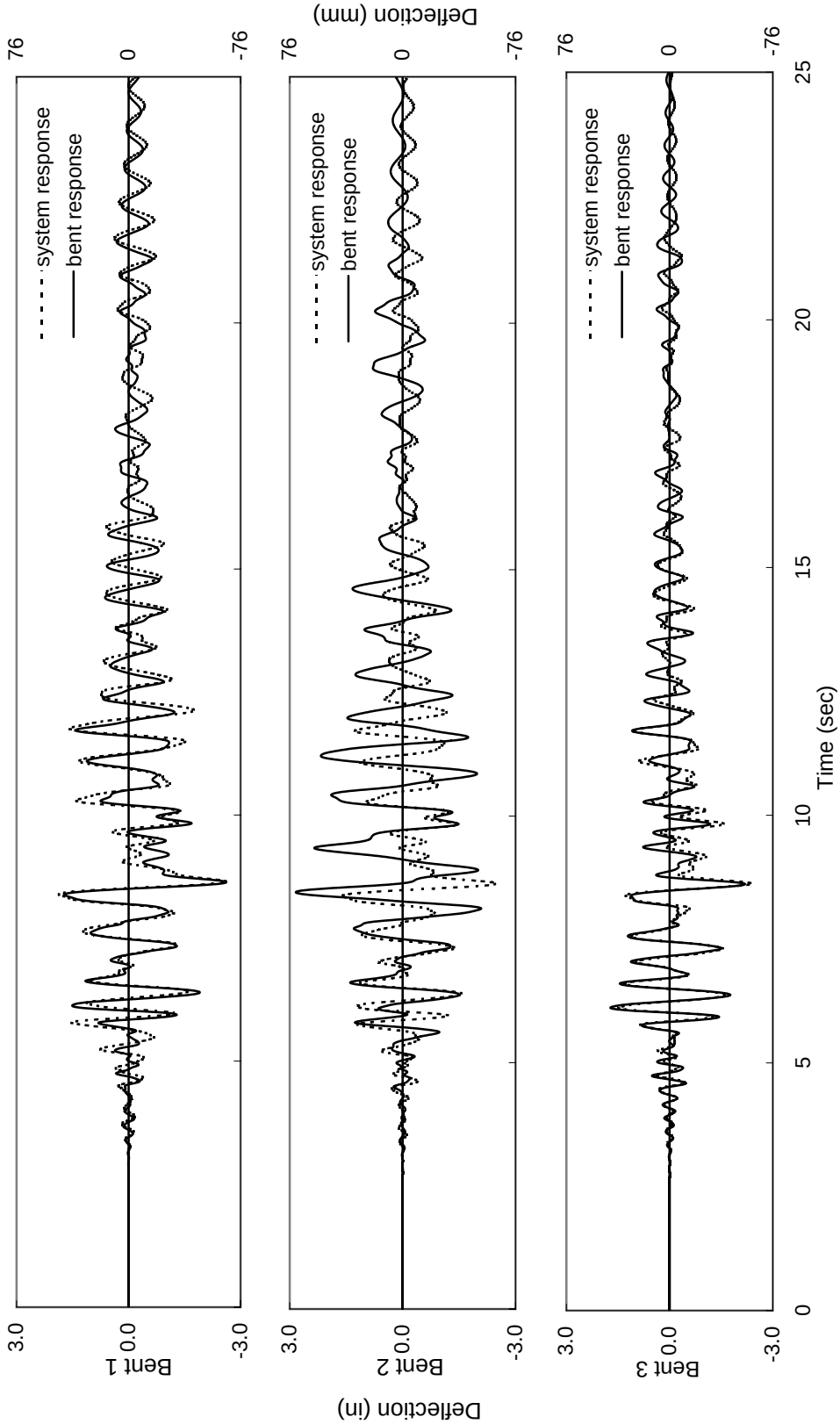

Figure 10-4: Comparison of calculated system and individual bent displacement response for bents 1-3 subjected to target motion of test 16.

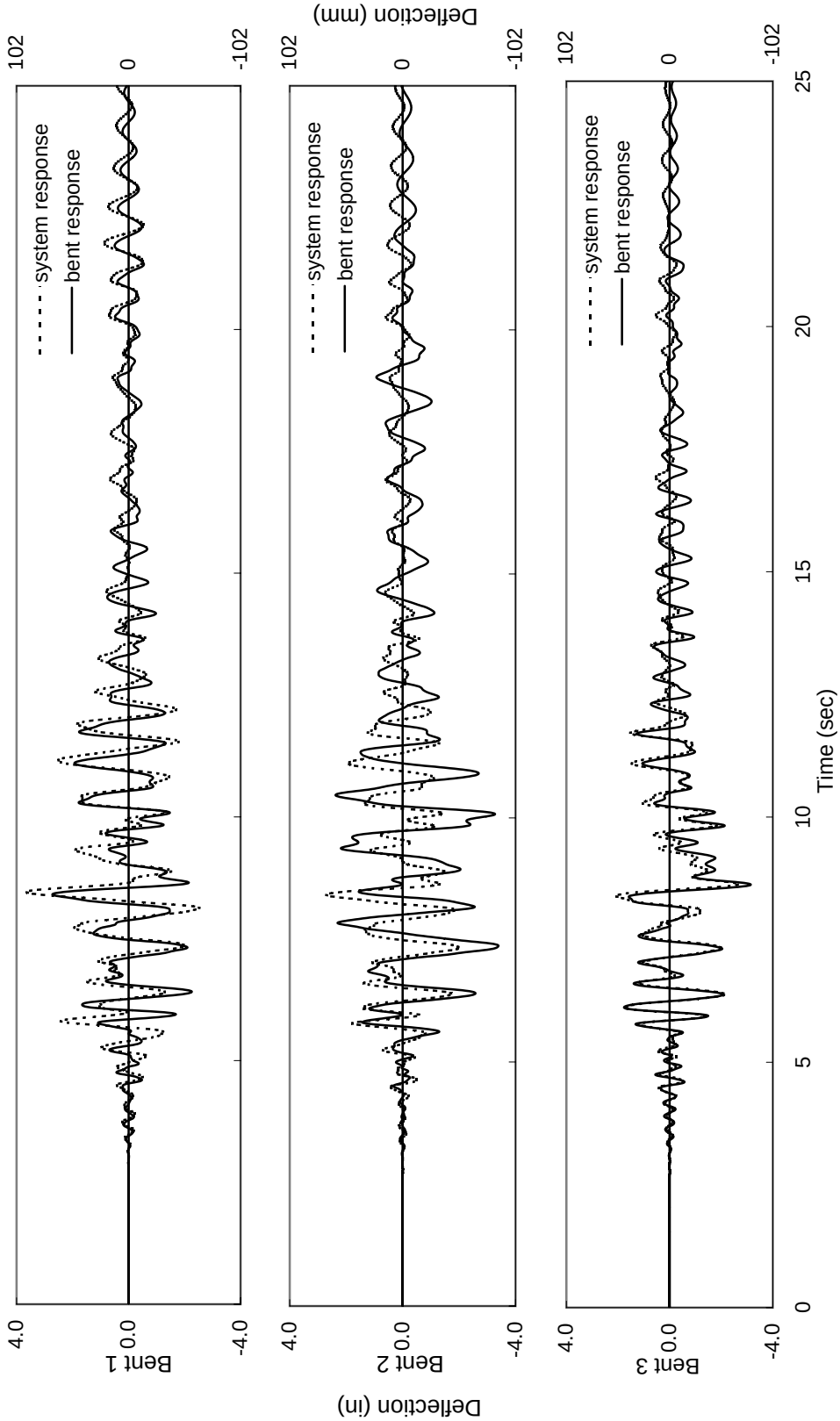

Figure 10-5: Comparison of calculated system and individual bent displacement response for bents 1-3 subjected to target motion of test 17.

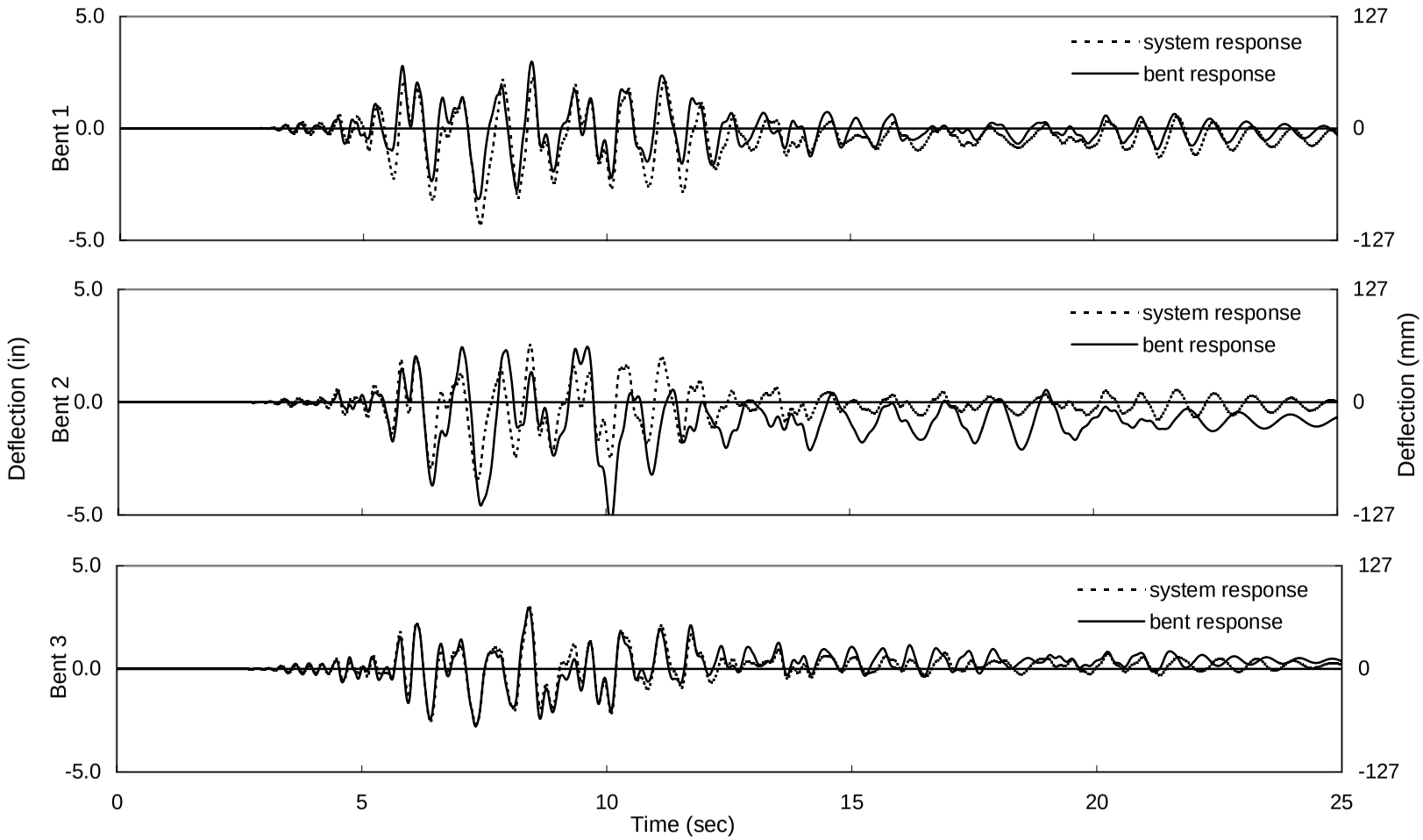

Figure 10-6: Comparison of calculated system and individual bent displacement response for bents 1-3 subjected to target motion of test 18.

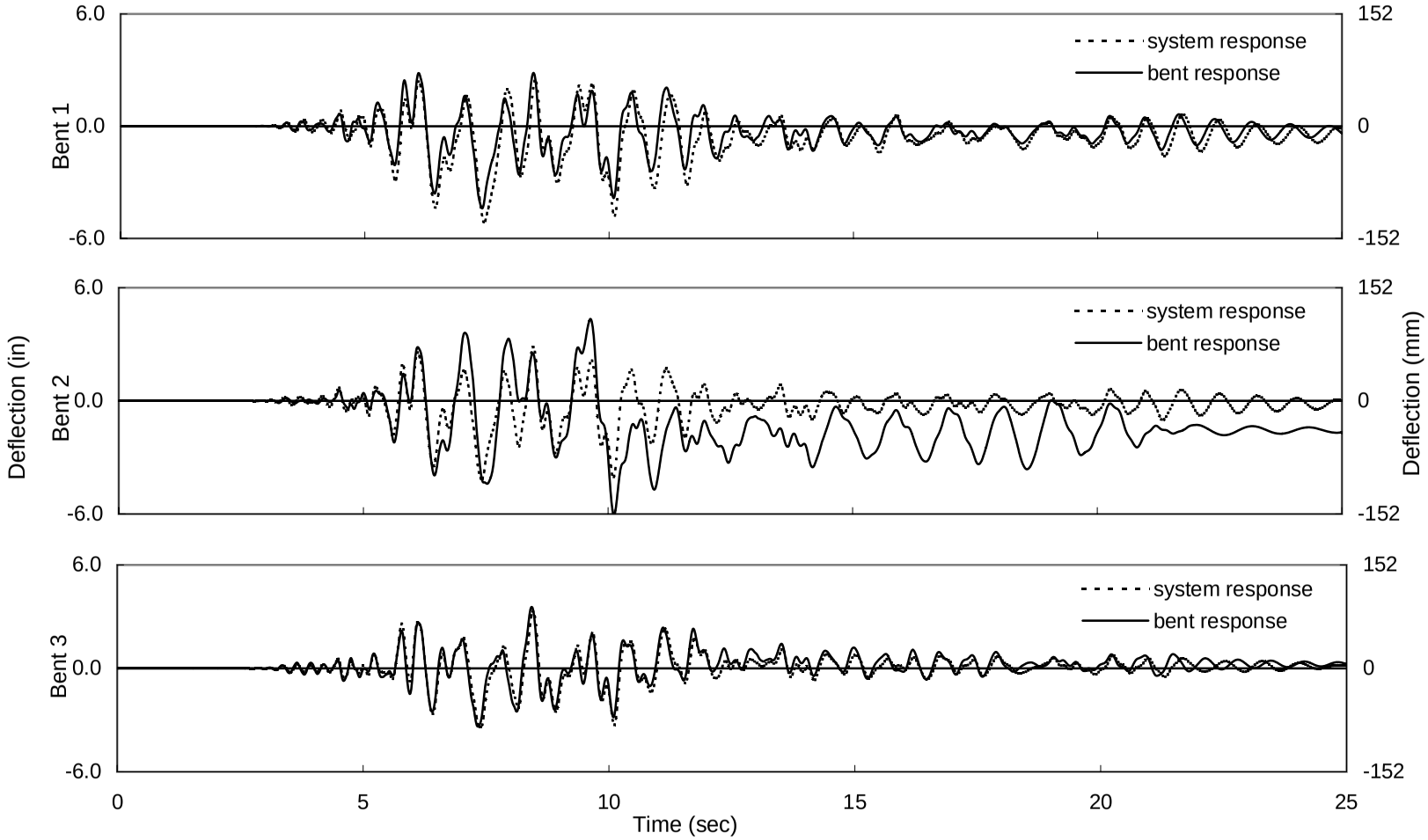

Figure 10-7: Comparison of calculated system and individual bent displacement response for bents 1-3 subjected to target motion of test 19.

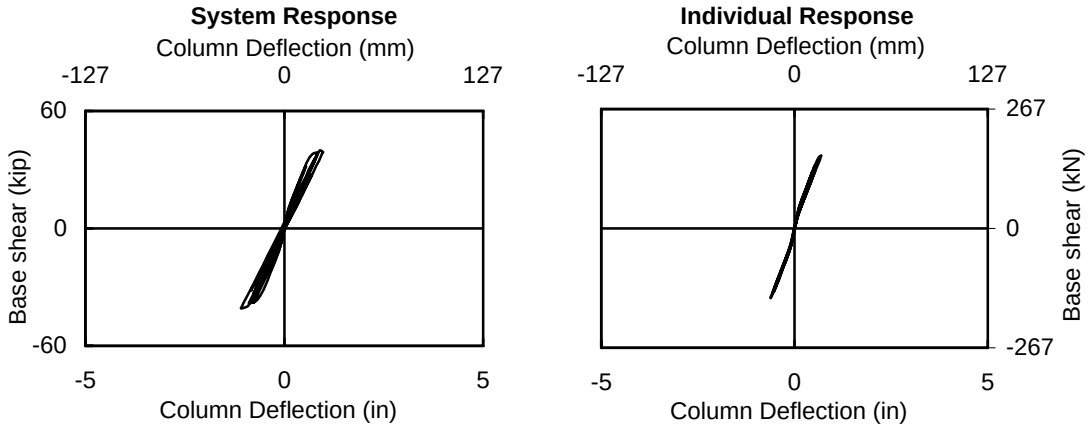

Figure 10-8 Comparison of calculated system and individual force-displacement hysteresis for bent 1 subjected to target motion of test 13.

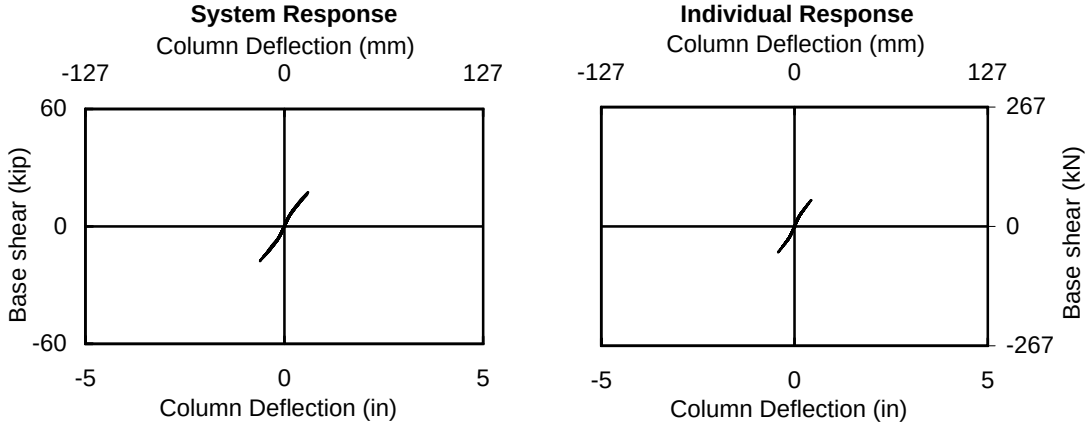

Figure 10-9 Comparison of calculated system and individual force-displacement hysteresis for bent 2 subjected to target motion of test 13.

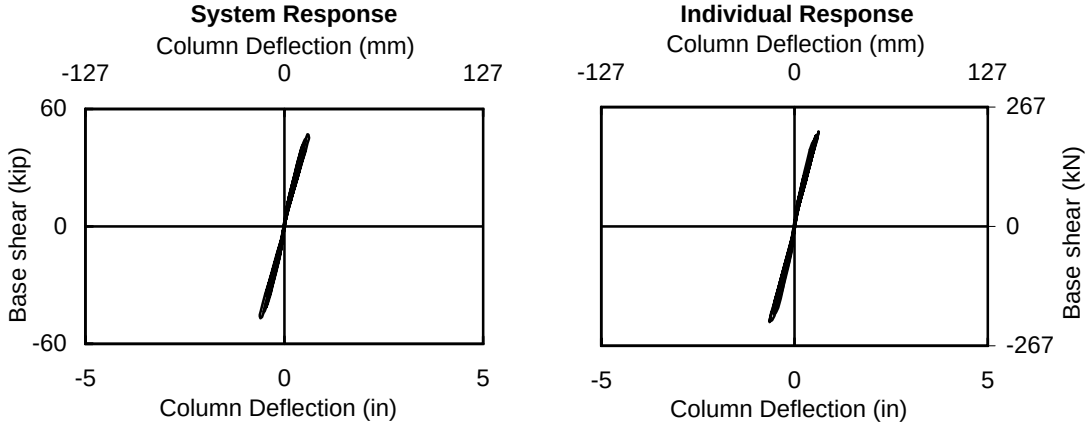

Figure 10-10 Comparison of calculated system and individual force-displacement hysteresis for bent 3 subjected to target motion of test 13.

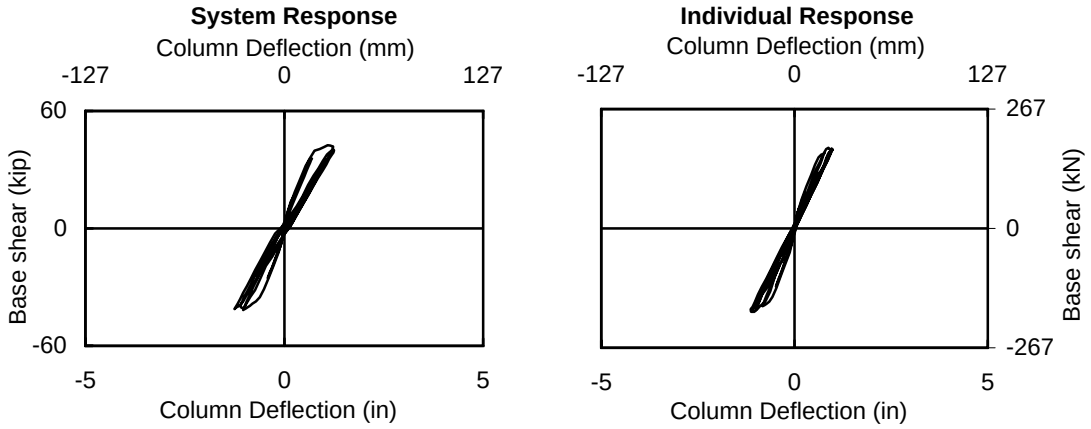

Figure 10-11 Comparison of calculated system and individual force-displacement hysteresis for bent 1 subjected to target motion of test 14.

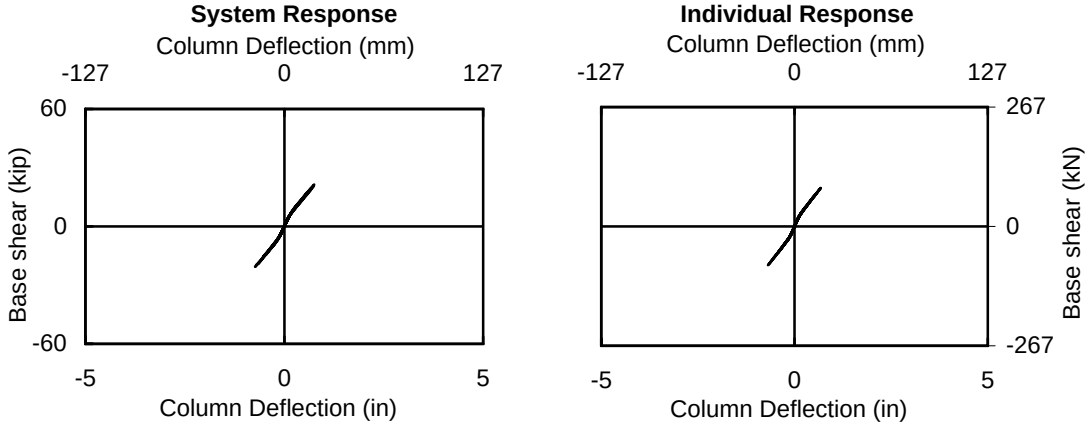

Figure 10-12 Comparison of calculated system and individual force-displacement hysteresis for bent 2 subjected to target motion of test 14.

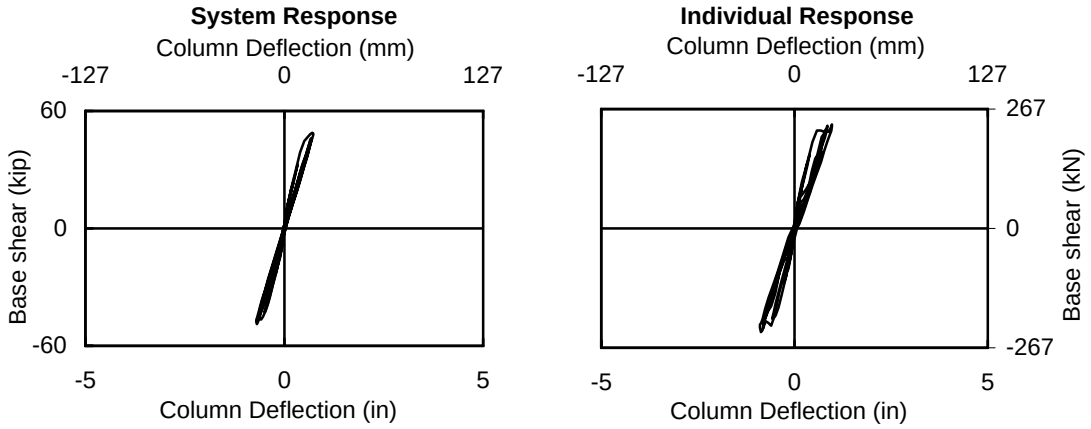

Figure 10-13 Comparison of calculated system and individual force-displacement hysteresis for bent 3 subjected to target motion of test 14.

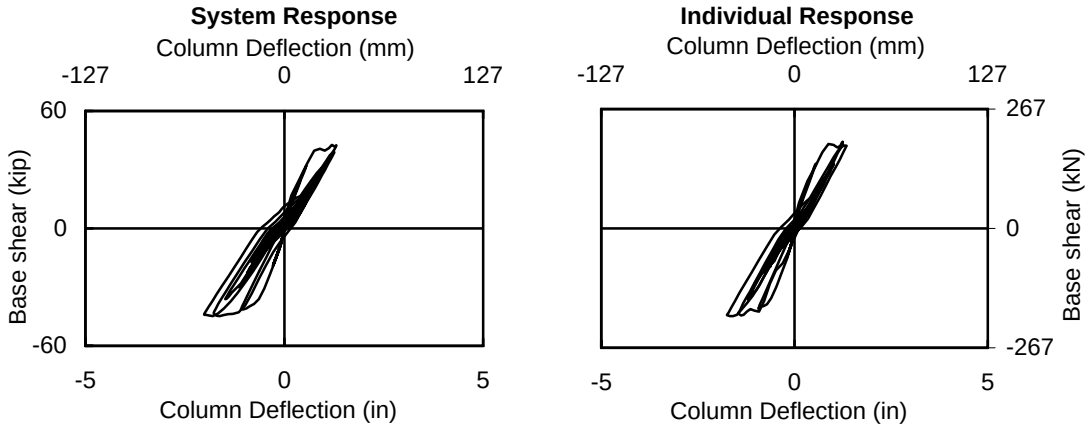

Figure 10-14 Comparison of calculated system and individual force-displacement hysteresis for bent 1 subjected to target motion of test 15.

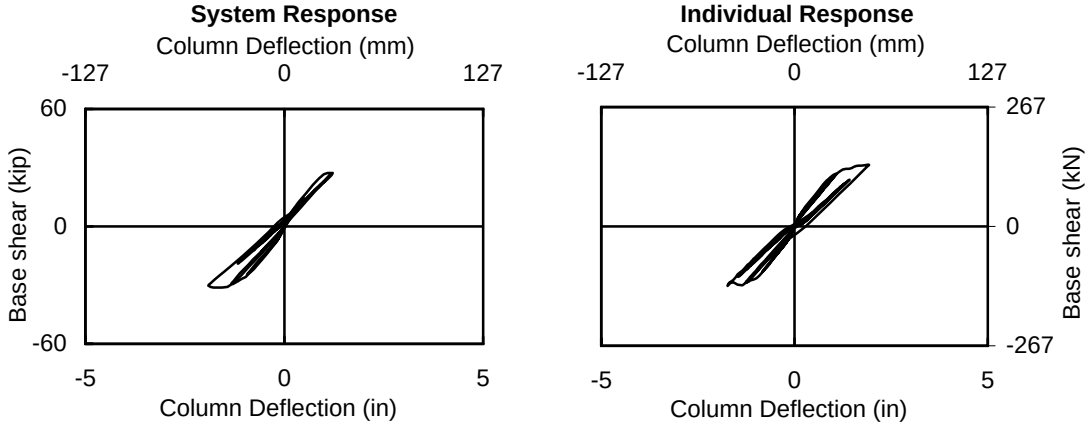

Figure 10-15 Comparison of calculated system and individual force-displacement hysteresis for bent 2 subjected to target motion of test 15.

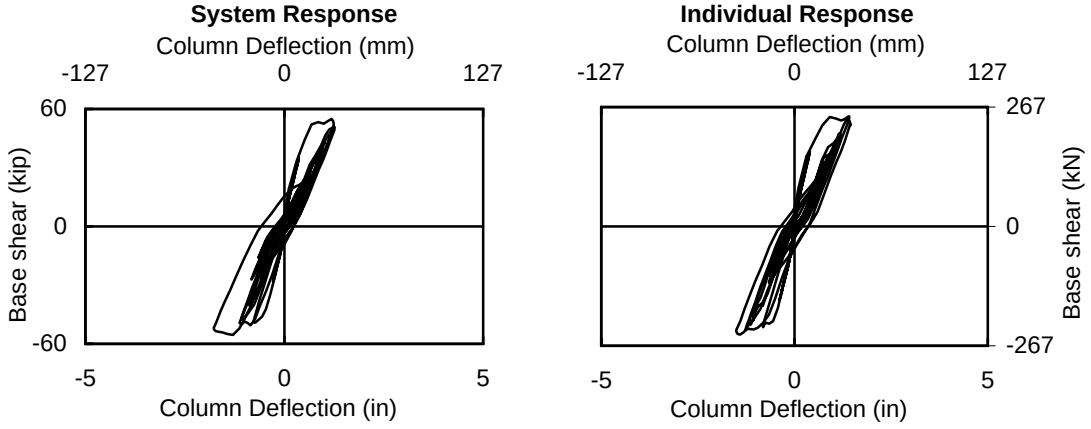

Figure 10-16 Comparison of calculated system and individual force-displacement hysteresis for bent 3 subjected to target motion of test 15.

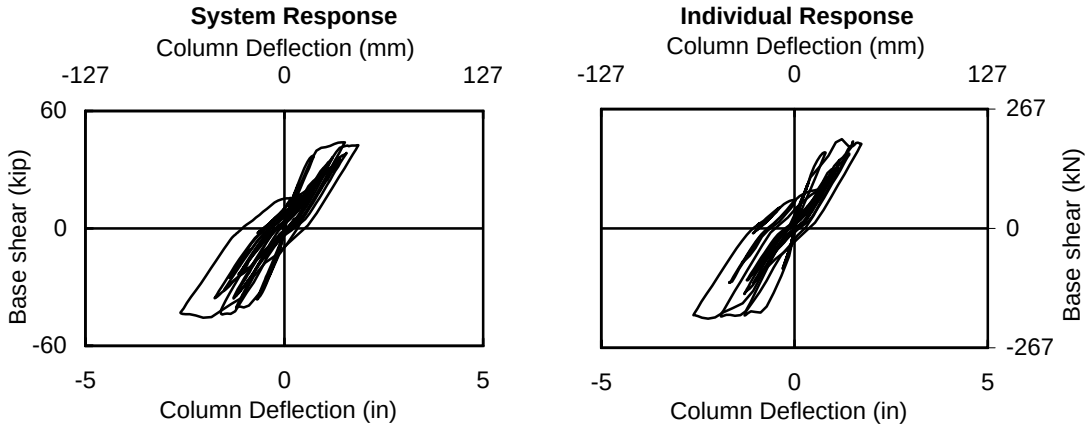

Figure 10-17 Comparison of calculated system and individual force-displacement hysteresis for bent 1 subjected to target motion of test 16.

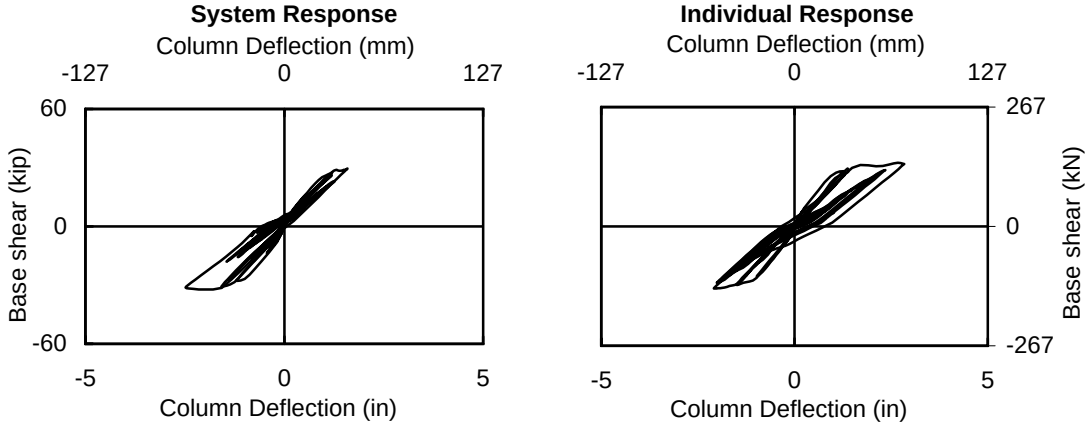

Figure 10-18 Comparison of calculated system and individual force-displacement hysteresis for bent 2 subjected to target motion of test 16.

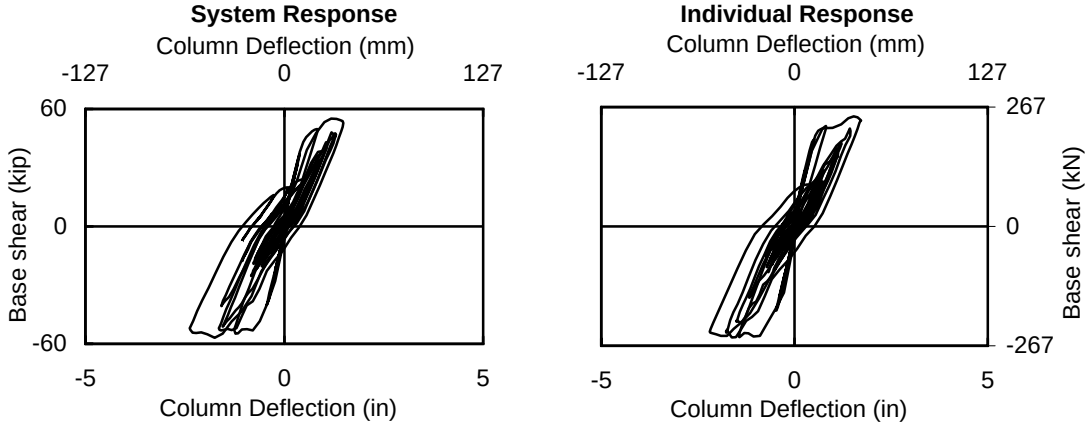

Figure 10-19 Comparison of calculated system and individual force-displacement hysteresis for bent 3 subjected to target motion of test 16.

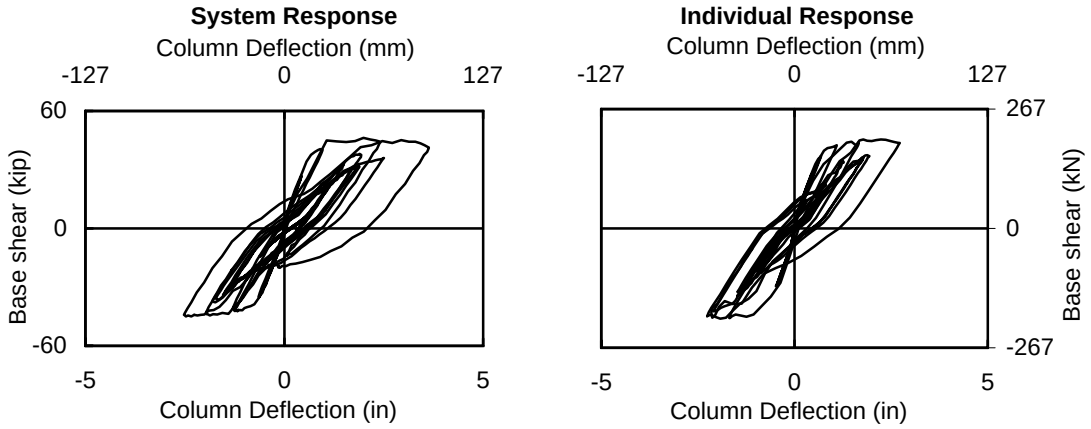

Figure 10-20 Comparison of calculated system and individual force-displacement hysteresis for bent 1 subjected to target motion of test 17.

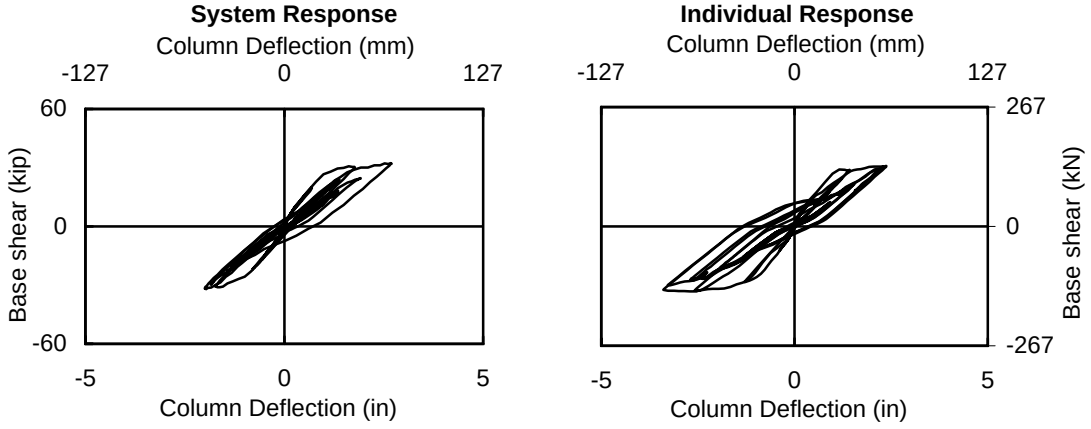

Figure 10-21 Comparison of calculated system and individual force-displacement hysteresis for bent 2 subjected to target motion of test 17.

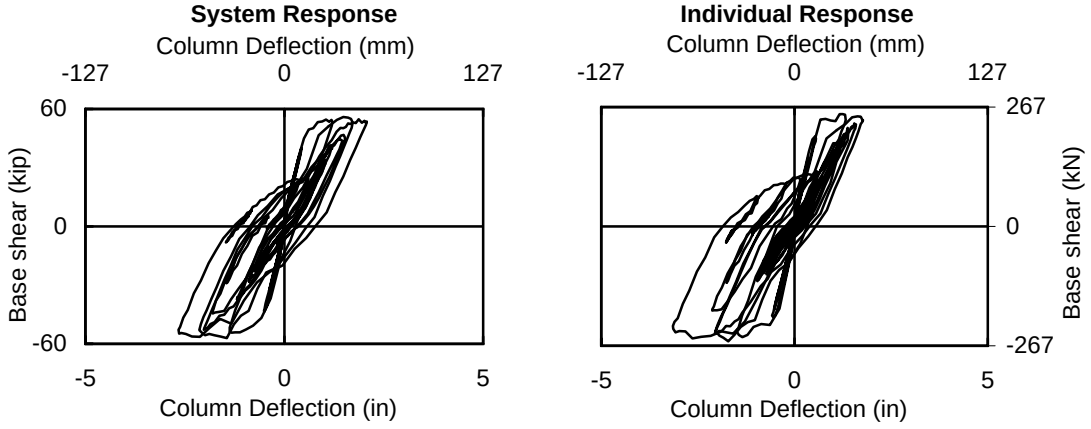

Figure 10-22 Comparison of calculated system and individual force-displacement hysteresis for bent 3 subjected to target motion of test 17.

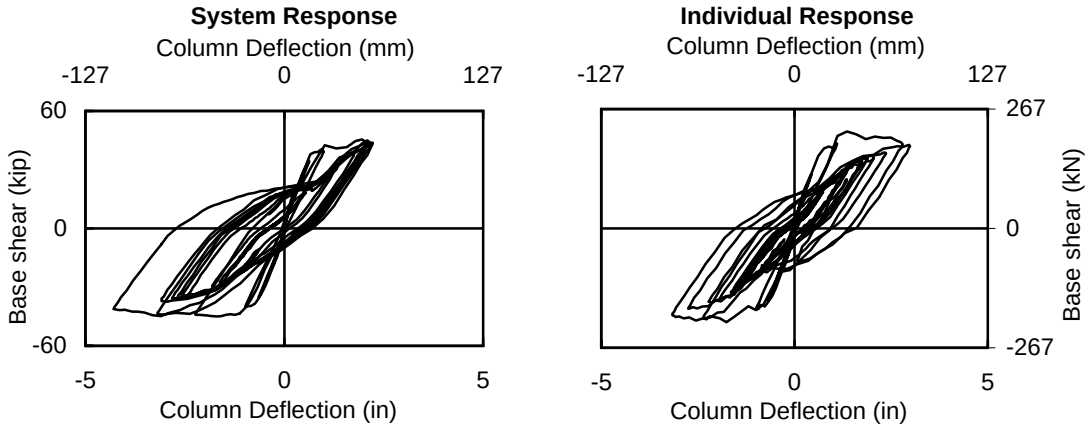

Figure 10-23 Comparison of calculated system and individual force-displacement hysteresis for bent 1 subjected to target motion of test 18.

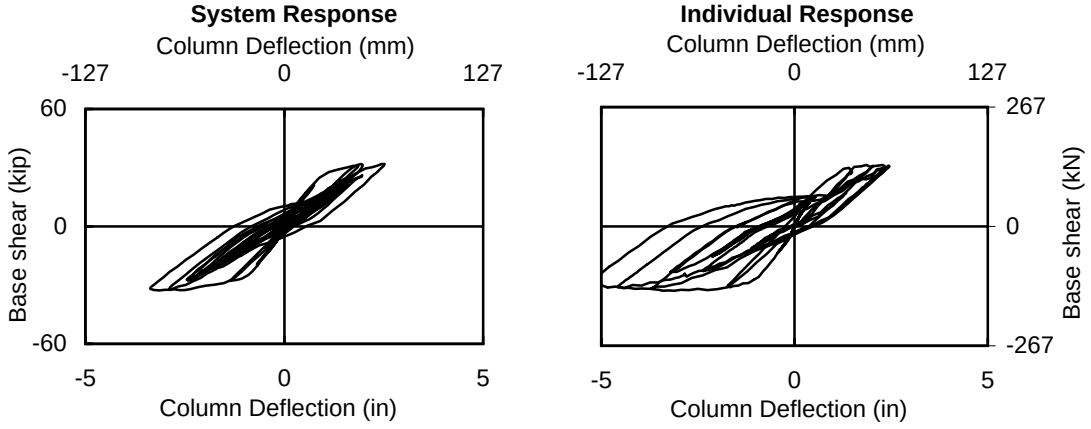

Figure 10-24 Comparison of calculated system and individual force-displacement hysteresis for bent 2 subjected to target motion of test 18.

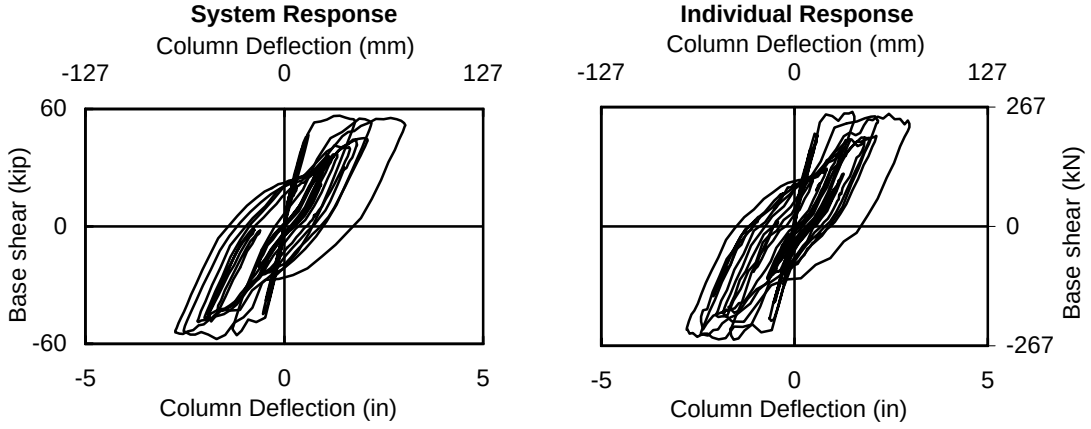

Figure 10-25 Comparison of calculated system and individual force-displacement hysteresis for bent 3 subjected to target motion of test 18.

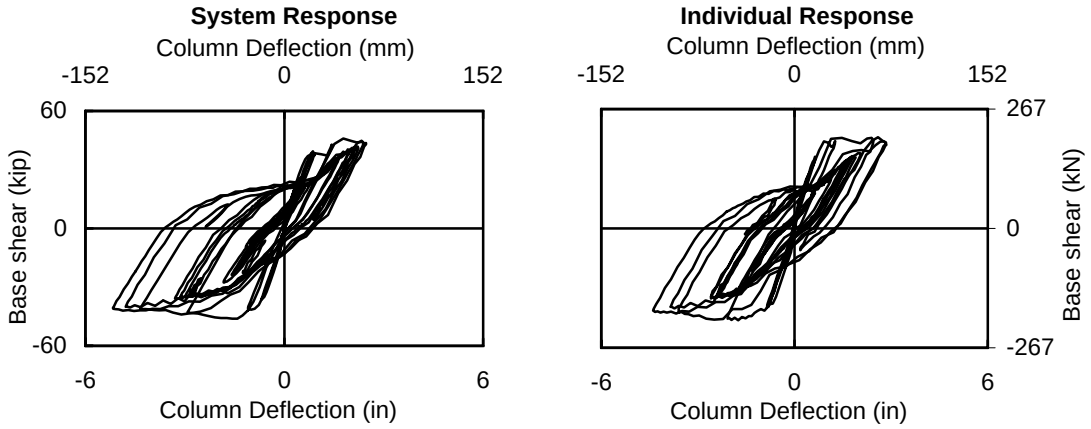

Figure 10-26 Comparison of calculated system and individual force-displacement hysteresis for bent 1 subjected to target motion of test 19.

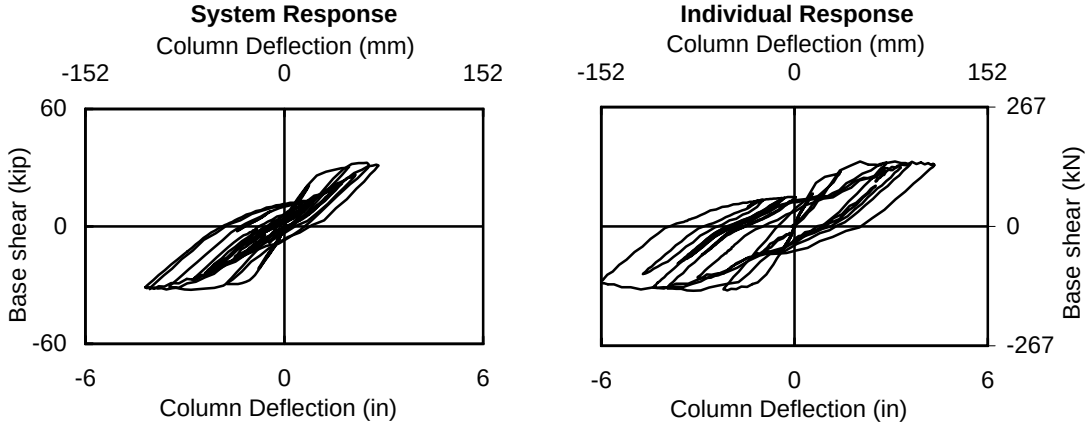

Figure 10-27 Comparison of calculated system and individual force-displacement hysteresis for bent 2 subjected to target motion of test 19.

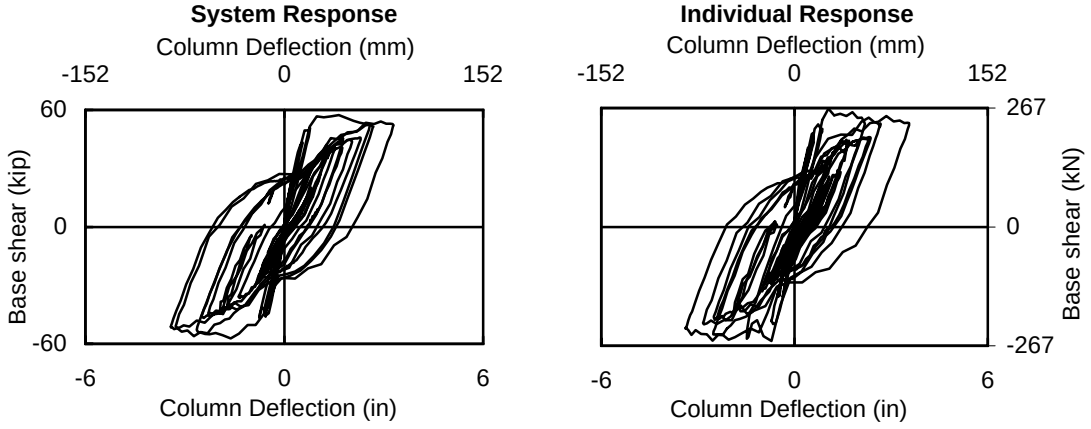

Figure 10-28 Comparison of calculated system and individual force-displacement hysteresis for bent 3 subjected to target motion of test 19.

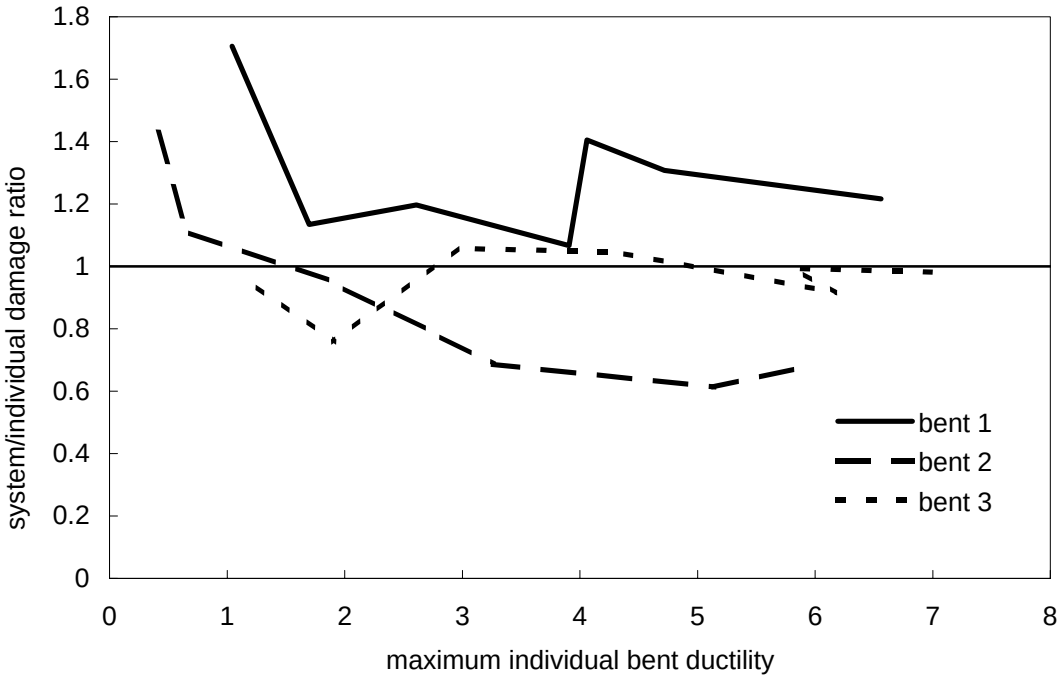

Figure 10-29: System/individual damage index ratio vs. maximum individual bent ductility for bents 1 through 3 using target motions 13 through 19.

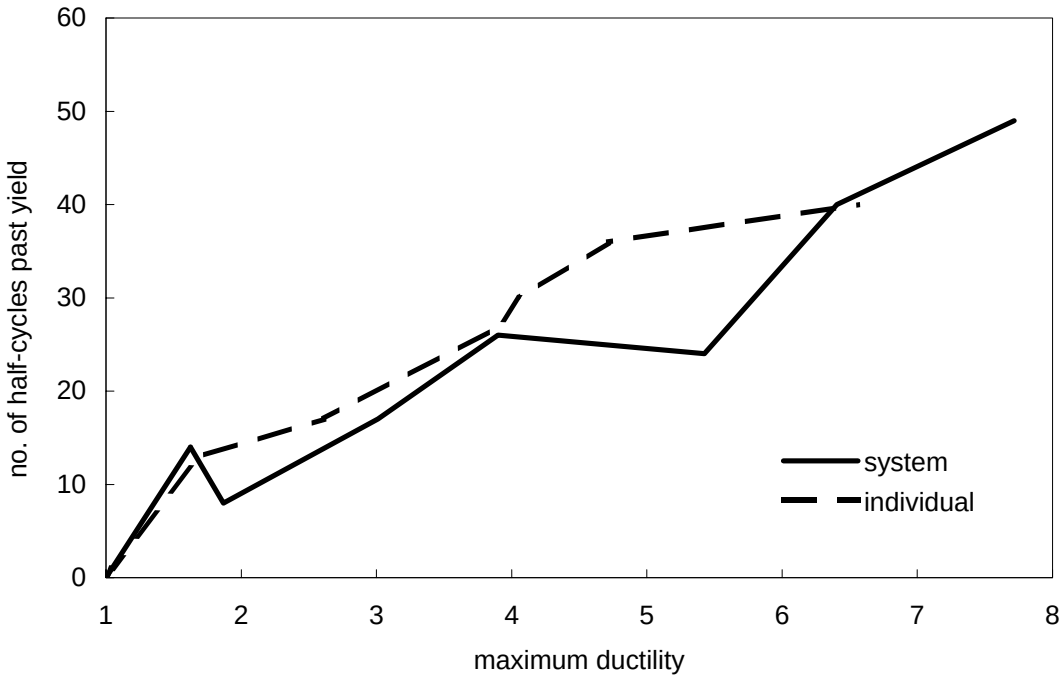

Figure 10-30: Number of cycles past yield vs. maximum ductility for bent 1 system and individual responses using target motions 13 through 19.

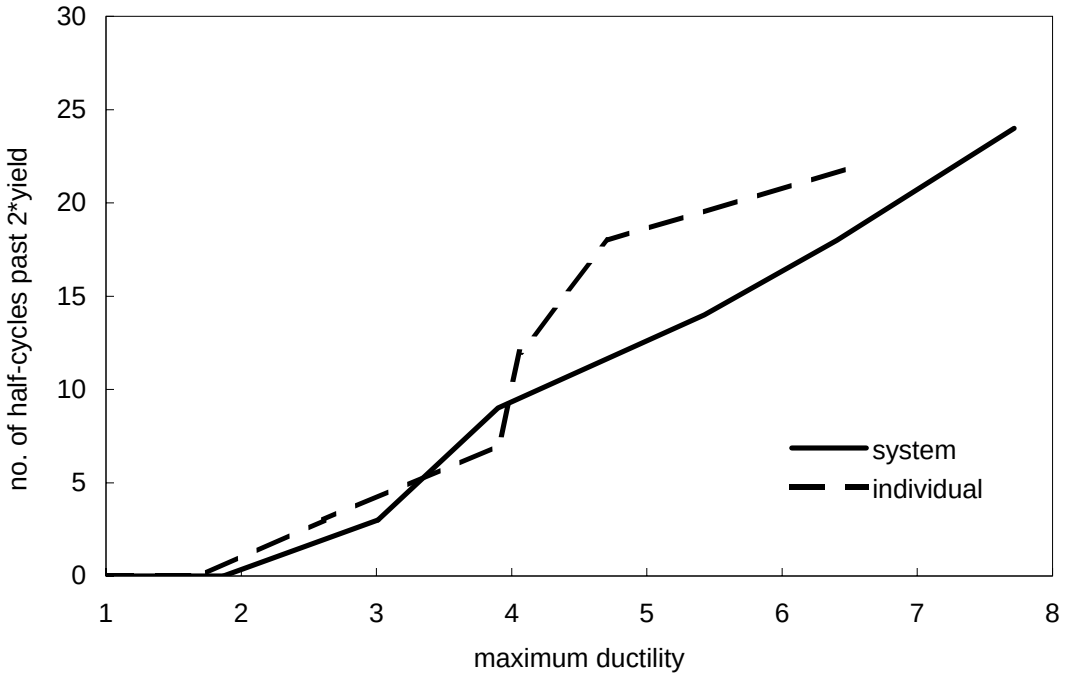

Figure 10-31: Number of cycles past 2*yield vs. maximum ductility for bent 1 system and individual responses using target motions 13 through 19.

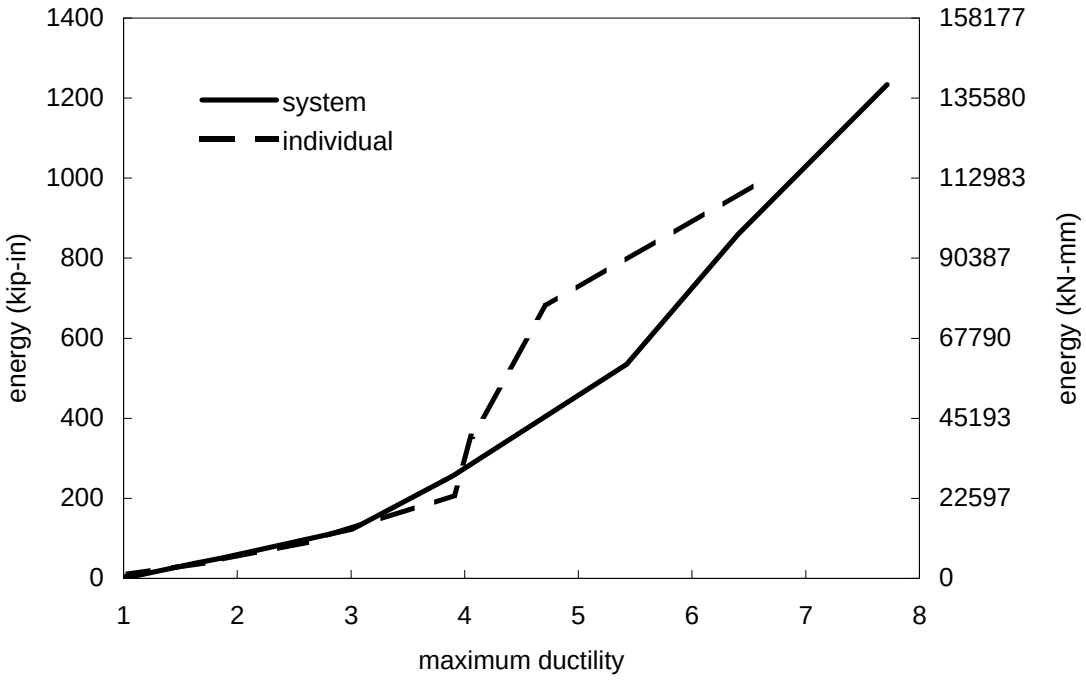

Figure 10-32: Dissipated hysteretic energy vs. maximum ductility for bent 1 system and individual responses using target motions 13 through 19.

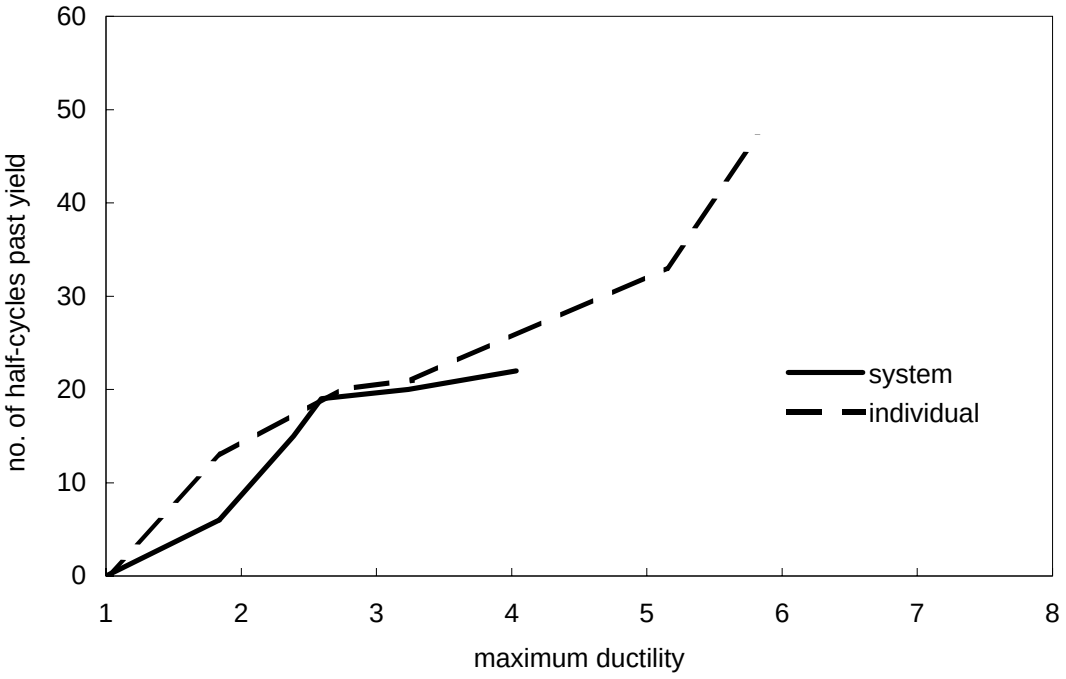

Figure 10-33: Number of cycles past yield vs. maximum ductility for bent 2 system and individual responses using target motions 13 through 19.

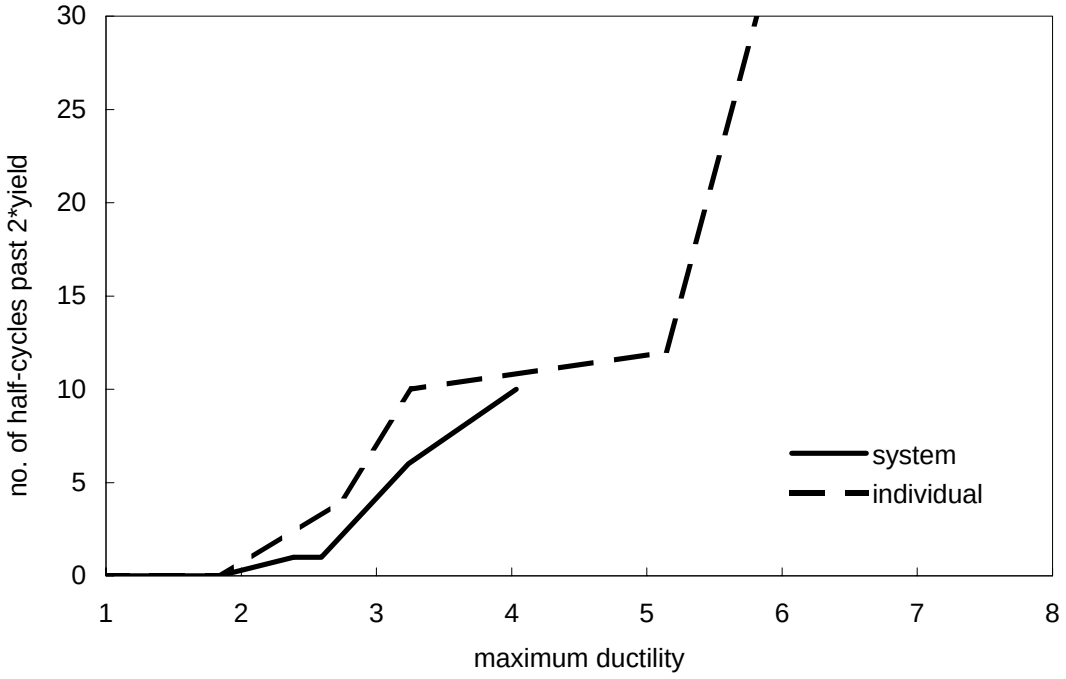

Figure 10-34: Number of cycles past 2*yield vs. maximum ductility for bent 2 system and individual responses using target motions 13 through 19.

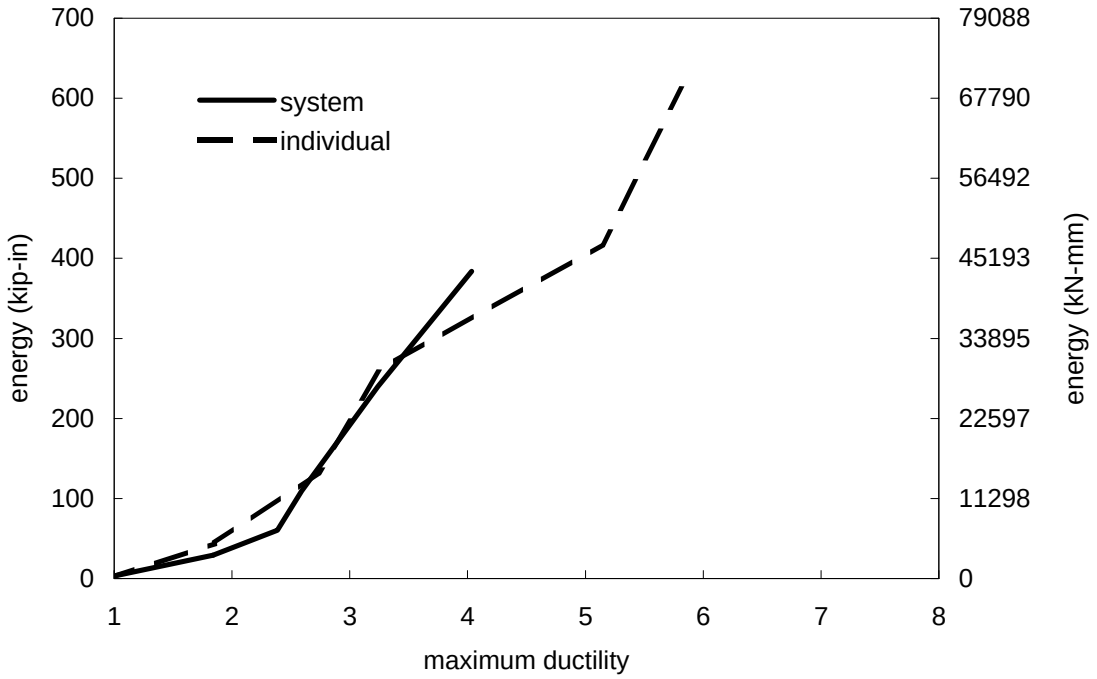

Figure 10-35: Dissipated hysteretic energy vs. maximum ductility for bent 2 system and individual responses using target motions 13 through 19.

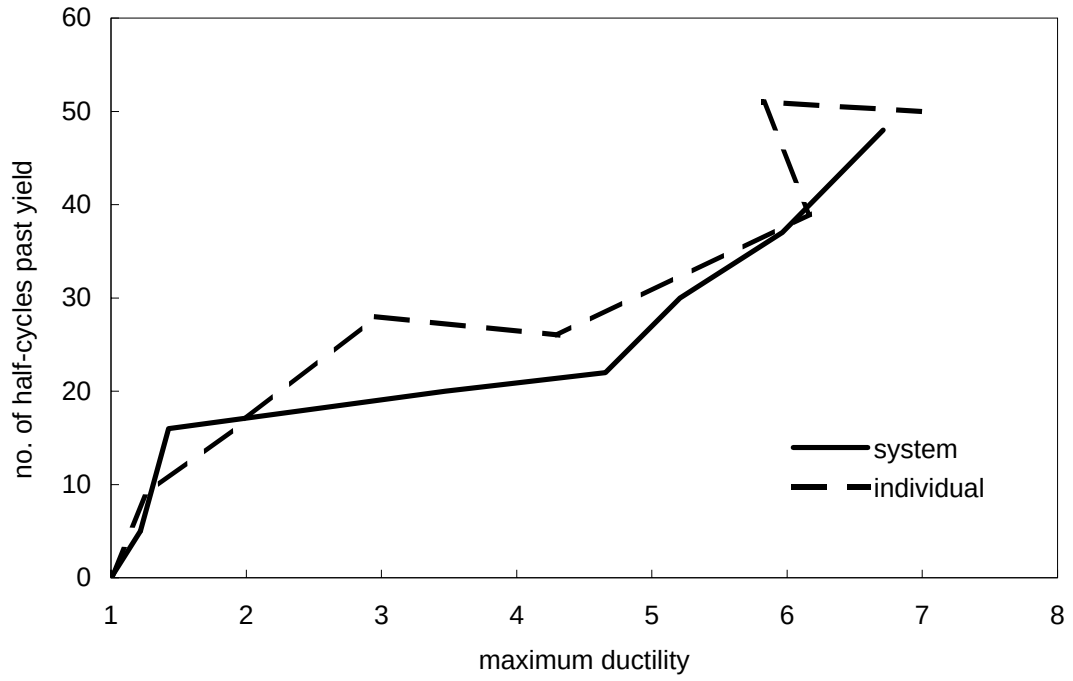

Figure 10-36: Number of cycles past yield vs. maximum ductility for bent 3 system and individual responses using target motions 13 through 19.

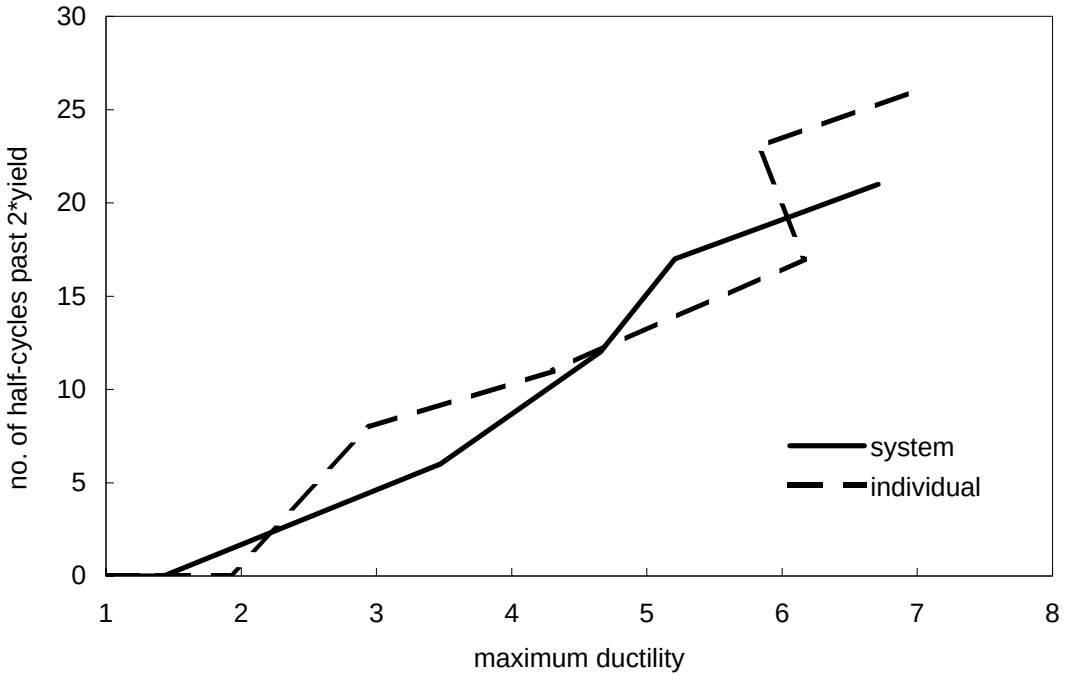

Figure 10-37: Number of cycles past 2*yield vs. maximum ductility for bent 3 system and individual responses using target motions 13 through 19.

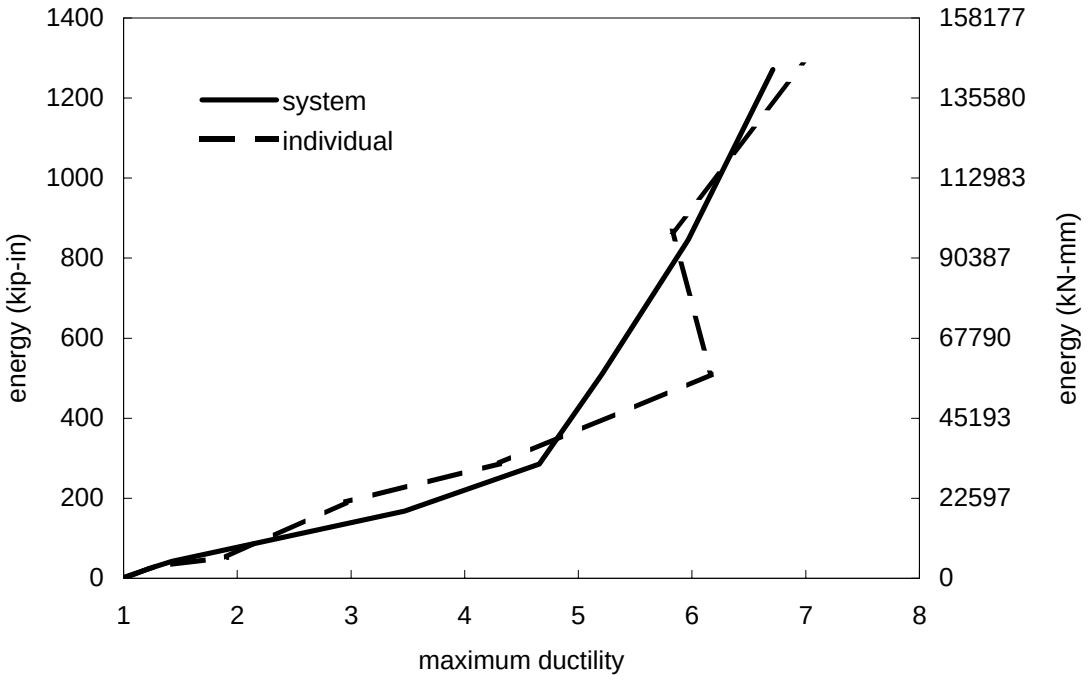

Figure 10-38: Dissipated hysteretic energy vs. maximum ductility for bent 3 system and individual responses using target motions 13 through 19.

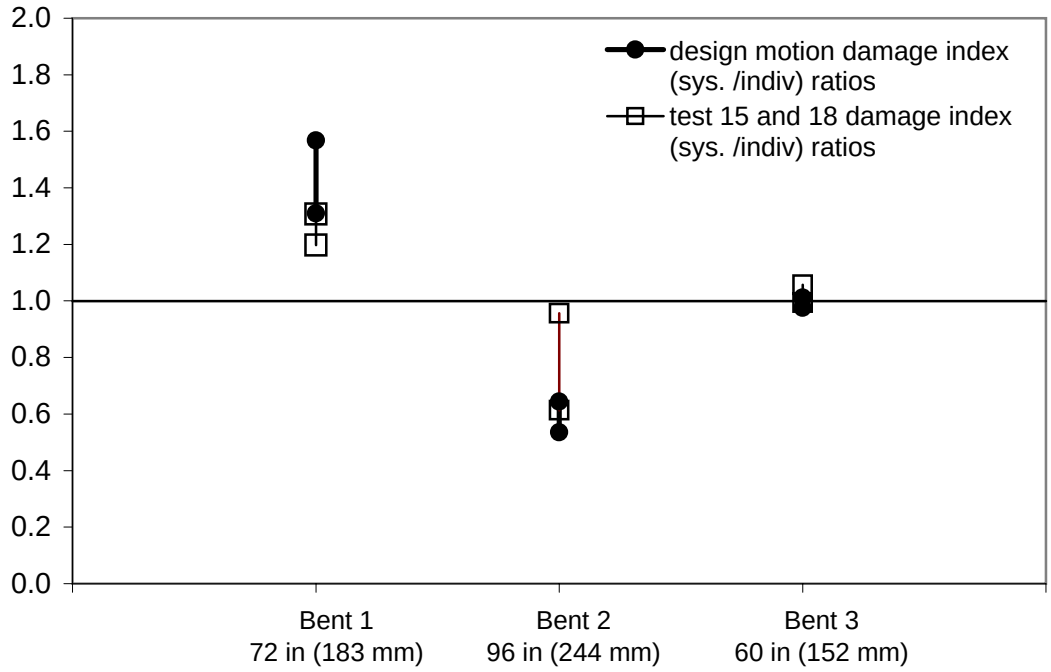

Figure 10-39: Range of damage index sys./indiv. ratios for each bent of test specimen using test motions and design motions.

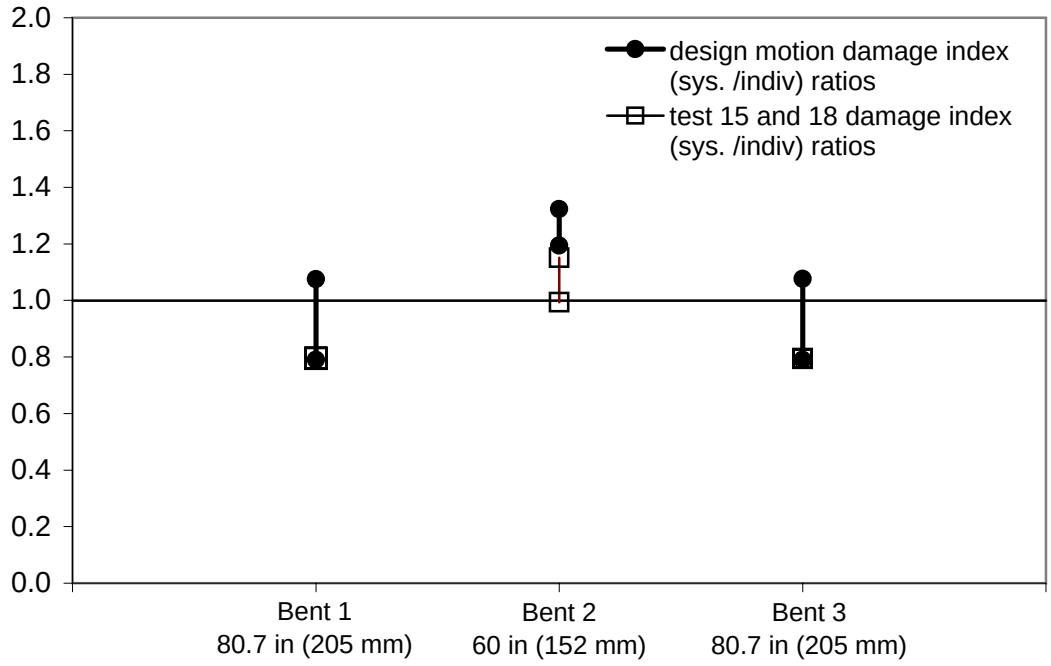

Figure 10-40: Range of damage index sys./indiv. ratios for each bent of system 1 using test motions and design motions.

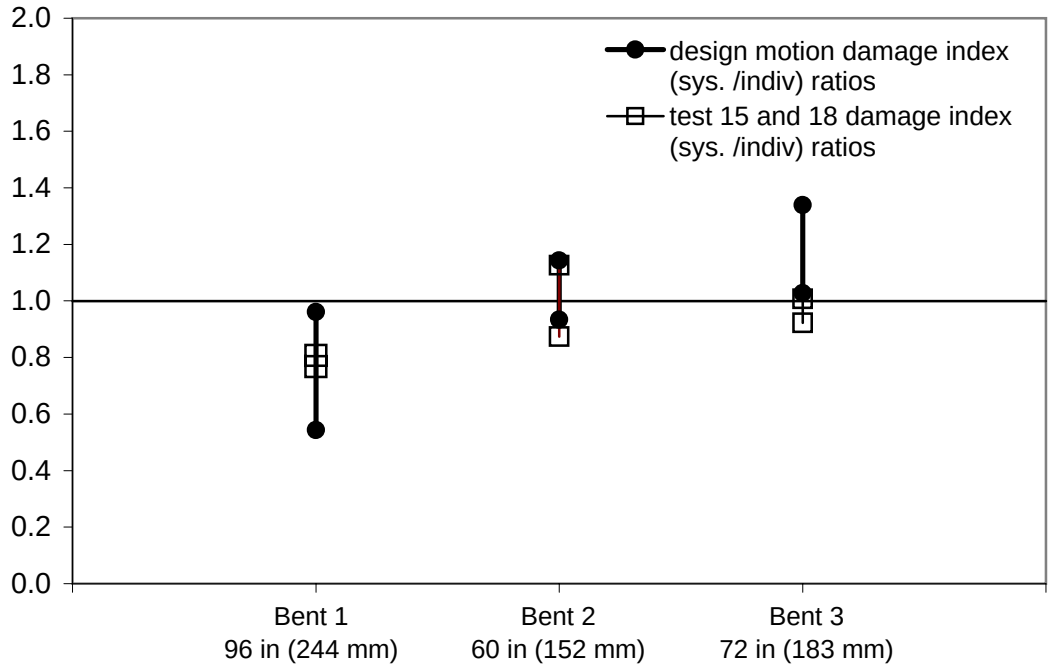

Figure 10-41: Range of damage index sys./indiv. ratios for each bent of system 2 using test motions and design motions.

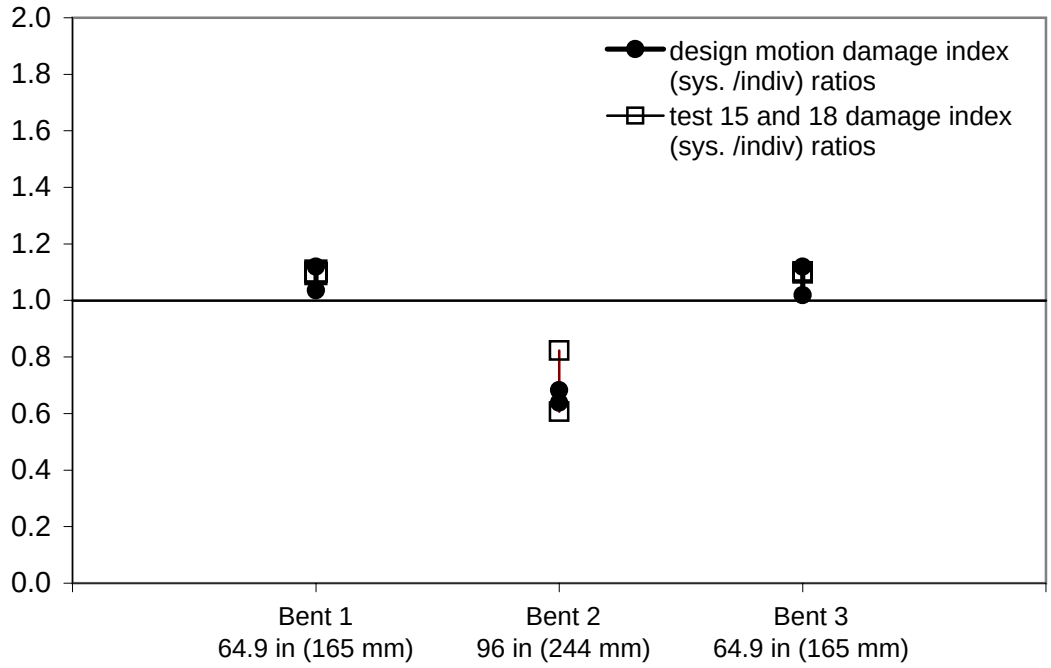

Figure 10-42: Range of damage index sys./indiv. ratios for each bent of system 3 using test motions and design motions.

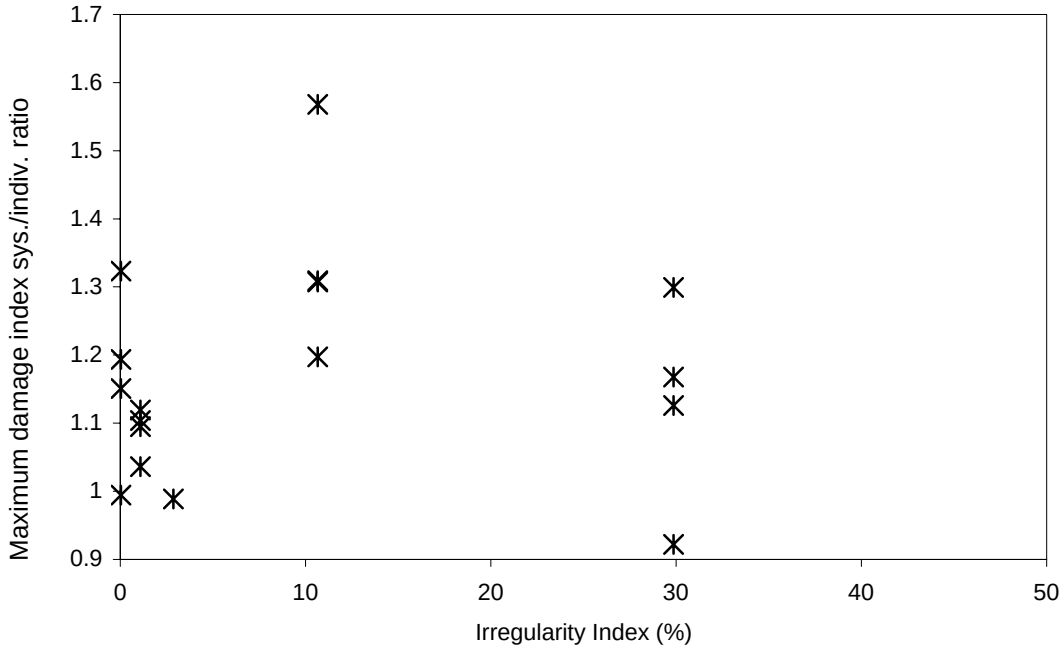

Figure 10-43: Maximum damage index sys./indiv. ratio compared to irregularity index for four bridge systems using all motions.

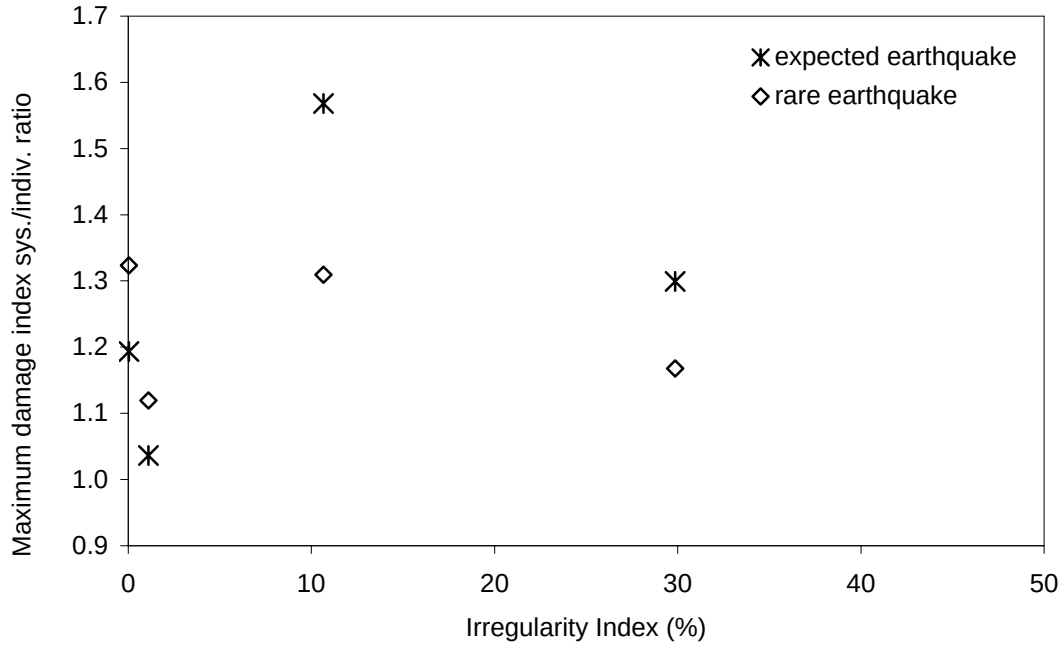

Figure 10-44: Maximum damage index sys./indiv. ratio compared to irregularity index for four bridge systems using rare and expected design earthquakes.

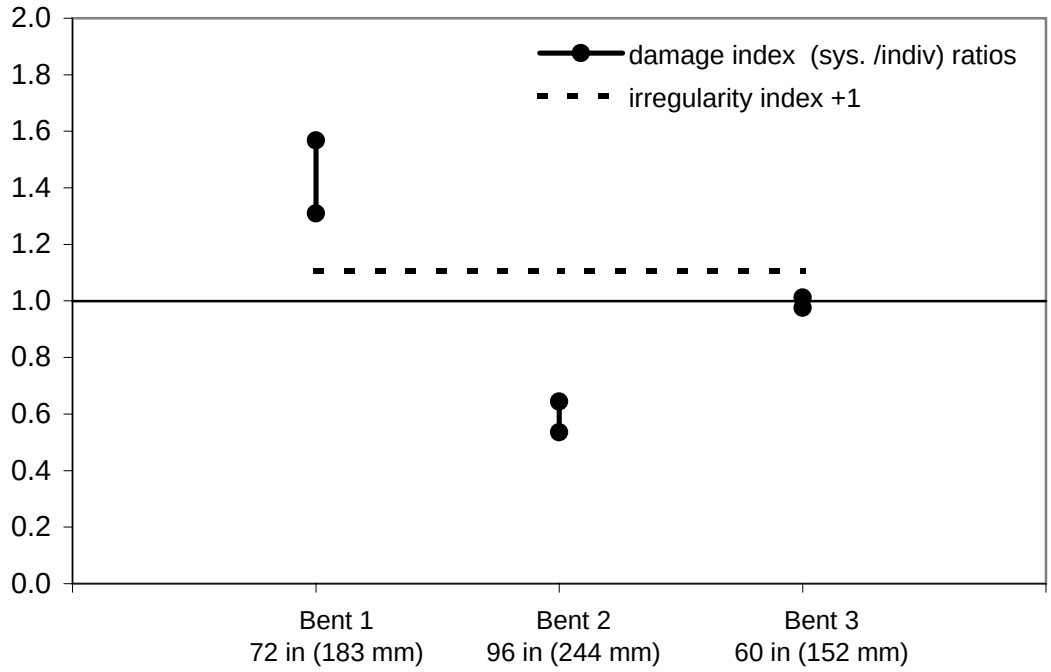

Figure 10-45: Range of damage index sys./indiv. ratios for each bent of test specimen using design motions, compared with system irregularity index.

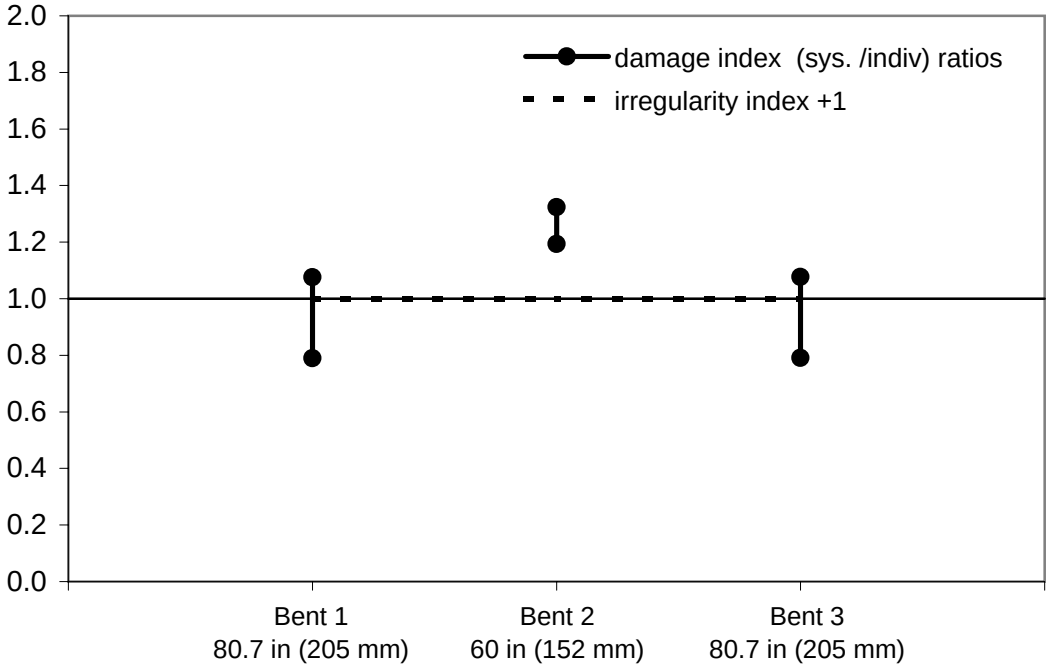

Figure 10-46: Range of damage index sys./indiv. ratios for each bent of system 1 using design motions, compared with system irregularity index.

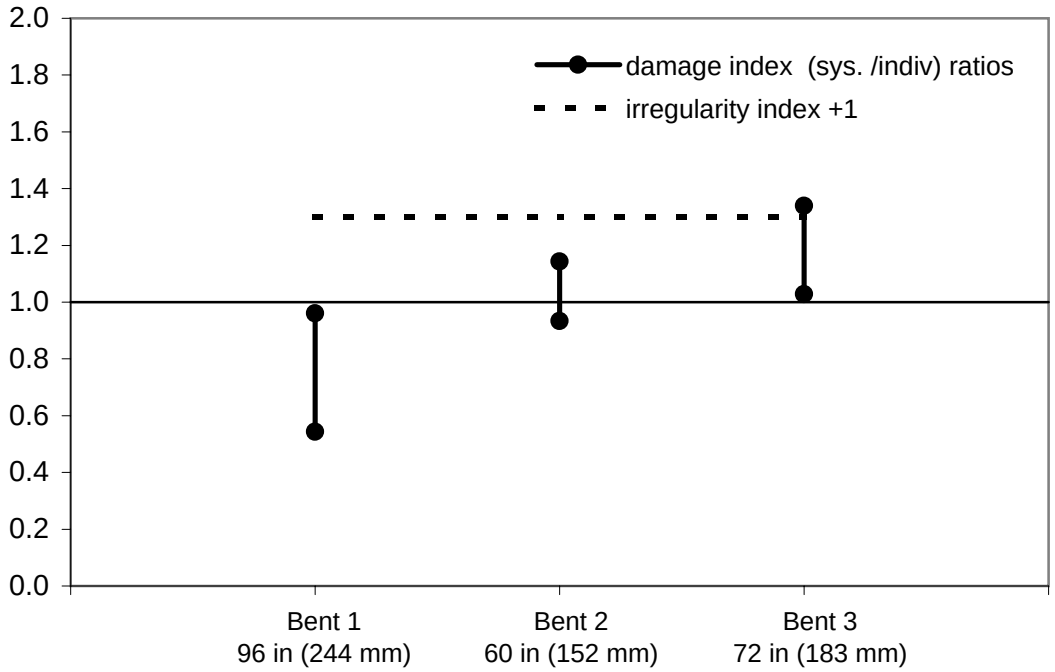

Figure 10-47: Range of damage index sys./indiv. ratios for each bent of system 2 using design motions, compared with system irregularity index.

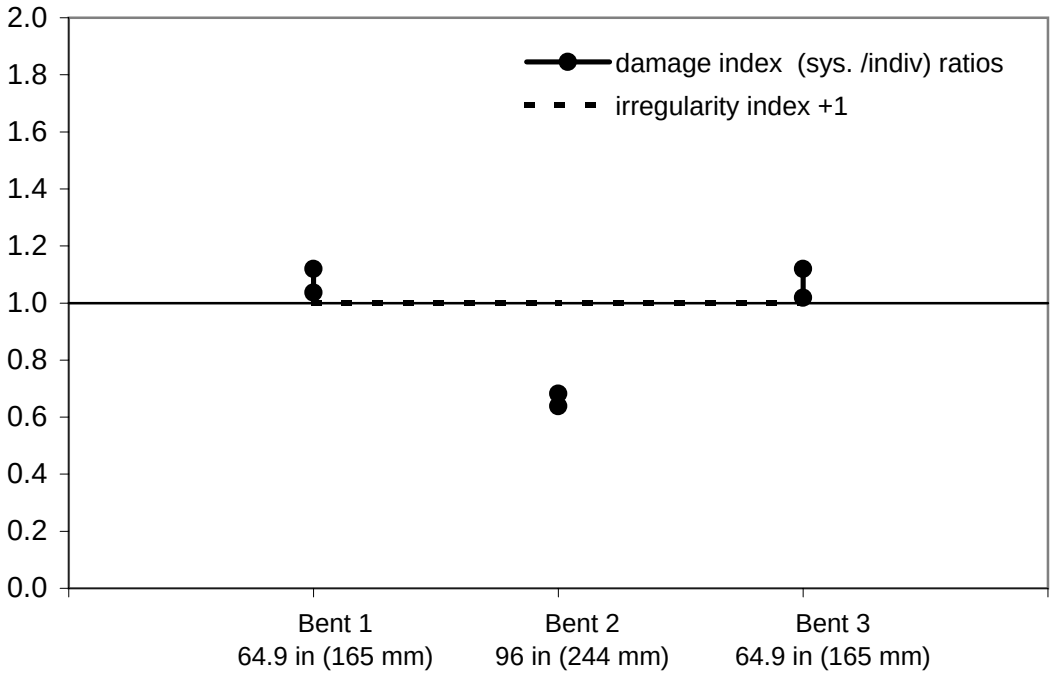

Figure 10-48: Range of damage index sys./indiv. ratios for each bent of system 3 using design motions, compared with system irregularity index.

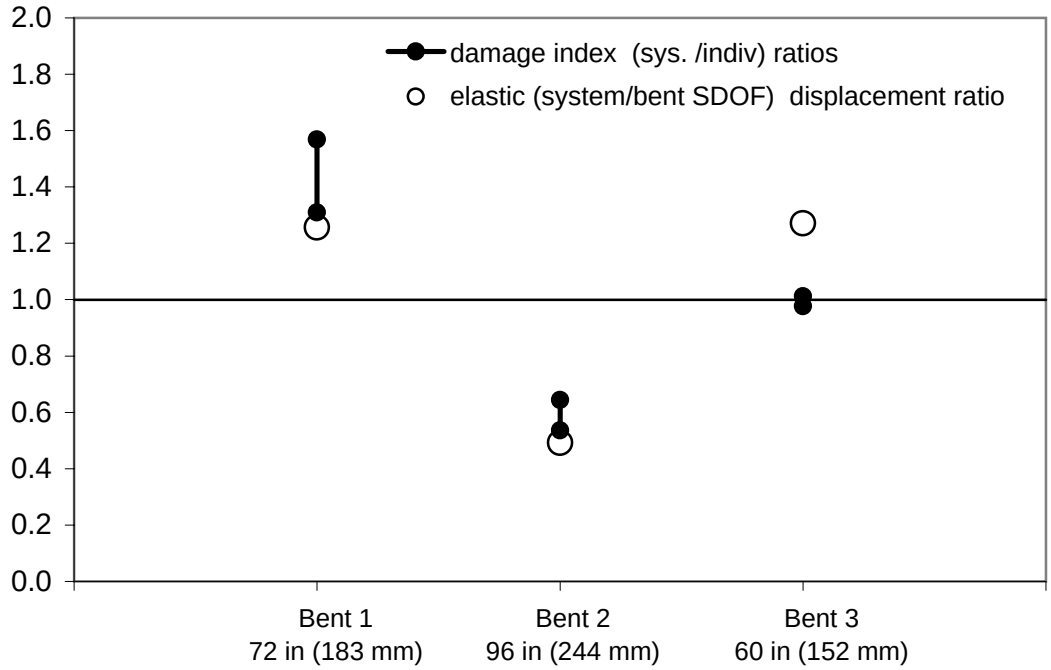

Figure 10-49: Range of damage index sys./indiv. ratios for each bent of test specimen using design motions, compared with elastic system/bent SDOF ratio.

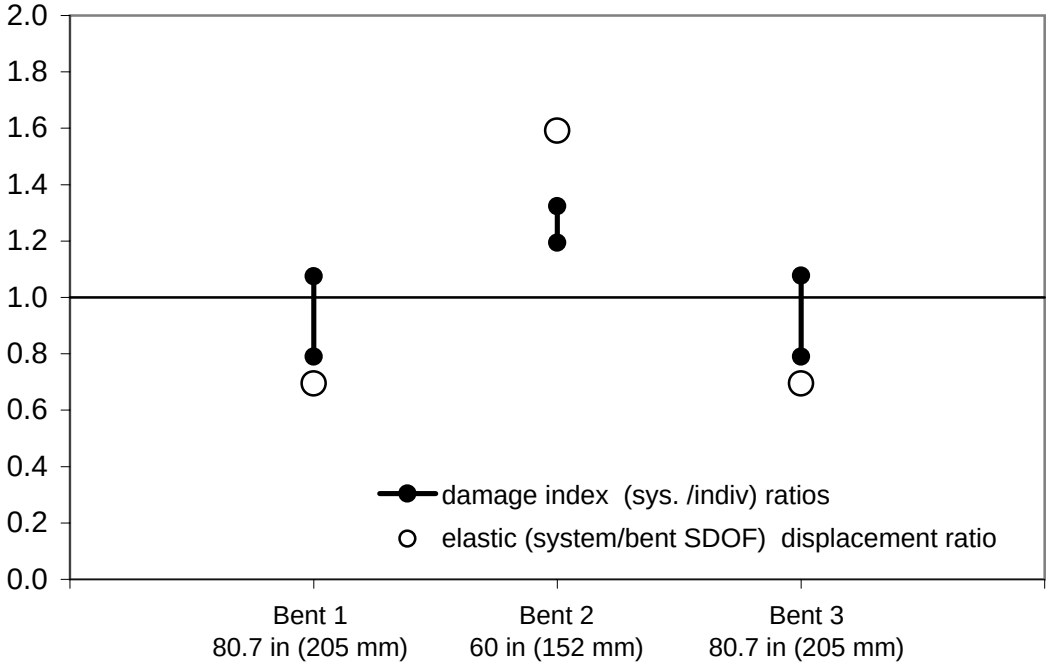

Figure 10-50: Range of damage index sys./indiv. ratios for each bent of system 1 using design motions, compared with elastic system/bent SDOF ratio.

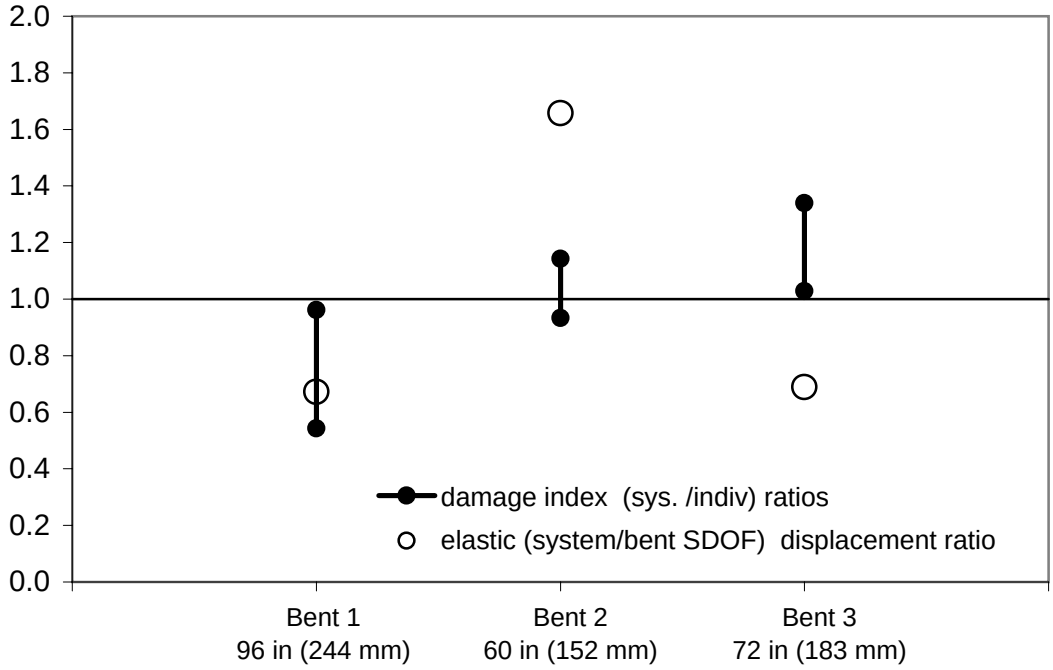

Figure 10-51: Range of damage index sys./indiv. ratios for each bent of system 2 using design motions, compared with elastic system/bent SDOF ratio.

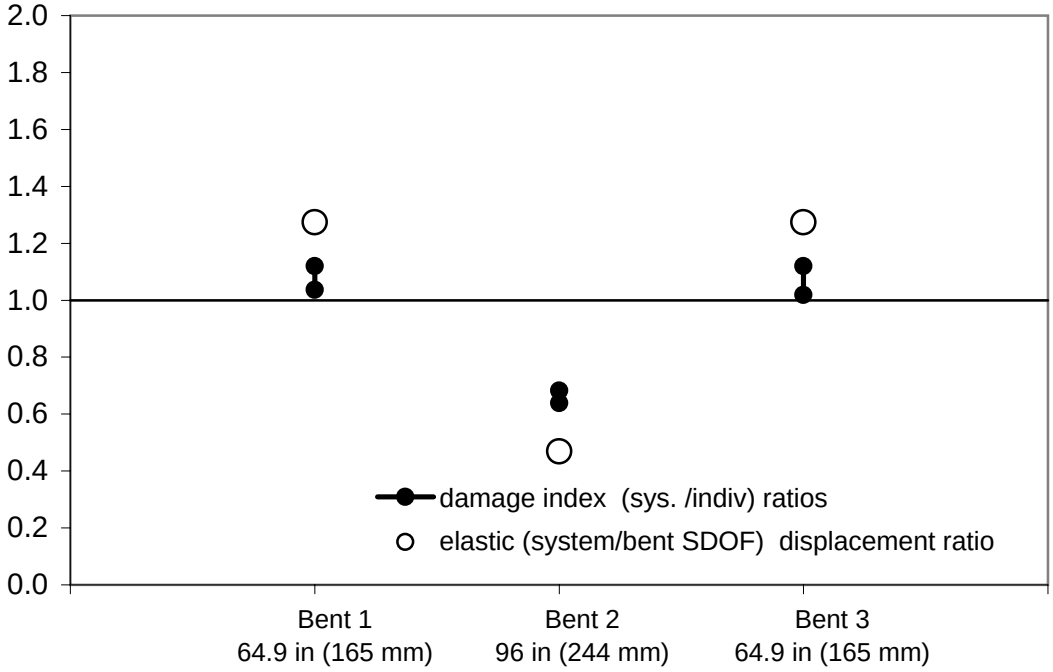

Figure 10-52: Range of damage index sys./indiv. ratios for each bent of system 3 using design motions, compared with elastic system/bent SDOF ratio.

Appendix A: Strain Histories for Column Strain Gauges

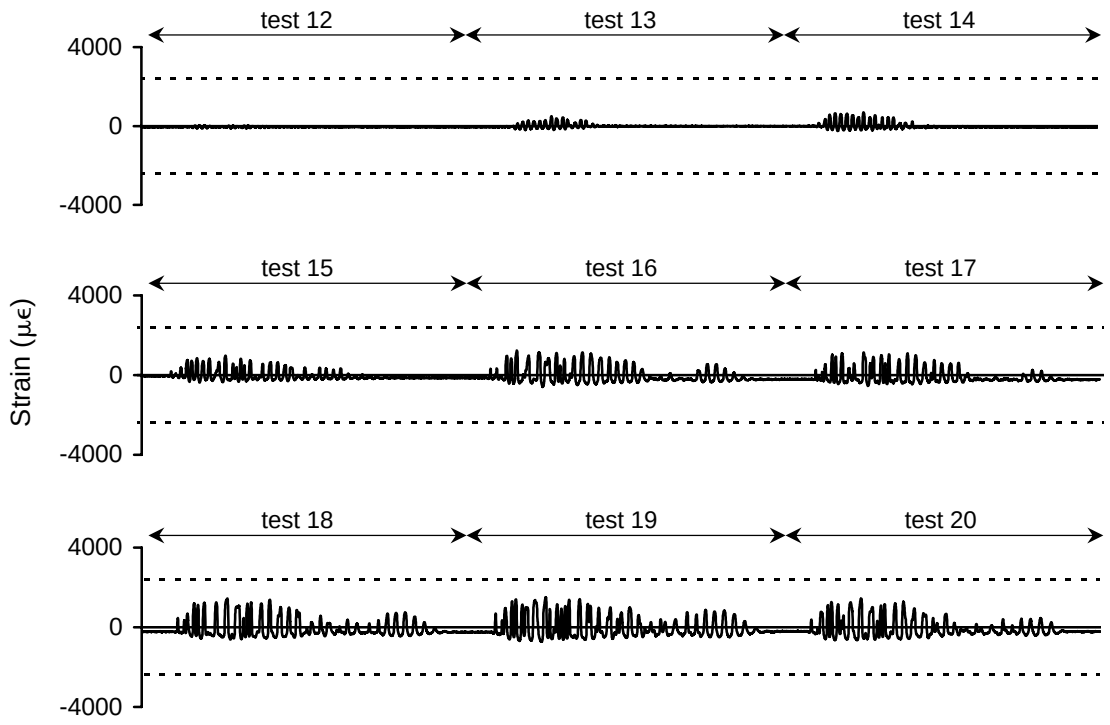

Figure A-1 Strain history for 1WTSL1 during high amplitude testing

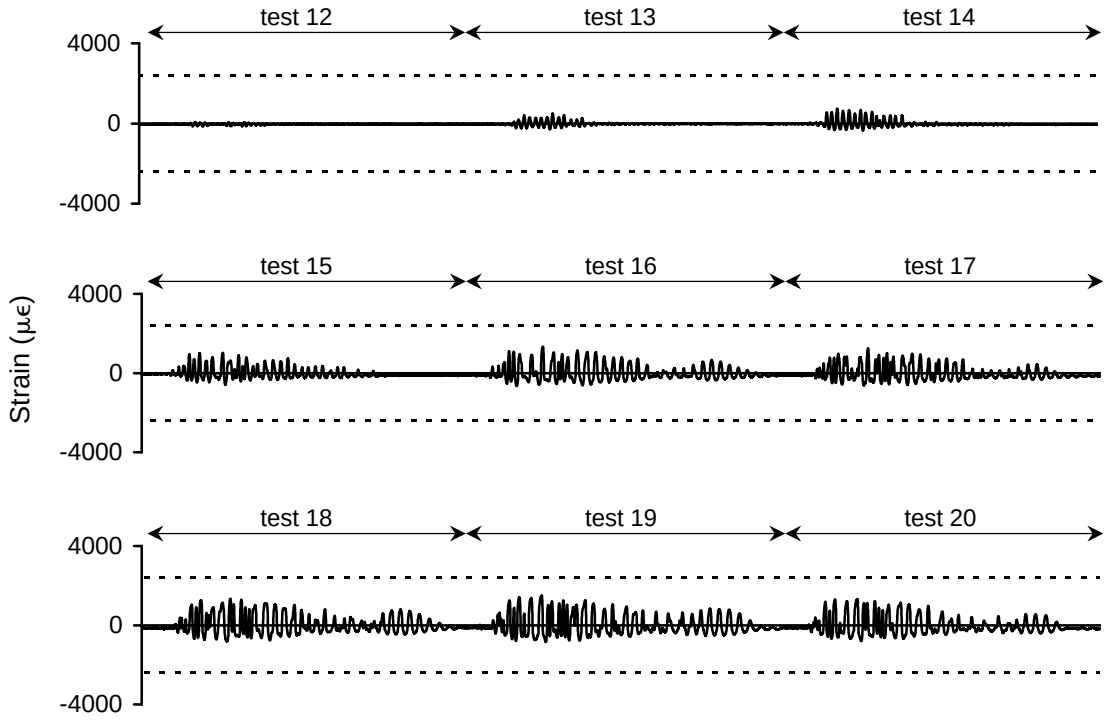

Figure A-2 Strain history for 1WTSL2 during high amplitude testing

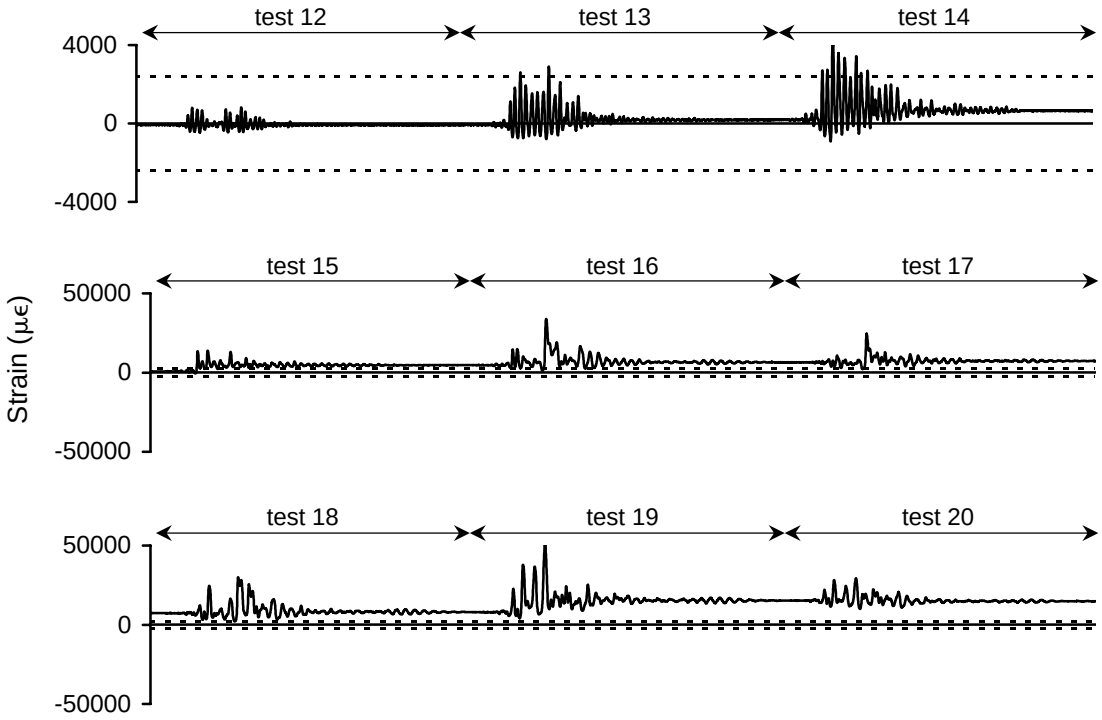

Figure A-3 Strain history for 1WTSL3 during high amplitude testing

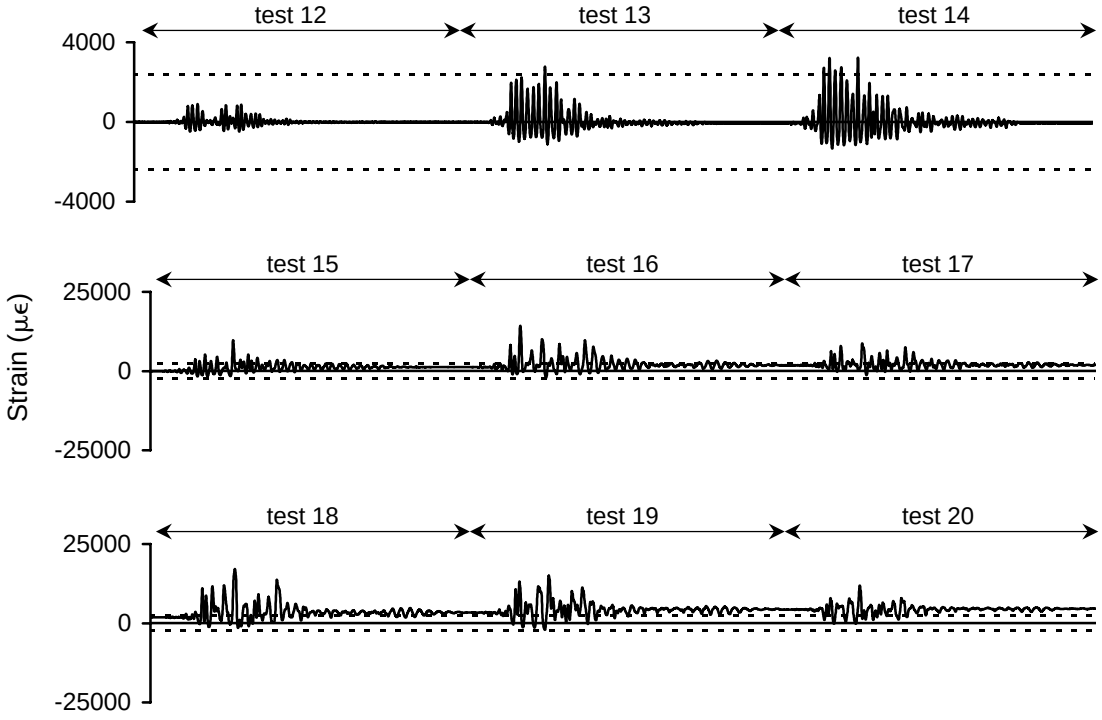

Figure A-4 Strain history for 1WTSL4 during high amplitude testing

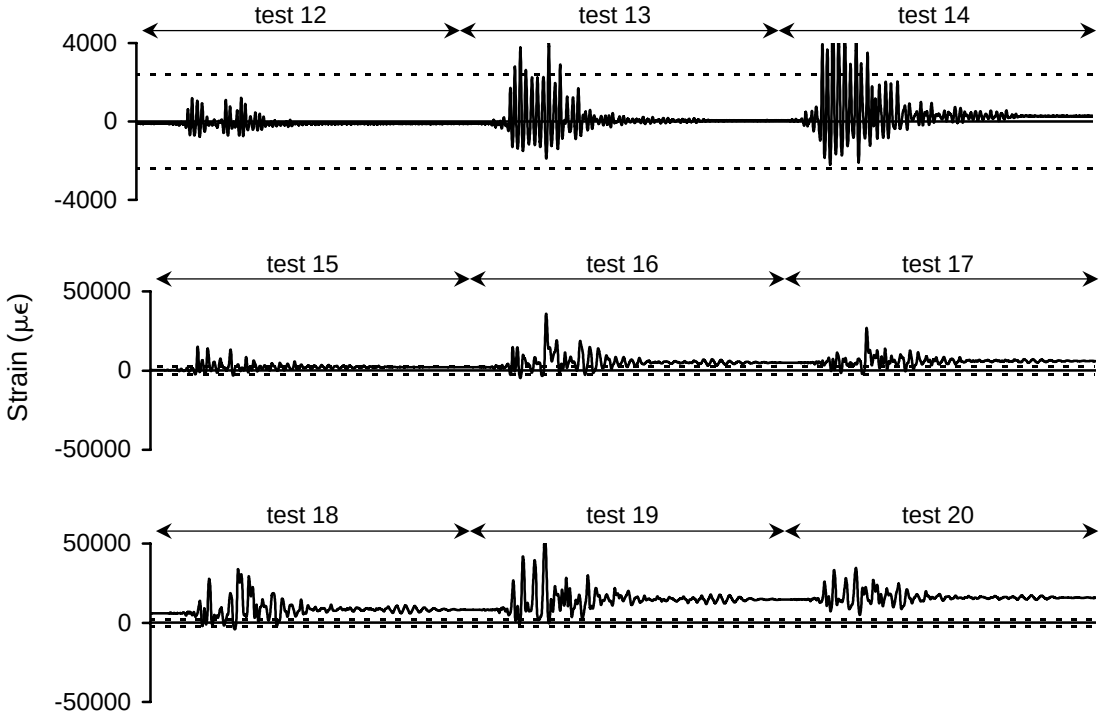

Figure A-5 Strain history for 1WTSL5 during high amplitude testing

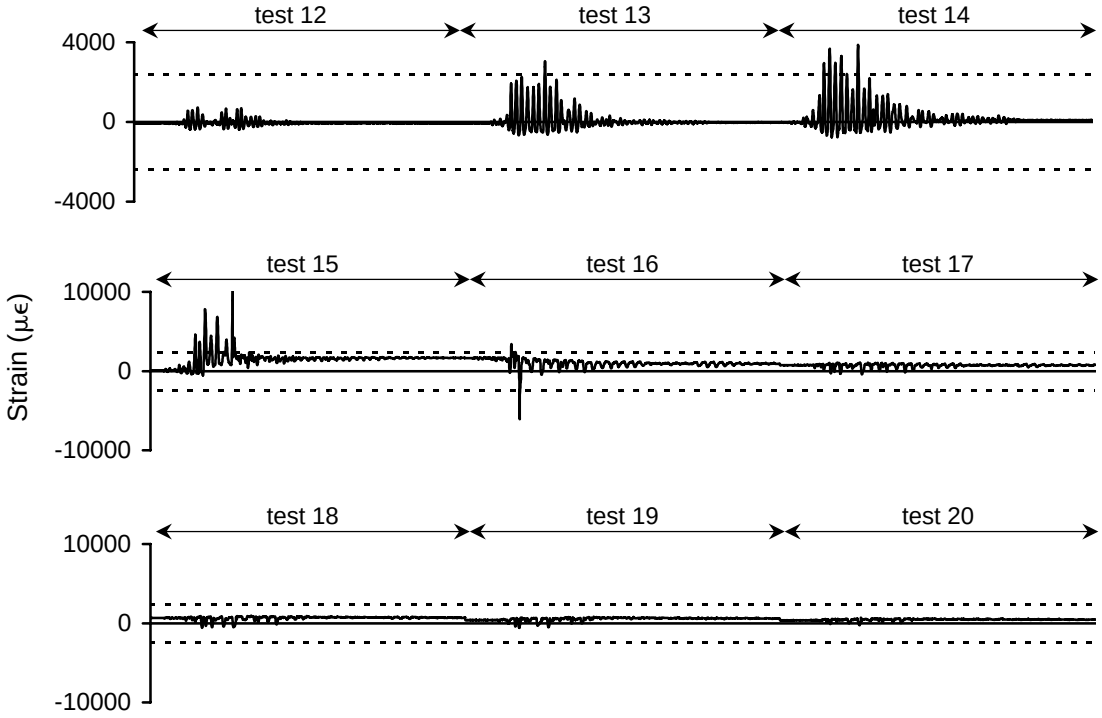

Figure A-6 Strain history for 1WTSL6 during high amplitude testing

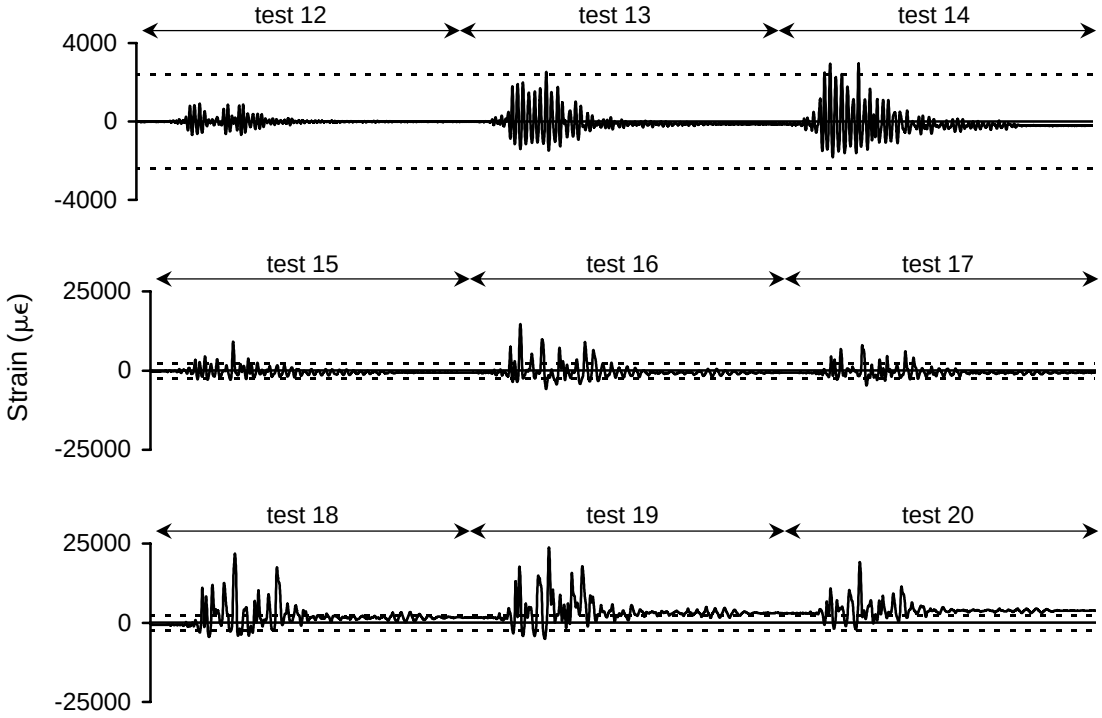

Figure A-7 Strain history for 1WTSL7 during high amplitude testing

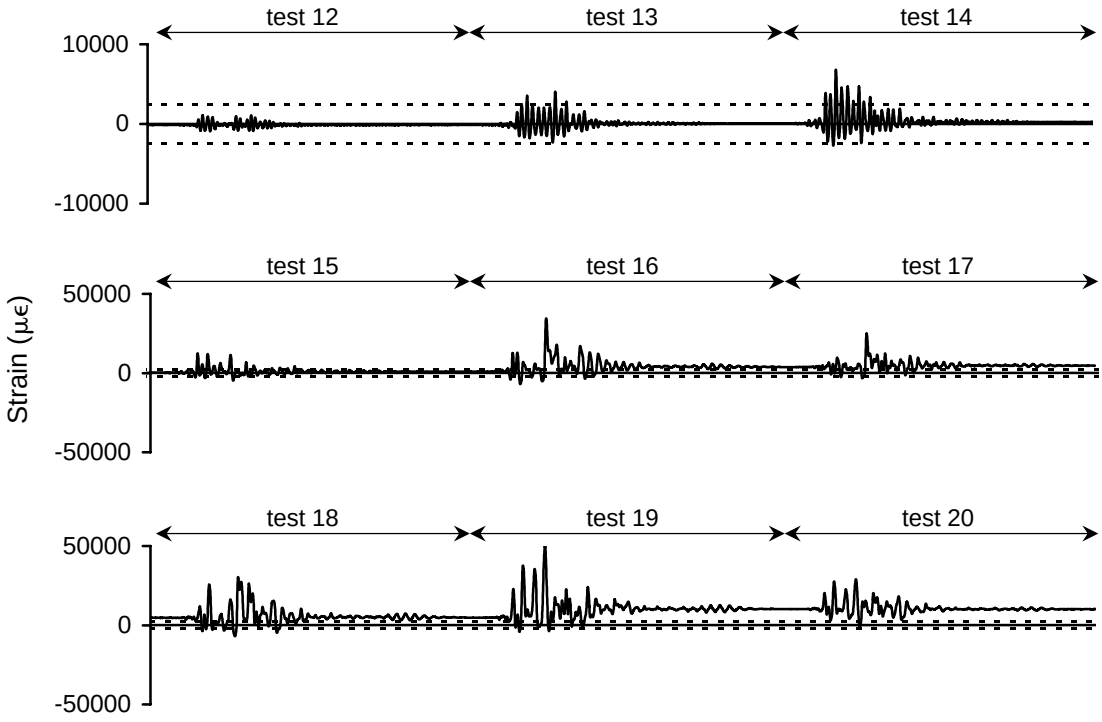

Figure A-8 Strain history for 1WTSL8 during high amplitude testing

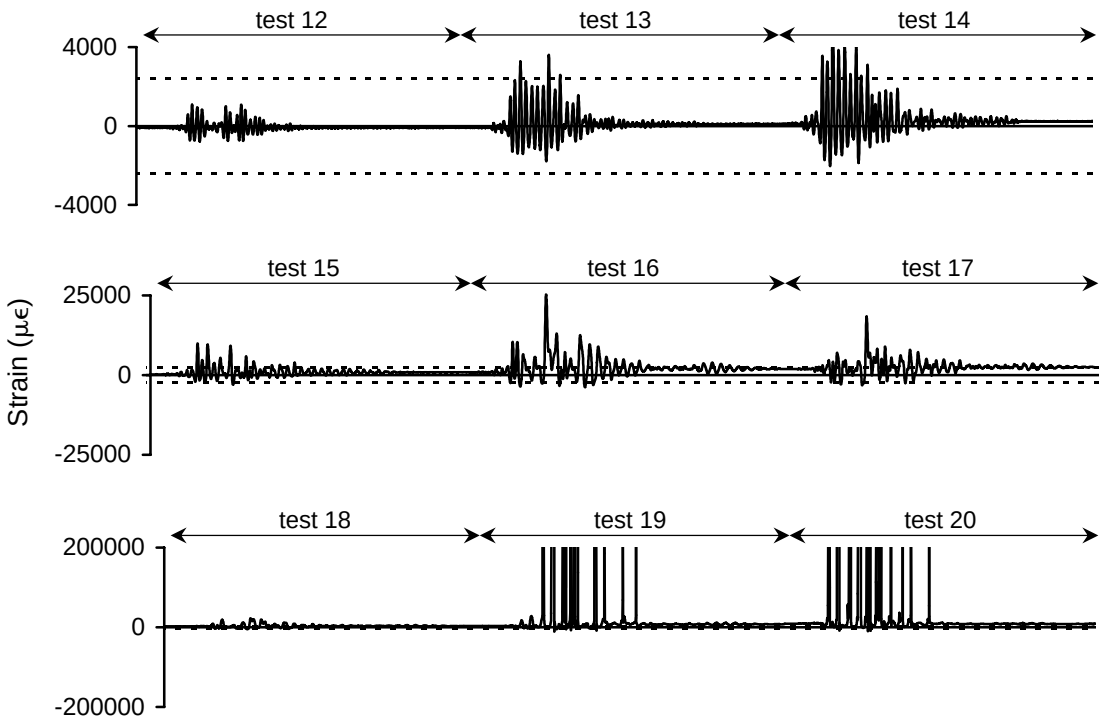

Figure A-9 Strain history for 1WBSL1 during high amplitude testing

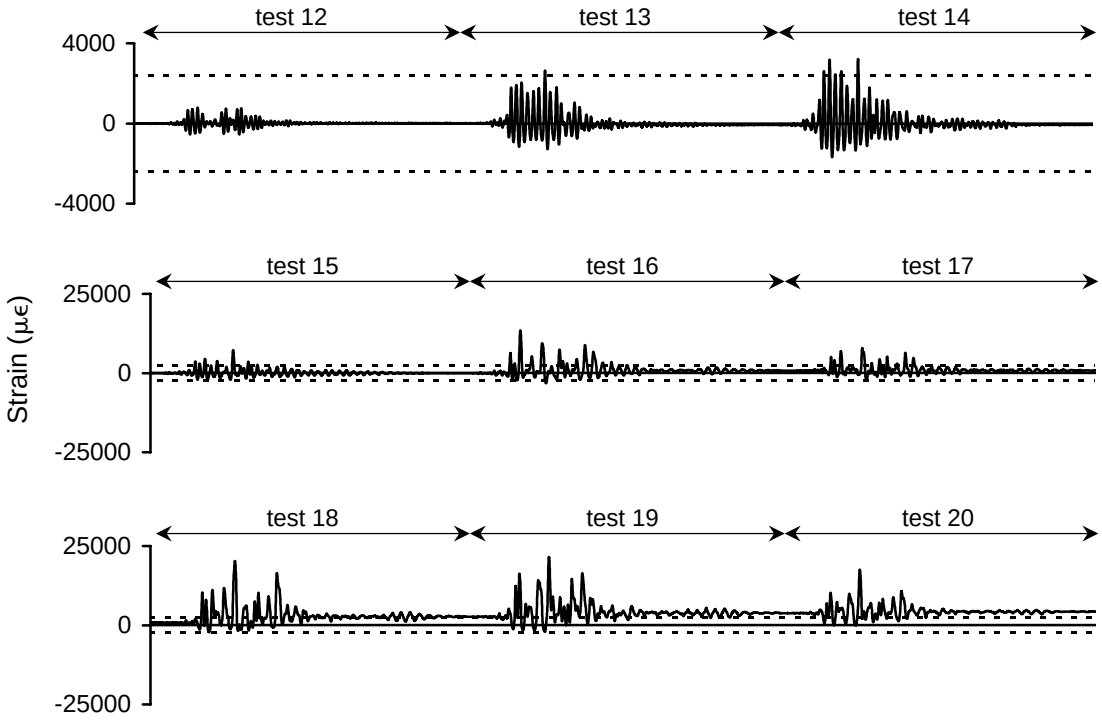

Figure A-10 Strain history for 1WBSL2 during high amplitude testing

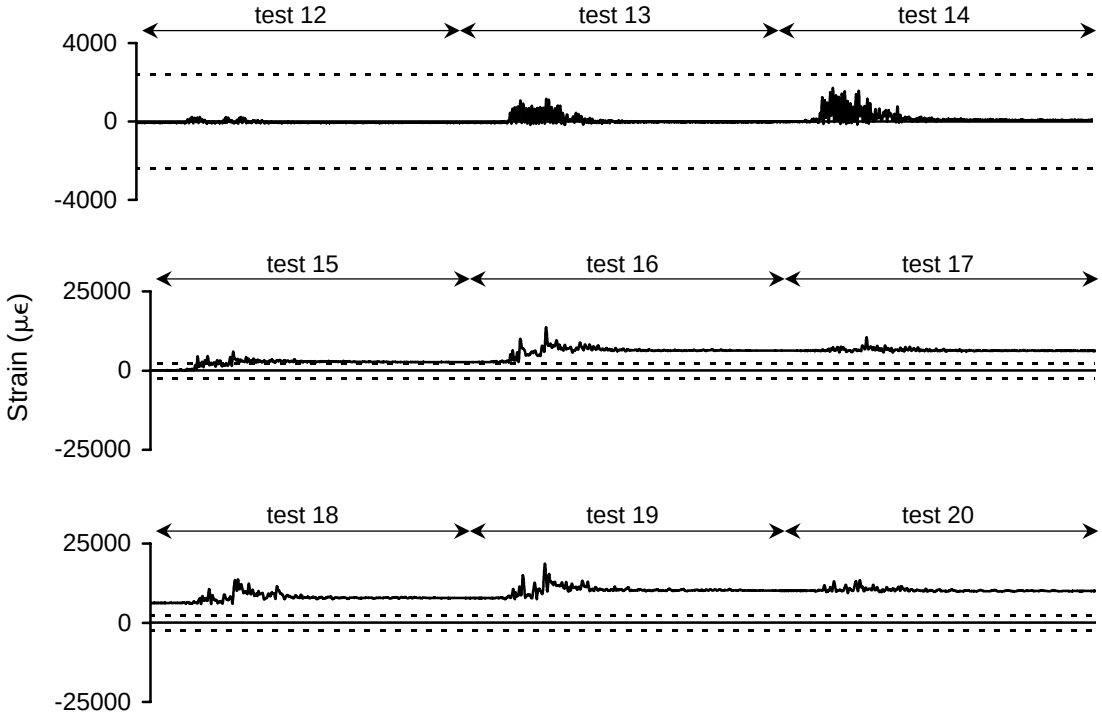

Figure A-11 Strain history for 1WBSL3 during high amplitude testing

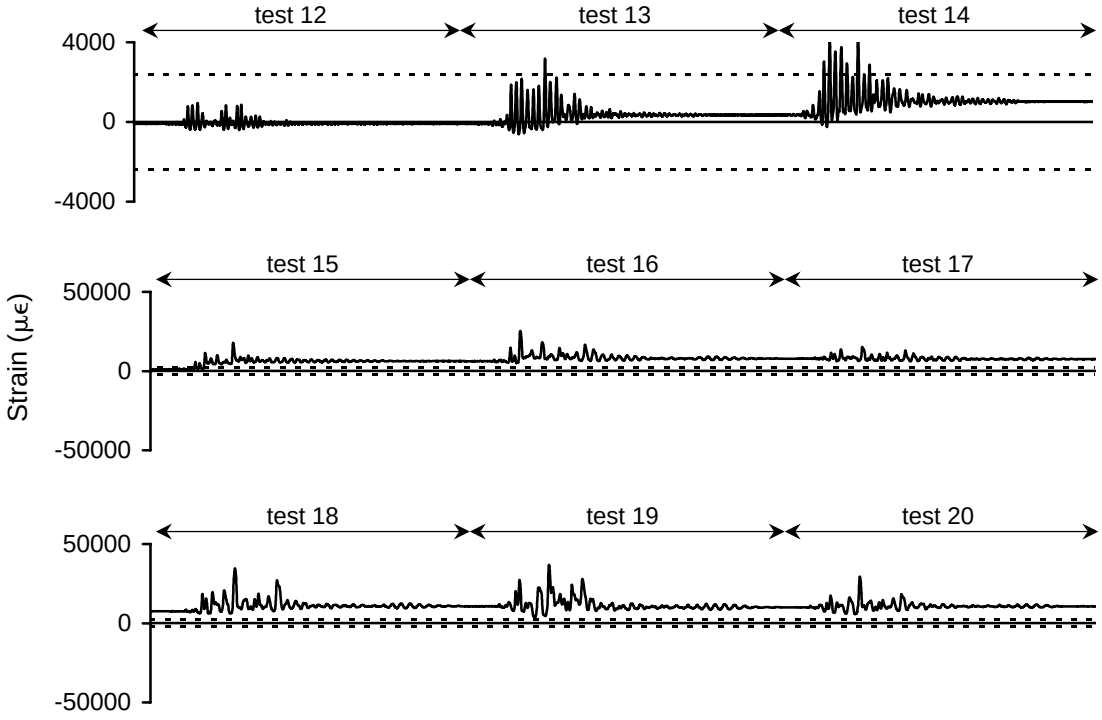

Figure A-12 Strain history for 1WBSL4 during high amplitude testing

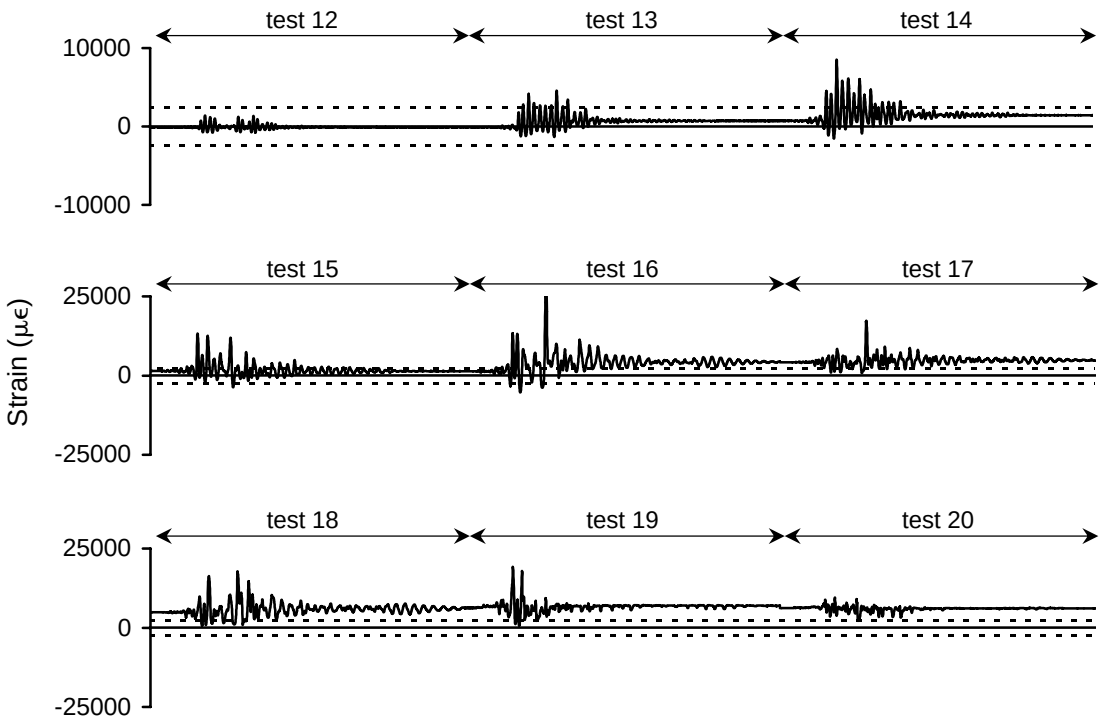

Figure A-13 Strain history for 1WBSL5 during high amplitude testing

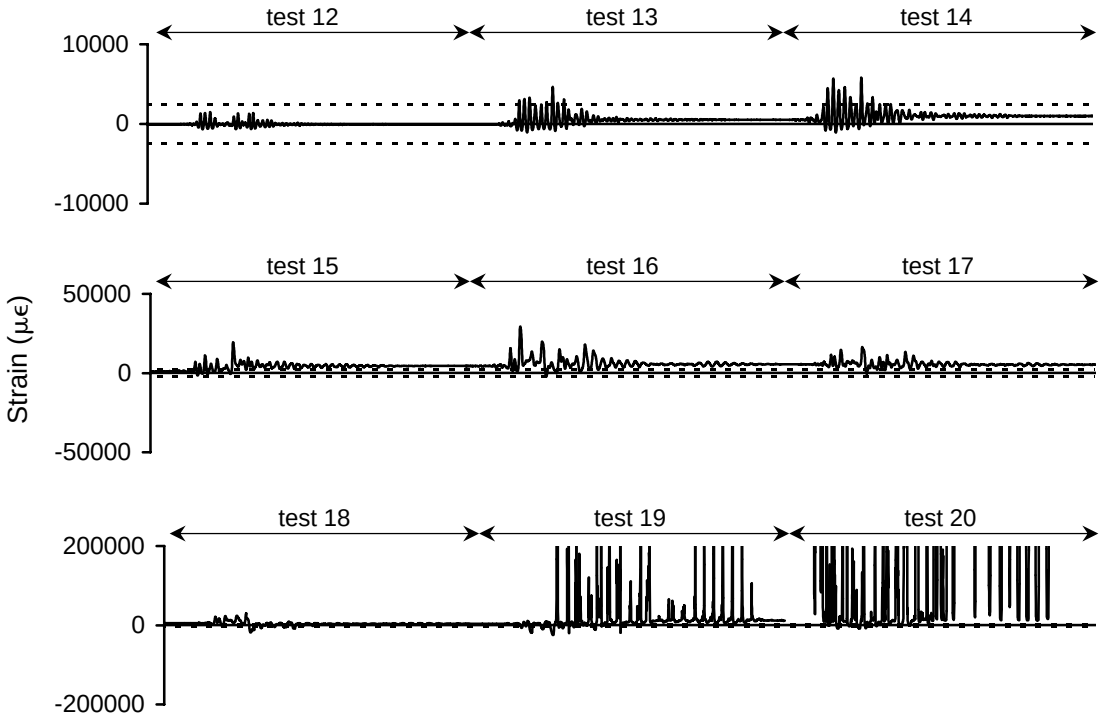

Figure A-14 Strain history for 1WBSL6 during high amplitude testing

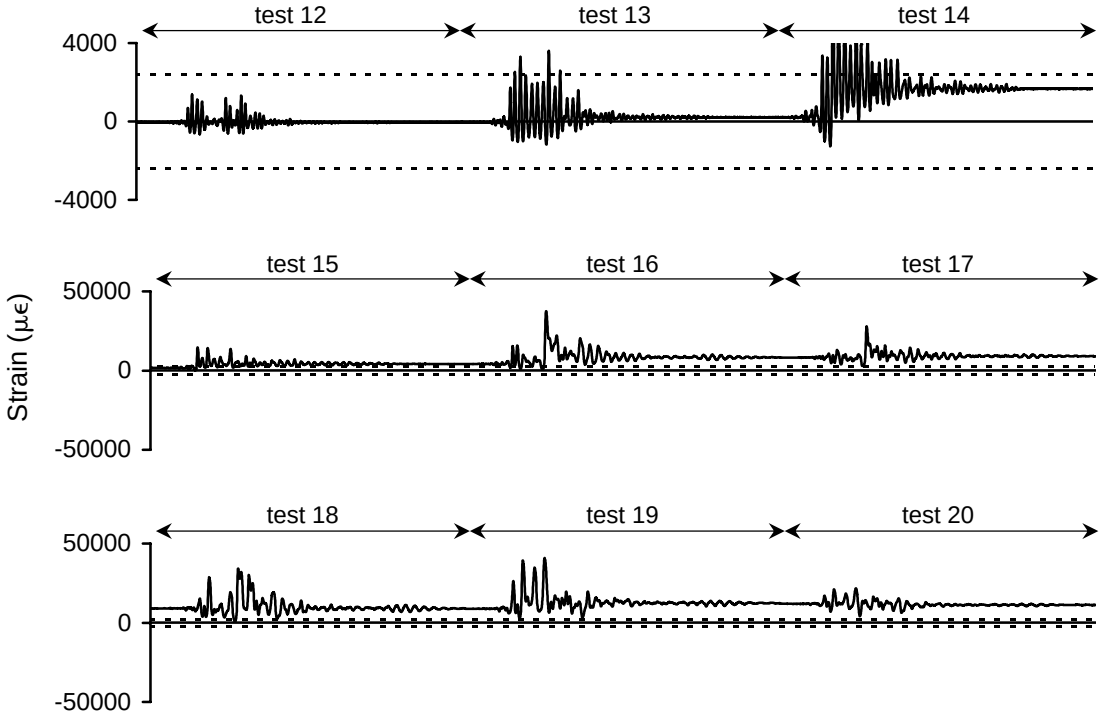

Figure A-15 Strain history for 1WBSL7 during high amplitude testing

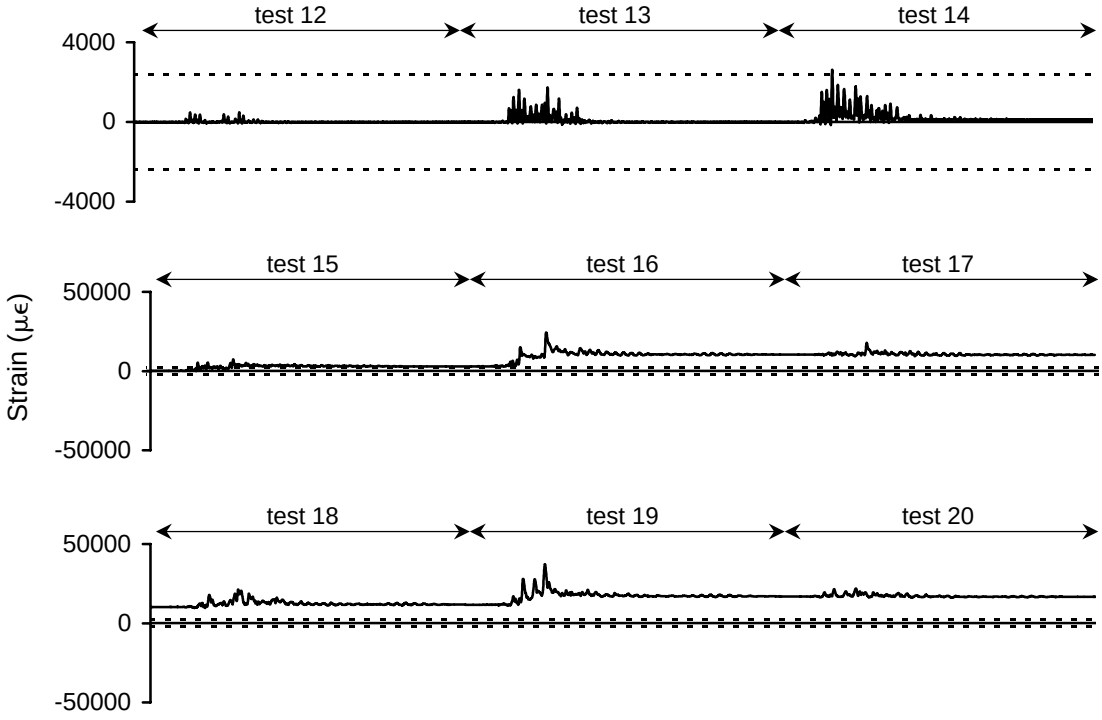

Figure A-16 Strain history for 1WBSL8 during high amplitude testing

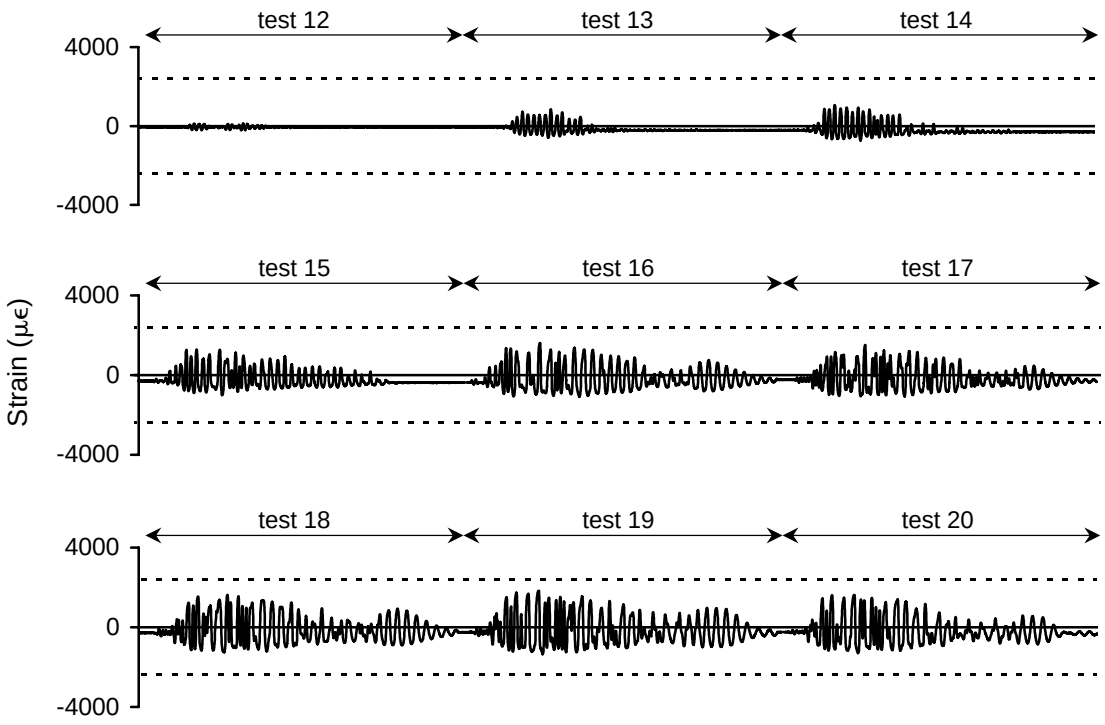

Figure A-17 Strain history for 1WBSL9 during high amplitude testing

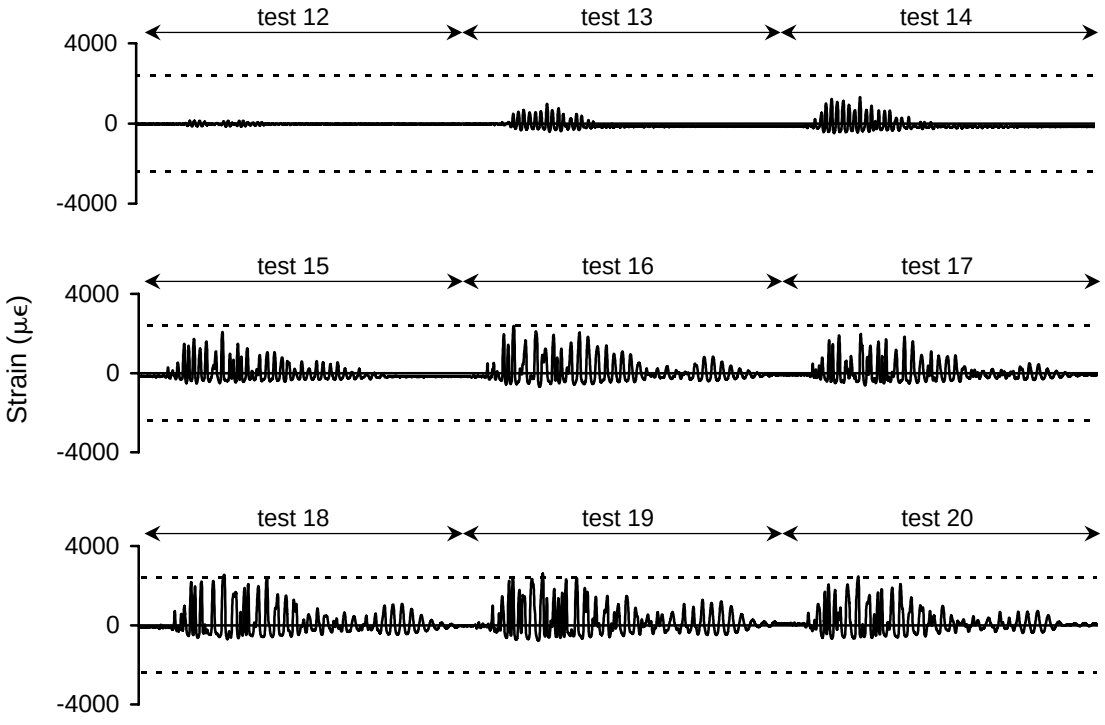

Figure A-18 Strain history for 1WBSL10 during high amplitude testing

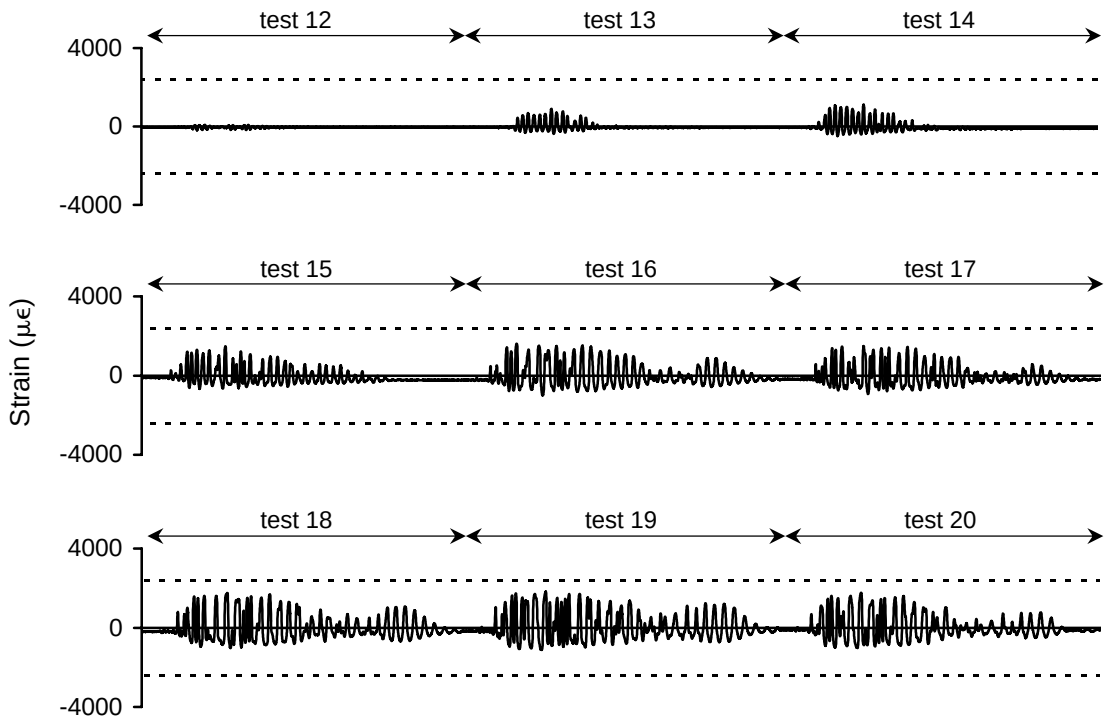

Figure A-19 Strain history for 1ETSL1 during high amplitude testing

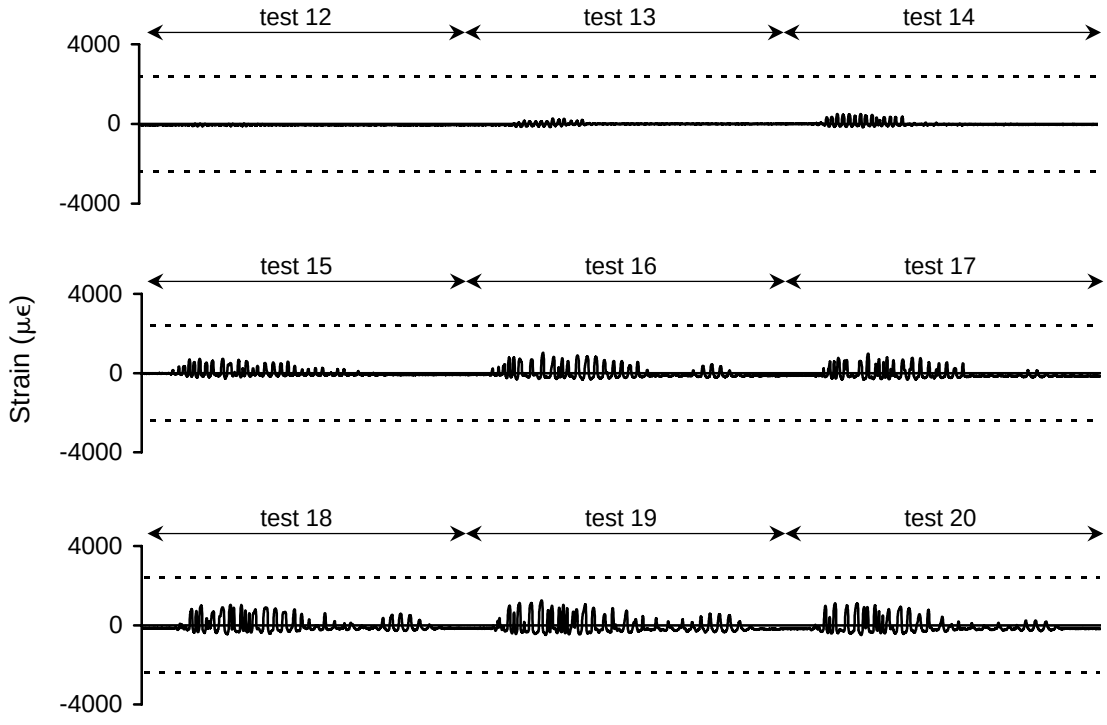

Figure A-20 Strain history for 1ETSL2 during high amplitude testing

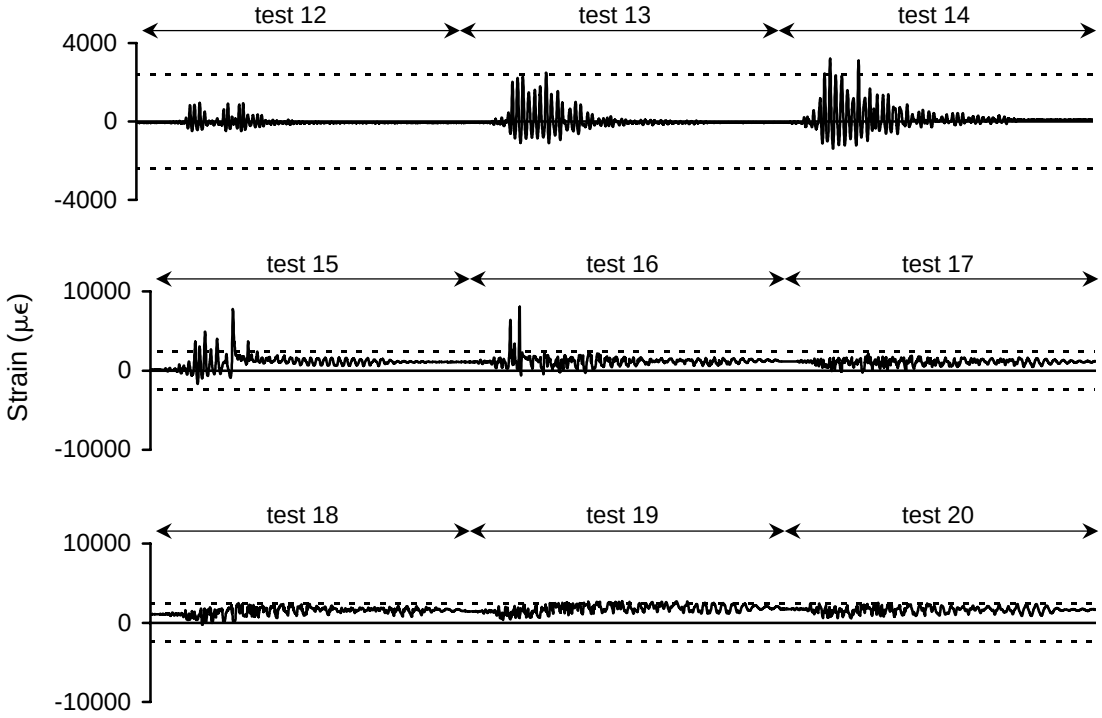

Figure A-21 Strain history for 1ETSL3 during high amplitude testing

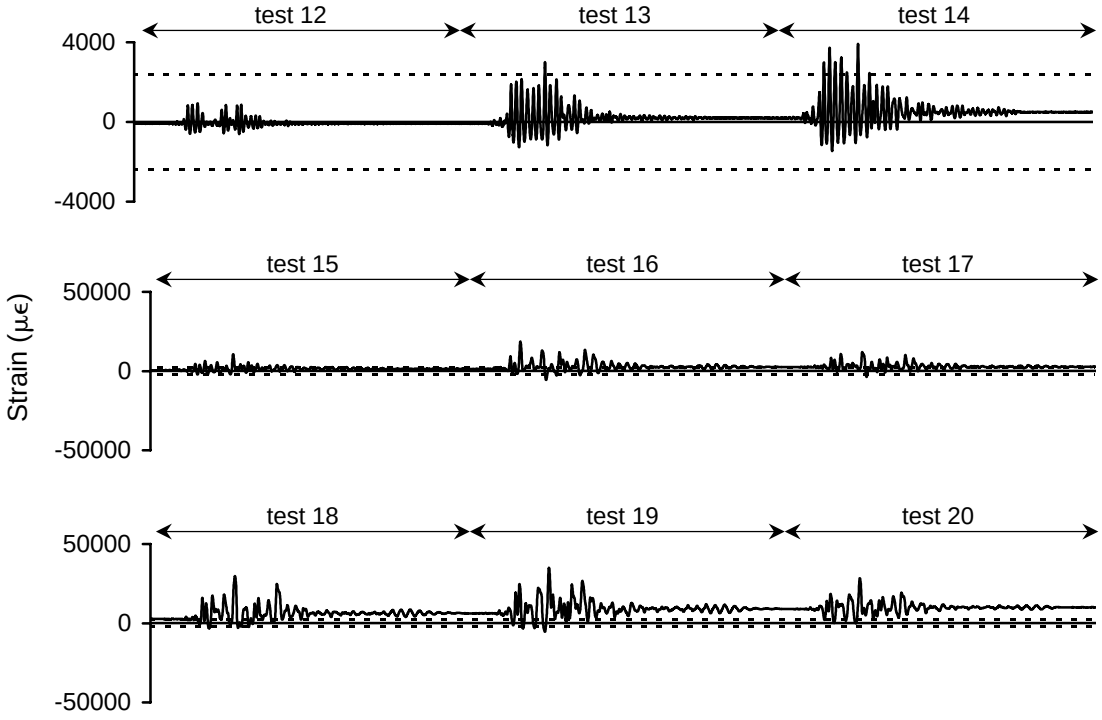

Figure A-22 Strain history for 1ETSL4 during high amplitude testing

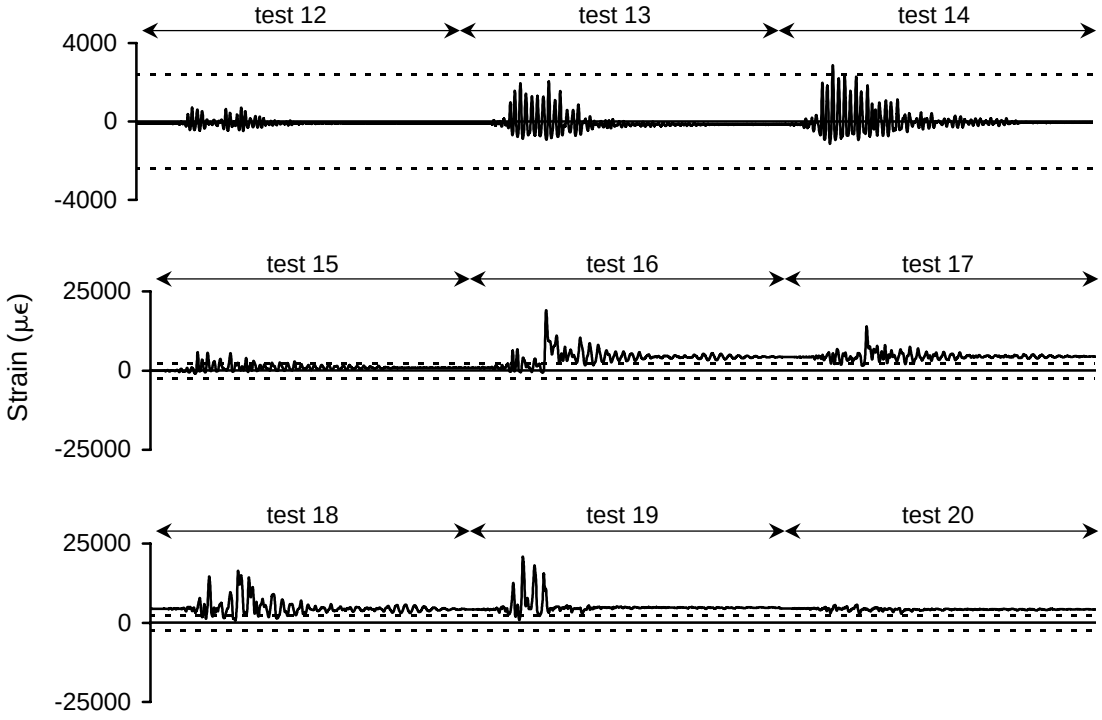

Figure A-23 Strain history for 1ETSL6 during high amplitude testing

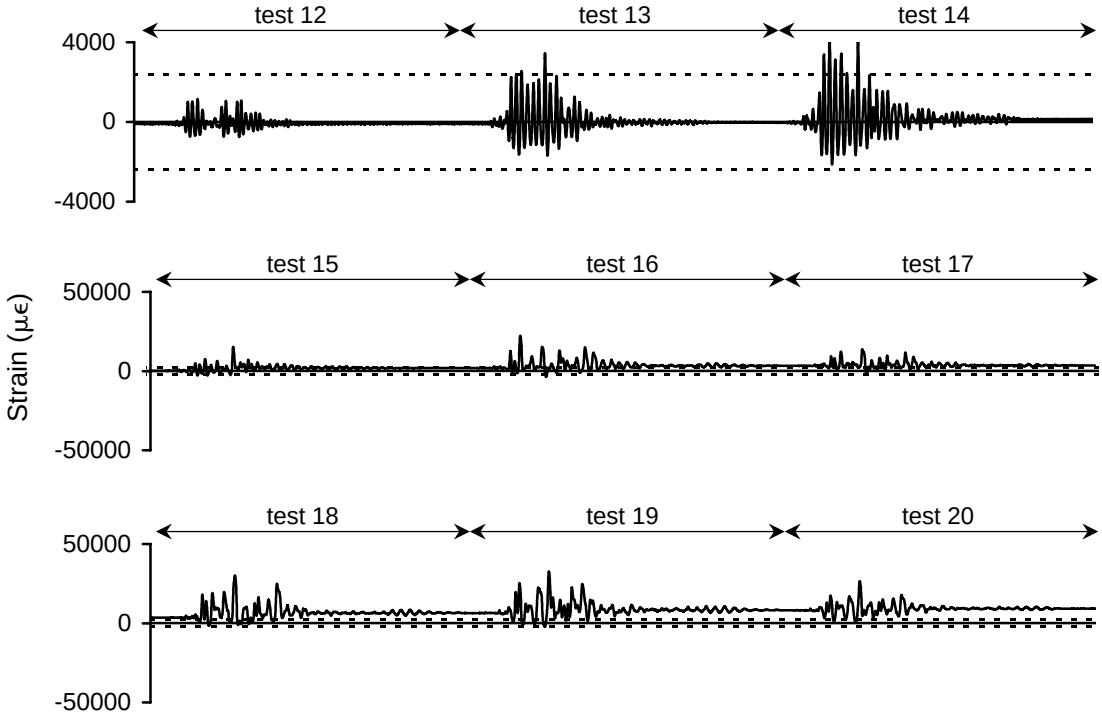

Figure A-24 Strain history for 1ETSL7 during high amplitude testing

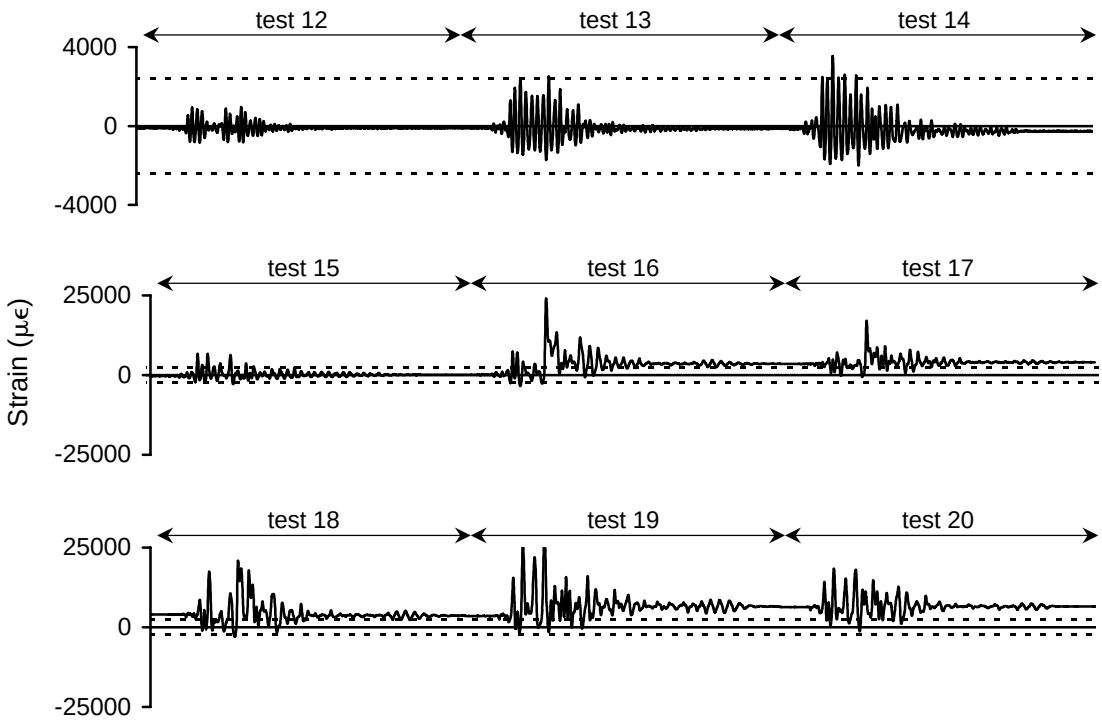

Figure A-25 Strain history for 1ETSL8 during high amplitude testing

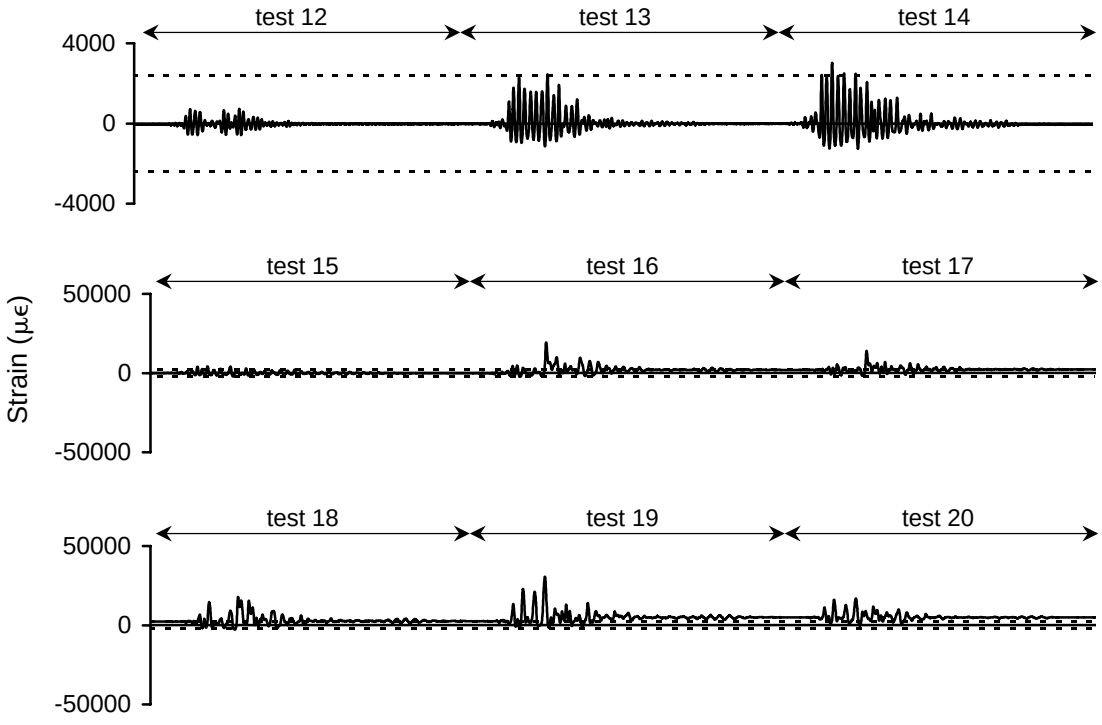

Figure A-26 Strain history for 1EBSL1 during high amplitude testing

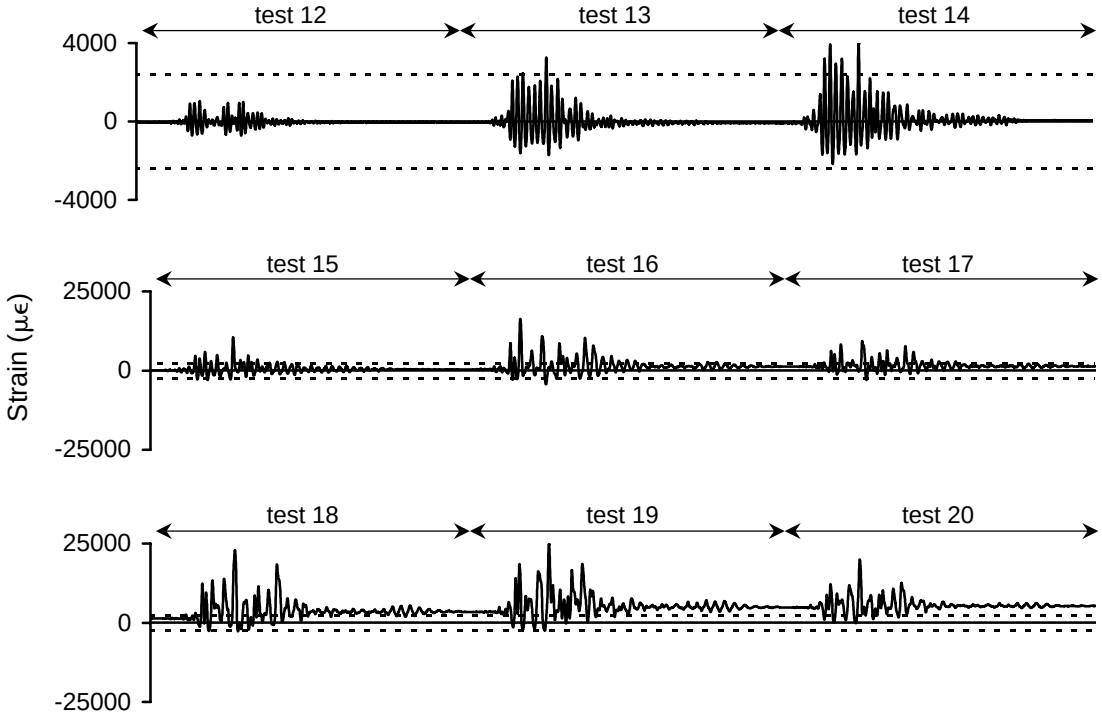

Figure A-27 Strain history for 1EBSL2 during high amplitude testing

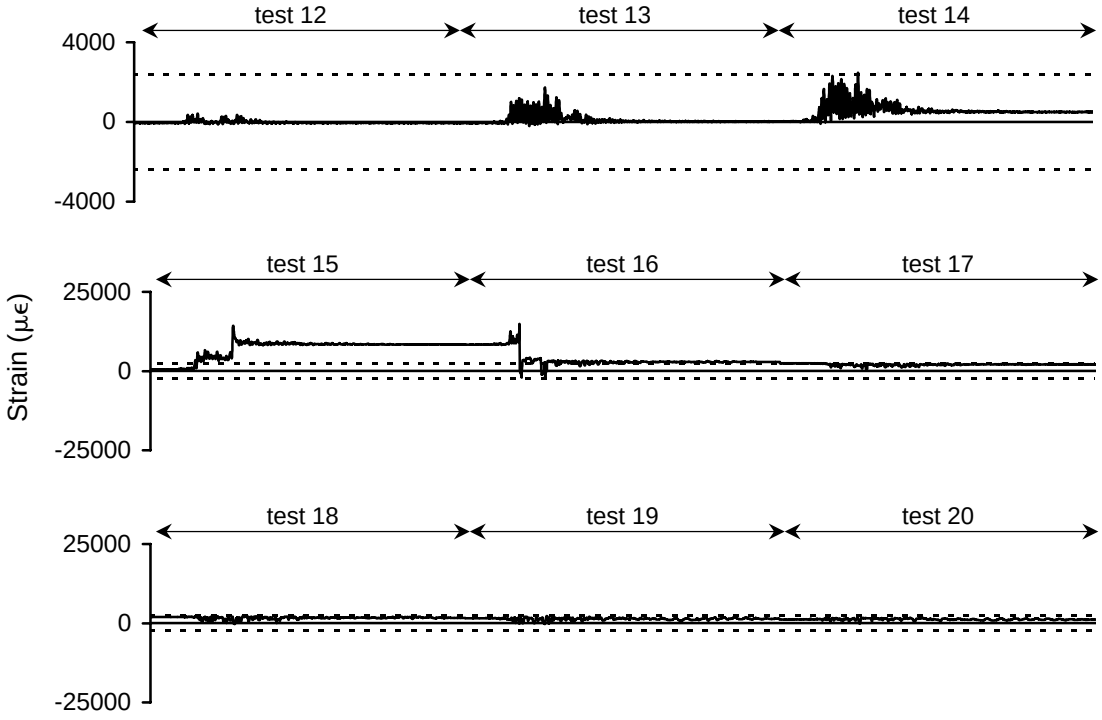

Figure A-28 Strain history for 1EBSL3 during high amplitude testing

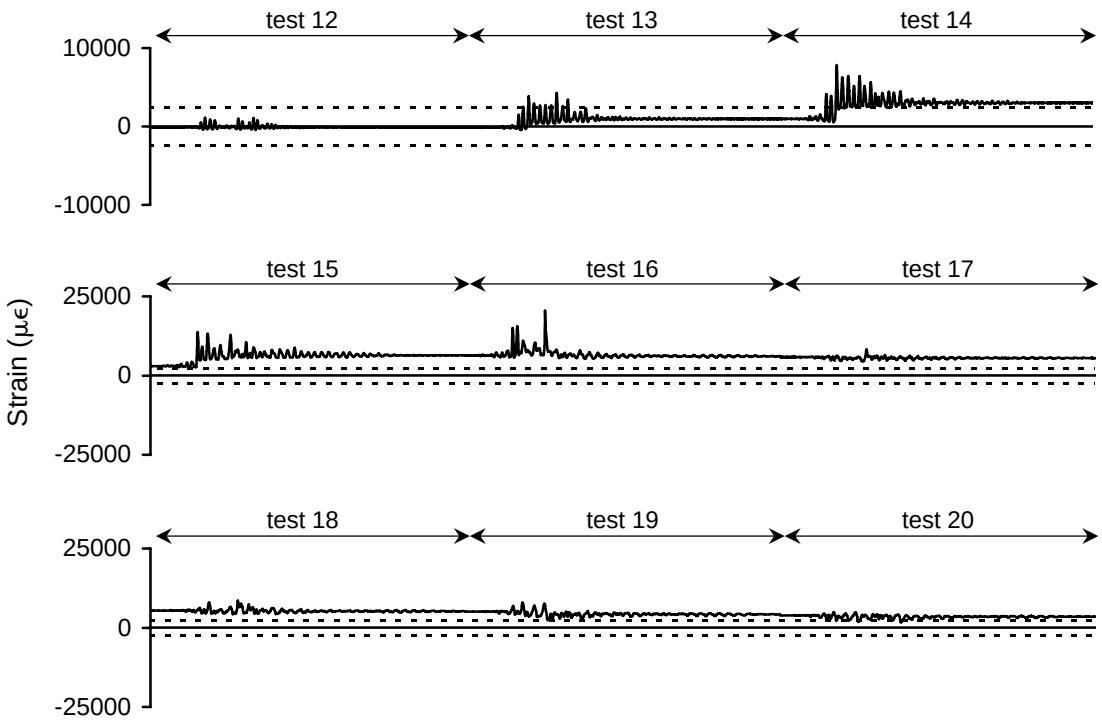

Figure A-29 Strain history for 1EBSL4 during high amplitude testing

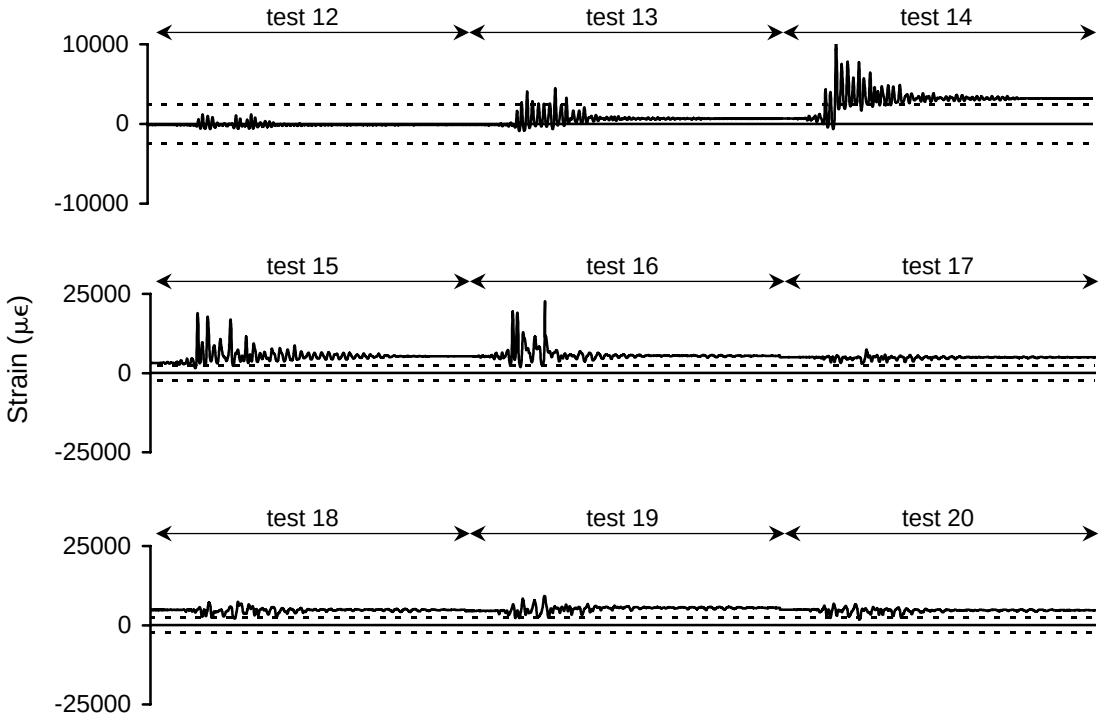

Figure A-30 Strain history for 1EBSL5 during high amplitude testing

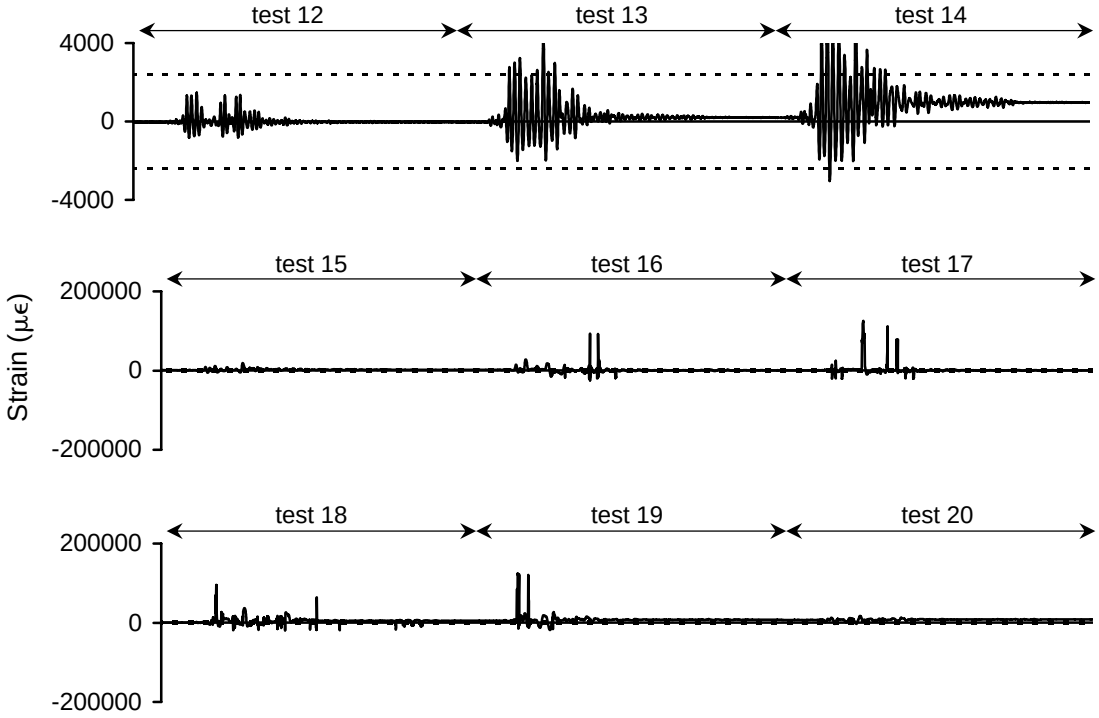

Figure A-31 Strain history for 1EBSL6 during high amplitude testing

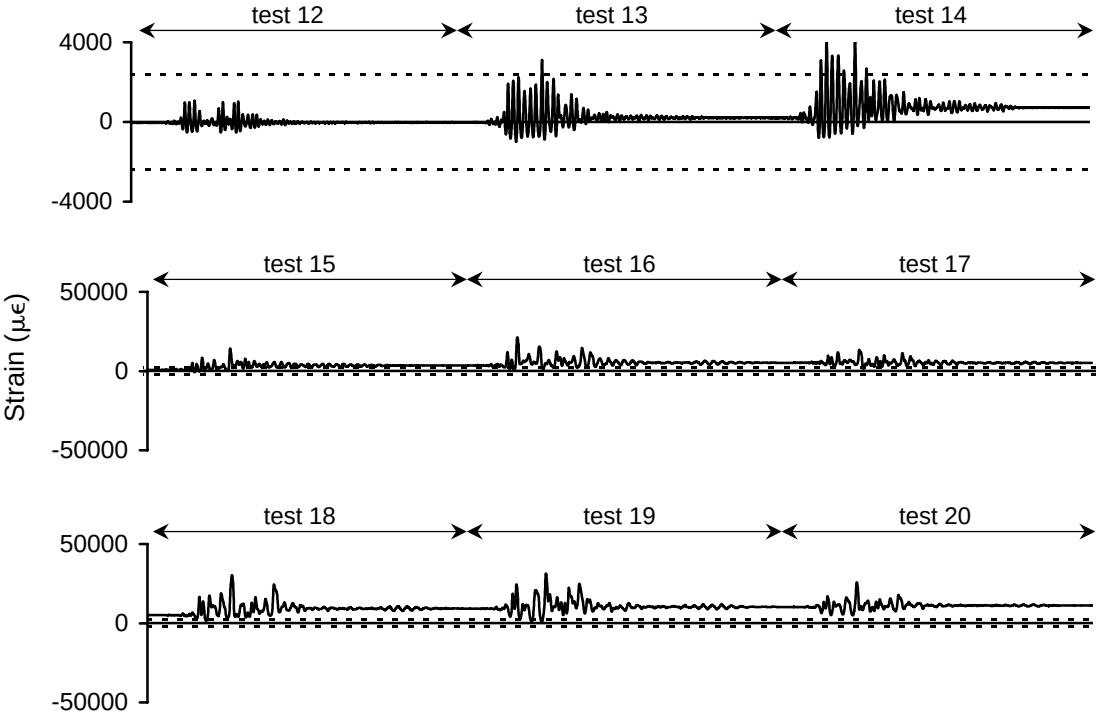

Figure A-32 Strain history for 1EBSL7 during high amplitude testing

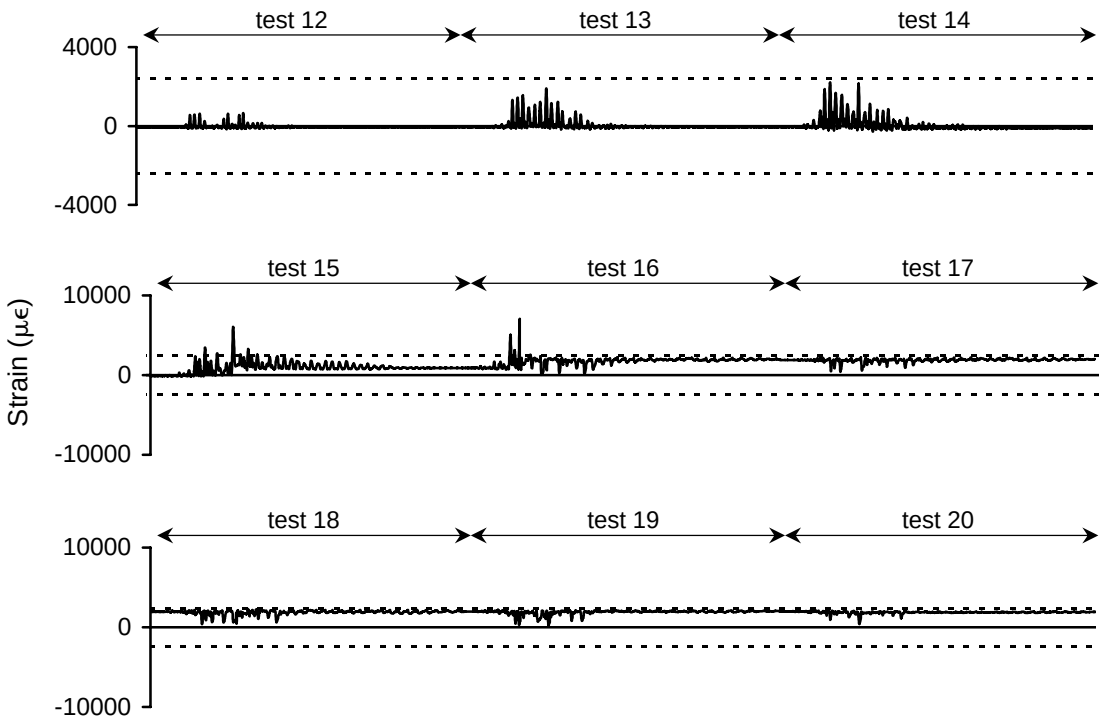

Figure A-33 Strain history for 1EBSL8 during high amplitude testing

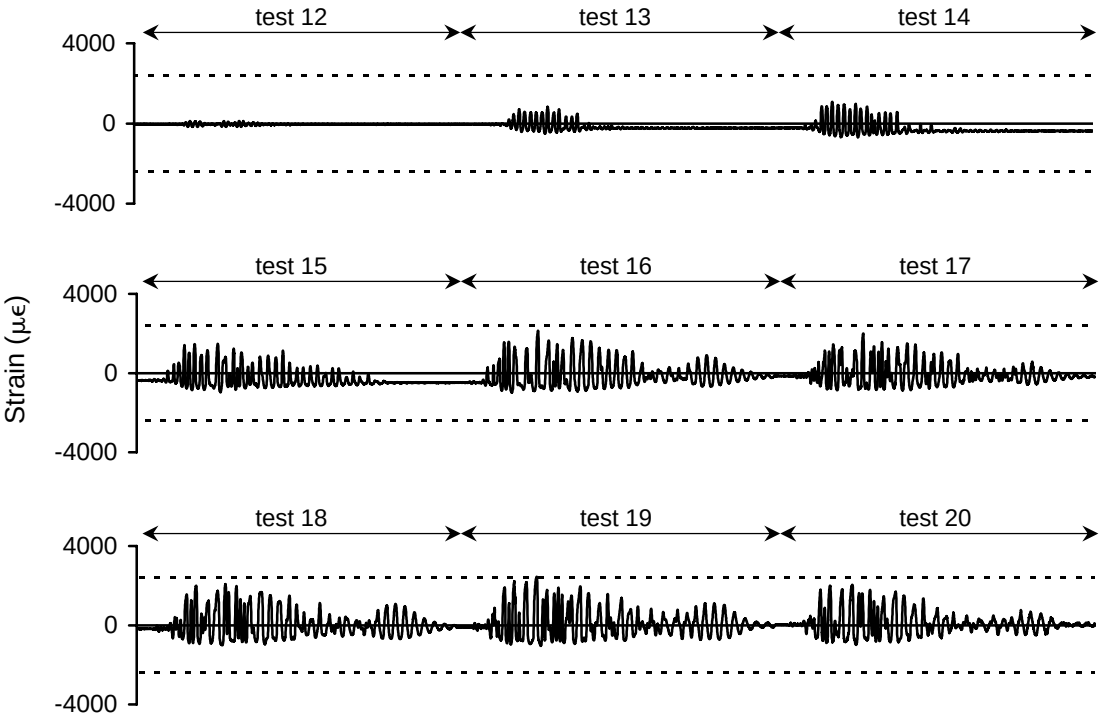

Figure A-34 Strain history for 1EBSL9 during high amplitude testing

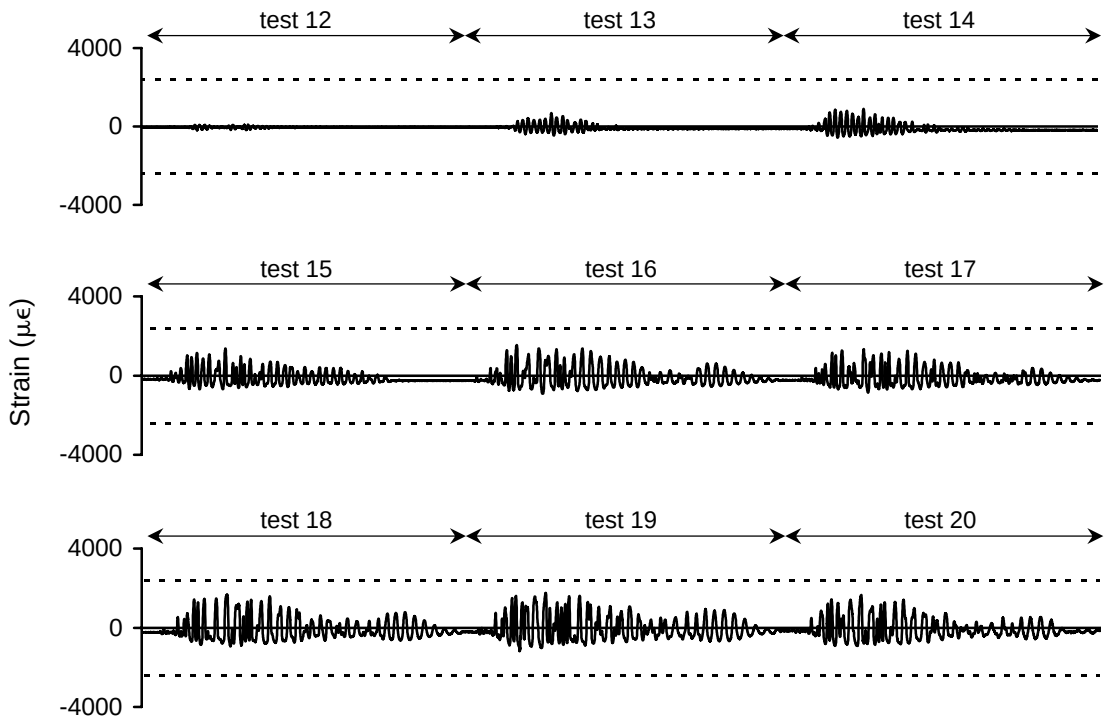

Figure A-35 Strain history for 1EBSL10 during high amplitude testing

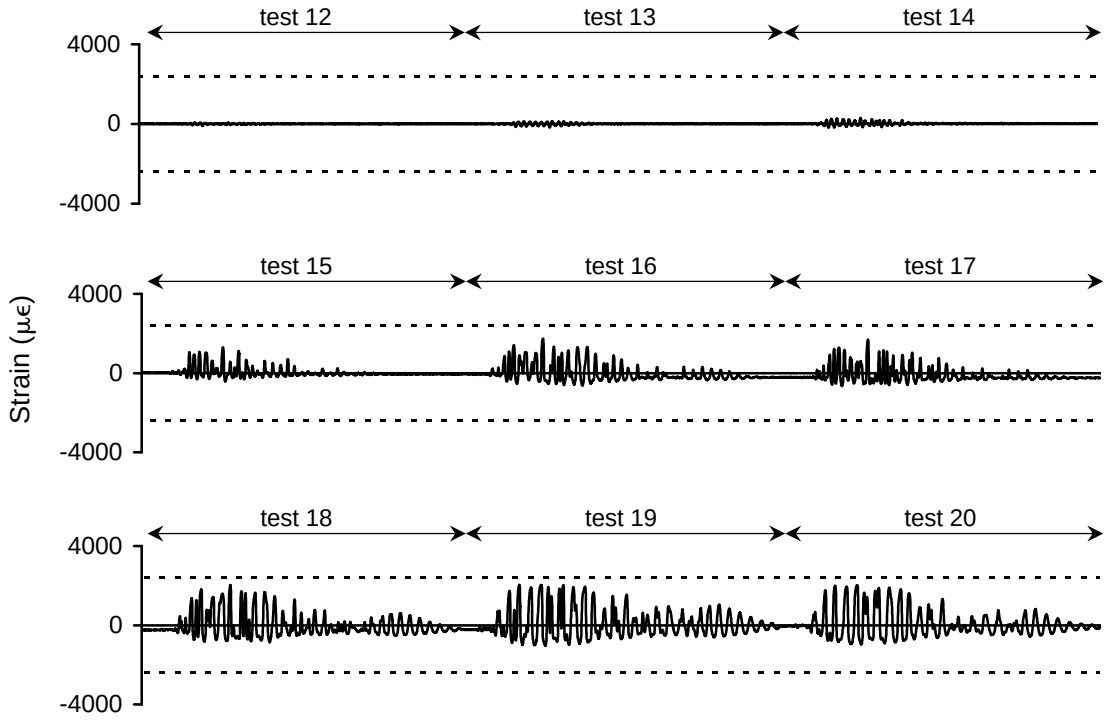

Figure A-36 Strain history for 2WTSL1 during high amplitude testing

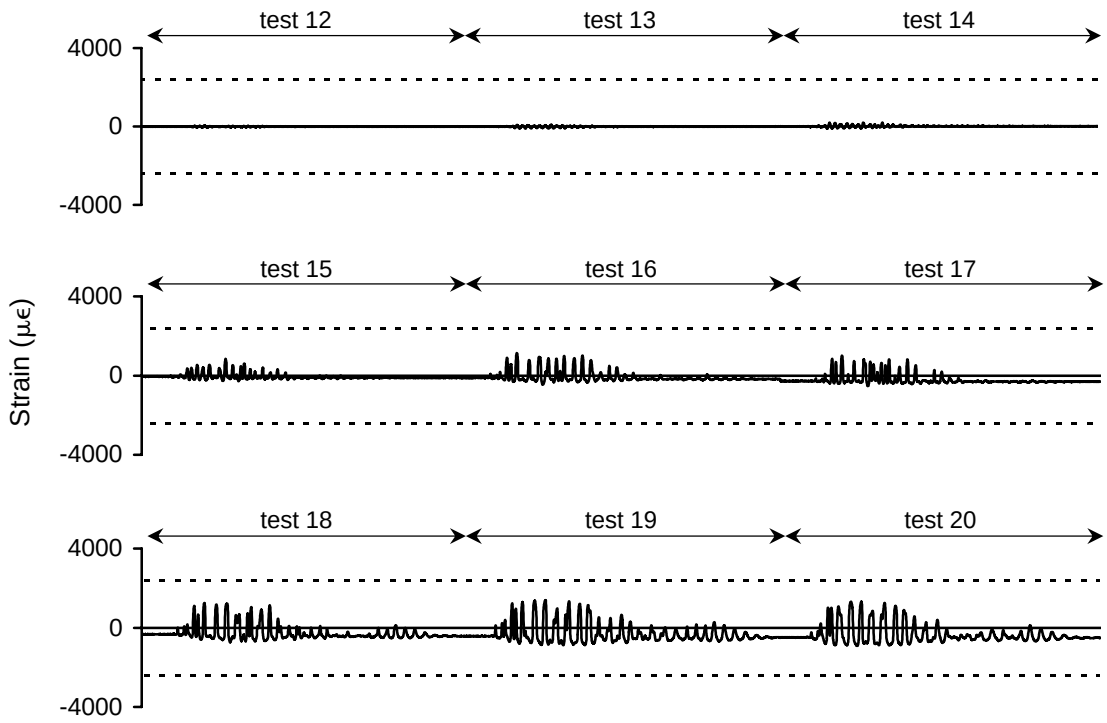

Figure A-37 Strain history for 2WTSL2 during high amplitude testing

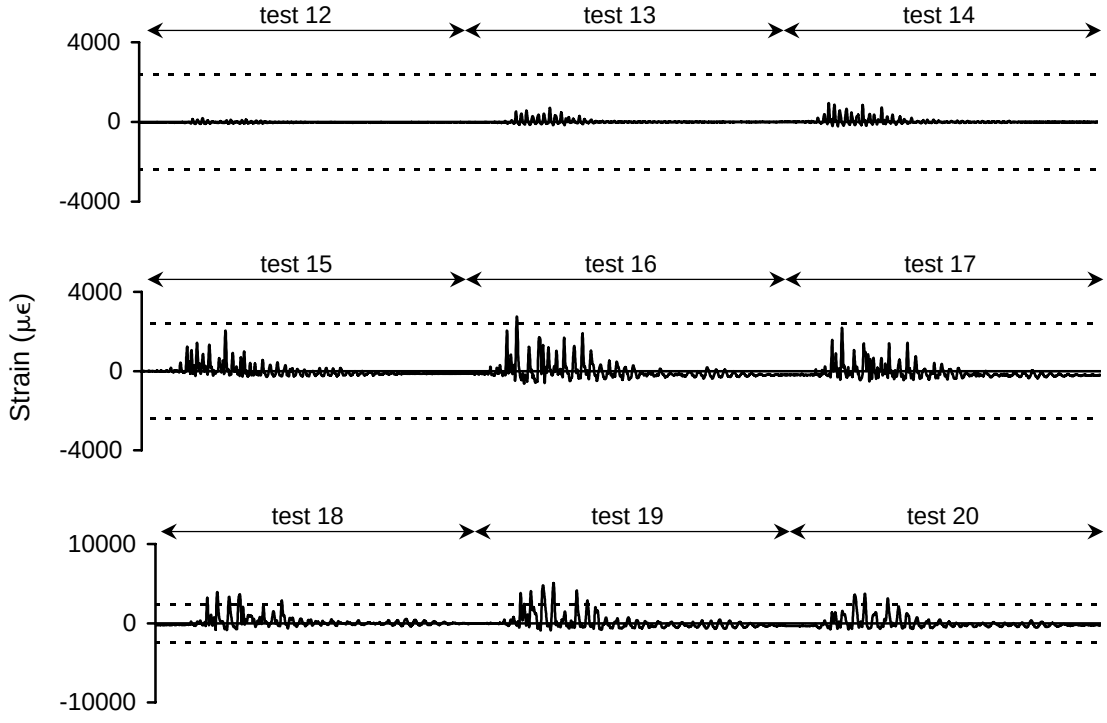

Figure A-38 Strain history for 2WTSL3 during high amplitude testing

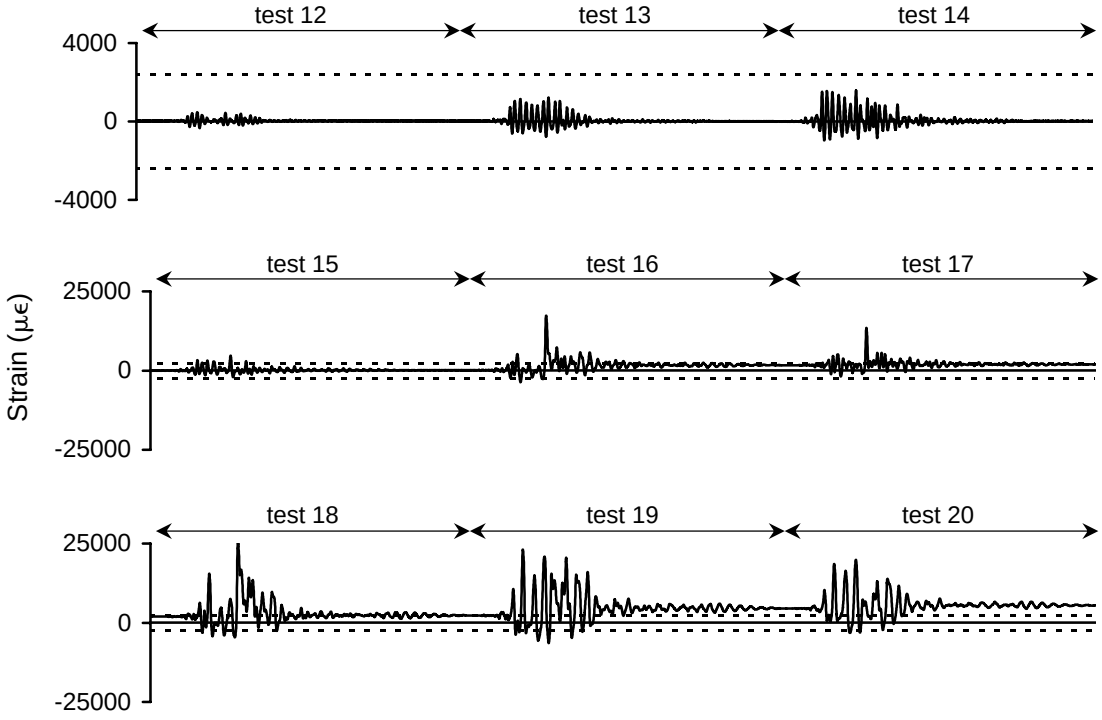

Figure A-39 Strain history for 2WTSL4 during high amplitude testing

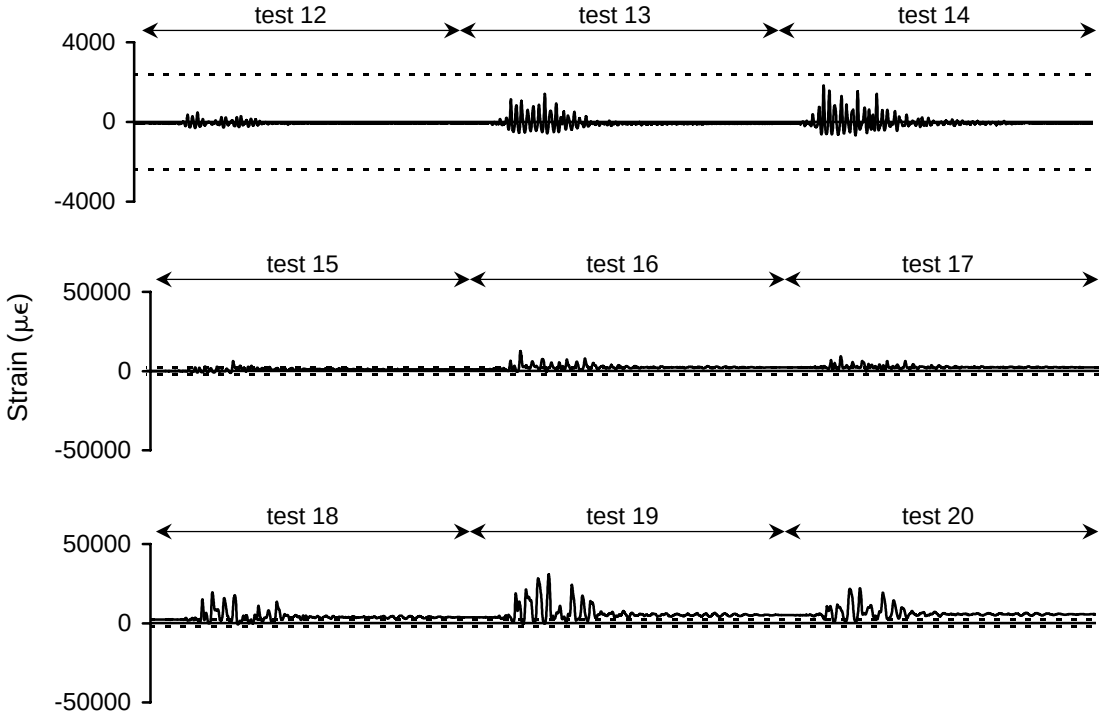

Figure A-40 Strain history for 2WTSL5 during high amplitude testing

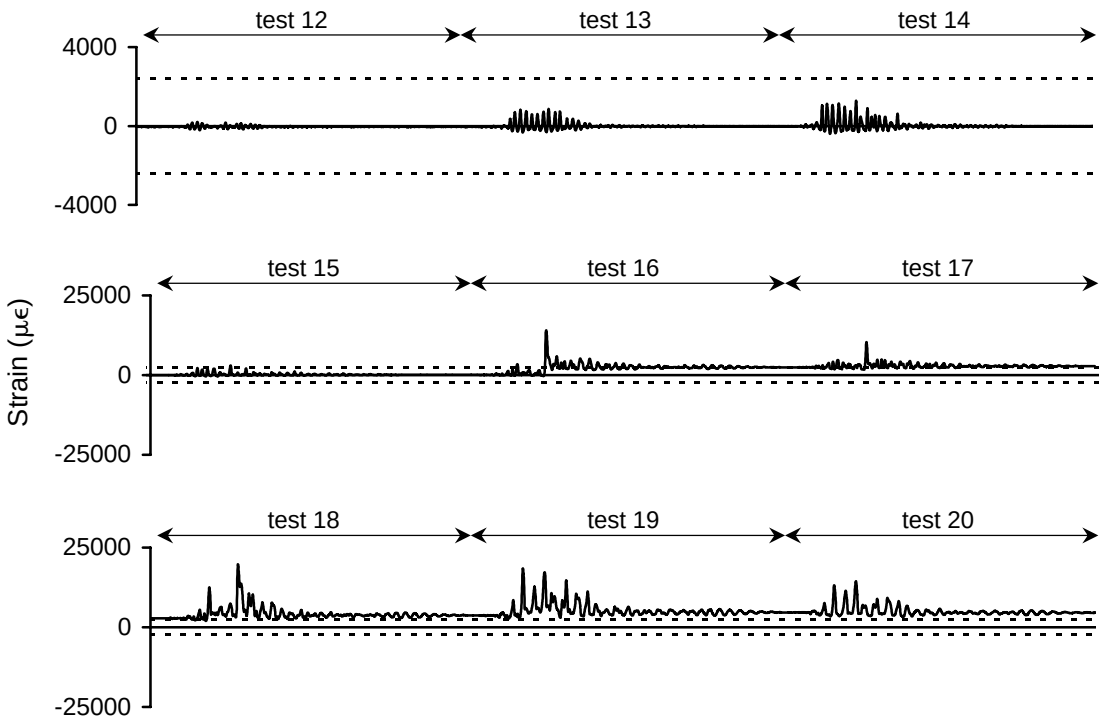

Figure A-41 Strain history for 2WTSL6 during high amplitude testing

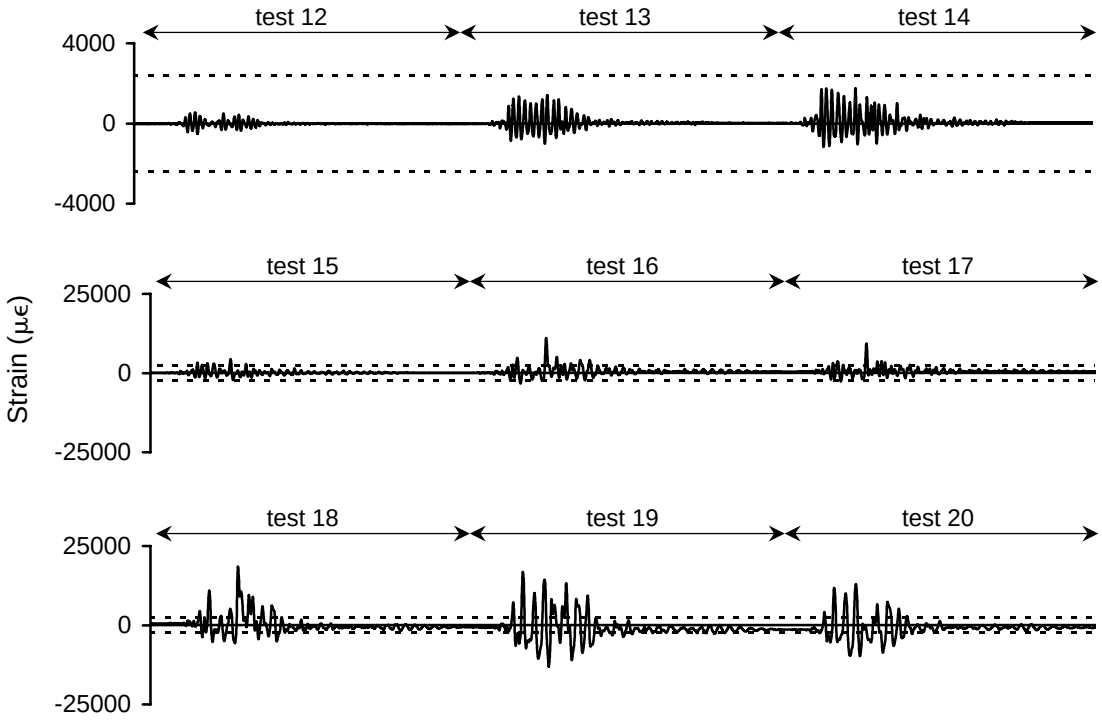

Figure A-42 Strain history for 2WTSL7 during high amplitude testing

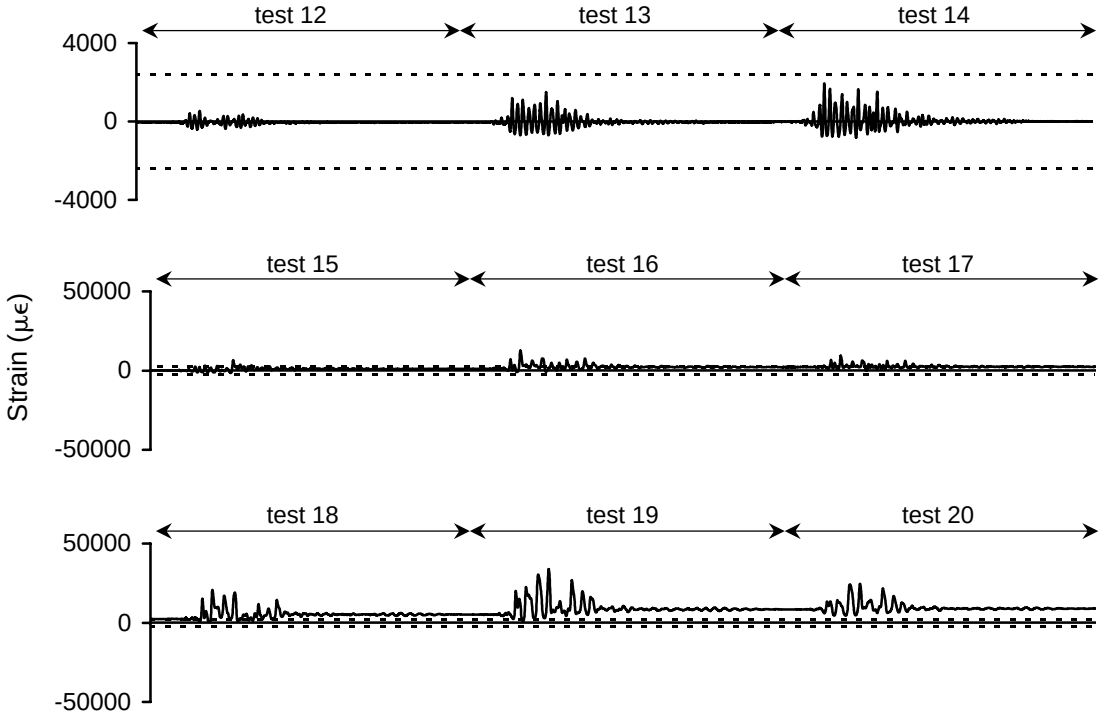

Figure A-43 Strain history for 2WTSL8 during high amplitude testing

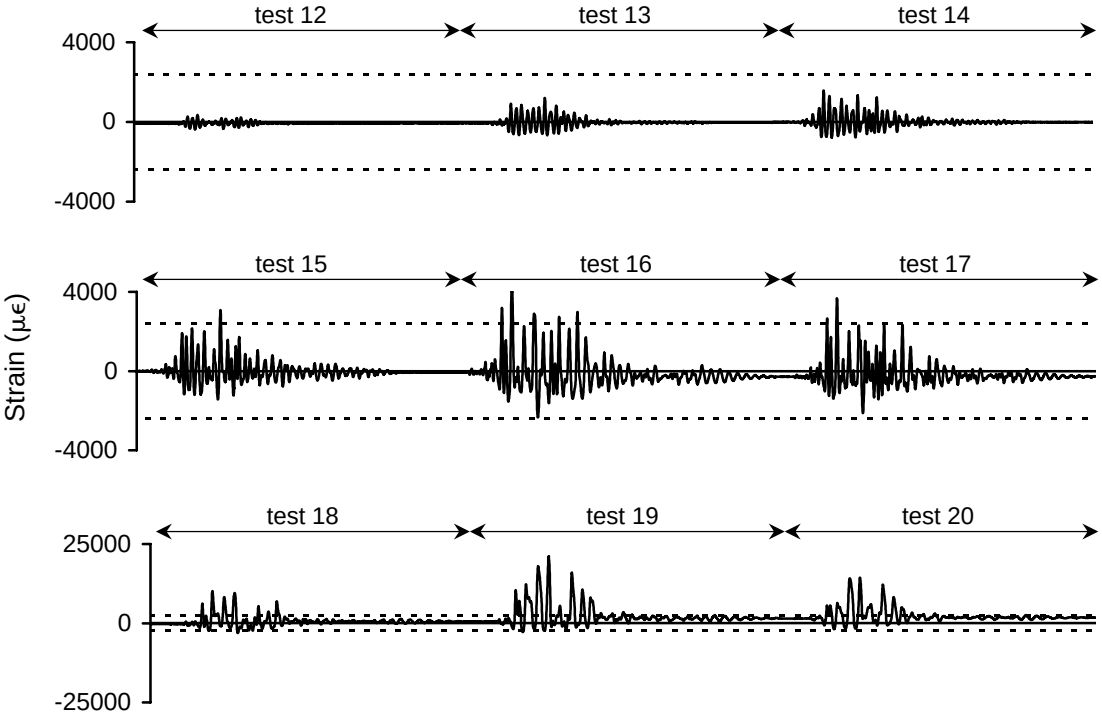

Figure A-44 Strain history for 2WBSL1 during high amplitude testing

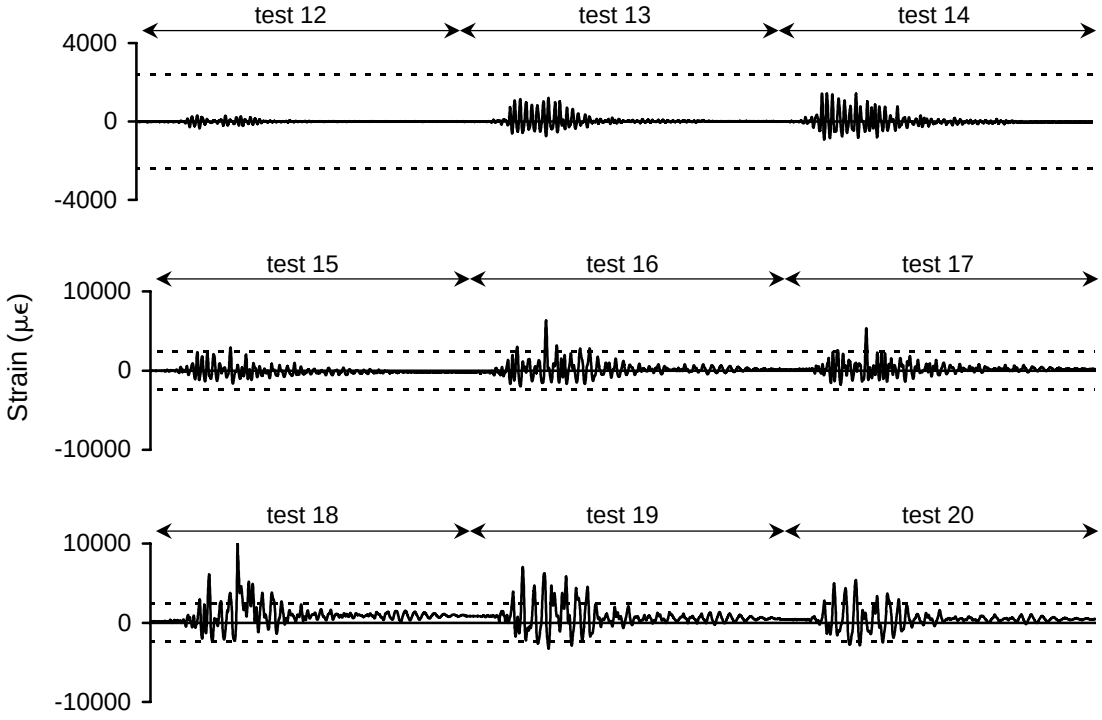

Figure A-45 Strain history for 2WBSL2 during high amplitude testing

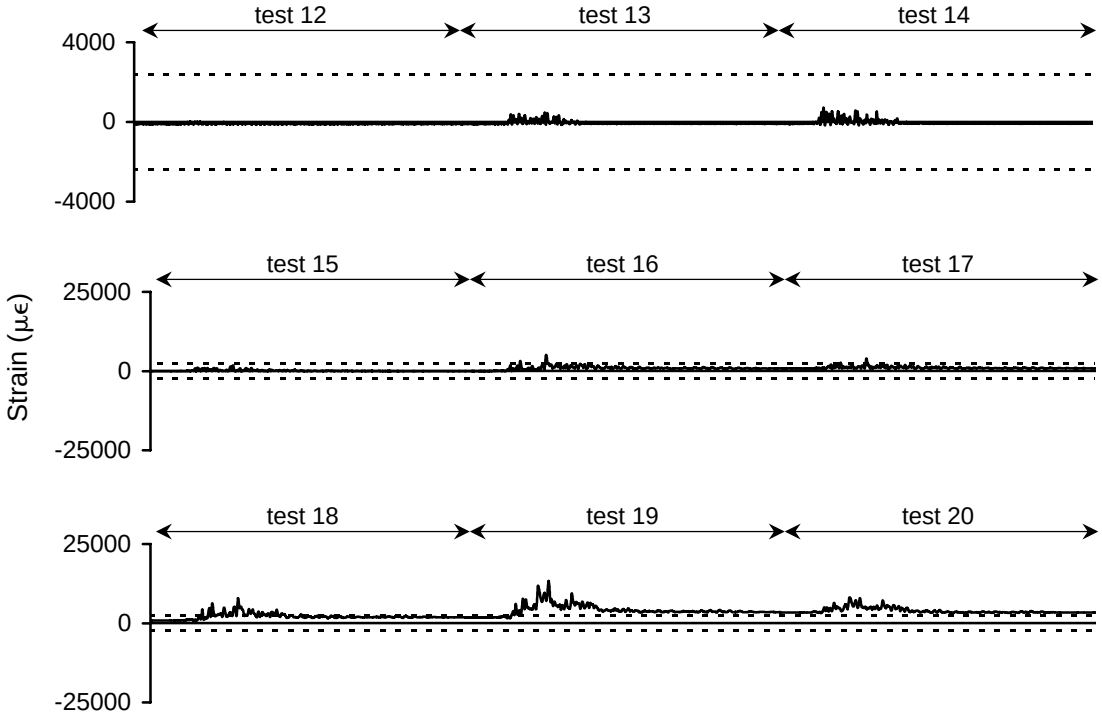

Figure A-46 Strain history for 2WBSL3 during high amplitude testing

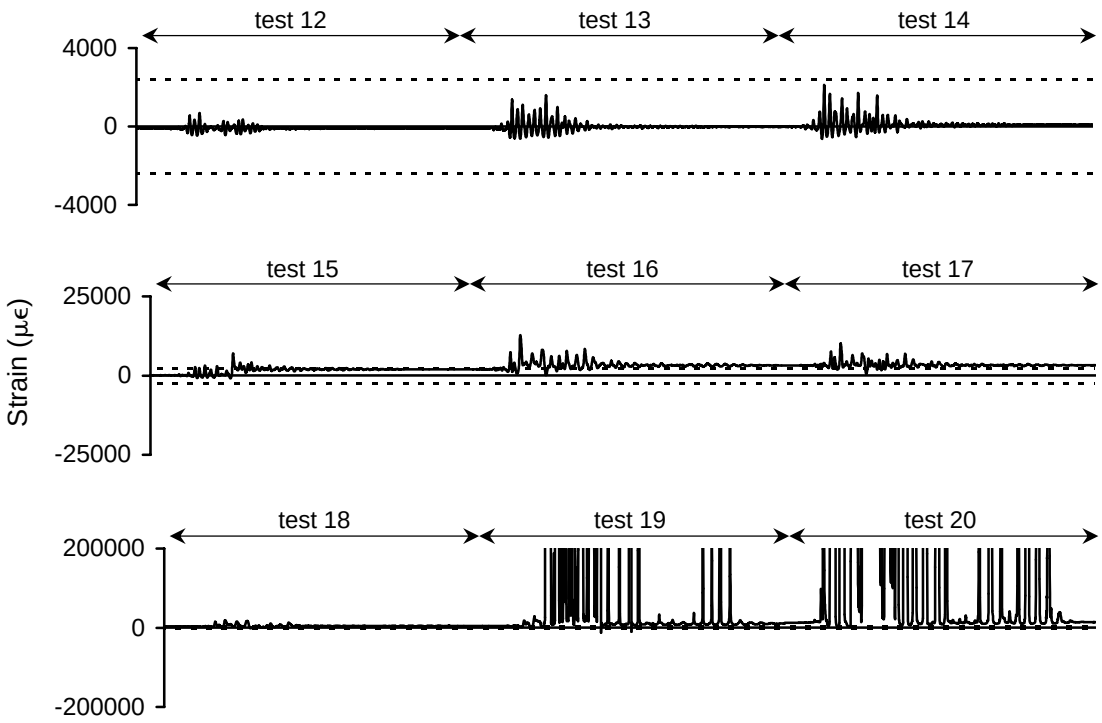

Figure A-47 Strain history for 2WBSL5 during high amplitude testing

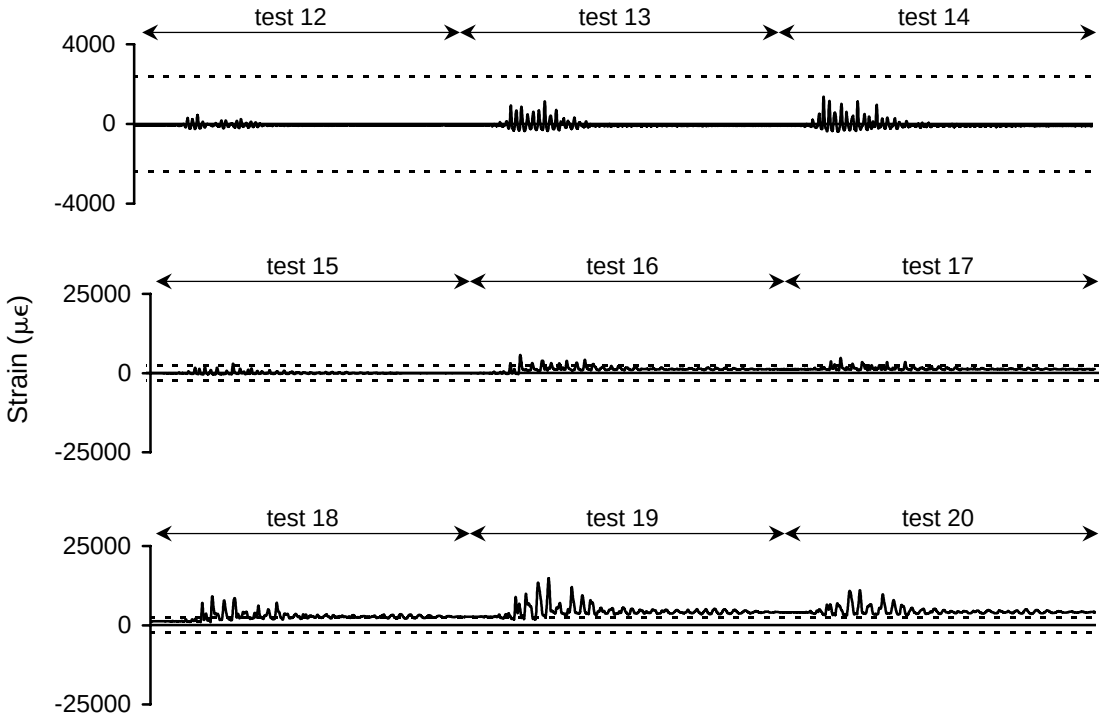

Figure A-48 Strain history for 2WBSL7 during high amplitude testing

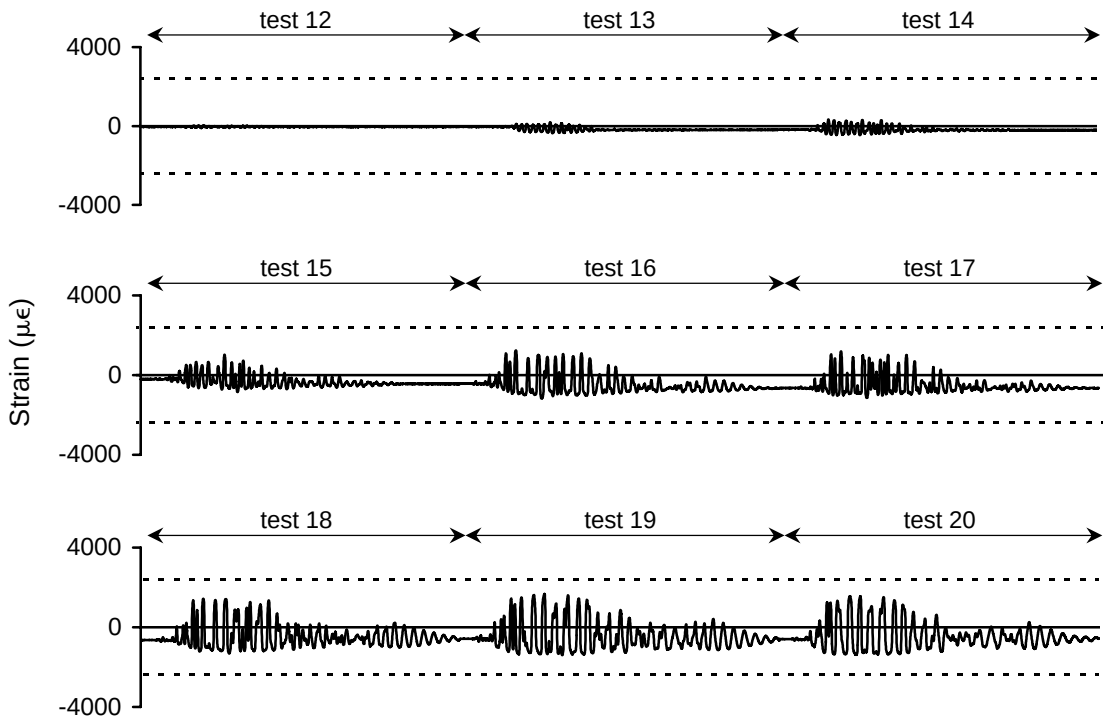

Figure A-49 Strain history for 2WBSL9 during high amplitude testing

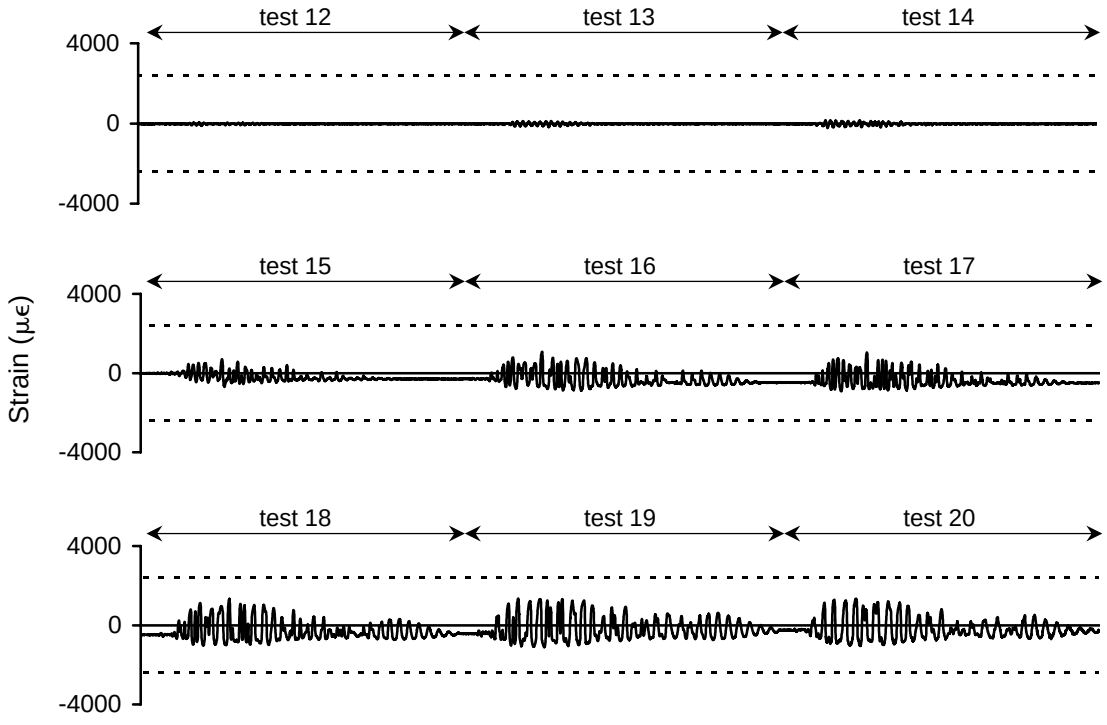

Figure A-50 Strain history for 2WBSL10 during high amplitude testing

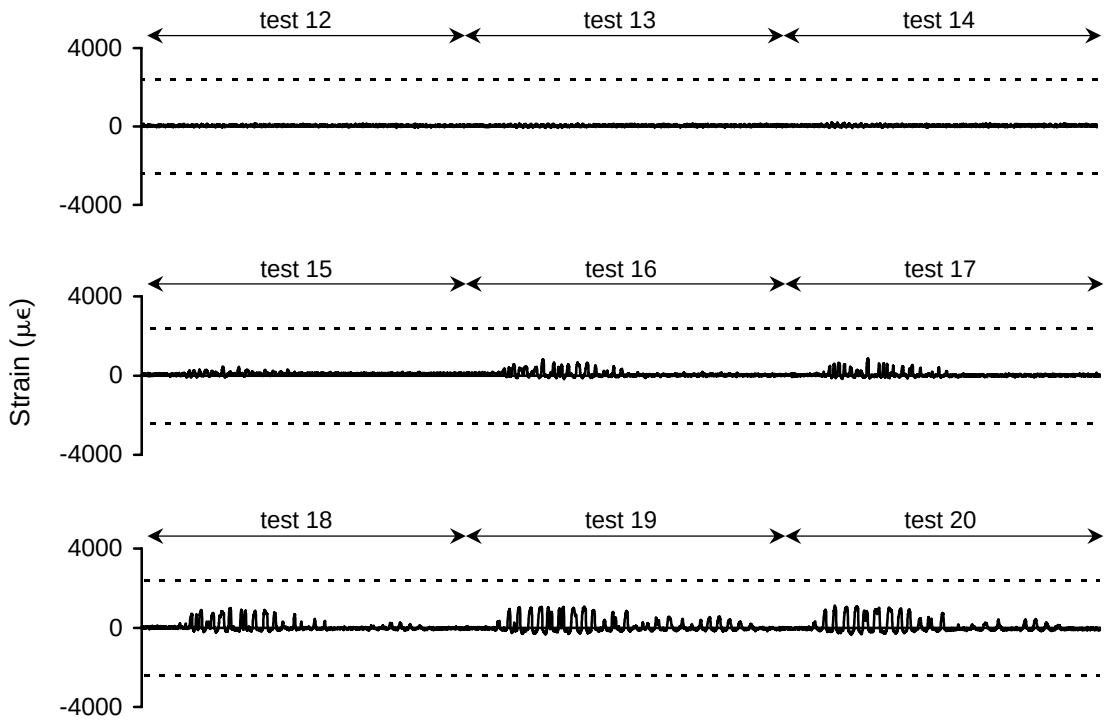

Figure A-51 Strain history for 2ETSL1 during high amplitude testing

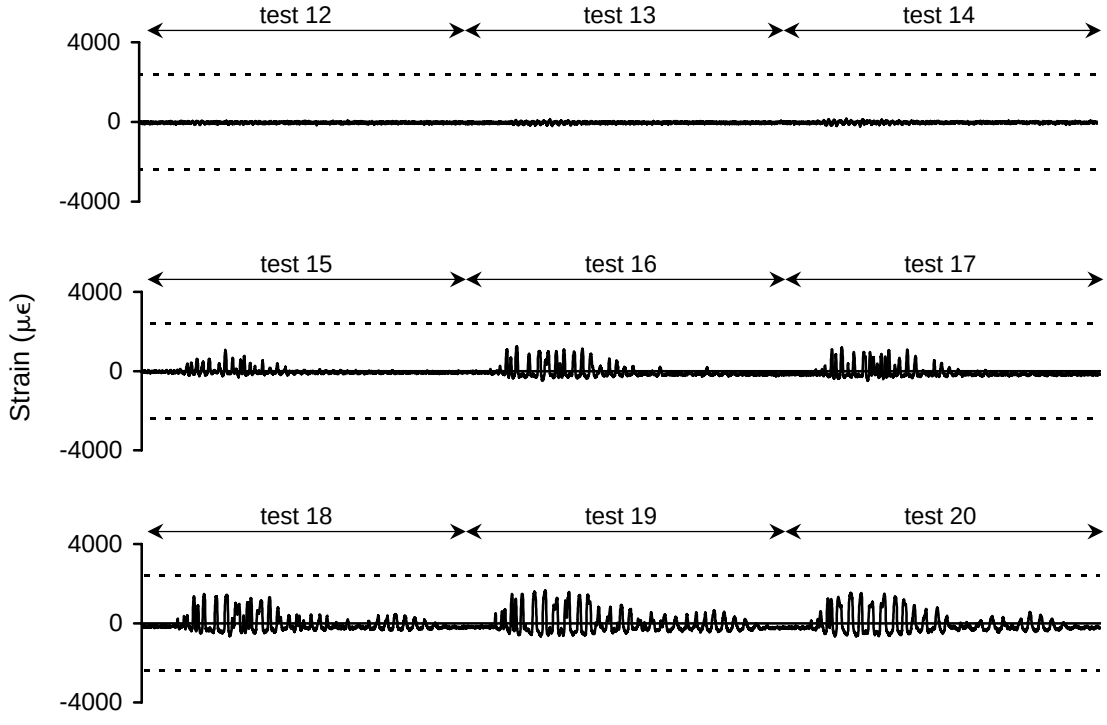

Figure A-52 Strain history for 2ETSL2 during high amplitude testing

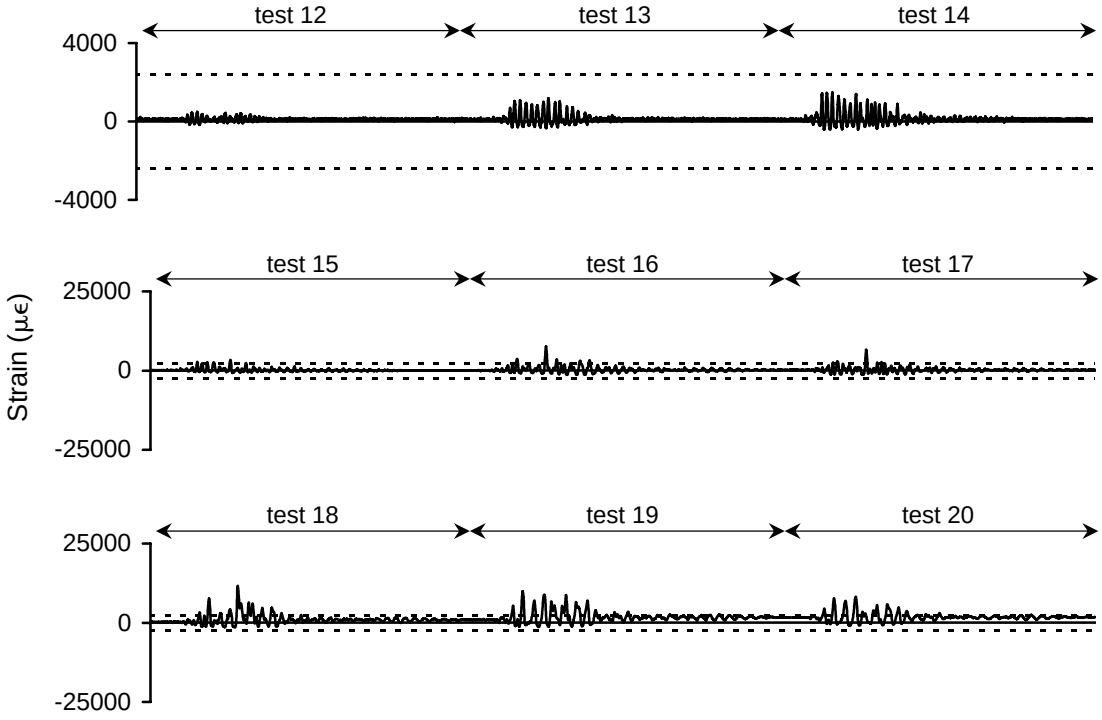

Figure A-53 Strain history for 2ETSL3 during high amplitude testing

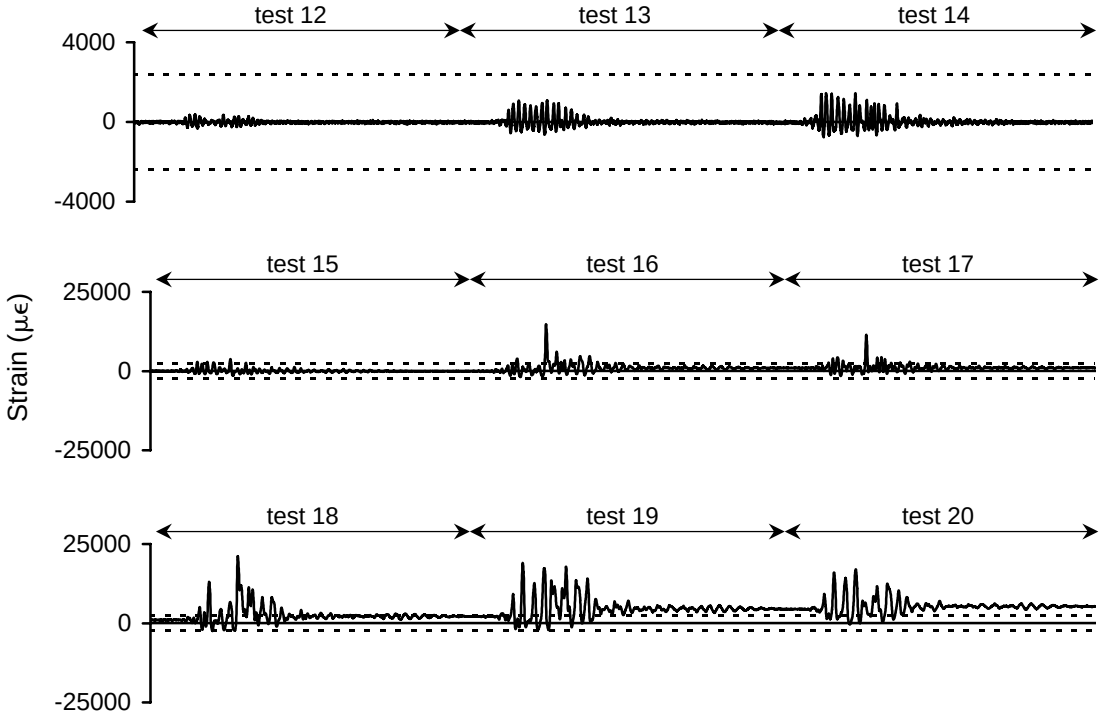

Figure A-54 Strain history for 2ETSL4 during high amplitude testing

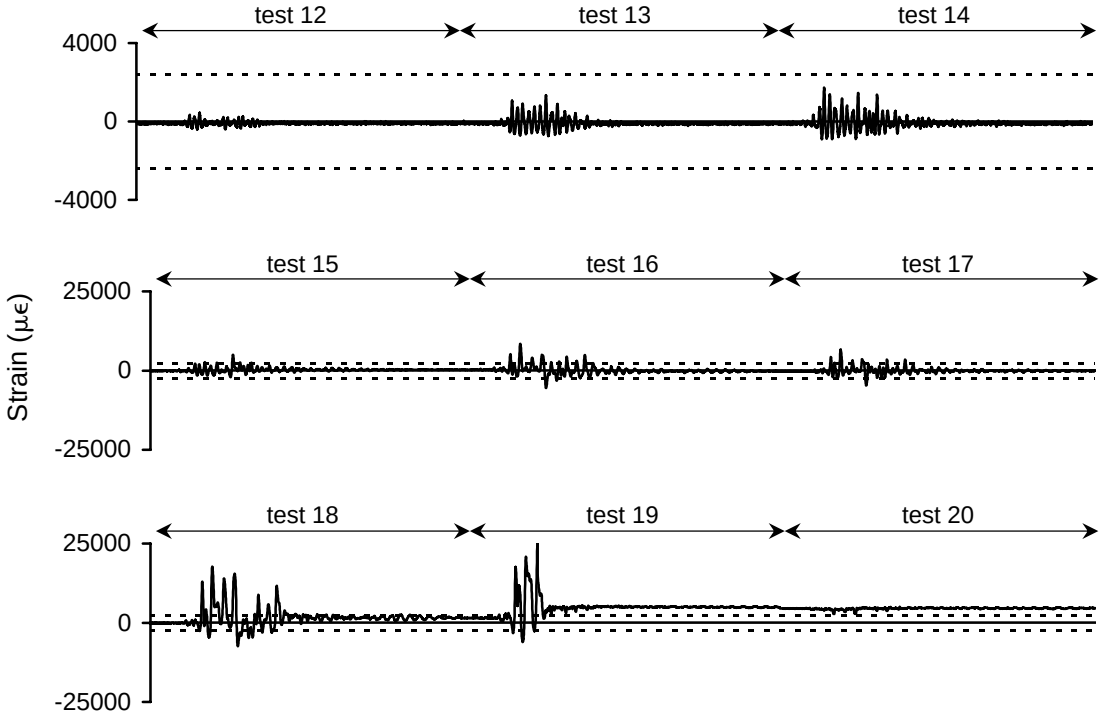

Figure A-55 Strain history for 2ETSL5 during high amplitude testing

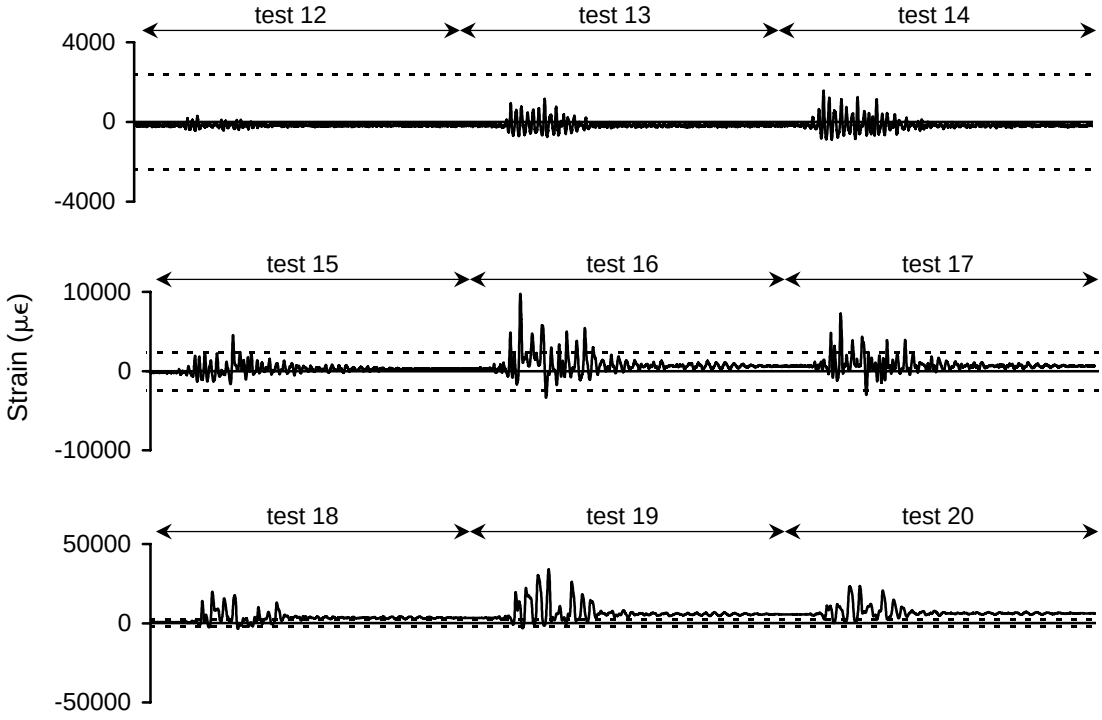

Figure A-56 Strain history for 2ETSL6 during high amplitude testing

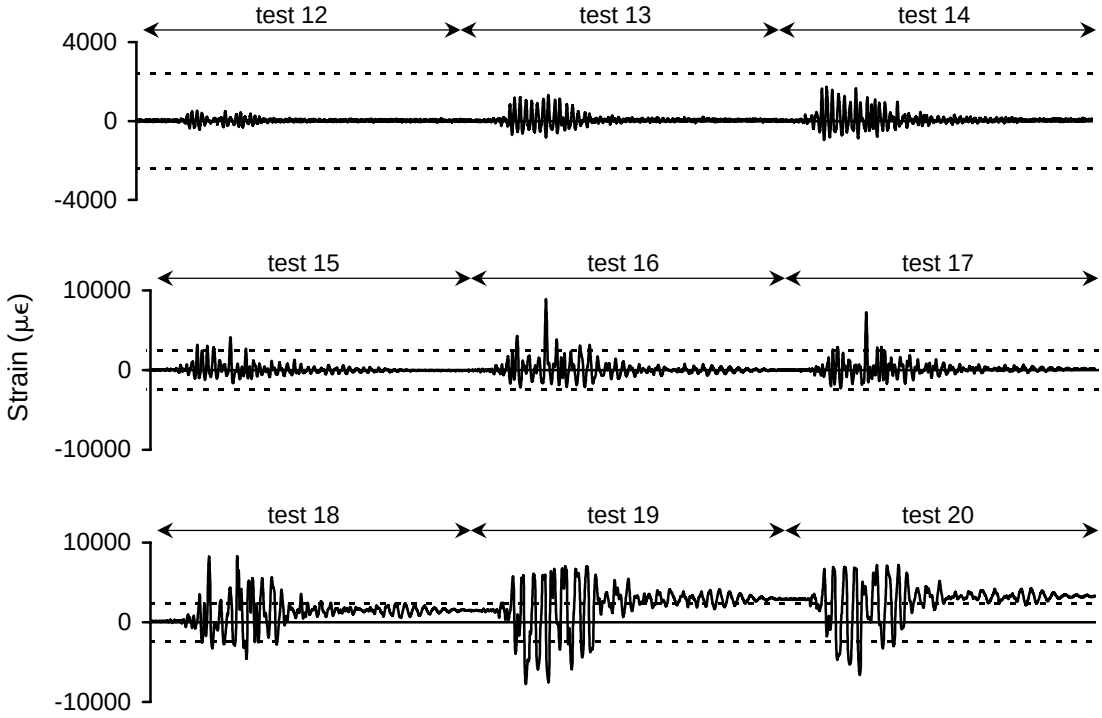

Figure A-57 Strain history for 2ETSL7 during high amplitude testing

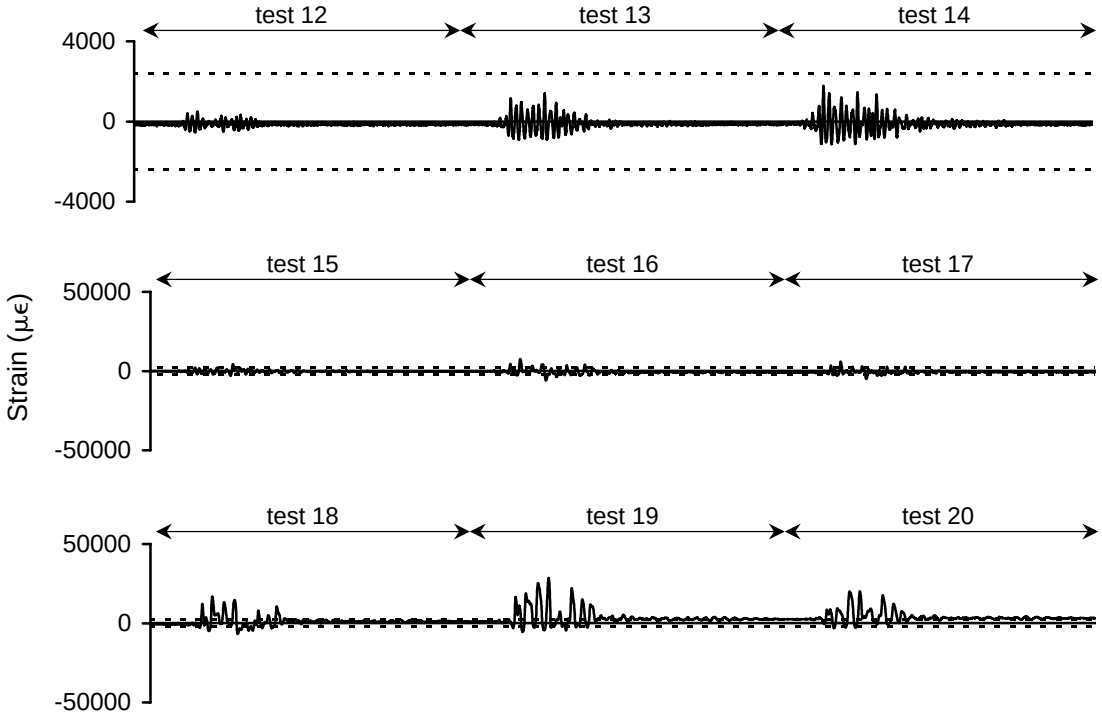

Figure A-58 Strain history for 2ETSL8 during high amplitude testing

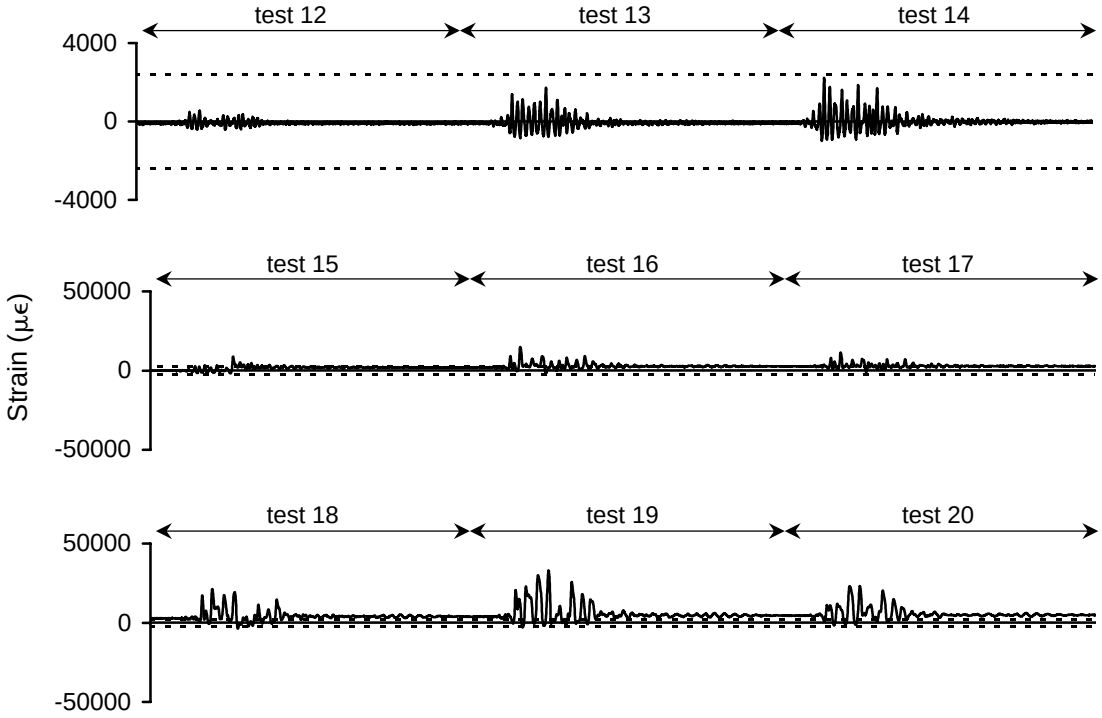

Figure A-59 Strain history for 2EBSL1 during high amplitude testing

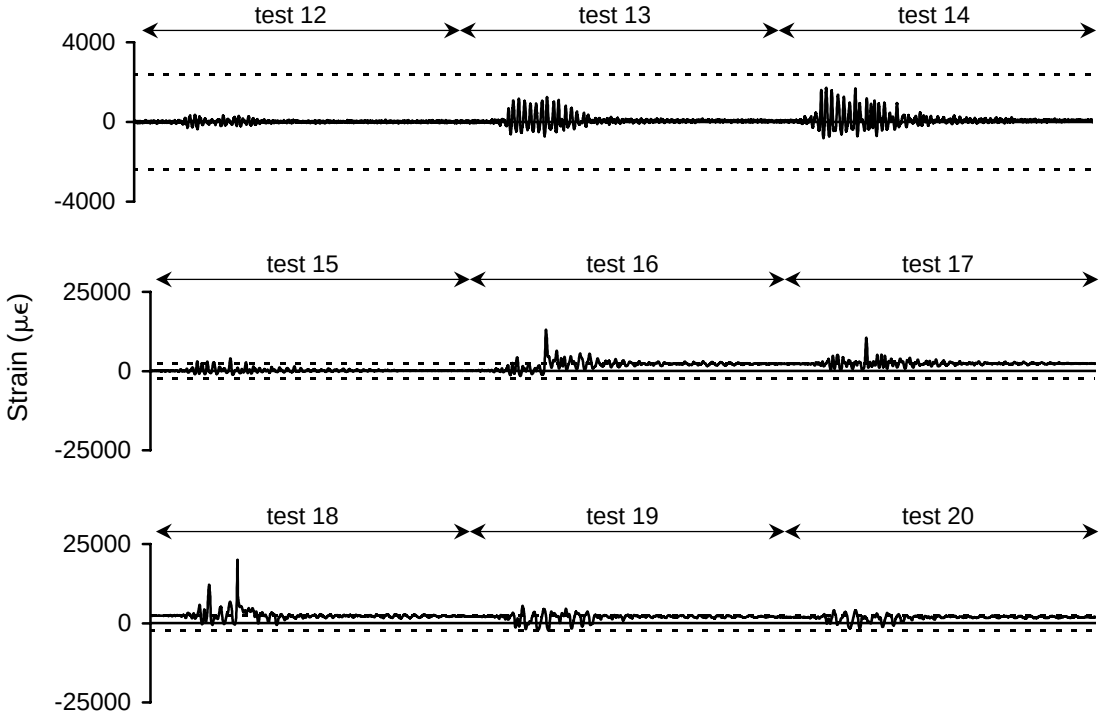

Figure A-60 Strain history for 2EBSL2 during high amplitude testing

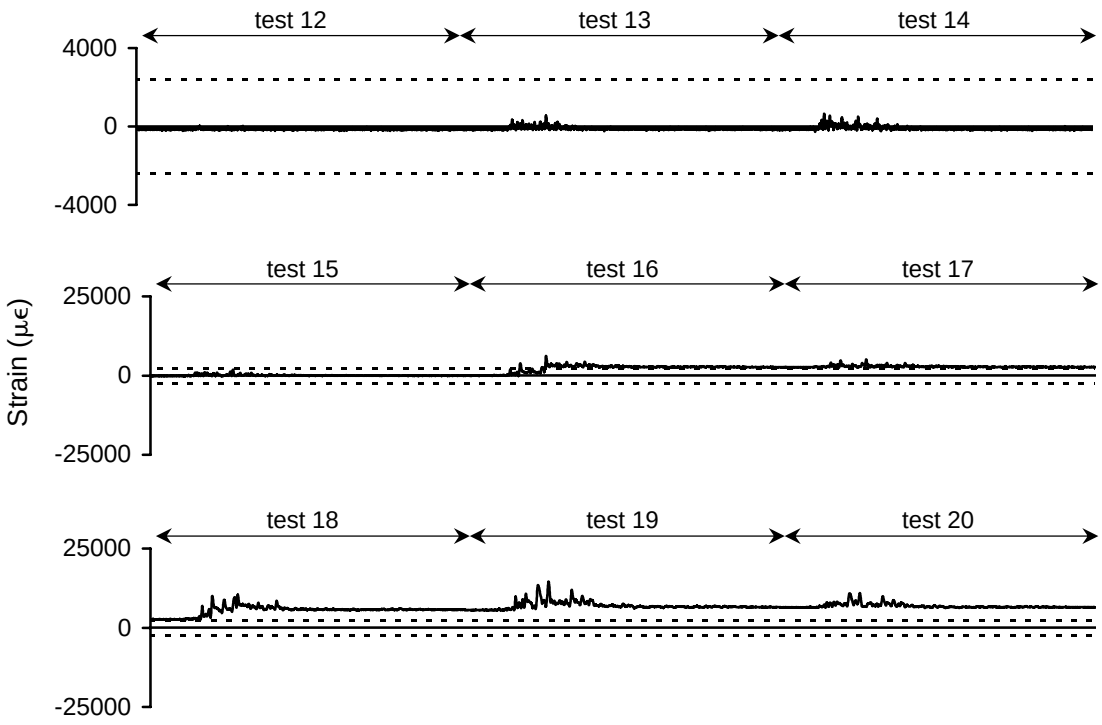

Figure A-61 Strain history for 2EBSL3 during high amplitude testing

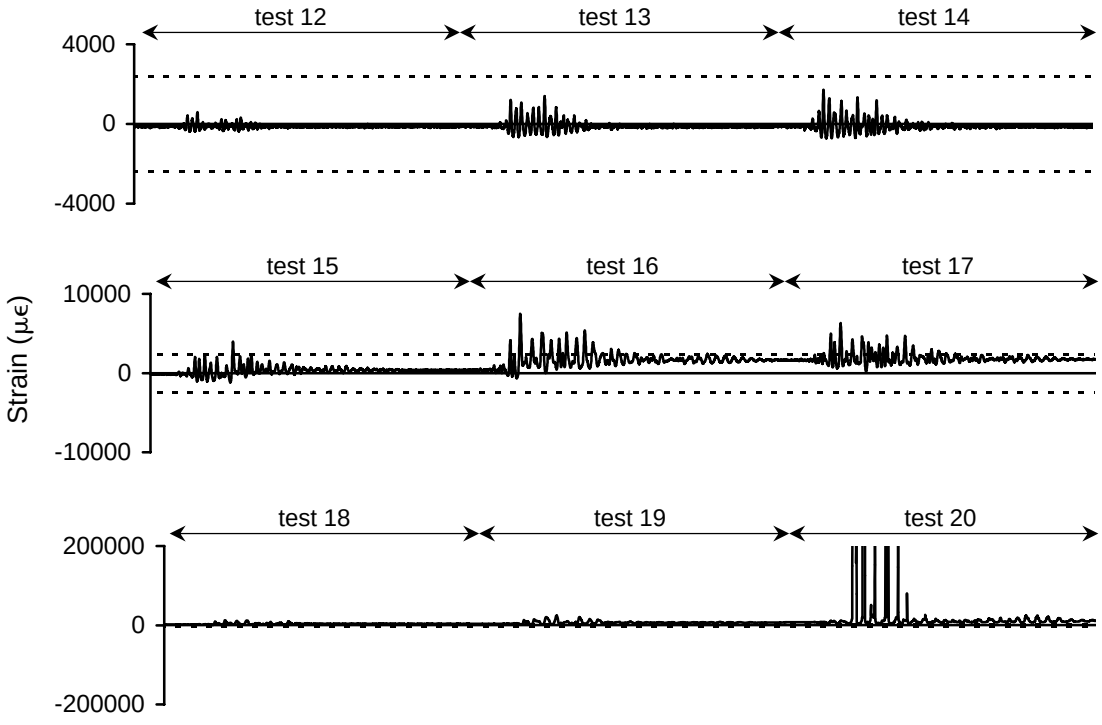

Figure A-62 Strain history for 2EBSL4 during high amplitude testing

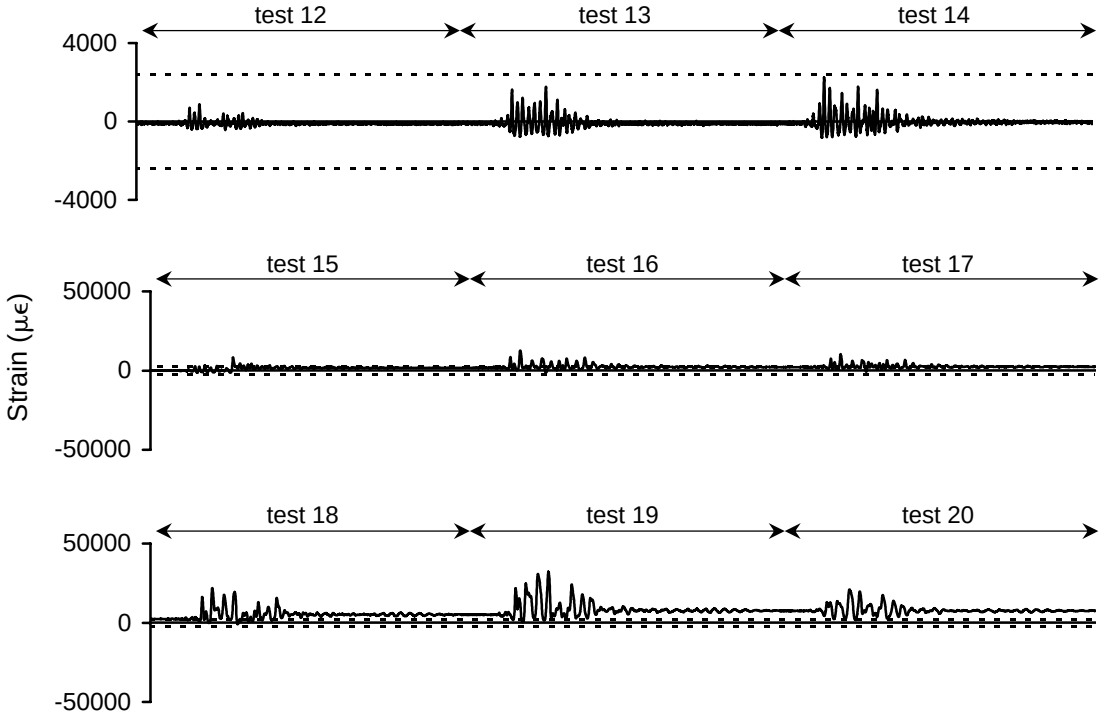

Figure A-63 Strain history for 2EBSL5 during high amplitude testing

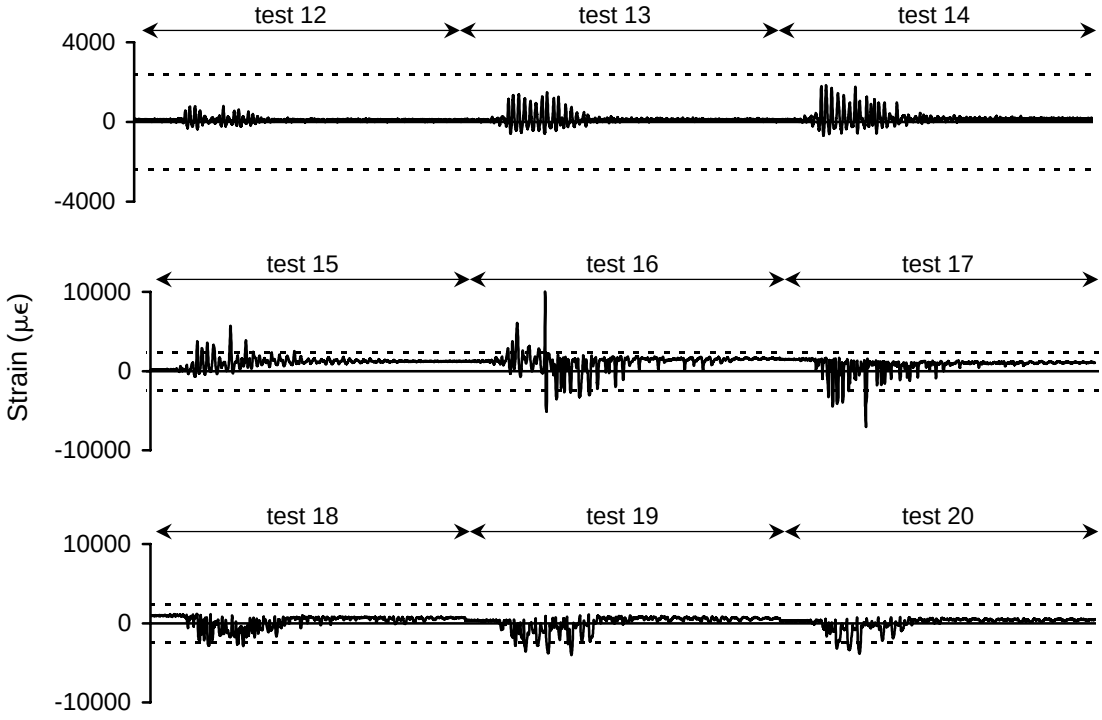

Figure A-64 Strain history for 2EBSL6 during high amplitude testing

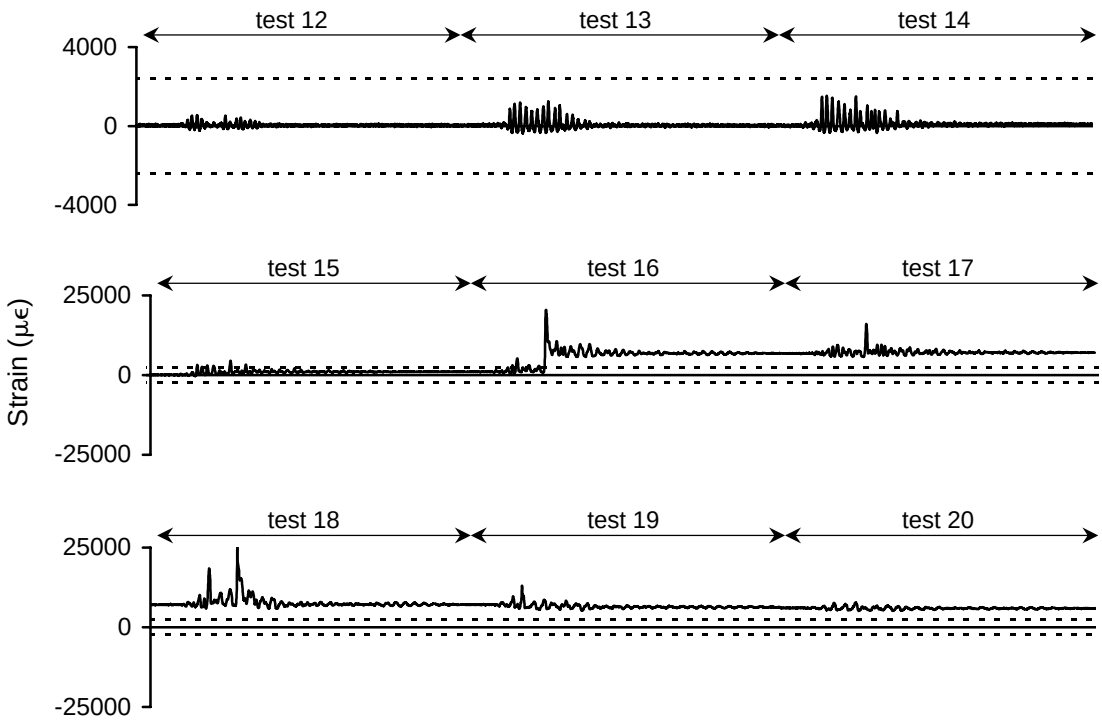

Figure A-65 Strain history for 2EBSL7 during high amplitude testing

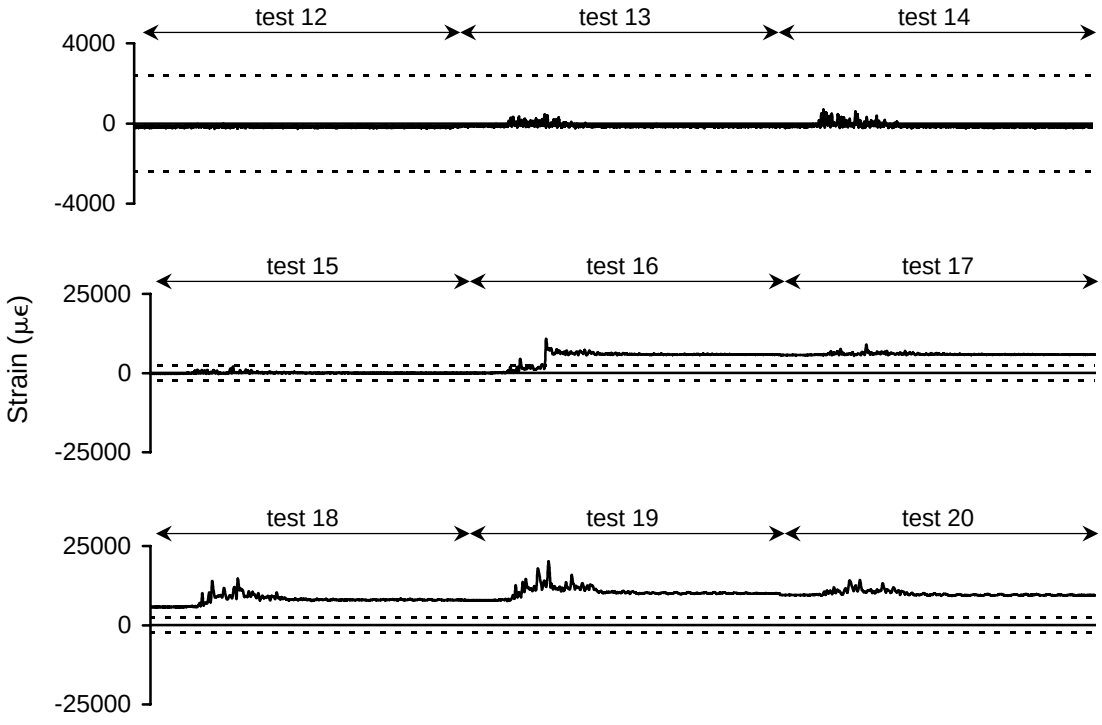

Figure A-66 Strain history for 2EBSL8 during high amplitude testing

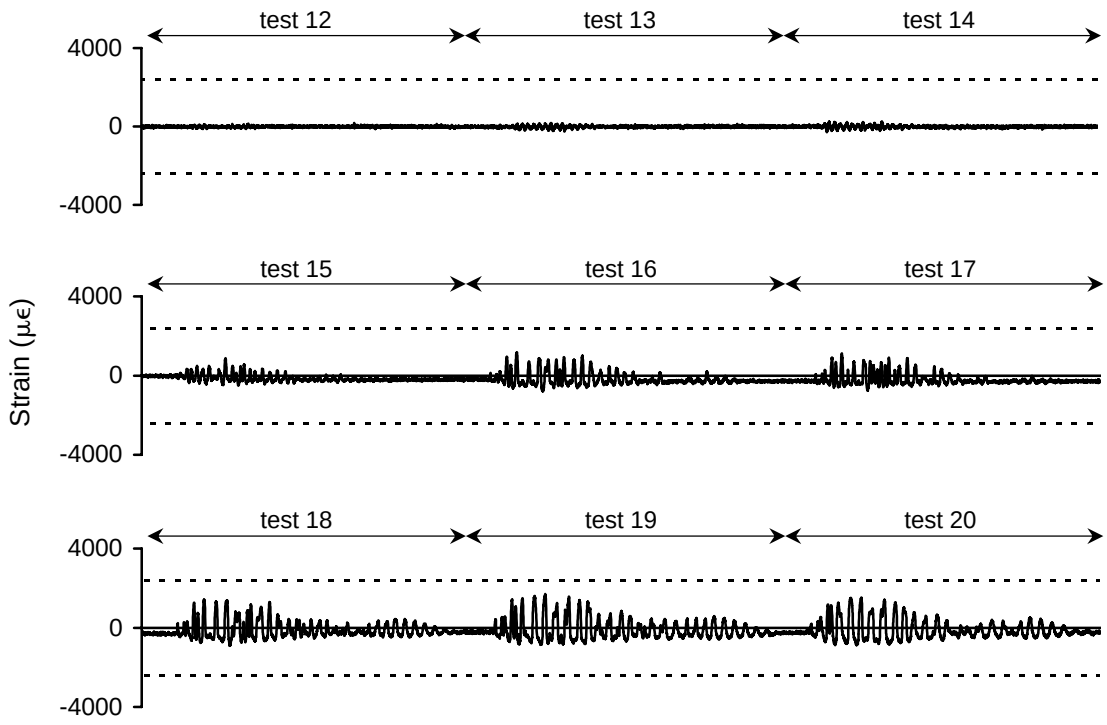

Figure A-67 Strain history for 2EBSL9 during high amplitude testing

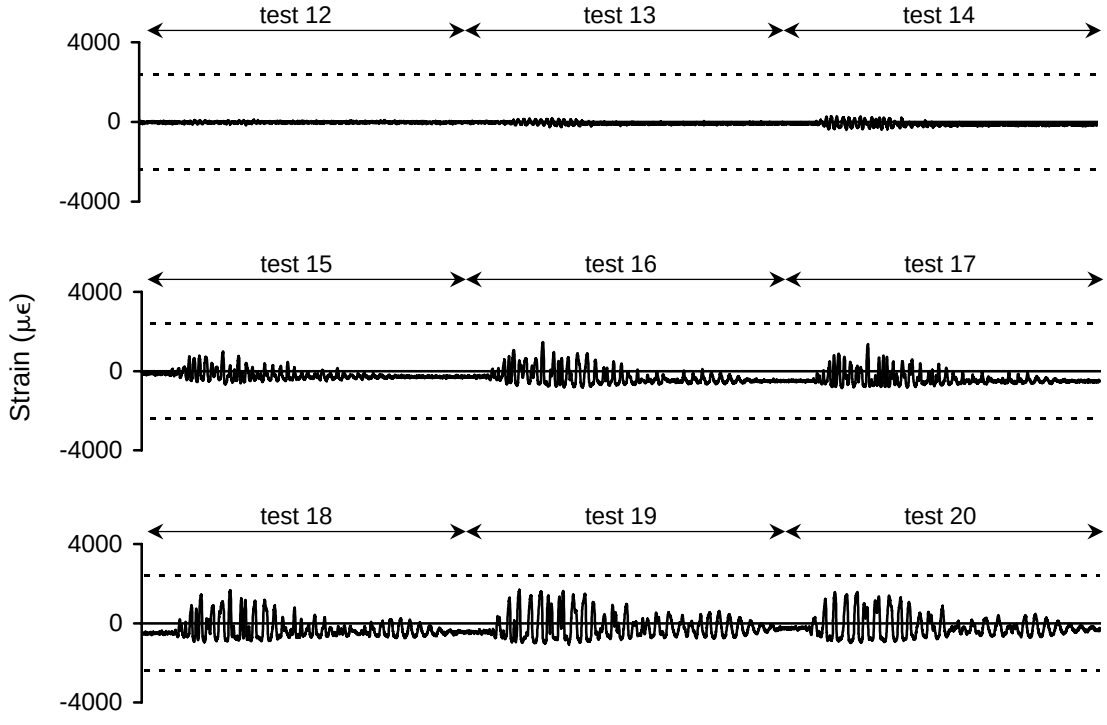

Figure A-68 Strain history for 2EBSL10 during high amplitude testing

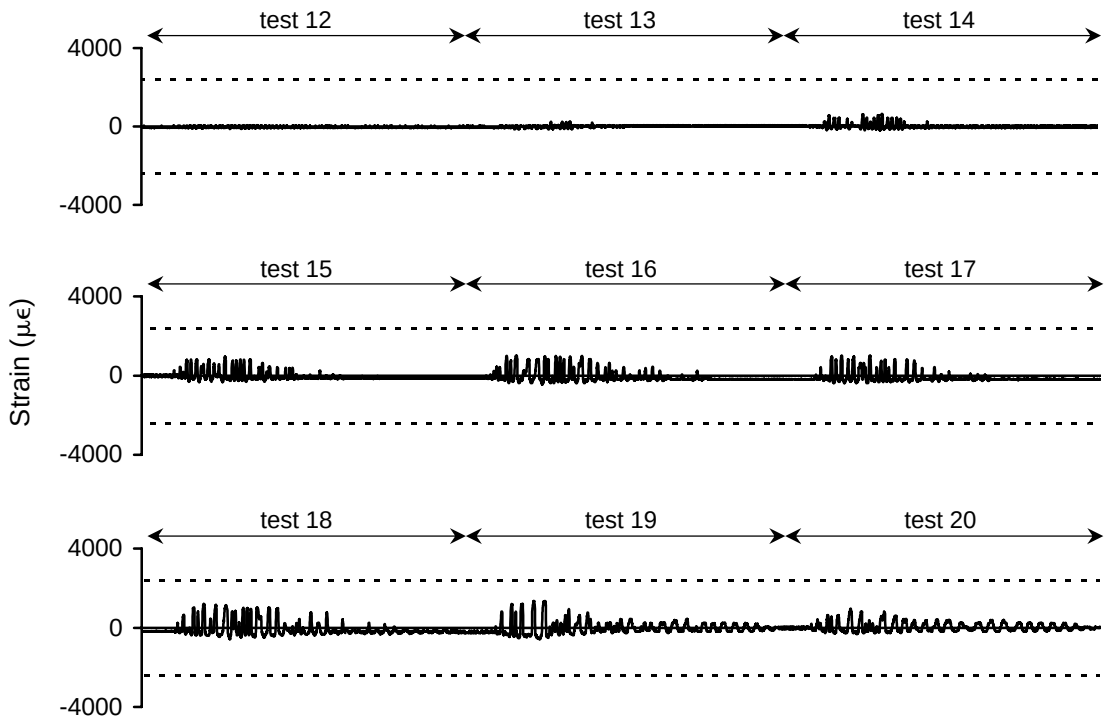

Figure A-69 Strain history for 3WTSL1 during high amplitude testing

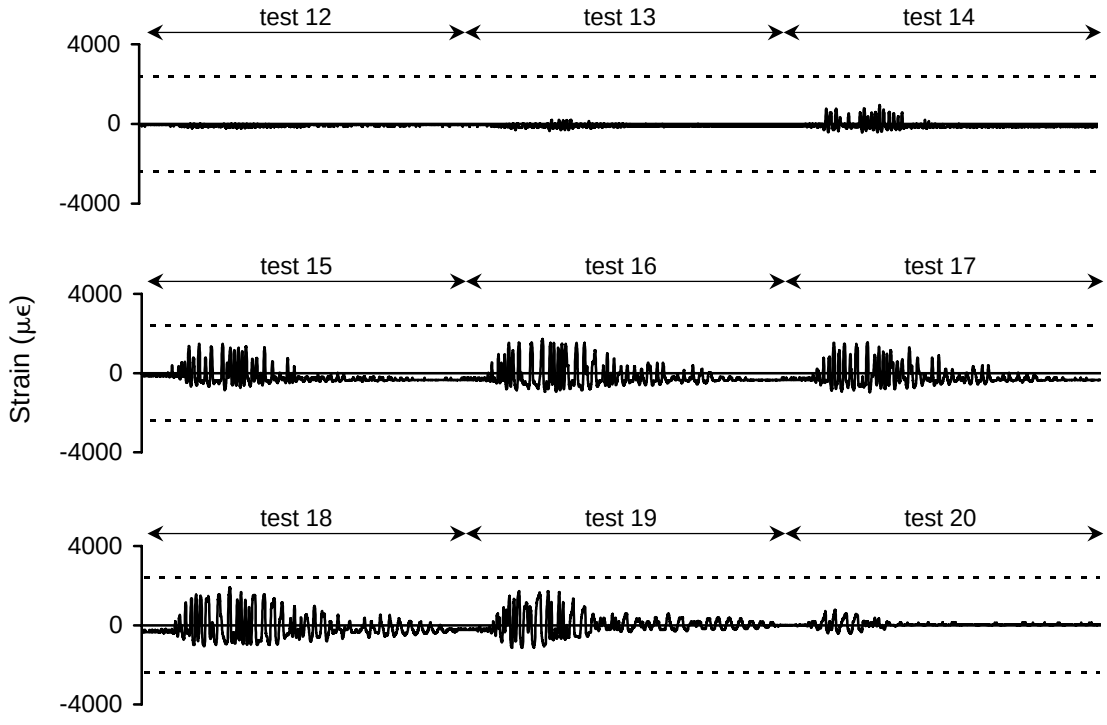

Figure A-70 Strain history for 3WTSL2 during high amplitude testing

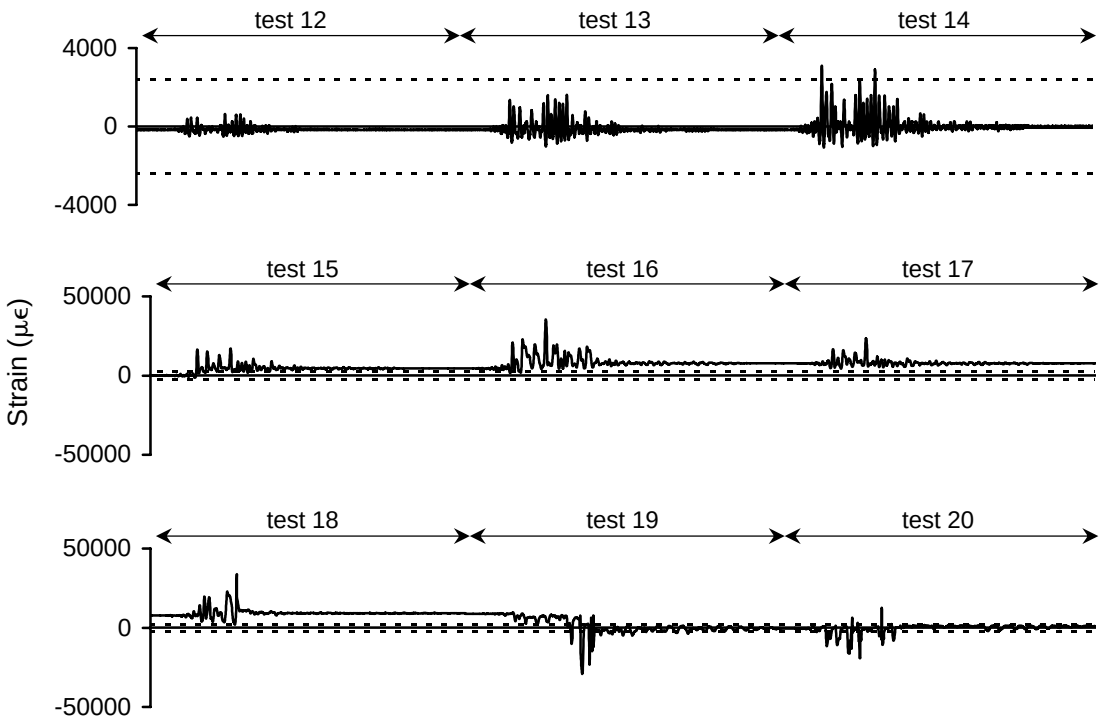

Figure A-71 Strain history for 3WTSL3 during high amplitude testing

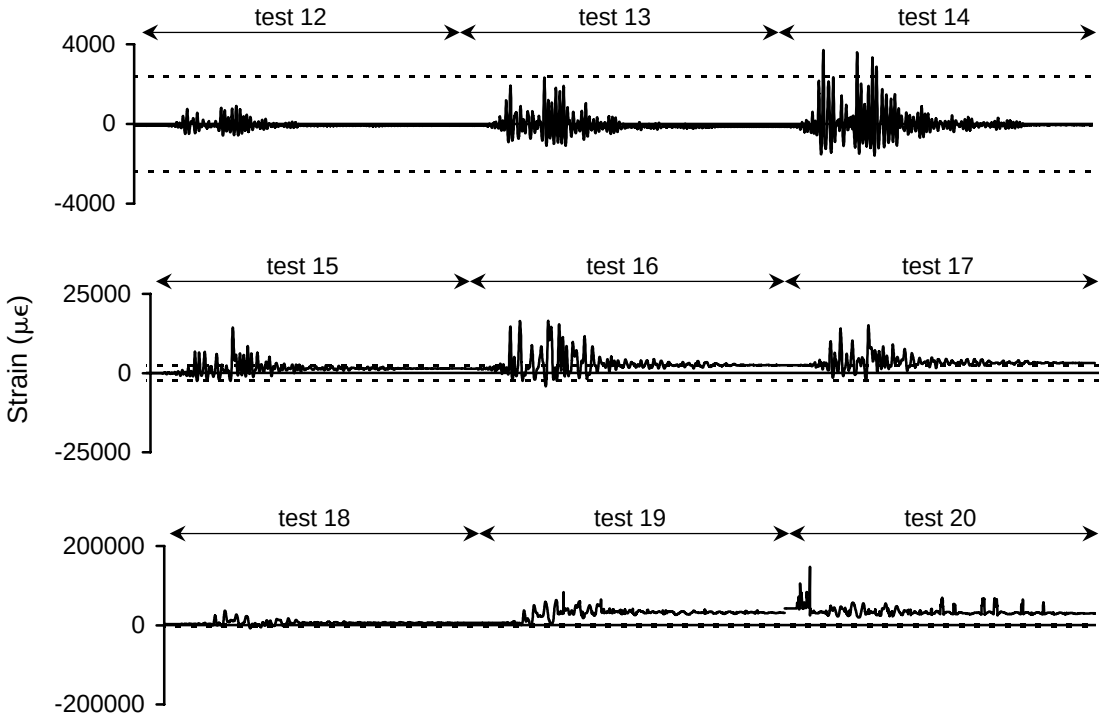

Figure A-72 Strain history for 3WTSL4 during high amplitude testing

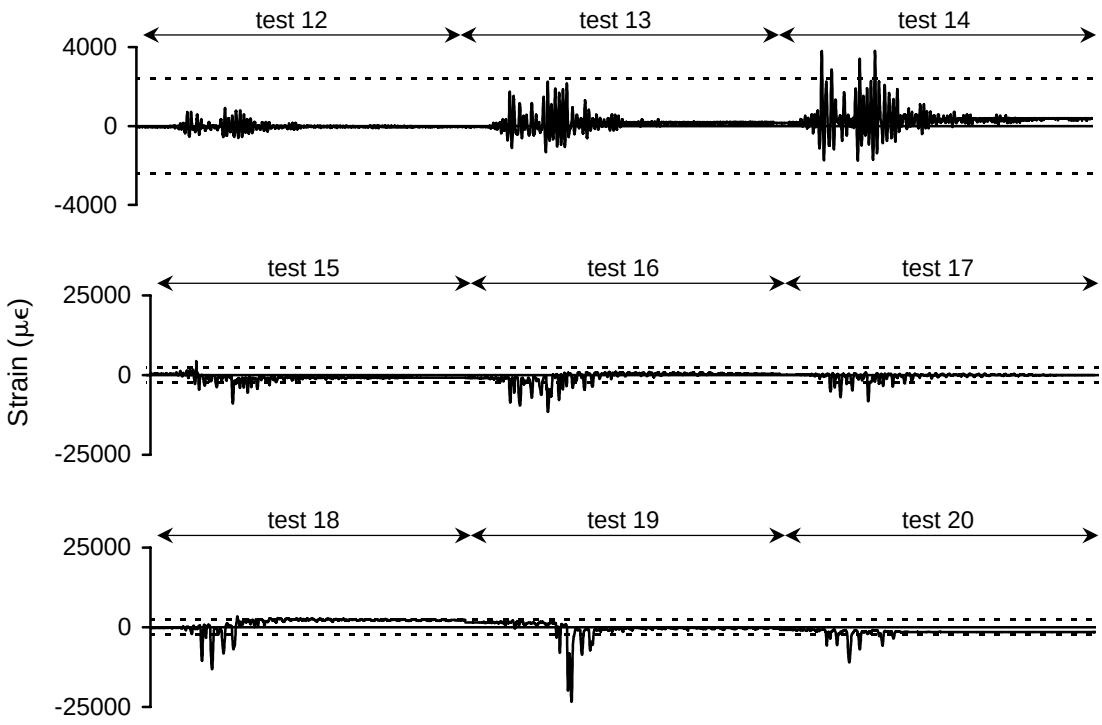

Figure A-73 Strain history for 3WTSL5 during high amplitude testing

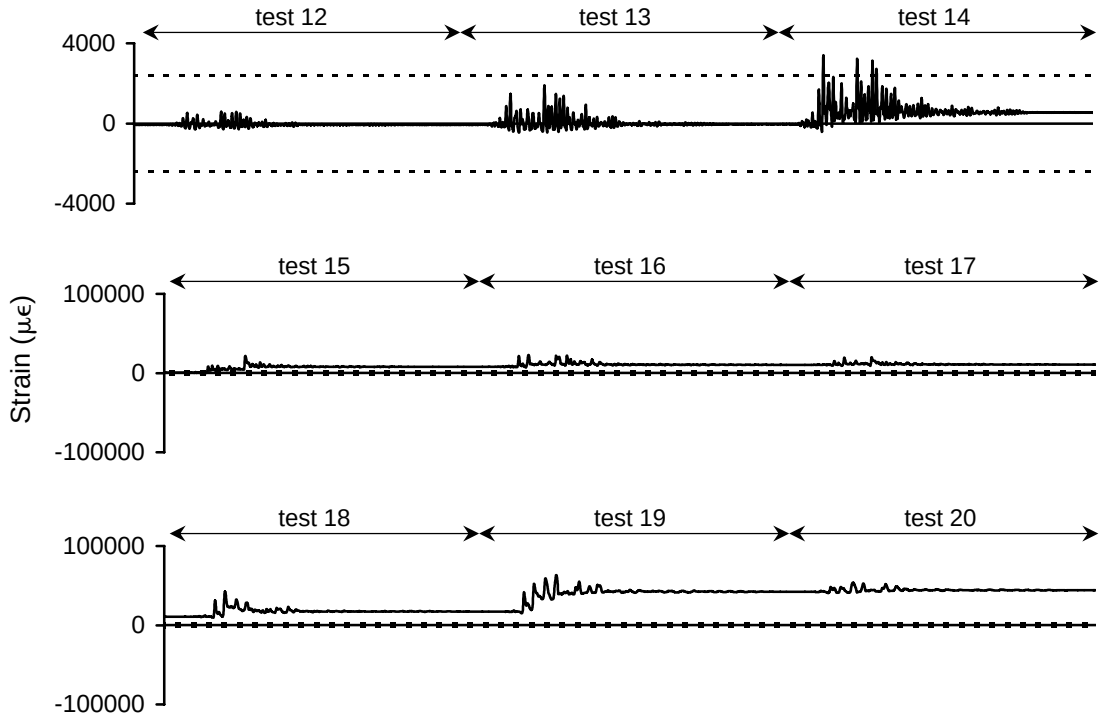

Figure A-74 Strain history for 3WTSL6 during high amplitude testing

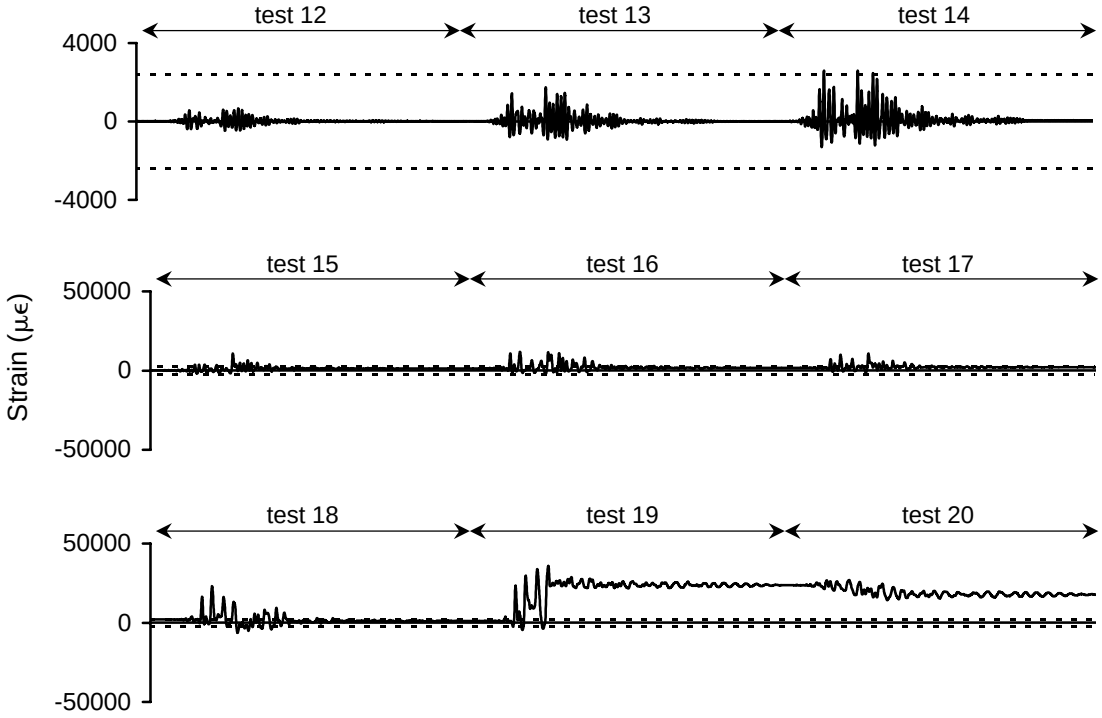

Figure A-75 Strain history for 3WTSL7 during high amplitude testing

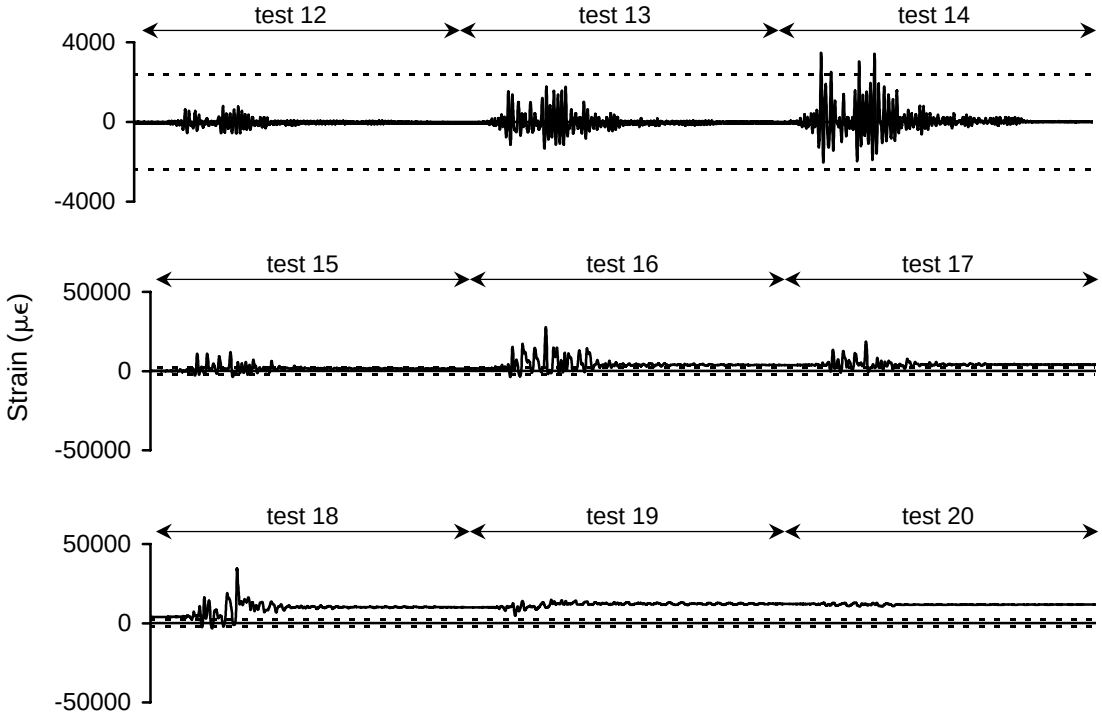

Figure A-76 Strain history for 3WTSL8 during high amplitude testing

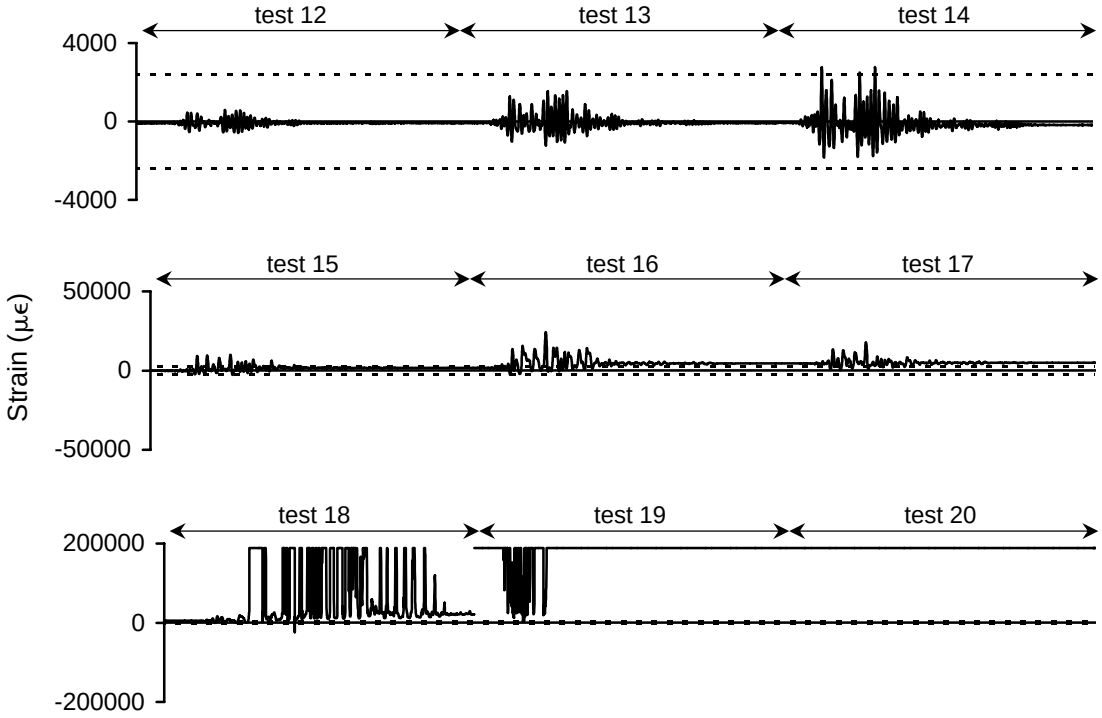

Figure A-77 Strain history for 3WBSL1 during high amplitude testing

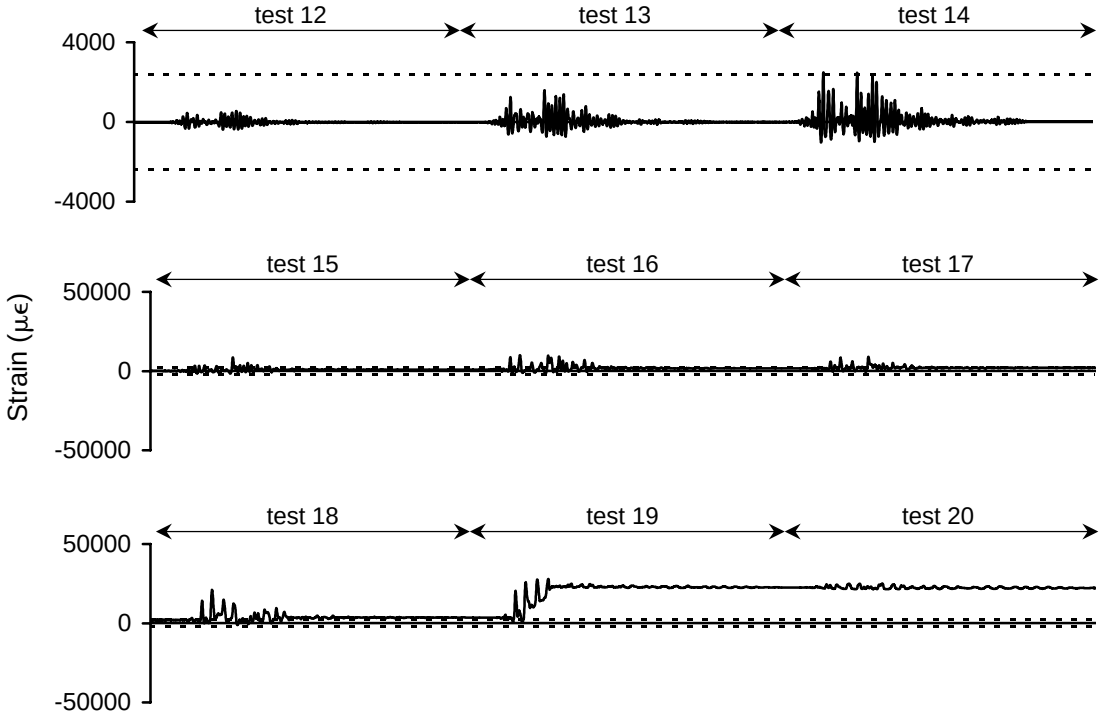

Figure A-78 Strain history for 3WBSL2 during high amplitude testing

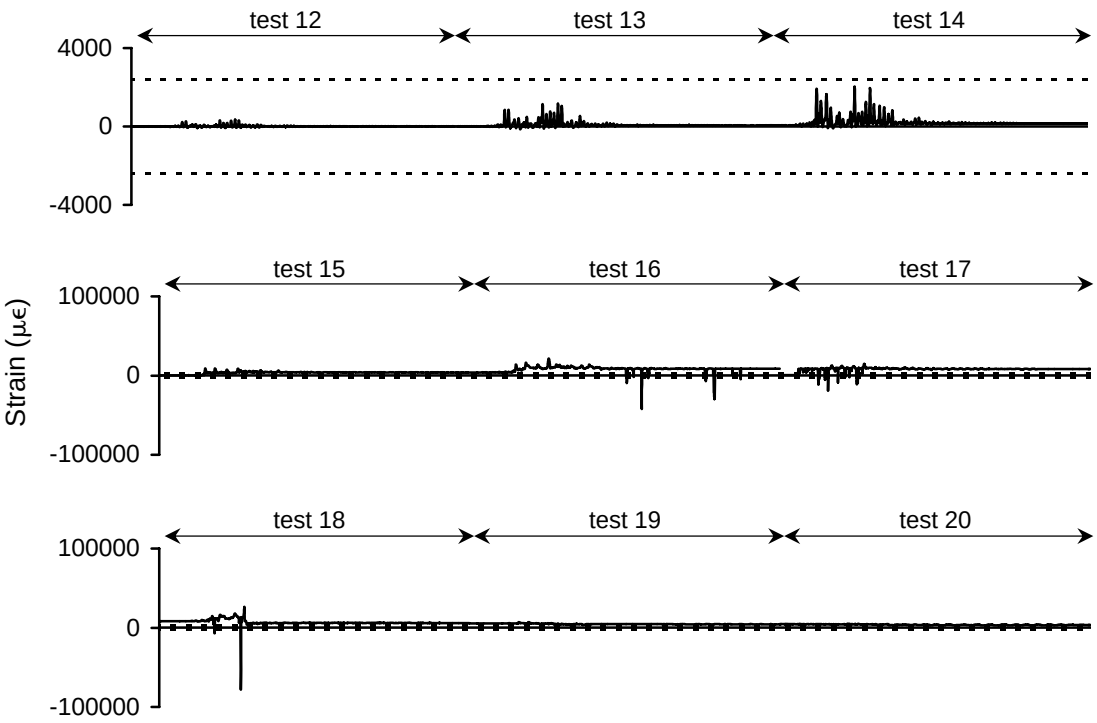

Figure A-79 Strain history for 3WBSL3 during high amplitude testing

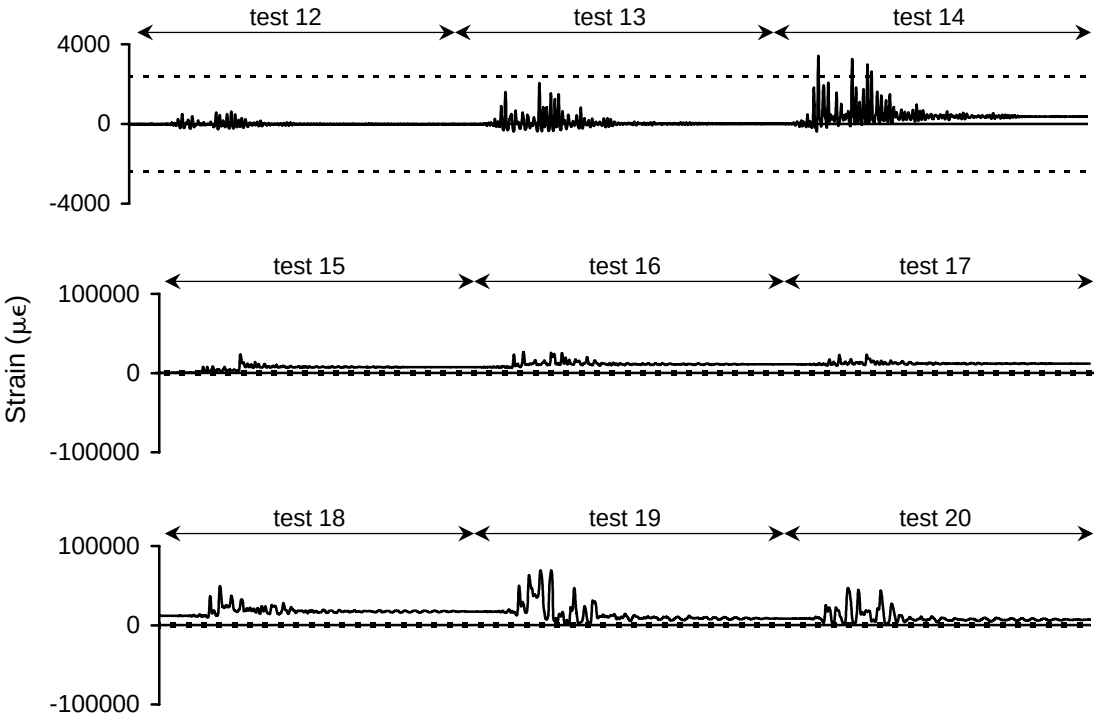

Figure A-80 Strain history for 3WBSL4 during high amplitude testing

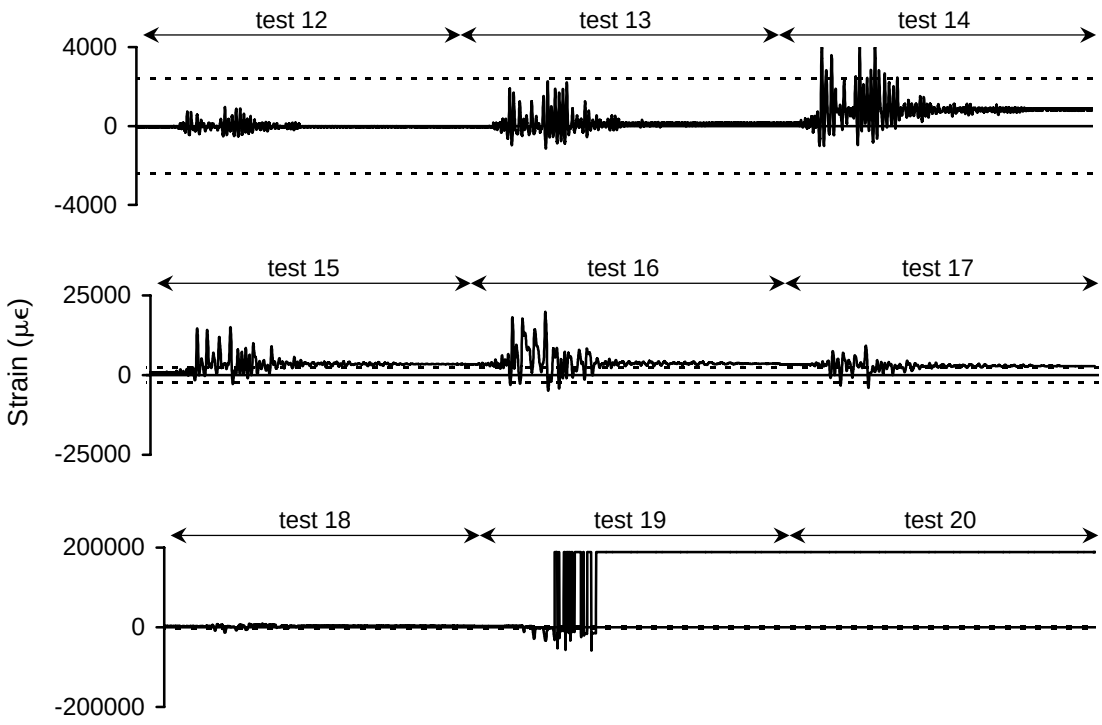

Figure A-80 Strain history for 3WBSL5 during high amplitude testing

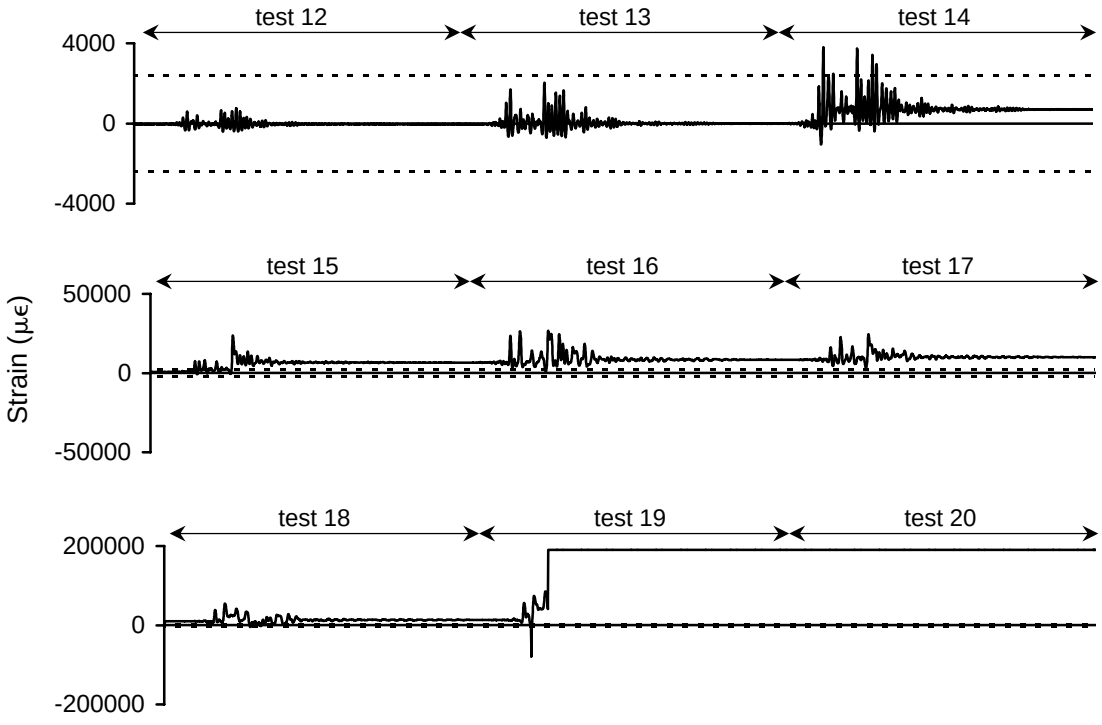

Figure A-81 Strain history for 3WBSL6 during high amplitude testing

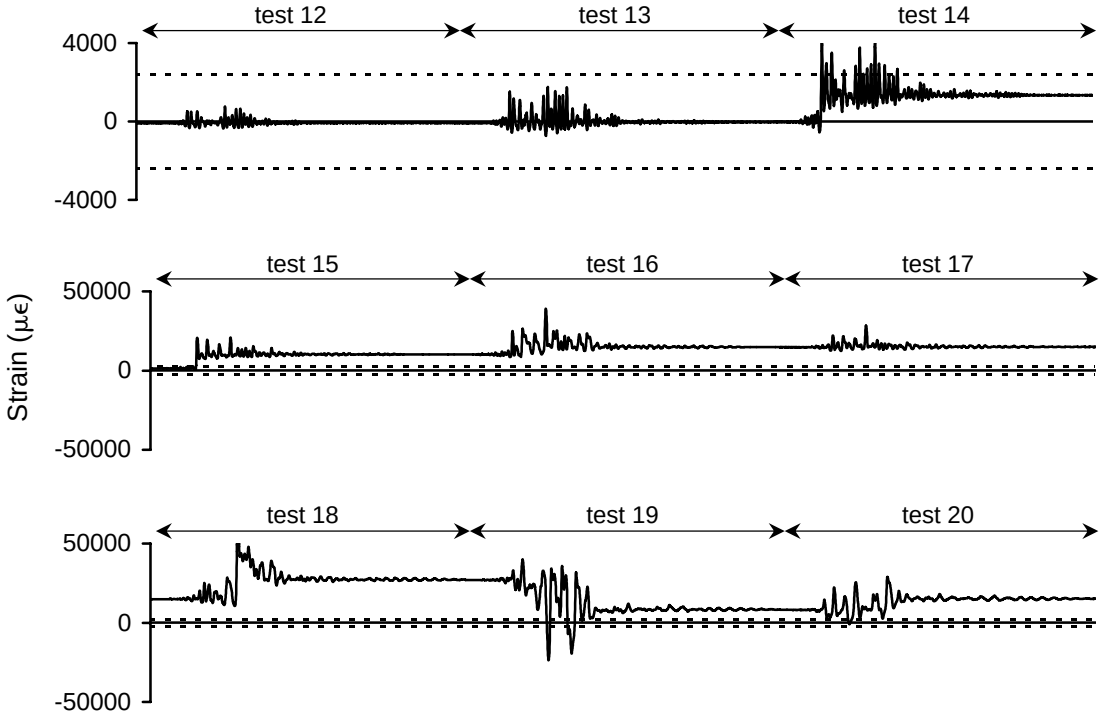

Figure A-82 Strain history for 3WBSL7 during high amplitude testing

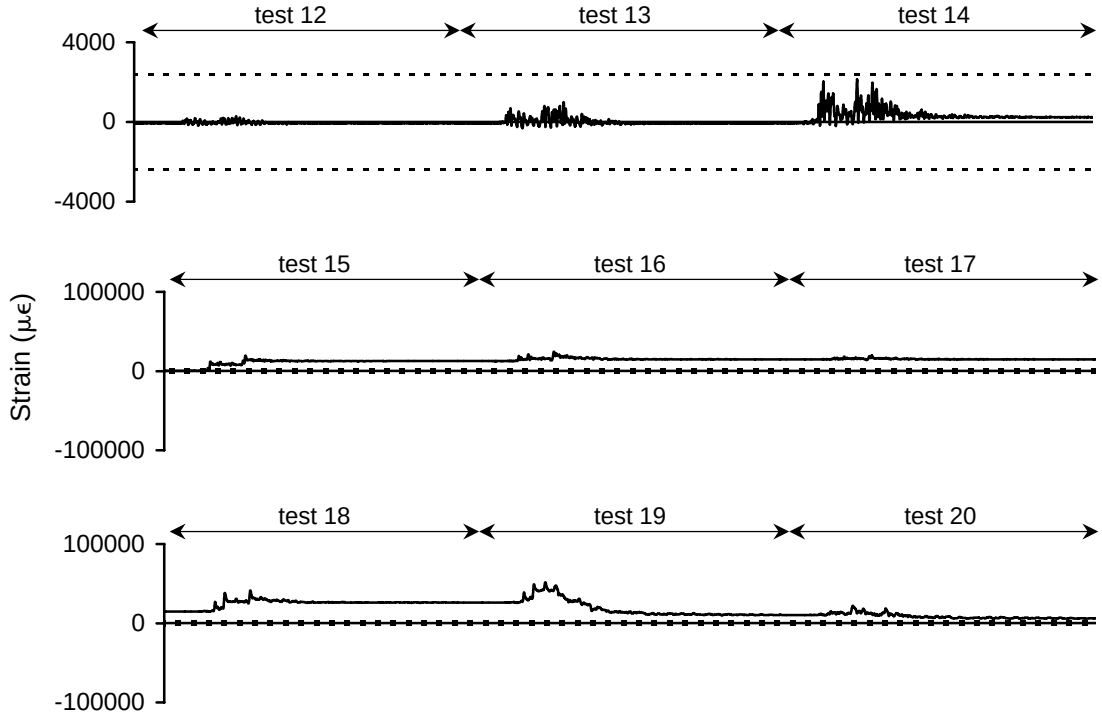

Figure A-83 Strain history for 3WBSL8 during high amplitude testing

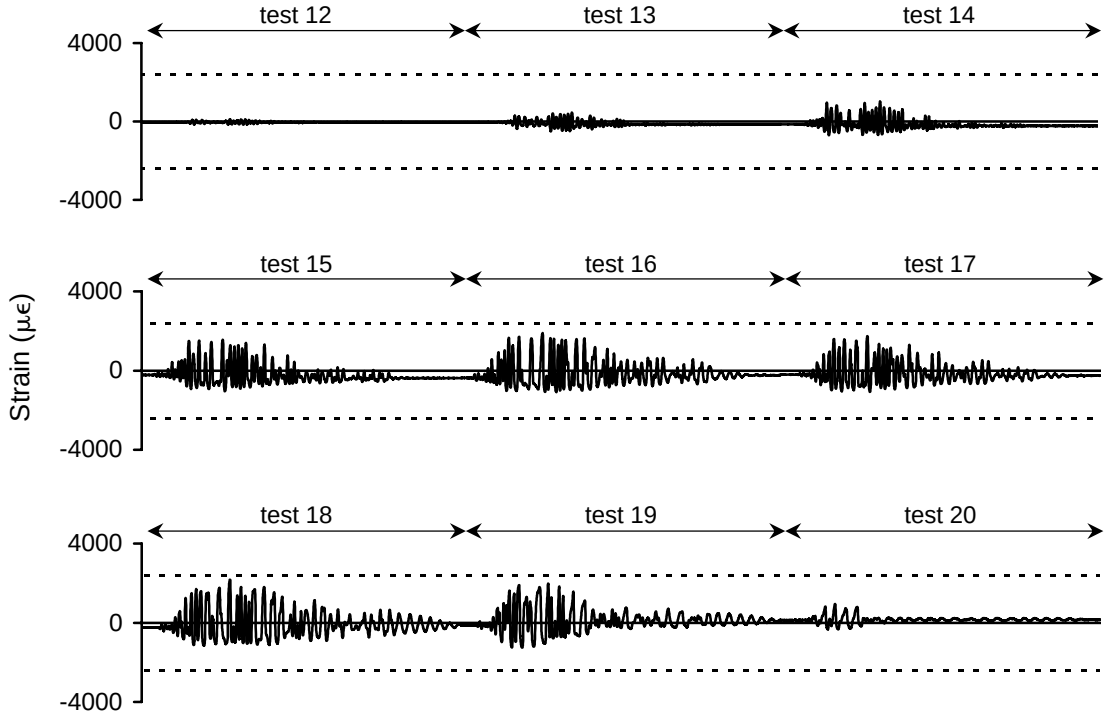

Figure A-84 Strain history for 3WBSL9 during high amplitude testing

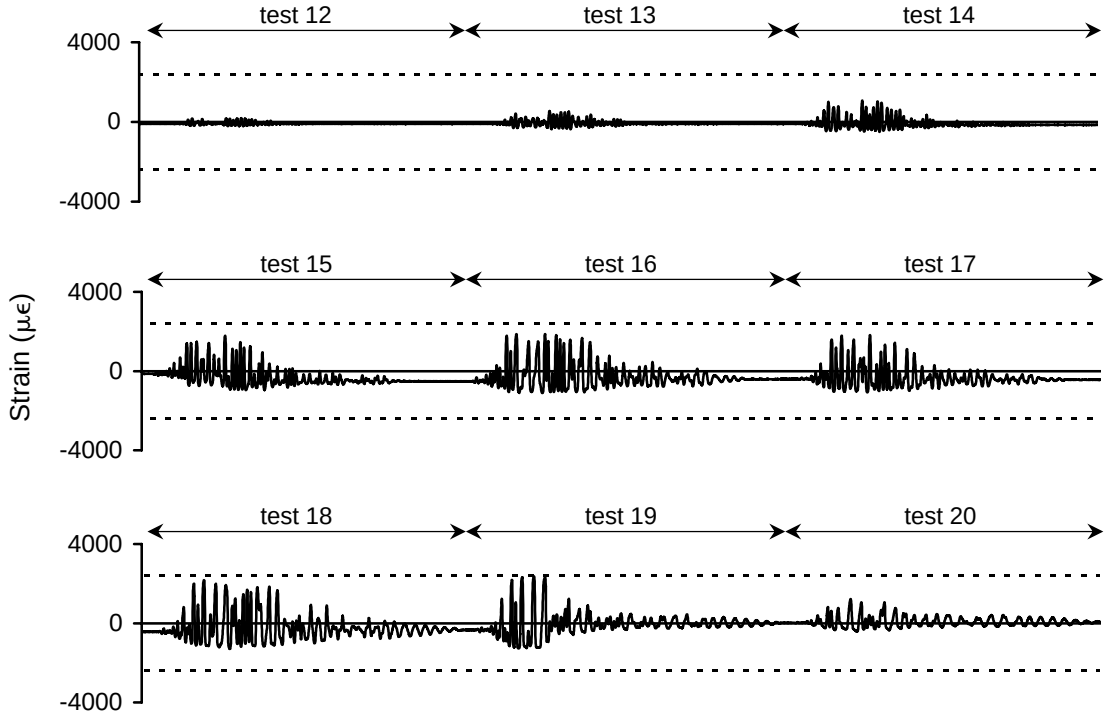

Figure A-85 Strain history for 3WBSL10 during high amplitude testing

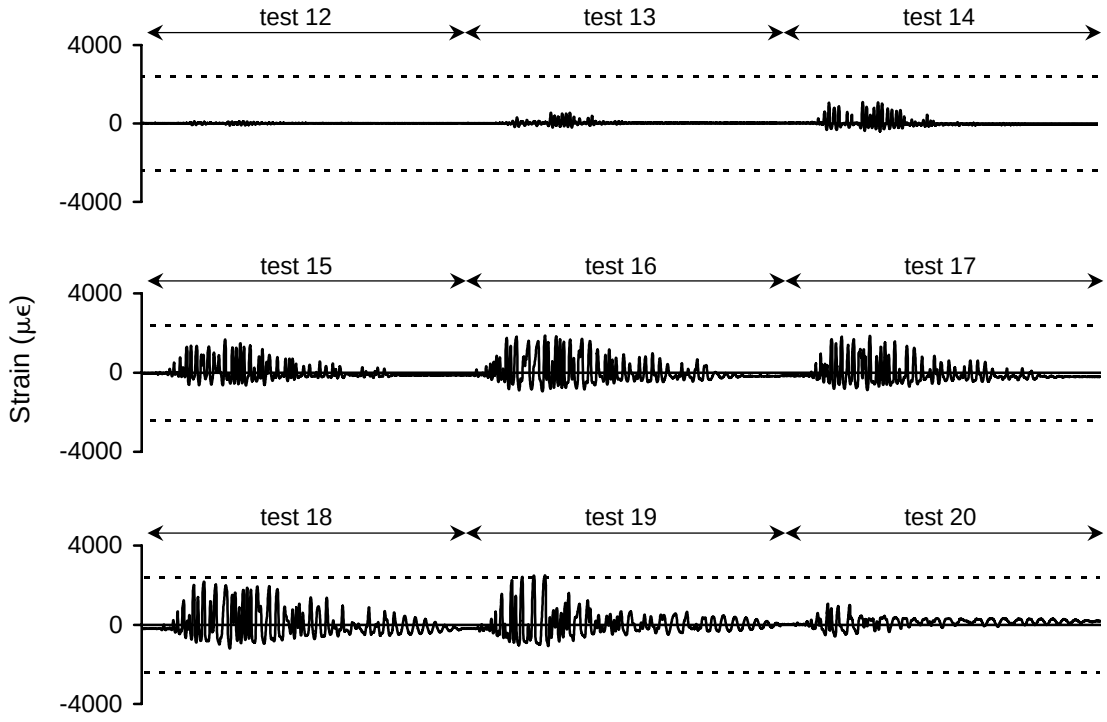

Figure A-86 Strain history for 3ETSL1 during high amplitude testing

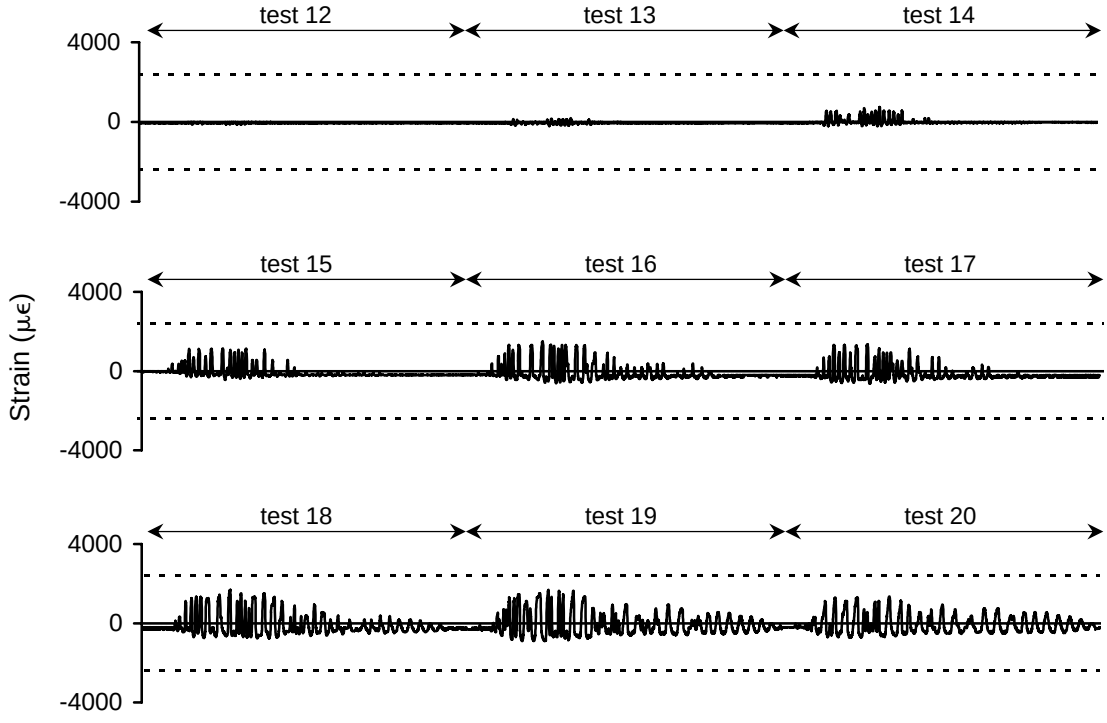

Figure A-87 Strain history for 3ETSL2 during high amplitude testing

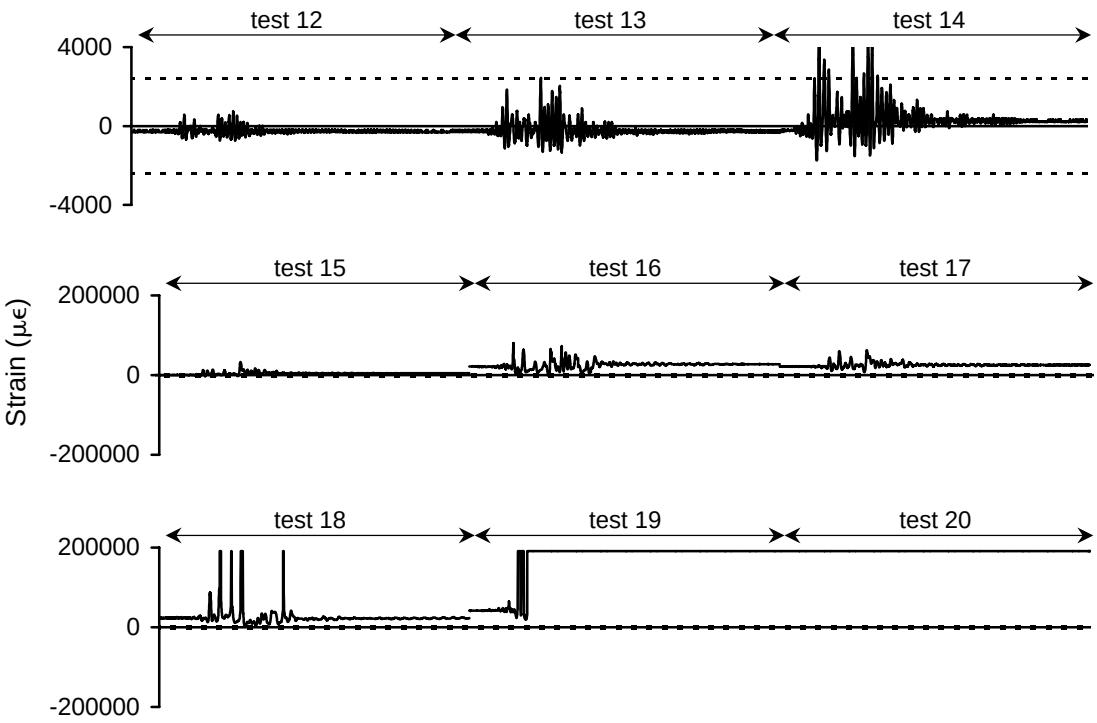

Figure A-89 Strain history for 3ETSL3 during high amplitude testing

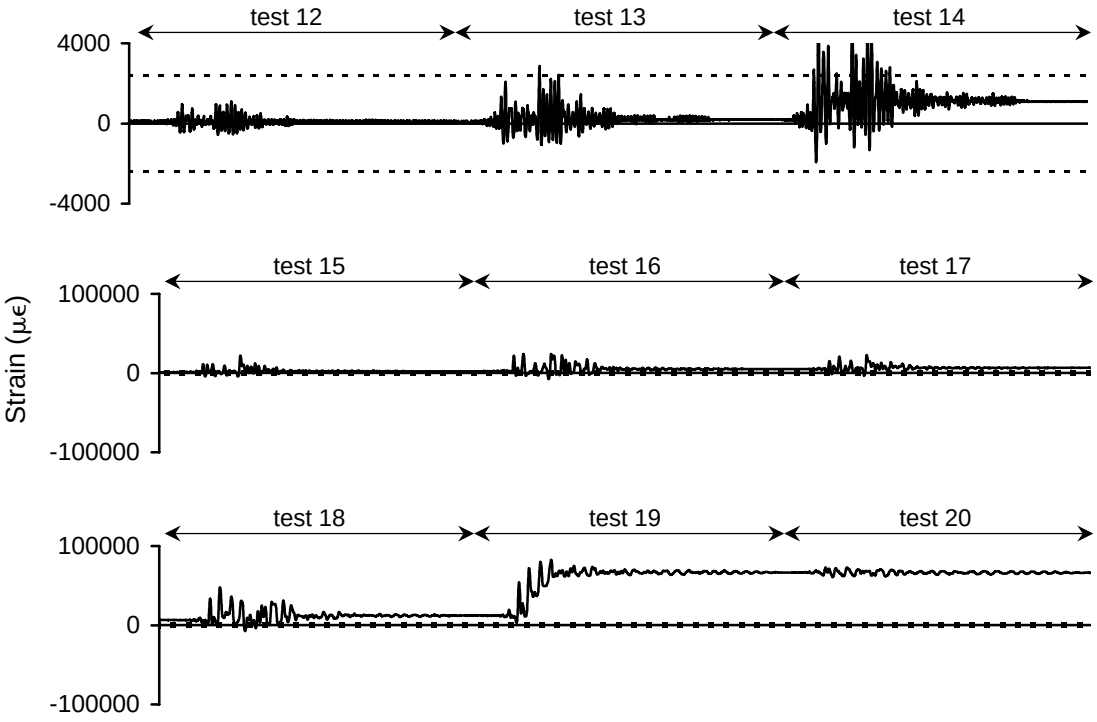

Figure A-90 Strain history for 3ETSL4 during high amplitude testing

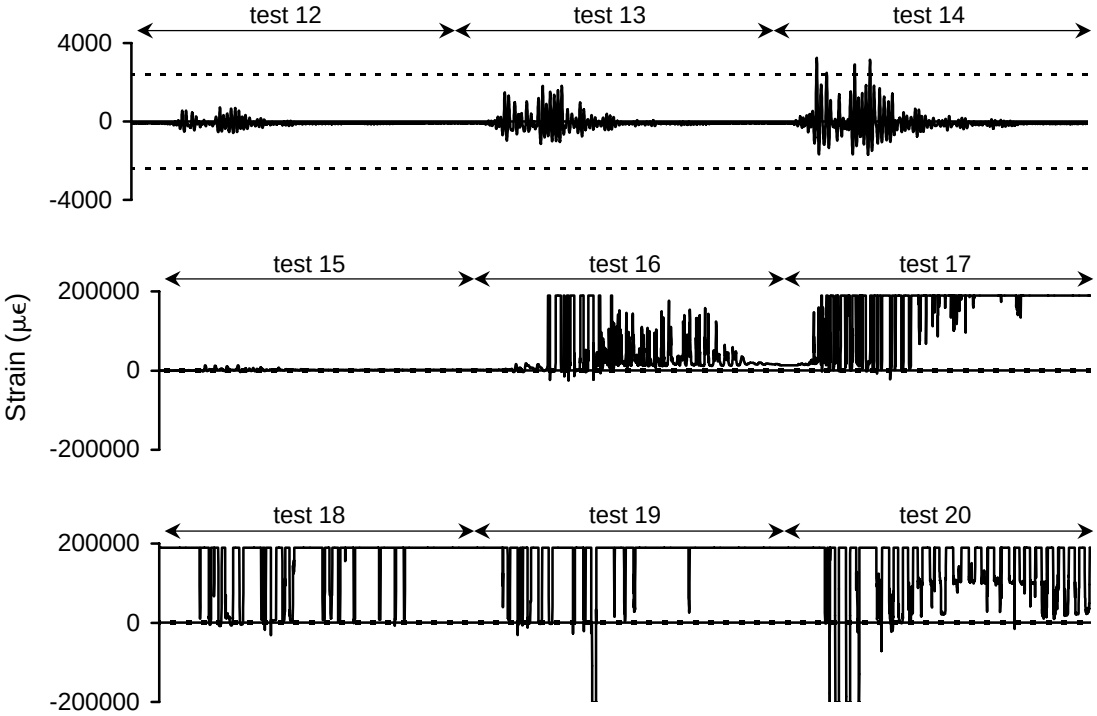

Figure A-91 Strain history for 3ETSL5 during high amplitude testing

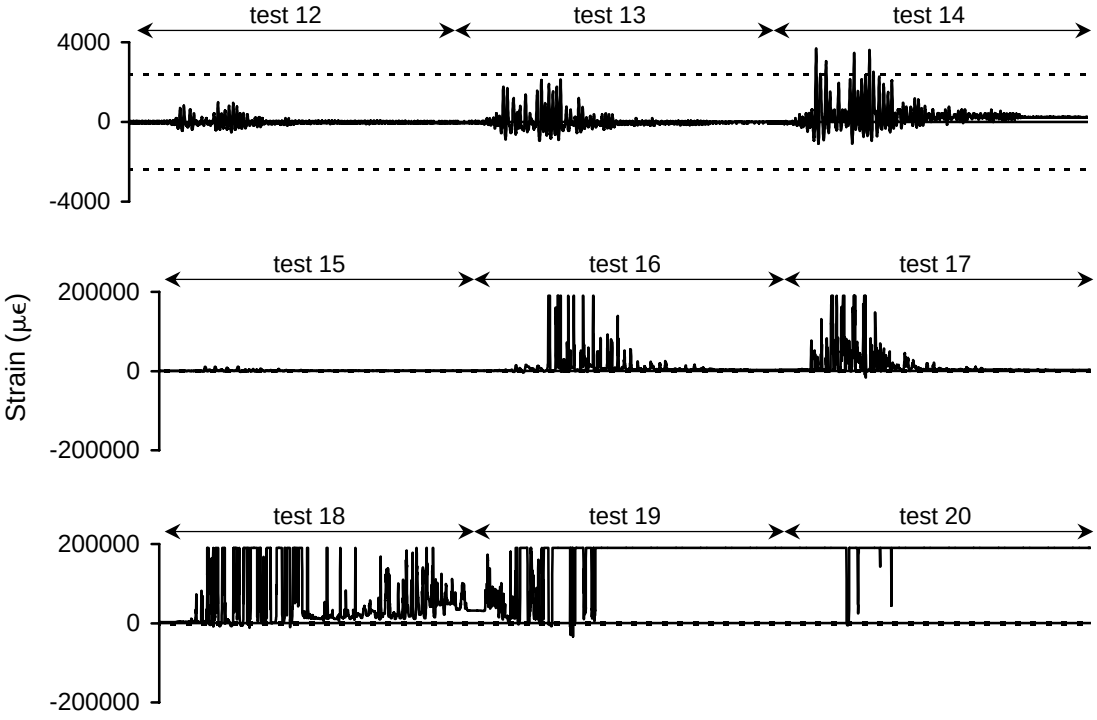

Figure A-92 Strain history for 3ETSL6 during high amplitude testing

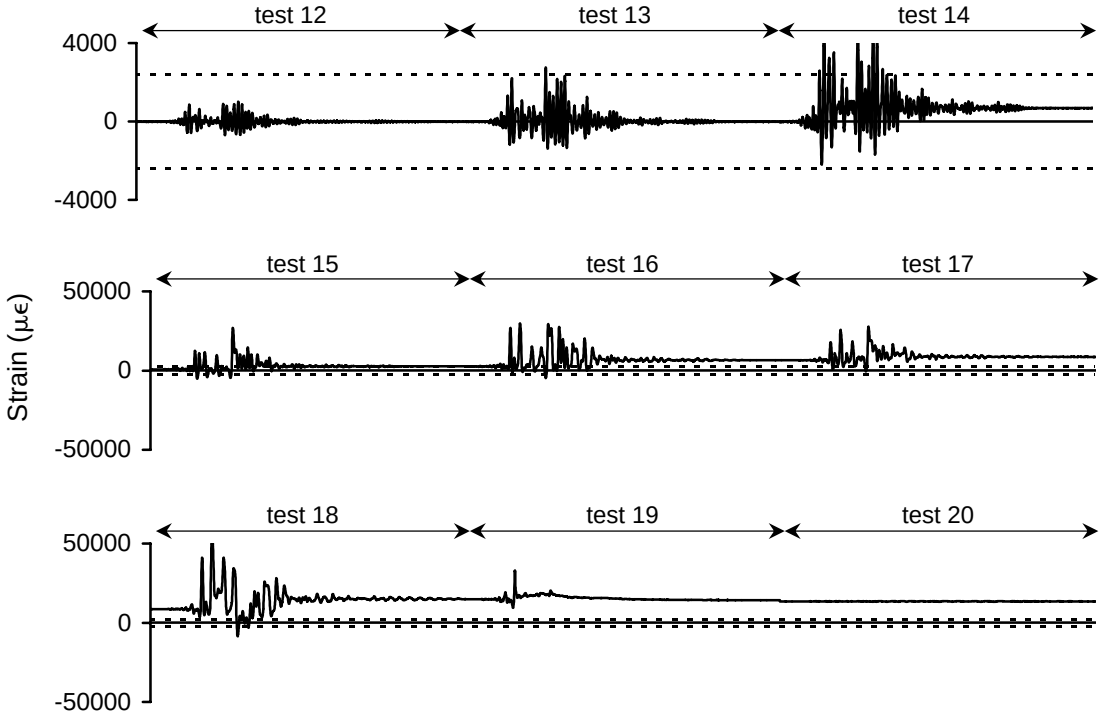

Figure A-93 Strain history for 3ETSL7 during high amplitude testing

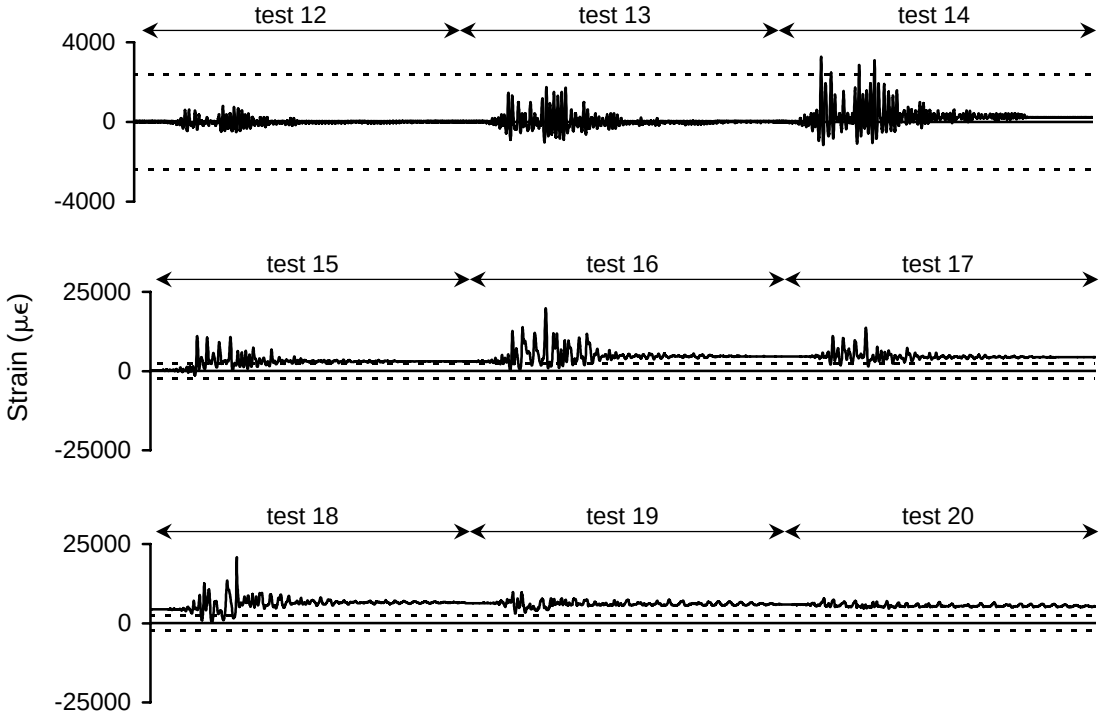

Figure A-94 Strain history for 3ETSL8 during high amplitude testing

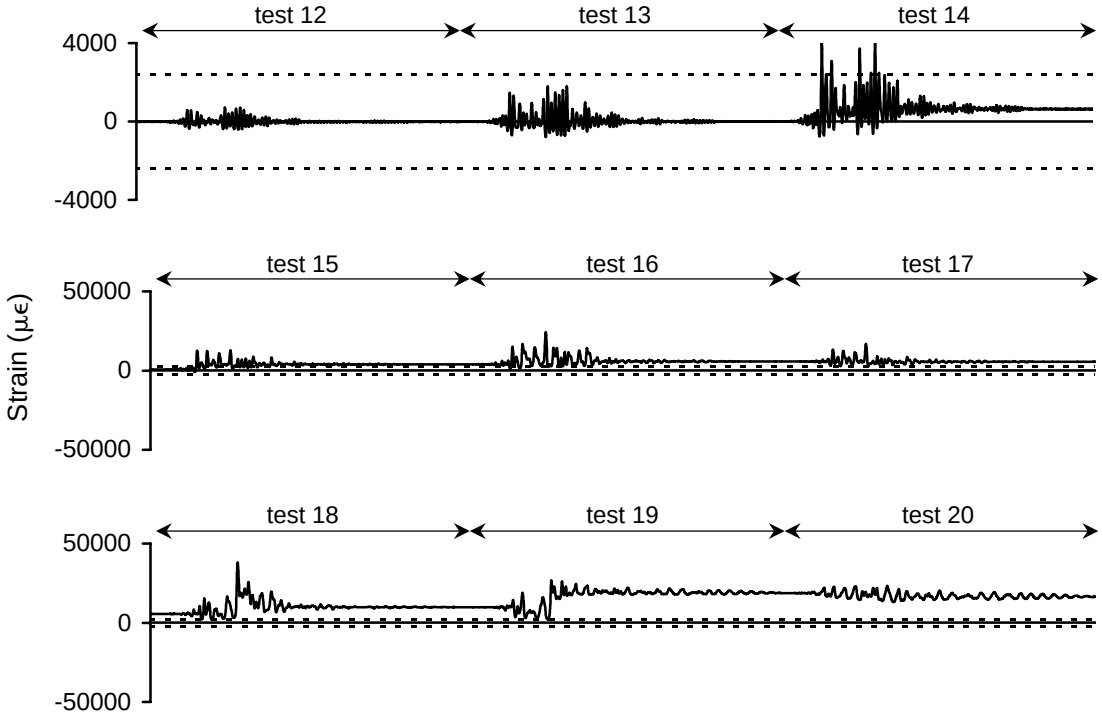

Figure A-95 Strain history for 3EBSL1 during high amplitude testing

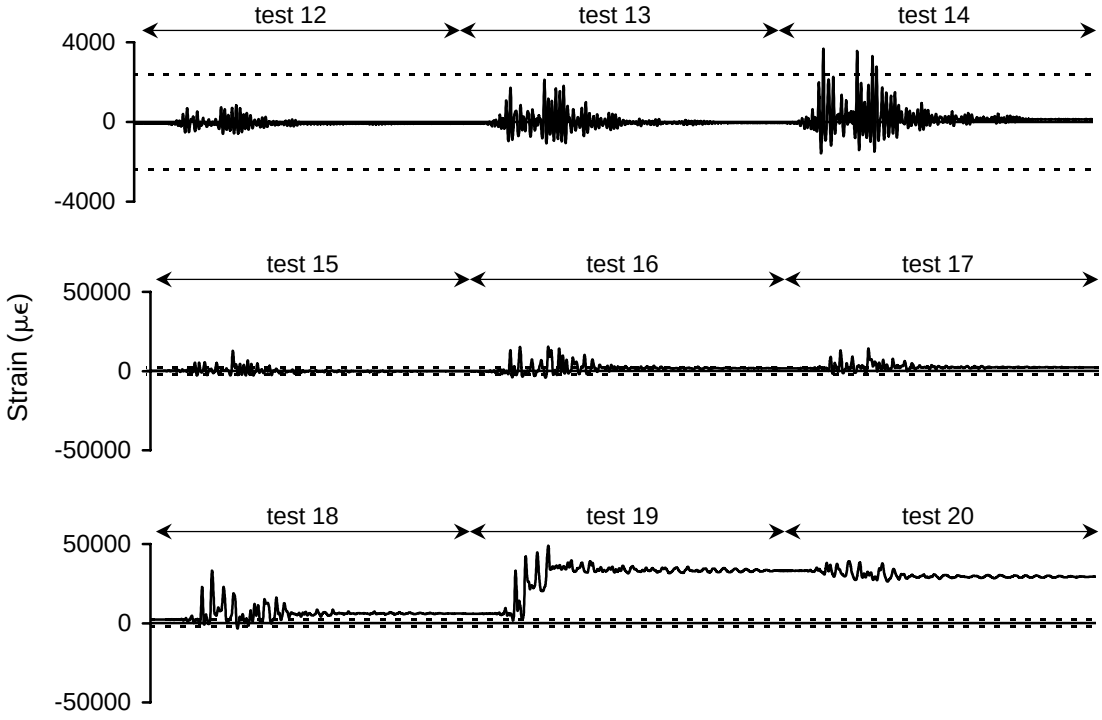

Figure A-96 Strain history for 3EBSL2 during high amplitude testing

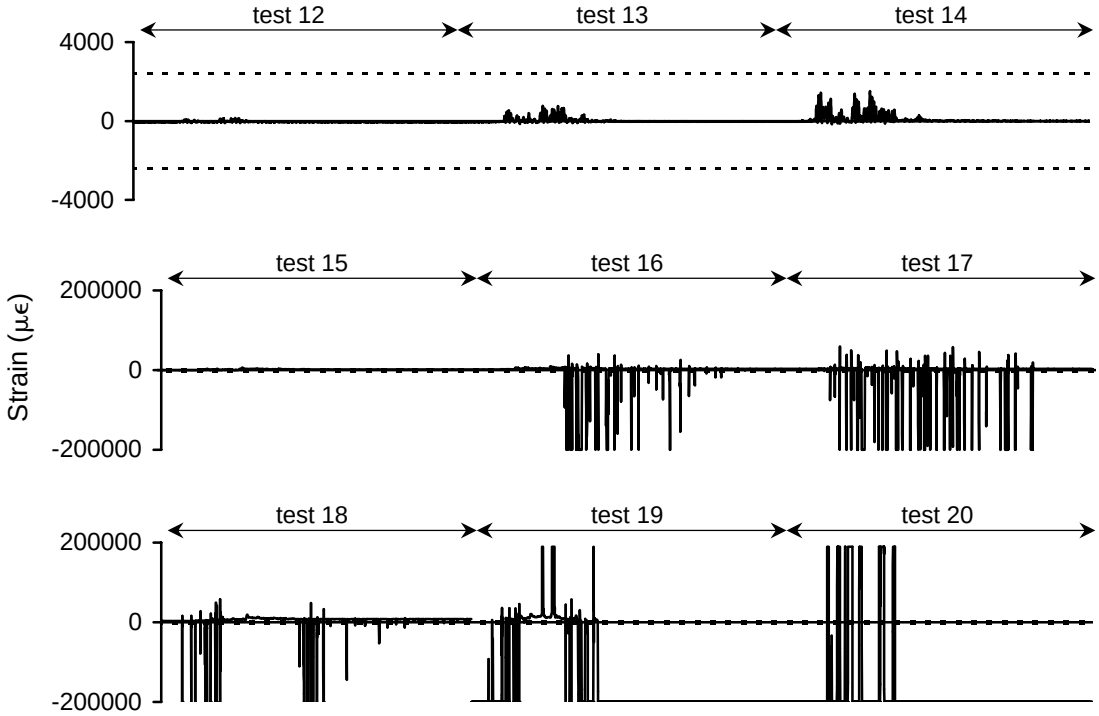

Figure A-97 Strain history for 3EBSL3 during high amplitude testing

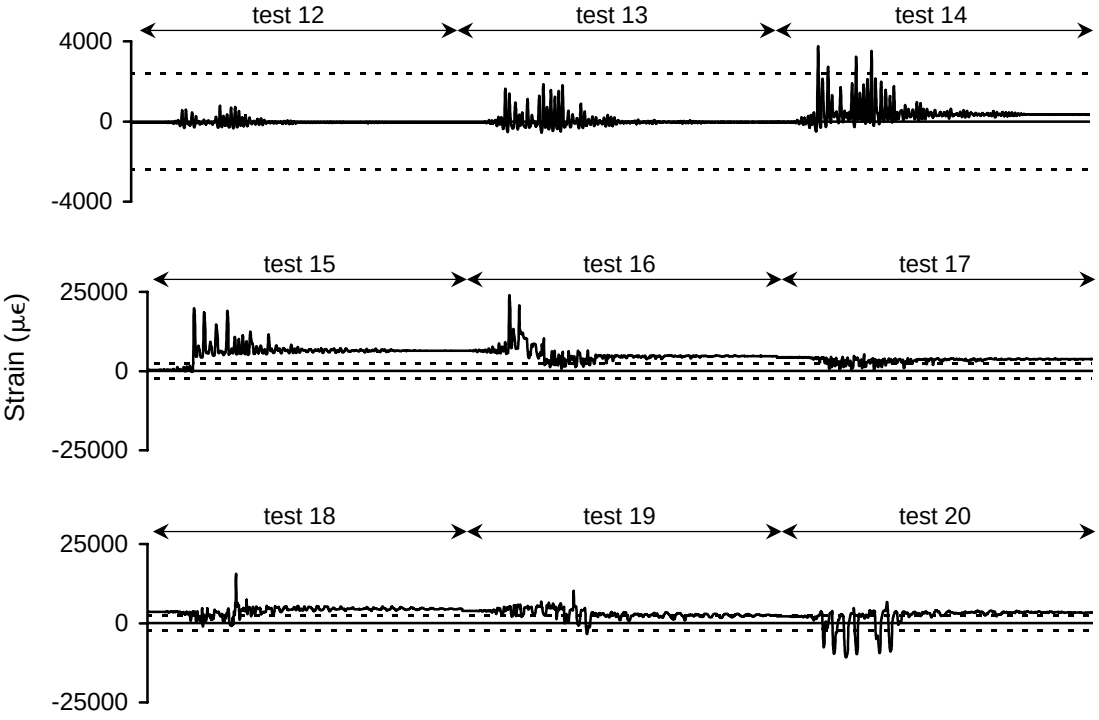

Figure A-98 Strain history for 3EBSL4 during high amplitude testing

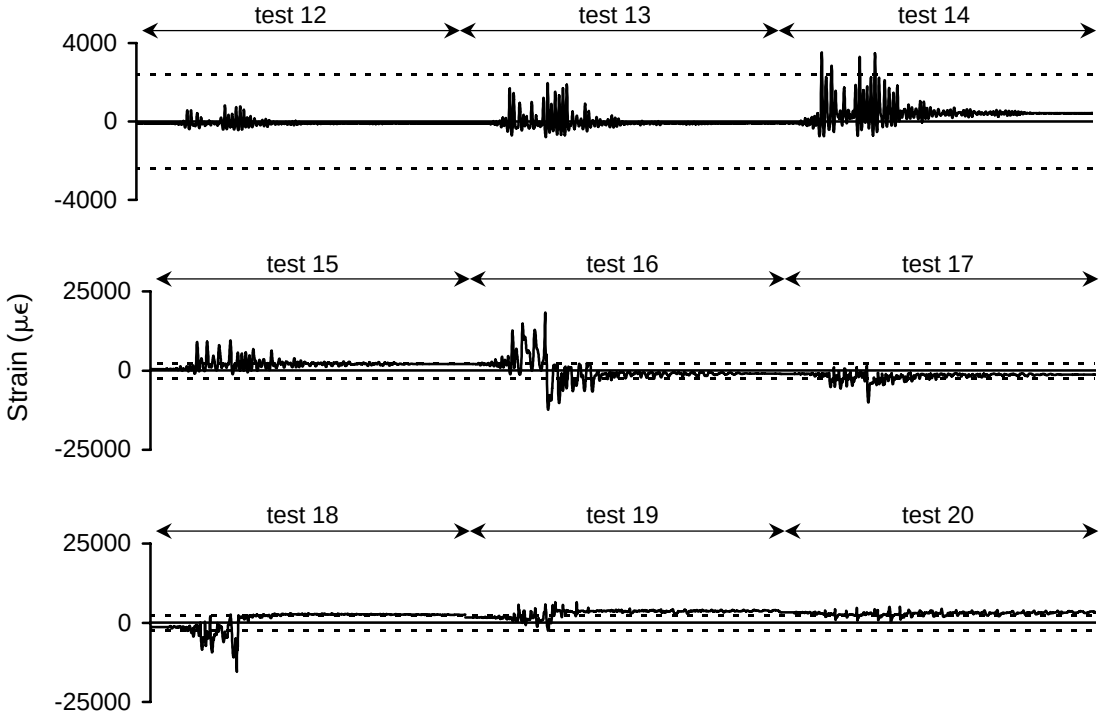

Figure A-99 Strain history for 3EBSL5 during high amplitude testing

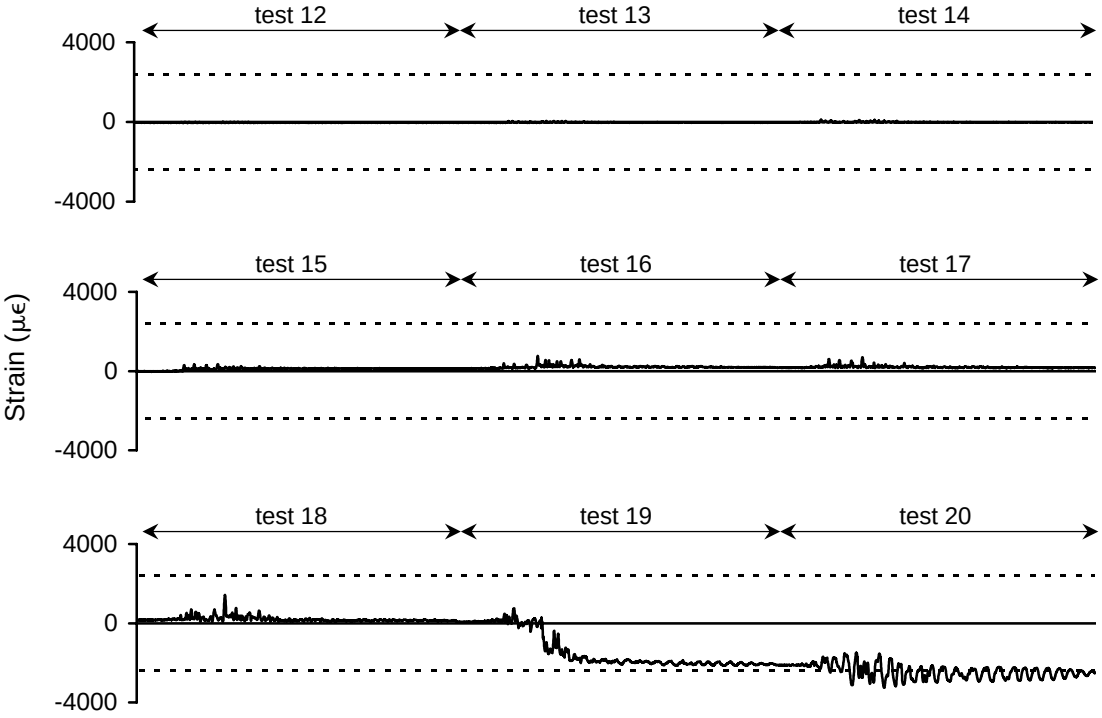

Figure A-100 Strain history for 3EBSL6 during high amplitude testing

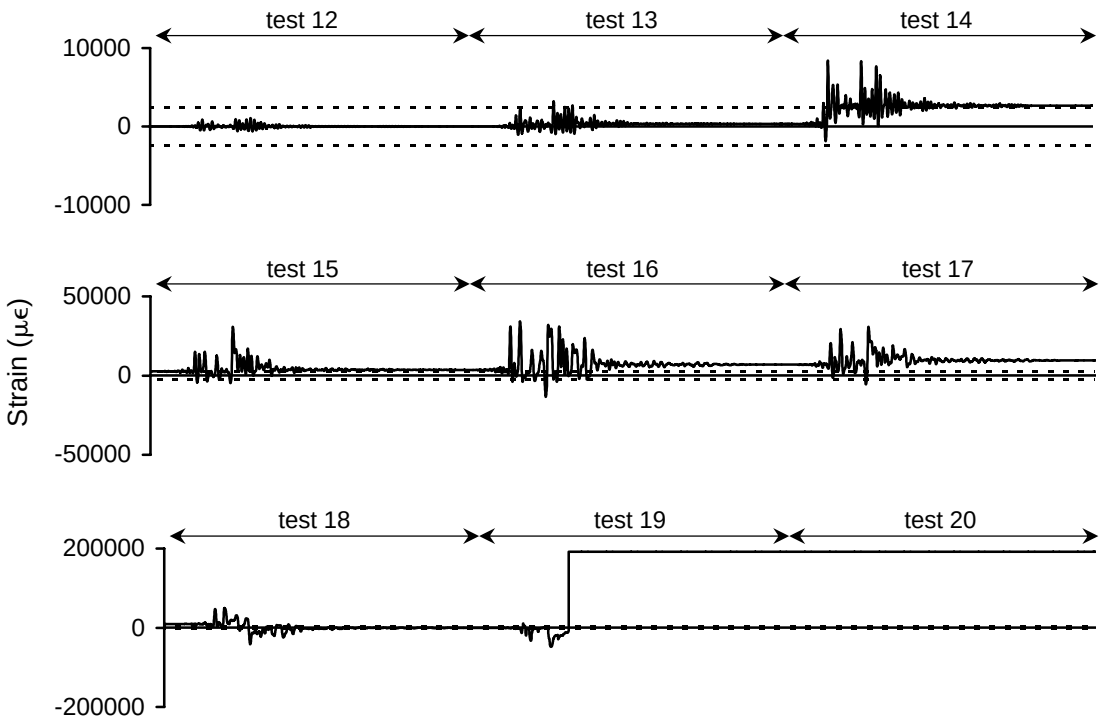

Figure A-101 Strain history for 3EBSL7 during high amplitude testing

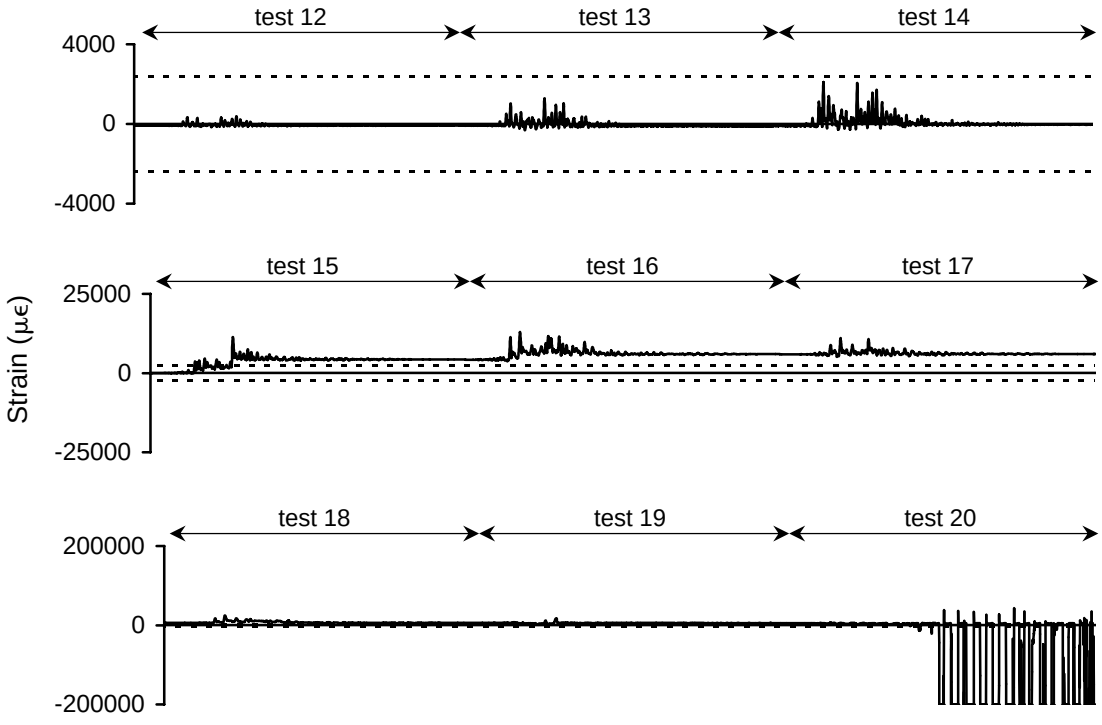

Figure A-102 Strain history for 3EBSL8 during high amplitude testing

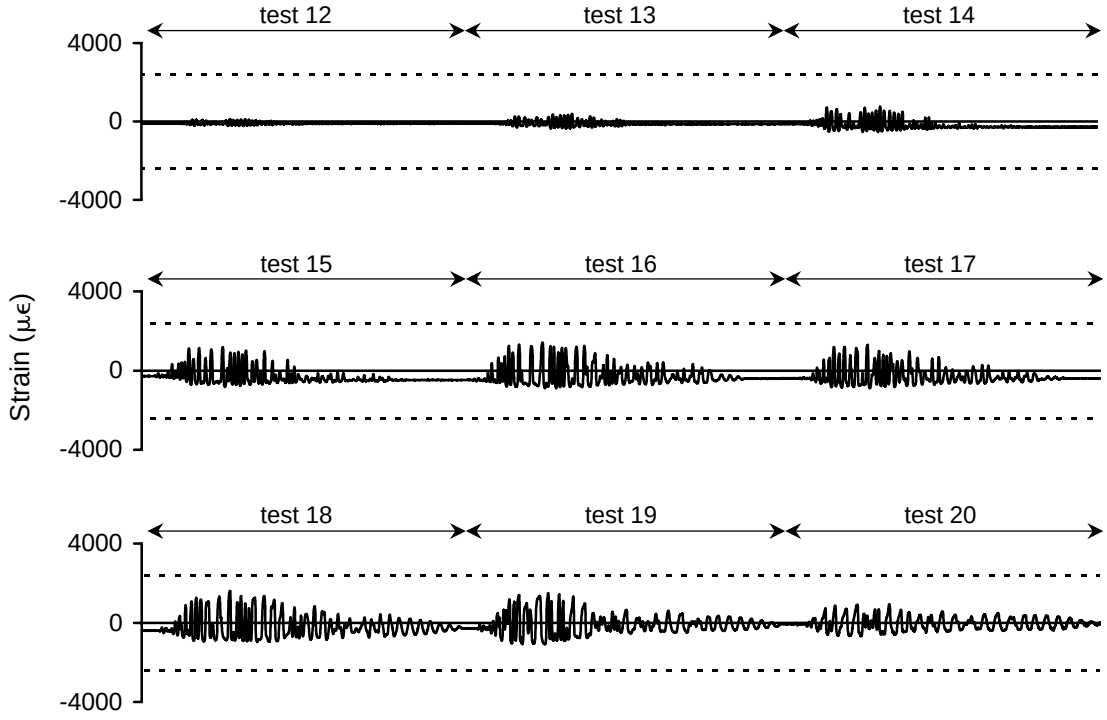

Figure A-103 Strain history for 3EBSL9 during high amplitude testing

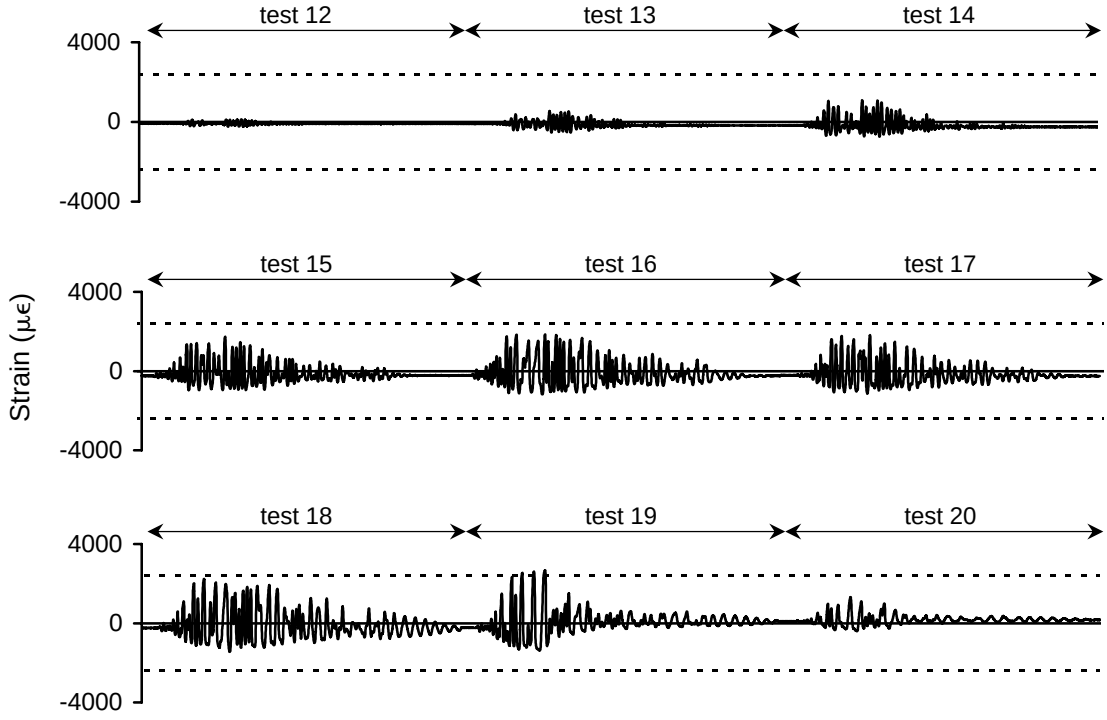

Figure A-104 Strain history for 3EBSL10 during high amplitude testing

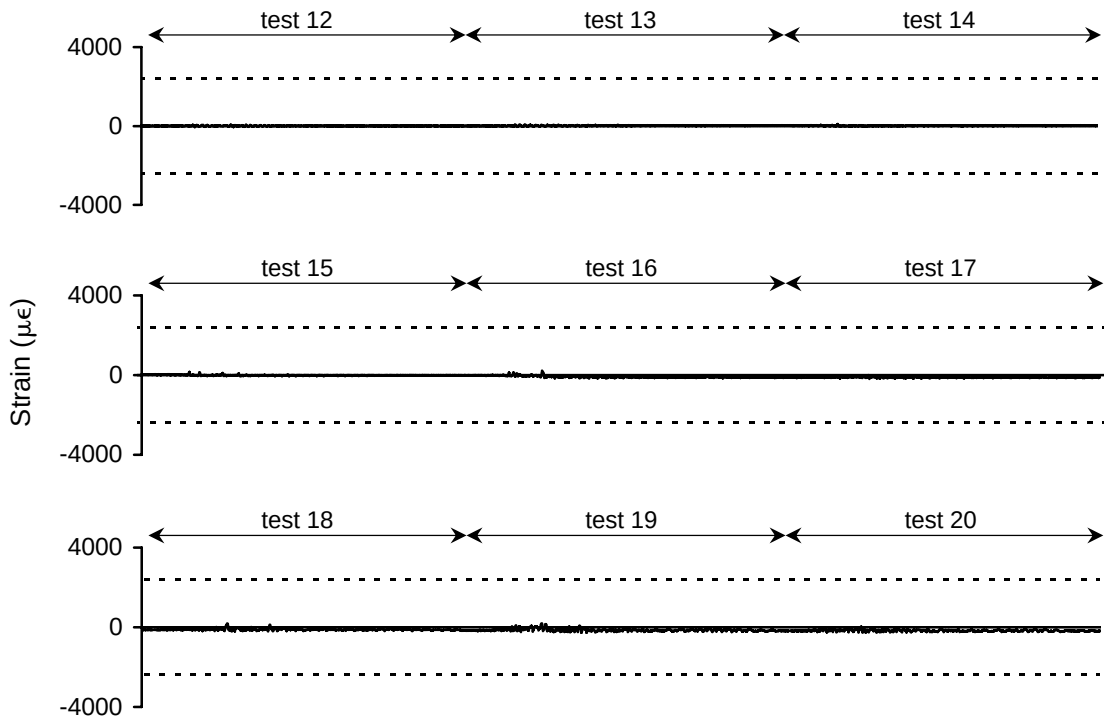

Figure A-105 Strain history for 1WTSH1 during high amplitude testing

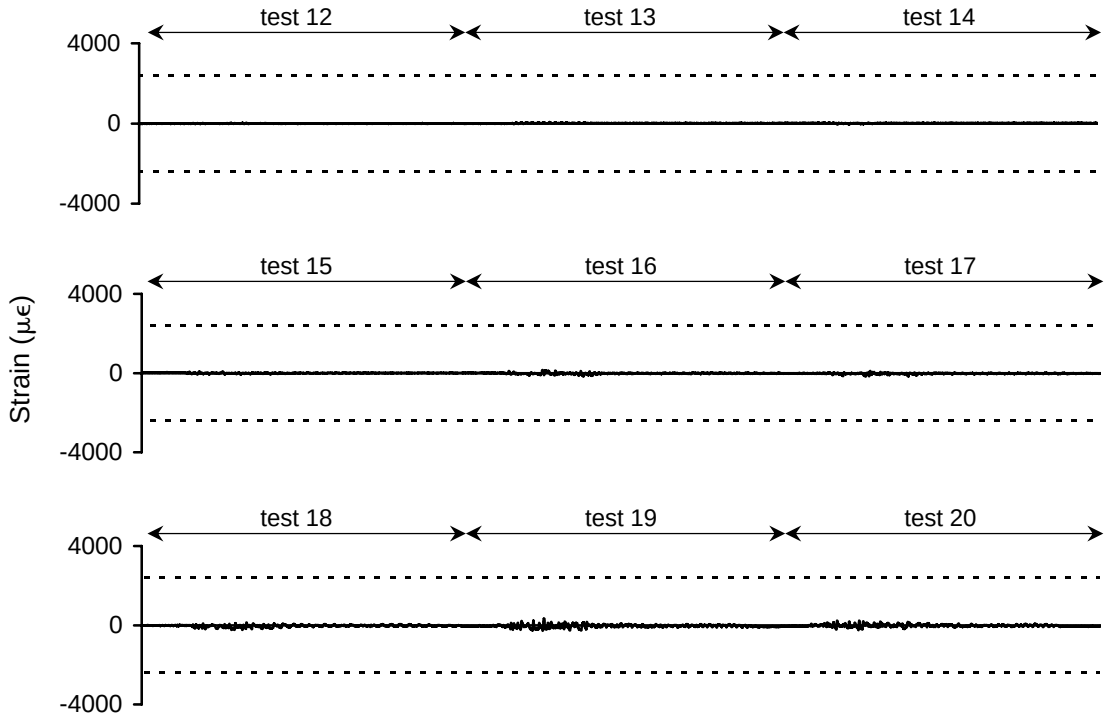

Figure A-106 Strain history for 1WTSH2 during high amplitude testing

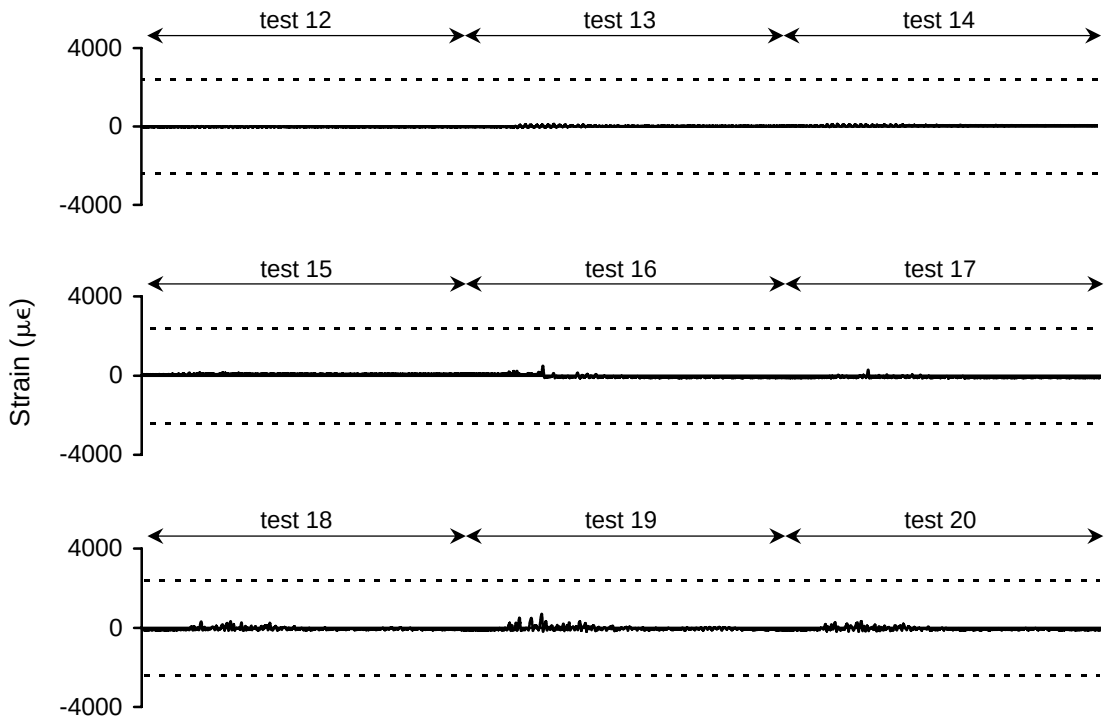

Figure A-107 Strain history for 1WTSH3 during high amplitude testing

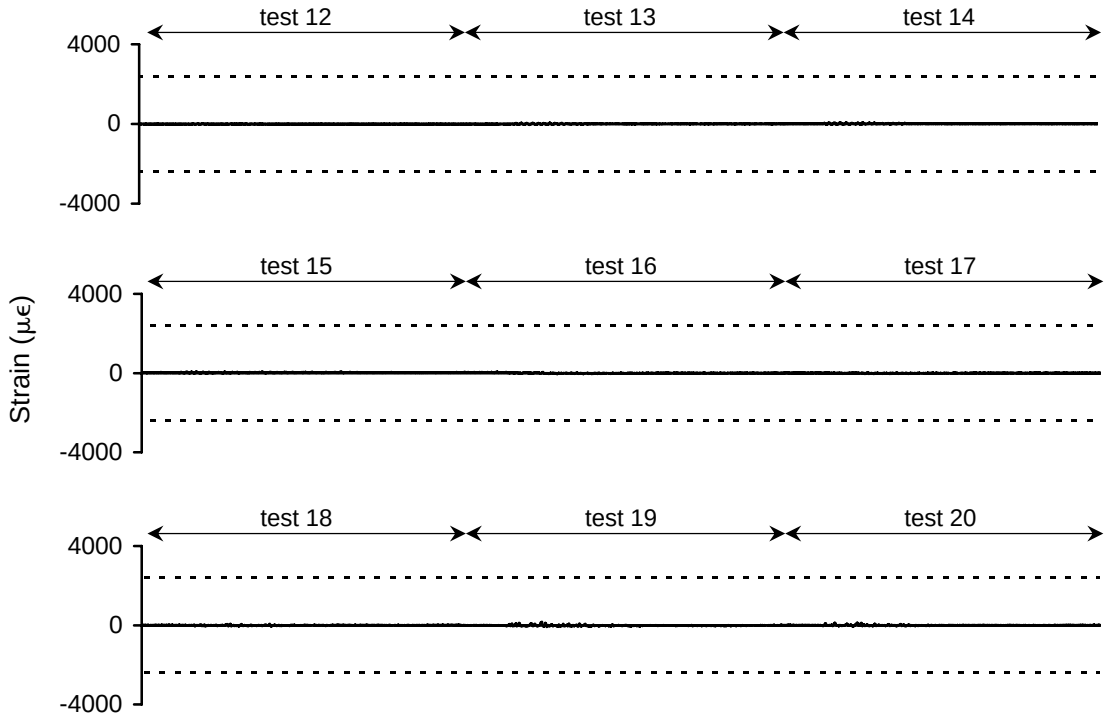

Figure A-108 Strain history for 1WTSH4 during high amplitude testing

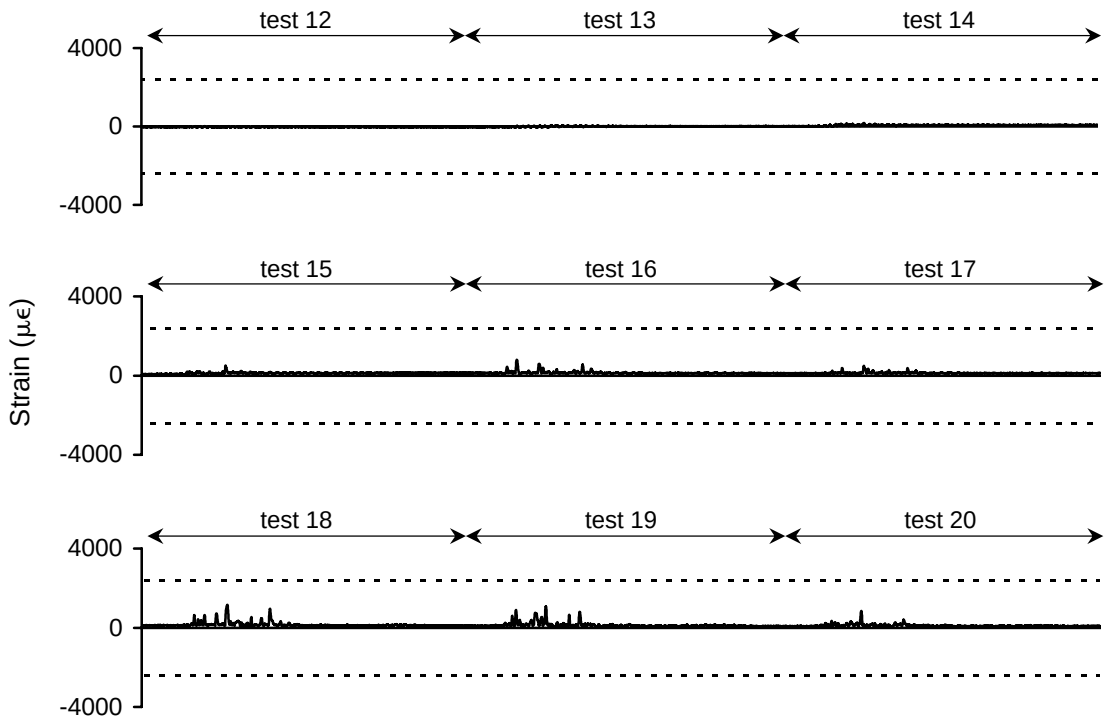

Figure A-109 Strain history for 1WBSH1 during high amplitude testing

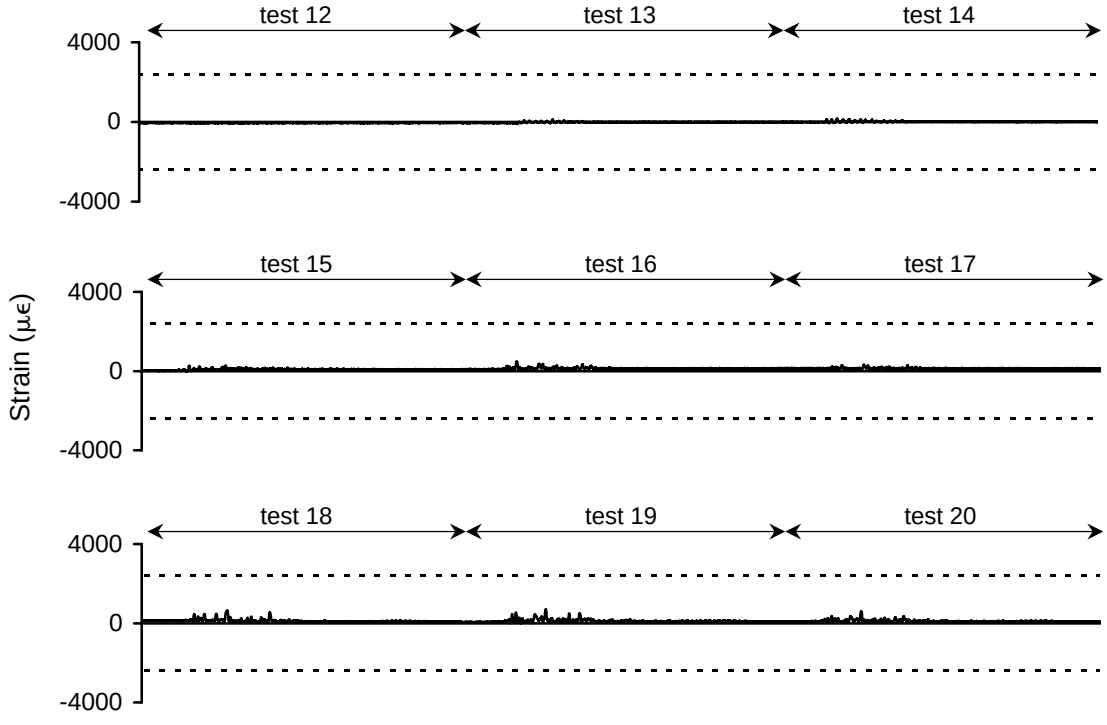

Figure A-110 Strain history for 1WBSH2 during high amplitude testing

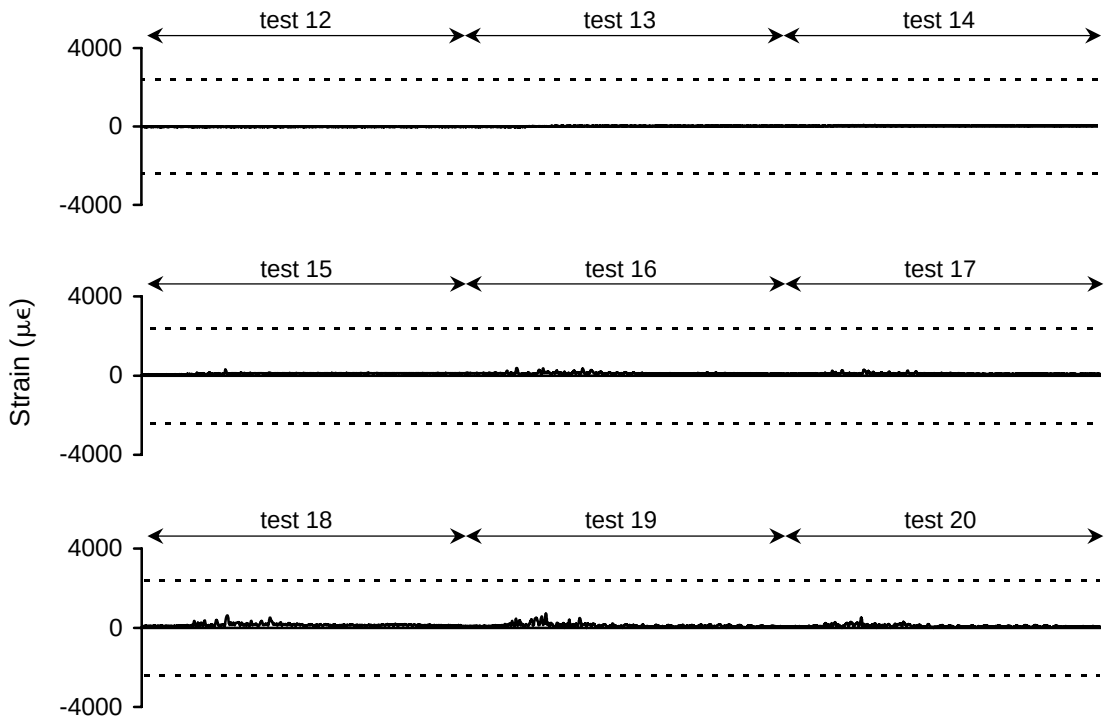

Figure A-111 Strain history for 1WBSH3 during high amplitude testing

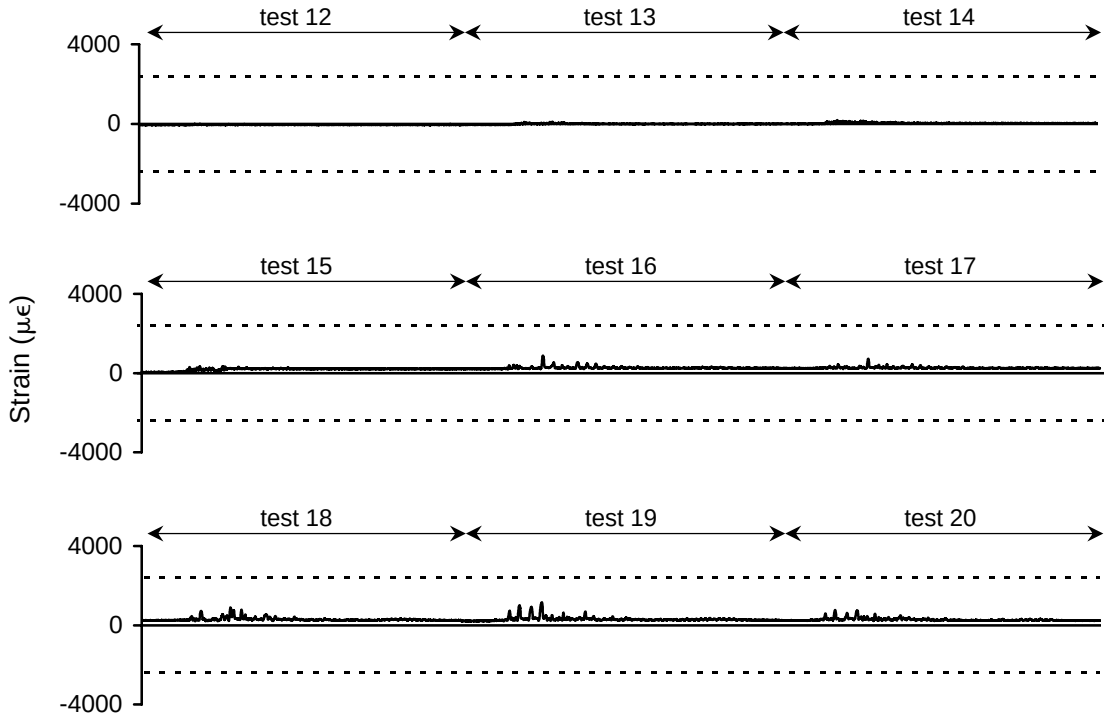

Figure A-112 Strain history for 1WBSH4 during high amplitude testing

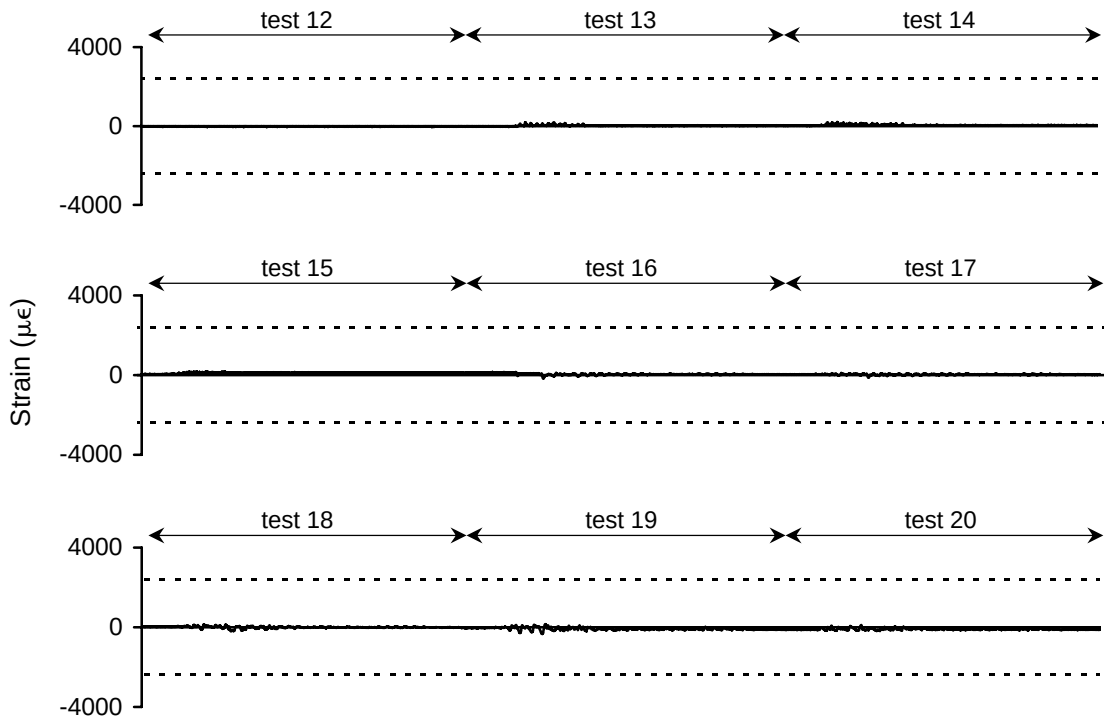

Figure A-113 Strain history for 1WBSH5 during high amplitude testing

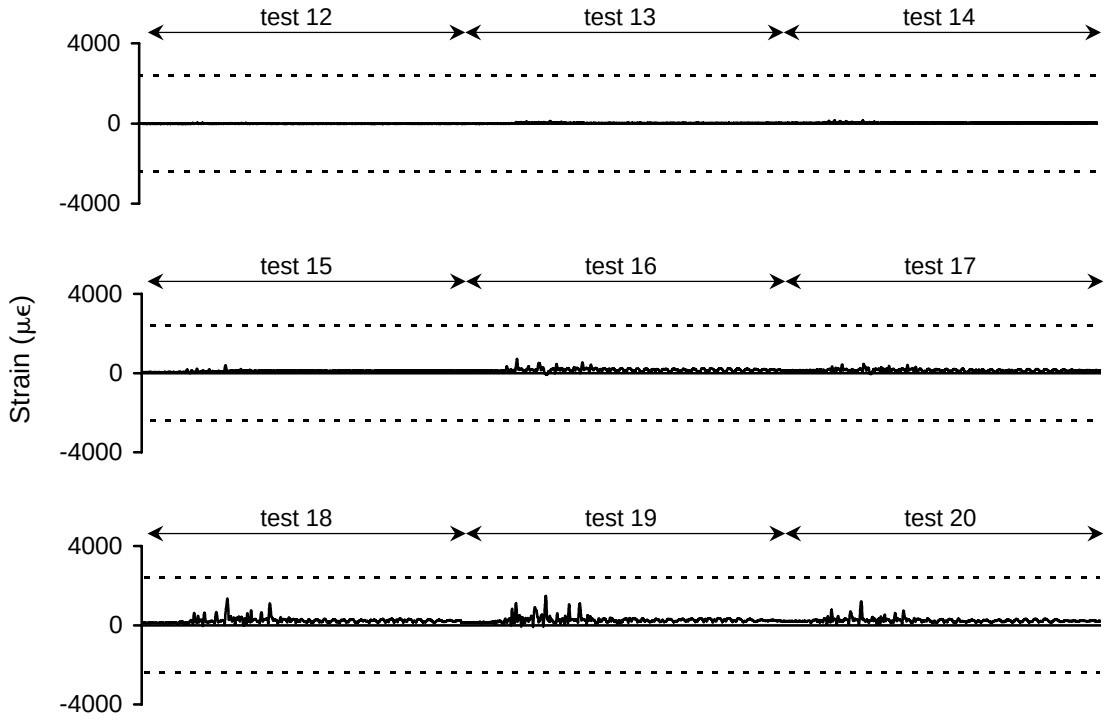

Figure A-114 Strain history for 1WBSH6 during high amplitude testing

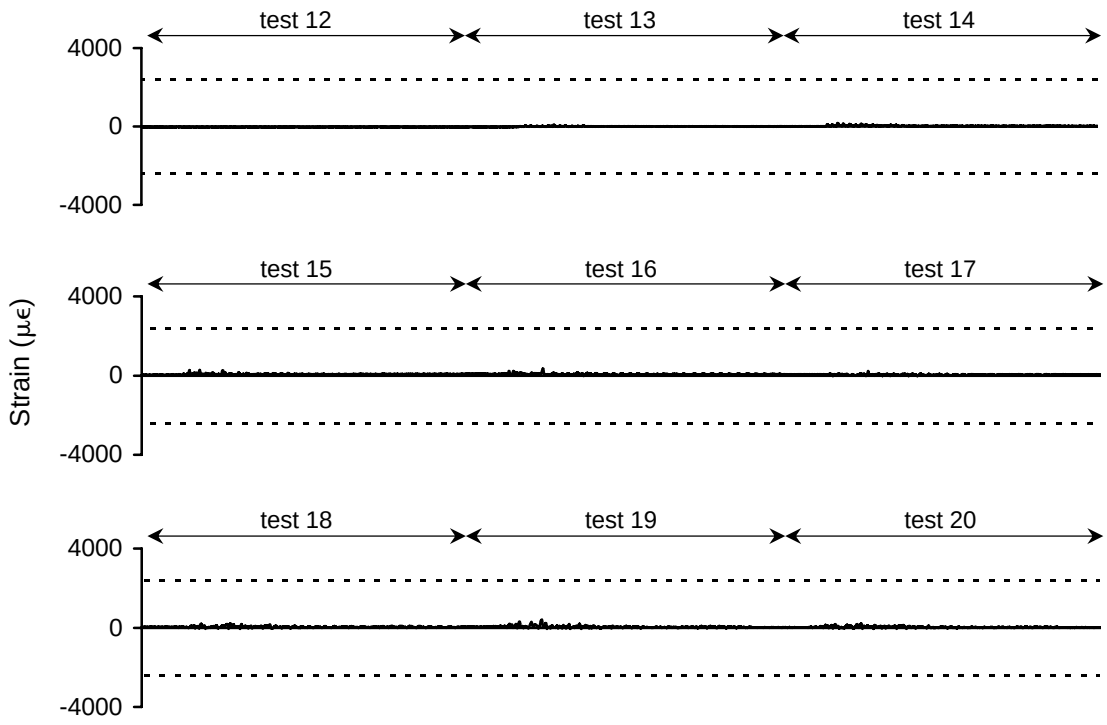

Figure A-115 Strain history for 1ETSH3 during high amplitude testing

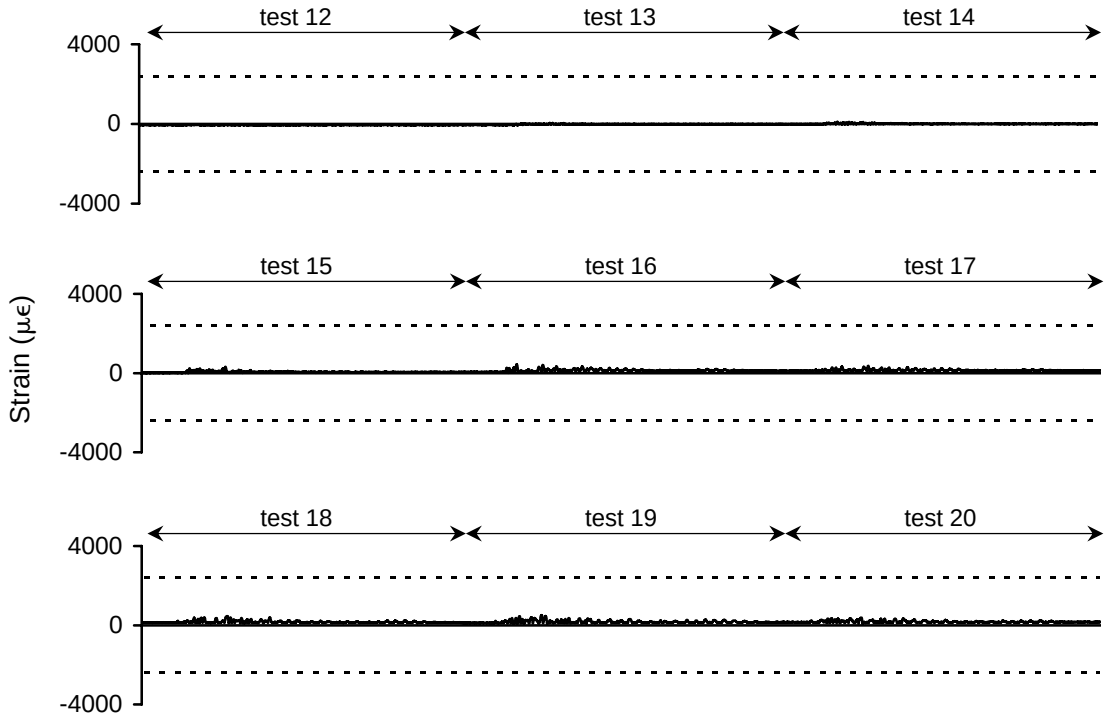

Figure A-116 Strain history for 1ETSH4 during high amplitude testing

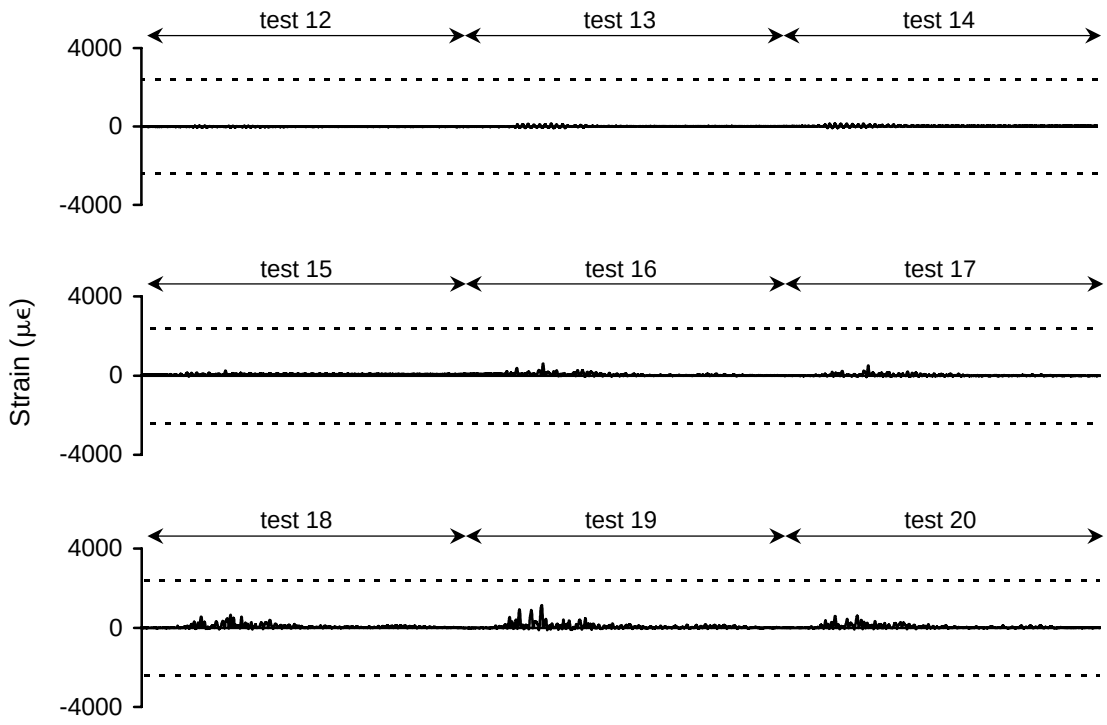

Figure A-117 Strain history for 1EBSH1 during high amplitude testing

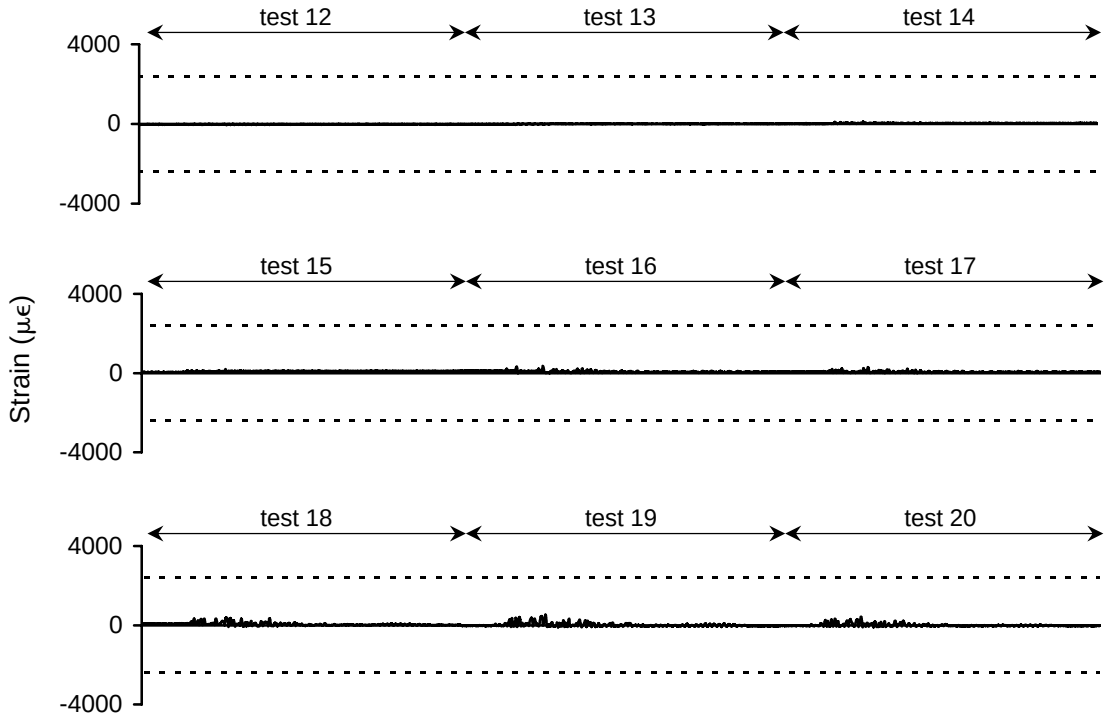

Figure A-118 Strain history for 1EBSH2 during high amplitude testing

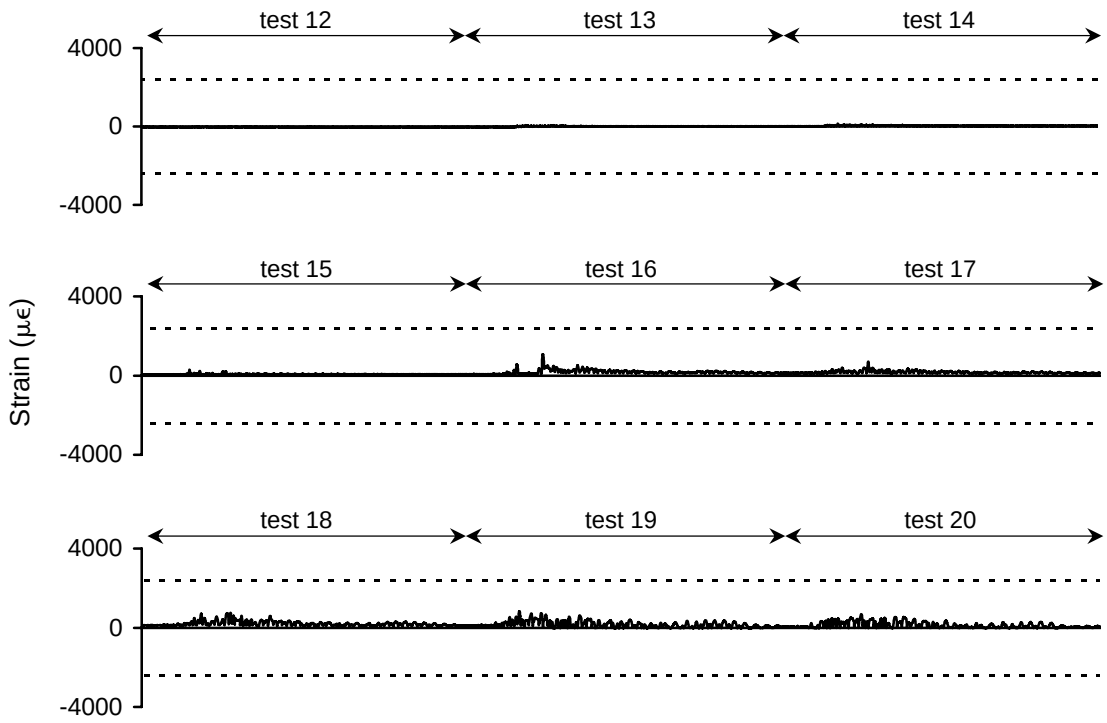

Figure A-119 Strain history for 1EBSH3 during high amplitude testing

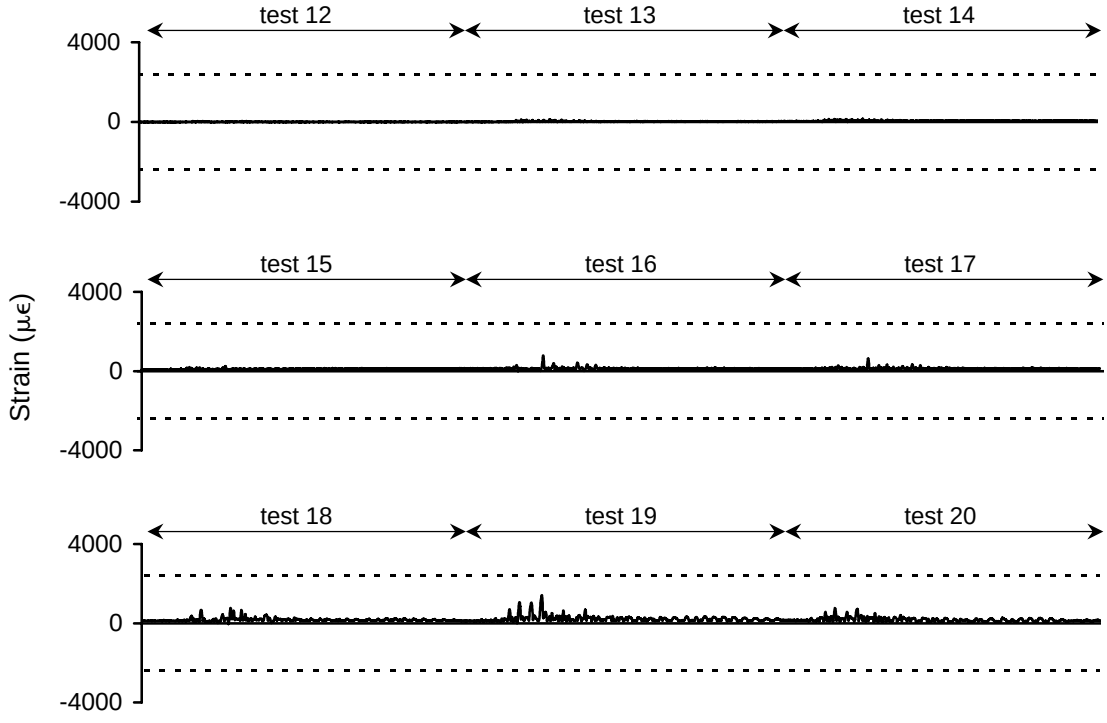

Figure A-120 Strain history for 1EBSH4 during high amplitude testing

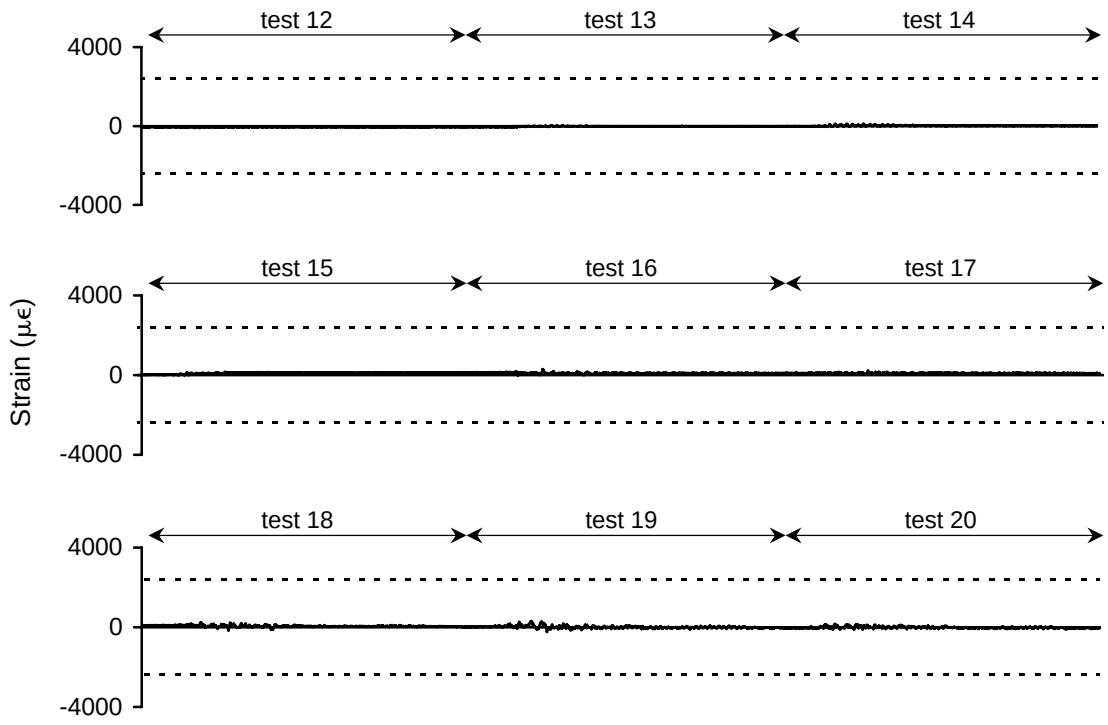

Figure A-129 Strain history for 1EBSH5 during high amplitude testing

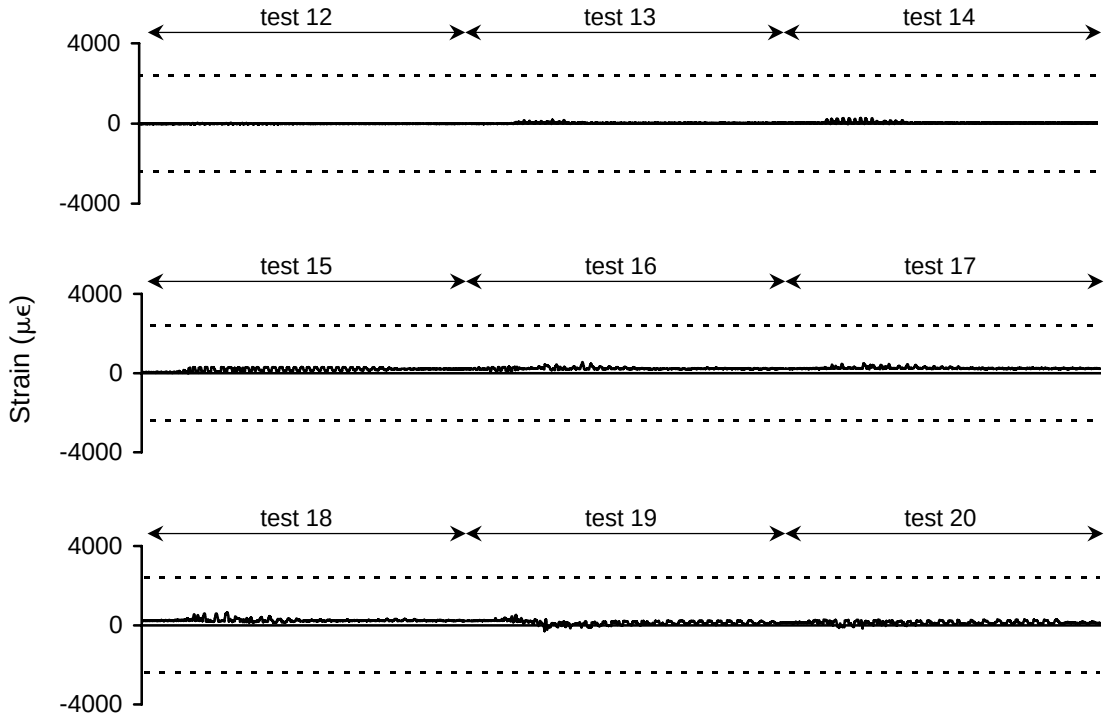

Figure A-130 Strain history for 1EBSH6 during high amplitude testing

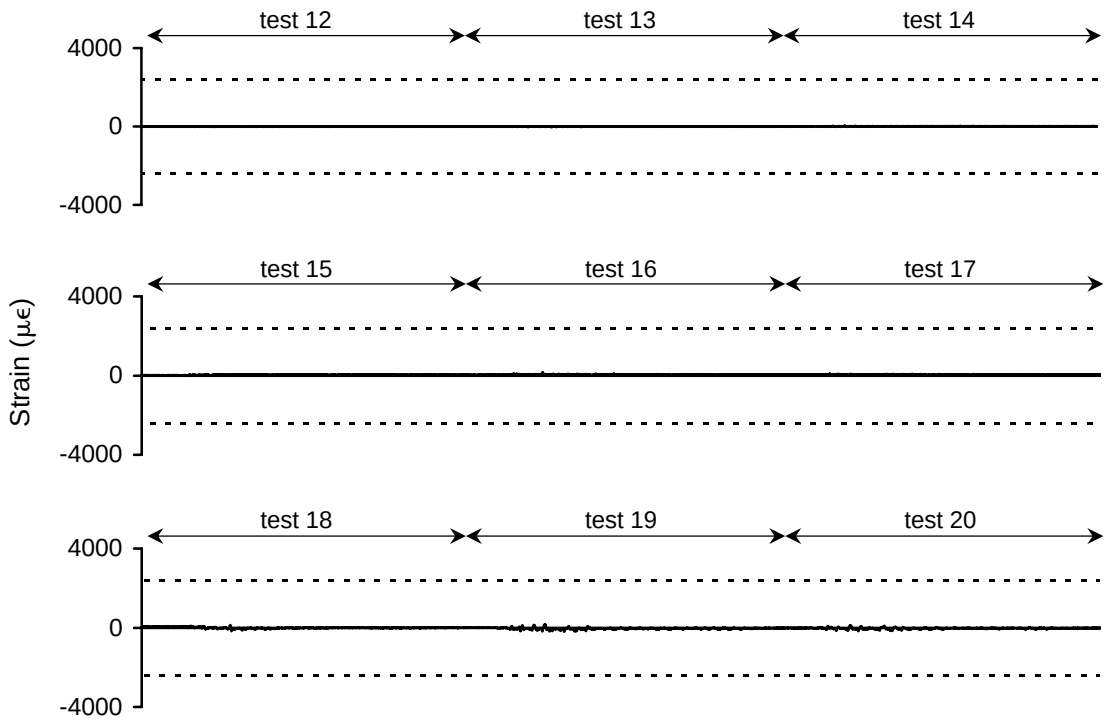

Figure A-131 Strain history for 2WTSH1 during high amplitude testing

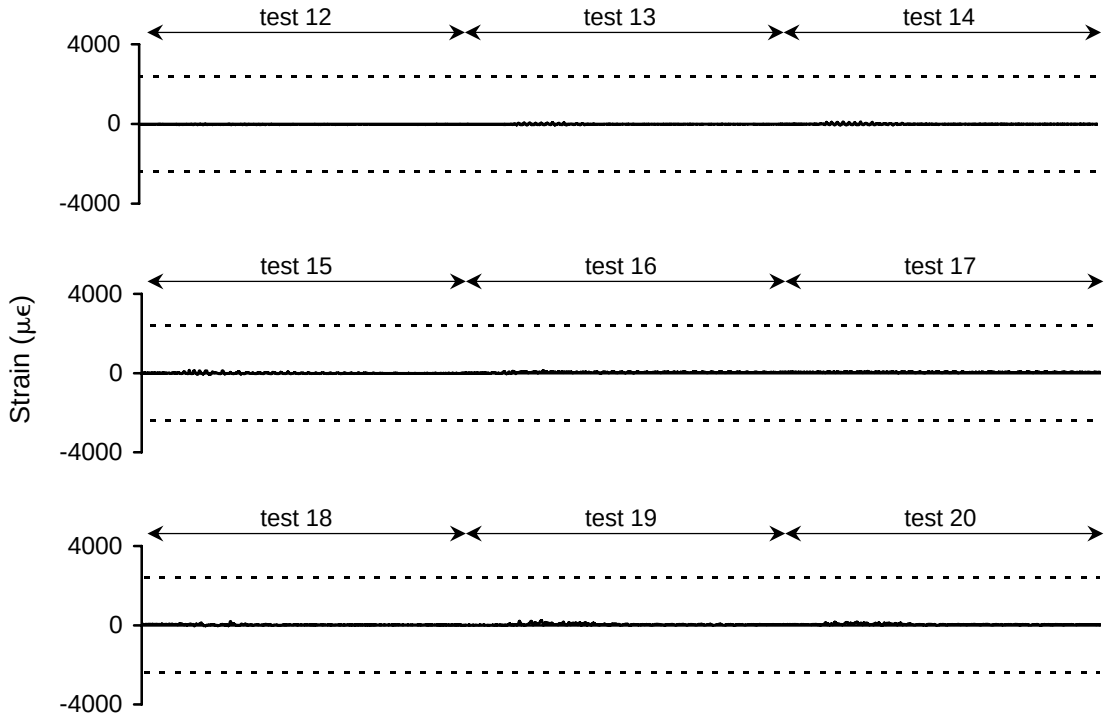

Figure A-132 Strain history for 2WTSH2 during high amplitude testing

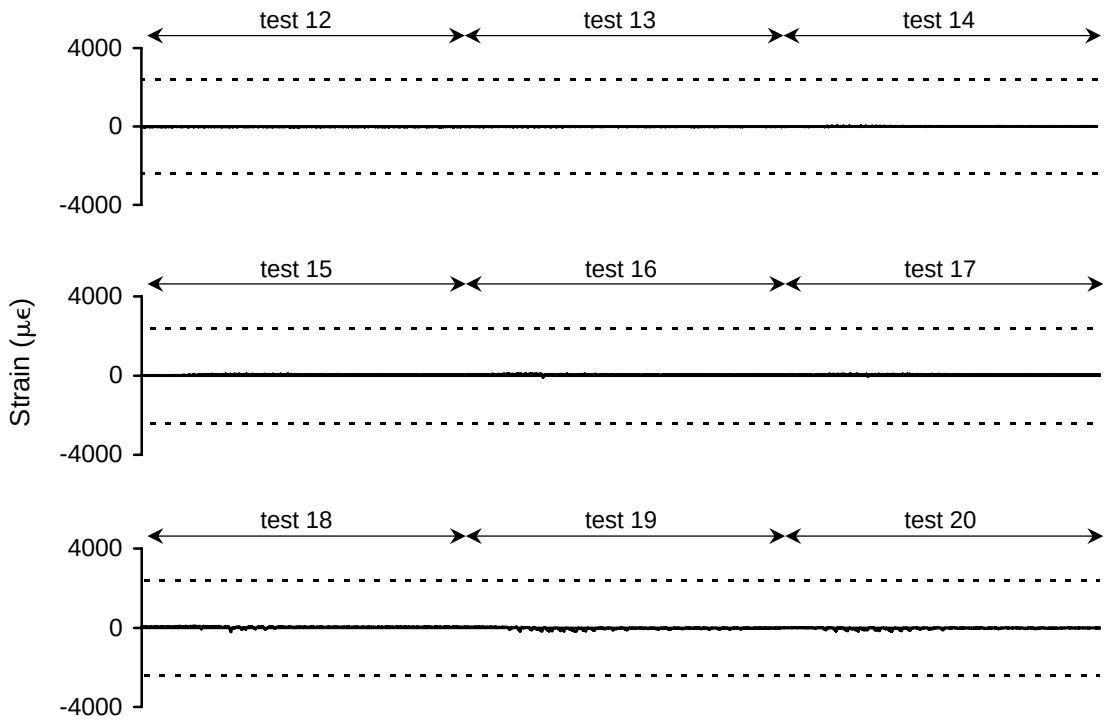

Figure A-133 Strain history for 2WTSH3 during high amplitude testing

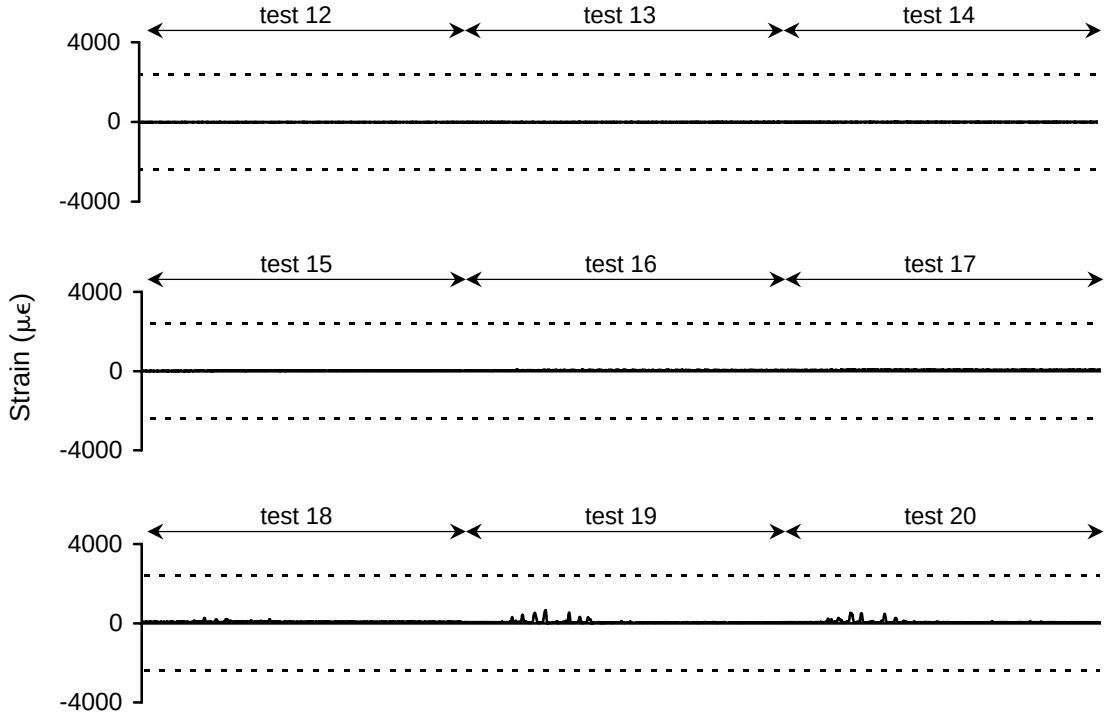

Figure A-134 Strain history for 2WBSH1 during high amplitude testing

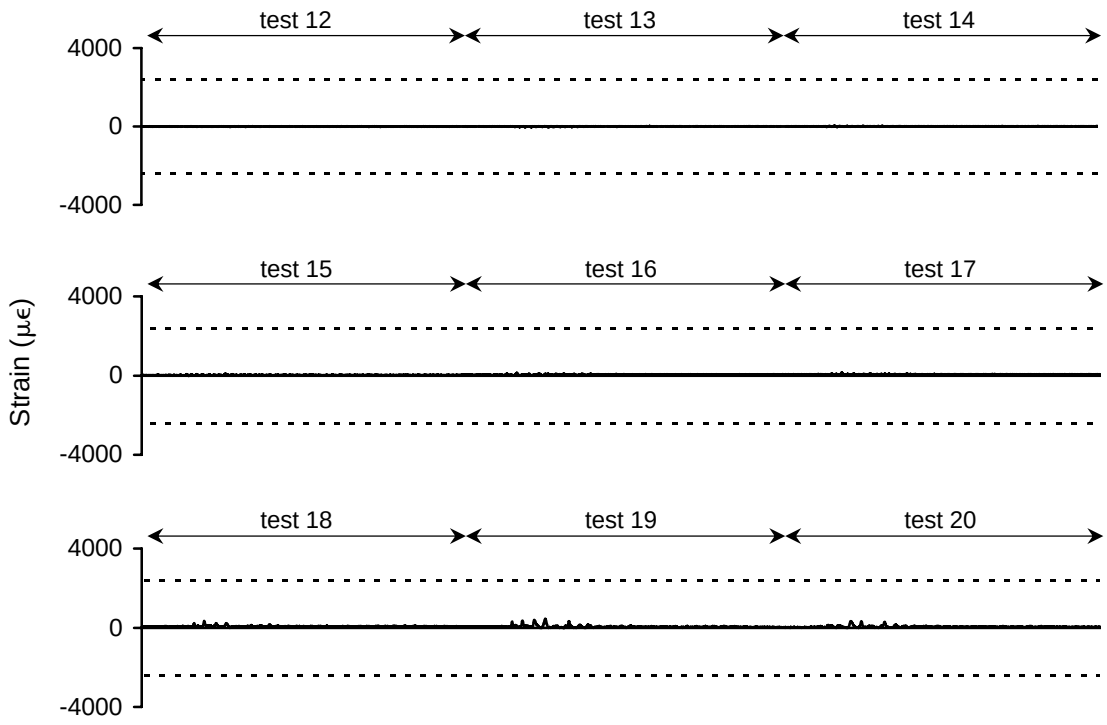

Figure A-135 Strain history for 2WBSH2 during high amplitude testing

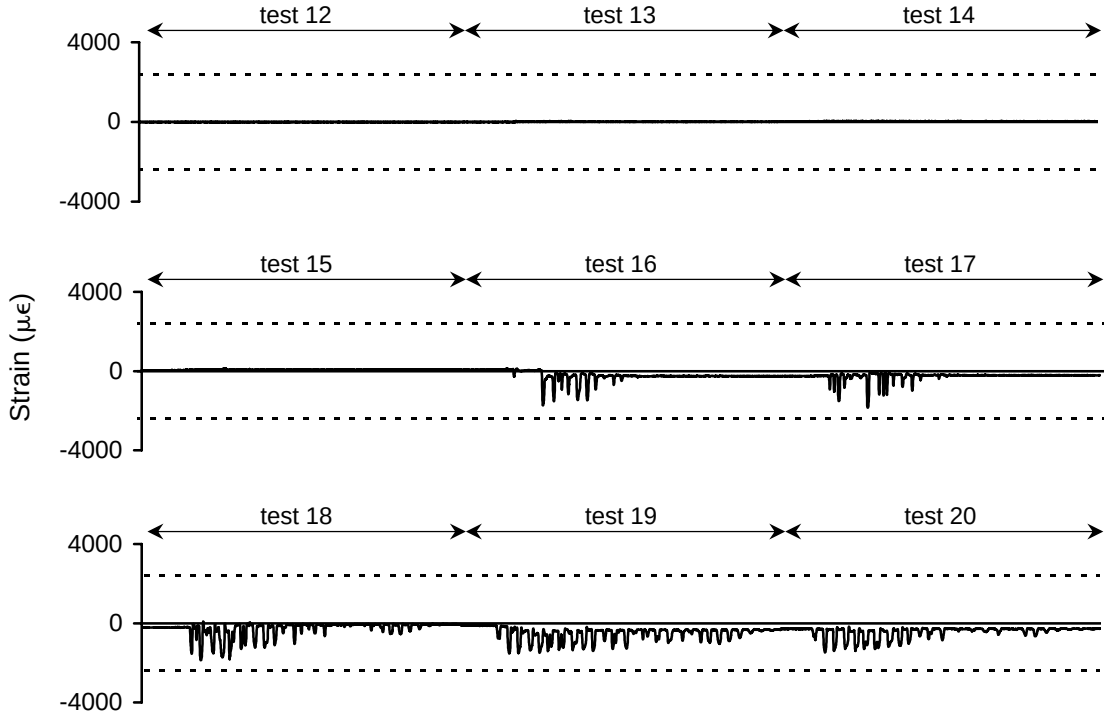

Figure A-136 Strain history for 2WBSH3 during high amplitude testing

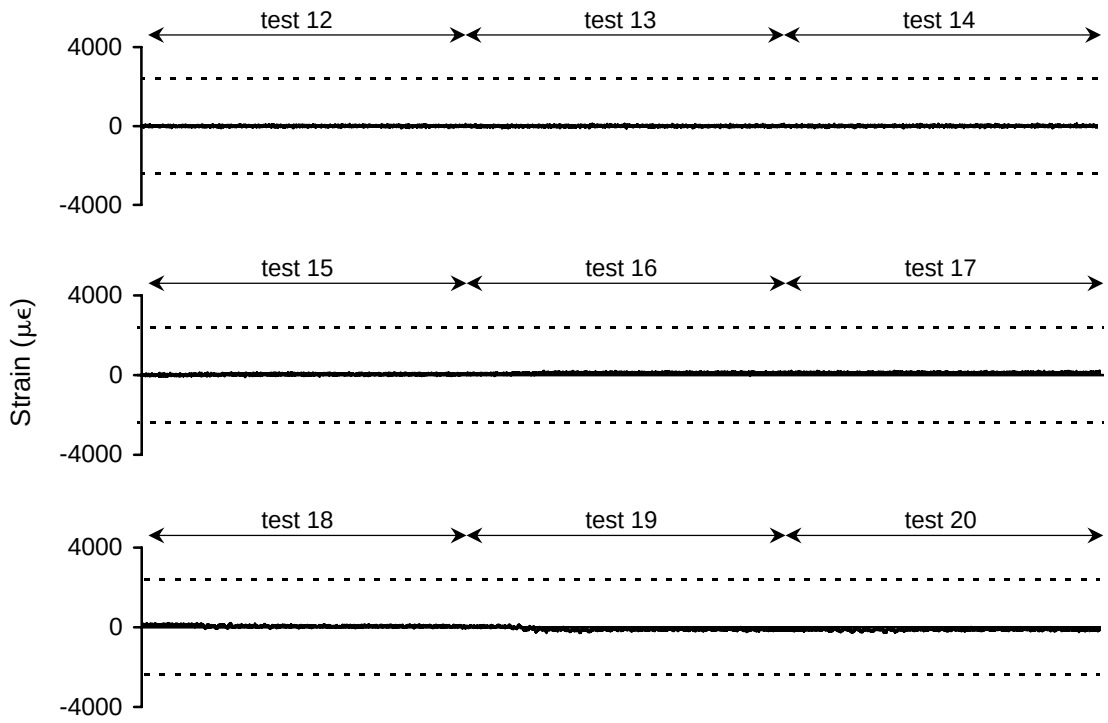

Figure A-129 Strain history for 2ETSH1 during high amplitude testing

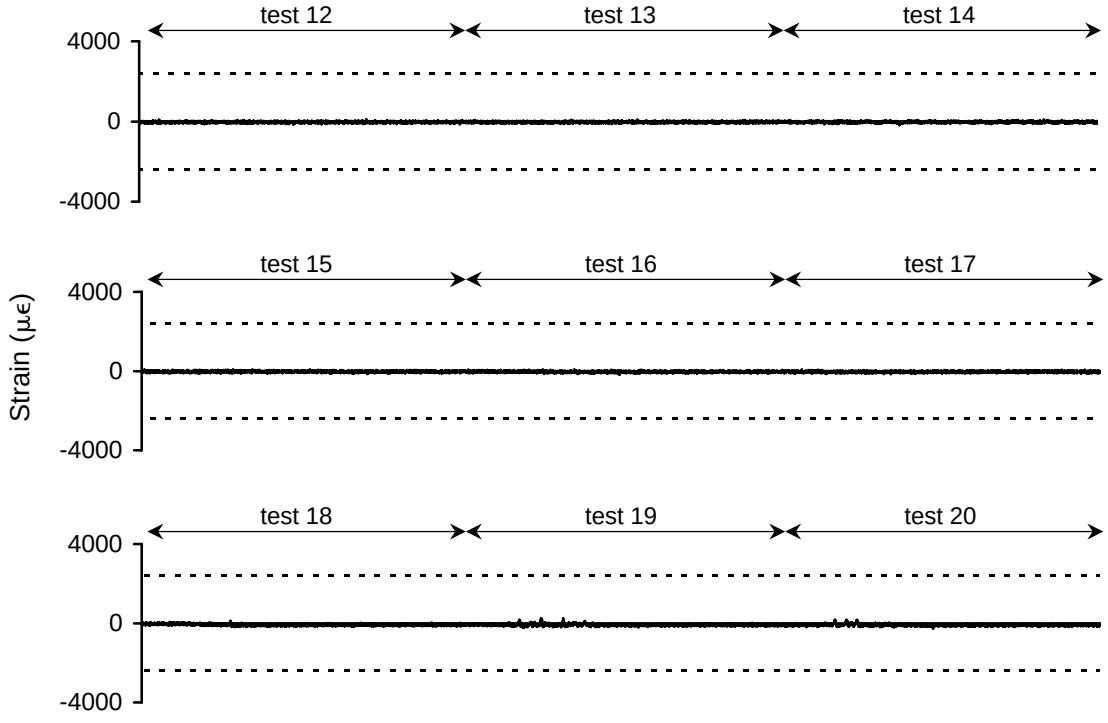

Figure A-130 Strain history for 2ETSH2 during high amplitude testing

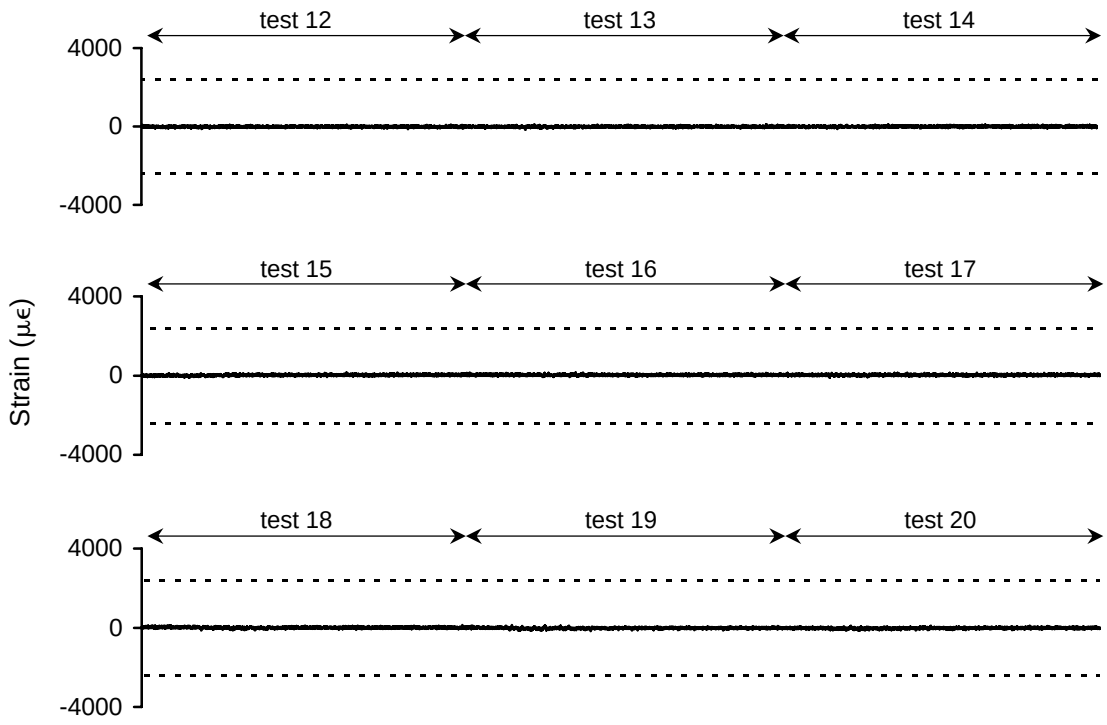

Figure A-131 Strain history for 2ETSH3 during high amplitude testing

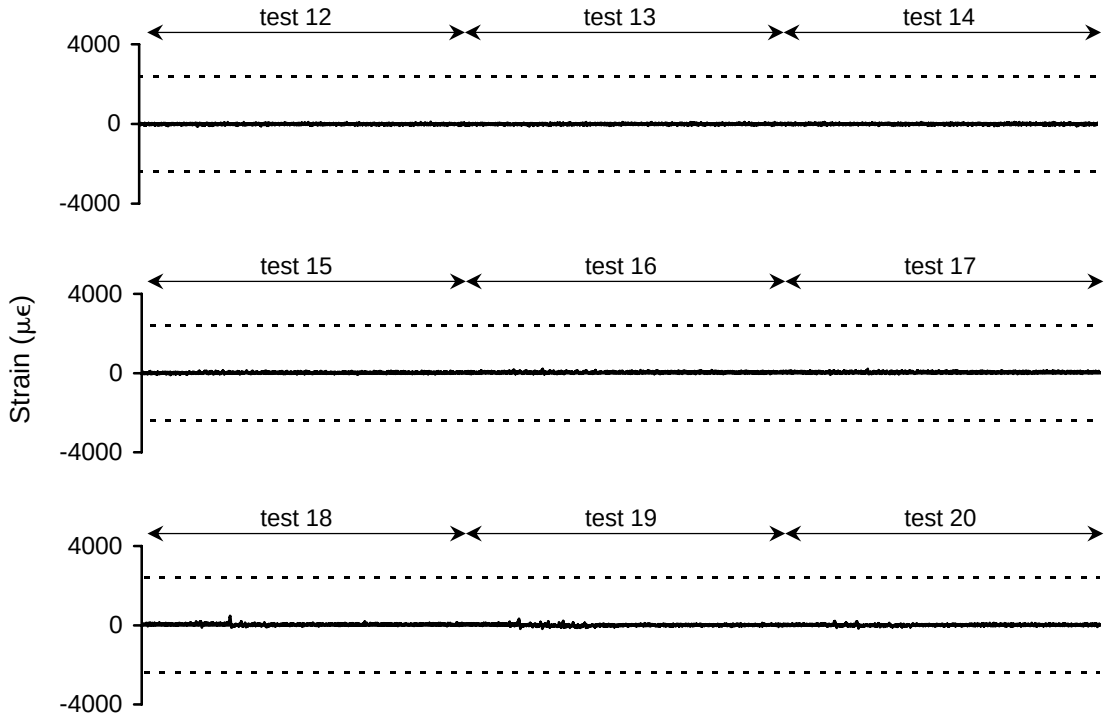

Figure A-132 Strain history for 2EBSH1 during high amplitude testing

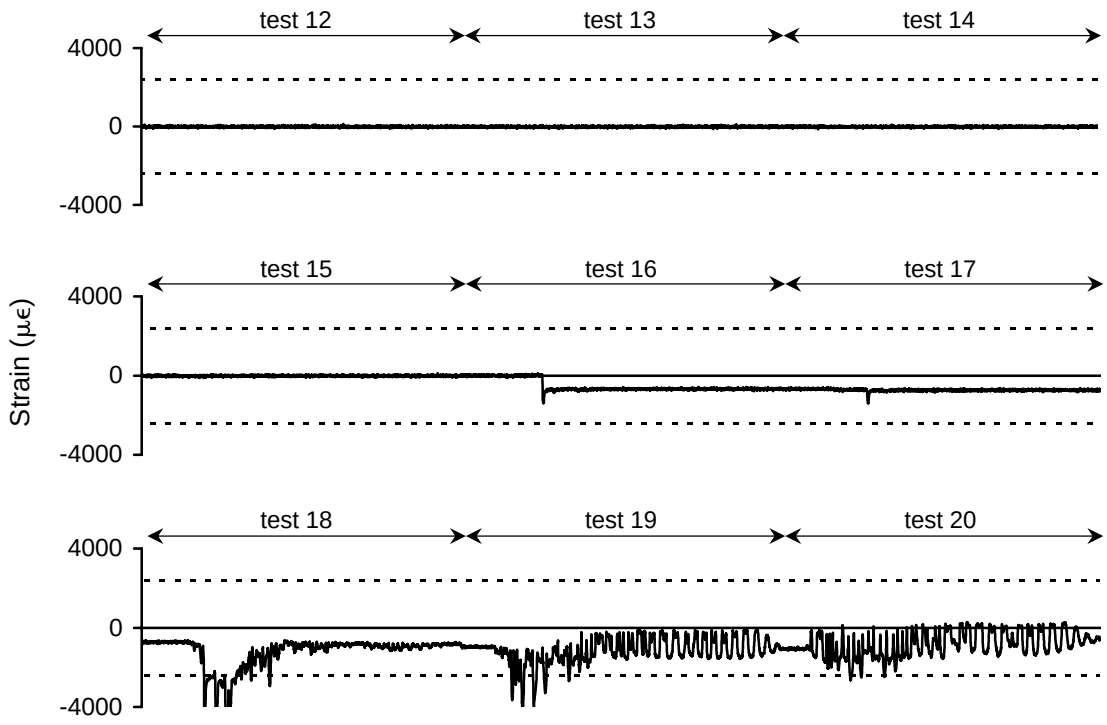

Figure A-133 Strain history for 2EBSH2 during high amplitude testing

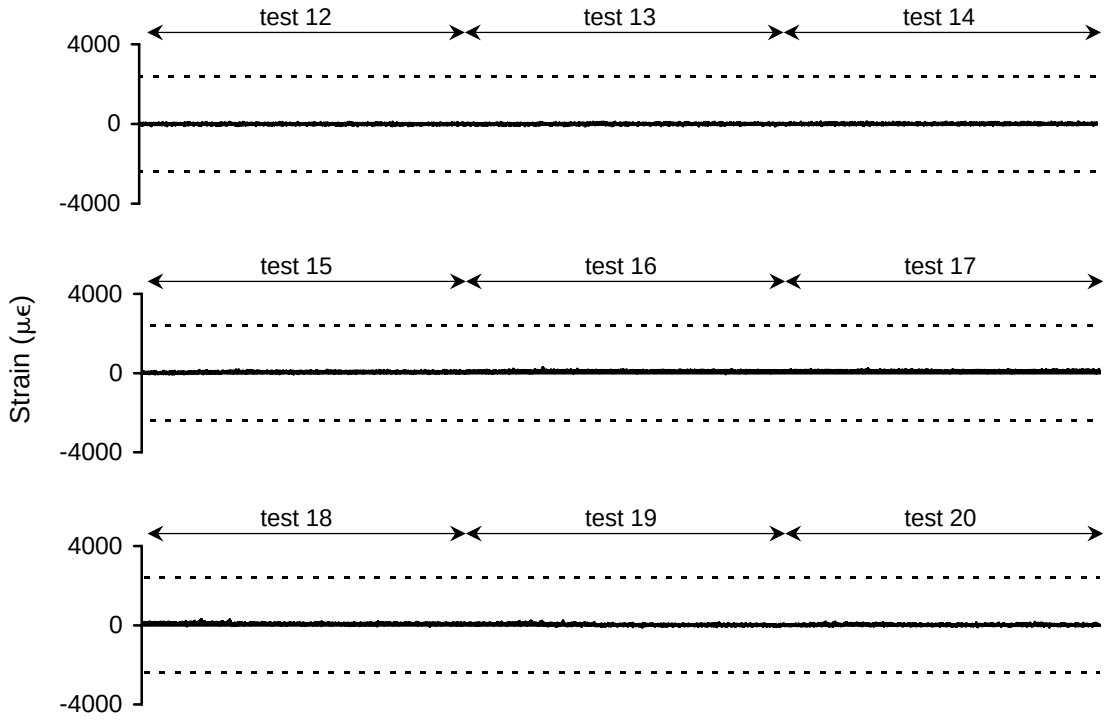

Figure A-134 Strain history for 2EBSH3 during high amplitude testing

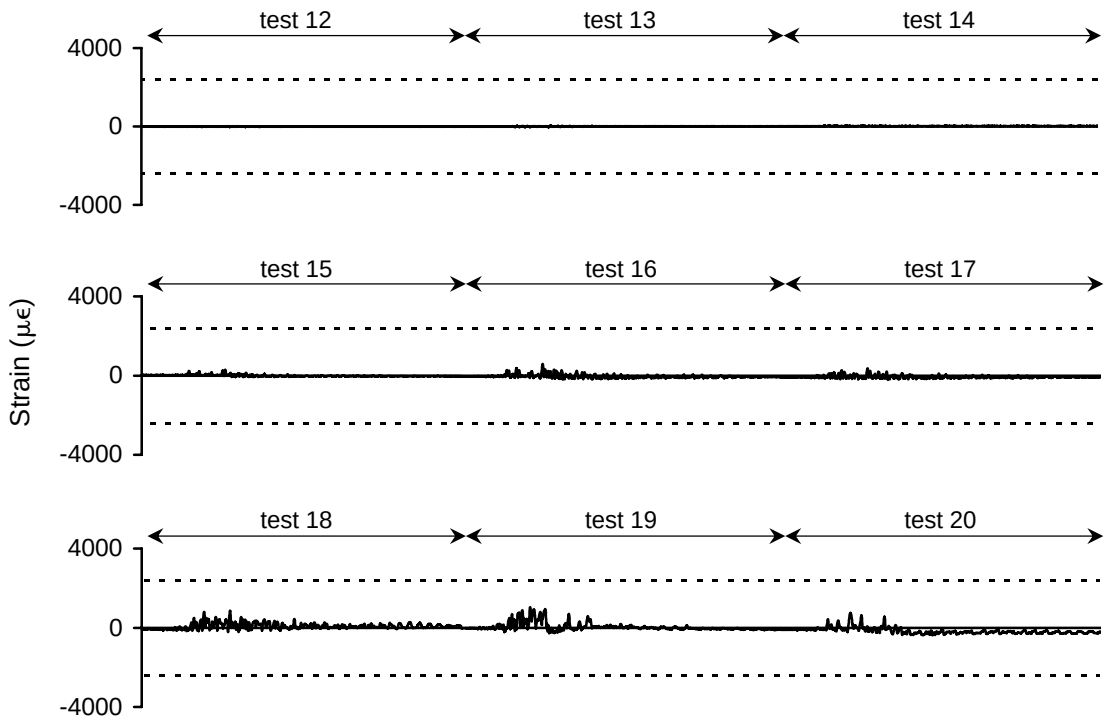

Figure A-135 Strain history for 3WTSH1 during high amplitude testing

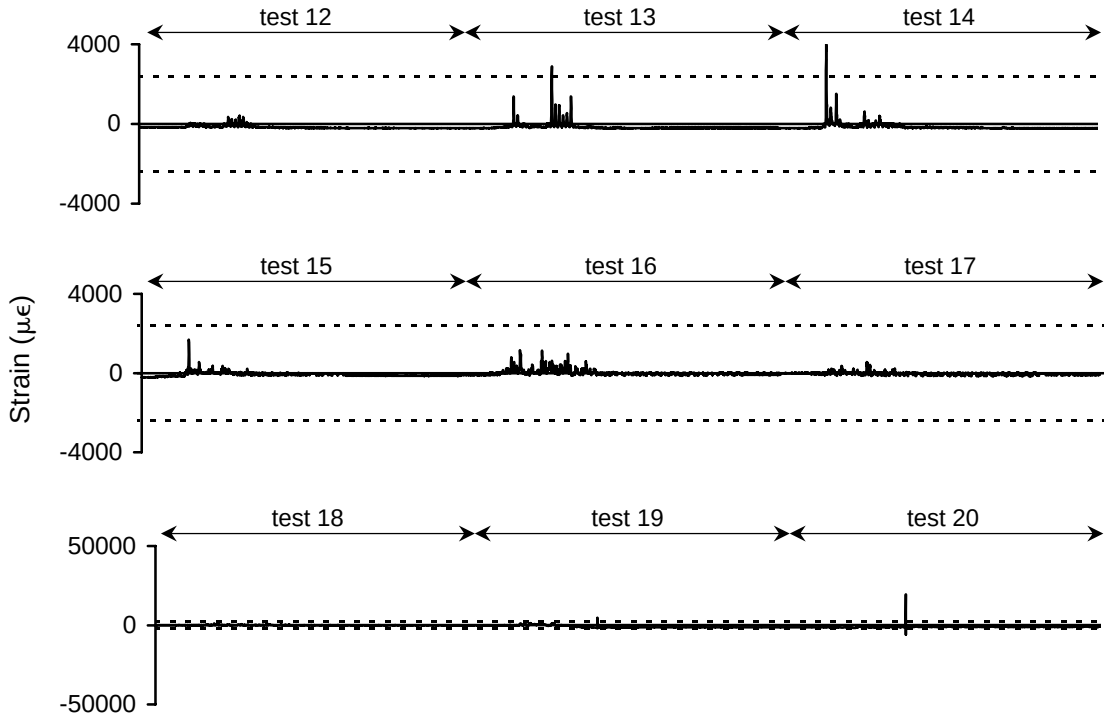

Figure A-136 Strain history for 3WTSH2 during high amplitude testing

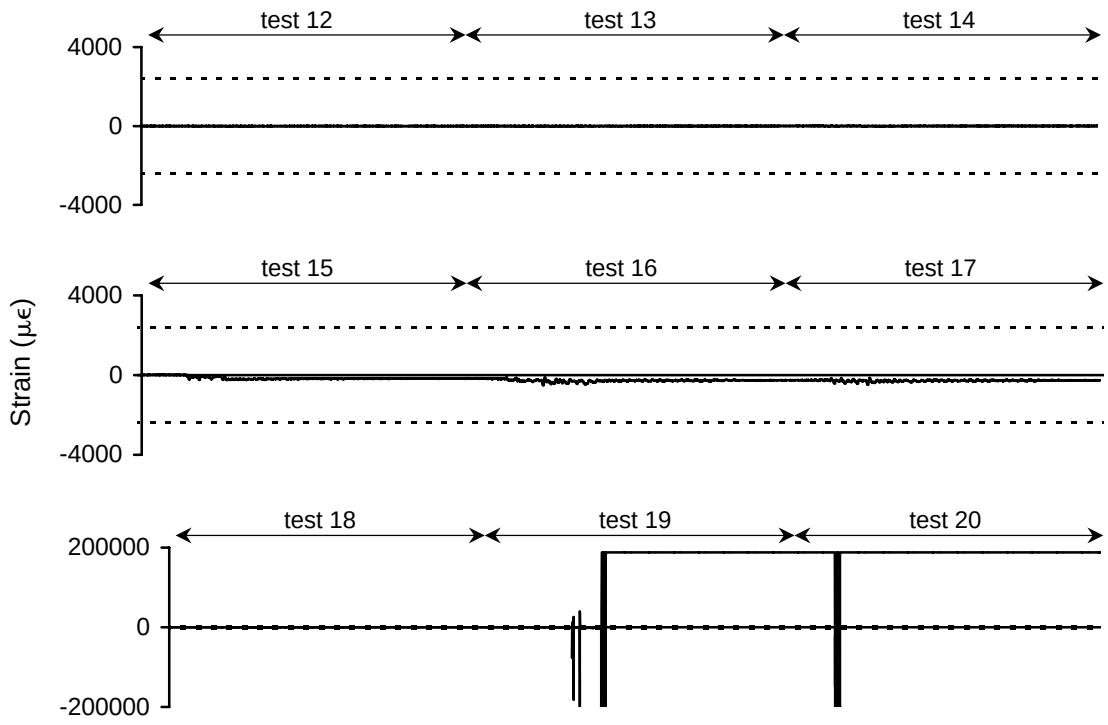

Figure A-137 Strain history for 3WTSH3 during high amplitude testing

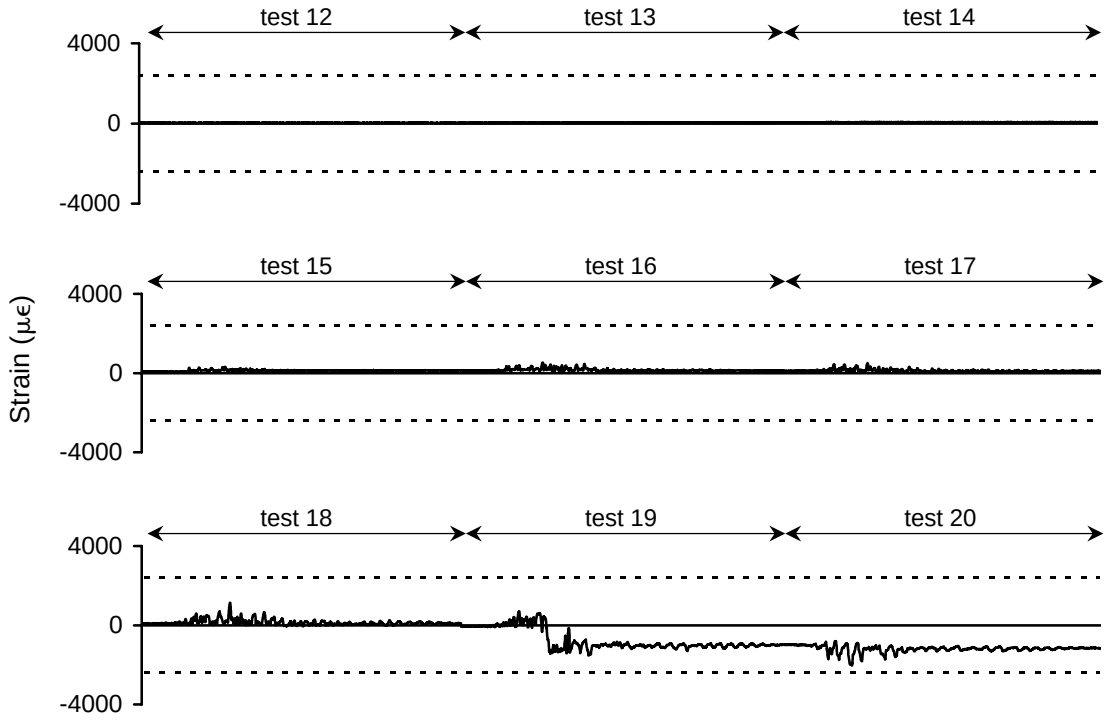

Figure A-138 Strain history for 3WTSH4 during high amplitude testing

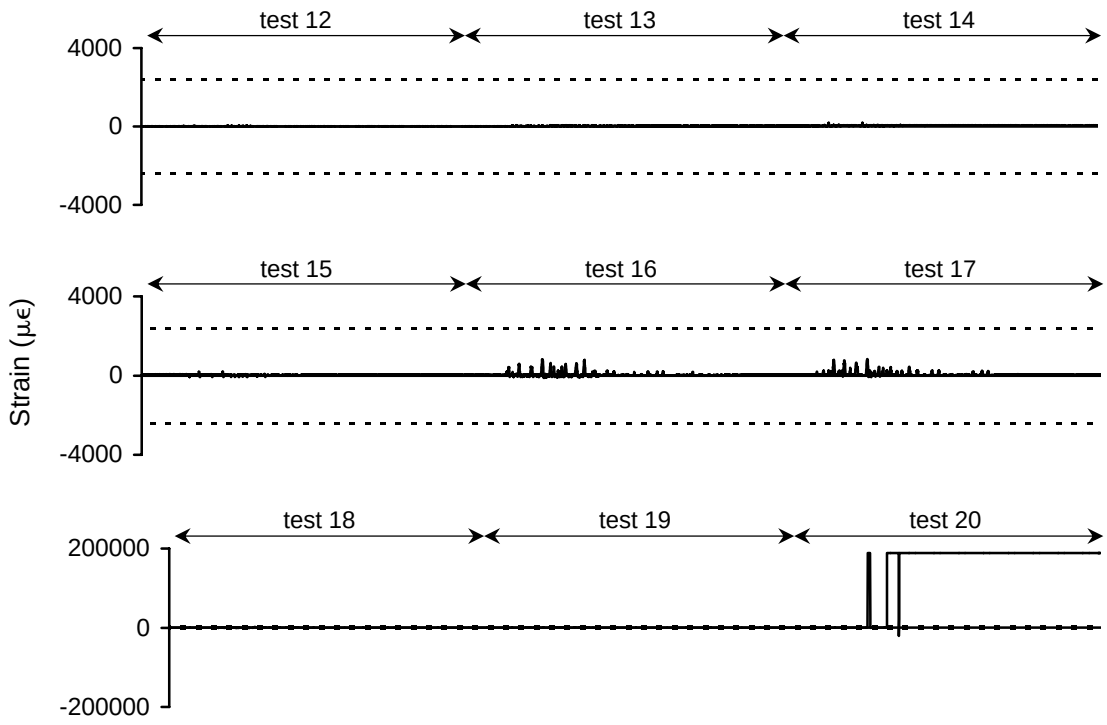

Figure A-139 Strain history for 3WTSH6 during high amplitude testing

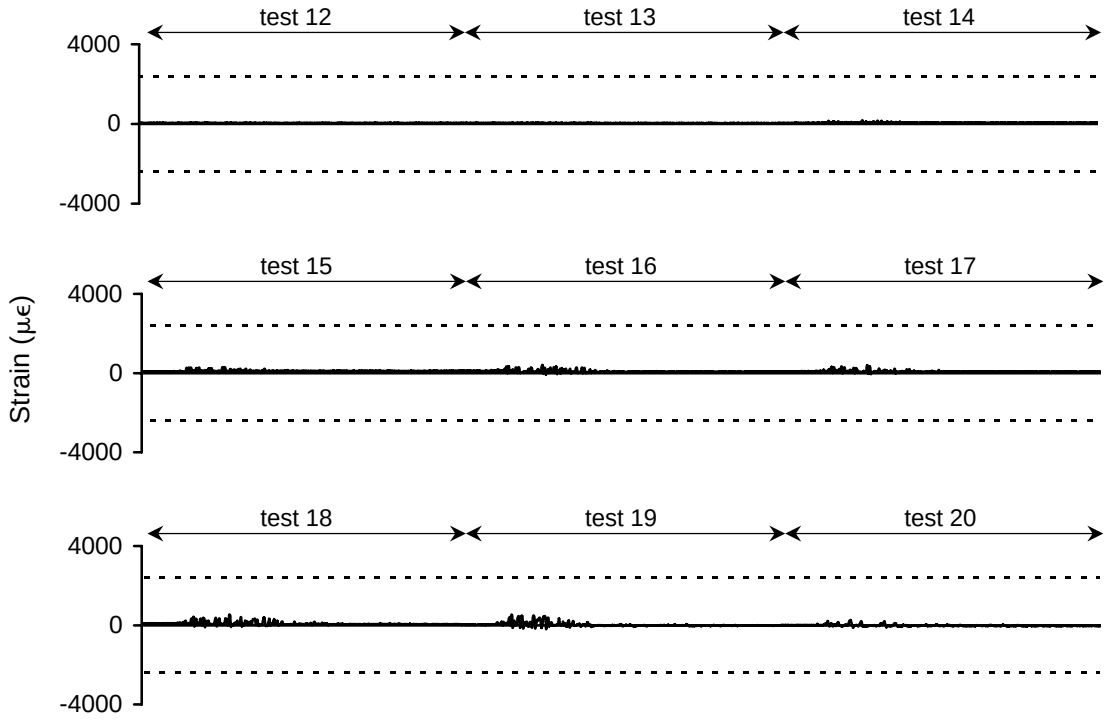

Figure A-140 Strain history for 3WTSH7 during high amplitude testing

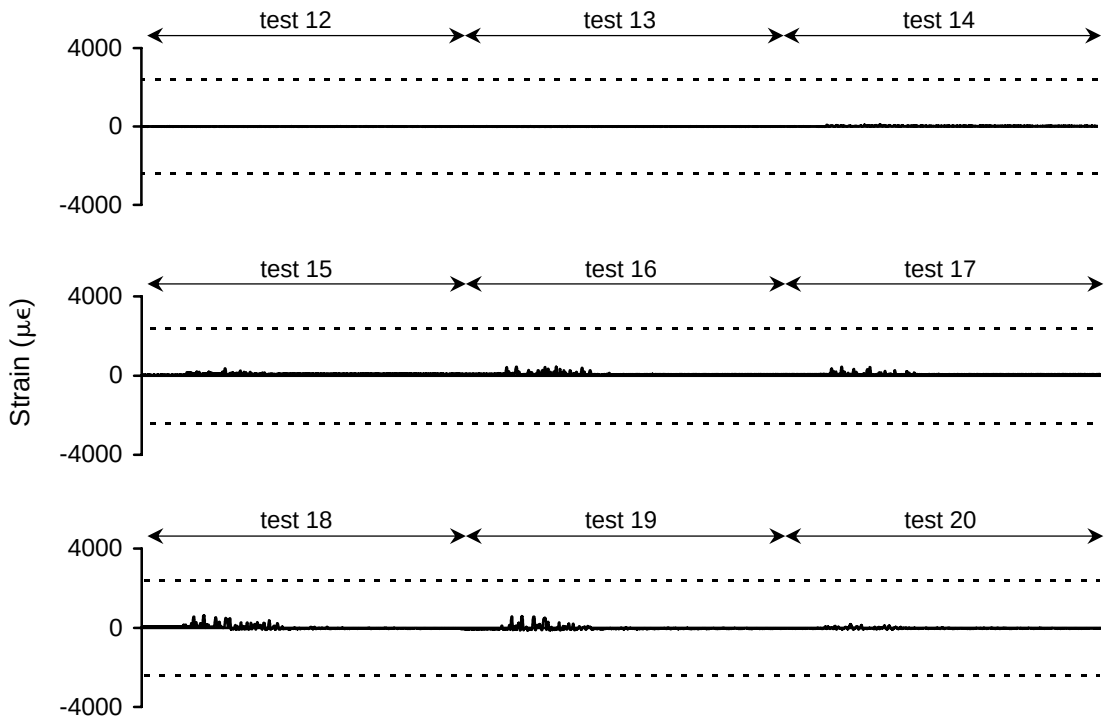

Figure A-141 Strain history for 3WBSH1 during high amplitude testing

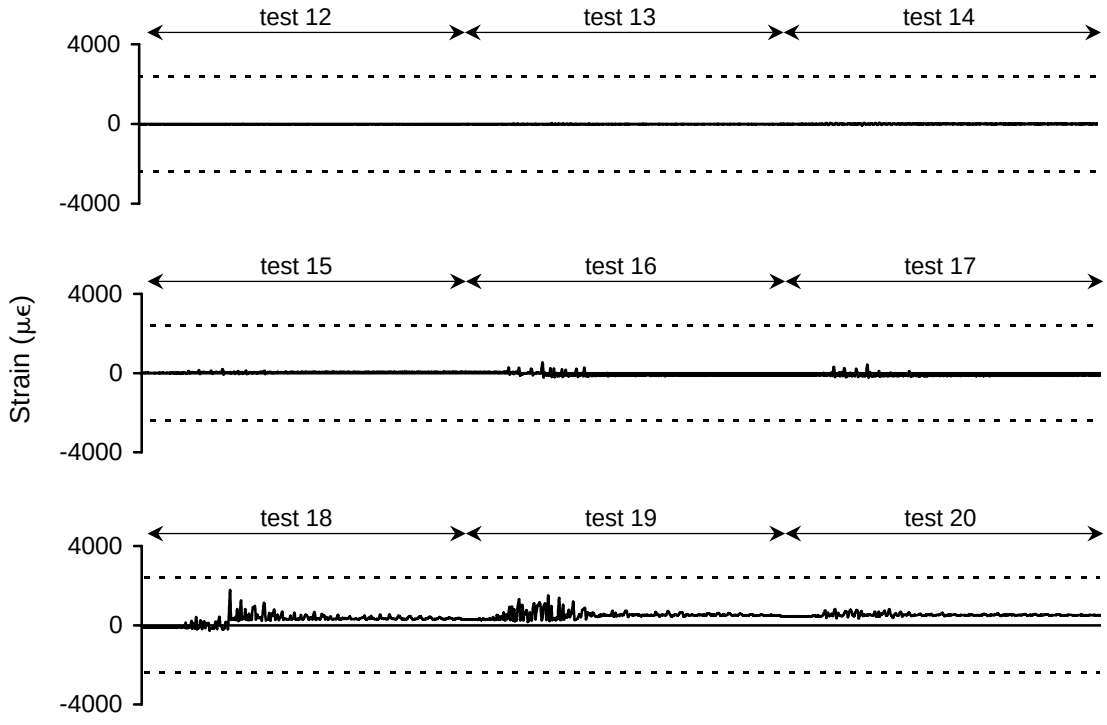

Figure A-142 Strain history for 3WBSH2 during high amplitude testing

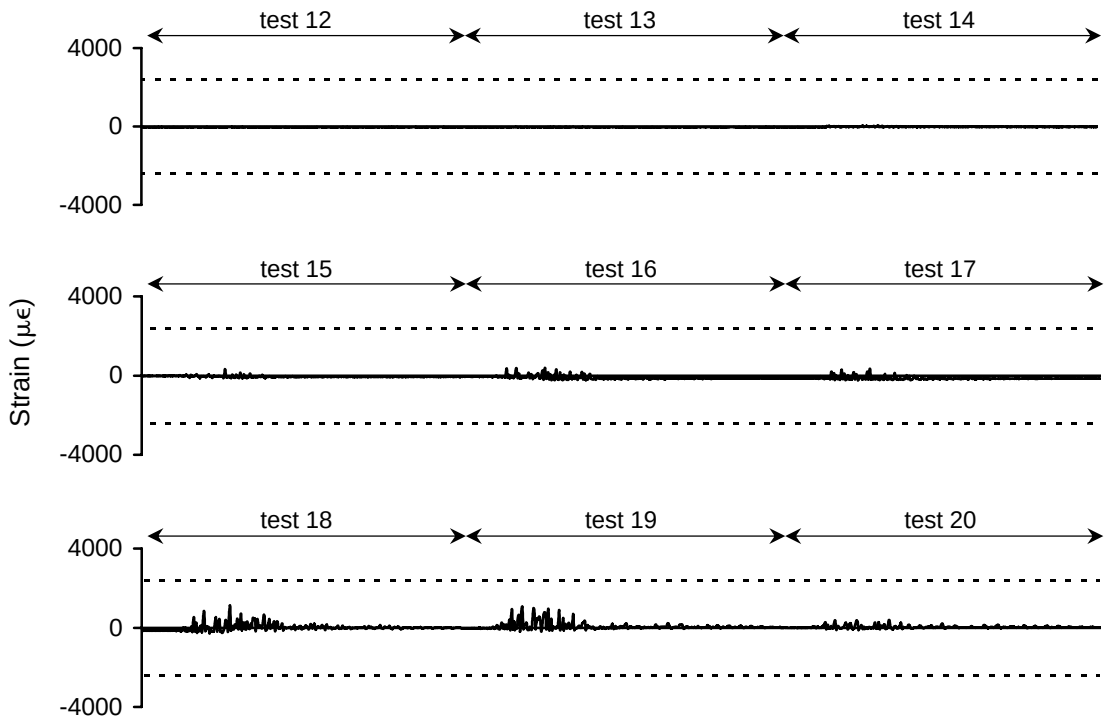

Figure A-143 Strain history for 3WBSH3 during high amplitude testing

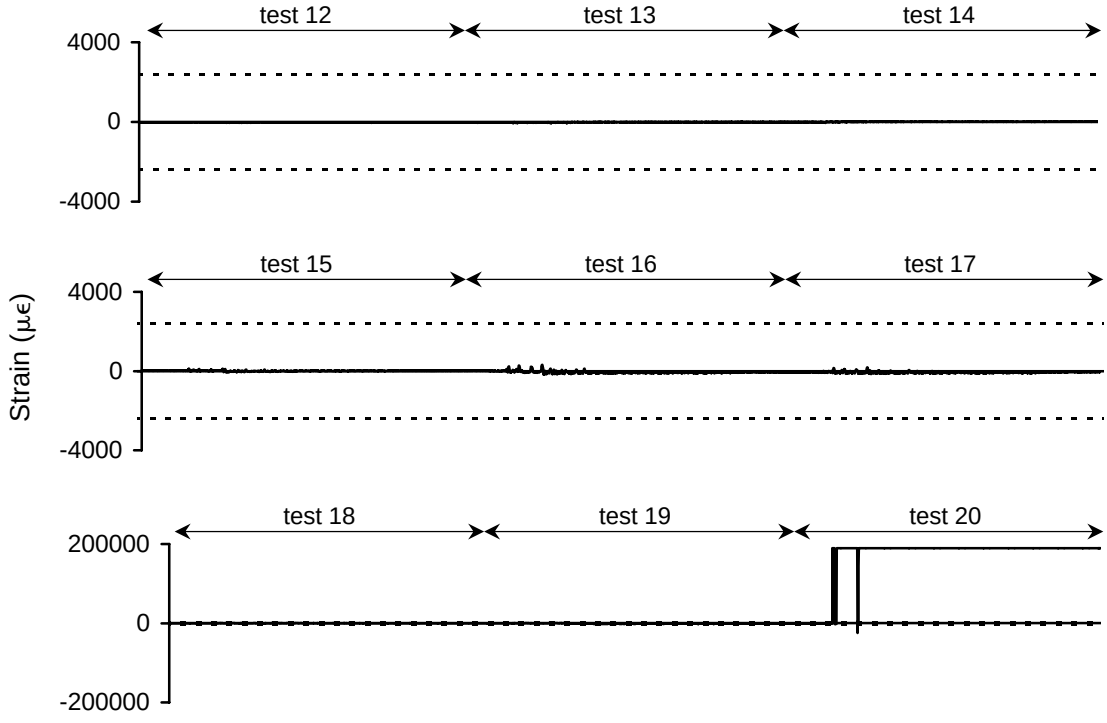

Figure A-144 Strain history for 3WBSH4 during high amplitude testing

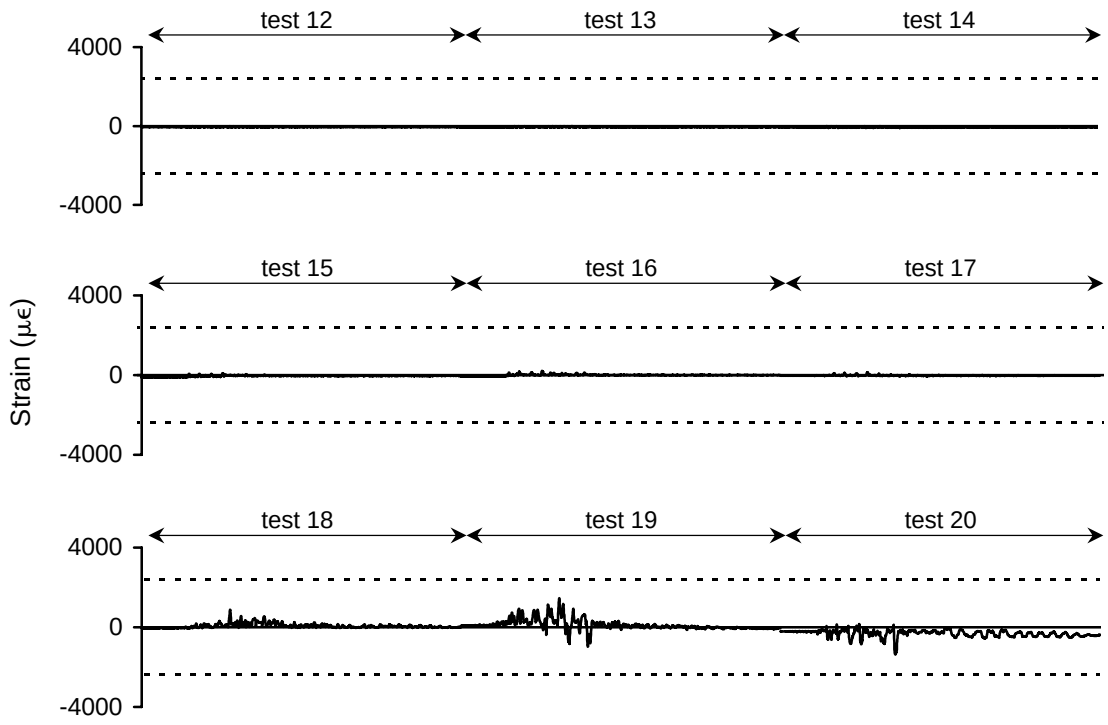

Figure A-145 Strain history for 3WBSH5 during high amplitude testing

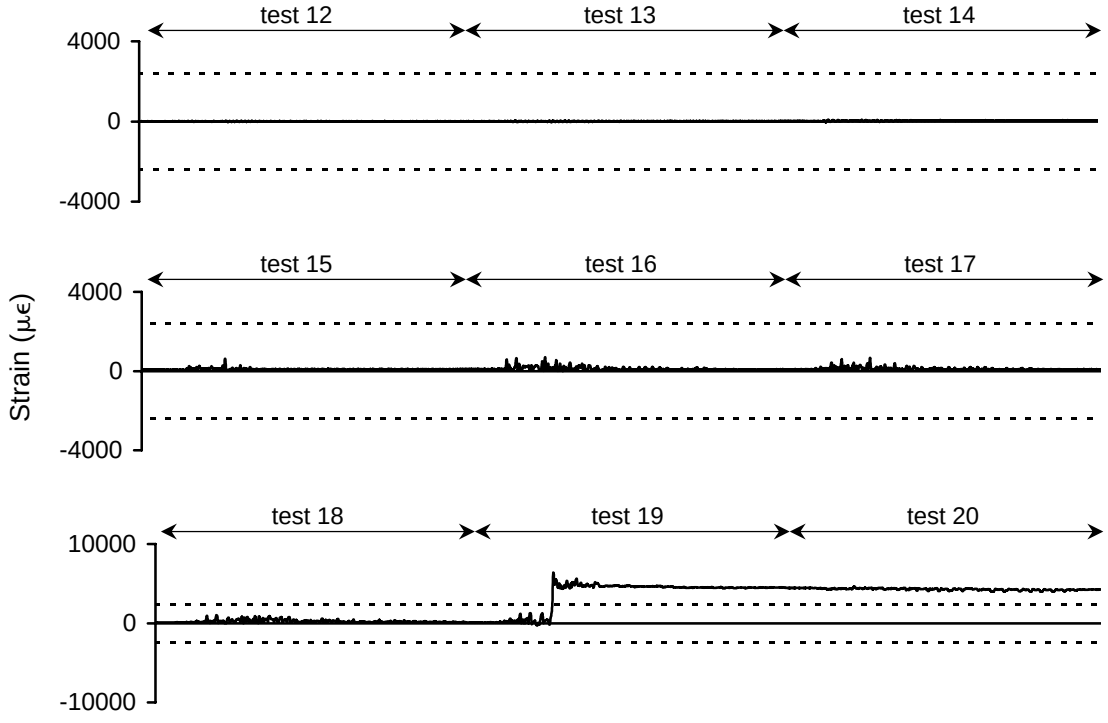

Figure A-146 Strain history for 3WBSH6 during high amplitude testing

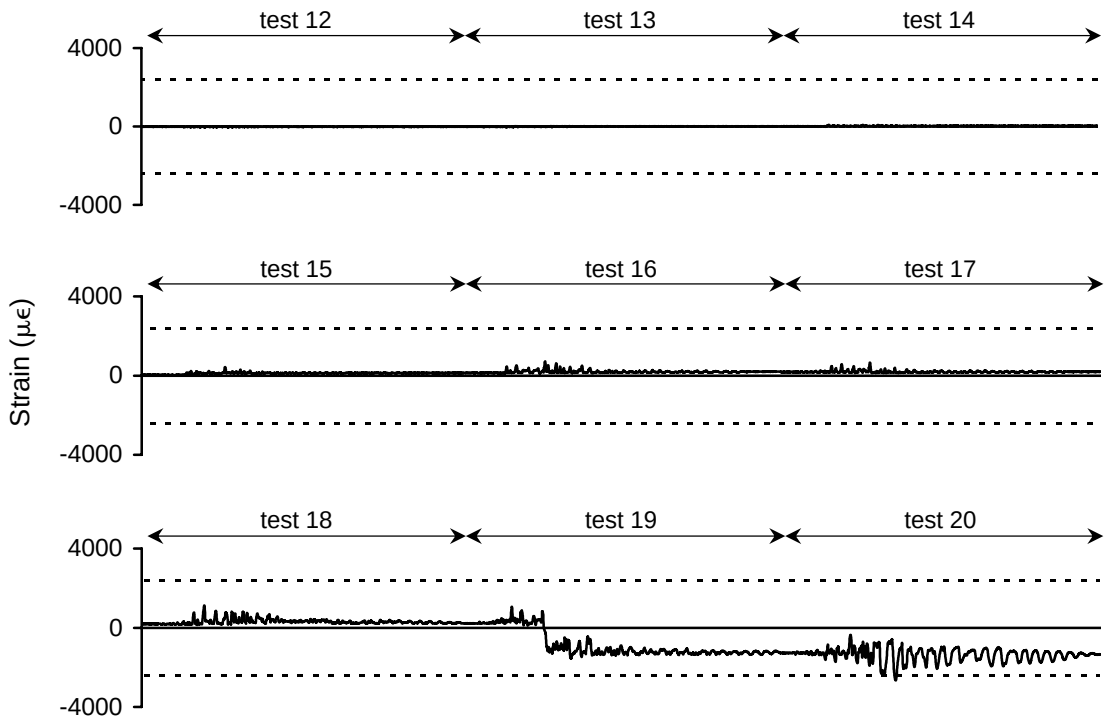

Figure A-147 Strain history for 3WBSH7 during high amplitude testing

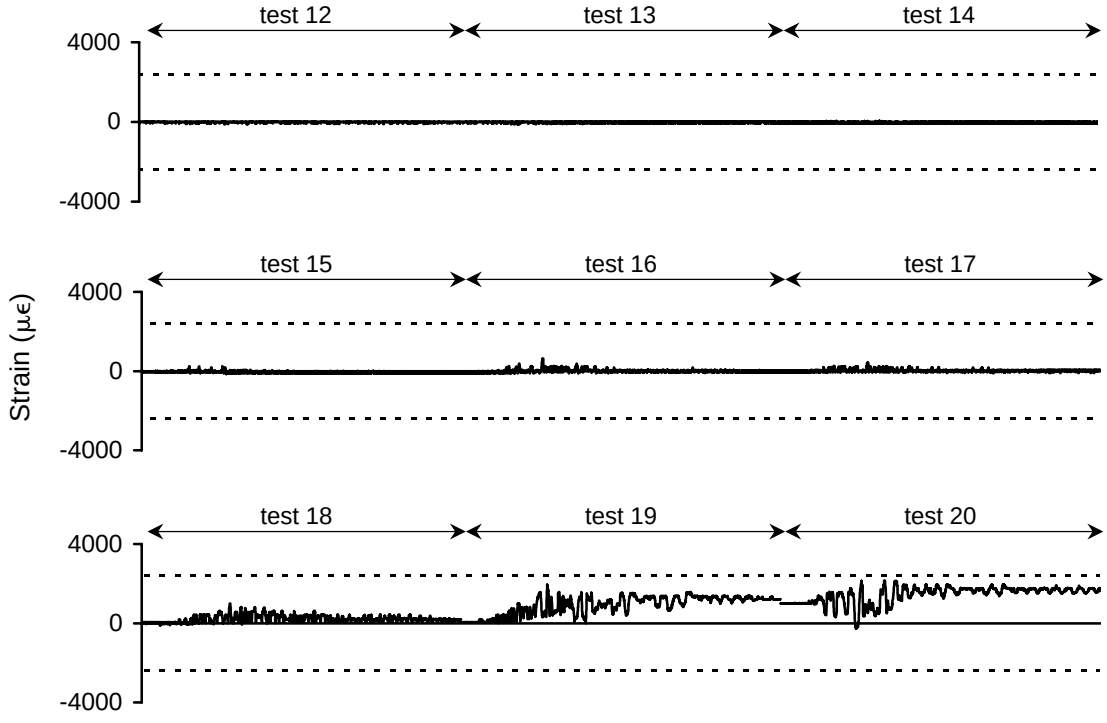

Figure A-148 Strain history for 3ETSH1 during high amplitude testing

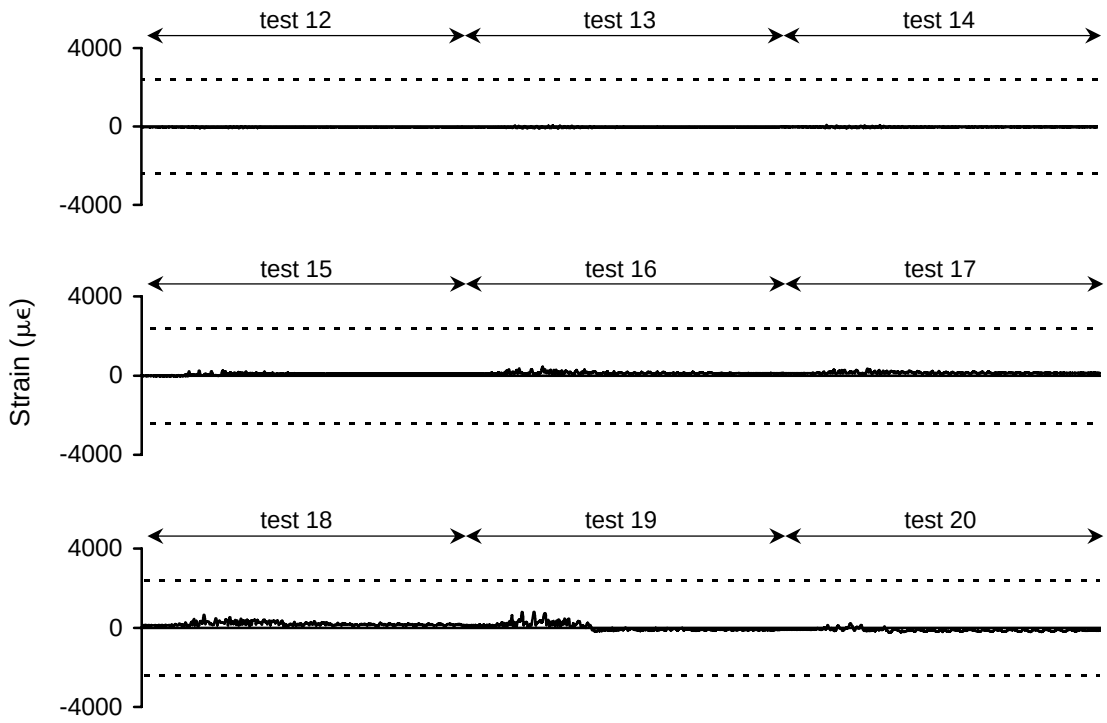

Figure A-149 Strain history for 3ETSH2 during high amplitude testing

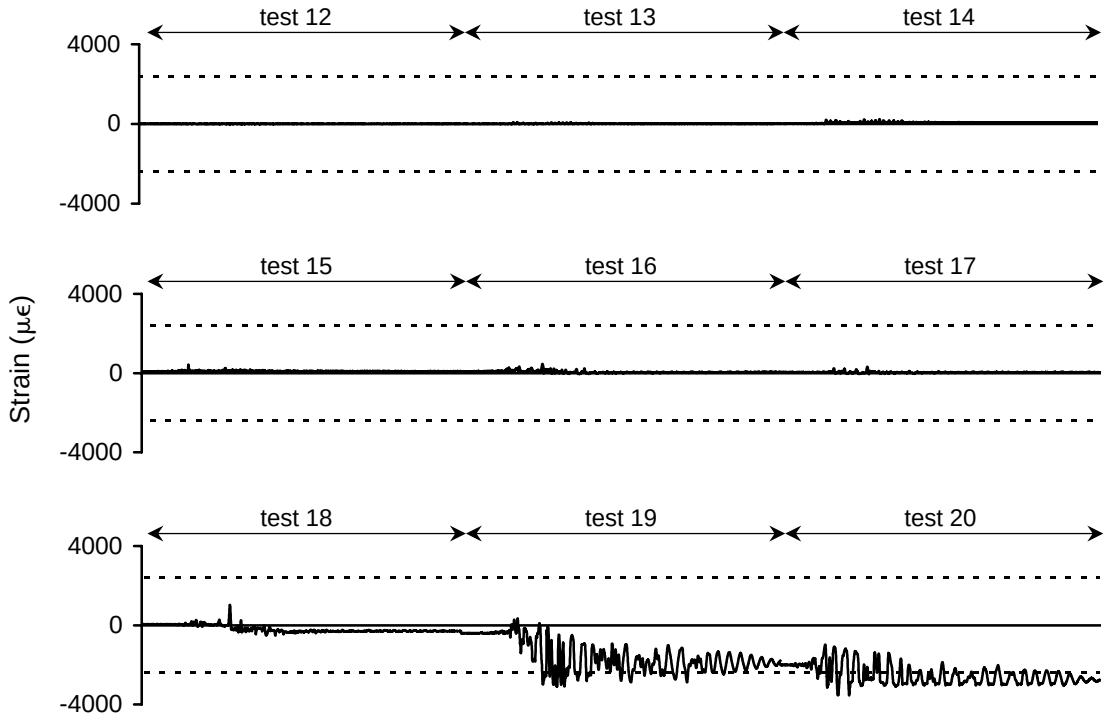

Figure A-150 Strain history for 3ETSH3 during high amplitude testing

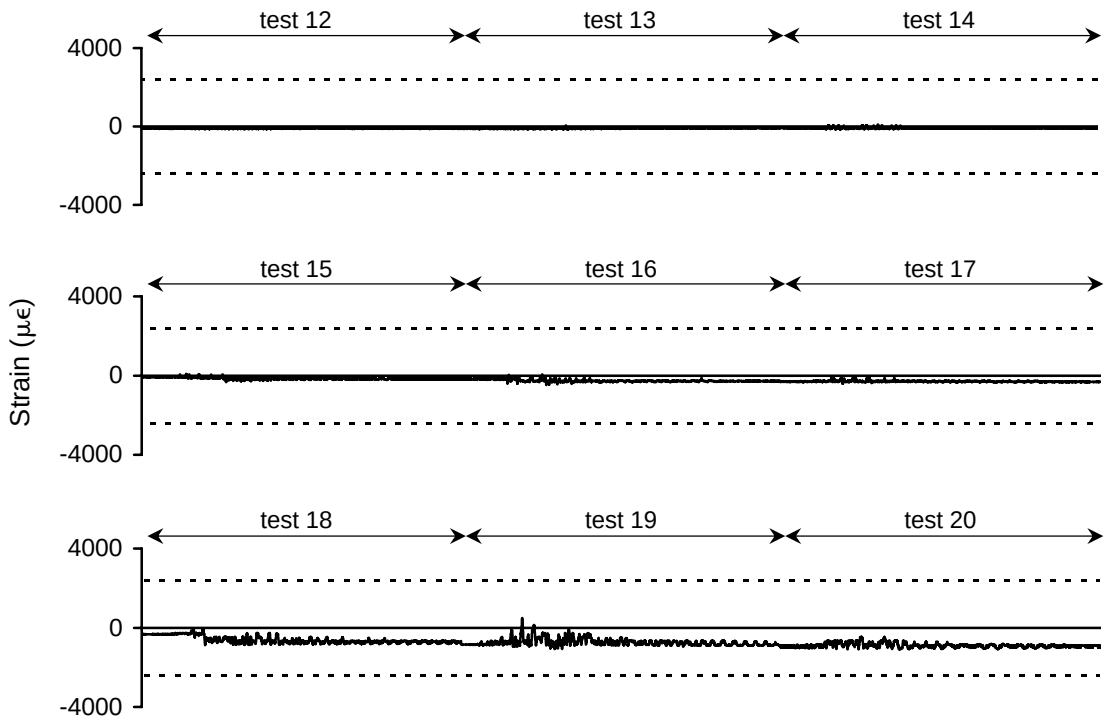

Figure A-151 Strain history for 3ETSH4 during high amplitude testing

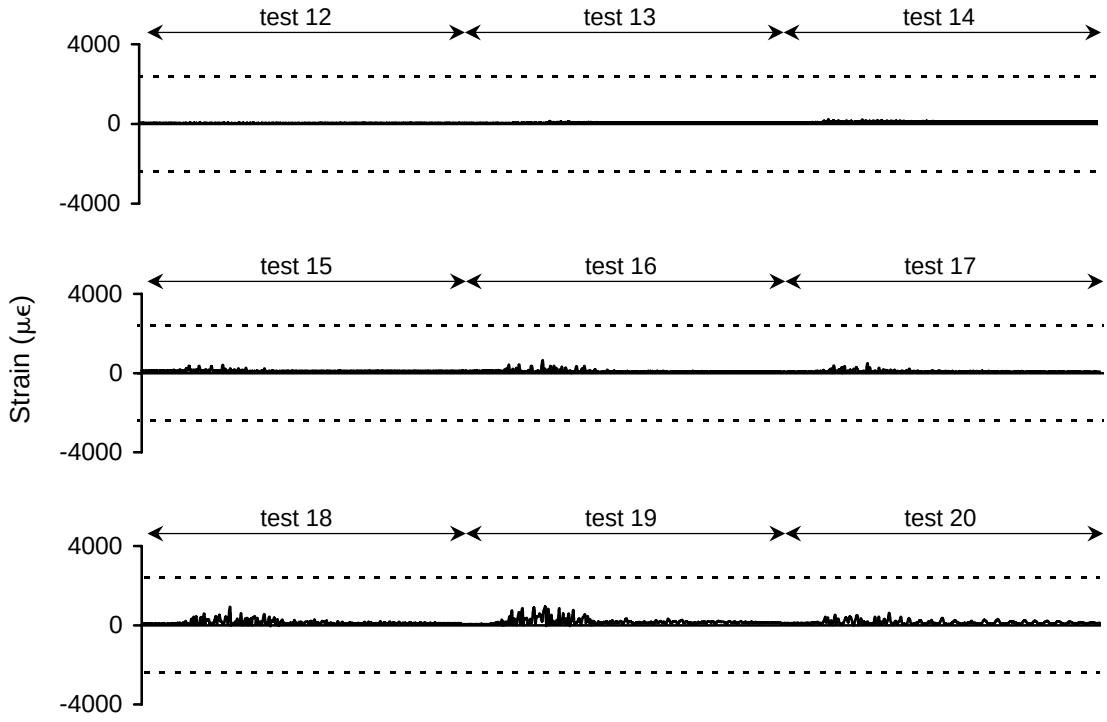

Figure A-152 Strain history for 3ETSH5 during high amplitude testing

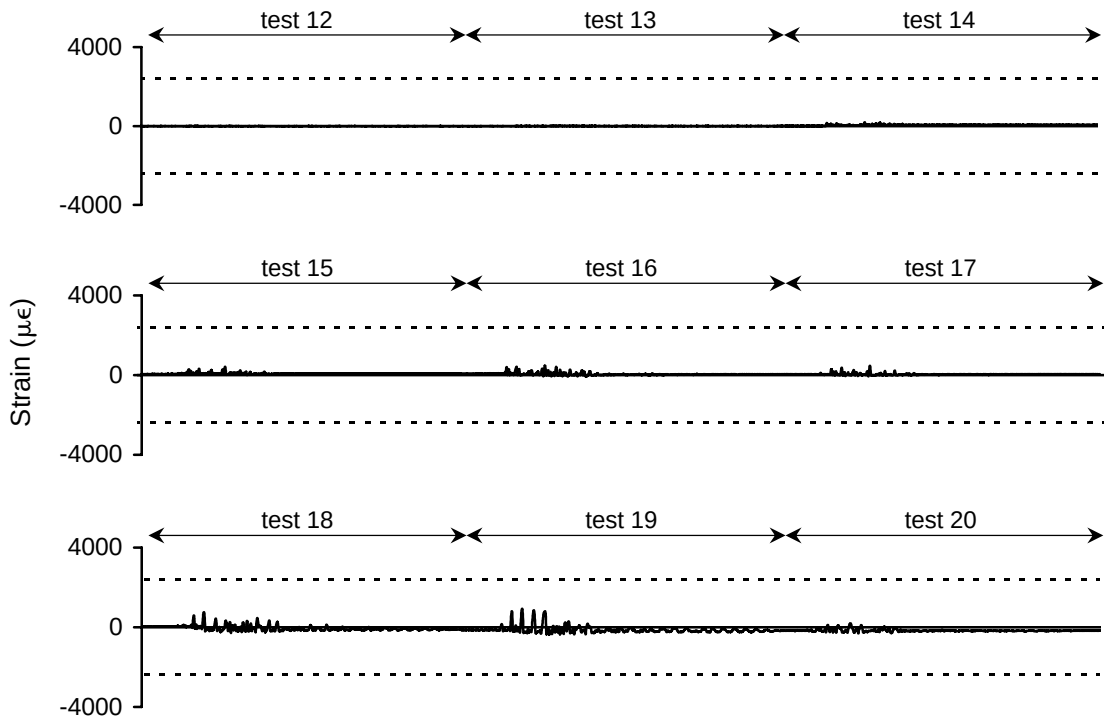

Figure A-153 Strain history for 3ETSH6 during high amplitude testing

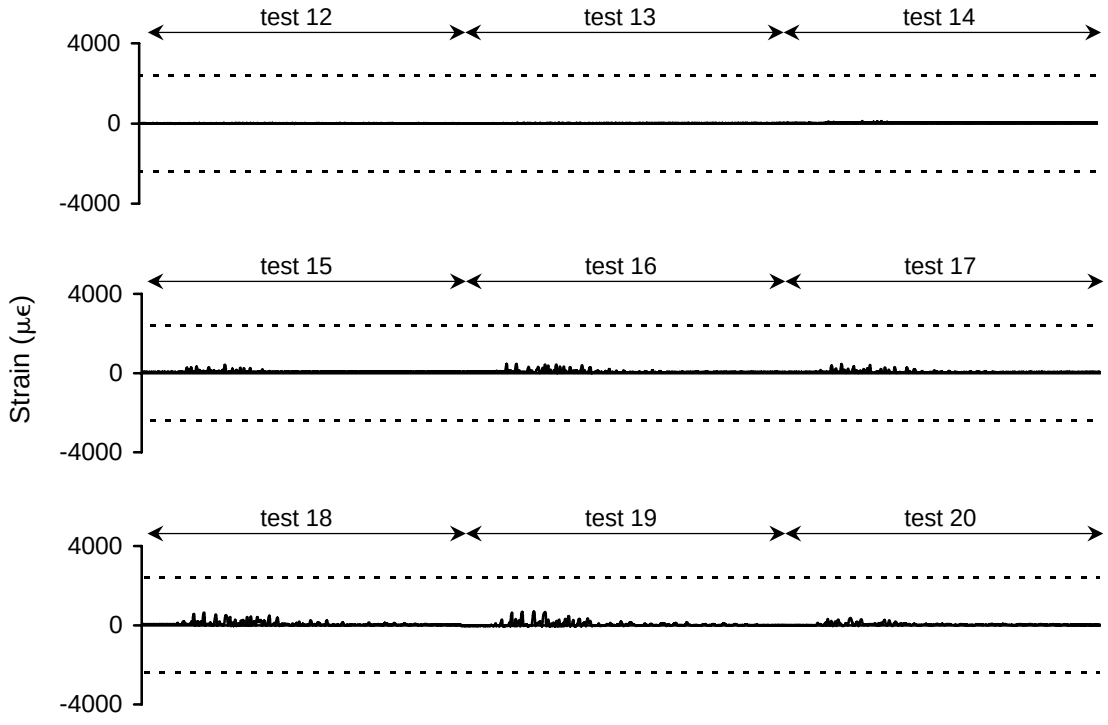

Figure A-154 Strain history for 3ETSH7 during high amplitude testing

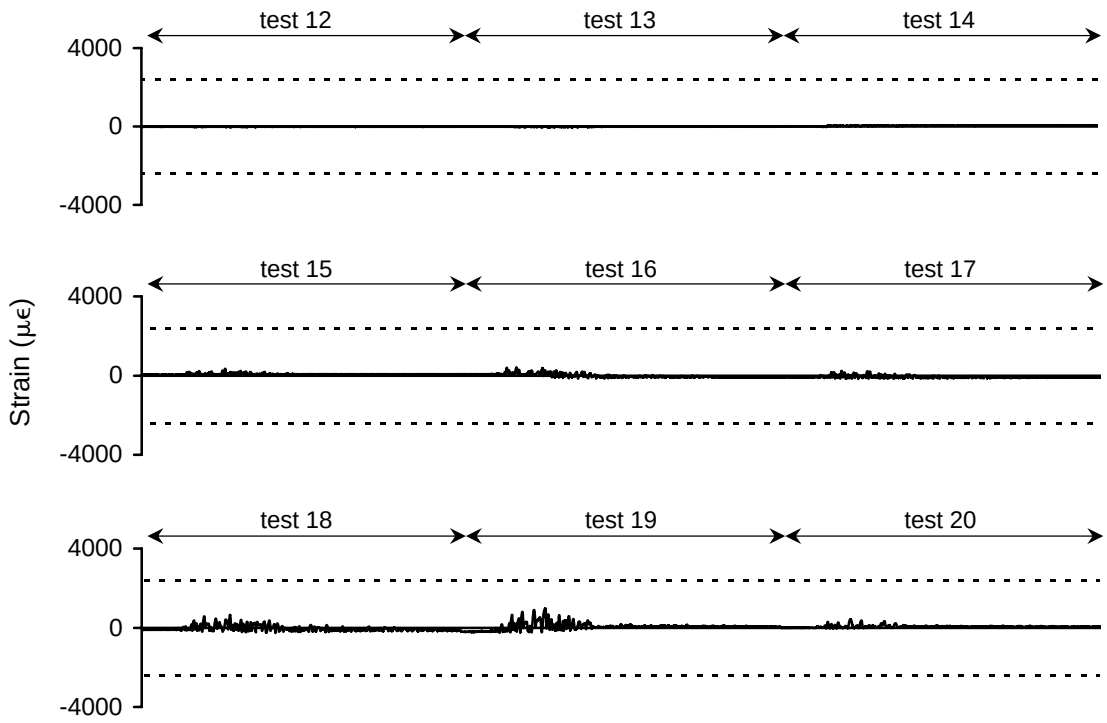

Figure A-155 Strain history for 3EBSH2 during high amplitude testing

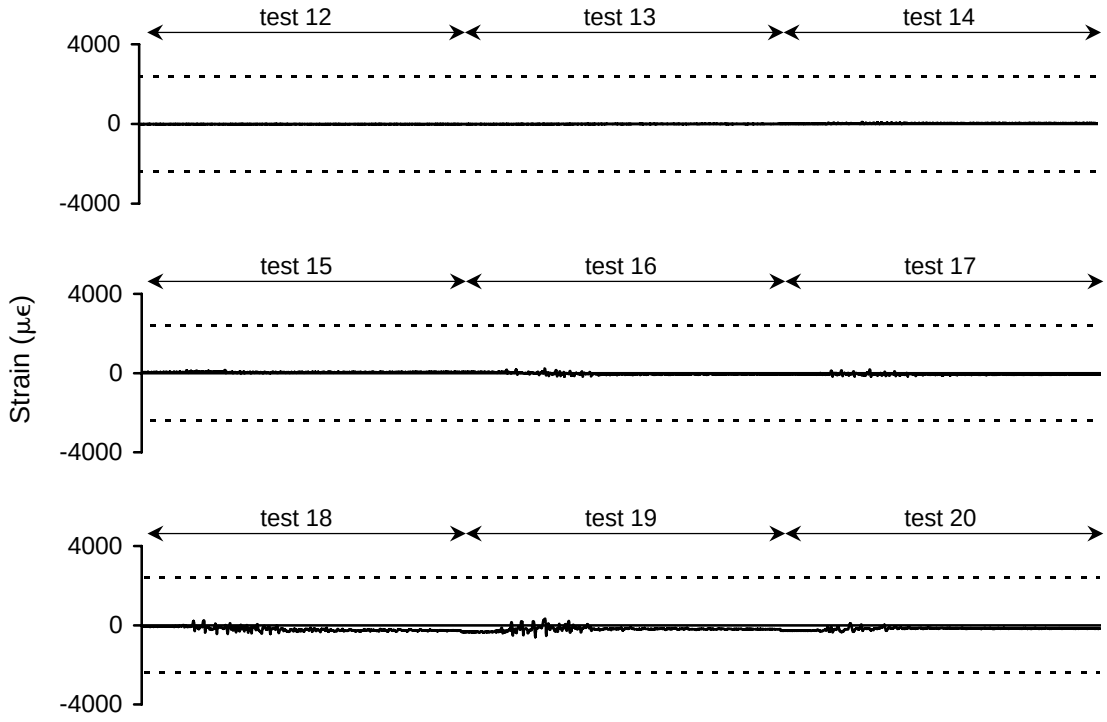

Figure A-156 Strain history for 3EBSH3 during high amplitude testing

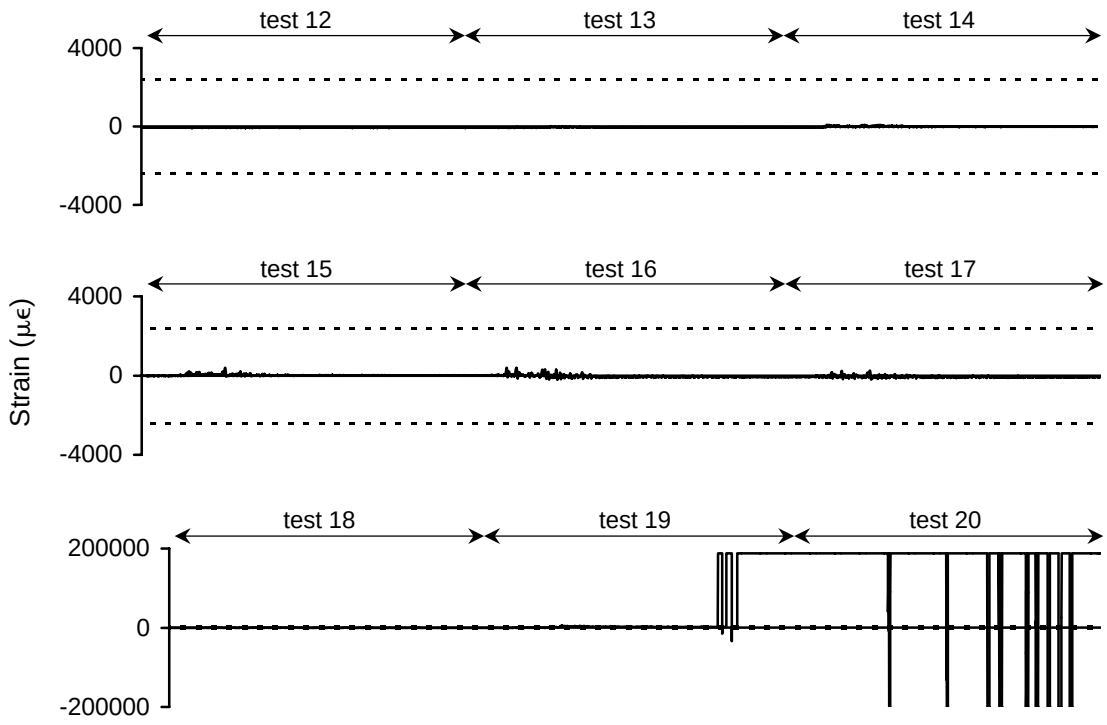

Figure A-157 Strain history for 3EBSH4 during high amplitude testing

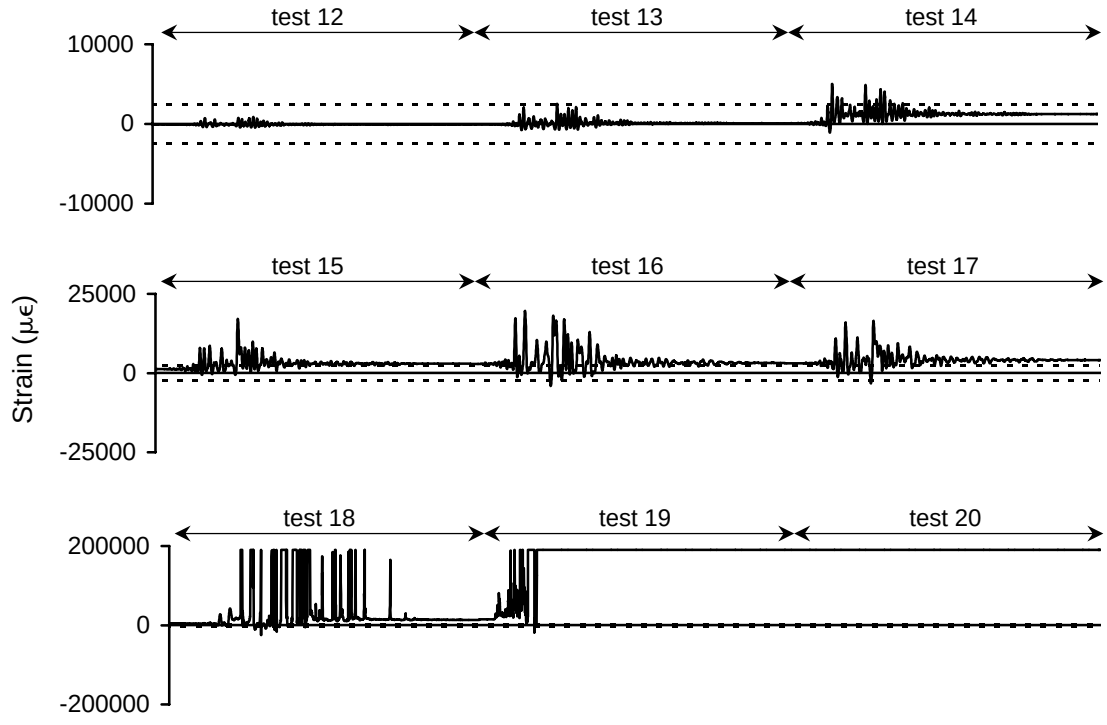

Figure A-158 Strain history for 3EBSH5 during high amplitude testing

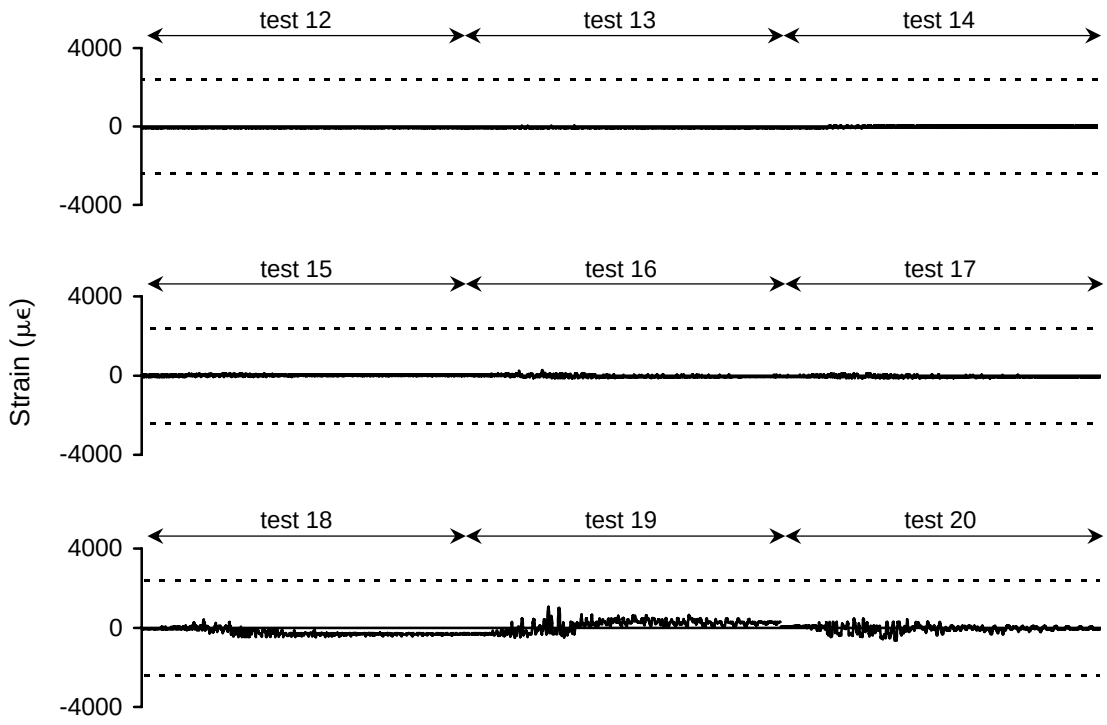

Figure A-159 Strain history for 3EBSH6 during high amplitude testing

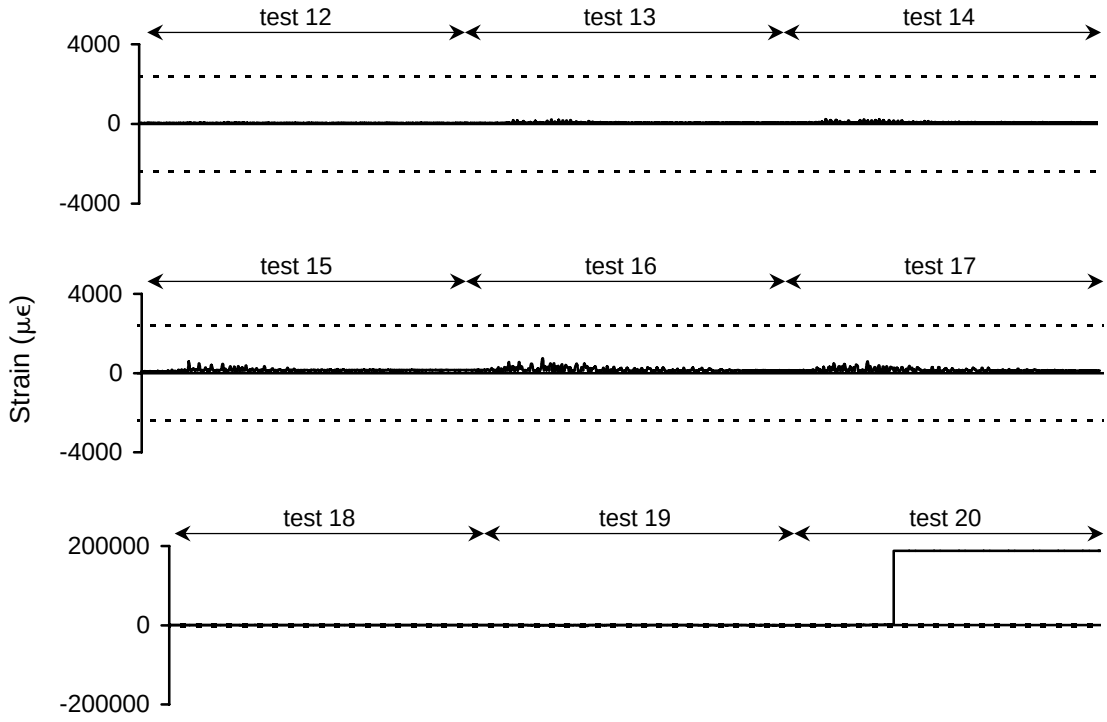

Figure A-160 Strain history for 3EBSH7 during high amplitude testing

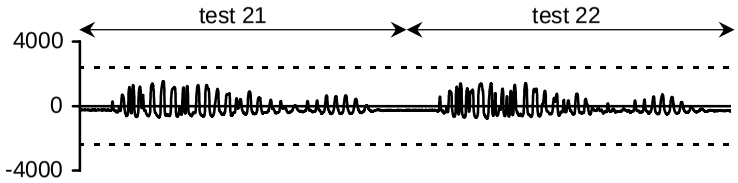

Figure A-161 Post-Test strain history for 1WTSL1

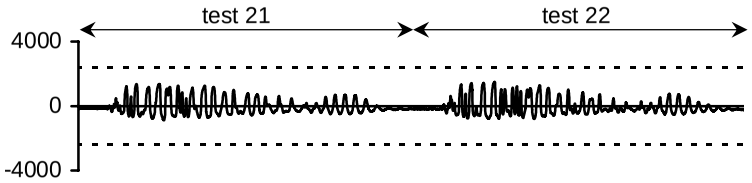

Figure A-162 Post-Test strain history for 1WTSL2

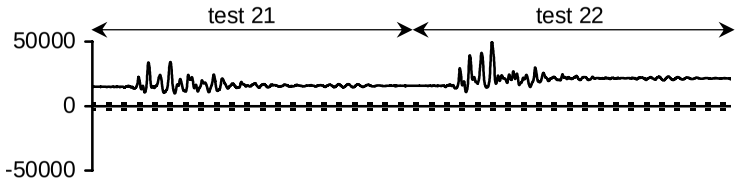

Figure A-163 Post-Test strain history for 1WTSL3

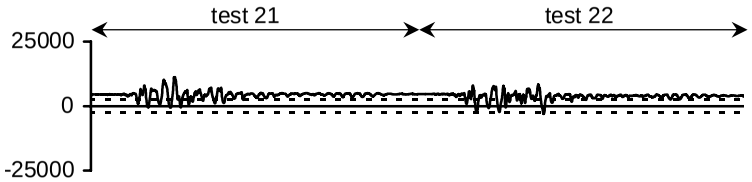

Figure A-164 Post-Test strain history for 1WTSL4

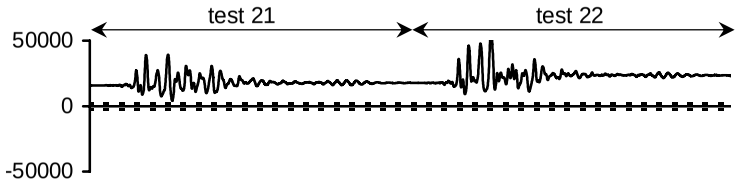

Figure A-165 Post-Test strain history for 1WTSL5

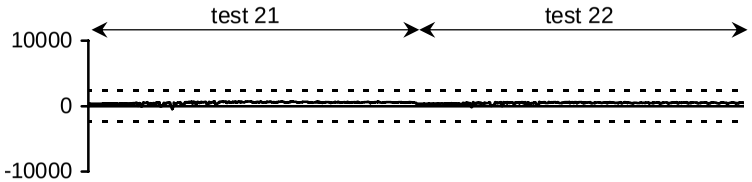

Figure A-166 Post-Test strain history for 1WTSL6

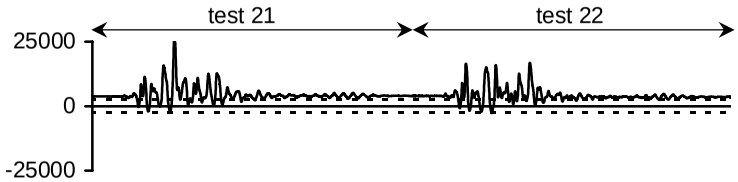

Figure A-167 Post-Test strain history for 1WTSL7

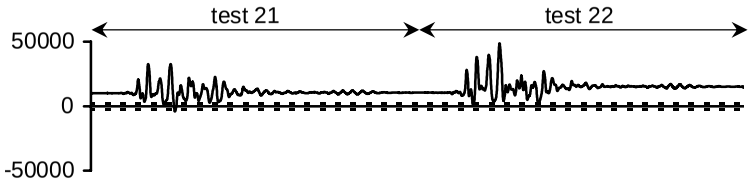

Figure A-168 Post-Test strain history for 1WTSL8

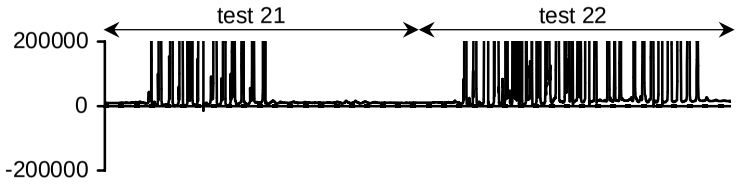

Figure A-169 Post-Test strain history for 1WBSL1

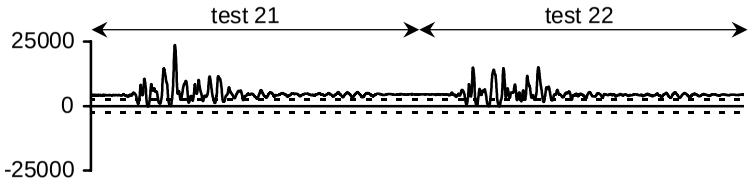

Figure A-170 Post-Test strain history for 1WBSL2

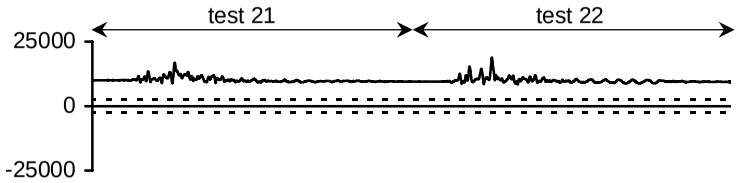

Figure A-171 Post-Test strain history for 1WBSL3

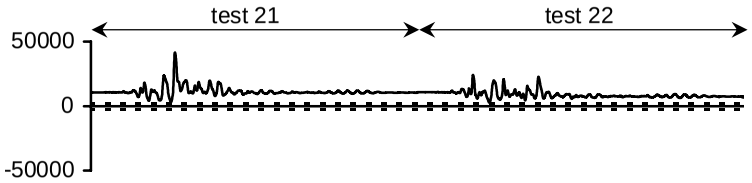

Figure A-172 Post-Test strain history for 1WBSL4

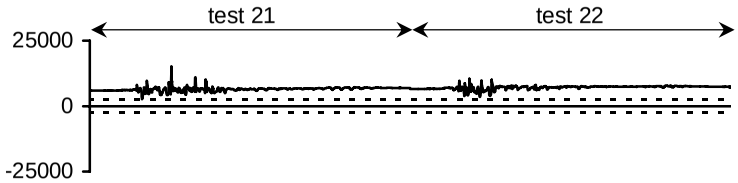

Figure A-173 Post-Test strain history for 1WBSL5

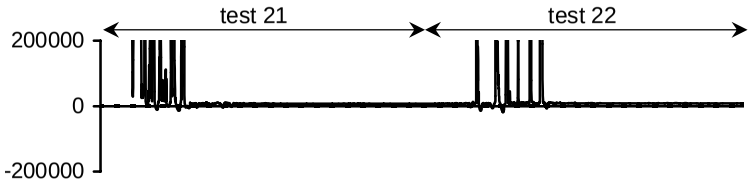

Figure A-174 Post-Test strain history for 1WBSL6

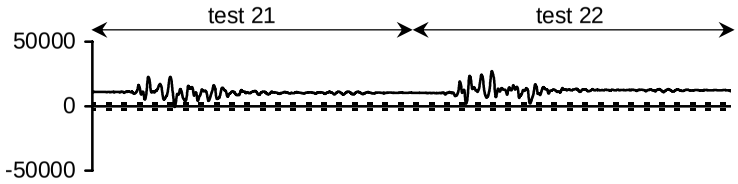

Figure A-175 Post-Test strain history for 1WBSL7

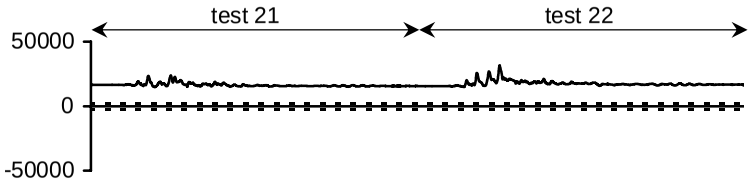

Figure A-176 Post-Test strain history for 1WBSL8

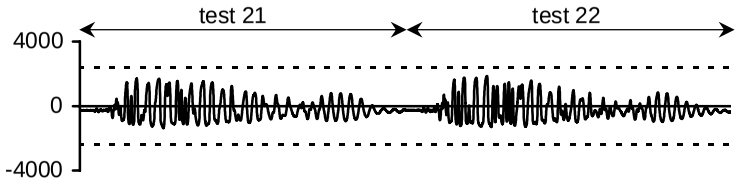

Figure A-177 Post-Test strain history for 1WBSL9

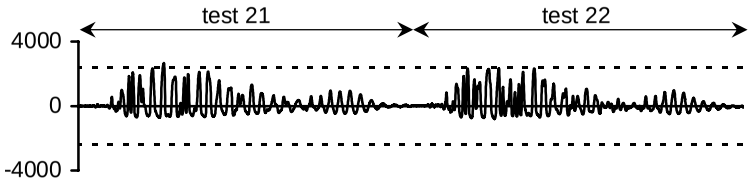

Figure A-178 Post-Test strain history for 1WBSL10

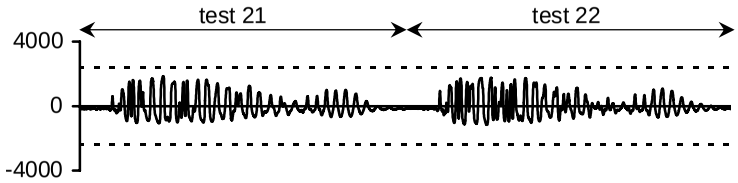

Figure A-179 Post-Test strain history for 1ETSL1

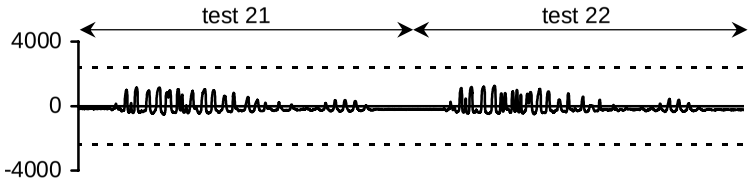

Figure A-180 Post-Test strain history for 1ETSL2

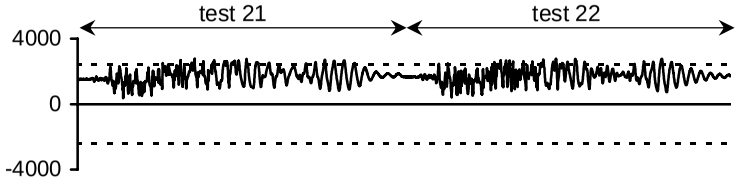

Figure A-181 Post-Test strain history for 1ETSL3

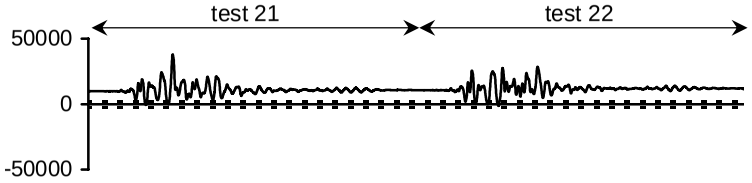

Figure A-182 Post-Test strain history for 1ETSL4

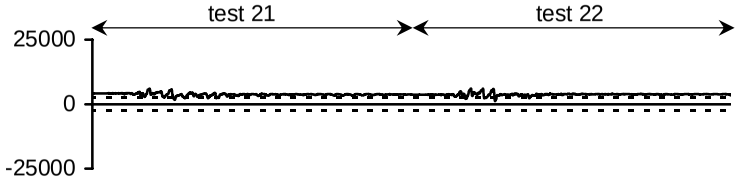

Figure A-183 Post-Test strain history for 1ETSL6

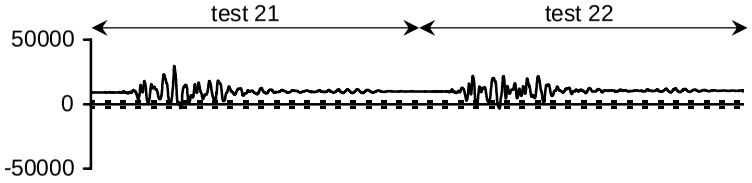

Figure A-184 Post-Test strain history for 1ETSL7

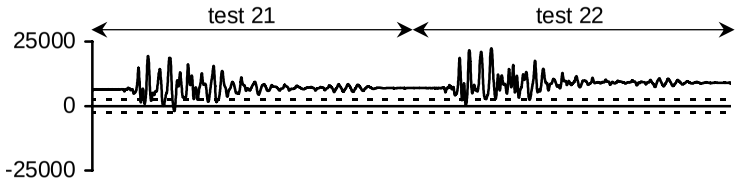

Figure A-185 Post-Test strain history for 1ETSL8

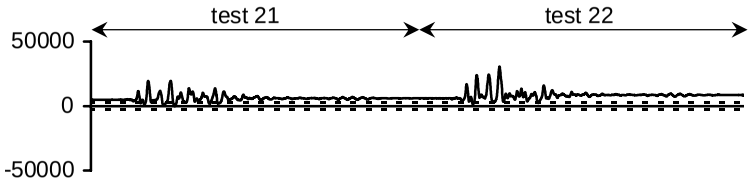

Figure A-186 Post-Test strain history for 1EBSL1

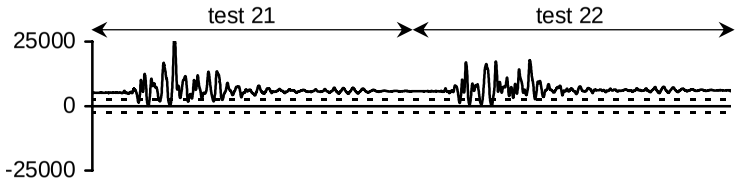

Figure A-187 Post-Test strain history for 1EBSL2

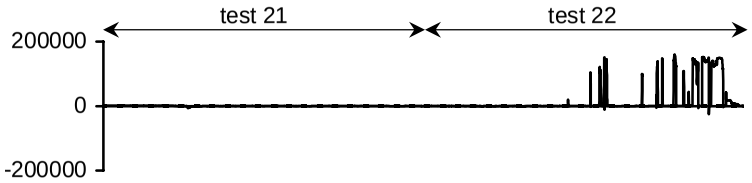

Figure A-188 Post-Test strain history for 1EBSL3

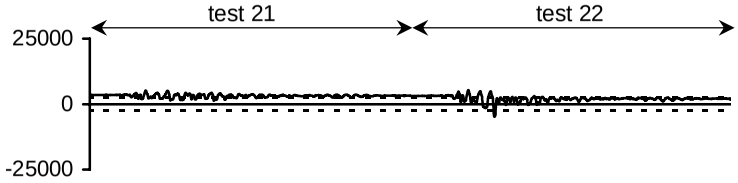

Figure A-189 Post-Test strain history for 1EBSL4

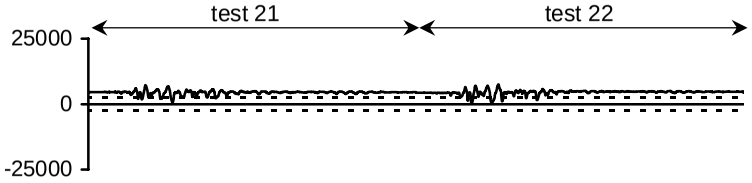

Figure A-190 Post-Test strain history for 1EBSL5

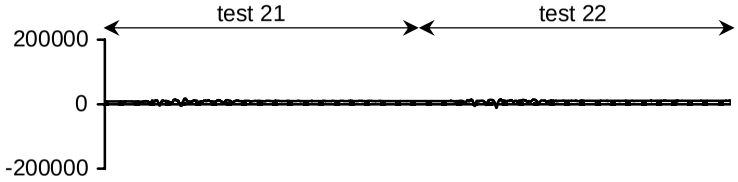

Figure A-191 Post-Test strain history for 1EBSL6

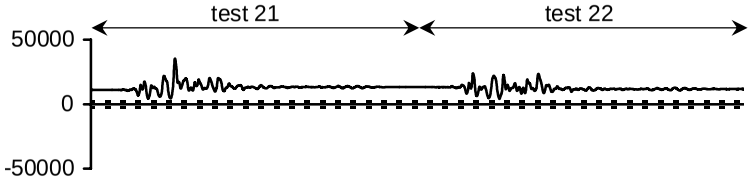

Figure A-192 Post-Test strain history for 1EBSL7

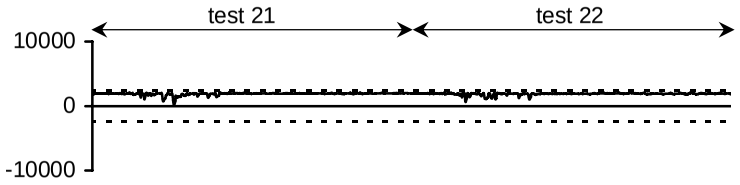

Figure A-193 Post-Test strain history for 1EBSL8

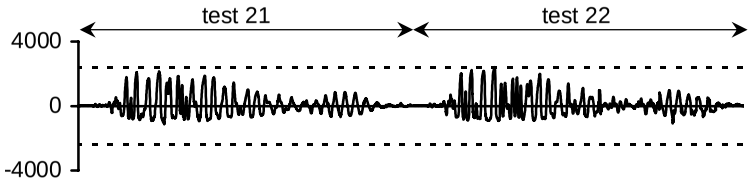

Figure A-194 Post-Test strain history for 1EBSL9

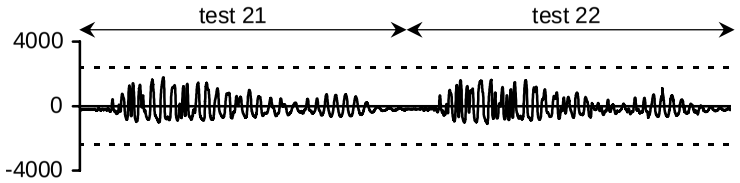

Figure A-195 Post-Test strain history for 1EBSL10

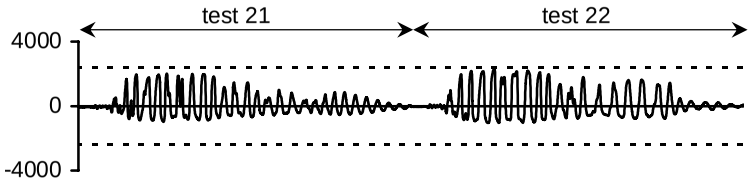

Figure A-196 Post-Test strain history for 2WTSL1

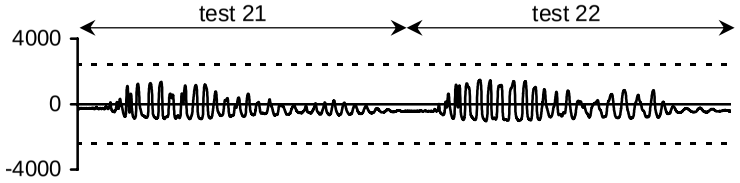

Figure A-197 Post-Test strain history for 2WTSL2

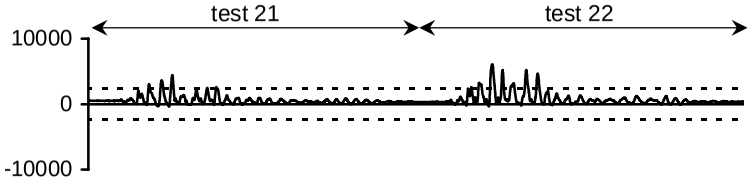

Figure A-198 Post-Test strain history for 2WTSL3

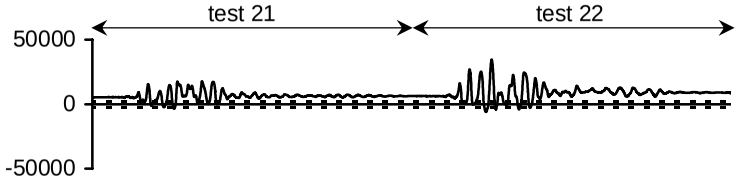

Figure A-199 Post-Test strain history for 2WTSL4

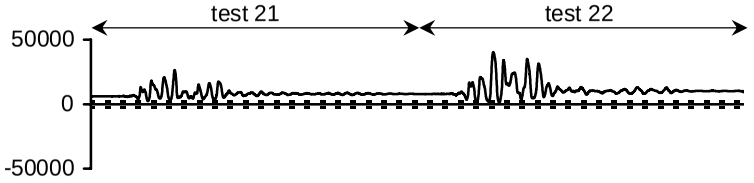

Figure A-200 Post-Test strain history for 2WTSL5

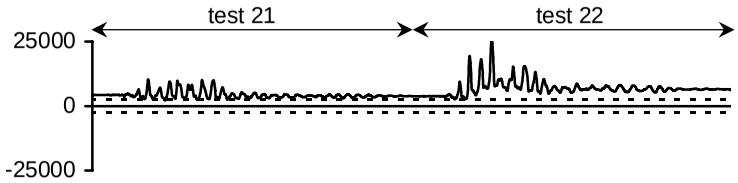

Figure A-201 Post-Test strain history for 2WTSL6

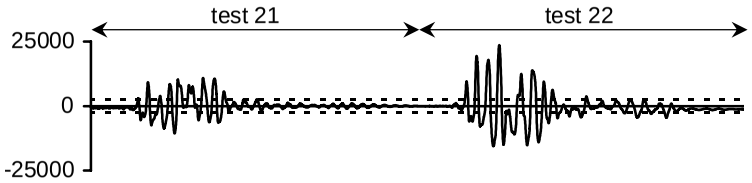

Figure A-202 Post-Test strain history for 2WTSL7

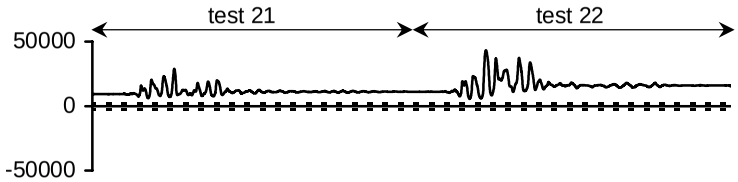

Figure A-203 Post-Test strain history for 2WTSL8

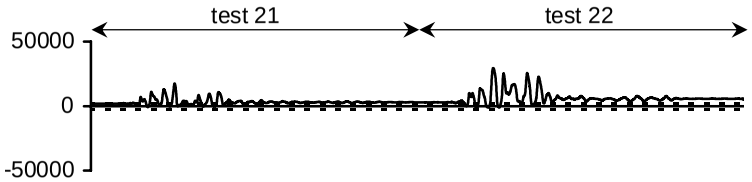

Figure A-204 Post-Test strain history for 2WBSL1

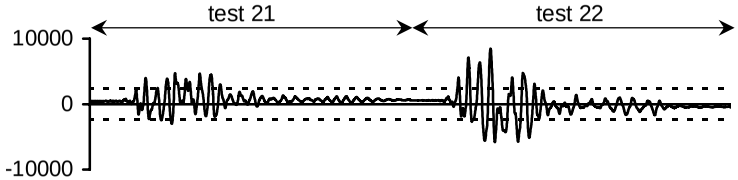

Figure A-205 Post-Test strain history for 2WBSL2

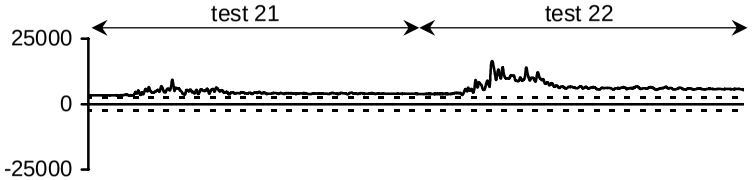

Figure A-206 Post-Test strain history for 2WBSL3

Figure A-207 Post-Test strain history for 2WBSL5

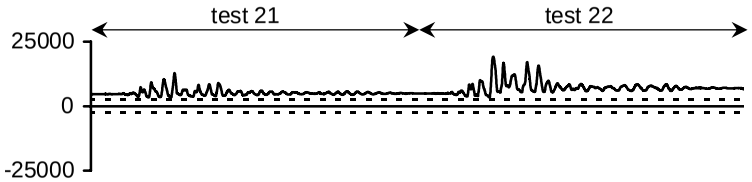

Figure A-208 Post-Test strain history for 2WBSL7

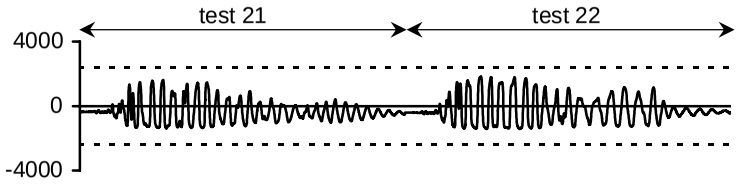

Figure A-209 Post-Test strain history for 2WBSL9

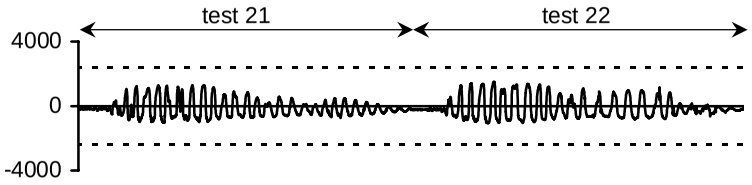

Figure A-210 Post-Test strain history for 2WBSL10

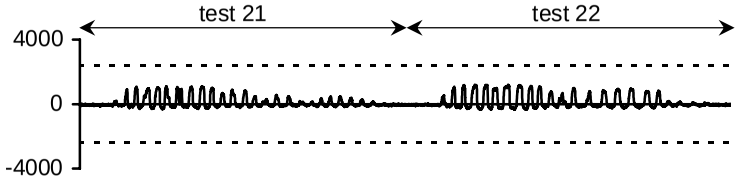

Figure A-211 Post-Test strain history for 2ETSL1

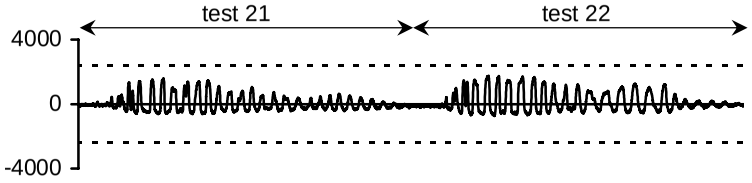

Figure A-212 Post-Test strain history for 2ETSL2

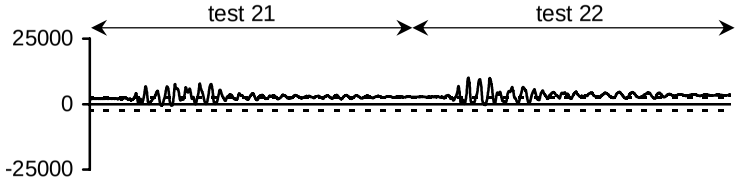

Figure A-213 Post-Test strain history for 2ETSL3

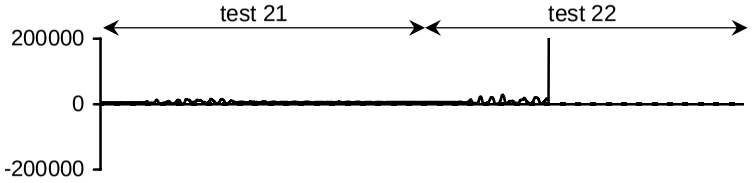

Figure A-214 Post-Test strain history for 2ETSL4

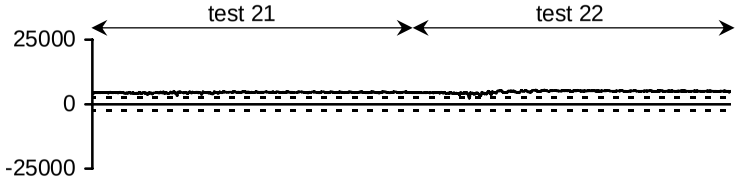

Figure A-215 Post-Test strain history for 2ETSL5

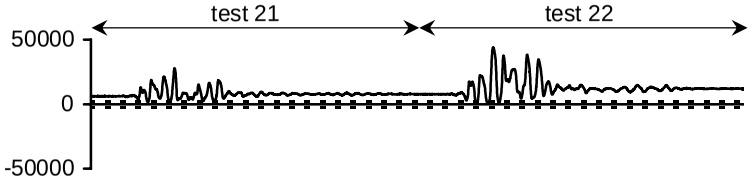

Figure A-216 Post-Test strain history for 2ETSL6

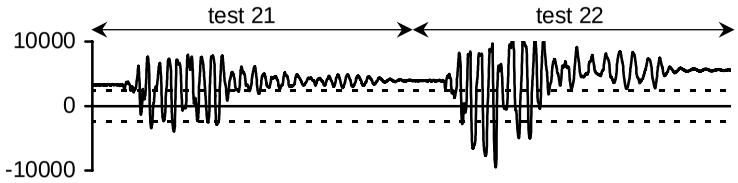

Figure A-217 Post-Test strain history for 2ETSL7

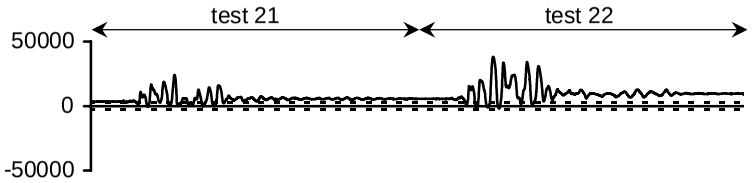

Figure A-218 Post-Test strain history for 2ETSL8

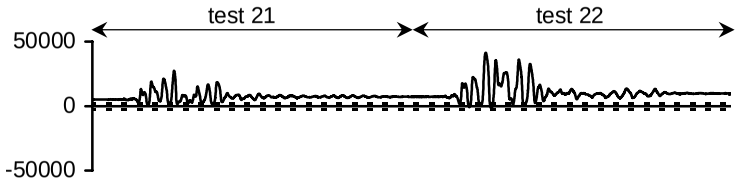

Figure A-219 Post-Test strain history for 2EBSL1

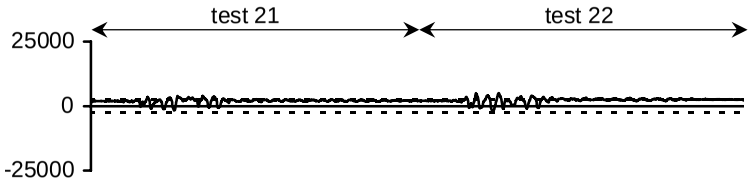

Figure A-220 Post-Test strain history for 2EBSL2

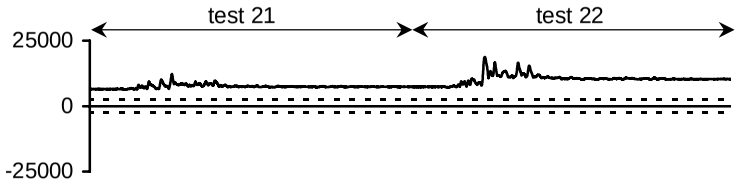

Figure A-221 Post-Test strain history for 2EBSL3

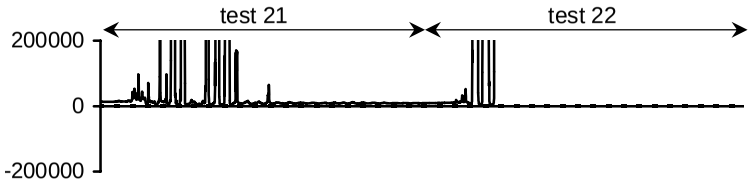

Figure A-222 Post-Test strain history for 2EBSL4

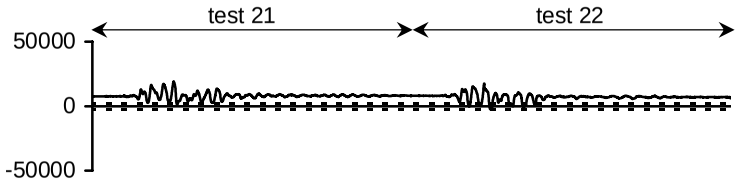

Figure A-223 Post-Test strain history for 2EBSL5

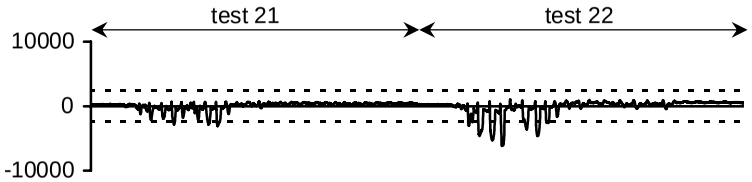

Figure A-224 Post-Test strain history for 2EBSL6

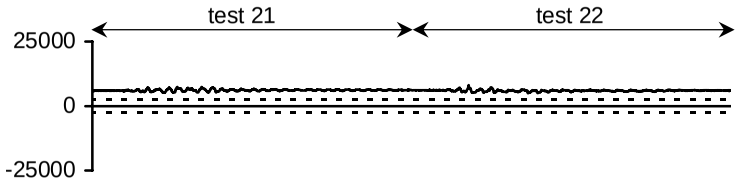

Figure A-225 Post-Test strain history for 2EBSL7

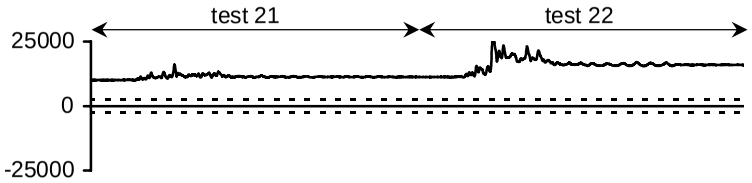

Figure A-226 Post-Test strain history for 2EBSL8

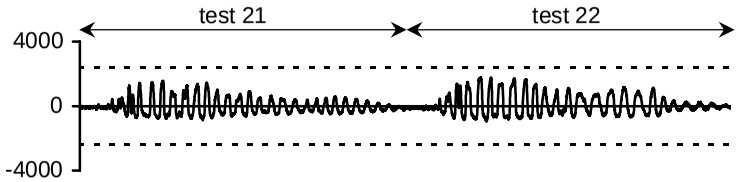

Figure A-227 Post-Test strain history for 2EBSL9

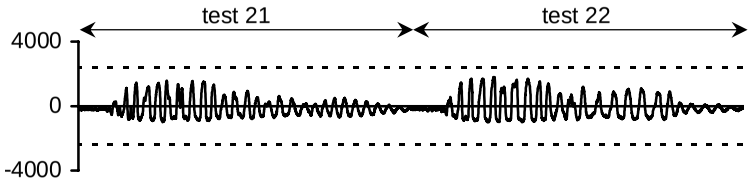

Figure A-228 Post-Test strain history for 2EBSL10

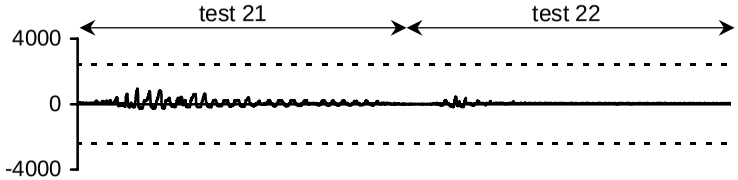

Figure A-229 Post-Test strain history for 3WTSL1

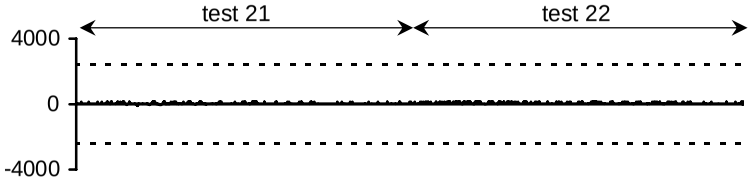

Figure A-230 Post-Test strain history for 3WTSL2

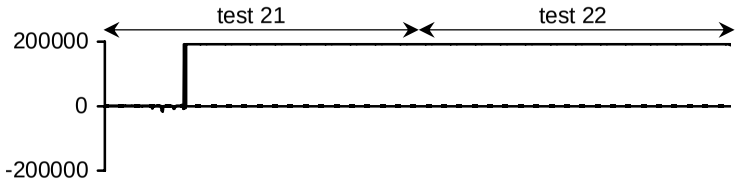

Figure A-231 Post-Test strain history for 3WTSL3

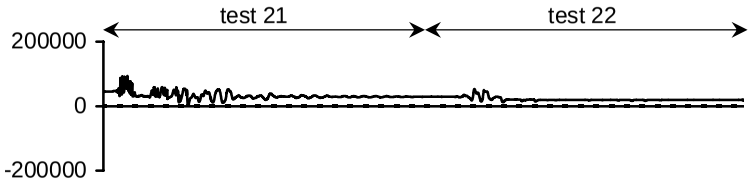

Figure A-232 Post-Test strain history for 3WTSL4

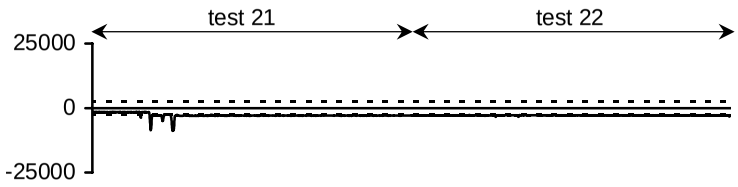

Figure A-233 Post-Test strain history for 3WTSL5

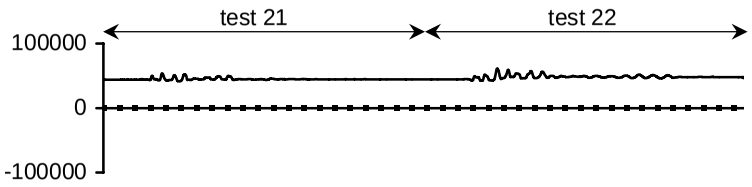

Figure A-234 Post-Test strain history for 3WTSL6

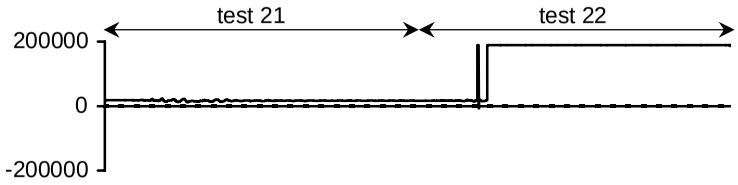

Figure A-235 Post-Test strain history for 3WTSL7

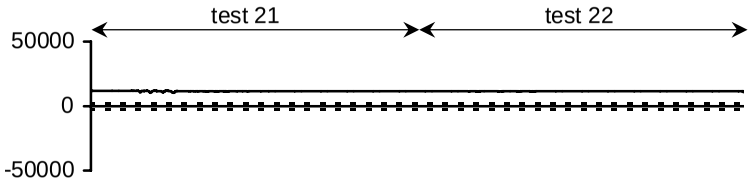

Figure A-236 Post-Test strain history for 3WTSL8

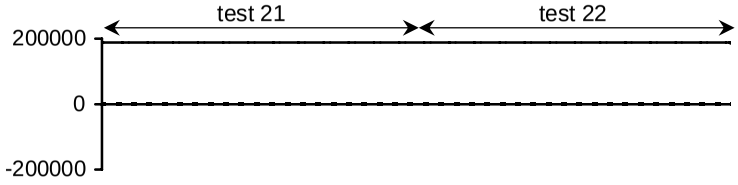

Figure A-237 Post-Test strain history for 3WBSL1

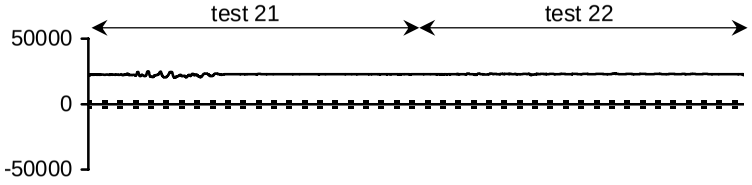

Figure A-238 Post-Test strain history for 3WBSL2

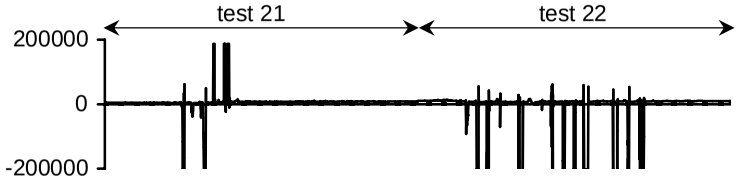

Figure A-239 Post-Test strain history for 3WBSL3

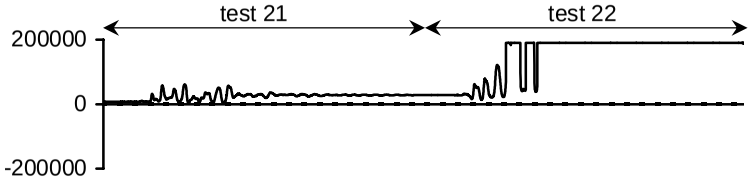

Figure A-240 Post-Test strain history for 3WBSL4

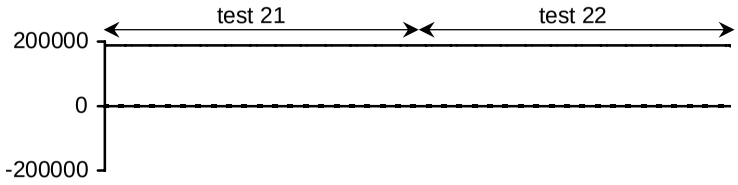

Figure A-241 Post-Test strain history for 3WBSL5

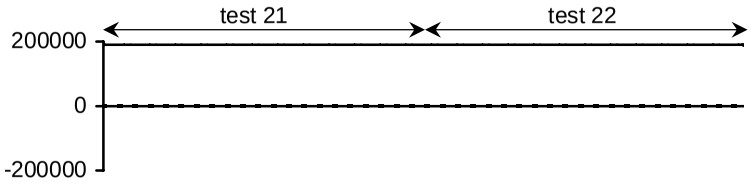

Figure A-242 Post-Test strain history for 3WBSL6

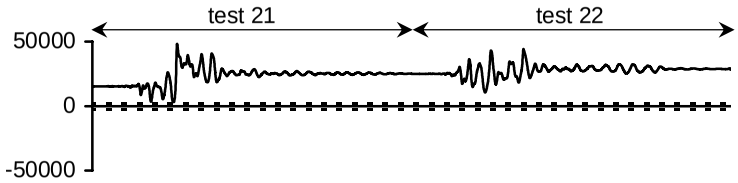

Figure A-243 Post-Test strain history for 3WBSL7

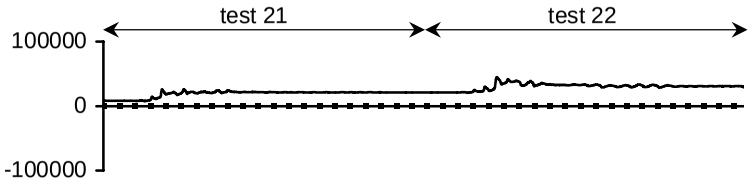

Figure A-244 Post-Test strain history for 3WBSL8

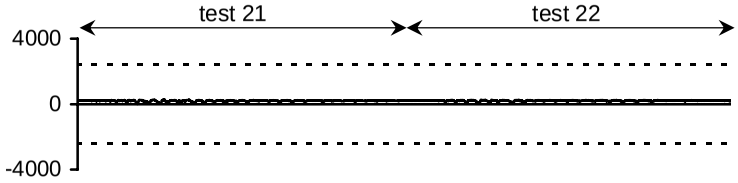

Figure A-245 Post-Test strain history for 3WBSL9

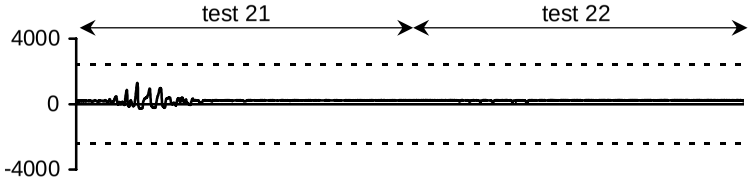

Figure A-246 Post-Test strain history for 3WBSL10

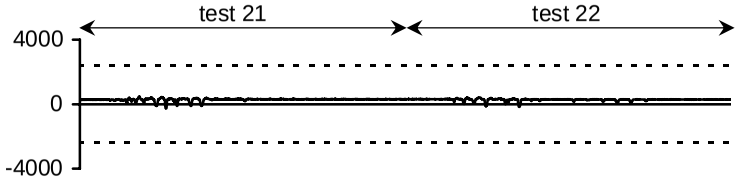

Figure A-247 Post-Test strain history for 3ETSL1

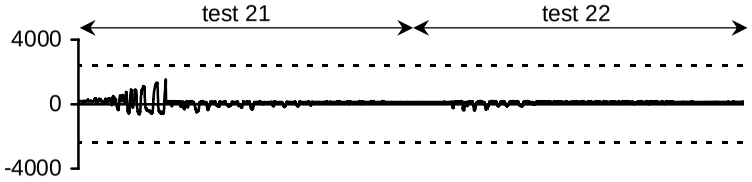

Figure A-248 Post-Test strain history for 3ETSL2

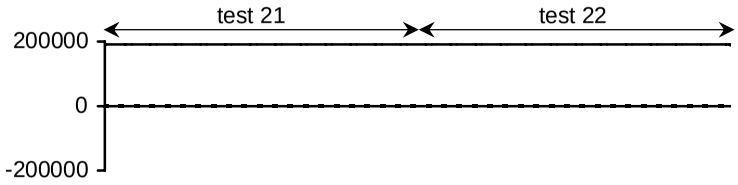

Figure A-249 Post-Test strain history for 3ETSL3

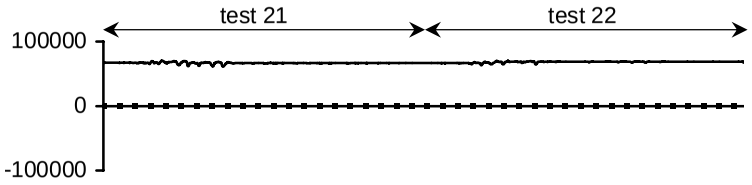

Figure A-250 Post-Test strain history for 3ETSL4

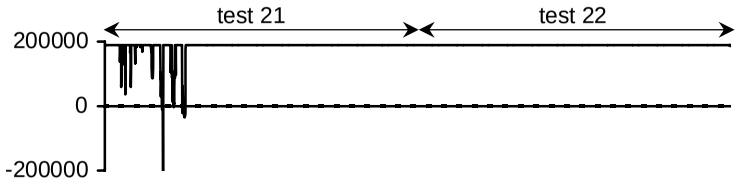

Figure A-251 Post-Test strain history for 3ETSL5

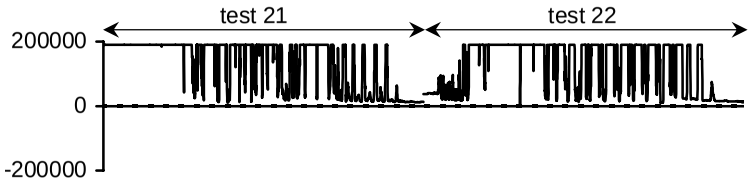

Figure A-252 Post-Test strain history for 3ETSL6

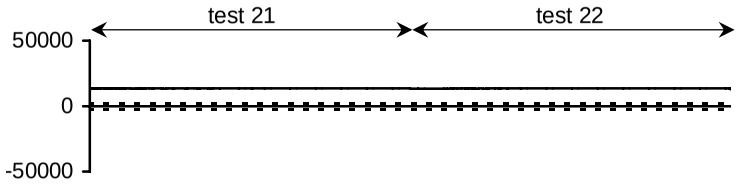

Figure A-253 Post-Test strain history for 3ETSL7

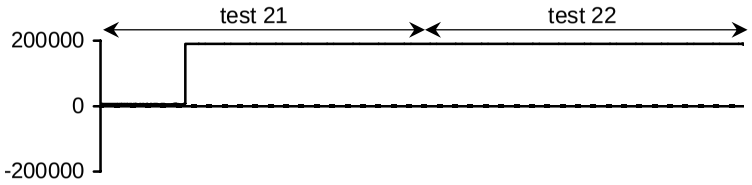

Figure A-254 Post-Test strain history for 3ETSL8

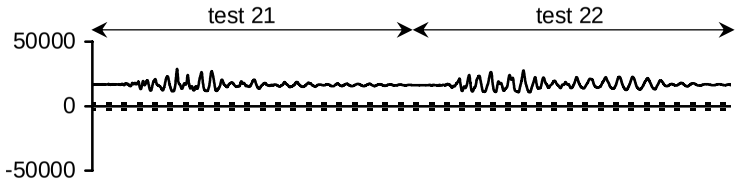

Figure A-255 Post-Test strain history for 3EBSL1

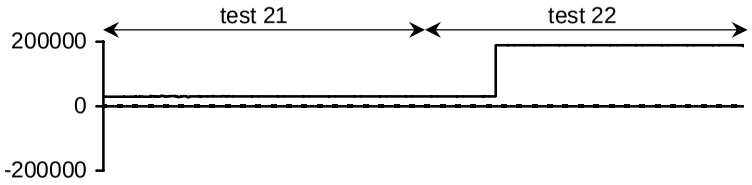

Figure A-256 Post-Test strain history for 3EBSL2

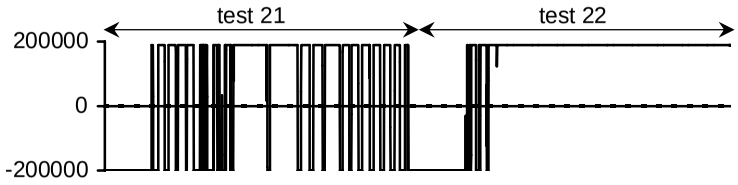

Figure A-257 Post-Test strain history for 3EBSL3

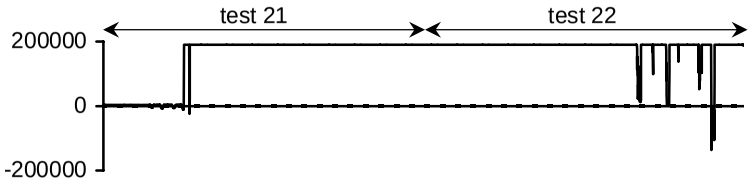

Figure A-258 Post-Test strain history for 3EBSL4

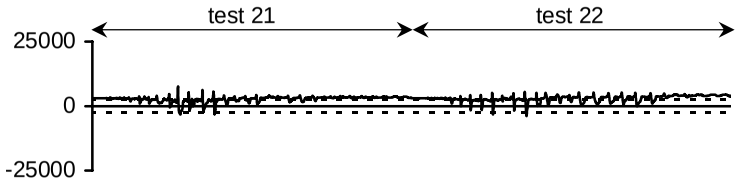

Figure A-259 Post-Test strain history for 3EBSL5

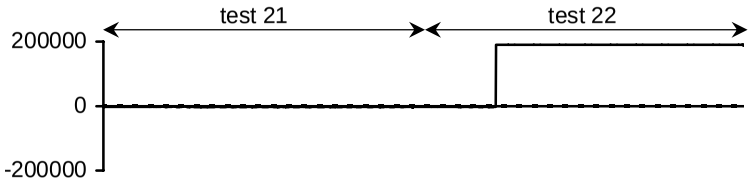

Figure A-260 Post-Test strain history for 3EBSL6

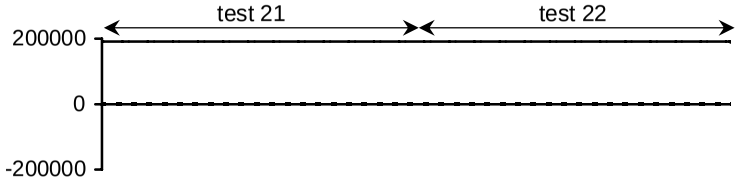

Figure A-261 Post-Test strain history for 3EBSL7

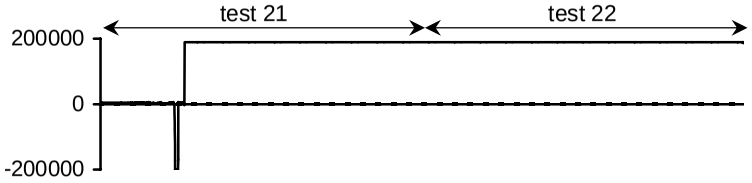

Figure A-262 Post-Test strain history for 3EBSL8

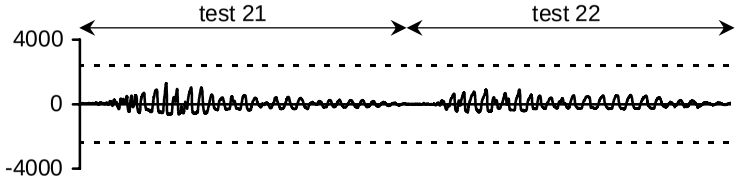

Figure A-263 Post-Test strain history for 3EBSL9

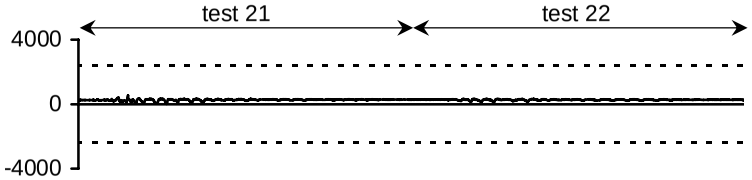

Figure A-264 Post-Test strain history for 3EBSL10

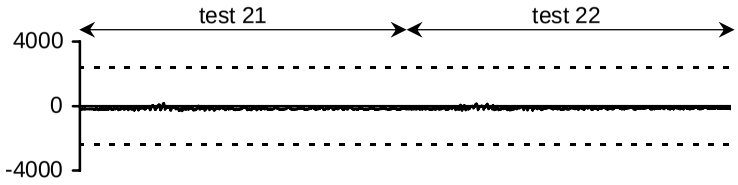

Figure A-265 Post-Test strain history for 1WTSH1

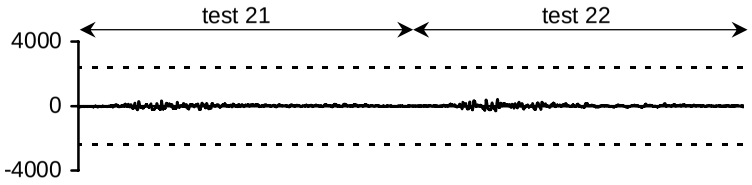

Figure A-266 Post-Test strain history for 1WTSH2

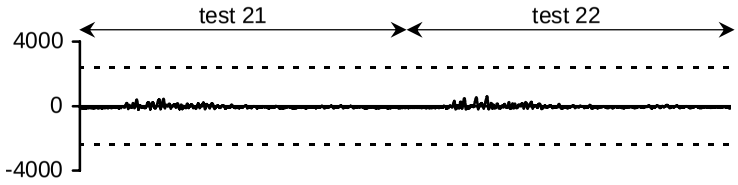

Figure A-267 Post-Test strain history for 1WTSH3

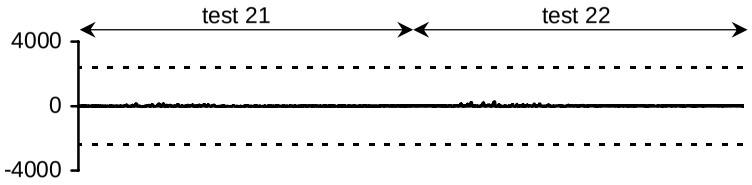

Figure A-268 Post-Test strain history for 1WTSH4

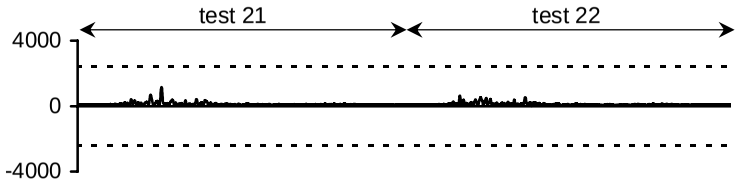

Figure A-269 Post-Test strain history for 1WBSH1

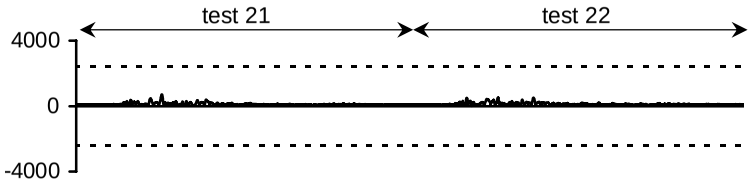

Figure A-270 Post-Test strain history for 1WBSH2

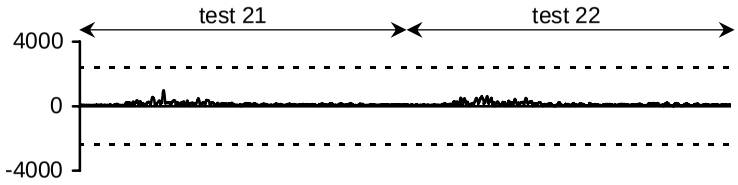

Figure A-271 Post-Test strain history for 1WBSH3

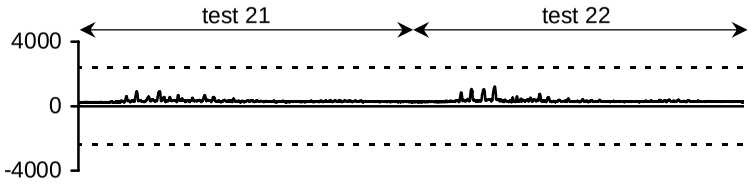

Figure A-272 Post-Test strain history for 1WBSH4

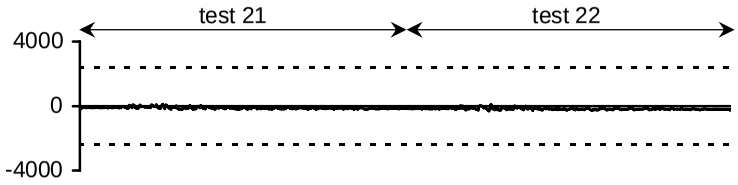

Figure A-273 Post-Test strain history for 1WBSH5

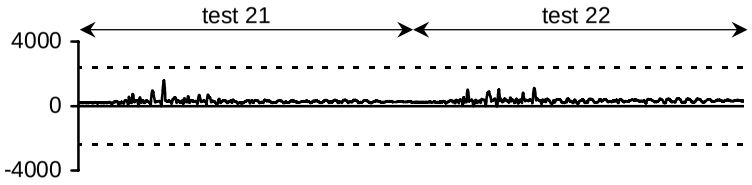

Figure A-274 Post-Test strain history for 1WBSH6

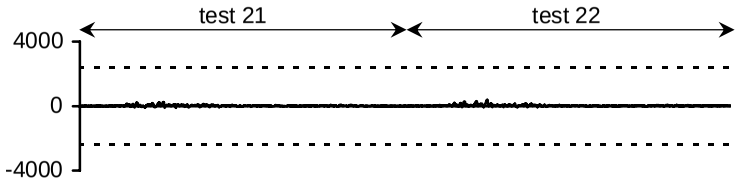

Figure A-275 Post-Test strain history for 1ETSH3

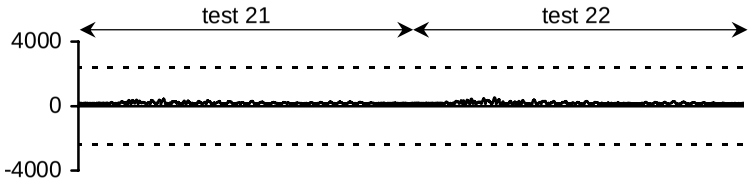

Figure A-276 Post-Test strain history for 1ETSH4

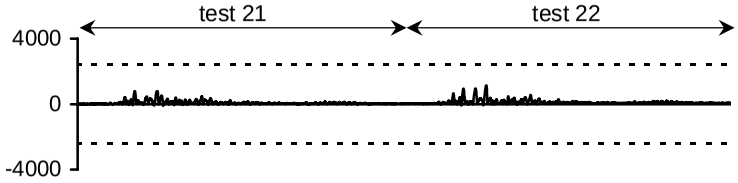

Figure A-277 Post-Test strain history for 1EBSH1

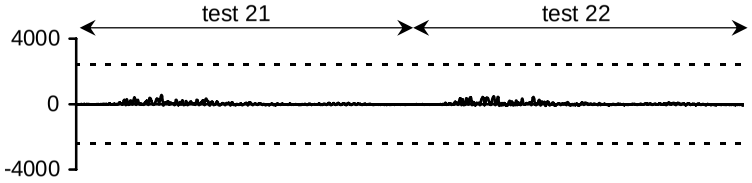

Figure A-278 Post-Test strain history for 1EBSH2

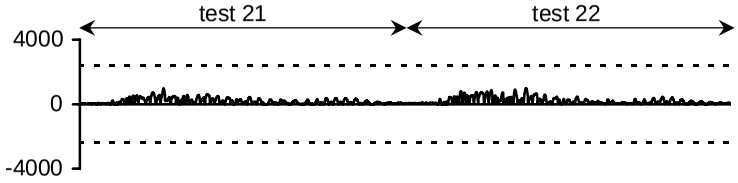

Figure A-279 Post-Test strain history for 1EBSH3

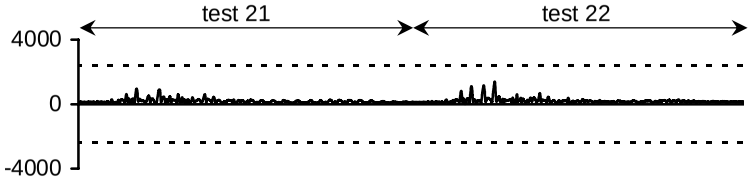

Figure A-280 Post-Test strain history for 1EBSH4

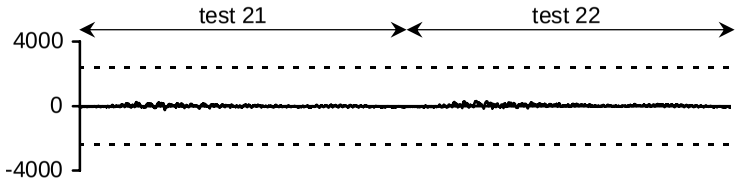

Figure A-281 Post-Test strain history for 1EBSH5

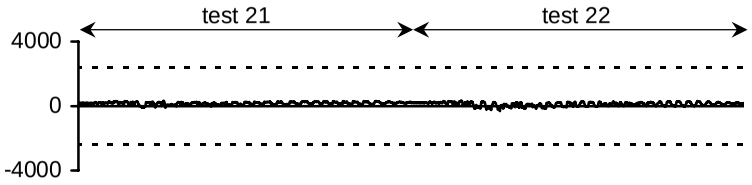

Figure A-282 Post-Test strain history for 1EBSH6

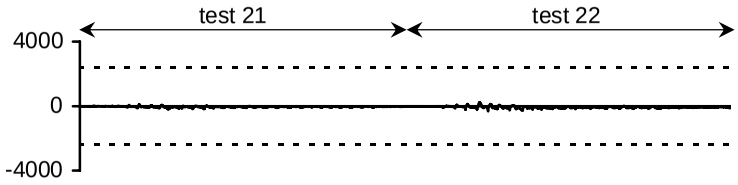

Figure A-283 Post-Test strain history for 2WTSH1

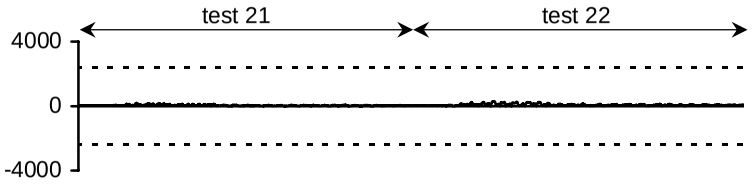

Figure A-284 Post-Test strain history for 2WTSH2

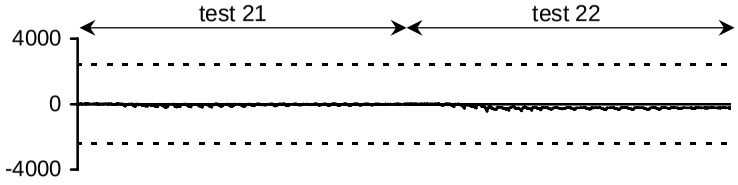

Figure A-285 Post-Test strain history for 2WTSH3

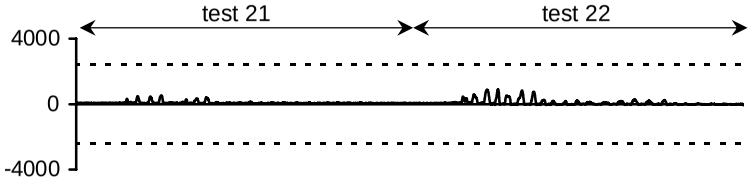

Figure A-286 Post-Test strain history for 2WBSH1

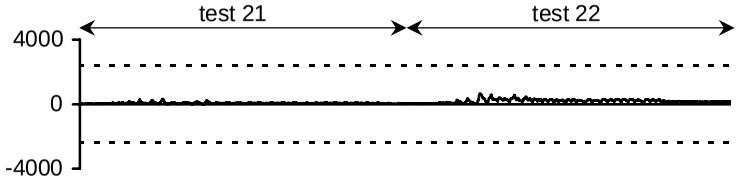

Figure A-287 Post-Test strain history for 2WBSH2

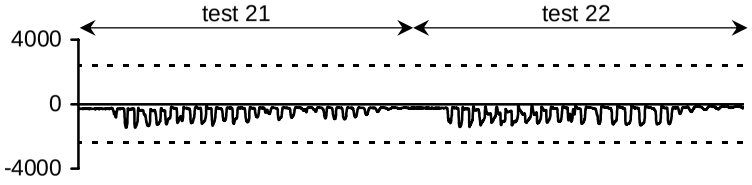

Figure A-288 Post-Test strain history for 2WBSH3

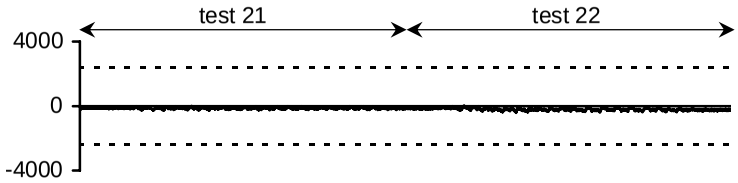

Figure A-289 Post-Test strain history for 2ETSH1

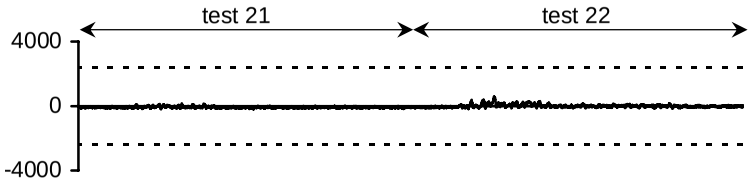

Figure A-290 Post-Test strain history for 2ETSH2

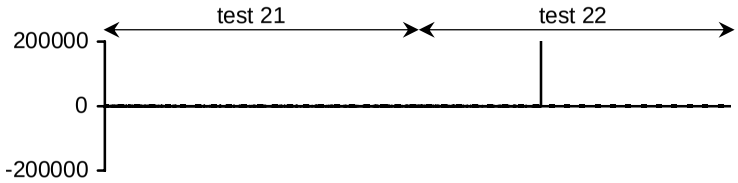

Figure A-291 Post-Test strain history for 2ETSH3

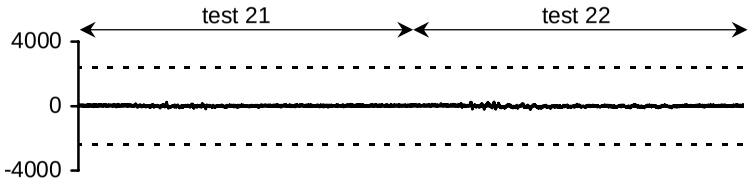

Figure A-292 Post-Test strain history for 2EBSH1

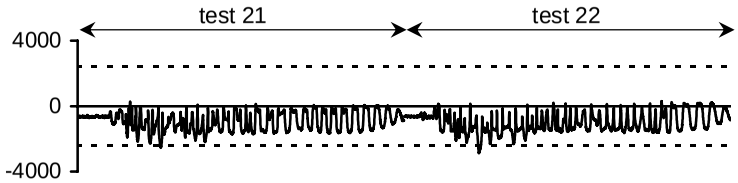

Figure A-293 Post-Test strain history for 2EBSH2

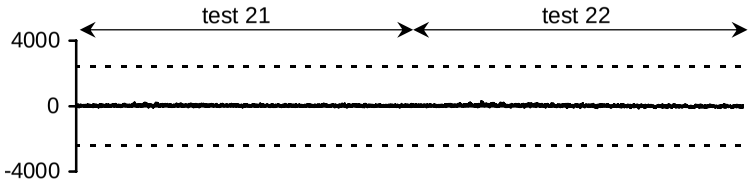

Figure A-294 Post-Test strain history for 2EBSH3

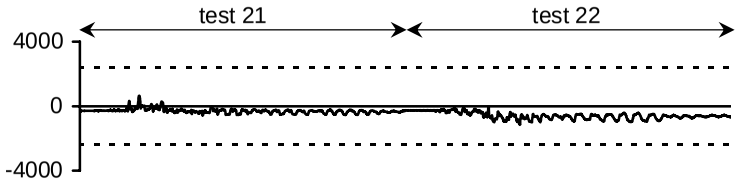

Figure A-295 Post-Test strain history for 3WTSH1

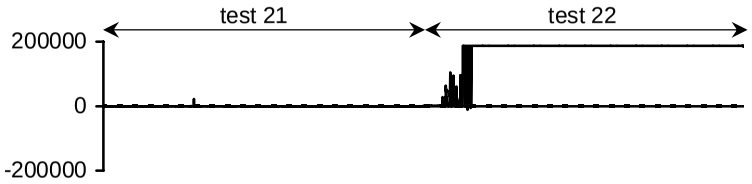

Figure A-296 Post-Test strain history for 3WTSH2

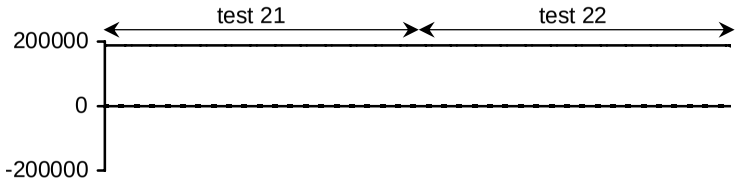

Figure A-297 Post-Test strain history for 3WTSH3

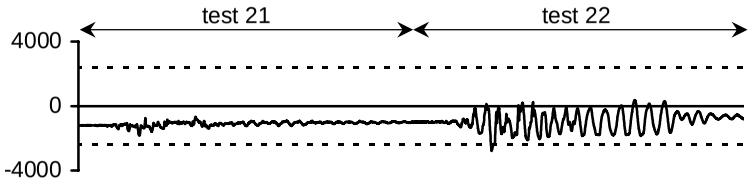

Figure A-298 Post-Test strain history for 3WTSH4

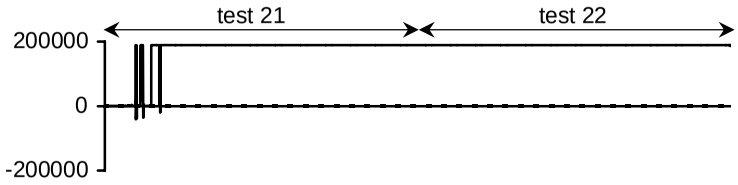

Figure A-299 Post-Test strain history for 3WTSH6

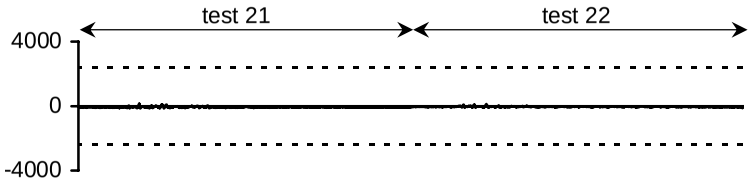

Figure A-300 Post-Test strain history for 3WTSH7

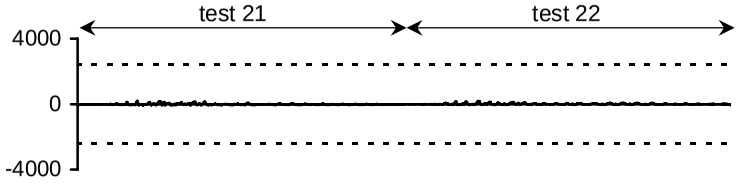

Figure A-301 Post-Test strain history for 3WBSH1

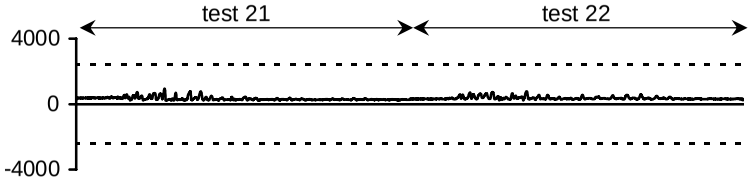

Figure A-302 Post-Test strain history for 3WBSH2

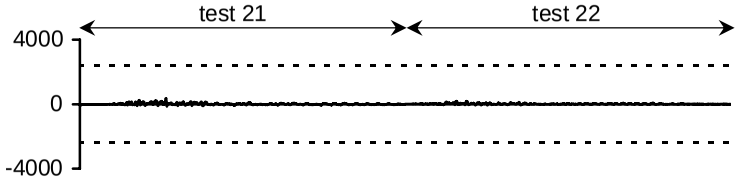

Figure A-303 Post-Test strain history for 3WBSH3

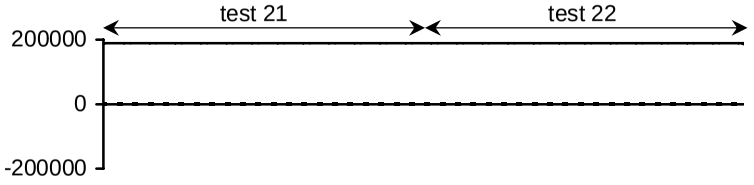

Figure A-304 Post-Test strain history for 3WBSH4

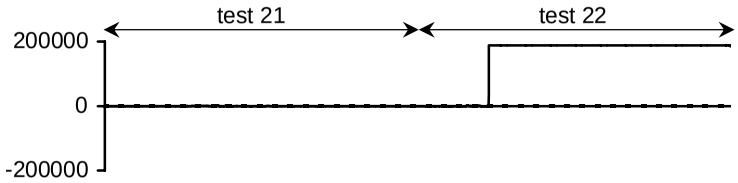

Figure A-305 Post-Test strain history for 3WBSH5

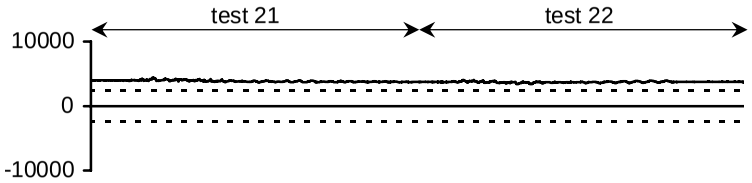

Figure A-306 Post-Test strain history for 3WBSH6

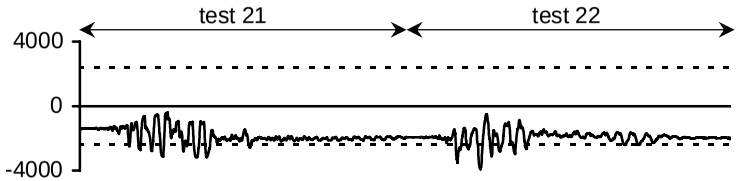

Figure A-307 Post-Test strain history for 3WBSH7

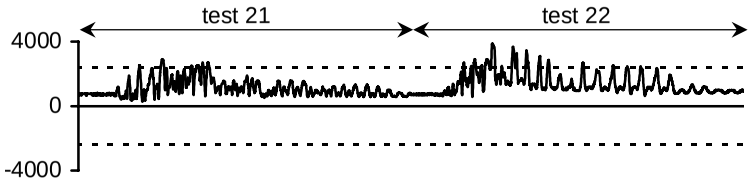

Figure A-308 Post-Test strain history for 3ETSH1

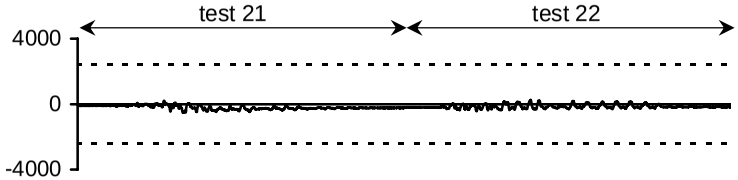

Figure A-309 Post-Test strain history for 3ETSH2

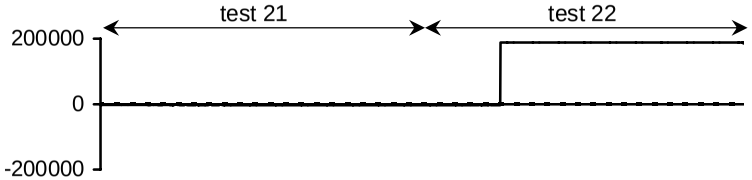

Figure A-310 Post-Test strain history for 3ETSH3

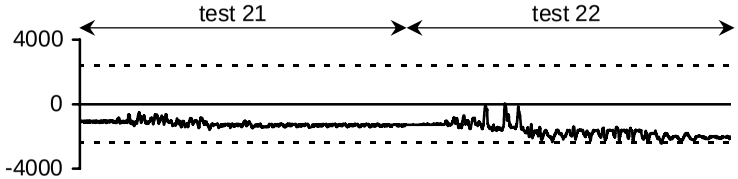

Figure A-311 Post-Test strain history for 3ETSH4

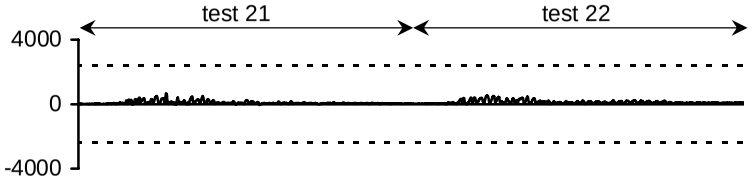

Figure A-312 Post-Test strain history for 3ETSH5

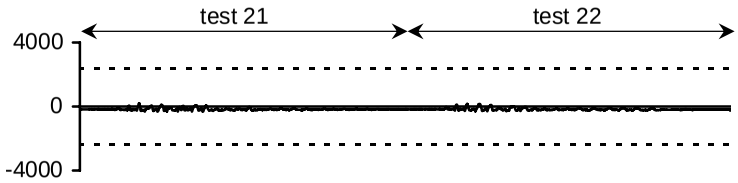

Figure A-313 Post-Test strain history for 3ETSH6

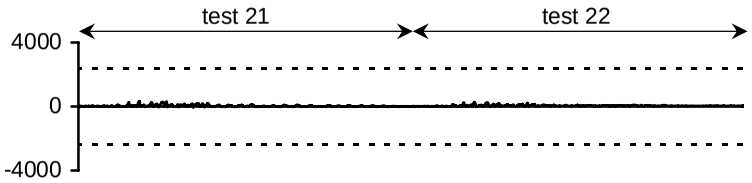

Figure A-314 Post-Test strain history for 3ETSH7

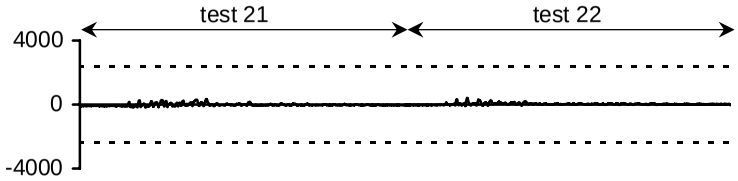

Figure A-315 Post-Test strain history for 3EBSH2

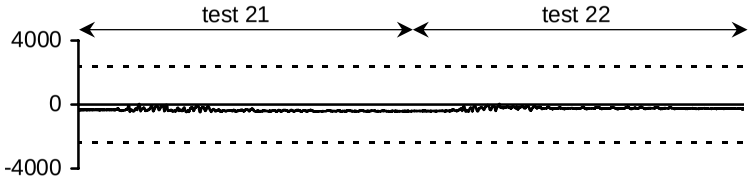

Figure A-316 Post-Test strain history for 3EBSH3

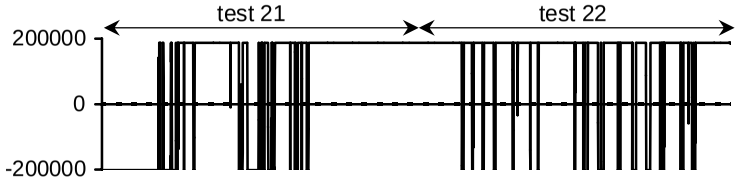

Figure A-317 Post-Test strain history for 3EBSH4

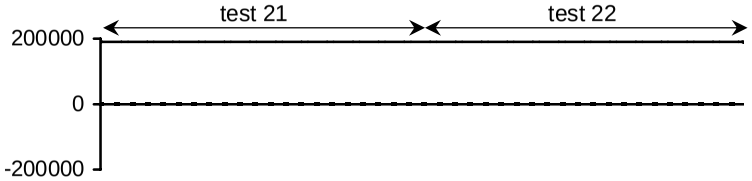

Figure A-318 Post-Test strain history for 3EBSH5

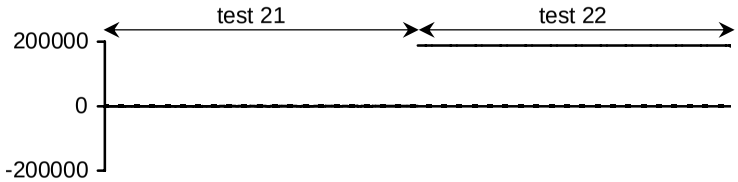

Figure A-319 Post-Test strain history for 3EBSH6

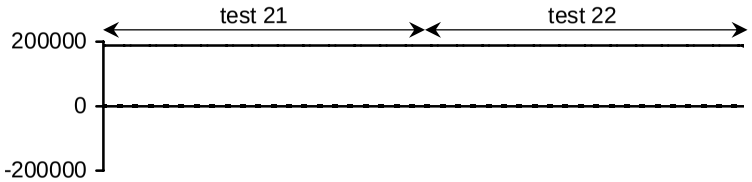

Figure A-320 Post-Test strain history for 3EBSH7

Appendix B: Extended Summary

B.1 Summary

As part of a multi-university collaborative project to study soil-foundation-structure interaction (SFSI), a quarter-scale two-span bridge frame containing three, two-column bents was tested to failure on the three shake table system at the University of Nevada, Reno. The project was conducted, in part, to examine the collaborative aspects of the NSF Network for Earthquake Engineering Simulation (NEES). The global objective of the multi-university project was to study SFSI using four experimental studies that could be combined to define the earthquake response of a prototype structure which was a post-tensioned reinforced concrete box girder bridge with pile foundations. The four experiments were: ¼ scale shake table tests of the superstructure and substructure of a two-span bridge frame at the University of Nevada, Reno; 1/52 scale centrifuge tests of bents and the bridge frame including soil and piles at the University of California, Davis; 1/4 scale and ½ scale structural component tests at Purdue University; and ¼ scale in-situ bent field tests at the University of Texas, Austin. These experimental studies are to be computationally integrated by research collaborators using calibrated OpenSees (OpenSees 2002) models to conduct further research of soil-foundation-structure-interaction (Wood et. al 2004).

B.1.1 Experimental Study

Research in this document focused on the experimental testing of the shake table bridge specimen and analytical study of the linear and nonlinear response of bridge systems. This includes the design of the prototype structure for the global project, development and implementation of an effective technique for experimentally testing bridges on multiple shake tables, and analytical modeling of bridge systems. The computational model that was developed and experimentally verified was used in conjunction with the measured data from testing to conduct further studies on bridge system response and shake table testing of bridges.

The bridge specimen was designed and tested with the intent to realistically model interaction between bridge bents of varied heights within a system. The earthquake design of the prototype was based on the National Cooperative Highway Research Program (NCHRP) 12-49 *Recommended LRFD Guidelines for the Seismic Design of Highway Bridges* (ATC/MCEER 2001). The total length of the quarter-scale bridge specimen was 67.3 ft (20.5 m) with two 30 ft (9.1 m) spans between bents. The three two-column bents, which were 12 in (0.305 m) in diameter, had clear heights of 60, 72, and 90 in (1.52, 1.83, and 2.29 m). The tall bent was in the center and the short and medium height bents were at each end of the bridge, which created coupling between the bents causing in-plane rotational modes for the transverse response. Columns had moment connection at the top to the superstructure and were fixed at the base to the rigid footings connected to the shake tables; therefore the columns were all subjected to double curvature in bending. Location of the base fixity to the shake tables coincides with the equivalent point of fixity in the pile foundations of the prototype.

The superstructure of the specimen was a solid post-tensioned slab with elastic bending properties about both bending axes that matched those of the prototype. It was composed of six precast beams in two sets that were transversely post tensioned to each other and longitudinally post tensioned to the cap beam of the center bent and the cantilevers/cap beams of the end bents. External weights were superimposed to the top of the superstructure of the specimen to account for the scaling effect so that the columns were subjected to the same axial stress as those of the prototype. The total weight of the superstructure including the superimposed axial loads was 270 kips (1200 kN). The axial load index of the columns was 7.3 percent for the middle bent and 8.3 percent for the two end bents.

The response of the bridge specimen was monitored utilizing 298 channels of accelerometers, displacement transducers, and strain gauges. Since this bridge was the first semi-rigid bridge system on multiple shake tables that was tested to failure, standard methods were not available for pre-test analysis. Prior to creating and testing the bridge model, nonlinear dynamic analysis was conducted to verify that the bridge system would not exceed the limits of the shake tables and to make sure that the tables could fail the bridge.

The bridge frame was subjected to a set of low amplitude (pre-yield), and high amplitude acceleration record target motions that were derived from the Century City accelerogram of the 1994 Northridge, California earthquake using Pro-shake and OpenSees to include the effects of soil depth. Low amplitude tests were scheduled such that the demands in the columns remained below 75 percent of the calculated moment where extreme longitudinal column reinforcement yielding was initiated. The low amplitude testing consisted of uniaxial coherent and incoherent motions and biaxial coherent motions. The incoherency was created by varying the amount of soil depth in the calculation of motions for the shake table input. Also in the low amplitude tests, the achieved centrifuge motions that corresponded to the small scale centrifuge test at UC Davis were applied so that the shake table tests could be better correlated with centrifuge tests by research collaborators. As expected during low amplitude tests, no damage was observed in the superstructure, and the reinforcement strain in the columns remained below yield.

High amplitude testing of the bridge consisted of uniaxial coherent target excitation with a motion that began with pre-yield amplitude and was applied at increased amplitudes until the first bent failure. Transverse excitation was used for high amplitude tests because the end conditions of the model were such that longitudinal response would only be accurate up to closure of the scaled prototype hinge gap. The target peak ground acceleration of high amplitude tests ranged from 0.075 g (test 12) to 1.66 g (test 19).

For tests 13 and 16, which were equivalent to the expected and rare design earthquakes, the columns satisfied both the service and damage level design code life safety performance objectives. During test 13, the maximum column displacement ductility demand was 0.95 in the medium height bent. During test 16, the maximum displacement ductility demand was 3.31 which was only 40 percent of the failure displacement. The bridge was considered to have failed during test 19 when the columns of bent 3 failed in flexure at a displacement ductility of 8.9. No signs of shear distress were observed or measured throughout the tests other than minor shear cracking in bent

3, the shortest of the bents. After the bent 3 failure, the bridge was subjected to an additional test, test 20, of reduced amplitude to attempt to further damage bents 1 and 2 and measure system response after the bent 3 failure. After test 20, the mass above bent 3 was removed and the bridge was subjected to two additional high amplitude motions as an attempt to induce more damage in the remaining bents 1 and 2.

The shake table tests provided a wealth of data that was used to evaluate numerical models and identify properties of the structural response that are unique to a large-scale asymmetric bridge system. Both bent accelerations and displacements were the primary measures that were compared in the analytical models. Modal frequencies were measured at each bent from low amplitude vibration testing between the earthquakes as damage in the bridge progressed. It was determined that the modal frequencies excited by low amplitude vibrations could be a valuable tool in assessing and quantifying post earthquake damage in bridge systems including identifying damage to certain components.

Since there was not a direct measurement of shear force in the columns, the bent shears during testing were monitored by top of bent accelerations. Upon reviewing the data it was discovered that the accelerations were effective in estimating the force of the columns that dominated the response, but this method was not accurate for all of the bents. The actuator pressures of each shake table were used to calculate the shear force and it was found that actuator pressure is an effective method to estimate bent shear for bridge system tests when load cells are not a viable option.

In both the pre-test and post-test analyses, the shear stiffness of columns was assumed to be the Park and Paulay (1975) elastic cracked shear stiffness. Instrumentation in bent 3 allowed for separation of the column shear deformation from the total deformation. The measured pre-yield shear stiffness of the column was a good match to the cracked stiffness equation. After column yielding, the shear stiffness of the bent was substantially reduced, however, upon comparison with the post-yield shear stiffness equation developed by Correal et al. (2004), it was found that the post-yield stiffness, which was not included in the analyses provided a good match to the measured results.

The Mander model (Mander et al. 1988) for confined concrete was used throughout the pre-test and post-test analyses. To better estimate the ductility capacity in the pre-test analyses, the failure rotation was assumed to be two times the rotation calculated for initial confined concrete crushing using the Mander concrete model. Using the displacement transducers and strain gauges at the critical sections of the columns, the maximum measured concrete compression strains were compared to the crushing strain predicted by the Mander model. The measured results showed that either the Mander model is conservative by a factor of at least 2, or that the displacement capacity failure occurs substantially later than crushing of the confined concrete occurs at the extreme confined compressive fiber.

B.1.2 Analytical Studies

Upon the completion of testing, analytical nonlinear response history modeling of the bridge for the high amplitude testing was conducted using SAP2000 (CSI 2005) and Drain-3DX (Prakash and Campbell 1994). This was conducted to determine the accuracy of contemporary modeling techniques and to develop a model to use for further study of

the shake table tests and bridge system response. A unique problem to testing on multiple shake tables that was encountered for the computational modeling of the high amplitude tests was that the achieved shake table motions for the synchronous input were asynchronous and therefore displacement records were required for analysis. Because the measured shake table displacements did not have the sufficient resolution to accurately define both the displacement and acceleration response of the shake tables, a method was developed to double integrate the measured acceleration of the tables so that the displacement input to the computer model had both acceleration and displacement content that matched the shake table motions.

Because nonlinearity is computationally demanding and most of the bridge components could be assumed to respond linearly, nonlinearity of the bridge was modeled at the column ends only. Fiber elements were used to define column nonlinearity in the computer models because characteristics such as axial load and biaxial bending, as well as moment-rotation hysteretic relationships are implicitly included. Prior to creating the analytical models, parametric studies were conducted to determine the optimal configurations of nonlinear elements so that the models would be sufficiently discretized to capture the desired response of the bridge, and have a minimal number of degrees of freedom to reduce the amount of time for computation. The number, length, as well as the fiber discretization of the nonlinear elements was included in the parametric studies. It was concluded that one fiber section at each column end having a length matching the plastic hinge length and a fiber section of four layers (1 unconfined, 2 confined, and 1 reinforcement) and 8 slices was sufficient to adequately capture the global nonlinear response of the columns. A parametric study was also conducted to determine the integration time step to use so that the models converged on consistent displacements.

There were three primary differences between the SAP2000 and Drain-3DX computational models of the bridge. The first and second were for the nonlinear fiber elements. The Drain-3DX fiber element was of the distributed plasticity type where the moment-curvature relationship is integrated over the length of the element. In SAP2000, the fiber element is the lumped plasticity type where the moment-curvature relationship is multiplied by a hinge length and in assumed to be lumped at the center of the element. Drain-3DX includes a separate lumped plasticity fiber discretized model for modeling of bond-slip at the end of the nonlinear fiber element. The drain bond-slip model allowed the bar yield penetration and crack opening at the ends of the column to be explicitly defined. The SAP2000 column elements did not allow for explicit definition of bond-slip and therefore a slip relationship was included in the constitutive relationship of the reinforcement but crack opening was ignored. The third difference between the two models was the integration method. In SAP2000, the Newmark's integration method was used and the iteration convergence tolerance was specified as 10^{-7}. For Drain-3DX, a more direct method of integration was used where instead of iteration, the force error in each time step was applied during the next time step.

The results from the analytical modeling were compared to the measured data. It was shown that both models produced reasonable results. However, the specialized reinforcement bond slip element that was utilized in the Drain-3DX model and the more refined distributed plasticity element, combined with the method of numerical integration

proved the Drain-3DX model to be more accurate, consume less processing time, and to provide more stable results. Consequently, the Drain model was selected over the SAP2000 model to proceed with further investigation of the shake table model response, system response, and response of related bridge systems. It was found that the current analysis tools using conventional methods can be effective to predict the response of a reinforced concrete bridge structure with column aspect ratios as low as 2 from the pre-yield state through failure.

Single bent models from the Drain-3DX analysis were used to determine the effects of cap beam stiffness for the analytical models and bridge specimen relative to the prototype bridge. It was concluded that the effects of cap beam stiffness were negligible relative to the yield moments of the columns. The Drain-3DX results were also used to aid in the verification of the force estimates from the shake table actuator pressures.

The experimentally verified Drain-3DX model was used to study three topics relating to the system response of the bridge. The first was the measured and calculated performance of the bridge model compared to the life safety performance criteria of the NCHRP 12-49 code that was used for design. The spectra of the rare and expected design earthquakes were amplified to control the design of the bridge so that after R-factor reduction both spectra had demand matching the capacity of the bridge. Shake table tests with spectral accelerations that approximately matched the two design spectra were used to evaluate the measured performance for a more direct determination of the bridge performance subjected to design earthquakes. Two artificial motions were calculated using program SIMQKE (Gasparini and Vanmarcke, 1976). The two motions were input to the Drain-3DX model and the performance of each was compared to the code criteria. Both the measured response from shake table tests, and the analytical response based on the design spectra, satisfied the performance criteria. For the expected motion, the bridge performance satisfied both “immediate use”, and “minimal damage”. For the rare motion, the bridge performance satisfied both “significant disruption” and “severe damage” criteria. These comparisons provided an experimentally verified evaluation that validated the NCHRP design methodology.

The second topic that was studied using the analytical model of the bridge was the effect of the achieved shake table motions on the damage progression of the bridge. Since the measured motions were input into the computer models, differences between the achieved and target motions did not have a significant impact on this test. However, because this was the first multiple shake table test of its kind, deviations between the achieved and target motions could be potentially important and hence their effect was studied. This is a complex issue since there is unpredictability in the response of the specimens tested on shake tables, there is a delay in implementing compensation of table motions due to changes in the specimen dynamic characteristics, and the force feedback comes not only from the bridge response, but also from cross coupling of shake tables through the bridge specimen.

Four state-of-the-art methods were used to improve the response of the shake tables. It was observed during testing and through measured results that bent 3 was subjected to significantly larger demand than that predicted by the pre-test analyses, which predicted failure of bent 1. Both the effects of acceleration overshoot and incoherent displacements were explored through the computational model. Although

there were significant pseudo-static forces that were caused by the differential displacements of the shake tables, the displacement errors were not significant before yielding of the columns and did not cause the failure of bent 3. It was determined that the large demand that led to the failure of bent 3 was due to acceleration overshoot due to delayed compensation in adjusting the shake table controllers for the yielding of the bents. Two possibilities for solution to the achieved motion errors were presented and discussed.

The third topic that was studied using the computational models was the system and individual response of the bents (system effect). Past research on reinforced concrete columns has either been pseudo-static testing of single bents, or the more superior single bent testing with tributary mass on shake tables which is used because of the inclusion of dynamic effects. Experiments that include the system interaction provide yet another complexity that defines the performance of bents. The system effects were measured using maximum displacement demand and a mechanistic measure of damage that includes the hysteretic energy and maximum displacement.

The first system comparison was made was using the computational model of the shake table specimen and models of the individual bents with tributary mass. It was shown that for all of the columns in this study, there was generally not an increase in hysteretic energy or large displacement cycles from system response at given values of displacement demand. The response of the bents for each high amplitude test motion was also compared. It was shown that the response of bent 3 is generally the same whether modeled in the system or individually. Bent 1 had up to a 41 percent increase in damage index and 36 percent increase in displacement ductility demand for the post-yield motions when modeled as part of the system. When modeled as part of the system, bent 2 had as much as a 39 percent decrease in damage index and 37 percent decrease in displacement ductility demand for post-yield motions.

In addition to the shake table model, four bridge systems were used in a parametric study to determine the system effect. The total pier stiffness was the same in all systems. So that there was not a bias toward the analyses due to slight shifting in response frequency, most comparisons were made using the synthetic motions based on design spectra. In comparing the other systems, it was determined that the symmetric version of the bridge specimen, which contained the same height center bent as the specimen but no in-plane rotational response, was very comparable in nonlinear performance to the bridge specimen for the same high amplitude demand. The uniform system was also shown to have a comparable performance for high amplitude response.

The five different bridge configurations were compared to irregularity indices to evaluate the effectiveness of the measures in predicting the differences in system and individual bent response. The first was a regularity index that is typically used to determine whether single mode analysis is sufficient for design. The second reflected the elastic response of each bent in the system in comparison with the elastic response of individual bents having tributary mass. It was determined that the second index is a good indicator of the difference in system and individual bent response. However this method can not be used to quantify the magnitude of difference because of the interaction of nonlinear effects, system restraint, torsion, and variations of earthquake spectral demand.

Prior to single bent component testing on shake tables, an estimate can be used to determine whether the system would affect the bent response significantly.

LIST OF CCEER PUBLICATIONS

Report No.	Publication
CCEER-84-1	Saiidi, M., and R. Lawver, "User's Manual for LZAK-C64, A Computer Program to Implement the Q-Model on Commodore 64," Civil Engineering Department, Report No. CCEER-84-1, University of Nevada, Reno, January 1984.
CCEER-84-2	Douglas, B. and T. Iwasaki, "Proceedings of the First USA-Japan Bridge Engineering Workshop," held at the Public Works Research Institute, Tsukuba, Japan, Civil Engineering Department, Report No. CCEER-84-2, University of Nevada, Reno, April 1984.
CCEER-84-3	Saiidi, M., J. Hart, and B. Douglas, "Inelastic Static and Dynamic Analysis of Short R/C Bridges Subjected to Lateral Loads," Civil Engineering Department, Report No. CCEER-84-3, University of Nevada, Reno, July 1984.
CCEER-84-4	Douglas, B., "A Proposed Plan for a National Bridge Engineering Laboratory," Civil Engineering Department, Report No. CCEER-84-4, University of Nevada, Reno, December 1984.
CCEER-85-1	Norris, G. and P. Abdollaholiaee, "Laterally Loaded Pile Response: Studies with the Strain Wedge Model," Civil Engineering Department, Report No. CCEER-85-1, University of Nevada, Reno, April 1985.
CCEER-86-1	Ghusn, G. and M. Saiidi, "A Simple Hysteretic Element for Biaxial Bending of R/C in NEABS-86," Civil Engineering Department, Report No. CCEER-86-1, University of Nevada, Reno, July 1986.
CCEER-86-2	Saiidi, M., R. Lawver, and J. Hart, "User's Manual of ISADAB and SIBA, Computer Programs for Nonlinear Transverse Analysis of Highway Bridges Subjected to Static and Dynamic Lateral Loads," Civil Engineering Department, Report No. CCEER-86-2, University of Nevada, Reno, September 1986.
CCEER-87-1	Siddharthan, R., "Dynamic Effective Stress Response of Surface and Embedded Footings in Sand," Civil engineering Department, Report No. CCEER-86-2, University of Nevada, Reno, June 1987.
CCEER-87-2	Norris, G. and R. Sack, "Lateral and Rotational Stiffness of Pile Groups for Seismic Analysis of Highway Bridges," Civil Engineering Department, Report No. CCEER-87-2, University of Nevada, Reno, June 1987.
CCEER-88-1	Orie, J. and M. Saiidi, "A Preliminary Study of One-Way Reinforced Concrete Pier Hinges Subjected to Shear and Flexure," Civil Engineering Department, Report No. CCEER-88-1, University of Nevada, Reno, January 1988.
CCEER-88-2	Orie, D., M. Saiidi, and B. Douglas, "A Micro-CAD System for Seismic Design of Regular Highway Bridges," Civil Engineering Department, Report No. CCEER-88-2, University of Nevada, Reno, June 1988.
CCEER-88-3	Orie, D. and M. Saiidi, "User's Manual for Micro-SARB, a Microcomputer Program for Seismic Analysis of Regular Highway Bridges," Civil Engineering Department, Report No. CCEER-88-3, University of Nevada, Reno, October 1988.
CCEER-89-1	Douglas, B., M. Saiidi, R. Hayes, and G. Holcomb, "A Comprehensive Study of the Loads and Pressures Exerted on Wall Forms by the Placement of Concrete," Civil Engineering Department, Report No. CCEER-89-1, University of Nevada, Reno, February 1989.

CCEER-89-2 Richardson, J. and B. Douglas, "Dynamic Response Analysis of the Dominion Road Bridge Test Data," Civil Engineering Department, Report No. CCEER-89-2, University of Nevada, Reno, March 1989.

CCEER-89-2 Vrontinos, S., M. Saiidi, and B. Douglas, "A Simple Model to Predict the Ultimate Response of R/C Beams with Concrete Overlays," Civil Engineering Department, Report NO. CCEER-89-2, University of Nevada, Reno, June 1989.

CCEER-89-3 Ebrahimpour, A. and P. Jagadish, "Statistical Modeling of Bridge Traffic Loads - A Case Study," Civil Engineering Department, Report No. CCEER-89-3, University of Nevada, Reno, December 1989.

CCEER-89-4 Shields, J. and M. Saiidi, "Direct Field Measurement of Prestress Losses in Box Girder Bridges," Civil Engineering Department, Report No. CCEER-89-4, University of Nevada, Reno, December 1989.

CCEER-90-1 Saiidi, M., E. Maragakis, G. Ghusn, Y. Jiang, and D. Schwartz, "Survey and Evaluation of Nevada's Transportation Infrastructure, Task 7.2 - Highway Bridges, Final Report," Civil Engineering Department, Report No. CCEER 90-1, University of Nevada, Reno, October 1990.

CCEER-90-2 Abdel-Ghaffar, S., E. Maragakis, and M. Saiidi, "Analysis of the Response of Reinforced Concrete Structures During the Whittier Earthquake 1987," Civil Engineering Department, Report No. CCEER 90-2, University of Nevada, Reno, October 1990.

CCEER-91-1 Saiidi, M., E. Hwang, E. Maragakis, and B. Douglas, "Dynamic Testing and the Analysis of the Flamingo Road Interchange," Civil Engineering Department, Report No. CCEER-91-1, University of Nevada, Reno, February 1991.

CCEER-91-2 Norris, G., R. Siddharthan, Z. Zafir, S. Abdel-Ghaffar, and P. Gowda, "Soil-Foundation-Structure Behavior at the Oakland Outer Harbor Wharf," Civil Engineering Department, Report No. CCEER-91-2, University of Nevada, Reno, July 1991.

CCEER-91-3 Norris, G., "Seismic Lateral and Rotational Pile Foundation Stiffnesses at Cypress," Civil Engineering Department, Report No. CCEER-91-3, University of Nevada, Reno, August 1991.

CCEER-91-4 O'Connor, D. and M. Saiidi, "A Study of Protective Overlays for Highway Bridge Decks in Nevada, with Emphasis on Polyester-Styrene Polymer Concrete," Civil Engineering Department, Report No. CCEER-91-4, University of Nevada, Reno, October 1991.

CCEER-91-5 O'Connor, D.N. and M. Saiidi, "Laboratory Studies of Polyester-Styrene Polymer Concrete Engineering Properties," Civil Engineering Department, Report No. CCEER-91-5, University of Nevada, Reno, November 1991.

CCEER-92-1 Straw, D.L. and M. Saiidi, "Scale Model Testing of One-Way Reinforced Concrete Pier Hinges Subject to Combined Axial Force, Shear and Flexure," edited by D.N. O'Connor, Civil Engineering Department, Report No. CCEER-92-1, University of Nevada, Reno, March 1992.

CCEER-92-2 Wehbe, N., M. Saiidi, and F. Gordaninejad, "Basic Behavior of Composite Sections Made of Concrete Slabs and Graphite Epoxy Beams," Civil Engineering Department, Report No. CCEER-92-2, University of Nevada, Reno, August 1992.

CCEER-92-3 Saiidi, M. and E. Hutchens, "A Study of Prestress Changes in A Post-Tensioned Bridge During the First 30 Months," Civil Engineering Department, Report No. CCEER-92-3, University of Nevada, Reno, April 1992.

CCEER-92-4 Saiidi, M., B. Douglas, S. Feng, E. Hwang, and E. Maragakis, "Effects of Axial Force on Frequency of Prestressed Concrete Bridges," Civil Engineering Department, Report No. CCEER-92-4, University of Nevada, Reno, August 1992.

CCEER-92-5 Siddharthan, R., and Z. Zafir, "Response of Layered Deposits to Traveling Surface Pressure Waves," Civil Engineering Department, Report No. CCEER-92-5, University of Nevada, Reno, September 1992.

CCEER-92-6 Norris, G., and Z. Zafir, "Liquefaction and Residual Strength of Loose Sands from Drained Triaxial Tests," Civil Engineering Department, Report No. CCEER-92-6, University of Nevada, Reno, September 1992.

CCEER-92-7 Douglas, B., "Some Thoughts Regarding the Improvement of the University of Nevada, Reno's National Academic Standing," Civil Engineering Department, Report No. CCEER-92-7, University of Nevada, Reno, September 1992.

CCEER-92-8 Saiidi, M., E. Maragakis, and S. Feng, "An Evaluation of the Current Caltrans Seismic Restrainer Design Method," Civil Engineering Department, Report No. CCEER-92-8, University of Nevada, Reno, October 1992.

CCEER-92-9 O'Connor, D., M. Saiidi, and E. Maragakis, "Effect of Hinge Restrainers on the Response of the Madrone Drive Undercrossing During the Loma Prieta Earthquake," Civil Engineering Department, Report No. CCEER-92-9, University of Nevada, Reno, February 1993.

CCEER-92-10 O'Connor, D., and M. Saiidi, "Laboratory Studies of Polyester Concrete: Compressive Strength at Elevated Temperatures and Following Temperature Cycling, Bond Strength to Portland Cement Concrete, and Modulus of Elasticity," Civil Engineering Department, Report No. CCEER-92-10, University of Nevada, Reno, February 1993.

CCEER-92-11 Wehbe, N., M. Saiidi, and D. O'Connor, "Economic Impact of Passage of Spent Fuel Traffic on Two Bridges in Northeast Nevada," Civil Engineering Department, Report No. CCEER-92-11, University of Nevada, Reno, December 1992.

CCEER-93-1 Jiang, Y., and M. Saiidi, "Behavior, Design, and Retrofit of Reinforced Concrete One-way Bridge Column Hinges," edited by D. O'Connor, Civil Engineering Department, Report No. CCEER-93-1, University of Nevada, Reno, March 1993.

CCEER-93-2 Abdel-Ghaffar, S., E. Maragakis, and M. Saiidi, "Evaluation of the Response of the Aptos Creek Bridge During the 1989 Loma Prieta Earthquake," Civil Engineering Department, Report No. CCEER-93-2, University of Nevada, Reno, June 1993.

CCEER-93-3 Sanders, D.H., B.M. Douglas, and T.L. Martin, "Seismic Retrofit Prioritization of Nevada Bridges," Civil Engineering Department, Report No. CCEER-93-3, University of Nevada, Reno, July 1993.

CCEER-93-4 Abdel-Ghaffar, S., E. Maragakis, and M. Saiidi, "Performance of Hinge Restrainers in the Huntington Avenue Overhead During the 1989 Loma Prieta Earthquake," Civil Engineering Department, Report No. CCEER-93-4, University of Nevada, Reno, June 1993 (in final preparation).

CCEER-93-5 Maragakis, E., M. Saiidi, S. Feng, and L. Flournoy, "Effects of Hinge Restrainers on the Response of the San Gregorio Bridge During the Loma Prieta Earthquake," (in final preparation) Civil Engineering Department, Report No. CCEER-93-5, University of Nevada, Reno.

CCEER-93-6 Saiidi, M., E. Maragakis, S. Abdel-Ghaffar, S. Feng, and D. O'Connor, "Response of

Bridge Hinge Restrainers During Earthquakes -Field Performance, Analysis, and Design," Civil Engineering Department, Report No. CCEER-93-6, University of Nevada, Reno, May 1993.

CCEER-93-7 Wehbe, N., Saiidi, M., Maragakis, E., and Sanders, D., "Adequacy of Three Highway Structures in Southern Nevada for Spent Fuel Transportion, Civil Engineering Department, Report No. CCEER-93-7, University of Nevada, Reno, August 1993.

CCEER-93-8 Roybal, J., Sanders, D.H., and Maragakis, E., "Vulnerability Assessment of Masonry in the Reno-Carson City Urban Corridor," Civil Engineering Department, Report No. CCEER-93-8, University of Nevada, Reno, May 1993.

CCEER-93-9 Zafir, Z. and Siddharthan, R., "MOVLOAD: A Program to Determine the Behavior of Nonlinear Horizontally Layered Medium Under Moving Load," Civil Engineering Department, Report No. CCEER-93-9, University of Nevada, Reno, August 1993.

CCEER-93-10 O'Connor, D.N., Saiidi, M., and Maragakis, E.A., "A Study of Bridge Column Seismic Damage Susceptibility at the Interstate 80/U.S. 395 Interchange in Reno, Nevada," Civil Engineering Department, Report No. CCEER-93-10, University of Nevada, Reno, October 1993.

CCEER-94-1 Maragakis, E., B. Douglas, and E. Abdelwahed, "Preliminary Dynamic Analysis of a Railroad Bridge," Report CCEER-94-1, January 1994.

CCEER-94-2 Douglas, B.M., Maragakis, E.A., and Feng, S., "Stiffness Evaluation of Pile Foundation of Cazenovia Creek Overpass," Civil Engineering Department, Report No. CCEER-94-2, University of Nevada, Reno, March 1994.

CCEER-94-3 Douglas, B.M., Maragakis, E.A., and Feng, S., "Summary of Pretest Analysis of Cazenovia Creek Bridge," Civil Engineering Department, Report No. CCEER-94-3, University of Nevada, Reno, April 1994.

CCEER-94-4 Norris, G.M. and Madhu, R., "Liquefaction and Residual Strength of Sands from Drained Triaxial Tests, Report 2," Civil Engineering Department, CCEER-94-4, University of Nevada, Reno, August 1994.

CCEER-94-5 Saiidi, M., Hutchens, E., and Gardella, D., "Prestress Losses in a Post-Tensioned R/C Box Girder Bridge in Southern Nevada," Civil Engineering Department, CCEER-94-5, University of Nevada, Reno, August 1994.

CCEER-95-1 Siddharthan, R., El-Gamal, M., and Maragakis, E.A., "Nonlinear Bridge Abutment , Verification, and Design Curves," Civil Engineering Department, CCEER-95-1, University of Nevada, Reno, January 1995.

CCEER-95-2 Norris, G.M., Madhu, R., Valceschini, R., and Ashour, M., "Liquefaction and Residual Strength of Loose Sands from Drained Triaxial Tests," Report 2, Civil Engineering Department, Report No. CCEER-95-2, University of Nevada, Reno, February 1995.

CCEER-95-3 Wehbe, N., Saiidi, M., Sanders, D., and Douglas, B., "Ductility of Rectangular Reinforced Concrete Bridge Columns with Moderate Confinement,"Civil Engineering Department, Report No. CCEER-95-3, University of Nevada, Reno, July 1995.

CCEER-95-4 Martin, T., Saiidi, M., and Sanders, D., “Seismic Retrofit of Column-Pier Cap Connections in Bridges in Northern Nevada,” Civil Engineering Department, Report No. CCEER-95-4, University of Nevada, Reno, August 1995.

CCEER-95-5 Darwish, I., Saiidi, M., and Sanders, D., “Experimental Study of Seismic Susceptibility

Column-Footing Connections," Civil Engineering Department, Report No. CCEER-95-5, University of Nevada, Reno, September 1995.

CCEER-95-6 Griffin, G., Saiidi, M., and Maragakis, E., "Nonlinear Seismic Response of Isolated Bridges and Effects of Pier Ductility Demand," Civil Engineering Department, Report No. CCEER-95-6, University of Nevada, Reno, November 1995.

CCEER-95-7 Acharya, S., Saiidi, M., and Sanders, D., "Seismic Retrofit of Bridge Footings and Column-Footing Connections," Report for the Nevada Department of Transportation, Civil Engineering Department, Report No. CCEER-95-7, University of Nevada, Reno, November 1995.

CCEER-95-8 Maragakis, E., Douglas, B., and Sandirasegaram, U., "Full-Scale Field Resonance Tests of a Railway Bridge," A Report to the Association of American Railroads, Civil Engineering Department, Report No. CCEER-95-8, University of Nevada, Reno, December 1995.

CCEER-95-9 Douglas, B., Maragakis, E., and Feng, S., "System Identification Studies on Cazenovia Creek Overpass," Report for the National Center for Earthquake Engineering Research, Civil Engineering Department, Report No. CCEER-95-9, University of Nevada, Reno, October 1995.

CCEER-96-1 El-Gamal, M.E. and Siddharthan, R.V., "Programs to Computer Translational Stiffness of Seat-Type Bridge Abutment," Civil Engineering Department, Report No. CCEER-96-1, University of Nevada, Reno, March 1996.

CCEER-96-2 Labia, Y., Saiidi, M., and Douglas, B., "Evaluation and Repair of Full-Scale Prestressed Concrete Box Girders," A Report to the National Science Foundation, Research Grant CMS-9201908, Civil Engineering Department, Report No. CCEER-96-2, University of Nevada, Reno, May 1996.

CCEER-96-3 Darwish, I., Saiidi, M., and Sanders, D., "Seismic Retrofit of R/C Oblong Tapered Bridge Columns with Inadequate Bar Anchorage in Columns and Footings," A Report to the Nevada Department of Transportation, Civil Engineering Department, Report No. CCEER-96-3, University of Nevada, Reno, May 1996.

CCEER-96-4 Ashour, M., Pilling, P., Norris, G., and Perez, H., "The Prediction of Lateral Load Behavior of Single Piles and Pile Groups Using the Strain Wedge Model," A Report to the California Department of Transportation, Civil Engineering Department, Report No. CCEER-96-4, University of Nevada, Reno, June, 1996.

CCEER-97-1-A Rimal, P. and Itani, A. "Sensitivity Analysis of Fatigue Evaluations of Steel Bridges", Center for Earthquake Research, Department of Civil Engineering, University of Nevada, Reno, Nevada Report No. CCEER-97-1-A, September, 1997.

CCEER-97-1-B Maragakis, E., Douglas, B., and Sandirasegaram, U. "Full-Scale Field Resonance Tests of a Railway Bridge," A Report to the Association of American Railroads, Civil Engineering Department, University of Nevada, Reno, May, 1996.

CCEER-97-2 Wehbe, N., Saiidi, M., and D. Sanders, "Effect of Confinement and Flares on the Seismic Performance of Reinforced Concrete Bridge Columns," Civil Engineering Department, Report No. CCEER-97-2, University of Nevada, Reno, September 1997.

CCEER-97-3 Darwish, I., M. Saiidi, G. Norris, and E. Maragakis, "Determination of In-Situ Footing Stiffness Using Full-Scale Dynamic Field Testing," A Report to the Nevada Department of Transportation, Structural Design Division, Carson City, Nevada, Report No. CCEER-97-3, University of Nevada, Reno, October 1997.

CCEER-97-4 Wehbe, N., and M. Saiidi, “User’s manual for RCMC v. 1.2 : A Computer Program for Moment-Curvature Analysis of Confined and Unconfined Reinforced Concrete Sections,” Center for Civil Engineering Earthquake Research, Department of Civil Engineering, University of Nevada, Reno, Nevada, Report No. CCEER-97-4, November, 1997.

CCEER-97-5 Isakovic, T., M. Saiidi, and A. Itani, “Influence of new Bridge Configurations on Seismic Performance,” Department of Civil Engineering, University of Nevada, Reno, Report No. CCEER-97-5, September, 1997.

CCEER-98-1 Itani, A., Vesco, T. and Dietrich, A., “Cyclic Behavior of “as Built” Laced Members With End Gusset Plates on the San Francisco Bay Bridge” Center for Civil Engineering Earthquake Research, Department of Civil Engineering, University of Nevada, Reno, Nevada Report No. CCEER-98-1, March, 1998.

CCEER-98-2 G. Norris and M. Ashour, “Liqueficiation and Undraned response evaluation of Sands from Drained Formulation.” Center for Civil Engineering Earthquake Research, Department of Civil Engineering, University of Nevada, Reno, Nevada, Report No. CCEER-98-2, May, 1998.

CCEER-98-3 Qingbin, Chen, B. M. Douglas, E. Maragakis, and I. G. Buckle, "Extraction of Nonlinear Hysteretic Properties of Seismically Isolated Bridges from Quick-Release Field Tests", Center for Civil Engineering Earthquake Research, Department of Civil Engineering, University of Nevada, Reno, Nevada, Report No. CCEER-98-3, June, 1998.

CCEER-98-4 Maragakis, E., B. M. Douglas, and C. Qingbin, "Full-Scale Field Capacity Tests of a Railway Bridge", Center for Civil Engineering Earthquake Research, Department of Civil Engineering, University of Nevada, Reno, Nevada, Report No. CCEER-98-4, June, 1998.

CCEER-98-5 Itani, A., Douglas, B., and Woodgate, J., “Cyclic Behavior of Richmond-San Rafael Retrofitted Tower Leg”. Center for Civil Engineering Earthquake Research, Department of Civil Engineering, University of Nevada, Reno. Report No. CCEER-98-5, June 1998

CCEER-98-6 Moore, R., Saiidi, M., and Itani, A., “Seismic Behavior of New Bridges with Skew and Curvature”. Center for Civil Engineering Earthquake Research, Department of Civil Engineering, University of Nevada, Reno. Report No. CCEER-98-6, October, 1998.

CCEER-98-7 Itani, A and Dietrich, A, “Cyclic Behavior of Double Gusset Plate Connections”, Center for Civil Engineering Earthquake Research, Department of Civil Engineering, University of Nevada, Reno, Nevada, Report No. CCEER-98-5, December, 1998.

CCEER-99-1 Caywood, C., M. Saiidi, and D. Sanders, “ Seismic Retrofit of Flared Bridge Columns With Steel Jackets,” Civil Engineering Department, University of Nevada, Reno, Report No. CCEER-99-1, February 1999.

CCEER-99-2 Mangoba, N., M. Mayberry, and M. Saiidi, “Prestress Loss in Four Box Girder Bridges in Northern Nevada,” Civil Engineering Department, University of Nevada, Reno, Report No. CCEER-99-2, March 1999.

CCEER-99-3 Abo-Shadi, N., M. Saiidi, and D. Sanders, "Seismic Response of Bridge Pier Walls in the Weak Direction", Civil Engineering Department, University of Nevada, Reno, Report No. CCEER-99-3, April 1999.

CCEER-99-4 Buzick, A., and M. Saiidi, "Shear Strength and Shear Fatigue Behavior of Full-Scale Prestressed Concrete Box Girders", Civil Engineering Department, University of Nevada, Reno, Report No. CCEER-99-4, April 1999.

CCEER-99-5 Randall, M., M. Saiidi, E. Maragakis and T. Isakovic, "Restrainer Design Procedures For Multi-Span Simply-Supported Bridges", Civil Engineering Department, University of Nevada, Reno, Report No. CCEER-99-5, April 1999.

CCEER-99-6 Wehbe, N. and M. Saiidi, "User's Manual for RCMC v. 1.2, A Computer Program for Moment-Curvature Analysis of Confined and Unconfined Reinforced Concrete Sections", Civil Engineering Department, University of Nevada, Reno, Report No. CCEER-99-6, May 1999.

CCEER-99-7 Burda, J. and A. Itani, "Studies of Seismic Behavior of Steel Base Plates," Civil Engineering Department, University of Nevada, Reno, Report No. CCEER-99-7, May 1999.

CCEER-99-8 Ashour, M., and G. Norris, "Refinement of the Strain Wedge Model Program," Civil Engineering Department, University of Nevada, Reno, Report No. CCEER-99-8, March 1999.

CCEER-99-9 Dietrich, A., and A. Itani, "Cyclic Behavior of Laced and Perforated Steel Members on the San Francisco-Oakland Bay Bridge," Civil Engineering Department, University, Reno. December 1999.

CCEER 99-10 Itani, A., A. Dietrich, "Cyclic Behavior of Built Up Steel Members and their Connections," Civil Engineering Department, University of Nevada, Reno. December 1999.

CCEER 99-11 Itani, A., J. Woodgate, "Axial and Rotational Ductility of BuiltUp Structural Steel Members," Civil Engineering Department, University of Nevada, Reno December 1999.

CCEER-99-12 Sgambelluri, M., Sanders, D.H., and Saiidi, M.S., Behavior of One-Way Reinforced Concrete Bridge Column Hinges in the Weak Direction, Report No. Department of Civil Engineering, University of Nevada, Reno, December 1999.

CCEER-99-13 Laplace, P., Sanders, D.H., Douglas, B, and Saiidi, M, Shake Table Testing of Flexure Dominated Reinforced Concrete Bridge Columns, Report No. Department of Civil Engineering, University of Nevada, Reno, December 1999.

CCEER-99-14 Ahmad M. Itani, Jose A. Zepeda, and Elizabeth A. Ware "Cyclic Behavior of Steel Moment Frame Connections for the Moscone Center Expansion," December 1999.

CCEER 00-1 Ashour, M., and Norris, G. "Undrained Lateral Pile and Pile Group Response in Saturated Sand", Civil Engineering Department, University of Nevada, Reno, Report No. CCEER-00-1, May 1999. January 2000.

CCEER 00-2 Saiidi, M. and Wehbe, N., "A Comparison of Confinement Requirements in Different Codes for Rectangular, Circular, and Double-Spiral RC Bridge Columns," Civil Engineering Department, University of Nevada, Reno, Report No. CCEER-00-2, January 2000.

CCEER 00-3 McElhaney, B., M. Saiidi, and D. Sanders, "Shake Table Testing of Flared Bridge Columns With Steel Jacket Retrofit," Civil Engineering Department, University of Nevada, Reno, Report No. CCEER-00-3, January 2000.

CCEER 00-4 Martinovic, F., M. Saiidi, D. Sanders, and F. Gordaninejad, "Dynamic Testing of Non-Prismatic Reinforced Concrete Bridge Columns Retrofitted with FRP Jackets," Civil Engineering Department, University of Nevada, Reno, Report No. CCEER-00-4, January 2000.

CCEER 00-5 Itani, A., and M. Saiidi, "Seismic Evaluation of Steel Joints for UCLA Center for Health Science Westwood Replacement Hospital," Civil Engineering Department, University of Nevada, Reno, Report No. CCEER-00-5, February 2000.

CCEER 00-6 Will, J. and D. Sanders, "High Performance Concrete Using Nevada Aggregates," Civil Engineering Department, University of Nevada, Reno, Report No. CCEER-00-6, May 2000.

CCEER 00-7 French, C., and M. Saiidi, "A Comparison of Static and Dynamic Performance of Models of Flared Bridge Columns ," Civil Engineering Department, University of Nevada, Reno, Report No. CCEER-00-7, October 2000.

CCEER 00-8 Itani, A., H. Sedarat, "Seismic Analysis of the AISI LRFD Design Example of Steel Highway Bridges," Civil Engineering Department, University of Nevada, Reno, Report No. CCEER 00-08, November 2000.

CCEER 00-9 Moore, J., D. Sanders, and M. Saiidi, "Shake Table Testing of 1960's Two Column Bent with Hinges Bases," Civil Engineering Department, University of Nevada, Reno, Report No. CCEER 00-09, December 2000.

CCEER 00-10 Asthana, M., D. Sanders, and M. Saiidi, "One-Way Reinforced Concrete Bridge Column Hinges in the Weak Direction," Civil Engineering Department, University of Nevada, Reno, Report No. CCEER 00-10, April 2001.

CCEER 01-1 Ah Sha, H., D. Sanders, M. Saiidi, "Early Age Shrinkage and Cracking of Nevada Concrete Bridge Decks, "Civil Engineering Department, University of Nevada, Reno, Report No. CCEER 01-01, May 2001.

CCEER 01-2 Ashour, M. and G. Norris, "Pile Group program for Full Material Modeling an Progressive Failure." Civil Engineering Department, University of Nevada, Reno, Report No. CCEER 01-02, July 2001.

CCEER 01-3 Itani, A., C. Lanaud, and P. Dusicka, "Non-Linear Finite Element Analysis of Built-Up Shear Links." Civil Engineering Department, University of Nevada, Reno, Report No. CCEER 01-03, July 2001.

CCEER 01-4 Saiidi, M., J. Mortensen, and F. Martinovic, "Analysis and Retrofit of Fixed Flared Columns with Glass Fiber-Reinforced Plastic Jacketing," Civil Engineering Department, University of Nevada, Reno, Report No. CCEER 01-4, August 2001

CCEER 01-5 Saiidi, M., A. Itani, I. Buckle, and Z. Cheng," Performance of A Full-Scale Two-Story Wood Frame Structure Supported on Ever-Level Isolators," Civil Engineering Department, University of Nevada, Reno, Report No. CCEER 01-5, October 2001

CCEER 01-6 Laplace, P., D. Sanders, and M. Saiidi, "Experimental Study and Analysis of Retrofitted Flexure and Shear Dominated Circular Reinforced Concrete Bridge Columns Subjected to Shake Table Excitation, "Civil Engineering Department, University of Nevada, Reno, Report No. CCEER 01-6, June 2001.

CCEER 01-7 Reppi, F., and D. Sanders, "Removal and Replacement of Cast-in-Place, Post-tensioned, Box Girder Bridge," Civil Engineering Department, University of Nevada, Reno, Report No. CCEER 01-7, December 2001.

CCEER 02-1 Pulido, C., M. Saiidi, D. Sanders, and A. Itani, "Seismic Performance and Retrofitting of Reinforced Concrete Bridge Bents," Civil Engineering Department, University of Nevada, Reno, Report No. CCEER 02-1, January 2002.

CCEER 02-2 Yang, Q., M. Saiidi, H. Wang, and A. Itani, "Influence of Ground Motion Incoherency on Earthquake Response of Multi-Support Structures," Civil Engineering Department, University of Nevada, Reno, Report No. CCEER 02-2, May 2002.

CCEER 02-3 M. Saiidi, B. Gopalakrishnan, E. Reinhardt, and R. Siddharthan, A Preliminary Study of Shake Table Response of A Two-Column Bridge Bent on Flexible Footings Civil Engineering Department, University of Nevada, Reno, Report No. CCEER 02-03, June 2002.

CCEER 02-4 Not Published

CCEER 02-5 Banghart, A., Sanders, D., Saiidi, M., "Evaluation of Concrete Mixes for Filling the Steel Arches in the Galena Creek Bridge," Civil Engineering Department, University of Nevada, Reno, Report No. CCEER 02-05, June 2002.

CCEER 02-6 Dusicka, P., Itani, A., Buckle, I. G., "Cyclic Behavior of Shear Links and Tower Shaft Assembley of San Francisco – Oakland Bay Bridge Tower" Civil Engineering Department, University of Nevada, Reno, Report No. CCEER 02-06, July 2002.

CCEER 02-7 Mortensen, J., and M. Saiidi, " A Performance-Based Design Method for Confinement in Circular Columns," Civil Engineering Department, University of Nevada, Reno, Report No. CCEER 02-07, November 2002.

CCEER 03-1 Wehbe, N., and M. Saiidi, "User's manual for SPMC v. 1.0 : A Computer Program for Moment-Curvature Analysis of Reinforced Concrete Sections with Interlocking Spirals," Center for Civil Engineering Earthquake Research, Department of Civil Engineering, University of Nevada, Reno, Nevada, Report No. CCEER-03-1, May, 2003.

CCEER 03-2 Wehbe, N., and M. Saiidi, "User's manual for RCMC v. 2.0 : A Computer Program for Moment-Curvature Analysis of Confined and Unconfined Reinforced Concrete Sections," Center for Civil Engineering Earthquake Research, Department of Civil Engineering, University of Nevada, Reno, Nevada, Report No. CCEER-03-2, June, 2003.

CCEER 03-3 Nada, H., D. Sanders, and M. Saiidi, " Seismic Performance of RC Bridge Frames with Architectural-Flared Columns," Civil Engineering Department, University of Nevada, Reno, Report No. CCEER 03-3, January 2003.

CCEER 03-4 Reinhardt, E., M. Saiidi, and R. Siddharthan, " Seismic Performance of a CFRP/ Concrete Bridge Bent on Flexible Footings." Civil Engineering Department, University of Nevada, Reno. Report No. CCEER 03-4, August 2003.

CCEER 03-5 Johnson, N., M. Saiidi, A. Itani, and S. Ladkany, "Seismic Retrofit of Octagonal Columns with Pedestal and One-Way Hinge at the Base," Center for Civil Engineering Earthquake Research, Department of Civil Engineering, University of Nevada, Reno, Nevada, Report No. CCEER-03-5, August 2003.

CCEER 03-6 Mortensen, C., M. Saiidi, and S. Ladkany, "Creep and Shrinkage Losses in Highly Variable Climates," Center for Civil Engineering Earthquake Research, Department of Civil Engineering, University of Nevada, Reno, Nevada, Report No. CCEER-03-6, September 2003.

CCEER 03- 7 Ayoub, C., M. Saiidi, and A. Itani, "A Study of Shape-Memory-Alloy-Reinforced Beams and Cubes," Center for Civil Engineering Earthquake Research, Department of Civil Engineering, University of Nevada, Reno, Nevada, Report No. CCEER-03-7, October 2003.

CCEER 03-8 Chandane, S., D. Sanders, and M. Saiidi, "Static and Dynamic Performance of RC Bridge Bents with Architectural-Flared Columns," Center for Civil Engineering Earthquake Research, Department of Civil Engineering, University of Nevada, Reno, Nevada, Report No. CCEER-03-8, November 2003.

CCEER 04-1 Olaegbe, C., and Saiidi, M., "Effect of Loading History on Shake Table Performance of A Two-Column Bent with Infill Wall," Center for Civil Engineering Earthquake Research, Department of Civil Engineering, University of Nevada, Reno, Nevada, Report No. CCEER-04-1, January 2004.

CCEER 04-2 Johnson, R., Maragakis, E., Saiidi, M., and DesRoches, R., "Experimental Evaluation of Seismic Performance of SMA Bridge Restrainers," Center for Civil Engineering Earthquake Research, Department of Civil Engineering, University of Nevada, Reno, Nevada, Report No. CCEER-04-2, February 2004.

CCEER 04-3 Moustafa, K., Sanders, D., and Saiidi, M., "Impact of Aspect Ratio on Two-Column Bent Seismic Performance," Center for Civil Engineering Earthquake Research, Department of Civil Engineering, University of Nevada, Reno, Nevada, Report No. CCEER-04-3, February 2004.

CCEER 04-4 Maragakis, E., Saiidi, M., Sanchez-Camargo, F., and Elfass, S., "Seismic Performance of Bridge Restrainers At In-Span Hinges," Center for Civil Engineering Earthquake Research, Department of Civil Engineering, University of Nevada, Reno, Nevada, Report No. CCEER-04-4, March 2004.

CCEER 04-5 Ashour, M., Norris, G. and Elfass, S., "Analysis of Laterally Loaded Long or Intermediate Drilled Shafts of Small or Large Diameter in Layered Soil," Center for Civil Engineering Earthquake Research, Department of Civil Engineering, University of Nevada, Reno, Nevada, Report No. CCEER-04-5, June 2004.

CCEER 04-6 Correal, J., Saiidi, M. and Sanders, D., "Seismic Performance of RC Bridge Columns Reinforced with Two Interlocking Spirals," Center for Civil Engineering Earthquake Research, Department of Civil Engineering, University of Nevada, Reno, Nevada, Report No. CCEER-04-6, August 2004.

CCEER 04-7 Dusicka, P., Itani, A. and Buckle, I., "Cyclic Response and Low Cycle Fatigue Characteristics of Plate Steels," Center for Civil Engineering Earthquake Research, Department of Civil Engineering, University of Nevada, Reno, Nevada, Report No. CCEER-04-7, November 2004.

CCEER 04-8 Dusicka, P., Itani, A. and Buckle, I., " Built-up Shear Links as Energy Dissipaters for Seismic Protection of Bridges," Center for Civil Engineering Earthquake Research, Department of Civil Engineering, University of Nevada, Reno, Nevada, Report No. CCEER-04-8, November 2004.

CCEER 04-9 Sureshkumar, K., Saiidi, S., Itani, A. and Ladkany, S., "Seismic Retrofit of Two-Column Bents with Diamond Shape Columns," Center for Civil Engineering Earthquake Research, Department of Civil Engineering, University of Nevada, Reno, Nevada, Report No. CCEER-04-9, November 2004.

CCEER 05-1 Wang, H. and Saiidi, S., "A Study of RC Columns with Shape Memory Alloy and Engineered Cementitious Composites," Center for Civil Engineering Earthquake Research, Department of Civil Engineering, University of Nevada, Reno, Nevada, Report No. CCEER-05-1, January 2005.

CCEER 05-2 Johnson, R., Saiidi, S. and Maragakis, E., "A Study of Fiber Reinforced Plastics for Seismic Bridge Restrainers," Center for Civil Engineering Earthquake Research, Department of Civil Engineering, University of Nevada, Reno, Nevada, Report No. CCEER-05-2, January 2005.

CCEER 05-3 Carden, L.P., Itani, A.M., Buckle, I.G, "Seismic Load Path in Steel Girder Bridge Superstructures," Center for Civil Engineering Earthquake Research, Department of Civil Engineering, University of Nevada, Reno, Nevada, Report No. CCEER-05-3, January 2005.

CCEER 05-4 Carden, L.P., Itani, A.M., Buckle, I.G, "Seismic Performance of Steel Girder Bridge Superstructures with Ductile End Cross Frames and Seismic Isolation," Center for Civil Engineering Earthquake Research, Department of Civil Engineering, University of Nevada, Reno, Nevada, Report No. CCEER-05-4, January 2005.

CCEER 05-5 Goodwin, E., Maragakis, M., Itani, A. and Luo, S., "Experimental Evaluation of the Seismic Performance of Hospital Piping Subassemblies," Center for Civil Engineering Earthquake Research, Department of Civil Engineering, University of Nevada, Reno, Nevada, Report No. CCEER-05-5, February 2005.

CCEER 05-6 Zadeh M. S., Saiidi, S, Itani, A. and Ladkany, S., "Seismic Vulnerability Evaluation and Retrofit Design of Las Vegas Downtown Viaduct," Center for Civil Engineering Earthquake Research, Department of Civil Engineering, University of Nevada, Reno, Nevada, Report No. CCEER-05-6, February 2005.

CCEER 05-7 Phan, V., Saiidi, S. and Anderson, J., "Near Fault (Near Field) Ground Motion Effects on Reinforced Concrete Bridge Columns" Center for Civil Engineering Earthquake Research, Department of Civil Engineering, University of Nevada, Reno, Nevada, Report No. CCEER-05-7, August 2005.

CCEER 05-8 Carden, L., Itani, A. and Laplace, P., "Performance of Steel Props at the UNR Fire Science Academy subjected to Repeated Fire" Center for Civil Engineering Earthquake Research, Department of Civil Engineering, University of Nevada, Reno, Nevada, Report No. CCEER-05-8, August 2005.

CCEER 05-9 Yamashita, R. and Sanders, D., "Shake Table Testing and an Analytical Study of Unbonded Prestressed Hollow Concrete Column Constructed with Precast Segments" Center for Civil Engineering Earthquake Research, Department of Civil Engineering, University of Nevada, Reno, Nevada, Report No. CCEER-05-9, August 2005.

CCEER 05-10 Moustafa, K. Sanders, D., and Saiidi, M., "Seismic Behavior of R/C Bridge Bents with Architectural-Flared Columns Including both Horizontal and Vertical Gaps," Center for Civil Engineering Earthquake Research, Department of Civil Engineering, University of Nevada, Reno, Nevada, Report No. CCEER-05-10, February 2005.

CCEER 05-11 Carden, L., Itani., A., and Peckan, G., "Recommendations for the Design of Beams and Posts in Bridge Falsework," Center for Civil Engineering Earthquake Research, Department of Civil Engineering, University of Nevada, Reno, Nevada, Report No. CCEER-05-11, October 2005.

CCEER 06-01 Cheng, Z., Saiidi, M., and Sanders, D., "Development of a Seismic Design Method for Reinforced Concrete Two-Way Bridge Column Hinges," Center for Civil Engineering Earthquake Research, Department of Civil Engineering, University of Nevada, Reno, Nevada, Report No. CCEER-06-01, February 2006.